frontiers | Research Topics

Remote sensing application for precision agriculture, 2nd Edition

Edited by
Xiuliang Jin, Matthew McCabe, Chunyuan Diao and Zhenhai Li

Coordinated by
Dameng Yin

Published in
Frontiers in Plant Science

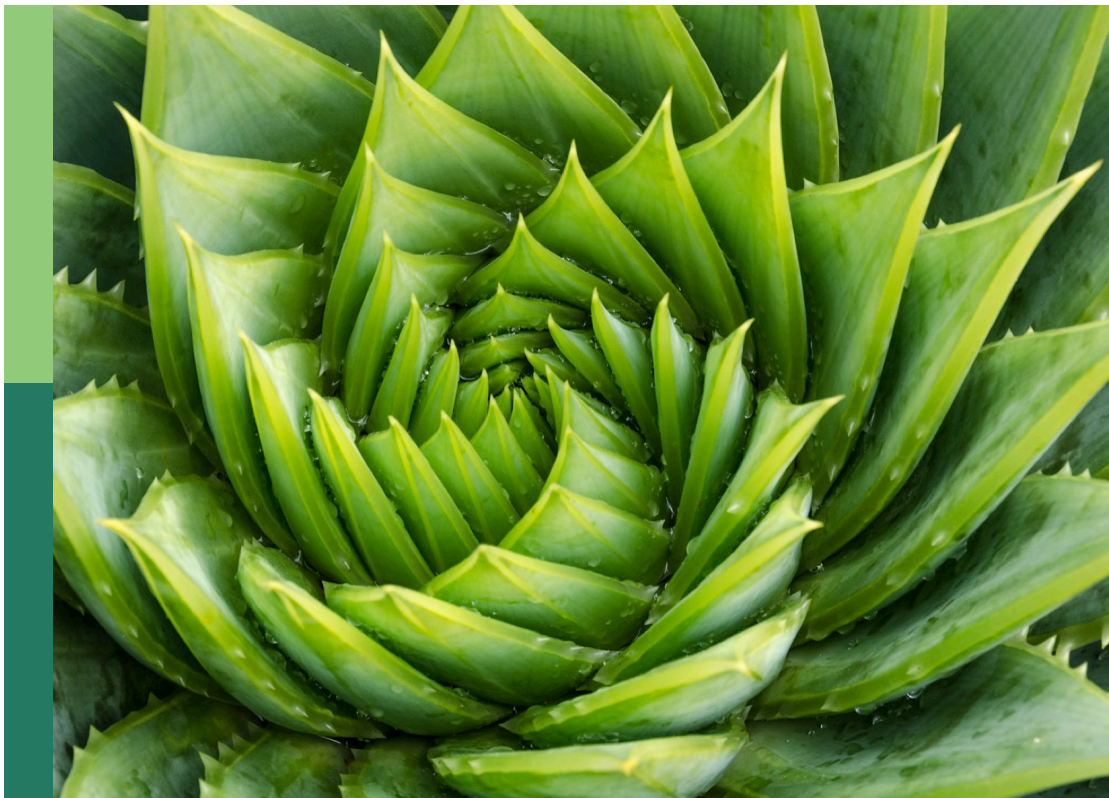

FRONTIERS EBOOK COPYRIGHT STATEMENT

The copyright in the text of individual articles in this ebook is the property of their respective authors or their respective institutions or funders. The copyright in graphics and images within each article may be subject to copyright of other parties. In both cases this is subject to a license granted to Frontiers.

The compilation of articles constituting this ebook is the property of Frontiers.

Each article within this ebook, and the ebook itself, are published under the most recent version of the Creative Commons CC-BY licence. The version current at the date of publication of this ebook is CC-BY 4.0. If the CC-BY licence is updated, the licence granted by Frontiers is automatically updated to the new version.

When exercising any right under the CC-BY licence, Frontiers must be attributed as the original publisher of the article or ebook, as applicable.

Authors have the responsibility of ensuring that any graphics or other materials which are the property of others may be included in the CC-BY licence, but this should be checked before relying on the CC-BY licence to reproduce those materials. Any copyright notices relating to those materials must be complied with.

Copyright and source acknowledgement notices may not be removed and must be displayed in any copy, derivative work or partial copy which includes the elements in question.

All copyright, and all rights therein, are protected by national and international copyright laws. The above represents a summary only. For further information please read Frontiers' Conditions for Website Use and Copyright Statement, and the applicable CC-BY licence.

ISSN 1664-8714
ISBN 978-2-8325-3182-2
DOI 10.3389/978-2-8325-3182-2

About Frontiers

Frontiers is more than just an open access publisher of scholarly articles: it is a pioneering approach to the world of academia, radically improving the way scholarly research is managed. The grand vision of Frontiers is a world where all people have an equal opportunity to seek, share and generate knowledge. Frontiers provides immediate and permanent online open access to all its publications, but this alone is not enough to realize our grand goals.

Frontiers journal series

The Frontiers journal series is a multi-tier and interdisciplinary set of open-access, online journals, promising a paradigm shift from the current review, selection and dissemination processes in academic publishing. All Frontiers journals are driven by researchers for researchers; therefore, they constitute a service to the scholarly community. At the same time, the *Frontiers journal series* operates on a revolutionary invention, the tiered publishing system, initially addressing specific communities of scholars, and gradually climbing up to broader public understanding, thus serving the interests of the lay society, too.

Dedication to quality

Each Frontiers article is a landmark of the highest quality, thanks to genuinely collaborative interactions between authors and review editors, who include some of the world's best academicians. Research must be certified by peers before entering a stream of knowledge that may eventually reach the public - and shape society; therefore, Frontiers only applies the most rigorous and unbiased reviews. Frontiers revolutionizes research publishing by freely delivering the most outstanding research, evaluated with no bias from both the academic and social point of view. By applying the most advanced information technologies, Frontiers is catapulting scholarly publishing into a new generation.

What are Frontiers Research Topics?

Frontiers Research Topics are very popular trademarks of the *Frontiers journals series*: they are collections of at least ten articles, all centered on a particular subject. With their unique mix of varied contributions from Original Research to Review Articles, Frontiers Research Topics unify the most influential researchers, the latest key findings and historical advances in a hot research area.

Find out more on how to host your own Frontiers Research Topic or contribute to one as an author by contacting the Frontiers editorial office: frontiersin.org/about/contact

Remote sensing application for precision agriculture, 2nd Edition

Topic editors

Xiuliang Jin — Key Laboratory of Crop Physiology and Ecology, Institute of Crop Sciences (CAAS), China

Matthew McCabe — King Abdullah University of Science and Technology, Saudi Arabia

Chunyuan Diao — University of Illinois at Urbana-Champaign, United States

Zhenhai Li — Shandong University of Science and Technology, China

Topic coordinator

Dameng Yin — Institute of Crop Sciences, Chinese Academy of Agricultural Sciences, China

Citation

Jin, X., McCabe, M., Diao, C., Li, Z., Yin, D., eds. (2023). *Remote sensing application for precision agriculture, 2nd Edition*. Lausanne: Frontiers Media SA.

doi: 10.3389/978-2-8325-3182-2

Publisher's note: In this 2nd edition, the following article has been added: Liu X, Li X, Gao L, Zhang J, Qin D, Wang K and Li Z (2023) Early-season and refined mapping of winter wheat based on phenology algorithms - a case of Shandong, China. Front. Plant Sci. 14:1016890. doi: 10.3389/fpls.2023.1016890

Table of contents

06 Estimation of Rice Aboveground Biomass by Combining Canopy Spectral Reflectance and Unmanned Aerial Vehicle-Based Red Green Blue Imagery Data
Zhonglin Wang, Yangming Ma, Ping Chen, Yonggang Yang, Hao Fu, Feng Yang, Muhammad Ali Raza, Changchun Guo, Chuanhai Shu, Yongjian Sun, Zhiyuan Yang, Zongkui Chen and Jun Ma

23 Cotton Yield Estimation Based on Vegetation Indices and Texture Features Derived From RGB Image
Yiru Ma, Lulu Ma, Qiang Zhang, Changping Huang, Xiang Yi, Xiangyu Chen, Tongyu Hou, Xin Lv and Ze Zhang

40 Mapping the Corn Residue-Covered Types Using Multi-Scale Feature Fusion and Supervised Learning Method by Chinese GF-2 PMS Image
Wancheng Tao, Yi Dong, Wei Su, Jiayu Li, Fu Xuan, Jianxi Huang, Jianyu Yang, Xuecao Li, Yelu Zeng and Baoguo Li

55 Estimating Maize Yield in the Black Soil Region of Northeast China Using Land Surface Data Assimilation: Integrating a Crop Model and Remote Sensing
Ying Cui, Suhong Liu, Xingang Li, Hao Geng, Yun Xie and Yuhua He

73 Rice Yield Estimation Based on Continuous Wavelet Transform With Multiple Growth Periods
Chen Gu, Shu Ji, Xiaobo Xi, Zhenghua Zhang, Qingqing Hong, Zhongyang Huo, Wenxi Li, Wei Mao, Haitao Zhao, Ruihong Zhang, Bin Li and Changwei Tan

88 Estimation Model of Potassium Content in Cotton Leaves Based on Wavelet Decomposition Spectra and Image Combination Features
Qiushuang Yao, Ze Zhang, Xin Lv, Xiangyu Chen, Lulu Ma and Cong Sun

108 Evaluation of important phenotypic parameters of tea plantations using multi-source remote sensing data
He Li, Yu Wang, Kai Fan, Yilin Mao, Yaozong Shen and Zhaotang Ding

127 An Intelligent Rice Yield Trait Evaluation System Based on Threshed Panicle Compensation
Chenglong Huang, Weikun Li, Zhongfu Zhang, Xiangdong Hua, Junya Yang, Junli Ye, Lingfeng Duan, Xiuying Liang and Wanneng Yang

141 Multi-dimensional variables and feature parameter selection for aboveground biomass estimation of potato based on UAV multispectral imagery
Shanjun Luo, Xueqin Jiang, Yingbin He, Jianping Li, Weihua Jiao, Shengli Zhang, Fei Xu, Zhongcai Han, Jing Sun, Jinpeng Yang, Xiangyi Wang, Xintian Ma and Zeru Lin

154 Combining spectral and wavelet texture features for unmanned aerial vehicles remote estimation of rice leaf area index
Cong Zhou, Yan Gong, Shenghui Fang, Kaili Yang, Yi Peng, Xianting Wu and Renshan Zhu

171 Multispectral remote sensing for accurate acquisition of rice phenotypes: Impacts of radiometric calibration and unmanned aerial vehicle flying altitudes
Shanjun Luo, Xueqin Jiang, Kaili Yang, Yuanjin Li and Shenghui Fang

190 Research hotspots and frontiers in agricultural multispectral technology: Bibliometrics and scientometrics analysis of the Web of Science
Yali Zhang, Dehua Zhao, Hanchao Liu, Xinrong Huang, Jizhong Deng, Ruichang Jia, Xiaoping He, Muhammad Naveed Tahir and Yubin Lan

207 Identification and picking point positioning of tender tea shoots based on MR3P-TS model
Lijie Yan, Kaihua Wu, Jia Lin, Xingang Xu, Jingcheng Zhang, Xiaohu Zhao, James Tayor and Dongmei Chen

219 Estimation of potato above-ground biomass based on unmanned aerial vehicle red-green-blue images with different texture features and crop height
Yang Liu, Haikuan Feng, Jibo Yue, Xiuliang Jin, Zhenhai Li and Guijun Yang

237 Field-scale rice yield estimation based on UAV-based MiniSAR data with Ku band and modified water-cloud model of panicle layer at panicle stage
Zhiyong Wang, Shuli Wang, Hongxiang Wang, Long Liu, Zhenjin Li, Yuandong Zhu and Kai Wang

253 Estimation of the nitrogen content of potato plants based on morphological parameters and visible light vegetation indices
Yiguang Fan, Haikuan Feng, Xiuliang Jin, Jibo Yue, Yang Liu, Zhenhai Li, Zhihang Feng, Xiaoyu Song and Guijun Yang

268 Rapid prediction of winter wheat yield and nitrogen use efficiency using consumer-grade unmanned aerial vehicles multispectral imagery
Jikai Liu, Yongji Zhu, Xinyu Tao, Xiaofang Chen and Xinwei Li

288 Universal detection of curved rice panicles in complex environments using aerial images and improved YOLOv4 model
Boteng Sun, Wei Zhou, Shilin Zhu, Song Huang, Xun Yu, Zhenyuan Wu, Xiaolong Lei, Dameng Yin, Haixiao Xia, Yong Chen, Fei Deng, Youfeng Tao, Hong Cheng, Xiuliang Jin and Wanjun Ren

303 Estimation of soybean yield parameters under lodging conditions using RGB information from unmanned aerial vehicles
Dong Bai, Delin Li, Chaosen Zhao, Zixu Wang, Mingchao Shao, Bingfu Guo, Yadong Liu, Qi Wang, Jindong Li, Shiyu Guo, Ruizhen Wang, Ying-hui Li, Li-juan Qiu and Xiuliang Jin

322 Evaluating how lodging affects maize yield estimation based on UAV observations
Yuan Liu, Chenwei Nie, Zhen Zhang, ZiXu Wang, Bo Ming, Jun Xue, Hongye Yang, Honggen Xu, Lin Meng, Ningbo Cui, Wenbin Wu and Xiuliang Jin

338 Integrating environmental and satellite data to estimate county-level cotton yield in Xinjiang Province
Ping Lang, Lifu Zhang, Changping Huang, Jiahua Chen, Xiaoyan Kang, Ze Zhang and Qingxi Tong

352 Early-season and refined mapping of winter wheat based on phenology algorithms - a case of Shandong, China
Xiuyu Liu, Xuehua Li, Lixin Gao, Jinshui Zhang, Dapeng Qin, Kun Wang and Zhenhai Li

frontiers | Frontiers in Plant Science

ORIGINAL RESEARCH
published: 27 May 2022
doi: 10.3389/fpls.2022.903643

Estimation of Rice Aboveground Biomass by Combining Canopy Spectral Reflectance and Unmanned Aerial Vehicle-Based Red Green Blue Imagery Data

*Zhonglin Wang[1,2], Yangming Ma[1,2], Ping Chen[3], Yonggang Yang[1,2], Hao Fu[1,2], Feng Yang[3], Muhammad Ali Raza[3], Changchun Guo[1,2], Chuanhai Shu[1,2], Yongjian Sun[1,2], Zhiyuan Yang[1,2], Zongkui Chen[1,2] and Jun Ma[1,2]**

[1]Rice Cultivation Laboratory, Rice Research Institute, Sichuan Agricultural University, Chengdu, China, [2]Crop Ecophysiology and Cultivation Key Laboratory of Sichuan Province, Chengdu, China, [3]Sichuan Engineering Research Center for Crop Strip Intercropping System, Chengdu, China

OPEN ACCESS

Edited by:
Xiuliang Jin,
Key Laboratory of Crop Physiology and Ecology, Institute of Crop Sciences (CAAS), China

Reviewed by:
Liang Wan,
Zhejiang University, China
Abbas Atefi,
California Polytechnic State University, United States

***Correspondence:**
Jun Ma
majunp2002@163.com

Specialty section:
This article was submitted to Sustainable and Intelligent Phytoprotection, a section of the journal Frontiers in Plant Science

Received: 24 March 2022
Accepted: 03 May 2022
Published: 27 May 2022

Citation:
Wang Z, Ma Y, Chen P, Yang Y, Fu H, Yang F, Raza MA, Guo C, Shu C, Sun Y, Yang Z, Chen Z and Ma J (2022) Estimation of Rice Aboveground Biomass by Combining Canopy Spectral Reflectance and Unmanned Aerial Vehicle-Based Red Green Blue Imagery Data. Front. Plant Sci. 13:903643. doi: 10.3389/fpls.2022.903643

Estimating the aboveground biomass (AGB) of rice using remotely sensed data is critical for reflecting growth status, predicting grain yield, and indicating carbon stocks in agroecosystems. A combination of multisource remotely sensed data has great potential for providing complementary datasets, improving estimation accuracy, and strengthening precision agricultural insights. Here, we explored the potential to estimate rice AGB by using a combination of spectral vegetation indices and wavelet features (spectral parameters) derived from canopy spectral reflectance and texture features and texture indices (texture parameters) derived from unmanned aerial vehicle (UAV) RGB imagery. This study aimed to evaluate the performance of the combined spectral and texture parameters and improve rice AGB estimation. Correlation analysis was performed to select the potential variables to establish the linear and quadratic regression models. Multivariate analysis (multiple stepwise regression, MSR; partial least square, PLS) and machine learning (random forest, RF) were used to evaluate the estimation performance of spectral parameters, texture parameters, and their combination for rice AGB. The results showed that spectral parameters had better linear and quadratic relationships with AGB than texture parameters. For the multivariate analysis and machine learning algorithm, the MSR, PLS, and RF regression models fitted with spectral parameters (R^2 values of 0.793, 0.795, and 0.808 for MSR, PLS, and RF, respectively) were more accurate than those fitted with texture parameters (R^2 values of 0.540, 0.555, and 0.485 for MSR, PLS, and RF, respectively). The MSR, PLS, and RF regression models fitted with a combination of spectral and texture parameters (R^2 values of 0.809, 0.810, and 0.805, respectively) slightly improved the estimation accuracy of AGB over the use of spectral parameters or texture parameters alone. Additionally, the bior1.3 of wavelet features at 947 nm and scale 2 was used to predict the grain yield and had good accuracy for the quadratic regression model. Therefore, the combined use of canopy spectral reflectance and texture information

has great potential for improving the estimation accuracy of rice AGB, which is helpful for rice productivity prediction. Combining multisource remotely sensed data from the ground and UAV technology provides new solutions and ideas for rice biomass acquisition.

Keywords: aboveground biomass, rice, vegetation indices, wavelet features, texture, unmanned aerial vehicle, machine learning

INTRODUCTION

Nitrogen is the most critical nutrient for promoting crop growth, increasing crop aboveground biomass (AGB), and improving grain yield. As an important predictor, AGB can reflect crop growth status and gross primary production (Harrell et al., 2011) and is related to grain yield (Wang et al., 2021b). Rapid and accurate assessment of crop AGB is essential for predicting grain yield and improvement of field nitrogen management strategies. The conventional approach for measuring AGB by collecting samples in the field and drying them indoors is destructive, time-consuming, laborious, and prone to human error. In recent years, remotely sensed technology has been successfully used to estimate crop AGB, other physiological parameters, and grain yield and quality. With the development of remotely sensed technology, more remotely sensed sensors and platforms have been developed and applied to agricultural condition monitoring.

Remotely sensed data for estimating rice AGB are acquired from the ground (Cheng et al., 2017), unmanned aerial vehicles (UAV; Jiang et al., 2019), and satellite platforms (Sharifi and Hosseingholizadeh, 2020). Remotely sensed data from the ground with hyperspectral information have received close attention and are widely used to estimate crop AGB because ground-based hyperspectral remote sensing has the advantages of high spectral resolution, continuous wavebands, high efficiency, and objectivity (Li et al., 2016a). Many studies have reported the close relationship between spectral parameters and rice biomass using ground-based hyperspectral remote sensing (Casanova et al., 1998; Gnyp et al., 2014; Kanke et al., 2016; Cheng et al., 2017). Ground-based hyperspectral remote sensing cannot directly observe the growth status of rice, nor can it satisfy the requirements of space–time, and it is difficult to estimate rice biomass and dry matter over large areas. Conversely, satellite platforms have an obvious advantage in monitoring rice growth status and estimating biomass over large areas (Mansaray et al., 2020; Sharifi and Hosseingholizadeh, 2020). A study reported using back-propagation artificial neural network models to estimate the grassland AGB from MODIS satellite imagery with high accuracy (R^2: 0.75–0.85; Yang et al., 2018). However, the estimation accuracy of crop AGB using satellite imagery data is often influenced by spatial and spectral resolution, cloud cover, and meteorological factors (Wu et al., 2005). In particular, the anticipated accuracy is not achieved for small field areas. Many studies have used UAV-based RGB imagery to overcome these constraints and drawbacks and to estimate rice AGB with high accuracy (Cen et al., 2019; Wan et al., 2020).

Multisource remotely sensed data are acquired to provide more approaches for the accurate, fast, and non-destructive monitoring of crop biomass. Researchers have developed various data-processing methods and mathematical models for remotely sensed data. Canopy spectral reflectance, multispectral imagery, and RGB imagery are often used to extract vegetation indices (VIs) for estimating AGB in maize, rice, and wheat (Jiang et al., 2019; Yue et al., 2019; Ma et al., 2020; Raya-Sereno et al., 2021). Spectral VIs (SVIs), such as the ratio vegetation index (RVI), difference vegetation index (DVI), and normalized difference vegetation index (NDVI), have proven to have close relationships with rice biomass (Gnyp et al., 2014). However, the relationship between remotely sensed data and physiological parameters is related to differences in crop species, remote sensing measurements, and growth conditions. When SVIs of the same wavebands are used in different crop species or growth conditions, crop biomass could be overestimated or underestimated, yielding larger errors. Therefore, extracting accurate wavebands to establish SVIs is necessary to improve the estimation accuracy of crop biomass. SVIs based on complete two-by-two combinations of spectral wavebands were calculated to accurately estimate leaf chlorophyll content (LCC; Wang et al., 2021b), canopy nitrogen content (Wang et al., 2022), leaf area index (Delegido et al., 2015), and grain yield (Rodrigues et al., 2018). Wavelet analysis is a widely utilized spectral analysis tool that uses mother wavelet functions by decomposing raw spectral reflectance data into multiple scales (Mallat, 1989; Cheng et al., 2011). Continuous wavelet transform (CWT) is superior to SVIs in noise and dimension reduction (Cheng et al., 2011). Our studies have confirmed that CWT has better performance than SVIs for estimating LCC (Wang et al., 2020) and carbon-nitrogen content (Chen et al., 2019; Wang et al., 2022). The wavelet coefficient calculated using mother wavelet functions can minimize the interference of the canopy structure and soil background on the spectral reflectance data (Cheng et al., 2012). Previous studies have analyzed the feasibility of wavelet analysis for estimating crop biomass and dry matter content using remotely sensed data (Li et al., 2013; Cheng et al., 2014). Wavelet analysis has been widely used to estimate physiological parameters (Guo et al., 2015; Wang et al., 2016), predict grain yield and protein content (Wang et al., 2021b), and detect weeds and diseases in the field (Zhang et al., 2014).

RGB imagery shows abundant color and texture features with temporal and spatial information, compensating for the defects of ground-hyperspectral remote sensing. However, extracting information from RGB imagery is more complicated than ground-hyperspectral remote sensing. Multiple RGB images obtained from the field are stitched to yield orthophotos and point cloud data, and then the digital number (DN) values and texture features are extracted to monitor the growth status of crops. Two complementary data sources are used simultaneously to improve the estimation accuracy of wheat biomass (Lu et al., 2019).

Generally, both RGB-based VIs (RGB-VIs) and texture features derived from RGB imagery are vital variables for estimating crop biomass. The estimation accuracy of crop biomass is gradually considered based on the influence of crop growth differences. The majority of previous studies have attempted to combine RGB-VIs and plant height information to improve the accuracy and have shown the best estimation performance (Bendig et al., 2014; Iqbal et al., 2017; Lu et al., 2019). One study found that coupled plant height and spectral reflectance data correlated with barley biomass (Bendig et al., 2015). Spectral reflectance data reflect the specific features (such as steps, reflection peaks, and absorption valleys) of physiological and biochemical information in crop tissues with a strong correlation. Therefore, establishing a multiple stepwise regression (MSR) model using texture features and SVIs (Yue et al., 2019) is a better approach to estimating crop biomass than plant height (Bendig et al., 2015; Roth and Streit, 2018). Satellite imagery and polarimetric radar data were combined to improve the estimation model of rice biomass on the Sanjiang Plain in Heilongjiang Province, Northeast China (Koppe et al., 2013). The combination of multisource remotely sensed data is receiving extensive attention for estimating the physiological parameters and productivity of crops.

Multivariate analysis and machine learning algorithms have great potential in remotely sensed data mining and crop biomass estimation, with higher accuracy than convenient algorithms (Meyer and Neto, 2008; Mansaray et al., 2020). The MSR model established by a combination of SVIs and texture indices can explain more variability of rice AGB ($R^2 = 0.87$) than linear and exponential regression models for the pre-heading stage (Zheng et al., 2019). The random forest (RF) regression model was used to achieve a better prediction result ($R^2 = 0.90$) than linear and exponential regression models for rice AGB (Jiang et al., 2019). Few studies have investigated multivariate analysis and machine learning algorithms for estimating rice AGB by combining SVIs and wavelet features (spectral parameters) derived from canopy spectral reflectance and RGB-VIs, texture features and texture indices (texture parameters) derived from RGB imagery. Consequently, this study examines whether RGB-VIs and texture parameters can compete with spectral parameters for estimating rice AGB. We determine whether the combination of canopy spectral reflectance and RGB imagery leads to a more accurate estimation of rice AGB. Last, we evaluate the performance of estimation models of rice AGB established using univariate analysis, multivariate analysis, and machine learning algorithm from canopy spectral reflectance and RGB imagery.

MATERIALS AND METHODS

Field Experimental Details

The field experiment was conducted in 2021 at the Sichuan Agricultural University Modern Agricultural Research and Development Base in Chongzhou city (30°33′N, 103°38′E, altitude 540 m), Sichuan Province, China (**Figure 1**). The experimental location is in a subtropical humid monsoon climate zone; the average temperature is 23.7°C, and precipitation is 908.4 mm from May to September during the rice-growing season.

In a randomized complete block design, experimental treatments were carried out with three replications for three nitrogen rates, two nitrogen application percentages, and two cultivars during three growth stages. The nitrogen rates were applied as urea (46.7% N) at N0 ($0\,kg\,ha^{-1}$), N1 ($150\,kg\,ha^{-1}$), and N2 ($180\,kg\,ha^{-1}$). The nitrogen fertilizer was applied in two percentages as follows: i) approximately 70% of urea was applied as basal fertilizer, and another 30% of urea was applied at the tillering stage (M1 = 7: 3); and ii) 30% of urea was applied as basal fertilizer, 30% of urea was applied at the tillering stage, and another 40% of urea was applied at the heading stage (M2 = 3: 3: 4). Two rice cultivars, "Fyou498" with loose type and "Jingliangyou534" with compact type, were sown on April 14, rice seedlings were transplanted with a row space of 0.33 m and plant distance of 0.17 m on May 16. Rice grain was harvested on September 12. A total of 30 plots were used for the experiment, and the individual plot size was $11 \times 4\,m^2$. The plant density was 1.8×10^5 plants ha^{-1}. Other basal fertilizers of phosphorus as calcium superphosphate (12% P_2O_5) at $75\,kg\,ha^{-1}$ and potassium as potassium chloride (60% K_2O) at $150\,kg\,ha^{-1}$ were applied to all plots. Weeds and insect populations were controlled with herbicides and pesticides, respectively.

Data Acquisition

Acquisition of RGB Imagery

Acquisition of RGB imagery was performed at the tillering (June 22), booting (July 21), and full-heading (August 03) stages. RGB imagery and canopy spectral reflectance were acquired under clear sky conditions between 10:00 and 14:00 (Beijing local time). We used a UAV platform with four propellers and a visible RGB camera (DJI Mavic 2 Zoom, DJI, Shenzhen, China) to fly over the rice field and evaluate the RGB-VIs and texture features for estimating rice biomass. The detailed specifications of the aircraft, camera, and flight settings are shown in **Table 1**. The aircraft was flown before the measurement of canopy spectral reflectance to avoid the human campaigns from destroying the canopy status, which would have affected the RGB imagery. According to the settings of camera specifications and flight details, the nine routes were automatically fielded from west to east. Nine images were acquired for each route, for 81 images. The aircraft was always stable during flight, and flight planning was not changed during the whole season. Orthophotos were generated using Agisoft PhotoScan software (Agisoft, LLC., St. Petersburg, Russia) to extract DN values and texture features.

Measurement of Canopy Spectral Reflectance

After acquiring RGB imagery, ground-based canopy spectral reflectance data were measured using a field spectroradiometer with a 25° field-of-view fiber optic probe (AvaSpec-2048, Avantes, Apeldoorn, Netherlands). The device has a full spectral range from 350 nm to 2,500 nm, and the sampling intervals are 0.6 nm from 350 nm to 1,100 nm and 6 nm from 1,100 nm to 2,500 nm. The probe was vertically placed from 1 m above the rice canopy and 0.445 m view diameter to obtain spectral information. A $25\pi\ m^2$ $BaSO_4$ white panel

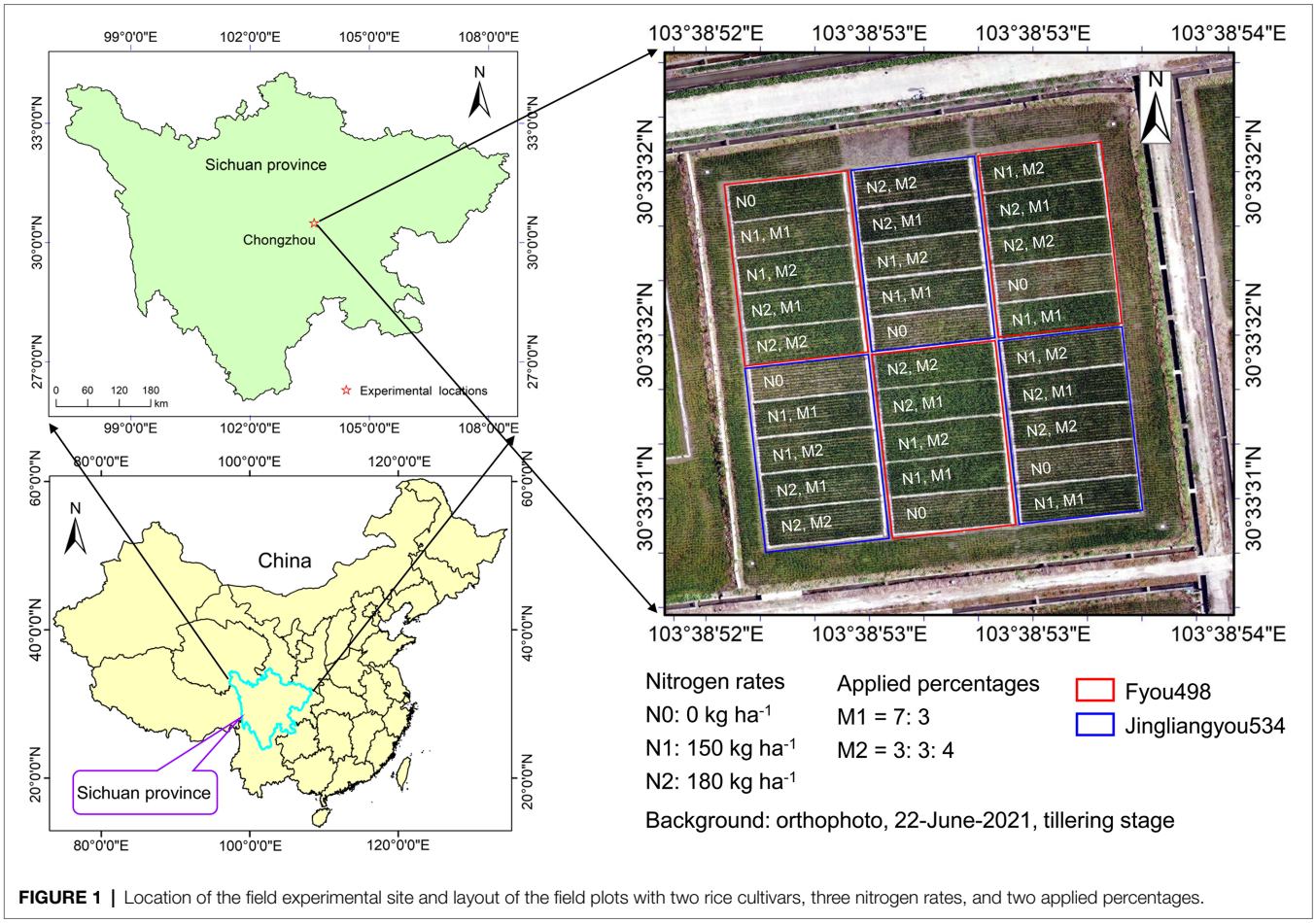

FIGURE 1 | Location of the field experimental site and layout of the field plots with two rice cultivars, three nitrogen rates, and two applied percentages.

TABLE 1 | Basic information on aircraft, cameras, and flight settings.

Aircraft		Camera		Flying details	
Take-off weight	905 g	Camera model	FC2204	Height	30 m
Maximum flying speed	20 m s^{-1}	Effective pixels	12 million	Speed	2.2 m s^{-1}
Maximum flying height	6,000 m	CCD	1-inch CMOS	Shutter interval	4 s
GNSS	GPS + GLONASS	Angle	85°	Ground resolution	1.1 cm pixel^{-1}
		Photo resolution	4,000 × 3,000	Forward overlap	80%
		Bit depth	24	Side overlap	70%
		Aperture	f/2.8		
		Focal length	4.386 mm		
		ISO	ISO-100		
		Exposure	1/640 s		
		Photo format	JEPG (RAW)		

was used to calibrate spectral reflectance before and after vegetation measurement by using three scans each time. Canopy spectral reflectance was measured for three samples in a plot, and average reflectance was recorded by scanning three times for one sample.

Measurement of Aboveground Biomass and Grain Yield

After measuring canopy spectral reflectance, rice plants were uprooted and taken to the laboratory to remove the dirt and soil. Then, the roots of the rice plants were cut off and placed in paper bags. Samples were oven-dried at 105°C for 0.5 h and 70°C until constant weight. Subsequently, dry weight (including stems, leaves, and panicles) was weighed and recorded. Rice AGB (kg m^{-2}) was calculated as the product of dry weight per plant (kg plant^{-1}) and plant density (plant m^{-2}; Li et al., 2016b).

Rice grain yield (t ha^{-1}) for each plot was harvested individually by manual means at the maturity stage. The collected rice grain was air-dried to a 13.5% moisture level and weighed using an electronic balance.

Data Analysis

Texture Analysis

This study generated a gray level co-occurrence matrix (GLCM) at the tillering, booting, and full-heading stages to analyze the texture features for AGB estimation (**Figure 2**). Eight texture features were computed in the IDL/ENVI 5.3 environment (Exelis Visual Information Solutions, Boulder, Colorado, United States), including the mean (ME), variance (VAR), homogeneity (HOM), contrast (CON), dissimilarity (DIS), entropy (ENT), second moment (SEM), and correlation (COR). Window size represents detailed texture information and is an important parameter for texture analysis. Appropriate window sizes often contain texture features of the soil background and crop plants (Zheng et al., 2019). Rice was transplanted with a row spacing of 0.33 m and a plant spacing of 0.17 m; thus, texture analysis was performed using the smallest window size of 3 × 3 pixels. The texture features of the red, green, and blue wavebands were calculated separately, and twenty-four features were finally generated. Texture features from RGB imagery were used to evaluate rice AGB.

Vegetation Indices and Texture Indices

Orthophotos were processed to extract DN values (including R, G, and B values) using the region of interest tool in IDL/ENVI software. Then DN values were normalized to reduce the illumination effect (Cheng et al., 2001). Five RGB-VIs were studied to correlate with crop physiological parameters and calculated using normalized DN values (i.e., *r*, *g*, and *b*). Based on the RVI, DVI, and NDVI, texture indices were defined as the ratio texture index (TRVI), difference texture index (TDVI), and normalized difference texture index (TNDVI) and produced using complete two-by-two combinations of eight texture features with three wavebands (red, green, and blue wavebands). Texture indices were determined based on a previous study (Zheng et al., 2019). The waveband range of 1,050–2,500 nm was removed because of the exorbitant signal-to-noise ratio. Canopy spectral reflectance with an exorbitant signal-to-noise ratio could affect the sensitive wavebands analysis of rice AGB. Thus, this study used the waveband range of 350–1,050 nm to analyze the relationships between rice AGB and spectral parameters. Eight SVIs of ground-based canopy spectral reflectance were calculated to correlate with rice AGB, including SVIs of complete two-by-two combinations of spectral wavebands within a spectral range of 350–1,050 nm and SVIs of specific spectral wavebands. These indices are defined and listed in **Table 2**.

Wavelet Analysis

Five wavelet features, namely daubechies6 (db6), symlets3 (sym3), biorthogonal1.3 (bior1.3), reverse biorthogonal5.5 (rbio5.5), and gaussian3 (gaus3), were executed to transform the spectral reflectance data into wavelet coefficients at a dyadic scale of 1–256 in MATLAB Version 9.2 (MathWorks, Inc., Natick, MA, United States). The definition and equation of wavelet analysis were described in our previous study (Wang et al., 2021b). In this study, spectral reflectance of 350–1,050 nm was used to produce a wavelet coefficient matrix and analyze the correlation between wavelet coefficients and rice AGB on a scale of 1 to 256. Finally, the correlation coefficient matrix diagram, best correlation coefficient (*r*), corresponding waveband, and scale were output to establish the estimation model of rice AGB.

Model Performance Estimation

Data involving various cultivars, nitrogen rates, and growth stages were integrated to form a comprehensive dataset. The comprehensive dataset was randomly divided into the calibration and validation datasets. 70% of samples were used as the calibration dataset for modeling, and 30% of samples were used as the validation dataset for validating model performance, as shown in **Table 3**.

Three regression methods were selected to evaluate rice AGB, namely, univariate analysis, multivariate analysis, and machine learning algorithm. SVIs, wavelet features, texture features, and texture indices were respectively employed to establish simple linear and quadratic regression models using the calibration dataset

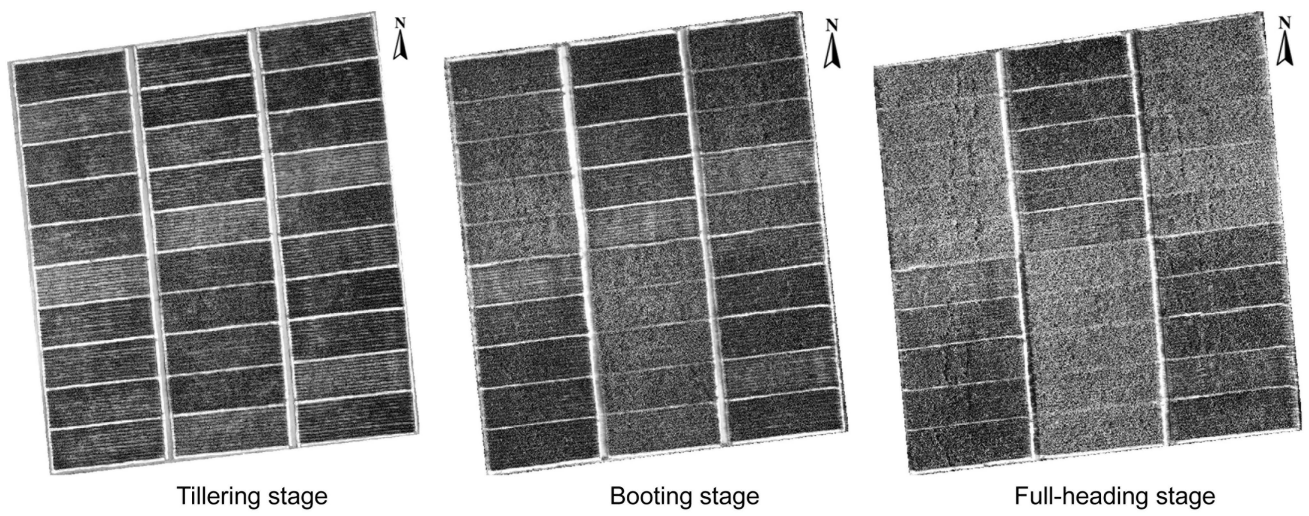

FIGURE 2 | Gray level co-occurrence matrix of rice RGB imagery at the tillering, booting, and full-heading stages.

TABLE 2 | Definition of RGB-VIs and SVIs.

Category	Name	Definition	References
RGB-VIs	Excessive green index	$ExG = 2*g-r-b$	Woebbecke et al., 1995
	Excessive red index	$ExR = (1.4*R-G)/(R+G+B)$	Meyer and Neto, 2008
	Excessive blue index	$ExB = (1.4*B-G)/(R+G+B)$	Mao et al., 2003
	Excess green minus excess red	$ExGR = ExG-ExR$	Camargo Neto, 2004
	Red green blue vegetation index	$RGBVI = (G^2-B*R)/(G^2+B*R)$	Bendig et al., 2015
Two-by-two combinations of spectral wavebands	Ratio vegetation index	$RVI = R_i/R_j$	Pearson and Miller, 1972
	Difference vegetation index	$DVI = R_i-R_j$	Jordan, 1969
	Normalized difference vegetation index	$NDVI = (R_i-R_j)/(R_i+R_j)$	Rouse et al., 1974
Specific spectral wavebands	Red-edge chlorophyll index	$CI_{rededge} = R_{800}/R_{720}-1$	Gitelson et al., 2003
	Renormalized difference vegetation index	$RDVI = (R_{800}-R_{670})/(R_{800}+R_{670})^{1/2}$	Roujean and Breon, 1995
	Optimized soil adjusted vegetation index	$OSAVI = (1+0.16)*(R_{800}-R_{670})/(R_{800}+R_{670}+0.16)$	Tremblay et al., 2003
	Transformed chlorophyll absorption reflectance index	$TCARI = 3*((R_{700}-R_{670})-0.2*(R_{700}-R_{550})*(R_{700}/R_{670}))$	Haboudane et al., 2002
	Plant pigment ratio index	$PRR = (R_{550}-R_{450})/(R_{550}+R_{450})$	Metternicht, 2003

R, G, and B represent the DN values of red, green, and blue, respectively; r = R/(R + G + B), g = G/(R + G + B), b = B/(R + G + B); R_i and R_j indicate the spectral reflectance for wavebands i and j, respectively.

TABLE 3 | Statistical results of rice AGB and grain yield for calibration and validation datasets.

	AGB (kg m^{-2})		Grain yield (t ha^{-1})	
	Cal. dataset	Val. dataset	Cal. dataset	Val. dataset
Samples	160	68	20	10
Minimum	0.113	0.140	5.839	6.176
Maximum	1.928	2.013	9.204	10.568
Mean	0.885	0.881	8.091	8.352
Standard deviation	0.469	0.490	0.909	1.318
Coefficient of variation (%)	53.0	55.5	11.2	15.8

for univariate analysis. The MSR and partial least square (PLS) were fitted for multivariate analysis using spectral parameters, texture parameters, and their combination. The MSR can explain the reliability of independent variables and eliminate variables that cause collinearity (Li et al., 2016b). No more than three variables were introduced into the MSR models to avoid overfitting (Zheng et al., 2019). Variables with collinearity and $p > 0.05$ were eliminated for the MSR models.

The PLS regression technique is successfully used to monitor rice biomass (Wang et al., 2021a). The PLS can effectively reduce dimensionality, eliminate the collinearity between variables, and improve the reliability and accuracy of estimation models (Fu et al., 2014). In this study, the PLS regression technique was implemented in MATLAB software, and the modeling results were finally output as regression coefficients, constant, predicted values, and R^2.

The RF algorithm is an ensemble machine learning algorithm that combines a large set of decision trees to improve the accuracy of classification and regression trees (Mutanga et al., 2012). Two important parameters were adjusted and optimized to achieve the best prediction performance: the number of variables to be tested for each node of tree (*mtry*) and the number of trees (*ntree*). The parameter *mtry* was generally determined from the default value (1/3 of the total number of input variables; Mutanga et al., 2012; Oliveira et al., 2012). In this study, the out-of-bag error rate was calculated to acquire the optimal *mtry*, and the *mtry* with the lowest out-of-bag error rate was selected. Subsequently, we adjusted the parameter *ntree* to achieve the best training results. Finally, *mtry* and *ntree* were determined to operate the RF algorithm using spectral parameters (*mtry* = 1, *ntree* = 1,000), texture parameters (*mtry* = 4, *ntree* = 1,600), and their combinations (*mtry* = 7, *ntree* = 400). The RF algorithm was implemented using the "*randomForest*" package within the R statistical software (R Development Core Team, 2022).

The predictive accuracy of the estimation models was assessed using the R^2, root mean square error (RMSE), and the ratio of performance to deviation (RPD). The following equations calculated three accuracy metrics:

$$R^2 = \frac{\sum_{i=1}^{n}\left(y_i - y_i^{'}\right)^2}{\sum_{i-1}^{n}\left(y_i - \overline{y}\right)^2} \quad (1)$$

$$RMSE = \sqrt{\frac{\sum_{i=1}^{n}\left(y_i - y_i^{'}\right)^2}{n}} \quad (2)$$

$$RPD = \frac{Std_v}{RMSE_v} \quad (3)$$

where y_i and $y_i^{'}$ are the measured and predicted AGB values for sample i, respectively. $\overline{y}$ is the mean AGB. n is the number of samples for the calibration or validation dataset. Std_v and $RMSE_v$ are the standard derivation and RMSE of the validation dataset, respectively. Higher R^2 and lower RMSE values indicate better estimation accuracy for AGB estimation models. The RPD is classified into three levels: $RPD \geq 2$ represents good performance, $2 > RPD \geq 1.4$ represents intermediate

performance, and RPD < 1.4 represents low performance. The AGB model with the best validation accuracy was selected from all regression models. Rice AGB was used to analyze the relationship with grain yield using the linear model and as a bridge to link remotely sensed data to grain yield (Wang et al., 2021b). The approach indirectly uses remotely sensed data to estimate crop grain yield is more physiologically explanatory.

RESULTS

Estimation of Rice Aboveground Biomass Using Spectral Parameters

Figure 3 shows the correlation results for the relationships between rice AGB and spectral parameters. The $CI_{rededge}$, RDVI, OSAVI, TCARI, and PRR of specific spectral wavebands exhibited low positive correlations ($r < 0.64$, $p < 0.01$) with AGB. The correlation coefficient matrices were calculated using complete two-by-two combinations of wavebands (701 × 701 wavebands) for the DVI, RVI, and NDVI (**Supplementary Figures S1A–C**). The best correlation was selected from the correlation coefficient matrices, and the DVI (952, 947), RVI (775, 784), and NDVI (775, 784) showed better correlation than SVIs of specific spectral wavebands, and the correlation coefficients were 0.811, 0.806, and 0.806, respectively. No differences were found in correlations between the three SVIs. The correlation coefficient matrix diagram illustrates the correlation analysis between wavelet features and rice AGB (**Supplementary Figure S2**). The wavelet features had a high correlation coefficient ($|r| > 0.79$, $p < 0.001$), and the db6 of the wavelet features had the strongest correlation with AGB ($r = -0.876$, $p < 0.001$) at 469 nm and scale 6. Thus, the DVI (952, 947), RVI (775, 784), and NDVI (775, 784) of SVIs and five wavelet features were adopted to establish the linear and quadratic regression models.

As shown in **Figure 4**, the accuracy of linear and quadratic regression models is compared to estimate rice AGB using spectral parameters. Generally, the accuracy of the quadratic regression model is superior to that of the linear regression model. The db6 (469, 6) of the wavelet features achieved the best estimation performance for linear ($R^2 = 0.767$, RMSE = 0.227 kg m^{-2}) and quadratic ($R^2 = 0.777$, RMSE = 0.223 kg m^{-2}) regression models. Linear and quadratic regression models had proximate curves and similar accuracies for the db6 (469, 6), sym3 (468, 6), and rbio5.5 (467, 6) of the wavelet features. Furthermore, these models were validated with the validation dataset, and the validation accuracy is shown in the scatter plots of 1:1 (**Figure 5**). The validation results demonstrated that the performance of the SVIs and wavelet features estimates varied with R^2 values of 0.56–0.67 and 0.58–0.76, RMSE of 0.27–0.32 kg m^{-2} and 0.24–0.32 kg m^{-2}, and RPD of 1.51–1.79 and 1.55–2.05, respectively. The wavelet features had a better performance than the SVIs. The quadratic regression model of rice AGB was determined to have the best

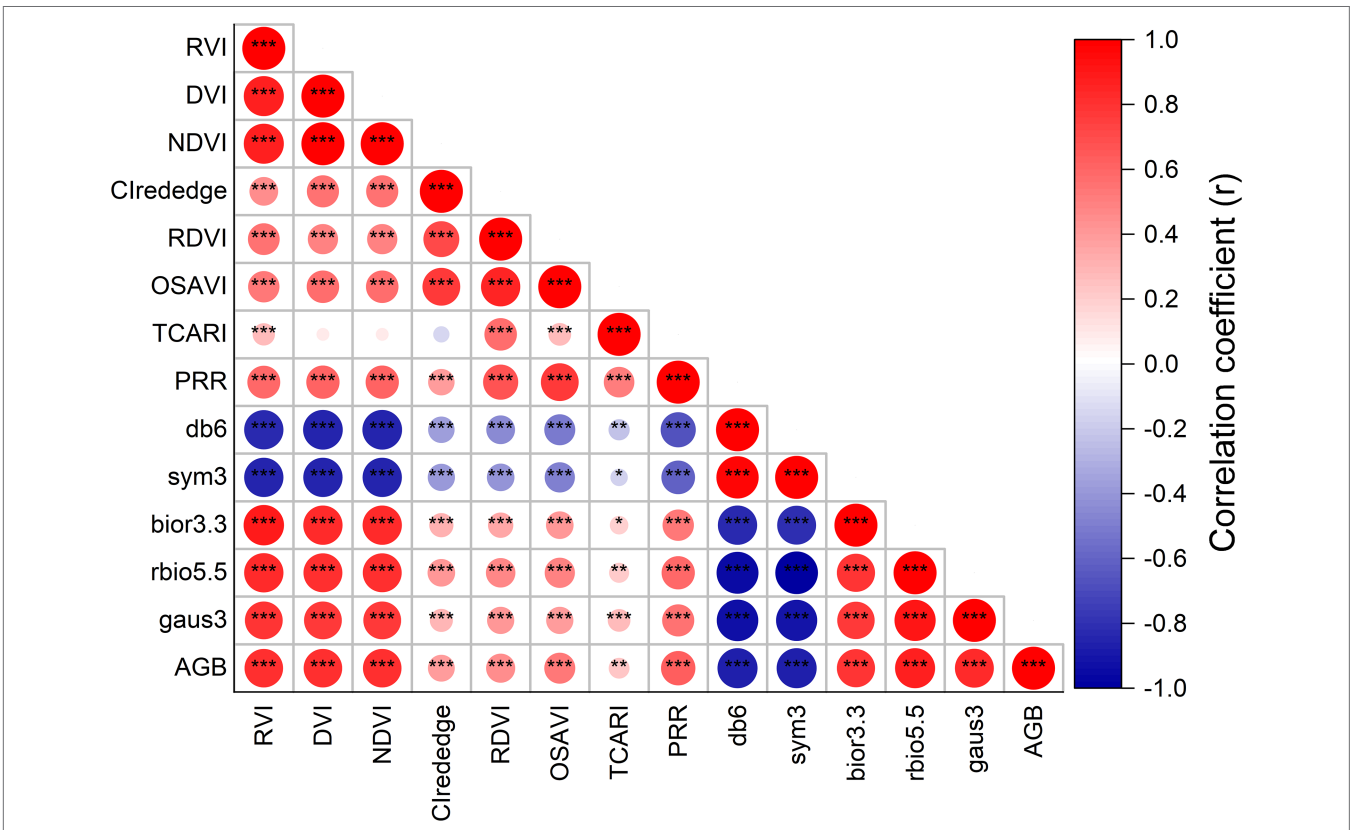

FIGURE 3 | The correlation coefficient between rice AGB and spectral parameters. * indicates significant correlation at the $p < 0.05$ level, ** indicates the significant correlation at the $p < 0.01$ level, *** indicates the significant correlation at the $p < 0.001$ level.

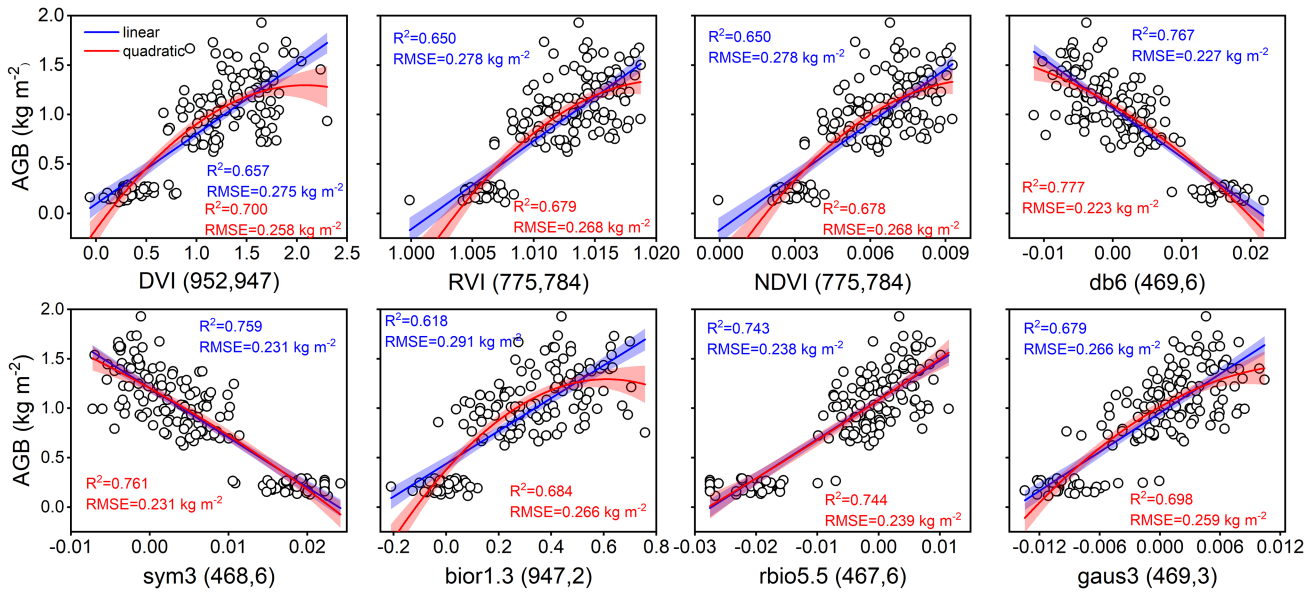

FIGURE 4 | Linear and quadratic regression models using spectral parameters for estimating rice AGB ($n = 160$). The shaded band is the prediction interval at the 95% confidence level. DVI (952, 947) indicates the DVI at wavebands 952 nm and 947 nm. Others are the same as it. db6 (469, 6) indicates the db6 of wavelet features at waveband 469 nm and scale 6. Others are the same as it.

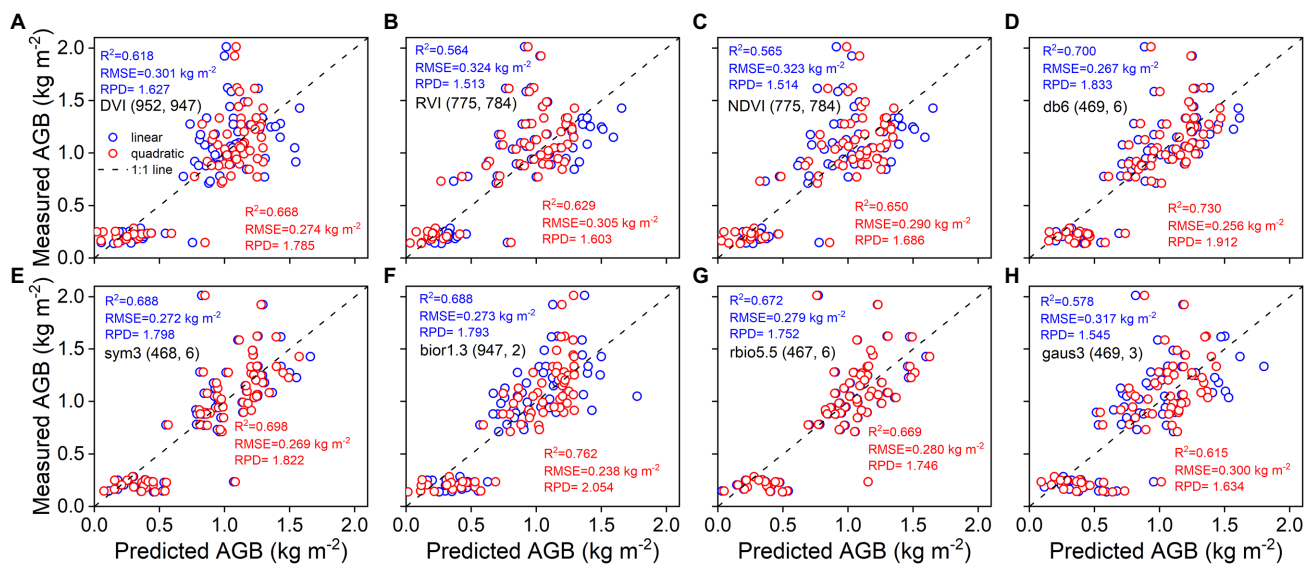

FIGURE 5 | Predicted and measured values of rice AGB with linear and quadratic regression models ($n = 68$). Uppercase letters **(A–H)** are represented in sequence as DVI (952, 947), RVI (775, 784), NDVI (775, 784), db6 (469, 6), sym3 (468, 6), bior1.3 (947, 2), rbio5.5 (467, 6), and gaus3 (469, 3), respectively.

validation performance ($R^2 = 0.762$, RMSE = 0.238 kg m^{-2}, RPD = 2.054) using the bior1.3 (947, 2) of the wavelet features.

Estimation of Rice Aboveground Biomass Using Texture Parameters

The correlation results of rice AGB with RGB-VIs and texture parameters are shown in **Figure 6**. RGB-VIs exhibited extremely low correlation coefficients with rice AGB, and the maximum correlation coefficient was only 0.277 ($p < 0.01$) with the RGBVI. For the texture features of red, green, and blue wavebands, eleven of twenty-four texture features showed strongly positive or negative correlations with correlation coefficient values from 0.53 to 0.69 (VAR_R, HOM_R, CON_R, DIS_R, VAR_G, HOM_G, CON_G, DIS_G, VAR_B, CON_B, and DIS_B). The strongest correlation was found in VAR_G ($r = 0.688$, $p < 0.001$) with AGB. The correlation coefficient matrices of texture indices were calculated using

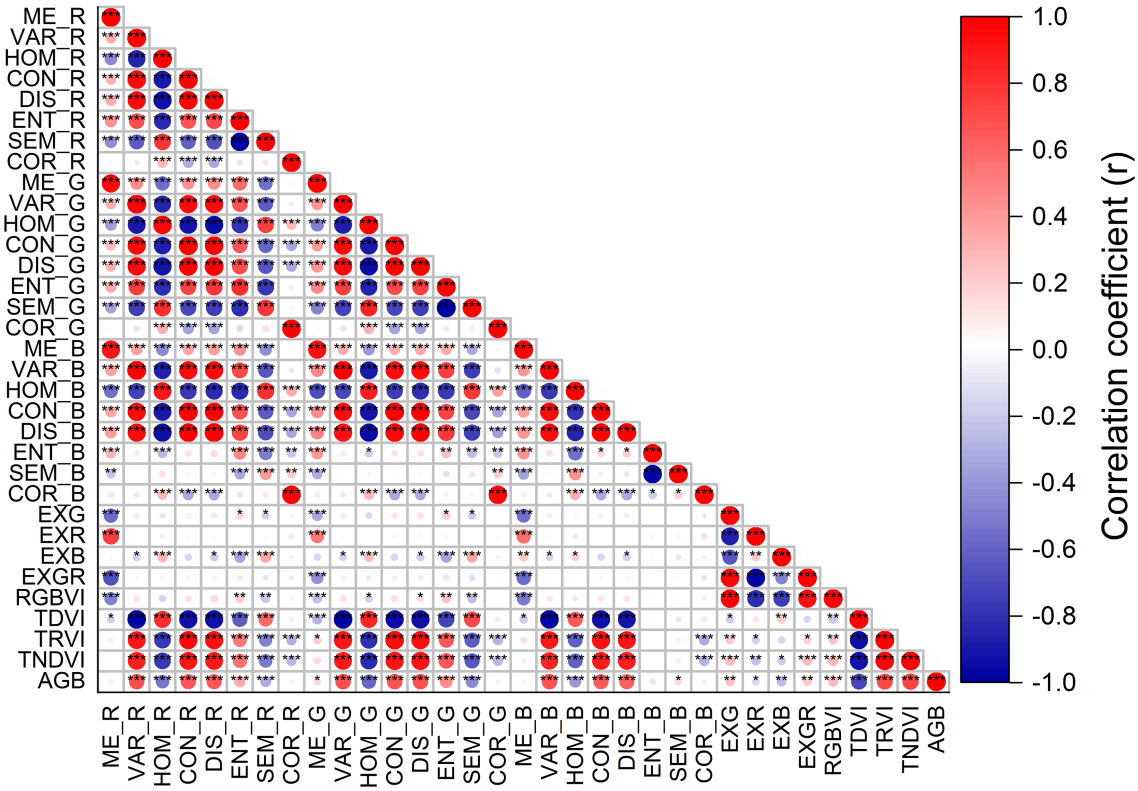

FIGURE 6 | The correlation coefficient between rice AGB and RGB-VIs and texture parameters. * indicates significant correlation at the $p < 0.05$ level, ** indicates the significant correlation at the $p < 0.01$ level, *** indicates the significant correlation at the $p < 0.001$ level.

complete two-by-two combinations of wavebands (24 × 24 wavebands) for the TDVI, TRVI, and TNDVI (**Supplementary Figures S1D–F**). Texture indices were better correlated with AGB than texture features, with correlation coefficients of −0.708, 0.719, and 0.727 for TDVI (VAR_G, ME_B), TRVI (ME_B, VAR_R), and TNDVI (DIS_B, CON_G), respectively. Thus, RGB-VIs and texture features with low correlation were not used to establish the estimation models of rice AGB.

The calibration accuracy for linear and quadratic regression models between rice AGB and texture parameters is presented in **Figure 7**. All estimation models using texture parameters yielded weaker correlations ($0.28 < R^2 < 0.55$, $0.32\,kg\,m^{-2} < RMSE < 0.40\,kg\,m^{-2}$) than spectral parameters. The TDVI (VAR_G, ME_B) of texture indices achieved the best calibration performance for quadratic ($R^2 = 0.548$, $RMSE = 0.317\,kg\,m^{-2}$) regression models. However, the validation results were unsatisfactory for linear and quadratic regression models using texture parameters (**Figure 8**), with R^2 values of 0.14–0.44, RMSE of 0.37–0.46 kg m^{-2}, and RPD of 1.07–1.33. These models exhibited low performance (RPD < 1.4) by using texture parameters to estimate rice AGB.

Estimation of Rice Aboveground Biomass Using Multivariate Analysis and Machine Learning Algorithm

A combination of spectral parameters, selected texture features, and texture indices was used to investigate rice AGB estimates when using MSR, PLS, and RF techniques. The relationship between the predicted and estimated AGB is shown in **Figure 9**. The results demonstrated that RF regression using spectral parameters achieved the best calibration ($R^2 = 0.808$, $RMSE = 0.205\,kg\,m^{-2}$) and validation ($R^2 = 0.747$, $RMSE = 0.245\,kg\,m^{-2}$, $RPD = 2.001$) accuracy among the three techniques, and MSR and PLS regression had similar accuracy in calibration and validation performance. For selected texture features and texture indices, PLS regression showed better calibration ($R^2 = 0.555$, $RMSE = 0.312\,kg\,m^{-2}$) and validation ($R^2 = 0.455$, $RMSE = 0.362\,kg\,m^{-2}$, $RPD = 1.354$) accuracy than MSR and RF regression techniques. When using combined spectral parameters, selected texture features, and texture indices, PLS regression was found to have the best calibration ($R^2 = 0.810$, $RMSE = 0.204\,kg\,m^{-2}$) and validation ($R^2 = 0.751$, $RMSE = 0.244\,kg\,m^{-2}$, $RPD = 2.010$) accuracy. Similar accuracy was achieved using MSR and RF regression techniques. The validation accuracy of the three regression techniques was slightly better than that of the linear and quadratic regression models.

Estimation of Rice Grain Yield Using Remotely Sensed Data

As shown in **Figure 10A**, a strong linear relationship of grain yield was found with rice AGB ($R^2 = 0.654$, $RMSE = 0.521\,t\,ha^{-1}$, $p < 0.0001$). The quadratic regression model established by the bior1.3 (947, 2) of the wavelet features with the highest validation

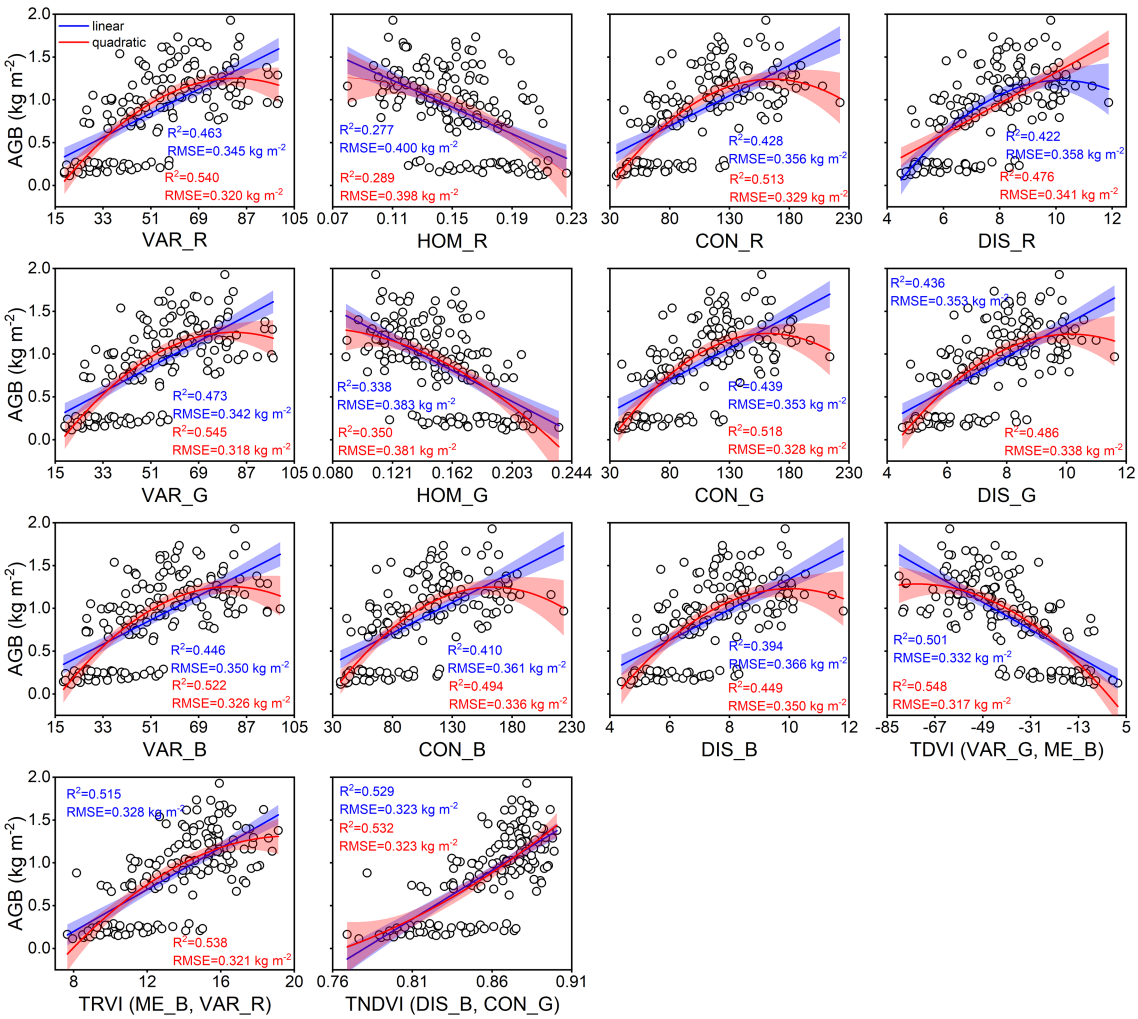

FIGURE 7 | Linear and quadratic regression models using texture parameters for estimating rice AGB ($n = 160$). The shaded band is the prediction interval at the 95% confidence level. TDVI (VAR_G, ME_B) indicates the TDVI at VAR_G and ME_B of texture features. Others are the same as it.

accuracy was selected to investigate the relationship with grain yield. The "AGB-grain yield" linear model was linked with the "bior1.3-AGB" quadratic regression model to generate a spectral estimation model for grain yield. The 1:1 scatter plots of predicted and estimated grain yield are shown for calibration (**Figure 10B**) and validation (**Figure 10C**) performance. The results indicated that the bior1.3 (947, 2) of the wavelet features was used to estimate the grain yield with good calibration ($R^2 = 0.836$, RMSE = 0.394 t ha^{-1}) and validation ($R^2 = 0.758$, RMSE = 0.683 t ha^{-1}, RPD = 1.930) performance. Ground-based remotely sensed data exhibited a good ability for predicting rice grain yield.

DISCUSSION

Relationships Between Rice Aboveground Biomass and Remotely Sensed Data

In this study, the SVIs of specific spectral wavebands from previous studies were found to have low correlations with rice AGB. Generalizing previous studies with our study, the SVIs of specific spectral wavebands were difficult to adapt to the current study (Fu et al., 2014; Bendig et al., 2015; Ren et al., 2018; Wang et al., 2020, 2021b, 2022) because VIs were limited by crop species and the measurement environment of the remotely sensed data. These VIs appeared to be used only for comparison with the new VIs to emphasize the advantages and performance of the new VIs. The sensitive wavebands of rice AGB were found in the red-edge and near-infrared (NIR) regions for the DVI, RVI, NDVI, and bior1.3 of the wavelet features and in the blue wavebands for other wavelet features. According to previous studies, the blue, red-edge, and NIR regions were sensitive to crop biomass (Kanke et al., 2016; Yang et al., 2021). The db6, sym3, and rbio5.5 of the wavelet features showed better calibration performance than the SVIs, which was related to the 467–469 nm of sensitive wavebands and the consistent scale (scale 6). UAV-based RGB imagery is complex and is composed of soil, water, leaves, stems, and panicles (Yue et al., 2019). Although the soil background was

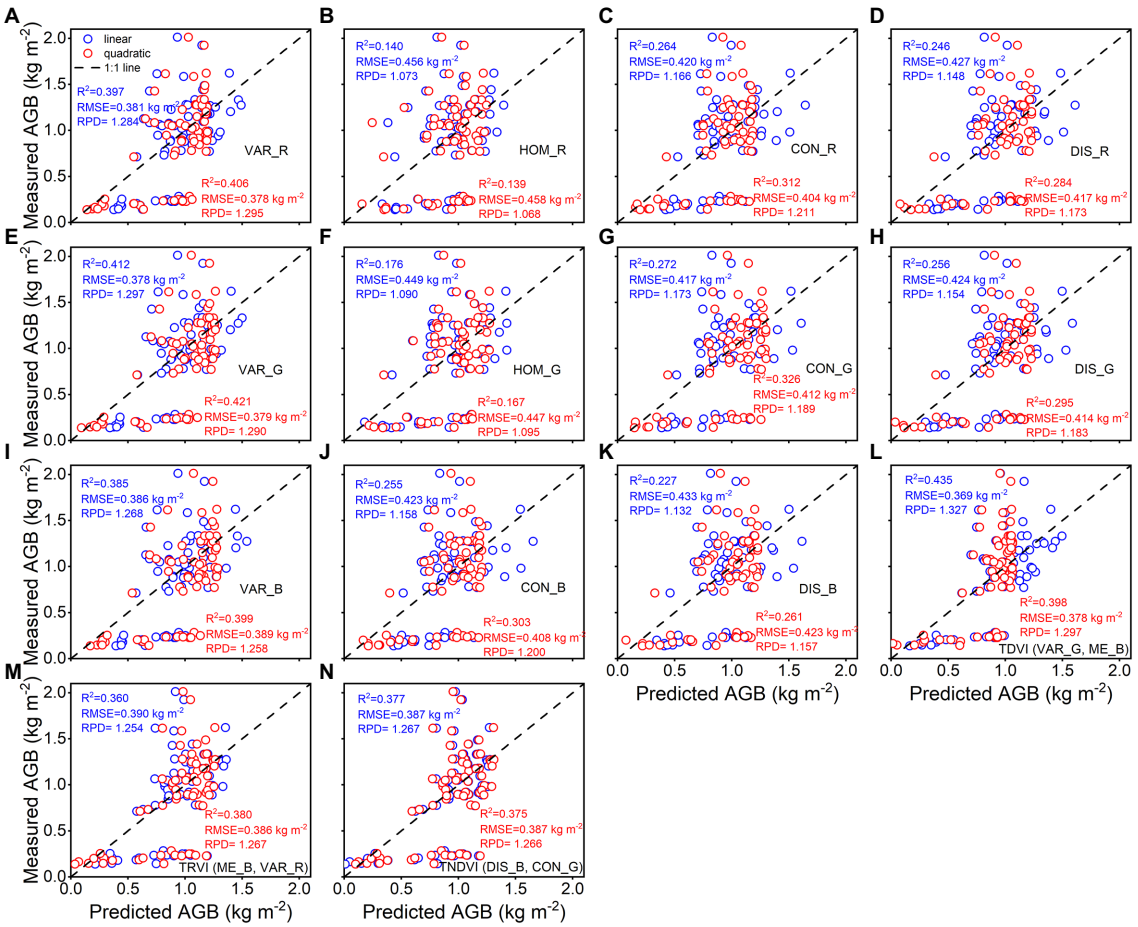

FIGURE 8 | Predicted and measured values of rice AGB with linear and quadratic regression models ($n = 68$). Uppercase letters **(A–N)** are represented in sequence as VAR_R, HOM_R, CON_R, DIS_R, VAR_G, HOM_G, CON_G, DIS_G, VAR_B, CON_B, DIS_B, TDVI, TRVI, and TNDVI, respectively.

effectively classified using a supervised classification method (i.e., RF classifier), DN values were still disturbed by water and soil background, influencing the linear relationship between RGB-VIs and rice AGB. Additionally, the GLCM was used to clearly distinguish crop canopy (dark pixels) and soil background (bright pixels; Haralick et al., 1973), and the correlation with rice AGB was higher than RGB-VIs. The texture imagery showed that the cultivar "Fyou498" had bright pixels with high DN values at the full-heading stage (**Figure 2**). However, rice crops generally had dark pixels with low DN values, and bright pixels deteriorated the estimation accuracy of rice AGB using texture parameters. The bright pixels might be related to the low chlorophyll content and panicles of cultivar "Fyou498."

Multivariate analysis and machine learning algorithms have been widely used to predict the AGB and grain yield of crops (Kanke et al., 2016; Cen et al., 2019; Li et al., 2020; Wan et al., 2020; Zhou et al., 2021). Linear and quadratic regression models are the simplest modeling methods used to determine the relationship between two quantitative variables. However, the dependent variable is often related to two or more independent variables. Linear and quadratic regression cannot solve more complex problems and achieve the anticipated prediction ability. In the current study, the MSR, PLS, and RF regression algorithms were able to explain the differences in AGB estimates by multiple variables while improving the prediction accuracy. As the texture features were affected by the water and soil background, the validation accuracy of the MSR, PLS, and RF regression models using texture parameters alone was still unacceptable, as with linear and quadratic regression (RPD < 1.4). Although RGB imagery data have little effective information and are easily affected by complex backgrounds, they cannot eliminate the advantages of RGB imagery data for the monitoring of crop growth status and the estimation of physiological parameters (Li et al., 2016b; Zhou et al., 2020, 2021). The PLS regression algorithm was used to estimate AGB with the best performance by combining spectral and texture parameters (**Figure 9H**), which explained 2.1%, 1.9%, and 0.2% higher variability than the spectral parameters used and explained 50.0%, 45.9%, and 67.0% higher variability than the texture parameters used for the MSR, PLS, and RF regression algorithms, respectively. Notably, for the three regression algorithms, the difference in estimation accuracy was very small between the spectral parameters and the combination of spectral and texture parameters. RGB imagery provided the texture features with

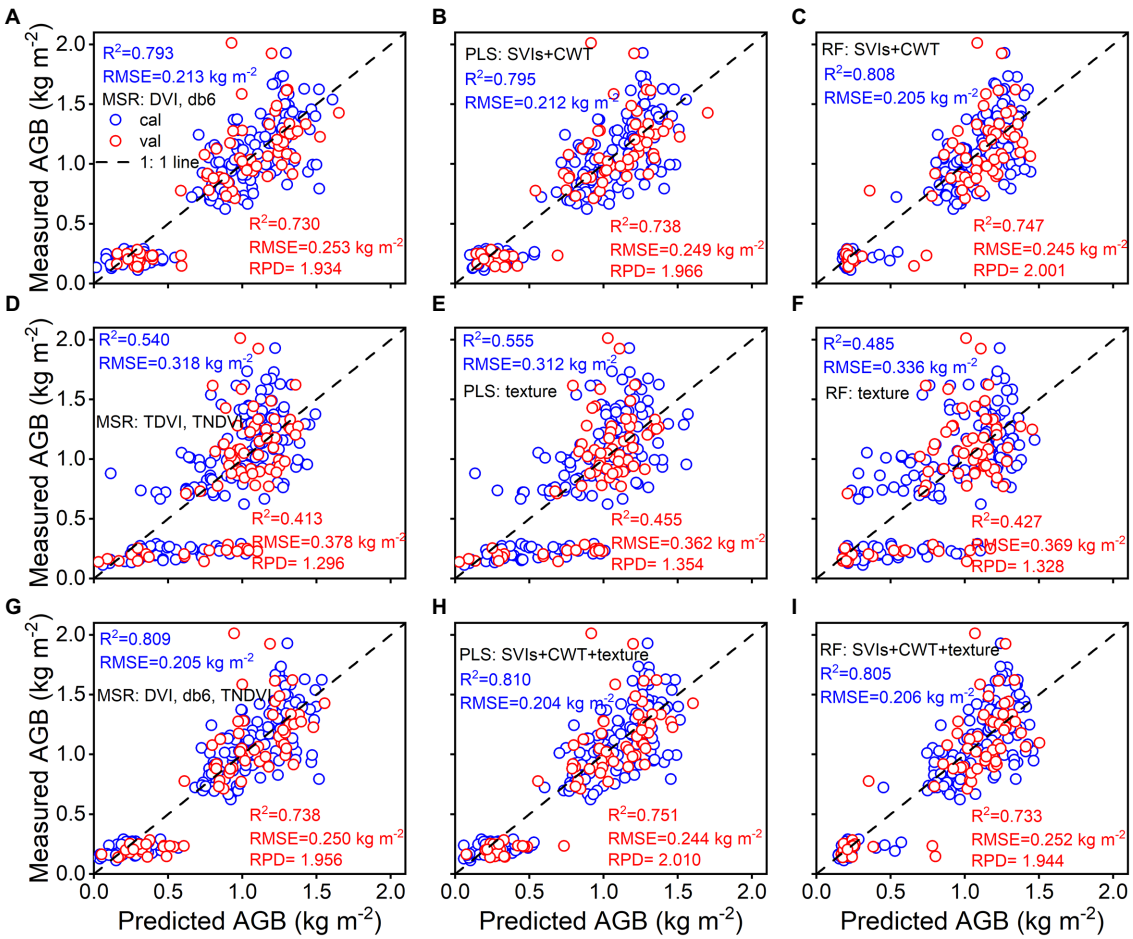

FIGURE 9 | Predicted and measured values of rice AGB with MSR, PLS, and RF regression models from spectral parameters **(A–C)**, texture parameters **(D–F)**, and the combined spectral and texture parameters (**G–I**; cal: $n = 160$, val: $n = 68$).

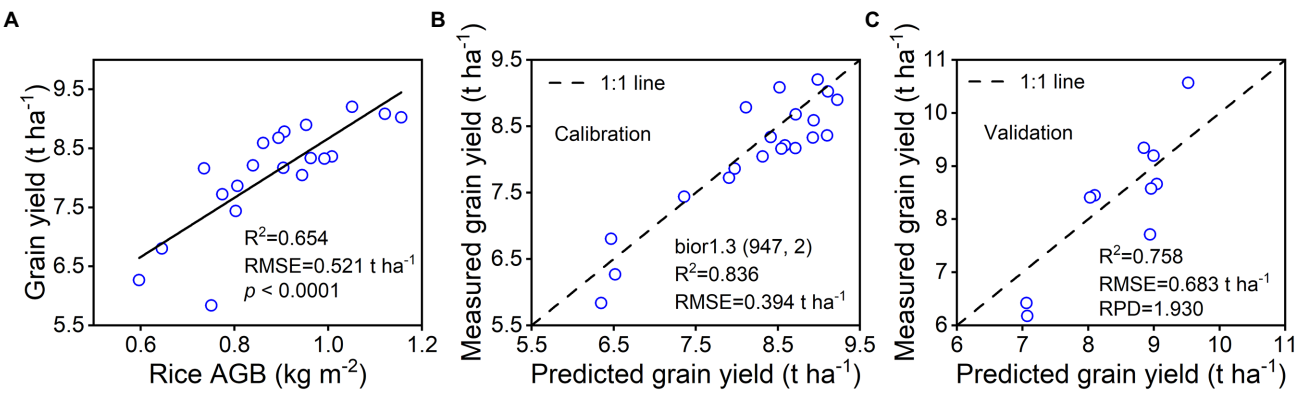

FIGURE 10 | Spectral estimation of rice grain yield by using bior1.3 (947, 2) of wavelet features. **(A)** represents the linear relationship between rice AGB and grain yield ($n = 20$), **(B)** represents the calibration accuracy of the grain yield estimation model ($n = 20$), and **(C)** represents the validation accuracy of predicted and measured grain yield ($n = 10$).

little effective information, and the spectral parameters masked the contribution of texture parameters. It may also be related to the physiological information, canopy structure, and texture information provided by spectral reflectance. Therefore, as important variables, the spectral parameters greatly contribute to the three regression algorithms. In future work, we will

further optimize the RGB imagery data to improve the estimation accuracy by identifying and segmenting the background.

Collinearity and Importance of Variables for the Multivariate Analysis and Machine Learning Algorithm

The DVI, RVI, and NDVI of the complete two-by-two combination of spectral wavebands showed a high correlation with rice AGB. However, linear and quadratic regression models for the RVI and NDVI (**Figure 4**) exhibited similar scatter distributions and prediction intervals (at the 95% confidence level), resulting in approximate calibration and validation accuracy. The predicted values of the linear and quadratic regression models established by the RVI and NDVI were analyzed (**Figure 11**), the slope and R^2 value reached 1 between the predicted values, and the scatter plots were close to the 1:1 line. **Figures 3**, **11** indicated that the RVI and NDVI had a strong positive correlation ($r = 1$, $p < 0.001$), which also confirmed the strong collinearity of these two VIs. The same wavebands were selected to calculate the RVI, and the NDVI was the main reason for strong collinearity and "perfect" predicted values. Therefore, the relationship between spectral reflectance data and rice AGB, along with the collinearity risk, should be improved.

A parsimonious variable selection method such as MSR is set to no more than three variables to prevent overfitting and collinearity problems (Zheng et al., 2019). When more variables are introduced into the MSR model to estimate rice AGB, collinearity between independent variables should be considered to avoid undermining the stability and reliability of the model. Tolerance and the variance inflation factor (VIF) were employed to assess the collinearity of variables; variables with a tolerance less than 0.1 and a VIF greater than 10 were considered collinear and were not introduced into the MSR model (Dormann et al., 2013). The collinearity diagnosis of the MSR model for estimating rice AGB is shown in **Supplementary Table S1**. The variables introduced by the MSR model did not have collinearity and achieved a significant level ($p < 0.05$). Some variables were not collinear, but these variables were removed because they did not satisfy the MSR model ($p > 0.05$). For example, the RVI, NDVI, bior1.3, and gaus3 of the wavelet features did not exhibit collinearity but were not employed in the MSR model. The introduction of other variables masks the strong collinearity between the RVI and NDVI. The sym3 and rbio5.5 of the wavelet features and the TRVI always maintained strong collinearity with the other variables. Strong collinear variables will inevitably affect the test accuracy and model application for estimating rice AGB. PLS and RF regression models can accommodate collinearity without deteriorating the predictive performance of rice AGB (Dingstad et al., 2004). Thus, the collinearity of the PLS and RF regression models is not discussed in this study.

The variable importance is supposed to assess the contribution and explanation to rice AGB. The standard regression coefficient (SRC) for the PLS regression model (Prasad et al., 2008) and the percentage increase in mean square error (IncMSE%) for the RF regression model (Oliveira et al., 2012) were used to indicate the variable importance (**Figure 12**). The larger the absolute value of SRC and IncMSE% is, the greater the influence of the variable on the AGB estimation model. The db6, sym3, and rbio5.5 of the wavelet features had high absolute values of SRC and IncMSE% in the PLS and RF regression models based on spectral parameters and combined spectral and texture parameters. For the correlation analysis between wavelet features and rice AGB, the db6, sym3, and rbio5.5 of the wavelet features were strongly correlated with rice AGB. These three wavelet features were determined to contribute greatly to the estimation of rice AGB. The TDVI, TRVI, and TNDVI of the texture indices significantly contributed to the PLS and RF regression models based on texture parameters. For the combined spectral and texture parameters, the spectral parameters were the main contributions, and the improved estimation accuracy of the MSR and PLS regression models may have been due to the dominant

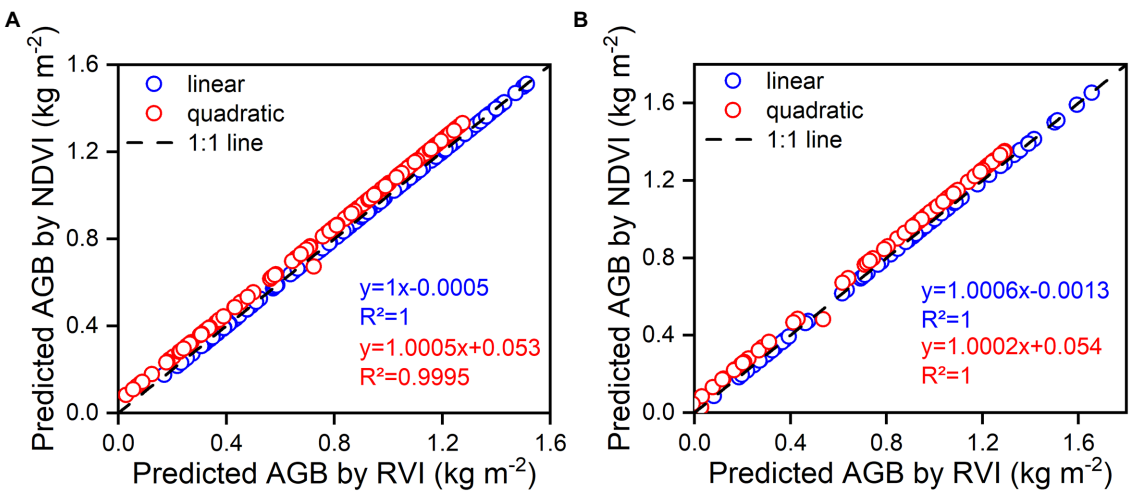

FIGURE 11 | The relationships between predicted values of estimation models using RVI and NDVI for linear and quadratic regression models. **(A)** represents the calibration models, **(B)** represents the validation models.

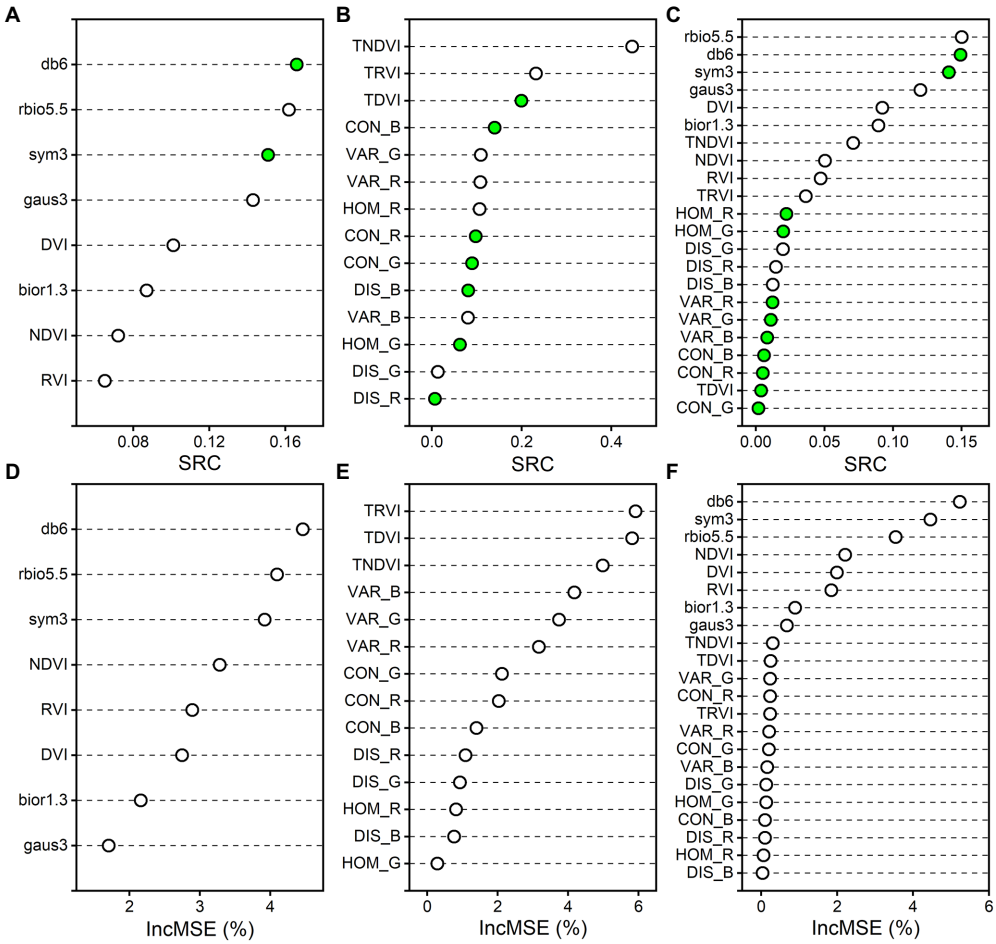

FIGURE 12 | The variable importance measures for the PLS and RF regression models. **(A–C)** indicate the standard regression coefficient (SRC) of PLS regression model for spectral parameters, texture parameters, and the combined spectral and texture parameters, respectively. **(D–F)** indicate the percentage increase in mean square error (IncMSE%) of RF regression model for spectral parameters, texture parameters, and the combined spectral and texture parameters, respectively. Green solid circles indicate absolute values of negative SRC.

role of spectral parameters. When spectral parameters were coupled with texture parameters, the calibration and validation accuracy of the RF regression model was slightly reduced (**Figures 9C,F,I**). This may have been because the texture parameters were introduced into the RF algorithm, and the estimation accuracy was weakened for estimating rice AGB. Variables with low contributions tend to be removed. However, the MSR and PLS regression models were slightly improved, reminding us that texture parameter contributions cannot be ignored.

Sensitivity of Rice Aboveground Biomass

Several studies have demonstrated that AGB data in winter wheat and rice were universally underestimated at the late-reproductive growth stages due to high canopy coverage and plant density (Fu et al., 2014; Kanke et al., 2016; Lu et al., 2019; Zheng et al., 2019). However, samples with high AGB values are not always underestimated (Li et al., 2020; Yang et al., 2021). The underestimation problem can be addressed well by texture parameters and canopy height (Bendig et al., 2015; Yue et al., 2019). The predicted AGB did not suffer from the underestimation problem in this study. Notably, the AGB values derived from the 0–0.5 kg m^{-2} range at the tillering stage were always overestimated (**Figures 5**, **8, 9**). The spectral reflectance and RGB imagery data were not sensitive to rice AGB in the range of 0–0.5 kg m^{-2} (**Figures 4**, **7**). Bare soil and water background during the tillering stage may be the main reasons that interfere with the spectral reflectance and DN values. When the spectral and texture parameters were combined, the predicted AGB values were overestimated, which improved compared to the spectral parameters alone and the texture parameters alone. A study demonstrated that texture information provides the advantage of structural information when spectral information deteriorates biomass estimation accuracy at the heading stage (Lu and Batistella, 2005). The sensitivity of texture parameters at the early vegetative growth stages to vegetation canopy structure remains to be further studied and discussed. Canopy height as an indicator had a suitable and robust relationship with crop biomass and was used to overcome the underestimation problem (Tilly et al., 2015; Li

et al., 2016b). We will explore whether canopy height can optimize and improve the overestimation problem of rice AGB.

Previous studies have reported that multivariate analysis and machine learning algorithms, such as MSR (Gab-Sue et al., 2006), PLS (Kawamura et al., 2018), RF (Mariano and Mónica, 2021), and neural networks (Zhou et al., 2021), demonstrate excellent advantages in estimating crop grain yield. However, using machine learning algorithms to predict grain yield is difficult to explain physiologically through physiological parameters and lacks a mechanism. Because AGB is closely related to photosynthetically active radiation and dry matter accumulation in crops, it is a critical predictor of grain yield. SVIs, wavelet features, and texture features were successfully used to estimate crop grain yield (Rodrigues et al., 2018; Maimaitijiang et al., 2020; Wang et al., 2021b). A combination of spectral and texture parameters to predict rice grain yield requires further work. More diverse remotely sensed data are available for improving the estimation models and application areas (Li et al., 2016b). Meanwhile, dry matter is stored in leaves and stems during the vegetative growth stages and then transported at the grain filling stage to form the grain yield. The sensitivity of AGB at the different growth stages was different for grain yield. Therefore, it is essential to seek sensitive stages to predict grain yield using multisource remotely sensed data.

CONCLUSION

This study compared the estimation performance of linear, quadratic, MSR, PLS, and RF regression models for rice AGB estimation with spectral parameters (SVIs and wavelet features), texture parameters (texture features and texture indices), and their combination. The results showed that spectral parameters were strongly correlated with rice AGB, and eleven selected texture features and texture indices were found to have significant but weaker correlations. Spectral parameters were superior to texture parameters in estimating rice AGB for the linear and quadratic regression models. For the MSR, PLS, and RF regression models, a combination of spectral and texture parameters slightly improved estimation performance over the use of spectral parameters or texture parameters alone. Combined remotely sensed data may help overcome the overestimation of rice AGB in the range of 0–0.5 $kg\,m^{-2}$. At the same time, rice grain yield can be predicted well with bior1.3 of the wavelet features. However, this study was limited to one growing season and an area with few datasets. Future work will further optimize texture information and combine spectral reflectance to improve the estimation accuracy of rice AGB and grain yield. More years and growth areas should be examined to test the stability and reliability of the estimation models.

DATA AVAILABILITY STATEMENT

The original contributions presented in the study are included in the article/**Supplementary Material**, further inquiries can be directed to the corresponding author.

AUTHOR CONTRIBUTIONS

JM and ZW designed the research. JM supervised the research. ZW, YM, PC, YY, and HF performed the experimental work and acquired the data. ZW wrote the first manuscript. ZW, YM, and PC analyzed the data. ZW, FY, MR, CG, and CS revised the manuscript. FY, YS, ZY, and ZC provided helpful suggestions for the experimental work. All authors contributed to the article and approved the submitted version.

FUNDING

The work was supported by the Rice Breeding Project Foundation of the Sichuan Provincial Science and Technology Department (grant no. 2021YFYZ0005) and the National Modern Agricultural Industry Technology System Sichuan Innovative Rice Innovation Team Project (sccxtd-2021-01).

SUPPLEMENTARY MATERIAL

The Supplementary Material for this article can be found online at: https://www.frontiersin.org/articles/10.3389/fpls.2022.903643/full#supplementary-material

REFERENCES

Bendig, J., Bolten, A., Bennertz, S., Broscheit, J., Eichfuss, S., and Bareth, G. (2014). Estimating biomass of barley using crop surface models (CSMs) derived from UAV-based RGB imaging. *Remote Sens.* 6, 10395–10412. doi: 10.3390/rs61110395

Bendig, J., Yu, K., Aasen, H., Bolten, A., Bennertz, S., Broscheit, J., et al. (2015). Combining UAV-based plant height from crop surface models, visible, and near infrared vegetation indices for biomass monitoring in barley. *Int. J. Appl. Earth Obs. Geoinf.* 39, 79–87. doi: 10.1016/j.jag.2015.02.012

Camargo Neto, J. (2004). A combined statistical-soft computing approach for classification and mapping weed species in minimum -tillage systems. Ph.D., The University of Nebraska - Lincoln.

Casanova, D., Epema, G. F., and Goudriaan, J. (1998). Monitoring rice reflectance at field level for estimating biomass and LAI. *Field Crops Res.* 55, 83–92. doi: 10.1016/S0378-4290(97)00064-6

Cen, H., Wan, L., Zhu, J., Li, Y., Li, X., Zhu, Y., et al. (2019). Dynamic monitoring of biomass of rice under different nitrogen treatments using a lightweight UAV with dual image-frame snapshot cameras. *Plant Methods* 15, 32. doi: 10.1186/s13007-019-0418-8

Chen, J., Li, F., Wang, R., Fan, Y., Raza, M. A., Liu, Q., et al. (2019). Estimation of nitrogen and carbon content from soybean leaf reflectance spectra using wavelet analysis under shade stress. *Comput. Electron. Agric.* 156, 482–489. doi: 10.1016/j.compag.2018.12.003

Cheng, H. D., Jiang, X. H., Sun, Y., and Wang, J. (2001). Color image segmentation: advances and prospects. *Pattern Recogn.* 34, 2259–2281. doi: 10.1016/S0031-3203(00)00149-7

Cheng, T., Rivard, B., and Sánchez-Azofeifa, A. (2011). Spectroscopic determination of leaf water content using continuous wavelet analysis. *Remote Sens. Environ.* 115, 659–670. doi: 10.1016/j.rse.2010.11.001

Cheng, T., Rivard, B., Sánchez-Azofeifa, A. G., Féret, J.-B., Jacquemoud, S., and Ustin, S. L. (2012). Predicting leaf gravimetric water content from

foliar reflectance across a range of plant species using continuous wavelet analysis. *J. Plant Physiol.* 169, 1134–1142. doi: 10.1016/j.jplph.2012.04.006

Cheng, T., Rivard, B., Sánchez-Azofeifa, A. G., Féret, J.-B., Jacquemoud, S., and Ustin, S. L. (2014). Deriving leaf mass per area (LMA) from foliar reflectance across a variety of plant species using continuous wavelet analysis. *ISPRS J. Photogramm. Remote Sens.* 87, 28–38. doi: 10.1016/j.isprsjprs.2013.10.009

Cheng, T., Song, R., Li, D., Zhou, K., Zheng, H., Yao, X., et al. (2017). Spectroscopic estimation of biomass in canopy components of Paddy Rice using dry matter and chlorophyll indices. *Remote Sens.* 9, 319. doi: 10.3390/rs9040319

Delegido, J., Verrelst, J., Rivera, J. P., Ruiz-Verdú, A., and Moreno, J. (2015). Brown and green LAI mapping through spectral indices. *Int. J. Appl. Earth Obs. Geoinf.* 35, 350–358. doi: 10.1016/j.jag.2014.10.001

Dingstad, G. I., Westad, F., and Næs, T. (2004). Three case studies illustrating the properties of ordinary and partial least squares regression in different mixture models. *Chemometrics Intellig. Lab. Syst.* 71, 33–45. doi: 10.1016/j.chemolab.2003.11.002

Dormann, C. F., Elith, J., Bacher, S., Buchmann, C., Carl, G., Carré, G., et al. (2013). Collinearity: a review of methods to deal with it and a simulation study evaluating their performance. *Ecography* 36, 27–46. doi: 10.1111/j.1600-0587.2012.07348.x

Fu, Y., Yang, G., Wang, J., Song, X., and Feng, H. (2014). Winter wheat biomass estimation based on spectral indices, band depth analysis and partial least squares regression using hyperspectral measurements. *Comput. Electron. Agric.* 100, 51–59. doi: 10.1016/j.compag.2013.10.010

Gab-Sue, J., Kenneth, A. S., Suk Young, H., Newell, R. K., and Harlan, L. P. (2006). Relating Hyperspectral image bands and vegetation indices to corn and soybean yield. *Korean J. Remote. Sens.* 22, 183–197. doi: 10.7780/kjrs.2006.22.3.183

Gitelson, A. A., Gritz, Y., and Merzlyak, M. N. (2003). Relationships between leaf chlorophyll content and spectral reflectance and algorithms for non-destructive chlorophyll assessment in higher plant leaves. *J. Plant Physiol.* 160, 271–282. doi: 10.1078/0176-1617-00887

Gnyp, M. L., Miao, Y., Yuan, F., Ustin, S. L., Yu, K., Yao, Y., et al. (2014). Hyperspectral canopy sensing of paddy rice aboveground biomass at different growth stages. *Field Crops Res.* 155, 42–55. doi: 10.1016/j.fcr.2013.09.023

Guo, Y., Zhou, Y., and Tan, J. (2015). Wavelet analysis of pulse-amplitude-modulated chlorophyll fluorescence for differentiation of plant samples. *J. Theor. Biol.* 370, 116–120. doi: 10.1016/j.jtbi.2015.01.041

Haboudane, D., Miller, J. R., Tremblay, N., Zarco-Tejada, P. J., and Dextraze, L. (2002). Integrated narrow-band vegetation indices for prediction of crop chlorophyll content for application to precision agriculture. *Remote Sens. Environ.* 81, 416–426. doi: 10.1016/S0034-4257(02)00018-4

Haralick, R. M., Shanmugam, K., and Dinstein, I. (1973). Textural features for image classification. *IEEE Trans. Syst. Man Cybern.* SMC-3, 610–621. doi: 10.1109/TSMC.1973.4309314

Harrell, D. L., Tubaña, B. S., Walker, T. W., and Phillips, S. B. (2011). Estimating Rice grain yield potential using normalized difference vegetation index. *Agron. J.* 103, 1717–1723. doi: 10.2134/agronj2011.0202

Iqbal, F., Lucieer, A., Barry, K., and Wells, R. (2017). Poppy crop height and capsule volume estimation from a single UAS flight. *Remote Sens.* 9, 647. doi: 10.3390/rs9070647

Jiang, Q., Fang, S., Peng, Y., Gong, Y., Zhu, R., Wu, X., et al. (2019). UAV-based biomass estimation for Rice-combining spectral, TIN-based structural and meteorological features. *Remote Sens.* 11, 890. doi: 10.3390/rs11070890

Jordan, C. F. (1969). Derivation of leaf-area index from quality of light on the Forest floor. *Ecology* 50, 663–666. doi: 10.2307/1936256

Kanke, Y., Tubaña, B., Dalen, M., and Harrell, D. (2016). Evaluation of red and red-edge reflectance-based vegetation indices for rice biomass and grain yield prediction models in paddy fields. *Precis. Agric.* 17, 507–530. doi: 10.1007/s11119-016-9433-1

Kawamura, K., Ikeura, H., Phongchanmaixay, S., and Khanthavong, P. (2018). Canopy Hyperspectral sensing of Paddy fields at the booting stage and PLS regression can assess grain yield. *Remote Sens.* 10, 1249. doi: 10.3390/rs10081249

Koppe, W., Gnyp, M. L., Hütt, C., Yao, Y., Miao, Y., Chen, X., et al. (2013). Rice monitoring with multi-temporal and dual-polarimetric TerraSAR-X data. *Int. J. Appl. Earth Obs. Geoinf.* 21, 568–576. doi: 10.1016/j.jag.2012.07.016

Li, X., Luo, L., He, Y., and Xu, N. (2013). Determination of dry matter content of tea by near and middle infrared spectroscopy coupled with wavelet-based data mining algorithms. *Comput. Electron. Agric.* 98, 46–53. doi: 10.1016/j.compag.2013.07.014

Li, W., Niu, Z., Chen, H., Li, D., Wu, M., and Zhao, W. (2016b). Remote estimation of canopy height and aboveground biomass of maize using high-resolution stereo images from a low-cost unmanned aerial vehicle system. *Ecol. Indic.* 67, 637–648. doi: 10.1016/j.ecolind.2016.03.036

Li, L., Ren, T., Ma, Y., Wei, Q., Wang, S., Li, X., et al. (2016a). Evaluating chlorophyll density in winter oilseed rape (Brassica napus L.) using canopy hyperspectral red-edge parameters. *Comput. Electron. Agric.* 126, 21–31. doi: 10.1016/j.compag.2016.05.008

Li, B., Xu, X., Zhang, L., Han, J., Bian, C., Li, G., et al. (2020). Above-ground biomass estimation and yield prediction in potato by using UAV-based RGB and hyperspectral imaging. *ISPRS J. Photogramm. Remote Sens.* 162, 161–172. doi: 10.1016/j.isprsjprs.2020.02.013

Lu, D., and Batistella, M. (2005). Exploring TM image texture and its relationships with biomass estimation in Rondônia. *Brazilian Amazon. Acta Amazon.* 35, 249–257. doi: 10.1590/S0044-59672005000200015

Lu, N., Zhou, J., Han, Z., Li, D., Cao, Q., Yao, X., et al. (2019). Improved estimation of aboveground biomass in wheat from RGB imagery and point cloud data acquired with a low-cost unmanned aerial vehicle system. *Plant Methods* 15:17. doi: 10.1186/s13007-019-0402-3

Ma, D., Maki, H., Neeno, S., Zhang, L., Wang, L., and Jin, J. (2020). Application of non-linear partial least squares analysis on prediction of biomass of maize plants using hyperspectral images. *Biosyst. Eng.* 200, 40–54. doi: 10.1016/j.biosystemseng.2020.09.002

Maimaitijiang, M., Sagan, V., Sidike, P., Hartling, S., Esposito, F., and Fritschi, F. B. (2020). Soybean yield prediction from UAV using multimodal data fusion and deep learning. *Remote Sens. Environ.* 237:111599. doi: 10.1016/j.rse.2019.111599

Mallat, S. G. (1989). A theory for multiresolution signal decomposition: the wavelet representation. *IEEE* 11, 674–693. doi: 10.1109/34.192463

Mansaray, L. R., Zhang, K., and Kanu, A. S. (2020). Dry biomass estimation of paddy rice with sentinel-1A satellite data using machine learning regression algorithms. *Comput. Electron. Agric.* 176:105674. doi: 10.1016/j.compag.2020.105674

Mao, W., Wang, Y., and Wang, Y. (2003). "Real-Time Detection of Between-Row Weeds Using Machine Vision", in: ASAE Annual Meeting. (St. Joseph, MI: ASABE).

Mariano, C., and Mónica, B. (2021). A random forest-based algorithm for data-intensive spatial interpolation in crop yield mapping. *Comput. Electron. Agric.* 184:106094. doi: 10.1016/j.compag.2021.106094

Metternicht, G. (2003). Vegetation indices derived from high-resolution airborne videography for precision crop management. *Int. J. Remote Sens.* 24, 2855–2877. doi: 10.1080/01431160210163074

Meyer, G. E., and Neto, J. C. (2008). Verification of color vegetation indices for automated crop imaging applications. *Comput. Electron. Agric.* 63, 282–293. doi: 10.1016/j.compag.2008.03.009

Mutanga, O., Adam, E., and Cho, M. A. (2012). High density biomass estimation for wetland vegetation using WorldView-2 imagery and random forest regression algorithm. *Int. J. Appl. Earth Obs. Geoinf.* 18, 399–406. doi: 10.1016/j.jag.2012.03.012

Oliveira, S., Oehler, F., San-Miguel-Ayanz, J., Camia, A., and Pereira, J. M. C. (2012). Modeling spatial patterns of fire occurrence in Mediterranean Europe using multiple regression and random Forest. *For. Ecol. Manag.* 275, 117–129. doi: 10.1016/j.foreco.2012.03.003

Pearson, R. L., and Miller, L. D. (1972). "Remote Mapping of Standing Crop Biomass for Estimation of the Productivity of the Shortgrass Prairie", in: Remote Sensing of Environment, VIII, 1355.

Prasad, V. K., Badarinath, K. V. S., and Eaturu, A. (2008). Effects of precipitation, temperature and topographic parameters on evergreen vegetation greenery in the Western Ghats. *India. Int. J. Climatol.* 28, 1807–1819. doi: 10.1002/joc.1662

R Development Core Team (2022). R: A Language and Environment for Statistical Computing. R Foundation for Statistical Computing, Vienna, Austria. Available at: https://www.r-project.org/ (Assessed April 22, 2022).

Raya-Sereno, M. D., Ortiz-Monasterio, J. I., Alonso-Ayuso, M., Rodrigues, F. A., Rodríguez, A. A., González-Perez, L., et al. (2021). High-resolution airborne

Hyperspectral imagery for assessing yield, biomass, grain N concentration, and N output in spring wheat. *Remote Sens.* 13:1373. doi: 10.3390/rs13071373

Ren, H., Zhou, G., and Zhang, F. (2018). Using negative soil adjustment factor in soil-adjusted vegetation index (SAVI) for aboveground living biomass estimation in arid grasslands. *Remote Sens. Environ.* 209, 439–445. doi: 10.1016/j.rse.2018.02.068

Rodrigues, F. A., Blasch, G., Defourny, P., Ortiz-Monasterio, J. I., Schulthess, U., Zarco-Tejada, P. J., et al. (2018). Multi-temporal and spectral analysis of high-resolution Hyperspectral airborne imagery for precision agriculture: assessment of wheat grain yield and grain protein content. *Remote Sens.* 10:930. doi: 10.3390/rs10060930

Roth, L., and Streit, B. (2018). Predicting cover crop biomass by lightweight UAS-based RGB and NIR photography: an applied photogrammetric approach. *Precis. Agric.* 19, 93–114. doi: 10.1007/s11119-017-9501-1

Roujean, J.-L., and Breon, F.-M. (1995). Estimating PAR absorbed by vegetation from bidirectional reflectance measurements. *Remote Sens. Environ.* 51, 375–384. doi: 10.1016/0034-4257(94)00114-3

Rouse, J. W., Haas, R. H., Schell, J. A., and Deering, D. W. (1974). "Monitoring Vegetation Systems in the Great Plains with Erts," in NASA special Publica, 309.

Sharifi, A., and Hosseingholizadeh, M. (2020). Application of Sentinel-1 data to estimate height and biomass of Rice crop in Astaneh-ye Ashrafiyeh. *Iran. Iran. J Indian Soc. Remote Sens.* 48, 11–19. doi: 10.1007/s12524-019-01057-8

Tilly, N., Aasen, H., and Bareth, G. (2015). Fusion of plant height and vegetation indices for the estimation of barley biomass. *Remote Sens.* 7, 11449–11480. doi: 10.3390/rs70911449

Tremblay, N., Haboudane, D., and Miller, J. (2003). "Corn OSAVI as related to soil electrical conductivity and nitrogen fertilization rates." in *IGARSS 2003. 2003 IEEE International Geoscience and Remote Sensing Symposium. Proceedings (IEEE Cat. No.03CH37477)*; July 21–25, 2003; 2230–2232.

Wan, L., Cen, H., Zhu, J., Zhang, J., Zhu, Y., Sun, D., et al. (2020). Grain yield prediction of rice using multi-temporal UAV-based RGB and multispectral images and model transfer – a case study of small farmlands in the south of China. *Agric. For. Meteorol.* 291:108096. doi: 10.1016/j.agrformet.2020.108096

Wang, Z., Chen, J., Fan, Y., Cheng, Y., Wu, X., Zhang, J., et al. (2020). Evaluating photosynthetic pigment contents of maize using UVE-PLS based on continuous wavelet transform. *Comput. Electron. Agric.* 169:105160. doi: 10.1016/j.compag.2019.105160

Wang, L., Chen, S., Li, D., Wang, C., Jiang, H., Zheng, Q., et al. (2021a). Estimation of Paddy Rice nitrogen content and accumulation Both at leaf and plant levels from UAV Hyperspectral imagery. *Remote Sens.* 13, 2956. doi: 10.3390/rs13152956

Wang, Z., Chen, J., Zhang, J., Fan, Y., Cheng, Y., Wang, B., et al. (2021b). Predicting grain yield and protein content using canopy reflectance in maize grown under different water and nitrogen levels. *Field Crops Res.* 260:107988. doi: 10.1016/j.fcr.2020.107988

Wang, Z., Chen, J., Zhang, J., Tan, X., Ali Raza, M., Ma, J., et al. (2022). Assessing canopy nitrogen and carbon content in maize by canopy spectral reflectance and uninformative variable elimination. *Crop J.* doi: 10.1016/j.cj.2021.12.005 [Epub ahead of print].

Wang, H., Huo, Z., Zhou, G., Liao, Q., Feng, H., and Wu, L. (2016). Estimating leaf SPAD values of freeze-damaged winter wheat using continuous wavelet analysis. *Plant Physiol. Biochem.* 98, 39–45. doi: 10.1016/j.plaphy.2015.10.032

Woebbecke, D. M., Meyer, G. E., Von Bargen, K., and Mortensen, D. A. (1995). Color indices for weed identification Under various soil, residue, and lighting conditions. *Trans. ASAE* 38, 259–269. doi: 10.13031/2013.27838

Wu, G., de Leeuw, J., Skidmore, A. K., Prins, H. H. T., and Liu, Y. (2005). "Exploring the possibility of estimating the aboveground biomass of *Vallisneria spiralis* L. using Landsat TM image in Dahuchi, Jiangxi Province, China." in *International Society of Photo-Optical Instrumentation Engineers (SPIE) Conference Series MIPPR 2005: Geospatial Information, Data Mining, and Applications*, 60452P; December 2, 2005.

Yang, S., Feng, Q., Liang, T., Liu, B., Zhang, W., and Xie, H. (2018). Modeling grassland above-ground biomass based on artificial neural network and remote sensing in the Three-River headwaters region. *Remote Sens. Environ.* 204, 448–455. doi: 10.1016/j.rse.2017.10.011

Yang, H., Li, F., Wang, W., and Yu, K. (2021). Estimating above-ground biomass of potato using random Forest and optimized Hyperspectral indices. *Remote Sens.* 13:2339. doi: 10.3390/rs13122339

Yue, J., Yang, G., Tian, Q., Feng, H., Xu, K., and Zhou, C. (2019). Estimate of winter-wheat above-ground biomass based on UAV ultrahigh-ground-resolution image textures and vegetation indices. *ISPRS J. Photogramm. Remote Sens.* 150, 226–244. doi: 10.1016/j.isprsjprs.2019.02.022

Zhang, J., yuan, L., Pu, R., Loraamm, R. W., Yang, G., and Wang, J. (2014). Comparison between wavelet spectral features and conventional spectral features in detecting yellow rust for winter wheat. *Comput. Electron. Agric.* 100, 79–87. doi: 10.1016/j.compag.2013.11.001

Zheng, H., Cheng, T., Zhou, M., Li, D., Yao, X., Tian, Y., et al. (2019). Improved estimation of rice aboveground biomass combining textural and spectral analysis of UAV imagery. *Precis. Agric.* 20, 611–629. doi: 10.1007/s11119-018-9600-7

Zhou, J., Zhou, J., Ye, H., Ali, M. L., Chen, P., and Nguyen, H. T. (2021). Yield estimation of soybean breeding lines under drought stress using unmanned aerial vehicle-based imagery and convolutional neural network. *Biosyst. Eng.* 204, 90–103. doi: 10.1016/j.biosystemseng.2021.01.017

Zhou, J., Zhou, J., Ye, H., Ali, M. L., Nguyen, H. T., and Chen, P. (2020). Classification of soybean leaf wilting due to drought stress using UAV-based imagery. *Comput. Electron. Agric.* 175:105576. doi: 10.1016/j.compag.2020.105576

Conflict of Interest: The authors declare that the research was conducted in the absence of any commercial or financial relationships that could be construed as a potential conflict of interest.

Publisher's Note: All claims expressed in this article are solely those of the authors and do not necessarily represent those of their affiliated organizations, or those of the publisher, the editors and the reviewers. Any product that may be evaluated in this article, or claim that may be made by its manufacturer, is not guaranteed or endorsed by the publisher.

Copyright © 2022 Wang, Ma, Chen, Yang, Fu, Yang, Raza, Guo, Shu, Sun, Yang, Chen and Ma. This is an open-access article distributed under the terms of the Creative Commons Attribution License (CC BY). The use, distribution or reproduction in other forums is permitted, provided the original author(s) and the copyright owner(s) are credited and that the original publication in this journal is cited, in accordance with accepted academic practice. No use, distribution or reproduction is permitted which does not comply with these terms.

frontiers | Frontiers in Plant Science

ORIGINAL RESEARCH
published: 15 June 2022
doi: 10.3389/fpls.2022.925986

Cotton Yield Estimation Based on Vegetation Indices and Texture Features Derived From RGB Image

Yiru Ma[1†], Lulu Ma[1†], Qiang Zhang[1], Changping Huang[2], Xiang Yi[1], Xiangyu Chen[1], Tongyu Hou[1], Xin Lv[1] and Ze Zhang[1*]*

[1]Xinjiang Production and Construction Crops Oasis Eco-Agriculture Key Laboratory, College of Agriculture, Shihezi University, Shihezi, China, [2]Aerospace Information Research Institute, Chinese Academy of Sciences, Beijing, China

OPEN ACCESS

Edited by:
Zhenhai Li,
Shandong University of Science and Technology, China

Reviewed by:
Paulo Flores,
North Dakota State University, United States
Quanlong Feng,
China Agricultural University, China

***Correspondence:**
Xin Lv
luxin@shzu.edu.cn
Ze Zhang
zhangze1227@shzu.edu.cn

[†]These authors have contributed equally to this work and share first authorship

Specialty section:
This article was submitted to Sustainable and Intelligent Phytoprotection, a section of the journal Frontiers in Plant Science

Received: *22 April 2022*
Accepted: *23 May 2022*
Published: *15 June 2022*

Citation:
Ma Y, Ma L, Zhang Q, Huang C, Yi X, Chen X, Hou T, Lv X and Zhang Z (2022) Cotton Yield Estimation Based on Vegetation Indices and Texture Features Derived From RGB Image. Front. Plant Sci. 13:925986. doi: 10.3389/fpls.2022.925986

Yield monitoring is an important parameter to evaluate cotton productivity during cotton harvest. Nondestructive and accurate yield monitoring is of great significance to cotton production. Unmanned aerial vehicle (UAV) remote sensing has fast and repetitive acquisition ability. The visible vegetation indices has the advantages of low cost, small amount of calculation and high resolution. The combination of the UAV and visible vegetation indices has been more and more applied to crop yield monitoring. However, there are some shortcomings in estimating cotton yield based on visible vegetation indices only as the similarity between cotton and mulch film makes it difficult to differentiate them and yields may be saturated based on vegetation index estimates near harvest. Texture feature is another important remote sensing information that can provide geometric information of ground objects and enlarge the spatial information identification based on original image brightness. In this study, RGB images of cotton canopy were acquired by UAV carrying RGB sensors before cotton harvest. The visible vegetation indices and texture features were extracted from RGB images for cotton yield monitoring. Feature parameters were selected in different methods after extracting the information. Linear and nonlinear methods were used to build cotton yield monitoring models based on visible vegetation indices, texture features and their combinations. The results show that (1) vegetation indices and texture features extracted from the ultra-high-resolution RGB images obtained by UAVs were significantly correlated with the cotton yield; (2) The best model was that combined with vegetation indices and texture characteristics RF_ELM model, verification set R^2 was 0.9109, and RMSE was 0.91277 t.ha^{-1}. rRMSE was 29.34%. In conclusion, the research results prove that UAV carrying RGB sensor has a certain potential in cotton yield monitoring, which can provide theoretical basis and technical support for field cotton production evaluation.

Keywords: yield, UAV, RGB image, vegetation indices, texture feature

INTRODUCTION

Cotton is an important cash crop, providing one of the world's best high-quality fiber and natural crops, serving as one of the largest raw material supplies in the textile industry (Khan et al., 2020). In order to reduce production costs, reduce farmers' labor burden, and improve cotton harvest efficiency, cotton harvest efficiency, use of machine for cotton cultivation has expanded over large areas (Wu and Chen, 2015). Spraying defoliating agent is the key technology of mechanized cotton harvesting (Sun et al., 2020), and the amount of defoliating agent and spraying time had significant effect on cotton yield (Xin et al., 2021). Analysis of the yield variation of the cotton harvest period is very important to determine the harvest time and evaluate the productivity of cotton (Tedesco-Oliveira et al., 2020). Therefore, it is of great significance to estimate cotton yield quickly and accurately before the cotton harvest.

The traditional yield survey method is based on the experience of farmers or professionals, which is time-consuming, laborious, and is mainly based on fixed point destructive sampling, which has a certain degree of uncertainty and cannot accurately evaluate the distribution of cotton yield in the region (Çopur et al., 2010). In recent years, the combination of artificial intelligence and remote sensing technology has been widely applied in agriculture (Xu et al., 2021). At present, relevant scholars have also proposed various methods for cotton yield prediction, such as the use of a yield detector mounted on the cotton picker (Pelletier et al., 2019), yield estimation based on crop growth models (Masasi et al., 2020), and yield monitoring realized based on multi-source satellite data (Meng et al., 2019). Compared to traditional methods, remote sensing methods are more economical and effective when it comes to cotton yield monitoring. However, existing remote sensing for crop yield monitoring has shortcomings such as a large amount of data, difficulty in data processing, or limitations in terms of resolution. With the development of remote sensing technology, unmanned aerial vehicle (UAV) low-altitude remote sensing platforms have become increasingly popular in the development of precision agriculture (Tsouros et al., 2019), At present, unmanned aerial vehicles can carry more sensors, such as hyperspectral, thermal image, RGB images, and LiDAR (Maddikunta et al., 2021). Compared with satellite remote sensing, UAV remote sensing platforms have strong flexibility, low cost, small atmospheric impact, and relatively high spatial and temporal resolution. Relevant researchers have studied the relationship between remote sensing information obtained by drones and crop yields. Tao et al. (2020) showed that the partial least squares regression (PLSR) allows the accurate estimation of crop yield from hyperspectral remote sensing data, and the combination of the vegetation indices and plant height allows the most accurate yield estimation. Maimaitijiang et al. (2020) used a UAV equipped with three sensors (RGB, multispectral, and thermal) to obtain remote sensing data, and a deep neural network framework was used to achieve multi-modal data fusion, to forecast soybean yield and effectively improve the accuracy of the prediction model.

At present, digital imagery provides the easiest and most common image information. The cost of RGB information acquisition is also very low, and it has been widely used in crop monitoring (Yamaguchi et al., 2021). Among the sensors typically carried by UAVs, RGB cameras have the advantages of small size, high resolution, and simple operation. RGB imagery can record the brightness digital number (DN) value of red, green, and blue wave segments, and color space conversion can be carried out according to this, and vegetation indices can be calculated. Compared with a spectral image or multi-source data fusion, RGB imagery is associated with a small amount of data and is easy to process. It is more beneficial to reduce the cost and complexity of monitoring, by obtaining RGB images with a UAV and fully mining the image information. Previous studies have extracted vegetation indices from RGB imagery to realize crop monitoring. For example, cotton yield monitoring research has been based on unmanned aerial vehicle multi-sensor realization (Feng et al., 2020)，extracting the boll number from RGB imagery (Yeom et al., 2018); the cotton pixels were then separated using image processing technique and k-means with 5 class (Maja et al., 2016), or base UAV visible light remote sensing images extracted boll opening pixel percentage, and vegetation indices during the blooming period were used for estimating single boll weight (Xu et al., 2020). Most of the existing researches are based on image processing technology and need large amount of calculation and high hardware requirements. However, direct monitoring of cotton yield through the use of the visible vegetation indices combined with texture features has been studied less.

Vegetation indices, calculated based on visible and near infrared spectra, will appear to be saturated when the vegetation coverage is high during the growth stage of crops (Yue et al., 2019). Vegetation indices constructed based on RGB imagery also encounter the same problem, as they are calculated based on the brightness values of the R, G, and B bands only, less information, and small changes in vegetation indices. RGB images can be subjected to color space conversion and texture feature calculation. In the current research, mostly in the ground scale are by converting the color space achieved background segmentation and classification (Mao et al., 2020; Riehle et al., 2020). But there is a lack of research on monitoring cotton yield with different color space models at the ground scale. In addition, considering the centimeter-level high-resolution RGB images obtained by UAVs, the fusion of texture features and color features can lead to information complementarity and extracting more meaningful information from the imagery. Previous studies have shown that image texture features extracted based on gray level co-occurrence matrix (GLMC) are effective in nitrogen content estimation (Zheng et al., 2020) and the classification of diseases (Kurale and Vaidya, 2018), the results of which showed good performance.

There have been a lot of studies on cotton yield estimation using low-altitude UAV remote sensing, but few of them have utilized deep mining for RGB images. However, in terms of crop growth monitoring, (Yue et al., 2019) high-resolution RGB images and texture features obtained by UAV were used to monitor wheat biomass. Fernandez-Gallego (Fernandez-Gallego et al., 2019) estimated wheat yield using visible vegetation indices and color space. Therefore, in this study, UAV was used to obtain high-resolution RGB images from which vegetation index, texture features were extracted and converted color space model, and

their combination were used to estimate cotton yield before harvest. Provide technical support for mechanical cotton harvesting and accurate management.

MATERIALS AND METHODS

Experimental Design and Yield Investigation

For this study, a field experiment was carried out at the Shihezi University Teaching and Testing Ground, Shihezi, Xinjiang, China (**Figure 1**; 44°19′N, 85°59′E; altitude, 443 m). The study area is characterized by a temperate continental climate, in an arid and semiarid region, with an average annual precipitation of 125.9–207.7 mm, a large temperature difference between day and night, and a high soil nutrient content in the test area. Two local varieties of cotton (Xinluzao 50 and Xinluzao 33) were planted for two years (in 2019 and 2020). Six groups were planted per year, as shown in **Figure 1D**. Two cotton varieties, four defoliant concentrations, and six application time treatments were used to increase the yield differences. Taking Xinluzao 50 and Xinluzao 33, the main cotton varieties in the Xinjiang region, as the research objects, the defoliant concentration treatment included C1: clear water (CK); C2: defoliant 150 ml•hm^{-2} + special additives 750 ml•hm^{-2} + ethephon 1.2 l•hm^{-2}; C3: defoliant 300 ml•hm^{-2} + special additives 750 ml•hm^{-2} + ethephon 1.2 l•hm^{-2}; and C4: defoliant 450 ml•hm^{-2} + special additives 750 ml•hm^{-2} + ethephon 1.2 l•hm^{-2}. A defoliant (Total active ingredient content, 540 g•L^{-1}; diuron content, 180 g•L^{-1}; thidiazuron content, 360 g•L^{-1}, as a suspension agent) and special auxiliaries by the materials company Bayer AG production were used in this test. Defoliant was sprayed on August 20 (T1), August 23 (T2), August 30 (T3), September 7 (T4), September 14 (T5), and September 21 (T6) as shown in **Figure 1D.** Cotton was harvested after different defoliant spraying times and concentrations. Defoliant concentration tests (C1, C2, C3, and C4) of different varieties of cotton were carried out in the six experimental groups under the different spraying time treatments (T1, T2, T3, T4, T5, and T6). Theoretical yield investigation was carried out on the 3rd, 6th, 9th, 12th, and 15th days after the application of defoliant in the cotton opening period and before harvest. Yield per unit area was calculated by counting the number of bolls at the opening and the weight of a single boll in each plot. The single boll weight used in this study is the average weight calculated by selecting ten consecutive cotton plants in each plot (2.5 m*10 m), investigating their yield and boll number as given in equation (1).

$$single\ boll\ weight = \frac{10\ plants\ yield}{10\ plants\ boll\ number} \quad (1)$$

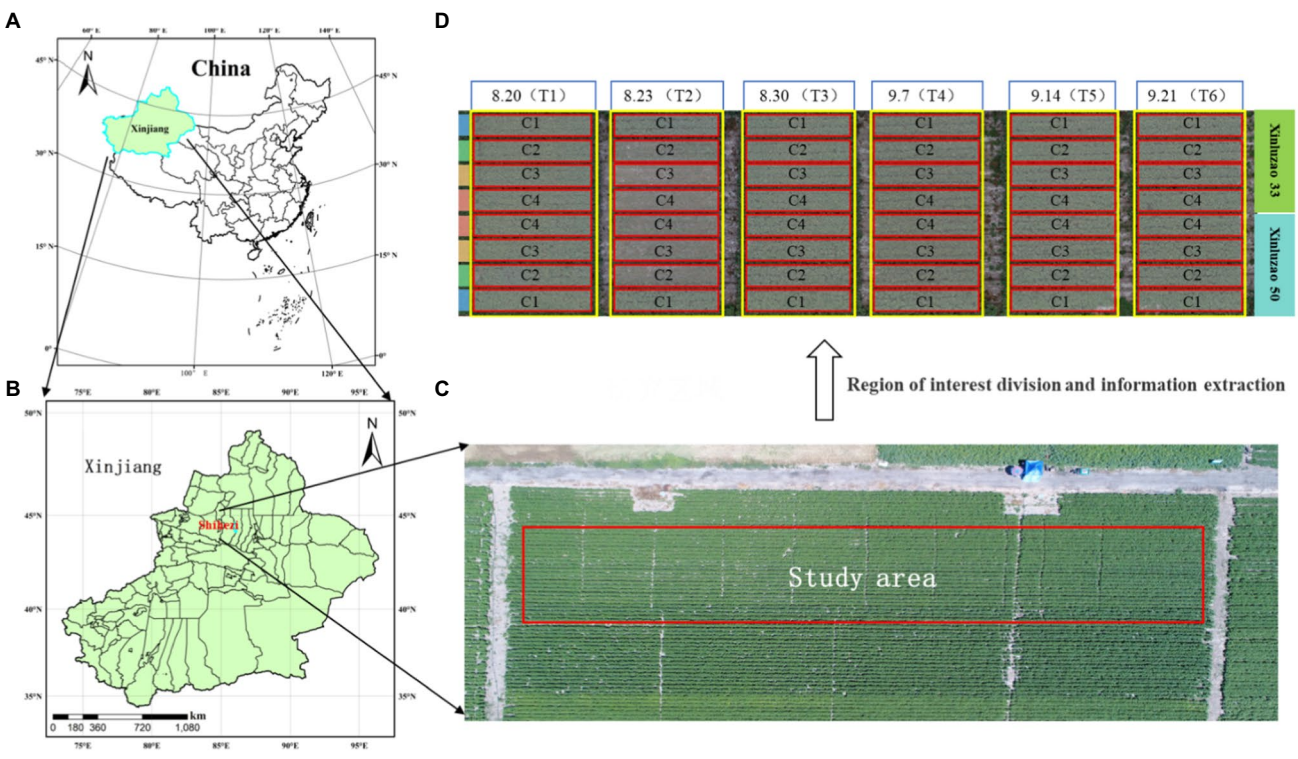

FIGURE 1 | Study area and experimental design: cotton experiment at Shihezi University Teaching and Testing Ground, Shihezi, Xinjiang, China in 2019–2020. Experimental including two local varieties of cotton. C1, C2, C3, and C4 denote different defoliant concentrations. T1–T3 denote different sprayed times. **(A)** Geographical location of Xinjiang; **(B)** Geographical location of Shihezi; **(C)** Study area; **(D)** Experimental design.

$$Theoretical\ yield = sigle\ boll\ weight \times boll\ number \quad (2)$$

UAV Canopy RGB Image Data Collection and Processing

Before the cotton harvest, the Phantom 4 Advanced Aerial Photography UAV (Shenzhen, DJI, China) was used to capture high resolution color images of the entire experimental area. The drone image acquisition was done between 12:00 PM and 1:00 PM. During image acquisition, the camera (sensor size 5,472 × 3,648 pixels) was set to be vertically downward and set to equal time intervals. The flight height was set as 10 m above ground, with forward and side overlap set to 80%, the camera shutter time was 1/240 s, and the ISO value was 100. A total of 387 images were obtained from the experimental area. These images were stitched into orthophotographs with the Pix4D Mapper software (Pix4D, Switzerland), and stored in a TIFF format. The orthomosaics retain the gray-scale information of red, green, and blue colors of the ground objects. Each color contained 8-bit information, with a numerical range from 0 to 255. According to the plots distribution, the stitched cotton field image was cut into 48 regions of interest.

Feature Extraction and Analysis of RGB Images

Extraction of Vegetation Indices

Some color space models and vegetation indices based on RGB were selected from previous studies (**Table 1**). The region of interest (ROI) is divided based on each test cell, and DN values of the three colors (red, green, and blue) were included for orthomosaics. We used MATLAB 2019A to obtain the DN values of three color channels, calculate the average DN value of each color channel, and calculate the normalized value of the three colors (R, G, and B), to calculate the vegetation indices. The equations used to calculate normalized values and vegetation indices are shown in **Table 1**.

The color features of each divided ROI were converted from RGB color space model to HSV, and LA * B *, and YIQ were calculated based on corresponding functions in MATLAB. YCrCb model conversion formula are shown in **Table 1**.

Spatial Features: Texture Features Based on Gray-Scale Co-occurrence Matrix (GLMC)

Ultra-high-resolution images (ground resolution of 0.3 cm/pixel) were obtained from a UAV flying at an altitude of 10 meters above ground level. Four texture features were calculated from four different angles (0°, 45°, 90°, and 135°), based on the gray-level co-occurrence matrix (GLMC), and the average value of the four texture features was obtained. The three bands of the RGB image were calculated as gray values, and then, the texture features were calculated. The texture features were calculated using the following equations:

$$Asm = \sum_i \sum_j P(i,j)^2 \quad (3)$$

$$Ent = \sum_i \sum_j P(i,j) log P(i,j) \quad (4)$$

$$Con = \sum_i \sum_j (i,j)^2 P(i,j) \quad (5)$$

$$Cor = \frac{\sum_i \sum_j (i,j) P(i,j) - \mu_x \mu_y}{\sigma_x \sigma_y} \quad (6)$$

Construction and Evaluation of Cotton Yield Estimation Model

The flowchart shown in **Figure 2** illustrates the experimental methods of this study, including field data collection, feature selection, model construction, and validation. In this study, vegetation indices and texture features, alone or combined, were used to estimate cotton yield. To further study the estimation accuracy of the yield estimation model, the cross-validation method was used to divide the data into training and validation datasets, with 315 samples for the 199 training dataset and 116 samples for the validation dataset. The descriptive statistics are shown in **Table 2**. There are significant differences between the data of training set and validation set.

Optimal Feature Parameter Screening

The four methods of correlation, maximum information coefficient (MIC), random forest (RF), and recursive feature elimination (RFE) were adopted to select the optimal feature parameters for the model establishment, respectively, to eliminate the obvious collinearity among the parameters. The above methods are based on Python3.8 sklearn library. Parameter screening probability is to normalize the scores given by each method so that the values fall between 0 and 1.

Model

In the current research, the methods for establishing the relationship between remote sensing information and agricultural parameters mainly include three types: physical, statistical, and semiempirical models. In this study, a statistical model was established to achieve cotton yield monitoring. The statistical model mainly analyzed the correlation between the obtained UAV data and the measured output on the ground, and establishes regression models, including linear and nonlinear models. The linear regression model is fast and simple. Each characteristic variable can obtain a fixed weight, but the model structure is fixed and immutable. The nonlinear model is flexible, has a strong monitoring ability, and can eliminate certain collinearity; however, there is no fixed weight for each characteristic variable, it requires a large amount of data, takes a long time to calculate, and the output is a model framework, rather than a fixed formula. For this study, three linear regression methods were selected: partial least squares regression (PLSR), elastic neural network (Elastic Net), and kernel ridge regression (KRR). Three nonlinear regression methods were used to

TABLE 1 | Review of the color space and vegetation indices used in this study.

Data type	Band and vegetation indices	Equations	References
Color space	R	DN value of the red band	
	G	DN value of the green band	
	B	DN value of the blue band	
	R	$r = \frac{R}{(R+G+B)}$	
	G	$g = \frac{G}{(R+G+B)}$	
	B	$b = \frac{B}{(R+G+B)}$	
	Y	$Y = 0.299R + 0.587G + 0.114B$	
	Cb	$Cb = 0.568(B-Y)+128$	
	Cr	$Cr = 0.713(R-Y)+128$	
	U	$U = 0.493(B-Y2))$	
Vegetation indices	NGRDI	$\mathrm{NGRDI} = (g-r)/(g+r)$	Hamuda et al., 2016
	MGRVI	$MGRVI = \frac{(g^2-r^2)}{(g^2+r^2)}$	Bendig et al., 2015
	RGBVI	$RGBVI = \frac{(g^2-br)}{(g^2+br)}$	Bendig et al., 2015
	NDI	$NDI = \frac{(r-g)}{(r+g+0.01)}$	Hamuda et al., 2016
	VARI	$VARI = \frac{(g-r)}{(g+r-b)}$	Gitelson et al., 2002
	WI	$WI = \frac{(g-b)}{(r-g)}$	Bendig et al., 2015
	CIVE	$CIVE = 0.441r - 0.881g + 0.385b + 18.78745$	Kataoka et al., 2003
	GLA	$GLA = \frac{(2G-B-R)}{(2G+B+R)}$	Chianucci et al., 2016
	ExG	$ExG = 2g - b - r$	Hamuda et al., 2016
	ExR	$ExR = 1.4r - g$	Hamuda et al., 2016
	ExGR	$ExGR = 3g - 2.4r - b$	Hamuda et al., 2016
	GLI	$GLI = \frac{(2g-b-r)}{(2g+b+r)}$	Louhaichi et al., 2001
	NGBDI	$RGBVI = \frac{(g-b)}{(g+b)}$	Hunt et al., 2005

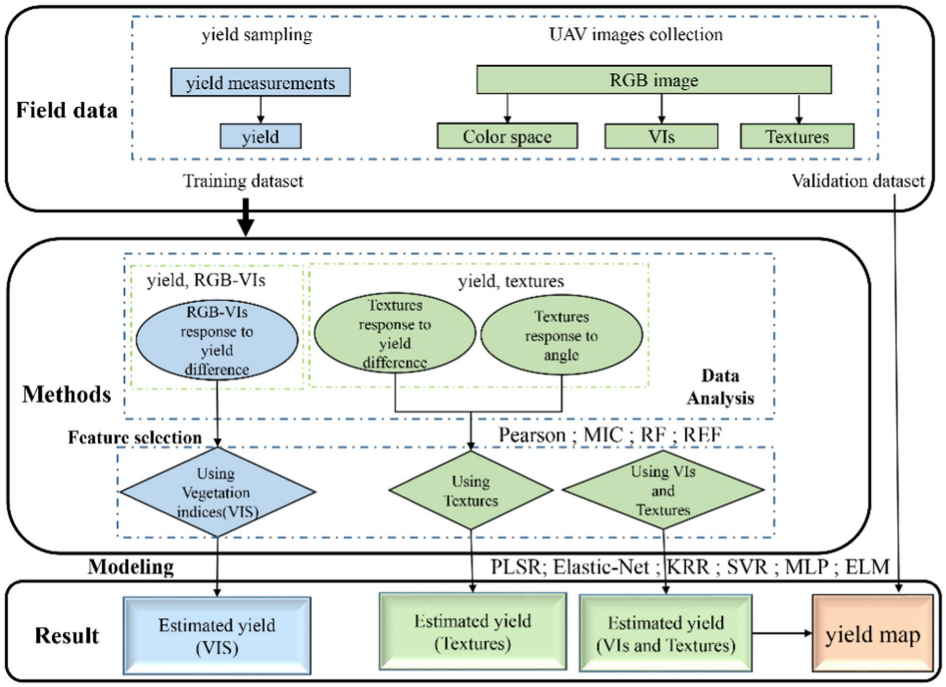

FIGURE 2 | This study involves the flowchart of data acquisition, data processing, and model construction.

TABLE 2 | Cotton yield descriptive statistics.

Dataset	Samples	Min (t.ha^{-1})	Mean (t.ha^{-1})	Max (t.ha^{-1})	Standard deviation (t.ha^{-1})	Coefficient of variation(%)
Training set	199	0.00	3.00	11.58	2.91	97.08%
Validation dataset	116	0.00	3.08	9.83	2.75	89.25%

establish the cotton yield monitoring model: support vector regression (SVR), multilayer perceptron (MLP), and extreme Learning Machine (ELM). The above methods are based on Python3.8 sklearn library, and GridSearchCV of sklearn library is used to optimize model parameters.

Precision Evaluation

In this study, the coefficient of determination (R^2), root-mean-square error (RMSE), and relative root-mean-square error (rRMSE) were used to evaluate the model performance. Higher R^2 and smaller RMSE, rRMSE, denote higher model precision, accuracy, and stability. Those metrics were calculated as follows:

$$R^2 = \frac{\sum_{i=1}^{n}(x_i - \bar{x})2(y_i - \bar{y})2}{n\sum_{i=1}^{n}(x_i - \bar{x})2n\sum_{i=1}^{n}(y_i - \bar{y})2} \quad (7)$$

$$\mathrm{RMSE} = \sqrt{\frac{1}{n}\sum_{i=1}^{n}(y_i - x_i)2} \quad (8)$$

$$rRMSE = \frac{RMSE}{\bar{x}} \quad (9)$$

where i represents the data of the i th sample point; x_i is the measured value of the cotton yield for the i th sample point (in t.ha^{-1}); y_i is the predicted cotton yield value at sample point i, estimated according to the model (in t.ha^{-1}); $\bar{x}$ is the average value of measured cotton yield (in t.ha^{-1}); and $\bar{y}$ is the average value of cotton yield estimated by the model (in t.ha^{-1}).

RESULTS

Relationship Between Vegetation Indices, Texture Characteristics, and Yield

The red area represents a positive correlation, the blue area represents a negative correlation, and the lighter the color, the weaker the correlation. As shown in **Figure 3**, cotton yield was most correlated with NDI, NGRDI and MGRVI, with the correlation being 0.55, −0.55, and − 0.55, respectively.

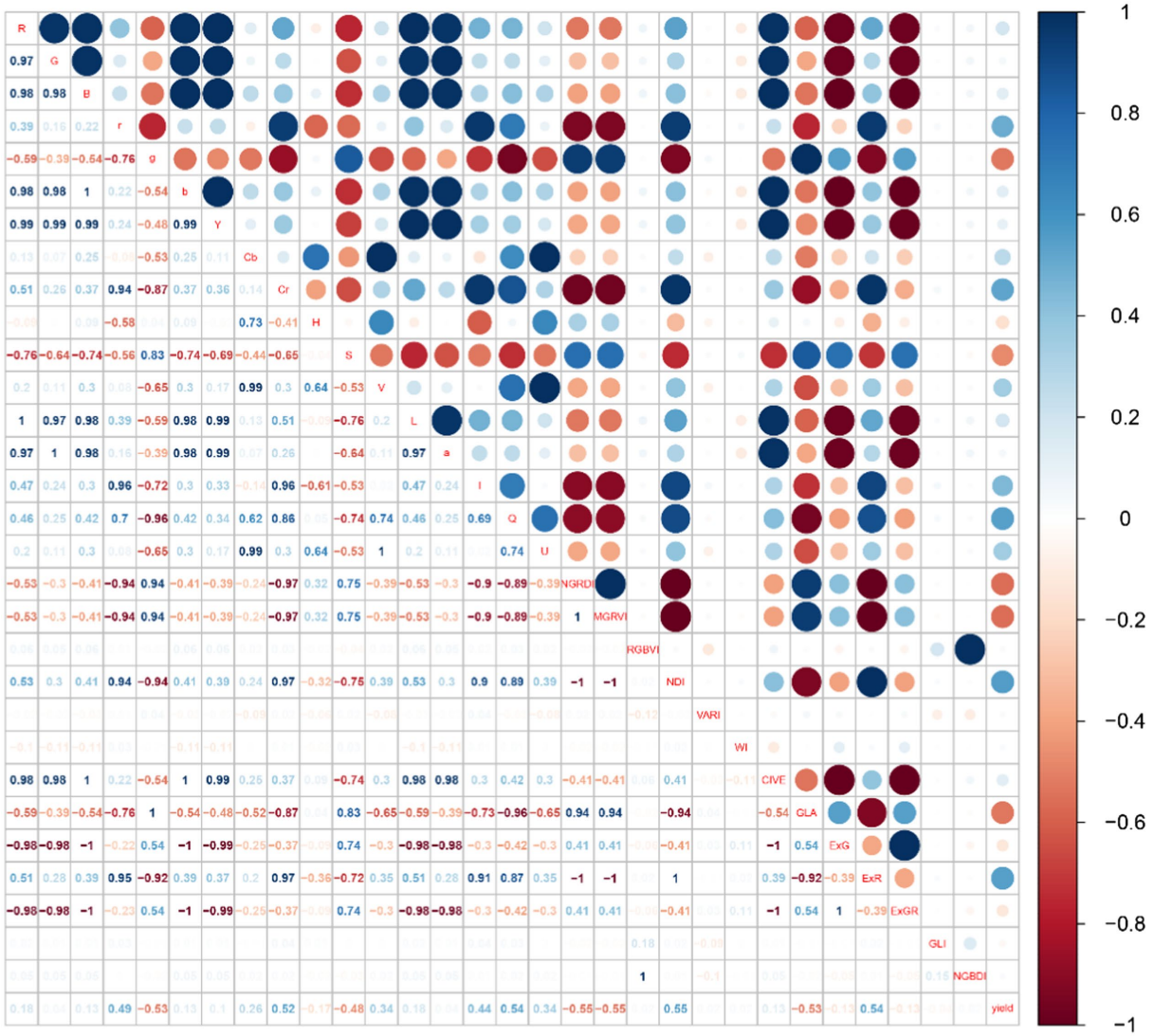

FIGURE 3 | Correlation between different vegetation indices and cotton yield.

But there is serious collinearity among the three. As shown in **Figure 4**, cotton yield is positively correlated with ASM and COR at different angles, and negatively correlated with Ent and Con at different angles. The correlation with CON-SD was −0.51, indicating that with the increase in yield, the difference of Con in different directions became smaller and smaller. The distribution of image texture features is more and more uniform. Collinearity between texture features is also strong.

Feature Selection

To effectively eliminate the collinearity among variables and accurately estimate cotton yield, the optimal features were found from vegetation indices and texture features, based on the correlation coefficient, MIC, RF, and RFE. Then, different machine learning models were established, based on the six optimal features. **Figure 5** shows the screening results of each method, in which the red bar indicates the optimal feature selected, and the feature parameters selected from each screening method are different. In combination with **Figures 3, 4**, it can be seen that the correlation between the characteristic parameters selected by RF was the lowest.

Estimation of Cotton Yield Based on Vegetation Indices

Table 3 shows the results of linear regression (PLSR, Elastic-Net, and KRR) and nonlinear regression (SVR, MLP, and ELM) monitoring models based only on vegetation indices. **Figure 6** shows the fitting relationship between measured and predicted values of the model training and validation sets. The results showed that: (1) In the linear regression model, the RF_KRR model performed the best, the training set R^2 was 0.6087,

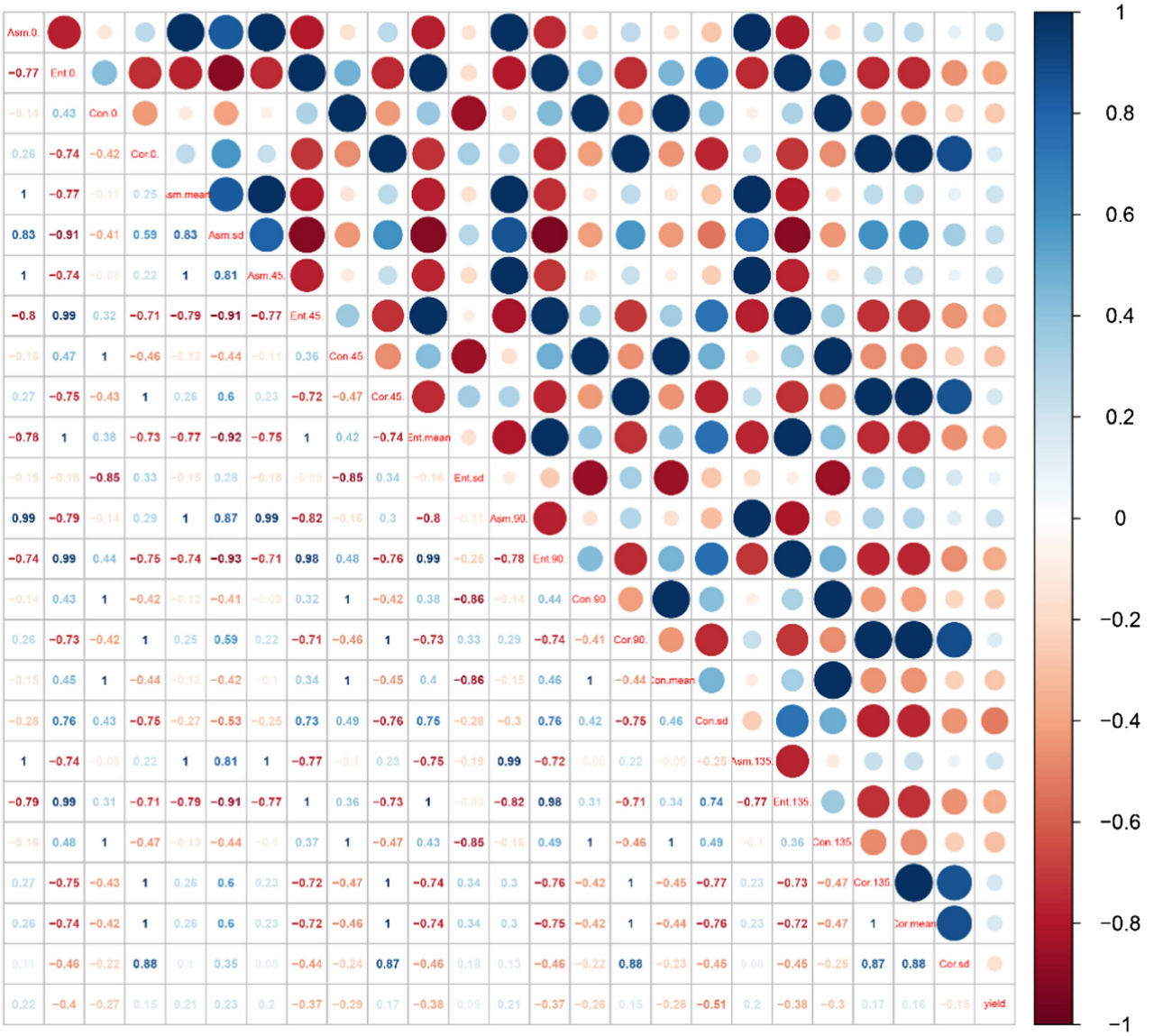

FIGURE 4 | Correlation between different texture characteristics and cotton yield.

the RMSE was 1.7156 t.ha^{-1}, and the rRMSE was 60.95%. But the verification set R^2 only 0.3884, the RMSE was 2.4805 t. ha^{-1}, and the rRMSE was 71.46%, among which. In the nonlinear regression models, the RFE_ELM model had the best effect. Training set $R^2 = 0.7310$, RMSE = 1.4285 t.ha^{-1}, rRMSE = 47.57%. The verification set $R^2 = 0.7244$, the RMSE = 1.4418 t.ha^{-1}, and the rRMSE = 49.23%, where the nonlinear models were better than the linear models, and the best model was the RFE_ELM model (2) **Figure 7** shows the yield estimation model based on vegetation indices underestimated the high yield samples; the higher the yield, the worse the estimation ability. RFE_ELM effectively improved the estimation accuracy of high yield samples and, thus, improved the accuracy of the model.

Cotton Yield Estimation Based on Texture Features

Table 4 shows the R^2, RMSE, and rRMSE of the monitoring model using only texture features, based on linear regression (PLSR, Elastic-Net, KRR) and nonlinear regression (SVR, MLP, ELM) methods. **Figure 8** shows the results indicated that: (1) The optimal linear regression model was the RF_ KRR model (training set $R^2 = 0.6004$, RMSE = 1.7164 t.ha^{-1}, rRMSE = 60.97%; verification set $R^2 = 0.5858$, RMSE = 2.0112 t. ha^{-1}, rRMSE = 57.97%), while the optimal nonlinear regression model was the RFE_ELM model (training set $R^2 = 0.8619$, RMSE = 1.0941 t.ha^{-1}, rRMSE = 38.46%; verification set $R^2 = 0.8379$, RMSE = 1.1705 t.ha^{-1}, rRMSE = 34.54%). Furthermore, the best nonlinear model was better than the

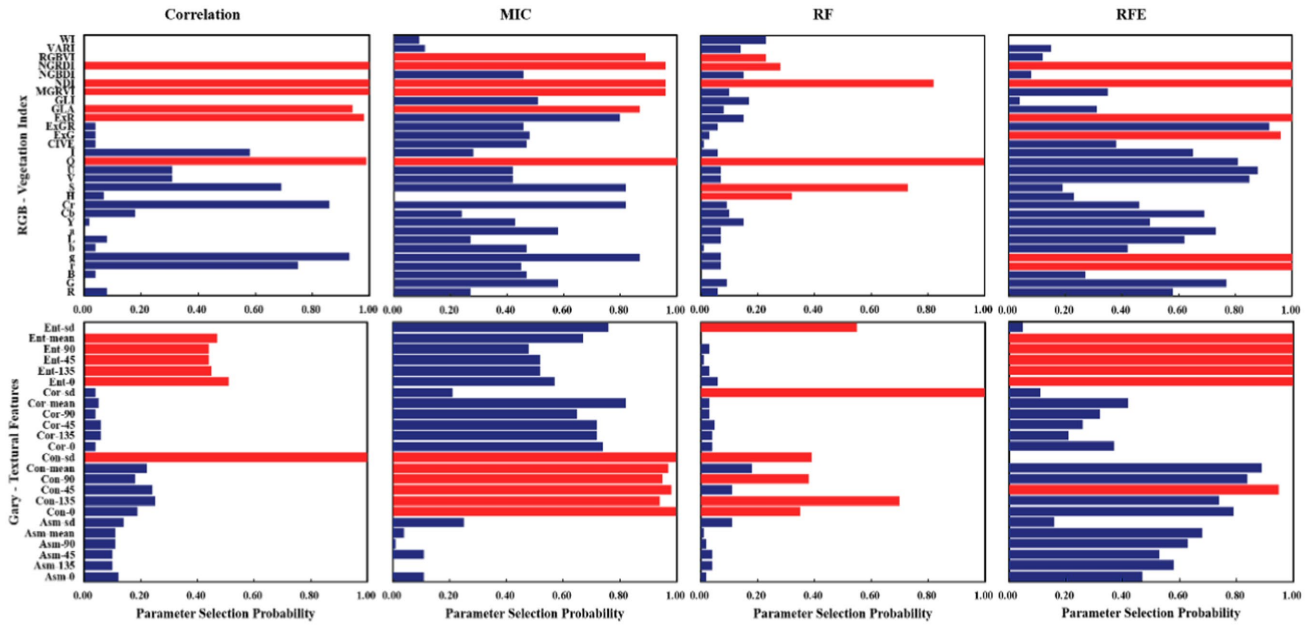

FIGURE 5 | Optimal feature selection based on different screening methods.

best linear model (2) **Figure 9** shows fitting relationship between the predicted and measured values of the training set and the verification set of the monitoring model. The yield estimation model based on texture features underestimated the high yield samples, but the effect was better than that of the yield estimation model based on vegetation indices.

Cotton Yield Estimation Based on Vegetation Indices and Texture Features

Table 5 shows the results of establishing linear and nonlinear regression monitoring models by selecting the three vegetation indices and texture features with the highest selection probability as feature parameters. **Figure 10** shows the results indicated that: (1) In the linear regression models, the training set R^2 was 0.4306–0.7250, the RMSE was 2.0754–1.4283 t.ha^{-1}, and the rRMSE was 73.73–50.74%, while the verification set R^2 was 0.3348–0.6184, the RMSE was 2.5277–1.9348 t.ha^{-1}, and the rRMSE was 72.82–55.74%, where the best model was RF_KRR. In the nonlinear regression models, the training set R^2 was 0.3706–0.9316, the RMSE was 2.1631–0.7279 t.ha^{-1}, and the rRMSE was 76.84–25.88%, while the verification set R^2 was 0.3947–0.9109, the RMSE was 2.4377–0.9127 t.ha^{-1}, and the rRMSE was 70.23–29.34%, among which the best model was the RFE_ELM model (2) **Figure 11** shows the fitting results of measured and predicted values on the training and validation sets for the monitoring model, the yield estimation model based on vegetation indices and texture features underestimated the high yield samples, but the effect was better than that based on vegetation indices.

Cotton Yield Inversion Map Based on UAV RGB Image

Based on the UAV RGB images covering 48 plots, vegetation indices and texture features were extracted, and the linear and nonlinear models with the best results (as described above) were selected for preharvest yield inversion. The results showed that the best linear model, RF_KRR, was able to monitoring the yields of <3.62 t.ha^{-1} accurately when estimating plots with low yield. However, as the yield increased gradually, the monitoring accuracy became lower and lower, and the yield of high-yielding plots was significantly underestimated such that yields greater than 8.33 t.ha^{-1} were not estimated. As for the RFE_ELM model, the estimation performance was better than that of the RF_KRR model, and its estimation results were similar to the measured values; however, yields <3.63 t. ha^{-1} were overestimated (**Supplementary Figure 1**).

DISCUSSION

At present, crop yield estimation based on remote sensing means is mainly realized based on satellite remote sensing data or unmanned aerial vehicles carrying multiple sensors. However, these methods have some limitations, mainly regarding the following aspects: (1) the resolution of satellite imagery is too course for that kind of application; and (2) multiple sensors acquire more information and, therefore, capture a large amount of redundant data, might require both large volume of hard drive space for storage and large amount of computer power to process the data. Therefore, for this study, we used an unmanned aerial vehicle carrying an RGB camera

TABLE 3 | Cotton yield estimation based on vegetation indices.

Feature selection	Data set	PLSR			Elastic-Net			KRR			SVR			MLP			ELM		
		R^2	RMSE ($t.ha^{-1}$)	rRMSE (%)	R^2	RMSE ($t.ha^{-1}$)	rRMSE (%)	R^2	RMSE ($t.ha^{-1}$)	rRMSE (%)	R^2	RMSE ($t.ha^{-1}$)	rRMSE (%)	R^2	RMSE ($t.ha^{-1}$)	rRMSE (%)	R^2	RMSE ($t.ha^{-1}$)	rRMSE (%)
P	Cal	0.35	2.1833	77.56	0.34	2.2054	78.35	0.47	1.9694	69.96	0.38	2.1379	75.45	0.37	2.1512	76.42	0.56	1.8191	63.70
	Val	0.26	2.6585	76.59	0.27	2.6521	76.41	0.32	2.5701	74.04	0.28	2.6446	76.19	0.26	2.6484	76.30	0.52	2.0215	65.55
MIC	Cal	0.36	2.1768	77.33	0.35	2.1960	78.01	0.50	1.9288	68.52	0.38	2.1374	75.93	0.3	2.1600	76.73	0.67	1.5799	55.89
	Val	0.26	2.6597	76.62	0.27	2.6538	76.46	0.32	2.5866	74.52	0.27	2.6573	76.56	0.23	2.7400	78.94	0.61	1.7314	57.55
RF	Cal	0.36	2.1675	77.00	0.36	2.1836	77.57	**0.61**	**1.7156**	**60.95**	0.43	2.0644	73.34	0.43	2.0475	72.74	0.56	1.8812	63.04
	Val	0.29	2.6074	75.12	0.30	2.6120	75.25	**0.39**	**2.4805**	**71.46**	0.36	2.5325	72.96	0.33	2.5268	72.80	0.41	2.1842	69.46
RFE	Cal	0.37	2.1531	76.49	0.36	2.1819	77.51	0.56	1.8106	64.32	0.47	1.9710	70.02	0.50	1.9305	68.58	**0.73**	**1.4285**	**47.57**
	Val	0.27	2.6515	76.39	0.27	2.6559	76.52	0.39	2.4342	70.13	0.32	2.5926	74.69	0.33	2.5404	78.19	**0.72**	**1.4418**	**49.23**

The values in bold represent models with the best results in linear and nonlinear methods.

to obtain digital images with a high ground resolution and extracted vegetation indices and texture features to estimate cotton yield.

Crop yield monitoring is very important in crop management. Many studies have been devoted to using different methods to improve the accuracy of yield estimation models. Commonly used methods include establishing the model through vegetation indices (Zhang et al., 2020), multi-sensor monitoring (Feng et al., 2020), or deep learning (Escalante et al., 2019). RGB images are the most common type of image in daily life, which are characterized by simple acquisition and easy processing. More and more RGB images have been used for yield monitoring. Although these methods can effectively improve the accuracy of the yield estimation model, there is still room for improvement; for example, Liu et al. (2019) used the vegetation indices extracted from RGB imagery of a rice canopy to estimate its yield. The accuracy R^2 of the model was improved, but only reached 0.7074. Fathipoor et al. (2019) used UAV RGB imagery to estimate forage yield, and the verification accuracy of their estimation model was 0.74, with a relative RMSE of 12.39%. In this paper, the RFE_ELM model was found to be the best model to estimate the yield through the use of vegetation indices, with $R^2 = 0.7310$, RMSE = 1.4285, and rRMSE = 47.57% on the training set, and $R^2 = 0.7244$, RMSE = 1.4418, and rRMSE = 49.23% on the verification set, similar to the results of (Huang et al., 2016), who used UAV RGB imagery to extract plant height and count the number of cotton bolls to estimate cotton yield. However, the accuracy was significantly lower than that of the cotton yield monitoring model established by Feng et al. (2020) using multi-sensor imagery. In this paper, the vegetation indices extracted from the UAV RGB imagery were significantly correlated with the cotton yield, such that it is feasible to select the optimal parameter features for cotton yield monitoring; however, this still needs to be improved from the perspective of model accuracy. Therefore, more texture feature information or other color information should be mined from RGB imagery, to improve model accuracy.

Texture features are an important parameter of RGB imagery, for which there exist many extraction methods. GLCM is the most commonly used and effective extraction method. In this paper, GLCM was used to obtain four texture features at different angles (0°, 45°, 90°, and 135°). **Figure 2** shows that different cotton canopy grey values in the RGB imagery were used to extract texture features, some of which had significant correlations with cotton yield, where the difference had a significant correlation between different perspectives on the same parameters, namely according to different cotton canopy RGB image texture feature dependencies. This differed from the results of Zhang et al. (2017), in their study on satellite remote sensing texture feature extraction, and those of Zheng et al. (2020), who estimated nitrogen content in rice leaves by using an unmanned aerial vehicle to obtain multispectral images. As shown in **Supplementary Figure 2**, as we used a UAV with a flying height of 10 meters to capture high-resolution RGB images, no significant difference was found between each pixel, and we could select the ROI in an image, under the

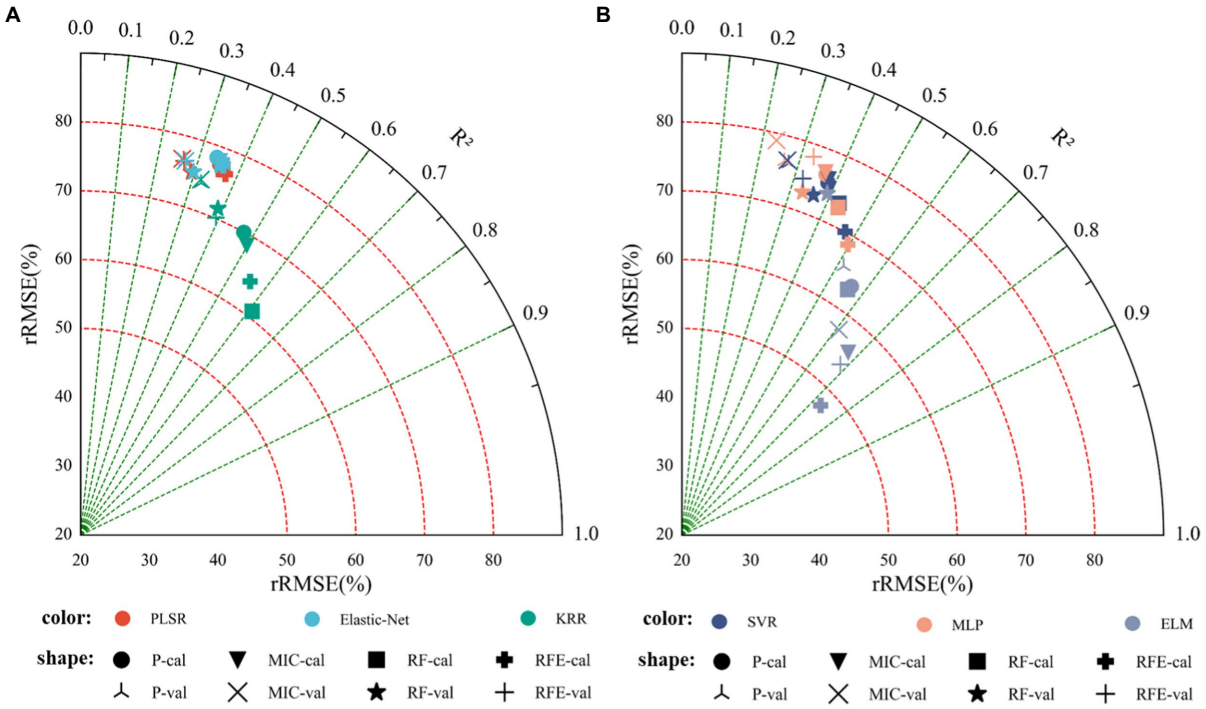

FIGURE 6 | Monitoring model result of cotton yield based on the visible vegetation indices (Note: P denotes feature parameters screened out based on Pearson's correlation coefficient, cal denotes training set; val denotes validation set. **(A)** Modeling results based on linear regression, **(B)** modeling results based on nonlinear regression).

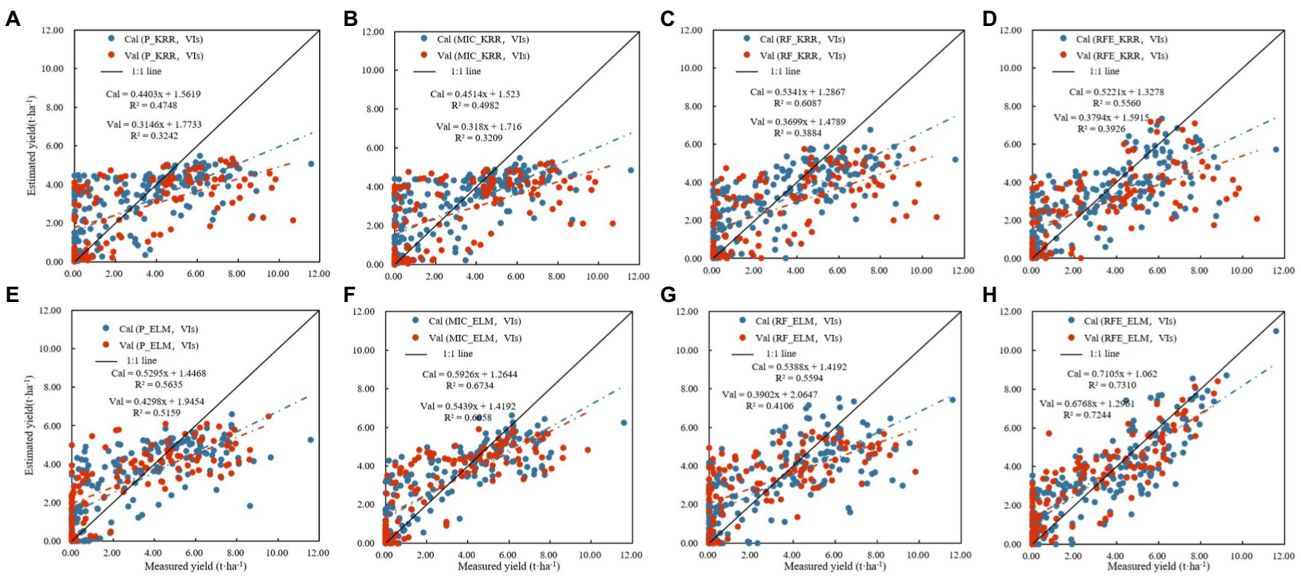

FIGURE 7 | Cotton yield estimation models established by best performing based on the visible vegetation indices by using the linear and nonlinear models (Note: **(A)** P_KRR model; **(B)** MIC_KRR model; **(C)** RF_KRR model; **(D)** RFE_KRR model; **(E)** P_ELM model; **(F)** MIC_ELM model; **(G)** MIC_ELM model; **(H)** RFE_ELM model).

same processing. This was because where cotton planting density was higher, the canopy distribution was relatively uniform. However, in the study by Zhang et al. (2017), the satellite image separation rate was high, the difference between each pixel was obvious, and the distribution of image feature information was uneven. In the study of Zheng et al. (2020), the UAV flew at a height of 100 m and the selected area was multi-row, such that there was a difference in crop distribution

TABLE 4 | Cotton yield estimation results based on texture features.

Feature selection	Data set	PLSR			Elastic-Net			KRR			SVR			MLP			ELM		
		R^2	RMSE ($t.ha^{-1}$)	rRMSE (%)	R^2	RMSE ($t.ha^{-1}$)	rRMSE (%)	R^2	RMSE ($t.ha^{-1}$)	rRMSE (%)	R^2	RMSE ($t.ha^{-1}$)	rRMSE (%)	R^2	RMSE ($t.ha^{-1}$)	rRMSE (%)	R^2	RMSE ($t.ha^{-1}$)	rRMSE (%)
P	Cal	0.29	2.2891	81.32	0.28	2.3116	82.12	0.43	2.0515	72.88	0.33	2.2290	79.19	0.30	2.2644	80.44	0.72	1.4666	50.09
	Val	0.27	2.6575	76.56	0.24	2.7222	78.43	0.41	2.3907	68.88	0.33	2.5235	72.70	0.24	2.6975	77.72	0.67	1.5518	57.96
MIC	Cal	0.28	2.2989	81.67	0.28	2.3107	82.09	0.31	2.2599	80.28	0.30	2.2868	81.24	0.29	2.2897	81.34	0.66	1.7020	53.09
	Val	0.25	2.6807	77.23	0.25	2.7053	77.94	0.36	2.5190	72.57	0.33	2.5240	72.72	0.29	2.6043	75.03	0.57	1.8765	56.86
RF	Cal	0.52	1.8897	67.13	0.50	1.9702	67.00	**0.60**	**1.7164**	**60.97**	0.57	1.7760	63.09	0.57	1.7789	63.19	0.77	1.3601	42.93
	Val	0.44	2.3066	66.45	0.43	2.3906	68.87	**0.59**	**2.0112**	**57.94**	0.58	2.0398	58.77	0.54	2.0940	60.33	0.74	1.4065	44.42
RFE	Cal	0.22	2.4007	85.28	0.20	2.4267	86.21	0.38	2.1502	76.38	0.24	2.3826	84.68	0.24	2.3685	84.14	**0.86**	**1.0941**	**38.46**
	Val	0.16	2.8485	82.07	0.12	2.9104	83.85	0.34	2.5443	73.30	0.18	2.8473	82.03	0.17	2.8186	81.20	**0.83**	**1.1705**	**34.54**

The values in bold represent models with the best results in linear and nonlinear methods.

due to the planting mode and, so, there was an obvious correlation in a certain direction.

Compared with the three estimation models based on vegetation indices, texture features, and their fusion, as used in this paper, texture features showed better performance than vegetation indices in cotton yield estimation, where the best model was the ELM model. The R^2 increased by 17.91%, the RMSE decreased by 23.41%, and the rRMSE decreased by 19.15%, while for the verification dataset, the R^2 increased by 15.67%, the RMSE decreased by 18.82%, and the rRMSE decreased by 29.84%. However, the performance of the monitoring model based on vegetation indices and texture features was better than that based on either vegetation indices or texture features alone, and the ELM model still performed the best. Compared with the model based on vegetation indices, the modeling results for the combined model, in terms of the R^2, RMSE, and rRMSE, were increased by 27.44, 49.04, and 45.60%, respectively. For the verification dataset, the R^2 increased by 25.75%, the RMSE decreased by 40.93%, and the rRMSE decreased by 35.73%. In conclusion, using both vegetation indices and texture feature information for cotton yield estimation can improve the accuracy of the model. This was similar to the results of Guo et al. (2021a), who monitored wheat yellow rust by using vegetation indices and texture features, and Yue et al. (2019), who estimated winter wheat biomass by using texture features and vegetation indices derived from the gray-scale correlation matrix of canopy imagery. However, in these two studies, the estimation performance when using the vegetation indices was better than that with the texture features. The analysis of vegetation indices and texture characteristics can be sensitive to the growth period, as the cotton leaves fall off gradually, and a more prominent G component (green) change is observed in the image but, in the later growth stage, when the dry leaves fall off, the G component decreases to a constant, while the yield is still changing. Therefore, vegetation indices are insensitive to yield changes associated with such gradual changes. Therefore, models based on vegetation indices tend to underestimate high yield plots, while texture features are calculated based on image gray values, which can effectively reflect the changes in the image feature; however, the dependence on the G component is weak, and the sensitivity to the changes of yield in the later growth period is reduced (but is still better than when using vegetation indices). In this study, the vegetation indices and texture features were combined to compensate for the saturation of vegetation index when the yield was high by virtue of the accuracy of vegetation index texture features in color, so as to improve the accuracy of the model to a certain extent. In previous studies, Zhang et al. (2021) used texture features, color and vegetation index to estimate wheat growth parameters, and also used texture features to compensate for index saturation and effectively improve the accuracy of the model. Zhou et al. (2021) used drones to diagnose water stress in winter wheat. Zhang et al. (2022) also introduced the combination of texture features and vegetation index to improve the model accuracy in the study of maize leaf area index estimation

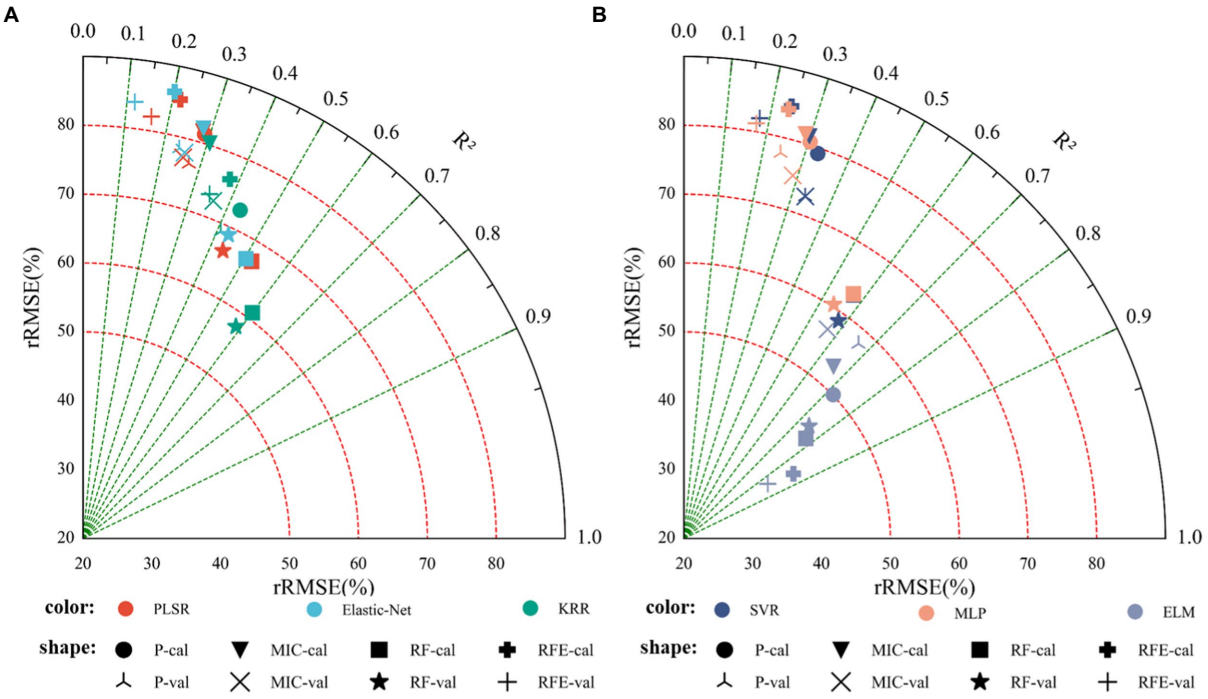

FIGURE 8 | Cotton yield monitoring model based on texture features. **(A)** Modeling results based on linear regression, **(B)** modeling results based on nonlinear regression.

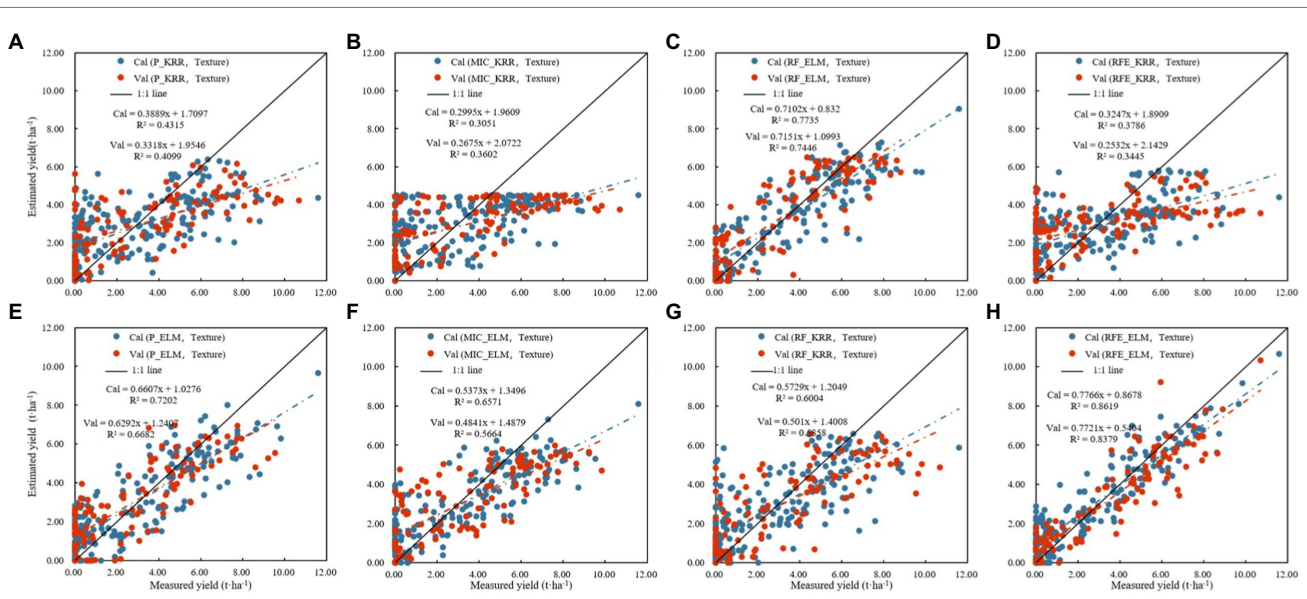

FIGURE 9 | Cotton yield estimation models established by best performing based on the texture features by using the linear and nonlinear models. **(A)** Modeling results based on linear regression, **(B)** modeling results based on nonlinear regression.

by UAV. Combined with the results of this study, it is feasible to improve the accuracy of cotton yield monitoring model by combining vegetation index and texture feature. Combined with the results of this study, it is feasible to improve the accuracy of cotton yield monitoring model by combining vegetation index and texture feature. As shown in **Supplementary Figure 3**, among the models established by integrating different pre-treatment methods, the best linear model was the model established by the KRR method, while the best nonlinear model was the ELM model; among these two, the ELM model had the best performance. This was similar to the results of Guo et al. (2021b), who used machine learning methods to predict rice yield by integrating phenological and meteorological data.

TABLE 5 | Cotton yield estimation results based on vegetation indices and texture features.

Feature selection	Data set	PLSR			Elastic-Net			KRR			SVR			MLP			ELM		
		R^2	RMSE (t.ha^{-1})	rRMSE (%)	R^2	RMSE (t.ha^{-1})	rRMSE (%)	R^2	RMSE (t.ha^{-1})	rRMSE (%)	R^2	RMSE (t.ha^{-1})	rRMSE (%)	R^2	RMSE (t.ha^{-1})	rRMSE (%)	R^2	RMSE (t.ha^{-1})	rRMSE (%)
P	Cal	0.47	1.9824	70.42	0.47	1.9971	70.95	0.55	1.7202	64.66	0.51	1.9044	67.65	0.37	2.1631	76.84	0.75	1.4971	48.48
	Val	0.38	2.4432	70.39	0.38	2.4650	71.02	0.45	2.3235	66.94	0.42	2.3757	68.44	0.39	2.4377	70.23	0.70	1.6364	48.61
MIC	Cal	0.49	1.9446	69.66	0.49	1.9608	69.66	0.59	1.7382	61.75	0.53	1.8661	66.29	0.54	1.8334	65.13	0.78	1.3561	42.63
	Val	0.39	2.4048	69.28	0.40	2.4267	69.91	0.49	2.2275	64.17	0.44	2.3258	67.01	0.45	2.3142	66.67	0.75	1.5028	47.06
RF	Cal	0.44	2.0358	72.32	0.43	2.0754	73.73	**0.73**	**1.4283**	**50.74**	**0.63**	1.6923	60.12	0.65	1.6184	57.49	0.91	0.9277	29.34
	Val	0.33	2.5277	72.82	0.36	2.5190	72.57	**0.62**	**1.9348**	**55.74**	**0.52**	2.2403	64.54	0.49	2.2237	64.07	0.80	1.1699	37.64
RFE	Cal	0.47	1.9738	70.05	0.44	2.0503	72.76	0.53	1.8581	65.94	0.48	1.9775	70.18	0.46	1.9960	70.83	**0.93**	**0.7279**	**25.88**
	Val	0.38	2.4559	70.87	0.35	2.5136	72.54	0.45	2.3231	67.04	0.41	2.4028	69.34	0.31	2.5709	74.19	**0.91**	**0.8516**	**31.64**

The values in bold represent models with the best results in linear and nonlinear methods.

In this study, cotton yield monitoring based on simple RGB image provides technical support for cotton production and harvest. However, the model constructed in this study still lacks universality in different regions, different years, and different data acquisition conditions. In the future, more data set optimization models will be added, while image processing technology will eliminate the environmental impact of data acquisition to improve the model accuracy.

CONCLUSION

In this study, ultra-high-resolution UAV RGB images were used to monitor the cotton yield before harvest. Vegetation indices, color spaces, texture features, and their combination were used to estimate the cotton yield before harvest from the RGB imagery. The results indicated the following:

1. The vegetation indices and texture features extracted from the ultra-high-resolution RGB images obtained by UAVs were significantly correlated with the cotton yield and, as such, can feasibly be used in cotton yield monitoring.
2. Comparing the modeling methods of linear and nonlinear regression, the cotton yield estimation model established by the nonlinear regression method had higher accuracy and stronger stability.
3. Comparing the cotton yield monitoring models based on vegetation indices or texture features, their fusion can further improve the monitoring ability of the cotton yield estimation model. The best model was the RFE_ELM model, the verification dataset $R^2 = 0.9109$, RMSE = 0.91277 t.ha^{-1}, and rRMSE = 29.34%.

DATA AVAILABILITY STATEMENT

The raw data supporting the conclusions of this article will be made available by the authors, without undue reservation.

AUTHOR CONTRIBUTIONS

YM, XL, and ZZ involved in research idea and scheme. YM, LM, and TH involved in experiment design. YM, XY, and TH UAV involved in data acquisition and processing. YM, QZ, and LM involved in ground data acquisition and analysis. YM, LM, and CH involved in data processing, model building, and validation. CH, TH, XL, and ZZ involved in resources. YM involved in writing original draft preparation. YM, LM, ZZ, XL, and CH involved in writing—review and editing. CH, XL, and ZZ involved in funding acquisition. All authors have read and agreed to the published version of the manuscript.

FUNDING

This study was supported by the National Natural Science Foundation of China (No. 42061658; 41971321), Key Research Program of Frontier Sciences, CAS (No. ZDBS-LY-DQC012),

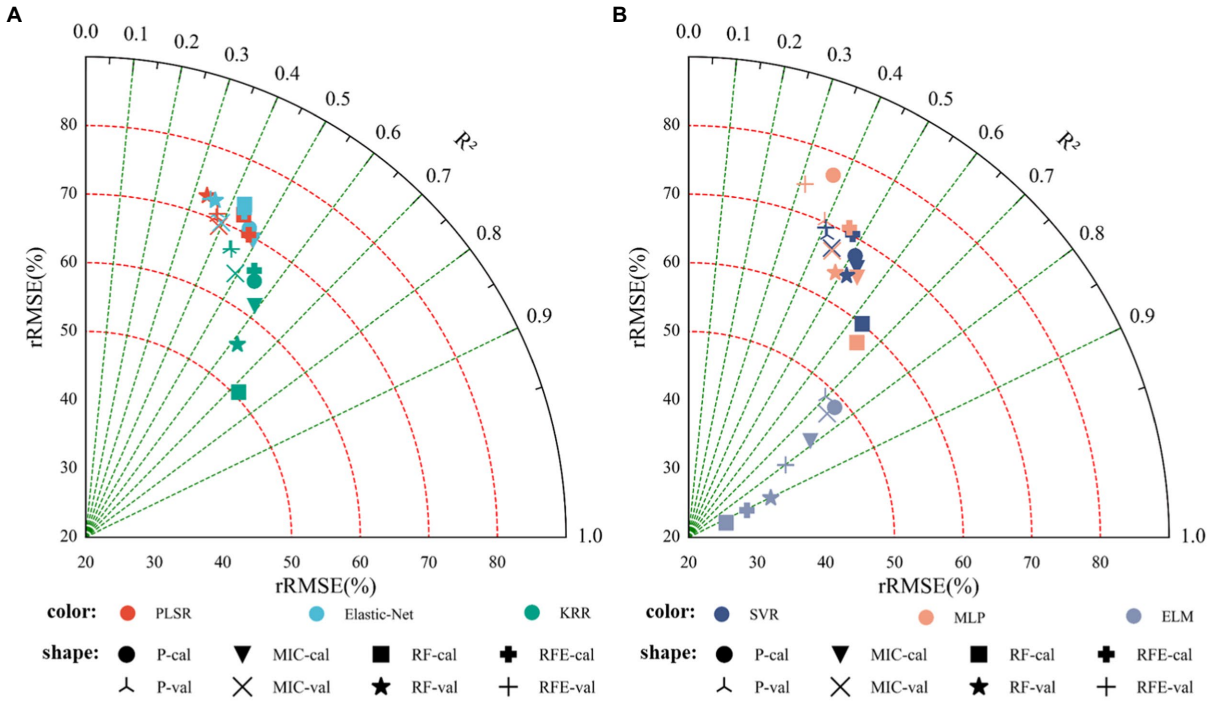

FIGURE 10 | Cotton yield monitoring model based on the fusion of vegetation indices and texture features. **(A)** Modeling results based on linear regression, **(B)** modeling results based on nonlinear regression.

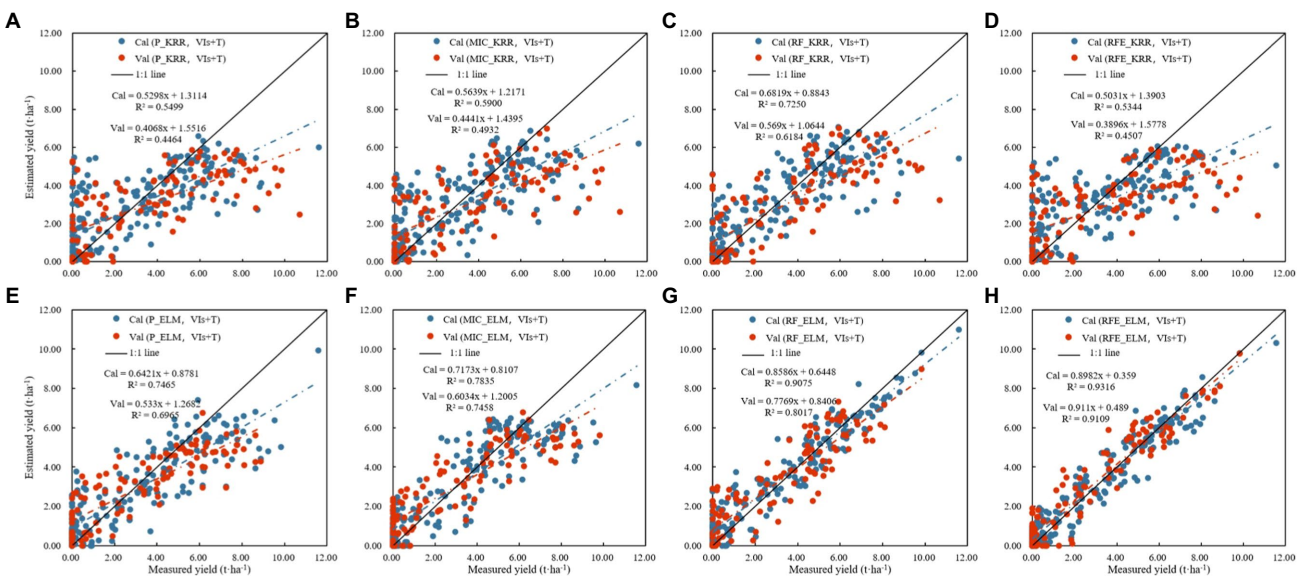

FIGURE 11 | Cotton yield estimation models established by best performing based on the vegetation indices and texture features by using the linear and nonlinear models. (Note: **(A)** P_KRR model; **(B)** MIC_KRR model; **(C)** RF_KRR model; **(D)** RFE_KRR model; **(E)** P_ELM model; **(F)** MIC_ELM model; **(G)** MIC_ELM model; **(H)** RFE_ELM model).

Key Scientific and Technological Research Program of XPCC (No.2020AB005), The Common Application Support Platform for Land Observation Satellites of China's Civil Space Infrastructure (CASPLOS_CCSI).

ACKNOWLEDGMENTS

We are very grateful to the teachers and students who helped us in the process of experiment and article writing. We are also grateful

to the reviewers for their comments and suggestions that significantly improved this paper.

SUPPLEMENTARY MATERIAL

The Supplementary Material for this article can be found online at: https://www.frontiersin.org/articles/10.3389/fpls.2022.925986/full#supplementary-material

Supplementary Figure 1 | Cotton yield inversion based on 2020's UAV RGB imagery: **(A)** make cotton yield inversion map based on measured yield; **(B)** make cotton yield inversion map based on the vegetation indices and texture features by KRR model; **(C)** make cotton yield inversion map based on the vegetation indices and texture features by ELM model.

Supplementary Figure 2 | Difference of texture features under different treatments.

Supplementary Figure 3 | Comparison of results of different modeling methods.

REFERENCES

Bendig, J., Yu, K., Aasen, H., Bolten, A., Bennertz, S., Broscheit, J., et al. (2015). Combining UAV-based plant height from crop surface models, visible, and near infrared vegetation indices for biomass monitoring in barley. *Int. J. Appl. Earth Obs. Geoinf.* 39, 79–87. doi: 10.1016/j.jag.2015.02.012

Chianucci, F., Disperati, L., Guzzi, D., Bianchini, D., Nardino, V., Lastri, C., et al. (2016). Estimation of canopy attributes in beech forests using true colour digital images from a small fixed-wing UAV. *Int. J. Appl. Earth Obs. Geoinf.* 47, 60–68. doi: 10.1016/j.jag.2015.12.005

Çopur, O., Demirel, U., Polat, R., and Gür, M. A. (2010). Effect of different defoliants and application times on the yield and quality components of cotton in semi-arid conditions. *Afr. J. Biotechnol.* 9, 2095–2100. doi: 10.4314/ajb.v9i14

Escalante, H. J., Rodríguez-Sánchez, S., Jiménez-Lizárraga, M., Morales-Reyes, A., De La Calleja, J., and Vazquez, R. (2019). Barley yield and fertilization analysis from UAV imagery: a deep learning approach. *Int. J. Remote Sens.* 40, 2493–2516. doi: 10.1080/01431161.2019.1577571

Fathipoor, H., Arefi, H., Shah-Hosseini, R., and Moghadam, H. (2019). Corn forage yield prediction using unmanned aerial vehicle images at mid-season growth stage. *JARS* 13:034503. doi: 10.1117/1.JRS.13.034503

Feng, A., Zhou, J., Vories, E. D., Sudduth, K. A., and Zhang, M. (2020). Yield estimation in cotton using UAV-based multi-sensor imagery. *Biosyst. Eng.* 193, 101–114. doi: 10.1016/j.biosystemseng.2020.02.014

Fernandez-Gallego, J. A., Kefauver, S. C., Vatter, T., Aparicio Gutiérrez, N., Nieto-Taladriz, M. T., and Araus, J. L. (2019). Low-cost assessment of grain yield in durum wheat using RGB images. *Eur. J. Agron.* 105, 146–156. doi: 10.1016/j.eja.2019.02.007

Gitelson, A. A., Kaufman, Y. J., Stark, R., and Rundquist, D. (2002). Novel algorithms for remote estimation of vegetation fraction. *Remote Sens. Environ.* 80, 76–87. doi: 10.1016/S0034-4257(01)00289-9

Guo, Y., Fu, Y., Hao, F., Zhang, X., Wu, W., Jin, X., et al. (2021b). Integrated phenology and climate in rice yields prediction using machine learning methods. *Ecol. Indic.* 120:106935. doi: 10.1016/j.ecolind.2020.106935

Guo, A., Huang, W., Dong, Y., Ye, H., Ma, H., Liu, B., et al. (2021a). Wheat yellow rust detection using UAV-based Hyperspectral technology. *Remote Sens.* 13:123. doi: 10.3390/rs13010123

Hamuda, E., Glavin, M., and Jones, E. (2016). A survey of image processing techniques for plant extraction and segmentation in the field. *Comput. Electron. Agric.* 125, 184–199. doi: 10.1016/j.compag.2016.04.024

Huang, Y., Brand, H. J., Sui, R., Thomson, S. J., Furukawa, T., and Ebelhar, M. W. (2016). Cotton yield estimation using very high-resolution digital images acquired with a low-cost small unmanned aerial vehicle. *Trans. ASABE* 59, 1563–1574. doi: 10.13031/trans.59.11831

Hunt, E. R., Cavigelli, M., Daughtry, C. S. T., Mcmurtrey, J. E., and Walthall, C. L. (2005). Evaluation of digital photography from model Aircraft for Remote Sensing of crop biomass and nitrogen status. *Precision Agric* 6, 359–378. doi: 10.1007/s11119-005-2324-5

Kataoka, T., Kaneko, T., Okamoto, H., and Hata, S. (2003). "Crop growth estimation system using machine vision," in *Proceedings 2003 IEEE/ASME international conference on advanced intelligent mechatronics (AIM 2003)*; July 20, 2003.

Khan, M. A., Wahid, A., Ahmad, M., Tahir, M. T., Ahmed, M., Ahmad, S., et al. (2020). "World cotton production and consumption: An overview," in *Cotton Production and Uses: Agronomy, Crop Protection, and Postharvest Technologies*. eds. S. Ahmad and M. Hasanuzzaman (Singapore: Springer), 1–7.

Kurale, N. G., and Vaidya, M. V. (2018). "Classification of leaf disease using texture feature and neural network classifier," in *2018 International Conference on Inventive Research in Computing Applications (ICIRCA)*; July 11, 2018.

Liu, K., Li, Y., Han, T., Yu, X., Ye, H., Hu, H., et al. (2019). Evaluation of grain yield based on digital images of rice canopy. *Plant Methods* 15:28. doi: 10.1186/s13007-019-0416-x

Louhaichi, M., Borman, M. M., and Johnson, D. E. (2001). Spatially located platform and aerial photography for documentation of grazing impacts on wheat. *Geocarto Int.* 16, 65–70. doi: 10.1080/10106040108542184

Maddikunta, P. K. R., Hakak, S., Alazab, M., Bhattacharya, S., Gadekallu, T. R., Khan, W. Z., et al. (2021). Unmanned aerial vehicles in smart agriculture: applications, requirements, and challenges. *IEEE Sensors J.* 21, 17608–17619. doi: 10.1109/JSEN.2021.3049471

Maimaitijiang, M., Sagan, V., Sidike, P., Hartling, S., Esposito, F., and Fritschi, F. B. (2020). Soybean yield prediction from UAV using multimodal data fusion and deep learning. *Remote Sens. Environ.* 237:111599. doi: 10.1016/j.rse.2019.111599

Maja, J. M. J., Campbell, T., Neto, J. C., and Astillo, P. (2016). Predicting cotton yield of small field plots in a cotton breeding program using UAV imagery data. *Aut. Air Ground Sensing Sys. Agri. Optimization Phenotyping (SPIE)* 9866, 39–45. doi: 10.1117/12.2228929

Mao, S., Li, Y., Ma, Y., Zhang, B., Zhou, J., and Wang, K. (2020). Automatic cucumber recognition algorithm for harvesting robots in the natural environment using deep learning and multi-feature fusion. *Comput. Electron. Agric.* 170:105254. doi: 10.1016/j.compag.2020.105254

Masasi, B., Taghvaeian, S., Gowda, P. H., Marek, G., and Boman, R. (2020). Validation and application of AquaCrop for irrigated cotton in the southern Great Plains of US. *Irrig. Sci.* 38, 593–607. doi: 10.1007/s00271-020-00665-4

Meng, L., Liu, H., Zhang, X., Ren, C., Ustin, S., Qiu, Z., et al. (2019). Assessment of the effectiveness of spatiotemporal fusion of multi-source satellite images for cotton yield estimation. *Comput. Electron. Agric.* 162, 44–52. doi: 10.1016/j.compag.2019.04.001

Pelletier, M. G., Wanjura, J. D., and Holt, G. A. (2019). Electronic Design of a Cotton Harvester Yield Monitor Calibration System. *Agri. Eng.* 1, 523–538. doi: 10.3390/agriengineering1040038

Riehle, D., Reiser, D., and Griepentrog, H. W. (2020). Robust index-based semantic plant/background segmentation for RGB- images. *Comput. Electron. Agric.* 169:105201. doi: 10.1016/j.compag.2019.105201

Sun, X., Liu, L., Wang, D., Xu, P., Ma, Z., Zhang, X., et al. (2020). "Research on the progress of key technology of cotton harvester," in *2020 ASABE Annual International Virtual Meeting*; July 12-15, 2020.

Tao, H., Feng, H., Xu, L., Miao, M., Yang, G., Yang, X., et al. (2020). Estimation of the yield and plant height of winter wheat using UAV-based Hyperspectral images. *Sensors* 20:1231. doi: 10.3390/s20041231

Tedesco-Oliveira, D., Pereira da Silva, R., Maldonado, W., and Zerbato, C. (2020). Convolutional neural networks in predicting cotton yield from images of commercial fields. *Comput. Electron. Agric.* 171:105307. doi: 10.1016/j.compag.2020.105307

Tsouros, D. C., Bibi, S., and Sarigiannidis, P. G. (2019). A review on UAV-based applications for precision agriculture. *Information* 10:349. doi: 10.3390/info10110349

Wu, J., and Chen, X. (2015). Present situation, problems and countermeasures of cotton production mechanization development in Xinjiang Production and Construction Corps. Available at: https://www.ingentaconnect.com/content/tcsae/tcsae/2015/00000031/00000018/art00002 (Accessed April 1, 2022).

Xin, W. E. I., Qingqian, M. A., Chunyan, L. I., Haijiang, X. U., Zipiao, Z., Chunping, L. I., et al. (2021). Effects of defoliant spraying time on cotton yield, quality and chemical composition of seed. *Xinjiang Agri. Sci.* 58:1648. doi: 10.6048/j.issn.1001-4330.2021.09.010

Xu, Y., Liu, X., Cao, X., Huang, C., Liu, E., Qian, S., et al. (2021). Artificial intelligence: A powerful paradigm for scientific research. *Innovation* 2:100179. doi: 10.1016/j.xinn.2021.100179

Xu, W., Yang, W., Chen, S., Wu, C., Chen, P., and Lan, Y. (2020). Establishing a model to predict the single boll weight of cotton in northern Xinjiang by using high resolution UAV remote sensing data. *Comput. Electron. Agric.* 179:105762. doi: 10.1016/j.compag.2020.105762

Yamaguchi, T., Tanaka, Y., Imachi, Y., Yamashita, M., and Katsura, K. (2021). Feasibility of combining deep learning and RGB images obtained by unmanned aerial vehicle for leaf area index estimation in Rice. *Remote Sens.* 13:84. doi: 10.3390/rs13010084

Yeom, J., Jung, J., Chang, A., Maeda, M., and Landivar, J. (2018). Automated open cotton boll detection for yield estimation using unmanned aircraft vehicle (UAV) data. *Remote Sens.* 10:1895. doi: 10.3390/rs10121895

Yue, J., Yang, G., Tian, Q., Feng, H., Xu, K., and Zhou, C. (2019). Estimate of winter-wheat above-ground biomass based on UAV ultrahigh-ground-resolution image textures and vegetation indices. *ISPRS J. Photogramm. Remote Sens.* 150, 226–244. doi: 10.1016/j.isprsjprs.2019.02.022

Zhang, X., Cui, J., Wang, W., and Lin, C. (2017). A study for texture feature extraction of high-resolution satellite images based on a direction measure and gray level co-occurrence matrix fusion algorithm. *Sensors* 17:1474. doi: 10.3390/s17071474

Zhang, J., Qiu, X., Wu, Y., Zhu, Y., Cao, Q., Liu, X., et al. (2021). Combining texture, color, and vegetation indices from fixed-wing UAS imagery to estimate wheat growth parameters using multivariate regression methods. *Comput. Electron. Agric.* 185:106138. doi: 10.1016/j.compag.2021.106138

Zhang, X., Zhang, K., Sun, Y., Zhao, Y., Zhuang, H., Ban, W., et al. (2022). Combining spectral and texture features of UAS-based multispectral images for maize leaf area index estimation. *Remote Sens.* 14:331. doi: 10.3390/rs14020331

Zhang, M., Zhou, J., Sudduth, K. A., and Kitchen, N. R. (2020). Estimation of maize yield and effects of variable-rate nitrogen application using UAV-based RGB imagery. *Biosyst. Eng.* 189, 24–35. doi: 10.1016/j.biosystemseng.2019.11.001

Zheng, H., Ma, J., Zhou, M., Li, D., Yao, X., Cao, W., et al. (2020). Enhancing the nitrogen signals of Rice canopies across critical growth stages through the integration of textural and spectral information from unmanned aerial vehicle (UAV) multispectral imagery. *Remote Sens.* 12:957. doi: 10.3390/rs12060957

Zhou, Y., Lao, C., Yang, Y., Zhang, Z., Chen, H., Chen, Y., et al. (2021). Diagnosis of winter-wheat water stress based on UAV-borne multispectral image texture and vegetation indices. *Agric. Water Manag.* 256:107076. doi: 10.1016/j.agwat.2021.107076

Conflict of Interest: The authors declare that the research was conducted in the absence of any commercial or financial relationships that could be construed as a potential conflict of interest.

Publisher's Note: All claims expressed in this article are solely those of the authors and do not necessarily represent those of their affiliated organizations, or those of the publisher, the editors and the reviewers. Any product that may be evaluated in this article, or claim that may be made by its manufacturer, is not guaranteed or endorsed by the publisher.

Copyright © 2022 Ma, Ma, Zhang, Huang, Yi, Chen, Hou, Lv and Zhang. This is an open-access article distributed under the terms of the Creative Commons Attribution License (CC BY). The use, distribution or reproduction in other forums is permitted, provided the original author(s) and the copyright owner(s) are credited and that the original publication in this journal is cited, in accordance with accepted academic practice. No use, distribution or reproduction is permitted which does not comply with these terms.

frontiers | Frontiers in Plant Science

ORIGINAL RESEARCH
published: 21 June 2022
doi: 10.3389/fpls.2022.901042

Mapping the Corn Residue-Covered Types Using Multi-Scale Feature Fusion and Supervised Learning Method by Chinese GF-2 PMS Image

Wancheng Tao[1,2], Yi Dong[1,2], Wei Su[1,2], Jiayu Li[1,2], Fu Xuan[1,2], Jianxi Huang[1,2], Jianyu Yang[1,2], Xuecao Li[1,2], Yelu Zeng[1,2] and Baoguo Li[1]*

[1] College of Land Science and Technology, China Agricultural University, Beijing, China, [2] Key Laboratory of Remote Sensing for Agri-Hazards, Ministry of Agriculture, Beijing, China

The management of crop residue covering is a vital part of conservation tillage, which protects black soil by reducing soil erosion and increasing soil organic carbon. Accurate and rapid classification of corn residue-covered types is significant for monitoring crop residue management. The remote sensing technology using high spatial resolution images is an effective means to classify the crop residue-covered areas quickly and objectively in the regional area. Unfortunately, the classification of crop residue-covered area is tricky because there is intra-object heterogeneity, as a two-edged sword of high resolution, and spectral confusion resulting from different straw mulching ways. Therefore, this study focuses on exploring the multi-scale feature fusion method and classification method to classify the corn residue-covered areas effectively and accurately using Chinese high-resolution GF-2 PMS images in the regional area. First, the multi-scale image features are built by compressing pixel domain details with the wavelet and principal component analysis (PCA), which has been verified to effectively alleviate intra-object heterogeneity of corn residue-covered areas on GF-2 PMS images. Second, the optimal image dataset (OID) is identified by comparing model accuracy based on the fusion of different features. Third, the 1D-CNN_CA method is proposed by combining one-dimensional convolutional neural networks (1D-CNN) and attention mechanisms, which are used to classify corn residue-covered areas based on the OID. Comparison of the naive Bayesian (NB), random forest (RF), support vector machine (SVM), and 1D-CNN methods indicate that the residue-covered areas can be classified effectively using the 1D-CNN-CA method with the highest accuracy (*Kappa*: 96.92% and overall accuracy (*OA*): 97.26%). Finally, the most appropriate machine learning model and the connected domain calibration method are combined to improve the visualization, which are further used to classify the corn residue-covered areas into three covering types. In addition, the study showed the superiority of multi-scale image features by comparing the contribution of the different image features in the classification of corn residue-covered areas.

Keywords: crop residue covering, multi-scale image features, machine learning, GF-2 PMS image, high spatial resolution remote sensing

OPEN ACCESS

Edited by:
Zhenhai Li,
Shandong University of Science and Technology, China

Reviewed by:
Xinghua Li,
Wuhan University, China
Weiwei Sun,
Ningbo University, China

***Correspondence:**
Wei Su
suwei@cau.edu.cn

Specialty section:
This article was submitted to Sustainable and Intelligent Phytoprotection, a section of the journal Frontiers in Plant Science

Received: *21 March 2022*
Accepted: *01 June 2022*
Published: *21 June 2022*

Citation:
Tao W, Dong Y, Su W, Li J, Xuan F, Huang J, Yang J, Li X, Zeng Y and Li B (2022) Mapping the Corn Residue-Covered Types Using Multi-Scale Feature Fusion and Supervised Learning Method by Chinese GF-2 PMS Image. Front. Plant Sci. 13:901042. doi: 10.3389/fpls.2022.901042

INTRODUCTION

The precious black soils in Northeast China, classified as dark Chernozems and called Mollisols, are the most suitable soils for cereal production and commodity grains, as they have abundant organic matter and show high soil fertility (Yao et al., 2017; Zheng et al., 2018). However, black soil has been facing severe problems of soil degradation due to unscientific cultivation. To avoid continuing degradation, the balance of soil productivity must range from degradation processes to conservation practices with crop residue management (Unger et al., 1991). In the traditional management patterns, the crop residue is often burned or removed, resulting in the thinning of black soil and serious air pollution (Freebairn and Boughton, 1985). In contrast, the crop residue cover can reduce soil erosion resulting from wind blowing and water washing (Pi et al., 2020; Wan et al., 2022). Furthermore, the decomposed residue will improve the content of soil organic matter slowly year by year (Kaur, 2017; Bhuvaneshwari et al., 2019; Jat et al., 2020; Lu, 2020). Consequently, mapping the crop residue-covered types accurately in regional areas is of great significance for monitoring conservation tillage application and black soil protection. Furthermore, the accurate map regarding the crop residue-covered type is a crucial input for the soil erosion equation.

Corn is the main crop planted on the inner *Golden Corn Belts* containing the black soil in Northeast China, and produces a large number of residues every year. In Northeast China, the corn is harvested in early and middle October, and the corn residue is left in cornfields from October to the next April on the black soil. Then it will be covered with snow on the black soil from the middle of November. Under the influence of frost and other adverse weather conditions, the traditional manual method to investigate the corn residue cover is time-consuming, laborious, and expensive, and can only be carried out in a limited sampling area. Remote sensing is a low-cost, labor-saving method that provides rapid access to regional surface information technology (Maxwell et al., 2018; Weiss et al., 2020; Khanal et al., 2021). Particularly, the Chinese GF-2 high spatial resolution image with the PMS sensor has a spatial resolution of 1 m, and it provides abundant information for land surface observation. Unfortunately, the high spatial resolution, like two sides to all technologies, also leads to severe spectral intra-object heterogeneity (i.e., the same object with different spectra), which brings significant challenges for automatically classifying corn residue-covered areas in GF-2 images. Consequently, many studies are exploring the effectiveness of multi-scale features for overcoming this challenge (Huang et al., 2007; Martis et al., 2013; Ai et al., 2015; Ma et al., 2020; Trivizakis et al., 2021). Therefore, this study will focus on mining the multi-scale feature images that are used for the classification of corn residue-covered types.

The fusion of different features, including multi-scale features, spectral bands, vegetation indexes, and other image features, is a vital approach to improve classification accuracy in remote sensing images (Munnaf et al., 2021). Moreover, the importance of fusion features has been demonstrated in many fields (Gu et al., 2017; Ma et al., 2017; Zhang et al., 2020). Zheng et al. (2013) studied the effectiveness of normalized difference tillage index using the object-based approaches to detect the crop residues from Landsat 7 and Landsat 5 imagery in Champaign County and Marshall County, respectively, and the overall accuracy of tillage classification ranged from 69 to 79%. Najafi et al. (2018) identified crop residue-covered area and tillage intensity using the mean of brightness, normalized difference tillage index, and gray-level co-occurrence matrix texture features from Landsat Operational Land Imager (OLI) satellite image in Maragheh, East Azerbaijan, Iran. However, it is not proper to use more features to get higher classification performance certainly and necessarily (Drotar et al., 2015). Sometimes, subsets of variables can achieve similar or better classification accuracy than multivariable feature methods (Wang et al., 2017). Therefore, selecting and optimizing image features is essential for classifying corn residue cover types.

At present, classification algorithms are widely used in geo-mapping. The supervised and the unsupervised classification methods are developed in the remote sensing context (Bruzzone and Persello, 2010). The result of unsupervised classification differs significantly from the actual classification due to insufficient prior knowledge, such as K-Mean and ISODATA (Abbas et al., 2016). In comparison, the supervised classification methods with prior categories show good classification performance in remote sensing images, such as naive Bayesian (NB), support vector machine (SVM), random forest (RF), and convolutional neural networks (CNN) (Shi et al., 2016; Bonaccorso, 2017; Zhong et al., 2019; Yan et al., 2021). These supervised methods have been generally used as potential classification models with high accuracy in remote sensing and other areas of research (Talukdar et al., 2020; Antoniadis et al., 2021), such as land cover classification (Tatsumi et al., 2016; Wang et al., 2021), fault diagnosis (Yin and Hou, 2016), deformation prediction (Feng et al., 2021), human activity recognition (Casale et al., 2011), etc. Therefore, supervised classification methods are used to classify corn residue-covered areas in this study.

Considering the above-mentioned facts, the fusion of the multi-scale features and supervised classification algorithms are used to classify corn residue-covered types for solving the problem of severe intra-object spectral difference in corn residue cover. The main objectives of this study are as follows: (1) Exploring the effective method of classifying corn residue-covered areas with intra-object heterogeneity by building multi-scale features using principal component analysis (PCA) and wavelet. (2) Analyzing the rate of contribution of different image features in classifying corn residue cover into three types. (3) Based on 1D-CNN and attention mechanism, designing 1D-CNN_CA method to classify corn residue-covered areas in this study. (4) Combining the most appropriate machine learning method and connected domain calibration method for mapping corn residue-covered types in the regional area.

The organization of this manuscript is as follows. In Section "Materials and Methods," we introduce the study area and the data collection. In addition, the details regarding the multi-scale fusion method, classification method, and assessment indexes are presented. In Section "Results and Analysis," the optimal image dataset (OID) is identified by comparing the fusion of different features. Then, we compare different classification methods based

on OID and acquire the classification of corn residue-covered areas on a GF-2 multispectral image. In Section "Discussion," the discussion about the strengths and weaknesses of the proposed method with respect to other relevant studies is given. Finally, in Section "Conclusion," considerations for future work and the conclusion of the study are presented.

MATERIALS AND METHODS

For solving the problem of spectral intra-object heterogeneity in the corn residue-covered area, we propose a multi-scale fusion method for this classification task using high-resolution GF-2 images. There are four steps in this study. First, the first component image is obtained by the PCA method from the GF-2 multispectral image. Second, the multi-scale features are created by compressing context space information of multi-scale images using the wavelet method. Third, the OID is identified by comparing the fusion of different features. Then, the machine learning models with optimal parameters are trained and verified using the sample dataset (training dataset: validation dataset = 7:3). Finally, the classification of corn residue-covered types is accomplished using the most appropriate model and image dataset, which is further optimized by the connected domain calibration method subsequently. The workflow is shown in **Figure 1**.

Study Area and Data Collection

Study Area

The study area is Lishu County and is in the southwest of Jilin Province, China, which is in the inner Golden Corn Belts on the Chinese Black Soil area of one of the worldwide well-known four black soil belts. In the study area, the corn plant is the primary cereal, with planting dates generally 1 week before and after 1 May each year and harvest dates are from October 1 to 20, and residue cover is produced after harvest.

Remote Sensing Data

The optimum time window for monitoring the corn residue-covered area with satellite images ranges from the end of October to the middle of November. So, the Chinese GF-2 PMS image acquired on 28 October 2017 is consistent with the field survey time and is used to classify corn residue types in this study. The original GF-2 image contains one panchromatic band with 1 m spatial resolution and four multispectral bands with 4 m spatial resolution, whose temporal resolution is 5 days and the width is 45 km. The GF-2 PMS image is preprocessed, including radiometric calibration, atmospheric correction, and pan-sharping fusion for obtaining the GF-2 multispectral image with about 1 m spatial resolution. The scope of cloud-free coverage and the number of GF-2 PMS images are limited by weather and a valid time window for obtaining images. We clip the multispectral image with 4,500 × 4,500 pixels (**Figure 2a**) as the study area in the GF-2 image with a central longitude of 124.75° and central latitude of 43.39°, and the red triangles in the figure indicate the observation points.

Sample Collection and Analysis

The accuracy verification of the classification results is based on the field survey data. In Lishu County, the stable corn residue covering after harvest is observed at the end of October and the middle of November each year. A large number of sample plots are available during this period and hence is the ideal time to conduct field observations in the study area. According to the high spatial resolution (1 m) of the GF-2 satellite image, 10 uniform plots with a size of 1 m × 1 m were randomly selected from the fields, and the height and the existing form of corn residue were measured and divided into three types. Moreover, the GF-2 sub-images and field survey photos for three kinds of corn residue-covered types are shown in **Figure 2b** and **Figure 2c**. For Type 1, the corn residue is stacked in the field after artificial harvesting, where the corn residue is bright and the soil is dark in the GF-2 image; thus, the zoomed image of Type 1 is seen as black and white alternating rows. Type 2 is mainly caused by large harvesters leaving more corn residue after harvesting. So, the zoomed image of Type 2 is highlighted in white. Type 3 is due to the stubble produced by taking the corn straw away after artificial harvesting, and there is little corn residue in the field; the zoomed image of Type 3 is seen as brown and black. Based on the field survey, a total of 3,102 samples are collected to build the sample dataset by visual interpretation method, including Type 1 (758), Type 2 (746), Type 3 (779), and other classes (819). The other classes include buildings, roads, forests, etc.

Through the analysis of the frequency distribution of the sample dataset (**Figure 3**), the gray values of different bands range from 130 to 255 in **Figure 3B**, and the gray values of different bands range from 25 to 175 in **Figure 3C**. So, Type 2 and Type 3 are the easiest to distinguish. The gray values of different bands range from 0 to 250 in **Figures 3A,D**. Compared with Type 2 and Type 3, the wide range of distribution of Type 1 and the other classes leads to severe intra-object differences in the spectra, which greatly interferes with classification accuracy.

Principal Component Analysis of GF-2 PMS Image

The PCA method is utilized to reduce the dimension of the GF-2 high-resolution multispectral images, which is a popular method for linear dimensionality reduction and feature extraction (Alhayani and Ilhan, 2017). Through the PCA transformation, the spectral GF-2 PMS image is transformed to the new coordinate system space to maximize the difference among band variables and make these variables independent (Kang et al., 2020). Assume that the GF-2 multispectral image is defined as $\boldsymbol{Z}$, which can be expressed as follows:

$$\mathbf{Z} = \left[\mathbf{Z}_1 \cdots \mathbf{Z}_d\right] = \begin{bmatrix} z_{11} & \cdots & z_{1d} \\ \vdots & \ddots & \vdots \\ z_{n1} & \cdots & z_{nd} \end{bmatrix} \quad (1)$$

where $\boldsymbol{Z} = \{\boldsymbol{Z}_i; i = 1,2,3, \ldots, d\}$, d is the total number of image bands, $\boldsymbol{Z}_i = \{\boldsymbol{Z}_{ij}; j = 1,2,3, \ldots, n\}$ is the i-th band image, n is the total pixel number of $\boldsymbol{Z}_i$ band image, and $\boldsymbol{Z}_{ij}$ is the j-th pixel of

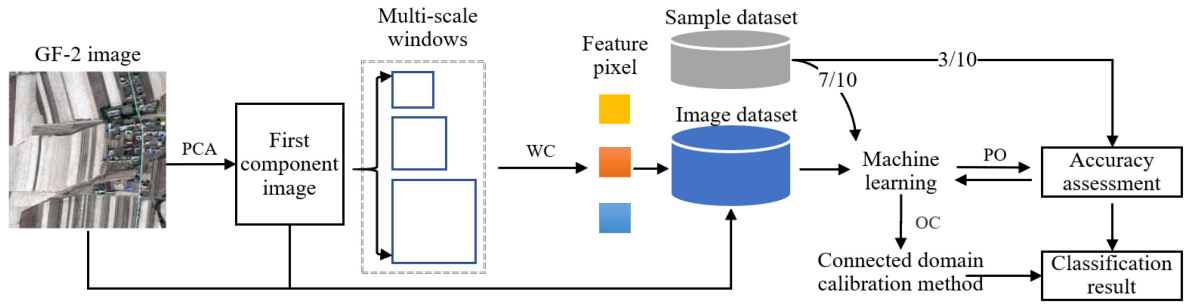

FIGURE 1 | Workflow of classification for corn residue-covered types. Notes: PCA: Principal component analysis. WC: Wavelet compression. PO: Parameter optimization. OC: Optimization classification.

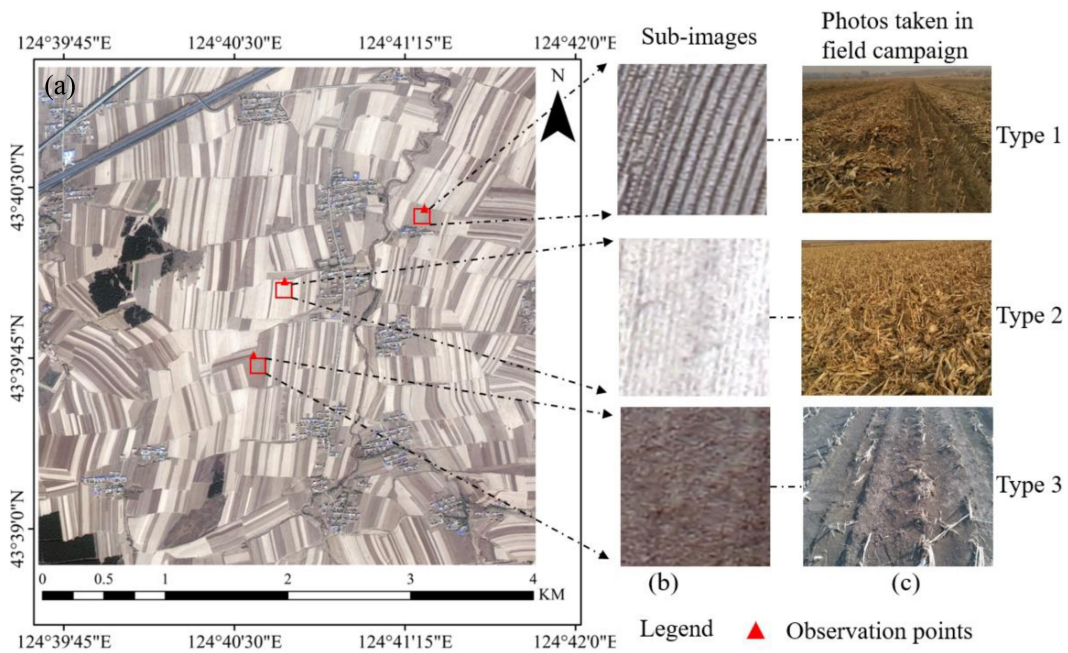

FIGURE 2 | The study area **(a)**. The GF-2 sub-images **(b)** and corresponding field survey photos **(c)** for three kinds of corn residue-covered types.

the *i*-th band. For the GF-2 PMS image, the PCA transformation is as follows:

$$X = A \times \mathbf{Z} \quad (2)$$

where $\boldsymbol{Z}$ is the pixel vector in the multispectral space of the GF-2 image. $\boldsymbol{X} = \{\boldsymbol{X}_i; i = 1,2,3, \ldots, d'\}$ is the pixel vector of the principal component space transformed by PCA, $\boldsymbol{X}_i$ is the *i*-th component image, and *d*' is the total number of component images. The matrix *A* is obtained by the transpose of the eigenvectors, and the eigenvectors are computed from the space covariance of the multispectral image $\boldsymbol{Z}$. The eigenvalue calculated from the eigenvector is used to describe the information contained by the corresponding component. Furthermore, the variance contribution rate can be calculated from the eigenvalues of one component divided by the sum of all the eigenvalues, which is used to describe the information proportion of the component.

The information contained in each component of $\boldsymbol{X}$ is different. Generally, it shows a decreasing trend, and the first component (PC1) after PCA transformation of the GF-2 image contains the most space and detailed information.

Multi-Scale Image Feature Extraction of the First Component Image by Wavelet

Wavelet transform can compress the spatial neighborhood information of high-resolution images to obtain multi-scale image features, so as to alleviate the problem of intra-object spectral differences in straw mulch. The multi-scale image features are obtained from PC1 using the wavelet method. The PC1 image can be represented as $\boldsymbol{X}_1 = \{x_{i,j}; i = 1,2,3, \ldots, r; j = 1,2,3, \ldots, c\}$, where *i* and *j* are the indexes of the rows and columns of the image. $x_{i,j}$ is the pixel of *i*-th rows and *j*-th column. *r* and *c* are the total number of the rows and

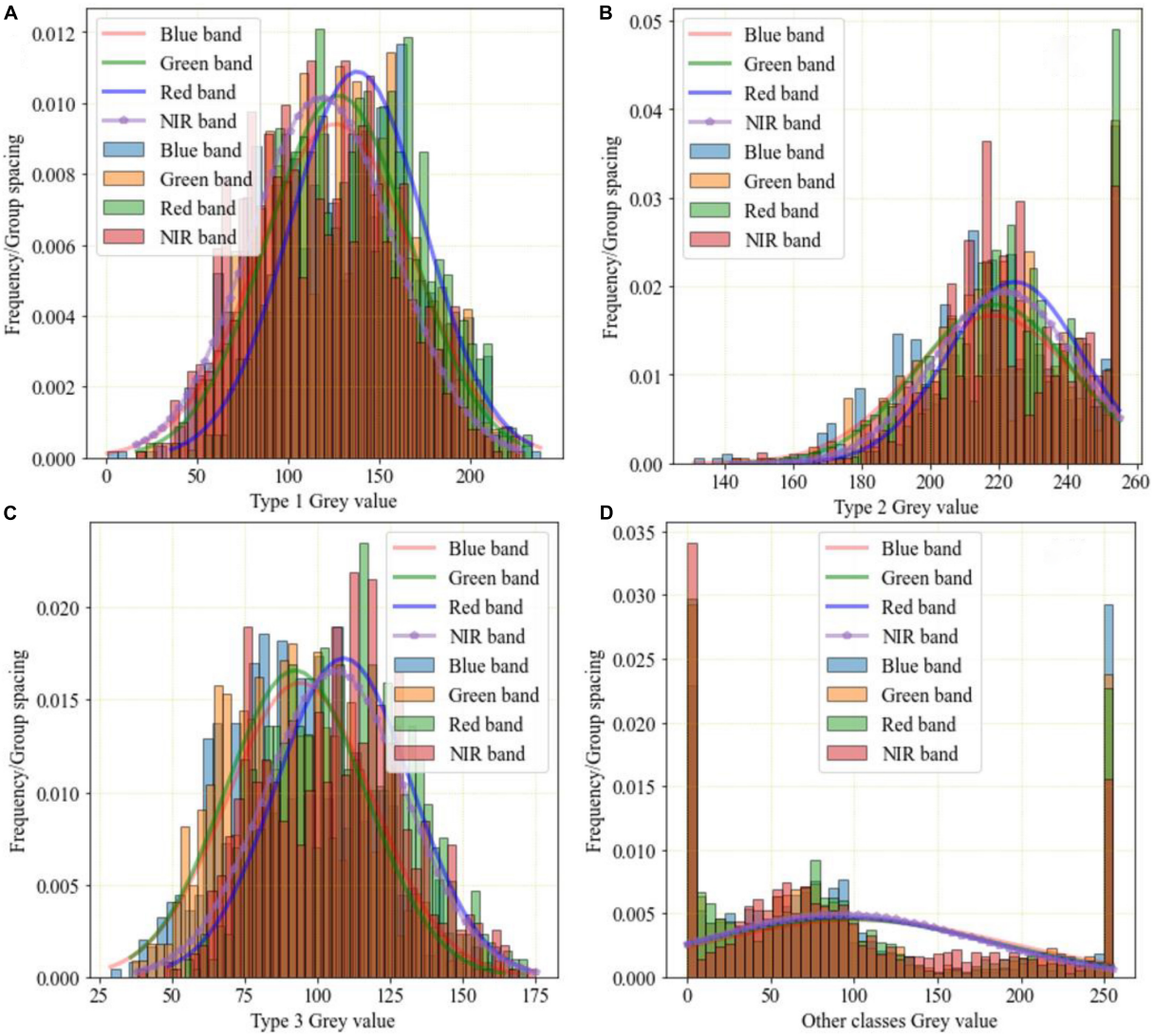

FIGURE 3 | Frequency distribution of sample points of GF-2 multispectral image. **(A)** Type 1 gray value. **(B)** Type 2 gray value. **(C)** Type 3 gray value. **(D)** Other classes gray value.

the column, respectively. The description of the multi-scale window settings is shown in **Figure 4**. Different sizes of pixel neighborhood windows are used as measurement units of multi-scale spatial domain images. For multi-scale features of the $x_{i,\ j}$ pixel in image $\boldsymbol{X}_1$, the multi-scale images are obtained through multi-scale windows with pixel $x_{i,\ j}$ as the center, and the multi-scale features of the $x_{i,\ j}$ pixel are extracted by using the wavelet method (Nunez et al., 1999) to compress spatial domain information of each multi-scale image into a single pixel. The scale of pixel neighborhood windows includes 2 × 2 (green box), 4 × 4 (brown box), 8 × 8 (yellow box), and so on.

The feature can be replaced by approximate coefficient and detail coefficient, and it can transform the image from space domain to frequency domain and generate sub-images with different frequencies domain. The wavelet coefficient of the multi-scale images at 2^m resolution is expressed by the formula is as follows:

$$A_m = f(s)_{m-1} \times \varphi_m^r \times C_m^r \times \varphi_m^c \times C_m^c \tag{3}$$

$$H_m = f(s)_{m-1} \times \varphi_m^r \times C_m^r \times \phi_m^c \times C_m^c \tag{4}$$

$$V_m = f(s)_{m-1} \times \phi_m^r \times C_m^r \times \varphi_m^c \times C_m^c \tag{5}$$

$$D_m = f(s)_{m-1} \times \phi_m^r \times C_m^r \times \phi_m^c \times C_m^c \tag{6}$$

where m is the decomposition level and A_m is low frequency (approximation coefficient). H_m, V_m, and D_m are the detail coefficients which are vertical high frequencies (horizontal

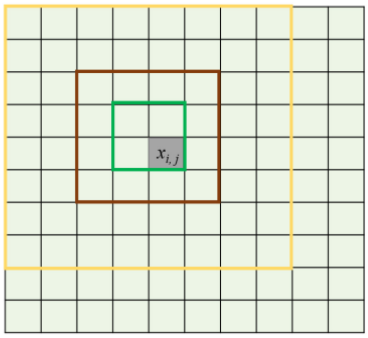

FIGURE 4 | Multi-scale image description of the different pixel neighborhood windows.

detail coefficient), horizontal high frequencies (vertical detail coefficient), and high frequency in both directions (diagonal detail coefficient) (Myint et al., 2002), respectively. $f(s)_{m-1}$ is the low frequency of the multi-scale images at the m-1 decomposition level. φ_m^r and φ_m^c are a one-dimensional scaling function. ϕ_m^r and ϕ_m^c are a one-dimensional wavelet function. C_m^r and C_m^c are down sampling along rows and columns at the m decomposition level. Moreover, the db3 wavelet basis function with vanishing moment 3 is selected in the experiment. In general, the larger the vanishing moment, the smoother the wavelet. The decomposition process is illustrated in **Figure 5**.

According to **Figure 5**, the detail sub-image (detail coefficient) and approximation sub-image (approximation coefficient) of the multi-scale images can be gained based on a one-dimensional filter along with rows and columns. First, the rows of the input image are convolved with a one-dimensional low-pass filter ($L1$). The downsampling with the scale of 2 along rows is used for filtered data. If the data after downsampling (Ds1) are convolved with a one-dimensional low-pass filter ($L2$) and the downsampling with the scale 2 along with columns, then the approximation sub-image (AI) can be obtained. If the data after downsampling (Ds1) are convolved with a one-dimensional high-pass filter ($H2$) and the downsampling with the scale of 2 along with columns, then the horizontal detail sub-image (HI) can be gained. Similarly, we also can obtain the vertical detail sub-image (VI) and the diagonal detail sub-image (DI).

The four sub-images (AI, HI, VI, and DI) obtained by each wavelet decomposition of the original image are the information sources of the multi-scale images. The wavelet coefficient or energy is significant where the brightness changes in the sub-image. Due to the meaningful details and edge feature information of the sub-images, we use the method of the larger absolute value of coefficients (Huang et al., 2007). Therefore, the multi-scale features are extracted by fusing the coefficients according to the selected maximum value of sub-images, ignoring the coefficients of lower energy.

Classification Algorithms

Naive Bayesian

Naïve Bayesian, based on Bayesian theory, is a widely used classification algorithm in machine learning and data mining. The NB algorithm is based on the assumption that the variables need to be predicted to agree with the Gaussian distribution, and all the variables are independent of each other. And the classification is accomplished in line with the conditional probability of each sample belonging to every class (Leung, 2007). Compared with other classification methods, there are no input parameters for the NB classifier, which is efficient and straightforward. In this study, the image dataset was provided as the input data for the NB to identify corn residue-covered types.

Support Vector Machine

Support vector machine classification is based on statistical learning theory, classifying the input sample features by solving the optimal hyperplane $f(x) = w^t + b$ among classes. The samples on plane $w^t + b = 1$ or $w^t + b = -1$ are called support vectors. The core of SVM is to solve the problem of dichotomy. For multi-classification problems, the "one-to-many" classification method is usually adopted. After selecting one class of samples, all other classes are grouped into one class. For n classes, n hyperplanes need to be solved. The n results will be obtained after discriminating n optimal hyperplanes for the predicted sample. Then the optimal class will be selected (Jakkula, 2006). The SVM is a small sample learning method with good robustness and accuracy, which was selected and used to classify corn residue-covered types.

Random Forest

The RF classification method is a machine learning algorithm based on the idea of ensemble learning, which generates decision trees randomly for classification and regression using the bagging method (Belgiu and Drăguţ, 2016). Each decision tree is distributed independently and identically, and its structure will be changed by splitting each node randomly. Moreover, the classification rules are formed by learning and training samples, which can analyze the classification features of complex geographic information. In the whole modeling process, randomness contains two meanings: the randomness of decision tree formation and the randomness of decision tree node segmentation (Strobl et al., 2007). Therefore, the RF method has high robustness and is used to classify the dataset for corn residue-covered types in this study.

In order to optimize the combination of feature images, the *Gini*-importance is used to determine the importance of each feature image, which can perform an implicit feature selection for the high-dimensional feature dataset (Rodriguez-Galiano et al., 2012). The formula expresses the *Gini*-importance as follows.

$$Gini = \sum_{i=1}^{N} P(y_i) \times Gini_m(y_i) \quad (7)$$

where *Gini* is the *Gini*-importance, y_i is the i-th set, i = (1,2,3, . . ., N), P(y_i) is the probability, and N is the total number of subsets. $Gini_m(y_i)$ is *Gini* impurity, that is, the probability that a random sample of the set is misclassified.

1D-CNN_CA Network

The features acquired by CNN through learning have stronger discrimination ability and generalization ability

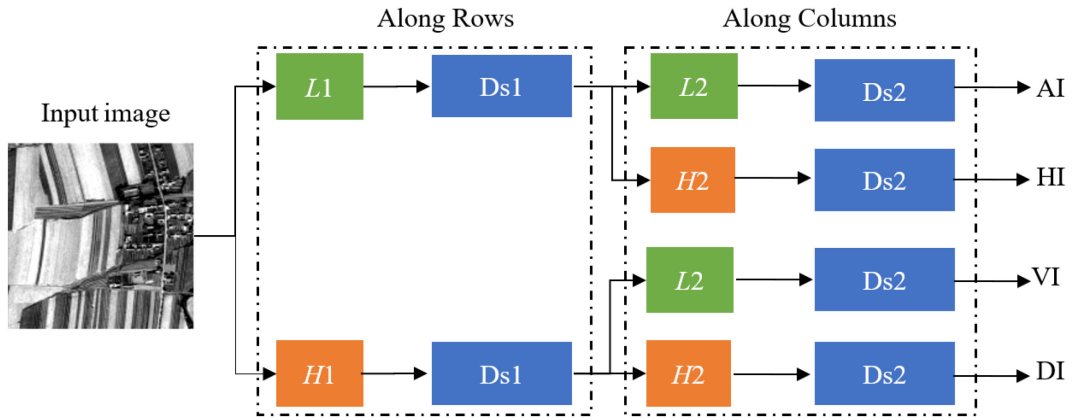

FIGURE 5 | Decomposition procedure of the multi-scale image. *L*1 is the first low-pass filter. *L*2 is the second low-pass filter. *H*1 is the first high-pass filter. *H*2 is the second high-pass filter. Ds1 is the first down sampling. Ds2 is the second down sampling. AI is an approximation sub-image. HI is a horizontal detail sub-image. VI is a vertical detail sub-image. DI is a diagonal detail sub-image.

(Wang et al., 2021). As a representative of deep learning, the CNN has great potential in remote sensing classification. The attention mechanism can effectively optimize CNN network feature information by giving different weights to features, which is the critical technology in deep learning. Therefore, the 1D-CNN_CA is proposed by fusing 1D-CNN and the attention mechanism, which is used for classifying corn residue-covered types in this study.

The network structure used is presented in **Table 1**. "n_f" is the number of features entered, and "n_class" is the number of output classes. First, multi-dimensional features of input data are obtained by one-dimensional convolution "Conv1D_1" and nonlinear activation function "Relu." Then, the optimized multi-dimensional features are acquired by channel attention. The mechanism (CAM) "CAM_1," and the formula of CAM is as follows:

$$\boldsymbol{F_c} = M(\mathbf{F}) \otimes \boldsymbol{F} \tag{8}$$

$$M(\boldsymbol{F}) = \delta\left(MLP\left(Avgpool(\boldsymbol{F})\right) MLP\left(Maxpool(\boldsymbol{F})\right)\right) \tag{9}$$

TABLE 1 | The network structure of 1D-CNN_CA.

Layer (type)	Output Shape
Conv1D_1	(None, n_f, 512)
Activation_1 (Activation = "Relu")	(None, n_f, 512)
CAM_1	(None, n_f, 512)
Flatten_1	(None, n_f × 512)
Droupout_1	(None, n_f × 512)
Dense_1 (Activation = "Relu")	(None, 2048)
Dense_2 (Activation = "Relu")	(None, 1024)
Dense_3 (Activation = " Liner")	(None, n_class)
Activation_2 ("Softmax")	(None, n_class)

CAM_1 is channel attention mechanism.

where $\boldsymbol{F_c}$ is the output feature by CAM, and $\boldsymbol{F}$ is the input feature of CAM. The $\otimes$ is element-wise multiplication, and δ is the sigmoid function. $Avgpool(\boldsymbol{F})$ and $Maxpool(\boldsymbol{F})$ are the global average pooling and maximum global pooling of $\boldsymbol{F}$. *MLP* is multilayer perceptron.

Then, the optimized multi-dimensional features are converted to one-dimensional features by "Flatten_1." The "Dropout_1" prevents the networks from overfitting, which is set to 0.4. Subsequently, the dense layers "Dense_1," "Dense_2," and "Dense_3" are used, with the activation function "Relu," "Relu," and "Liner," respectively. Finally, the "Softmax" activation function is used to output the classification results.

Optimization of Classification Based on Connected Domain Calibration Method

In the study area, the corn residue-covered areas generally have the natural characteristics of being connected in a large area. However, corn residue-covered areas are classified based on the pixel level, and there will be fine spots in the results. Therefore, it is necessary to use the connected domain calibration method to optimize each type globally. The flow of the connected domain calibration method is shown in **Figure 6**. Assume that **Figure 6A** is a sub-image of classification results, the number 1 represents one Type, and the number 2 represents another Type. The green area is a 4 connected domain sliding window. The connected domains of different types are marked by sliding windows (**Figure 6B**). At the same time, the smallest connected domain is deleted to obtain the optimization result (**Figure 6C**). By setting a reasonable threshold, the classification results are calibrated and optimized in this way globally.

Accuracy Assessment of Classification of Corn Residue-Covered Types

There are three kinds of indexes used to assess the classification performance of classification models for corn residue-covered types (Kirasich et al., 2018; Foody, 2020), which are *Kappa*,

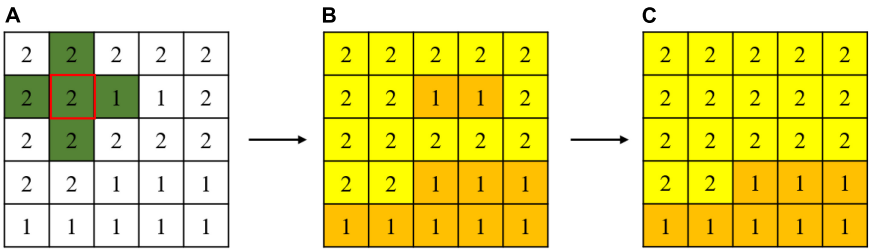

FIGURE 6 | Connected domain calibration process is **(A)** a sub-image of classification results, **(B)** the connected domains of different types, and **(C)** the optimization result.

overall accuracy (*OA*), and time cost (*TC*), respectively. The *Kappa* measures the spatial consistency and spatial changes of classification results, and the following formula can express it:

$$Kappa = \frac{OA - P_k}{1 - P_k} \tag{10}$$

where *OA* is the proportion of correctly predicted pixels, and P_k is the probability of random agreement. The following formula expresses *OA*:

$$OA = \frac{p_{ii}}{p_{ii}p_{ij}} \tag{11}$$

where p_{ii} is the number of correctly classified samples, and p_{ij} is the number of incorrectly classified samples for corn residue-covered type classifications. *TC* is the time cost of model classification, which is determined by the following formula:

$$TC = T_{end} - T_{start} \tag{12}$$

where T_{end} is the end timestamp of model classification, and T_{start} is the start timestamp of model classification.

RESULTS AND ANALYSIS

Building Multi-Scale Image Features for Describing the Intra-Object Heterogeneity

The multi-scale image dataset is generated by PCA and wavelet from the GF-2 image (B_{blue} : blue band, B_{green} : green band, B_{red} : red band, and B_{nir} : near-infrared band). The PCA transform can reduce feature redundancy and improve the processing speed of image features, which is done to reduce the data dimensionality of the GF-2 image. So, we retain PC1 with interprets more than 97% of the information of image features and ignore the relatively unimportant features simultaneously (PC2: 2.08%, PC3: 0.53%, and PC4: 0.07%). Based on the PC1 of the GF-2 image, the multi-scale image features (B_{ms2}, B_{ms4}, B_{ms8}, B_{ms16}, B_{ms32}, and B_{ms64}) are extracted using different window sizes ranging from 2 × 2 to 64 × 64 by the wavelet.

The multi-scale image features are quantified by using the variance method to describe intra-object heterogeneity. Each image feature is split into 25 blocks according to the size of 900 × 900 pixels (**Figure 7**). From **Figures 5A-F**, the variances of images are 4,023.3, 3,759.2, 3,435.7, 3,109.6, 2,725.7, and 2,268.4 in sequence, and the variance of each block also shows an apparent decreasing trend. These results reveal that the intra-object heterogeneity decreases with the increase of pixel neighborhood window size of multi-scale image features.

Optimizing Image Dataset

The contribution of each feature in the image dataset is different, so the *Gini*-importance is used to evaluate the importance of features quantitatively in the classification of corn residue cover. Moreover, the mean values of ten *Gini*-importance experiments are used to rank feature contributions. The importance (**Figure 8**) of the feature images from high to low is in the order of B_{ms64} (16.24%) > B_{ms32} (13.42%) > B_{nir} (12.97%) > B_{blue} (12.49%) > B_{ms16} (10.83%) > B_{green} (9.46%) > B_{red} (9.31%) > B_{ms8} (4.93%) > B_{ms4} (4.37%) > B_{ms2} (3.03%) > PC1 (2.91%). This importance ranking shows that the three most important feature images are B_{ms64}, B_{ms32}, and B_{nir}. The PC1 has the least contribution. It proves the importance of multi-scale image features for classifying corn residue cover.

The combination of different features will cause significant differences in classification results. The construction of each model is established on a dataset that adds features in order of the *Gini*-importance. The optimal dataset is chosen by comparing model performance (**Table 2**). The results reveal that Model 9 has the best performance with *Kappa* and *OA* values of 94.73% and 95.37%, respectively. Compared with Model 9, the performances of Model 1 to Model 8 and Model 10 to Model 13 are reduced by 47.73%/41.86%, 28.12%/24.76%, 8.27%/7.29%, 3.16%/2.78%, 2.45%/2.17%, 1.89%/1.67%, 0.07%/0.07%, 0.49%/0.44%, 0.28%/0.25%, 0.77%/0.68%, 8.98%/7.91%, and 7.02%/6.18% in Kappa/OA, respectively. Compared with Model 12 and Model 13, the Model 9 improve 8.98%/7.91%, 7.02%/6.18% in *Kappa*/*OA*, respectively. Therefore, the features (B_{blue}, B_{green}, B_{red}, B_{nir}, B_{ms4}, B_{ms8}, B_{ms16}, B_{ms32}, and B_{ms64}) with the best performance in Model 9 are chosen as the optimal image dataset (OID).

Exploring the Optimal Machine Learning Algorithm for Classification

The performance of different machine learning methods varies greatly, so five machine learning methods (NB, RF, SVM, 1D-CNN, and 1D-CNN_CA) are selected for comparison based on the OID. To ensure the fairness of the comparison in

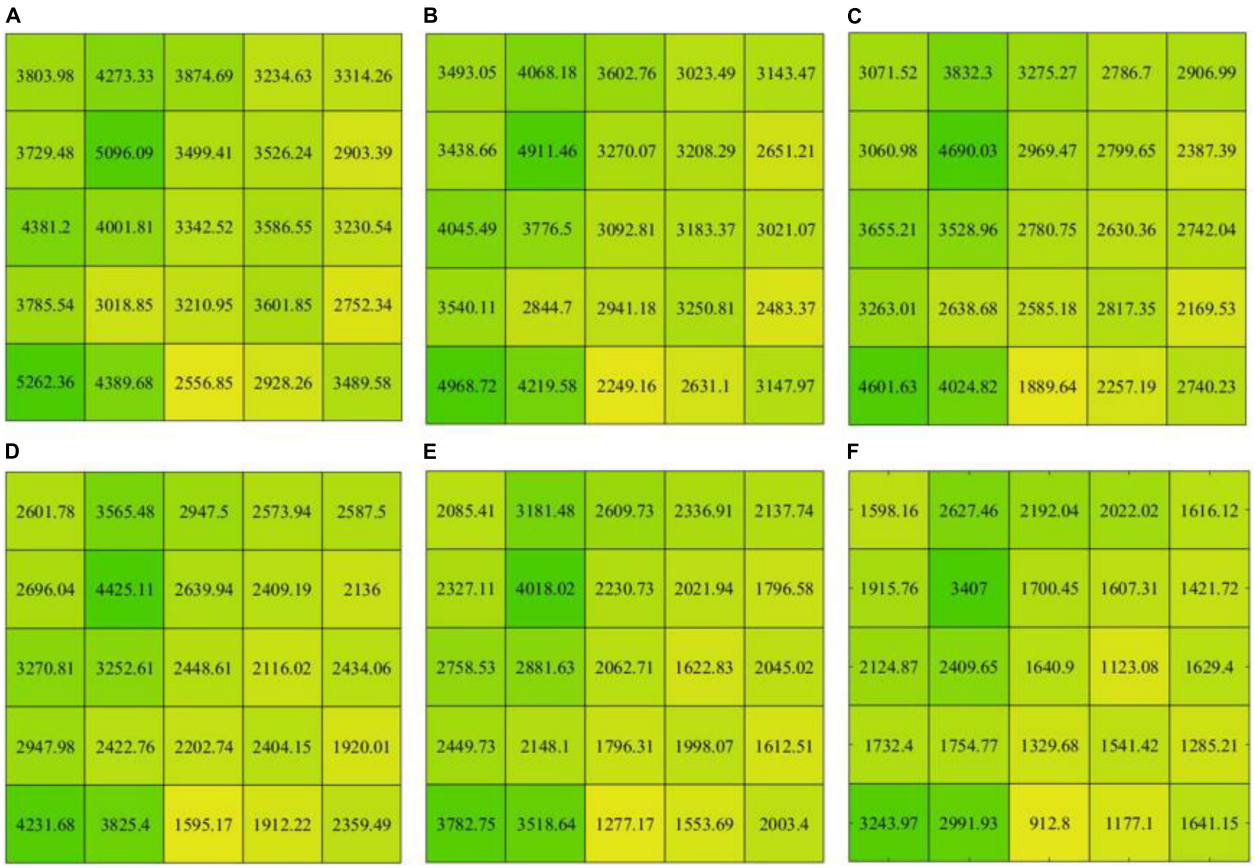

FIGURE 7 | The variance of the multi-scale feature images. **(A–F)** correspond to the variance of the B_{ms2}, B_{ms4}, B_{ms8}, B_{ms16}, B_{ms32}, and B_{ms64}, respectively.

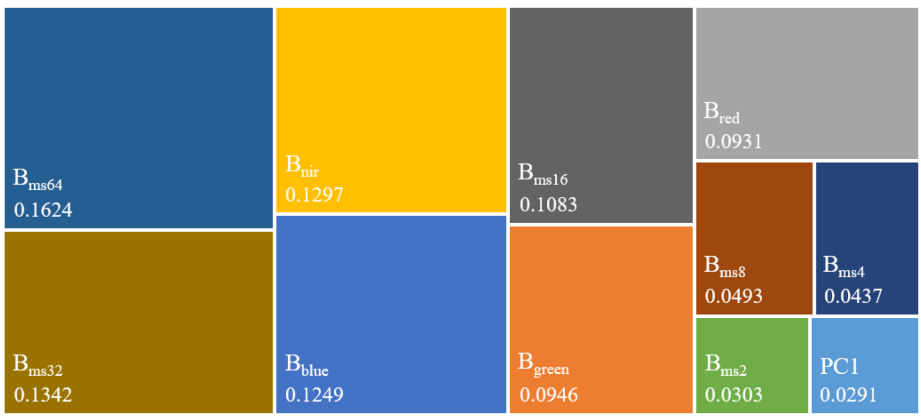

FIGURE 8 | The *Gini*-importance of image features. B_{blue}, B_{green}, B_{red}, and B_{nir} are the bands of GF-2 multispectral image. PC1 is the first principal component image. B_{ms2}, B_{ms4}, B_{ms8}, B_{ms16}, B_{ms32}, and B_{ms64} are multi-scale feature images with 2 × 2, 4 × 4, 8 × 8, 16 × 16, 32 × 32, and 64 × 64 neighborhood windows, respectively.

the experiments, the experiments are carried out under the same environmental configuration. Furthermore, considering that the parameters of machine learning methods are random, the optimal model parameters are identified by combining the random search and grid search. The main parameter of NB is prior probability, and the maximum likelihood method is used to calculate the prior probability automatically. The RF model parameters on OID are set as follows: the number of the decision tree is 1,411, the maximum depth of the decision tree is 281, and max features is sqrt.' The RF model parameters on DT1 are set as

TABLE 2 | The performance of different models based on features combinations.

	B_{blue}	B_{green}	B_{red}	B_{nir}	PC1	B_{ms2}	B_{ms4}	B_{ms8}	B_{ms16}	B_{ms32}	B_{ms64}	*Kappa*/%	*OA*/%
Model 1	–	–	–	–	–	–	–	–	–	–	+	47.00	53.51
Model 2	–	–	–	–	–	–	–	–	–	+	+	66.61	70.61
Model 3	–	–	–	+	–	–	–	–	–	+	+	86.46	88.08
Model 4	+	–	–	+	–	–	–	–	–	+	+	91.57	92.59
Model 5	+	–	–	+	–	–	–	–	+	+	+	92.28	93.20
Model 6	+	+	–	+	–	–	–	–	+	+	+	92.84	93.70
Model 7	+	+	+	+	–	–	–	–	+	+	+	94.66	95.30
Model 8	+	+	+	+	–	–	–	+	+	+	+	94.24	94.93
Model 9	**+**	**+**	**+**	**+**	–	–	**+**	**+**	**+**	**+**	**+**	**94.73**	**95.37**
Model10	+	+	+	+	-	+	+	+	+	+	+	94.45	95.12
Model11	+	+	+	+	+	+	+	+	+	+	+	93.96	94.69
Model12	+	+	+	+	–	–	–	–	-–	–	–	85.75	87.46
Model13	+	+	+	+	+	–	–	–	–	–	–	87.71	89.19

From B_{blue} to B_{nir} are the bands of GF-2 multispectral image. PC1 is the first principal component image. From B_{ms2} to B_{ms64} are multi-scale feature images with 2 × 2, 4 × 4, 8 × 8, 16 × 16, 32 × 32, and 64 × 64 neighborhood windows. "+" represents the added modeling features, and "–" represents the removed modeling features. The bold values represent the model with the best performance.

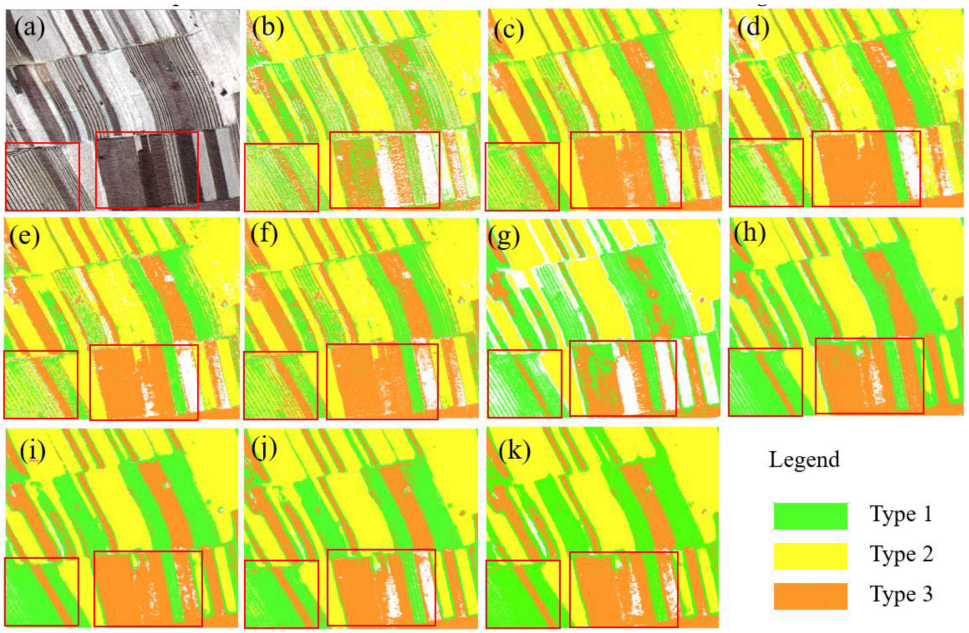

FIGURE 9 | Visualization of the classification result for different machine learning methods in sub-images. The original sub-image is **(a)** (R/B_{red}, G/B_{green}, and B/B_{blue}). **(b–f)** correspond to the classification results of NB, RF, SVM, 1D-CNN, and 1D-CNN_CA methods, respectively, using the image dataset DT1 (B_{blue}, B_{green}, B_{red}, and B_{nir}). **(g–k)** correspond to the classification results of NB, RF, SVM, 1D-CNN, and 1D-CNN_CA, respectively, using OID (B_{blue}, B_{green}, B_{red}, B_{nir}, B_{ms4}, B_{ms8}, B_{ms16}, B_{ms32}, and B_{ms64}).

TABLE 3 | The performances of different methods based on different dataset types.

Methods	**NB**		**RF**		**SVM**		**1D-CNN**		**1D-CNN_CA**	
DT	**DT1**	**OID**	**DT1**	**OID**	**DT1**	**OID**	**DT1**	**OID**	**DT1**	**OID**
Kappa/%	54.34	73.21	86.80	94.94	87.64	96.70	87.31	96.85	87.59	96.92
OA/%	59.62	76.41	88.39	95.55	89.13	97.09	88.94	97.15	89.08	97.26
Time/s	8.47	14.69	1687.98	2986.31	415.46	460.28	3650.06	4809.48	3658.72	4811.47

DT is the dataset type. DT1 is the image dataset constructed using four spectral features (B_{blue}, B_{green}, B_{red}, and B_{nir}). OID is the optimal image dataset (B_{blue}, B_{green}, B_{red}, B_{nir}, B_{ms4}, B_{ms8}, B_{ms16}, B_{ms32}, and B_{ms64}).

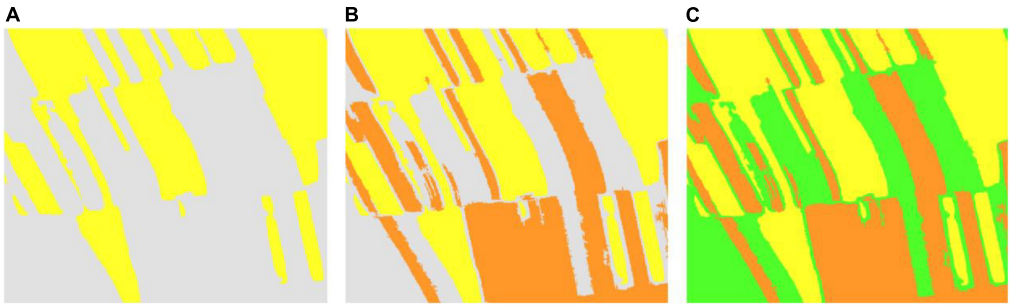

FIGURE 10 | The classification results are optimized based on the connected domain calibration method. **(A)** Type 2 optimized classification results. **(B)** Type 2 and Type 3 optimized classification results. **(C)** Optimal classification results of corn residue-covered areas.

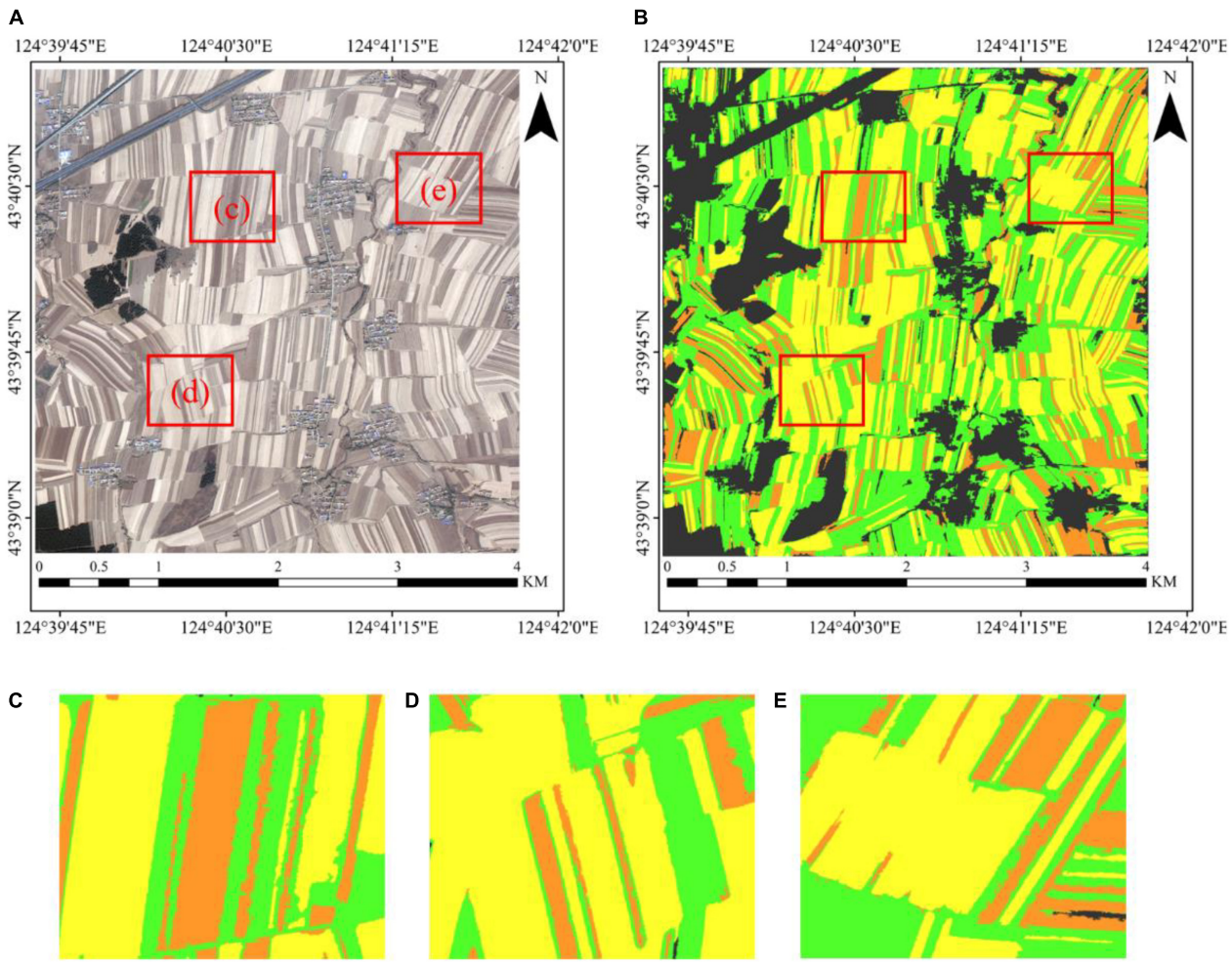

FIGURE 11 | The classification result of corn residue-covered types. **(A)** The GF-2 PMS image (R/B_{red}, G/B_{green}, and B/B_{blue}). **(B)** The classification result of corn residue-covered types. **(C–E)** The zoomed sub-image of the classification result.

follows: the number of the decision tree is 1,091, the maximum depth of the decision tree is 381, and max features is 'auto.' The SVM parameters on DT1 and OID are set as follows: cost or slack parameter is 510.0, gamma value is "scale," and the kernel type is radial basis function. The 1D-CNN and the 1D-CNN_CA have the same parameter settings on OID and DT1, "epochs" is 150, "batch_size" is 20, and the initial learning rate is 0.01.

The classification results of the sub-images (650 pixel × 580 pixel) are displayed in **Figure 9**. Images shown in **Figure 9a** are the original sub-images. Images shown in **Figures 9b-f**

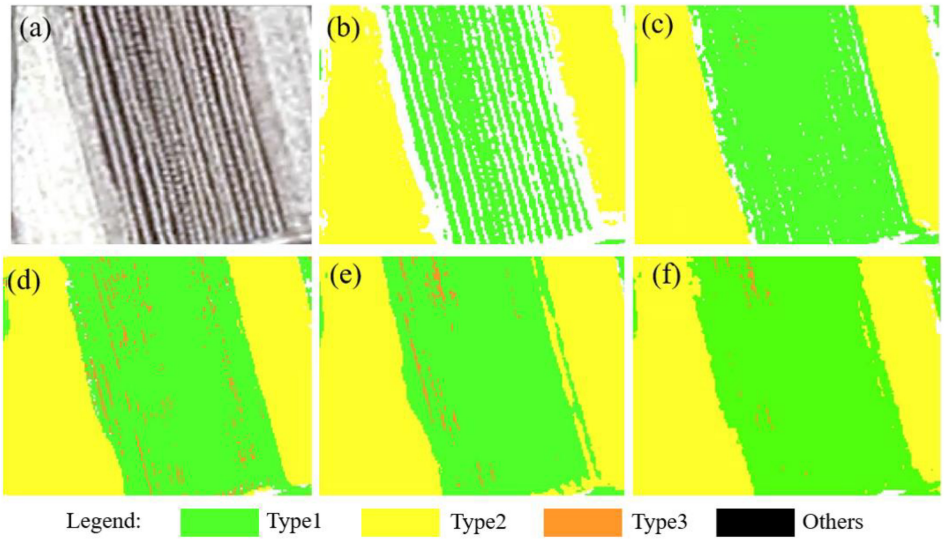

FIGURE 12 | The classification result of five methods. **(a)** The GF-2 PMS sub-image (R/B_{red}, G/B_{green}, and B/B_{blue}). **(b–f)** Correspond to the classification results of NB, RF, SVM, 1D-CNN, and 1D-CNN_CA using OID.

correspond to the classification results of NB, RF, SVM, 1D-CNN, and 1D-CNN_CA based on DT1 (B_{blue}, B_{green}, B_{red}, and B_{nir}), which have serious noise of salt-and-pepper and a lot of misclassifications due to intra-object heterogeneity. Images shown in **Figures 9g-k** correspond to the classification results of NB, RF, SVM,1D-CNN, and 1D-CNN_CA based on the OID, which have relatively good field edge details and fewer salt-and-pepper problems. Moreover, the classification results of the RF, SVM, and SVM have better visual effects, low noise, and low misclassification, and retain field edge details, especially the SVM classification results. The performances of different methods are presented in **Table 3**.

Regarding time cost, the NB method has the fastest classification speed, but it was the worst for the datasets in classification accuracy. 1D-CNN_CA is the slowest, which is related to model parameters. Compared with the NB, RF, SVM, 1D-CNN, and 1D-CNN_CA methods based on DT1 in **Table 3**, these methods using the OID show improved results, that is, 18.87% / 16.79% / 6.22s, 8.14% / 7.16% / 1298.33s, 9.06% / 7.96% / 44.82s, 9.54% / 8.21% / 1159.42s and 9.33% / 8.18% / 1152.75s in *Kappa* / *OA* / *TC*. The results show that using the OID with more features consumes some *TC* but greatly improves the classification accuracy (*Kappa* and *OA*), which also explains the superiority of the fusion multi-scale feature dataset. For the NB, RF, SVM, and 1D-CNN methods, based on the OID, the 1D-CNN_CA method showed improved results, that is, 23.71% / 20.85% / 4796.78s, 1.98% /1.71% / 1825.16s, 0.22% /0.17% / 4351.19s and 0.07% / 0.11% / 1.99s in *Kappa* / *OA* / *TC*. The results show that the 1D-CNN_CA method has the highest accuracy (*Kappa* and *OA*), which also reflects the effectiveness of the attention mechanism. Compared with SVM and 1D-CNN, the improvement in 1D-CNN-CA is slight. Therefore, considering the trade-off of time-saving and accuracy, the SVM method is selected to classify corn residue-covered types.

Optimizing and Mapping the Residue-Covered Types

The comparison experiments in Section "Exploring the Optimal Machine Learning Algorithm for Classification" reveal that the SVM is suitable for the classification task in this study. Considering that the classification result still has some noise, the connected domain calibration method is chosen to optimize classification to ensure the integrity of the plot area. From the visual point of view, the plot areas in the results of Type 2 are the most complete, so the connected domain calibration method with a threshold of 60 pixels is used to denoise Type 2 first, as shown in **Figure 10A**. Then, we use a similar method to denoise Type 3 and Type 1, as shown in **Figure 10B** and **Figure 10C**.

The optimized classification result is shown in **Figure 11**. **Figure 11A** is the original GF-2 PMS image dataset (R/red band, G/green band, and B/blue band), and **Figure 11B** is the corresponding classification result. **Figures 11C-E** represents the zoomed sub-images from **Figure 11B**. **Figures 11B-E** reveals that the classification result is satisfactory, and the three types of corn residue cover can be distinguished clearly. The results show that the proposed method is suitable for corn residue cover with severe spectral intra-object heterogeneity from the GF-2 image, classifying corn residue cover effectively and accurately.

DISCUSSION

Compared with the low and medium spatial resolution remote sensing, the high spatial resolution GF-2 PMS images have more details and spatial information. However, the spectral information of the high-resolution image is not as stable as the low- and medium-resolution images (Wang et al., 2018),

which had severe intra-object heterogeneity resulting from the different straw mulching ways. Therefore, we explored a multi-scale feature fused method to classify the corn residue cover using Chinese high-resolution GF-2 PMS images. Compared with previous studies (Huang et al., 2007; Martis et al., 2013; Ma et al., 2020), our study achieved the following objectives: (1) We extracted multi-scale features by compressing the spatial information of pixels neighborhood using wavelet and PCA in GF2 images, which can alleviate the problem of intra-object spectral differences effectively in corn residue cover. (2) By comparing NB, RF, SVM, and 1D-CNN methods, the designed 1D-CNN_CA method based on 1D-CNN and attention mechanism had the highest classification accuracy in the classification task. (3) Considering the classification performance and the integrity of the plot, the most appropriate machine learning method and connected domain calibration method were combined to map corn residue-covered types effectively and accurately in the regional area. According to the analysis in Section "Optimizing Image Dataset," it can be seen that the spectrum has a small contribution to straw mulching classification, so this work totally ignored the soil moisture, crop residue moisture, and residue decomposing effect on the cropland spectra (Yue et al., 2020). Due to the limitation of the spectral range of the Chinese GF-2 remote sensing images (B_{blue}, B_{green}, B_{red}, and B_{nir}), some spectral indices of the crop residue cover are difficult to apply to this study (Wan et al., 2022).

The performance of different models in each corn residue-covered type is different. **Figure 12** shows the classification effect of Type 1 and Type 2 residues, with Type 1 exhibiting clear spectral differences. By visual contrast, the 1D-CNN_CA (**Figure 12f**) method has obvious advantages in the classification of Type 1 residues, as the classification results have low noise. The SVM (**Figure 12d**) and the RF (**Figure 12c**) have a better classification effect on Type 2. **Figure 9** shows that the SVM shows superiority in Type 3. Therefore, future research objectives should focus on combining the advantages of different models in a certain category of classification. In addition, the data fusion of multispectral information and multi-resolution remote sensing image features, which have the potential to improve the classification performance of the crop residue cover, should be considered in the future.

It plays an increasingly important role in agricultural development to obtain crop information accurately and quickly by using high-resolution satellite remote sensing images. The retention of crop residue in fields can be considered vital in promoting physical, chemical, and biological attributes of soil health in the agricultural systems of developing countries (Turmel et al., 2015; Goswami et al., 2020). The classification map of crop residue cover was obtained accurately and quickly by the method used in this study, which can be used for monitoring the implementation of conservation tillage, statistics of the amount of crop residue in the region, clean energy production, and formulation of agricultural subsidy policies.

CONCLUSION

Rapid and accurate classification of corn residue-covered types in the regional area is vital for black soil protection. In order to improve the classification performance, multi-scale feature fusion is proposed for solving the problem of intra-object heterogeneity in this study. The key conclusions are as follows:

(1). The contribution of different features in the image dataset to classification was determined by *Gini*-importance. It is found that multi-scale features obtained by compressing spatial information of pixel neighborhood with the wavelet method show the highest contribution, particularly the multi-scale feature images with 32×32 and 64×64 neighborhood windows.

(2). Compared with DT1, the machine learning method based on the OID can obtain better classification performance. By comparing five methods, including the NB, RF, SVM, 1D-CNN, and 1D-CNN_CA models, the 1D-CNN_CA model has the highest accuracy, and the SVM model is time-saving and has high accuracy in classifying corn residue cover types.

(3). The combination of the SVM model and connected domain calibration method can improve the visualization effect effectively, which is used to classify the GF-2 image and obtain satisfactory classification results. The results reveal that the method proposed in this paper can effectively alleviate intra-object heterogeneity for corn residue cover.

Due to the limitation in the coverage of Chinese GF-2 PMS images, the classification is done only in a $4{,}500 \times 4{,}500$ pixels area in this study. In the future, we will combine transfer learning and a broader range of image sources to achieve a broader range for corn residue-covered classification.

DATA AVAILABILITY STATEMENT

The original contributions presented in this study are included in the article/supplementary material, further inquiries can be directed to the corresponding author/s.

AUTHOR CONTRIBUTIONS

This work was cooperated by our research team, and the contributions are as followed. WT and WS: conceptualization and methodology. WT: original draft preparation. WS, YZ, and XL: review and editing. JH and FX: visualization. JL and YD: validation. BL and JY: supervision. All authors have read and agreed to the published version of the manuscript.

FUNDING

This research was funded by the National Natural Science Foundation of China under the projects "Retrieving corn residue fraction by harmonizing LiDAR points and optimal remote sensing images" (No. 42171331) and the 2115 Talent development Program of China Agricultural University.

REFERENCES

Abbas, A. W., Minallh, N., Ahmad, N., Abid, S. A. R., and Khan, M. A. A. (2016). K-means and ISODATA clustering algorithms for landcover classification using remote sensing. *Sindh Univ. Res. J. SURJ* 48, 315–318.

Ai, D., Yang, J., Wang, Z., Fan, J., Ai, C., and Wang, Y. (2015). Fast multi-scale feature fusion for ECG heartbeat classification. *EURASIP J. Adv. Signal Process.* 2015:46. doi: 10.1186/s13634-015-0231-0

Alhayani, B., and Ilhan, H. (2017). Hyper spectral image classification using dimensionality reduction techniques. *Int. J. Innov. Res. Electr. Electron. Instrum. Control Eng.* 5, 71–74. doi: 10.17148/IJIREEICE.2017.5414

Antoniadis, A., Lambert-Lacroix, S., and Poggi, J. M. (2021). Random forests for global sensitivity analysis: a selective review. *Reliabil. Eng. Syst. Saf.* 206:107312. doi: 10.1016/j.ress.2020.107312

Belgiu, M., and Drăguţ, L. (2016). Random forest in remote sensing: a review of applications and future directions. *ISPRS J. Photogramm. Remote Sens.* 114, 24–31. doi: 10.1016/j.isprsjprs.2016.01.011

Bhuvaneshwari, S., Hettiarachchi, H., and Meegoda, J. N. (2019). Crop residue burning in India: policy challenges and potential solutions. *Int. J. Environ. Res. Public Health* 16:832. doi: 10.3390/ijerph16050832

Bonaccorso, G. (2017). *Machine Learning Algorithms*. Birmingham: Packt Publishing Ltd.

Bruzzone, L., and Persello, C. (2010). "Recent trends in classification of remote sensing data: active and semisupervised machine learning paradigms," in *Proceedings of the 2010 IEEE International Geoscience and Remote Sensing Symposium* (Washington, DC: IEEE), 3720–3723. doi: 10.1109/IGARSS.2010.5651236

Casale, P., Pujol, O., and Radeva, P. (2011). "Human activity recognition from accelerometer data using a wearable device," in *Proceedings of the Iberian Conference on Pattern Recognition and Image Analysis* (Berlin: Springer), 289–296. doi: 10.1007/978-3-642-21257-4_36

Drotar, P., Gazda, J., and Smekal, Z. (2015). An experimental comparison of feature selection methods on two-class biomedical datasets. *Comput. Biol. Med.* 66, 1–10. doi: 10.1016/j.compbiomed.2015.08.010

Feng, T., Wang, C., Zhang, J., Wang, B., and Jin, Y. F. (2021). An improved artificial bee colony-random forest (IABC-RF) model for predicting the tunnel deformation due to an adjacent foundation pit excavation. *Underground Space.* 6, 1–14 doi: 10.1016/j.undsp.2021.11.004

Foody, G. M. (2020). Explaining the unsuitability of the kappa coefficient in the assessment and comparison of the accuracy of thematic maps obtained by image classification. *Remote Sens. Environ.* 239:111630. doi: 10.1016/j.rse.2019.111630

Freebairn, D., and Boughton, W. (1985). Hydrologic effects of crop residue management practices. *Soil Res.* 23, 23–35. doi: 10.1016/j.scitotenv.2015.10.066

Goswami, S. B., Mondal, R., and Mandi, S. K. (2020). Crop residue management options in rice–rice system: a review. *Arch. Agron. Soil Sci.* 66, 1218–1234. doi: 10.1080/03650340.2019.1661994

Gu, Y. F., Chanussot, J., Jia, X. P., and Benediktsson, J. A. (2017). Multiple kernel learning for hyperspectral image classification: a review. *IEEE Transact. Geosci. Remote Sens.* 55, 6547–6565. doi: 10.1109/TGRS.2017.2729882

Huang, X., Zhang, L. P., and Li, P. X. (2007). Classification of high spatial resolution remotely sensed imagery based upon fusion of multiscale features and SVM. *J. Remote Sens. Beijing* 11:48.

Jakkula, V. (2006). Tutorial on support vector machine (svm). *Sch. EECS Wash. State Univ.* 37:3

Jat, H. S., Jat, R. D., Nanwal, R. K., Lohan, S. K., Yadav, A. K., Poonia, T., et al. (2020). Energy use efficiency of crop residue management for sustainable energy and agriculture conservation in NW India. *Renew. Energy* 155, 1372–1382. doi: 10.1016/j.renene.2020.04.046

Kang, X. D., Duan, P. H., and Li, S. (2020). Hyperspectral image visualization with edge-preserving filtering and principal component analysis. *Inf. Fusion* 57, 130–143. doi: 10.1016/j.inffus.2019.12.003

Kaur, A. (2017). Crop residue in Punjab agriculture-status and constraints. *J. Krishi Vigyan* 5, 22–26. doi: 10.5958/2349-4433.2017.00005.8

Khanal, S., Klopfenstein, A., Kushal, K. C., Ramarao, V., Fulton, J., Douridas, N., et al. (2021). Assessing the impact of agricultural field traffic on corn grain yield using remote sensing and machine learning. *Soil Tillage Res.* 208:104880. doi: 10.1016/j.still.2020.104880

Kirasich, K., Smith, T., and Sadler, B. (2018). Random forest vs logistic regression: binary classification for heterogeneous datasets. *SMU Data Sci. Rev.* 1:9.

Leung, K. M. (2007). Naive Bayesian classifier. *Polytech. Univ. Depart. Comput. Sci. Finance Risk Eng.* 2007, 123–156.

Lu, X. (2020). A meta-analysis of the effects of crop residue return on crop yields and water use efficiency. *PLoS One* 15:e0231740. doi: 10.1371/journal.pone.0231740

Ma, H., Liu, D., Yan, N., Li, H., and Wu, F. (2020). End-to-end optimized versatile image compression with wavelet-like transform. *IEEE Trans. Pattern Anal. Mach. Intell.* 44, 1247–1263. doi: 10.1109/TPAMI.2020.3026003

Ma, L., Li, M., Ma, X., Cheng, L., Du, P., and Liu, Y. (2017). A review of supervised object-based land-cover image classification. *ISPRS J. Photogramm. Remote Sens.* 130, 277–293. doi: 10.1016/j.isprsjprs.2017.06.001

Martis, R. J., Acharya, U. R., and Min, L. C. (2013). ECG beat classification using PCA, LDA, ICA and discrete wavelet transform. *Biomed. Signal Process. Control* 8, 437–448. doi: 10.1016/j.bspc.2013.01.005

Maxwell, A. E., Warner, T. A., and Fang, F. (2018). Implementation of machine-learning classification in remote sensing: an applied review. *Int. J. Remote Sens.* 39, 2784–2817. doi: 10.1080/01431161.2018.1433343

Munnaf, M. A., Haesaert, G., and Mouazen, A. M. (2021). Map-based site-specific seeding of seed potato production by fusion of proximal and remote sensing data. *Soil Tillage Res.* 206:104801. doi: 10.1016/j.still.2020.104801

Myint, S. W., Lam, N., and Tyler, J. (2002). An evaluation of four different wavelet decomposition procedures for spatial feature discrimination in urban areas. *Transact. GIS* 6, 403–429. doi: 10.1111/1467-9671.00120

Najafi, P., Navid, H., Feizizadeh, B., and Eskandari, I. (2018). Object-based satellite image analysis applied for crop residue estimating using Landsat OLI imagery. *Int. J. Remote Sens.* 39, 6117–6136. doi: 10.1080/01431161.2018.1454621

Nunez, J., Otazu, X., Fors, O., Prades, A., Pala, V., and Arbiol, R. (1999). Multiresolution-based image fusion with additive wavelet decomposition. *IEEE Transact. Geosci. Remote Sens.* 37, 1204–1211. doi: 10.1109/36.763274

Pi, H., Webb, N. P., Huggins, D. R., and Sharratt, B. (2020). Critical standing crop residue amounts for wind erosion control in the inland Pacific Northwest, USA. *Catena* 195:104742. doi: 10.1016/j.catena.2020.104742

Rodriguez-Galiano, V. F., Ghimire, B., Rogan, J., Chica-Olmo, M., and Rigol-Sanchez, J. P. (2012). An assessment of the effectiveness of a random forest classifier for land-cover classification. *ISPRS J. Photogramm. Remote Sens.* 67, 93–104. doi: 10.1016/j.isprsjprs.2011.11.002

Shi, Z. K., Li, P. J., and Sun, Y. (2016). "An outlier generation approach for one-class random forests: an example in one-class classification of remote sensing imagery," in *Proceedings of the 2016 IEEE International Geoscience and Remote Sensing Symposium (IGARSS)*, Beijing, 5107–5110. doi: 10.1109/IGARSS.2016.7730331

Strobl, C., Boulesteix, A. L., Zeileis, A., and Hothorn, T. (2007). Bias in random forest variable importance measures: illustrations, sources and a solution. *BMC Bioinformatics* 8:25. doi: 10.1186/1471-2105-8-25

Talukdar, S., Singha, P., Mahato, S., Pal, S., Liou, Y. A., and Rahman, A. (2020). Land-use land-cover classification by machine learning classifiers for satellite observations—a review. *Remote Sens.* 12:1135. doi: 10.3390/rs12071135

Tatsumi, K., Yamashiki, Y., Morante, A. K. M., FernÁndez, L. R., and Nalvarte, R. A. (2016). Pixel-based crop classification in Peru from Landsat 7 ETM+ images using a random forest model. *J. Agric. Meteorol.* 72, 1–11. doi: 10.2480/agrmet.D-15-00010

Trivizakis, E., Ioannidis, G. S., Souglakos, I., Karantanas, A. H., Tzardi, M., and Marias, K. (2021). A neural pathomics framework for classifying colorectal cancer histopathology images based on wavelet multi-scale texture analysis. *Sci. Rep.* 11:15546. doi: 10.1038/s41598-021-94781-6

Turmel, M. S., Speratti, A., Baudron, F., Verhulst, N., and Govaerts, B. (2015). Crop residue management and soil health: a systems analysis. *Agric. Syst.* 134, 6–16. doi: 10.1016/j.agsy.2014.05.009

Unger, P. W., Stewart, B. A., Parr, J. F., and Singh, R. P. (1991). Crop residue management and tillage methods for conserving soil and water in semiarid regions. *Soil Tillage Res.* 20, 219–240. doi: 10.1016/0167-1987(91)90041-U

Wan, W., Liu, Z., Li, B., Fang, H., Wu, H., and Yang, H. (2022). Evaluating soil erosion by introducing crop residue cover and anthropogenic disturbance intensity into cropland C-factor calculation: novel estimations from a cropland-dominant region of Northeast China. *Soil Tillage Res.* 219:105343. doi: 10.1016/j.still.2022.105343

Wang, N., Li, Q., Du, X., Zhang, Y., Zhao, L., and Wang, H. (2017). Identification of main crops based on the univariate feature selection in Subei. *Remote Sens.* 21, 519–530.

Wang, W., Li, W., Zhang, C., and Zhang, W. (2018). Improving object-based land use/cover classification from medium resolution imagery by Markov chain geostatistical post-classification. *Land* 7:31. doi: 10.3390/land7010031

Wang, Y., Zhang, Z., Feng, L., Ma, Y., and Du, Q. (2021). A new attention-based CNN approach for crop mapping using time series Sentinel-2 images. *Comput. Electron. Agric.* 184:106090. doi: 10.1016/j.compag.2021.106090

Weiss, M., Jacob, F., and Duveiller, G. (2020). Remote sensing for agricultural applications: a meta-review. *Remote Sens. Environ.* 236:111402. doi: 10.1016/j.rse.2019.111402

Yan, T., Xu, W., Lin, J., Duan, L., Gao, P., Zhang, C., et al. (2021). Combining multi-dimensional convolutional neural network (CNN) with visualization method for detection of *Aphis gossypii* glover infection in cotton leaves using hyperspectral imaging. *Front. Plant Sci.* 12:74. doi: 10.3389/fpls.2021.604510

Yao, Q., Liu, J. J., Yu, Z. H., Li, Y. S., Jin, J., Liu, X. B., et al. (2017). Three years of biochar amendment alters soil physiochemical properties and fungal community composition in a black soil of Northeast China. *Soil Biol. Biochem.* 110, 56–67. doi: 10.1016/j.soilbio.2017.03.005

Yin, Z., and Hou, J. (2016). Recent advances on SVM based fault diagnosis and process monitoring in complicated industrial processes. *Neurocomputing* 174, 643–650. doi: 10.1016/j.neucom.2015.09.081

Yue, J., Tian, Q., Dong, X., and Xu, N. (2020). Using broadband crop residue angle index to estimate the fractional cover of vegetation, crop residue, and bare soil in cropland systems. *Remote Sens. Environ.* 237:111538. doi: 10.1016/j.rse.2019.111538

Zhang, L., Liu, Z., Ren, T. W., Liu, D. Y., Ma, Z., Tong, L., et al. (2020). Identification of seed maize fields with high spatial resolution and multiple spectral remote sensing using random forest classifier. *Remote Sens.* 12:362. doi: 10.3390/rs12030362

Zheng, B. J., Campbell, J. B., Shao, Y., and Wynne, R. H. (2013). Broad-scale monitoring of tillage practices using sequential Landsat imagery. *Soil Sci. Soc. Am. J.* 77, 1755–1764. doi: 10.2136/sssaj2013.03.0108

Zheng, H. B., Liu, W. R., Zheng, J. Y., Luo, Y., Li, R. P., Wang, H., et al. (2018). Effect of long-term tillage on soil aggregates and aggregate-associated carbon in black soil of Northeast China. *PLoS One* 13:e0199523. doi: 10.1371/journal.pone.0199523

Zhong, L., Hu, L., and Zhou, H. (2019). Deep learning based multi-temporal crop classification. *Remote Sens. Environ.* 221, 430–443. doi: 10.1016/j.rse.2018.11.032

Conflict of Interest: The authors declare that the research was conducted in the absence of any commercial or financial relationships that could be construed as a potential conflict of interest.

Publisher's Note: All claims expressed in this article are solely those of the authors and do not necessarily represent those of their affiliated organizations, or those of the publisher, the editors and the reviewers. Any product that may be evaluated in this article, or claim that may be made by its manufacturer, is not guaranteed or endorsed by the publisher.

Copyright © 2022 Tao, Dong, Su, Li, Xuan, Huang, Yang, Li, Zeng and Li. This is an open-access article distributed under the terms of the Creative Commons Attribution License (CC BY). The use, distribution or reproduction in other forums is permitted, provided the original author(s) and the copyright owner(s) are credited and that the original publication in this journal is cited, in accordance with accepted academic practice. No use, distribution or reproduction is permitted which does not comply with these terms.

frontiers | Frontiers in Plant Science

ORIGINAL RESEARCH
published: 23 June 2022
doi: 10.3389/fpls.2022.915109

Estimating Maize Yield in the Black Soil Region of Northeast China Using Land Surface Data Assimilation: Integrating a Crop Model and Remote Sensing

Ying Cui[1,2], Suhong Liu[1,2], Xingang Li[1,2], Hao Geng[1,2], Yun Xie[1,2] and Yuhua He[3]*

[1] Faculty of Geographical Science, Beijing Normal University, Beijing, China, [2] Beijing Key Laboratory of Environmental Remote Sensing and Digital Cities, Beijing Normal University, Beijing, China, [3] Land Satellite Remote Sensing Application Center, Ministry of Natural Resources of the People's Republic of China, Beijing, China

OPEN ACCESS

Edited by:
Xiuliang Jin,
Key Laboratory of Crop Physiology and Ecology (CAAS), China

Reviewed by:
Yunshan Yang,
Shihezi University, China
Chenyao Yang,
University of Trás-os-Montes and Alto Douro, Portugal
Albert Thembinkosi Modi,
University of KwaZulu-Natal, South Africa

***Correspondence:**
Suhong Liu
liush@bnu.edu.cn

Specialty section:
This article was submitted to Sustainable and Intelligent Phytoprotection, a section of the journal Frontiers in Plant Science

Received: *07 April 2022*
Accepted: *30 May 2022*
Published: *23 June 2022*

Citation:
Cui Y, Liu S, Li X, Geng H, Xie Y and He Y (2022) Estimating Maize Yield in the Black Soil Region of Northeast China Using Land Surface Data Assimilation: Integrating a Crop Model and Remote Sensing. Front. Plant Sci. 13:915109. doi: 10.3389/fpls.2022.915109

Accurate yield estimation at the regional scale has always been a persistent challenge in the agricultural sector. With the vigorous emergence of remote sensing land surface observations in recent decades, data assimilation methodology has become an effective means to promote the accuracy and efficiency of yield estimation by integrating regional data and point-scale crop models. This paper focuses on the black soil area of Northeast China, a national strategic grain production base, applying the AquaCrop crop growth model to simulate the fractional vegetation cover (FVC) and maize yield from 2000 to 2020 and then forming a reliable FVC optimization dataset based on an ensemble Kalman filter (EnKF) assimilation algorithm with remote sensing products. Using the random forest model, the regression relationship between FVC and yield was established from the long-term time series data, which is crucial to achieve better yield estimation through the optimized FVC. The major findings include the following: (1) The R^2 of the assimilated FVC and maize yield can reach 0.557. (2) When compared with the local statistical yield, our method reduced the mean absolute error (MAE) from 1.164 ton/ha (based on GLASS FVC products) to 1.004 ton/ha (based on the calibrated AquaCrop model) and then to 0.888 ton/ha (the result after assimilation). The above results show that we have proposed a yield estimation method to provide accurate yield estimations by combining data assimilation and machine learning. This study provided deep insights into understanding the variations in FVC and revealed the spatially explicit yield prediction ability from the time series land surface parameters, which has significant potential for optimizing water and soil resource management.

Keywords: AquaCrop model, Kalman filter, remote sensing, yield prediction, random forest, data assimilation

INTRODUCTION

Agricultural production is the foundation of human survival. Accurate prediction of crop yield enables farmers to estimate profits and adjust crop-planting patterns. Governments also benefit from yield prediction information, which helps to promote the development and reform of food security, sustainable utilization of water and soil resources, agricultural trade and many other aspects (Feng et al., 2021).

The northeastern Chinese black soil area is a major black soil zone of the world and a strategic guarantee base for national food security by producing crops such as maize and soybean (Lin et al., 2019). The special soil properties and natural geographical conditions make its rain-fed agricultural production mode different from other main grain-producing areas. Atmospheric precipitation has become one of the main influencing factors of crop yield (Cui et al., 2021). According to these characteristics of this area, there is an urgent need to carry out detailed research on crop yield estimation, especially on maize with large planting scale and appreciable economic benefits (Qian et al., 2018).

Crop growth models are an important tool to quantitatively describe the growth and yield formation process of specific crops under specific environments based on point scales (Van et al., 1989; Monteith, 1996; Steduto et al., 2009), and it is difficult to characterize the spatial low of crop growth due to the limitation of scale. The current research trend is to run models on a regional scale and then establish the response system of crop growth to soil and meteorological environment changes to provide macro decision-making for precision agriculture. Different from photosynthetic effective radiation driving mechanism of WOFOST model and the other crop model (Todorovic et al., 2009), AquaCrop model is driven by water factors and simulates crop yield based on water use efficiency (Raes et al., 2009) and is widely used in arid and rain-fed areas with great research prospects in water-efficient utilization (Eshete et al., 2020). This model evolved from the crop water response equation in the irrigation and drainage Document No. 33 of the Food and Agriculture Organization of the United Nations (FAO) (Passioura, 1996). Several studies have applied AquaCrop model to simulate and evaluate typical crops growth in different regions and got great results. Iqbal et al. (2014) demonstrated that the yield of winter wheat in North China Plain simulated by AquaCrop model performed unsatisfied under strong water stress, and the accuracy is significantly improved after parameter calibration. Sandhu and Irmak (2019) found the AquaCrop simulated yield and evapotranspiration quite well in Midwestern America, but encountered substantial difficulties in simulating biomass and soil-water. The AquaCrop model driven by water has advantages for crop research in Northeast China, but relevant research has lacked.

Simulation and observation are two basic strategies of geoscience research (Li, 2016). Since almost all surface variables have high spatiotemporal heterogeneity, there is bound to be deviation and uncertainty in any parameterization process. From the perspective of simulation, although the crop model has sorted out the material cycle and other growth processes very clearly on the micro level, complex error transmission will accumulate, and the uncertainty reflected will be amplified in the simulation results when it is extended to the macro scale. From the perspective of observations, field measurements have high accuracy but low spatial representation. Obtaining abundant observations will be very laborious when studying a large-scale area with high heterogeneity. Although remote sensing observations already provide sufficient surface data, a sophisticated inversion algorithm is needed to gain effective information indirectly. The inversion and sensor accuracy greatly limit the reliability of remote sensing data. Therefore, integrating multisource observations and decreasing the uncertainty of the simulation is key to ameliorating the limitations of model application.

Data assimilation (DA) is an important integrating methodology that automatically adjusts the process model forward direction continuously by relying on observations and then generates the minimum-deviation state variable set with spatiotemporal consistency, which is usually used for modeling and dynamic prediction of complex systems (Li and Bai, 2010; Qin et al., 2018). With the rapid development of remote sensing technology, a large amount of earth observation data has emerged as crucial support for regional precision agriculture research. By reanalyzing the prior crop growth model with multi-temporal observation data, the reliability of the simulation results is improved, which is of great significance to agricultural dynamic monitoring, yield prediction, and regional resource management.

Looking at the relevant studies integrating crop model and remote sensing data in recent years (**Table 1**), the most common crop models are WOFOST, CERES and AquaCrop. The main crop types are winter wheat and other food crops. Optical remote sensing data is generally used for remote sensing observation data, and a few literatures show that InSAR has a good effect on retrieving soil water content (Wigneron et al., 2017). The assimilation variable generally selects LAI (leaf area index) for various crop models, while there are different options for AquaCrop model. In terms of assimilation algorithm, both cost function algorithm and filtering algorithm have more applications and innovations. The research objectives mostly focus on improving the accuracy of yield estimation. Most of the available studies using short-term data, mostly less than three growing seasons and may neglect the inter-annual variability in environmental conditions.

Although many studies have indicated the effectiveness of using crop models and remote sensing data assimilation for yield mapping, the expansion accuracy from the field to regional scale still lacks exploration (Steele-Dunne et al., 2017). Silvestro et al. (2017) used the updating assimilation method, the ensemble Kalman filter (EnKF), assimilated leaf area index (LAI) into the SAFY model, and used the calibration assimilation method, PSO, and assimilated canopy cover (CC) into the AquaCrop model to demonstrate the possibility of estimating wheat yield. The results show that the relative root-mean-square error (RRMSE) between the predicted and the measured yield ranges from 0.18 to 0.24 t/ha. SAFY with the EnKF method was more suitable than Aquacrop with PSO, which is mainly due to the high computational cost and the difficult calibration of the AquaCrop model. For the AquaCrop model, CC achieved a lower RMSE than LAI. Another finding of this article is that the accuracy of the assimilation method is greatly limited by the number of remote sensing images, three or four images with an error in LAI estimation of 30% and an error in the yield estimation of approximately 18%. Feng et al. (2019) used the multivariable linear regression model (MLR) and the RF model as external modifications of the APSIM crop model to predict wheat yield, while RF has a higher accuracy gain than MLR. The R^2 and

TABLE 1 | Research status of the crop model and remote sensing data assimilation.

Authors	Model	Crop	Data	Variable	Method	Objective	Region	Period
Hank et al., 2015	PROMET	Winter wheat	Landsat-TM; RapidEye	LAI	Filter	Regional yield estimation	Germany	2010-2011
Jin X. et al., 2016	AquaCrop	Winter wheat	Hyperspectral	AGB	PSO	Yield estimation	Beijing, China	2008-2011
Jin H. et al., 2016	CERES-Maize	Maize	MOD09A1	LAI	SA	LAI estimation	Jilin, China	2010
Xie et al., 2016	CERES-Wheat	Winter wheat	Landsat	LAI; SWC; AGB	PF	Yield estimation	Shanxi, China	2007-2014
Iqbal et al., 2014	AquaCrop; SAFY	Wheat	HJ-1; Landsat-8	LAI; CC	EnKF; PSO	Yield estimation	Yangling, China	2012-2015
Li et al., 2017	CERES-Wheat	Winter wheat	GF-1; HJ-1; Landsat-8	LAI	PF; 4DVar	Yield estimation	Hebei, China	2014
Gilardelli et al., 2019	WARM	Rice	Landsat-7/8; Sentinel-2	LAI	Downhill simplex method	Yield estimation	Italy	2014-2016
Hu et al., 2019	SWAP-WOFOST	Sugarcane	(Field experiment)	LAI; SWC	Forcing method; calibration method; EnKF	Yield estimation	Guangxi, China	2016-2017
Li et al., 2019	WheatSM	Winter wheat	MCD15A3; MCD15A3H	LAI	EnKF; SCE-UA	Yield estimation	Henan, China	2013-2017
Pique et al., 2020	SAFY-CO_2	Winter Wheat	Sentinel-2; SPOT-2/4/5	GAI	SAFY-CO_2	Assessing annual carbon budget	France	2005-2014
Tewes et al., 2020	LINTUL5	Winter Wheat	(Field experiment)	LAI	EnKF; WM	Yield estimation	France; Germany; Netherlands	2016-2017
Wu et al., 2021	WOFOST	Winter wheat	HJ-1; GF-1	LAI	ABT-4DVar	Yield estimation	Hebei, China	2013-2014
Peng et al., 2021	SAFY	Maize	UAV	LAI	EnKF	Yield estimation	Inner Mongolia, China	2019

AGB: Above ground biomass. CC: Canopy cover. PSO: Particle swarm optimization. SA: Simulated annealing. SCE-UA: Shuffled complex evolution. LAI: leaf area index. GAI: Green area index. UAV: unmanned aerial vehicle. LSOA: Least squares optimization algorithm. SWC: Soil water content. PF: particle filter. WM: Weighted Mean.

root-mean-square error (RMSE) between the predicted yield and the measured yield were 0.81 and 0.54 t/ha and 0.61 and 0.86 t/ha, respectively, before and after combining RF. Hu et al. (2019) used forcing, calibration, and EnKF, three assimilation methods for improving sugarcane crop simulation. The results show that EnKF performed the best in estimating soil water content, LAI development, and sugarcane yield. Assimilating LAI alone works better than assimilating LAI and SWC both under slight water stress levels, which demonstrates that the choice of assimilated variable relies on a reasonable diagnosis of the environment. In summary, the direct assimilation of remote sensing data to update vegetation assessments is very promising. Very limited literature available in Northeast China for yield estimation using data assimilation, especially for long-term study.

This study completed the calibration and validation of the AquaCrop model in Northeast China via field test data and applied 21 years of regional-scale simulations from 2000 to 2020. Then we selected FVC for AquaCrop model assimilation not only because it is one of the outputs of AquaCrop but also because it considers the important role it plays in surface process simulation. Due to the accumulation of sufficient assimilated FVC data and crop yield data, which reflect various environmental conditions, the relationship between yield and environmental factors was established through the machine learning method of random forest. Relying on the FVC assimilation curve, a high-precision estimation of crop yield can be obtained. This study aims to establish an assimilation system to better monitor FVC growth and provide better maize yield estimation, which is significant for local agricultural management.

MATERIALS AND METHODS

Study Area

The Songnen Plain (42°56′ ∼ 50°03′ N, 122°05′ ∼ 128°12′ E) is located in the middle of the Songliao black soil basin in Northeast China, with a total area of approximately 206404.3 km^2 and a large part of it is dominated by rain-fed agriculture. It has a temperate continental monsoon climate, the average annual temperature is approximately 0.4°C, the average annual precipitation is approximately 534 mm, and the altitude is approximately 250∼450 m. In 2021 Liu et al. (2021) classified the phaeozem and chernozem as typical black soil that is covered with a high content of organic matter dark humus and mapped three typical black soil areas in Northeast China which are Sanjiang, Songnen and Mengdong. This study took the Songnen typical black soil region as the study area, composed of Songnen Phaeozem region and Songnen chernozem region. Most farmland in the study area was planted with soybeans and maize without irrigation scheduling. The irrigation scenario was not

set up in the subsequent application of crop model. This paper established a database from 28 meteorological stations and 155 practical soil profile samples, scattered as shown in **Figure 1**. The phenological information of maize is shown in **Table 2**.

Meteorological Data

This study collected meteorological data from 28 weather stations from 2000 to 2020, including daily rainfall (mm), minimum and maximum temperature (°C) and solar radiation (MJ m^{-2} day^{-1}), as input to the AquaCrop meteorological module (see **Appendix A** for details). These data can be downloaded from National Meteorological Information Center[1]. Meanwhile, the reference evapotranspiration is calculated through the FAO ET_0 calculator.

Soil Sampling

Soil properties have a major impact on crop yield chiefly because they affect the ability of soil to retain water and transfer water to crops (Bakker et al., 2007). AquaCrop model provides reference soil parameters for all kinds of soil texture, which reduces the difficulty of regional soil-property-information measurement. Therefore, a large number of measured soil texture data are used for establishing the corresponding soil module parameters of the AquaCrop model to ensure that the model considers the impact of soil hydraulic properties of different soil texture structures on crop growth. This study matched the nearest meteorological station data for 155 soil survey points by spatial location, and conducts regional AquaCrop simulations on these 155 units. The soil texture of 155 survey points in the Songnen black soil area is classified into 27 categories and can be further divided into 56 subcategories according to the thickness of each layer (**Figure 2**). The AquaCrop model assigns 56 groups of parameters in soil module according to these soil testure subcategories. The classification results show the high soil heterogeneity in Songnen Plain, although there are only four different textures. Soil classification improves the efficiency of regional model operation.

TABLE 2 | Phenological information of maize in the black soil area of Northeast China.

Growth Stages	Length days	Date
Sowing	1	1 May
Emergence	6	7 May
Maximum canopy cover	54	24 June
Maximum rooting depth	108	17 August
Start of canopy senescence	107	16 August
Maturity	150	27 September
Flowering	66 – 79	6 July – 19 July
Yield formation	66 – 150	6 July – 27 September

Satellite-Based Data

GLASS fractional vegetation cover (FVC) products from 2000 to 2020 were collected for regional data assimilation. Multisource high-resolution optical remote sensing images in 2018 and 2020 were collected for relative accuracy verification of the GLASS FVC product and assimilation tests.

GLASS FVC is a global fractional vegetation cover product, with 500 meters spatial resolution and 8 days temporal resolution, published by the National Earth System Science Data Center[2]. The inversion algorithm is based on multisource remote sensing data and measured site data (Jia et al., 2015). This study adopted the GLASS FVC data with tile number h26v04 from 2000 to 2020.

[1]http://data.cma.cn/site/index.html

[2]http://www.cresda.com/CN/Data

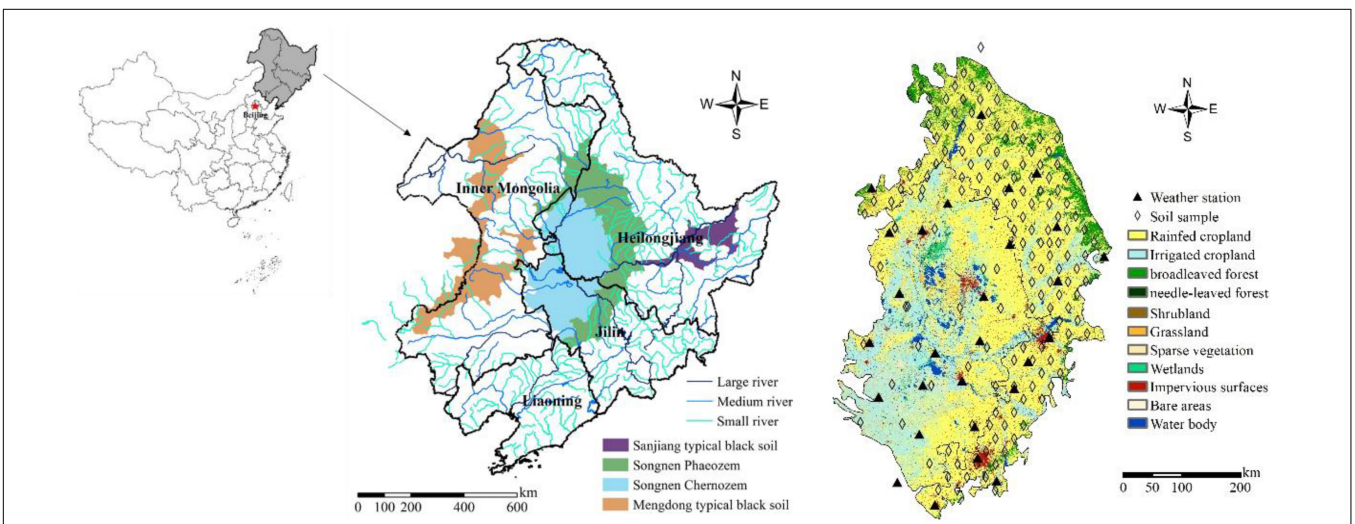

FIGURE 1 | Distribution of phaeozem, chernozem and rivers in Northeast China **(left)**; distribution of 30 m-resolution land cover type, meteorological stations and soil sampling points in Songnen Plain in 2020 **(right)**.

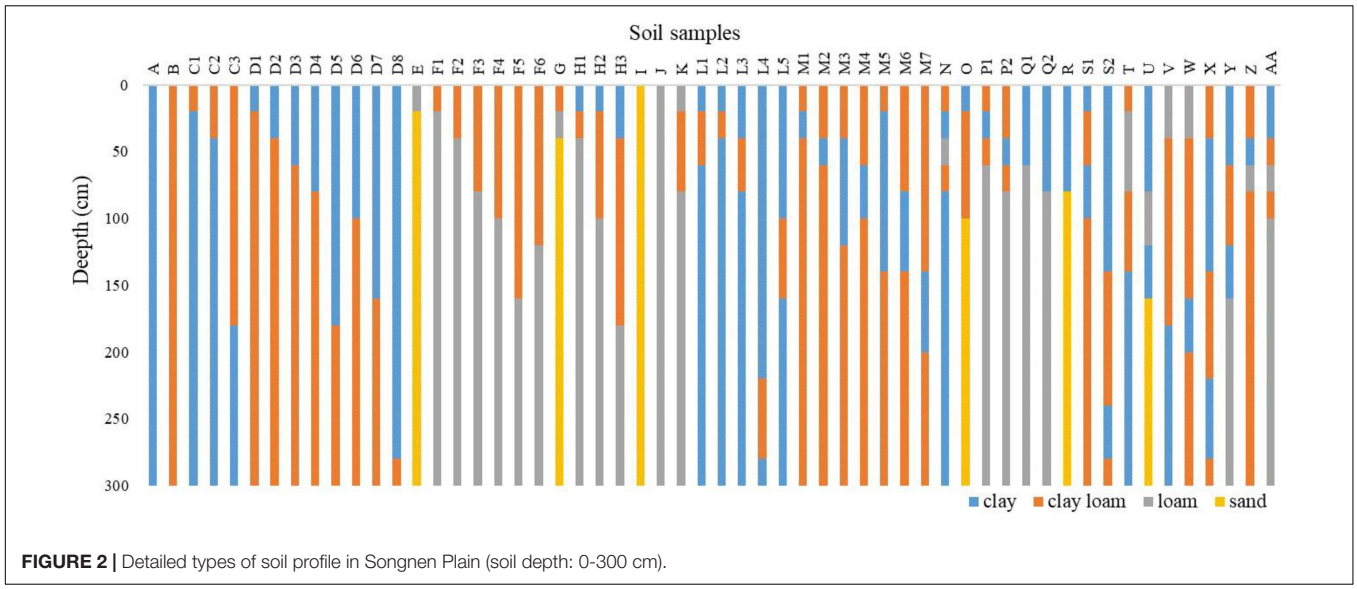

FIGURE 2 | Detailed types of soil profile in Songnen Plain (soil depth: 0-300 cm).

TABLE 3 | List of satellite imagery collected in Nenjiang County and Lishu County.

Area	Data	Satellite	Sensor	Path/Row	Area	Data	Satellite	Sensor	Path/Row
LS	2020-04-04	GF-6	WFV	589/63	NJ	2018-05-05	LS-8	OLI	120/26
LS	2020-05-28	GF-6	WFV	594/63	NJ	2018-05-07	GF-1	PMS2	597/72
LS	2020-06-12	GF-1	WFV4	601/81	NJ	2018-06-21	GF-1	PMS1	597/72
LS	2020-06-28	GF-1	WFV3	597/81	NJ	2018-06-21	ZY-3-2	TMS	884/102
LS	2020-07-15	GF-1	WFV4	603/81	NJ	2018-07-27	GF-2	PMS1	1004/103
LS	2020-07-23	GF-1	WFV3	600/81	NJ	2018-07-27	GF-2	PMS2	1003/113
LS	2020-07-23	GF-1	WFV4	600/81	NJ	2018-08-01	GF-1	WFV3	596/72
LS	2020-08-16	GF-1	WFV3	596/81	NJ	2018-08-05	GF-1	WFV2	598/72
LS	2020-08-21	GF-1	WFV4	601/81	NJ	2018-08-18	GF-1	WFV3	598/72
LS	2020-09-06	GF-1	WFV3	600/81	NJ	2018-08-18	LS-8	OLI	119/26
LS	2020-09-26	GF-1	WFV2	595/81	NJ	2018-08-22	GF-1	WFV3	599/72
LS	2020-09-26	GF-1	WFV3	595/81	NJ	2018-09-10	ZY-3	MUX	884/102
LS	2020-10-13	GF-1	WFV4	601/81	NJ	2018-09-15	ZY-3	MUX	883/101
LS	2020-10-27	GF-6	WFV	603/60	NJ	2018-10-17	ZY-3-2	TMS	884/102
LS	2020-11-05	GF-6	WFV	594/63	NJ	2018-10-18	GF-2	PMS1	1004/113
LS	2020-11-08	GF-1D	PMS	654/82	NJ	2018-10-18	GF-2	PMS2	1004/112
LS	2020-11-13	GF-1B	PMS	653/82					

Nenjiang is located at 49°10′ N, 125°13′ E, altitude of 242.2 meters, and Lishu is located at 43°10′ N, 124°19′ E, altitude of 165.7 meters. These two counties are the northernmost and southernmost parts of the Songnen black soil area, respectively. This study collected multiscene domestic GaoFen-1 satellite remote sensing images of Nenjiang County, Heilongjiang Province, in 2018 and Lishu County, Jilin Province, in 2020 with 8-meter spatial resolution and 4-day temporal resolution. Several domestic ZiYuan-3 satellite images and Landsat-8 images were collected as supplements with 6-meter spatial resolution and 5-day temporal resolution and 30-meter spatial resolution and 16-day temporal resolution (**Table 3**). The absolute calibration coefficient and solar irradiance are from the official website of the China Resources Satellite Application Center[3].

[3]http://www.geodata.cn/thematicView/GLASS.html

After geometric correction and radiometric correction, the fractional vegetation cover (FVC) can be retrieved according to the pixel dichotomy:

$$FVC = \frac{VI - V_s}{V_v - V_s} \quad (1)$$

where VI is the NDVI of the pixel, V_s is the NDVI of the pure soil pixel, and V_v is the NDVI of the pure vegetation pixel.

The remote sensing FVC curves obtained from different sensors and inversion methods are roughly the same, reflecting the reliability of the GLASS FVC product in Northeast China. **Figure 3** shows the time sequence FVC of the two main maize-producing areas on the Songnen Plain. In the early stage of maize growth, the FVC was almost less than 0.15. From approximately 40 to 80 days, the FVC in most areas increased rapidly from 0.20 to 0.9. After approximately 120 days, FVC reached a high level, and maize started to mature. Some leaves began to curl,

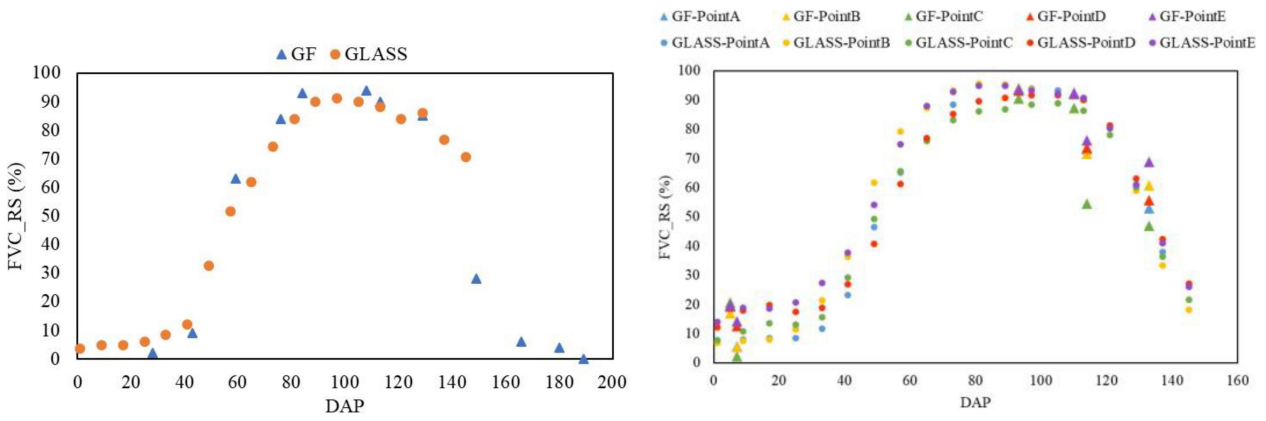

FIGURE 3 | Verifying GLASS FVC with GF satellite image inversion. Lishu County in 2020 **(left)**; Nenjiang County in 2018 **(right)**.

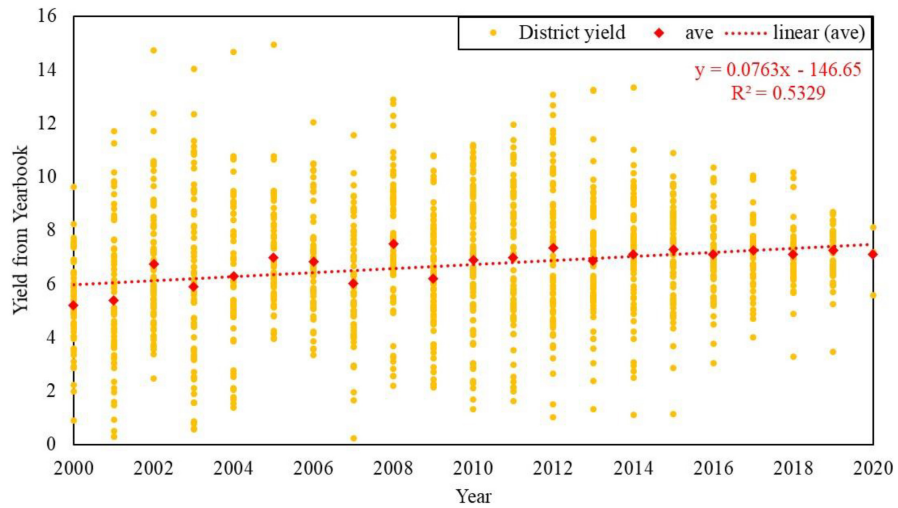

FIGURE 4 | Maize yield (t/ha) dataset from 2000 to 2020's Statistical Yearbook.

and those at the lower part of the canopy began to turn yellow. FVC showed a decreasing trend. By approximately 140 days, the FVC decreased to 0.6, and maize was ready to mature. By approximately 150 days, maize was harvested, and the FVC was below 0.2. The surface of black land was mainly cut straw.

Statistical Yield

National statistical yearbooks are formed by governments' sampling surveys and have acknowledged the authenticity. This study collected province yearbooks from 2000 to 2020 for Jilin, Heilongjiang, Liaoning and Inner Mongolia, which are under the coverage of the Songnen Plain. The established yield dataset of Northeast China included 3666 statistical maize yields per unit area of 258 districts and counties, which was used to establish the regression relationship between FVC and yield based on spatial location. The linear fitting results of yearly yield are shown in **Figure 4**, which need "detrending" to eliminate the impact of these unquantifiable factors on the simulation accuracy (Wang X. et al., 2020), considering the progress of corn varieties and planting technology over the past 21 years while we applied field management measures in 2018.

MODELS AND METHODS

The methodology adopted in this study mainly involved three parts: regional application of the AquaCrop model, FVC data assimilation by model outputs and remote sensing products, and yield estimation relying on the RF regression model (**Figure 5**).

AquaCrop Model

The AquaCrop model simulates the transpiration process of crops by inputting climate, crop, soil, and field management data and finally outputs the daily prediction results of CC, rooting depth, biomass and yield (Raes et al., 2009; Steduto et al., 2009). A significant difference from other crop models is that AquaCrop uses CC instead of LAI as the basis for calculating transpiration, separates soil evaporation from leaf transpiration and avoids the

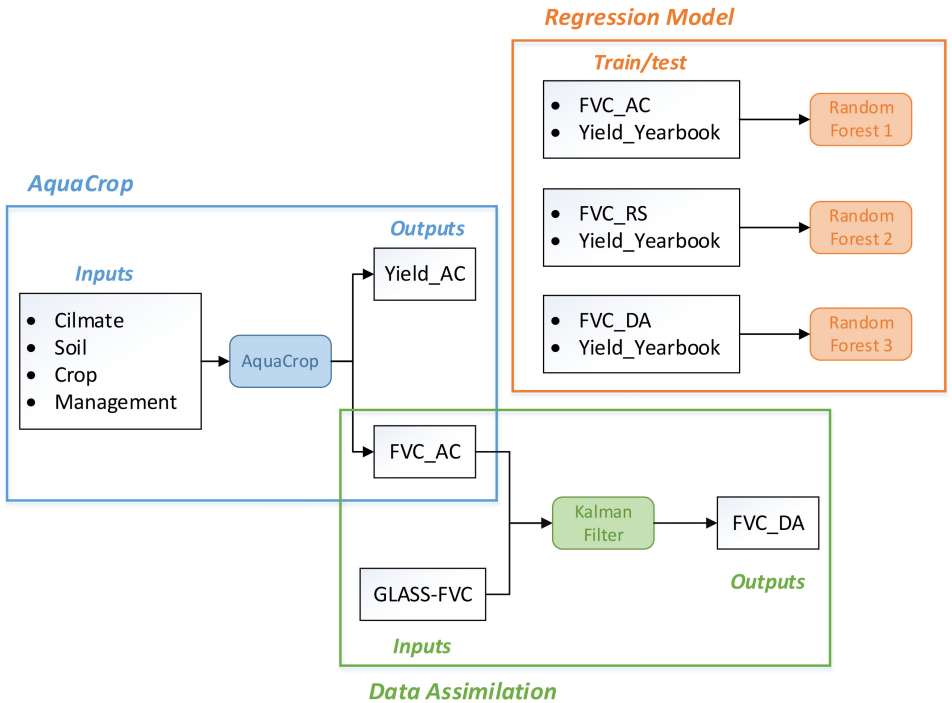

FIGURE 5 | Flowchart of the methodology applied.

TABLE 4 | AquaCrop model soil database (Van Gaelen and Raes, 2016).

Soil tape	TAW (mm/m)	PWP (vol%)	FC (vol%)	SAT (vol%)	Ksat (mm/day)	tau	CN	REW (mm)
Sand	70	6.0	13.0	36.0	3,000.0	1.00	46A	4
loamy sand	80	8.0	16.0	38.0	2,200.0	1.00	46A	5
sandy loam	120	10.0	22.0	41.0	1,200.0	1.00	46A	7
Loam	160	15.0	31.0	46.0	500.0	0.76	61B	9
silt loam	200	13.0	33.0	46.0	575.0	0.80	61B	11
Silt	240	9.0	33.0	43.0	500.0	0.76	61B	11
sandy clay loam	120	20.0	32.0	47.0	225.0	0.58	72C	9
clay loam	160	23.0	39.0	50.0	125.0	0.47	72C	11
silty clay loam	210	23.0	44.0	52.0	150.0	0.50	72C	13
sandy clay	120	27.0	39.0	50.0	35.0	0.30	77D	10
silty clay	180	32.0	50.0	54.0	100.0	0.43	72C	14
Clay	150	39.0	54.0	55.0	35.0	0.30	77D	14

Thickness is set to 4.00 m in the model. PWP: permanent wilting point. FC: field capacity. CN: Curve Number. REW: Readily Evaporable Water.

confusion effect of unproductive water consumption (Equations 2-3). This variable obviously simplifies the simulation and integrates the leaf expansion growth, angle and distribution into an overall growth function. Another advantage is that CC can be easily obtained from remote sensing sources to check analog CC or as input of AquaCrop. Equation 4 and Equation 5 are the two stages of CC growth and the stage of CC decline, respectively.

$$Tr = Kc_{Tr} \times ET_0 \tag{2}$$

$$Kc_{Tr} = CC^{*} \times Kc_{Tr,x} \tag{3}$$

where Tr is the leaf transpiration. Kc_{Tr} is the crop transpiration coefficient. ET_0 is the relative evapotranspiration without stress. CC^{*} is the adjusted canopy cover. $Kc_{Tr,x}$ is the coefficient for maximum crop transpiration, which represents an integration of the effects of the characteristics that distinguish the crop with a complete canopy from reference grass.

$$\begin{cases} CC = CC_0 \times e^{CGC \times t}, CC \leq \frac{CC_x}{2} \\ CC = CC_x - (CC_x - CC_0) \times e^{-CGC \times t}, CC > \frac{CC_x}{2} \end{cases} \tag{4}$$

$$CC = CC_x \left[1 - 0.05 \left(\exp^{\frac{CDC}{CC_x} t - 1} \right) \right] \tag{5}$$

CC is canopy coverage (%). t is the time accumulated from emergence. CC_0 is the initial canopy coverage (%), generally taking the average seedling coverage at 90% emergence. CC_x is

the maximum value of canopy coverage (%). CGC is the canopy coverage growth rate, which indicates the increase in canopy coverage per unit growth degree day (% GDD^{-1}). CDC is the canopy coverage decrease rate, which represents the reduction in daily canopy coverage per unit growth degree day (% GDD^{-1}).

The accumulated biomass is calculated by daily transpiration (Tr_i), daily atmospheric evapotranspiration demand ($ET_{0,i}$) and normalized water productivity (WP*), and crop yield is calculated by the biomass and harvest index, as shown in Equations 6-7.

$$B_i = WP^* \times \left(\frac{Tr_i}{ET_{0,i}}\right) \quad (6)$$

$$Y = B \times HI \quad (7)$$

A soil database can be established according to the layered structure of soil texture in the AquaCrop model, which covers 13 soil types (**Table 4**). The 155 measured soil texture data in Songnen black soil region can be flexibly set to found 57 groups of the corresponding parameters based on this table.

After the sensitivity analyzed and parameters calibrated in the Hebei basin of Nenjiang County based on field experiments from 2011-2018, AquaCrop model has a good prediction effect on a point scale in Northeast China (Xie et al., 2003; Cui et al., 2021). Present research carry on using the same set of cultivar parameters from the previous study (see **Appendix B** for details).

Sequential Filter Assimilation

Referring to the application summary of remote sensing and crop model assimilation, modern data assimilation methods are mainly divided into the following two categories: parameter optimization methods based on cost functions and sequential filtering methods based on estimation theory (Huang et al., 2018). The former minimizes the difference between the remote sensing observation value and the model simulation value using iterations to achieve the optimal estimation, while the latter constantly relies on external observations to adjust the model simulation trajectory in real time to achieve the optimal prediction. For the yield estimation proposition, filter assimilation is more widely used because of its real-time performance. The most representative method is the EnKF, which is based on linear and Gaussian assumptions. In the context that the AquaCrop model simulated a daily FVC curve in the growing season and the GLASS FVC also provides multitemporal FVC values, it is possible to make FVC as the assimilation variable attempt to obtain a higher accuracy estimation based on ensemble Kalman filter (EnKF) algorithm.

KF is an assimilation algorithm that uses the linear system state equation to estimate the optimal system state through the system input and output observation data. Since the observation data include the influence of noise and interference in the system, the optimal estimation can also be regarded as a filtering process. The AquaCrop simulated FVC_AC and remote sensing inversion calculated FVC_RS contribute to the following dynamic models, which are constructed to evolve FVC in time and used to provide short-range prediction of FVC:

$$FVC_t = F_t \times FVC_{t-1} + w_t \quad (8)$$

$$w_t = FVC_RS_t - FVC_AC_t \quad (9)$$

where FVC_{t-1} is the FVC value of the previous time, FVC_t represents the present FVC value, w_t is the model error. FVC_RS_t represents the FVC data observated from GLASS FVC products at time t. FVC_AC_t represents the FVC data simulated by the AquaCrop model at time t, which is from the daily dataset during the crop growth period. F_t is a linear state transition operator:

$$F_t = 1 + \frac{1}{|FVC_AC_t + \varepsilon|} \times \frac{dFVC_AC_t}{dt} \quad (10)$$

where is an uncertainty factor that is set to 0.0001 to prevent the denominator from being 0. The observation operator is set to 1 due to the same parameter of simulation and observation.

EnKF integrates the model forward with the new observation data to obtain a set of analysis field sets, which are updated by the KF equation; the updated set, as the background field of the next moment, continues to make forward short-term forecasts and is assimilated with the new observation data of the next moment. EnKF overcomes the weakness that KF is limited to dealing with linear problems and solves the problem caused by the KF method requiring too much computing resources when calculating the covariance of prediction error. For KF assimilation, the observation operator H in EnKF is set to 1, but the process model error is set to 5% of the predicted value, the observation error is set to 5%, and the number of set elements is set to 20, 100, and 200.

Random Forest

In order to extend the improvement of FVC accuracy to yield estimation accuracy, this section build a regression model of time series FVC and maize yield in a data-driven approach. Machine learning is currently the most effective and rapidly developing data research method, which enable algorithmic models to learn knowledge from data autonomously and then have the ability of judge and predict in new problems. Random forest (RF) is a typical classifier that uses multiple decision trees to train and predict from input samples. It determines the category of test samples by voting and then takes the average output of each decision tree as the final result.

Referring to the Scikit-learn python machine learning library, this study uses the daily FVC value to estimate yield optimally through the RF model. In order to compare the impact on yield estimation accuracy before and after FVC assimilation, three random forest models were established to describe the regression relationship between the FVC curve and yield. The difference is in the input FVC, including the FVC simulated by AquaCrop, the FVC provided by the GLASS remote sensing product and the FVC obtained by data assimilation. Finally, the model with the highest accuracy is selected for maize yield prediction, so as to achieve the research goal of optimal yield estimation.

The total dataset of RF1-3 is composed of 21 growing seasons from 2000 to 2020, three types of FVC data of 155

simulation units and the corresponding statistical yield data. Each RF model should have 3255 records, each record have a set of FVC and a statistical yield. The actual number of records is finally determined by the amount of data with well assimilation effect. The scale of statistical yearbook data is suitable, which is of 258 districts and counties can be matched with the three series of FVC data on 155 simulation units. Another consideration of choosing statistical yield instead of AquaCrop simulated yield is to avoid the accuracy interference caused by the same model output as FVC_AC, and more objectively reflect the real harvest. The samples were randomly divided into two parts with a ratio of 8:2 the large part used for training and the other part used for accuracy evaluation (**Table 5**). The accuracy verification is indicated by MAE (mean absolute error) and R^2, using Equations 11-12.

$$\mathrm{MAE} = \frac{1}{m}\sum_{i=1}^{m}\left|(y_i - \widehat{y_i})\right| \tag{11}$$

$$R^2 = 1 - \frac{\sum (y_i - \widehat{y_i})^2}{\sum (y_i - \overline{y})^2} \tag{12}$$

RESULTS AND ANALYSIS

Regional Continuous Simulation of the AquaCrop Model

Running the AquaCrop model of multithread scheduling for the 155 soil representative cells in Songnen black soil region from 2000 to 2020, we explored the spatial pattern of predicted yield by mapping the results after two empirical Bayesian Kriging interpolation to **Figure 6**.

In general, the spatial distribution and the temporal differences of predicted yield are reasonable reproduced, which is consistent with that of statistical yield (shown in **Figure 7**). Among them, the output of the southeast is the highest, followed by the southwest, and the northeast is the lowest. This spatial pattern is mainly caused by temperature and soil texture. During the growing season, the northern part of the study area is approximately 5°C lower than the southern part as a whole, as shown in **Appendix A**. A lower temperature makes it more difficult for crops to reach the effective accumulated temperature required for maturity, resulting in a lower final yield. Regarding the soil texture difference, although the fertility of chernozem is higher than that of phaeozem, it requires supplementary irrigation to effectively improve growth due to its relatively poor water storage capacity. For Northeast China, which relies on precipitation to provide water supply, phaeozem is more suitable for cultivated land than chernozem.

In terms of time series, the inter-annual differences were mainly caused by the differences of hydrothermal conditions in each growing season, especially the water factor. The output showed a stable trend, with 2000, 2001, 2004, 2007, 2010, 2017 being the good harvest years for the entire region, while other years clearly make out the spatial difference. Abnormal precipitation events during crop growth period, especially in the process of yield formation after flowering, are easy to cause low crop yields. Mild and continuous natural precipitation provides optimal water conditions for crop growth and development. The neglected soil erosion and the administration policies also affect the estimation accuracy.

Field Scale Assimilation of Fractional Vegetation Cover

This study implements a multithreaded univariate EnKF assimilation algorithm based on MATLAB language, which can realize the optimal estimation combining the daily FVC simulated by the AquaCrop model and the multitemporal remote sensing FVC in the corresponding growing season. The results show that EnKF assimilation can indeed integrate remote sensing data into simulation results, achieve higher spatiotemporal resolution and provide FVC estimation with good accuracy. All the assimilation results are defined into 4 types (**Figure 8**). Including: a) Approximately 80% of FVC_Optimal showed excellent assimilation results due to the similar shape of FVC_AC and FVC_RS. b) Approximately 1% of FVC_Optimal showed poor performance owing to the abnormal maize canopy growth reflected by FVC_AC, which differed greatly from the remote sensing observations at these points. c) A few FVC_RS fails to maintain coherence and showed the FVC inversion results of some phases may be distorted, which lead to doubts about the reliability of FVC_Optimal after correction according to the observed value. d) Approximately 10% of FVC_RS is generally lower than the corresponding FVC_AC, indicating an obvious failure to achieve the desired high level in canopy growth. It can be considered that maize planting failed at these locations.

The unsatisfactory assimilation results were probably caused by mixed-pixel RS inversion, spatial mismatch and inaccurate

TABLE 5 | Data composition of the random forest model.

Name	Year	Area	Input (FVC)	FVC frequency	Output (Yield)
RF1	2000-2020	Songnen typical black soil region	FVC_AC	150	Y_ yearbook
RF2	2000-2020	Songnen typical black soil region	FVC_RS	17	Y_yearbook
RF3	2000-2020	Songnen typical black soil region	FVC_DA	150	Y_yearbook

FVC_AC is the FVC simulated by the AquaCrop model. FVC_RS is the GLASS FVC data. FVC_DA is the assimilation result. The FVC frequency shows the FVC number of a data array. The AquaCrop model gives daily output during the 150-day growth period. GLASS FVC provides observations every 8 days.

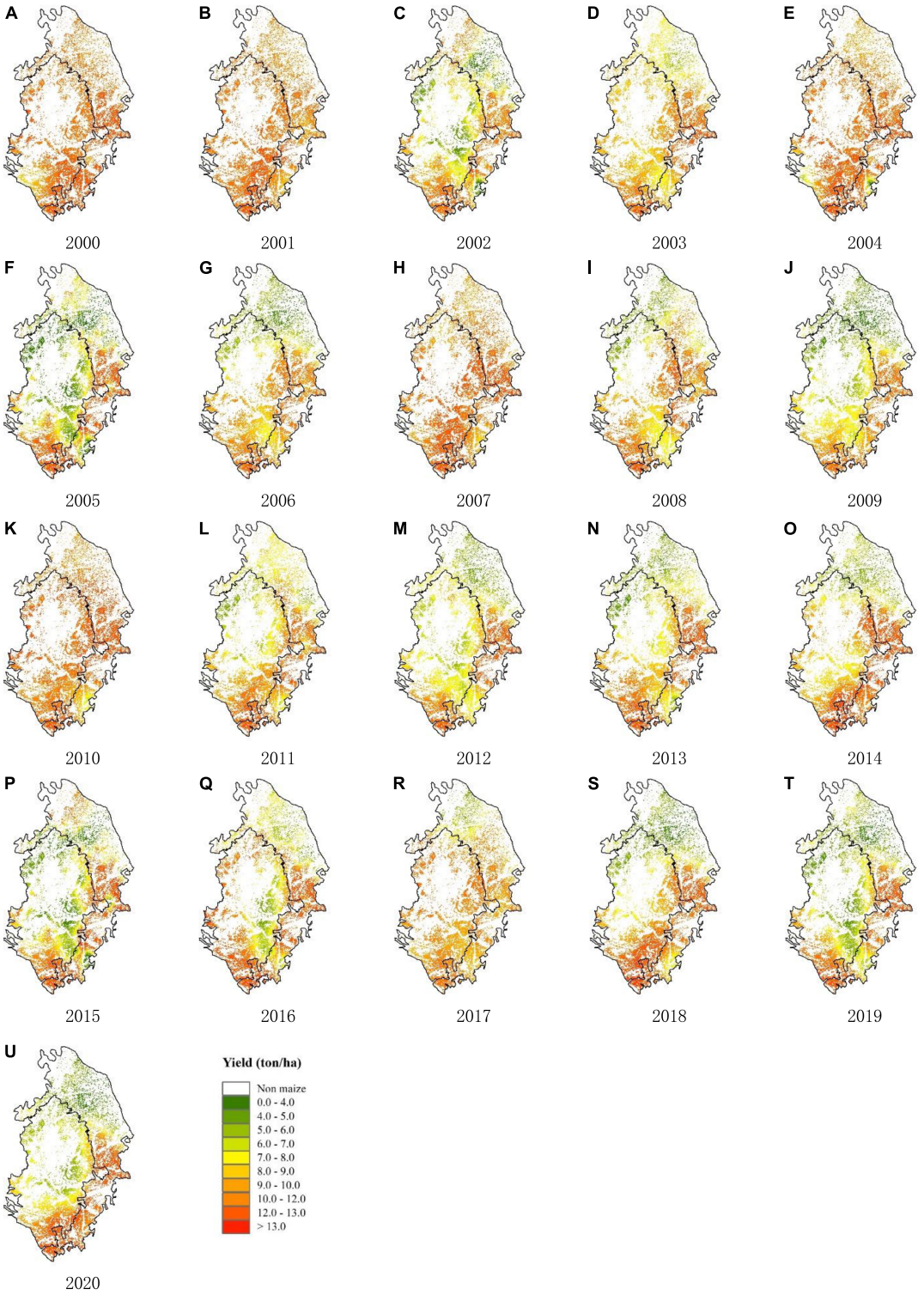

FIGURE 6 | Maize yield map (ton/ha) for Songnen Plain simulated by AquaCrop model from 2000–2020.

phenological parameters that led to discrepancies between the simulation and reality. It should be noted that remote sensing data can reflect real surface information only when the spatial resolution is sufficiently high. The accuracy of the method will be dramatically promoted when the resolution of remote sensing input data is improved.

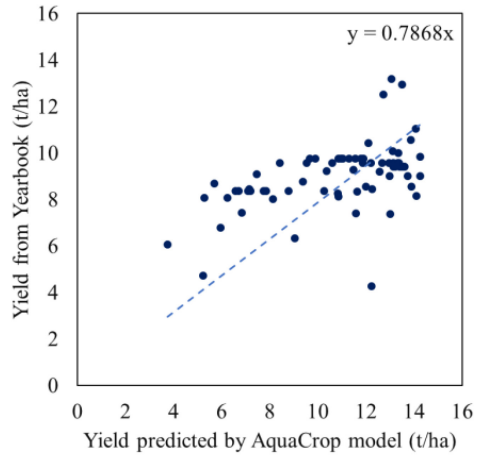

FIGURE 7 | Comparison of random AquaCrop simulated yield and the corresponding statistical yield.

At the end of the growth period, FVC observed by remote sensing is not of maize crops, but background interference such as surface weeds, it will have no impact on yield simulation by removing the last 10 days of data before adding to the RF model.

Random Forest Model of Regression Between Fractional Vegetation Cover and Yield

Based on the FVC array and yield data in the last 20 years, this study established three RF models to describe the regression relationship between the three FVCs and the yield of the statistical yearbook. RF1 used the FVC simulated by the AquaCrop model, RF2 used the remote sensing GLASS FVC product, and RF3 used the optimal FVC assimilated by the two. Considering that the unsatisfactory assimilation results reflected the unreliability of FVC_AC or FVC_RS, the three random forest models only used the data corresponding to well-assimilated fraction of FVC in **Figure 8**. The verification results of the predicted yields of random forests are shown in **Figure 9**. As a typical data-driven machine learning model, random forest strongly shows the dependence of prediction results on input data, and they objectively reflect the invisible relationship between FVC and yield.

Based on the optimal FVC curve, RF3 showed the best performance on maize yield prediction in the black soil area of Northeast China. RF3 is slightly better than RF1, which proves that the addition of remote sensing observation data still has a gain on the yield simulation model, R^2 increases from 0.555 to 0.557, and MAE decreases from 1.004 ton/ha to 0.888 ton/ha. RF2, the yield estimation model based on remote sensing values alone has the lowest accuracy, probably because the amount of data input is far less than that of the other two models, and the quality of the data is greatly influenced by the scale effect. RF3 proved the feasibility of estimating yield with optimal FVC curve.

DISCUSSION

Yield Estimation Benefits From Assimilating Fractional Vegetation Cover

From the results, the addition of assimilation only nets a slight improvement to the yield estimation accuracy, which may lead to doubts about the method effectiveness. Therefore, we establish the following assumptions to explain the benefit of the assimilation algorithm on yield estimation accuracy:

First, assume that Fs(t) is the FVC simulated by the AquaCrop model at time t, Fo(t) is the FVC observed by remote sensing at time t, and Ft(t) is the real FVC, which is unknown. Then, there are two errors, observation error $_o$ and simulation errors $_s$:

$$\varepsilon_o = F_o(t) - F_t(t) \tag{13}$$

$$\varepsilon_s = F_s(t) - F_t(t) \tag{14}$$

Furthermore, assuming that the error of observation value and the simulation value are unbiased and have no correlation:

$$E(\varepsilon_o) = E(\varepsilon_s) = 0 \tag{15}$$

$$E(\varepsilon_o \varepsilon_s) = 0 \tag{16}$$

At this time, by calculating the variance of the observation error σ_o^2 and variance of simulation error σ_s^2 and determining the corresponding weight coefficient, we obtained an FVC estimation value $F_a(t)$ that is closer to Ft(t). The reciprocal of variance is defined as the data precision.

$$F_a(t) = aF_o(t) + bF_s(t) \tag{17}$$

Assuming that the estimated value is unbiased:

$$E(F_a) = E(F_t) \tag{18}$$

$$a + b = 1 \tag{19}$$

Then, minimize the variance σ_a^2 of the estimated value $F_a(t)$:

$$\sigma_a^2 = E[F_a(t) - F_t(t)]^2 = E(aF_o(t) - F_t(t)) + (bF_s(t) - F_t(t))^2 \tag{20}$$

$$= E\left[(a\varepsilon_o + b\varepsilon_s)^2\right] = a^2\sigma_o^2 + b^2\sigma_s^2 \tag{21}$$

$$a = \frac{\sigma_s^2}{\sigma_o^2 + \sigma_s^2} \tag{22}$$

$$b = \frac{\sigma_o^2}{{}_o^2 + \sigma_s^2} \tag{23}$$

$$\sigma_a^2 = \frac{\sigma_o^2}{1 + \left(\frac{\sigma_o}{\sigma_s}\right)^2} < \sigma_o^2 \tag{24}$$

$$\sigma_a^2 = \frac{\sigma_s^2}{1 + \left(\frac{\sigma_s}{\sigma_o}\right)^2} < \sigma_s^2 \tag{25}$$

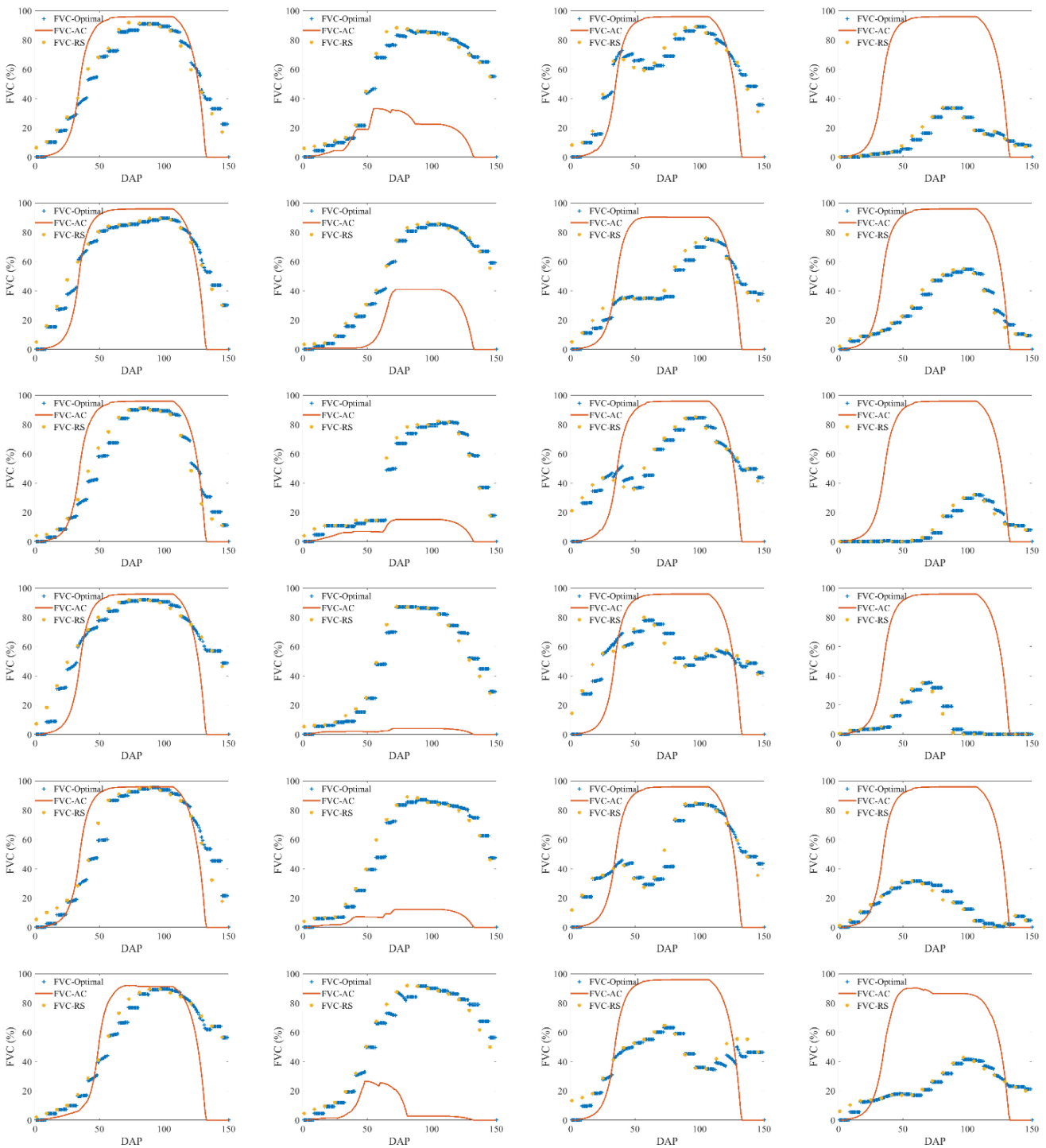

FIGURE 8 | Several examples of FVC assimilation based on the EnKF multithreaded algorithm.

Obviously, the variance of the estimated value is always less than the observation error variance and simulation error variance. The coupling of observation and model simulation information is confirmed to obtain a better state estimation value.

However, no data source can guarantee the unbiased of its error nature. In terms of remote sensing data, if the observations are collectively higher than the true values, the addition of observed values during assimilation will lead the simulation

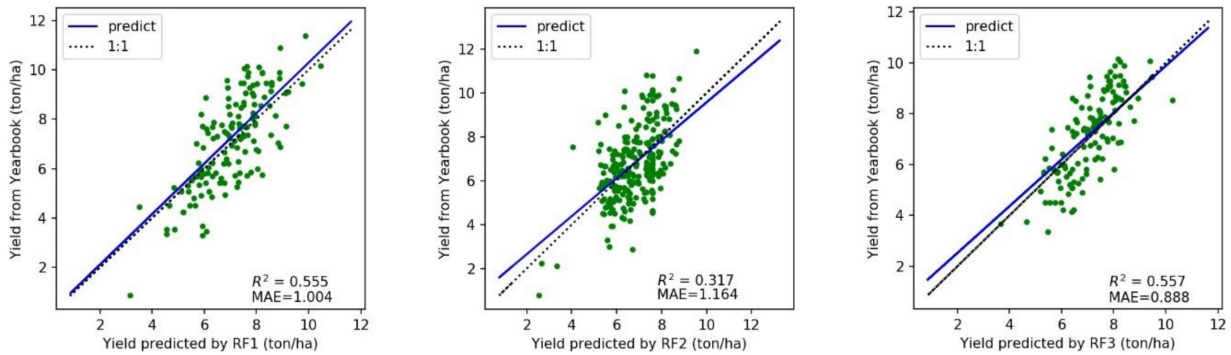

FIGURE 9 | Comparison of accuracy between the three random forest models. (RF1: input FVC_AC; RF2: input FVC_RS; RF1: input FVC_Optimal).

process to a higher direction but make the estimation results more distorted. Therefore, it is necessary to control and reduce the reliability of each input data of the assimilation algorithm to ensure the final prediction effect. This requires the continued development of remote sensing technology and traditional mechanism models.

Uncertainties and Future Work

This paper mainly has uncertainty and limitations in the following two aspects: data assimilation by remote sensing and machine learning. In the ideal case, the AquaCrop model assimilation system coupled with multitemporal remote sensing products integrates the advantages of the two. On the one hand, the addition of a mechanism model makes up for the lack of biophysical significance of the system. On the other hand, the addition of remote sensing observations improves the reliability of the system and expands the application scope. But in fact, the analog of state variables in the crop model is not detailed enough, and many variation characteristics of FVC observed by remote sensing are not reflected in the simulation results. It should also focus on developing regional crop models to allow the input and output of surface parameters to better integrate and utilize regional products and serve regional research. In regional studies, remote sensing data are generally expected to be used due to their large scale and ready availability. However, the unverifiable authenticity of remote sensing data caused by mixed pixels must not be overlooked, and the final error may be three times the input LAI error (Fang et al., 2018). Although high spatial resolution imagery ensures the maximum number of pure pixels, the time resolution and width are sacrificed, resulting in high costs in regional applications. Research should balance the system investment and its efficiency. Above all, deliberately combining the advantages of different data resources to improve the practical value of crop models is still a valuable problem for agricultural research.

Introducing the data-driven method, this study established the regression relationship between time series FVC and yield based on the machine learning method of random forest. According to the crop yield predicted by the assimilated FVC and the statistical yield, the R^2 of random forest reached 0.557, demonstrating that the construction logic of the system is tenable. It revealed that crop yield is not only reflected by FVC, which may account for 55.7% of the representation. The maize yield estimation accuracy was limited by the correlation between FVC and maize yield itself, which can hardly be surpassed by technology. For regional yield estimation, this is still a rare attempt to provide a relatively accurate yield forecast based only on time series FVC data.

Several previous studies have also found the significant association between surface state variables and crop yield, and all committed to estimating yield through these variables. Present yield estimation accuracy of 0.888 ton/ha through FVC assimilation has an advantage over previous assimilation studies. Hank et al., 2015) estimated winter wheat yield by assimilating LAI into PROMET model, the R^2 was 0.93 and the RMSE was 1.15 ton/ha. Gilardelli et al. (2019) estimated rice yield in northern Italy by assimilating LAI into WARM rice model, the MAE was 0.66 ton/ha and the RRMSE was 13.8%. Their study got higher accuracy by using fine spatial resolution (30 meters) on an area lower than 3 km^2, while our study using 500 m resolution product so as to achieved 20 km^2 of yield estimation. Li et al., 2019) estimated winter wheat yield by assimilating LAI into WheatSM model, the RMSE was 1.641 ton/ha through SCE-UA assimilation method and 1.587 ton/ha through EnKF assimilation method. Wang P. X. et al. (2020) integrated remote sensing LAI of 4 phases to CERES-Maize model based on EnKF data assimilation approach in North China, the R^2 of the estimated yield was 0.33, and the root mean square error (RMSE) was 0.371 ton/ha. Their study has only been verified in 8 research points for 5 years, while our study verified on 155 points for 21 years.

The results of this paper also show that there are many potential development space for the method of yield estimation based on the assimilation of surface state variable and machine learning. This finding is similar to those reported by Silva et al. (2020), which concluded that "big data" are useful to characterize cropping systems at the regional scale but need more progress to explain yield variability. Directions for improvement including optimizing machine learning algorithms to isolate and enhance the effect of FVC features on crop yield; and exploring multivariable joint assimilation integrating relevant biophysical indicators, such as evapotranspiration and temperature. It may also be necessary to apply continuous assimilation of multiple images into crop models to retain their spatial information.

CONCLUSION

This study proposed a yield prediction method based on a crop model and remote sensing data assimilation for maize in the black soil region of Northeast China. The calibrated AquaCrop model already has a good simulation effect at the point scale, which confirms the availability of the AquaCrop model in this area. Profit from the physiological response of crops to environmental and management conditions is intuitively reflected by the AquaCrop model. We applied the model to simulate the growth of maize crops in the Songnen black soil area from 2000 to 2020 and accumulated a large database. After confirming the accuracy of the remote sensing surface parameter products, synchronous time series observations are added to the AquaCrop simulation results of 21 years through the EnKF filtering assimilation algorithm, and an optimal FVC dataset is established. Using the optimal FVC and the regression relationship between FVC and statistical yield trained by random forest, a yield estimation method is formed. Data assimilation combines the two geodetic research methodologies of simulation and observation, while this study proposed that the method further integrates the idea of a mechanism model and machine learning and provides a feasible idea for crop yield estimation. Overall, the main contribution of current study is offering new insights and perspectives for the following two issues: one is how to integrate satellite remote sensing data into the crop model at the regional scale; the second is how to obtain more useful yield information from the available surface parameter data.

DATA AVAILABILITY STATEMENT

The raw data supporting the conclusions of this article will be made available by the authors, without undue reservation.

AUTHOR CONTRIBUTIONS

YC: conceptualization, methodology, software, formal analysis, investigation, and writing—review and editing. SL: conceptualization, writing—review and editing, supervision, and project administration. XL and HG: visualization. YX: data curation, conceptualization, and supervision. YH: data curation. All authors have read and agreed to the published version of the manuscript.

FUNDING

This study was supported by the National Key Research and Development Program of China (Grant No. 2021YFD1500705).

REFERENCES

Bakker, M. M., Govers, G., Jones, R. A., and Rounsevell, M. D. A. (2007). The effect of soil erosion on Europe's crop yields. *Ecosystems* 10, 1209–1219. doi: 10.1007/s10021-007-9090-3

Cui, Y., Lin, H., Xie, Y., and Liu, S. (2021). Application study of crop yield prediction based on aquacrop model in black soil region of northeast china. *Acta Agron. Sin.* 47, 159–168. doi: 10.3724/SP.J.1006.2021.03016

Eshete, D. G., Sinshaw, B. G., and Legese, K. G. (2020). Critical review on improving irrigation water use efficiency: advances, challenges, and opportunities in the Ethiopia context. *Water Energy Nexus* 3, 143–154. doi: 10.1016/j.wen.2020.09.001

Fang, H., Liang, S., Hoogenboom, G., Teasdale, J., and Cavigelli, M. (2018). Corn-yield estimation through assimilation of remotely sensed data into the CSM-CERES-Maize model. *Int. J. Remote Sens.* 29, 3011–3032. doi: 10.1080/01431160701408386

Feng, L., Wang, Y., Zhang, Z., and Du, Q. (2021). Geographically and temporally weighted neural network for winter wheat yield prediction. *Remote Sens. Environ.* 262:112514. doi: 10.1016/j.rse.2021.112514

Feng, P., Wang, B., Liu, D. L., Waters, C. M., and Yu, Q. (2019). Incorporating machine learning with biophysical model can improve the evaluation of climate extremes impacts on wheat yield in south-eastern Australia. *Agric. For. Meteorol.* 275, 100–113. doi: 10.1016/j.agrformet.2019.05.018

Gilardelli, C., Stella, T., Confalonieri, R., Ranghetti, L., Campos-Taberner, M., Garcia-Haro, F. J., et al. (2019). Downscaling rice yield simulation at sub-field scale using remotely sensed LAI data. *Eur. J. Agron.* 103, 108–116. doi: 10.1016/j.eja.2018.12.003

Hank, T., Bach, H., and Mauser, W. (2015). Using a remote sensing-supported hydro-agroecological model for field-scale simulation of heterogeneous crop growth and yield: application for wheat in central Europe. *Remote Sens.* 7, 3934–3965. doi: 10.3390/rs70403934

Hu, S., Shi, L., Huang, K., Zha, Y., Hu, X., Ye, H., et al. (2019). Improvement of sugarcane crop simulation by SWAP-WOFOST model via data assimilation. *Field Crops Res.* 232, 49–61. doi: 10.1016/j.fcr.2018.12.009

Huang, J., Huang, H., Ma, H., Zhou, W., and Zhu, D. (2018). Review on data assimilation of remote sensing and crop growth models. *Trans. Chinese Soc. Agric. Eng.* 34, 144–156. doi: 10.11975/j.issn.1002-6819.2018.21.018

Iqbal, M. A., Shen, Y., Stricevic, R., Pei, H., Sun, H., Amiri, E., et al. (2014). Evaluation of the FAO aquacrop model for winter wheat on the north china plain under deficit irrigation from field experiment to regional yield simulation. *Agric. Water Manage.* 135, 61–72. doi: 10.1016/j.agwat.2013.12.012

Jia, K., Liang, S., Liu, S., Li, Y., Xiao, Z., Yao, Y., et al. (2015). Global land surface fractional vegetation cover estimation using general regression neural networks from MODIS surface reflectance. *IEEE Trans. Geosci. Remote Sens.* 53, 4787–4796. doi: 10.1109/TGRS.2015.2409563

Jin, H., Li, A., Wang, J. D., and Bo, Y. (2016). Improvement of spatially and temporally continuous crop leaf area index by integration of CERES-Maize model and MODIS data. *Eur. J. Agron.* 78, 1–12. doi: 10.1016/j.eja.2016.04.007

Jin, X., Kumar, L., Li, Z., Xu, X., Yang, G., and Wang, J. (2016). Estimation of winter wheat biomass and yield by combining the AquaCrop model and field hyperspectral data. *Remote Sens.* 8:972. doi: 10.3390/rs8120972

Li, H. (2016). *A Study On The Uncertainty Of Regional Winter Wheat Growth Simulation From A Crop Model Using Remote Sensing Data Assimilation*. Beijing: Chinese Academy of Agricultural Sciences.

Li, H., Chen, Z., Liu, G., Jiang, Z., and Huang, C. (2017). Improving winter wheat yield estimation from the CERES-wheat model to assimilate leaf area index with different assimilation methods and spatio-temporal scales. *Remote Sens.* 9:190. doi: 10.3390/rs9030190

Li, X., and Bai, Y. (2010). A Bayesian filter framework for sequential data assimilation. *Adv. Earth Sci.* 25, 515–522. doi: 10.3788/gzxb20103907.1340

Li, Y., Chen, H. L., Tian, H. W., and Yu, W. D. (2019). Estimation of winter wheat yield based on coupling remote sensing information and WheatSM model. *Chinese J.Ecol.* 38, 2258–2264. doi: 10.13292/j.1000-4890.201907.039

Lin, H., Xie, Y., Liu, G., Zhai, J., and Li, S. (2019). Soybean and maize simulation under different degrees of soil erosion. *Field Crops Res.* 230, 1–10. doi: 10.1016/j.fcr.2018.10.004

Liu, B. Y., Zhang, G. L., Xie, Y., Shen, B., and Liu, B. (2021). Delineating the black soil region and typical black soil region of northeastern China. *Chinese Sci. Bull.* 66, 96–106. doi: 10.1360/TB-2020-0178

Monteith, J. L. (1996). The quest for balance in crop modeling. *Agron. J.* 88, 695–697. doi: 10.2134/agronj1996.00021962008800050003x

Passioura, J. B. (1996). Simulation models: science, snake oil, education, or engineering? *Agron. J.* 88, 690–694. doi: 10.2134/agronj1996.00021962008800050002x

Peng, X., Han, W., Ao, J., and Wang, Y. (2021). Assimilation of LAI derived from UAV multispectral data into the SAFY model to estimate maize yield. *Remote Sens.* 13:1094. doi: 10.1016/j.agrformet.2021.108345

Pique, G., Fieuzal, R., Bitar, A. A., Veloso, A., Tallec, T., Brut, A., et al. (2020). Estimation of daily CO2 fluxes and of the components of the carbon budget for winter wheat by the assimilation of Sentinel 2-like remote sensing data into a crop model. *Geoderma* 376:114428. doi: 10.1016/j.geoderma.2020.114428

Qian, X., Zang, H., Xu, H., Ren, C., Guo, L., Wang, C., et al. (2018). Relay strip intercropping of oat with maize, sunflower and mung bean in semi-arid regions of Northeast China: yield advantages and economic benefits. *Field Crops Res.* 223, 33–40. doi: 10.1016/j.fcr.2018.04.004

Qin, Q. M., Fan, W. J., and Ren, H. Z. (2018). *Theory, Method And Application Of Farmland Quantitative Remote Sensing*. Beijing: Science Press.

Raes, D., Steduto, P., Hsiao, T. C., and Fereres, E. (2009). AquaCrop—the FAO crop model to simulate yield response to water: II. Main algorithms and software description. *Agron. J.* 101, 438–447. doi: 10.2134/agronj2008.0140s

Sandhu, R., and Irmak, S. (2019). Performance of AquaCrop model in simulating maize growth, yield, and evapotranspiration under rainfed, limited and full irrigation. *Agric. Water Manage.* 223:105687. doi: 10.1016/j.agwat.2019.105687

Silva, J. V., Tenreiro, T. R., Spätjens, L., Anten, N. P. R., Ittersum, M. K. V., and Reidsma, P. (2020). Can big data explain yield variability and water productivity in intensive cropping systems? *Field Crops Res.* 255:107828. doi: 10.1016/j.fcr.2020.107828

Silvestro, P. C., Pignatti, S., Pascucci, S., Yang, H., Li, Z., Yang, G., et al. (2017). Estimating wheat yield in China at the field and district scale from the assimilation of satellite data into the Aquacrop and simple algorithm for yield (SAFY) models. *Remote Sens.* 9:509. doi: 10.3390/rs9050509

Steduto, P., Hsiao, T. C., Raes, D., and Fereres, E. (2009). AquaCrop—The FAO crop model to simulate yield response to water: I. Concepts and underlying principles. *Agron. J.* 101, 426–437. doi: 10.2134/agronj2008.0139s

Steele-Dunne, S. C., Mcnairn, H., Monsivais-Huertero, A., Judge, J., Liu, P. W., and Papathanassiou, K. (2017). Radar remote sensing of agricultural canopies: a review. *IEEE J. Sel. Top. Appl. Earth Obs. Remote Sens.* 10, 2249–2273. doi: 10.1109/JSTARS.2016.2639043

Tewes, A., Hoffmann, H., Krauss, G., Schafer, F., Kerkhoff, C., and Gaiser, T. (2020). New approaches for the assimilation of LAI measurements into a crop model ensemble to improve wheat biomass estimations. *Agronomy* 10:446. doi: 10.3390/agronomy10030446

Todorovic, M., Albrizio, R., Zivotic, L., Abi Saab, M. T., Stöckle, C., and Steduto, P. (2009). Assessment of AquaCrop, CropSyst, and WOFOST models in the simulation of sunflower growth under different water regimes. *Agron. J.* 101, 509–521. doi: 10.2134/agronj2008.0166s

Van Gaelen, H., and Raes, D. (2016). *AquaCrop Training Handbooks–Book II Running AquaCrop[J]*. Rome: Food and Agriculture Organization of the United Nations.

Van, D. C. A., Wolf, J., and Rappoldt, V. K. H. (1989). WOFOST: a simulation model of crop production. *Soil Use Manage.* 5, 16–24. doi: 10.1111/j.1475-2743.1989.tb00755.x

Wang, P. X., Hu, Y. J., Li, L., and Xu, L. X. (2020). Estimation of maize yield based on ensemble kalman filter and random forest for regression. *Trans. Chinese Soc. Agric. Machinery* 51, 135–143. doi: 10.6041/j.issn.1000-1298.2020.09.016

Wang, X., Huang, J., Feng, Q., and Yin, D. (2020). Winter wheat yield prediction at county level and uncertainty analysis in main wheat-producing regions of China with deep learning approaches. *Remote Sens.* 12:1744. doi: 10.3390/rs12111744

Wigneron, J. P., Jackson, T. J., Neill, P. O., Lannoy, D. G., Rosnay, D. P., Walker, J. P., et al. (2017). Modelling the passive microwave signature from land surfaces: a review of recent results and application to the L-band SMOS & SMAP soil moisture retrieval algorithms. *Remote Sens. Environ.* 192, 238–262. doi: 10.1016/j.rse.2017.01.024

Wu, S., Yang, P., Chen, Z., Ren, J., Li, H., and Sun, L. (2021). Estimating winter wheat yield by assimilation of remote sensing data with a four-dimensional variation algorithm considering anisotropic background error and time window. *Agric. For. Meteorol.* 30:108345.

Xie, Y., Kiniry, J. R., and Williams, J. R. (2003). The ALMANAC model's sensitivity to input variables. *Agric. Syst.* 78, 1–16. doi: 10.1016/S0308-521X(03)00002-7

Xie, Y., Wang, P. X., Wang, L., Zhang, S., and Liu, J. (2016). Estimation of wheat yield based on crop and remote sensing assimilation models. *Trans. Chinese Soc. Agric. Eng.* 32, 179–186. doi: 10.11975/j.issn.1002-6819.2016.20.023

Conflict of Interest: The authors declare that the research was conducted in the absence of any commercial or financial relationships that could be construed as a potential conflict of interest.

Publisher's Note: All claims expressed in this article are solely those of the authors and do not necessarily represent those of their affiliated organizations, or those of the publisher, the editors and the reviewers. Any product that may be evaluated in this article, or claim that may be made by its manufacturer, is not guaranteed or endorsed by the publisher.

Copyright © 2022 Cui, Liu, Li, Geng, Xie and He. This is an open-access article distributed under the terms of the Creative Commons Attribution License (CC BY). The use, distribution or reproduction in other forums is permitted, provided the original author(s) and the copyright owner(s) are credited and that the original publication in this journal is cited, in accordance with accepted academic practice. No use, distribution or reproduction is permitted which does not comply with these terms.

APPENDIX

Appendix A: Meteorological Data

TABLE A1 | Weather station information in Songnen Plain.

Station ID	Latitude	Longitude	Altitude (m)	Province	County
50557	49.17	125.23	242.2	Heilongjiang	Nenjiang
50639	48.00	122.73	306.5	Inner Mongolia	Zhalantun
50656	48.28	126.52	269.7	Heilongjiang	Beian
50658	48.05	125.88	236.0	Heilongjiang	Keshan
50674	48.05	125.88	236.0	Heilongjiang	Keshan
50739	47.33	123.18	190.0	Heilongjiang	Longjiang
50742	47.80	124.48	162.7	Heilongjiang	Fuyu
50745	47.38	123.92	147.1	Heilongjiang	Qiqihaer
50756	47.45	126.97	239.2	Heilongjiang	Hailun
50758	47.18	125.90	246.0	Heilongjiang	Mingshui
50844	46.40	123.45	138.8	Heilongjiang	Tailai
50853	46.62	126.97	179.6	Heilongjiang	Beilin
50854	46.38	125.32	149.3	Heilongjiang	Anda
50862	46.98	128.02	210.5	Heilongjiang	Tieli
50936	45.63	122.83	155.3	Jilin	Baicheng
50945	45.50	124.27	137.6	Jilin	Da'an
50948	45.00	124.02	146.3	Jilin	Qian'an
50949	45.08	124.87	136.2	Jilin	Qianguo
50950	45.70	125.25	148.7	Heilongjiang	Zhaozhou
50953	45.75	126.77	142.3	Heilongjiang	Harbin
50955	45.38	126.30	166.4	Heilongjiang	Shuangcheng
54041	44.80	123.07	150.0	Jilin	Tongyu
54049	44.25	123.97	188.9	Jilin	Changling
54063	44.97	126.00	196.8	Jilin	Fuyu
54064	44.38	125.15	170.2	Jilin	Nong'an
54142	43.50	123.53	114.9	Jilin	Shuangliao
54157	43.17	124.33	165.7	Jilin	Siping
54161	43.90	125.22	236.8	Jilin	Changchun
54165	43.55	125.63	219.5	Jilin	Shuangyang

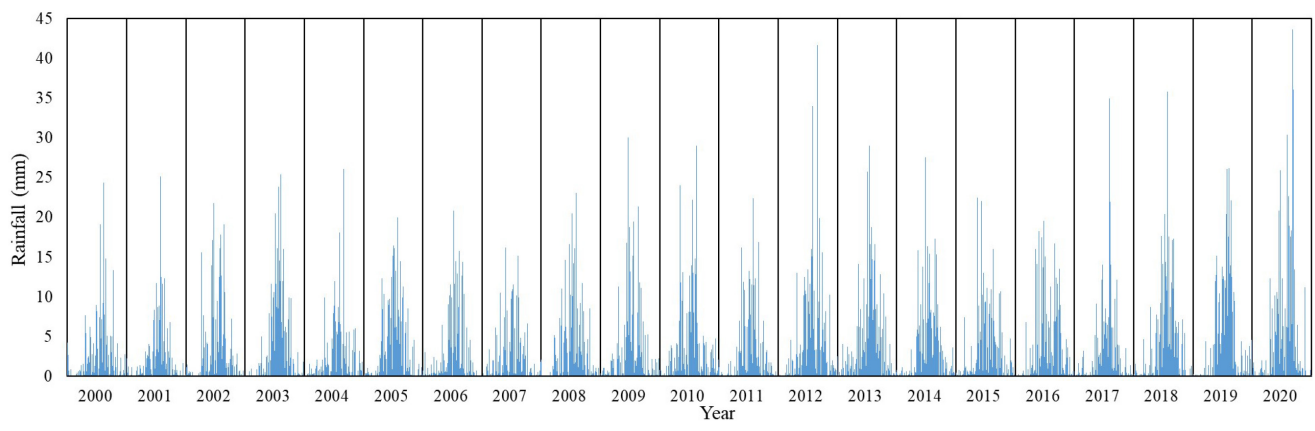

FIGURE A1 | Average daily precipitation in Songnen Plain from 2000 to 2020.

TABLE A2 | Statistics of annual precipitation on the Songnen Plain.

Year	2000	2001	2002	2003	2004	2005	2006
Sum	394.450	308.154	472.461	541.175	362.904	567.989	457.154
Std dev	2.171	1.991	2.547	2.668	2.056	2.530	2.368
Year	2007	2008	2009	2010	2011	2012	2013
Sum	360.679	491.032	492.386	524.946	449.171	619.689	646.086
Std dev	2.015	2.482	2.555	2.634	2.316	3.085	2.982
Year	2014	2015	2016	2017	2018	2019	2020
Sum	527.464	514.336	554.368	469.113	591.448	652.820	711.384
Std dev	2.501	2.365	2.539	2.784	2.885	3.003	3.915

2020 has both the highest total precipitation and the highest standard deviation in the past two decades, which alerts for climate anomalies in the future, and abnormal precipitation will have a serious impact on agricultural production.

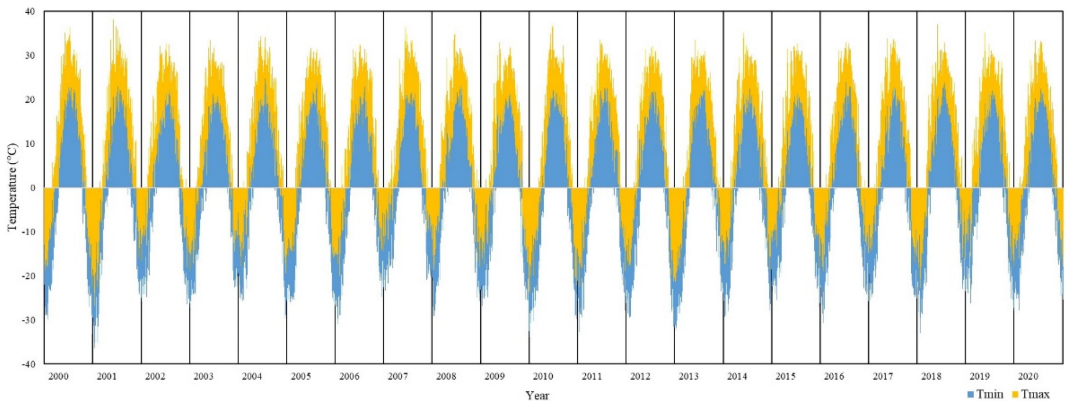

FIGURE A2 | The average daily temperature in the Songnen Plain from 2000 to 2020 is close to the average long-term situation. The gentle temperature change provides a better planting environment and is conducive for crops to adapt to environmental changes.

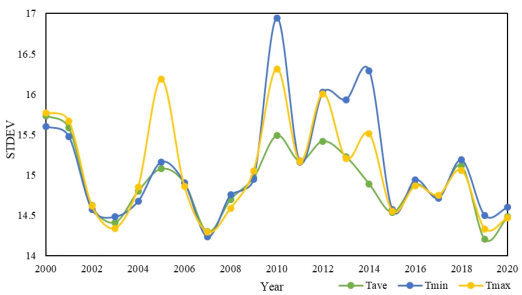

FIGURE A3 | Standard deviation of annual average temperature in Songnen Plain from 2000 to 2020.

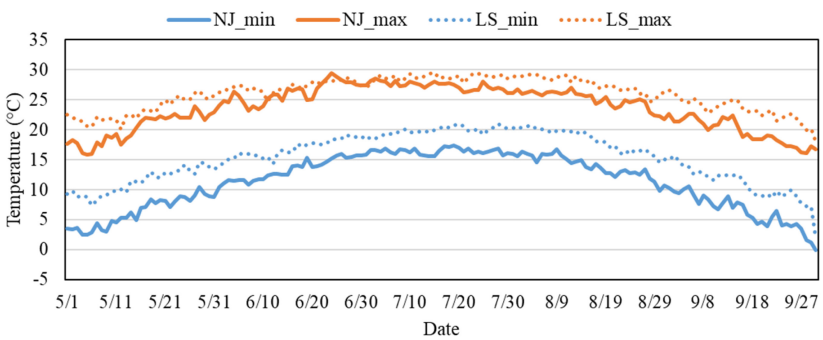

FIGURE A4 | Average temperature of the northern and southern parts of the Songnen black soil region during the recent 21-maize growth season.

Appendix B: AquaCrop Model Parameters

TABLE A1 | Parameter calibration of the AquaCrop model simulating the growth of maize in the Northeast Chinese black soil area.

Notation	Description	Unit	Default value	Calibration value
Pexp-lw	Soil water depletion threshold for canopy expansion – lower threshold	% of TAW	0.25	0.14
Pexshp	Shape factor for Water stress coefficient for canopy expansion	–	3.0	2.9
DeKcTr,x	Decline of crop coefficient as a result of aging, nitrogen deficiency	% d-1	0.150	0.300
KcTr,x	Crop coefficient before canopy formation and senescence	–	1.10	1.05
Rexshp	Shape factor describing root zone expansion	–	1.5	1.3
Zx	Maximum effective rooting depth	m	1.0	2.3
WP*	Water productivity normalized for ET0 and CO2	g m-2	17.0	33.7
CCx	Maximum canopy cover	%	80	96
CGC	Canopy growth coefficient	% d-1	15.0	15.8
CDC	Canopy decline coefficient	% d-1	12.8	11.7
HI0	Reference harvest index	%	50	58

TAW: total available water in the root zone.

frontiers | Frontiers in Plant Science

ORIGINAL RESEARCH
published: 01 July 2022
doi: 10.3389/fpls.2022.931789

Rice Yield Estimation Based on Continuous Wavelet Transform With Multiple Growth Periods

*Chen Gu[1], Shu Ji[1], Xiaobo Xi[1], Zhenghua Zhang[1], Qingqing Hong[1], Zhongyang Huo[1], Wenxi Li[2], Wei Mao[2], Haitao Zhao[1], Ruihong Zhang[1], Bin Li[1] and Changwei Tan[1]**

[1]Jiangsu Key Laboratory of Crop Genetics and Physiology, Jiangsu Co-Innovation Center for Modern Production Technology of Grain Crops, Joint International Research Laboratory of Agriculture and Agri-Product Safety of the Ministry of Education of China, Key Laboratory of Cultivated Land Quality Monitoring and Evaluation (Jiangsu) Ministry of Agriculture and Rural Affairs, Jiangsu Engineering Centre for Modern Agricultural Machinery and Agronomy Technology, Jiangsu Province Engineering Research Center of Knowledge Management and Intelligent Service, Yangzhou University, Yangzhou, China, [2]Station of Land Protection of Yangzhou City, Yangzhou, China

OPEN ACCESS

Edited by:
Chunyuan Diao,
University of Illinois at Urbana-Champaign, United States

Reviewed by:
Jibo Yue,
Henan Agricultural University, China
Jakub Nalepa,
Silesian University of Technology, Poland

***Correspondence:**
Changwei Tan
cwtan@yzu.edu.cn

Specialty section:
This article was submitted to Sustainable and Intelligent Phytoprotection, a section of the journal Frontiers in Plant Science

Received: 29 April 2022
Accepted: 14 June 2022
Published: 01 July 2022

Citation:
Gu C, Ji S, Xi X, Zhang Z, Hong Q, Huo Z, Li W, Mao W, Zhao H, Zhang R, Li B and Tan C (2022) Rice Yield Estimation Based on Continuous Wavelet Transform With Multiple Growth Periods. Front. Plant Sci. 13:931789. doi: 10.3389/fpls.2022.931789

Yield is an important indicator in evaluating rice planting, and it is the collective result of various factors over multiple growth stages. To achieve a large-scale accurate prediction of rice yield, based on yield estimation models using a single growth stage and conventional spectral transformation methods, this study introduced the continuous wavelet transform algorithm and constructed models under the premise of combined multiple growth stages. In this study, canopy reflectance spectra at four important stages of rice elongation, heading, flowering and milky were selected, and then, a rice yield estimation model was constructed by combining vegetation index, first derivative and wavelet transform based on random forest algorithm or multiple stepwise regression. This study found that the combination of multiple growth stages significantly improved the model accuracy. In addition, after two validations, the optimal model combination for rice yield estimation is first derivative-wavelet transform-vegetation index-random forest model based on four growth stages, with the coefficient of determination (R^2) of 0.86, the root mean square error (RMSE) of 35.50 g·m^{-2} and the mean absolute percentage error (MAPE) of 4.6% for the training set, R^2 of 0.85, RMSE of 33.40 g.m^{-2} and MAPE 4.30% for the validation set 1, and R^2 of 0.80, RMSE of 37.40 g·m^{-2} and MAPE of 4.60% for the validation set 2. The research results demonstrated that the established model could accurately predict rice yield, providing technical support and a foundation for large-scale statistical estimating of rice yield.

Keywords: remote sensing, hyperspectral, yield, wavelet transform, multi-growth stage, rice

INTRODUCTION

Rice is one of the important food crops in China and occupies an important position in agricultural production, so the production work of rice is also related to our food security and sustainable agricultural development. In recent years, with the improvement of people's economic level, people's research on rice has gradually shifted to the quality aspect, but the

yield is still an aspect that we cannot ignore. Large-scale estimating of rice yield is of great importance to ensure national food security and regulate food crop production.

The information of different bands in spectral data, the vegetation indices, and hyperspectral characteristic parameters of various band combinations can directly or indirectly tell the growth status of crops, and they are a comprehensive reflection of the effects of various factors on field crops (Curran, 1989). The research of hyperspectral technology on rice focuses on using various independent variables such as original reflectance spectrum, differential transformation, vegetation index, area variable, and location to initially establish prediction models for rice leaf area index (LAI), biomass, yield, etc., and then achieves rice yield estimates (Feng et al., 2021; Miclea et al., 2022). Regarding the current research, the research on nitrogen content and protein content of crops are relatively mature (Xue et al., 2004; Zhu et al., 2007; Wang et al., 2012; Zheng et al., 2020), but the model accuracy of yield study still has more potential for improvement in practical production work. For example, Shen et al. (2009) used data assimilation method to predict rice yield based on radar image data with the root mean square error of 113 $g{\cdot}m^{-2}$. Yang et al. (2019) used unmanned aerial vehicle multispectral images to train a convolutional neural network model to predict rice yield with the root mean square error of 65.8 $g{\cdot}m^{-2}$. In the field of hyperspectral pre-processing, Yu et al. (2020a) used wavelet transform to pre-process unmanned aerial vehicle hyperspectral images and developed a nitrogen content estimation model in rice. Osco et al. (2020) used the first derivative transformation method to process the hyperspectral data to filter out the most appropriate wavelength to predict the nutrient content in orange leaves. Amirhossein et al. (2020) developed a yield estimation model for snap beans by using continuum removal. Yang et al. (2021b) used wavelet transform to remove hyperspectral noise and developed a model for estimating corn yield. He et al. (2018) estimated the canopy chlorophyll content of winter wheat based on the wavelet transform. Jin and Wang (2016) successfully traced the canopy transpiration of a desert plant by using first derivative spectra. Therefore, preprocessing crop canopy spectra with first derivative transformation, continuum removal, and wavelet transform is based on the certain study. However, few studies have used these preprocessing methods in combination, and this research attempts to use them in combination to be able to significantly improve the accuracy of the model.

On the other hand, most studies on canopy-level spectra adopted a single growth stage, usually the mature stage (Inoue et al., 1998; Zheng et al., 2016; Sampaio et al., 2018; Tuvdendorj et al., 2019; Yu et al., 2020b; Shao et al., 2021). Modeling studies based on the combination of multiple growth stages were not common. In fact, rice yield is a collective result of multiple growth stages. Relevant studies have revealed that rice yield was affected by various factors such as water, light, fertilizer, and quality. These impacts were exerted on every growth stage, exhibited as variations in growth, and eventually shown as differences in yield. Therefore, in addition to the spectral information of the maturity stage, the canopy spectral information of the important growth stages before the mature stage should also be included in the study to improve the yield estimation accuracy analysis. At present, there are two main methods for rice yield estimation using spectral data, statistical regression (Chang et al., 2005; Nguyen and Lee, 2006; Xue and Yang, 2008; Bajwa et al., 2010) and data assimilation (Huang et al., 2016; Xie et al., 2017; Mokhtari et al., 2018). Data assimilation could significantly improve the estimates of model parameters and model dynamic simulation ability to improve estimation accuracy (Reichle, 2008; Wang and Yu, 2021). However, this method requires the input of phenological characteristics, weather, soil, and variety coefficient, which are not easy to get and are complicated parameters. It seriously reduces the practical performance of the model, and the accuracy needs to be improved too (Wang et al., 2020). For example, Huang et al. (2015) collected weather and soil climate data and used convolutional neural network algorithm to build a winter wheat yield prediction model with an accuracy of 73.2 $g{\cdot}m^{-2}$. Ren et al. (2008) built a winter wheat yield prediction model based on Moderate-resolution Imaging Spectroradiometer (MODIS) products and used statistical regression method with an accuracy of 21.4 $g{\cdot}m^{-2}$. Therefore, in this study, two modeling methods, multiple stepwise regression and random forest, are chosen to compare the accuracy and finally select the best yield estimation model.

Therefore, this study selected four key stages of rice growth, the elongation stage, the heading stage, the flowering stage, and the milky stage, to study the impact of the combinations of spectral information of multiple growth stages on the yield prediction model.

MATERIALS AND METHODS

As shown in **Figure 1**. This was a flowchart of the entire study, and the approach used had four main stages: data collection, data processing, model build, and model validation. A detailed description of the steps was given as follows.

Experimental Design

Experimental site 1 was located in Yangzhou University experiment base, Jiangsu Province, China. The field experiment was a continuous experiment between 2015 and 2016, which was set up as three different experimental varieties (Nangeng 9,108, Yangnongdao No.1, and Yangdao No.6) with the same fertilizer variety for a total of 60 plots (N0: 0, N1: 100 $kg.ha^{-1}$, N2: 200 $kg.ha^{-1}$, N3: 300 $kg.ha^{-1}$, N4: 400 $kg.ha^{-1}$).

Experiment site 2 was set up at the test field in Gongdao Town, Yangzhou City, Jiangsu Province, China in 2019. The experiment was set up into a total of 60 plots of 2 rice variety (Nangeng 9,108, Yangliangyou 013), in which 5 N fertilizer levels (N0, N1, N2, N3, and N4) were set at 0, 100 $kg.ha^{-1}$, 200 $kg.ha^{-1}$, 300 $kg.ha^{-1}$ and 400 $kg.ha^{-1}$, 5 K fertilizer levels (K0, K1, K2, K3, and K4) were set at 0, 50 $kg.ha^{-1}$, 100 $kg.ha^{-1}$, 150 $kg.ha^{-1}$ and 200 $kg.ha^{-1}$, 5 P fertilizer levels (P0, P1, P2, P3, and P4) were set at 0,

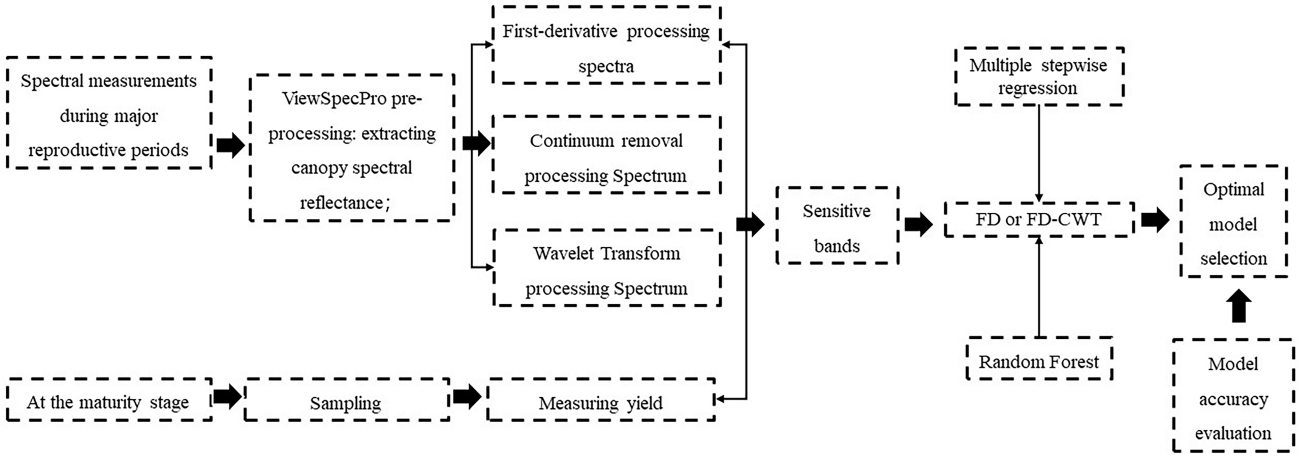

FIGURE 1 | A flowchart of the research process.

100 kg.ha^{-1}, 200 kg.ha^{-1}, 300 kg.ha^{-1} and 400 kg.ha^{-1}, respectively. **Figure 2** shows the geographical location of the experimental area. **Figure 3** is an experimental plot distribution map.

Data Collection

Field Canopy Spectra Measurement

Measurements were made with a Fieldspec®3 (350–2,500 nm) Hi-Res spectrometer from ASD (Analytical Spectral Devices, Inc., CO, United States), with sampling intervals of 1.3 nm (in the 350–1,000 nm interval) and 2 nm (in the 1,000–2,500 nm interval). The spectra were measured in clear weather, without wind or with low wind speed, from 10:30 to 14:00 British Summer Time (BST). The probe was measured vertically downward at a distance of 0.6 m from the top of the plant crown, and the reflectance spectrum was the average of 10 repetitions within the plot (each measurement was made at a randomly selected location within the plot). The measurements were taken once at each of the four critical stages of rice, namely, elongation, heading, flowering, and milky, each measurement was calibrated by using a standard white reflectance panel (the standard white panel reflectance was 1).

Yield Determination

At the rice maturity stage, rice was harvested at a randomly selected 1 m^2 area in each experimental field (avoiding the field edge). After harvest, the grains were threshed, sun-dried to a constant weight, and weighed to determine the rice yield of each experimental plot.

Spectral Variables

By reviewing the literature and results of related studies, it was found that spectral parameters such as red edge, yellow edge, and blue edge were frequently used in quality monitoring and prediction in the fields such as quality (Guo et al., 2019; Olivares Díaz et al., 2019; Yang et al., 2021a). Therefore, in this study, spectral characteristic parameters such as field canopy spectrum, first derivative spectrum of field canopy, four vegetation indices, and three edge parameters (red edge, blue edge, and yellow edge) were selected for parameter screening and model establishment, as listed in **Table 1**.

Hyperspectral Data Processing

Data Preprocessing

The hyperspectral data had large noise in the range of 350–2,500 nm. Therefore, the Savitsky-Golay (SG) filter (Savitzky and Golay, 1964) in Matlab 2016b version was used to smooth the original canopy reflectance spectrum, and the processed spectrum was marked as Original Reflectance (OR).

Conventional Spectral Transformation

To further eliminate the impact of noise and truly exhibit the spectral characteristics of ground objects, this study selected two conventional spectral transformation methods, first derivative transformation and continuum removal transformation of spectral reflectance. The spectrum obtained by first-derivative transformation after being pre-processed by the SG filter was noted as First-derivative (FD).

The spectrum obtained by continuum removal transformation after pre-processed by SG filter was noted as Continuum Removal (CR). The equation for calculation is as follows (Yang and Du, 2021).

$$\boldsymbol{S_{cr} = R / R_{C_0}}$$

where S_{cr} is the continuum removed spectral reflectance, R is the original spectral reflectance, and R_{C_0} is the continuum linear reflectance.

Wavelet Transform

The property of wavelet transform is that time-domain features are added based on the Fourier transform. By decomposing the signals in time and frequency domains, wavelet transform

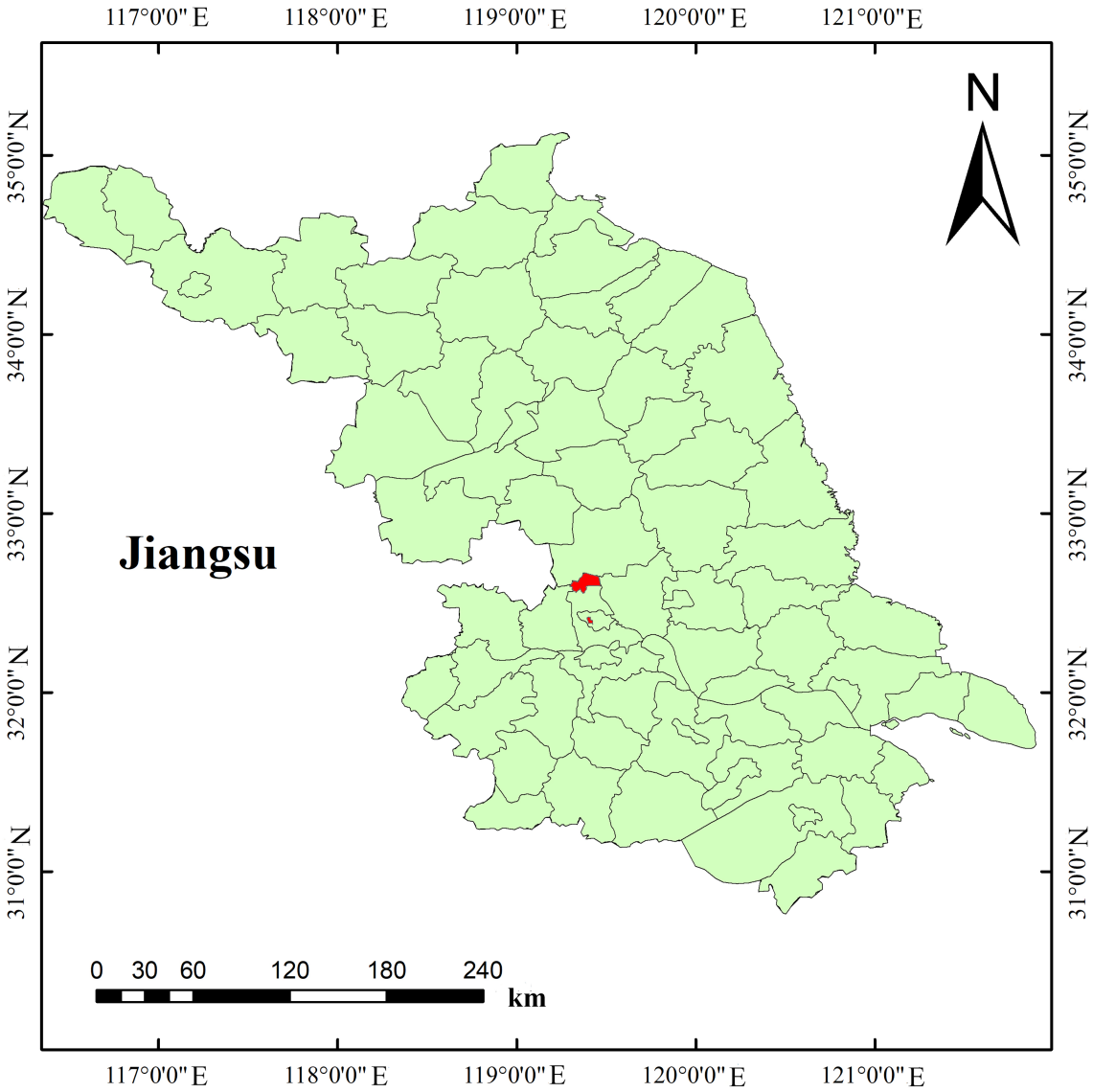

FIGURE 2 | Experimental area overview.

achieves the separation and extraction of characteristic signals to obtain more effective information. Wavelet transforms are divided into two groups, continuous wavelet transform (CWT), and discrete wavelet transform (DWT). In this study, CWT was used to decompose the canopy reflectance spectral data at various scales. The equation for calculation is as follows.

$$W_f(a,b) = \int_{-\infty}^{+\infty} f(\lambda)\psi_{a,b}(\lambda)d\lambda$$

$$\psi_{a,b}(\lambda) = \frac{1}{\sqrt{a}}\psi\left(\frac{\lambda - b}{a}\right)$$

where $f(\lambda)$ is the spectral reflectance; λ is the number of spectral bands in the range of 350–2,500 nm; $\psi_{a,b}$ is the wavelet basis function; a is the scale factor; and b is the translation factor. The wavelet coefficient $W_f(a,b)$ contains two-dimensional data, the band and scale. The behavioral scales were generated and listed as the matrix of bands.

CWT on the rice canopy spectra was conducted in Matlab 2016b, and the 10 decomposition scales [1, 10] were set (Lamb et al., 2002), namely 2^1, 2^2, …, 2^{10}. Correlation analysis was carried out between the transformation results under the 10 scales and rice yield, and the results were used to screen characteristic bands.

Training Set and Validation Sets

The experimental data for 2015, 2016, and 2019 were selected, including the spectral data of the elongation stage,

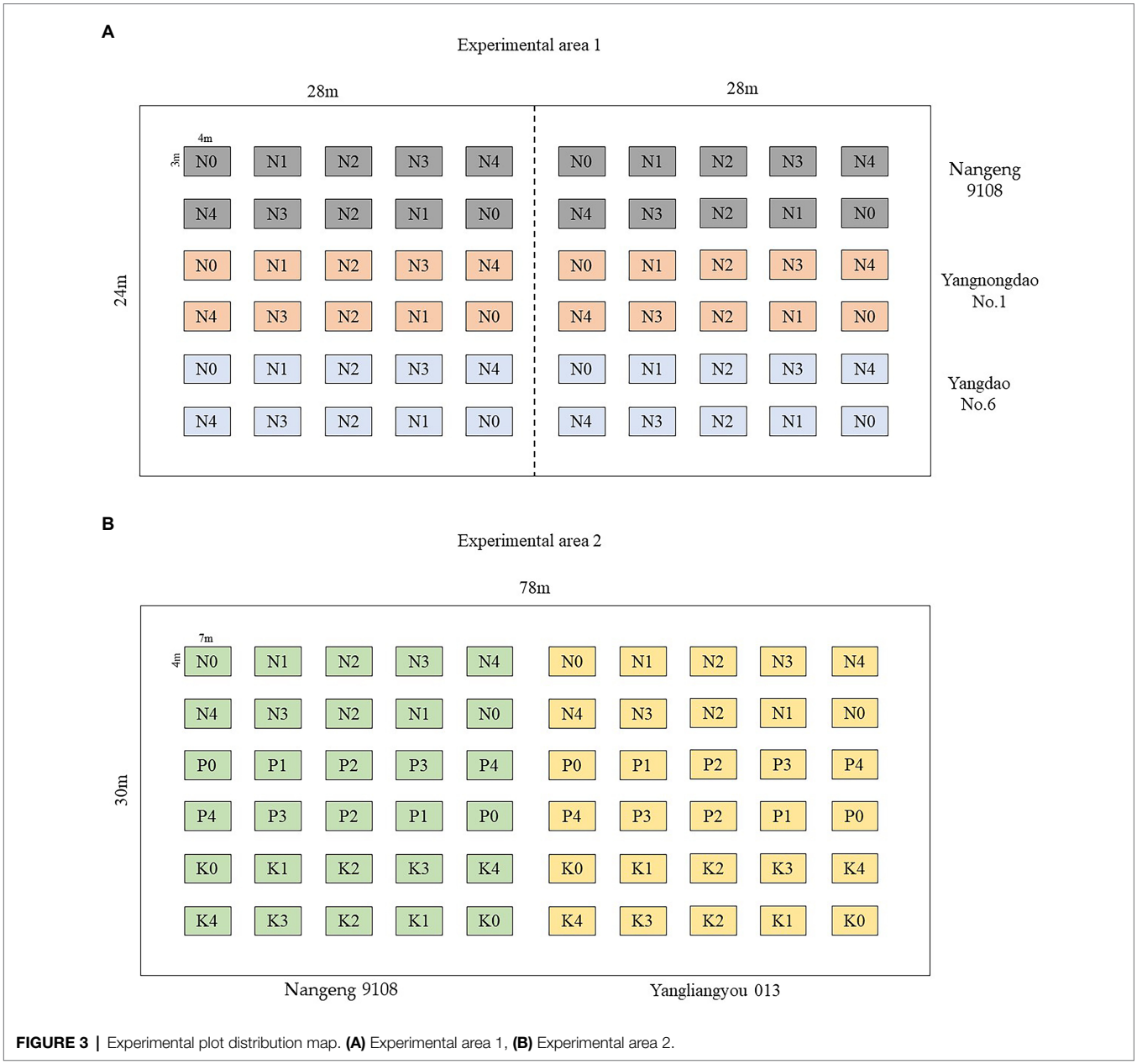

FIGURE 3 | Experimental plot distribution map. **(A)** Experimental area 1, **(B)** Experimental area 2.

the heading stage, the flowering stage, and the milky stage. The sample size was 180. The samples from 2015 ($n = 60$) were used as the training set to establish a production estimation model. And the samples in 2016 ($n = 60$) and 2019 ($n = 60$) were, respectively, used as the validation set to verify the accuracy of the production estimation model. **Table 2** shows the data characteristics.

Model Building and Result Validation

The multivariate stepwise regression (MSR) method was used to establish a multiple linear regression model with multiple parameters. The central idea is to introduce independent variables one by one, on the condition of significantly improved coefficient of partial determination (partial R^2) after introduction. At the same time, after introducing each new independent variable, the old independent variables should be tested one by one to remove those with insignificant partial R^2. This process of introducing while removing was conducted until neither a new variable was introduced nor an old variable was removed. Its essence is to establish the "optimal" multiple linear regression equation. The equation for this type of model is (Uyanık and Güler, 2013):

$$y = b_0 + b_1 x_1 + b_2 x_2 + b_n x_n + e$$

TABLE 1 | Spectral variables.

Type		Symbol	Name	Definition	References
Vegetation index		NDVI	Normalized vegetation index	(NIR-R)/(NIR + R)	Huete, 1988
		DVI	Difference vegetation index	NIR-R	Gitelson et al., 2002
		RVI	Ratio vegetation index	R/NIR	Pearson and Miller, 1972
		EVI	Enhanced vegetation index	2.5(NIR-R)/(1 + NIR + 2.4R)	Jiang et al., 2008
Hyperspectral characteristic variable		λ_r	Red edge position	Wavelength position of D_r	Gong et al., 2002
	Red	D_r	Red edge slope	First derivative spectral maximum within the red edge	Gong et al., 2002
	edge	SD_r	Red edge area	Area of the first derivative spectrum within the red edge	Gong et al., 2002
		λ_b	Blue edge position	Wavelength position of D_b	Gong et al., 2002
	Blue	D_b	Blue edge slope	First derivative spectral maximum within the blue edge	Gong et al., 2002
	edge	SD_b	Blue edge area	Area of the first derivative spectrum within the blue edge	Gong et al., 2002
		λ_y	Yellow edge position	Wavelength position of D_y	Gong et al., 2002
	Yellow	D_y	Yellow edge slope	First derivative spectral maximum within the yellow edge	Gong et al., 2002
	edge	SD_y	Yellow edge area	Area of the first derivative spectrum within the yellow edge	Gong et al., 2002

NIR is any reflectivity in the wavelength range of 760–2,500 nm, R is any reflectivity in the wavelength range of 620–700 nm.

TABLE 2 | Data characteristics.

Sample set	Number of samples	Minimum (g·m^{-2})	Maximum (g·m^{-2})	Mean value	Standard deviation	Variance	Coefficient of variation
Training	60	520	925	686.3	107.9	11633.7	0.16
Validation 1	60	450	925	659.6	102.1	10417.3	0.15
Validation 2	60	443	788	600.6	74.0	5469.7	0.12

where y is the dependent variable, $x_1, x_2, \ldots, x_n$ are the n independent variables used in the modeling, b_0, $b_1, b_2, \ldots, b_n$ are the constant terms corresponding to each independent variable, and e is the error term.

Random forest (RF) is a machine learning algorithm first proposed by Breiman. The algorithm uses the bootstrap resampling method to collect samples from the original sample and performs decision tree modeling for each sample extracted, combining them into multiple decision trees for prediction. The advantage of random forest is that the training is relatively fast and no cross-validation is required (Breiman, 2001). Therefore, random forest is widely used in the classification and prediction of remote sensing. When the random forest is applied to regression problems, the average of the results of each decision tree is the predicted value of the dependent variable.

The indicators selected for the model test were coefficient of determination (R^2), root mean square error (RMSE), and mean absolute percentage error (MAPE).

$$R^2 = \frac{\sum_{i=1}^{n}\left(x_i - \hat{x}_i\right)^2}{\sum_{i=1}^{n}\left(x_i - \bar{x}\right)^2}$$

$$\mathbf{RMSE} = \sqrt{\frac{\sum_{i=1}^{n}\left(x_i - \hat{x}_i\right)^2}{n}}$$

$$\mathbf{MAPE} = \frac{\sum_{i=1}^{n}\left|\frac{x_i - \hat{x}_i}{\hat{x}_i}\right|}{n} \times 100\%$$

Where n is the number of sample sets, $\bar{x}$ is the mean value of rice yield, x_i is the measured value of rice yield, and $\hat{x}_i$ is the predicted value of the model.

The higher the value of R^2, the better the goodness of fit of the corresponding model. RMSE and MAPE tell how accurate the predictions are, and they are two indicators evaluating the regression model. The smaller the values of RMSE and MAPE, the more accurate the model predicts.

RESULTS AND ANALYSIS

Analysis of Canopy Spectral Transformation of Rice in Various Growth Stages

The first derivative, continuum removal, and wavelet transform were performed on the original reflectance. All three methods showed varied curves from the pattern of OR (**Figures 4, 5**). As shown in **Figure 4**, the reflectance of OR and CR was quite different in the four stages in the range of 800–1,100 nm, whereas it was difficult for the FD treatment to intuitively show the difference in spectral reflectance in various stages. **Figure 5** shows the patterns of rice canopy spectra for 10 scales of transformations at various stages. It can be seen from **Figure 5** that the patterns of the four stages were relatively flat on scale [1, 5], with no clear spectral features, were all wave-shaped on scale [6, 8], turned to parabolic on scale [9, 10], and were approaching a straight line beyond 2000 nm. Overall, the spectral features were more distinct than the original spectrum after being transformed at scale 6, 7, 8, 9, and 10.

Correlation Analysis

Correlation Between Rice Yield and Conventional Spectral Transformations

To further take advantage of the rice canopy spectra to predict the rice yield, based on the correlation analysis between the original reflectance and rice yield, this study also conducted a correlation analysis between the first derivative spectra and rice yield, and between the reflectance spectra after continuum removal and rice yield (**Figure 6**). It can be seen that the original spectrum at the jointing stage was significantly correlated with the yield in the range of 400–720 nm. After the first derivative of the spectrum was processed, most of the sensitive bands were still retained in the visible light range, in addition, the range for sensitive bands selection was extended to the near-infrared region beyond 800 nm, such as 910–925 nm, 935–966 nm, 983–1,010 nm, etc. At the heading stage, the strongest correlation after the first-derivative treatment increased to $r'_{1283}\,\mathrm{nm} = -0.73$ from $r_{694}\,\mathrm{nm} = -0.69$ in the original spectrum. The result of the flowering stage was similar that the strongest correlation increased from $r_{705}\,\mathrm{nm} = -0.67$ to $r'_{686}\,\mathrm{nm} = -0.71$. Compared with the previous three stages, the sensitive bands of the milky stage were narrower, and overall, the correlation was decreased as well. Considering the correlation performance of the three treatments, FD > OR > CR, therefore, the spectral spectrum after FD treatment was selected as an independent variable to be introduced into the yield prediction model.

Correlation Between Rice Yield and Wavelet Transform

Figure 7 shows the correlation coefficient matrix of rice yield and rice canopy spectra after 10-dimensional CWT at various stages. As shown in **Figure 7**, the sensitive bands related to rice yield mainly focused on the decomposition at scale [4, 9], and the correlations were weak at scale [1, 3] and [10]. The result after the wavelet transform was compared with the result after the first derivative transform. It was shown that at the elongation stage, the maximum correlation coefficient r appeared at scale [4] at 683 nm with a value of 0.74, significantly higher than the maximum *r*-value of 0.64 at 440 nm of first derivative transform. At the heading stage, the maximum correlation coefficient r was at scale [8] at 732 nm with a value of 0.81, higher than the maximum correlation of −0.73 at 1283 nm of the first derivative transform. At the flowering stage, the maximum correlation coefficient was 0.74 at scale [5] at 675 nm, slightly higher than the maximum correlation of −0.71 at 426 nm of the first-derivative. At the milky stage, the maximum correlation coefficient was 0.65 at scale [4] at 570 nm, significantly higher than the maximum correlation of −0.51 at 557 nm of the first derivative transform. In addition, the number of sensitive bands of spectral reflectance to rice yield under the first derivative treatment was significantly less than that treated by CWT. Therefore, the overall results demonstrated that CWT was significantly better than FD. The effective spectral signals were better displayed after wavelet transform, and it was conducive to digging into the information to facilitate subsequent research and analysis.

To explore which scales of the wavelet transform have the most potential in retrieving rice yield, the 10 dimensions under each growth stage were analyzed independently (**Supplementary Figure 1**). The results showed that at the elongation stage, the absolute values of the correlation coefficients between spectral reflectance and rice yield under wavelet transform at scale [4, 6] and [8] were increased significantly, and the number of sensitive bands also increased substantially compared with the FD transform. The improvement by wavelet transform was more distinct at the heading and flowering stages, with dominant scales concentrated in [4, 9]. While the milky stage was significantly improved at scales [4, 5] and [7, 8]. Therefore, the overall results indicated that the wavelet transform of the original spectrum had strong adaptability at scale [8], and performed well across all the four growth stages.

Correlation Between Vegetation Indices and Rice Yield

Four vegetation index (VI), Normalized Difference Vegetation Index (NDVI), Ratio Vegetation Index (RVI), Difference Vegetation Index (DVI), and Enhanced Vegetation Index (EVI), were calculated using the red and near-infrared bands, and the correlation between each of them with measured

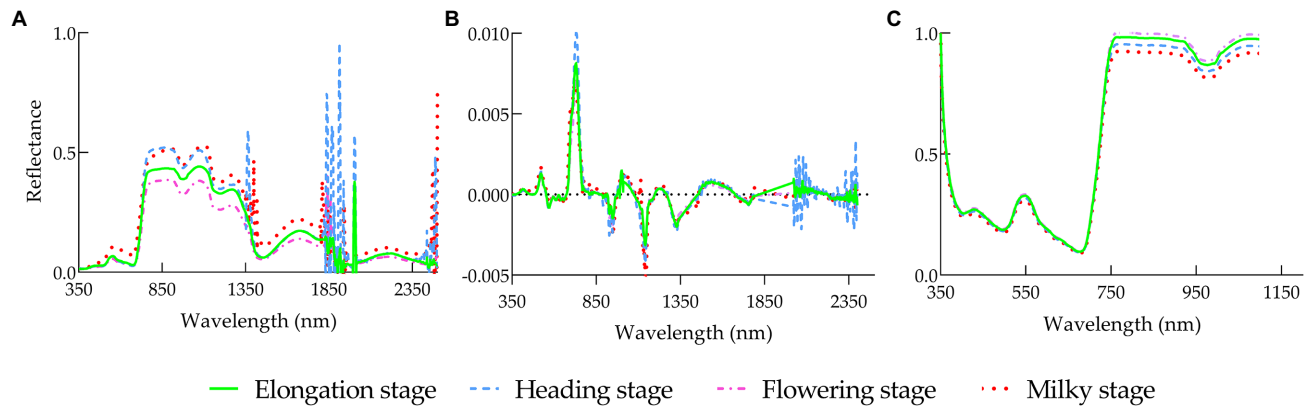

FIGURE 4 | Spectral reflectance of rice leaf canopy under different treatments in various growth stages: **(A)** OR, **(B)** FD, **(C)** CR.

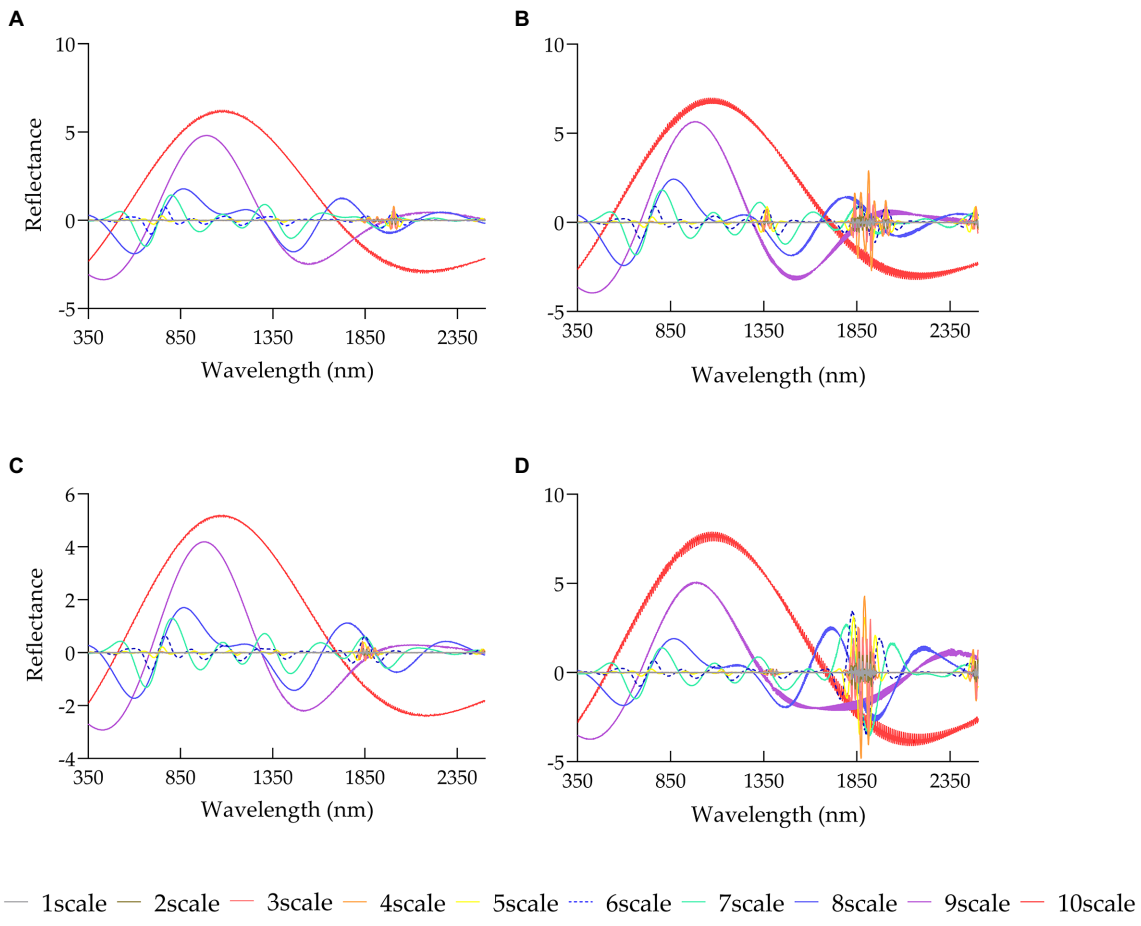

FIGURE 5 | Changes in reflectance of wavelet transform of rice canopy spectra in various growth stages: **(A)** elongation stage, **(B)** heading stage, **(C)** flowering stage, **(D)** milky stage.

yield was analyzed. The results are shown in **Table 3**. It is exhibited that the Pearson correlation coefficients of the four vegetation indices all increased first and then decreased as the growth stage advanced and peaked at the heading stage. Therefore, it is speculated that the vegetation indices at the heading and flowering stages would perform better for the prediction of rice yield in the later stage.

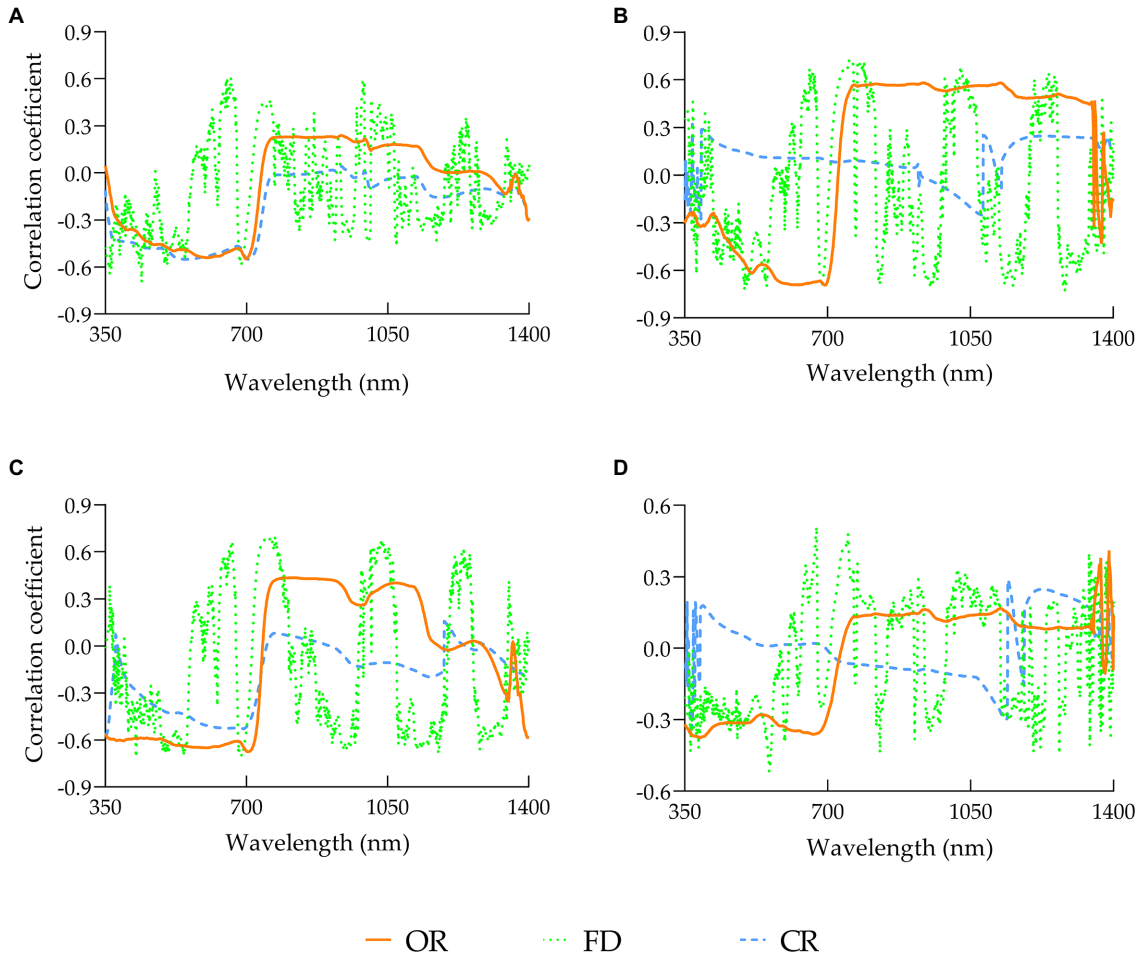

FIGURE 6 | Correlation between rice yield and conventional spectral transformations in various growth stages: **(A)** elongation stage, **(B)** heading stage, **(C)** flowering stage, **(D)** milky stage.

Correlation Between FD-Based Hyperspectral Characteristic Parameters and Rice Yield

The characteristic parameters such as red edge, yellow edge, and blue edge were calculated, and further, they were normalized and differentially calculated. The correlation analysis was carried out between the obtained values and rice yield, and the results are shown in **Table 4**. As shown, the correlation coefficients between the hyperspectral parameters and yield at the heading and flowering stages were generally higher than those at the elongation and milky stages. And the three hyperspectral parameters, λ_r, SD_r/SD_b, and $(SD_r - SD_b)/(SD_r + SD_b)$, performed best regarding adaptation and were strongly correlated with the yield at all four stages.

Construction of Rice Yield Prediction Models

The yield of rice is a collective result of multiple growth stages, and each growth contributed spectral variables that are closely related to yield. Therefore, this study combined the spectral variables of multiple growth stages to predict rice yield and adopted MSR and RF to establish prediction models to determine the optimal combination of growth stages. In addition, to verify whether the wavelet transform could improve the prediction accuracy of the yield estimation model, two prediction models were established in this study. One was the yield prediction model based on the first derivative transform, the other one was based on first derivative-wavelet transform.

TABLE 3 | Summary of optimal parameters of vegetation index.

Stage	RVI	NDVI	DVI	EVI
	Correlation coefficient	Correlation coefficient	Correlation coefficient	Correlation coefficient
Elongation stage	0.58	0.59	0.34	0.43
Heading stage	0.74	0.73	0.62	0.67
Flowering stage	0.72	0.71	0.56	0.64
Milky stage	0.61	0.63	0.24	0.34

Comparison of Different Models Based on First Derivative Transform

The MSR and RF models established based on the first derivative transformation of multiple growth stages are shown in **Table 5**. As far as the results of a single growth stage were concerned, the model of the heading stage performed the best. The optimal MSR models at the corresponding four growth stages were the heading stage model, the heading-milky stage model, the elongation-heading-milky stage model, and the elongation-heading-flowering-milky stage model, respectively. The optimal RF models were the heading stage model, the heading-flowering model, the elongation-heading-milky model, the elongation-heading-flowering-milky model.

TABLE 4 | Correlation analysis between spectral characteristics variable and rice yield at different stages.

Hyperspectral characteristic	Correlation coefficient			
variable	Elongation stage	Heading stage	Flowering stage	Milky stage
λ_r	0.59	0.66	0.71	0.61
λ_b	−0.12	0.23	0.30	0.07
λ_y	0.12	0.18	0.01	0.45
D_r	0.34	0.61	0.58	0.21
D_b	−0.39	−0.40	−0.58	−0.21
D_y	−0.12	−0.21	−0.03	−0.38
SD_r	0.28	0.58	0.51	0.22
SD_b	−0.47	−0.54	−0.63	−0.25
SD_y	−0.14	−0.03	−0.20	0.11
$SD_r - SD_b$	0.32	0.61	0.56	0.26
$SD_r - SD_y$	0.30	0.60	0.54	0.22
$SD_b - Sd_y$	−0.45	−0.67	−0.60	−0.40
SD_r/SD_b	0.58	0.73	0.72	0.63
SD_r/SD_y	0.52	0.72	0.42	−0.17
SD_b/SD_y	−0.39	−0.62	−0.46	−0.39
$(SD_r - SD_b)/(SD_r + SD_b)$	0.64	0.73	0.72	0.67
$(SD_r - SD_y)/(SD_r + SD_y)$	0.52	0.73	0.51	0.11

λ_b is blue edge position, D_b is blue edge slope, SD_b is blue edge area; λ_y is yellow edge position, D_y is yellow edge slope, SD_y is yellow edge area; λ_r is red edge position, D_r is red edge slope, SD_r is red edge area.

Comparison of Different Models Based on First Derivative-Wavelet Transform

The MSR models and RF models established based on first derivative-wavelet transform of multiple growth stages are shown in **Table 6**. Regarding the modeling results of a single growth stage, the model of the heading stage performed the best. Comparing the models of each growth stage, it can be seen that the optimal MSR models for the corresponding four growth stages were the heading stage model, the heading-flowering stage model, the elongation-heading-flowering stage model, and the elongation-heading-flowering-milky model, respectively. The optimal RF models were the heading stage, the heading-milky stage, the elongation-heading-milky stage, the elongation-heading-flowering-milky stage.

A comprehensive comparison of **Tables 5, 6** showed that the most suitable growth stage combinations for rice yield estimation was the elongation-heading-flowering-milky stage. In the model validation section, this study validated the MSR model and RF model for the four stages combinations.

Validation of the Predictive Model

The evaluation results of the two modeling methods based on validation set 1 were shown in the table (**Table 7**). VI was combined with FD and FD-CWT, respectively, for a comparative analysis of the two modeling approaches. For the MSR model,

TABLE 5 | Rice yield prediction model based on first derivative transform.

Stage combination	MSR			RF		
	R^2	RMSE ($g \cdot m^{-2}$)	MAPE (%)	R^2	RMSE ($g \cdot m^{-2}$)	MAPE (%)
Elongation	0.46	92.50	11.80	0.49	83.70	8.70
Heading	0.50	67.60	7.50	0.55	63.10	7.10
Flowering	0.44	72.50	8.40	0.46	75.00	8.20
Milky	0.49	80.40	8.30	0.51	74.50	8.10
Elongation-heading	0.48	73.80	8.30	0.50	65.50	7.70
Elongation-flowering	0.50	67.20	8.50	0.55	63.90	8.00
Elongation-milky	0.50	70.10	8.10	0.61	60.90	7.20
Heading-flowering	0.51	69.80	7.50	0.59	60.40	6.90
Heading-milky	0.55	64.10	7.10	0.50	69.50	7.60
Flowering-milky	0.49	66.50	7.40	0.53	63.30	8.10
Elongation-heading-flowering	0.60	63.60	7.70	0.62	57.60	6.80
Elongation-heading-milky	0.62	58.30	6.90	0.67	52.60	6.50
Elongation-flowering-milky	0.54	65.70	7.80	0.55	60.50	7.50
Heading-flowering-milky	0.58	63.50	7.10	0.60	55.50	6.60
Elongation-heading-flowering-milky	0.70	50.30	5.60	0.77	45.10	5.50

TABLE 6 | Rice yield prediction model based on first derivative-wavelet transform.

Stage combination	MSR			RF		
	R^2	RMSE ($g \cdot m^{-2}$)	MAPE (%)	R^2	RMSE ($g \cdot m^{-2}$)	MAPE (%)
Elongation	0.54	88.30	10.20	0.50	76.60	9.90
Heading	0.64	60.90	7.90	0.66	58.00	7.80
Flowering	0.56	64.50	8.20	0.58	66.40	7.90
Milky	0.48	72.40	9.00	0.53	69.90	8.70
Elongation-heading	0.65	58.10	7.30	0.67	58.30	6.70
Elongation-flowering	0.60	65.40	8.70	0.60	60.80	6.90
Elongation-milky	0.66	60.90	8.10	0.61	60.20	6.50
Heading-flowering	0.68	57.50	7.00	0.62	57.20	6.60
Heading-milky	0.65	59.60	7.80	0.69	54.60	6.20
Flowering-milky	0.60	61.30	7.90	0.65	54.80	6.70
Elongation-heading-flowering	0.73	47.10	6.50	0.74	47.40	5.90
Elongation-heading-milky	0.67	50.30	6.80	0.75	46.00	5.70
Elongation-flowering-milky	0.66	54.70	7.20	0.71	58.40	6.40
Heading-flowering-milky	0.68	48.30	6.60	0.73	50.90	6.00
Elongation-heading-flowering-milky	0.81	37.60	4.80	0.86	35.50	4.60

TABLE 7 | Comparison of the two modeling approaches.

			Training set			Validation set		
Stage combination	Model algorithm	Independent variable	R^2	RMSE ($g \cdot m^{-2}$)	MAPE (%)	R^2	RMSE ($g \cdot m^{-2}$)	MAPE (%)
Elongation-Heading-Flowering-Milky	MSR	FD-VI	0.70	50.30	5.60	0.68	51.80	6.10
		CWT-FD-VI	0.81	37.60	4.80	0.77	36.30	4.70
	RF	FD-VI	0.77	45.10	5.60	0.80	45.20	5.00
		CWT-FD-VI	0.86	35.50	4.60	0.85	33.40	4.30

the combination of VI with CWT-FD improved the modeling set R^2 by 0.11 and reduced the RMSE and MAPE by 12.70 $g \cdot m^{-2}$ and 0.80%, respectively, while the validation set R^2 improved by 0.11 and reduced the RMSE and MAPE by 15.5 $g \cdot m^{-2}$ and 1.4%, respectively. For the RF model, the modeling set R^2 improved by 0.09 and RMSE and MAPE decreased by 9.60 $g \cdot m^{-2}$ and 1.00%, respectively, and the validation set R^2 improved by 0.05 and RMSE and MAPE decreased by 11.80 $g \cdot m^{-2}$ and 0.70%, respectively. Consequently, the most suitable combination of independent variables for estimating rice yield was VI-FD-CWT. In terms of the effect of different modeling algorithms, the RF algorithm gave the best results with modeling sets R^2, RMSE, and MAPE of 0.86, 35.50 $g \cdot m^{-2}$, and 4.60%, respectively, and validation sets R^2, RMSE, and MAPE of 0.85, 33.40 $g \cdot m^{-2}$, and 4.30%, respectively. Based on the four growth stages and CWT-FD-VI combination, the RF model was the best estimation model for rice yield.

The optimal MSR and RF models generated by the two transformation methods based on combinations of four growth stages were tested. The validation sets were independent sample sets, and the results are shown in **Supplementary Figures 2**, **3**.

To verify whether different varieties and nitrogen fertilizer levels affect the prediction accuracy of the models, completely independent validation sets were used in this study to re-evaluate the optimal MSR model and RF model. The evaluation results are shown in **Supplementary Figure 4**. The validation results of the validation set 2 showed that the RF model was superior to the MSR model, with R^2 improving by 0.08 and RMSE and MAPE decreasing by 6.3 $g \cdot m^{-2}$ and 1.3%, respectively.

DISCUSSION

Literature and previous studies have already proved that the spectral reflectance can tell the growth status of crops to various extents. However, the existing models are usually established based on the original spectrum without any processing, leaving a lot of room for improvement regarding the model accuracy. For example, Li et al. used a successive projection algorithm (SPA) to determine characteristic bands and then established an estimation model for estimating the pH of water body (Li and Guo, 2021). The spectral preprocessing methods such as first derivative and continuum removal which have been commonly used in recent years could amplify the effective information in the spectrum to

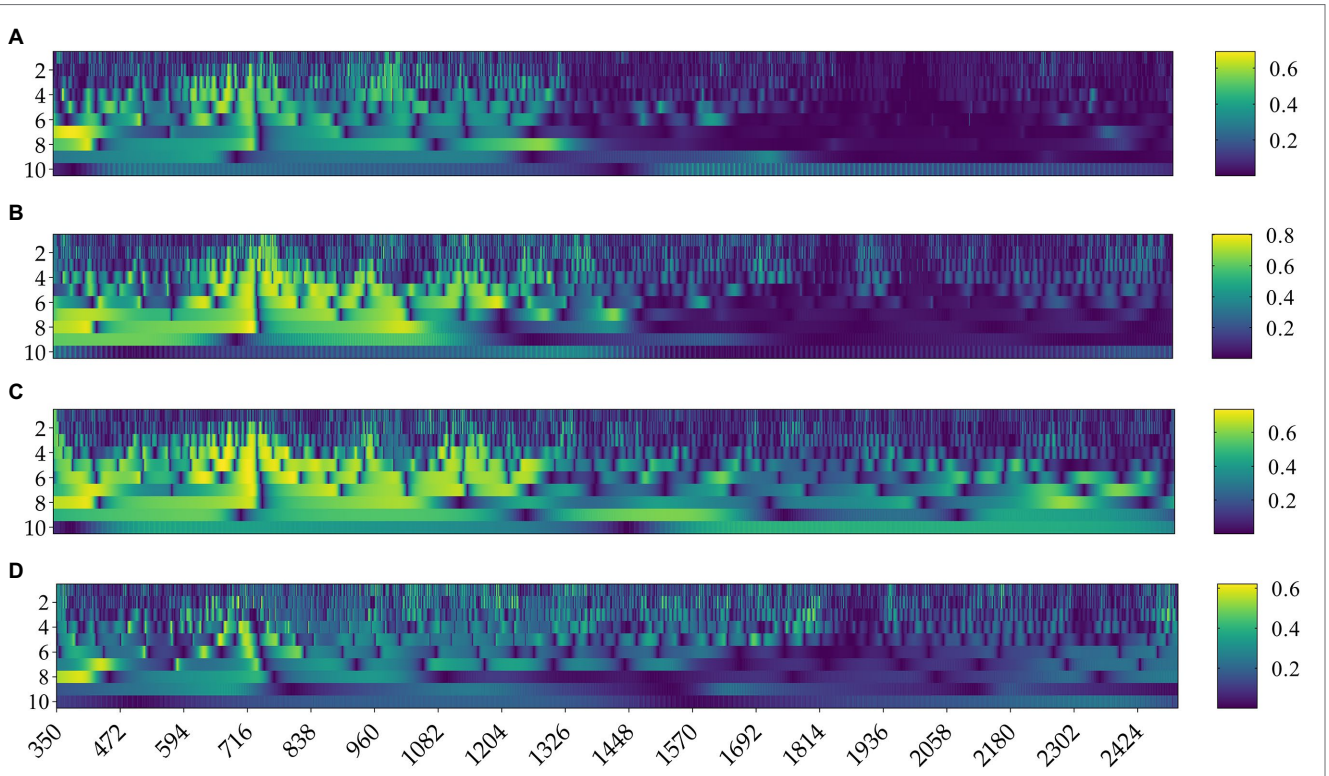

FIGURE 7 | Absolute value of correlation coefficients of different wavelet coefficients with rice yield in various growth stages: **(A)** elongation stage, **(B)** heading stage, **(C)** flowering stage, **(D)** milky stage.

a certain extent. For example, Yuan et al. used SG to smooth the hyperspectral data of the original spectrum, screened the sensitive bands, and identified the early rice blast disease with an accuracy of 90% (Yuan et al., 2021). Gao et al. adopted the first derivative and continuum removal in the estimation of the phosphorus content of grassland forages and pointed out that the first derivative was the most effective spectral preprocessing method (Gao et al., 2019). The range of characteristic spectral bands after processing by first derivative could be extended to the infrared region. This conclusion is consistent with the previous findings. Previous research of our lab revealed that the field rice canopy spectrum was the collective result of multiple factors including weather and rice variety. In addition, noise was also introduced into the canopy spectral data collected in the field due to human reasons and the machine itself. It is difficult for the conventional spectral preprocessing methods to deep excavate effective information. Therefore, in this study, the original spectrum after SG smoothing was taken and subjected to continuous wavelet transform to eliminate spectral noise. The results demonstrated that the wavelet transform of original spectrum could not only greatly boost its correlation with rice yield, but also increase the number of sensitive bands in various stages compared with the first derivative transform, with an especially distinct effect in the flowering and heading stages. At the same time, the comparative analysis also revealed that the wavelet transform under scale [8] was the most effective for mining effective information, and its strong ability was seen for all the four stages, basically consistent with the previous research results (Li et al., 2019; Zhou et al., 2021). Therefore, wavelet transform can be used in the next step of research to establish estimation models for important agronomic parameters in each growth stage.

In terms of hyperspectral parameter selection, correlation analysis showed that various parameters demonstrated different sensitivities in different growth stages. The parameters NDVI, RVI, and "tri-edge" parameters all performed nicely in all the four growth stages after difference, ratio, or normalization transformations. However, the correlations between them with rice yield were generally higher in the heading and flowering stags than in the other two growth stages. By analyzing the sensitive bands selected by various hyperspectral studies in recent years (Wu and Shi, 2004; Xie et al., 2014; Bagchi et al., 2016), it was found that most of them were in the near-infrared region, and there have been few related applications in the field of visible light. Nevertheless, in our study on the bands selected by the optimal models for different growth stages, it was shown that except for the red-edge parameter, all the others were distributed in the visible light range. The results of the present study demonstrated that the established prediction models based on wavelet transform could greatly reduce the difficulty of parameter acquisition and improve the practical model performance.

The comparison of previous studies showed that the established prediction model for yield was often limited to using a single vegetation index. For example, Lai et al. used NDVI at the mature stage to build a rice panicle differentiation prediction model (Lai and Lin, 2021). Nazir et al. used Sentinel-2 satellite images together with different single vegetation index to predict rice yield (Nazir et al., 2021). However, usually, this method had low accuracy, and in practical applications, issues such as overfitting were seen. Huang et al. pointed out that such disadvantages existed when simply using the relationship between vegetation index and crop yield to build a model (Huang et al., 2019). In addition, in the optimal models regarding combinations of different growth stages, the four vegetation indices checked in the study were not included in the final optimal model. It indicated that these four vegetation indices cannot be used to accurately estimate the yield of rice. In the next stage of research, we may consider replacing them with other vegetation indices, such as Soil-Adjusted Vegetation Index (SAVI), Optimized Soil-Adjusted Vegetation Index (OSAVI), Green Normalized Difference Vegetation Index (GNDVI), Normalized Difference Water Index (NDWI), etc.

In terms of growth stage selection, our study found that the heading and flowering stages were the best predictors of rice yield, followed by the jointing and milky stages. The trend was not a monotonically increasing curve following the growth stages, but a parabolic curve that first increased and then decreased. Presumably, it may be because of the strong interference of soil and weeds due to the low coverage rate of rice before the jointing stage. In addition, the nutrient accumulation of rice in the booting stage has not finished yet, and the spectral change is mainly affected by the growth of stems and leaves. Therefore, the spectral information of rice at the early growth stages was not suitable for yield estimation. The heading and flowering stages of rice were the key stages to yield. Gradually, rice transitioned from nutritional phase to reproductive phase, and the crop population was coordinated. Therefore, the hyperspectral information of these two stages contributed the most to the rice yield estimation model. Most of the current studies on rice yield were based on remote-sensing information of a single growth stage. For example, Jin et al. established a winter wheat yield estimation model using a combination of multiple vegetation indices at the heading stage and gave a verification R^2 of 0.69, but they did not explore much information on the growth stages (Jin et al., 2022). Therefore, the present study comprehensively utilized the information on multiple growth stages based on previous studies to verify and further explore the significance and role of the spectra of different combinations of growth stages on the rice yield prediction model.

The research results already demonstrated that the accuracies of the regression models based on the combinations of multiple growth stages were higher than those established by the parameters of single growth stages. Therefore, the introduction of information on multiple growth stages may significantly improve the accuracy of the prediction model. The optimal combination of growth stages was elongation-heading-flowering-milky. In addition, two validation sets were set up in this study considering the influence of variety and fertilizer variety on the accuracy of the model. In this study, to verify the generality of the optimal growth stage combination model, another validation set using a different variety and a different fertilizer test were used to verify the accuracy of the model. The R^2 of the MSR model decreased by 0.05 and the RMSE and MAPE increased by 7.40 $g \cdot m^{-2}$ and 1.2%, respectively. The R^2 of the RF model decreased by 0.05 and the RMSE and MAPE increased by 4.00 $g \cdot m^{-2}$ and 0.3%, respectively. Therefore, it proved that the generalizability of the RF model was higher than the MSR model.

At present, the research on estimating rice yield still faces many challenges, and more exploration is urgently needed. First, the hyperspectral prediction model has been applied in various fields in recent years, but its mechanism investigation remains insufficient. For example, the technology still cannot distinguish different varieties by spectrum. At present, most of the models were derived from empirical models. With the continuous advancement of science and technology, hyperspectral technology become more and more mature in the future. Secondly, with the continuous innovation in machine learning field in recent years, more and more algorithms have been applied to the field of agricultural remote sensing, such as the Support Vector Machine algorithm, Gaussian Process Regression algorithm, etc. Appropriate algorithms can significantly improve the accuracy of the prediction model and are a great help to practicability improvement. In addition, the full rise of agricultural drones will provide new directions for large-scale yield estimation too.

CONCLUSION

By comprehensive analysis and comparison of correlations and modeling, it was demonstrated that wavelet transform was the most effective spectral preprocessing method, followed by first-derivative. This study found that after the original spectrum was processed by the first-derivative and wavelet transform, the effective information was amplified and enhanced, and the ability to characterize rice yield became stronger. Therefore, the wavelet transform and first derivative transform methods have important application values in enhancing spectral characteristics. Secondly, the rice yield prediction models established based on combining multiple growth stages could significantly improve the prediction accuracy. The RF model established by combining first derivative-wavelet transform and the four growth stages (elongation-heading-flowering-milky) carried out the best prediction, with modeling set R^2 of 0.86, RMSE of 35.50 $g \cdot m^{-2}$, and MAPE of 4.60%. The validation set 1 had the results as R^2 of 0.85, RMSE of 33.40 $g \cdot m^{-2}$, and MAPE of 4.30%. The validation set 2 had the results as R^2 of 0.80, RMSE of 37.40 $g \cdot m^{-2}$, and MAPE of 4.60%.

DATA AVAILABILITY STATEMENT

The raw data supporting the conclusions of this article will be made available by the authors, without undue reservation.

AUTHOR CONTRIBUTIONS

CG and CT: conceptualization and formal analysis. CT: supervision. CG and SJ: data curation and validation. CG: prepared and revised the manuscript. SJ, QH, WL, RZ, ZZ and ZH: provided technical support. CG, WM, HZ, BL, XX: visualization and original draft. All authors contributed to the article and approved the submitted version.

FUNDING

This study was supported by the National Natural Science Foundation of China (32071902), the Key Research Program of Jiangsu Province, China (BE2020319), the Yangzhou University Interdisciplinary Research Foundation for Crop Science Discipline of Targeted Support (yzuxk202007 and yzuxk202008), and the Priority Academic Program Development of Jiangsu Higher Education Institutions (PAPD).

SUPPLEMENTARY MATERIAL

The Supplementary Material for this article can be found online at: https://www.frontiersin.org/articles/10.3389/fpls.2022.931789/full#supplementary-material

Supplementary Figure 1 | Comparison of the number of sensitive bands after wavelet transform at different scales in various growth stages: **(A)** elongation stage, **(B)** heading stage, **(C)** flowering stage, **(D)** milky stage.

Supplementary Figure 2 | Test results of four growth stages combination model based on first derivative transform: **(A)** MSR model, **(B)** RF model.

Supplementary Figure 3 | Test results of four growth stages combination model based on first derivative-wavelet transform: **(A)** MSR model, **(B)** RF model.

Supplementary Figure 4 | Model test results based on the validation set 2: **(A)** MSR model, **(B)** RF model.

REFERENCES

Amirhossein, H., Jan van, A., Sean Patrick, M., and Sarah Jane, P. (2020). Yield modeling of snap bean based on hyperspectral sensing: a greenhouse study. *J. Appl. Remote. Sens.* 14, 1–20. doi: 10.1117/1.JRS.14.024519

Bagchi, T. B., Sharma, S., and Chattopadhyay, K. (2016). Development of NIRS models to predict protein and amylose content of brown rice and proximate compositions of rice bran. *Food Chem.* 191, 21–27. doi: 10.1016/j.foodchem.2015.05.038

Bajwa, S. G., Mishra, A. R., and Norman, R. J. (2010). Canopy reflectance response to plant nitrogen accumulation in rice. *Precis. Agric.* 11, 488–506. doi: 10.1007/s11119-009-9142-0

Breiman, L. (2001). Random forests. *Mach. Learn.* 45, 5–32. doi: 10.1023/A:1010933404324

Chang, K.-W., Shen, Y., and Lo, J.-C. (2005). Predicting rice yield using canopy reflectance measured at booting stage. *Agron. J.* 97, 872–878. doi: 10.2134/agronj2004.0162

Curran, P. J. (1989). Remote sensing of foliar chemistry. *Remote Sens. Environ.* 30, 271–278. doi: 10.1016/0034-4257(89)90069-2

Feng, L., Wu, B., He, Y., and Zhang, C. (2021). Hyperspectral imaging combined with deep transfer learning for Rice disease detection. *Front. Plant Sci.* 12:693521. doi: 10.3389/fpls.2021.693521

Gao, J., Meng, B., Liang, T., Feng, Q., Ge, J., Yin, J., et al. (2019). Modeling alpine grassland forage phosphorus based on hyperspectral remote sensing and a multi-factor machine learning algorithm in the east of Tibetan plateau, China. *ISPRS J. Photogramm. Remote Sens.* 147, 104–117. doi: 10.1016/j.isprsjprs.2018.11.015

Gitelson, A. A., Kaufman, Y. J., Stark, R., and Rundquist, D. (2002). Novel algorithms for remote estimation of vegetation fraction. *Remote Sens. Environ.* 80, 76–87. doi: 10.1016/S0034-4257(01)00289-9

Gong, P., Pu, R., and Heald, R. C. (2002). Analysis of in situ hyperspectral data for nutrient estimation of giant sequoia. *Int. J. Remote Sens.* 23, 1827–1850. doi: 10.1080/01431160110075622

Guo, T., Tan, C., Li, Q., Cui, G., and Li, H. (2019). Estimating leaf chlorophyll content in tobacco based on various canopy hyperspectral parameters. *J. Amb. Inter. Hum. Comp.* 10, 3239–3247. doi: 10.1007/s12652-018-1043-5

He, R., Li, H., Qiao, X., and Jiang, J. (2018). Using wavelet analysis of hyperspectral remote-sensing data to estimate canopy chlorophyll content of winter wheat under stripe rust stress. *Int. J. Remote Sens.* 39, 4059–4076. doi: 10.1080/01431161.2018.1454620

Huang, J., Gómez-Dans, J. L., Huang, H., Ma, H., Wu, Q., Lewis, P. E., et al. (2019). Assimilation of remote sensing into crop growth models: current status and perspectives. *Agric. For. Meteorol.* 276-277:107609. doi: 10.1016/j.agrformet.2019.06.008

Huang, J., Ma, H., Tian, L., Pengxin, W., and Liu, J. (2015). Comparison of remote sensing yield estimation methods for winter wheat based on assimilating time-sequence LAI and ET. *Trans. Chin. Soc. Agric. Engineer.* 31, 197–203. doi: 10.3969/j.issn.1002-6819.2015.04.028

Huang, J., Sedano, F., Huang, Y., Ma, H., Li, X., Liang, S., et al. (2016). Assimilating a synthetic Kalman filter leaf area index series into the WOFOST model to improve regional winter wheat yield estimation. *Agric. For. Meteorol.* 216, 188–202. doi: 10.1016/j.agrformet.2015.10.013

Huete, A. R. (1988). A soil-adjusted vegetation index (SAVI). *Remote Sens. Environ.* 25, 295–309. doi: 10.1016/0034-4257(88)90106-X

Inoue, Y., Moran, M. S., and Horie, T. (1998). Analysis of spectral measurements in Paddy field for predicting Rice growth and yield based on a simple crop simulation model. *Plant Prod. Sci.* 1, 269–279. doi: 10.1626/pps.1.269

Jiang, Z., Huete, A. R., Didan, K., and Miura, T. (2008). Development of a two-band enhanced vegetation index without a blue band. *Remote Sens. Environ.* 112, 3833–3845. doi: 10.1016/j.rse.2008.06.006

Jin, N., Tao, B., Ren, W., He, L., Zhang, D., Wang, D., et al. (2022). Assimilating remote sensing data into a crop model improves winter wheat yield estimation based on regional irrigation data. *Agr. Water Manage.* 266:107583. doi: 10.1016/j.agwat.2022.107583

Jin, J., and Wang, Q. (2016). Hyperspectral indices based on first derivative spectra closely trace canopy transpiration in a desert plant. *Ecol. Inform.* 35, 1–8. doi: 10.1016/j.ecoinf.2016.06.004

Lai, J.-K., and Lin, W.-S. (2021). Assessment of the rice panicle initiation by using NDVI-based vegetation indexes. *Appl. Sci.* 11:10076. doi: 10.3390/app112110076

Lamb, D., Steyn-Ross, M., Schaares, P., Hanna, M., Silvester, W., and Steyn-Ross, A. (2002). Estimating leaf nitrogen concentration in ryegrass pasture using the chlorophyll red-edge: Modelling and experimental observations. *Int. J. Remote Sens.* 23, 3619–3648. doi: 10.1080/01431160110114529

Li, L., and Guo, S. (2021). A wavelength selection model based on successive projections algorithm for pH detection of water by VIS-NIR spectroscopy. *J. Phys. Conf. Ser.* 1813:012002. doi: 10.1088/1742-6596/1813/1/012002

Li, F., Wang, L., Liu, J., Wang, Y., and Chang, Q. (2019). Evaluation of leaf N concentration in winter wheat based on discrete wavelet transform analysis. *Remote Sens.* 11:1331. doi: 10.3390/rs11111331

Miclea, A. V., Terebes, R. M., Meza, S., and Cislariu, M. (2022). On spectral-spatial classification of hyperspectral images using image denoising and enhancement techniques, wavelet transforms and controlled data set partitioning. *Remote Sens.* 14, 1475–1489. doi: 10.3390/rs14061475

Mokhtari, A., Noory, H., and Vazifedoust, M. (2018). Improving crop yield estimation by assimilating LAI and inputting satellite-based surface incoming solar radiation into SWAP model. *Agric. For. Meteorol.* 250-251, 159–170. doi: 10.1016/j.agrformet.2017.12.250

Nazir, A., Ullah, S., Saqib, Z. A., Abbas, A., Ali, A., Iqbal, M. S., et al. (2021). Estimation and forecasting of Rice yield using phenology-based algorithm and linear regression model on sentinel-II satellite data. *Agriculture* 11:1026. doi: 10.3390/agriculture11101026

Nguyen, H. T., and Lee, B.-W. (2006). Assessment of rice leaf growth and nitrogen status by hyperspectral canopy reflectance and partial least square regression. *Eur. J. Agron.* 24, 349–356. doi: 10.1016/j.eja.2006.01.001

Olivares Díaz, E., Kawamura, S., Matsuo, M., Kato, M., and Koseki, S. (2019). Combined analysis of near-infrared spectra, colour, and physicochemical information of brown rice to develop accurate calibration models for determining amylose content. *Food Chem.* 286, 297–306. doi: 10.1016/j.foodchem.2019.02.005

Osco, L. P., Ramos, A. P., Faita Pinheiro, M. M., Moriya, É. A., Imai, N. N., Estrabis, N., et al. (2020). A machine learning framework to predict nutrient content in Valencia-Orange leaf Hyperspectral measurements. *Remote Sens.* 12:906. doi: 10.3390/rs12060906

Pearson, R. L., and Miller, L. D. (1972). Remote mapping of standing crop biomass for estimation of productivity of the Shortgrass prairie. *Remote Sens. Environ.* 2, 1357–1381.

Reichle, R. H. (2008). Data assimilation methods in the earth sciences. *Adv. Water Resour.* 31, 1411–1418. doi: 10.1016/j.advwatres.2008.01.001

Ren, J., Chen, Z., Zhou, Q., and Tang, H. (2008). Regional yield estimation for winter wheat with MODIS-NDVI data in Shandong, China. *Int. J. Appl. Earth Obs.* 10, 403–413. doi: 10.1016/j.jag.2007.11.003

Sampaio, P. S., Soares, A., Castanho, A., Almeida, A. S., Oliveira, J., and Brites, C. (2018). Optimization of rice amylose determination by NIR-spectroscopy using PLS chemometrics algorithms. *Food Chem.* 242, 196–204. doi: 10.1016/j.foodchem.2017.09.058

Savitzky, A., and Golay, M. J. (1964). Smoothing and differentiation of data by simplified least squares procedures. *Anal. Chem.* 36, 1627–1639. doi: 10.1021/ac60214a047

Shao, Y., Wang, Y., and Xuan, G. (2021). In-field and non-invasive determination of internal quality and ripeness stages of Feicheng peach using a portable hyperspectral imager. *Biosyst. Eng.* 212, 115–125. doi: 10.1016/j.biosystemseng.2021.10.004

Shen, S., Yang, S., Li, B., Tan, B., Li, Z., and Le Toan, T. (2009). A scheme for regional rice yield estimation using ENVISAT ASAR data. *Sci. China Ser. D Earth Sci.* 52, 1183–1194. doi: 10.1007/s11430-009-0094-z

Tuvdendorj, B., Wu, B., Zeng, H., Batdelger, G., and Nanzad, L. (2019). Determination of appropriate remote sensing indices for spring wheat yield estimation in Mongolia. *Remote Sens.* 11:2568. doi: 10.3390/rs11212568

Uyanık, G. K., and Güler, N. (2013). A study on multiple linear regression analysis. *Procedia. Soc. Behav. Sci.* 106, 234–240. doi: 10.1016/j.sbspro.2013.12.027

Wang, X., Huang, J., Feng, Q., and Yin, D. (2020). Winter wheat yield prediction at county level and uncertainty analysis in Main wheat-producing regions of China with deep learning approaches. *Remote Sens.* 12:1744. doi: 10.3390/rs12111744

Wang, W., Yao, X., Tian, Y., Liu, X., Ni, J., Cao, W., et al. (2012). Common spectral bands and optimum vegetation indices for monitoring leaf nitrogen accumulation in rice and wheat. *J. Integr. Agric.* 11, 2001–2012. doi: 10.1016/S2095-3119(12)60457-2

Wang, J., and Yu, Y. (2021). Comprehensive drought monitoring in Yunnan Province, China using multisource remote sensing data. *J. Mt. Sci.* 18, 1537–1549. doi: 10.1007/s11629-020-6333-7

Wu, J. G., and Shi, C. H. (2004). Prediction of grain weight, brown rice weight and amylose content in single rice grains using near-infrared reflectance spectroscopy. *Field Crop Res* 87, 13–21. doi: 10.1016/j.fcr.2003.09.005

Xie, Y., Wang, P., Bai, X., Khan, J., Zhang, S., Li, L., et al. (2017). Assimilation of the leaf area index and vegetation temperature condition index for winter wheat yield estimation using Landsat imagery and the CERES-wheat model. *Agric. For. Meteorol.* 246, 194–206. doi: 10.1016/j.agrformet.2017.06.015

Xie, L. H., Tang, S. Q., Chen, N., Luo, J., Jiao, G. A., Shao, G. N., et al. (2014). Optimisation of near-infrared reflectance model in measuring protein and amylose content of rice flour. *Food Chem.* 142, 92–100. doi: 10.1016/j.foodchem.2013.07.030

Xue, L., Cao, W., Luo, W., Dai, T., and Zhu, Y. (2004). Monitoring leaf nitrogen status in Rice with canopy spectral reflectance. *Agron. J.* 96, 135–142. doi: 10.2134/agronj2004.1350

Xue, L., and Yang, L. (2008). Recommendations for nitrogen fertiliser topdressing rates in rice using canopy reflectance spectra. *Biosyst. Eng.* 100, 524–534. doi: 10.1016/j.biosystemseng.2008.05.005

Yang, H., and Du, J. (2021). Classification of desert steppe species based on unmanned aerial vehicle hyperspectral remote sensing and continuum removal vegetation indices. *Optik* 247:167877. doi: 10.1016/j.ijleo.2021.167877

Yang, F., Liu, T., Wang, Q., Du, M., Yang, T., Liu, D., et al. (2021a). Rapid determination of leaf water content for monitoring waterlogging in winter wheat based on hyperspectral parameters. *J. Integr. Agric.* 20, 2613–2626. doi: 10.1016/S2095-3119(20)63306-8

Yang, W., Nigon, T., Hao, Z., Dias Paiao, G., Fernández, F. G., Mulla, D., et al. (2021b). Estimation of corn yield based on hyperspectral imagery and convolutional neural network. *Comput. Electron. Agric.* 184:106092. doi: 10.1016/j.compag.2021.106092

Yang, Q., Shi, L., Han, J., Zha, Y., and Zhu, P. (2019). Deep convolutional neural networks for rice grain yield estimation at the ripening stage using UAV-based remotely sensed images. *Field Crop Res* 235, 142–153. doi: 10.1016/j.fcr.2019.02.022

Yu, F., Feng, S., Du, W., Wang, D., Guo, Z., Xing, S., et al. (2020a). A study of nitrogen deficiency inversion in rice leaves based on the Hyperspectral reflectance differential. *Front. Plant Sci.* 11:573272. doi: 10.3389/fpls.2020.573272

Yu, F., Feng, S., Yao, W., Wang, D., Xing, S., and Xu, T. (2020b). BAS-ELM based UAV hyperspectral remote sensing inversion modeling of rice canopy nitrogen content. *Int. J. Presic. Agr. Aviat.* 1, 59–64. doi: 10.33440/j.ijpaa.20200303.105

Yuan, J. Q., Li, L., and Yan, W. (2021). Early identification of Rice leaf blast based on Hyperspectral imaging. *J. Phys. Conf. Ser.* 1944:012041. doi: 10.1088/1742-6596/1944/1/012041

Zheng, H., Cheng, T., Yao, X., Deng, X., Tian, Y., Cao, W., et al. (2016). Detection of rice phenology through time series analysis of ground-based spectral index data. *Field Crop Res* 198, 131–139. doi: 10.1016/j.fcr.2016.08.027

Zheng, H., Ma, J., Zhou, M., Li, D., Yao, X., Cao, W., et al. (2020). Enhancing the nitrogen signals of Rice canopies across critical growth stages through the integration of textural and spectral information from unmanned aerial vehicle (UAV) multispectral imagery. *Remote Sens.* 12:957. doi: 10.3390/rs12060957

Zhou, X., Sun, J., Zhang, Y., Tian, Y., Yao, K., and Xu, M. (2021). Visualization of heavy metal cadmium in lettuce leaves based on wavelet support vector machine regression model and visible-near infrared hyperspectral imaging. *J. Food Process Eng.* 44, 1378–1389. doi: 10.1111/jfpe.13897

Zhu, Y., Zhou, D., Yao, X., Tian, Y., and Cao, W. (2007). Quantitative relationships of leaf nitrogen status to canopy spectral reflectance in rice. *Aust. J. Agr. Res.* 58, 1077–1085. doi: 10.1071/AR06413

Conflict of Interest: The authors declare that the research was conducted in the absence of any commercial or financial relationships that could be construed as a potential conflict of interest.

Publisher's Note: All claims expressed in this article are solely those of the authors and do not necessarily represent those of their affiliated organizations, or those of the publisher, the editors and the reviewers. Any product that may be evaluated in this article, or claim that may be made by its manufacturer, is not guaranteed or endorsed by the publisher.

Copyright © 2022 Gu, Ji, Xi, Zhang, Hong, Huo, Li, Mao, Zhao, Zhang, Li and Tan. This is an open-access article distributed under the terms of the Creative Commons Attribution License (CC BY). The use, distribution or reproduction in other forums is permitted, provided the original author(s) and the copyright owner(s) are credited and that the original publication in this journal is cited, in accordance with accepted academic practice. No use, distribution or reproduction is permitted which does not comply with these terms.

frontiers | Frontiers in Plant Science

ORIGINAL RESEARCH
published: 13 July 2022
doi: 10.3389/fpls.2022.920532

Estimation Model of Potassium Content in Cotton Leaves Based on Wavelet Decomposition Spectra and Image Combination Features

Qiushuang Yao, Ze Zhang, Xin Lv*, Xiangyu Chen, Lulu Ma and Cong Sun*

The Key Laboratory of Oasis Eco-Agriculture, College of Agriculture, Shihezi University, Shihezi, China

Potassium (K) is one of the most important elements influencing cotton metabolism, quality, and yield. Due to the characteristics of strong fluidity and fast redistribution of the K in plants, it leads to rapid transformation of the K lack or abundance in plant leaves; therefore, rapid and accurate estimation of potassium content in leaves (LKC, %) is a necessary prerequisite to solve the regulation of plant potassium. In this study, we concentrated on the LKC of cotton in different growth stages, an estimation model based on the combined characteristics of wavelet decomposition spectra and image was proposed, and discussed the potential of different combined features in accurate estimation of the LKC. We collected hyperspectral imaging data of 60 main-stem leaves at the budding, flowering, and boll setting stages of cotton, respectively. The original spectrum (R) is decomposed by continuous wavelet transform (CWT). The competitive adaptive reweighted sampling (CARS) and random frog (RF) algorithms combined with partial least squares regression (PLSR) model were used to determine the optimal decomposition scale and characteristic wavelengths at three growth stages. Based on the best "CWT spectra" model, the grayscale image databases were constructed, and the image features were extracted by using color moment and gray level co-occurrence matrix (GLCM). The results showed that the best decomposition scales of the three growth stages were CWT-1, 3, and 9. The best growth stage for estimating LKC in cotton was the boll setting stage, with the feature combination of "CWT-9 spectra + texture," and its determination coefficients (R^2val) and root mean squared error (RMSEval) values were 0.90 and 0.20. Compared with the single R model (R^2val = 0.66, RMSEval = 0.34), the R^2val increased by 0.24. Different from our hypothesis, the combined feature based on "CWT spectra + color + texture" cannot significantly improve the estimation accuracy of the model, it means that the performance of the estimation model established with more feature information is not correspondingly better. Moreover, the texture features contributed more to the improvement of model performance than color features did. These results provide a reference for rapid and non-destructive monitoring of the LKC in cotton.

Keywords: hyperspectral imaging, potassium content in leaves, continuous wavelet transform, gray level co-occurrence matrix, cotton, growth stage

OPEN ACCESS

Edited by:
Zhenhai Li,
Shandong University of Science and Technology, China

Reviewed by:
Saeed Saadat,
Soil & Water Research Institute, Iran
Abbas Atefi,
California Polytechnic State University, United States

****Correspondence:***
Ze Zhang
zhangze1227@shzu.edu.cn
Xin Lv
luxin@shzu.edu.cn

Specialty section:
This article was submitted to Sustainable and Intelligent Phytoprotection, a section of the journal Frontiers in Plant Science

Received: *14 April 2022*
Accepted: *07 June 2022*
Published: *13 July 2022*

Citation:
Yao Q, Zhang Z, Lv X, Chen X, Ma L and Sun C (2022) Estimation Model of Potassium Content in Cotton Leaves Based on Wavelet Decomposition Spectra and Image Combination Features. Front. Plant Sci. 13:920532. doi: 10.3389/fpls.2022.920532

INTRODUCTION

Potassium (K) is an essential and favorite nutrient element in the growth of cotton. The level of K directly affects the growth and development of cotton and the quality of fiber (Pettigrew, 2008; Lewis et al., 2021). Affected by the parent material of soil formation, the soil in Xinjiang, China is rich in K. The content of available K in arable soil tends to be high in the north and low in the south, but in recent years, cotton fields in some areas have been deficient in K (Tian et al., 2020; Wang et al., 2021). Furthermore, Xinjiang has high-quality and high-yield cotton and a large demand for soil nutrients. Therefore, an excessive supply of potash fertilizer is usually used to avoid production reduction due to lack of the K, resulting in an increase in cotton production costs. However, the accurate method of element determination is time-consuming and laborious, so it is of great significance to monitor the potassium content in cotton leaves (LKC) quickly and without damage for the healthy growth of cotton, the recommendation of fertilizer application amounts and the reduction in resource waste.

Proximal hyperspectral remote sensing technology has become an effective means to evaluate precision agriculture (Pandey et al., 2017; Li et al., 2019), which can be divided into imaging spectra and non-imaging spectra. They can collect hyperspectral reflectance data from the visible, near-infrared (NIR) and short-wave infrared (SWIR) regions of the electromagnetic spectrum (Mertens et al., 2021), so that a wide variety of physiological traits of crops can be studied, such as crop nutrient deficiency (Furlanetto et al., 2021; Jiang et al., 2021; Mahajan et al., 2021, photosynthetic efficiency (El-Hendawy et al., 2017), water stress (Sun et al., 2021; Zhou et al., 2021), chlorophyll fluorescence (Zhao et al., 2021), heavy metal pollution (Lin et al., 2021) and early plant disease detection (El-Hendawy et al., 2017; Barros et al., 2020). On the other hand, hyperspectral imaging can simultaneously obtain the target spectrum and image information, and is regarded as a technique with high-throughput plant phenotype potential (Pandey et al., 2017). Although there are many studies on nutrition monitoring using near-end hyperspectral imaging, most of them focus on quantitative monitoring and diagnosis of crop nitrogen (N), such as wheat (Mahajan et al., 2014; Jiang et al., 2021), rice (Men et al., 2021), maize (Furlanetto et al., 2021), cotton (Oliveira et al., 2020), rape (Liu et al., 2020a), soybean (Chen et al., 2019), orange (Osco et al., 2019, 2020a), tea (Wang et al., 2020) and mango (Mahajan et al., 2021). At present, the quantitative monitoring research on crop K is also gradually carried out, but more studies often analyze the K together with other elements (Liu et al., 2020b; Osco et al., 2020a,b; Mahajan et al., 2021), and there are few studies only on the characteristics of single the K nutrient element. Indeed, a large group of K^+ transporters and channels has been identified in plants (Gierth and Maser, 2007), and cytoplasmic concentration of K^+ is maintained around 80–150 MM (Ahmad and Maathuis, 2014). Preserving this concentration range is important for many physiological processes as the enzyme activations, and stabilization of protein synthesis (Villette et al., 2020). These processes are present in all tissues and subcellular compartments of cells, which enables the precise quantification of foliar K attributes of the foliage. It has been shown that the 550–700 and 1,390–1,880-nanometer (nm) wavelengths were the best wavelengths to explain the difference in nutrient levels of N, P, and K in cotton (Oliveira et al., 2020; Wang et al., 2020). Thus, the research utilizing sensitive characteristic wavelengths or vegetation indexes to identify and estimate the K deficiency are common method in rice (Das et al., 2020), wheat (Hussain et al., 2017), and maize (Furlanetto et al., 2021). However, to which extent the K can be estimated using hyperspectral requires further investigations.

Continuous wavelet transform (CWT) has attracted increasing attention in image and spectral signal decomposition due to its rich wavelet basis function, multi-resolution, and time-frequency locality (Chen et al., 2010; Yue et al., 2020). Because the CWT can perform multi-scale decomposition of spectrum and has good performance in characteristic wavelength selection and fine spectral signal extraction (Chen et al., 2019), it has been widely used in crop biochemical parameter inversion of hyperspectral data (Zhang et al., 2014), including estimating the above-ground biomass of wheat (Yao et al., 2018; Yue et al., 2020), analyzing the relationship between leaf copper content and spectrum (Lin et al., 2021) and rapidly detecting the chlorophyll fluorescence parameters of potato leaves (Zhao et al., 2021). Therefore, it is of great significance to improve the accuracy of spectral monitoring to construct a quantitative regression relationship between the wavelet coefficients and nutrient parameters (Mahajan et al., 2014).

As an imaging spectrometer can provide very high spatial and spectral resolution data (Pandey et al., 2017), it is necessary to consider the spatial information (e.g., color and texture) in hyperspectral images in addition to the spectral information to estimate crop nutrients. Image color can express the color distribution and range of image, while image texture reflects the information of uniformity, sharpness and spatial arrangement of image gray distribution. Although there are few studies on the role of image features in hyperspectral nutrient monitoring, it has important application potential in the field of hyperspectral imaging (Jiang et al., 2021). Zheng et al. (2017) extracted 14 vegetation indices related to color features to segment corn, and the accuracy rate over 90.19%. Zou et al. (2019) segmented broccoli seedlings from weeds and soil by extracting GLCM features and color features, and achieved higher accuracy. In the existing studies have demonstrated that the K deficiency causes discoloration of crop leaf tips and edges [such as wheat (Mahajan et al., 2014), rice (Sun et al., 2018), soybean (Ghosal et al., 2018), and cotton (Oliveira et al., 2020)], then gradually spread to the center of the leaf, develop into brown spots, and finally wither and necrosis, resulting in changes in leaf color and texture (Laddi et al., 2013). Also, vegetation coverage and NDVI value are significantly reduced (Severtson et al., 2016). Besides, through the calculation of crop RGB image, it was found that the extension rate of the K deficient leaves slowed down and the wilting rate accelerated (Sun et al., 2018). However, the potential for the image features of leaf hyperspectral imaging data for estimating crop nutrients stress (e.g., K) is not well documented.

Hence, using the high-resolution proximal hyperspectral imaging data of cotton leaves in different growth stages, this study

proposed an estimation model of the LKC in cotton based on the combined characteristics of "CWT spectra + image." The main objectives of this study were to (1) clarify the characteristics of hyperspectral response of cotton LKC at different growth stages, and the effective characteristic wavelengths of the best decomposition scale was determined combined with CWT and PLSR, (2) construct a gray image database of characteristic wavelengths in different growth periods to extract and screen sensitive image features, and (3) evaluate the potential of different "CWT spectra + image" combination features to estimate the LKC of cotton at different growth stages.

MATERIALS AND METHODS

Experimental Design

The research area was located in Erlian (85°59′41″E, 44°19′54″N), the teaching experiment field of Shihezi University. Sunshine duration is 2,721–2,818 h, ≥ 0°C active accumulated temperature is 4,023–4,118°C, ≥10°C active accumulated temperature is 3,570–3,729°C and frost-free period is 168–171 days. The soil texture was loam, and the 0–20 cm soil layer contained 19.06 g·kg^{-1} organic matter, 12.8 mg·kg^{-1} total nitrogen, 20.8 mg·kg^{-1} available phosphorus, and 165.1 mg·kg^{-1} available potassium. The soil pH is 8.17 and electrical conductivity (EC) is 0.42 ms·cm^{-1}. During the whole growth period of cotton, nitrogen, phosphorus, and potassium fertilizer were applied with water drops. The urea (N, 46%) of 276 kg·hm$^{-2,}$ monoammonium phosphate (P_2O_5, 61%) of 174 kg·hm^{-2} and potassium sulfate (K_2O, 50%) was used as a potassium fertilizer. A total of 9-times drips were given during the whole growth period, and the fertilization ratios of the three fertilizers (N, P, and K) were 2.5, 7.7, and 0% (June 7), 7.5, 11.7, and 6.7% (June 15), 7.5, 11.7, and 6.7% (June 24), 12.5, 19.2, and 20% (July 2), 20, 19.2, and 20% (July 18), 25, 15.4, and 13.3% (July 26), 15, 15.4, and 13.3% (Aug 5), 10, 0, and 13.3% (Aug 15), 0, 0, and 6.7% (Aug 25). At each fertilization, the three fertilizers weighed in proportion are poured into the corresponding differential pressure fertilization tank to dissolve, and then drip irrigation was applied to the plot.

The experiment was carried out in the study area from April to September 2020. The variety Xinluzao 53 was selected for the experiment. The planting pattern was "one film, three tubes, and six rows" and the plant spacing was 10 + 66 + 10 cm. Four K application levels were set, namely, blank (0 kg·hm^{-2}), low K (75 kg·hm^{-2}), conventional K (225 kg·hm^{-2}), and high K (375 kg·hm^{-2}). We used a random block design with 3 replicates on a total of 12 plots with a single plot area of 25 m^2 (**Figure 1**). The sowing date was 18 April 18 2020, the topping date was 9 July 202 and the sampling periods were the budding stage (30 June 2020), flowering stage (12 July 2020) and boll setting stage (30 July 2020). Five pieces of cotton main-stem leaves with similar growth in the middle and upper parts were randomly collected from each plot, a total of 60 main-stem leaves were collected in one growth period, and a total of 180 main-stem leaves were collected in three growth periods.

Hyperspectral Image Data Acquisition

The SOC710-VP portable visible-near-infrared hyperspectral imaging spectrometer (Surface Optics Corporation, USA) was used for data acquisition. The spectral resolution is 5 nm, the image resolution is 692 × 520 and the spectral range is 376–1,044 nm, with a total of 128 bands. After removing the front and rear spectral noises, each hyperspectral image cube selected a wavelength in the range of 400–950 nm, with a total of 106 image bands. To reduce the influence of natural light, all images were captured in a dark box (**Figure 2**).

Cotton main-stem leaves are the main source organs providing assimilates to cotton bolls (Pace et al., 1999). Fresh main-stem leaves at the three key growth stages were selected to be tiled in a dark box with a low-reflectivity black background plate according to the order of leaf position. At the same time, a standard gray plate was placed 5 cm away from the leaf edge to assist black-and-white correction. To reduce the influence of light source intensity, exposure time, and dark current in the sensor during spectral scanning, the instrument should be preheated for 30 min. The scanning parameters of the hyperspectral imager were as follows: object distance, 88 cm, scanning rate, 150–200 frames·s^{-1}, aperture, 5.6. The collected spectral data were digital (DN) and were converted into spectral reflectance through spectral calibration and radiometric calibration in SRAnal 710 software according to the grayscale reference panel in each original image. The average spectral reflectance of the whole leaf was extracted as the original spectral data of this sample (Lin et al., 2021).

Determination of Total Potassium Content in Plants

The total potassium content in leaves was determined using a H_2SO_4-H_2O_2 flame photometer (Bao, 2000). Fresh leaves were dried at 85°C for 30 min and then at 105°C until reaching a constant weight. The dried leaf samples were ground, weighed and then digested with H_2O_2-H_2SO_4, and the K was determined using a laboratory flame photometer (FP640, Yidian Co., Ltd, Shanghai, China). The total LKC was calculated according to the following formula:

$$K(\%) = \frac{\rho \times V \times ts \times 10^{-4}}{m} \quad (1)$$

where ρ is the mass concentration of K obtained from the standard curve (ug·mL^{-1}), V is the measuring liquid volume (ml), t_s is the separation multiple, and m is the dry sample mass (g).

Data Processing

Continuous Wavelet Transform

Continuous wavelet transform (CWT) is an effective signal processing tool to decompose an original signal into multidimensional signals, mainly including discrete wavelet transform and continuous wavelet transform (Liu et al., 2020b). In the CWT, the algorithm uses the selected mother wavelet to decompose the hyperspectral data into a series of wavelet

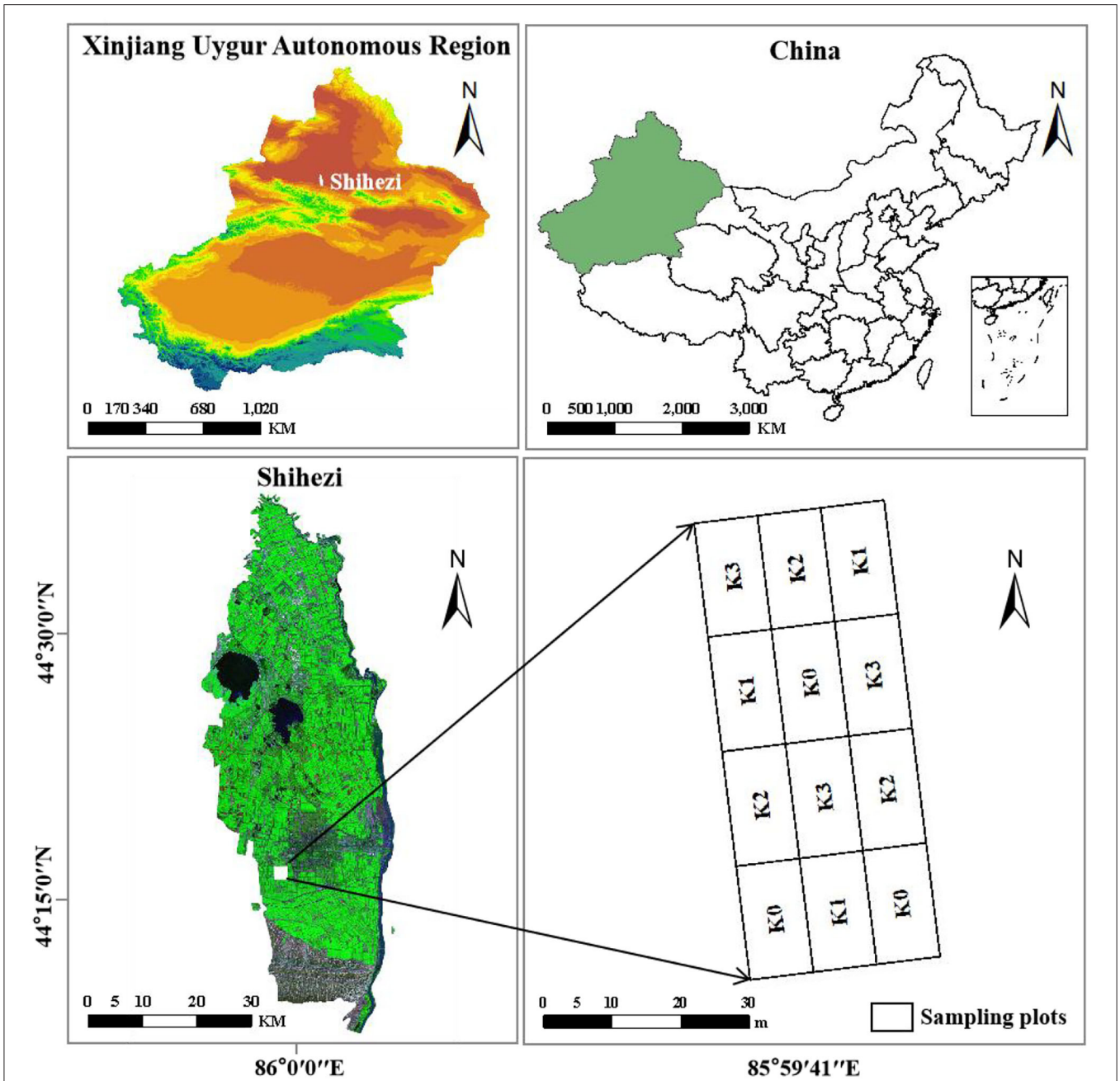

FIGURE 1 | The study site and the location of the experiments.

coefficients of different scales, which is a linear transformation. Its transformation formula is as follows:

$$W_f(a,b) = \int_{-\infty}^{\infty} f(\lambda)\psi_{a,b}d\lambda \quad (2)$$

$$\psi_{a,b}(\lambda) = \frac{1}{\sqrt{a}}\psi\left(\frac{\lambda - b}{a}\right) \quad (3)$$

where $f(\lambda)$ is the leaf hyperspectral reflectance, λ is the wavelength within 400–950 nm, $\psi_{a,b}$ is the wavelet basis function, a is the scale factor, b is the translocation factor, and $W_f(a, b)$ is a two-dimensional matrix, including i and j, where i represents the decomposition scale ($i = 1, 2, 3, \ldots, m$) and j represents the band range of the spectrum ($j = 1, 2, 3, \ldots, n$), forming an m by n matrix. In this study, the spectral data of cotton leaves at three growth stages were obtained, and each leaf sample included 106 bands. As the setting of the decomposition scale has a certain influence on spectral feature recognition (Liu et al., 2020; Lin et al., 2021), the decomposition scale in this study was set as 2^1, 2^2, 2^3, …, 2^{10}, scales 1–10. Among them, the decomposition

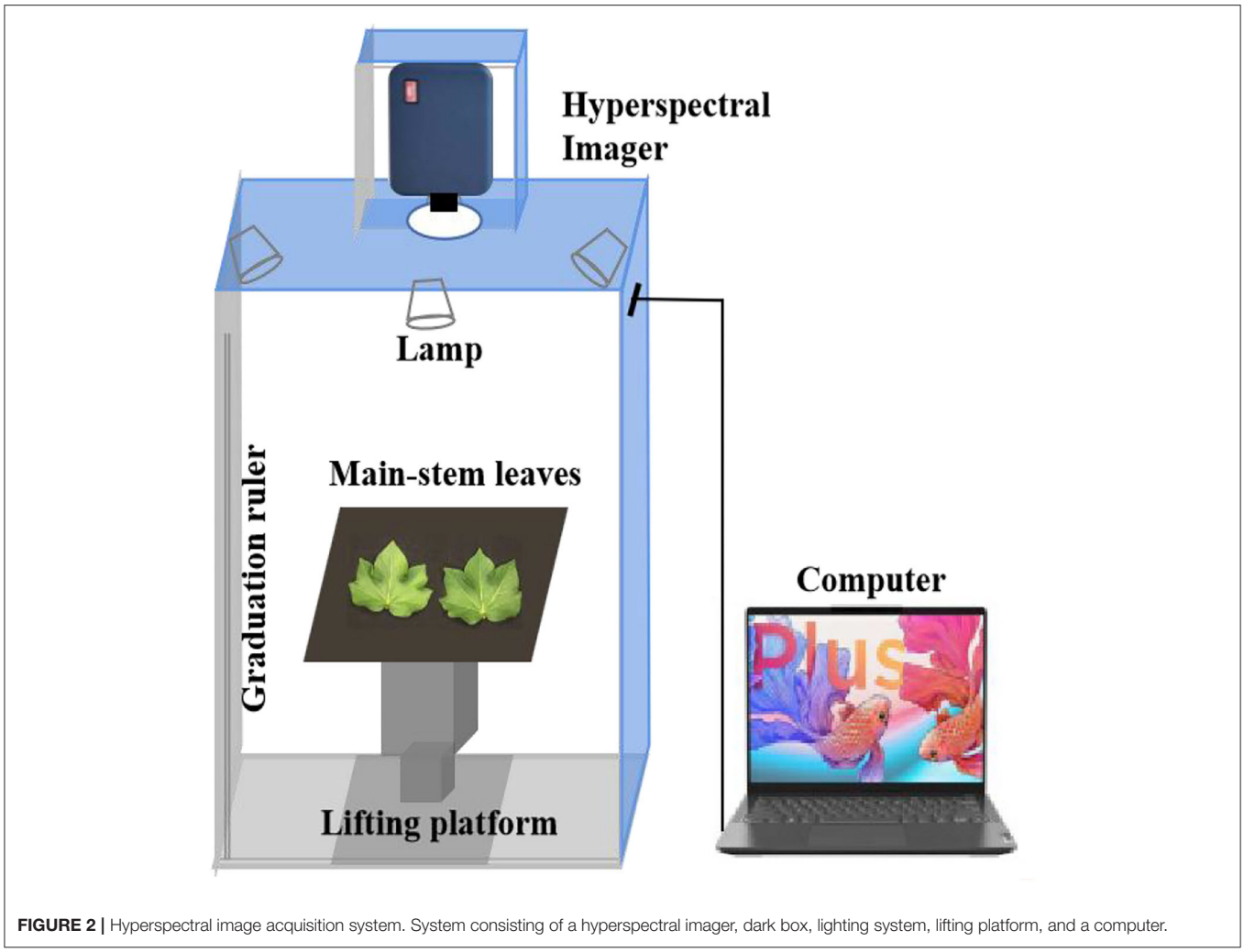

FIGURE 2 | Hyperspectral image acquisition system. System consisting of a hyperspectral imager, dark box, lighting system, lifting platform, and a computer.

scales 1–3 and 4–7 belong to low frequency and middle frequency, respectively, and the rest belong to high frequency. Sym2 was selected as the wavelet basis function, and then, a PLSR model was used to quantitatively analyze the relationship between the wavelet coefficients of each decomposition scale and the LKC so as to determine the optimal decomposition scale and effective wavelength.

Selection Method of Characteristic Variables

Different feature selection methods lead to different features being selected. To select spectral and image features sensitive and stable to the LKC in cotton, the competitive adaptive reweighted sampling (CARS), and random frog (RF) algorithms were used in this study to screen features.

Competitive adaptive reweighted sampling selects wavelength points with a large coefficient absolute value in the model through the Monte Carlo strategy and removes wavelength points with a low weight (Sun et al., 2021). The subset with the lowest root mean squared error of cross validation (RMSECV) value is retained as the feature selection result by cross-validation. In this study, the Monte Carlo strategy was set to run 50 times, using 5-fold cross-validation.

Random frog is an algorithm to measure the importance of variables (El-Hendawy et al., 2017). The main steps are as follows: (1) a subset of initial variables containing m variables is randomly initialized, (2) variables in the initial variable subset are continuously selected into the candidate subset, and the number of variables in the candidate subset increases and decreases with the number of iterations, (3) the selection probability of each variable is calculated as a measure of the importance of the variable, and (4) the characteristic wavelength is selected according to the probability of the occurrence of recorded variables in each iteration. In this study, the selection probability of each wavelength was used to screen the feature information, and the running results are presented in descending order. The number of iterations was set as 10,000, and the selection probability thresholds of the three growth periods were 0.40, 0.21, and 0.23, respectively.

TABLE 1 | The calculation equations for the characteristics of the GLCM.

Feature	Equation
ENE	$ENE = \sum_{i=0}^{k}\sum_{j=0}^{k} P(i,j)^2$
ENT	$ENT = -\sum_{i=0}^{k}\sum_{j=0}^{k} P(i,j)\cdot \ln P(i,j)$
CON	$CON = \sum_{i=0}^{k}\sum_{j=0}^{k} P(i,j)\cdot (i,j)^2$
COR	$COR = \sum_{i=0}^{k}\sum_{j=0}^{k} P(i,j)\frac{(i-MEA)\cdot(j-MEA)}{\sqrt{VARi\cdot VARj}}$
MEA	$MEA = \sum_{i=0}^{k}\sum_{j=0}^{k} P(i,j)\cdot i$
VAR	$VAR = \sum_{i=0}^{k}\sum_{j=0}^{k} P(i,j)\cdot (i-MEA)^2$

Image Feature Extraction

The most common gray level co-occurrence matrix (GLCM) algorithm was adopted to extract texture features (Yang et al., 2021). In this study, the energy (ENE), entropy (ENT), contrast (CON), correlation (COR), and their mean (MEA) and variance (VAR) in four directions were calculated by using the gray comatrix function. The calculation equation is shown in **Table 1**, where the $P(i, j)$ is the value of the GLCM in the ith row and jth column, k is the number of gray levels in the GLCM. The gray level is 256, the step size is 1, the angle is 0°, 45°, 90°, and 135°. Finally, each characteristic wavelength grayscale image will eventually produce 24 ($4 \times 4 + 8$) texture features.

Color moments are used to represent the color distribution in the image (Ge et al., 2021). Since the color information is mainly distributed in low-order moments, first-order moments (mean, MEA), second-order moments (variance, VAR), and third-order moments (skewness, SKE) are sufficient to express the color distribution of the image. Its formula is as follows:

$$MEA = \sum_{j=1}^{n} \frac{1}{n} Pij \tag{4}$$

$$VAR = \sqrt{\frac{1}{n}\sum_{j=1}^{n} (Pij - MEAi)^2} \tag{5}$$

$$SKE = \sqrt[3]{(\frac{1}{n}\sum_{j=1}^{n} P(Pij - MEAi)^3} \tag{6}$$

where Pij is the color value of the jth pixel on the ith color channel, i is the number of color channels of the image. The image in this study is grayscale image, so $i = 1$; MEAi is the color mean of the ith color channel of all pixels. Finally, each characteristic wavelength grayscale image will eventually produce three color features.

Notably, the named representation of combined features is as follows: (1) The characteristic wavelength-texture feature-direction, such as 400 nm-ENE-0°, which means the texture feature is ENE in the 0° direction of the 400-nm grayscale image and (2) characteristic wavelength-color feature, such as 400-nm MEA, which means the color feature is MEA of the 400-nm grayscale image.

Modeling and Analysis Methods

Partial least squares regression (PLSR) is one of the most widely used modeling methods in spectral analysis, which can be used for dimensionality reduction and comprehensive screening of spectral data, with high modeling stability and reliability. The PLSR is widely favored in hyperspectral analysis (Lin et al., 2021; Zhao et al., 2021) because it can solve the collinearity and overfitting characteristics of hyperspectral data compared with other multivariate models.

The determination coefficients (R^2) and RMSE values were used to evaluate the performance of the model. In general, better performing models have higher R^2 and lower RMSE values. Original hyperspectral data were extracted by ENVI5 3. The CWT, PLSR, and GLCM analyses of leaf spectral data were carried out by Matlab R2018a (The MathWorks, Inc., Natick MA, USA). Origin 2020 was used for creating graphs (OriginLab Corporation, Northampton, MA, USA).

$$\mathrm{R}^2 = 1 - \frac{\sum_{i=1}^{n} \left(y_i - \hat{y}_i\right)^2}{\sum_{i=1}^{n} \left(y_i - \bar{y}\right)^2} \tag{7}$$

$$\mathrm{RMSE} = \sqrt{\frac{1}{n}\sum_{i=1}^{n} \left(y_i - \hat{y}_i\right)^2} \tag{8}$$

where R^2cal is expressed as the determination coefficient of calibration sets, R^2val is expressed as the determination coefficient of validation sets, n is the number of samples, y_i and $\hat{y}_i$, are, respectively, the measured and estimated values of sample i in the corresponding sample set, $\bar{y}$ is the average value of y_i.

RESULTS

Analysis of Spectral Characteristics

Statistical Data of Cotton Leaf Sample Set

The total LKC in three key growth stages of cotton was measured (**Table 2**). The concentration gradient method (Liu et al., 2015) was used to divide the total samples into 40 calibration sets and 20 validation sets in a ratio of 2:1. The range of the K content in the calibration set including the validation set was 3.56–0.51, 2.80–0.57, and 2.30–0.40% in the three growth stages, respectively, indicating that the calibration set could well represent the entire datasets. The coefficients of variation in the calibration sets and validation sets were both between 37 and 50%, show that the LKC in cotton studied had a wide range and had good representativeness and coverage.

Spectral Reflectance Analysis

The single-band threshold segmentation method (**Figure 3**) was used to extract the average spectrum of the whole cotton leaves from hyperspectral images as the original spectrum (R) and a

TABLE 2 | Statistical results of calibration and validation sets.

Growth Stage	Sets	Size	Max. (%)	Min. (%)	Mean (%)	SD[a] (%)	CV[b] (%)
Budding stage	All sets	60	3.56	0.51	1.63	0.81	49.47
	Calibration sets	40	3.56	0.51	1.63	0.81	49.78
	Validation sets	20	3.51	0.51	1.64	0.82	50.12
Flowering stage	All sets	60	2.80	0.57	1.18	0.44	37.47
	Calibration sets	40	2.80	0.57	1.18	0.45	38.20
	Validation sets	20	2.43	0.57	1.18	0.43	36.93
Boll setting stage	All sets	60	2.30	0.40	1.25	0.56	44.67
	Calibration sets	40	2.30	0.40	1.25	0.56	44.88
	Validation sets	20	2.30	0.46	1.25	0.57	45.42

[a]*SD, standard deviation.*
[b]*CV (%), coefficient of variation.*

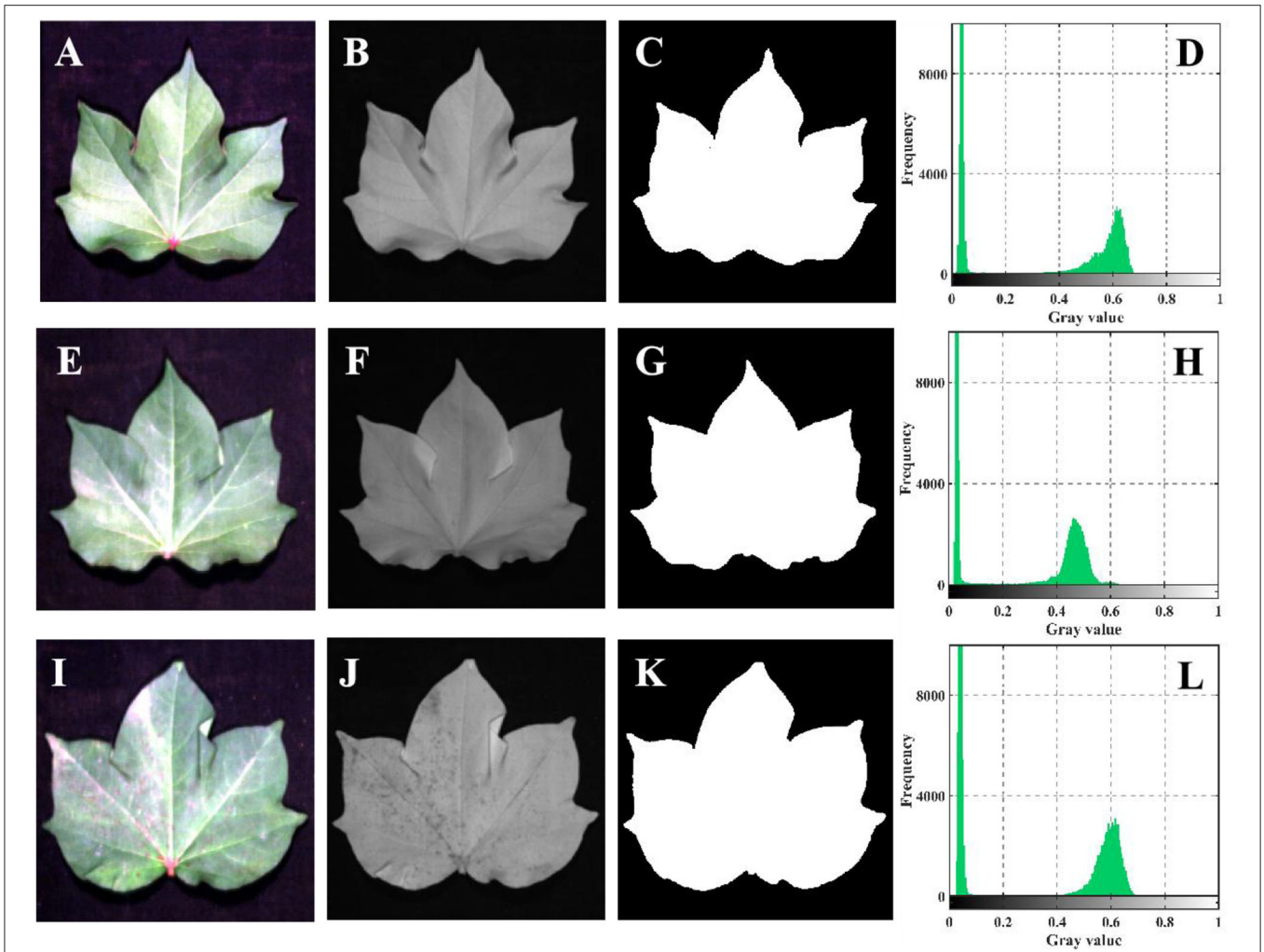

FIGURE 3 | ROI extraction process by single band threshold segmentation. **(A–D)** Budding stage. **(E–H)** Flowering stage. **(I–L)** Boll setting stage. **(A,E,I)** The true color picture synthesized by ENVI cannot completely represent the true color of leaf. **(B,F,J)** The grayscale image of 800 nm. This grayscale image can display the outline of cotton leaves more completely in terms of brightness and clarity, so 800 nm is selected as the segmentation band. **(C,G,K)** Mask image. **(D,H,L)** Gray histogram.

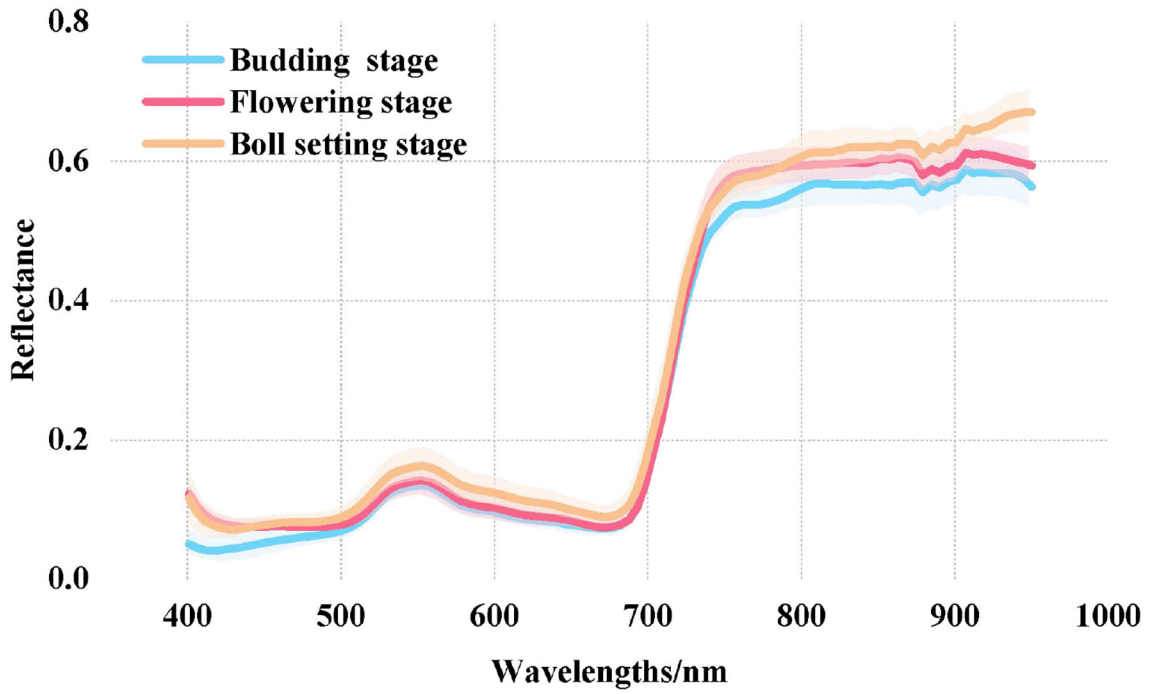

FIGURE 4 | R spectral curves of the LKC in cotton at different growth stages.

region of interest (ROI). The threshold was set to 0.25–0.3098, and the sample area lower than 0.25 was the background plate.

The spectral curves of cotton leaves at the three growth stages were consistent with the spectral characteristics of green plants (**Figure 4**). There were strong absorption peaks at 450 and 680 nm and a strong reflection peak at 550 nm. Due to the many cavities in the mesophyll sponge structure, the reflectance increases sharply near the red edge region (690–760 nm), and a highly reflective platform appears in the NIR region (760–950 nm). Among them, the spectral reflectance of cotton leaves at different growth stages differed significantly in the NIR region, which showed as boll setting stage > flowering stage > budding stage. This may be because after mid-July, the redistribution and utilization of the K nutrients during fruit development and the fluidity of potassium make the K in leaves gradually transfer to cotton bolls at the flowering and boll setting stages (Singh et al., 2019), leading to the decrease in LKC, while the lack of the K in leaves increases the thickness of leaves, and the palisade tissue and parenchymal cells shrink and partially break (Zhao et al., 2001; Ramírez-Soler et al., 2021). Finally, the spectral reflectance of the boll setting stage was higher than that of the budding stage in the NIR region.

Correlation Analysis Between CWT Spectra and the LKC

The R spectrum of cotton leaves was decomposed by the CWT at 10 scales. Correlation analysis was performed between the wavelet coefficients generated under each decomposition scale and the LKC, and the results were expressed as the absolute value of the correlation coefficient ($|R|$). The correlation between the wavelet coefficient and the LKC was relatively high, especially at the flowering stage of cotton growth (**Figure 5**). Under the calculation of different scales and movement factors, the regions with high correlation at the budding stage are mainly focused in the range of 500–550 and 640–660 nm on the mesoscales 3–5 and 7, with the highest correlation $|R| = 0.74$ (**Figure 5A**). The flowering stage showed obvious regional distribution, with a high correlation in the low dimension on scale 3, with the highest correlation $|R| = 0.86$ (**Figure 5B**). At the boll setting stage, the high-correlation area was mainly distributed in mesoscales 3–6, and the highest correlation $|R| = 0.70$ (**Figure 5C**). In addition, the wavelengths of 500–530, 640–660, and 740–760 nm showed higher correlation in the three growth stages.

Characteristic Wavelength Screening of R Spectrum and CWT Spectra

To further screen out characteristic wavelengths for the rapid estimation of the LKC in cotton, reduce the analytical dimension of spectral data and highlight the timeliness and convenience of spectral monitoring, the CARS and RF algorithms were selected to screen the R spectra and the CWT spectra (scales 1–10) of the three growth periods, and the selected characteristic wavelengths did not exceed 10. In the whole spectrum, the selected characteristic wavelengths of the three growth stages were similar, but there are significant differences in the screening methods of different characteristic wavelengths. The characteristic wavelengths selected based on the CARS algorithm were evenly distributed in the range of 400–950 nm, mainly

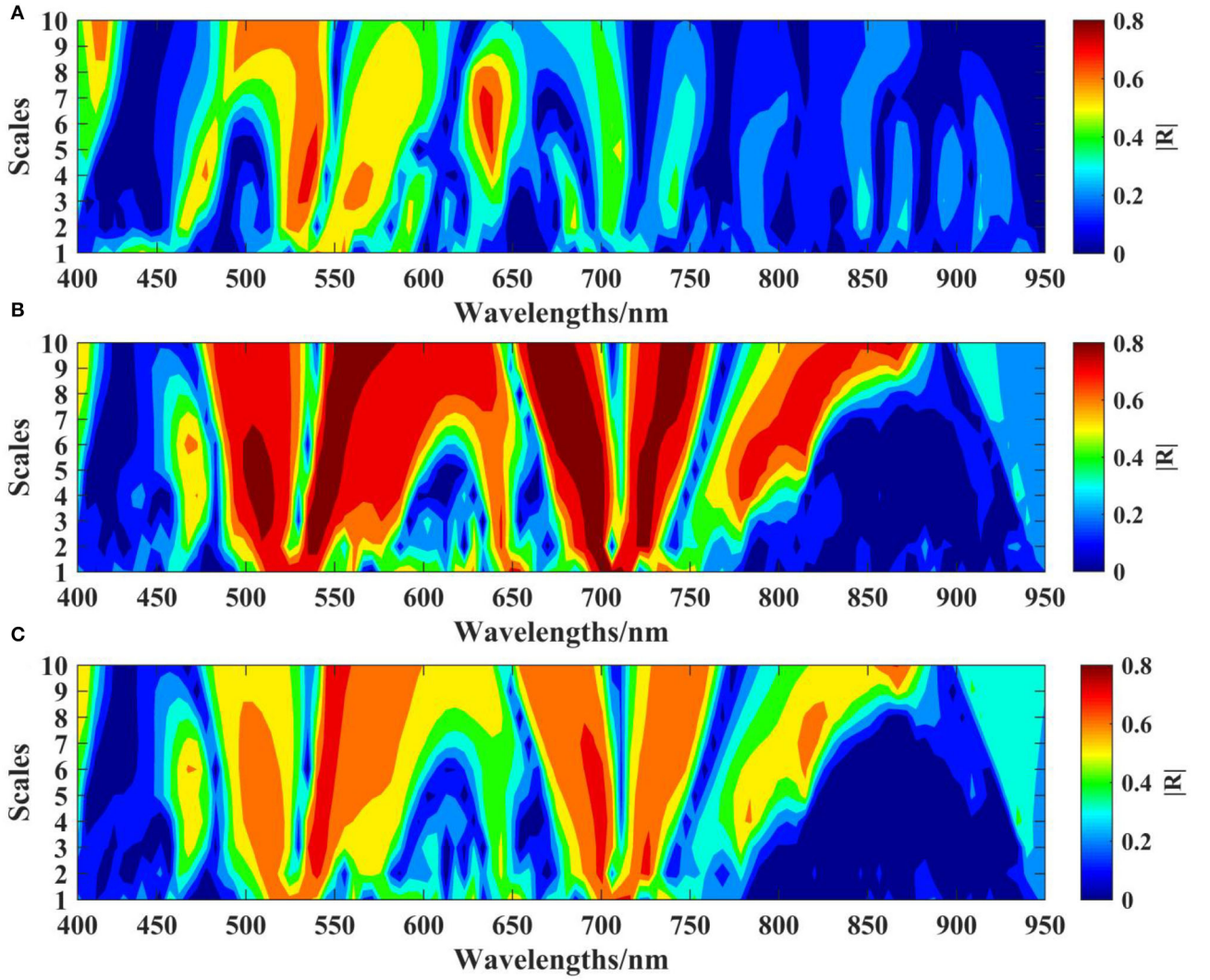

FIGURE 5 | Correlation analysis between the LKC and CWT coefficient. **(A)** Budding stage. **(B)** Flowering stage. **(C)** Boll setting stage.

located in the visible (500 nm), red edge (700 nm), and NIR regions (900 nm) (**Figures 6A–C**). The characteristic wavelengths screened by the RF algorithm were mainly concentrated in the visible and NIR regions in the whole spectrum, but more characteristic wavelengths appear in the visible region (**Figures 6D–F**). The characteristic wavelengths located in the visible region reflect the information of leaf pigment, especially the characteristic bands distributed near the strong absorption and reflection of chlorophyll. Red edge is closely related to the physical and chemical parameters of plants, is generally used to describe the health status of plants and is affected by leaf pigment and leaf area index. The characteristic wavelengths were in the range of 800–950 nm, reflecting the structure of cotton leaves and some water absorption.

The PLSR Model Based on R Spectrum and CWT Spectra

To explore the quantitative regression relationship between cotton leaf spectral data and the LKC, a quantitative estimation model was established to realize the quantification of spectral monitoring. Using the R spectrum and CWT spectra composed of characteristic wavelengths screened by CARS and RF as independent variables and the LKC as a dependent variable, PLSR estimation models of the LKC at different growth stages were established (**Table 3**). The calibration and validation sets perform differently in estimating the effect of the LKC model at different growth stages and decomposition scales. At the budding stage, the model R^2cal and R^2val both were >0.6136 (RF-CWT-7) and 0.2675 (CARS-CWT-4). At the flowering stage,

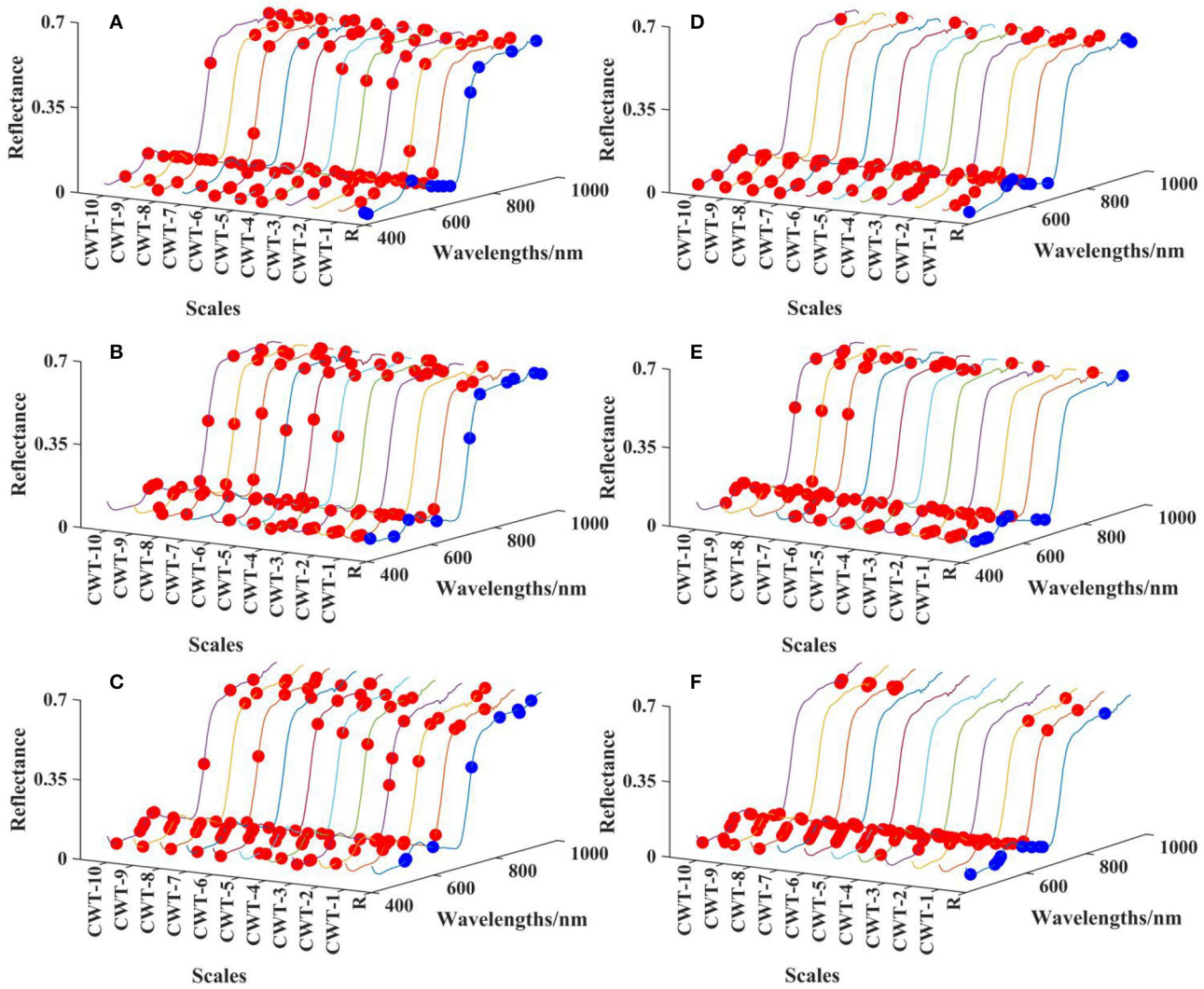

FIGURE 6 | Characteristic wavelengths of the R spectrum and CWT spectra screened by CARS and RF algorithms. The red and blue dots represent the characteristic wavelengths of CWT spectra and R spectrum, respectively. **(A)** Budding stage, CARS. **(B)** Flowering stage, CARS. **(C)** Boll setting stage, CARS. **(D)** Budding stage, RF. **(E)** Flowering stage, RF. **(F)** Boll setting stage, RF.

the model R^2cal and R^2val were >0.7311 (RF-CWT-10) and 0.6158 (CARS-CWT-2). In the boll setting period, the model R^2cal and R^2val were both >0.5717 (RF-CWT-3) and 0.5430 (RF-CWT-6).

The all model R^2val and RMSEval results are shown in **Figure 7**. The results showed that compared with the R spectrum, the CWT spectra could significantly improve the prediction performance of the LKC (**Figures 7D–F**). The optimal estimation model of the R spectrum at the budding, flowering and boll growth stages was constructed using the characteristic wavelengths selected by the CARS algorithm, indicating that CARS had a better estimation performance than the RF algorithm, this is similar to previous studies (Sun et al., 2021). The R^2val values were 0.6613, 0.753, and 0.6643 and the RMSEval values were 0.5292, 0.2202, and 0.3405, respectively. Using the multi-decomposition scale CWT method, the best decomposition scales of the three growth stages were found to be CWT-1, CWT-3 and CWT-9 spectrum (**Table 3**). The best estimation models for the LKC were CARS-CWT-1 at the budding stage, RF-CWT-3 at the flowering stage and CARS-CWT-9 at the boll setting stage. The R^2val values were 0.7918, 0.79, and 0.808 and the RMSEval values were 0.368, 0.1987 and 0.2508, respectively (**Figures 7A–C**). Compared with the single R spectrum model, the improved R^2 values at the three growth stages were 0.13, 0.04, and 0.15, respectively. Higher R^2val values and lower RMSEval values indicate that these models have a good fitting degree and accuracy, and the decomposed CWT spectra can effectively extract weak information, but there are significant differences in the prediction accuracy of the CWT spectra at different decomposition scales, and the screening

TABLE 3 | CARS and RF algorithms are used to screen the characteristic wavelengths of the wavelet coefficient spectra, the PLSR estimation model of cotton LKC in different growth stages is established, and emphasize the relatively better performances of these the wavelet coefficient spectra in LKC estimation.

Growth Stage	Scales	CARS				RF			
		R^2 cal	RMSE cal	R^2 val	RMSE val	R^2 cal	RMSE cal	R^2 val	RMSE val
Budding stage	R	0.8003	0.3578	0.6613	0.5292	0.7225	0.4217	0.4978	0.6141
	CWT-1	0.8104	0.3485	0.7918	0.3680	0.7537	0.3973	0.7306	0.4421
	CWT-2	0.7568	0.3947	0.5333	0.5737	0.8168	0.3426	0.7157	0.4298
	CWT-3	0.8325	0.3277	0.5471	0.5514	0.7269	0.4183	0.6853	0.4816
	CWT-4	0.6616	0.4657	0.2675	0.7251	0.6257	0.4898	0.3837	0.6761
	CWT-5	0.7274	0.4180	0.5457	0.5823	0.6871	0.4478	0.6176	0.5225
	CWT-6	0.7507	0.3997	0.5647	0.5565	0.6415	0.4793	0.4836	0.6198
	CWT-7	0.7503	0.4000	0.5755	0.5539	0.6136	0.4976	0.5314	0.5943
	CWT-8	0.7545	0.3966	0.5205	0.5722	0.7395	0.4086	0.5549	0.5479
	CWT-9	0.7648	0.3882	0.5200	0.5779	0.6585	0.4678	0.6487	0.4892
	CWT-10	0.7289	0.4168	0.5888	0.5232	0.7333	0.4134	0.5557	0.5549
Flowering stage	R	0.8397	0.1789	0.7530	0.2202	0.8183	0.1905	0.7377	0.2227
	CWT-1	0.8688	0.1619	0.6942	0.2388	0.8017	0.1990	0.7395	0.2190
	CWT-2	0.8585	0.1681	0.6158	0.2627	0.8673	0.1628	0.6757	0.2413
	CWT-3	0.8141	0.1927	0.6598	0.2480	0.8405	0.1785	0.7900	0.1987
	CWT-4	0.8429	0.1771	0.7566	0.2094	0.7571	0.2202	0.6882	0.2444
	CWT-5	0.8007	0.1995	0.7473	0.2187	0.7679	0.2153	0.6279	0.2629
	CWT-6	0.8064	0.1966	0.6772	0.2432	0.7829	0.2082	0.6098	0.2674
	CWT-7	0.8155	0.1919	0.7500	0.2176	0.7453	0.2255	0.5956	0.2708
	CWT-8	0.8074	0.1961	0.7905	0.2070	0.7405	0.2276	0.6960	0.2381
	CWT-9	0.8104	0.1946	0.7710	0.2118	0.7952	0.2022	0.7121	0.2309
	CWT-10	0.8174	0.1910	0.7360	0.2227	0.7311	0.2317	0.6704	0.2477
Boll setting stage	R	0.6487	0.3274	0.6643	0.3405	0.6471	0.3281	0.5476	0.3993
	CWT-1	0.7217	0.2914	0.6441	0.3474	0.8070	0.2426	0.5499	0.4049
	CWT-2	0.7323	0.2858	0.6736	0.3564	0.7493	0.2766	0.6722	0.4169
	CWT-3	0.6212	0.3400	0.6598	0.3229	0.5717	0.3615	0.7481	0.2795
	CWT-4	0.6433	0.3299	0.6869	0.3173	0.6093	0.3453	0.6802	0.3146
	CWT-5	0.5966	0.3508	0.7610	0.2793	0.6182	0.3413	0.6635	0.3301
	CWT-6	0.6380	0.3323	0.7581	0.2820	0.4192	0.4210	0.5430	0.3771
	CWT-7	0.6200	0.3405	0.7254	0.3042	0.5955	0.3513	0.5573	0.3697
	CWT-8	0.6162	0.3422	0.7157	0.3047	0.5794	0.3582	0.7972	0.2734
	CWT-9	0.6310	0.3356	0.8080	0.2508	0.5983	0.3501	0.6917	0.3238
	CWT-10	0.7118	0.2965	0.6867	0.4988	0.6031	0.3480	0.6973	0.3076

results of the CARS and RF algorithms also show different model effects.

Image Feature Analysis

Leaf Grayscale Image Database

To find image features that could optimize the estimation model of the LKC in cotton, gray image databases of leaves at the budding, flowering, and boll setting stages were constructed according to the selected characteristic wavelengths (**Figure 8**). Among them, the number of effective characteristic wavelengths in the three growth stages are 10, 10, and 9, respectively. Therefore, the total number of grayscale images in budding, flowering, and boll setting stages are 60 × 10, 60 × 10 and 60 × 9, respectively.

Image Feature Extraction and Determination

After the mask processing for all images, three color features and 24 texture features of each characteristic wavelength grayscale image were successively calculated. Finally, the color and texture data extracted from the three growth periods were stored in 3 × 30 and 3 × 240 matrices, and a correlation analysis was performed with the LKC, respectively. The results are shown in **Figure 10**, where a square represents a feature.

For color features, the correlation between MEA and VAR was higher than that with SKE at the budding, flowering, and boll setting stages. The highest correlations of color features in the three growth stages were obtained for 532 nm-VAR ($R = 0.39$, $p < 0.01$), which reached extremely significant correlation,

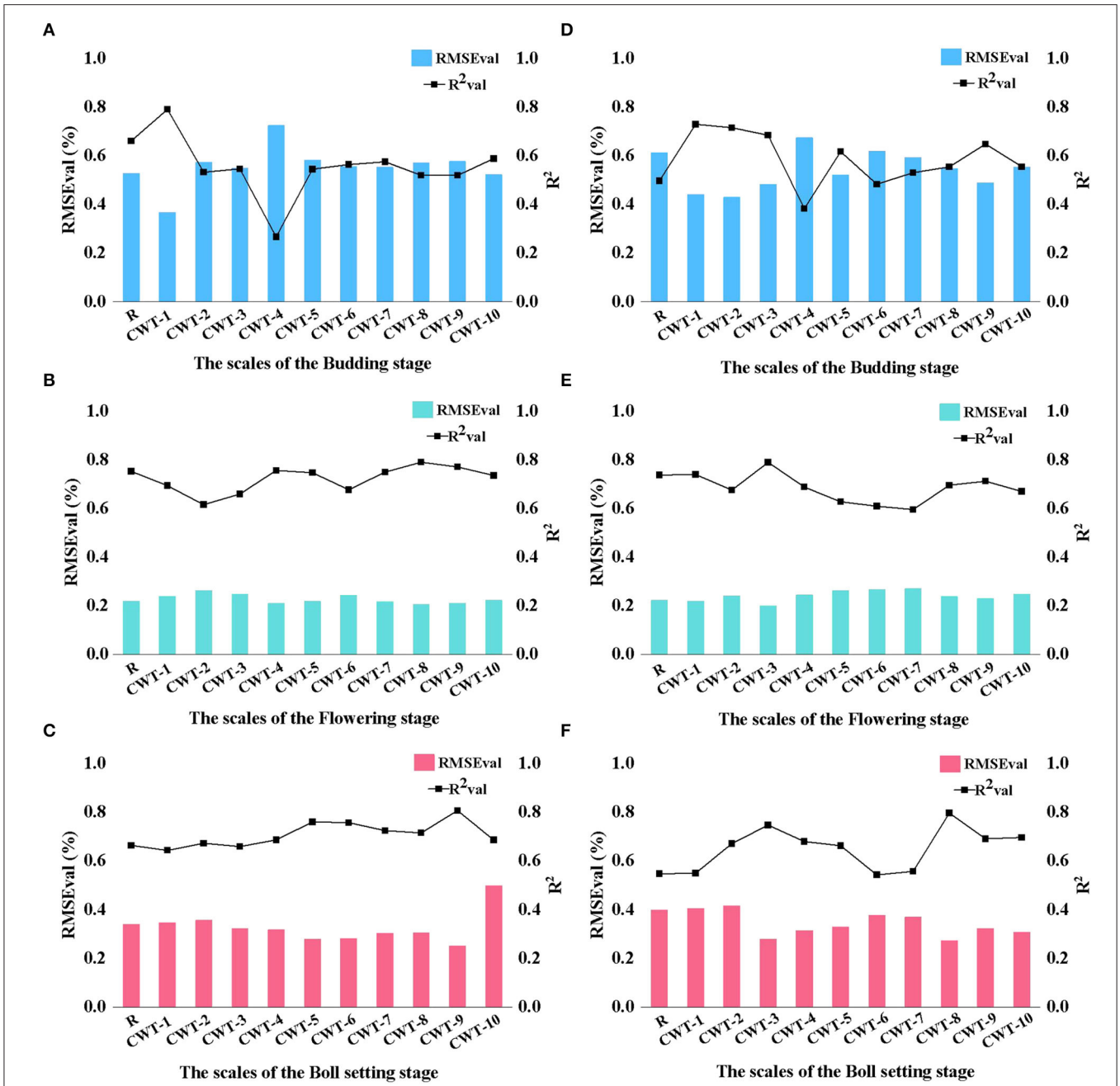

FIGURE 7 | PLSR estimation model of the LKC in cotton based on R and CWT spectra (validation sets). **(A)** CARS-Budding stage. **(B)** CARS-Flowering stage. **(C)** CARS-Boll setting stage. **(D)** RF-Budding stage. **(E)** RF-Flowering stage. **(F)** RF-Boll setting stage.

461 nm-MEA ($R = 0.18$, $p < 0.05$) and 522 nm-MEA ($R = -0.33$, $p < 0.05$). The results showed that the overall brightness and color distribution of images were closely related to the LKC. The texture features with a high correlation between the budding, flowering, and boll setting stage were different. The high correlation at the budding stage was mainly the CON of 471, 512, and 641 nm grayscale images in the 90° and 135° directions, and the highest correlation was 641 nm-CON-135° ($R = -0.48$). The results showed that the furrow depth of the cotton leaf surface at the budding stage was negatively correlated with K content. The texture features with high correlation at the flowering stage was mainly the COR of the characteristic wavelength of visible light (e.g., 476 nm) in the direction of 135°, especially 476 nm-COR-135° ($R = -0.38$). During the boll setting stage, highly correlated texture features were concentrated in the CON at the characteristic wavelength of NIR (e.g., 799 nm), and the highest correlation was obtained at 799 nm-VAR (CON) ($R = -0.44$), indicating that the uniformity of the leaf surface texture was

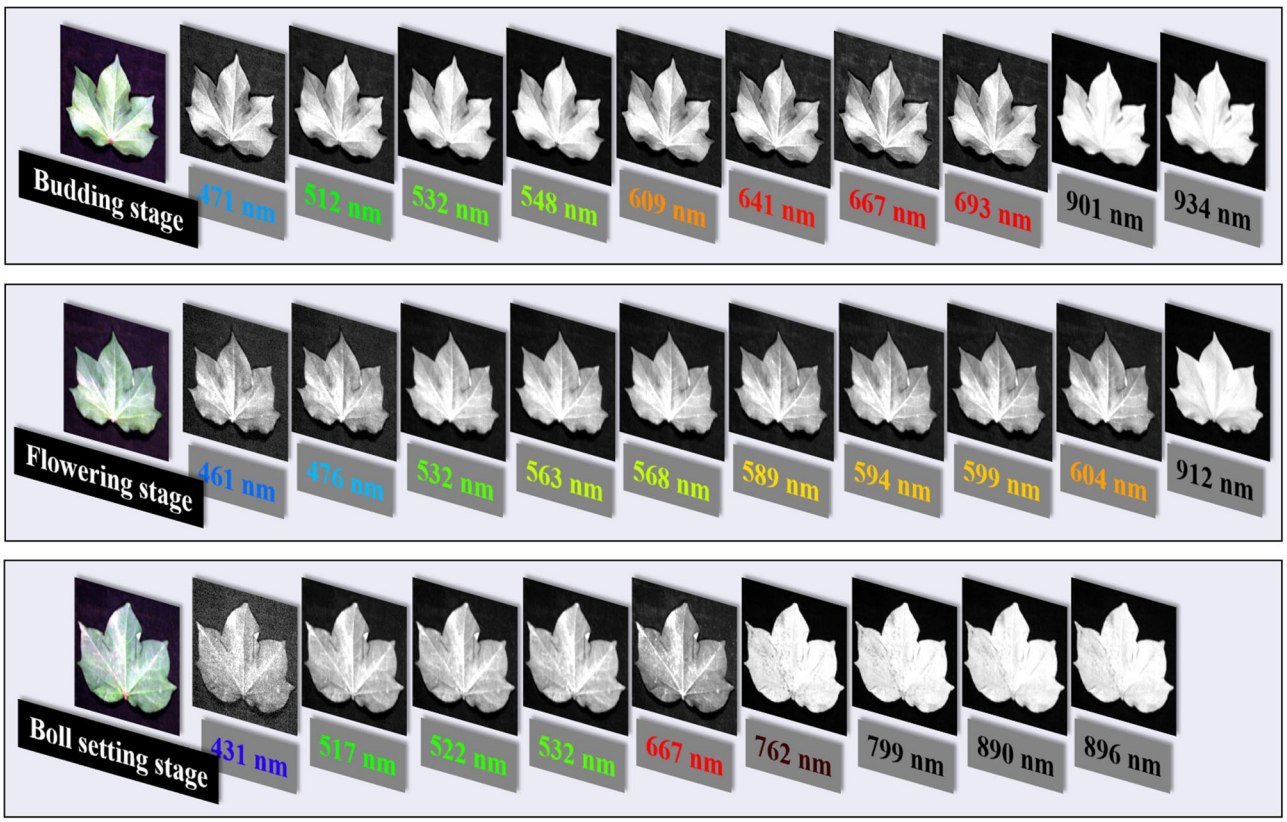

FIGURE 8 | Characteristic wavelength grayscale image databases based on CWT-1, CWT-3, and CWT-9 wavelet coefficients.

significantly negatively correlated with the K at the flowering and boll setting stages.

As can be seen from **Figure 9**, the color and texture feature dimensions of each growth period have higher dimensions and contain a large amount of invalid information. Therefore, we choose the CARS algorithm with better performance and combined correlation analysis to determine the effective image features. The screening results are shown in **Table 4**.

Model Establishment and Validation

Estimation Model of the LKC Based on Combination Feature

Table 5 shows the results of the PLSR estimation model of the LKC in cotton at different growth stages was created based on the combined characteristics of "CWT spectra + image." Compared with the R spectrum and CWT spectra models, the fusion of image features can improve the accuracy of the K estimation model at the three growth stages, but the performance of models constructed based on CWT spectra fusion with either "color" or "texture" or with "color + texture" features is different. Among them, the best estimation model was "CWT-1 + texture" for the budding stage, "CWT-3 + color" for the flowering stage and "CWT-9 + texture" for the boll setting stage. Based on the "spectra + image" combination, the best estimation models of the LKC in cotton at the budding, flowering, and boll setting stages had 16, 14, and 12 features, respectively. Moreover, texture features contribute more to the model performance improvement than color features do. These results provide a reference for rapid and non-destructive monitoring of the K.

Comparison of Model Between Single Spectrum and "Spectrum + Image" Feature

Figure 10 shows the best inversion model of the LKC in cotton at three growth stages. The optimal LKC estimation model constructed based on the characteristic wavelengths of R spectra at budding, flowering, and boll setting stages had R^2val s of 0.6613, 0.7530, and 0.6643; and RMSEvals of 0.5292, 0.2202, and 0.3405, respectively (**Figures 10A–C**). Based on the "CWT spectra + image" feature, the accuracy R^2val values of the best LKC estimation model for the three growth stages had R^2val s of 0.8652, 0.8261, and 0.8952 and the RMSEval of 0.3009, 0.1821, and 0.2019, respectively (**Figures 10D,F**). Compared with the single R spectrum, the model accuracy R^2 increased by 0.2, 0.08, and 0.23, respectively, indicating the feasibility of estimating the LKC in cotton based on CWT analysis and image feature fusion and achieving high-precision and rapid monitoring. The best estimation of the LKC in cotton was at the boll setting stage. Furthermore, because the fusion image features at the

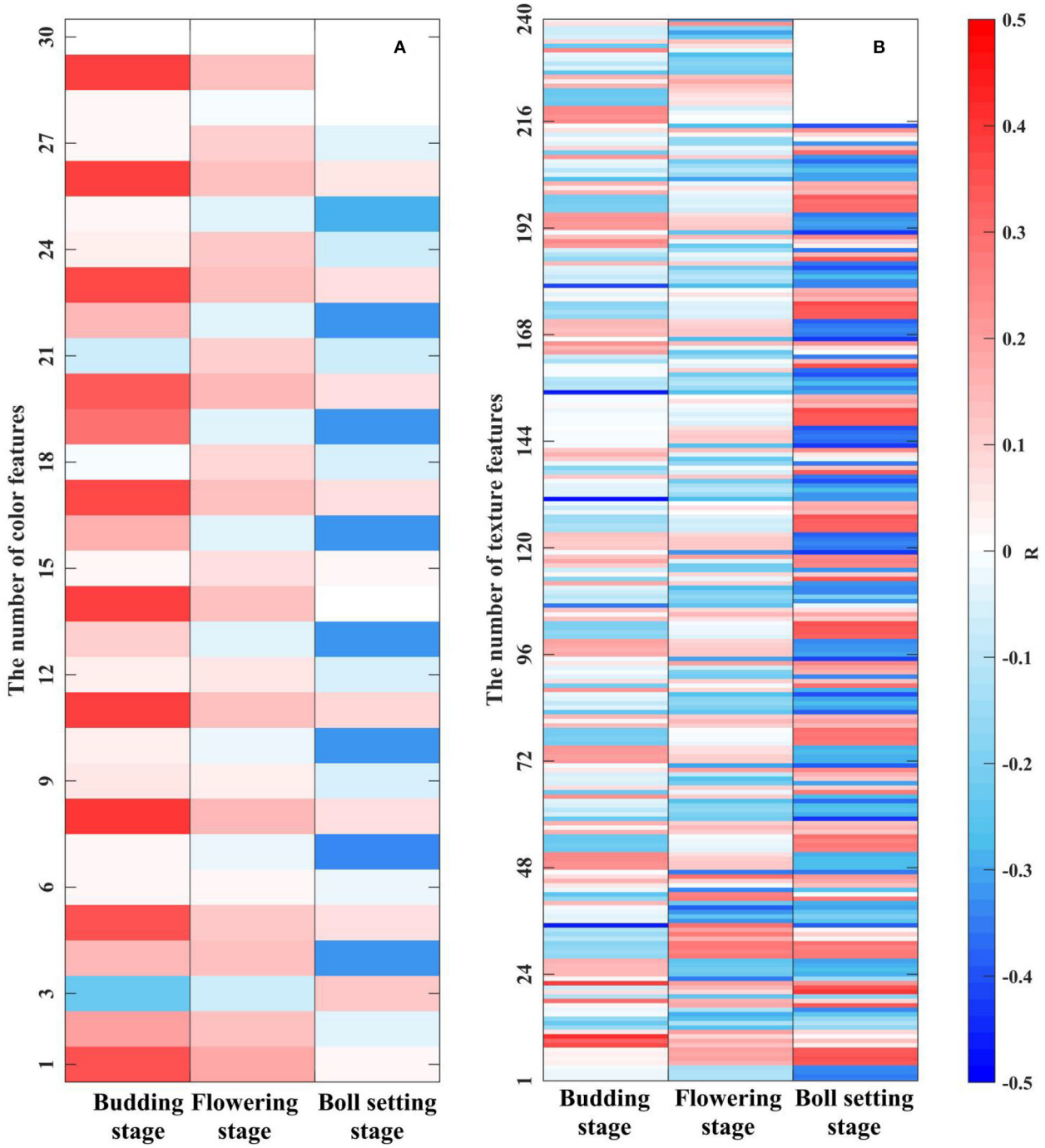

FIGURE 9 | Correlation analysis of the LKC with grayscale image features. **(A)** Color features. There were 10 × 3, 10 × 3 and 9 × 3 color features in three growth stages, respectively. **(B)** Texture features. There were 10 × 24, 10 × 24, and 9 × 24 texture features in three growth stages, respectively.

flowering stage contributed little to the improvement of the model accuracy, it indicated that the quantitative inversion of the K in the growth stage could be satisfied only by R spectral data, and the model had high stability.

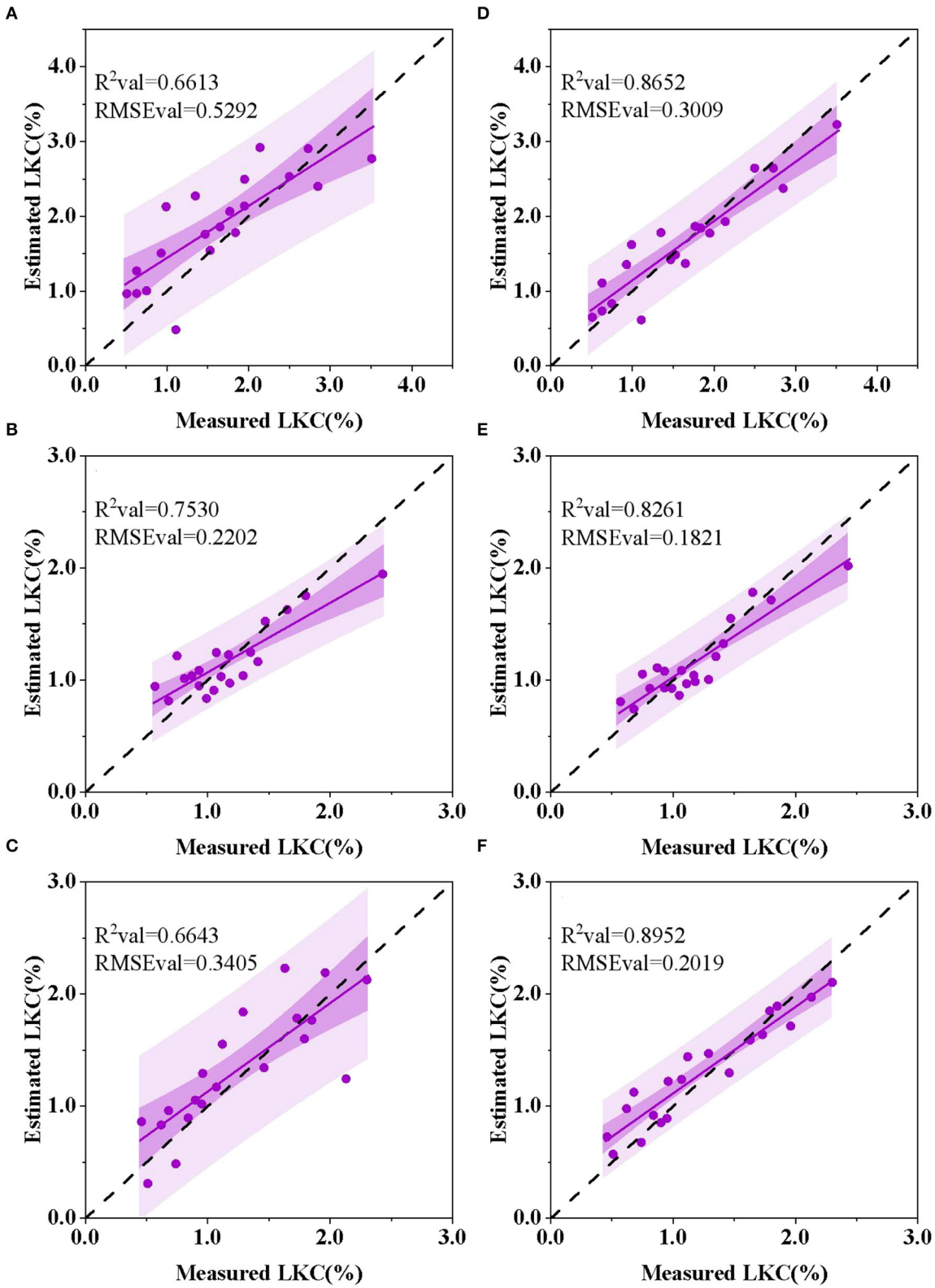

FIGURE 10 | Optimal PLSR estimation model of the LKC in cotton at different growth stages. **(A)** Budding stage, R spectrum. **(B)** Flowering stage, R spectrum. **(C)** Boll setting stage, R spectrum. **(D)** Budding stage, CWT-1 + texture. **(E)** Flowering stage, CWT-3 + color. **(F)** Boll setting stage, CWT-9 + texture.

DISCUSSION

Selection of Characteristic Wavelength

In our study, there was a high correlation between CWT spectra with the LKC at the three key growth stages of cotton. However, it should be noted that LKC in cotton is not highly correlated with wavelet coefficients in the whole band of 400–950 nm but only in some important spectral regions (**Figure 5**). Therefore, to reduce collinearity between spectral data dimensions and adjacent wavelengths, screening several effective wavelengths containing maximum spectral information plays an important role in reducing model complexity and improving estimation ability (Lu et al., 2019b; Ruffing et al., 2021). In this study, characteristic wavelengths of the R spectrum and CWT spectra at three growth periods were screened based on the CARS and RF algorithms (**Table 3**). In general, the characteristic wavelengths were mainly concentrated in the visible and NIR regions in the whole spectrum. The research found that the characteristic wavelengths of the LKC of six degraded vegetation types in the green, red and NIR regions (Peng et al., 2020). Studies have shown that the K deficiency in leaves has a significant impact on the content of photosynthetic pigments (e.g., chlorophyll, carotenoid, and lutein), and the cell structure of leaves (e.g., leaf area, leaf thickness, and cell space) (Curran, 1989; Hu et al., 2020a,b), which is a key factor affecting the light absorption and utilization of plant leaves, leading to the change in reflectance (Peuelas and Filella, 1998). When crops are subjected to the K stress, the spectral reflectance of the visible and near-infrared regions increases, while chlorophyll concentration decreases (Zhao et al., 2001). At the same time, the chlorophyll ultrastructure is significantly damaged, leaf thickness increases, palisade tissue and parenchyma cells contract, and local rupture occurs (Lu et al., 2019a). In conclusion, the K deficiency symptoms can significantly affect the absorption and reflection of light by cotton leaves, change the path of light reflection and refraction and produce different spectral reflectance curves. In addition, studies have shown that the spectral reflectance of the SWIR (1,300–2,000 nm) band of rice was sensitive to K level and significantly correlated with the LKC in rice (Lu et al., 2019a). Pimstein et al. (2011) pointed out that the SWIR (1,450 nm) reflectance was significantly correlated with LKC in wheat. Sibanda et al. (2015) also showed that the SWIR spectroscopy can be used to determine *K* value defense on steppe.

TABLE 4 | Grayscale image feature extraction results.

Growth Stage	Image Feature	Number	Combined Feature Name
Budding stage	Color	1	548 nm-MEA
			471 nm-CON-90°, 471 nm-CON-0°,
	Texture	6	934 nm-ENT-45°, 471 nm-COR-135°, 641 nm-CON-135°, 512 nm-ENT-135°
Flowering stage	Color	4	461 nm-MEA, 532 nm-SKE, 589 nm-MEA, 599 nm-SKE
			532 nm-ENE-135°, 568 nm-COR-135°,
	Texture	8	912 nm-VAR (COR), 594 nm-MEA (CON), 532 nm-MRA (CON), 599 nm-ENT-0°, 604 nm-ENE-90°, 461 nm-MEA (COR)
Boll setting stage	Color	2	667 nm-VAR, 532 nm-VAR
	Texture	3	799 nm-ENE-135°, 522 nm-ENT-90°, 890 nm-ENT-135°

TABLE 5 | PLSR estimation models of the LKC with different combinations of features.

Growth Stage	Method	Feature Combination	Calibration sets		Validation sets	
			R^2cal	RMSEcal	R^2val	RMSEval
Budding stage	CARS	R spectrum	0.8003	0.3578	0.6613	0.5292
		CWT-1	0.8104	0.3485	0.7918	0.3680
		CWT-1 + color	0.8124	0.3467	0.8127	0.3488
		CWT-1 + texture	0.8017	0.3564	0.8652	0.3009
		CWT-1+ color + texture	0.8344	0.3258	0.7980	0.3602
Flowering stage	CARS	R spectrum	0.8397	0.1789	0.7530	0.2202
	RF	CWT-3	0.8405	0.1785	0.7900	0.1987
	CARS	CWT-3 + color	0.8530	0.1714	0.8261	0.1821
		CWT-3 + texture	0.8400	0.1788	0.8012	0.1952
		CWT-3 + color + texture	0.8621	0.1660	0.7960	0.2007
Boll setting stage		R spectrum	0.6487	0.3274	0.6643	0.3405
		CWT-9	0.6310	0.3356	0.8080	0.2508
	CARS	CWT-9 + color	0.6333	0.3345	0.8111	0.2463
		CWT-9 + texture	0.6948	0.3052	0.8952	0.2019
		CWT-9 + color + texture	0.7603	0.2704	0.8272	0.2450

Estimation of the LKC Based on CWT Algorithm

The CWT can decompose hyperspectral data in the time domain and frequency domain simultaneously and estimate the physiological and biochemical components of plants by looking for the best signals at different decomposition scales. The estimation model of the LKC in cotton constructed in this study using CTW spectral data has good prediction accuracy. Based on spectral data, the accuracy R^2 value of the best CWT spectral models constructed for the three growth stages was 0.13, 0.04, and 0.15 higher, than that of the R spectral data model (**Figure 7**). Since CWT can further continuously decompose spectral data, the decomposed wavelet coefficients can correspond to the R spectrum so as to extract subtle signals in spectral data more effectively and improve spectral monitoring accuracy (Li et al., 2019). However, it should be noted that when using the CWT method, the mother wavelet function should be selected first, rather than the commonly used mother wavelet function (Sun et al., 2021; Zhao et al., 2021). A large number of studies have shown that spectral data transformed by CWT have achieved a high accuracy in the inversion of crop nutrients, chlorophyll, and agronomic traits that is superior to models obtained by traditional conversion methods (Yue et al., 2020; Lin et al., 2021; Zhao et al., 2021). Therefore, when crops are under nutrient stress, CWT can effectively mine more complete spectral information, which has great potential in feature selection, noise elimination and weak information extraction.

Estimation Model of the LKC in Cotton

The single feature extracted from the hyperspectral image has limited abilities to estimate nutrient content. Our comparison of the model performance evaluation resulting from different feature combinations (**Table 5**) showed that the estimation of the LKC in cotton based on "CWT spectra + image" features had high accuracy and stability at the three key growth stages, but there were differences in the modeling results of different feature combinations. Contrary to our hypothesis, it was not the case that more feature information led to better model performance. In this study, the estimation model constructed based on the features of "CWT spectra + color + texture" did not show significantly improved accuracy. Instead, the performance of models based on "CWT spectra + color" or "CWT spectra + texture" features is improved. It indicates that when constructing the model based on the feature information of "CWT spectra + color + texture," some invalid information is added, which is interference for improving the accuracy and stability of the prediction model (Li et al., 2019). It should be noted that although the combination feature of the best estimation model of the LKC at the flowering stage is "cwt-3 + color," and the model accuracy R^2val and RMSEval are 0.8261 and 0.1821, the absolute values of the difference between R^2val R^2val and RMSEval based on the "CWT-3 + color" and "CWT-3 + texture" models are 0.0249 and 0.0131 (**Table 5**). This slight difference may be influenced by the feature parameter selection algorithm, as can be seen from **Table 4**, the number of color features selected by CARS during the flowering stage is relatively a little more than in other growth periods. On the other hand, statistically speaking, the difference between the two models is negligible. Therefore, it cannot be fully stated that the combined characteristics of the best estimation model for the LKC at the flowering stage is "CWT-3 + color." Moreover, this study aimed at extracting image features of grayscale images with feature wavelengths, and different feature selection methods may obtain different feature wavelengths (Sun et al., 2021), which will lead to extracting different image feature values. Therefore, future studies will further explore the relationship between the selection of feature wavelengths and image features.

Compared with texture, color features did not contribute significantly to the estimation of the LKC. This is similar to the results of the Jamil et al. (2015) study, which showed that in the taxonomic identification of 455 Chinese herbal medicines, single texture features were superior to color or shape features, with a recognition rate of 92%. In our study, the reason for this discrepancy may be that the image we studied was a single-band grayscale image that contained different information about color and texture characteristics. For color features, we use low-dimensional color moments composed of mean, variance, and skewness to represent the color characteristics of single-band grayscale images, and because the number of channels is 1, the number of color features obtained by calculation is relatively small. In addition, for the color features we extracted, it can also be considered as another expression of spectral information, because each grayscale image has a corresponding wavelength, and perhaps there is interference information between them, reducing the additional effect of color features. However, further investigation needs to be done to positively confirmed the claim. For texture features, we used the GLCM algorithm to extract 240, 240, and 216 high-dimensional texture features from three reproductive periods, including 4 texture features in 4 directions, and its advantage may be that a larger number of feature parameters are conducive to the selection of sensitive parameters. Further, images of different wavelengths of grayscale can clearly show the veins and mesophyll parts of cotton leaves and their degree of brightness and shade (**Figure 8**), while texture is another feature that can be used in plant identification to describe the vein structure or leaf's surface, and it is considered as an additional feature to better describe properties of the leaves (Jamil et al., 2015). These reasons explain, as far as possible, why when we build cotton LKC estimation models, the texture features are better than the color features, and the mechanism of the relationship between LKC and texture features needs further study. Therefore, near-range hyperspectral images with high spatial and hyperspectral resolution can provide more details (Pandey et al., 2017), the model based on "CWT spectra + image" features provide a potential method for estimating the LKC in cotton.

Previous studies mainly focused on using hyperspectral data (Das et al., 2020; Furlanetto et al., 2021) or RGB images (Ghosal et al., 2018; Sun et al., 2018) for analytical modeling of the estimation of the LKC in crop. Ge et al. (2019) constructed a low-cost, non-destructive, and high-throughput maize multiphysiological parameter (including K) estimation model based on the full spectrum band (VIS-NIR-SWIR) through

PLSR and SVM methods. The results for K nutrients show that the modeling results of PLSR are similar to those of SVM, and the and the model accuracy R^2val is 0.586 and 0.543, respectively. The performance of the model largely depends on the sensitivity of input parameters. Compared with their research, we established the model based on the characteristic wavelength sensitive to the LKC in cotton, rather than the full wavelength, but we do not have the SWIR region, which is a deficiency. Although our study used a PLSR model to estimate the LKC with good robustness, the analysis of hyperspectral image data for large samples needs to be further explored, especially as the continuous optimization of deep learning algorithms may be beneficial to LKC estimation (Mahajan et al., 2021; Mertens et al., 2021). Das et al. (2020) studied the content changes of eight nutrient elements (K, Na, Ca, Mg, Fe, Mn, Zn, and Cu) in rice leaves under salt stress and constructed different coupled machine learning models. The results showed that the most accurate estimation of the LKC based on the PLSR-ELNET model (r = 0.928). Liu et al. (2020a) proposed a novel ensemble-modeling framework to transform the rape canopy reflectance data of the selected bands into more distinguishable probability features and identify the N, P, and K deficiency levels using the probabilities. The overall accuracy of nutritional deficiency analysis of this framework is 80.76%, it shows a competitive advantage in severe and moderate potassium deficiency. In this regard, we will study more predictive model algorithms in future work to provide a reference for rapid and non-destructive monitoring of the LKC in cotton.

CONCLUSIONS

The CWT method and PLSR model were used to estimate the LKC in cotton, which had high spectral prediction accuracy and feasibility. The CARS and RF algorithms combined with the PLSR model were used to determine the optimal decomposition scales of CWT at three growth stages, which were CWT-1, CWT-3, and CWT-9 spectra. Also, the CARS is better than RF in Characteristics selection. Compared with the single R spectrum model, the R^2 values were improved by 0.13, 0.04, and 0.15, respectively.

Compared with the best estimation model of the R spectrum and CWT spectra, the PLSR model accuracy was improved after the fusion of image features at the three growth stages. The best feature combination of estimation models was "CWT-1 + texture" at the budding stage, "CWT-3 + color" at the flowering stage and "CWT-9 + texture" at the boll setting stage. Compared with the single R spectrum model, the accuracy R^2 values increased by 0.2, 0.08, and 0.24, respectively.

Using characteristic wavelength to fuse image information can optimize the performance of the LKC estimation model and improve the stability and accuracy of the model. Based on the combination of "CWT spectra + image," the best growth stage for assessing LKC in cotton was the boll setting stage, with the feature combination of "CWT-9 spectra + texture," and its R^2val and RMSEval values were 0.90 and 0.20. However, the optimal growth stage for estimating LKC only by R spectral estimation is the flowering stage. The model did not show significantly improved prediction accuracy and had high stability after integrating image features, indicating that the quantitative estimation of the LKC based on spectral data can be satisfied in this growth stage.

DATA AVAILABILITY STATEMENT

The raw data supporting the conclusions of this article will be made available by the authors, without undue reservation.

AUTHOR CONTRIBUTIONS

QY conceived the study, analyzed the data, and wrote the manuscript. CS finished the laboratory experiment. XC and LM trained the algorithms. ZZ and XL proofread and made comments on the manuscript. All authors discussed in the review process and contributed to the article and approved the submitted version.

FUNDING

This study was supported by the National Natural Science Foundation of China (42061058) and the Corps' key areas of research projects (2020AB005).

ACKNOWLEDGMENTS

QY thank CS for supporting and helping in the experiment. ZZ and XL for revising the article.

REFERENCES

Ahmad, I., and Maathuis, F. (2014). Cellular and tissue distribution of potassium: physiological relevance, mechanisms and regulation. *J. Plant Physiol.* 171, 708–714. doi: 10.1016/j.jplph.2013.10.016

Bao, S. D. (2000). *Soil and Agricultural Chemistry Analysis, 3rd Edn*. Beijing: China Agriculture Press.

Barros, P., Schutze, I. X., Filho, F., Yamamoto, P. T., Fiorio, P. R., and Demattê, J. A. M. (2020). Monitoring bemisia tabaci gennadius (hemiptera: aleyrodidae) infestation in soybean using by proximal sensing. *Insects* 12, 47. doi: 10.3390/insects12010047

Chen, J. X., Li, F., Wang, R., Fan, Y. F., Muhammad, A. R., Liu, Q. L., et al. (2019). Estimation of nitrogen and carbon content from soybean leaf reflectance spectra using wavelet analysis under shade stress. *Comput. Electron. Agric.* 156, 482–489. doi: 10.1016/j.compag.2018.12.003

Chen, P., Haboudane, D., Tremblay, N., Wang, J., Vigneault, P., and Li, B. (2010). New spectral indicator assessing the efficiency of crop nitrogen treatment in corn and wheat. *Remote Sens. Environ.* 114, 1987–1997. doi: 10.1016/j.rse.2010.04.006

Curran, P. J. (1989). Remote sensing of foliar chemistry. *Remote Sens. Environ.* 30, 271–278. doi: 10.1016/0034-4257(89)90069-2

Das, B., Manohara, K. K., Mahajan, G. R., and Sahoo, R. N. (2020). Spectroscopy based novel spectral indices, pca- and plsr-coupled machine learning models for salinity stress phenotyping of rice. *Spectrochim. Acta A Mol. Biomol. Spectrosc.* 229, 117983. doi: 10.1016/j.saa.2019.117983

El-Hendawy, S., Al-Suhaibani, N., Hassan, W., Tahir, M., and Schmidhalter, U. (2017). Hyperspectral reflectance sensing to assess the growth and photosynthetic properties of wheat cultivars exposed to different irrigation rates in an irrigated arid region. *PLoS ONE* 12:e0183262. doi: 10.1371/journal.pone.0183262

Furlanetto, R. H., Nanni, M. R., Crusiol, L. G. T., Silva, G. F. C., and Sibaldelli, R. N. R. (2021). Identification and quantification of potassium (K+) deficiency in maize plants using an unmanned aerial vehicle and visible/near-infrared semi-professional digital camera. *Int. J. Remote Sens.* 42, 8783–8804. doi: 10.1080/01431161.2020.1871091

Ge, H., Xiang, H., Ma, F., Li, Z., and Du, C. (2021). Estimating plant nitrogen concentration of rice through fusing vegetation indices and color moments derived from uav-rgb images. *Remote Sens*. 13, 1620. doi: 10.3390/rs13091620

Ge, Y., Atefi, A., Zhang, H., Miao, C., Ramamurthy, R. K., and Sigmon, B., et al. (2019). High-throughput analysis of leaf physiological and chemical traits with VIS–NIR–SWIR spectroscopy: a case study with a maize diversity panel. *Plant Methods* 15, 66. doi: 10.1186/s13007-019-0450-8

Ghosal, S., Blystone, D., and Singh, A. K. (2018). An explainable deep machine vision framework for plant stress phenotyping. *Proc. Nat. Acad. Sci. U. S. A.* 115, 4613–4618. doi: 10.1073/pnas.1716999115

Gierth, M., and Maser, P. (2007). Potassium transporters in plants – involvement in k + acquisition, redistribution and homeostasis. *FEBS Lett.* 581, 2348–2356. doi: 10.1016/j.febslet.2007.03.035

Hu, N., Li, W., Du, C., Zhang, Z., and Wang, Z. (2020a). Predicting micronutrients of wheat using hyperspectral imaging. *Food Chem*. 343, 128473. doi: 10.1016/j.foodchem.2020.128473

Hu, W. S., Lu, Z. F., Meng, F. J., Li, X. K., Cong, R. H., Ren, T., et al. (2020b). The reduction in leaf area precedes that in photosynthesis under potassium deficiency: the importance of leaf anatomy. *New Phytol.* 227, 1749–1763. doi: 10.1111/nph.16644

Hussain, A., Sahoo, R. N., Kumar, D., and Pradhan, S. (2017). Relationship of hyperspectral reflectance indices with leaf n and p concentration, dry matter accumulation and grain yield of wheat. *J. Indian Soc. Remote Sens*. 45, 773–784. doi: 10.1007/s12524-016-0633-y

Jamil, N., Hussin, N., Nordin, S., and Awang, K. (2015). Automatic plant identification: is shape the key feature? *Proc. Comput. Sci*. 76, 436–442. doi: 10.1016/j.procs.2015.12.287

Jiang, J., Zhu, J., Wang, X., Cheng, T., Tian, Y., Zhu, Y., et al. (2021). Estimating the leaf nitrogen content with a new feature extracted from the ultra-high spectral and spatial resolution images in wheat. *Remote Sens.* 13, 739. doi: 10.3390/rs13040739

Laddi, A., Sharma, S., Kumar, A., and Kapur, P. (2013). Classification of tea grains based upon image texture feature analysis under different illumination conditions. *J. Food Eng.* 115, 226–231. doi: 10.1016/j.jfoodeng.2012.10.018

Lewis, K., Morgan, G., Frame, W. H., Fromme, D., and Nichols, R. L. (2021). Cotton yield response to soil applied potassium across the United States cotton belt. *Agron. J.* 113, 3600–3614. doi: 10.1002/agj2.20719

Li, F. L.,Wang, L., Liu, J., Wang, Y., and Chang, Q. (2019). Evaluation of leaf n concentration in winter wheat based on discrete wavelet transform analysis. *Remote Sens.* 11, 1331. doi: 10.3390/rs11111331

Lin, D., Li, G., Zhu, Y., Liu, H., and Jiao, Q. (2021). Predicting copper content in chicory leaves using hyperspectral data with continuous wavelet transforms and partial least squares. *Comput. Electron. Agric.* 187, 106293. doi: 10.1016/j.compag.2021.106293

Liu, N., Xing, Z., Zhao, R., Qiao, L., Li, M., Liu, G., et al. (2020b). Analysis of chlorophyll concentration in potato crop by coupling continuous wavelet transform and spectral variable optimization. *Remote Sens*. 12, 2826. doi: 10.3390/rs12172826

Liu, S., Zhai, R., and Hui, P. (2015). "Non-destructive detection of the pH value of cold fresh pork using hyperspectral imaging technique," in *9th IFIP WG 5.14 International Conference on Computer and Computing Technologies in Agriculture (CCTA), Vol. 478*, 266–274. doi: 10.1007/978-3-319-48357-3_26

Liu, S. S., Yang, X., Guan, Q. F., Lu, Z., and Lu, J. (2020a). An ensemble modeling framework for distinguishing nitrogen, phosphorous and potassium deficiencies in winter oilseed rape (*Brassica napus* L.) using hyperspectral data. *Remote Sens.* 12, 4060. doi: 10.3390/rs12244060

Lu, J., Yang, T., Su, X., Qi, H., Yao, X., Cheng, T., et al. (2019a). Monitoring leaf potassium content using hyperspectral vegetation indices in rice leaves. *Precis. Agric.* 21, 324–348. doi: 10.1007/s11119-019-09670-w

Lu, N., Wang, W., Zhang, Q., Li, D., and Cheng, T. (2019b). Estimation of nitrogen nutrition status in winter wheat from unmanned aerial vehicle based multi-angular multispectral imagery. *Front. Plant Sci*. 10:1601. doi: 10.3389/fpls.2019.01601

Mahajan, G. R., Das, B., Murgaokar, D., Herrmann, I., and Kulkarni, R. M. (2021). Monitoring the foliar nutrients status of mango using spectroscopy-based spectral indices and PLSR-combined machine learning models. *Remote Sensing*. 13, 641. doi: 10.3390/rs13040641

Mahajan, G. R., Sahoo, R. N., Pandey, R. N., Gupta, V. K., and Kumar, D. (2014). Using hyperspectral remote sensing techniques to monitor nitrogen, phosphorus, sulphur and potassium in wheat (*Triticum aestivum* L.). *Precis. Agric.* 15, 499–522. doi: 10.1007/s11119-014-9348-7

Men, H., Yuan, H., Shi, Y., Liu, M., and Liu, J. (2021). A residual network with attention module for hyperspectral information of recognition to trace the origin of rice. *Spectrochim. Acta A Mol. Biomol. Spectrosc.* 263, 120155. doi: 10.1016/j.saa.2021.120155

Mertens, S., Verbraeken, L., Sprenger, H., Demuynck, K., and Wuyts, N. (2021). Proximal hyperspectral imaging detects diurnal and drought-induced changes in maize physiology. *Front. Plant Sci*. 12:640914. doi: 10.3389/fpls.2021.640914

Oliveira, M. R. R., Queiroz, T. R. G., Teixeira, A. D., Moreira, L. C. J., and Leao, R. A. D. (2020). Reflectance spectrometry applied to the analysis of nitrogen and potassium deficiency in cotton. *Rev. Cienc. Agron.* 51, e20196705. doi: 10.5935/1806-6690.20200074

Osco, L. P., Ramos, A. P. M., Faita Pinheiro, M. M., Moriya, É. A. S., Imai, N. N., Estrabis, N., et al. (2020a). A machine learning framework to predict nutrient content in valencia-orange leaf hyperspectral measurements. *Remote Sens.* 12, 906. doi: 10.3390/rs12060906

Osco, L. P., Ramos, A. P. M., Moriya, E. A. S., de Souza, M., Marcato Junior, J., Matsubara, E. T., et al. (2020b). Improvement of leaf nitrogen content inference in valencia-orange trees applying spectral analysis algorithms in UAV mounted-sensor images-sciencedirect. *Int. J. Appl. Earth Observ. Geoinform.* 83, 101907. doi: 10.1016/j.jag.2019.101907

Osco, L. P., Ramos, A. P. M., Pereira, D. R., Moriya, E. A. S., Imai, N. N., Matsubara, E. T., et al. (2019). Predicting canopy nitrogen content in citrus-trees using random forest algorithm associated to spectral vegetation indices from uav-imagery. *Remote Sens*. 11, 2925. doi: 10.3390/rs11242925

Pace, P. F., Cralle, H. T., Cothren, J. T., and Senseman, S. A. (1999). Photosynthate and dry matter partitioning in short and long-season cotton cultivars. *Crop Sci*. 39, 1065–1069. doi: 10.2135/cropsci1999.0011183X003900040018x

Pandey, P., Ge, Y. F., Stoerger, V., and Schnable, J. C. (2017). high throughput *in vivo* analysis of plant leaf chemical properties using hyperspectral imaging. *Front. Plant Sci.* 8:1348. doi: 10.3389/fpls.2017.01348

Peng, Y., Zhang, M., Xu, Z., Yang, T., Su, Y., Zhou, T., et al. (2020). Estimation of leaf nutrition status in degraded vegetation based on field survey and hyperspectral data. *Sci. Rep*.10, 4361. doi: 10.1038/s41598-020-61294-7

Pettigrew, W. T. (2008). Potassium influences on yield and quality production for maize, wheat, soybean and cotton. *Physiol. Plant.* 133, 670–681. doi: 10.1111/j.1399-3054.2008.01073.x

Peuelas, J., and Filella, I. (1998). Visible and near-infrared reflectance techniques for diagnosing plant physiological status. *Trends Plant Sci*. 3, 151–156. doi: 10.1016/S1360-1385(98)01213-8

Pimstein, A., Karnieli, A., Bansal, S. K., and Bonfil, D. J. (2011). Exploring remotely sensed technologies for monitoring wheat potassium and phosphorus using field spectroscopy. *Field Crop Res*. 121, 125–135. doi: 10.1016/j.fcr.2010.12.001

Ramírez-Soler, C. H., Magnitskiy, M., Martínez, S. S. E., Alvarez-Flórez, F., and Melgarejo, L. M. (2021). Photosynthesis, biochemical activity, and leaf anatomy of tree tomato (*Solanum betaceum* cav.) plants under potassium deficiency. *J. Appl. Bot. Food Qual*. 94, 75–81. doi: 10.5073/JABFQ.2021.094.009

Ruffing, A. M., Anthony, S. M., Strickland, L. M., Lubkin, I., and Dietz, C. R. (2021). Identification of metal stresses in arabidopsis thaliana using hyperspectral reflectance imaging. *Front. Plant Sci.* 12:624656. doi: 10.3389/fpls.2021.624656

Severtson, D., Callow, N., Flower, K., Neuhaus, A., Olejnik, M., and Nansen, C. (2016). Unmanned aerial vehicle canopy reflectance data detects potassium

deficiency and green peach aphid susceptibility in canola. *Precis. Agric.* 17, 659–677. doi: 10.1007/s11119-016-9442-0

Sibanda, M., Mutanga, O., Rouget, M., and Odindi, J. (2015). Exploring the potential of in situ hyperspectral data and multivariate techniques in discriminating different fertilizer treatments in grasslands. *J. Appl. Remote Sens.* 9, 1931–3195. doi: 10.1107/S010876738708303X

Singh, J., Singh, N. P., Sangwan, A. K., Gill, P. S., Gill, B. S., Kaur, S., et al. (2019). Standardization of litchi leaf nutrient composition for tissue analysis in sub tropics of India. *Commun. Soil Sci. Plant Anal.* 50, 2889–2898. doi: 10.1080/00103624.2019.1689253

Sun, J., Yang, W., Zhang, M., Feng, M., and Ding, G. (2021). Estimation of water content in corn leaves using hyperspectral data based on fractional order savitzky-golay derivation coupled with wavelength selection. *Comput. Electron. Agric.* 182, 105989. doi: 10.1016/j.compag.2021.105989

Sun, Y., Tong, C., He, S., Wang, K., and Chen, L. (2018). Identification of nitrogen, phosphorus, and potassium deficiencies based on temporal dynamics of leaf morphology and color. *Sustainability* 10, 762. doi: 10.3390/su10030762

Tian, L. W., Qi, Y. C., Dai, L., Cui, J. P., Guo, R. S.,Xu, H. J., et al. (2020). Evaluation of soil nutrient content and its distribution of cultivated land in south of Xinjiang: taking Aksu prefecture as an example. *J. Nucl. Agric. Sci.* 34, 214–223.

Villette, J., T., Cuéllar, Verdeil, J. L., Delrot, S., and Gaillard, I. (2020). Grapevine potassium nutrition and fruit quality in the context of climate change. *Front. Plant Sci.* 11:123. doi: 10.3389/fpls.2020.00123

Wang, A. Y., Liu, Y. H., and Sheng, J. D. (2021). Spatial-temporal variation of soil nutrients in typical drip irrigation cotton fields in Xinjiang. *Tianjin Agric. Sci.* 27, 86–90. doi: 10.3969/j.issn.1006-6500.2021.11.019

Wang, Y. J., Jin, G., Li, L. Q., Liu, Y., Kalkhajeh, Y. K., Ning, J. M., et al. (2020). NIR hyperspectral imaging coupled with chemometrics for non-destructive assessment of phosphorus and potassium contents in tea leaves. *Infrared Phys. Technol.* 108, 103365. doi: 10.1016/j.infrared.2020.103365and

Yang, Y., Nie, J., Kan, Z., Yang, S., Zhao, H., and Li, J. (2021). Cotton stubble detection based on wavelet decomposition and texture features. *Plant Methods* 17, 113. doi: 10.1186/s13007-021-00809-3

Yao, X., Si, H. Y., Cheng, T., Jia, M., Chen, Q., and Tian, Y. C. (2018). Hyperspectral estimation of canopy leaf biomass phenotype per ground area using a continuous wavelet analysis in wheat. *Front. Plant Sci.* 9:1360. doi: 10.3389/fpls.2018.01360

Yue, J., Zhou, C., Guo, W., Feng, H., and Xu, K. (2020). Estimation of winter-wheat above-ground biomass using the wavelet analysis of unmanned aerial vehicle-based digital images and hyperspectral crop canopy images. *Int. J. Remote Sens.* 42, 1602–1622. doi: 10.1080/01431161.2020.1826057

Zhang, J. C., Yuan, L., Pu, R. L., Loraamm, R. W., Yang, G. J., and Wang, J. H. (2014). Comparison between wavelet spectral features and conventional spectral features in detecting yellow rust for winter wheat. *Comput. Electron. Agric.* 100, 79–87. doi: 10.1016/j.compag.2013.11.001

Zhao, D., Oosterhuis, D. M., and Bednarz, C. W. (2001). Influence of potassium deficiency on photosynthesis, chlorophyll content, and chloroplast ultrastructure of cotton plants. *Photosynthetica* 39, 103–109. doi: 10.1023/A:1012404204910

Zhao, R., An, L., Song, D., Li, M., and Sun, H. (2021). Detection of chlorophyll fluorescence parameters of potato leaves based on continuous wavelet transform and spectral analysis. *Spectrochim. Acta A Mol. Biomol. Spectrosc.* 259, 119768. doi: 10.1016/j.saa.2021.119768

Zheng, Y., Zhu, Q. B., Huang, M., Guo, Y., and Qin, J. W. (2017). Maize and weed classifcation using color indices with support vector data description in outdoor fields. *Comput. Electron. Agric.* 141, 215–222. doi: 10.1016/j.compag.2017.07.028

Zhou, J. J., Zhang, Y. H., Han, Z. M., Liu, X. Y., Jian, Y. F., and Hu, C. G. (2021). Evaluating the performance of hyperspectral leaf reflectance to detect water stress and estimation of photosynthetic capacities. *Remote Sens.* 13, 2160. doi: 10.3390/rs13112160

Zou, K. L., Ge, L. Z., Zhang, C. L., Yuan, T., and Li, W. (2019). Broccoli seedling segmentation based on support vector machine combined with color texture features. *IEEE Access* 7, 168565–168574. doi: 10.1109/ACCESS.2019.2954587

Conflict of Interest: The authors declare that the research was conducted in the absence of any commercial or financial relationships that could be construed as a potential conflict of interest.

Publisher's Note: All claims expressed in this article are solely those of the authors and do not necessarily represent those of their affiliated organizations, or those of the publisher, the editors and the reviewers. Any product that may be evaluated in this article, or claim that may be made by its manufacturer, is not guaranteed or endorsed by the publisher.

Copyright © 2022 Yao, Zhang, Lv, Chen, Ma and Sun. This is an open-access article distributed under the terms of the Creative Commons Attribution License (CC BY). The use, distribution or reproduction in other forums is permitted, provided the original author(s) and the copyright owner(s) are credited and that the original publication in this journal is cited, in accordance with accepted academic practice. No use, distribution or reproduction is permitted which does not comply with these terms.

frontiers | Frontiers in Plant Science

TYPE Original Research
PUBLISHED 22 July 2022
DOI 10.3389/fpls.2022.898962

Check for updates

OPEN ACCESS

EDITED BY
Zhenhai Li,
Shandong University of Science and Technology, China

REVIEWED BY
Klára Kosová,
Crop Research Institute (CRI), Czechia
Zhang Kaixing,
Shandong Agricultural University, China

*CORRESPONDENCE
Zhaotang Ding
dzttea@163.com

SPECIALTY SECTION
This article was submitted to Sustainable and Intelligent Phytoprotection, a section of the journal Frontiers in Plant Science

RECEIVED 18 March 2022
ACCEPTED 28 June 2022
PUBLISHED 22 July 2022

CITATION
Li H, Wang Y, Fan K, Mao Y, Shen Y and Ding Z (2022) Evaluation of important phenotypic parameters of tea plantations using multi-source remote sensing data.
Front. Plant Sci. 13:898962.
doi: 10.3389/fpls.2022.898962

COPYRIGHT
© 2022 Li, Wang, Fan, Mao, Shen and Ding. This is an open-access article distributed under the terms of the Creative Commons Attribution License (CC BY). The use, distribution or reproduction in other forums is permitted, provided the original author(s) and the copyright owner(s) are credited and that the original publication in this journal is cited, in accordance with accepted academic practice. No use, distribution or reproduction is permitted which does not comply with these terms.

Evaluation of important phenotypic parameters of tea plantations using multi-source remote sensing data

He Li[1], Yu Wang[1], Kai Fan[1], Yilin Mao[1], Yaozong Shen[1] and Zhaotang Ding[1,2]*

[1]Tea Research Institute, Qingdao Agricultural University, Qingdao, China, [2]Tea Research Institute, Shandong Academy of Agricultural Sciences, Jinan, China

Tea height, leaf area index, canopy water content, leaf chlorophyll, and nitrogen concentrations are important phenotypic parameters to reflect the status of tea growth and guide the management of tea plantation. UAV multi-source remote sensing is an emerging technology, which can obtain more abundant multi-source information and enhance dynamic monitoring ability of crops. To monitor the phenotypic parameters of tea canopy more efficiently, we first deploy UAVs equipped with multispectral, thermal infrared, RGB, LiDAR, and tilt photography sensors to acquire phenotypic remote sensing data of tea canopy, and then, we utilize four machine learning algorithms to model the single-source and multi-source data, respectively. The results show that, on the one hand, using multi-source data sets to evaluate H, LAI, W, and LCC can greatly improve the accuracy and robustness of the model. LiDAR + TC data sets are suggested for assessing H, and the SVM model delivers the best estimation (Rp^2 = 0.82 and RMSEP = 0.078). LiDAR + TC + MS data sets are suggested for LAI assessment, and the SVM model delivers the best estimation (Rp^2 = 0.90 and RMSEP = 0.40). RGB + TM data sets are recommended for evaluating W, and the SVM model delivers the best estimation (Rp^2 = 0.62 and RMSEP = 1.80). The MS +RGB data set is suggested for studying LCC, and the RF model offers the best estimation (Rp^2 = 0.87 and RMSEP = 1.80). On the other hand, using single-source data sets to evaluate LNC can greatly improve the accuracy and robustness of the model. MS data set is suggested for assessing LNC, and the RF model delivers the best estimation (Rp^2 = 0.65 and RMSEP = 0.85). The work revealed an effective technique for obtaining high-throughput tea crown phenotypic information and the best model for the joint analysis of diverse phenotypes, and it has significant importance as a guiding principle for the future use of artificial intelligence in the management of tea plantations.

KEYWORDS

UAV, multispectral, LiDAR, RGB, thermal, tilt photography, tea plants phenotype

Introduction

Tea [*Camellia sinensis (L.) O. Kuntze*] is an evergreen cash crop, which is widely cultivated all over the world. Phenotypic parameters, such as height (H), leaf area index (LAI), leaf water content (W), leaf chlorophyll, and nitrogen concentration (LCC and LNC), are important indicators to estimate the growth and development of tea plants. Using these parameters on large scale can effectively guide the daily management of tea plantations in field. However, the conventional measurement methods of these parameters have some problems, such as time-consuming and labor-intensive, low efficiency, high cost, and poor accuracy, which seriously restrict growth, development, and smart yield of tea on larger scale. Therefore, it is important to find better, faster, and smarter way of phenotyping methods for more accurate results.

In recent years, with the rise of new remote sensing tools around the world, UAV system has gradually become an important means to obtain the phenotypic information of field crops with the advantages of flexibility, adaptability to complex farmland environment, high efficiency, and low cost (Herwitz et al., 2004). At the present, UAV sensors mostly comprise optical sensors, thermal sensors, and three-dimensional reconstruction sensors.

As we know that, optical sensors could obtain spectral reflectance and texture information of vegetation (Kalaitzidis et al., 2008; Chianucci et al., 2016), and optical information had been successfully applied to crop phenotype analysis. For example, the density of maize plants was estimated using UAV RGB data (Štambuk et al., 2021). The vegetation index of soybean canopy was obtained by UAV RGB image, and the canopy volume model was constructed to estimate soybean biomass (Maimaitijiang et al., 2019). The hyperspectral image of UAV and the lodging characteristics of rice were used to establish the rice yield detection model (Wang et al., 2021). The UAV multispectral data were used to estimate the biochemical components of tea canopy leaves (Luo et al., 2021). However, the optical sensors that were utilized to monitor the dense field crops suffered from the challenge of progressive saturation, which caused it harder to obtain the structural parameters and canopy temperature of the crops.

The thermal sensor could be able to obtain the canopy temperature of field crops. The obtained temperature information had a high correlation with plant water content in field. Therefore, thermal sensors were mostly used to monitor the temporal and spatial changes in crop water content and evaluate the drought degree of crops (Abdelhakim et al., 2021). Some researchers also use thermal infrared data to evaluate plant leaf area index and chlorophyll content (Lin et al., 2021). Infrared imaging is mainly used to monitor the water content of plants. The monitoring of other phenotypic parameters needs to be further explored.

To get accurate information on crop canopy structure, the three-dimensional reconstruction sensor is the fundamental sensor. The three-dimensional reconstruction sensor is the main sensor to obtain the crop canopy structure information. It generates point cloud data through the structure from motion (SFM) to establish a three-dimensional (3D) model (Brook et al., 2021). There are two main methods to build 3D models. One is to obtain omnidirectional images, *via* multi-angle oblique photography technique, and then splice the omnidirectional images to establish a three-dimensional model. The other is to launch the laser beam through the LiDAR sensor and then locate the laser beam hitting the spot of the object to establish the three-dimensional model (Perez and Costes, 2018). These two methods have made good progress in agricultural application: for instance, combining oblique and vertical photography technologies from a UAV to create a 3D model to estimate the plant height and leaf area of maize growing in a field (Ying et al., 2020), and using 3D rotating LiDAR sensor to establish a three-dimensional model to estimate the canopy density of perennial horticultural crops (Lowe et al., 2021). In contrast, the tilt photography sensor has low cost and is suitable for large-scale popularization in the field. However, this is a passive technology with less density and information than the point cloud generated by LiDAR sensors (Luo et al., 2019).

In recent years, the continuous development of computer hardware has facilitated the progress of machine learning, which has become an active research area in agricultural quantitative remote sensing (Liu et al., 2021). For example, Luo et al. (2021) used the UAV equipped with multispectral sensors to obtain the spectral data of tea canopy leaves and used support vector regression (SVR) and partial least square regression (PLSR) to estimate the nitrogen content, polyphenols, and caffeine. Liu et al. (2021) used the UAV equipped with multispectral, RGB and thermal infrared to obtain the multi-source data of corn canopy and established regression models using RNN, PLS, RF, and SVM to evaluate the LAI.

Single-source remote sensing has made good progress in monitoring various parameters of crops, but it has limitations. Because the information collected by different sensors is different, if only relying on a single sensor to monitor crops, some data will be lost, which will affect the accuracy of the model. Moreover, in the study of maize and soybean phenotypes, it has been proved that the accuracy of modeling with multi-source data is higher than that with single-source data, as shown in Table 1. Therefore, it is of great significance to study the multi-source remote sensing monitoring of tea plant growth indicators.

In this research work, we smartly use multi-source remote sensing data, including RGB images, multispectral images, TM images, LiDAR images, and TC images, collected from a UAV crop high-throughput phenotyping platform, to develop a multimodal data processing framework to estimate the H, LAI, W, LCC, and LNC of tea plants in field. The proposed

TABLE 1 Results of estimating relevant indexes of field crops using multi-source remote sensing data.

Sensor type	Phenotypic	Crop	Algorithm	Accuracy	References
RGB	LAI	Maize	DCNN	$R^2 = 0.82$	Liu et al., 2021
			RF	$R^2 = 0.71$	
MS	LAI	Maize	DCNN	$R^2 = 0.7$	
			RF	$R^2 = 0.68$	
TM	LAI	Maize	DCNN	$R^2 = 0.51$	
			RF	$R^2 = 0.54$	
RGB+MS+TM	LAI	Maize	DCNN	$R^2 = 0.89$	
			RF	$R^2 = 0.76$	
LiDAR	H	Maize	RF	$R^2 = 0.76$	Yue et al., 2018
	AGB		SVM	$R^2 = 0.74$	
RGB	H	Maize	RF	$R^2 = 0.69$	
	AGB		SVM	$R^2 = 0.64$	
HS	H	Maize	RF	$R^2 = 0.56$	
	AGB		SVM	$R^2 = 0.54$	
LiDAR+RGB+MS	H	Maize	RF	$R^2 = 0.82$	
	AGB		SVM	$R^2 = 0.8$	
MS	AGB	Soybean	SVM	$R^2 = 0.52$	Maimaitijiang et al., 2020
RGB	AGB	Soybean	SVM	$R^2 = 0.42$	
TM	AGB	Soybean	SVM	$R^2 = 0.26$	
MS+RGB+MS	AGB	Soybean	SVM	$R^2 = 0.67$	

framework is mainly based on four key machine learning methods: back propagation (BP), support vector machine (SVM), random forest (RF), and partial least squares (PLS). This work makes several contributions: (1) It proposes a framework for processing fused, multi-source remote sensing data, which produces multimodal data sets to improve estimates of the H, LAI, W, LCC, and LNC; (2) comparing the robustness and adaptability of multi-mode data fusion and single-source data evaluation models to estimate H, LAI, W, LCC, and LNC of tea plant and found an optimal estimation model for different phenotypes; (3) the tea phenotypic model constructed by RF and SVM algorithm has the highest accuracy and robustness.

Materials and methods

Study area

The study areas were located in Bi Hai Lan Tian Tea plantations (120.61°E, 36.27°N, Figure 1), Laoshan District, Qingdao City, Shandong Province. It covers an area of about 65 hectares, with an average altitude of 55 meters. The soil texture is sandy, the unit weight is 1.45 g/cm^3, the organic matter is 1.63%, and the pH value is 6.0. The annual average precipitation is 719.2 mm, the annual average sunshine hours are 2,392 h, and the annual average temperature is 13.5°C (the annual maximum/minimum temperature is 39.6/−19.6°C), which is suitable for the growth and development of tea plants. The experimental areas were divided into three tea plantations at different growth stages, the age of tea plants in young tea garden (YTG) is 4 years old, mature tea garden (MTG) is 10 years old, and aging tea garden (ATG) is 22 years old. The location of the test area is shown in Figure 1.

The field experiment was conducted in November 2020. The three tea plantations were divided into experimental units. YTG is divided into 70 test subunits, each of which is 3 m^2; MTG is divided into 50 test subunits, each with 4 m^2; ATG is divided into 60 test subunits, each of which is 3 m^2. Three tea plantations were watered and fertilized. YTG watering is 45 mm, MTG watering is 120 mm, and ATG watering is 120 mm. Drip irrigation is adopted. The fertilizer is organic fertilizer. Mechanical trenching is adopted for fertilization. YTG is applied with 75 kg hm^{-2}, MTG is applied with 112 kg hm^{-2}, and ATG is applied with 85 kg hm^{-2}.

Data collection

Field data collection

Field data were collected on July 1, 2021, and five tea plant phenotypic parameters were measured in this study, including LAI (m^2 m^{-2}), H (m), W (%), LCC (SPAD value), and LNC (mg g^{-1}) (Table 2). All five parameters were measured between July

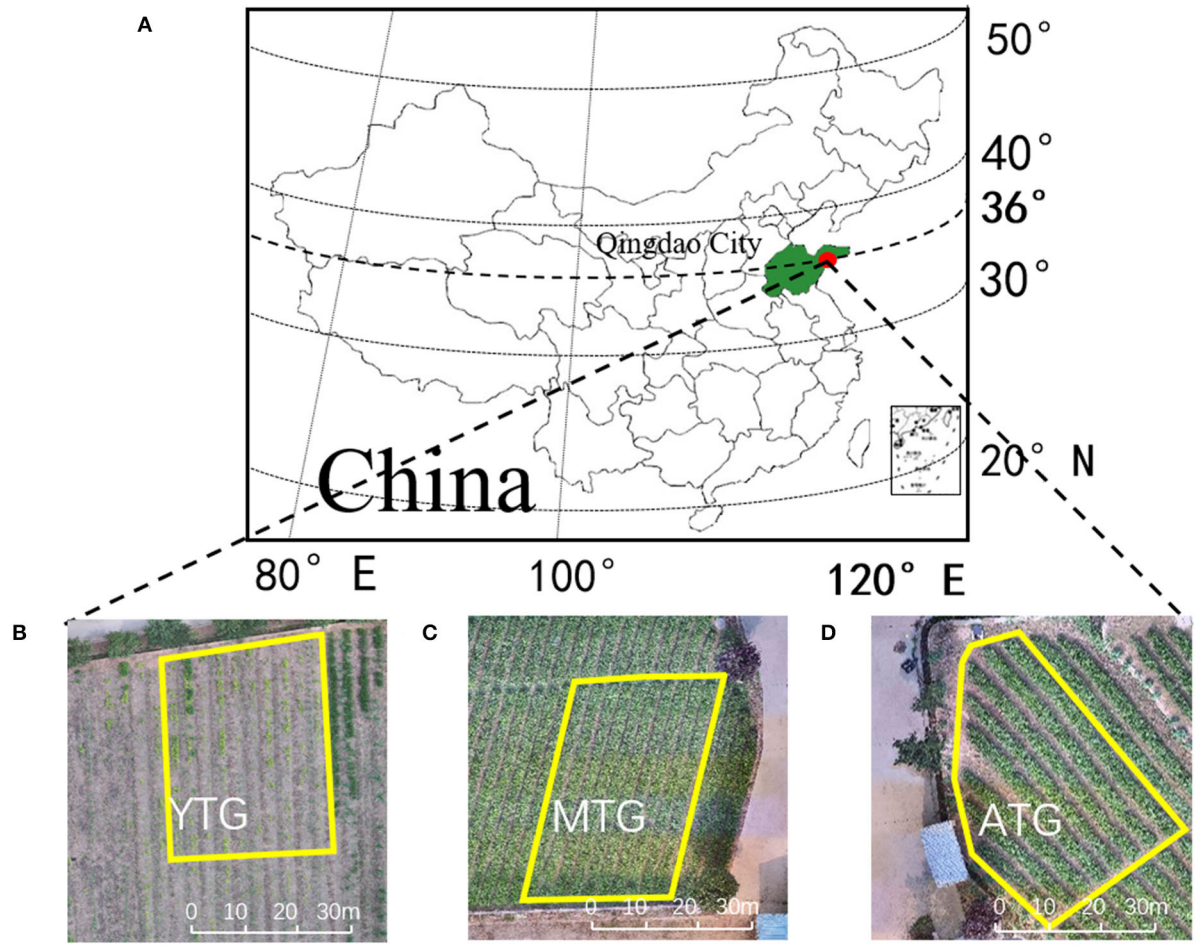

FIGURE 1
(A) Geographical location of the study area (Qingdao); **(B)** young tea garden (YTG); **(C)** mature tea garden (MTG); **(D)** aging tea garden (ATG).

1 and July 2, 2021 (Figure 2). All tea plants in the tea gardens were pruned, and the fresh shoots were picked before phenotypic parameters were measured and flight missions were performed. As a result, our measurements of leaf values are based on mature leaves. To verify the typicality of the collected samples and minimize measurement error, we randomly measure the leaves of multiple tea plants in the test unit and then use the average as the final input data.

The LAI was measured by the plant canopy Digital Image Analyzer CI-110 (CID USA). The final result is the average value of three measurements in each test area (Brand and Zonta, 2016). The H was measured by hand using a ruler, and the final result is the average of six measurements taken in each test area. The W was measured by oven. Ten mature leaves from each test area were taken and dried to constant weight in an oven at 90°C to constant weight. The LCC and LNC were measured by plant Nutrition analyzer (Tuopu Zhejiang, China), carefully avoiding the leaf veins during whole measurement for accuracy of results. The final average data were calculated according to the prescribed formula of W as follows:

$$W = \frac{m1 - m2}{m2} \times 100\% \quad (1)$$

where m1(g) is the total weight of the blade, and m2 (g) is the weight after drying.

UAV multi-sensor data acquisition

To ensure flight quality and safety, we choose sunny weather and low wind speed conditions to perform the flight mission. On July 1, 2021, three UAVs were equipped with four sensors to perform flight tasks (Figure 3). The DJ M300 RTK (DJI, Inc., Shenzhen, China) was equipped with Meditation L1 (DJI, Inc., Shenzhen, China) and Meditation P1 (DJI, Inc., Shenzhen,

TABLE 2 Descriptive statistics were used to analyze the phenotypic parameters of tea plantations.

Tea parameters	Number	Min	Mean	Max	SD
LAI (m^2 m^{-2})	Field all = 180	0.53	2.4	5.10	1.31
	Field YTG = 70	0.53	1.14	2.07	0.35
	Field MTG = 60	3.23	4.13	5.10	0.42
	Field ATG = 50	1.1	2.41	4.03	0.71
H (m)	Field all = 180	0.21	0.36	0.52	0.079
	Field YTG = 70	0.21	0.34	0.46	0.054
	Field MTG = 60	0.40	0.47	0.52	0.025
	Field ATG = 50	0.22	0.31	0.38	0.036
W (%)	Field all = 180	61	68.54	76	3.91
	Field YTG = 70	68	72.40	76	1.52
	Field MTG = 60	61	66.03	73	2.64
	Field ATG = 50	62	66.11	75	2.91
LCC (SPAD)	Field all = 180	61.3	69.23	76.5	4.22
	Field YTG = 70	61.3	64.57	75.2	2.09
	Field MTG = 60	65.4	71.76	75.3	1.97
	Field ATG = 50	68.1	72.56	76.5	1.75
N (mg g^{-1})	Field all = 180	17.1	20.88	26.4	1.59
	Field YTG = 70	19.7	22.07	26.4	1.31
	Field MTG = 60	17.1	20.10	23.8	1.46
	Field ATG = 50	17.4	20.14	23.6	1.10

China), respectively. DJ M200 V2 (DJI, Inc., Shenzhen, China) was equipped with MS600 (Yusense, Inc., Qingdao, China) and Meditation XT2 (DJI, Inc., Shenzhen, China). The specific information about the UAV system and its flight mission are shown in Table 3.

Further processing of UAV remote sensing data

Figure 4 shows the overall framework for evaluating tea phenotype based on multi-source remote sensing data. First, 65 variables are extracted from LiDAR, TC, MS, RGB, and TM images. Second, the variables were screened by Pearson's correlation analysis. Then, using four machine learning methods, five tea phenotypic data are used to model the selected variables. R^2, RMSE, and NRMSE are used to evaluate the quality of the model. To eliminate the influence of flight altitude on the data set, we extract the marked coordinate points from the LiDAR image and input the marked coordinate points in other images during the splicing process.

a) The LiDAR data collected by Meditation L1 were used to establish point cloud model by DJI SmartMap software (DJI, Inc., Shenzhen, China). The processing process includes screening the high-density point cloud, output coordinate system location CGRS93, point cloud accuracy optimization, and reconstruction.
b) The TC data collected by Meditation P1 were used to establish point cloud model by DJI SmartMap software. The processing process includes selecting high-definition images, oblique and orthographic shooting scenes, and reshaping.
c) The MS data collected by MS600 were spliced by Yusense Map V1.0 (Yusense, Inc., Qingdao, China). The processing process includes generating the registration parameters for image registration, inputting white board reflectivity radiometric calibration, and splicing multispectral images (Luo et al., 2021).
d) The TM and RGB data collected by Meditation XT2 were spliced by Yusense Map V1.0. The processing process includes data import, camera parameter generation, image splicing, and temperature calibration.
e) For LiDAR and OC data, Alandur Platform Free software (ALD. Inc., Chengdu, China) was used to cut plots and extract variables. For MS and RGB data, ENVI 5.2 software was used for plot clipping, band, and texture extraction. For TM data, FLIR Tools (Teledyne FLIR, USA) software was used for cropping of plots and extraction of temperature information. For MS and RGB data, ENVI 5.2 software was used for plot clipping, band, and texture extraction. Python 3.7 and MATLAB 2020



FIGURE 2
(A) Determination of the W; **(B)** determination of the H; **(C)** determination of the LCC and LCN; **(D)** determination of the LAI.

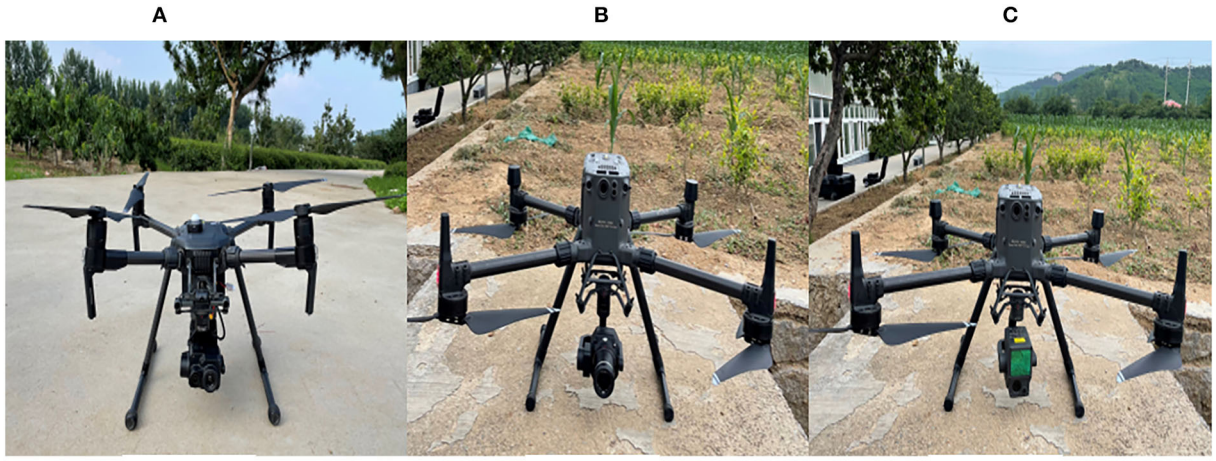

FIGURE 3
(A) M200 V2 carries with MS600 and Meditation XT2; **(B)** the M300 RTK carries Meditation P1; **(C)** the M300 RTK carries with Meditation L1.

TABLE 3 Specific information on UAV systems and their flight missions.

UAV platforms	Sensors	Flight height (m)	Flying speed (m s^{-1})	Overlap (%)	Accuracy (cm $pixel^{-1}$)
M300 RTK	Meditation L1	50	6	70 (front) 80 (side)	0.8
M300 RTK	Meditation P1	50	6	70 (front) 80 (side)	0.7
M200 V2	MS600	15	2	55 (front) 75 (side)	1.2
M200 V2	Meditation XT2	15	2	55 (front) 75 (side)	1.0

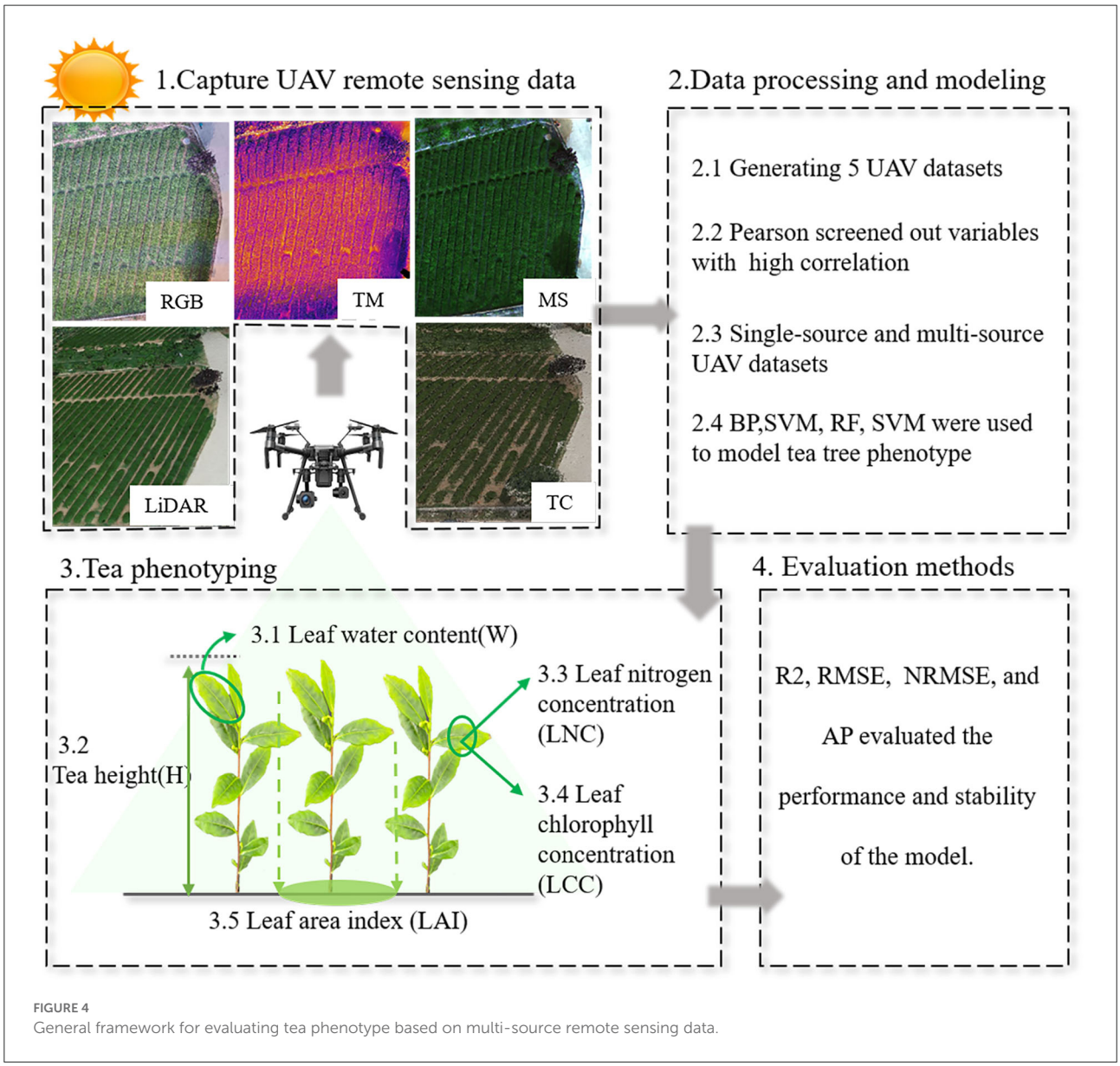

FIGURE 4
General framework for evaluating tea phenotype based on multi-source remote sensing data.

TABLE 4 Definitions of the features extracted from different sensors and imagery.

Sensor	Fentures	Formula	References
LiDAR	Point cloud density	L.PCD = NOPC	Su et al., 2016
	Laser penetration index	L.LPI = NOGPC/NOGPC+NOCPC	
	Porosity	L.Fgap = NOGPCE/TNOPCE	
	Height mean	Mean height of tree crown	
	Height maximum	Maximum height of tree crown	
	Height percentile (5, 15, 25, 35, 45, 55, 65, 75, 85, 95%)	Percentile height of echo return point	
TC	Point cloud density	P.PCD = NOPC	Su et al., 2016; Ying et al., 2020
	Porosity	P.Fgap = NOGPE/TNOPE	
	Height mean	Mean height of tree crown	
	Height maximum	Maximum height of tree crown	
	Height percentile (5, 15, 25, 35, 45, 55, 65, 75, 85, 95%)	Percentile height of echo return point	
MS	450, 555, 660, 720, 750, 840 nm	The raw value of each band	
	Normalized difference vegetation index	NDVI = (NIR–R)/(NIR+R)	Peñuelas et al., 1997
	Ratio vegetation index	RVI = NIR/R	Jordan, 1969
	Difference vegetation index	DVI = NIR–R	Richardson and Wiegand, 1977
	Enhanced vegetation index	EVI = 2.5(NIR–R)/(NIR+6R−7.5B+1)	Hui and Huete, 1995
	Renormalized difference vegetation index	RDVI = (NIR–R)/($\sqrt{NIR + R}$)	Roujean and Breon, 1995
	Triangular vegetation index	TVI = 60(NIR–G) – 100(R–G)	Broge and Leblanc, 2001
	Soil-adjusted vegetation index	SAVI = 1.5(NIR–R)/(NIR+R+0.5)	Huete, 1988
	Nonlinear vegetation index	NIR = (NIR^2-R)/(NIR^2+R)	Goel and Qin, 1994
	Red-edge chlorophyll index	RECI = NIR/R−1	Gitelson et al., 2006
	Modified nonlinear vegetation index	MNLI = 1.5 (NIR^2-R)/(NIR^2+R+0.5)	Peng et al., 2003
	Optimization of soil-adjusted vegetation index	OSAVI = 1.16(NIR–R)/(NIR+R+0.16)	Rondeaux et al., 1996
	Green normalized difference vegetation index	GNDVI = (NIR–G)/(NIR +G)	Gitelson et al., 1996
	Red-edge NDVI	RENDVI = (R750–R720)/(R750+R710)	Gitelson and Merzlyak, 1996
RGB	Gray-level co-occurrence matrix (GLCM)	ME, VA, HO, CO, DI, EN, SE, CO	Haralick et al., 1973
TM	Temperature maximum	TMAX	Zhu et al., 2021
	Temperature minimum	TMIN	
	Temperature mean	TI/I	

NP, number of point clouds; NOGPC, number of ground point clouds; NOCPC, number of canopy point clouds; NOGPCE, number of ground point clouds echoes; TNOPCE, total number of point cloud echoes.

were used for further processing and analysis of remote sensing data.

The extraction of UAV remote sensing information

To clearly display the remote sensing indicators used in this article, we classify and rank the variables extracted from LiDAR, TC, MS, RGB, and TM data, as shown in Table 4.

Extraction of LiDAR information

The point cloud model of LiDAR data was further processed by Alandur Platform Free software. The processing process includes denoising, filtering, normalization, and generating DSM model and DEM models. DSM model subtracts DEM model to further generate canopy height model (CHM). In this way, five variables can be extracted: point cloud density (PCD), laser penetration index (LPI), porosity (Fgap), height mean (Hmean), and height maximum (Hmax). The height information was related to the Z coordinate system of point cloud data. Therefore, the Z coordinate system of the point cloud model was rearranged by Python 3.8 to obtain a total of 10 variables of height percentile, namely H5th, H15th, H25th, H35th, H45th, H55th, H65th, H75th, H85th, and H95th. Therefore, the LiDAR data set contains 5 + 10 = 15 variables.

Extraction of TC information

The extraction of TC information was basically the same as that of LiDAR information, but there were

no LPI variables. Thus, the TC data set contained $4 + 10 = 14$ variables.

Extraction of MS information

MS data were extracted into six original bands through ENVI 5.2, including 450, 555, 660, 720, 750, and 840 nm. In addition, we applied 13 vegetation indices commonly used in previous studies. Therefore, the MS data set contains $6 + 13 = 19$ variables.

Extraction of RGB information

Because MS data provide spectral information, we use high-resolution RGB data to extract texture information. The texture information was extracted from the gray-level co-occurrence matrix (GLCM) of green, red, and blue bands by ENVI 5.2 software, and the processing window is 3 lines × 3 columns. GLCM texture includes eight indexes: mean, variance, homogeneity, contrast, dissimilarity, entropy, second moment, and correlation. Therefore, the RGB data set includes $3 \times 8 = 24$ variables.

Extraction of TM information

For thermal sensors, temperature is the most important information. Therefore, we use FLIR Tools software to extract three temperature variables from TM data, namely temperature maximum (Tmax), temperature minimum (Tmin), and temperature mean (Tmean).

Data modeling and validation

In this study, BP, SVM, RF, and PLS neural networks were used to analyze the data and establish the model. BP neural network had the ability of data integration and analysis, which could be used to analyze the nonlinear relationship between parameters affecting phenotypes (Liu et al., 2016). SVM had unique advantages in solving small sample, nonlinear, and high-dimensional pattern recognition problems, and its network structure is more complex, with strong generalization and prediction ability (Qin and He, 2005). PLS combined the advantages of principal component analysis, canonical correlation analysis, and multiple linear regression analysis and can handle the problem of multicollinearity between feature attributes (Lin et al., 2016). RF can balance errors for unbalanced data sets and has fast training speed, and it was easy to make a parallelization method (Iverson et al., 2008).

The variables of multi-source data sets and single-source data sets were screened by Pearson's correlation analysis, and the variables with high correlations were selected to be input into the four networks. To further expand the number of samples and ensure the accuracy of the algorithm, this study uses the method of 10-fold cross-validation to divide the data set into 10 parts, of which nine parts were used as the training set and one part was used as the test set, repeated 100 times, and finally calculate the average value of the results. The performance of the model was evaluated by determining R Square (R^2), root mean square error (RMSE), and normalized root mean square error (NRMSE). The larger R^2, the smaller RMSE and NRMSE, indicating the better performance of the model. The stability of the data set to different models was evaluated by average precision (AP). R^2, RMSE, NRMSE, and AP were as follows:

$$R^2 = \frac{\sum_{i=1}^{n} (x_i - \bar{x})^2 \times (y_i - \bar{y})^2}{\sum_{i=1}^{n} (x_i - \bar{x})^2 \times \sum_{i=1}^{n} (y_i - \bar{y})^2} \quad (2)$$

$$RMSE = \sqrt{\frac{\sum_{i=1}^{n} (y_i - x_i)^2}{n}} \quad (3)$$

$$NRMSE = \frac{RMSE}{\bar{x}} \quad (4)$$

$$AP = \frac{\sum_{i=1}^{n} R_i}{n} \quad (5)$$

Results and analysis

Phenotypic analysis of tea crowns at different growth stages

To obtain the phenotypic information of tea crown, LAI, H, W, LCC, and LNC were measured by artificial method (Figure 5). The H of MTG is about 0.5 m, and the LAI is about 5 m^2m^{-2}, which is the largest among the three tea gardens, indicating that the canopy of MTG is the densest. The LAI of YTG is about 0.1 m^2m^{-2}, which is the smallest of the three tea gardens, indicating that the tea plant is in the growth stage. For W, the water content of tea leaves in YTG is the largest, which is 73%, and the W of MTG and ATG is lower. For LCC, the chlorophyll of ATG tea leaves is the largest, and the SPAD value is about 73. The chlorophyll of YTG tea leaves is the smallest, and the SPAD value is about 65. For LNC, the average LNC of MTG and ATG is about 20 mg g^{-1}, which indicates that tea plants are seriously deficient in nitrogen.

Contribution of single-source remote sensing data to estimation of tea crown phenotypic

Screening of single-source UAV remote sensing data

To screen out the variables with high correlation, we performed Pearson's correlation analysis between all variables of five single-source remote sensing data sets and tea crown phenotype data. In addition, we selected 1–9 variables with high

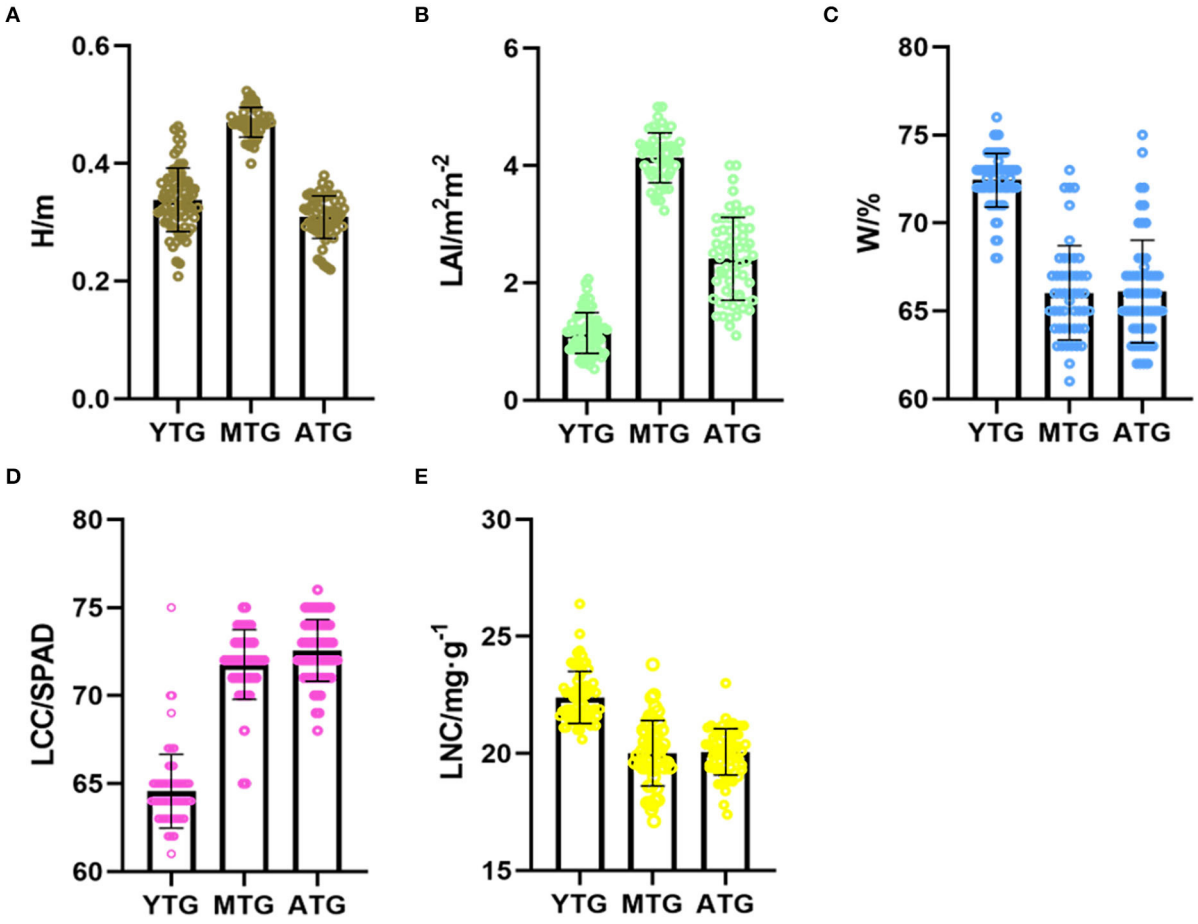

FIGURE 5
Phenotypes of tea crowns at different growth stages. **(A)** H; **(B)** LAI; **(C)** W; **(D)** LCC; **(E)** LNC.

correlation as the input of single-source remote sensing data to establish the model (Figure 6). In Figure 6, * and ** represent the significance levels of $P < 0.05$ and $P < 0.01$, respectively.

To evaluate the H of tea crown, L.Hmax, L.Hmean, L.H85th, and L.H95th variables of LiDAR were selected for modeling; P.Hmax, P.H65th, P.H75th, P.H85th, and P.H95th variables of TC were selected for modeling; RV, RContrast, GV, Gcontrast, and BV variables of RGB were selected for modeling; MEAN.B.450 and MEAN.R.660 variables of MS were selected for modeling; Tmax variable of TM was selected for modeling.

To evaluate the LAI of tea crown, L.Fgap, L.H35th, L.H45th, L.H55th, L.H65th, and L.H75th variables of LiDAR were selected for modeling; P.Fgap, P.H35th, P.H45th, and P.H55th variables of TC were selected for modeling; RV, Rcontrast, GV, Gcontrast, BV, and Bcontrast variables of RGB were selected for modeling; MEAN.R.660, PVI, RECI, and RENDVI variables of MS were selected for modeling; Tmax and Tmin variables of TM were selected for modeling.

To evaluate the W of tea crown, L.Fgap, L.H35th, L.H45th, L.H55th, L.H65th, and L.H75th variables of LiDAR were selected for modeling; P.Fgap, P.H15th, P.H25th, P.H35th, and P.H45th variables of TC were selected for modeling; RM, RASM, GM, GCorrelation, BM, and BASM variables of RGB were selected for modeling; SAVI, MNLI, GNDVI, and RENDVI variables of MS were selected for modeling; Tmax and Tmin variables of TM were selected for modeling.

To evaluate the LCC of tea crown, L.Fgap, L.H35th, L.H45th, L.H55th, L.H65th, and L.H75th variables of LiDAR were selected for modeling; P.Fgap, P.H15th, P.H 25th, P.H35th, and P.H45th variables of TC were selected for modeling; RM, RASM, RCorrelation, GM, GASM, GCorrelation, BM, BASM, and BCorrelation variables of RGB were selected for modeling; MEAN.RE.720, MEAN. NIR. 750, EVI, RDVI, and MNLI variables of MS were selected for modeling; Tmax and Tmin variables of TM were selected for modeling.

To evaluate the LNC of tea crown, L.Fgap, L.H35th, L.H45th, L.H55th, L.H65th, and L.H75th variables of LiDAR were selected for modeling; P.Fgap, P.H25th, P.H35th, and P.H45th variables of TC were selected for modeling; RM, RASM, RCorrelation, GM GASM, GCorrelation, BM,

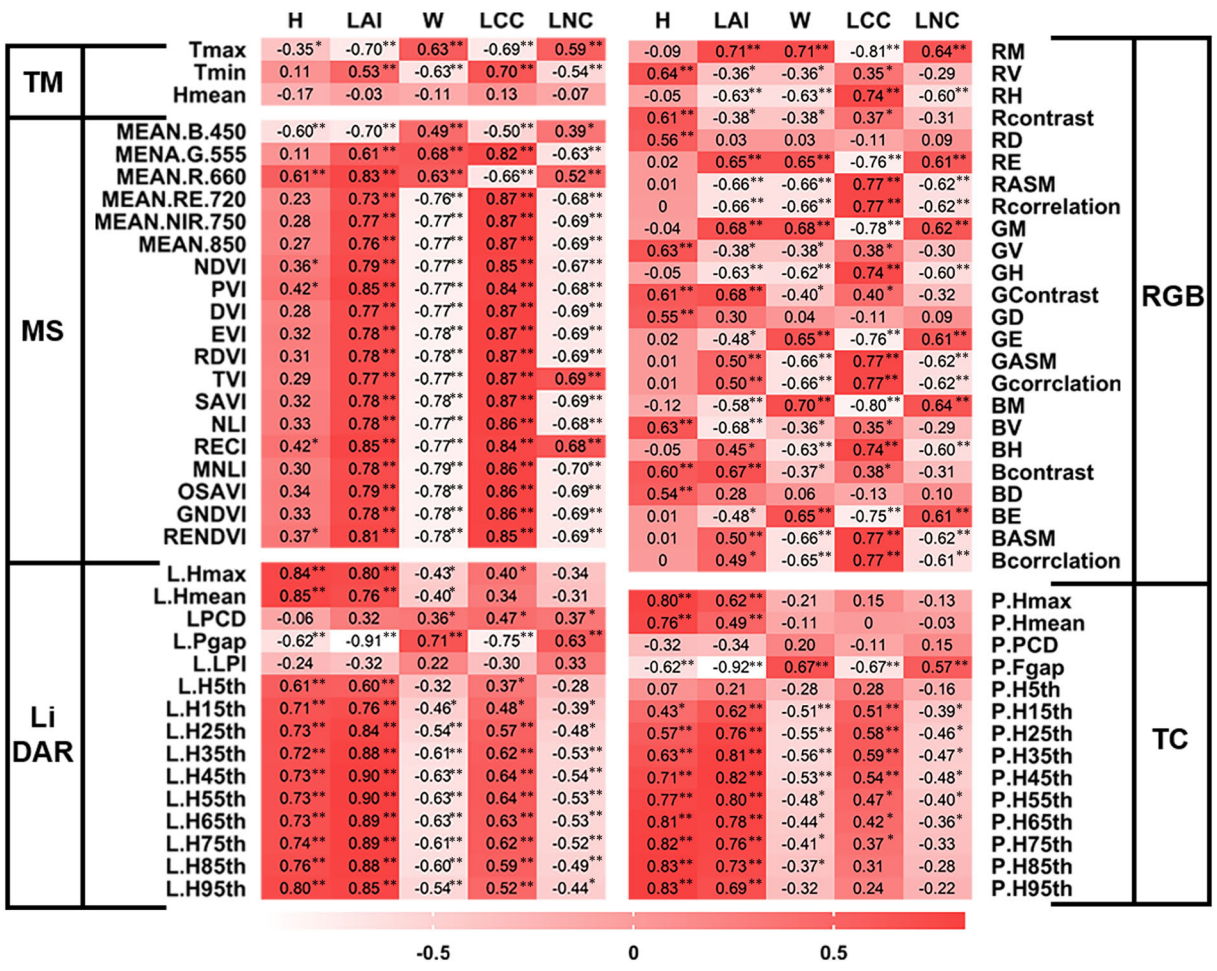

FIGURE 6
Selected single-source remote sensing variables with high correlation. * and ** represent the significance levels of $P < 0.05$ and $P < 0.01$, respectively.

BASM, and BCorrelation variables of RGB were selected for modeling; MEAN.NIR. 750, MEAN. 840, EVI, SAVI, RDVI, MNLI, and GNDVI variables of MS were selected for modeling; Tmax and Tmin variables of TM were selected for modeling.

Performance of single-source UAV data on tea plant phenotyping

After selecting the appropriate single-source data, BP, SVM, RF, and PLS of machine learning methods were used to model the single-source remote sensing data and tea crown phenotype data. The results showed that the evaluation of crown phenotype by data from various sensors was significantly different (Figures 7, 8).

For the estimation of H, the model established by LiDAR and TC data has higher accuracy, and the AP value in the model established by LiDAR data is higher. The data from MS, RGB, and TM are not suitable for estimating tea plant height. The RF model established by LiDAR data has the best evaluation effect ($Rp^2 = 0.82$, RMSEP = 0.031, and NRMSEP = 0.089).

For the estimation of LAI, the model established by TC, LiDAR, and MS data has high accuracy. In the model established by TC data, the AP value is the largest, so its stability is the highest. The SVM model established by TC data has the highest accuracy ($Rp^2 = 0.84$, RMSEP = 0.45, and NRMSEP = 0.19).

For the estimation of W, the model established by RGB and TM data has high accuracy. In comparison, the AP value in the model established from RGB data is higher, so its stability is higher. The RF model established from TM data has the best evaluation effect ($Rp^2 = 0.72$, RMSEP = 1.9, and NRMSEP = 0.03).

For the estimation of LCC, the performance and stability of the model established by MS data are the best. The BP model

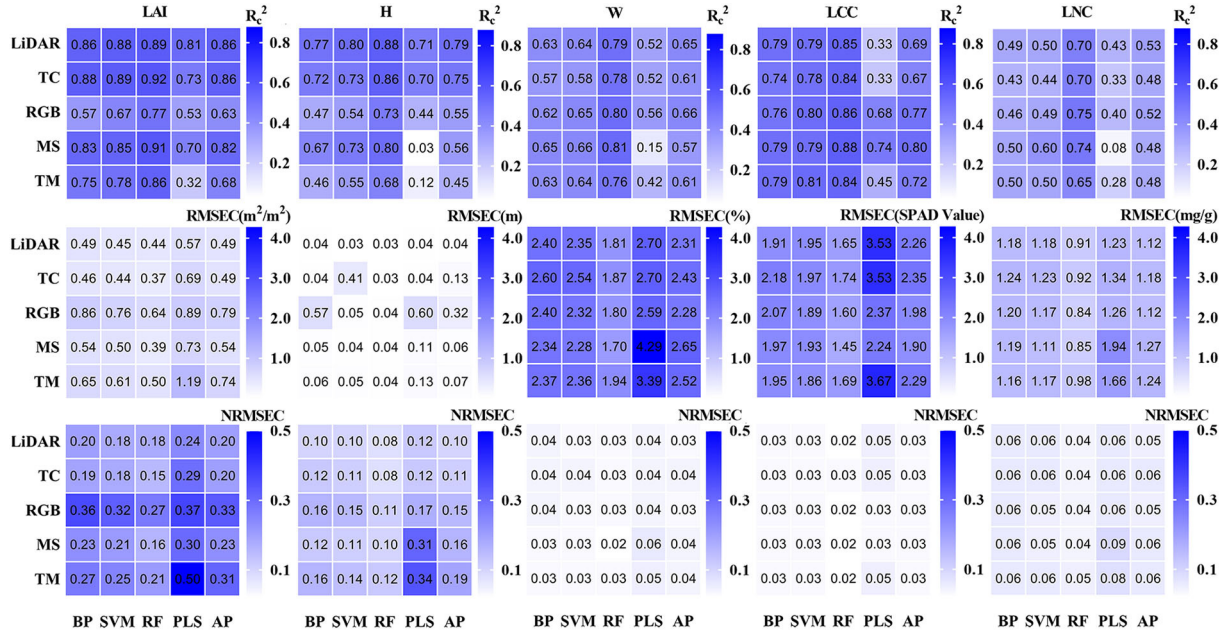

FIGURE 7
Result of the training set.

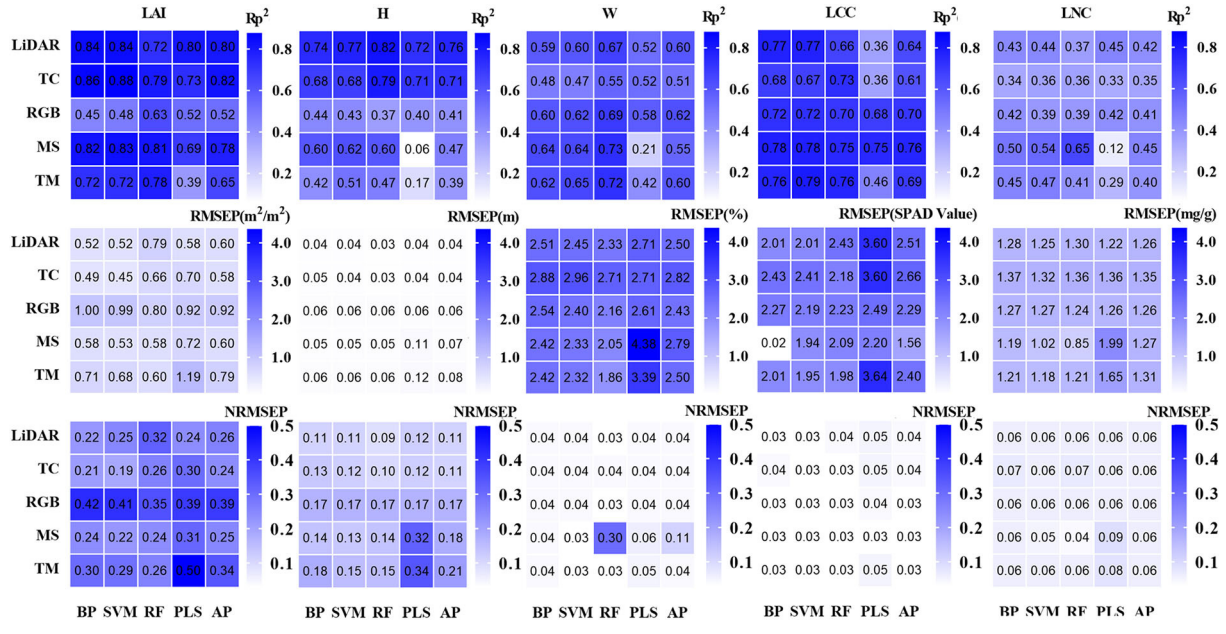

FIGURE 8
Result of the test set.

established by MS data has the highest accuracy (Rp^2 = 0.78, RMSEP = 1.9, and NRMSEP = 0.029).

For the estimation of LNC, the AP value and accuracy of the model established by each data are low. In comparison, the RF model established by MS data has the highest accuracy (Rp^2 = 0.65, RMSEP = 0.85, and NRMSEP = 0.04).

In conclusion, LiDAR and TC data are better in evaluating H and LAI of tea crowns. MS data

are better in evaluating LAI, LCC, and LNC of tea crowns. RGB and TM data are better to evaluate the W of tea crowns.

Contribution of multi-source remote sensing data to estimation of tea crown phenotypic

Screening of multi-source UAV remote sensing data

To evaluate the effect of multi-source remote sensing data on tea phenotype, we screened 2–7 variables with high correlation as the input of multi-source remote sensing data to establish model. To eliminate the influence of the number of variables on the comparison of single-source data and multi-source data, we keep the number of input variables unchanged. To evaluate the H of tea crown, L.Hmax, L.Hmean, P.H85th, and P.H95th variables of LiDAR + TC were selected for modeling. To evaluate the LAI of tea crown, L.Fgap, L.H45th, P.Fgap, and PVI variables of LiDAR + TC + MS were selected for modeling. To evaluate the W of tea crown, RM and Tmax variables of RGB+ TM were selected for modeling. To evaluate the LCC of tea crown, RM, MEAN.RE.720, MEAN.NIR. 750, EVI, and RDVI variables of RGB+ MS were selected for modeling. To evaluate the LNC of tea crown, L.Fgap, RM, BM, Tmax, SAVI, MNLI, and GNDVI variables of LiDAR + RGB + MS + TM were selected for modeling.

Performance of multi-source UAV data on tea plant phenotyping

After selecting the appropriate multi-source remote sensing data, BP, SVM, RF, and PLS of machine learning methods were used to model the multi-source remote sensing data and tea crown phenotype data. The results show that the multi-source remote sensing data from multiple sensors have a good effect on the evaluation of tea crown phenotype (Table 5). For the estimation of H, the effect of SVM model is the best ($Rc^2 = 0.87$, $Rp^2 = 0.82$, RMSEC = 0.03, RMSEP = 0.04, NRMSEC = 0.078, and NRMSEP = 0.09); for the estimation of LAI, the effect of SVM model is the best ($Rc^2 = 0.91$, $Rp^2 = 0.90$, RMSEC = 0.39, RMSEP = 0.40, NRMSEC = 0.15, and NRMSEP = 0.17); for the estimation of W, the effect of SVM model is the best ($Rc^2 = 0.68$, $Rp^2 = 0.62$, RMSEC = 1.8, RMSEP = 1.8, NRMSEC = 0.03, and NRMSEP = 0.03); for the estimation of LCC, the effect of RF model is the best ($Rc^2 = 0.89$, $Rp^2 = 0.85$, RMSEC = 1.4, RMSEP = 1.8, NRMSEC = 0.02, and NRMSEP = 0.03); for the estimation of LNC, the effect of RF model is the best ($Rc^2 = 0.73$, $Rp^2 = 0.57$, RMSEC = 0.85, RMSEP = 0.92, NRMSEC = 0.04, and NRMSEP = 0.04). Figure 9 shows the scatter plot of the predicted value and actual value distribution of the model with the highest accuracy among the five phenotypic parameters.

Comparison of single-source and multi-source remote sensing data to evaluate the results of tea crowns phenotype

To more clearly and intuitively compare the evaluation results of multi-source remote sensing data and single-source remote sensing data on the phenotypic parameters of tea crowns, we calculated the difference between the evaluation results from the multi-source remote sensing data model and the evaluation results of the single-source remote sensing data model with the highest accuracy (Figure 10). To eliminate the influence of the number of variables, we keep the same number of variables input from multi-source data and single-source data. Table 6 shows the validation statistics of tea phenotypic parameters evaluated by single-source data set model with the highest accuracy and multi-source data set model. The results show that in evaluating the H of tea crowns, the accuracy of the model established by the fused LiDAR and TC data is greatly improved than that of LiDAR data, and the accuracy of the RF model is the highest. In evaluating the LAI of tea crowns, the accuracy of the model established by the fused LiDAR, TC, and MS data is improved than that of TC data; in evaluating the W of tea crowns, the accuracy of the model established by the fused RGB and TM data is greatly improved than that of RGB data, and the accuracy of the RF model is the highest. In evaluating the LCC of tea crowns, the accuracy of the model established by the fused MS and RGB data is greatly improved than that of the MS data. In evaluating the LNC of tea crowns, the accuracy of the model established by the fused LiDAR, MS, RGB, and TM data is significantly less than that of MS data, and the accuracy of the PLS model is the highest.

Discussion

To select suitable single-source remote sensing data set to evaluate the phenotypic parameters of tea crowns

The results of this study verify that UAV remote sensing data sets from different sources are suitable for specific tea phenotypic parameters. LiDAR and TC sensors are dominant in monitoring H and LAI. The data obtained by the two sensors can establish a three-dimensional point cloud model to restore the crown structure of tea plants. Previously, researchers used LiDAR sensors to establish 3D point cloud models to monitor the forest canopy structure (Schneider et al., 2019). Some researchers also used oblique camera to establish 3D point cloud models to monitor the height and leaf area index of corn (Ying et al., 2020). These results are in accordance with our findings. The canopy structure of plants may be monitored using LiDAR and a TC camera. It is because LiDAR is an active sensor that the modeling accuracy of LiDAR data is higher than that of the

TABLE 5 Phenotypic evaluation of tea plants based on multi-source remote sensing.

		Training sets			Test sets		
Phenotype	**Model**	**Rc^2**	**RMSEC**	**NRMSEC**	**Rp^2**	**RMSEP**	**NRMSEP**
H	BP	0.82	0.03	0.09	0.80	0.03	0.09
	SVM	0.87	0.03	0.08	0.82	0.04	0.09
	RF	0.90	0.02	0.07	0.81	0.04	0.09
	PLS	0.78	0.04	0.10	0.77	0.04	0.10
	AP	0.84	0.03	0.08	0.80	0.04	0.10
LAI	BP	0.9	0.4	0.16	0.88	0.46	0.19
	SVM	0.91	0.39	0.15	0.9	0.40	0.17
	RF	0.93	0.3	0.12	0.89	0.45	0.19
	PLS	0.84	0.5	0.21	0.84	0.51	0.22
	AP	0.89	0.39	0.16	0.85	0.49	0.22
W	BP	0.65	1.9	0.03	0.58	1.8	0.04
	SVM	0.68	1.8	0.03	0.62	1.8	0.03
	RF	0.78	1.8	0.03	0.49	1.9	0.04
	PLS	0.59	1.9	0.04	0.53	1.9	0.04
	AP	0.69	1.9	0.04	0.56	1.9	0.04
LCC	BP	0.78	2	0.03	0.75	1.9	0.03
	SVM	0.8	1.9	0.03	0.76	1.9	0.03
	RF	0.89	1.4	0.02	0.85	1.8	0.03
	PLS	0.75	2.1	0.03	0.74	2.2	0.03
	AP	0.81	1.85	0.03	0.79	2	0.03
LNC	BP	0.5	1.2	0.06	0.48	1.2	0.06
	SVM	0.52	1.2	0.06	0.46	1.2	0.06
	RF	0.73	0.85	0.04	0.57	0.92	0.04
	PLS	0.47	1.18	0.06	0.46	1.2	0.06
	AP	0.56	1.1	0.05	0.5	1.1	0.06

TC data. The principle of LiDAR data acquisition is to transmit laser signals, which are reflected by tea plants and collected by the receiving system, so the penetration is better. However, we advocate utilizing TC cameras to monitor canopy structure for certain tea plants with low canopy structure. On the one hand, the TC camera can provide high-precision RGB data and 3D point cloud data; on the other hand, the TC camera is far less expensive than LiDAR.

RGB and MS sensors are dominant in monitoring LCC and LNC indexes of tea plants. Previous studies used multispectral data to estimate the nitrogen concentration of winter wheat (Tao et al., 2020). Here, we evaluated the accuracy of textural characteristics and spectral information in assessing the LCC of tea crowns, unlike aforementioned investigation. Our approach transforms in a model with a greater level of accuracy than one based on texture characteristics. We can utilize hyperspectral sensors for intensive analysis if we want to better monitor the LCC of the tea canopy, and hyperspectral sensors can collect more spectral information. Zhu et al. (2021) utilized hyperspectral data to determine the chlorophyll content of maize leaves.

The TM sensor has great potential in monitoring the water content of tea crown leaves. This was mainly because the thermal sensor could obtain the canopy temperature of crops, and there was a certain relationship between the temperature information and leaf water content (Luz and Crowley, 2010). In recent years, thermal sensors were more and more widely used in monitoring crop leaf water content (Maimaitijiang et al., 2020), such as researchers used thermal sensors to monitor changes in wheat moisture content and achieved good results (Abdelhakim et al., 2021). However, in this study, the accuracy of leaf water content prediction model is low, which may be due to the complexity and uncontrollability of field environment affecting the acquisition of temperature information. Therefore, if we can accurately obtain the changing trend of field environmental factors, such as wind speed, temperature, and humidity, it will help us to improve the accuracy of the model, which needs further research in the later stage.

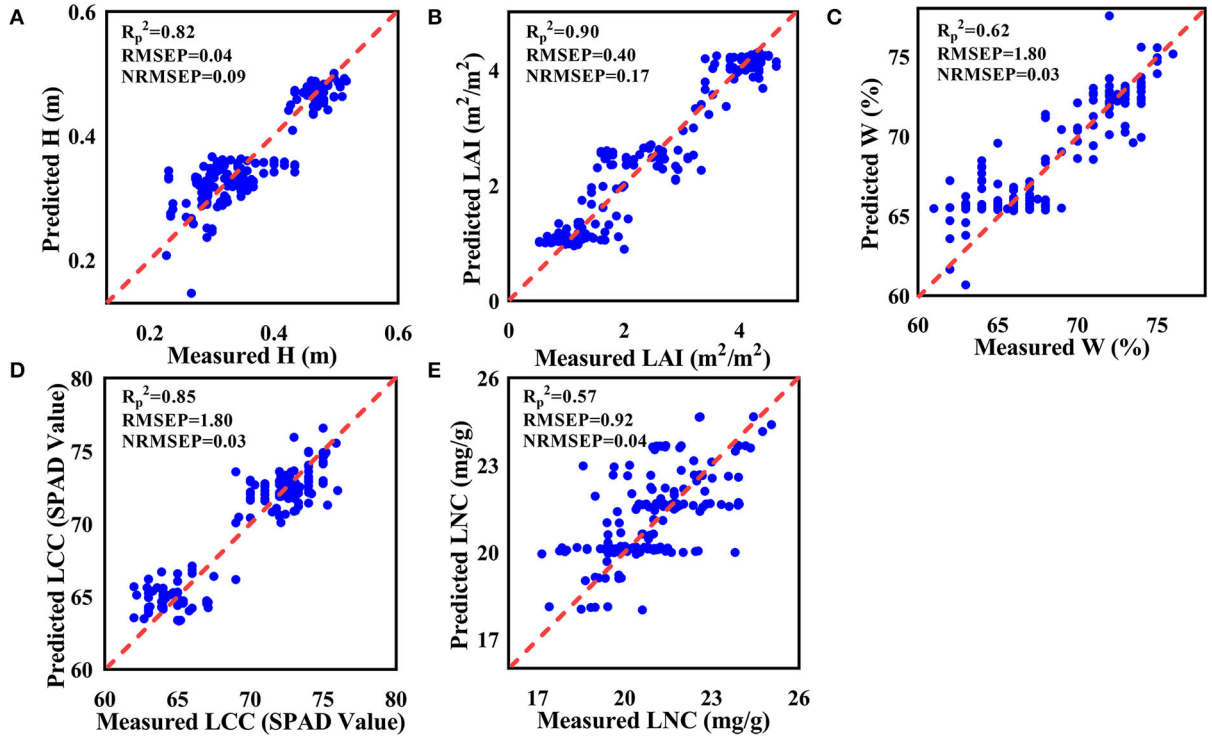

FIGURE 9
Scatter plot of predicted and actual values of the model. **(A)** H; **(B)** LAI; **(C)** W; **(D)** LCC; **(E)** LNC.

To select suitable multi-source remote sensing data set to evaluate the phenotypic parameters of tea crowns

In this research, the accuracy of the model established by the combined LiDAR and TC data is much greater than that of the model established by single-source data while evaluating H of tea crown. This may be due to the strong fault tolerance of multi-source data, which reduces the impact of environmental factors on specific types of data, improves spatial resolution, and enriches remote sensing image information; the accuracy of the model established by the fused LiDAR, TC, and MS data is small improved than that of the model established by single-source data while evaluating the LAI of tea crowns. However, previous researchers used multi-source remote sensing data to evaluate LAI of maize, which greatly improved the accuracy of the model (Liu et al., 2021). We analyze the reasons for the difference in accuracy between the tea plants and maize. On the one hand, because tea plants have the characteristics of high canopy density, especially in mature tea gardens, the measuring instrument is difficult to reach the center to measure the LAI. Therefore, there are errors in the measurement, which will affect the accuracy of the model. On the other hand, the evaluation of maize LAI is based on the fusion of RGB, MS, and TM data, while the evaluation of tea leaf area index is based on the fusion of LiDAR, TC, and MS data. Different data types may lead to different improvement of model accuracy. The accuracy of the model established by the fused LiDAR, MS, RGB, and TM data is much higher than that of the model established by single-source data while evaluating the W of tea crowns. Previously, researchers used the fusion of RGB texture features and vegetation index to evaluate the water content of rice, and the research results were consistent with our research results (Wan et al., 2020). However, different from our research method, we have more data types and larger amount of data to evaluate the water content of tea leaves, so the improvement of model accuracy is also greater. The accuracy of the model established by multi-source remote sensing data is improved than that of the model established by single-source remote sensing data while evaluating the LCC of tea crowns. Previously, multi-source remote sensing data were used to evaluate corn LCC and also proved that the accuracy of multi-source remote sensing data model is higher than that of single-source model in evaluating LCC (Zhu et al., 2021). The accuracy of the model established by MS data is improved than that of the model established by LiDAR + RGB + MS + TM data while evaluating the LNC of tea crowns. This may be because the LNC of tea plant only has a strong response to spectral information, but has a weak response to thermal information and texture information. At present, there are few literature on

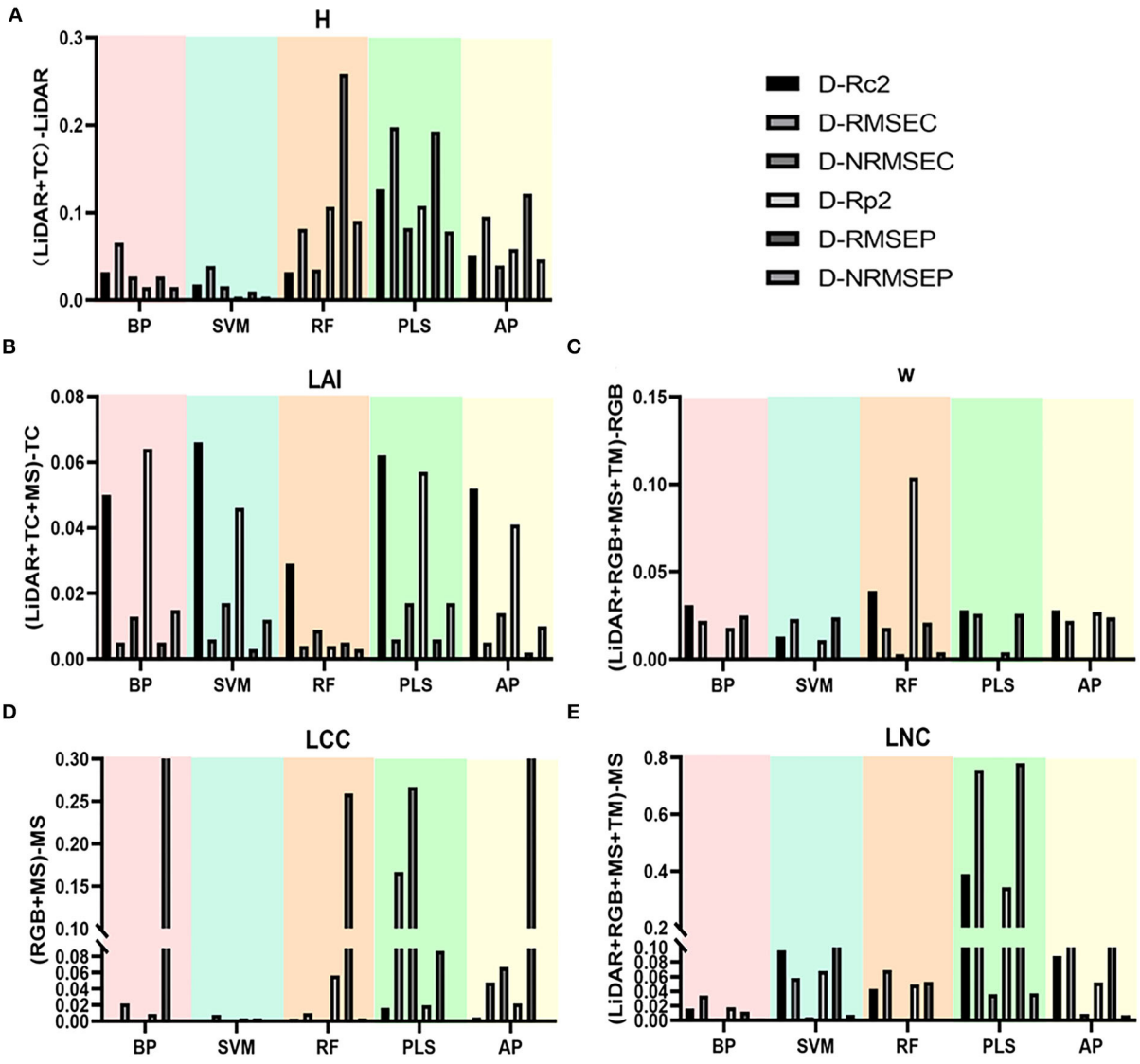

FIGURE 10
Evaluation results of single source and multi-source UAV data on tea crown phenotype. **(A)** H; **(B)** LAI; **(C)** W; **(D)** LCC; **(E)** LNC.

the evaluation of crop nitrogen content by multi-source remote sensing data.

Effects of different machine learning algorithms on phenotypic evaluation of tea crown

While examining tea phenotypes, the accuracy of SVM, RF, and BP models is distinct by using a single data set. Among them, the SVM model has the highest accuracy in evaluating LAI, the RF model has the highest accuracy in evaluating H, W, and LNC, and the BP model has the highest accuracy in evaluating LCC. However, the stability of the BP model is low, and the accuracy decreases in the evaluation of LAI and W. As consistent with previous studies, using BP algorithm to establish corn leaf area index and leaf water content model, the number of samples is too small, resulting in low model accuracy. Therefore, BP neural network is suitable for large sample modeling. For small sample modeling, the stability is poor, and the parameters need to be adjusted constantly (Zhu et al., 2021). The accuracy of the PLS model is the lowest and in evaluating LCC and W of tea canopy, $Rp^2 < 0.3$. This is consistent with previous studies. SVM, BP, and PLS algorithms were used to build the prediction model of nitrogen, tea polyphenols, and amino acid content in

TABLE 6 Validation statistics of tea phenotypic parameters evaluated by single-source data set model with the highest accuracy and multi-source data set model.

Phenotypic parameters	Sensor type	No. of feature	Metrics	BP	SVM	RF	PLS	AP
H	LiDAR	4	Rp^2	0.74	0.77	0.81	0.72	0.76
			RMSEP	0.040	0.039	0.031	0.043	0.038
			NRMSEP	0.11	0.11	0.089	0.12	0.11
	LiDAR+TC	4	Rp^2	0.80	0.82	0.81	0.77	0.80
			RMSEP	0.034	0.036	0.036	0.037	0.036
			NRMSEP	0.094	0.094	0.092	0.10	0.095
LAI	TC	4	Rp^2	0.86	0.88	0.79	0.73	0.81
			RMSEP	0.49	0.45	0.66	0.70	0.58
			NRMSEP	0.21	0.19	0.26	0.30	0.24
	LiDAR+TC+MS	4	Rp^2	0.88	0.9	0.89	0.84	0.85
			RMSEP	0.46	0.42	0.45	0.51	0.49
			NRMSEP	0.19	0.19	0.19	0.22	0.22
W	TM	2	Rp^2	0.55	0.6	0.49	0.49	0.52
			RMSEP	2.4	2.3	3.4	3.4	2.5
			NRMSEP	0.035	0.034	0.030	0.049	0.037
	RGB+TM	2	Rp^2	0.58	0.62	0.49	0.53	0.56
			RMSEP	1.8	1.8	1.9	1.9	1.9
			NRMSEP	0.04	0.03	0.04	0.04	0.04
LCC	MS	5	Rp^2	0.78	0.77	0.75	0.75	0.76
			RMSEP	2.2	1.9	2.1	2.2	1.6
			NRMSEP	0.029	0.028	0.030	0.032	0.03
	RGB+MS	5	Rp^2	0.75	0.78	0.85	0.74	0.79
			RMSEP	1.9	1.9	1.8	2.2	2
			NRMSEP	0.03	0.03	0.03	0.03	0.03
LNC	MS	7	Rp^2	0.50	0.54	0.65	0.12	0.45
			RMSEP	1.2	1.02	0.85	2.0	1.3
			NRMSEP	0.057	0.049	0.040	0.095	0.060
	LiDAR+RGB+MS+TM	7	Rp^2	0.48	0.46	0.57	0.46	0.5
			RMSEP	1.2	1.2	0.92	1.2	1.1
			NRMSEP	0.06	0.06	0.04	0.06	0.06

tea leaves, of which the prediction model established by PLS algorithm had the lowest accuracy (Luo et al., 2021). This may be because the principle of PLS algorithm is combined with principal component analysis (PCA) to reduce the dimension of data. Although this will improve the running speed of the model, it will also lose some data information, resulting in low accuracy of the model (Wold et al., 2001). When applied to an evaluation of the tea phenotype using multi-source data, the RF and SVM modeling algorithms provide more accurate results. Among them, the RF algorithm is the most effective one for establishing LCC and LNC content prediction models of tea crowns. This is due to the fact that RF is able to balance the faults and errors of different types of data sets and is simple to parallelize (Yuan et al., 2017). SVM algorithm is better to establish LAI, H, and W content prediction models of tea crowns, and this is because the SVM network structure is more complex and has strong generalization and prediction ability (Yuan et al., 2017). The accuracy of BP model based on multi-source remote sensing data is higher than that of BP model based on single-source remote sensing data. This may be due to the increase in the number of samples, which increases the fitting degree of the model and gives full play to the advantages of BP algorithm.

In our research, we found that RF and SVM models have stable performance and high accuracy. Our results are consistent with other researchers using machine learning method to establish phenotypic models of rice and maize (Cen et al., 2019; Lin et al., 2021; Wang et al., 2021). We prefer to use RF algorithm, because RF algorithm has simpler network structure and faster running speed.

Conclusion

In this study, the UAV is equipped with MS, TM, RGB, LiDAR, and TC sensors to monitor the tea height, leaf area index, leaf water content, leaf chlorophyll, and nitrogen concentration of the tea plantations in the three growth stages and obtain the structure information, spectral information, texture information, and temperature information of the tea plants. Remote sensing data were utilized to model with BP, SVM, RF, and PLS of machine learning algorithms, and the performance of single-source and multi-source remote sensing data sets to evaluate the crown phenotype of tea plants was studied. The main conclusions are as follows: On the one hand, using multi-source data sets to evaluate H, LAI, W, and LCC can greatly improve the accuracy and robustness of the model. For the evaluation of H, LiDAR + TC data sets are recommended for analysis, and SVM model provides the best estimation (Rp^2 = 0.82 and RMSEP = 0.078). For the evaluation of LAI, LiDAR + TC + MS data sets are recommended, and SVM model provides the best estimation (Rp^2 = 0.90 and RMSEP = 0.40). For the evaluation of W, RGB + TM data sets are recommended, and SVM model provides the best estimation (Rp^2 = 0.62 and RMSEP = 1.80). For the evaluation of LCC, MS +RGB data set is recommended for analysis, and RF model provides the best estimation (Rp^2 = 0.87 and RMSEP = 1.80). On the other hand, using single-source data sets to evaluate LNC can greatly improve the accuracy and robustness of the model. For the evaluation of LNC, MS data set is recommended for analysis, and RF model provides the best estimation (Rp^2 = 0.65 and RMSEP = 0.85).

Data availability statement

The original contributions presented in the study are included in the article/supplementary material, further inquiries can be directed to the corresponding author.

Author contributions

HL carried out the experiment, collected and organized data, processed the multi-source remote sensing data, and wrote the manuscript. YM provided the modification of the article's picture. ZD, YW, and KF proposed the hypothesis for this work, designed the experiment, helped organize the manuscript structure, and directed the study. YS participated in the design of the experiment and directed the study. All authors contributed to the article and approved the submitted version.

Funding

This research was funded by the Significant Application Projects of Agriculture Technology Innovation in Shandong Province (SD2019ZZ010), the Technology System of Modern Agricultural Industry in Shandong Province (SDAIT-19-01), the Special Foundation for Distinguished Taishan Scholar of Shangdong Province (ts201712057), the Livelihood Project of Qingdao City (19-6-1-64-nsh), and the Project of Agricultural Science and Technology Fund in Shandong Province (2019LY002, 2019YQ010, and 2019TSLH0802).

Conflict of interest

The authors declare that the research was conducted in the absence of any commercial or financial relationships that could be construed as a potential conflict of interest.

Publisher's note

All claims expressed in this article are solely those of the authors and do not necessarily represent those of their affiliated organizations, or those of the publisher, the editors and the reviewers. Any product that may be evaluated in this article, or claim that may be made by its manufacturer, is not guaranteed or endorsed by the publisher.

References

Abdelhakim, L. O. A., Rosenqvist, E., and Wollenweber, B. (2021). Investigating combined drought- and heat stress effects in wheat under controlled conditions by dynamic image-based phenotyping. *Agronomy* 11, 364. doi: 10.3390/agronomy11020364

Brand, O. Z. N., and Zonta, J. H. (2016). Hemispherical photography to estimate biophysical variables of cotton. *Rev. Bras. Eng. Agríc. Ambient* 20, 789. doi: 10.1590/1807-1929/agriambi.v20n9p789-794

Broge, N. H., and Leblanc, E. (2001). Comparing prediction power and stability of broadband and hyperspectral vegetation indices for estimation of green leaf area index and canopy chlorophyll density. *Remote Sens. Environ.* 76, 156–172. doi: 10.1016/S0034-4257(00)00197-8

Brook, A., Tal, Y., Markovich, O., and Rybnikova, N. (2021). Canopy volume as a tool for early detection of plant drought and fertilization stress: banana plant fine-phenotype. *bioRxiv2021*. doi: 10.1101/2021.03.04.433868

Cen, H., Wan, L., and Zhu, J. (2019). Dynamic monitoring of biomass of rice under different nitrogen treatments using a lightweight UAV with dual image-frame snapshot cameras. *Plant Methods* 15, 32. doi: 10.1186/s13007-019-0418-8

Chianucci, F., Disperati, L., Guzzi, D., Bianchini, D., Nardino, V., and Lastri, C. (2016). Estimation of canopy attributes in beech forests using true colour digital images from a small fixed-wing UAV. *Int. J. Appl. Earth Observ. Geoinform.* 47, 60–68. doi: 10.1016/j.jag.2015.12.005

Gitelson, A. A., Kaufman, Y. J., and Merzlyak, M. N. (1996). Use of a green channel in remote sensing of global vegetation from EOS-MODIS. *Remote Sens. Environ.* 58, 289–298. doi: 10.1016/S0034-4257(96)00072-7

Gitelson, A. A., Keydan, G. P., and Merzlyak, M. N. (2006). Three-band model for noninvasive estimation of chlorophyll, carotenoids, and anthocyanin contents in higher plant leaves. *Geophys. Res.* 33, 431–433. doi: 10.1029/2006GL026457

Gitelson, A. A., and Merzlyak, M. N. (1996). Signature analysis of leaf reflectance spectra: algorithm development for remote sensing of chlorophyll. *Plant Physiol.* 148, 494–500 doi: 10.1016/S0176-1617(96)80284-7

Goel, N. S., and Qin, W. (1994). Influences of canopy architecture on relationships between various vegetation indices and LAI and Fpar: a computer simulation. *Remote Sens.* 10, 309–347. doi: 10.1080/027572594095 32252

Haralick, R. M., Shanmugam, K., and Dinstein, I. (1973). "Textural features for image classification," in *IEEE Transactions on Systems, Man, and Cybernetics SMC-3*, 610–621.

Herwitz, S. R., Johnson, L. F., and Dunagan, S. E. (2004). Imaging from an unmanned aerial vehicle: agricultural surveillance and decision support. *Comp. Electron. Agric.* 44, 49–61. doi: 10.1016/j.compag.2004.02.006

Huete, A. R. (1988). A soil-adjusted vegetation index (SAVI). *Remote Sens. Environ.* 25, 295–309. doi: 10.1016/0034-4257(88)90106-X

Hui, Q. L., and Huete, A. (1995). A feedback based modification of the NDVI to minimize canopy background and atmospheric noise. *IEEE Trans. Geosci. Remote Sens. Environ.* 33, 457–465. doi: 10.1109/36.377946

Iverson, L. R., Prasad, A. M., Matthews, S. N., and Peters, M. (2008). Estimating potential habitat for 134 eastern US tree species under six climate scenarios. *Forest Ecol. Manage.* 254, 390–406. doi: 10.1016/j.foreco.2007.07.023

Jordan, C. (1969). Derivation of leaf-area index from quality of light on the forestfloor. *Ecology* 50, 663–666. doi: 10.2307/1936256

Kalaitzidis, C., Caporn, S., and Cutler, M. (2008). Estimating foliar nitrogen concentration of heather (*Calluna vulgaris*) from field and laboratory spectra. *Water Air Soil Pollut.* 194, 57–66. doi: 10.1007/s11270-008-9698-8

Lin, D., Shuo, S., Jian, Y., Jia, S., and Wei, G. (2016). Using different regression methods to estimate leaf nitrogen content in rice by fusing hyperspectral LiDAR data and laser-induced chlorophyll fluorescence data. *Remote Sens. Environ.* 8, 526–526. doi: 10.3390/rs8060526

Lin, W., Jiating, L., Lin, Z., Biquan, Z., Geng, B., Yufeng, G., et al. (2021). "Investigate the potential of UAS-based thermal infrared imagery for maize leaf area index estimation," in *Proc.SPIE.*

Liu, H., Zhu, H., and Ping, W. (2016). Quantitative modelling for leaf nitrogen con-tent of winter wheat using UAV-based hyperspectral data. *Int. J. Remote Sens.* 38, 2117–2134. doi: 10.1080/01431161.2016.1253899

Liu, S., Jin, X., Nie, C., Wang, S., and Liu, Y. (2021). Estimating leaf area index using unmanned aerial vehicle data: shallow vs. deep machine learning algorithms. *Plant Physiol.* 187, 1551–1576. doi: 10.1093/plphys/kiab322

Lowe, T., Moghadam, P., Edwards, E., and Williams., J. (2021). Canopy density estimation in perennial horticulture crops using 3D spinning LiDAR SLAM. *J. Field Robot.* 38, 598–618. doi: 10.1002/rob.22006

Luo, D., Gao, Y., Wang, Y., Shi, Y., Chen, S., Ding, Z., et al. (2021). Using UAV image data to monitor the effects of different nitrogen application rates on tea quality. *J. Sci. Food Agric.* 102, 1540–1549. doi: 10.1002/jsfa.11489

Luo, S., Wang, C., Xi, X., Nie, S., Fan, X., and Chen, H. (2019). Combining hyperspectral imagery and LiDAR pseudo-waveform for predicting crop LAI, canopy height and above-ground biomass. *Ecol. Indic.* 102, 801–812. doi: 10.1016/j.ecolind.2019.03.011

Luz, B., and Crowley, J. K. (2010). Identification of plant species by using high spatial and spectral resolution thermal infrared (8.0–13.5μm) imagery *J. Remote Sens. Environ.* 114, 404–413. doi: 10.1016/j.rse.2009.09.019

Maimaitijiang, M., Sagan, V., and Sidike, P. (2019). Vegetation index weighted canopy volume model (CVMVI) for soybean biomass estimation from Unmanned Aerial System-based RGB imagery. *ISPRS* 151, 27–41. doi: 10.1016/j.isprsjprs.2019.03.003

Maimaitijiang, M., Sagan, V., Sidike, P., Hartling, S., Esposito, F., and Fritschi, F. B. (2020). Soybean yield prediction from UAV using multimodal data fusion and deep learning. *Remote Sens. Environ.* 237, 111599. doi: 10.1016/j.rse.2019. 111599

Peng, G., Pu, R., Biging, G., and Larrieu, M. (2003). Estimation of forest leaf area index using vegetation indices derived from Hyperion hyperspectral data. *IEEE Trans. Geosci. Remote Sens.* 41, 1355–1362. doi: 10.1109/TGRS.2003.812910

Peñuelas, J., Isla, R., Filella, I., and Araus, J. (1997). Visible and near-infrared reflec-tance assessment of salinity effects on barley. *Crop Sci.* 37, 198–202. doi: 10.2135/cropsci1997.0011183X003700010033x

Perez, R. P. A., and Costes, E. (2018). 3D plant model assessed by terrestrial LiDAR and hemispherical photographs: a useful tool for comparing light interception among oil palm progenies. *Agric. Forest Meteorol.* 249, 250–263. doi: 10.1016/j.agrformet.2017.11.008

Qin, J., and He, Z. S. (2005). "A SVM face recognition method based on Gabor-featured key points," in: *Machine Learning and Cybernetics, 2005. Proceedings of 2005 International Conference on*.

Richardson, A. J., and Wiegand, C. L. (1977). Distinguishing vegetation from soil background information. *Photogramm. Eng. Remote Sens.* 43, 1541–1552.

Rondeaux, G., Steven, M., and Baret, F. (1996). Optimization of soil-adjusted vegetation indices. Furrow irrigation and salinization. *Remote Sens. Environ.* 55, 95–107. doi: 10.1016/0034-4257(95)00186-7

Roujean, J. L., and Breon, F. M. (1995). Estimating PAR absorbed by vegetation from bidirectional reflectance measurements. *Remote Sens. Environ.* 51, 375–384. doi: 10.1016/0034-4257(94)00114-3

Schneider, F. D., Kukenbrink, D., Schaepman, M. E., Schimel, D. S., and Morsdorf, F. (2019). Quantifying 3D structure and occlusion in dense tropical and temperate forests using close-range LiDAR. *Agric. For. Meteorol.* 268, 249–257. doi: 10.1016/j.agrformet.2019.01.033

Štambuk, P., Šikuten, I., and Preiner, D. (2021). Estimates of maize plant density from UAV RGB images using Faster-RCNN detection model: impact of the spatial resolution of the spatial resolution. *Plants* 10, 661. doi: 10.3390/plants10040661

Su, W., Zhan, J., Zhang, M., Wu, D., and Zhang, R. (2016). Estimation method of crop leaf area index based on airborne LiDAR data. *Trans. Chin. Soc. Agric. Mach.* 47, 272–277. doi: 10.6041/j.issn.1000-1298.2016.03.038

Tao, H., Feng, H., Xu, L., Miao, M., Yang, G., and, X., et al. (2020). Estimation of the yield and plant height of winter wheat using uav-based hyperspectral images. *Sensors* 20, 1231. doi: 10.3390/s20041231

Wan, L., Cen, H., Zhu, J., Zhang, J., Du, X., and He, Y. (2020). Using fusion of texture features and vegetation indices from water concentration in rice crop to UAV remote sensing monitor. *Smart Agric.* 2, 58–67. doi: 10.12133/j.smartag.2020.2.1.201911-SA002

Wang, J., Wu, B., Kohnen, M. V., Lin, D., Yang, C., Wang, X., et al. (2021). Classification of rice yield using UAV-based hyperspectral imagery and lodging feature. *Plant Phenom.* 2021, 9765952. doi: 10.34133/2021/9765952

Wold, S., Sjöström, M., and Eriksson, L. (2001). PLS-regression: a basic tool of chemometrics. *Chemom Intell. Lab. Syst.* 58, 109–130. doi: 10.1016/S0169-7439(01)00155-1

Ying, P. C., Qing, W., Zi, W. X., Long, Z., Shuang, W. L., Fang, H., et al. (2020). Estimation of maize plant height and leaf area index dynamics using an unmanned aerial vehicle with oblique and nadir photography. *Ann. Bot.* 126, 765–773. doi: 10.1093/aob/mcaa097

Yuan, H., Yang, G., Li, C., Wang, Y., Liu, J., and Yu, H. (2017). Retrieving soybean leaf area index from unmanned aerial vehicle hyperspectral remote sensing: analysis of RF, ANN, and SVM regression models. *Remote Sens.* 9, 309. doi: 10.3390/rs9040309

Yue, J., Feng, H., Jin, X., Yuan, H., Li, Z., Zhou, C., et al. (2018). A comparison of crop parameters estimation using images from UAV-mounted snapshot hyperspectral sensor and high-definition digital camera. *Remote Sens.* 10, 1138. doi: 10.3390/rs10071138

Zhu, W., Sun, Z., Huang, Y., Yang, T., Li, J., Zhu, K., et al. (2021). Optimization of multi-source UAV RS agro-monitoring schemes designed for field-scale crop phenotyping. *Prec. Agric.* 22, 1768–1802. doi: 10.1007/s11119-021-09811-0

frontiers | Frontiers in Plant Science

ORIGINAL RESEARCH
published: 22 July 2022
doi: 10.3389/fpls.2022.900408

An Intelligent Rice Yield Trait Evaluation System Based on Threshed Panicle Compensation

*Chenglong Huang†, Weikun Li†, Zhongfu Zhang, Xiangdong Hua, Junya Yang, Junli Ye, Lingfeng Duan, Xiuying Liang and Wanneng Yang**

National Key Laboratory of Crop Genetic Improvement, National Center of Plant Gene Research (Wuhan), College of Engineering, Huazhong Agricultural University, Wuhan, China

High-throughput phenotyping of yield-related traits is meaningful and necessary for rice breeding and genetic study. The conventional method for rice yield-related trait evaluation faces the problems of rice threshing difficulties, measurement process complexity, and low efficiency. To solve these problems, a novel intelligent system, which includes an integrated threshing unit, grain conveyor-imaging units, threshed panicle conveyor-imaging unit, and specialized image analysis software has been proposed to achieve rice yield trait evaluation with high throughput and high accuracy. To improve the threshed panicle detection accuracy, the Region of Interest Align, Convolution Batch normalization activation with Leaky Relu module, Squeeze-and-Excitation unit, and optimal anchor size have been adopted to optimize the Faster-RCNN architecture, termed 'TPanicle-RCNN,' and the new model achieved F1 score 0.929 with an increase of 0.044, which was robust to indica and japonica varieties. Additionally, AI cloud computing was adopted, which dramatically reduced the system cost and improved flexibility. To evaluate the system accuracy and efficiency, 504 panicle samples were tested, and the total spikelet measurement error decreased from 11.44 to 2.99% with threshed panicle compensation. The average measuring efficiency was approximately 40 s per sample, which was approximately twenty times more efficient than manual measurement. In this study, an automatic and intelligent system for rice yield-related trait evaluation was developed, which would provide an efficient and reliable tool for rice breeding and genetic research.

Keywords: rice panicle, yield traits, high-throughput, Faster-RCNN, cloud computation

OPEN ACCESS

Edited by:
Xiuliang Jin,
Key Laboratory of Crop Physiology and Ecology, Institute of Crop Sciences (CAAS), China

Reviewed by:
Md Nashir Uddin,
The University of Tokyo, Japan
Kang Yu,
Technical University of Munich, Germany

***Correspondence:**
Wanneng Yang
ywn@mail.hzau.edu.cn

† These authors have contributed equally to this work

Specialty section:
This article was submitted to Sustainable and Intelligent Phytoprotection, a section of the journal Frontiers in Plant Science

Received: *20 March 2022*
Accepted: *22 June 2022*
Published: *22 July 2022*

Citation:
Huang C, Li W, Zhang Z, Hua X, Yang J, Ye J, Duan L, Liang X and Yang W (2022) An Intelligent Rice Yield Trait Evaluation System Based on Threshed Panicle Compensation. Front. Plant Sci. 13:900408. doi: 10.3389/fpls.2022.900408

INTRODUCTION

Rice is the staple food for over half of the world's population (Zhang, 2007; Sandhu et al., 2019), the yield of which is of great significance to human security and development (Tester and Langridge, 2010). In rice research, the evaluation of rice yield-related traits is an essential step for rice breeding (Qian et al., 2016; Yang et al., 2020) and functional gene analysis (Sakamoto and Matsuoka, 2008). Generally, rice yield is determined by crucial factors, including the number of panicles (Xing and Zhang, 2010), the number of filled spikelet's (Borrell et al., 2014), and 1,000 grain weight (Richards, 2000). However, the traditional method for rice yield-related trait evaluation is manual and faces

the problems of rice threshing difficulties, measurement process complexity, and low efficiency. Therefore, an efficient and reliable tool for rice yield-related trait evaluation is urgently needed.

With the rapid development of machine vision, a growing number of image-based technologies have been applied in agriculture (Sankaran et al., 2010; Rebolledo et al., 2016; Confalonieri et al., 2017), and several studies on rice yield-related trait evaluation have been reported. Since it is difficult to thresh all the spikelet's in the panicle, most of the studies focus on grain traits measurement. ImageJ, a Java-based open source software, was used for isolated grain trait measurement (Igathinathane et al., 2009), and Smart Grain, an open source software, was released for grain trait measurement in complicated situations (Tanabata et al., 2012). Duan developed a yield traits scorer for automatic extraction of yield-related traits with high throughput (Duan et al., 2011). However, panicle threshing performance is still a bottleneck that some unfilled spikelet's would remain in the threshed panicle, which would have a great negative effect on the measurement of rice yield-related traits. Some researchers have attempted to directly analyze rice panicles without threshing processes. Sandhu proposed a method for rice panicle maturity evaluation based on three-dimensional point cloud construction and analysis (Sandhu et al., 2019). Hu developed a 22 yield-related trait extraction method based on X-ray computed tomography imaging (Hu et al., 2020). P-TRAP, a commercial software program, was designed for yield spread-related trait analysis (Al-Tam et al., 2013). However, the low measurement efficiency and high cost had a negative impact on the practical application. Thus, an automatic panicle analysis system with high efficiency and high accuracy would have great application prospects.

According to existing research, there are generally two ways to obtain rice yield traits. The most common method was to investigate the grain traits by threshing the panicle manually (Yang et al., 2014), because the unfilled spikelet's were hard to be completely taken off by the threshing machine, which limited the efficiency and accuracy of rice yield traits extraction. On the other hand, the X-ray technology was able to be used for filled and unfilled spikelet's identification (Hu et al., 2020), but it is difficult to be widely used in practical rice yield traits extraction, because of the high cost, low efficiency, and radiation. In order to solve the problem of residual panicle spikelet's by threshing machine, we promote a new way with threshed panicle compensation, which would identify the number of residual spikelet's in the threshed panicle and compensate it into the evaluation of spikelet yield traits. In order to achieve it, a robust and reliable method for threshed panicle identification is needed.

In recent years, artificial intelligence technology has been significantly promoted and widely used in agriculture (Chen et al., 2018; Escamilla-Garcia et al., 2020; van Klompenburg et al., 2020; Dhaka et al., 2021; Kattenborn et al., 2021). Sun developed a soybean yield prediction model based on a convolutional neural network (Sun et al., 2019) and a long short-term memory network (Hochreiter and Schmidhuber, 1997). Zhou analyzed drone images for maize leaf coverage based on the Deeplabv3 plus model (Zhou et al., 2019). Object detection is an important research field of deep learning image processing, which is widely used in various agricultural scenes. The state-of-the-art methods can be categorized into two main types: one-stage methods and two stage-methods. One-stage methods prioritize inference speed, and example models include YOLO, SSD, and Retina (Liu et al., 2016; Redmon et al., 2016; Lin et al., 2020). Two-stage methods prioritize detection accuracy, and example models include Faster R-CNN, Mask R-CNN, and Cascade R-CNN (Ren et al., 2015; He et al., 2017; Cai et al., 2018). Faster RCNN is a classical two-stage object detector consisting of object proposal, feature extraction, and bounding box regression, which formulates detection as a coarse-to-fine process. The Deep–Fruits model was proposed for fruit identification based on Faster-RCNN (Sa et al., 2016). Faster-RCNN has also been applied for pest detection (Shen et al., 2018; He et al., 2020; Li et al., 2021) and panicle spikelet counting (Wu et al., 2019; Deng et al., 2021; Yu et al., 2021). Therefore, we adopted a two-stage detector, Faster R-CNN, as the basis for the threshed panicle detection. However, the current Faster R-CNN detector has shown weak performances with small and overlapped objects (Tong et al., 2020), and the grain size is approximately 30 × 60 pixels in the threshed panicle image of 2,048 × 4,096 pixels. Building on these preliminary observations, appropriate improvement for the Faster R-CNN architecture should be performed to achieve accurate detection of the threshed panicle.

The aim of this study is to build an automatic and intelligent system for rice yield trait evaluation. Firstly, a new deep learning architecture was proposed to achieve threshed panicle compensation on the basis of the Faster R-CNN architecture, termed 'TPanicle-RCNN.' Then, equipped with automatic control, machine vision, and deep learning algorithms, we developed a novel intelligent system, which includes an integrated threshing unit, grain conveyor-imaging units, and threshed panicle conveyor-imaging unit, and specialized image analysis software. Finally, the threshed panicle compensation was performed to achieve automatic and accurate acquisition of rice yield-related traits.

MATERIALS AND METHODS

System Design

The system sketch is shown in **Figure 1A**, which mainly consists of the panicle threshing unit, servo air separator, and three conveyor imaging units. The threshing unit is derived from a semi-feeding drum thresher (TSL-150A, Top Cloud-AGRI, China) and is driven by a servo motor (Panasonic, Japan). The operator holds the panicle and puts it into the thresher; as a result, all the filled spikelet's and most of the unfilled spikelet's are threshed from the panicle. Then, the threshed spikelet's spread out on the first conveyor by the vibration feeder. The servo air separator is designed with a cross-flow fan and is fixed between two grain conveyor lines; as a result, the filled spikelet's are separated from the unfilled spikelet's. The conveyor-imaging units are constructed with a panicle conveyor line and two grain conveyor lines; as a result, images of threshed panicles, total spikelet's, and filled spikelet's are obtained, which were grayscale images saved in PNG format. Finally, the filled

spikelet's and unfilled spikelet's are individually collected from the specific outlets.

The details of the conveyor imaging units are shown in **Figure 1B**. The linear camera (SG-11-02K40-00-R, DASLA, Canada) is equipped with a 28 mm lens (Nikon, Japan), the charge-coupled device (CCD) size is $14\mu m \times 2048$, and the field of vision (FOV) is 204.8 mm with a pixel resolution of $100\mu m$. Motion control is conducted by a programmable logic

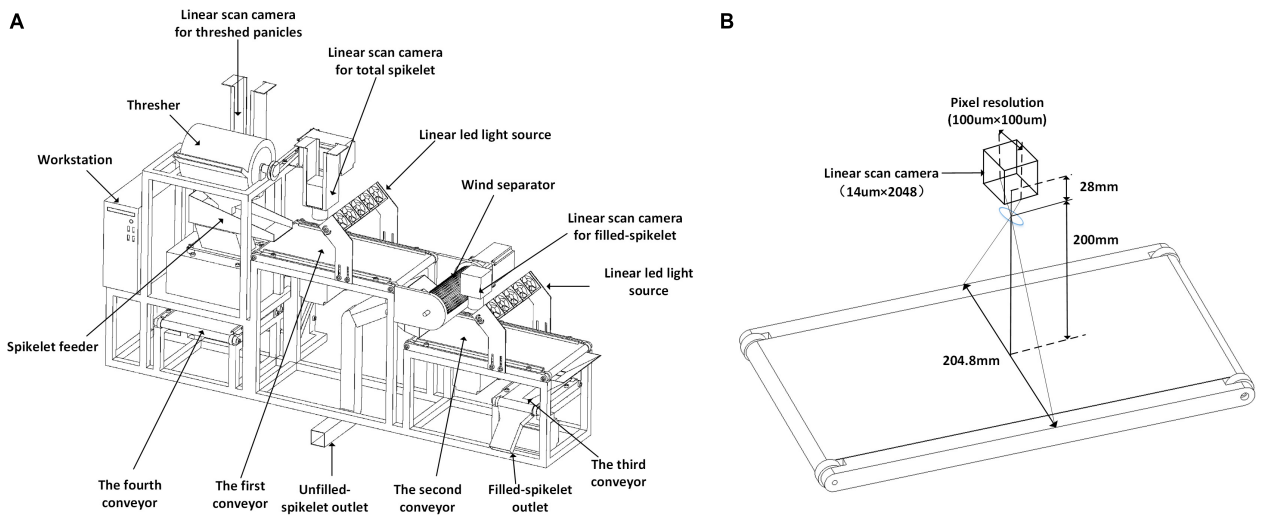

FIGURE 1 | System sketch of automatic rice yield-related trait evaluation: **(A)** system composition details and **(B)** conveyor imaging unit.

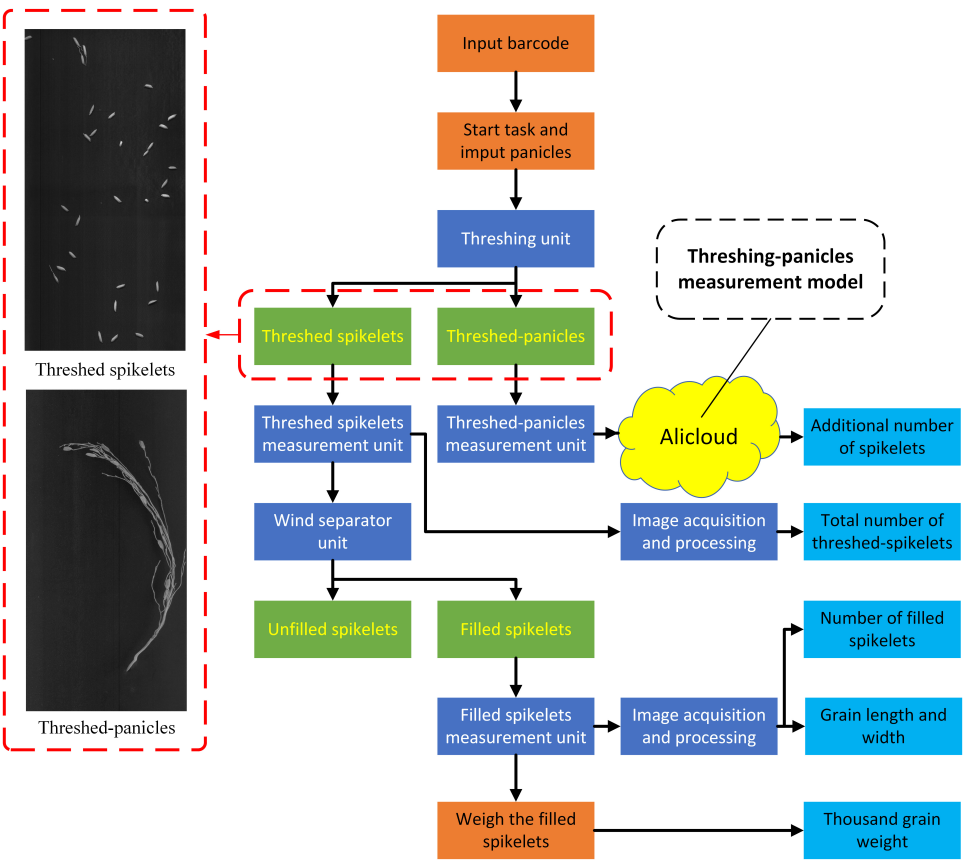

FIGURE 2 | System workflow for yield related trait measurement.

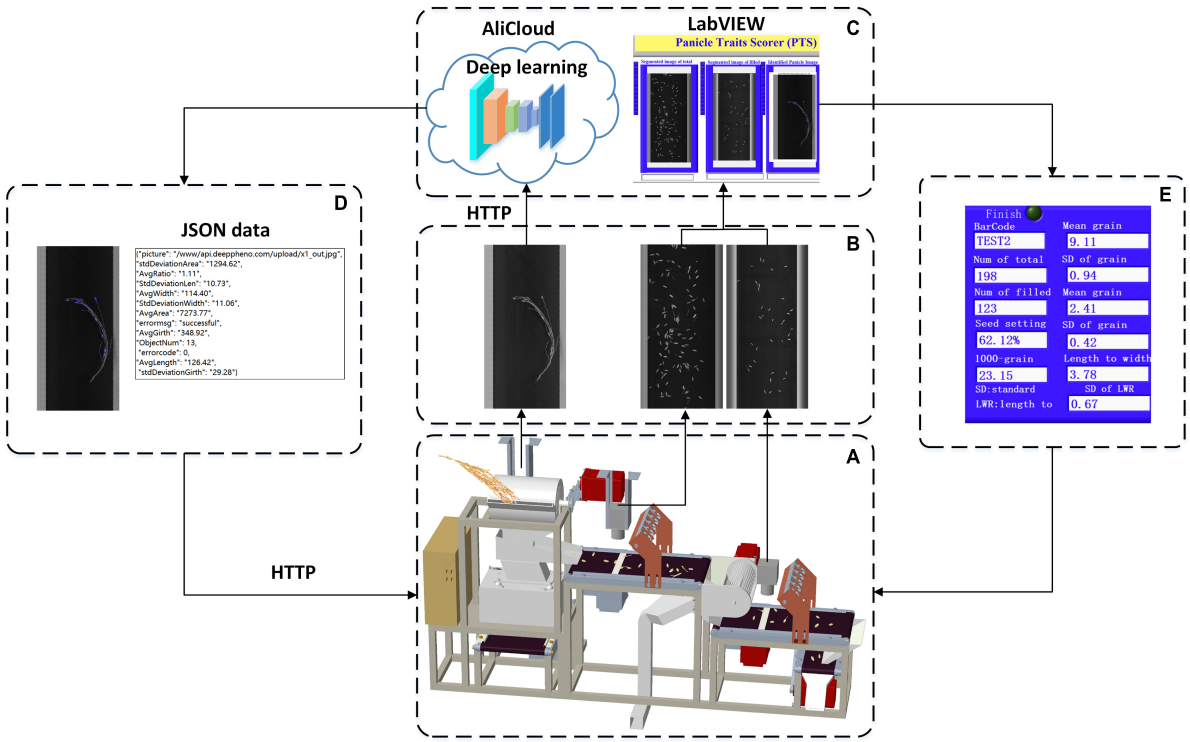

FIGURE 3 | Software workflow in the system: **(A)** system control, **(B)** image acquisition, **(C)** image analysis, **(D)** cloud communication, and **(E)** result exhibition.

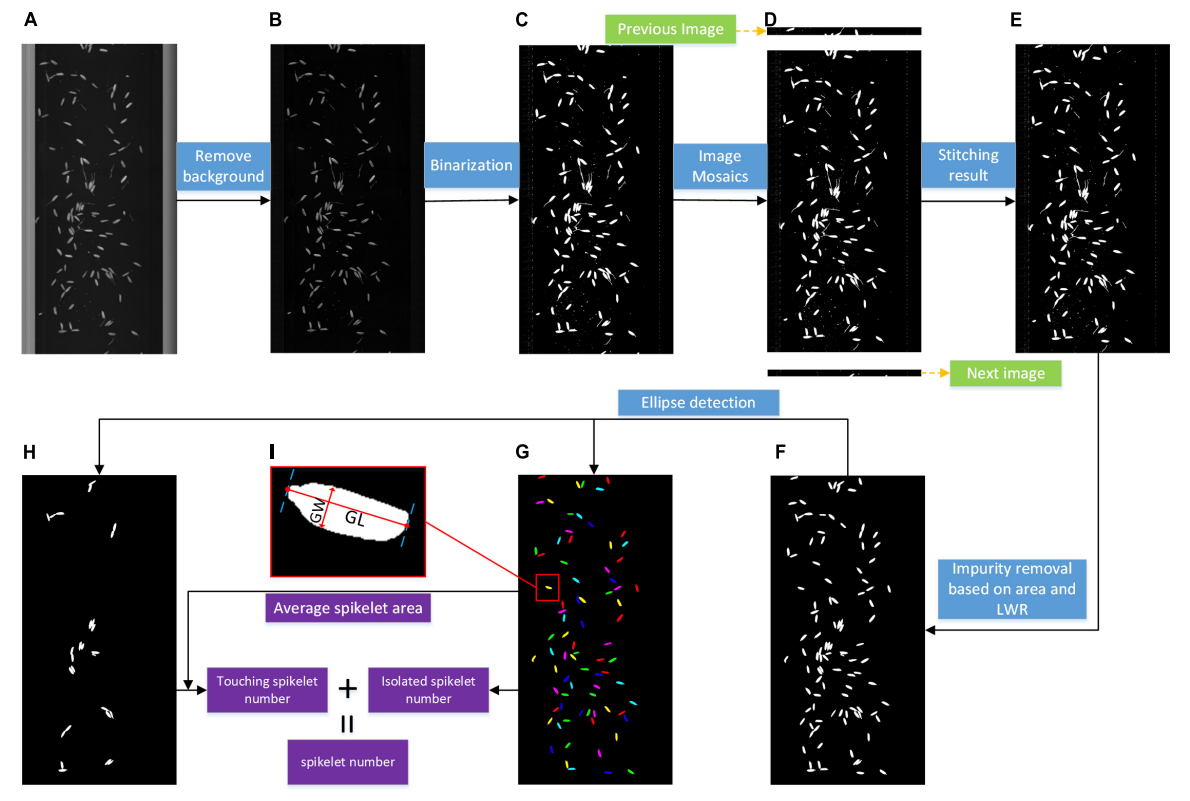

FIGURE 4 | Pipeline for the grain image analysis.

controller (PLC, Omron, Japan) programed by CX-Programmer 9.5 (Omron, Japan). The workstation m415 (Lenovo, China) is equipped with an i5-7500 CPU, 8 GB memory, and 1 T hard disk, and the Alibaba cloud (Alibabacloud) is adopted, with the configuration of a Tesla M40, 16 GB memory, and 30 GB cloud storage.

System Workflow

The system workflow is depicted in **Figure 2**: (1) First, the operator started the system and inputs the barcode. (2) Second, the panicle is held and put into the thresher after which the threshed panicle is placed on the fourth conveyor line for image acquisition, while all the threshed grains spread out onto the first conveyor line with a spikelet's feeder for image acquisition. (3) Then, the grains go through a wind separator that blows the unfilled spikelet's away, while the filled spikelet's falls onto the second conveyor for image acquisition. (4) Next, all the filled spikelet's are collected and weighed by the third conveyor and weighing device. (5) Finally, the images of threshed panicles, total spikelet's, and filled spikelet's are analyzed by specific local algorithms and cloud-deployed deep learning models for yield-related trait evaluation. The system workflow is shown in **Supplementary Video 1**.

Software Design

The software workflow in the system is shown in **Figure 3** and was developed to achieve the functions of PLC communication, image acquisition, image analysis, and data storage. First, PLC communication was designed to control the panicle thresher, vibration feeder, conveyor lines, and wind separator, as shown in **Figure 3A**. Second, image acquisition was achieved by the NI-Vision module (National Instruments, United States) to obtain images of threshed panicles, total spikelet's, and filled spikelet's, as shown in **Figure 3B**. The image analysis algorithms were written in C + + and complied with the Dynamic Link Library (DLL), which was invoked by the user software developed by LabVIEW 8.6 (National Instruments, United States), and the threshed panicle identification model was trained in the local server and deployed in the Alibaba cloud. Finally, as shown in **Figure 3E**, the measurement results were displayed on the software interface, and the data were saved in one Excel file.

Pipeline for the Grain Image Analysis

The grain image analysis pipeline is presented in **Figure 4**. First, background subtraction was conducted to enhance the foreground contrast shown in **Figure 4B**. Second, a fixed threshold was applied to obtain the binary image shown in

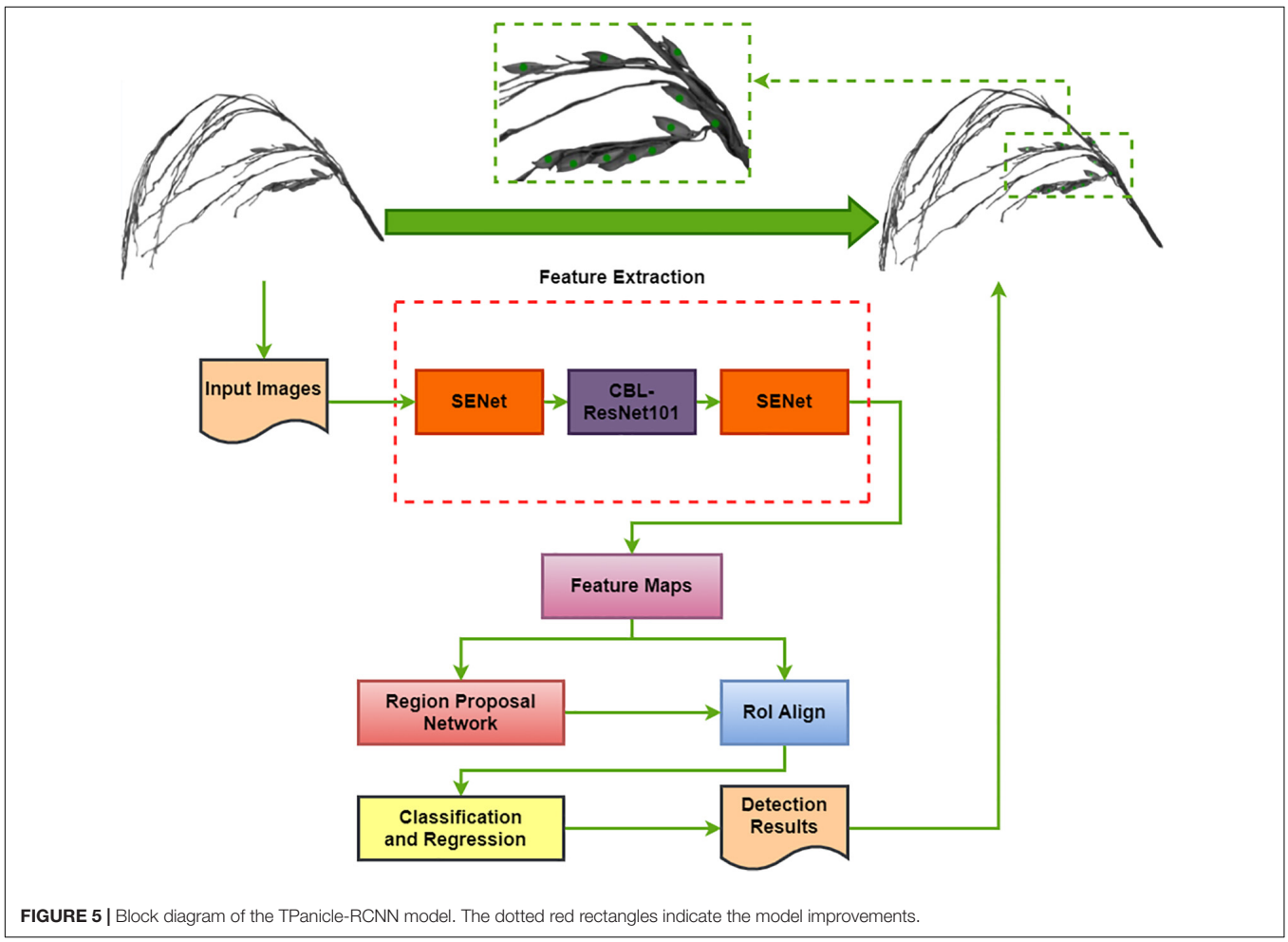

FIGURE 5 | Block diagram of the TPanicle-RCNN model. The dotted red rectangles indicate the model improvements.

Figure 4C. Because of continuous linear scanning, the grain was probably distributed on two adjacent images; therefore, sequence image stitching was implemented based on the bottom connected region shown in **Figure 4D**, and a binary image with complete grains (**Figure 4E**) was obtained. Then, the impurity removal algorithm was carried out based on the optimal thresholds of the area and length width ratio (LWR), as shown in **Figure 4F**, which was determined by the distribution of the grain size and a large number of experiments. Next, ellipse detection was used to obtain the isolated grain image (**Figure 4G**) and touching grain image (**Figure 4H**), and the range of minor and major axis lengths was set according to grain size; the minimum match score was set to 800, while 1,000 represented a perfect match.

Based on the above image processing, the number of connected regions in the isolated grain image was taken as the isolated spikelet number, while the areas of the connected regions in the touching grain image were divided by the average area of isolated grains, and the sum of the results was regarded as the

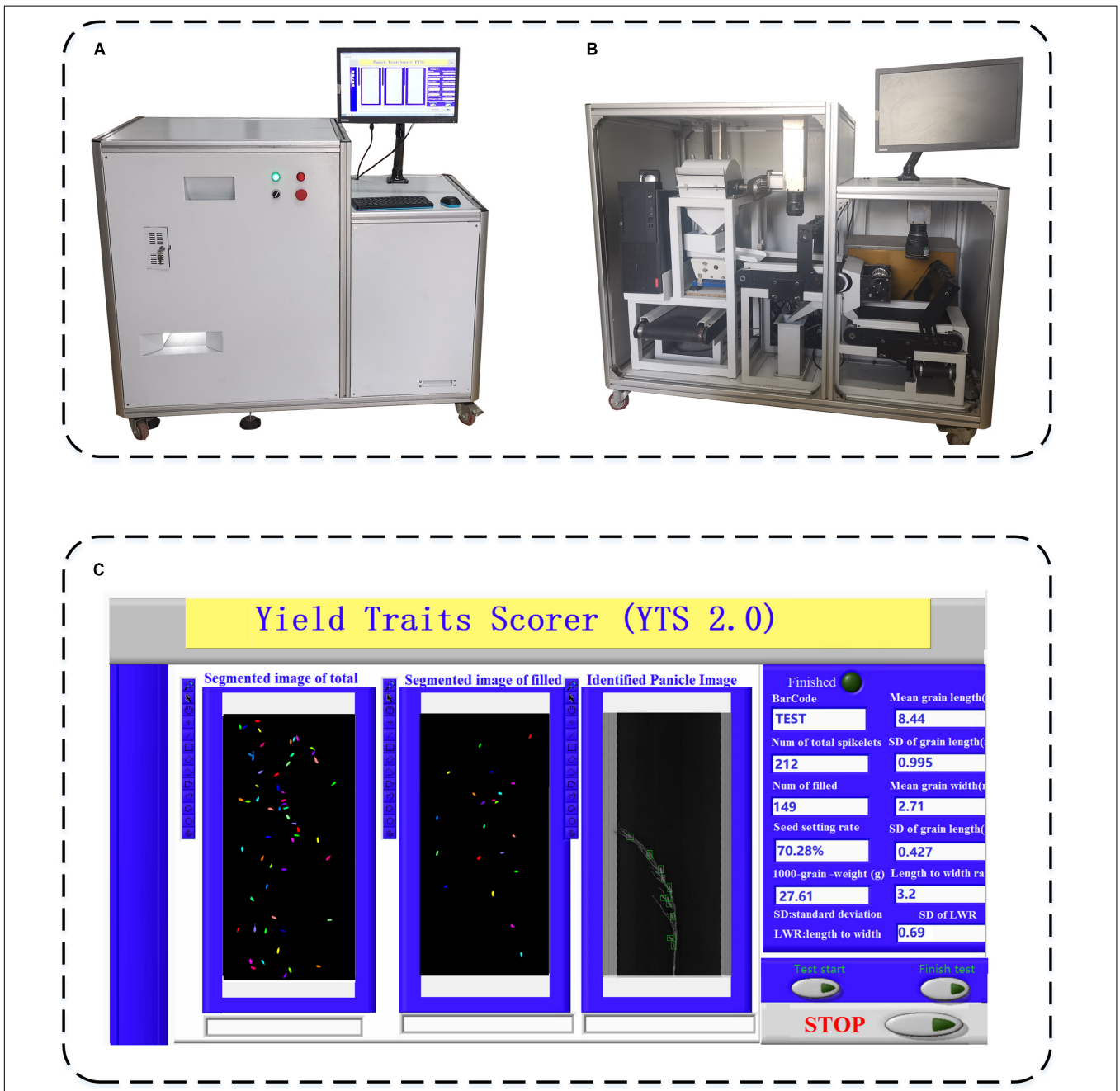

FIGURE 6 | The prototype of an automatic rice yield-related trait evaluation system, **(A)** system hardware composition, **(B)** system internal structure, and **(C)** system software interface.

touching spikelet number. The total number was calculated by adding the isolated spikelet number and touching the spikelet number. The filled spikelet number could also be calculated. Moreover, the grain shape parameters were extracted by the following contour computation method based on the filled isolated grain image. The Euclidean distance between the two farthest points of the contour is regarded as the grain length (GL), and the maximum perpendicular distance is regarded as the grain width (GW).

Pipeline for the Threshed Panicle Analysis

Since Faster-RCNN is a classical two-stage object detector that formulates detection as a coarse-to-fine process, the deep learning architecture for threshed panicle analysis was proposed on the basis of Faster-RCNN, termed 'TPanicle-RCNN,' while two feature extraction networks, VGG (Simonyan and Zisserman, 2014) and RESNET (He et al., 2016), were studied. To construct the model, 1,072 rice panicles, including 536 indica and 536 japonica panicles, were threshed by the threshing unit, a total of 1,072 threshed panicle images were captured and manually labeled with Labelimg (LabelImg.), and all the ground-truth bounding boxes and annotation files saved in the PASCAL VOC data format (Krizhevsky et al., 2012). Then the dataset was divided into a training set and a test set at a ratio of 4:1, with half indica and half japonica in each data set. Then, the datasets were augmented four times by image flipping and brightness adjustment, while 3,432 training images and 856 testing images were obtained. All the training and testing data are available at https://pan.baidu.com/s/1-XawHGseIc5bboVOP48Fkw?pwd=153w with the extraction code '153w' for non-commercial research purposes.

Model Improvement

The Block diagram of the TPanicle-RCNN model is depicted in **Figure 5**, while the red rectangles indicate the model improvements compared with the original Faster R-CNN architecture. The RoIPool operation had adopted two quantization processes, which would result in a deviation of the ultimate box, while the location error would put a great negative effect on the threshed panicle detection, especially when the grains were close or slightly overlapped. To improve it, the Region of Interest Align (RoIAlign) designed in Mask R-CNN architecture, was applied to calculate the exact values of the candidate-box coordinates in this method. The original Faster R-CNN architecture used nine anchors to detect regional proposals consisting of three scales 128^2, 256^2, and 512^2, and three aspect ratios, 1:1, 1:2, and 2:1, which were not suitable for the small object detection. Therefore the scale vectors were optimized to 32^2, 64^2, and 128^2 based on the sizes of the grain. The integration of Convolution, Batch normalization, and Leaky Relu (CBL) was used to replace the traditional convolution and activation in the Res101 network (Wu and He, 2018), which was helpful to speed up the training efficiency and improve the accuracy. Moreover, the squeeze-and-excitation unit had been embedded into the head and tail of the feature extraction net Res101[48], and the channel attention layer had merged global average pooling and maximum pooling, which was able to enhance the effective information and improve model accuracy. In conclusion, the RoIAlign, CBL module, Squeeze-and-Excitation unit, and optimal anchor size had been adopted in the TPanicle-RCNN model.

Model Training

Pytorch 1.7.1 was adopted as a deep learning framework, and python 3.6 was applied. Since the training dataset was small, the fine-tuning training technique had been applied. The Faster-RCNN and TPanicle-RCNN models were initialized with pre-trained weights obtained by training the ImageNet dataset (Ioffe and Szegedy, 2015). And then the models were trained on the 3,432 training set to further optimize the pre-trained net. During the fine-tuning stage, the batch-size was set to four to achieve the maximum utilization of graphic processing unit GPU memory. The intersection-over-union (IoU) was set to 0.5, which means that when its IoU was $\geq$ 0.5, the predicted bounding box was regarded as positive. The number of region proposals was set to 600, the shortest side of the image was set to 1,000 pixels, and the longest side of the image was set to 2,000 pixels, in accordance with grain number and image size. Other parameters were configured by the default settings of the Faster R-CNN network. Finally, the optimal model was deployed on Alibaba cloud for threshed panicle analysis, and the spikelet number was returned as the total spikelet compensation.

System Evaluation

To evaluate the threshed panicle model performance, 856 testing images were tested, and the indicators of precision, recall, PR curve, $F1$ values, and average precision (AP) were used, the calculations of which are shown in Equations 1–4. T_P represents the true positive targets, where the targets were correctly identified, F_P represents the false positive targets, where the background was identified as the target, and F_N represents the false negative targets, where the targets were missed.

$$Precision = \frac{T_P}{T_P + F_P} \tag{1}$$

$$Recall = \frac{T_P}{T_P + F_{\mathrm{N}}} \tag{2}$$

$$F1 = \frac{2 \times Precision \times Recall}{Precision + Recall} \tag{3}$$

$$AP = \int_0^1 P(r)dr \tag{4}$$

To evaluate the system accuracy, 504 randomly selected panicle samples were tested, and the results of the system measurement were compared with manual measurements, including the threshed panicle spikelet number (TPSN), unfilled spikelet number, and filled spikelet number, and the mean value of three manual measurements was taken as the ground truth. Additionally, the indicators of R square, the mean absolute percentage error (MAPE), and the root mean square error (RMSE) were computed using Equations 5–7 to evaluate the

system performance. Additionally, 200 randomly selected panicle samples were tested to evaluate the system efficiency.

$$R^2 = \frac{\sum_{i=1}^{n}(X_{ai} - \overline{X_m})^2}{\sum_{i=1}^{n}(X_{mi} - \overline{X_m})^2} \quad (5)$$

$$MAPE = \frac{1}{\mathrm{n}}\sum_{i=1}^{n}\frac{|X_{ai} - X_{mi}|}{X_{mi}} \quad (6)$$

$$RMSE = \sqrt{\frac{1}{\mathrm{n}}\sum_{i=1}^{n}(X_{ai} - X_{mi})^2} \quad (7)$$

where n is the total number of measurements; X_{mi} is the manual measurement results; X_{ai} is the system measurement results; and $\overline{X_m}$ is the mean of the manual measurements.

RESULTS

The prototype of the automatic rice yield-related trait evaluation system is shown in **Figure 6**. The system hardware composition is shown in **Figure 6A**, and the details of the system's internal structure are depicted in **Figure 6B**, while the system software interface is exhibited in **Figure 6C**. From the results, the specific functions of system hardware and software were realized, and images of threshed panicles, total spikelet's, and filled spikelet's were analyzed for rice yield-related traits, including the total spikelet number, seed setting rate, grain shape, and grain weight. To demonstrate the system, the performance with different object detection models and rice varieties were studied, and furthermore, the accuracy and efficiency of the system were evaluated in detail.

Evaluation of Models on the Testing Dataset

The models were evaluated by the 856 testing dataset, while comparisons of precision–recall curves of Faster R-CNN and TPanicle-RCNN models are shown in **Figure 7**, which showed that the average precision (AP) with the IoU $\geq$ 0.5 was 0.836, 0.873, 0.903 for the Faster-RCNN based on vgg16 (**Figure 7A**), resl01 (**Figure 7B**), and TPanicle-RCNN based on ResNet101 (**Figure 7C**), respectively. The results indicated that the res101 network had better performance than vgg16 in the feature extraction of small objects, therefore the Faster-RCNN improvement was based on ResNet101. Based on the advantages of RoIAlign, CBL module, Squeeze-and-Excitation unit, and optimal anchor size, the precision of TPanicle-RCNN was significantly greater than that of the original Faster R-CNN under the same recall conditions for threshed panicle, and the AP has reached 0.903, with an increase of 0.03. With the confidence threshold set as 0.5, the *F*1 value of improved Faster-RCNN was 0.929, an increase of 0.044.

TABLE 1 | The performance of the threshed panicle identification models.

Class	Data	Model	Recall	Precision	*F*1
Indica	428	Faster-RCNN	0.832	0.856	0.844
		TPanicle-RCNN	0.881	0.900	0.890
Japonica	428	Faster-RCNN	0.914	0.936	0.925
		TPanicle-RCNN	0.975	0.958	0.967

The Performance for Indica and Japonica

The threshed panicle identification performance for the indica and japonica varieties in the testing dataset was analyzed to evaluate the reliability and flexibility of the system, and the results are shown in **Table 1** with 428 indica and 428 japonica samples. With the Faster-RCNN based on ResNet101, the recall, precision, and F1 scores were 0.832, 0.856, and 0.844 for indica varieties, while the recall, precision, and F1 scores were 0.914, 0.936, and 0.925 for japonica varieties, respectively. With the TPanicle-RCNN, the recall, precision, and F1 scores were 0.881, 0.900, and 0.891 for indica varieties, while the recall, precision, and F1 scores were 0.975, 0.958, and 0.967 for indica varieties, respectively. From the results, the TPanicle-RCNN yielded better performance than the original Faster-RCNN in general, the improvements in recall, and precision was 0.049, 0.044 for indica, and 0.061, 0.018 for japonica, which indicated that the TPanicle-RCNN was able to greatly improve the recall rate and recognition accuracy of the threshed panicle. Additionally, the models performed better

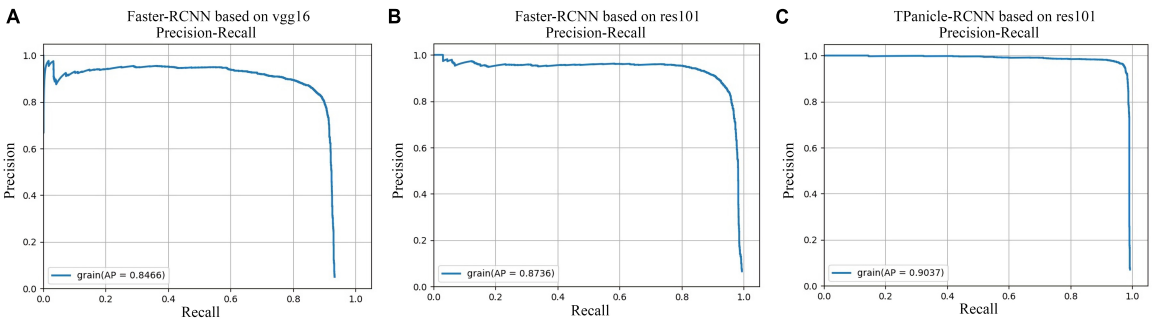

FIGURE 7 | Comparisons of precision–recall curves, **(A)** Faster-RCNN based on vgg16, **(B)** Faster-RCNN based on ResNet101, **(C)** TPanicle-RCNN based on ResNet101.

on the japonica varieties than the indica varieties, because the spikelet number in the japonica threshed panicles was obviously less than that in the indica threshed panicles, which led to an increase in the recall rate, and in the results, the average gap between the *F*1 values was 0.076 for the improved Faster-RCNN.

The threshed panicle spikelet number (TPSN) was measured manually and identified by the model inference, while the scatter plots of manual *vs.* model measurement and error distribution diagrams for the 428 indica and 428 japonica rice samples are shown in **Figure 8**, without positive and negative sample division based on IoU. From the results, the R^2 and RMSE of the improved Faster-RCNN were 0.968 and 1.18, respectively, for the indica varieties, with an improvement of 0.014 and 53%. Meanwhile, the R^2 and RMSE of the improved Faster-RCNN were 0.981 and 0.690, respectively, for the japonica varieties, with an improvement of 0.015 and 61.23%. The results demonstrated high consistency with manual measurements and a significant improvement compared with the original Faster-RCNN. The error distribution diagrams also indicated that the error distribution was normal in general, and 80% of identification errors constituted fewer than 2 spikelet's. On the basis of these results, the error distribution of indica varieties was more discrete than that of japonica, and the improved Faster-RCNN has greatly decreased the error, which was preferred and used in the system.

Accuracy of the Automatic Rice Yield-Related Trait Evaluation System

To test the system accuracy, 504 randomly selected panicle samples were measured, and the scatter plots of manual *vs.* system measurements are shown in **Figure 9**. From the results, yield-related traits, including total spikelet number and seed setting rate, were mainly analyzed to evaluate the effect of threshed panicle compensation. If threshed panicle compensation was not conducted, the R^2 and MAPE of the total spikelet measurement were 0.96 and 11.44%, respectively, which were improved to 0.99 and 2.99% by threshed panicle compensation. Additionally, the R^2 and MAPE of the seed setting rate measurement were 0.92 and 8.84%, respectively, which were improved to 0.98 and 3.47% by threshed panicle compensation. In conclusion, the accuracy of the entire system was significantly improved by threshed panicle compensation, enhancing the reliability of the automatic rice yield-related trait evaluation system.

System Efficiency Evaluation

To evaluate the system efficiency, 200 randomly selected panicle samples were tested, while the time costs of panicle threshing, image acquisition, and image analysis were recorded individually. The results proved that the average efficiency was approximately 40 s, in which the time costs of panicle threshing, panicle image acquisition, and image analysis were approximately 25, 5, and 10 s, respectively, as shown in **Figure 10**. Additionally, the spikelet image analysis was performed in parallel with the panicle analysis, in which the time cost was approximately 4 s. Therefore, the whole system efficiency was approximately 40 sper panicle, which was approximately 20 times more efficient than manual measurement.

DISCUSSION

The results demonstrated that the system measurement accuracy mainly depended on the threshed panicle compensation, which had a high correlation with the threshing effect. To evaluate the

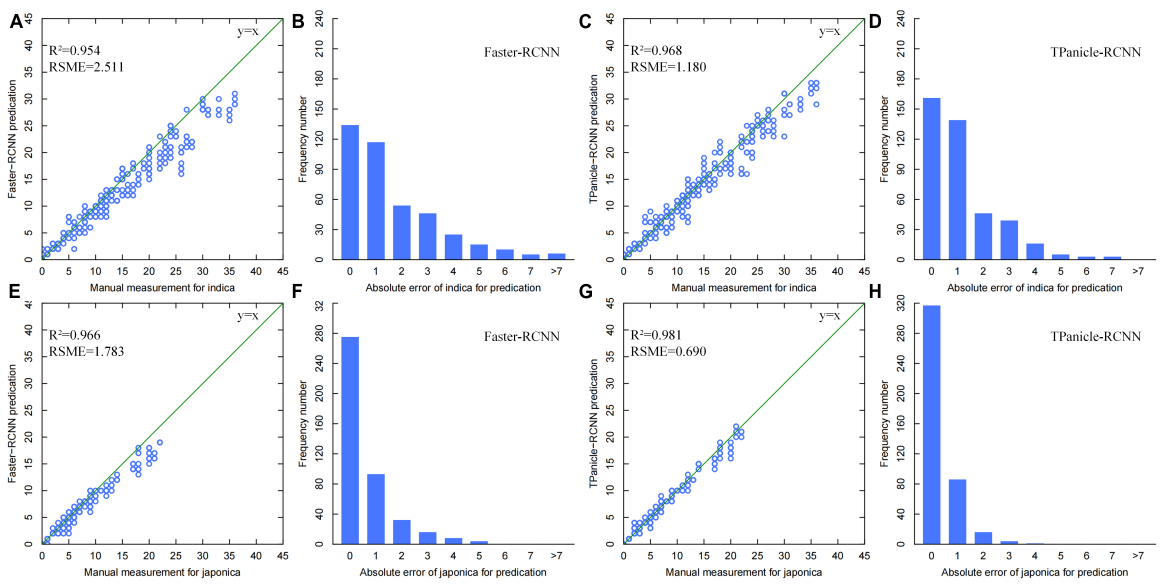

FIGURE 8 | (A,B) Threshed panicle spikelet number scatter plots of manual versus model measurement and error distribution diagrams for indica rice samples with Faster-RCNN measurement (Brichet et al., 2017), TPanicle-RCNN measurement **(C,D)**, and japonica rice samples with Faster-RCNN measurement **(E,F)**, TPanicle-RCNN measurement **(G,H)**.

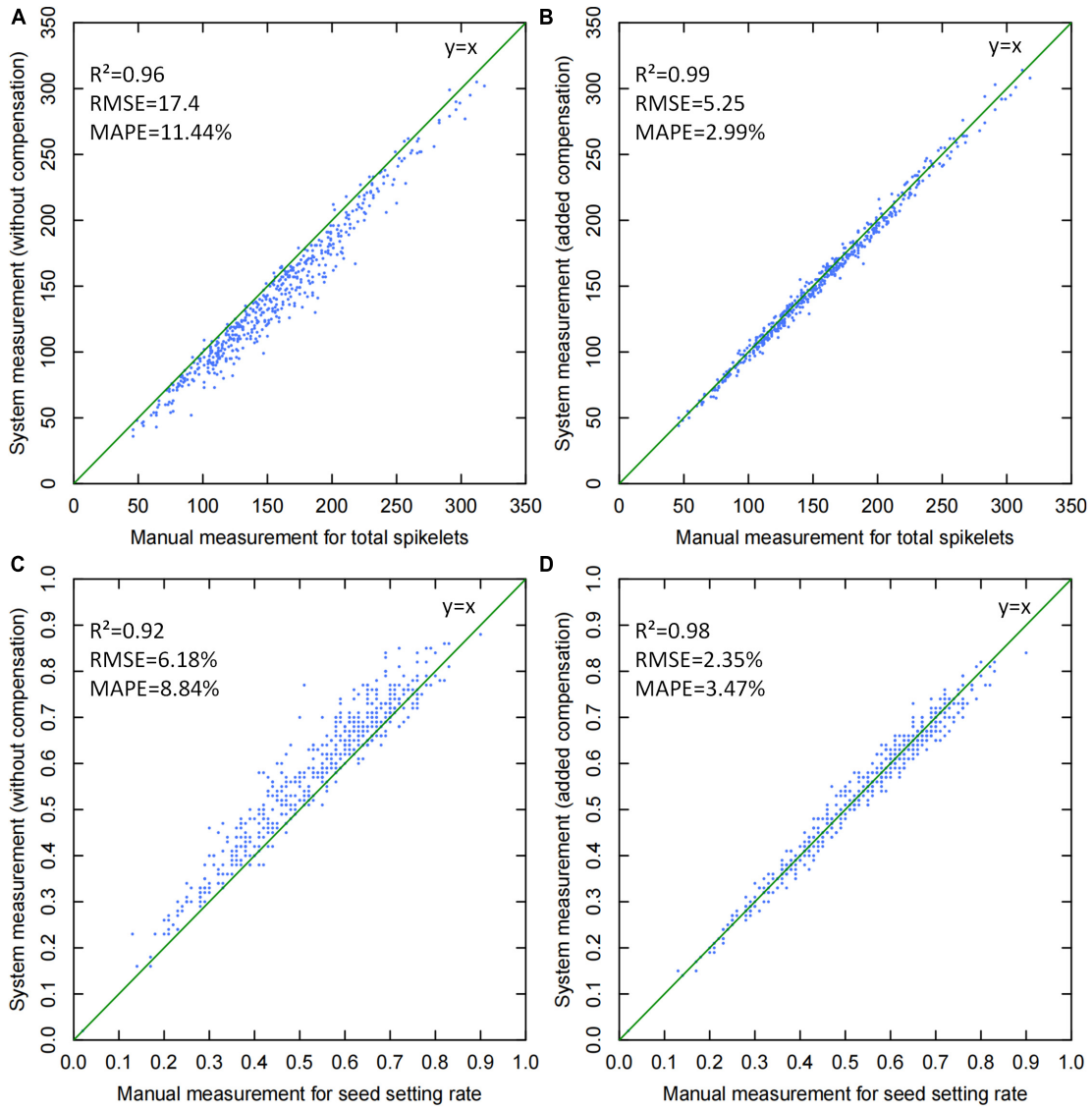

FIGURE 9 | Scatter plots of manual versus system measurements for yield-related trait evaluation: **(A)** total spikelet measurement without threshed panicle compensation, **(B)** total spikelet measurement with threshed panicle compensation, **(C)** seed setting rate measurement without threshed panicle compensation, and **(D)** seed setting rate measurement with threshed panicle compensation.

threshing effect, the spikelet's in the threshed panicle, unfilled spikelet outlet, and filled spikelet outlet were counted manually to obtain the threshing error percentage, and the results of 504 panicle samples are shown in **Figure 11**. The threshing results demonstrated that the filled spikelet's were able to be threshed well but a few unfilled spikelet's remained in the panicle, and the average spikelet number in the threshed panicle was 10.48, which led to a 9.37% average threshing error percentage. Additionally, the results showed great fluctuation in the threshing performance due to the panicle type and threshing time. In general, the threshing error contributed 81.9% of the total spikelet measurement error, while the threshed panicle compensation decreased the threshing error by 90.18%, which was of great significance to automatic yield-related trait evaluation.

Compared with the original Faster-RCNN architecture, it was demonstrated that the TPanicle-RCNN had significantly increased the performance, and the detailed prediction cases are shown in **Figure 12**, including indica varieties (**Figure 12A**) and japonica varieties (**Figure 12B**). The results proved that the CBL module, Squeeze-and-Excitation unit, and optimal anchor size were able to help extract more effective features, so as to improve the model accuracy, while the RoIAlign was able to significantly improve the regression accuracy of the target box. Therefore the TPanicle-RCNN had performed a higher recall rate and grain position accuracy, which was indicated by the red arrow in **Figure 12**. Regarding the performance of the japonica and indica varieties, the results showed that the spikelet's in indica threshed panicles were dense, and the

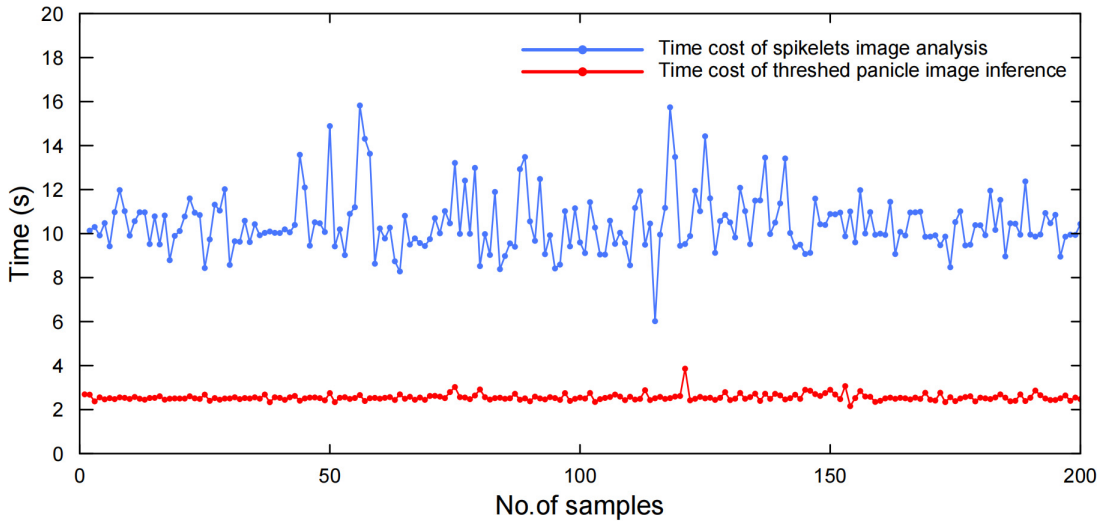

FIGURE 10 | Efficiency evaluation with 200 randomly selected panicle samples.

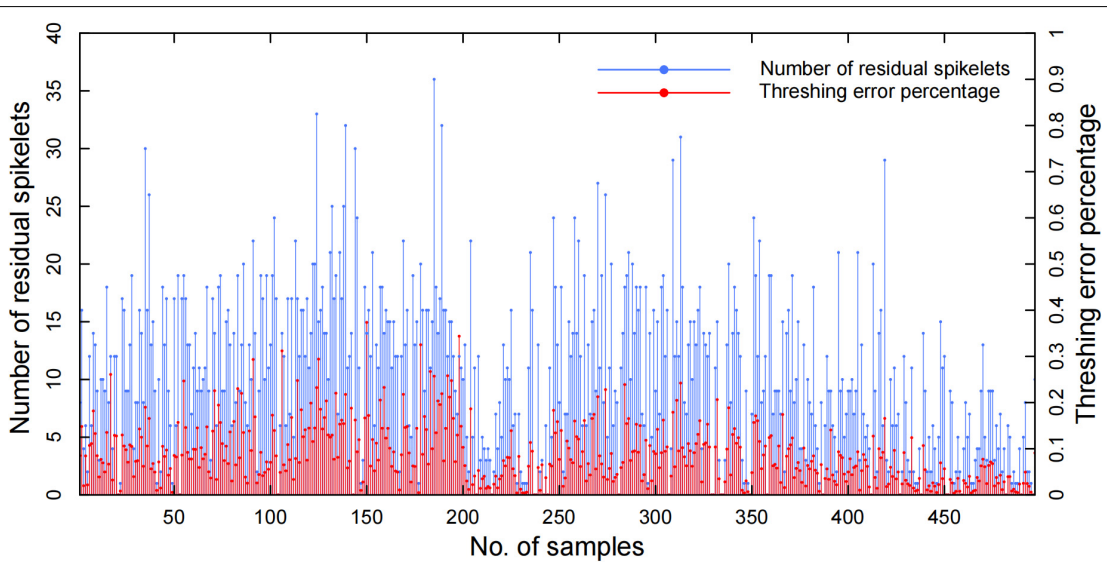

FIGURE 11 | Automatic threshing performance of the residual spikelet number and threshing error percentage.

threshed panicle structure was more complex, while the japonica panicles were easier to thresh. Therefore, the recall rate and precision value of indica varieties were lower than that of japonica varieties. Overall, the TPanicle-RCNN had a better performance of adaptability and reliability, regardless of panicle varieties and density.

According to the time cost of each step, the system efficiency was mainly decided by the threshing time, and the share of threshed panicle image inference was approximately one in eight, which indicated that the cloud computing mode did not distinctly decrease the system efficiency. In contrast, cloud computing dramatically reduced the system cost and improved the system flexibility. Thus, this study demonstrated a novel automatic system for rice yield-related trait evaluation with high accuracy and efficiency, which was of great significance to rice breeding and genetic research.

In the past studies on rice yield traits evaluation, it was difficult to balance the accuracy, automation, and practicality. For example, using X-ray computed tomography to analyze rice panicle traits could reach an R2 of 0.98 for grain number (Hu et al., 2020). However, this method required 2 min to scan and reconstruct each panicle, while the cost and radiation risk limited the practical application. We have also tried to design threshing equipment that could improve the threshing performance, and the threshing error is about 5%. However, the complicated mechanical structure and threshing error limited its popularization (Huang et al., 2013). Therefore, the existing research and equipment are still unable to meet the needs of

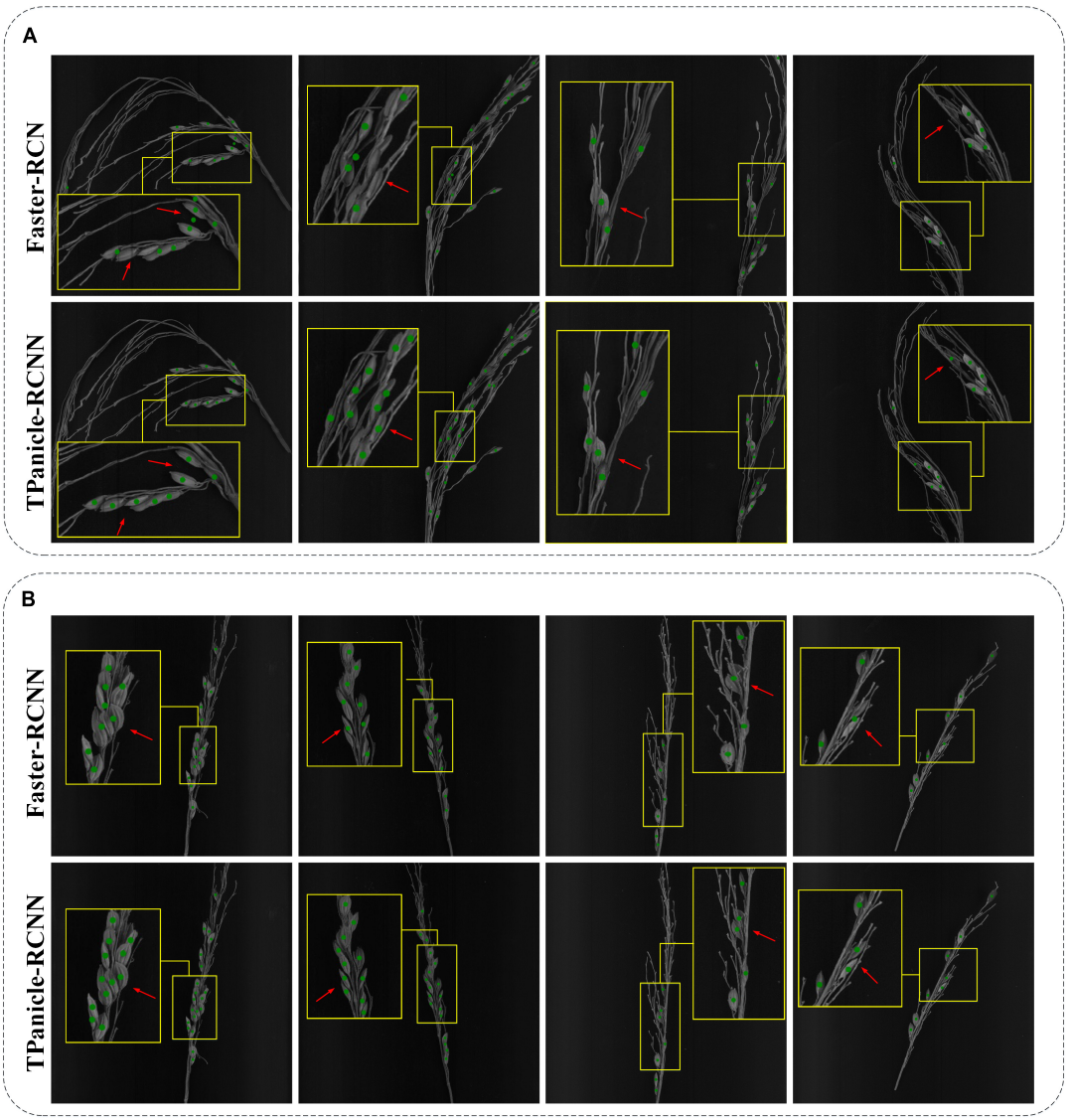

FIGURE 12 | Threshed panicle identification of the indica **(A)** and japonica **(B)** subspecies for the Faster-RCNN model and TPanicle-RCNN model. The red arrow indicates the comparison of the identification results by different models.

the practical rice yield traits evaluation with high accuracy and efficiency. In this research, we have demonstrated an intelligent method that could solve the threshing problem by threshed panicle compensation, and provide an efficient and reliable tool for rice breeding and genetic research.

CONCLUSION

This study developed a novel automatic system, for rice yield-related trait evaluation based on the technologies of automatic control, machine vision, and deep learning, in which the threshing problem has been skillfully solved by threshed panicle compensation. Moreover, a new deep learning architecture for threshed panicle analysis was proposed on the basis of Faster-RCNN, termed 'TPanicle-RCNN' and deployed in the cloud, which increased automation and improved measurement accuracy. The TPanicle-RCNN was improved by integration of the RoIAlign, CBL module, Squeeze-and-Excitation unit, and optimal anchor size, while various datasets were used to evaluate the threshed panicle identification model. The results indicated that the TPanicle-RCNN showed good performance on both japonica and indica varieties, while the F1 score was 0.929 with an increase of 0.044. To evaluate the system accuracy, 504 panicle samples were tested, and the total spikelet measurement error decreased from 11.44 to 2.99% with threshed panicle compensation. The results also proved that the system measurement was approximately 20 times more efficient than manual measurement and that cloud computing dramatically reduced the system cost and improved the system flexibility. In

conclusion, this study provides a novel and powerful tool for phenotyping yield-related traits that will benefit rice breeding and genetic research in the future.

DATA AVAILABILITY STATEMENT

The raw data supporting the conclusions of this article will be made available by the authors, without undue reservation.

AUTHOR CONTRIBUTIONS

CH and WL designed the research, performed the experiments, analyzed the data, and wrote the manuscript. ZZ, XH, JYe, JYa, LD, and XL contributed to the experiments. WY supervised the project and wrote the manuscript. All authors contributed to the article and approved the submitted version.

FUNDING

This work was supported by grants from the National Natural Science Foundation of China (U21A20205 and 31600287), key projects of Natural Science Foundation of Hubei Province (2021CFA059), major science and technology projects in Hubei Province, Fundamental Research Funds for the Central Universities (2662018JC004 and 2021ZKPY006), and HZAU-AGIS Cooperation Fund (SZYJY2022014).

SUPPLEMENTARY MATERIAL

The Supplementary Material for this article can be found online at: https://www.frontiersin.org/articles/10.3389/fpls.2022.900408/full#supplementary-material

Supplementary Video 1 | The system workflow and operation procedures of YTS-2.0.

REFERENCES

Al-Tam, F., Adam, H., Dos Anjos, A., Lorieux, M., Larmande, P., Ghesquiere, A., et al. (2013). P-TRAP: a Panicle Trait Phenotyping tool. *BMC Plant Biol.* 13:122. doi: 10.1186/1471-2229-13-122

Borrell, A. K., Mullet, J. E., George-Jaeggli, B., Van Oosterom, E. J., Hammer, G. L., Klein, P. E., et al. (2014). Drought adaptation of stay-green sorghum is associated with canopy development, leaf anatomy, root growth, and water uptake. *J. Exp. Bot.* 65, 6251–6263. doi: 10.1093/jxb/eru232

Brichet, N., Fournier, C., Turc, O., Strauss, O., Artzet, S., Pradal, C., et al. (2017). A robot-assisted imaging pipeline for tracking the growths of maize ear and silks in a high-throughput phenotyping platform. *Plant Methods* 13:96. doi: 10.1186/s13007-017-0246-7

Cai, Z., Vasconcelos, N., and IEEE (2018). *Cascade R-CNN: Delving into High Quality Object Detection*. Salt Lake City, UT: 31st IEEE/CVF Conference on Computer Vision and Pattern Recognition (CVPR), 6154–6162. doi: 10.1109/CVPR.2018.00644

Chen, L.-C., Papandreou, G., Kokkinos, I., Murphy, K., and Yuille, A. L. (2018). DeepLab: Semantic Image Segmentation with Deep Convolutional Nets, Atrous Convolution, and Fully Connected CRFs. *IEEE Trans. Pattern Anal. Machine Intell.* 40, 834–848. doi: 10.1109/TPAMI.2017.2699184

Confalonieri, R., Paleari, L., Foi, M., Movedi, E., Vesely, F. M., Thoelke, W., et al. (2017). PocketPlant3D: analysing canopy structure using a smartphone. *Biosyst. Eng.* 164, 1–12. doi: 10.1016/j.biosystemseng.2017.09.014

Deng, R., Tao, M., Huang, X., Bangura, K., Jiang, Q., Jiang, Y., et al. (2021). Automated Counting Grains on the Rice Panicle Based on Deep Learning Method. *Sensors* 21:281. doi: 10.3390/s21010281

Dhaka, V. S., Meena, S. V., Rani, G., Sinwar, D., Kavita., Ijaz, M. F., et al. (2021). A Survey of Deep Convolutional Neural Networks Applied for Prediction of Plant Leaf Diseases. *Sensors* 21:4749. doi: 10.3390/s21144749

Duan, L., Yang, W., Huang, C., and Liu, Q. (2011). A novel machine-vision-based facility for the automatic evaluation of yield-related traits in rice. *Plant Methods* 7:44. doi: 10.1186/1746-4811-7-44

Escamilla-Garcia, A., Soto-Zarazua, G. M., Toledano-Ayala, M., Rivas-Araiza, E., and Gastelum-Barrios, A. (2020). Applications of Artificial Neural Networks in Greenhouse Technology and Overview for Smart Agriculture Development. *Appl. Sci. Basel* 10:3835. doi: 10.3390/app10113835

He, K., Zhang, X., Ren, S., Sun, J., and IEEE (2016). *Deep Residual Learning for Image Recognition*. Las Vegas, NV: 2016 IEEE Conference on Computer Vision and Pattern Recognition. doi: 10.1109/CVPR.2016.90

He, K. M., Gkioxari, G., Dollar, P., Girshick, R., and IEEE (2017). *Mask R-CNN*. Venice: 16th IEEE International Conference on Computer Vision (ICCV), 2980–2988. doi: 10.1109/ICCV.2017.322

He, Y., Zhou, Z., Tian, L., Liu, Y., and Luo, X. (2020). Brown rice planthopper (Nilaparvata lugens Stal) detection based on deep learning. *Precision Agricult.* 21, 1385–1402. doi: 10.1007/s11119-020-09726-2

Hochreiter, S., and Schmidhuber, J. (1997). Long short-term memory. *Neural Comput.* 9, 1735–1780. doi: 10.1162/neco.1997.9.8.1735

Hu, W., Zhang, C., Jiang, Y., Huang, C., Liu, Q., Xiong, L., et al. (2020). Nondestructive 3D Image Analysis Pipeline to Extract Rice Grain Traits Using X-Ray Computed Tomography. *Plant Phenom.* 2020, 3414926–3414926. doi: 10.34133/2020/3414926

Huang, C., Duan, L., Liu, Q., and Yang, W. (2013). Development of a whole-feeding and automatic rice thresher for single plant. *Mathe. Comp. Modell.* 58, 684–690. doi: 10.1016/j.mcm.2011.10.033

Igathinathane, C., Pordesimo, L. O., and Batchelor, W. D. (2009). Major orthogonal dimensions measurement of food grains by machine vision using ImageJ. *Food Res. Int.* 42, 76–84. doi: 10.1016/j.foodres.2008.08.013

Ioffe, S., and Szegedy, C. (2015). *Batch Normalization: Accelerating Deep Network Training by Reducing Internal Covariate Shift*. Lille: 32nd International Conference on Machine Learning, 448–456.

Kattenborn, T., Leitloff, J., Schiefer, F., and Hinz, S. (2021). Review on Convolutional Neural Networks (CNN) in vegetation remote sensing. *ISPRS J. Photogram. Rem. Sens.* 173, 24–49. doi: 10.1016/j.isprsjprs.2020.12.010

Krizhevsky, A., Sutskever, I., and Hinton, G. (2012). ImageNet Classification with Deep Convolutional Neural Networks. *Adv. Neural Inform. Process. Syst.* 25, 1097–1105.

Li, W., Wang, D., Li, M., Gao, Y., Wu, J., and Yang, X. (2021). Field detection of tiny pests from sticky trap images using deep learning in agricultural greenhouse. *Comp. Electron. Agric.* 183:106048. doi: 10.1016/j.compag.2021.106048

Lin, T.-Y., Goyal, P., Girshick, R., He, K., and Dollar, P. (2020). Focal Loss for Dense Object Detection. *IEEE Trans. Pattern Anal. Machine Intell.* 42, 318–327. doi: 10.1109/TPAMI.2018.2858826

Liu, W., Anguelov, D., Erhan, D., Szegedy, C., Reed, S., Fu, C.-Y., et al. (2016). *SSD: Single Shot MultiBox Detector*. Amsterdam: 14th European Conference on Computer Vision (ECCV), 21–37. doi: 10.1007/978-3-319-46448-0_2

Qian, Q., Guo, L., Smith, S. M., and Li, J. (2016). Breeding high-yield superior quality hybrid super rice by rational design. *Natl. Sci. Rev.* 3, 283–294. doi: 10.1038/nplants.2017.31

Rebolledo, M. C., Pena, A. L., Duitama, J., Cruz, D. F., Dingkuhn, M., Grenier, C., et al. (2016). Combining Image Analysis, Genome Wide Association Studies and Different Field Trials to Reveal Stable Genetic Regions Related to Panicle Architecture and the Number of Spikelets per Panicle in Rice. *Front. Plant Sci.* 7:1384. doi: 10.3389/fpls.2016.01384

Redmon, J., Divvala, S., Girshick, R., Farhadi, A., and Ieee. (2016). *You Only Look Once: Unified, Real-Time Object Detection*. Seattle, WA: 2016 IEEE Conference

on Computer Vision and Pattern Recognition (CVPR), 779–788. doi: 10.1109/CVPR.2016.91

Ren, S., He, K., Girshick, R., and Sun, J. (2015). "Faster R-CNN: towards real-time object detection with region proposal networks," in *Proceedings of the 29th Annual Conference on Neural Information Processing Systems (NIPS), Dec 07-12, 2015*, Montreal, QC. doi: 10.1109/TPAMI.2016.2577031

Richards, R. A. (2000). Selectable traits to increase crop photosynthesis and yield of grain crops. *J. Exp. Bot.* 51, 447–458. doi: 10.1093/jexbot/51.suppl_1.447

Sa, I., Ge, Z., Dayoub, F., Upcroft, B., Perez, T., and Mccool, C. (2016). DeepFruits: A Fruit Detection System Using Deep Neural Networks. *Sensors* 16:1222. doi: 10.3390/s16081222

Sakamoto, T., and Matsuoka, M. (2008). Identifying and exploiting grain yield genes in rice. *Curr. Opin. Plant Biol.* 11, 209–214. doi: 10.1016/j.pbi.2008.01.009

Sandhu, J., Zhu, F., Paul, P., Gao, T., Dhatt, B. K., Ge, Y., et al. (2019). PI-Plat: a high-resolution image-based 3D reconstruction method to estimate growth dynamics of rice inflorescence traits. *Plant Methods* 15:162. doi: 10.1186/s13007-019-0545-2

Sankaran, S., Mishra, A., Ehsani, R., and Davis, C. (2010). A review of advanced techniques for detecting plant diseases. *Comp. Electron. Agric.* 72, 1–13.

Shen, Y., Zhou, H., Li, J., Jian, F., and Jayas, D. S. (2018). Detection of stored-grain insects using deep learning. *Comp. Electron. Agric.* 145, 319–325.

Simonyan, K., and Zisserman, A. (2015). "Very deep convolutional networks for large-scale image recognition," in *Proceedings of the 3rd International Conference on Learning Representations (ICLR 2015) May 7, 2015 - May 9, 2015*, San Diego, CA.

Sun, J., Di, L., Sun, Z., Shen, Y., and Lai, Z. (2019). County-Level Soybean Yield Prediction Using Deep CNN-LSTM Model. *Sensors* 19:4363. doi: 10.3390/s19204363

Tanabata, T., Shibaya, T., Hori, K., Ebana, K., and Yano, M. (2012). SmartGrain: High-Throughput Phenotyping Software for Measuring Seed Shape through Image Analysis. *Plant Physiol.* 160, 1871–1880. doi: 10.1104/pp.112.205120

Tester, M., and Langridge, P. (2010). Breeding Technologies to Increase Crop Production in a Changing World. *Science* 327, 818–822. doi: 10.1126/science.1183700

Tong, K., Wu, Y., and Zhou, F. (2020). Recent advances in small object detection based on deep learning: A review. *Image Vision Comp.* 97:103910.

van Klompenburg, T., Kassahun, A., and Catal, C. (2020). Crop yield prediction using machine learning: A systematic literature review. *Comp. Electron. Agric.* 177:105709.

Wu, W., Liu, T., Zhou, P., Yang, T., Li, C., Zhong, X., et al. (2019). Image analysis-based recognition and quantification of grain number per panicle in rice. *Plant Methods* 15:122. doi: 10.1186/s13007-019-0510-0

Wu, Y. X., and He, K. M. (2018). *Group Normalization*. Munich: 15th European Conference on Computer Vision (ECCV), 3–19. doi: 10.1007/978-3-030-01261-8_1

Xing, Y., and Zhang, Q. (2010). Genetic and Molecular Bases of Rice Yield. *Ann. Rev. Plant Biol.* 61, 421–442. doi: 10.1146/annurev-arplant-042809-112209

Yang, W., Feng, H., Zhang, X., Zhang, J., Doonan, J. H., Batchelor, W. D., et al. (2020). Crop Phenomics and High-Throughput Phenotyping: Past Decades, Current Challenges, and Future Perspectives. *Mol. Plant* 13, 187–214. doi: 10.1016/j.molp.2020.01.008

Yang, W., Guo, Z., Huang, C., Duan, L., Chen, G., Jiang, N., et al. (2014). Combining high-throughput phenotyping and genome-wide association studies to unlock the genetic architecture underlying the natural variation of rice. *Nat. Commun.* 5:5087. doi: 10.1038/ncomms6087

Yu, L., Shi, J., Huang, C., Duan, L., Wu, D., Fu, D., et al. (2021). An integrated rice panicle phenotyping method based on X-ray and RGB scanning and deep learning. *Crop J.* 9, 42–56. doi: 10.1016/j.cj.2020.06.009

Zhang, Q. (2007). Strategies for developing green super rice. *Proc. Natl. Acad. Sci. U. S. A.* 104, 16402–16409. doi: 10.1073/pnas.0708013104

Zhou, C., Ye, H., Xu, Z., Hu, J., Shi, X., Hua, S., et al. (2019). Estimating Maize-Leaf Coverage in Field Conditions by Applying a Machine Learning Algorithm to UAV Remote Sensing Images. *Appl. Sci. Basel* 9:2389. doi: 10.3390/app9112389

Conflict of Interest: The authors declare that the research was conducted in the absence of any commercial or financial relationships that could be construed as a potential conflict of interest.

Publisher's Note: All claims expressed in this article are solely those of the authors and do not necessarily represent those of their affiliated organizations, or those of the publisher, the editors and the reviewers. Any product that may be evaluated in this article, or claim that may be made by its manufacturer, is not guaranteed or endorsed by the publisher.

Copyright © 2022 Huang, Li, Zhang, Hua, Yang, Ye, Duan, Liang and Yang. This is an open-access article distributed under the terms of the Creative Commons Attribution License (CC BY). The use, distribution or reproduction in other forums is permitted, provided the original author(s) and the copyright owner(s) are credited and that the original publication in this journal is cited, in accordance with accepted academic practice. No use, distribution or reproduction is permitted which does not comply with these terms.

frontiers | Frontiers in Plant Science

TYPE Original Research
PUBLISHED 29 July 2022
DOI 10.3389/fpls.2022.948249

Check for updates

OPEN ACCESS

EDITED BY
Xiuliang Jin,
Institute of Crop Sciences (CAAS), China

REVIEWED BY
Hormoz Sohrabi,
Tarbiat Modares University,
Iran
Liang Wan,
Zhejiang University,
China

*CORRESPONDENCE
Yingbin He
heyingbin@caas.cn
Jianping Li
lijianping@caas.cn

†These authors have contributed equally to this work

SPECIALTY SECTION
This article was submitted to Sustainable and Intelligent Phytoprotection, a section of the journal Frontiers in Plant Science

RECEIVED 19 May 2022
ACCEPTED 07 July 2022
PUBLISHED 29 July 2022

CITATION
Luo S, Jiang X, He Y, Li J, Jiao W, Zhang S, Xu F, Han Z, Sun J, Yang J, Wang X, Ma X and Lin Z (2022) Multi-dimensional variables and feature parameter selection for aboveground biomass estimation of potato based on UAV multispectral imagery.
Front. Plant Sci. 13:948249.
doi: 10.3389/fpls.2022.948249

COPYRIGHT
© 2022 Luo, Jiang, He, Li, Jiao, Zhang, Xu, Han, Sun, Yang, Wang, Ma and Lin. This is an open-access article distributed under the terms of the Creative Commons Attribution License (CC BY). The use, distribution or reproduction in other forums is permitted, provided the original author(s) and the copyright owner(s) are credited and that the original publication in this journal is cited, in accordance with accepted academic practice. No use, distribution or reproduction is permitted which does not comply with these terms.

Multi-dimensional variables and feature parameter selection for aboveground biomass estimation of potato based on UAV multispectral imagery

Shanjun Luo[1,2,3†], Xueqin Jiang[3†], Yingbin He[1,2*], Jianping Li[1*], Weihua Jiao[4], Shengli Zhang[5], Fei Xu[5], Zhongcai Han[5], Jing Sun[5], Jinpeng Yang[1], Xiangyi Wang[1], Xintian Ma[1] and Zeru Lin[6]

[1]Institute of Agricultural Resources and Regional Planning, Chinese Academy of Agricultural Sciences, Beijing, China, [2]Collaborative Innovation Center on Forecast and Evaluation of Meteorological Disasters, Nanjing University of Information Science & Technology, Nanjing, China, [3]School of Remote Sensing and Information Engineering, Wuhan University, Wuhan, China, [4]Center for Agricultural and Rural Economic Research, Shandong University of Finance and Economics, Jinan, China, [5]Potato Science Institute, Jilin Academy of Vegetables and Flower Sciences, Changchun, China, [6]School of Economics and Management, Tiangong University, Tianjin, China

Aboveground biomass (AGB) is an essential assessment of plant development and guiding agricultural production management in the field. Therefore, efficient and accurate access to crop AGB information can provide a timely and precise yield estimation, which is strong evidence for securing food supply and trade. In this study, the spectral, texture, geometric, and frequency-domain variables were extracted through multispectral imagery of drones, and each variable importance for different dimensional parameter combinations was computed by three feature parameter selection methods. The selected variables from the different combinations were used to perform potato AGB estimation. The results showed that compared with no feature parameter selection, the accuracy and robustness of the AGB prediction models were significantly improved after parameter selection. The random forest based on out-of-bag (RF-OOB) method was proved to be the most effective feature selection method, and in combination with RF regression, the coefficient of determination (R^2) of the AGB validation model could reach 0.90, with root mean square error (RMSE), mean absolute error (MAE), and normalized RMSE (nRMSE) of 71.68g/m^2, 51.27g/m^2, and 11.56%, respectively. Meanwhile, the regression models of the RF-OOB method provided a good solution to the problem that high AGB values were underestimated with the variables of four dimensions. Moreover, the precision of AGB estimates was improved as the dimensionality of parameters increased. This present work can contribute to a rapid, efficient, and non-destructive means of obtaining AGB information for crops as well as provide technical support for high-throughput plant phenotypes screening.

KEYWORDS

remote sensing phenotypes, spectral indices, texture, geometric parameters, frequency-domain indicators, variables preference

Introduction

One of the 4th largest staples in the world, the potato enjoys an unparalleled position when it comes to food safety (Li et al., 2018b). Aboveground biomass (AGB) is a key metric to evaluate crop performance and is inextricably linked to yield, and its dynamics directly reflect the strength and trophic state of the crop (Zheng et al., 2019). Therefore, accurate and efficient monitoring of AGB can provide timely messages on crop growth and production estimation, which matters to guide fine farming management.

Currently, unmanned aerial vehicle (UAV) remote sensing technology has gained widespread attention in crop AGB monitoring due to the virtues of its flexible application, simple operation, and access to high space–time resolution images (Watanabe et al., 2017; Yang et al., 2017). The multispectral sensors can be compatible with the advantages of the hyperspectral and RGB sensors, such as being economically suitable, containing the red-edge and near-infrared bands, and allowing comparable spectral data to be obtained through radiometric calibration, thus gaining widespread interest in quantitative remote sensing in agriculture (Deng et al., 2018). Therefore, it is necessary to discuss the application of multispectral imagery in AGB estimation (Han et al., 2019).

The parameters that can be extracted from UAV images to characterize crop growth can be broadly classified into the following four categories. (i) Spectral variable (SV): Spectral indices (e.g., vegetation indices, VIs) are the most extensively employed parameters in precision agriculture since they have explicit physical meaning, but for many crops, the accuracy of the model is prone to saturation due to canopy closure during the late growth stage (Zheng et al., 2019). (ii) Texture variable (TV): Textures reflect the gray-scale properties of images and the spatial position of image pixels, which makes it possible to combine them with spectral variables to reduce the underestimation of crop parameters using VIs alone and thus improve the applicability of the estimation model (Li et al., 2020). The most prevalent and effective texture available is the gray level co-occurrence matrix (GLCM). (iii) Geometric variable (GV): Canopy height and fractional vegetation cover (FVC) are frequently used and valid indicators of geometric variables, reflecting the growth of the crop in both vertical and horizontal directions (Wan et al., 2020). (iv) Frequency-domain variable (FDV): The frequency-domain variable is characterized by a spectrum representing the distribution of energy. The algorithm represented by the Fourier transform converts the imagery from space to frequency dimension containing only different frequency information (high- and low-frequency information), which can highlight or suppress the details and noise of the image (Yang et al., 2019).

The joint employment of some of the above variables is presently common in precision agriculture, but few reports reveal the contribution of different dimensional variables and how they were selected. Therefore, with such a large number of variables, it is necessary to effectively extract the most appropriate variables for AGB prediction. The selection of feature variables has rarely been considered in most studies (Zheng et al., 2019; Liao et al., 2020; Maimaitijiang et al., 2020; Wan et al., 2020). The commonly applied methods for feature parameter selection are RReliefF (Li et al., 2020; Acikgoz, 2022) and machine learning (Janitza et al., 2018) such as random forest (RF). However, the difference and effectiveness of these methods for variable selection have been less studied. Moreover, there are few studies on biomass estimation in potato crops and the predictive variables are mainly focused on spectral indices and height (Li et al., 2020).

Considering that few studies have used variables from the above four dimensions simultaneously to predict AGB and to explore the impact of different feature parameter selection methods, in this study, parameters of the spectral, texture, geometric, and frequency domain were extracted from UAV multispectral images and three methods were chosen to calculate the importance of the variables, and finally, the most important parameters were selected to predict potato AGB. The major targets of the article are to (1) extract as many multi-dimensional parameters as possible that have the predictive potential for potato AGB; (2) compare the differences of three feature parameter selection methods in determining the importance of different dimensional variables and their impact on potato AGB estimation; and (3) predict potato AGB with combinations of different dimensional variables and compare their performance.

Materials and methods

Experimental design

The potato plant trials were conducted from May to August 2021 in Changchun City, Jilin Province, China (43.45°N, 124.99°E). Four widely cultivated varieties (Dongnong #310, Jishu #1, Chunshu #10, and Xuechuan #1) were involved. Different fertilizer treatments (N, P, and K) were used to simulate differentiated field cropping conditions. A total of four gradients (N1P1K1: no fertilization; N2P2K2: half of the normal fertilization; N3P3K3: normal fertilization; and N4P4K4: twice of normal fertilization) and three repetitions were set. The whole experimental area was divided into 48 small plots of the same size, with an area of about 15 m^2 (6 m × 2.5 m). Figure 1C shows the experimental design details.

UAV data acquisition

The MS600 PRO multispectral sensor was installed on a DJI Matrice 200 drone at a 40-m altitude to collect the centimeter-level images with an 18.8 mm spatial resolution. Six independent camera lenses [central bands of 450@35 (B), 555@25 (G), 660@20 (R), 720@10 (RE1), 750@15 (RE2), and 840@35 nm (NIR)] were equipped. The camera can realize automatic recognition of gray plate, real-time calculation of reflectance data, and synchronous preservation of reflectance images. In addition, its high-precision radiometric calibration and downline light sensor can ensure that users get a stable and accurate reflectance of ground objects, thus improving the consistency of data acquisition at different times and

under different environments. After the route flights (overlap both across-and along-track was 80%, flight speed was 2 m/s), Yusense Map software (Changguang Yusense Information Technology and Equipment Co., Ltd., Qingdao, China) was used to complete data preprocessing and generate DSM data. The process of acquiring reflectance images includes taking vertical downward shots of the matching calibration panels with the UAV in hand before takeoff, importing the original images and the calibration panels images into the software and framing the calibration area, and automatically conducting radiometric calibration and calculating reflectance according to the calibration panel DN values by the software. During the potato growth periods, we completed three flights from 11:00–13:00 on June 18 (seedling period, SP), July 17 (flowering period, FP), and August 9 (tuber period, TP). After obtaining the reflectance images, a rectangular region of interest (ROI) was defined for each plot, and the mean reflectance within the region was treated as the plot-level reflectance of the plot.

Field data measurement

Field measured data include canopy height, hyperspectral curves of different endmembers, and AGB of each plot. The millimeter-scale ruler was used to measure the true value of potato canopy height at each period. After the execution of each flight, three potato plants in each plot were randomly dug out, then the roots were subtracted, and the rest were dried indoors. These plants were ovened at 110°C for a few minutes before being kept at 75°C until the weight remained unchanged. Finally, the electronic balance was applied to weigh them and AGB was calculated in combination with the planting density. Hyperspectral curves of different endmembers at three stages were measured by the ASD spec four spectrometers.

Multi-dimensional parameters extraction based on UAV images

After each plot of the imagery was defined to acquire plot-level reflectance, several VIs (plot-level VIs) commonly used in precision agriculture (shown in Table 1) were computed according to the plot-level reflectance.

In practice, most of the pixels obtained by sensors are mixed pixels, and there is little detailed description information about the components, so it is difficult to give a more accurate description inside the pixels. The linear model is extensively used in spectral mixture analysis (SMA) due to its simpleness and clear physical meanings (Chang, 2017). In this study, the linear model of fully constrained least-square (LM-FCL) was used to obtain pure vegetation information.

$$R_{mp}=\sum_{i=1}^{M} Abd_i R_i+\mu \qquad (1)$$

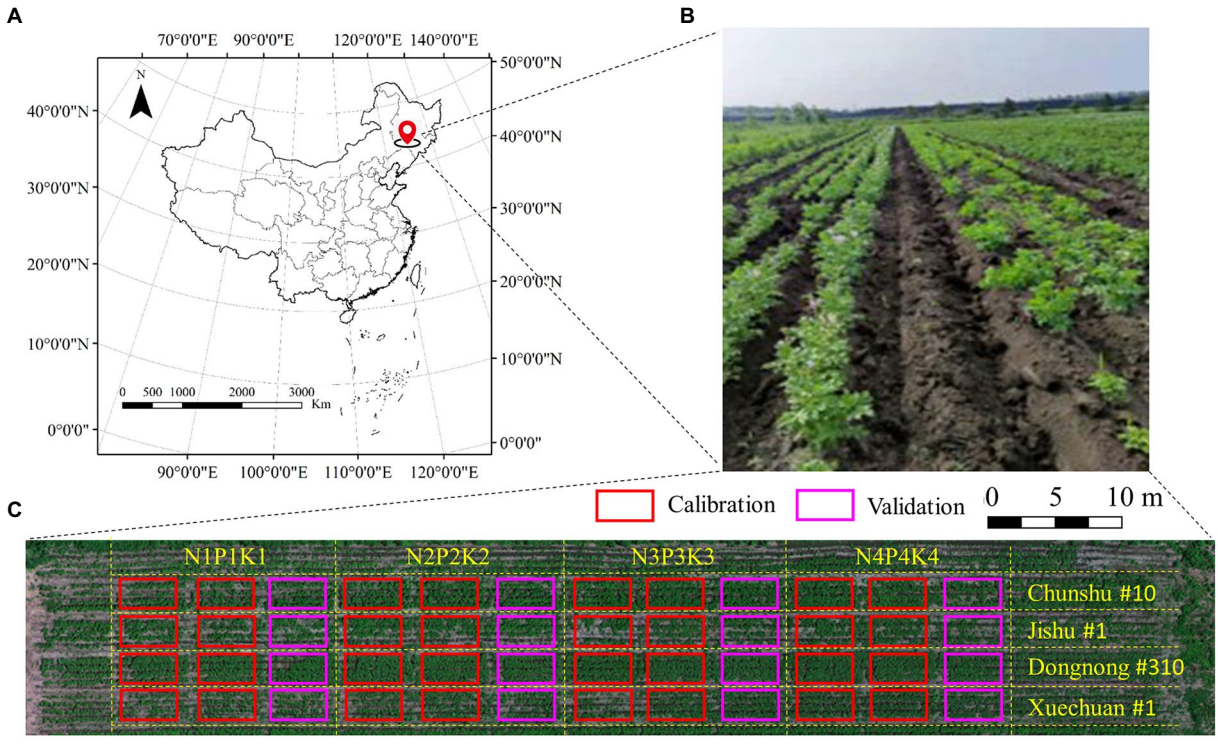

FIGURE 1
Potato trial layout: **(A)** the trail location; **(B)** the field scene photo; **(C)** experimental design details.

TABLE 1 VIs of different band combinations for predicting potato AGB.

Vegetation indices	Formula	References
NDVI	$(R_{840nm} - R_{660nm})/(R_{840nm} + R_{660nm})$	Rouse et al., 1974
NDRE	$(R_{840nm} - R_{720nm})/(R_{840nm} + R_{720nm})$	Gitelson and Merzlyak, 1997
MTCI	$(R_{840} - R_{720nm})/(R_{720} + R_{660nm})$	Dash and Curran, 2004
EVI2	$2.5(R_{840nm} - R_{660nm})/(R_{840nm} + 2.4_{R660nm} + 1)$	Jiang et al., 2008
VARI	$(R_{555nm} - R_{660nm})/(R_{555nm} + R_{660nm})$	Gitelson et al., 2002
OSAVI	$(1 + 0.16)(R_{840nm} - R_{660nm})/(R_{840nm} + R_{660nm} + 0.16)$	Rondeaux et al., 1996

$$\mathbf{0} \le \boldsymbol{Abd_i} \le \mathbf{1} \quad (2)$$

$$\sum_{i=1}^{M} \boldsymbol{Abd_i} = \mathbf{1} \quad (3)$$

where R_{mp} and R_i represent the reflectance of the mixed pixel and pure endmember, respectively. Abd is the abundance of different endmembers, M denotes the endmember amounts, and ε shows the error.

GLCM was considered to be the combined likelihood distributed of the pixel couple (Haralick et al., 1973). Six GLCM-based textures, variance (VAR), homogeneity (HOM), contrast (CON), dissimilarity (DIS), entropy (ENT), and second moment (SEC), were selected to participate in the AGB prediction.

Geometric variables, such as canopy height (Jiang et al., 2019) and FVC (Wan et al., 2020), were considered as the important predictors of crop biomass and yield. The canopy height can be accessed by subtracting the ground DEM from DSM. For assurance of the FVC precision achieved, the dimidiate pixel model (DPM) and the image classification method were used to check each other. The blue, green, and red bands were extracted from the multispectral images, and the true color synthesis was realized by RGB superposition. The support vector machine was applied for image classification to extract vegetation parts, and then, the FVC data can be obtained *via* the division of the plant pixel count by the overall. Moreover, the NDVI-based DPM was employed in the FVC estimation (Yan et al., 2022). Equation (4) shows the calculation principle.

$$FVC = (NDVI_M - NDVI_{NS})/(NDVI_{PP} - NDVI_{NS}) \quad (4)$$

where $NDVI_M$, $NDVI_{NS}$, and $NDVI_{PP}$ denote NDVI values of mixed, naked soil, and pure plant pixels, respectively. In this paper, due to the inevitable noise, the maximum and minimum values of $NDVI_{veg}$ and $NDVI_{soil}$ were set within the range of 98% confidence.

By transforming each spectral curve into ensembles of sine and cosine functions (see Eq. 5), the spectral domain data [$R_j = (r_1, r_2, \ldots, r_n)$, j is the band serial number (j = 1, 2, …, n), r is the reflectance, and n is band number] is converted into the frequency domain, thus obtaining parameters such as constant terms ($A_0/2$), amplitude (A_t, B_t, C_t), and phase (φ_t) that characterize the function (Jiang et al., 2021).

$$\begin{aligned} \boldsymbol{r(j)} &= \frac{\boldsymbol{A_0}}{\mathbf{2}} + \sum_{t=1}^{\infty} \left[\boldsymbol{A_t} \cos\left(\mathbf{2}\pi \boldsymbol{tj} / \boldsymbol{n}\right) + \boldsymbol{B_t} \sin\left(\mathbf{2}\pi \boldsymbol{tj} / \boldsymbol{n}\right) \right] \\ &= \frac{\boldsymbol{A_0}}{\mathbf{2}} + \sum_{t=1}^{\infty} \boldsymbol{C_t} \sin\left(\mathbf{2}\pi \boldsymbol{tj} / \boldsymbol{n} + \boldsymbol{\varphi_t}\right) \end{aligned} \quad (5)$$

$$\frac{\boldsymbol{A_0}}{\mathbf{2}} = \frac{\mathbf{1}}{\boldsymbol{n}} \left(\boldsymbol{r_1} + \boldsymbol{r_2} + .. + \boldsymbol{r_n} \right) \quad (6)$$

$$\boldsymbol{A_t} = \frac{\mathbf{2}}{\boldsymbol{n}} \sum_{j=1}^{n} \boldsymbol{r_j} \cos\left(\mathbf{2}\boldsymbol{t}\pi \boldsymbol{j} / \boldsymbol{n}\right) \quad (7)$$

$$\boldsymbol{B_t} = \frac{\mathbf{2}}{\boldsymbol{n}} \sum_{j=1}^{n} \boldsymbol{r_j} \sin\left(\mathbf{2}\boldsymbol{t}\pi \boldsymbol{j} / \boldsymbol{n}\right) \quad (8)$$

$$\boldsymbol{C_t} = \sqrt{\left(\boldsymbol{A_t}^2 + \boldsymbol{B_t}^2 \right)} \quad (9)$$

$$\boldsymbol{\varphi_t} = \arctan\left(\boldsymbol{A_t} / \boldsymbol{B_t} \right) \quad (10)$$

where *t* is the decomposition times.

Feature parameter selection methods

RReliefF algorithm

RReliefF algorithm is a feature selection method based on statistical correlation (Robnik-Sikonja and Kononenko, 2003). By randomly selecting a sample R in the training set, and then, searching its adjacent samples (the same class H and diverse class M), weights of each feature are updated according to the distance between R, H, and M. For continuous feature values, the difference [*Dif*(F, R_1, R_2)] between two samples R_1 and R_2 for feature F is defined as:

$$Dif\left(F, R_1, R_2\right) = \frac{\left| R_1(F) - R_2(F) \right|}{\max - \min} \quad (11)$$

where Max and Min represent the maximum value of F.

The weight [W(F)] of feature F can be given by approximate probability distribution:

$$W(F) = P(Dif(F, R_1, R_2)|M) - P(Dif(F, R_1, R_2)|H) \quad (12)$$

For the regression problem, two resampling probabilities are introduced to judge if they are in the same class. Probabilistic

determinations make it possible to model and forecast the corresponding intervals between two resamples.

$$P_1 = P(Dif(F)|H) \quad (13)$$

$$P_2 = P(Dif(prediction)|H) \quad (14)$$

where P_1 and P_2 are the simulated and predicted values of the distance probability of two similar samples.

According to the conditional probability:

$$P_{2|1} = P(Dif(prediction)|Dif\ (F)|H) \quad (15)$$

Combined with Eq. (12) and Eq. (15):

$$W(F) = (P_{2|1} \times P_1)/P_2 - [(1 - P_{2|1}) \times P_1]/(1 - P_2) \quad (16)$$

RF algorithm based on Gini index and error of out-of-bag

Bootstrap resampling technology is used in RF to collect a certain amount of samples in the target dataset. In each round of random sampling of bagging, some data in the training set are not selected (out-of-bag, OOB). This part is not engaged in the data simulation and thus serves to check the model's robustness.

The Gini index selection standard can be expressed that each sub-node reaches the highest purity (Boulesteix et al., 2012), that is, all observations falling in the sub-node belong to the same classification. For the decision tree (DT) in RF, there are v (v = 1, 2, …, q) classes of samples altogether. Assuming a sample falls into class v with probability p_v, the probability distribution of Gini index [G(PD)] can be defined as Eq. (17).

$$G(PD) = \sum_{v=1}^{q} p_v(1 - p_v) = 1 - \sum_{v=1}^{q} p_v^2 \quad (17)$$

Procedure for measuring the importance of features through the error of OOB includes:

(i) The OOB data that correspond to every DT was chosen to compute the error (E_1)
(ii) The noise is appended to F to compute the OOB error (E_2)
(iii) The assumption is that there are a total of K DTs, the importance of F (IMP_F) can be calculated:

$$IMP_F = \sum (E_2 - E_1)/K \quad (18)$$

IMP_F is able to account for the importance of F in that if there is a marked reduction in the precision of the OOB data after the addition of noise (i.e., an increase in E_2), this indicates that F strongly influences the predicted outcome.

Regression algorithms and accuracy evaluation

In this paper, the selected multi-dimensional feature parameters were used to estimate potato AGB in multiple periods by two regression algorithms (partial least squares regression, PLSR; random forest regression, RFR). The model precision was quantitatively characterized by R^2, RMSE, MAE, and nRMSE (Dong et al., 2020) using a separate validation dataset (Figure 1C).

Results

Acquisition of SVs based on the SMA of dynamic endmembers

The spectral endmembers in the field become more and more complex with the growth and development of potatoes. At SP, the light leaf (LL), shaded leaf (SL), light soil (LS), and shaded soil (SS) were included. At FP, the flower was added. At TP, the leaves can be divided into green and yellow ones. Thus, unlike FP, the light green leaf (LGL), shaded green leaf (SGL), and yellow leaf (YL) were added. By taking the mean value of measured spectral reflectance in the corresponding band range, spectral endmembers used for SMA in different periods are shown in Figure 2.

The results of LM-FCL-based SMA in different periods using dynamic endmembers are shown in Figure 3. It can be indicated that there are significant differences in abundance images of the same endmember at different stages (the more colored parts represents the greater abundance). For example, at SP, the colored parts of the leaf abundance (including LL and SL) are relatively lower than that at FP and TP and the soil abundance (including LS and SS) images show the opposite. Moreover, with the arrival of TP, the abundance of the flower and YL increases.

The VI calculated by the plot-level reflectance was defined as VI[plot]. To obtain the vegetation spectral parameters without soil background information, the product of the sum of abundances excluding soil and VI[plot] was defined as VI[v]. The correlation between potato AGB and VIs with different definitions is shown in Figure 4. It is seen that all listed VIs[v] were more correlated with the potato AGB than VIs[plot]. Thus, the VIs[v] were regarded as the SVs to predict the potato AGB.

Extraction of TVs in different bands and computational directions

Six bands of the multispectral images were used to calculate textures in three different directions [parallel ($D_{//}$) and perpendicular ($D_{\perp}$) to the ridge, and an angle of 45° ($D_{\angle}$) to the ridge]. The correlation in Figure 5 shows that HOM and SEC were negatively correlated with AGB, while VAR, CON, DIS, and ENT

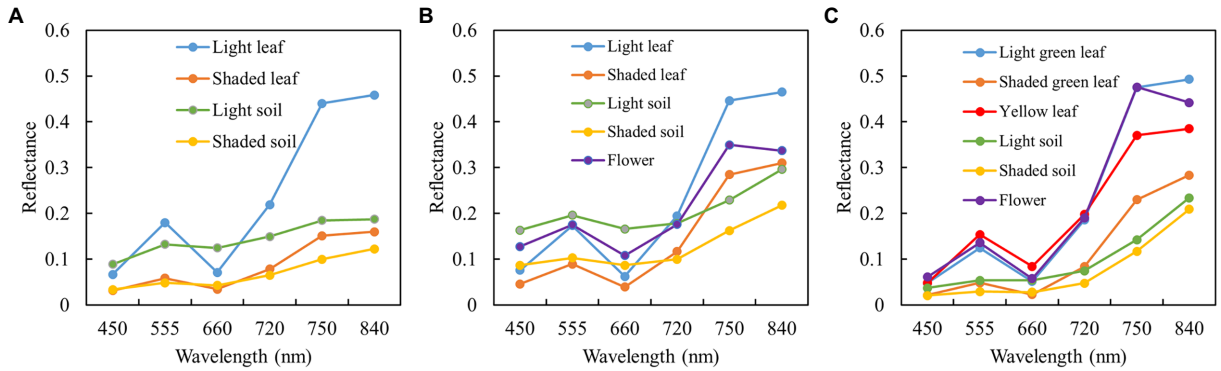

FIGURE 2
Field measured spectra of endmembers in different potato periods: **(A)** June 18; **(B)** July 17; **(C)** August 9.

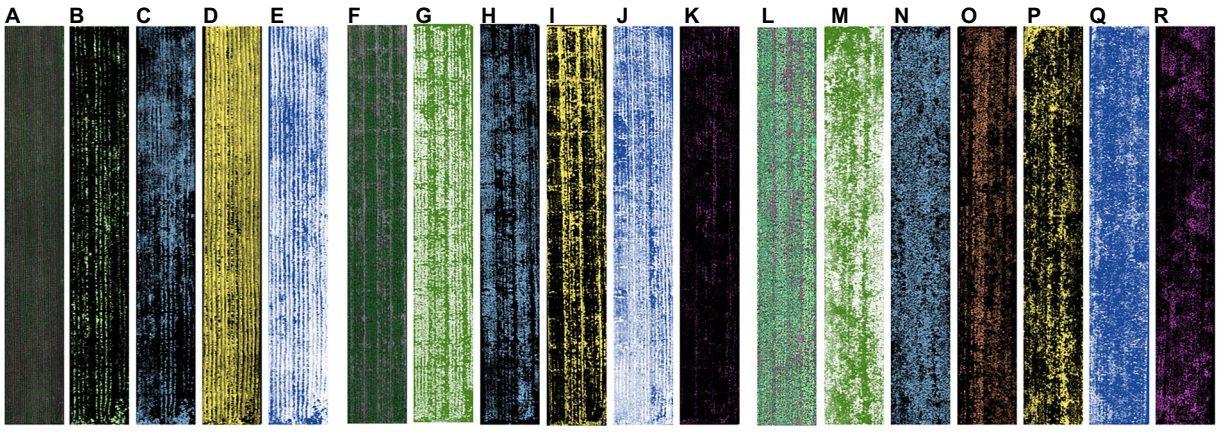

FIGURE 3
The abundance images of different potato growth stages: **(A–E)** LL, SL, LS, SS at SP; **(F–K)** LL, SL, LS, SS, flower at FP; **(L–R)** LGL, SGL, YL, LS, SS, flower at TP.

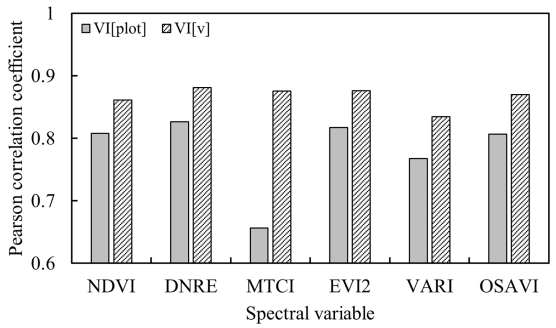

FIGURE 4
Correlation between potato AGB and VIs.

were positively correlated with AGB. Furthermore, the correlation between VAR, ENT, SEC, and AGB was consistent in different directions, while the correlation between HOM, CON, DIS, and AGB was significantly different in three directions.

In terms of different bands, the B, RE2, and NIR-based textures had a high correlation with AGB. The textures of other bands showed instability in different directions. Therefore, the B-based textures in the $D_{\perp}$direction with the highest correlation with AGB were referred to as TVs.

Extraction and validation of GVs

The UAV-based canopy heights were compared with the manually measured values (Figure 6A). The results showed that the heights acquired by UAV were highly correlated with the observed values ($R^2 = 0.9262$, RMSE = 0.0404 m). In addition, the comparison of two methods of obtaining FVC (DPM and SVM) was performed (Figure 6B). It can be observed that the FVC obtained by these two methods has a good consistency ($R^2 = 0.9786$ and RMSE = 0.0256). Therefore, we have reason to believe the accuracy of the FVC data extracted in this paper.

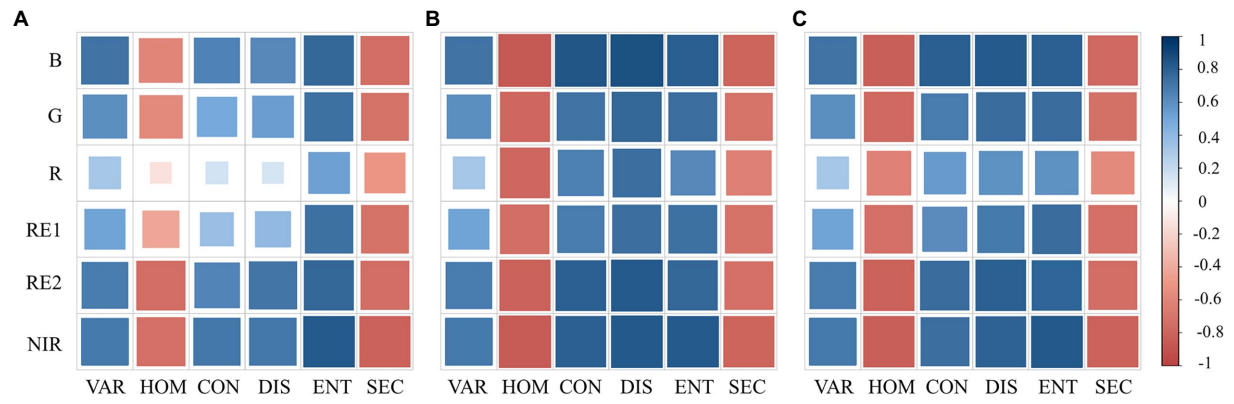

FIGURE 5
Correlation between potato AGB and textures based on different bands and calculation directions: **(A)** $D_{\parallel}$; **(B)** $D_{\perp}$; **(C)** $D_{\angle}$.

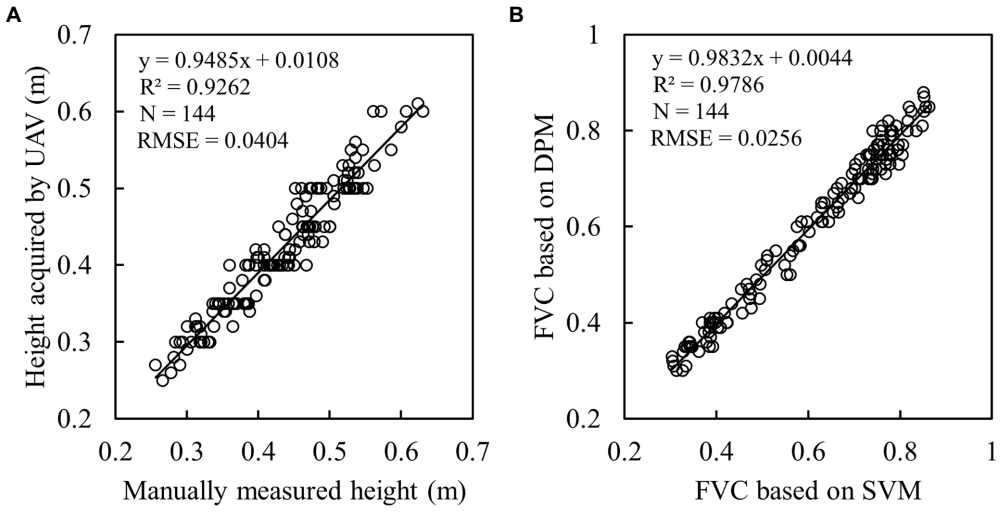

FIGURE 6
Verification of geometric parameters: **(A)** canopy height of potato; **(B)** canopy FVC of potato.

Acquisition of FDVs based on harmonic decomposition

To explain the harmonic decomposition process, the spectra of an arbitrary potato plot were selected as an example, and the harmonic decomposition parameters were calculated six times according to the formula of $C_t\sin(2\pi tj/n+\varphi_t)$. Figure 7 shows that the maximum amplitude appears in the sixth decomposition, and the amplitudes of the first five decompositions show little difference. Different amplitudes can represent high- and low-frequency information in the spectra.

The correlation between potato AGB and harmonic parameters of six decompositions is shown in Figure 8. The results indicated that except for the sixth decomposition, A and C obtained by the first five decompositions had a strong correlation with AGB. Also, the parameters of B obtained by six times of decomposition were strongly correlated with AGB. The correlation between φ and AGB obtained by all the decomposition times was weak. It concluded that low-frequency spectral information is more suitable for predicting potato AGB in multiple periods for FDVs.

RRelieff and RF for feature variables selection

In this paper, 39 variables of spectra were extracted. And three feature selection algorithms were used to calculate the importance of different parameters. Figure 9 shows the ranking results of feature importance values. The top 10 feature variables were exhibited in the dotted box. The results indicate that there are great differences among the top 10 important indices extracted

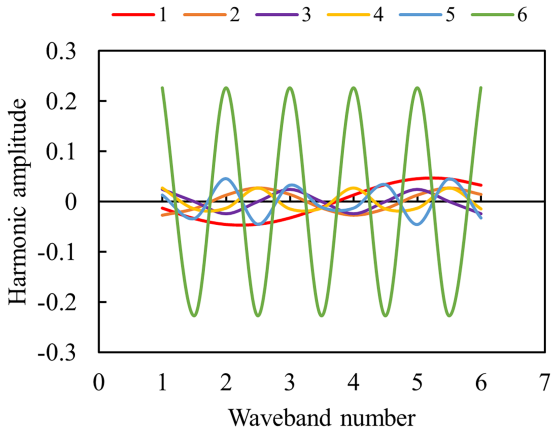

FIGURE 7
Schematic diagram of different harmonic decomposition times.

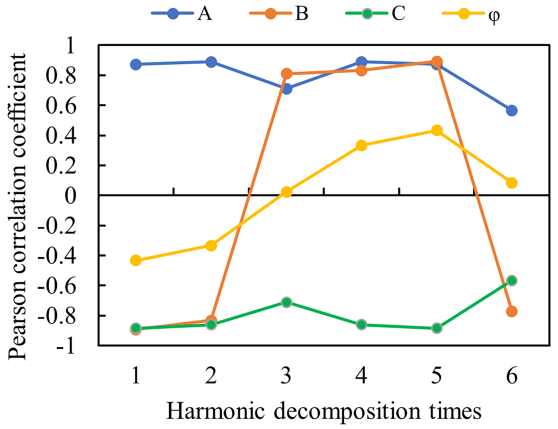

FIGURE 8
Correlation between potato AGB and harmonic parameters of different decomposition times.

by the three methods, especially the RReliefF and RF-based methods. The importance of the variable calculated by RReliefF is based on the correlation with AGB. The higher the correlation, the greater the weight value. The top 10 important variables extracted by the two RF-based methods are very similar and parameters selected by RF-Gini are also highly correlated with AGB. However, the RF-OOB selected φ_1 which is not highly correlated with AGB.

AGB estimation using different regression algorithms and multi-dimensional variables

The AGB prediction accuracy of calibration and validation datasets are shown in Table 2. It can be found that the accuracy without any feature variable selection is similar to that based on RReliefF and RF-Gini for the calibration dataset, but there is an obvious difference in the accuracy of the validation dataset. The accuracy of all parameters-based models (including PLSR and RFR) is much lower than that of the RReliefF and RF-Gini-based models, which shows that amount of parameters for forecasting is not the more the better, and the redundant variables will reduce the robustness of the models.

In terms of the feature selection method, the variables extracted by RF-OOB have the highest prediction accuracy of potato AGB ($R^2 = 0.90$, RMSE = 71.68 g/m^2, MAE = 51.27 g/m^2, and nRMSE = 11.56% for the validation dataset). From the perspective of the regression algorithm, the RFR has more advantages than PLSR for all variable selection scenarios in this paper.

A comparison chart of measured versus estimated AGB values in the validation dataset is shown in Figure 10 (the dashed line indicates the 1:1 line). It can be seen that for all feature selection methods (including no selection), the PLSR algorithm tends to produce negative values at low values of AGB. Moreover, the None, RReliefF, and RF-Gini-based models are prone to underestimate at high AGB values, especially in the range of 500–700 g/m^2. The RF-OOB-based models are a good solution to the problem of underestimation of high-value AGB (the regression line almost coincides with the 1:1 line). Hence, the RF-OOB-RFR model works best for the estimation of multi-period potato AGB using multi-dimensional variables derived from multispectral imagery.

To measure the contribution of spectra and other variables to the potato AGB estimates, the variables of the four dimensions were combined into seven combinations. RF-OOB was then used to select the top ten most important parameters for modeling and validation (all variables would be selected if there were fewer than 10 variables). As shown in Table 3, for the same regression algorithm, the accuracy of different combinations increases with the increasing dimensionality of the variables. For the same combination of variables, RFR models have higher precision compared to that of PLSR, except for SV + TV. This suggests that the selections of variables and regression algorithms are equally important for AGB prediction.

Discussion

Crop AGB is an essential indicator of crop growth as well as crop breeding and management, and is one of the key factors affecting crop yield and profitability (Zhao et al., 2021). Potato has an irreplaceable role in ensuring food security, and the use of remote sensing technology to obtain potato AGB information can provide a basis for its yield estimation and provide decision-making information for farm production management and markets (Luo et al., 2020). The advent of remote sensing technology, especially UAV remote sensing, has made it possible to non-destructively and rapidly estimate crop AGB at the plot level (Osco et al., 2021).

Soil background or shadows can frequently affect the estimation of plant canopy parameters by radiation values (Wang et al., 2022). As shown in Figure 2, the spectral differences between components such as potato plants and background at different

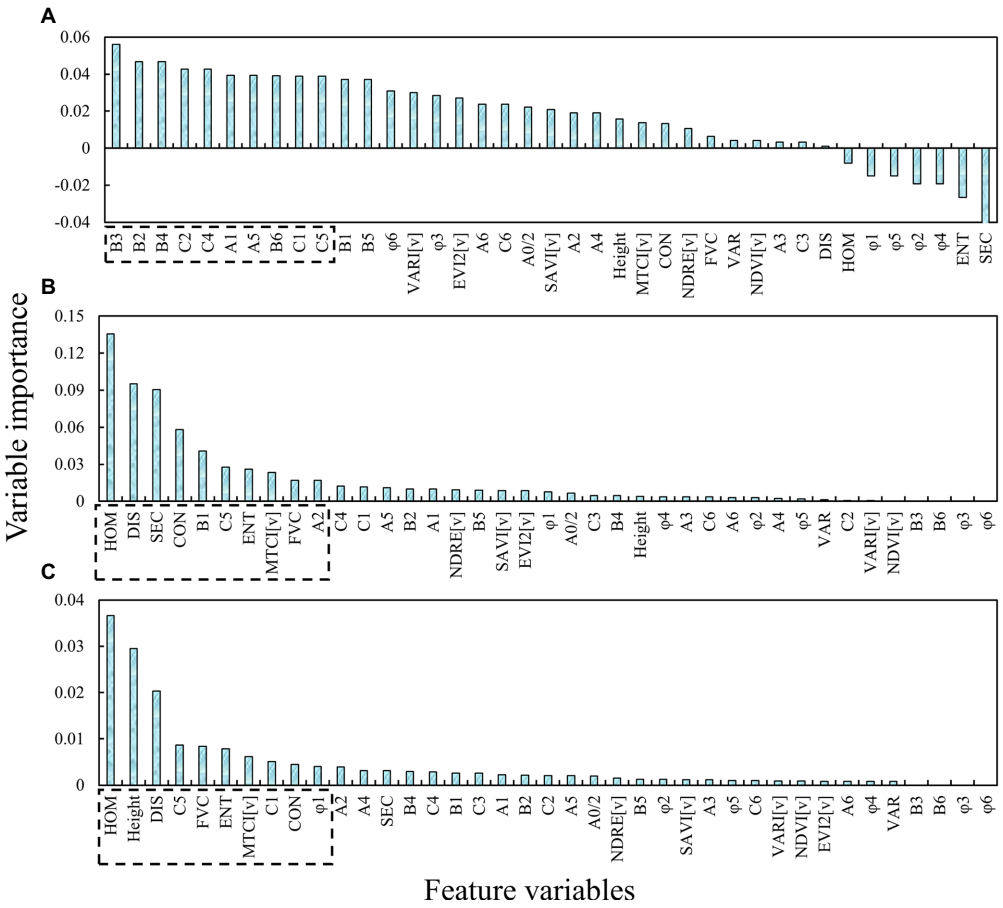

FIGURE 9
Variable importance ranking of different feature parameter selection methods: **(A)** RReliefF; **(B)** RF-Gini; **(C)** RF-OOB.

TABLE 2 Potato AGB prediction results based on different feature selection methods and regression algorithms.

Feature selection methods	Regression methods	Calibration				Validation			
		R^2	RMSE (g/m^2)	MAE (g/m^2)	nRMSE (%)	R^2	RMSE (g/m^2)	MAE (g/m^2)	nRMSE (%)
None	PLSR	0.86	83.17	59.25	13.55	0.82	93.68	63.78	15.11
	RFR	0.87	80.34	58.51	13.08	0.83	90.79	63.61	14.64
RReliefF	PLSR	0.87	80.77	58.82	13.15	0.85	85.22	61.19	13.75
	RFR	0.88	77.21	55.82	12.57	0.87	80.48	58.59	12.98
RF-Gini	PLSR	0.85	85.32	61.25	13.90	0.84	88.30	62.23	14.24
	RF	0.87	80.45	58.66	13.10	0.85	85.64	61.50	13.81
RF-OOB	PLSR	0.89	73.54	53.85	11.98	0.88	77.15	56.37	12.44
	RF	0.91	68.76	49.18	11.20	0.90	71.68	51.27	11.56

growth periods of potato were quite pronounced, and the proportion of different components (Figure 3) also changed significantly as can be seen by the abundance maps of each component. Therefore, spectral unmixing often results in good background removal when estimating crop parameters using spectral indices (Yang et al., 2007; Wang et al., 2022). The combination of VI and spectral unmixing results was often used to enhance the prediction of pure spectra (Zhou et al., 2018; Duan et al., 2019). In this paper, the product of VI and the abundance of vegetation was used to characterize the spectral information of potato, and the results showed that the correlation with AGB was significantly improved based on VI[plot] (Figure 4).

Moreover, the computational window scale has been shown no impact on the estimation of AGB when it comes to texture calculations (Li et al., 2020), but the choice involving specific orientation has been less reported. The results in Figure 5

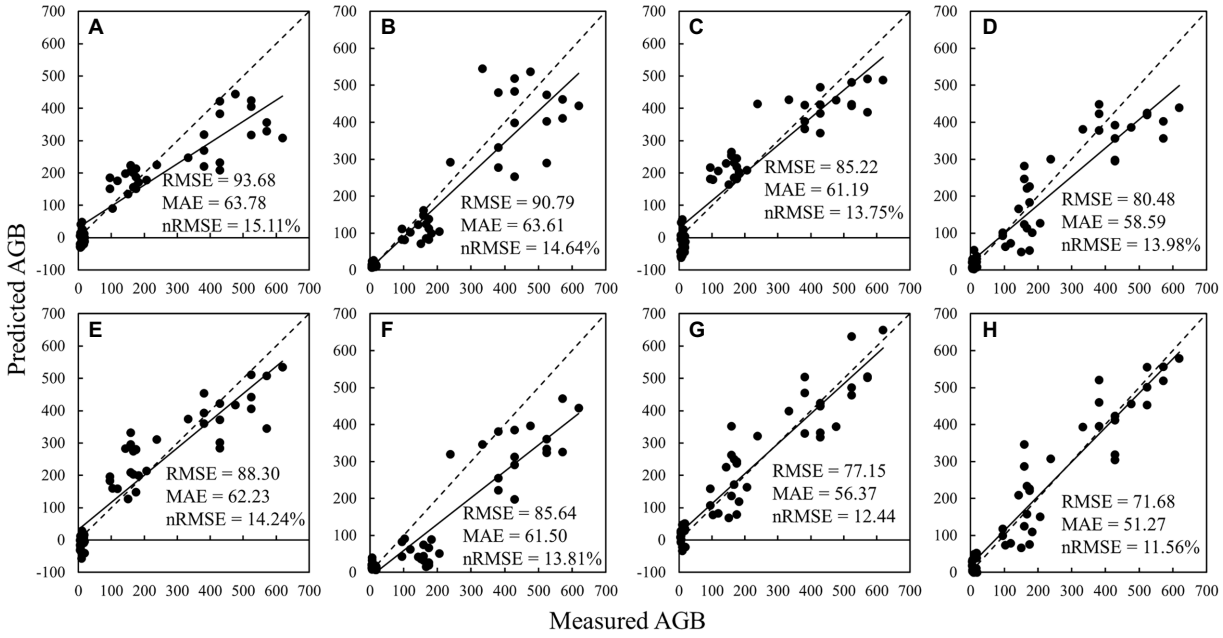

FIGURE 10
Comparison of measured and predicted AGB using different feature selection and regression algorithms: **(A)** None-PLSR; **(B)** None-RFR; **(C)** RReliefF-PLSR; **(D)** RReliefF-RFR; **(E)** RF-Gini-PLSR; **(F)** RF-Gini-RFR; **(G)** RF-OOB-PLSR; **(H)** RF-OOB-RFR.

TABLE 3 Potato AGB prediction results based on different variable combinations and regression algorithms.

Variable combinations	Regression methods	Calibration				Validation			
		R^2	RMSE (g/m^2)	MAE (g/m^2)	nRMSE (%)	R^2	RMSE (g/m^2)	MAE (g/m^2)	nRMSE (%)
SV + TV	PLSR	0.80	99.49	67.66	16.20	0.81	95.26	65.55	15.36
	RFR	0.82	93.74	63.82	15.27	0.80	98.93	67.04	15.96
SV + GV	PLSR	0.83	90.63	62.98	14.76	0.81	95.39	66.02	15.39
	RFR	0.85	85.29	61.30	13.89	0.83	90.56	63.28	14.61
SV + FDV	PLSR	0.82	93.87	64.02	15.29	0.81	96.33	66.89	15.54
	RFR	0.85	85.28	61.20	13.89	0.83	89.25	62.88	14.40
SV + TV + GV	PLSR	0.85	85.10	61.09	13.86	0.84	88.27	62.63	14.24
	RFR	0.87	80.54	58.75	13.12	0.87	80.86	58.97	13.04
SV + TV + FDV	PLSR	0.84	88.04	62.13	14.34	0.82	93.56	63.85	15.09
	RFR	0.88	77.39	56.04	12.60	0.86	83.26	59.34	13.43
SV + GV + FDV	PLSR	0.85	85.46	61.25	13.92	0.83	89.66	62.58	14.46
	RFR	0.88	77.03	56.15	12.55	0.87	80.61	58.31	13.00
SV + TV + GV + FDV	PLSR	0.89	73.54	53.85	11.98	0.88	77.15	56.37	12.44
	RFR	0.91	68.76	49.18	11.20	0.90	71.68	51.27	11.56

demonstrated that among the six selected textures, VAR, ENT, and SEC are not affected by the computational direction, which is due to the fact that the computational equations of these three textures contain texture statistics reflecting the inside of the computational window, and a change in the computational direction does not cause a change in them, nor does it cause a change in the statistical values of all pixels within the window. In contrast, the calculation equations of HOM, CON, and DIS all contain information in different calculation directions, reflecting the texture statistics in the calculation direction within the window. Therefore, when there is an obvious texture pattern with direction in the image, a change in the calculation direction will have an obvious effect on these three textures. Potatoes are a planted-by-ridge crop, and their field morphology is directional, especially in the first and middle stages. Initially, there was a flat soil background in most of the canopy images, and seedlings only accounted for a small portion (Figure 3A), at which time the image homogeneity was high and heterogeneity was low. As the

plants grow, seedlings grow a large number of new leaves in all directions, and the proportion of soil background decreases and the proportion of disordered leaves increases in the images (Figure 3B), leading to a weakening of image homogeneity and an increase in heterogeneity. After flowering, as well as the appearance of yellow leaves, the complexity was further increased (Figure 3C). Therefore, during the growth of rice, the homogeneity of images kept weakening and heterogeneity kept increasing with the accumulation of biomass, leading to a negative correlation between textures reflecting homogeneity (HOM and SEC) and biomass, and positive correlation between textures reflecting heterogeneity (VAR, CON, DIS, and ENT) and biomass. And the trend of this correlation does not change with orientations. The correlations of three directions suggested that the texture perpendicular to ridges reflected the potato growth information best (Figure 5). This may be due to the fact that the texture parallel to the ridges gives more expression to the spatial relationship between the potato plants, while the texture perpendicular to the ridges characterizes the relationship between the plants and the background, which is more indicative of the growth of the vegetation. It also provides a reference for texture selection of other ridge crops.

In addition to spectra and textures, parameters such as height and FVC are frequently exploited to improve the accuracy of crop biomass and yield estimation (Ashapure et al., 2020; Xu et al., 2022). In this study, the canopy height derived from DSM and DEM and FVC cross-validated by DPM and SVM (Figure 6) were obtained to participate in variable importance ranking and to improve the accuracy of AGB estimation. This is due to the fact that each of these parameters can characterize plant growth and development in different ways. For example, canopy height can provide stereoscopic information about the crop to compensate for the lack of canopy spectral information for estimating AGB (). LAI, which characterizes stereoscopic growth information of potato, was used to estimate yield and the results showed that its estimation was better than that of spectra (Luo et al., 2020). Therefore, more variables that can characterize plant stereo information (e.g., parameters obtained by LiDAR) are worth exploring for estimating crop AGB and yield. FVC, which represents the lushness of plant growth, has good parameter estimation ability, especially before crop closure of the canopy (Wan et al., 2020). Moreover, harmonic parameters were shown to be effective in crop biophysical parameter inversion (Zhuo et al., 2020; Jiang et al., 2021). However, the application of harmonic parameters in biomass estimation has been rarely reported. The results in Figures 7, 8 show that parameters highly correlated with the AGB could be extracted from both high-frequency and low-frequency spectral information. After the parameters of four dimensions were extracted, feature parameter selection becomes a new challenge (Faris et al., 2018).

Feature selection is critical in crop yield prediction, parameter inversion, and data preprocessing strategy, and overly redundant variables can even lead to reduced model robustness and accuracy (Li et al., 2018a, 2020). Thus, in potato biomass estimation, direct prediction of variables with multiple dimensions is evident to be inappropriate and necessary for feature selection. The results based on the three feature parameter selection methods show that RReliefF mainly conducts variable sorting according to the correlation with the target parameter (de Oliveira et al., 2017), which will lead to the failure to remove redundant features effectively and reduce the robustness of the model. RF-Gini, while similar to RF-OOB, leaves out important parameters such as height. Height has been shown to perform a vital part in AGB and yield estimation (Li et al., 2020; Maimaitijiang et al., 2020; Wan et al., 2020), which limits the accuracy of the model. The parameters selected by RF-OOB include not only highly correlated variables but also parameters such as height and φ_1, although the correlation with AGB may not be high (Figure 9). This method mainly aims to reduce the error of the model.

The results of RF-OOB-RFR demonstrate that there is informational variability and complementarity between the parameters of different dimensions and that all these indices contribute to the estimation of AGB to different degrees. Additionally, RF-OOB algorithms are good at proposing indices with complementary information from parameters of different dimensions for the accurate estimation of AGB (Figure 10). This study can contribute to a scientific basis for timely and lossless monitoring of AGB in potatoes and other crops.

Conclusion

In this study, four dimensions of variables (SV, TV, GV, and FDV, see Table 4) and three methods of feature parameter selection (RReliefF, RF-Gini, and RF-OOB) were used to analyze and compare the estimation accuracy of potato AGB. When extracting parameters in different dimensions from the UAV images, the LM-FCL-based SMA method using dynamic endmembers was found to be effective in removing the influence of background, thus improving the correlation between VIs and AGB. In addition, the B-based textures in the $D_{\perp}$ direction could show the ridge distribution of potatoes well. Variables of different dimensions were subsequently exploited for PLSR and RFR modeling and validation. It was found that the accuracy of the models continuously improved with the addition of variables of different dimensions, but this happened with the feature variable selection. Without any variable selection, the robustness of the model was very poor. Furthermore, the PLSR was prone to produce negative values at low values of AGB, while the RFR models could accurately predict AGB, especially when using four-dimensional variables and RF-OOB, and the underestimation problem for high values of AGB was well solved. According to the above results, the RFR model combined with four-dimensional variables and RF-OOB proposed in this paper is promising for accurate prediction of AGB and provides technical and theoretical support for rapid extraction of remote sensing phenotypic information of crops and high-throughput screening of plant phenotypes.

TABLE 4 The short glossary of terms in this study.

Full spelling words	Abbreviated glossary	Full spelling words	Abbreviated glossary
Aboveground biomass	AGB	Variance	VAR
Coefficient of determination	R^2	Homogeneity	HOM
Root mean square error	RMSE	Contrast	CON
Mean absolute error	MAE	Dissimilarity	DIS
Normalized RMSE	nRMSE	Entropy	ENT
Unmanned aerial vehicle	UAV	Second moment	SEC
Spectral variable	SV	Dimidiate pixel model	DPM
Vegetation indices	VIs	Out-of-bag	OOB
Texture variable	TV	Decision tree	DT
Gray level co-occurrence matrix	GLCM	Light leaf	LL
Geometric variable	GV	Shaded leaf	SL
Fractional vegetation cover	FVC	Light soil	LS
Frequency-domain variable	FDV	Shaded soil	SS
Random forest	RF	Light green leaf	LGL
Flowering period	FP	Shaded green leaf	SGL
Tuber period	TP	Yellow leaf	YL
Spectral mixture analysis	SMA	Partial least squares regression	PLSR
Linear model of fully constrained least-square	LM-FCL	Random forest regression	RFR

Data availability statement

The raw data supporting the conclusions of this article will be made available by the authors, without undue reservation.

Author contributions

SL wrote the manuscript. YH and JL provided the study ideas and completed the experimental design. WJ provided suggestions and edited the manuscript. SZ, FX, ZH, and JS measured the experimental data. JY and XW conducted the UAV flights. XM and ZL provided comments on the revision of the manuscript. All authors contributed to the article and approved the submitted version.

Funding

This work was supported by the National Natural Science Foundation of China's "Study on temporally and spatially precise assessment on potato cultivation suitability based on dynamic process-oriented mode" (41771562) and "Innovation Project" of the Chinese Academy of Agricultural Sciences (2021–2025, IARRP).

Conflict of interest

The authors declare that the research was conducted in the absence of any commercial or financial relationships that could be construed as a potential conflict of interest.

Publisher's note

All claims expressed in this article are solely those of the authors and do not necessarily represent those of their affiliated organizations, or those of the publisher, the editors and the reviewers. Any product that may be evaluated in this article, or claim that may be made by its manufacturer, is not guaranteed or endorsed by the publisher.

References

Acikgoz, H. (2022). A novel approach based on integration of convolutional neural networks and deep feature selection for short-term solar radiation forecasting. *Appl. Energy* 305:117912. doi: 10.1016/j.apenergy.2021.117912

Ashapure, A., Jung, J. H., Chang, A. J., Oh, S., Yeom, J., Maeda, M., et al. (2020). Developing a machine learning based cotton yield estimation framework using multi-temporal UAS data. *ISPRS J. Photogramm. Remote Sens.* 169, 180–194. doi: 10.1016/j.isprsjprs.2020.09.015

Boulesteix, A. L., Bender, A., Bermejo, J. L., and Strobl, C. (2012). Random forest Gini importance favours SNPs with large minor allele frequency: impact, sources and recommendations. *Brief. Bioinform.* 13, 292–304. doi: 10.1093/bib/bbr053

Chang, C. I. (2017). Adaptive linear spectral mixture analysis. *IEEE Trans. Geosci. Remote Sens.* 55, 1240–1253. doi: 10.1109/tgrs.2016.2620494

Dash, J., and Curran, P. J. (2004). The MERIS terrestrial chlorophyll index. *Int. J. Remote Sens.* 25, 5403–5413. doi: 10.1080/0143116042000274015

de Oliveira, M. P. G., Bocca, F. F., and Rodrigues, L. H. A. (2017). From spreadsheets to sugar content modeling: A data mining approach. *Comput. Electron. Agric.* 132, 14–20. doi: 10.1016/j.compag.2016.11.012

Deng, L., Mao, Z. H., Li, X. J., Hu, Z. W., Duan, F. Z., and Yan, Y. N. (2018). UAV-based multispectral remote sensing for precision agriculture: A comparison between different cameras. *ISPRS J. Photogramm. Remote Sens.* 146, 124–136. doi: 10.1016/j.isprsjprs.2018.09.008

Dong, J., Lu, H. B., Wang, Y. W., Ye, T., and Yuan, W. P. (2020). Estimating winter wheat yield based on a light use efficiency model and wheat variety data. *ISPRS J. Photogramm. Remote Sens.* 160, 18–32. doi: 10.1016/j.isprsjprs.2019.12.005

Duan, B., Fang, S. H., Zhu, R. S., Wu, X. T., Wang, S. Q., Gong, Y., et al. (2019). Remote estimation of rice yield with unmanned aerial vehicle (UAV) data and spectral mixture analysis. *Front. Plant Sci.* 10:14. doi: 10.3389/fpls.2019.00204

Faris, H., Mafarja, M. M., Heidari, A. A., Aljarah, I., Al-Zoubi, A. M., Mirjalili, S., et al. (2018). An efficient binary Salp swarm algorithm with crossover scheme for feature selection problems. *Knowledge Based Syst.* 154, 43–67. doi: 10.1016/j.knosys.2018.05.009

Gitelson, A. A., Kaufman, Y. J., Stark, R., and Rundquist, D. (2002). Novel algorithms for remote estimation of vegetation fraction. *Remote Sens. Environ.* 80, 76–87. doi: 10.1016/s0034-4257(01)00289-9

Gitelson, A. A., and Merzlyak, M. N. (1997). Remote estimation of chlorophyll content in higher plant leaves. *Int. J. Remote Sens.* 18, 2691–2697. doi: 10.1080/014311697217558

Han, L., Yang, G. J., Dai, H. Y., Xu, B., Yang, H., Feng, H. K., et al. (2019). Modeling maize above-ground biomass based on machine learning approaches using UAV remote-sensing data. *Plant Methods* 15:10. doi: 10.1186/s13007-019-0394-z

Haralick, R. M., Shanmugam, K., and Dinstein, I. (1973). Textural features for image classification. *IEEE Trans. Syst. Man Cybern. SMC3* SMC-3, 610–621. doi: 10.1109/tsmc.1973.4309314

Janitza, S., Celik, E., and Boulesteix, A. L. (2018). A computationally fast variable importance test for random forests for high-dimensional data. *Adv. Data Anal. Classif.* 12, 885–915. doi: 10.1007/s11634-016-0276-4

Jiang, Q., Fang, S. H., Peng, Y., Gong, Y., Zhu, R. S., Wu, X. T., et al. (2019). UAV-based biomass estimation for rice-combining spectral, TIN-based structural and meteorological features. *Remote Sens. (Basel)* 11:19. doi: 10.3390/rs11070890

Jiang, Z. Y., Huete, A. R., Didan, K., and Miura, T. (2008). Development of a two-band enhanced vegetation index without a blue band. *Remote Sens. Environ.* 112, 3833–3845. doi: 10.1016/j.rse.2008.06.006

Jiang, X. Q., Luo, S. J., Fang, S. H., Cai, B. W., Xiong, Q., Wang, Y. Y., et al. (2021). Remotely sensed estimation of total iron content in soil with harmonic analysis and BP neural network. *Plant Methods* 17:116. doi: 10.1186/s13007-021-00812-8

Li, J. D., Cheng, K. W., Wang, S. H., Morstatter, F., Trevino, R. P., Tang, J. L., et al. (2018a). Feature selection: a data perspective. *ACM Comput. Surv.* 50, 1–45. doi: 10.1145/3136625

Li, Q., Li, H. B., Zhang, L., Zhang, S. Q., and Chen, Y. L. (2018b). Mulching improves yield and water-use efficiency of potato cropping in China: a meta-analysis. *Field Crop Res* 221, 50–60. doi: 10.1016/j.fcr.2018.02.017

Li, B., Xu, X. M., Zhang, L., Han, J. W., Bian, C. S., Li, G. C., et al. (2020). Above-ground biomass estimation and yield prediction in potato by using UAV-based RGB and hyperspectral imaging. *ISPRS J. Photogramm. Remote Sens.* 162, 161–172. doi: 10.1016/j.isprsjprs.2020.02.013

Liao, Z. M., He, B. B., and Quan, X. W. (2020). Potential of texture from SAR tomographic images for forest aboveground biomass estimation. *Int. J. Appl. Earth Obs. Geoinf.* 88:102049. doi: 10.1016/j.jag.2020.102049

Luo, S., He, Y. B., Li, Q., Jiao, W. H., Zhu, Y. Q., and Zhao, X. H. (2020). Nondestructive estimation of potato yield using relative variables derived from multi-period LAI and hyperspectral data based on weighted growth stage. *Plant Methods* 16:150. doi: 10.1186/s13007-020-00693-3

Maimaitijiang, M., Sagan, V., Sidike, P., Hartling, S., Esposito, F., and Fritschi, F. B. (2020). Soybean yield prediction from UAV using multimodal data fusion and deep learning. *Remote Sens. Environ.* 237:111599. doi: 10.1016/j.rse.2019.111599

Osco, L. P., Marcato, J., Ramos, A. P. M., Jorge, L. A. D., Fatholahi, S. N., Silva, J. D., et al. (2021). A review on deep learning in UAV remote sensing. *Int. J. Appl. Earth Obs. Geoinf.* 102:102456. doi: 10.1016/j.jag.2021.102456

Robnik-Sikonja, M., and Kononenko, I. (2003). Theoretical and empirical analysis of relief F and RReliefF. *Mach. Learn.* 53, 23–69. doi: 10.1023/a:1025667309714

Rondeaux, G., Steven, M., and Baret, F. (1996). Optimization of soil-adjusted vegetation indices. *Remote Sens. Environ.* 55, 95–107. doi: 10.1016/0034-4257(95)00186-7

Rouse, J. W., Haas, R. H., Schell, J. A., and Deering, D. W. (1974). Monitoring vegetation systems in the great plains with ERTS. *NASA Spec. Publ.* 351:309.

Wan, L., Cen, H. Y., Zhu, J. P., Zhang, J. F., Zhu, Y. M., Sun, D. W., et al. (2020). Grain yield prediction of rice using multi-temporal UAV-based RGB and multispectral images and model transfer - a case study of small farmlands in the south of China. *Agric. For. Meteorol.* 291:108096. doi: 10.1016/j.agrformet.2020.108096

Wang, W., Zheng, H., Wu, Y., Yao, X., Zhu, Y., Cao, W., et al. (2022). An assessment of background removal approaches for improved estimation of rice leaf nitrogen concentration with unmanned aerial vehicle multispectral imagery at various observation times. *Field Crop Res* 283:108543. doi: 10.1016/j.fcr.2022.108543

Watanabe, K., Guo, W., Arai, K., Takanashi, H., Kajiya-Kanegae, H., Kobayashi, M., et al. (2017). High-throughput phenotyping of sorghum plant height using an unmanned aerial vehicle and its application to genomic prediction modeling. *Front. Plant Sci.* 8:11. doi: 10.3389/fpls.2017.00421

Xu, L., Zhou, L. F., Meng, R., Zhao, F., Lv, Z., Xu, B. Y., et al. (2022). An improved approach to estimate ratoon rice aboveground biomass by integrating UAV-based spectral, textural and structural features. *Precis. Agric.* 23, 1276–1301. doi: 10.1007/s11119-022-09884-5

Yan, K., Gao, S., Chi, H. J., Qi, J. B., Song, W. J., Tong, Y. Y., et al. (2022). Evaluation of the vegetation-index-based dimidiate pixel model for fractional vegetation cover estimation. *IEEE Trans. Geosci. Remote Sens.* 60, 1–14. doi: 10.1109/tgrs.2020.3048493

Yang, C. G., Everitt, J. H., and Bradford, J. M. (2007). Airborne hyperspectral imagery and linear spectral unmixing for mapping variation in crop yield. *Precis. Agric.* 8, 279–296. doi: 10.1007/s11119-007-9045-x

Yang, G. J., Liu, J. G., Zhao, C. J., Li, Z. H., Huang, Y. B., Yu, H. Y., et al. (2017). Unmanned aerial vehicle remote sensing for field-based crop phenotyping: current status and perspectives. *Front. Plant Sci.* 8:26. doi: 10.3389/fpls.2017.01111

Yang, B. H., Wang, M. X., Sha, Z. X., Wang, B., Chen, J. L., Yao, X., et al. (2019). Evaluation of aboveground nitrogen content of winter wheat using digital imagery of unmanned aerial vehicles. *Sensors* 19:18. doi: 10.3390/s19204416

Zhao, L., Zhou, W., Peng, Y. P., Hu, Y. M., Ma, T., Xie, Y. K., et al. (2021). A new AG-AGB estimation model based on MODIS and SRTM data in Qinghai Province, China. *Ecol. Indic.* 133:108378. doi: 10.1016/j.ecolind.2021.108378

Zheng, H. B., Cheng, T., Zhou, M., Li, D., Yao, X., Tian, Y. C., et al. (2019). Improved estimation of rice aboveground biomass combining textural and spectral analysis of UAV imagery. *Precis. Agric.* 20, 611–629. doi: 10.1007/s11119-018-9600-7

Zhou, K., Cheng, T., Zhu, Y., Cao, W. X., Ustin, S. L., Zheng, H. B., et al. (2018). Assessing the impact of spatial resolution on the estimation of leaf nitrogen concentration over the full season of paddy rice using near-surface imaging spectroscopy data. *Front. Plant Sci.* 9:18. doi: 10.3389/fpls.2018.00964

Zhuo, W., Shi, R. H., Zhang, C., Gao, W., Liu, P. D., Wu, N., et al. (2020). A novel method for leaf chlorophyll retrieval based on harmonic analysis: a case study on *Spartina alterniflora*. *Earth Sci Inform* 13, 747–762. doi: 10.1007/s12145-020-00465-6

frontiers | Frontiers in Plant Science

TYPE Original Research
PUBLISHED 04 August 2022
DOI 10.3389/fpls.2022.957870

Check for updates

OPEN ACCESS

EDITED BY
Xiuliang Jin,
Institute of Crop Sciences (CAAS), China

REVIEWED BY
Saeed Hamood Alsamhi,
Ibb University, Yemen
Liang Wan,
Zhejiang University, China

*CORRESPONDENCE
Yan Gong
gongyan@whu.edu.cn

SPECIALTY SECTION
This article was submitted to Sustainable and Intelligent Phytoprotection, a section of the journal Frontiers in Plant Science

RECEIVED 31 May 2022
ACCEPTED 11 July 2022
PUBLISHED 04 August 2022

CITATION
Zhou C, Gong Y, Fang S, Yang K, Peng Y, Wu X and Zhu R (2022) Combining spectral and wavelet texture features for unmanned aerial vehicles remote estimation of rice leaf area index.
Front. Plant Sci. 13:957870.
doi: 10.3389/fpls.2022.957870

COPYRIGHT
© 2022 Zhou, Gong, Fang, Yang, Peng, Wu and Zhu. This is an open-access article distributed under the terms of the Creative Commons Attribution License (CC BY). The use, distribution or reproduction in other forums is permitted, provided the original author(s) and the copyright owner(s) are credited and that the original publication in this journal is cited, in accordance with accepted academic practice. No use, distribution or reproduction is permitted which does not comply with these terms.

Combining spectral and wavelet texture features for unmanned aerial vehicles remote estimation of rice leaf area index

Cong Zhou[1], Yan Gong[1,2]*, Shenghui Fang[1,2], Kaili Yang[1], Yi Peng[1,2], Xianting Wu[2,3] and Renshan Zhu[2,3]

[1]School of Remote Sensing and Information Engineering, Wuhan University, Wuhan, China, [2]Lab for Remote Sensing of Crop Phenotyping, Wuhan University, Wuhan, China, [3]College of Life Sciences, Wuhan University, Wuhan, China

Estimating the crop leaf area index (LAI) accurately is very critical in agricultural remote sensing, especially in monitoring crop growth and yield prediction. The development of unmanned aerial vehicles (UAVs) has been significant in recent years and has been extensively applied in agricultural remote sensing (RS). The vegetation index (VI), which reflects spectral information, is a commonly used RS method for estimating LAI. Texture features can reflect the differences in the canopy structure of rice at different growth stages. In this research, a method was developed to improve the accuracy of rice LAI estimation during the whole growing season by combining texture information based on wavelet transform and spectral information derived from the VI. During the whole growth period, we obtained UAV images of two study areas using a 12-band Mini-MCA system and performed corresponding ground measurements. Several VI values were calculated, and the texture analysis was carried out. New indices were constructed by mathematically combining the wavelet texture and spectral information. Compared with the corresponding VIs, the new indices reduced the saturation effect and were less sensitive to the emergence of panicles. The determination coefficient (R^2) increased for most VIs used in this study throughout the whole growth period. The results indicated that the estimation accuracy of LAI by combining spectral information and texture information was higher than that of VIs. The method proposed in this study used the spectral and wavelet texture features extracted from UAV images to establish a model of the whole growth period of rice, which was easy to operate and had great potential for large-scale auxiliary rice breeding and field management research.

KEYWORDS

leaf area index (LAI), vegetation index (VI), unmanned aerial vehicle (UAV), remote sensing (RS), texture, wavelet, rice

Introduction

Rice is the staple food for more than 50% of the global population (Yuan, 2014). A useful index to monitor crop growth is the leaf area index (LAI), which is defined as the total leaf area per unit ground area. LAI is commonly used as an important parameter for photosynthesis, respiration, and productivity of vegetation (Gower et al., 1999; Liang et al., 2015). In the practical application of precision agriculture, LAI is also an effective indicator for diagnosing crop growth, estimating biomass, and predicting yield (Liu et al., 2005; Zhou et al., 2017; Fang et al., 2019). Therefore, it is very important to obtain crop LAI accurately, which can obviously improve the monitoring of crop growth and yield prediction in agricultural remote sensing.

Although the crop measurements based on the traditional manual methods are effective, they are labor-intensive and time-consuming. Therefore, it is not possible to quickly obtain temporal and spatial information on crops in detail on a large scale. The remote sensing technique, which is non-destructive and often applied at large scale, has achieved satisfactory results in the estimation of crop LAI and becomes more and more important. There are two main techniques to estimate LAI by remote sensing images: empirical statistical models (ESMs) (Zarate-Valdez et al., 2012) and radiative transfer models (RTMs) (Dorigo, 2012). Although RTM approaches can simulate the radiation transmission process of the optical signal in the canopy, they need many input parameters and high computational costs. In general, regression models are used to establish the relationship between LAI and vegetation indices (VIs). Numerous optical VIs are calculated from the combinations of two or more different spectral bands, mostly distributed in the visible and near-infrared regions of the spectrum. Through band combinations, the VI can highlight vegetation information which is in the reflectance spectrum, inhibit the effects of other interfering factors such as the structure of leaves and canopy (Herrmann et al., 2011; Verrelst et al., 2015), and reduce the soil, atmosphere, and solar–target–sensor geometry effects as much as possible (Moulin, 1999; Matsushita et al., 2007; Viña et al., 2011). In the 1970s, the normalized difference vegetation index (NDVI) and ratio vegetation index (RVI) were first applied by Rouse for estimating vegetation growth characteristics (Rouse et al., 1974). In recent years, many VIs have been applied in the estimation of LAI (Fang et al., 2019). Viña et al. (2011) evaluated several VIs to estimate the green leaf area index of corn and soybean, in which the chlorophyll index (CI_{green}, MTCI, and $CI_{red\ edge}$) showed a very significant linear relationship with green LAI. Qiao et al. (2020) used six VIs derived from MERIS data to establish LAI seasonal tracks for different types of vegetation, including deciduous forest, evergreen forest, and crops. Dong et al. (2019) proved the potential of VIs based on red-edge reflectance derived from multi-temporal RapidEye images in the LAI estimation of spring wheat and rape. Indices that incorporated the reflectance of red-edge bands had increased potential for estimating LAI. Liang et al. (2015) proposed a hybrid inversion method for estimating the crop LAI and evaluated 43 VIs to determine the best VIs in the estimation of LAI. However, there are still some problems to be settled in the estimation of rice LAI.

The changes in the canopy morphology and structure of rice are more obvious and complex than those of other vegetation types in different growth periods (Sakamoto et al., 2011; He et al., 2019). Rice seeds are transplanted into soil or water after germination. With the tillering and jointing of rice, the leaves gradually increase in size and leaf area. At this time, the canopy is blocked by leaves, and the soil background is almost invisible. When 20% of panicles have exserted from the sword leaf sheath, the plants enter the heading stage. The rice panicles are slender and rough in shape. When the rice enters the ripening stage, the panicles begin to droop and change color from green to golden. Meanwhile, the leaf begins to wither and falls from bottom to top, which makes the canopy structure of the crop more complex (Reza et al., 2019; Zha et al., 2020). The effect of remote estimation of rice LAI during the whole growth stage is greatly affected by the sophisticated changes in rice phenology.

In the early growth stage, the canopy reflectance is strongly influenced by the soil background (Zarco-Tejada et al., 2001; Croft et al., 2014; Tian et al., 2014). When the rice canopy closes, VIs tend to saturate in high coverage conditions (Viña et al., 2011). After the heading stage, the panicles begin to appear and are disorderly distributed. Remote sensing reflectance data contain not only leaf information but also panicle information. At the same time, the leaves begin to wither and yellow, and the canopy spectrum is greatly affected (Yang Q. et al., 2022). The VIs are very easy to be saturated in the late growth stage of rice, and LAI is relatively stable from the tillering to the jointing stage, but its value range is wide. Therefore, it is necessary to estimate LAI accurately in the later stages of growth. Wang et al. (2019) estimated LAI of rice before and after heading stages using 10 VIs. It was found that VARI was susceptible to the emergence of panicles, and the accuracy of estimation of LAI was affected by the panicles. Zhou et al. (2017) also found that panicles reduced the accuracy of grain yield estimation at the late growth stages of rice. Therefore, the model of rice LAI estimation without considering the variability of different fertility periods is flawed and ignores the complexity of rice. Differences in the canopy structure during rice growth must be taken into account to make more accurate estimates. In addition, for professionals, observing whether paddy plots are heading is a laborious and time-consuming job. Consequently, the estimation of rice LAI for the whole growing season is important.

Texture analysis plays an important role in image processing and is usually used to define the variability of pixel values between adjacent pixels of the analysis window (Kelsey and Neff, 2014). In recent years, many studies have considered image texture features when estimating LAI

(Zhang et al., 2021, 2022), AGB (Hlatshwayo et al., 2019; Yue et al., 2019), N nutrition parameters (Zheng et al., 2020), and plant potassium accumulation (PKA) (Lu et al., 2021). Li S. et al. (2019) used the UAV and RGB images to build the NDTI model. The indices based on the RGB images were combined with the calculated the NDTI to improve the accuracy of rice LAI estimation. Duan et al. (2019) proposed a method using Fourier spectral energy percentage (FSEP) and found that the FSEP extracted from VI images could obtain a more accurate rice LAI estimation model than the VI. In addition, the VI is highly susceptible to saturation in late rice growth stages, resulting in unsatisfactory LAI estimation. The combination of texture features and VIs is helpful in improving the accuracy of LAI estimation. However, the existing research methods cannot accurately reflect the complex changes in the rice canopy structure at different growth stages. On this foundation, it is necessary to find a texture feature that can adapt to multi-temporal changes of rice to assist the VI to improve the sensitivity of LAI estimation, especially in the canopy closure stage and post-heading stage. Wavelet texture features can quantify the differences in image texture features (Ren et al., 2021) and reveal the differences in the canopy structure in the process of rice growth.

In recent years, wavelet analysis with time–frequency and multi-resolution characteristics has become an effective tool for texture analysis (Huan and Hou, 2008), and it has been widely used for feature extraction (Ghazali et al., 2007), image denoising (Gökdağ et al., 2019), and object/tissue detection (Jain and Salau, 2019). The image is decomposed by the two-dimensional (2D) discrete wavelet transform (DWT) into four sub-bands: LL, reflecting the approximate information of the image, and LH, HH, and HL, reflecting vertical, diagonal, and horizontal detail information of the image, respectively. Most of the energy is concentrated in the LL sub-band, which mainly reflects the approximate component information of the original image (Chang and Kuo, 1993; Bruce et al., 2002; Quandt et al., 2015). The DWT, which is considered to be an efficient method for extracting hyperspectral features, is applied to quantify pigment concentration (Blackburn, 2007), retrieve soil moisture (Peng et al., 2013), and estimate LNC (Li F. et al., 2019) and crop residue quality (Sahadevan et al., 2014). In addition, energy is often used as a texture feature extracted by wavelet transform (Salari and Ling, 1995; Banskota et al., 2013), which can represent texture features in space from the point of energy distribution in the frequency domain and has great texture representation capability (Ren et al., 2021). The combination of texture features and spectral features has shown great potential in LAI estimation (Zheng et al., 2020). Wavelet texture features can enhance the discrimination ability of spatial information (Eckert, 2012). VIs contain rich spectral information, and wavelet texture features can provide spatial structure information of multiple growth stages of rice. Therefore, the advantage of wavelet texture features in capturing the difference in the canopy structure at different growth stages makes it a suitable index to improve the accuracy of rice LAI estimation combined with spectrum features.

Unmanned aerial vehicles (UAVs) have developed rapidly in recent years and have become a promising technology in disaster rescue, transportation, agriculture, and environmental monitoring (Alsamhi et al., 2021, 2022; Saif et al., 2021; Amarasingam et al., 2022; Yang Z. et al., 2022). UAV images are also applied in precision agriculture due to high resolution and low cost. For example, Jin et al. (2017) introduced a method to estimate wheat density using UAV images obtained at very low altitudes. Pádua et al. (2018) conducted multi-temporal monitoring of vineyard vegetation using UAVs equipped with consumer-grade RGB sensors. High-resolution UAV images can also help extract texture features, so it is necessary to consider texture features when monitoring vegetation growth.

In this study, a method for LAI estimation by combining spectral features and wavelet texture features is developed, given the differences in the rice canopy structure at different growth stages. The main purpose of this study is to discuss the potential of the combination of wavelet texture features and spectral features on the LAI estimation throughout the entire growth stage of rice based on UAV images, which have low cost, high flexibility, and high resolution.

Materials and methods

Study area

The two experiments were carried out in two different study areas: One was located in the hybrid rice experiment base of Wuhan University in Lingshui, Hainan, China (18°31′47″N, 110°03′34″E), and the other was located in Ezhou, Hubei, China (30°22′31″N 114°44′50″E) (**Figure 1**). Except for rice varieties, field management was the same for the two experiments. The planting density was 22.5 bundles per square meter, and the fertilizer supply was 12 kg per hectare. Moreover, in order to ensure the normal growth of the rice plant, the corresponding irrigation measures were carried out in the key growth period. In total, 42 varieties were selected for the experiment in Lingshui, and 48 varieties were selected for the experiment in Ezhou. Each cultivar was placed on the corresponding field plot, and several eye-catching whiteboards were placed at the outer edge of each plot. These whiteboards were used to help us identify different fields and rice varieties in the acquired UAV images. To minimize the effect of destructive sampling on remote sensing canopy spectral features, both experiments divided each hybrid sample plot into a subplot for non-destructively extracting spectral information and a subplot for destructively sampling LAI. The date of LAI sampling, UAV

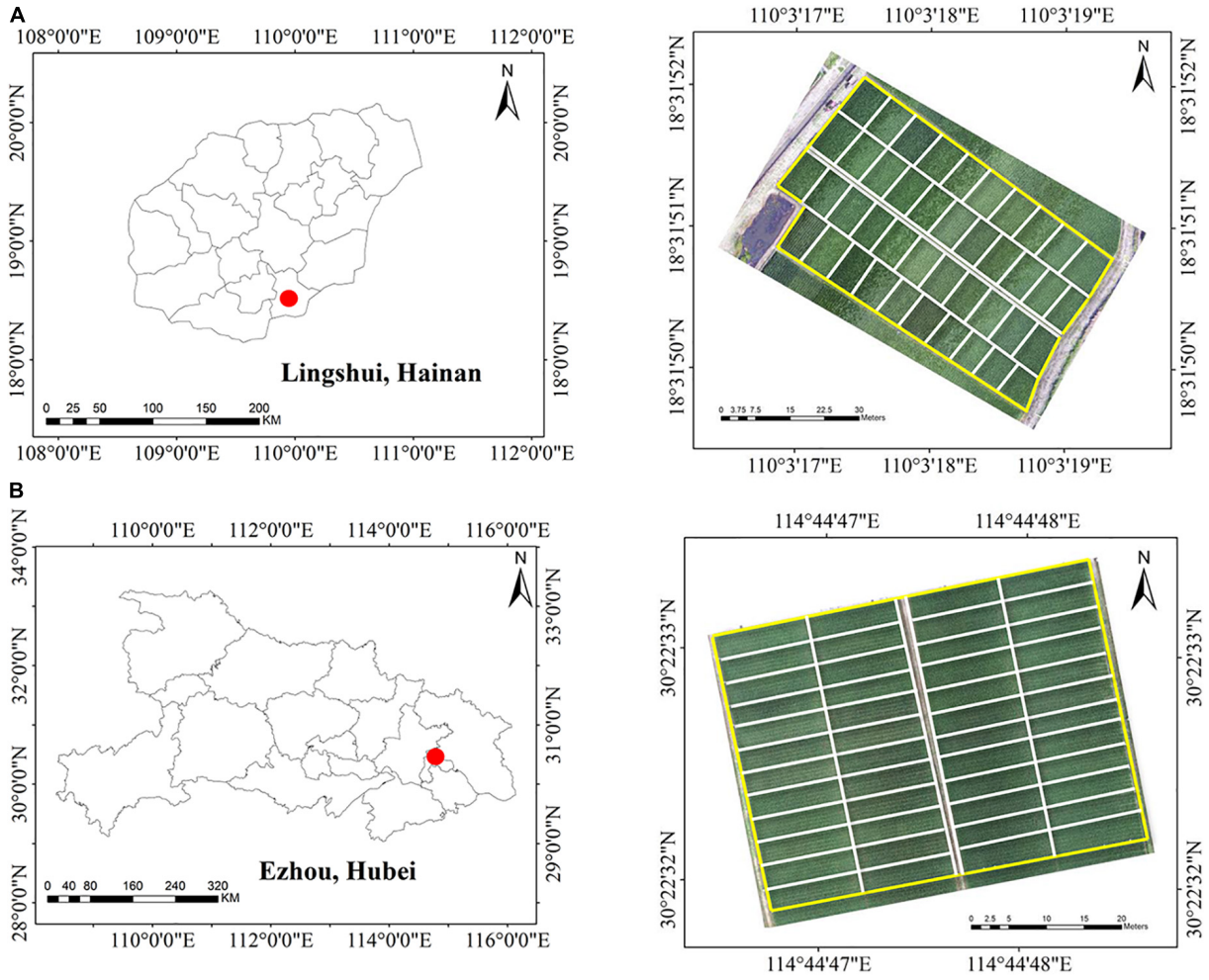

FIGURE 1
Two experiments were conducted in two study areas. **(A)** Experiment 1 in Hainan. **(B)** Experiment 2 in Hubei.

flight, and transplanting of the two experiments are shown in Table 1.

Experiment 1 lasted for three months in Hainan, with the rice plants transplanted in February 2018 and harvested in April 2018. Hainan has a tropical monsoon climate, with high temperatures the whole year. Lingshui has higher temperatures than the mainlands of China in winter, so it is suitable for rice overwintering growth. We selected 42 rice cultivars for sowing on 10 December 2017. The seedlings were transplanted on 8 January 2018 to 42 plots, each of which covered an area of about 63 m^2.

Experiment 2 in Hubei lasted for 4 months and was carried out from June to September 2019. Ezhou has a subtropical monsoon climate, and the annual average temperature is 15°C. We selected 48 varieties for sowing on 11 May 2019. The seedlings were transplanted on 9 June 2019 to 48 plots, each of which covered an area of about 36 m^2.

Measurements of leaf area index

During the entire growth process of rice, we destructively sampled each plot to obtain LAI data of rice. We randomly dug out three bundles of rice plants from the soil in the sampling area, and the sampling process was the same for each plot. The excavated rice plants were quickly put in a bucket and brought back to the laboratory. The samples brought back to the laboratory were measured immediately to obtain LAI data of rice and recorded accurately and in detail. The rice plants were measured after certain treatments to ensure that green leaves were separated from other components, especially withered and yellow leaves and panicles. We used LI-3100C (LI-COR Corporate, Lincoln, NE, United States) to obtain the leaf area of the measured plants. In order to calculate the plot-level LAI, the average area of the three bundles of plants was calculated as the leaf area (LA) of a single plant in each plot: $LAI = \frac{LA}{3} \times \rho$, where LA was the leaf area of all three bundles of rice and ρ was

TABLE 1 Details of data acquisition for the two experiments.

Experiment	Location	Year	DAT	Growth stage	UAV images	LAI sampling
Experiment 1	Hainan	2018	27,48	Tillering	2,26 February	4,25 February
			60	Jointing	11 March	9 March
			70	Booting and heading	18 March	19 March
			82,99	Ripening	1,15 April	31 March, 17 April
Experiment 2	Ezhou	2019	17,23,27,37,42,47	Tillering	26 June, 2,6,14,22,27July	26 June, 2,6,16,21,26 July
			53,58	Jointing	1,6 August	1,6 August
			63,69,73	Booting and heading	11,16,22August	11,17,21 August
			78,85	Ripening	29 August, 3 September	26 August, 3 September

the planting density with 22.5 bundles per square meter. The variation of LAI with the growth period for all fields is shown in Figure 2. LAI of all fields gradually increased in the early growth stage, slowed down at the booting and heading stages, and began to decrease slightly at the ripening stage. LAI changed sharply from the tillering to the jointing stage. However, LAI was relatively stable from the jointing to the ripening stage. The value range was wide, and LAI varied from 2 to 8 at the ripening stage.

Unmanned aerial vehicle image acquisition and processing

The Mini-MCA 12 multispectral camera (Tetracam Inc., Chatsworth, CA, United States) mounted on an M8 UAV (Beijing TT Aviation Technology Co., Ltd., Beijing, China) was used to obtain multispectral images of the two study areas during the entire growth period of rice. The Mini-MCA had 12 bands with different bandwidths (Table 2), which were mainly in the visible and near-infrared regions and contained abundant information on vegetation.

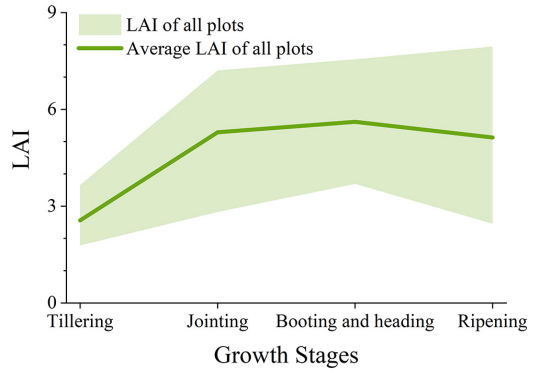

FIGURE 2
Variation in LAI at different growth stages.

For the corresponding pixels of each lens to overlap on the same focal plane in space, we registered each camera in the laboratory before the flight. The UAV was equipped with a gimbal stable platform to assist the UAV in normal flight and ensure the quality of the images captured. In order to reduce the influence of the changes in the solar altitude angle on the experiments, we carried out every flight from 10 a.m. to 2 p.m. local time. In sunny and windless weather, the UAV was used to collect remote sensing images to avoid the impact of clouds on the images. The flight height of the two experiments was 100 m, and the spatial resolution was 5.5 cm/pixel.

A total of eight calibration targets with stable reflectance values of 0.03, 0.06, 0.12, 0.24, 0.36, 0.48, 0.56, and 0.80, respectively, were observed by the MCA system. Since in this study, the weather was clear during the flight, the DN values of the target and their corresponding reflectance values were used to establish the linear correction equation. The reflectance data of the image were obtained by using the established linear correction equation, thus converting the original images with DN values into reflectance images (Farrand et al., 1994; Fang et al., 2016).

Then, the reflectance images of different bands were used in band mathematics to obtain VI images. The VI was calculated by mathematical combinations between several different bands, which can highlight vegetation features contained in the spectrum. The formula of VIs used in the experiment is given in Table 3, and these indices have been widely used in LAI estimation and biomass prediction. For each plot, a rectangle of appropriate size that reflected the information about the plot was defined. The average of all pixels in the defined rectangle was calculated. Thus, we obtained the plot-level values of the canopy reflectance and VI for subsequent calculations.

Wavelet spectrum texture extraction

In recent years, wavelet analysis has increasingly become an effective technique to analyze textures with its multi-resolution characteristics and its capability to simultaneously represent

TABLE 2 Bandwidth of the 12 bands of the Mini-MCA camera.

Spectral band	Center wavelength (nm)	Band width(nm)	Spectral band	Center wavelength (nm)	Band width (nm)
Blue	490	10		700	10
	520	10	Red edge	720	10
Green	550	10	NIR	800	10
	570	10		850	10
Red	670	10		900	20
	680	10		950	40

TABLE 3 VIs used in this study.

VI	Formula	References
Red-edge Chlorophyll Index ($CI_{red\ edge}$)	$R_{800nm}/R_{720nm} - 1$	Gitelson et al., 2014
Green Chlorophyll Index (CI_{green})	$R_{800nm}/R_{550nm} - 1$	Gitelson et al., 2014
Normalized Difference Vegetation Index (NDVI)	$(R_{800nm} - R_{670nm})/(R_{800nm} + R_{670nm})$	Rouse et al., 1974
Green Normalized Difference Vegetation Index (GNDVI)	$(R_{800nm} - R_{550nm})/(R_{800nm} + R_{550nm})$	Gitelson et al., 1996
Normalized Difference Red-edge Vegetation Index (NDRE)	$(R_{800nm} - R_{720nm})/(R_{800nm} + R_{720nm})$	Fitzgerald et al., 2010
MERIS Terrestrial Chlorophyll Index (MTCI)	$(R_{800nm} - R_{720nm})/(R_{720nm} - R_{670nm})$	Dash and Curran, 2010
Wide Dynamic Range Vegetation Index (WDRVI)	$(\alpha \times R_{800nm} - R_{670nm})/(\alpha \times R_{800nm} + R_{670nm}), \alpha = 0.2$	Gitelson, 2004
Two-band Enhanced Vegetation Index (EVI2)	$2.5 \times (R_{800nm} - R_{670nm})/(1 + R_{800nm} + 2.4 \times R_{670nm})$	Jiang et al., 2008
Visible Atmospherically Resistant Index (VARI)	$(R_{550nm} - R_{670nm})/(R_{550nm} + R_{670nm})$	Gitelson et al., 2002
Optimized Soil-Adjusted Vegetation Index (OSAVI)	$(1 + 0.16) \times (R_{800nm} - R_{720nm})/(R_{800nm} + R_{720nm} + 0.16)$	Rondeaux et al., 1996
Simple Ratio Index (SR)	R_{800nm}/R_{550nm}	Jordan, 1969; Xue et al., 2004
Ratio Vegetation Index (RVI)	R_{800nm}/R_{720nm}	Pearson and Miller, 1972; Zhou et al., 2017

local features of signal in the time–frequency domain (Huan and Hou, 2008). In this study, the discrete wavelet transform (DWT) was used to process the MCA images and extract the energy texture features, which were combined with VIs to establish a rice LAI estimation model.

The energy of the wavelet function $\Psi(t)$ can decay quickly to 0. If $\Psi(t)$ is scaled and panned, we can obtain a series of functions (Wang and Du, 2019):

$$\Psi_{a,b}(t) = |a|^{-0.5}\Psi\left(\frac{t-b}{a}\right) \quad (a, b \in R, a \neq 0) \tag{1}$$

where a refers to the scale factor and b refers to the shift factor. If $f(t) \in L^2(R)$ is the signals with finite energy, the continuous wavelet transform (CWT) function $W_f(a, b)$ is defined as follows:

$$W_f(a, b) = \int_{-\infty}^{\infty} f(t)\overline{\Psi_{a,b}(t)}dt \tag{2}$$

where $\overline{\Psi_{a,b}(t)}$ is the complex conjugate function of $\Psi_{a,b}(t)$. The discrete wavelet transform (DWT) discretizes a and b, $a = a_0^m (a_0 > 1)$, $b = nb_0a_0^m$, $\left(b_0 \in R, (m, n) \in Z^2\right)$. Generally, $a_0 = 2, b_0 = 1$. For signals with finite energy $f(t) \in L^2(R)$, the discrete wavelet transform (DWT) function $D_f(m, n)$ is defined as follows:

$$D_f(m, n) = \int_{-\infty}^{\infty} f(t)\overline{\Psi_{m,n}(t)}dt \tag{3}$$

where $\overline{\Psi_{m,n}(t)}$ is the complex conjugate function of $\Psi_{m,n}(t)$.

The discrete wavelet transform (DWT) is usually applied to extract relevant information by decomposing the signals into different frequency bands with different resolutions for further analysis. In this study, we used the level 1 Haar wavelet transform to extract texture information by decomposing the

rice reflectance images. The Haar wavelet can be defined as follows (Kausar et al., 2019):

$$\Psi(t) = \begin{cases} 1; 0 \le t \le \frac{1}{2} \\ -1; \frac{1}{2} \le t < 1 \\ 0; otherwise \end{cases} \quad (4)$$

Compared with other wavelet transforms, the level 1 Haar wavelet is computationally simpler and more efficient in decomposing 2D images, and it has a high speed (Ghazali et al., 2007). The image is decomposed by the 2D discrete wavelet transform (DWT) into four sub-bands: LL, reflecting the approximate information of the image, and LH, HH, and HL, reflecting vertical, diagonal, and horizontal detail information of the image, respectively. Rows and columns are filtered at the same time, where H corresponds to high-pass filtering and L corresponds to low-pass filtering. The rice reflectance images and the sub-band images decomposed by level 1 Haar wavelet transform are shown for reference in **Figure 3**. Most of the energy of the image was concentrated in the LL sub-band and was very high (Shukla et al., 2022). The LL sub-band reflected the outline of the image and contained most of the information of the image. Therefore, using the texture features extracted from the LL sub-band for LAI estimation can give better results.

The energy feature was extracted from the LL sub-band obtained by wavelet decomposition (Ren et al., 2021). In addition to the textural information, this feature was also able to amplify the dissimilarities that may be present between two regions and represent texture features in space from the point of energy distribution in the frequency domain with less computation and strong texture representation ability. The wavelet energy (Ene_{800nm}) was calculated as follows:

$$Ene_{800nm} = \frac{1}{9}\sum_{i=1}^{3}\sum_{j=1}^{3}|f(x,y)|^2 \quad (5)$$

where $f(x,y)$ is the value of the LL image decomposed by wavelet transform of the 800 nm reflectance image.

The near-infrared (NIR) spectral characteristics of the crop are related to the canopy structure of the crop, and the reflectivity changes more obviously than that of visible bands. Therefore, the $Ene_{800\ nm}$ obtained from the 800 nm reflectance images contained abundant texture information reflecting the canopy structure. Some studies have also proved the potential of texture features including NIR bands in biological parameter estimation (Colorado et al., 2020; Lu et al., 2021). Multiplication is a common feature combination method in the estimation of crop growth parameters (Badgley et al., 2017; Zeng et al., 2019, 2021; Wang et al., 2020; Hao et al., 2021). To highlight the target leaf information and limit the influence of the soil background and panicles, the plot-level values of VI and $Ene_{800\ nm}$ were multiplied to obtain a new index, recorded as WT-VI. A total of 12 WT-VIs were calculated according to the corresponding VIs (**Figure 3**).

Wavelet texture features were used as supplementary information of spectral features to broaden the data dimension of UAV images to improve the accuracy of rice LAI estimation. The performance of the calculated WT-VIs in the estimation of rice LAI was evaluated and compared with the traditional VIs in this study.

Model validation

The final model of rice LAI estimation was established using the method of k-fold cross-verification in this experiment. It divided all samples into k disjoint sets (k = 10 in this study). Each time, one of the subsets is used as the test set and the other k-1 sets as the training set. The k-1 sets are repeatedly applied to calibrate the coefficients ($Coef_i$) and coefficients of determination ($R^2{}_i$) for the established algorithm. We repeat the aforementioned steps k times, and the average values of root mean square error (RMSE) and relative root mean square error (rRMSE) based on the test set will be obtained (Peng et al., 2019):

$$Coef^2 = \frac{1}{k}\sum_{i=1}^{k} Coef_i{}^2; R^2 = \frac{1}{k}\sum_{i=1}^{k} R_i{}^2;$$

$$RMSE = \frac{1}{k}\sum_{i=1}^{k} RMSE_i, rRMSE = \frac{1}{k}\sum_{i=1}^{k} rRMSE_i \quad (6)$$

The training process of the model is repeated k times, and each sample is used for one validation, allowing the model to be optimized.

Result

Relationships between vegetation index and leaf area index of rice

To explore the relationships between rice LAI and VIs based on UAV images, we established the linear regression models of the VI and LAI and obtained R^2, as shown in **Table 4**. The linear regression model was the most common model for crop parameter estimation (Jiang et al., 2019). **Figure 4** presents the scatter plots of the VI and rice LAI, which reflected the variation of the VI with LAI throughout the growing season. The distribution of the VI in the two study areas was similar. The scattered plots were marked with four colors according to the growth stages of rice: tillering, jointing, booting and heading, and ripening. The results in **Table 4** indicated that R^2 values for all VIs throughout the entire growth period of rice were very low, not more than 0.4 except for OSAVI and EVI2, and VARI particularly was the lowest (R^2 was less than 0.1).

10.3389/fpls.2022.957870

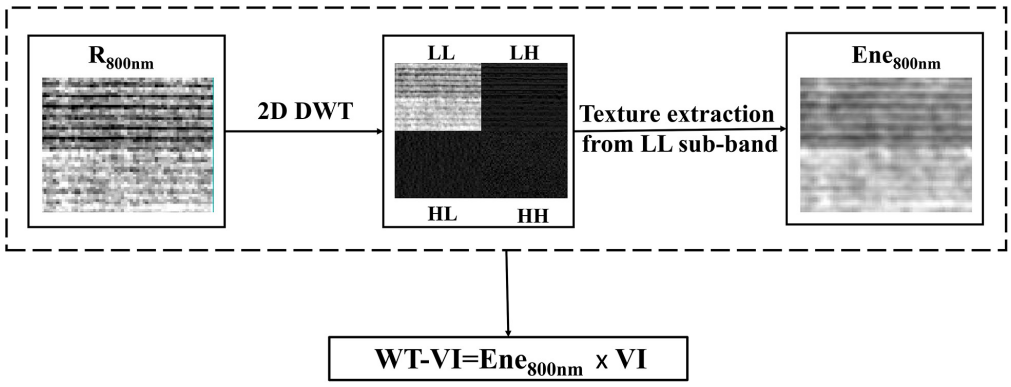

FIGURE 3
Process of calculating WT-VIs. $R_{800\ nm}$ means reflectance of 800 nm. $Ene_{800\ nm}$ represents the energy texture features extracted by the wavelet transform.

TABLE 4 R^2 of the linear regression of rice LAI with VIs.

VI	VARI	WDRVI	SR	CI_{green}	NDVI	MTCI	$CI_{red\ edge}$	RVI	NDRE	GNDVI	OSAVI	EVI2
R^2	0.020	0.307	0.315	0.315	0.316	0.334	0.335	0.335	0.366	0.368	0.426	0.540

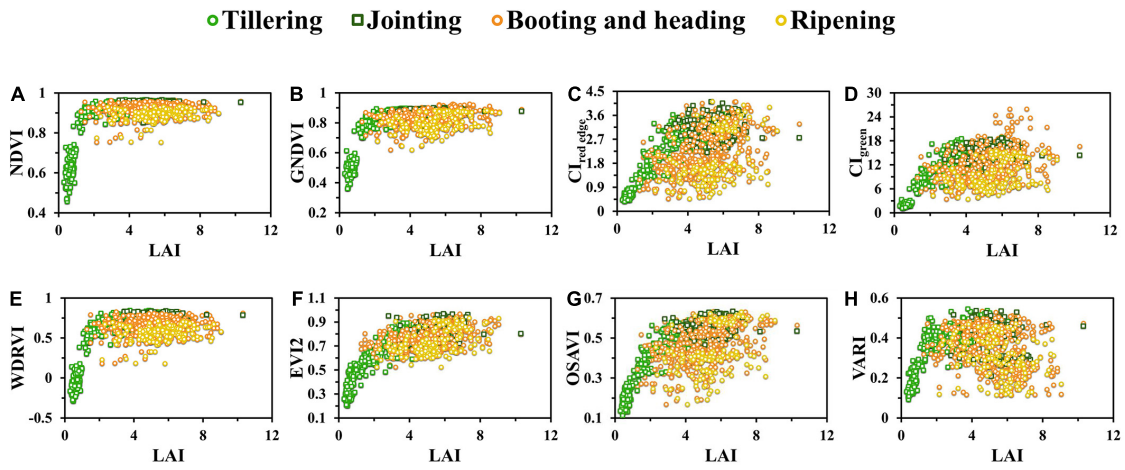

FIGURE 4
Variation of LAI plotted against vegetation indices: **(A)** NDVI, **(B)** GNDVI, **(C)** $CI_{red\ edge}$, **(D)** CI_{green}, **(E)** WDRVI, **(F)** EVI2, **(G)** OSAVI, and **(H)** VARI. The scattered points were marked with four colors according to the growth stages of rice: tillering, jointing, booting and heading, and ripening.

Among all tested VIs, EVI2 and OSAVI held the highest R^2 values of 0.426 and 0.540 (Table 4), respectively. The scattered points between pre-heading and post-heading stages of the ratio indices ($CI_{red\ edge}$ and CI_{green}) (Figures 4C,D) and VARI were severely separated, of which VARI was most separated (Figure 4H), while that of EVI2 was slightly weaker (Figure 4F).

As shown in Figure 4, when LAI was higher than 3, the sensitivity of all VIs to LAI decreased and saturation occurred, with normalized indices (NDVI and GNDVI) (Figures 4A,B) being the most obvious, which reduced the monitoring accuracy of the established model.

Estimation of rice leaf area index with texture features

In this study, we used WT-VIs to estimate rice LAI. VIs and WT-VIs were used to establish linear models with LAI, respectively. The fitting results of several VIs and WT-VIs are shown in Figure 5, and the performance of LAI estimation was compared.

Among all VIs, the scatter points in WT-VIs after heading were less separated than those in initial VIs. Compared with the VI, the WT-VI was less affected by the saturation effect.

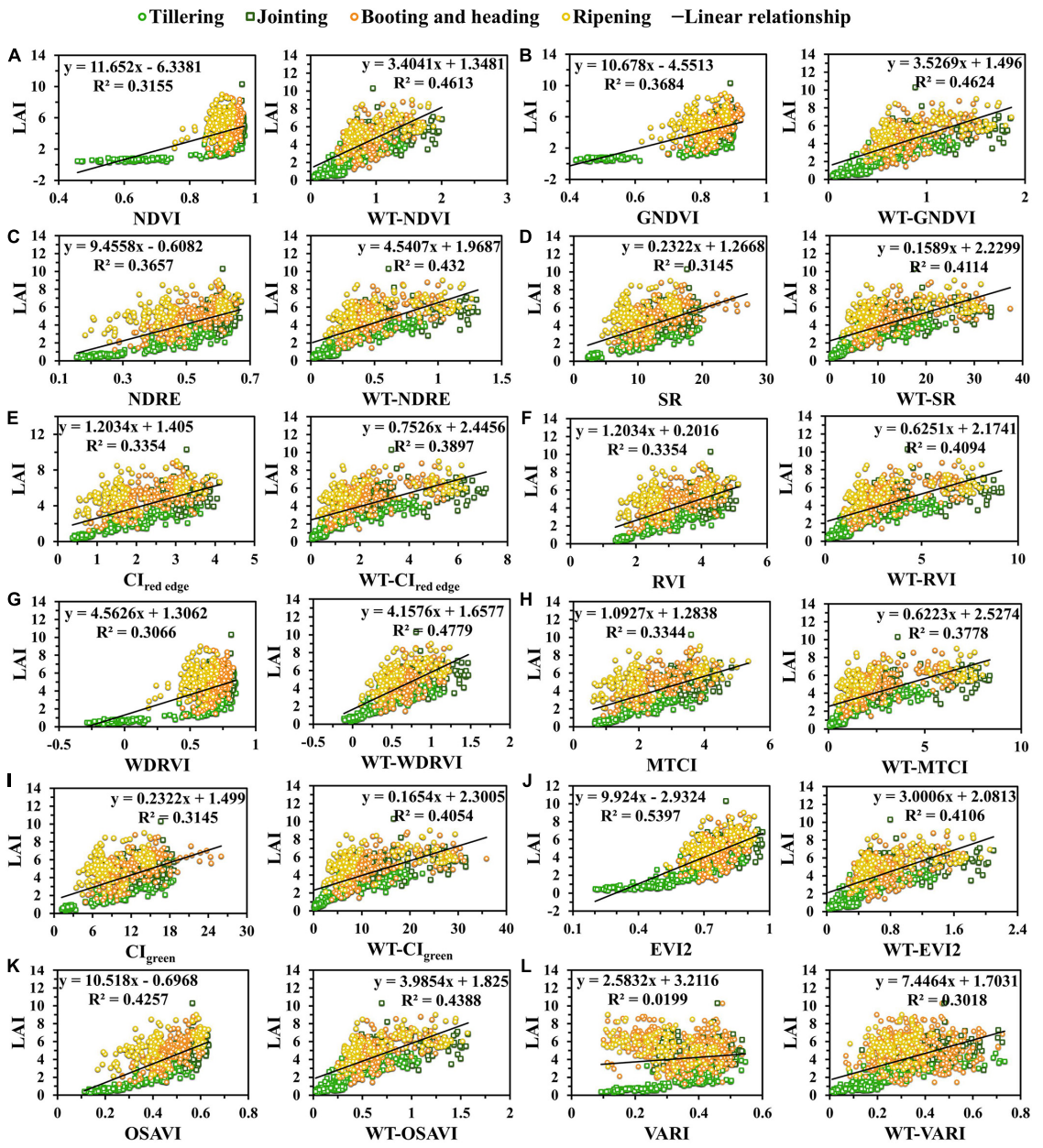

FIGURE 5
Two models of VIs and WT-VIs: **(A)** NDVI, **(B)** GNDVI, **(C)** NDRE, **(D)** SR, **(E)** $CI_{red\ edge}$, **(F)** RVI, **(G)** WDRVI, **(H)** MTCI, **(I)** CI_{green}, **(J)** EVI2, **(K)** OSAVI, and **(L)** VARI. The scattered points were marked with four colors according to the growth stages of rice: tillering, jointing, booting and heading, and ripening.

For the normalized indices (NDVI, GNDVI, and NDRE) in Figures 5A–C, the saturation effect of the original VIs began to appear when LAI increased to a certain extent, which seriously affected the effect of LAI estimation, while the saturation effect of the corresponding WT-VIs had been significantly improved (Figure 5A). Combined with the wavelet texture feature $Ene_{800\ nm}$, the scatter points of the WT-NDVI after the heading stage became less separated. In addition, in terms of improving the separation effect before and after the heading stage, the performance of the ratio indices ($CI_{red\ edge}$ and CI_{green}) (Figures 5E,I) was not as good as that of the normalized indices (Figure 5A). The scatter points of VARI after the heading stage showed an opposite trend to that before the heading stage, while the severe separation before and after the heading stage was greatly attenuated in the WT-VARI (Figure 5L).

From the scatter plots in Figure 5G, the scatter points of the WT-WDRVI and LAI were the closest to a straight line among all WT-VIs. It was obvious that the scatter after the heading

stage was more discrete in the WDRVI, while the scatter in WT-WDRVI was near a straight line with that before the heading stage. On the whole, the linear regression models established by the WT-VI and LAI performed better than VIs, which were less affected by the saturation effect and the separation before and after the heading stage.

K-fold cross-validation

In **Table 5**, the performances of rice LAI inversion with WT-VIs and VIs were compared by using the R^2 and RMSE after 10-fold cross-validation. By using 10-fold cross-validation, the R^2 of $Ene_{800\ nm}$ is 0.4022 and the RMSE is 1.4214. Most WT-VIs that contained texture information improved the accuracy of estimating LAI using VIs alone.

In addition, different types of VIs combined with texture features can improve the inversion effect of LAI. Compared with corresponding VI, R^2 of the WT-VI increased by more than 0.15 (WT-NDVI, WT-WDRVI, WT-VARI) and RMSE decreased by more than 0.2 (WT-WDRVI, WT-VARI). The rRMSE of WT-VARI decreased by more than 6%, as shown in **Figure 6**. The estimation accuracy of the WT-WDRVI was the highest, with an R^2 of 0.466 and an RMSE of 1.353. The inclusion of $Ene_{800\ nm}$ features did not significantly improve the accuracy of the models for OSAVI and EVI2, which were both the modified indices, and R^2 and RMSE were not significantly improved.

In general, the WT-VI-based model achieved higher accuracy than the model based on VIs for most indices. Based on the results of the model established by 10-fold cross-validation, we concluded that the models developed from the WT-WDRVI, WT-GNDVI, and WT-NDVI were the best models for estimating LAI of different rice varieties during the whole growing season. Therefore, we compared the relationships between the estimated LAI and the measured LAI, as shown in **Figure 7**, and the corresponding calculation formulas are as follows:

$$LAI = 4.16 \times (WT{-}WDRVI) + 1.66, RMSE = 1.353, rRMSE = 32.66\%$$

$$LAI = 3.53 \times (WT - GNDVI) + 1.50, RMSE = 1.373, rRMSE = 32.94\%$$

$$LAI = 3.40 \times (WT - NDVI) + 1.35, RMSE = 1.376, rRMSE = 33.07\%$$

Discussion

The main objective of this study was to improve the estimation of rice LAI based on the UAV remote sensing images. We introduced the texture feature $Ene_{800\ nm}$ based on the wavelet transform of the NIR image to increase the LAI estimation accuracy and reduce the influence of the saturation effect and the serious separation before and after heading.

In this research, we selected 12 VIs (NDVI, GNDVI, NDRE, SR, $CI_{red\ edge}$, CI_{green}, WDRVI, MTCI, EVI2, OSVAI, RVI, and VARI) to establish the model. These VIs had extensively been used in estimating LAI, aboveground biomass (Jiang et al., 2019), and yield of crops (Yuan et al., 2021). With the gradual growth of rice, all indices saturated rapidly before the heading stage, particularly for the normalized VIs such as NDVI and GNDVI. The scatter separation before and after the heading stage of VIs was severe for $CI_{red\ edge}$, VARI, and CI_{green}. This may be due to the transformation of rice from vegetative growth to reproductive growth in the late growth stage, resulting in a slight decrease in the leaf area. After rice heading, the appearance of panicles changes the spectral reflectance of the canopy. At the same time, the leaves are withered and yellow, and the leaf area is also changing, so the accuracy of the model is affected. It can be seen from **Figure 2** that the mean value of LAI was relatively stable from the jointing to the maturity stage, but the range of values was wide in the mature stage. At the same time, the vegetation indices were seriously saturated in high coverage conditions, which seriously affected the estimation effect of LAI in the late growth stage. Therefore, it was necessary to consider improving the LAI estimation effect at the late growth stage. Apparently, the VI only reflects spectral information and is deficient in its ability to describe the detailed texture features of the shape, size, and height of the crop canopy of images. The use of canopy reflectance and VI alone is not sufficient for LAI estimation. According to the characteristics of the vegetation spectral curve, the NIR images contain information on the vegetation canopy structure (Imran et al., 2020). Meanwhile, LAI calculated from the vegetation leaf area is an essential vegetation growth indicator for the canopy structure. Therefore, it was appropriate to use texture features based on NIR images to estimate LAI. To obtain the texture features of the remote sensing images of rice, the images were transformed from the spatial domain to the wavelet domain using the wavelet transform, and $Ene_{800\ nm}$ was calculated.

We combined texture features with the VI and built new models to improve the rice LAI estimation. The WT-VI can highlight the leaf information at different growth stages of rice and weaken the interference of the soil background and panicles. The complex canopy structural changes that were not well described by VI could be well described by texture features. Almost all VIs combined with the texture features could improve the estimation of rice LAI with similar patterns, and the effect of the WDRVI was more obvious and intuitive.

10.3389/fpls.2022.957870

TABLE 5 Comparison of the accuracy of VI and WT-VI models using 10-fold cross-validation.

	VI		WT-VI	
	R^2	RMSE	R^2	RMSE
NDVI	0.301	1.552	0.444	1.376
GNDVI	0.362	1.491	0.454	1.373
NDRE	0.356	1.497	0.429	1.402
SR	0.311	1.550	0.396	1.441
CIred edge	0.324	1.529	0.373	1.471
CIgreen	0.297	1.555	0.391	1.444
WDRVI	0.285	1.560	0.466	1.353
MTCI	0.328	1.531	0.367	1.481
EVI2	0.515	1.271	0.405	1.439
OSAVI	0.405	1.422	0.416	1.425
RVI	0.317	1.529	0.397	1.443
VARI	0.009	1.858	0.292	1.567

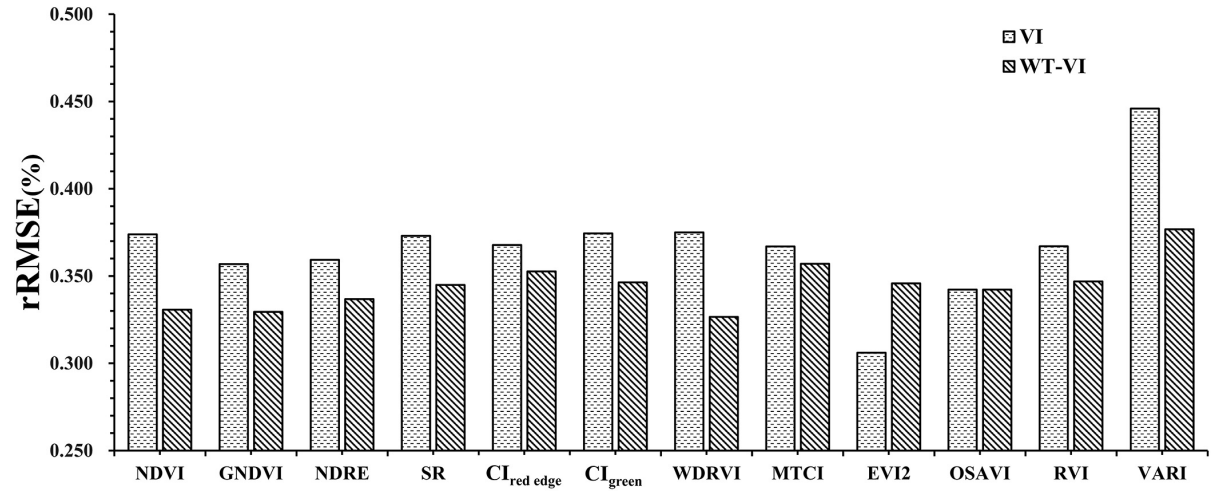

FIGURE 6
rRMSE of VI and WT-VI.

Therefore, taking WDRVI as an example, VI, $Ene_{800\ nm}$, and WT-WDRVI images in different growing stages are shown in Figure 8. The effects of the VI and WT-VI on LAI estimation were compared in detail in different growth stages in Figure 9.

In the tillering stage, it was observed from the scatter plot (Figure 9B) that the relationship between the VI and LAI was exponential and that between $Ene_{800\ nm}$ and LAI was linear. The scatter points of the WT-VI and LAI tended to approach a straight line. In Figure 9A, LAI was at a low level in the early tillering stage, and the values of the VI and $Ene_{800\ nm}$ were both small and less than 1. The values of the VI multiplied by $Ene_{800\ nm}$ were even smaller, and the corresponding scatter points would be more concentrated. The combination of the VI and texture features weakened the saturation effect of the VI in the late tillering stage. Texture features played a complementary role to the VI, which made the index of WT-VI very sensitive to LAI in the early stage of rice growth and had a strong linear relationship with LAI. Many studies have shown that the effect of the soil background is very significant at the initial stage of rice growth and decreases with the increase in vegetation coverage (Sun et al., 2017).

In the early tillering stage, the leaves of rice were smaller and the vegetation coverage was lower for irrigated paddy fields. Water and soil background significantly affected the plant canopy reflectance. Even when LAIs were similar, the differences of VIs were also large (Figure 9A). $Ene_{800\ nm}$ images blurred the edges of leaves and soil. As can be seen from the WT-VI image (Figure 8A), the bright lines were the leaves, and the dark lines were the soil background. The leaf information was highlighted clearly, and the effect of soil background was greatly

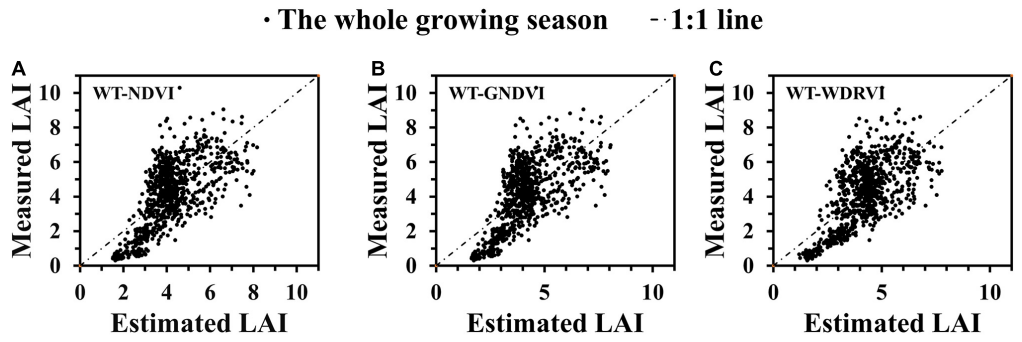

FIGURE 7
Relationships between measured LAI and estimated LAI. **(A)** WT-NDVI. **(B)** WT-GNDVI. **(C)** WT-WDRVI.

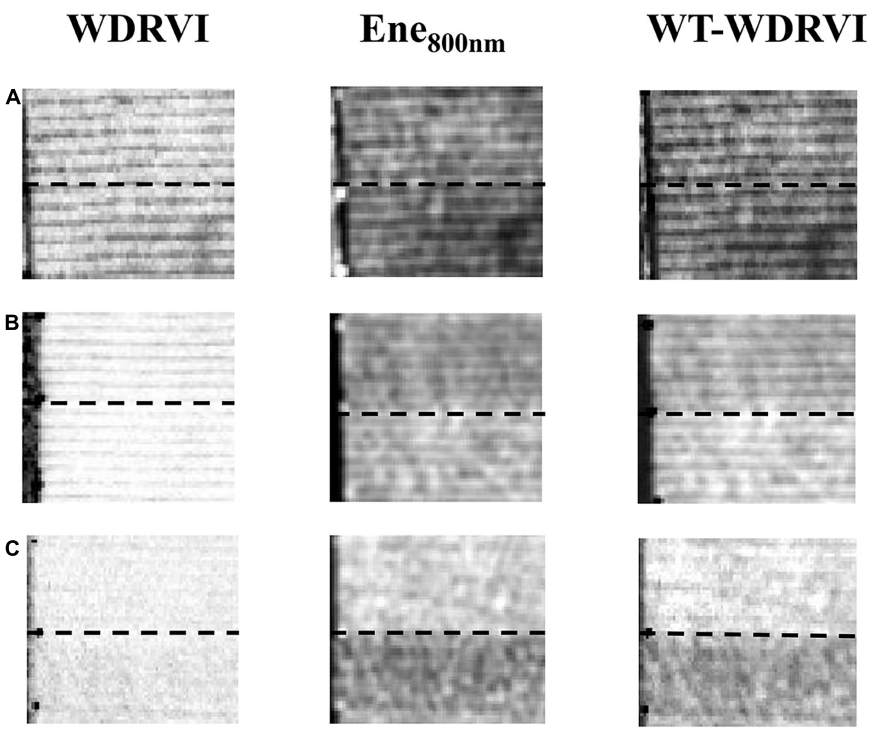

FIGURE 8
WDRVI, $Ene_{800\ nm}$, and WT-WDRVI images of two plots in different growth stages. **(A)** DAT 17, at the early tillering stage. **(B)** DAT 47, at the late tillering stage. **(C)** DAT 78, at the ripening stage. To better describe these features, two typical plots are selected to display. With the dotted line as the boundary, the upper field block is plot 1 and the lower field block is field plot 2.

diminished. By the late tillering stage, rice continued to grow and the leaves gradually became larger and more numerous. The difference between the two plots was small in the WDRVI image (Figure 8B) but obvious in the $Ene_{800\ nm}$ image (Figure 8B). $Ene_{800\ nm}$ was still sensitive to LAI, and the WT-VI greatly reduced the saturation effect.

In the jointing stage, it was observed from the scatter plot (Figure 9C) that LAI of rice increased rapidly, and the VI was obviously saturated. The values of LAI corresponding to similar VIs were quite different. In the late growth stage of rice, LAI was at a high level, and the WDRVI was already saturated, with values clustered to a small range. However, under the high vegetation coverage conditions, $Ene_{800\ nm}$ was not saturated, and the results of the multiplication of the VI and $Ene_{800\ nm}$ were mainly affected by the texture features and retained the sensitivity to LAI. As rice grew, the background of the soil was obscured by larger and more leaves. The differences in the canopy structure (leaf inclination, size, position distribution, etc.) were difficult to be accurately reflected by the VI, while the texture features could better describe it. When the canopy

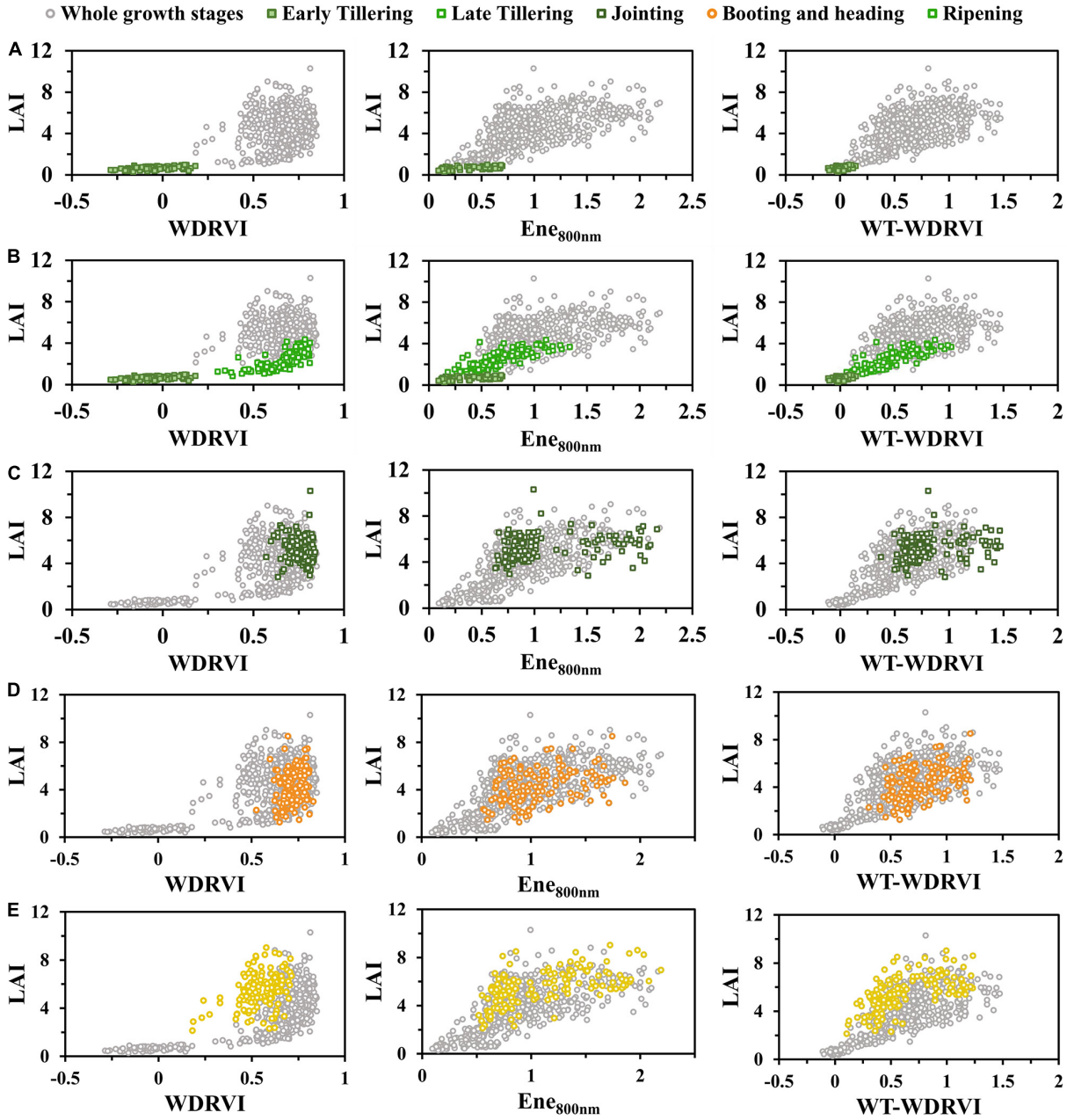

FIGURE 9
WDRVI vs LAI, $Ene_{800\ nm}$ vs LAI, and WT-WDRVI vs LAI of whole growth stages. **(A)** Early tillering. **(B)** Late tillering. **(C)** Jointing. **(D)** Booting and heading. **(E)** Ripening. To highlight the difference in texture features, the early tillering and late tillering stages are displayed separately.

of rice had closed, the addition of texture features reduced the saturation effect of the VI.

After rice heading, the appearance of panicles, and the yellowing and falling off of the leaves at the bottom of the canopy made the canopy structure more complex, which could affect the light distribution within the rice canopy and interfere with the spectral features of the canopy. Therefore, the VI contained not only the information on leaves but also the information on rice panicles. In the scatter diagram (Figures 9D,E), the VI results were relatively discrete. The texture features were less affected by the panicles, and the scatter points of $Ene_{800\ nm}$ with LAI were not so discrete. After the heading stage, the performance of LAI estimation by the WT-VI obtained by multiplying the VI and $Ene_{800\ nm}$ was more influenced by $Ene_{800\ nm}$. In Figure 8C, plot 1 in the $Ene_{800\ nm}$ texture image was relatively brighter with a larger leaf-to-panicle ratio, while plot 2 was darker with more panicles, and the panicles were drooping and cluttered. In the image of the WT-VI, plot 1 became brighter, and the

leaf information was more prominent when the panicles and leaves were mixed, so the panicles were suppressed. While plot 2 became darker, with the panicle being weakened. However, in the late stage of rice growth, the leaves of a small part of the fields withered and fell seriously. When the leaf-to-panicle ratio decreased, the inhibition of $Ene_{800\ nm}$ on panicles was not obvious, and there were some discrete points in **Figure 9E**, which led to the limited improvement.

In this study, the estimation accuracy of the WT-WDRVI was the highest in the whole growth period of rice (**Table 5**). The addition of $Ene_{800\ nm}$ can significantly improve the estimation effect of the normalized indices (NDVI, GNDVI, and NDRE) on LAI (**Figure 6**). The reason is that the normalized indices are susceptible to the influence of soil background and panicles, which can be weakened by the addition of $Ene_{800\ nm}$. The WT-VI was highly sensitive to LAI at the key growth stages of complex changes in the rice canopy structure, especially in the early tillering, late tillering, and post-heading stages. The improvement effect of texture features on the VI before the heading stage was better than that after the heading stage (**Figure 9**). The VI is the most widely used method to estimate LAI, and texture features are used to assist the VI to improve the accuracy of LAI estimation. The proposed method has an enhancement effect on most VIs. However, for the modified indices (EVI2), the improvement effect was not as good as the normalized indices given in **Figure 5J**. Neither R^2 nor RMSE had improved significantly (**Table 5**). OSAVI, which is the soil-adjusted VI, can reduce the effect of soil reflectance at low LAI. EVI2 is a 2-band version of the EVI that does not include the blue band, which retains the sensitivity of the EVI to high LAI vegetation (Liu et al., 2012). EVI2 has been found to remain sensitive to a wider range of LAI and resist to changes in soil background reflectance and atmospheric conditions (Jiang et al., 2008). The modified indices are less affected by the soil background than the normalized indices (**Figure 4**), so using only the modified indices to estimate LAI can get satisfactory results. Precisely for this reason, the improvement effect of our method on the modified indices is limited.

In this study, we used the 800 nm band for experiments. In addition, we also found that texture features of other NIR bands of the Mini-MCA 12 multispectral camera, except 800 nm, could also achieve similar accuracy, among which 900 nm had the best effect. NIR bands are related to the canopy structure of the vegetation. Therefore, the texture features extracted from NIR band images contain rich information related to the canopy structure. In addition, considering the R^2 and RMSE of VI, WT-VI, and $Ene_{800\ nm}$ in **Table 5**, it can be found from **Figure 9** that the performance of the WT-VI estimation of LAI depended on the texture features extracted from the NIR band images. Thus, although we only used 800 nm in this study, similar results could be achieved for all NIR bands of MCA.

In general, the WT-VI performed better than the VI in LAI estimation, with higher R^2 and lower RMSE and rRMSE (**Figure 6**), especially the normalized indices (NDVI, NDRE, and GNDVI). Wavelet texture features remained sensitive to the rice canopy structure, which varied greatly at different growth stages. The WT-VI reduced the effects of the soil background and panicles, which emerged at certain stages. The combination of texture information and spectral information weakened the saturation effect and the serious separation before and after the heading stage. The method proposed in this article can adapt to the multi-temporal differences in the rice canopy structure and avoid the time-consuming and laborious work of establishing models in each growth period. Compared with the physical model, the approach needs fewer parameters. The method we proposed in this article can be satisfactorily applied in precision agriculture, as well as for fields containing many breeding varieties. The model developed in this study was tested only on data from the two experiments together. However, this study provides a good example of applying remote sensing technology to accurately predict rice LAI, which has great potential in precision agriculture. Our future work is to apply this approach to different experiments to explore the transferability of the model and its robustness to factors such as species and image resolution.

Conclusion

In this study, we developed a method for LAI estimation by combining spectral features and wavelet texture features, given the differences in the rice canopy structure in different growth stages. For most VIs, compared with using the VI alone, the combination of the VI and $Ene_{800\ nm}$ can estimate rice LAI more accurately. The RMSE and rRMSE of linear fitting of the WT-NDVI decreased to 1.270 and 32.6%, respectively. Since texture features have high sensitivity to the canopy structure of rice in different growth stages, combining spectral features with texture features can improve the accuracy of rice LAI estimation. The combination of texture features and spectral features weakens the effects of the soil background and panicles and reduces the saturation effect when the rice canopy closes. Thus, the method we proposed can be well applied in precision agriculture and field management. In our future study, we will explore the transferability of the model and identify additional factors that may affect the LAI estimation. Other texture features can be considered to improve the LAI estimation of rice for the unique and complex canopy structure changes of rice.

Data availability statement

The original contributions presented in the study are included in the article/supplementary material, further inquiries can be directed to the corresponding author/s.

Author contributions

YG and CZ provided the main research ideas and gave guidance at critical moments. CZ conducted image processing and data analysis and completed the main experiments. KY provided important experimental and writing guidance. SF and RZ supplied professional equipment and experimental sites. XW and RZ provided advice from an agronomic point of view. CZ and YG completed this manuscript together. All authors agreed with the manuscript and contributed significantly to this manuscript.

Funding

This research was supported by Key R&D projects in Hubei Province (2020BBB058).

Conflict of interest

The authors declare that the research was conducted in the absence of any commercial or financial relationships that could be construed as a potential conflict of interest.

Publisher's note

All claims expressed in this article are solely those of the authors and do not necessarily represent those of their affiliated organizations, or those of the publisher, the editors and the reviewers. Any product that may be evaluated in this article, or claim that may be made by its manufacturer, is not guaranteed or endorsed by the publisher.

References

Alsamhi, S. H., Almalki, F., Ma, O., Ansari, M. S., and Lee, B. (2021). Predictive estimation of optimal signal strength from drones over iot frameworks in smart cities. *IEEE Trans. Mob. Comput.* 1:3074442. doi: 10.1109/TMC.2021.3074442

Alsamhi, S. H., Shvetsov, A. V., Kumar, S., Shvetsova, S. V., Alhartomi, M. A., Hawbani, A., et al. (2022). UAV computing-assisted search and rescue mission framework for disaster and harsh environment mitigation. *Drones* 6:154. doi: 10.3390/drones6070154

Amarasingam, N., Ashan Salgadoe, A. S., Powell, K., Gonzalez, L. F., and Natarajan, S. (2022). A review of Uav platforms, sensors, and applications for monitoring of sugarcane crops. *Remote Sens. Appl. Soc. Environ.* 26:100712. doi: 10.1016/j.rsase.2022.100712

Badgley, G., Field, C. B., and Berry, J. A. (2017). Canopy near-infrared reflectance and terrestrial photosynthesis. *Sci. Adv.* 3:e1602244. doi: 10.1126/sciadv.1602244

Banskota, A., Wynne, R., Thomas, V., Serbin, S., Kayastha, N., Gastellu-Etchegorry, J. P., et al. (2013). Investigating the utility of wavelet transforms for inverting a 3-d radiative transfer model using hyperspectral data to retrieve forest LAI. *Remote Sens.* 5, 2639–2659. doi: 10.3390/rs5062639

Blackburn, G. A. (2007). Wavelet decomposition of hyperspectral data: A novel approach to quantifying pigment concentrations in vegetation. *Int. J. Remote Sens.* 28, 2831–2855. doi: 10.1080/01431160600928625

Bruce, L. M., Koger, C. H., and Li, J. (2002). Dimensionality reduction of hyperspectral data using discrete wavelet transform feature extraction. *IEEE Trans. Geosci. Remote Sens.* 40, 2331–2338. doi: 10.1109/TGRS.2002.804721

Chang, T., and Kuo, C. J. (1993). Texture analysis and classification with tree-structured wavelet transform. *IEEE Trans. Image Process* 2, 429–441. doi: 10.1109/83.242353

Colorado, J. D., Calderon, F., Mendez, D., Petro, E., Rojas, J. P., Correa, E. S., et al. (2020). A novel nir-image segmentation method for the precise estimation of above-ground biomass in rice crops. *PLos One* 15:e239591. doi: 10.1371/journal.pone.0239591

Croft, H., Chen, J. M., and Zhang, Y. (2014). The applicability of empirical vegetation indices for determining leaf chlorophyll content over different leaf and canopy structures. *Ecol. Complex.* 17, 119–130. doi: 10.1016/j.ecocom.2013.11.005

Dash, J., and Curran, P. J. (2010). The meris terrestrial chlorophyll index. *Int. J. Remote Sens.* 25, 5403–5413. doi: 10.1080/0143116042000274015

Dong, T., Liu, J., Shang, J., Qian, B., Ma, B., Kovacs, J. M., et al. (2019). Assessment of red-edge vegetation indices for crop leaf area index estimation. *Remote Sens. Environ.* 222, 133–143. doi: 10.1016/j.rse.2018.12.032

Dorigo, W. A. (2012). Improving the robustness of cotton status characterisation by radiative transfer model inversion of multi-angular chris/proba data. *IEEE J. Sel. Top. Appl. Earth Obs. Remote Sens.* 5, 18–29. doi: 10.1109/JSTARS.2011.2171181

Duan, B., Liu, Y., Gong, Y., Peng, Y., Wu, X., Zhu, R., et al. (2019). Remote estimation of rice Lai based on fourier spectrum texture from UAV image. *Plant Methods* 15:124. doi: 10.1186/s13007-019-0507-8

Eckert, S. (2012). Improved forest biomass and carbon estimations using texture measures from worldview-2 satellite data. *Remote Sens.* 4, 810–829. doi: 10.3390/rs4040810

Fang, H., Baret, F., Plummer, S., and Schaepman Strub, G. (2019). An overview of global leaf area index (lai): Methods, products, validation, and applications. *Rev. Geophys.* 57, 739–799. doi: 10.1029/2018RG000608

Fang, S., Tang, W., Peng, Y., Gong, Y., Dai, C., Chai, R., et al. (2016). Remote estimation of vegetation fraction and flower fraction in oilseed rape with unmanned aerial vehicle data. *Remote Sens.* 8:416. doi: 10.3390/rs8050416

Farrand, W. H., Singer, R. B., and Merényi, E. (1994). Retrieval of apparent surface reflectance from aviris data: A comparison of empirical line, radiative transfer, and spectral mixture methods. *Remote Sens. Environ.* 47, 311–321. doi: 10.1016/0034-4257(94)90099-X

Fitzgerald, G., Rodriguez, D., and Leary, G. O. (2010). Measuring and predicting canopy nitrogen nutrition in wheat using a spectral index—the canopy chlorophyll content index (CCCI). *Field Crops Res.* 116, 318–324. doi: 10.1016/j.fcr.2010.01.010

Ghazali, K. H., Mansor, M. F., Mustafa, M. M., and Hussain, A. (2007). "Feature extraction technique using discrete wavelet transform for image classification," in *Proceedings of the 2007 5th Student Conference on Research and Development* (Selangor: IEEE).

Gitelson, A. A. (2004). Wide dynamic range vegetation index for remote quantification of biophysical characteristics of vegetation. *J. Plant Physiol.* 161, 165–173. doi: 10.1078/0176-1617-01176

Gitelson, A. A., Kaufman, Y. J., and Merzlyak, M. N. (1996). Use of a green channel in remote sensing of global vegetation from eos-modis. *Remote Sens. Environ.* 58, 289–298. doi: 10.1016/S0034-4257(96)00072-7

Gitelson, A. A., Kaufman, Y. J., Stark, R., and Rundquist, D. (2002). Novel algorithms for remote estimation of vegetation fraction. *Remote Sens. Environ.* 80, 76–87. doi: 10.1016/S0034-4257(01)00289-9

Gitelson, A. A., Peng, Y., Arkebauer, T. J., and Schepers, J. (2014). Relationships between gross primary production, green lai, and canopy chlorophyll content in maize: Implications for remote sensing of primary production. *Remote Sens. Environ.* 144, 65–72. doi: 10.1016/j.rse.2014.01.004

Gökdağ, Y. E., Şansal, F., and Gökdel, Y. D. (2019). Image denoising using 2-d wavelet algorithm for gaussian-corrupted confocal microscopy images. *Biomed. Signal Process. Control* 54:101594. doi: 10.1016/j.bspc.2019.101594

Gower, S. T., Kucharik, C. J., and Norman, J. M. (1999). Direct and indirect estimation of leaf area index, fapar, and net primary production of terrestrial ecosystems. *Remote Sens. Environ.* 70, 29–51. doi: 10.1016/S0034-4257(99)00056-5

Hao, D., Zeng, Y., Qiu, H., Biriukova, K., Celesti, M., Migliavacca, M., et al. (2021). Practical approaches for normalizing directional solar-induced fluorescence to a standard viewing geometry. *Remote Sens. Environ.* 255:112171. doi: 10.1016/j.rse.2020.112171

He, J., Zhang, N., Su, X., Lu, J., Yao, X., Cheng, T., et al. (2019). Estimating leaf area index with a new vegetation index considering the influence of rice panicles. *Remote Sens. (Basel, Switzerland)* 11:1809. doi: 10.3390/rs11151809

Herrmann, I., Pimstein, A., Karnieli, A., Cohen, Y., Alchanatis, V., Bonfil, D. J., et al. (2011). Lai assessment of wheat and potato crops by venμs and sentinel-2 bands. *Remote Sens. Environ.* 115, 2141–2151. doi: 10.1016/j.rse.2011.04.018

Hlatshwayo, S. T., Mutanga, O., Lottering, R. T., Kiala, Z., and Ismail, R. (2019). Mapping forest aboveground biomass in the reforested buffelsdraai landfill site using texture combinations computed from spot-6 pan-sharpened imagery. *Int. J. Appl. Earth Obs. Geoinf.* 74, 65–77. doi: 10.1016/j.jag.2018.09.005

Huan, Z., and Hou, Y. (2008). "An segmentation algorithm of texture image based on dwt," in *Proceedings of the 2008 Fourth International Conference on Natural Computation* (Jinan: IEEE).

Imran, H. A., Gianelle, D., Rocchini, D., Dalponte, M., Martín, M. P., Sakowska, K., et al. (2020). VIS-NIR, red-edge and nir-shoulder based normalized vegetation indices response to co-varying leaf and canopy structural traits in heterogeneous grasslands. *Remote Sens.* 12:2254. doi: 10.3390/rs12142254

Jain, S., and Salau, A. O. (2019). Detection of glaucoma using two dimensional tensor empirical wavelet transform. *SN Appl. Sci.* 1:1417. doi: 10.1007/s42452-019-1467-3

Jiang, Q., Fang, S., Peng, Y., Gong, Y., Zhu, R., Wu, X., et al. (2019). UAV-based biomass estimation for rice-combining spectral, tin-based structural and meteorological features. *Remote Sens.* 11:890. doi: 10.3390/rs11070890

Jiang, Z., Huete, A., Didan, K., and Miura, T. (2008). Development of a two-band enhanced vegetation index without a blue band. *Remote Sens. Environ.* 112, 3833–3845. doi: 10.1016/j.rse.2008.06.006

Jin, X., Liu, S., Baret, F., Hemerlé, M., and Comar, A. (2017). Estimates of plant density of wheat crops at emergence from very low altitude UAV imagery. *Remote Sens. Environ.* 198, 105–114. doi: 10.1016/j.rse.2017.06.007

Jordan, C. F. (1969). Derivation of leaf-area index from quality of light on the forest floor. *Ecology* 50, 663–666. doi: 10.2307/1936256

Kausar, T., Wang, M., Idrees, M., and Lu, Y. (2019). HWDCNN: Multi-class recognition in breast histopathology with haar wavelet decomposed image based convolution neural network. *Biocybern. Biomed. Eng.* 39, 967–982. doi: 10.1016/j.bbe.2019.09.003

Kelsey, K., and Neff, J. (2014). Estimates of aboveground biomass from texture analysis of landsat imagery. *Remote Sens.* 6, 6407–6422. doi: 10.3390/rs6076407

Li, F., Wang, L., Liu, J., Wang, Y., and Chang, Q. (2019). Evaluation of leaf n concentration in winter wheat based on discrete wavelet transform analysis. *Remote Sens.* 11:1331. doi: 10.3390/rs11111331

Li, S., Yuan, F., Ata-Ui-Karim, S. T., Zheng, H., Cheng, T., Liu, X. J., et al. (2019). Combining color indices and textures of UAV-based digital imagery for rice lai estimation. *Remote Sens.* 11:1763. doi: 10.3390/rs11151763

Liang, L., Di, L., Zhang, L., Deng, M., Qin, Z., Zhao, S., et al. (2015). Estimation of crop LAI using hyperspectral vegetation indices and a hybrid inversion method. *Remote Sens. Environ.* 165, 123–134. doi: 10.1016/j.rse.2015.04.032

Liu, J., Pattey, E., and Jégo, G. (2012). Assessment of vegetation indices for regional crop green lai estimation from landsat images over multiple growing seasons. *Remote Sens. Environ.* 123, 347–358. doi: 10.1016/j.rse.2012.04.002

Liu, X., Jin, J., Herbert, S. J., Zhang, Q., and Wang, G. (2005). Yield components, dry matter, lai and lad of soybeans in northeast china. *Field Crops Res.* 93, 85–93. doi: 10.1016/j.fcr.2004.09.005

Lu, J., Eitel, J. U. H., Engels, M., Zhu, J., Ma, Y., Liao, F., et al. (2021). Improving unmanned aerial vehicle (UAV) remote sensing of rice plant potassium accumulation by fusing spectral and textural information. *Int. J. Appl. Earth Obs. Geoinf.* 104:102592. doi: 10.1016/j.jag.2021.102592

Matsushita, B., Yang, W., Chen, J., Onda, Y., and Qiu, G. (2007). Sensitivity of the enhanced vegetation index (EVI) and normalized difference vegetation index (NDVI) to topographic effects: A case study in high-density cypress forest. *Sensors* 7, 2636–2651. doi: 10.3390/s7112636

Moulin, S. (1999). Impacts of model parameter uncertainties on crop reflectance estimates: A regional case study on wheat. *Int. J. Remote Sens.* 20, 213–218. doi: 10.1080/014311699213730

Pádua, L., Marques, P., Hruška, J., Adão, T., Peres, E., Morais, R., et al. (2018). Multi-temporal vineyard monitoring through UAV-based rgb imagery. *Remote Sens.* 10:1907. doi: 10.3390/rs10121907

Pearson, R., and Miller, L. (1972). "Remote mapping of standing crop biomass for estimation of productivity of the shortgrass prairie," in *Proceedings of the 8th International Symposium on Remote Sensing of Environment*, Ann Arbor, MI, 1355.

Peng, J., Shen, H., He, S. W., and Wu, J. S. (2013). Soil moisture retrieving using hyperspectral data with the application of wavelet analysis. *Environ. Earth Sci.* 69, 279–288. doi: 10.1007/s12665-012-1955-x

Peng, Y., Zhu, T. E., Li, Y., Dai, C., Fang, S., Gong, Y., et al. (2019). Remote prediction of yield based on lai estimation in oilseed rape under different planting methods and nitrogen fertilizer applications. *Agric. For. Meteorol.* 271, 116–125. doi: 10.1016/j.agrformet.2019.02.032

Qiao, K., Zhu, W., and Xie, Z. (2020). Application conditions and impact factors for various vegetation indices in constructing the lai seasonal trajectory over different vegetation types. *Ecol. Indic.* 112:106153. doi: 10.1016/j.ecolind.2020.106153

Quandt, V. I., Pacola, E. R., Pichorim, S. F., Gamba, H. R., and Sovierzoski, M. A. (2015). Pulmonary crackle characterization: Approaches in the use of discrete wavelet transform regarding border effect, mother-wavelet selection, and subband reduction. *Res. Biomed. Eng.* 31, 148–159. doi: 10.1590/2446-4740.0639

Ren, J., Chen, Q., Ma, D., Xie, R., Zhu, H., and Zang, S. (2021). Study on a fast ec measurement method of soda saline-alkali soil based on wavelet decomposition texture feature. *Catena* 203:105272. doi: 10.1016/j.catena.2021.105272

Reza, M. N., Na, I. S., Baek, S. W., and Lee, K. (2019). Rice yield estimation based on k-means clustering with graph-cut segmentation using low-altitude UAV images. *Biosyst. Eng.* 177, 109–121. doi: 10.1016/j.biosystemseng.2018.09.014

Rondeaux, G., Steven, M., and Baret, F. (1996). Optimization of soil-adjusted vegetation indices. *Remote Sens. Environ.* 55, 95–107. doi: 10.1016/0034-4257(95)00186-7

Rouse, J. W. Jr., Haas, R. H., Schell, J. A., and Deering, D. W. (1974). "Monitoring vegetation systems in the great plains with erts," in *Proceedings of the Third ERTS-1 Symposium NASA, NASA SP-351* (Washington, DC: Nasa Special Publication).

Sahadevan, A. S., Shrivastava, P., Das, B. S., and Sarathjith, M. C. (2014). Discrete wavelet transform approach for the estimation of crop residue mass from spectral reflectance. *IEEE J. Sel. Top. Appl. Earth Obs. Remote Sens.* 7, 2490–2495. doi: 10.1109/JSTARS.2013.2280894

Saif, A., Dimyati, K., Noordin, K. A., Alsamhi, S. H., and Hawbani, A. (2021). Multi-UAV andsar collaboration model for disaster management inb5g networks. *Internet Technol. Lett.* 23:e310. doi: 10.1002/itl2.310

Sakamoto, T., Shibayama, M., Kimura, A., and Takada, E. (2011). Assessment of digital camera-derived vegetation indices in quantitative monitoring of seasonal rice growth. *ISPRS J. Photogramm. Remote Sens.* 66, 872–882. doi: 10.1016/j.isprsjprs.2011.08.005

Salari, E., and Ling, Z. (1995). Texture segmentation using hierarchical wavelet decomposition. *Pattern Recognit.* 28, 1819–1824. doi: 10.1016/0031-3203(95)00054-2

Shukla, V., Khandekar, P., and Khaparde, A. (2022). Noise estimation in 2d mri using dwt coefficients and optimized neural network. *Biomed. Signal Process. Control* 71:103225. doi: 10.1016/j.bspc.2021.103225

Sun, T., Fang, H., Liu, W., and Ye, Y. (2017). Impact of water background on canopy reflectance anisotropy of a paddy rice field from multi-angle measurements. *Agric. For. Meteorol.* 233, 143–152. doi: 10.1016/j.agrformet.2016.11.010

Tian, Y., Gu, K., Chu, X., Yao, X., Cao, W., and Zhu, Y. (2014). Comparison of different hyperspectral vegetation indices for canopy leaf nitrogen concentration estimation in rice. *Plant Soil* 376, 193–209. doi: 10.1007/s11104-013-1937-0

Verrelst, J., Camps-Valls, G., Muñoz-Marí, J., Rivera, J. P., Veroustraete, F., Clevers, J. G. P. W., et al. (2015). Optical remote sensing and the retrieval of terrestrial vegetation bio-geophysical properties–a review. *ISPRS J. Photogramm. Remote Sens.* 108, 273–290. doi: 10.1016/j.isprsjprs.2015.05.005

Viña, A., Gitelson, A. A., Nguy-Robertson, A. L., and Peng, Y. (2011). Comparison of different vegetation indices for the remote assessment of green leaf area index of crops. *Remote Sens. Environ.* 115, 3468–3478. doi: 10.1016/j.rse.2011.08.010

Wang, C., Guan, K., Peng, B., Chen, M., Jiang, C., Zeng, Y., et al. (2020). Satellite footprint data from oco-2 and tropomi reveal significant spatio-temporal and

inter-vegetation type variabilities of solar-induced fluorescence yield in the U.S. Midwest. *Remote Sens. Environ.* 241:111728. doi: 10.1016/j.rse.2020.111728

Wang, J., and Du, Z. (2019). A method of processing color image watermarking based on the haar wavelet. *J. Vis. Commun. Image Represent.* 64:102627. doi: 10.1016/j.jvcir.2019.102627

Wang, Y., Zhang, K., Tang, C., Cao, Q., Tian, Y., Zhu, Y., et al. (2019). Estimation of rice growth parameters based on linear mixed-effect model using multispectral images from fixed-wing unmanned aerial vehicles. *Remote Sens.* 11:1371. doi: 10.3390/rs11111371

Xue, L., Cao, W., Luo, W., Dai, T., and Zhu, Y. (2004). Monitoring leaf nitrogen status in rice with canopy spectral reflectance. *Agron. J.* 96:135. doi: 10.2134/agronj2004.0135

Yang, Q., Shi, L., Han, J., Chen, Z., and Yu, J. (2022). A vi-based phenology adaptation approach for rice crop monitoring using UAV multispectral images. *Field Crops Res.* 277:108419. doi: 10.1016/j.fcr.2021.108419

Yang, Z., Yu, X., Dedman, S., Rosso, M., Zhu, J., Yang, J., et al. (2022). UAV remote sensing applications in marine monitoring: Knowledge visualization and review. *Sci. Total Environ.* 838:155939. doi: 10.1016/j.scitotenv.2022.155939

Yuan, L. (2014). Development of hybrid rice to ensure food security. *Rice Sci.* 21, 1–2. doi: 10.1016/S1672-6308(13)60167-5

Yuan, N., Gong, Y., Fang, S., Liu, Y., Duan, B., Yang, K., et al. (2021). UAV remote sensing estimation of rice yield based on adaptive spectral endmembers and bilinear mixing model. *Remote Sens.* 13:2190. doi: 10.3390/rs13112190

Yue, J., Yang, G., Tian, Q., Feng, H., Xu, K., Zhou, C., et al. (2019). Estimate of winter-wheat above-ground biomass based on UAV ultrahigh-ground-resolution image textures and vegetation indices. *ISPRS J. Photogramm. Remote Sens.* 150, 226–244. doi: 10.1016/j.isprsjprs.2019.02.022

Zarate-Valdez, J. L., Whiting, M. L., Lampinen, B. D., Metcalf, S., Ustin, S. L., and Brown, P. H. (2012). Prediction of leaf area index in almonds by vegetation indexes. *Comput. Electron. Agric.* 85, 24–32. doi: 10.1016/j.compag.2012.03.009

Zarco-Tejada, P. J., Miller, J. R., Noland, T. L., Mohammed, G. H., and Sampson, P. H. (2001). Scaling-up and model inversion methods with narrowband optical indices for chlorophyll content estimation in closed forest canopies with hyperspectral data. *IEEE Trans. Geosci. Remote Sens.* 39, 1491–1507. doi: 10.1109/36.934080

Zeng, Y., Badgley, G., Dechant, B., Ryu, Y., Chen, M., and Berry, J. A. (2019). A practical approach for estimating the escape ratio of near-infrared solar-induced chlorophyll fluorescence. *Remote Sens. Environ.* 232:111209. doi: 10.1016/j.rse.2019.05.028

Zeng, Y., Hao, D., Badgley, G., Damm, A., Rascher, U., Ryu, Y., et al. (2021). Estimating near-infrared reflectance of vegetation from hyperspectral data. *Remote Sens. Environ.* 267:112723. doi: 10.1016/j.rse.2021.112723

Zha, H., Miao, Y., Wang, T., Li, Y., Zhang, J., Sun, W., et al. (2020). Improving unmanned aerial vehicle remote sensing-based rice nitrogen nutrition index prediction with machine learning. *Remote Sens.* 12:215. doi: 10.3390/rs12020215

Zhang, J., Qiu, X., Wu, Y., Zhu, Y., Cao, Q., Liu, X., et al. (2021). Combining texture, color, and vegetation indices from fixed-wing uas imagery to estimate wheat growth parameters using multivariate regression methods. *Comput. Electron. Agric.* 185:106138. doi: 10.1016/j.compag.2021.106138

Zhang, X., Zhang, K., Sun, Y., Zhao, Y., Zhuang, H., Ban, W., et al. (2022). Combining spectral and texture features of uas-based multispectral images for maize leaf area index estimation. *Remote Sens.* 14:331. doi: 10.3390/rs14020331

Zheng, H., Ma, J., Zhou, M., Li, D., Yao, X., Cao, W., et al. (2020). Enhancing the nitrogen signals of rice canopies across critical growth stages through the integration of textural and spectral information from unmanned aerial vehicle (UAV) multispectral imagery. *Remote Sens.* 12:957. doi: 10.3390/rs12060957

Zhou, X., Zheng, H. B., Xu, X. Q., He, J. Y., Ge, X. K., Yao, X., et al. (2017). Predicting grain yield in rice using multi-temporal vegetation indices from UAV-based multispectral and digital imagery. *ISPRS J. Photogramm. Remote Sens.* 130, 246–255. doi: 10.1016/j.isprsjprs.2017.05.003

frontiers | Frontiers in Plant Science

TYPE Original Research
PUBLISHED 10 August 2022
DOI 10.3389/fpls.2022.958106

Check for updates

OPEN ACCESS

EDITED BY
Zhenhai Li,
Shandong University of Science and Technology, China

REVIEWED BY
Shangpeng Sun,
McGill University, Canada
Tao Yang,
Institute of Crop Sciences (CAAS), China

*CORRESPONDENCE
Shenghui Fang
shfang@whu.edu.cn

†These authors have contributed equally to this work

SPECIALTY SECTION
This article was submitted to Sustainable and Intelligent Phytoprotection, a section of the journal Frontiers in Plant Science

RECEIVED 31 May 2022
ACCEPTED 21 July 2022
PUBLISHED 10 August 2022

CITATION
Luo S, Jiang X, Yang K, Li Y and Fang S (2022) Multispectral remote sensing for accurate acquisition of rice phenotypes: Impacts of radiometric calibration and unmanned aerial vehicle flying altitudes. *Front. Plant Sci.* 13:958106. doi: 10.3389/fpls.2022.958106

COPYRIGHT
© 2022 Luo, Jiang, Yang, Li and Fang. This is an open-access article distributed under the terms of the Creative Commons Attribution License (CC BY). The use, distribution or reproduction in other forums is permitted, provided the original author(s) and the copyright owner(s) are credited and that the original publication in this journal is cited, in accordance with accepted academic practice. No use, distribution or reproduction is permitted which does not comply with these terms.

Multispectral remote sensing for accurate acquisition of rice phenotypes: Impacts of radiometric calibration and unmanned aerial vehicle flying altitudes

Shanjun Luo[1†], Xueqin Jiang[1†], Kaili Yang[1], Yuanjin Li[1] and Shenghui Fang[1,2*]

[1]School of Remote Sensing and Information Engineering, Wuhan University, Wuhan, China, [2]Lab for Remote Sensing of Crop Phenotyping, Wuhan University, Wuhan, China

As a promising method, unmanned aerial vehicle (UAV) multispectral remote sensing (RS) has been extensively studied in precision agriculture. However, there are numerous problems to be solved in the data acquisition and processing, which limit its application. In this study, the Micro-MCA12 camera was used to obtain images at different altitudes. The piecewise empirical line (PEL) method suitable for predicting the reflectance of different ground objects was proposed to accurately acquire the reflectance of multi-altitude images by comparing the performance of the conventional methods. Several commonly utilized vegetation indices (VIs) were computed to estimate the rice growth parameters and yield. Then the rice growth monitoring and yield prediction were implemented to verify and evaluate the effects of radiometric calibration methods (RCMs) and UAV flying altitudes (UAV-FAs). The results show that the variation trends of reflectance and VIs are significantly different due to the change in component proportion observed at different altitudes. Except for the milking stage, the reflectance and VIs in other periods fluctuated greatly in the first 100 m and remained stable thereafter. This phenomenon was determined by the field of view of the sensor and the characteristic of the ground object. The selection of an appropriate calibration method was essential as a result of the marked differences in the rice phenotypes estimation accuracy based on different RCMs. There were pronounced differences in the accuracy of rice growth monitoring and yield estimation based on the 50 and 100 m-based variables, and the altitudes above 100 m had no notable effect on the results. This study can provide a reference for the application of UAV RS technology in precision agriculture and the accurate acquisition of crop phenotypes.

KEYWORDS

multispectral remote sensing, unmanned aerial vehicle (UAV), radiometric calibration, UAV flying altitude, precision agriculture

Introduction

The precise, economical, and dynamic gathering of farmland information in time is critical for boosting agricultural economic development and reducing labor costs (Wang et al., 2021). Rice (*Oryza sativa* L.) being a significant global staple food crop, its growth status and yield level have always been of great concern (Wan et al., 2020; Duan et al., 2021). Exact and pre-harvest growth monitoring and yield prediction of rice is of much value for the implementation of field measures, policy formulation, and price judgment (Zheng et al., 2019; Wan et al., 2020).

Manual investigation and measurement in the fields are frequently used methods for collecting rice yield and phenotypic data. This includes labor- and time-intensive work with great uncertainty (Yang et al., 2017). Furthermore, some phenotypic parameters can only be gained by destroying the samplings, resulting in the interruption in obtaining growth parameters in the later periods (Zhao et al., 2021). Rice yield formation is a process of dynamic accumulation, which is associated with both vegetative and reproductive growth periods (Wan et al., 2020). Therefore, it is essential to continuously monitor the growth status of rice (Yue et al., 2019).

In contrast, the prominent merit of remote sensing (RS) is that a large area can be covered and the phenotype information can be obtained in a non-destructive way (Franch et al., 2021). The development of the RS technique makes it possible to forecast the crop yield in advance. At present, the prediction accuracy of satellite RS has reached a relatively high level (Li et al., 2014; Huang et al., 2015; Franch et al., 2021). However, the images derived from satellites generally have some insurmountable shortcomings. For example, the resolution is rarely up to centimeter level, and the occlusion of clouds is serious. Hence, the flexibility of getting plant phenotype information on time is limited. Moreover, the scale of satellite RS cannot meet the practical application needs in precision agriculture like the small plots in southern China (Peng et al., 2019). In recent years, unmanned aerial vehicle (UAV) RS technology has become a hot content in the field of agricultural research. The UAV provides a convenient tool for emerging sensors to obtain unparalleled images with high time–space–spectral resolution (Maes and Steppe, 2019).

The low-altitude UAV-based RS technology is of high significance to precision agriculture owing to its high efficiency, low cost, and macro size (Deng et al., 2018b; Han et al., 2019). Different types of sensors have also been applied to different scenes. For example, hyperspectral cameras were exploited to estimate crop leaf area index (LAI), leaf chlorophyll content, and leaf nitrogen content (Delegido et al., 2010; Xie et al., 2014; Raj et al., 2021). Thermal infrared sensors were utilized to retrieve the temperature and water status of the olive tree canopy (Noguera et al., 2020) and help to predict the soybean yield (Maimaitijiang et al., 2020). Moreover, the UAV-based LiDAR sensors were recently employed to determine the height of different crops (ten Harkel et al., 2020). Although they showed unique performance in precision agriculture, there are some difficulties in practical use. On the one hand, for the current UAVs, the weights of the sensors exceed the standard ones, which makes the flight difficult to last for a long time. On the other hand, these sensors are very expensive, and few people can afford the high cost. As non-quantitative RS equipment, the visible sensor (RGB camera) based on broadband is often used in precision agriculture due to its acceptable price and convenient operation. However, on account of the limitation of the number of bands and difficulty in calibration, it is generally applied to provide canopy height information and describe color changes (Deng et al., 2018b). Multispectral sensors cannot only meet the cost requirements but can also obtain high-resolution multispectral images, including red-edge and near-infrared (NIR) bands sensitive to vegetation growth (Huang et al., 2018). Therefore, the multispectral camera has great potential in precision agriculture. Vegetation indices (VIs) based on multispectral images have been extensively used in crop growth monitoring and yield prediction (Deng et al., 2018b; Gong et al., 2018; Duan et al., 2019).

For multispectral sensors, the premise of extracting accurate RS phenotype information is to obtain high-precision canopy spectral reflectance data. The observed reflectance data of the same ground object by different multispectral sensors are often different. The main reasons are as follows: (i) equipment and methods used for radiometric calibration (without considering the influence of the atmosphere), (ii) observation geometry, and (iii) differences in spectral response functions of different sensors in the corresponding bands (Deng et al., 2018a,b). When the multispectral sensor, observation target, and time are determined, the main factors affecting the observed reflectance are radiometric calibration methods (RCMs) and observation angles. In practical application, UAV control is flexible and changeable, resulting in flight altitudes ranging from dozens to hundreds of meters. Different flight altitudes will not only lead to changes in RS image resolution but also to differences in the observation angles of the same target. Currently, there are few reports on this aspect. Therefore, the impacts of UAV flying altitudes (UAV-FAs) on multispectral data are worth discussing.

In this study, the multispectral images derived from different UAV-FAs in some experiments (including different types of ground objects, different fertilizer gradients, and multi-cultivar rice experiments) were obtained to (i) compare the accuracy of reflectance and VIs achieved by different RCMs and put forward a unified calibration method suitable for the accurate acquisition of reflectance of different objects, (ii) analyze the variation trend and causes of reflectance and VIs at different UAV-FAs, and (iii) evaluate the effects of different RCMs and UAV-FAs on rice growth monitoring and yield prediction.

Materials and methods

Experimental area

This study involved three experimental areas, including Ezhou City, Hubei Province (30°22′31″N,114°44′50″E), Lingshui County, Hainan Province (18°31′47″N, 110°03′35″E), and Wuhan University Friendship Square, Hubei Province (30°31′48″N, 114°21′20″E), China.

Four experiments (named Tests 1, 2, 3, and 4) were conducted in this study. Test 1 was carried out from February to April 2018. A total of 42 rice plots including 42 cultivars were set up, and each plot covered an area of approximately 40 m^2. Except for different rice cultivars, the fertilization level and drainage and irrigation management were the same. For more details, see Jiang et al. (2019). Test 2 included three repetitions and four nitrogen gradients (0, 120, 180, and 240 kg/ha) and was conducted from February to April 2018. Two rice cultivars and 24 plots were randomly arranged, of which each plot was about 30 m^2. Black plastic film was laid between plots with different gradients to isolate water and fertilizer. Test 3 was the small rice plot experiment with an area of 1 m^2 of each plot and was conducted from July to September 2018. Multiple plots were selected to conduct the multi-altitude experiments. One rice cultivar was planted in each plot at an interval of 10 cm. In addition to their respective control variables (cultivar and nitrogen fertilizer), other field management measures (irrigation, weeding, pesticide application, etc.) were implemented under the guidance of professionals. The main purpose of Test 4 was to study some ground objects different from rice (grassland, smooth, and rough slabstone) for comparative analysis and to increase the universality of the results. We randomly selected and marked 17 locations, including grassland and slabstone, as the research objects on 23 July 2021.

Field data acquisition

In Test 1 and Test 2, rice growth parameters including LAI, above-ground biomass (AGB), and canopy chlorophyll content (CCC) at different growth durations (tillering, jointing, booting, heading, and milking stages) were measured directly or calculated indirectly.

The LAI (unitless) was measured by using LAI-2200C (LI-COR, Lincoln, Nebraska United States) at dusk or dawn. Three repeated measurements were conducted for each rice plot, and the mean value was treated as the plot-level LAI. Each repetition result is a reading of 10 random measurements (1 above and 10 below the rice canopy) with a 270° view cap. The LAI value obtained in this way can be regarded as the green LAI (LAI_{green}) due to the strong correlation with the manually measured value ($R^2 = 0.87$, $P < 0.001$) (Liu et al., 2017).

The SPAD (unitless) values, which were often used to reflect the chlorophyll content level of leaves (Uddling et al., 2007), were measured using SPAD-502 meter (Spetrum Technologies, Inc., Plainfield, IL, United States). At each growth stage of rice, 10 plants in every plot were selected to measure the SPAD values of four upper fully expanded leaves ($SPAD_{upper}$) at multi-locations (Peng et al., 1993), and the average was treated as the plot-level SPAD.

AGB (in g/m^2) was collected by destructive sampling. Three hills of plants were dug and taken back to the laboratory for drying. All samples with the underground parts removed were dried at 80°C until multiple weighing values remained constant. The plot-level AGB was the product of dry weight and density of samplings.

The CCC (in g/m^2) was calculated by exploiting the product of LAI_{green} and $SPAD_{upper}$ (Baret et al., 2007) to diagnose the canopy nitrogen content (Gitelson et al., 2005; Liu et al., 2017) and assess the total canopy-scale productivity of rice (Inoue et al., 2016).

The rice yield (in g/m^2) was surveyed by sampling 100 plants in each plot. The final rice yield of the plot was the average weight of spikes after threshing and drying multiplied by the transplanting density.

At different stages, the ASD Field Spec 4 spectrometer (Analytical Spectral Devices Inc., Boulder, CO, United States) was adopted to collect rice canopy spectra under cloudless and windless conditions. The multiple and multipoint measurements were implemented daily from 10:00 to 14:00 with a field-of-view (FOV) of 25°, and the results of five points and 10 measurements at each point were averaged to get the plot-level spectra.

Unmanned aerial vehicle multispectral image collection

The Micro-MCA camera fixed on the UAV (Duan et al., 2021) with a gimbal was utilized to obtain the multispectral images from 11:00 to 13:00. Twelve independent camera lenses (the image size of 1,280 × 1,024 pixels, with the horizontal and vertical FOV of 38.26 and 30.97°) were equipped with central bands of 490–950 nm. The visible to NIR bands widely employed in precision agriculture were covered (Kimes et al., 1981). The details of UAV multispectral data acquisition are shown in **Table 1**.

Data processing

The noise, vignetting, distortion correction, and band-to-band alignment of multispectral images were determined in the PixelWrench 2 software (Xu et al., 2019). Subsequently, three RCMs were applied to compare the reflectance conversion

10.3389/fpls.2022.958106

TABLE 1 The details of multispectral images for four experiments in Hubei and Hainan Provinces.

Experimental name	Study site	Number of plots	Date of UAV images collection (DAT/day)	UAV flying altitude (m)	Growth stage of rice
Test 1	Hainan	42	2018/02/02 (25)	100, 150, 200, 250	Tillering stage
			2018/02/26 (49)		Jointing stage
			2018/03/11 (62)		
			2018/03/18 (69)		Booting stage
			2018/04/01 (83)		Heading stage
			2018/04/26 (108)		Milking stage
Test 2	Hainan	24	2018/02/02 (27)	50, 100	Tillering stage
			2018/02/20 (45)		
			2018/03/03 (56)		Jointing stage
			2018/03/11 (64)		
			2018/03/25 (78)		Booting stage
			2018/04/01 (85)		Heading stage
			2018/04/26 (110)		Milking stage
Test 3	Hubei	Multiple	2018/08/15 (52)	60, 70, 80, 90, 100, 110, 120, 130, 150, 170, 190, 210, 230, 250	Tillering stage Jointing stage Booting stage Heading stage Milking stage
Test 4	Hubei	17	2021/07/23	60, 70, 80, 90, 100, 110, 120, 130, 150, 170, 190, 210	–

accuracy from the original digital number (DN) values. In this process, eight calibration targets (covering different reflectance ranges: 3, 6, 12, 24, 36, 48, 56, and 80%) with stable reflectance were laid within the imaging range of the UAV to obtain the reflectance of the target ground object. The eight 1.2 × 1.2 m grayscale calibration panels were fabricated using a specific lot of coated fabric for Tetracam Inc.

The conventional empirical line (EL) method was extensively employed when only two calibration targets were used for its straightforward, simple, and effective implementation (Smith and Milton, 1999; Laliberte et al., 2011; Wang and Myint, 2015). Since the fact that the increased number of observation targets could improve the accuracy and reliability of calibration was proved (Tucker, 1979), multiple calibration panels were utilized to obtain the reflectance by the EL method (Xu and Huang, 2008; Duan et al., 2019, 2021; Wan et al., 2020). However, in many vegetation scenes, it was found that the calibrated reflectance values of visible bands were negative, especially in blue and red bands (Deng et al., 2018b). In practice, it is worth noting that the linear relationship between reflectance and radiance does not always exist (Stow et al., 1996). Therefore, non-linear models need to be considered during the radiometric calibration. The subband empirical line (SEL) method was proposed to solve the problem of negative reflectance (Deng et al., 2018a,b). In the SEL method, different bands were divided into two groups (red, green, and blue bands with low reflectance and red edge and NIR bands with high reflectance), and the power and linear models were used for the reflectance calibration, respectively. The SEL method only studied the scene of vegetation's low reflectance in visible bands and did not consider other objects with high reflectance in these spectral regions. Moreover, the case of multiple calibration panels was ignored in the SEL method. In addition, the comparison of the linear and power models in visible bands with high reflectance was not performed. In this study, the piecewise empirical line (PEL) method was put forward to construct a general calibration method for reflectance acquisition of different types of objects. In all experiments, images obtained at a height of 100 m were selected for radiometric calibration comparison. The transformation relations of these three RCMs are shown in Eqs. (1–3).

$$y = a_1 \cdot x_i + b_1 \tag{1}$$

$$y = \begin{cases} a_2 \cdot x_i^{b_2} & i = 1, 2, 3, 4, 5, 6, 7 \\ a_3 \cdot x_i + b_3 & i = 8, 9, 10, 11, 12 \end{cases} \tag{2}$$

$$y = \begin{cases} a_4 \cdot x_i & y \le 0.03 \\ a_5 \cdot x_i + b_5 & y > 0.03 \end{cases} \tag{3}$$

where y is the reflectance after radiometric calibration, x is the DN value of different bands, i is the number of bands from 1 to 12, and the constants a and b are the corresponding slopes and intercepts of the fitted lines from the used calibration targets.

To compare the accuracy of the measured spectra using the ASD spectrometer (R_{ASD}) with the UAV multispectral reflectance (R_{MCA}), the R_{ASD} needs to be convolved by the spectral response function of the MCA camera (MCA-based

equivalent reflectance, $R_{MCA-ASD}$). The conversion of spectral reflectance was calculated by Eq. (4).

$$R_j = \frac{\int_s^e R_{ASD} \cdot S_j(\lambda) d\lambda}{\int_s^e S_j(\lambda) d\lambda} \quad (4)$$

where R_j is the $R_{MCA-ASD}$, λ is the wavelength, $S_j(\lambda)$ is the spectral response function of band j, and e and s are the starting and ending wavelengths of band j, respectively.

The plot-level canopy reflectance of rice derived from UAV images was obtained by defining a rectangular region of interest (ROI). For different UAV-FAs, the reflectance was acquired by adjusting the number of pixels in the ROI of the responding image according to the resolution. Additionally, several VIs, such as RVI (Jordan, 1969), NDVI (Tucker, 1979), NDRE (Gitelson and Merzlyak, 1994), VARI (Gitelson et al., 2002), EVI2 (Jiang et al., 2008), $CI_{rededge}$ (Gitelson et al., 2003), CI_{green} (Gitelson et al., 2003), MCARI (Daughtry et al., 2000), and WDRVI (Gitelson, 2004), frequently applied to rice growth monitoring and yield prediction were computed.

Methods and evaluation

In practical multispectral images, each pixel is usually a mixed pixel. The fluctuation in the reflectance of the mixed pixel can be regarded as the changes in the components (called endmember) and proportions of these components (called abundance). Mixed pixel decomposition is a process of calculating the abundance of each component by using the least-square method under the condition that the reflectance of the mixed pixel and each endmember is known. The fully constrained least-square linear spectral mixture (FCLS-LSM) model was employed in this study to obtain the abundance of endmembers of multispectral images derived from different UAV-FAs with the constrained conditions of Eqs. (5–6) (Gong et al., 2018; Duan et al., 2019).

$$R = \sum_{i=1}^{n} A_i R_i + e \quad (5)$$

$$0 \leq A_i \leq 1; \sum_{i=1}^{n} A_i = 1 \quad (6)$$

where R is the reflectance of the mixed pixel, A_i is the abundance of the endmember i, R_i is the reflectance of the endmember i, n is the number of the endmembers, and e is the error.

The prediction models of rice growth parameters and yield were constructed using linear regression and three machine learning algorithms of SVR, RFR, and ANN (Ashapure et al., 2020). The accuracy was described quantitatively by R^2, RMSE, and RRMSE (Duan et al., 2021). In addition, the mean relative percent error (MRPE) and RMSE were utilized to analyze and compare the effects of three RCMs. The relevant expressions for calculation are as follows:

$$MRPE = \frac{1}{n} \sum_{i=1}^{n} \left| \frac{\hat{y} - y}{y} \times 100 \right| \quad (7)$$

$$RMSE = \sqrt{\frac{\sum_{i=1}^{n} (\hat{y} - y)^2}{n}} \quad (8)$$

$$RRMSE = \frac{RMSE}{\bar{y}} \quad (9)$$

where y, $\hat{y}$, and $\bar{y}$ are the observed, estimated, and measured mean values, respectively. n is the number of samples. In the RCM evaluation, y is the $R_{MCA-ASD}$.

Results

Accuracy comparison of reflectance and vegetation indices based on three radiometric calibration methods

The reflectance of rice canopy

The $R_{MCA-ASD}$ of rice canopy during the whole growth period in Test 1 and Test 2 was used to compare with the R_{MCA} based on three RCMs (EL, SEL, and PEL). Since the differences among RCMs mainly lie in the visible and red-edge (700 nm) bands, these bands will be discussed emphatically. The accuracy comparison of several typical bands (490, 550, 670, and 700 nm) in Test 1 was shown as an example. As can be seen in **Figure 1**, each row represents a band and each column a RCM. In general, compared with EL, the accuracy of SEL- and PEL-based reflectance was improved at different stages (closer to the 1:1 line), particularly pronounced in the jointing, booting, and heading stages. In these periods, the rice canopy reflectance obtained based on EL was significantly underestimated, and even negative values appeared in the bands of 490 and 670 nm. In addition, the SEL- and PEL-based reflectance showed similarities. Furthermore, it was also found that SEL and PEL had a better ability to predict rice reflectance at the milking stage in the bands with low reflectance (490 and 670 nm), while EL and PEL had higher accuracy at tillering stage in the bands with relative high reflectance (490, 670, and 700 nm).

The MRPE and RMSE were computed to quantitatively evaluate the performance of three RCMs in the reflectance prediction of 12 bands in Test 1 and Test 2. It can be seen from **Table 2** that EL has a strong reflectance prediction ability in 720 nm and NIR bands (MPRE < 30% in Test 1 and < 15% in Test 2). In contrast to EL, SEL, and PEL improved the reflectance accuracy of 490, 670, and 680 nm by about 37–66% in Test 1 and 45–61% in Test 2. There is no more than a 5% accuracy difference among the three RCMs in 550 nm. PEL achieved

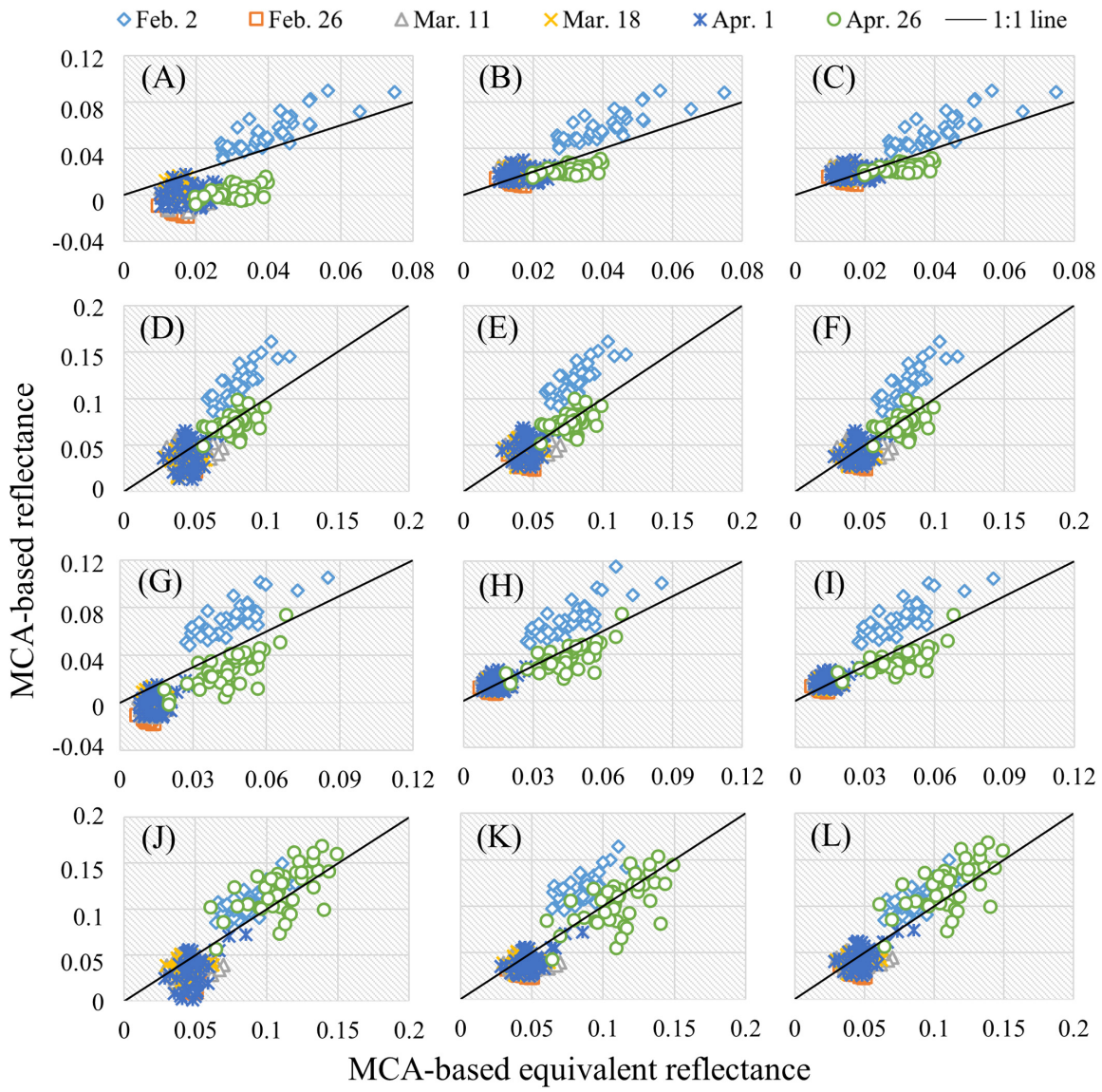

FIGURE 1
Comparison of R_{MCA} and $R_{MCA-ASD}$ in Test 1: **(A)** 490 nm and EL; **(B)** 490 nm and SEL; **(C)** 490 nm and PEL; **(D)** 550 nm and EL; **(E)** 550 nm and SEL; **(F)** 550 nm and PEL; **(G)** 670 nm and EL; **(H)** 670 nm and SEL; **(I)** 670 nm and PEL; **(J)** 700 nm and EL; **(K)** 700 nm and SEL; and **(L)** 700 nm and PEL.

the highest prediction accuracy in each band. Compared with SEL, PEL was slightly improved (less than 5%). Thus, in the estimation of canopy reflectance in the whole growth period of rice, the performance of SEL and PEL was significantly better than that of EL, but the accuracy improvement difference between SEL and PEL was limited.

The reflectance of grassland canopy and slabstone

The grasslands and slabstones were selected to obtain the R_{MCA} and $R_{MCA-ASD}$ simultaneously to evaluate the performance of the three RCMs in the reflectance predictions of different ground objects. The prediction accuracy of EL and PEL is identical for the observed slabstones due to the fact that the reflectance of each band is not less than 3%. It could be found in Table 3 that EL had a good prediction effect on the reflectance of grassland canopy and slabstone at 720 nm and NIR bands. For grassland, in the low reflectance bands (490, 670, and 680 nm), the performance of PEL was consistent with that of rice. The reflectance accuracy of PEL was significantly higher than that of EL and slightly stronger than that of SEL. However, in the bands of 550, 570, and 700 nm, the results of EL and PEL were similar and significantly better than SEL. For slabstone, EL (PEL) performed better than SEL in each compared band.

Vegetation indices of rice and grassland canopy

The VIs calculated based on R_{MCA} and $R_{MCA-ASD}$ of rice and grassland were compared to analyze the influence of RCMs. Here, only the accuracy comparison of RVI, NDVI, VARI, EVI2, CI_{green}, MCARI, and WDRVI was analyzed because the red-edge indices (NDRE and $CI_{rededge}$) were a combination of 720 nm and NIR bands, and the comparison of the three RCMs was not involved. The results presented in Table 4 demonstrated that the accuracy of VIs based on the three RCMs was consistent with the accuracy of reflectance. The PEL had the highest accuracy, and the accuracy of SEL and PEL was significantly higher than that of EL. However, CI_{green} in Test 4 showed higher precision of PEL and EL than SEL.

Responses of reflectance and vegetation indices to varying UAV flying altitudes

The variation of reflectance with UAV flying altitudes

In Test 3, the edge rice plots in the multispectral images at different stages were used to analyze the responses of reflectance

TABLE 2 Statistical results of reflectance accuracy of different RCMs in Test 1 and Test 2.

Band (nm)	MRPE (%)						RMSE					
	EL		SEL		PEL		EL		SEL		PEL	
	Test 1	Test 2	Test 1	Test 2	Test 1	Test 2	Test 1	Test 2	Test 1	Test 2	Test 1	Test 2
490	98.825	76.489	34.306	25.430	**32.287**	**21.616**	0.021	0.019	0.010	0.010	**0.009**	**0.009**
520	50.052	52.625	23.816	27.923	**21.619**	**24.966**	0.021	0.019	0.013	0.014	**0.011**	**0.013**
550	26.362	28.312	25.075	25.223	**22.955**	**24.663**	0.019	0.017	0.020	0.016	**0.018**	**0.016**
570	35.310	42.234	28.813	24.158	**24.423**	**22.241**	0.021	0.019	0.020	0.016	**0.017**	**0.014**
670	99.697	66.812	37.191	23.124	**35.888**	**21.598**	0.020	0.018	0.013	0.014	**0.012**	**0.014**
680	84.679	81.757	38.470	23.502	**37.775**	**20.608**	0.020	0.019	0.014	0.015	**0.013**	**0.014**
700	31.522	37.495	24.926	30.032	**20.724**	**28.137**	0.023	0.023	0.020	0.025	**0.016**	**0.020**
720	18.582	13.865	–	–	–	–	0.033	0.023	–	–	–	–
800	20.010	8.771	–	–	–	–	0.096	0.042	–	–	–	–
850	22.698	8.967	–	–	–	–	0.113	0.043	–	–	–	–
900	20.196	8.463	–	–	–	–	0.102	0.040	–	–	–	–
950	27.343	11.631	–	–	–	–	0.1218	0.046	–	–	–	–

The method with the best performance is represented by bold values.

TABLE 3 Statistical results of reflectance accuracy of different RCMs in Test 4.

Band (nm)	MRPE (%)					RMSE				
	EL		SEL		PEL	EL		SEL		PEL
	Grassland	Slabstone	Grassland	Slabstone	Grassland	Grassland	Slabstone	Grassland	Slabstone	Grassland
490	69.603	**29.806**	44.919	36.096	**42.607**	0.032	**0.043**	0.021	0.053	**0.020**
520	72.858	**35.562**	56.752	42.594	**51.435**	0.052	**0.053**	0.041	0.064	**0.037**
550	24.709	**24.070**	32.618	30.082	**24.709**	0.024	**0.043**	0.032	0.053	**0.024**
570	34.446	**25.030**	35.849	31.071	**34.446**	0.030	**0.043**	0.031	0.05	**0.030**
670	50.253	**24.224**	42.061	29.463	**41.636**	0.029	**0.049**	0.025	0.059	**0.025**
680	64.741	**26.298**	48.397	31.021	**43.571**	0.040	**0.052**	0.030	0.063	**0.027**
700	32.783	**23.615**	38.850	29.056	**32.783**	0.038	**0.050**	0.045	0.063	**0.038**
720	6.630	20.1980	–	–	–	0.016	0.044	–	–	–
800	4.390	17.735	–	–	–	0.017	0.045	–	–	–
850	3.354	17.295	–	–	–	0.014	0.047	–	–	–
900	5.445	16.326	–	–	–	0.025	0.046	–	–	–
950	5.034	24.287	–	–	–	0.022	0.074	–	–	–

The method with the best performance is represented by bold values.

10.3389/fpls.2022.958106

TABLE 4 Statistical results of VI accuracy of different radiometric calibration methods in Test 1, Test 2, and Test 4.

Error	Model	Experiment	RVI	NDVI	VARI	EVI2	CI_{green}	MCARI	WDRVI
MRPE (%)	EL	Test 1	99.517	4.967	99.321	11.993	42.889	90.532	72.578
		Test 2	99.329	9.860	75.488	11.935	53.042	59.763	90.445
		Test 4	123.900	18.678	84.619	16.780	46.732	36.054	812.925
	SEL	Test 1	31.765	2.091	10.084	9.157	33.601	26.437	41.533
		Test 2	36.040	6.761	43.082	10.999	46.632	23.116	89.540
		Test 4	79.514	15.648	56.319	14.237	67.477	36.914	744.887
	PEL	Test 1	**26.365**	**2.063**	**6.174**	**8.908**	**30.327**	**25.573**	**45.383**
		Test 2	**31.712**	**6.535**	**29.949**	**10.961**	**44.635**	**19.798**	**88.321**
		Test 4	**77.054**	**15.342**	**31.483**	**13.984**	**46.732**	**31.009**	**727.275**
RMSE	EL	Test 1	80.744	0.075	2.490	0.135	5.778	0.022	0.322
		Test 2	78.783	0.090	0.339	0.080	4.505	0.008	0.257
		Test 4	9.663	0.135	0.217	0.089	1.360	0.010	0.347
	SEL	Test 1	13.386	0.040	0.091	0.100	3.460	0.004	0.102
		Test 2	7.529	0.075	0.137	0.075	3.517	0.005	0.156
		Test 4	5.341	0.112	0.133	0.075	1.946	0.010	0.270
	PEL	Test 1	**11.002**	**0.038**	**0.062**	**0.099**	**3.099**	**0.004**	**0.101**
		Test 2	**7.428**	**0.075**	**0.090**	**0.074**	**3.426**	**0.004**	**0.155**
		Test 4	**5.201**	**0.110**	**0.081**	**0.074**	**1.360**	**0.008**	**0.264**

The method with the best performance is represented by bold values.

and VIs to UAV-FAs. In the same sensor and photographing mode, the resolution of the UAV-induced image was determined by the UAV-FAs. The UAV images of different scales (60–250 m) were converted according to the resolutions, and then the sizes of the ROI were calculated to represent the same study area. The mean value of all pixels within the ROI was taken as the plot-level reflectance.

It can be found from Figure 2 that the variation trend of rice reflectance (including visible to NIR bands) with UAV-FAs in different periods differs significantly. At the tillering stage (Figure 2A), the reflectance of the NIR bands (800, 850, 900, and 950 nm) decreases obviously with UAV-FAs, but the reflectance of the visible (490, 520, 550, 570, 670, and 680 nm) and red-edge bands (700 and 720 nm) shows a slight rise at first and then a slow decline. At the jointing stage (Figure 2B), in general, the variation trend of reflectance with UAV-FAs in all bands is similar to that at the previous stage, while in the visible and red-edge bands, the reflectance changes more violently within the first 100 m. At the heading stage, the variation in the reflectance of different bands is more gentle than at the jointing stage. Specifically, the variation in the reflectance of visible bands is slightly slow within the first 100 m, and the variation in the reflectance of NIR and red-edge bands is weakened (Figure 2C). At the milking stage, the reflectance of each band changes relatively steadily (Figure 2D).

The variation of vegetation indices with UAV flying altitudes

The changes in VIs with UAV-FAs in different periods are shown in Figure 3. It can be seen that almost all VIs show similar trends in different periods. At the tillering, jointing, and heading stages, VIs change sharply within 100 m with UAV-FAs, but become stable after 100 m. This is consistent with the variation in the reflectance of the visible bands with UAV-FAs. In addition, VIs at the milking stage are nearly unaffected by UAV-FAs. With the growth of rice, the variation in VIs gradually weakens within the first 100 m, that is, the most significant changes occur at tillering and jointing stages, then weaken significantly at the heading stage, and remain almost unchanged at the milking stage.

Analysis of contributing factors to reflectance variation with UAV flying altitudes

The FCLS-LSM model was used to analyze the reasons for the changes in reflectance obtained from the same area observed at different altitudes. Taking the edge plot at the jointing stage as an example, after six kinds of endmembers (light leaf, shaded leaf, light water, shaded water, light soil, and shaded soil) were selected and measured, the spectral curve of each endmember (Figure 4A) was obtained by convolution of the spectral response function of Mini-MCA12 camera. As shown in Figure 4A, in the NIR bands, the reflectance of rice was much higher than that of the background, but the opposite was true in the visible bands. The abundances (i.e., proportions) of different endmembers were acquired through unmixing, and the reflectance changes were described through the combinations of different endmembers (Figure 4B). The NIR band attenuation factor was defined as the sum of all background abundances (light water + shaded water + light soil + shaded soil), and the visible band enhancement factor was calculated by the

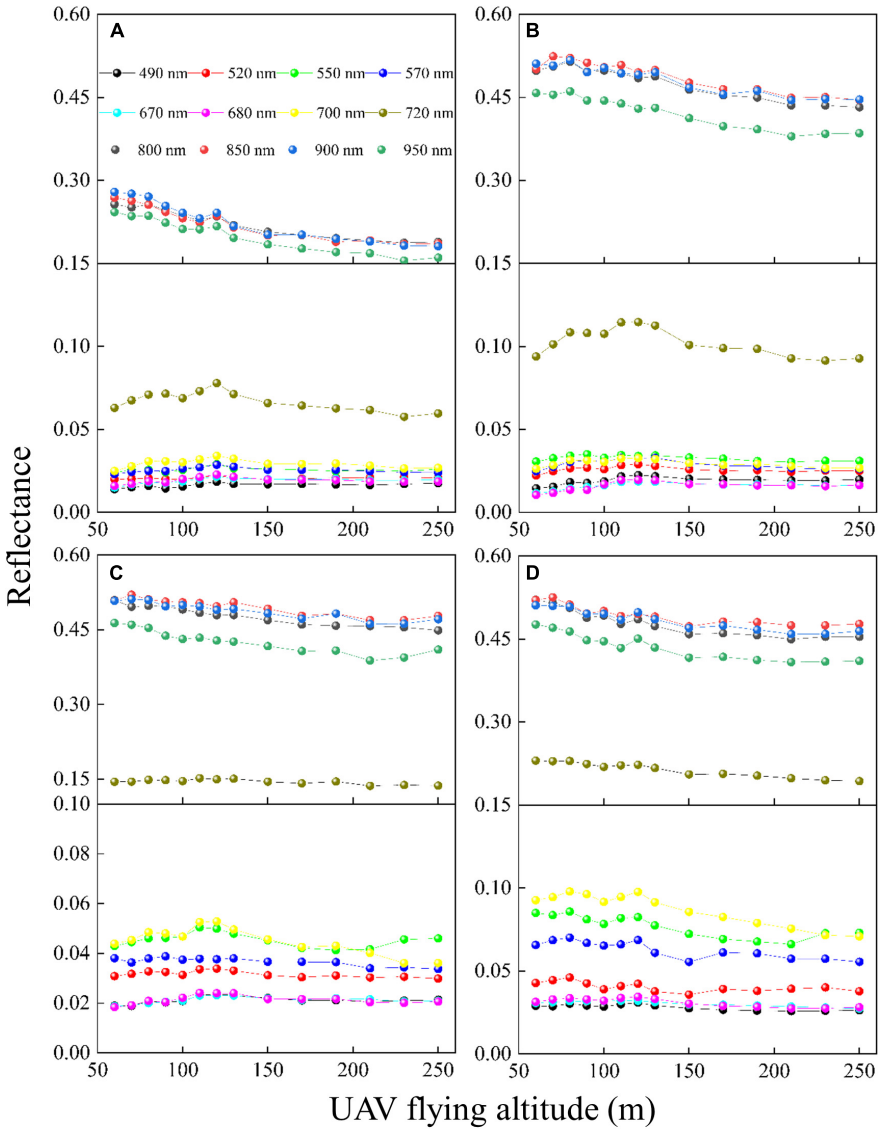

FIGURE 2
Variation in reflectance of rice with different UAV-FAs at **(A)** tillering stage; **(B)** jointing stage; **(C)** heading stage; and **(D)** milking stage.

combination of background abundances (light water + light soil + shaded soil – shaded water). The results in Figure 4B demonstrate that below 100 m, the visible band enhancement factor gradually increases with UAV-FAs, after which it remains stable. The NIR band attenuation factor increases with UAV-FAs until it changes slowly after 170 m. This shows no difference with the variation trend of NIR-band reflectance at the jointing stage (Figure 2B). Thus, as the background ratio increases, the reflectance of the NIR bands decreases, while the reflectance of the visible bands increases.

The observation angles of the same rice plot at different UAV-FAs are shown in Figure 4C. It can be seen that with the increase of UAV-FAs, the view zenith angle (VZA) of the same observation area gradually decreases. At a certain flight altitude, the edge-plot VZA of the image is equal to half of the FOV, so the distance from the study plot to the UAV in the vertical direction (d) can be calculated, and the variation in VZA at different UAV-FAs can be simulated according to the changing flight altitudes (H). The results in Figure 4D indicate that when the flight altitude rises from 50 to 100 m, the VZA drops sharply, and the trend gradually slows down after 100 m. The plot in this study is not located at the extreme edge of the image. Hence, the VZA at 100 m will shift to the right in Figure 4D, which is close to the stable state. At this point, the observation is closest to the orthotopic position.

Thus, observations at different altitudes are observations at different angles. The different proportions of the rice canopy and background observed at different angles, as well as the

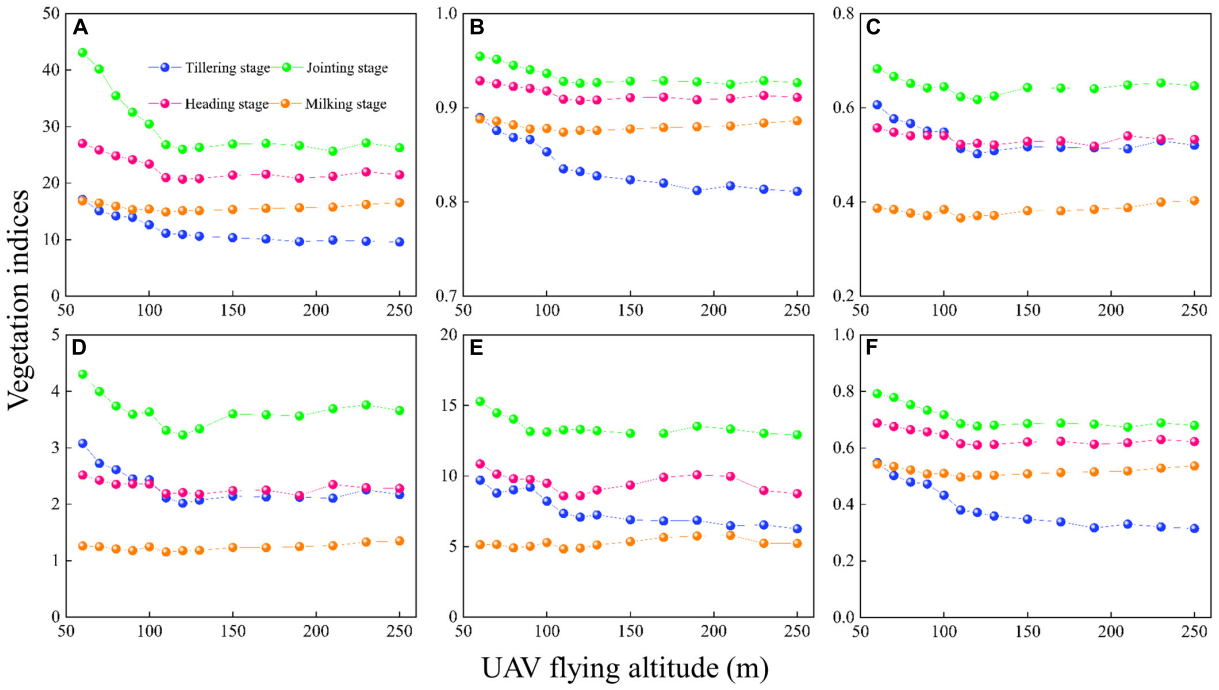

FIGURE 3
Variation in VIs with different UAV-FAs: **(A)** RVI; **(B)** NDVI; **(C)** NDRE; **(D)** $CI_{red\ edge}$; **(E)** CI_{green}; and **(F)** WDRVI.

differences in the proportion of light and shaded leaves in the canopy, make the observed reflectance of the rice plot show the characteristics of bidirectional reflection.

Impact of different radiometric calibration methods and UAV flying altitudes on rice growth monitoring

Different RCMs will produce large differences in reflectance and VIs (Figure 1 and Table 4). Thus, it is necessary to evaluate the impact of such differences in rice growth monitoring to guide practical applications. The EL-based reflectance often appears as outliers in the red bands, and the derived VIs will exceed the normal range (e.g., NDVI greater than 1). CI_{green} without red bands was selected to analyze the impact of different RCMs. To avoid the influence of bidirectional reflection, the 100 m images in Test 1 and Test 2 were used as the base map for calculating the CI_{green}. The linear regression models for estimating LAI, AGB, and CCC of rice are shown in Table 5. It turns out that the PEL performs better than EL and SEL methods in Test 1 and Test 2. In Test 1, the differences in LAI, AGB, and CCC prediction errors based on three RCMs are approximately 8, 2, and 10%, respectively. In Test 2, these differences are about 2%. In general, the PEL method has a stable advantage in rice growth monitoring.

As for the impact of different UAV-FAs on rice growth monitoring, the UAV-based images were processed by the PEL method. The results in Table 6 demonstrate that the differences in prediction results of rice growth parameters caused by UAV-FAs were more pronounced in Test 2 (50 and 100 m). In Test 1 (100–250 m), the differences in LAI, AGB, and CCC prediction errors based on different UAV-FAs were approximately 1, 2, and 1%, respectively. While in Test 2, these differences were about 8, 2, and 3%, respectively. The difference in LAI estimating results was the most significant.

Impact of different radiometric calibration methods and UAV flying altitudes on yield prediction

When analyzing the influence of different RCMs on yield prediction in a single stage, the images derived from an altitude of 100 m in Test 1 and Test 2 were selected. Moreover, the CI_{green} was also utilized to correlate with the yield of different stages. Quantitative evidence shown in Figure 5A indicates that the PEL reveals a better correlation with the yield at each stage in Test 1 and Test 2, particularly at the heading stage (significance changes).

The Pearson correlation coefficient between rice yield and PEL-based VIs at different UAV-FAs in Test 1 and Test 2 are shown in Figure 5. The darker and larger the colored

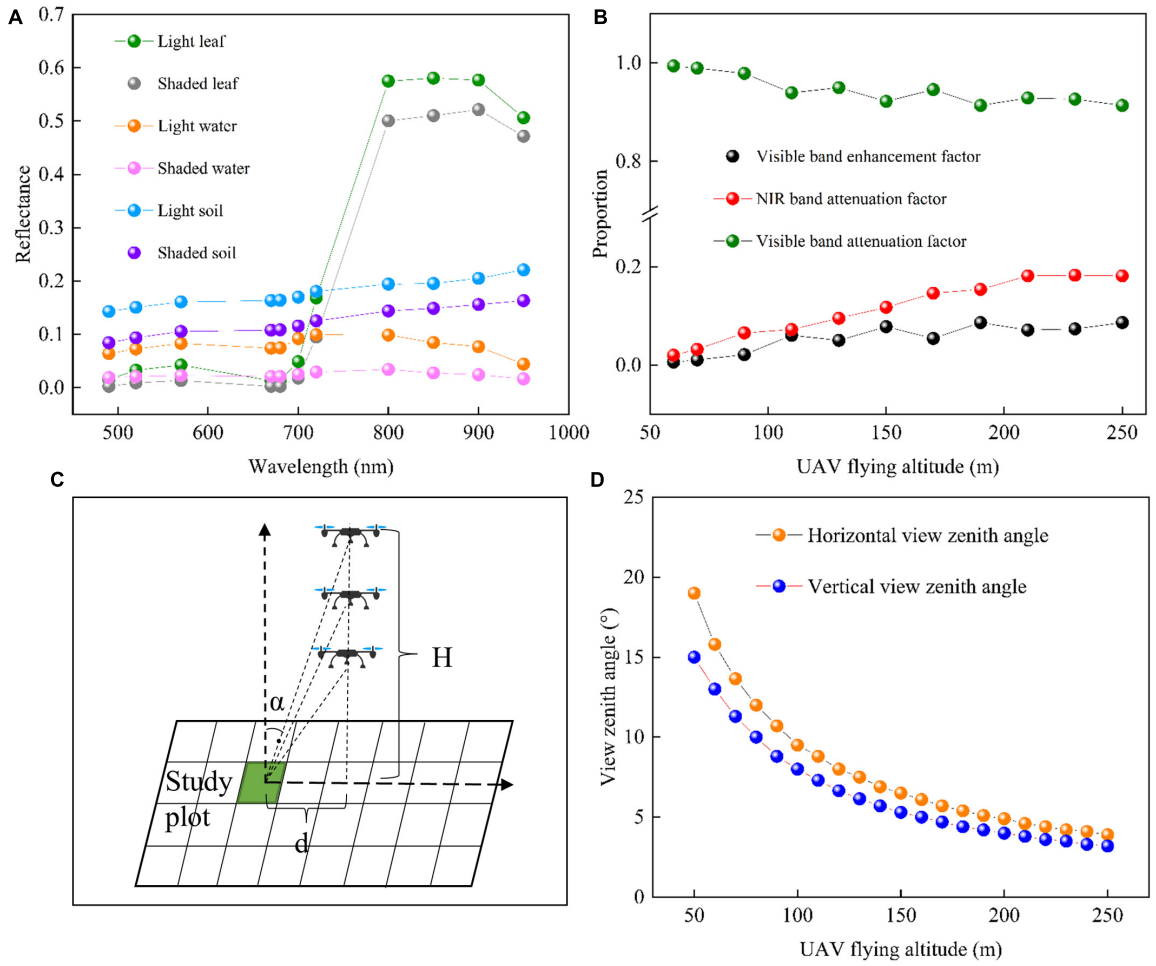

FIGURE 4
The changes caused by different UAV-FAs: **(A)** Reflectance of different endmembers in the rice field; **(B)** mixed pixel decomposition results; **(C)** schematic diagram of UAV observation angle change at different altitudes, α is the VZA and H is the UAV flying altitude; and **(D)** the changes in edge-plot FOV with the increase of UAV-FAs.

rectangles in the heat map, the stronger the correlation. It can be found that, as a whole, there was little difference in the correlation between VIs and yield at different altitudes in Test 1, but there was a significant difference in Test 2 at each stage. Indices with the strongest correlation with the rice yield at booting (EVI2) and heading stages (WDRVI) were selected for quantitative comparison. The linear regression models for predicting rice yield using PEL-based VIs at booting and heading stages in Test 2 are shown in Table 7. It can be seen that the difference in yield prediction errors based on 50 and 100 m altitudes is about 2%.

As for the yield estimation of multi-variety rice, VIs in the whole period in Test 1 was used for yield prediction by the machine learning methods (SVM, RFR, and ANN) with 10-fold cross-validation because the relationship between VIs and yield was not directly linear. Each model was run 10 times as a result group, and an analysis of variance (ANOVA) was conducted to analyze the differences among individual groups. CI_{green} and NDVI are employed in the differential analysis of RCMs and UAV-FAs, respectively. As shown in Figure 6, the averaged value of R^2 with the same lowercase letters (a, b, and c) is not significantly different by Tukey's test at a significance level of 5%. It turns out that the SEL- and PEL-based yield estimation accuracy is significantly higher than that of EL using RFR and ANN. The three RCMs share little difference when using SVM (Figure 6A). The RFR is proved to be the best predictor using the PEL method, and the performance of the three machine learning methods share little difference using EL and SEL methods (Figure 6B). The results in Figure 6C demonstrate that the altitude above 100 m has no significant effect on yield prediction. However, there are some differences between the results of different yield estimation methods (Figure 6D). The RFR has the highest prediction accuracy in multi-period rice yield estimation at

100–250 m altitude. Consequently, different RCMs and UAV-FAs have some impacts on single- and multi-period rice yield estimation.

Discussion

The comparison and selection of radiometric calibration methods

In precision agriculture, the selection of RCMs and the evaluation of reflectance accuracy are often ignored (Jiang et al., 2019; Rosas et al., 2020; Wan et al., 2020). The results presented in **Figure 1** and **Tables 2**, **3** show that the EL method is suitable for the conversion of high reflectance (e.g., the slabstone and the rice at the tillering stage), while the SEL method can obtain more accurate low reflectance (e.g., the grassland and the rice at jointing, booting, and heading stages). Therefore, the PEL method was proposed to combine the advantages of EL and SEL and to automatically obtain high-precision reflectance for different ground objects using multiple calibration panels. In the visible bands, SEL is useful for the low reflectance of the vegetation itself. However, when plants are mixed with high reflectance background (such as soil), the performance of SEL is worse than that of EL. When vegetation almost covered the background (e.g., rice and grassland with a closed canopy), the ability of SEL to obtain low reflectance is highlighted, while the PEL can automatically perform

TABLE 5 The linear regression models for monitoring rice growth parameters based on three RCMs in Test 1 and Test 2.

Experimental name	RCMs	Regression equation	R^2	RMSE	RRMSE%
Test 1	EL	$LAI = 0.2138 \times CI_{green} + 2.1213$	0.6159	1.1894	24.43
	SEL	$LAI = 0.3392 \times CI_{green} + 1.2471$	0.7714	0.9175	18.84
	PEL	$LAI = 0.3360 \times CI_{green} + 1.0176$	**0.8364**	**0.7772**	**15.96**
	EL	$AGB = 31.8780 \times CI_{green} + 58.2600$	0.6283	258.5627	47.60
	SEL	$AGB = 38.2660 \times CI_{green} + 46.7340$	0.5478	267.8949	49.32
	PEL	$AGB = 39.6540 \times CI_{green} + 3.7036$	**0.6534**	**255.5819**	**47.05**
	EL	$CCC = 8.7479 \times CI_{green} + 96.1880$	0.5419	56.6725	27.16
	SEL	$CCC = 14.7750 \times CI_{green} + 50.8720$	0.7689	40.2487	19.29
	PEL	$CCC = 14.3360 \times CI_{green} + 44.2940$	**0.8001**	**37.4370**	**17.94**
Test 2	EL	$LAI = 0.2944 \times CI_{green} + 0.6926$	0.8350	0.8195	18.38
	SEL	$LAI = 0.3210 \times CI_{green} + 0.6811$	0.8026	0.8755	19.63
	PEL	$LAI = 0.3390 \times CI_{green} + 0.4682$	**0.8533**	**0.7820**	**17.53**
	EL	$AGB = 42.1860 \times CI_{green} + 30.6610$	0.4654	271.4445	48.08
	SEL	$AGB = 45.0950 \times CI_{green} + 31.0940$	0.4403	277.7335	49.20
	PEL	$AGB = 47.5830 \times CI_{green} + 4.9777$	**0.4690**	**270.5139**	**47.92**
	EL	$CCC = 11.9540 \times CI_{green} + 28.8210$	0.8588	30.9864	17.05
	SEL	$CCC = 13.2190 \times CI_{green} + 26.1690$	0.8492	31.5024	17.33
	PEL	$CCC = 13.9210 \times CI_{green} + 17.8800$	**0.8975**	**27.5072**	**15.13**

The method with the best performance is represented by bold values.

TABLE 6 The linear regression models for monitoring rice growth parameters based on different UAV-FAs in Test 1 and Test 2.

Experimental name	UAV-FAs (m)	Regression equation	R^2	RMSE	RRMSE%
Test 1	100	$LAI = 0.3360 \times CI_{green} + 1.0176$	0.8364	0.7762	15.94
	150	$LAI = 0.3539 \times CI_{green} + 0.9984$	0.8546	0.7318	15.03
	200	$LAI = 0.3421 \times CI_{green} + 0.9721$	0.8317	0.7874	16.17
	250	$LAI = 0.3554 \times CI_{green} + 0.8772$	0.8411	0.7649	15.71
	100	$AGB = 39.6540 \times CI_{green} + 3.7036$	0.6534	162.6172	36.55
	150	$AGB = 43.5090 \times CI_{green} - 4.7125$	0.6363	165.2271	36.81
	200	$AGB = 38.6880 \times CI_{green} + 6.2879$	0.6133	171.7673	38.60
	250	$AGB = 40.1870 \times CI_{green} + 1.6108$	0.6130	171.8381	38.62
	100	$CCC = 14.3360 \times CI_{green} + 44.2940$	0.8001	37.4370	17.94
	150	$CCC = 14.6560 \times CI_{green} + 48.3090$	0.8103	35.0322	17.07
	200	$CCC = 15.0250 \times CI_{green} + 37.4670$	0.8430	33.1784	15.90
	250	$CCC = 15.5450 \times CI_{green} + 34.0210$	0.8455	32.9088	15.77
Test 2	50	$LAI = 0.2788 \times CI_{green} + 0.8889$	0.7761	1.1150	25.00
	100	$LAI = 0.3390 \times CI_{green} + 0.4682$	0.8533	0.7820	17.53
	50	$AGB = 39.5530 \times CI_{green} + 55.1480$	0.4301	280.2471	49.64
	100	$AGB = 47.5830 \times CI_{green} + 4.9777$	0.4690	270.5139	47.92
	50	$CCC = 11.4960 \times CI_{green} + 34.5720$	0.8228	33.9458	18.67
	100	$CCC = 13.9210 \times CI_{green} + 17.8800$	0.8975	27.5072	15.13

10.3389/fpls.2022.958106

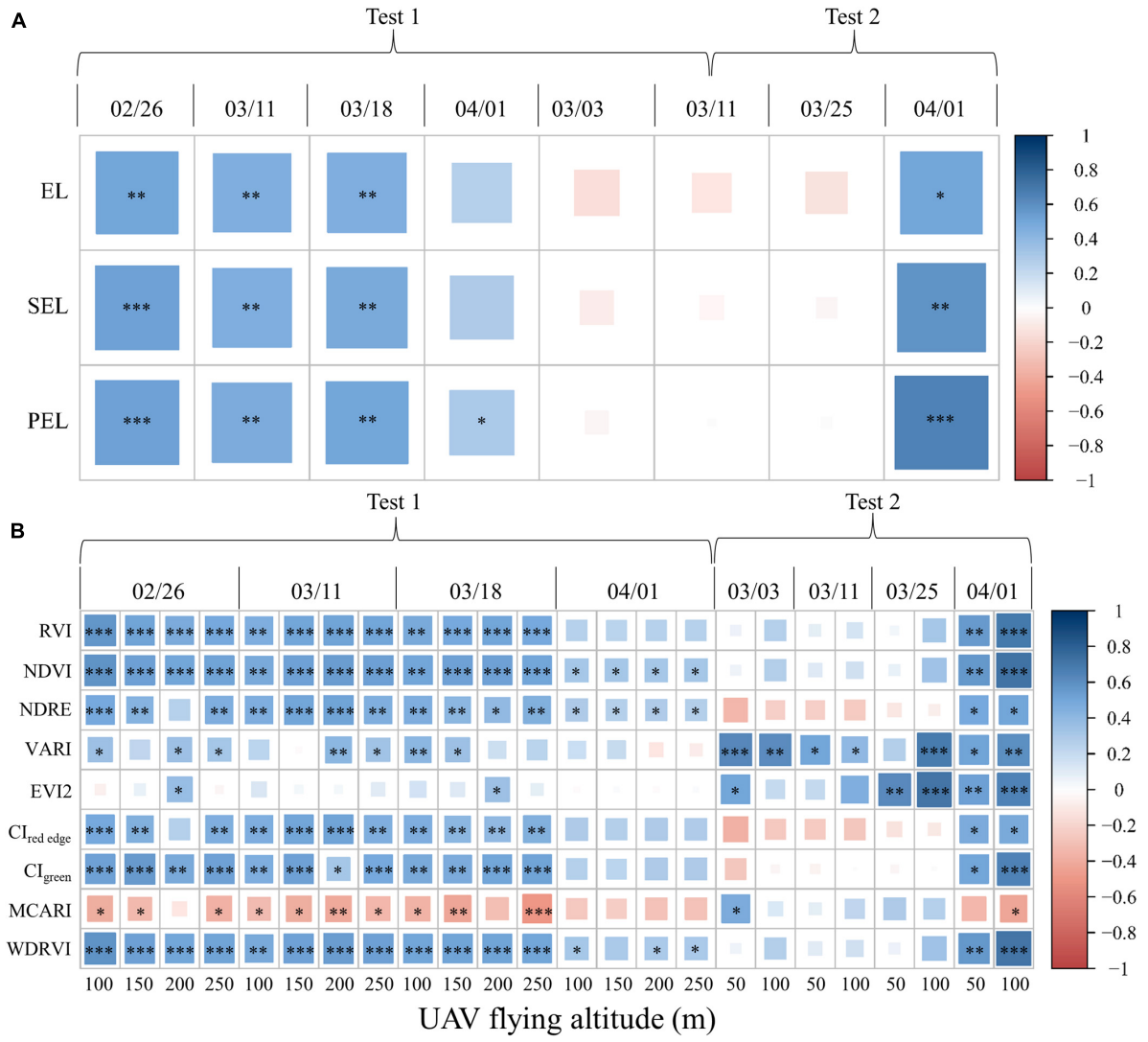

FIGURE 5
Impact of different RCMs and UAV-FAs on yield prediction: **(A)** Pearson correlation coefficient between rice yield and CI_{green} based on three RCMs in Test 1 and Test 2; **(B)** Pearson correlation coefficient between rice yield and VIs at different UAV-FAs in Test 1 and Test 2 (***, **, and * represent the significant correlation at the 0.001, 0.01, and 0.05 levels, respectively).

pixel-to-pixel reflectance conversion and obtain high-precision vegetation and background reflectance. This paves the way for analyzing the reflectance changes at different UAV-FAs.

The existing study shows that the accuracy of VIs derived from different sensors does not directly depend on the accuracy of reflectance (Deng et al., 2018b). That is to say, for different sensors, when the accuracy of reflectance is higher, it is not necessary that the accuracy of VIs should also be higher. The reasons are as follows: (i) the accuracy of reflectance of each band is different, (ii) bandwidths or central bands are different, and (iii) the reflectance is affected by the weather. However, in this study, the accuracy of VIs of the same sensor depends on its accuracy of reflectance. The results presented in **Table 4** demonstrate that SEL- and PEL-based VIs (except CI_{green} in Test 4) are more accurate than those based on EL in Test 1, Test 2, and Test 4. The accuracy of EL-based CI_{green} is higher than that of SEL in Test 4 due to the accuracy of the reflectance. The reflectance of 550, 570, and 700 nm of grassland in Test 4 has a higher accuracy based on EL (PEL) than SEL.

The response of reflectance and vegetation indices to different UAV flying altitudes

The vegetation canopy reflectance shows anisotropic characteristics with the change of incidence and observation angles, which is generally described by the bidirectional

TABLE 7 The linear regression models for predicting rice yield at booting and heading stages in Test 2.

Growth stage	UAV flying altitude (m)	Regression equation	R^2	RMSE	RRMSE%
Booting stage (03/25)	50	Yield = 3186.2660 × EVI2 - 2002.0312	0.3859	124.7462	15.4756
	100	Yield = 5475.6664 × EVI2 - 3455.1211	0.5177	110.5548	13.7151
Heading stage (04/01)	50	Yield = 1337.1689 × WDRVI - 120.3483	0.3165	131.6050	16.3265
	100	Yield = 2867.1955 × WDRVI - 1007.9788	0.5170	110.6357	13.7251

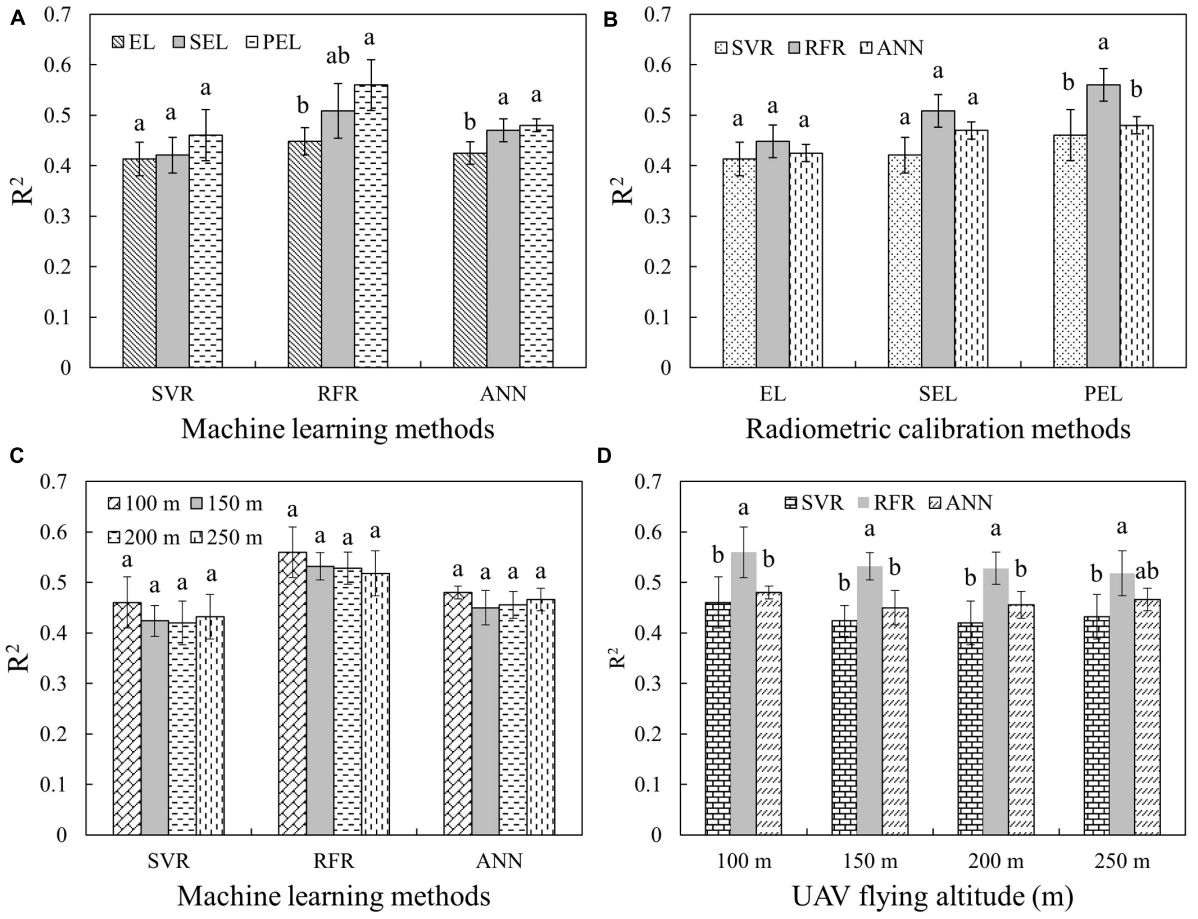

FIGURE 6
R^2-values of multi-stage rice yield prediction using machine learning methods with different RCMs or UAV-FAs: **(A)** Comparison of different RCMs and same machine learning methods using CI_{green}; **(B)** comparison of same RCMs and different machine learning methods using CI_{green}; **(C)** comparison of different RCMs and same UAV-FAs using NDVI; and **(D)** comparison of same UAV-FAs and different machine learning methods using NDVI.

reflection distribution function (BRDF) (Roy et al., 2016). The BRDF characteristics of vegetation canopy mainly depend on the following factors: (i) the optical characteristics of leaves and ground background; and (ii) canopy structure characteristics, including LAI, leaf inclination, canopy geometry, density, and distribution (Qiu et al., 2021). The changes in rice canopy reflectance with UAV-FAs at the same stage are mainly caused by the difference in the observation angles (Figure 6C).

The reflectance of rice at different altitudes and growth stages was obtained with high accuracy using PEL methods. The results in Figure 2 show that the reflectance variation in the different bands of rice at diverse UAV-FAs shares significant differences at different growth durations. To analyze the sensitivity of different bands to UAV-FAs, the reflectance curves of rice at the altitudes of 60–250 m in different periods are shown in Figure 7. The sensitivity is expressed as the ratio of the standard deviation (STD) of spectral reflectance at all altitudes to the reflectance (STDR) in the orthophoto direction (approximately substituted by the reflectance at 250 m). It can be seen that the variation range and sensitivity (STDR) of

10.3389/fpls.2022.958106

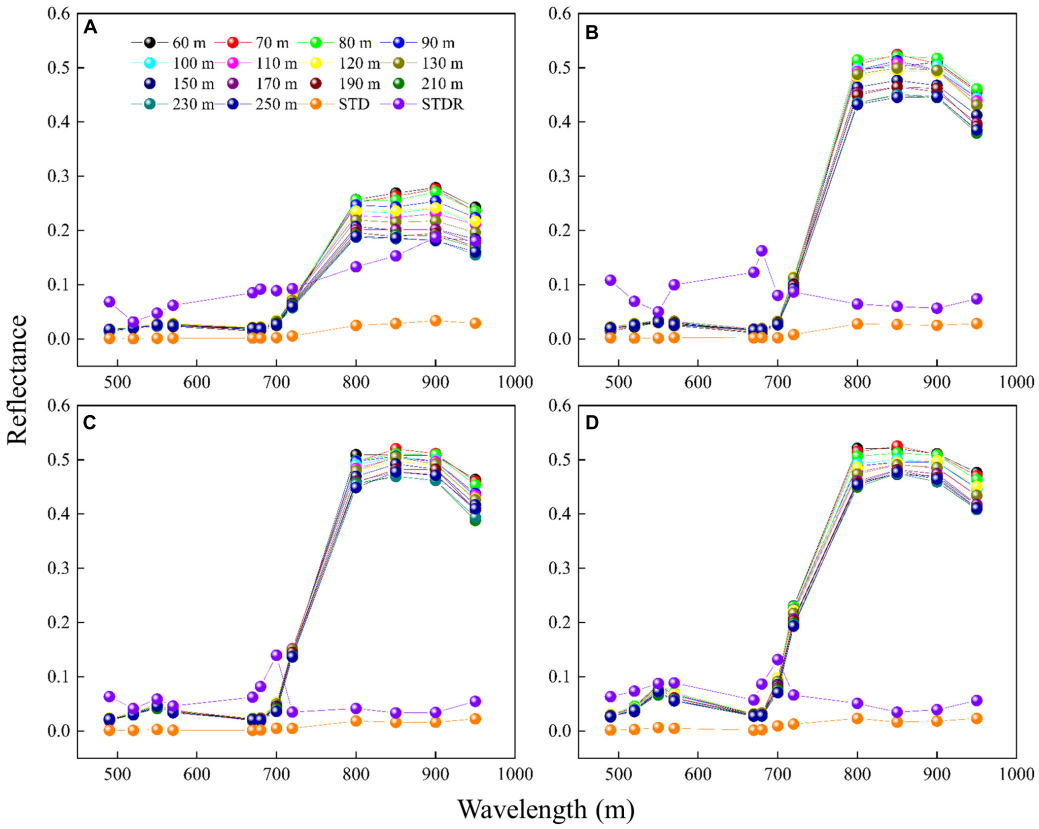

FIGURE 7
Reflectance spectral curves of rice at different altitudes and stages (STD represents the standard deviation of spectral reflectance at all altitudes and STDR is the ratio of the STD to the reflectance at 250 m): **(A)** Tillering stage; **(B)** jointing stage; **(C)** heading stage; **(D)** milking stage.

reflectance in NIR bands are more obvious than that in visible bands at the tillering stage (**Figure 7A**). This was due to the effect of water on the tillering stage, resulting in reduced sensitivity of visible bands (Gatebe and King, 2016). At the jointing, heading, and milking stages, the reflectance variation range of NIR bands is greater than that of visible bands, but the sensitivity is less than that of visible bands (**Figures 7A–D**). At these stages, the anisotropy effect of reflectance is the strongest in the red band (STDR > 0.1). In the NIR bands, the leaf absorption of vegetation is weak, and the reflectance and transmittance are high, which makes the multiple scattering effects inside the canopy stronger and reduces the anisotropy of vegetation in these bands, while the strong absorption of chlorophyll makes the anisotropy stronger in the red bands (Sandmeier et al., 1998). Therefore, the change of reflectance is distinctly weakened at the heading and milking stages because the appearance of the panicle makes the canopy not easy to be penetrated by light.

The FCLS-LSM model was used to analyze the changes in the components of multispectral images of paddy fields at the jointing stage. The results in **Figure 4B** showed that the fluctuations in the proportion of rice leaves and soil background, and the ratio of light and shaded leaves in the canopy are the reasons for the changes in canopy reflectance. The enhancement and attenuation factors in the visible bands change significantly before 100 m and then tend to be stable, while the NIR band attenuation factors keep unchanged after 170 m, because in the NIR bands, the reflectance of rice is much greater than that of the background (**Figure 4A**). In addition, the NIR bands have strong penetration, and the reflectance will decrease significantly as long as the background increases slightly. In the visible bands, the reflectance gap between the background and rice is relatively small, and the weak change of the background proportion will not lead to a drastic response of the reflectance. It can also be found in **Figure 4D** that after 100 m, the VZA variation of the plot at the edge of the image gradually becomes flat with the change of altitudes, which also proves that there is little fluctuation in the different components of the multispectral images after 100 m, and the edge plot at this altitude is close to the orthophoto direction. Therefore, the variation in the reflectance of different bands with UAV-FAs is related to the reflectance of the backgrounds.

The fluctuation in the reflectance will cause a change in VIs. It is found in **Figure 3** that the variation trend of VIs and reflectance of visible and red-edge bands in different periods

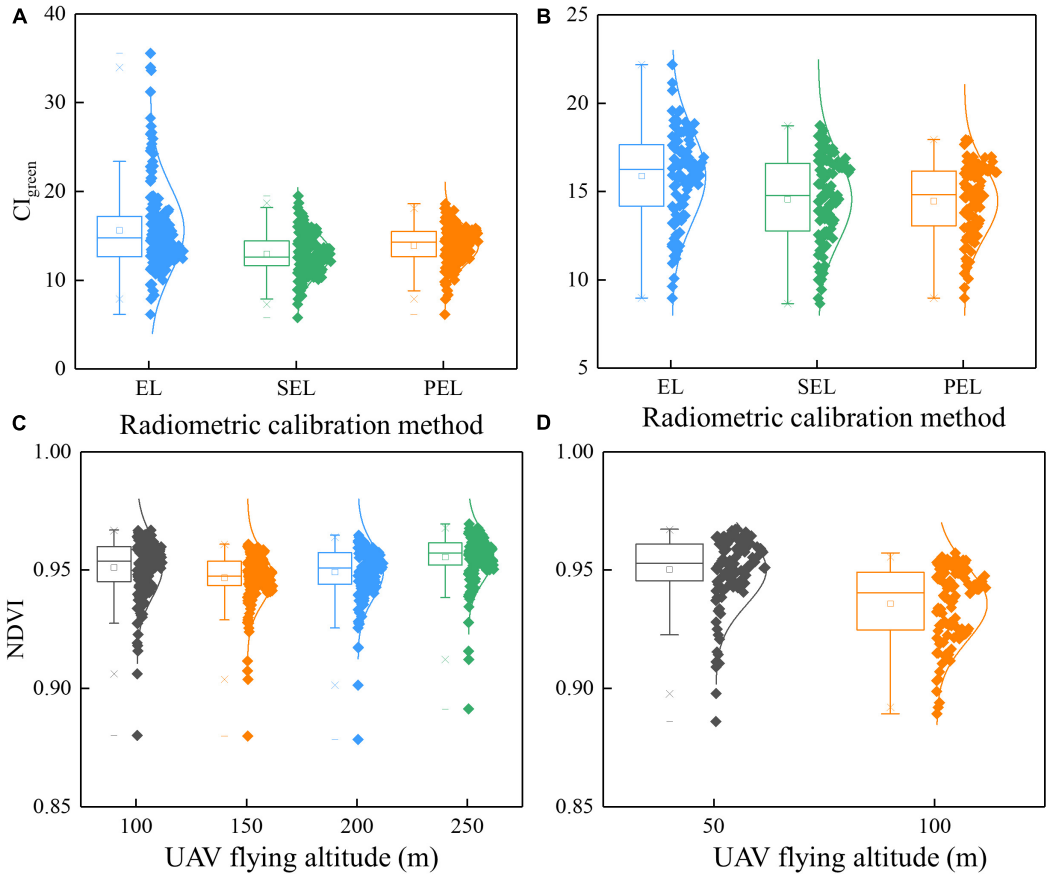

FIGURE 8
Boxplot for the comparison of VIs based on different RCMs and UAV-FAs: **(A)** CI_{green} based on different RCMs in Test 1; **(B)** CI_{green} based on different RCMs in Test 2; **(C)** NDVI based on different UAV-FAs in Test 1; **(D)** NDVI based on different UAV-FAs in Test 2.

are consistent, appearing that the VIs change significantly within 100 m at tillering, jointing, and heading stages, and remain unchanged beyond 100 m. The main reason for this phenomenon is that the reflectance of NIR bands is generally taken as the numerator in the calculation of VIs, while the reflectance of visible and red-edge bands can be taken as the denominator. Therefore, small changes in the denominator will eventually be amplified, and the influence of numerator changes will be much smaller.

Effects of radiometric calibration methods and UAV flying altitudes on the accurate acquisition of rice phenotypes

The VIs derived from the combination of reflectance in different bands have proven to be a good indicator to monitor crop growth and predict the yield (Deng et al., 2018b; Hassan et al., 2019; Luo et al., 2020). For crop growth monitoring (like LAI, AGB, and chlorophyll content), a multi-stage model is acceptable (Li et al., 2020). Both single-period and multi-period models are useful for yield estimation (Gong et al., 2018; Wang et al., 2019; Wan et al., 2020; Duan et al., 2021). Machine learning is the most widely used method in multi-period crop yield prediction. In this study, rice growth monitoring (multi-stage) and yield prediction (single and multi-stage) were carried out to verify and evaluate the effects of RCMs and UAV-FAs.

The results in **Table 5** and **Figure 5A** indicate that the PEL method holds the highest accuracy in LAI, AGB, CCC estimation, and single-stage yield prediction. The comparison of CI_{green} based on the three RCMs is shown in **Figures 8A,B**. It can be seen that the EL-based CI_{green} is different from the others (including range and distribution). Hence, the selection of appropriate RCMs has a very notable impact on precision agriculture (Deng et al., 2018b).

The results of different UAV-FAs presented in **Tables 6**, **7** and **Figure 5** show that the altitude change above 100 m has no conspicuous impact on growth parameter estimation and yield prediction. The variables based on 50 and 100 m have a great influence on single-period yield prediction and have a relatively weak impact on growth simulation. Of course, the size

and number of plots in Test 2 are less than those in Test 1. This reduces the impact of altitude to a certain extent because the plots in Test 2 are closer to the center of the image. The comparison of NDVI based on different UAV-FAs is shown in Figures 8C,D. The range and shape of NDVI based on 100–250 m are similar, and the difference between 50 and 100 m is prominent. At low altitudes, NDVI is larger and more easily saturated, which reduces the accuracy of the estimation model.

It is also crucial to select different machine learning methods for yield estimation with multi-period variables. For example, SVM can cover up the difference in yield estimation caused by different RCMs, while RFR and ANN can show the superiority of SEL and PEL (Figure 6A). The impact of different RCMs is also reflected in whether the advantages of machine learning methods can be highlighted: there is no significant difference in the estimation accuracy of the three machine learning methods when EL and SEL are used, while the accuracy of RFR is significantly higher than that of other methods when PEL is used (Figure 6B). Therefore, RCMs and machine learning methods have a mutual influence on yield estimation results, which should be paid attention to in the selection. The altitude change above 100 m does not have a significant impact on the multi-period yield estimation results (Figure 6C). The yield estimation accuracy of RFR is the highest, and there is no significant difference between SVR and ANN (Figure 6D).

Compared with the vertical downward observation at high altitude, the vegetation directional reflectance obtained by RS at low altitude contains abundant information on vegetation canopy structure. Therefore, more attention should be paid to the extraction of crop phenotype information from low-altitude images, particularly for sensors with large FOV.

Conclusion

Multispectral reflectance can be affected by RCMs and UAV-FAs. In this paper, the reflectance derived from different RCMs was compared, and accurate reflectance at different altitudes was obtained. It was found that the EL and SEL methods performed well in the prediction of high reflectance and low reflectance, respectively. The PEL method combining the advantages of EL and SEL showed the highest accuracy in rice growth monitoring (LAI, AGB, and CCC estimation) and yield prediction. In addition, the selection of machine learning methods would have a certain impact on multi-period rice yield estimation. Due to the differences in observation angles caused by UAV-FAs, the proportion changes of light and shaded rice and background made the reflectance fluctuate at different altitudes, which was apparent at tillering and jointing stages, and weakened at heading and milking stages. Likewise, VIs also showed certain variation rules, changing violently within 100 m and then remaining stable. The experimental data showed that the results of rice growth monitoring and yield prediction (using single and multi-period variables) differed significantly at different low altitudes (50 and 100 m) and shared little difference at high altitudes (100, 150, 200, and 250 m). The specific altitude value is determined by the FOV of the sensor and the characteristic of the ground object. In future work, more attention will be paid to the acquisition of crop phenotype information from low-altitude multispectral images as a result of the inclusion of more canopy structure information.

Data availability statement

The original contributions presented in this study are included in the article/supplementary material, further inquiries can be directed to the corresponding author.

Author contributions

SL wrote the manuscript. SF provided the study ideas and completed the experimental design. XJ provided suggestions and edited the manuscript. KY, YL, and SL measured the experimental data. YL and SL conducted the UAV flights. SF and XJ provided comments on the revision of the manuscript. All authors read and approved the final manuscript.

Funding

This work was supported by the National Key Research and Development Project (2016YFD0101105), the National High-tech Research and Development Program (863 Program) (2013AA102401), and the Phenomics Research and New Variety Creation of Hybrid Rice Based on UAV Remote Sensing (2020BBB058).

Conflict of interest

The authors declare that the research was conducted in the absence of any commercial or financial relationships that could be construed as a potential conflict of interest.

Publisher's note

All claims expressed in this article are solely those of the authors and do not necessarily represent those of their affiliated organizations, or those of the publisher, the editors and the reviewers. Any product that may be evaluated in this article, or claim that may be made by its manufacturer, is not guaranteed or endorsed by the publisher.

References

Ashapure, A., Jung, J. H., Chang, A. J., Oh, S., Yeom, J., Maeda, M., et al. (2020). Developing a machine learning based cotton yield estimation framework using multi-temporal UAS data. *ISPRS J. Photogramm. Remote Sens.* 169, 180–194. doi: 10.1016/j.isprsjprs.2020.09.015

Baret, F., Houles, V., and Guerif, M. (2007). Quantification of plant stress using remote sensing observations and crop models: The case of nitrogen management. *J. Exp. Bot.* 58, 869–880. doi: 10.1093/jxb/erl231

Daughtry, C. S. T., Walthall, C. L., Kim, M. S., de Colstoun, E. B., and McMurtrey, J. E. (2000). Estimating corn leaf chlorophyll concentration from leaf and canopy reflectance. *Remote Sens. Environ.* 74, 229–239. doi: 10.1016/s0034-4257(00)00113-9

Delegido, J., Alonso, L., Gonzalez, G., and Moreno, J. (2010). Estimating chlorophyll content of crops from hyperspectral data using a normalized area over reflectance curve (NAOC). *Int. J. Appl. Earth Obs. Geoinf.* 12, 165–174. doi: 10.1016/j.jag.2010.02.003

Deng, L., Mao, Z. H., Li, X. J., Hu, Z. W., Duan, F. Z., and Yan, Y. N. (2018b). UAV-based multispectral remote sensing for precision agriculture: A comparison between different cameras. *ISPRS J. Photogramm. Remote Sens.* 146, 124–136. doi: 10.1016/j.isprsjprs.2018.09.008

Deng, L., Hao, X. L., Mao, Z. H., Yan, Y. N., Sun, J., and Zhang, A. W. (2018a). A subband radiometric calibration method for UAV-based multispectral remote sensing. *IEEE J. Sel. Top Appl. Earth Obs. Remote Sens.* 11, 2869–2880. doi: 10.1109/jstars.2018.2842466

Duan, B., Fang, S. H., Gong, Y., Peng, Y., Wu, X. T., and Zhu, R. S. (2021). Remote estimation of grain yield based on UAV data in different rice cultivars under contrasting climatic zone. *Field Crops Res.* 267:108148. doi: 10.1016/j.fcr.2021.108148

Duan, B., Fang, S. H., Zhu, R. S., Wu, X. T., Wang, S. Q., Gong, Y., et al. (2019). Remote estimation of rice yield with unmanned aerial vehicle (UAV) data and spectral mixture analysis. *Front. Plant Sci.* 10: 204. doi: 10.3389/fpls.2019.00204

Franch, B., San Bautista, A., Fita, D., Rubio, C., Tarrazo-Serrano, D., Sanchez, A., et al. (2021). Within-field rice yield estimation based on Sentinel-2 satellite data. *Remote Sens.* 13:4095. doi: 10.3390/rs13204095

Gatebe, C. K., and King, M. D. (2016). Airborne spectral BRDF of various surface types (ocean, vegetation, snow, desert, wetlands, cloud decks, smoke layers) for remote sensing applications. *Remote Sens. Appl.* 179, 131–148. doi: 10.1016/j.rse.2016.03.029

Gitelson, A., and Merzlyak, M. N. (1994). Quantitative estimation of chlorophyll-a using reflectance spectra: Experiments with autumn chestnut and maple leaves. *J. Photochem. Photobiol. B* 22, 247–252. doi: 10.1016/1011-1344(93)06963-4

Gitelson, A. A. (2004). Wide dynamic range vegetation index for remote quantification of biophysical characteristics of vegetation. *J. Plant Physiol.* 161, 165–173. doi: 10.1078/0176-1617-01176

Gitelson, A. A., Gritz, Y., and Merzlyak, M. N. (2003). Relationships between leaf chlorophyll content and spectral reflectance and algorithms for non-destructive chlorophyll assessment in higher plant leaves. *J. Plant Physiol.* 160, 271–282. doi: 10.1078/0176-1617-00887

Gitelson, A. A., Kaufman, Y. J., Stark, R., and Rundquist, D. (2002). Novel algorithms for remote estimation of vegetation fraction. *Remote Sens. Environ.* 80, 76–87. doi: 10.1016/s0034-4257(01)00289-9

Gitelson, A. A., Vina, A., Ciganda, V., Rundquist, D. C., and Arkebauer, T. J. (2005). Remote estimation of canopy chlorophyll content in crops. *Geophys. Res. Lett.* 32:L08403,. doi: 10.1029/2005gl022688

Gong, Y., Duan, B., Fang, S. H., Zhu, R. S., Wu, X. T., Ma, Y., et al. (2018). Remote estimation of rapeseed yield with unmanned aerial vehicle (UAV) imaging and spectral mixture analysis. *Plant Methods* 14:70. doi: 10.1186/s13007-018-0338-z

Han, L., Yang, G. J., Dai, H. Y., Xu, B., Yang, H., Feng, H. K., et al. (2019). Modeling maize above-ground biomass based on machine learning approaches using UAV remote-sensing data. *Plant Methods* 15:10. doi: 10.1186/s13007-019-0394-z

Harkel, J., Bartholomeus, H., and Kooistra, L. (2020). Biomass and crop height estimation of different crops using UAV-based Lidar. *Remote Sens.* 12:17. doi: 10.3390/rs12010017

Hassan, M. A., Yang, M. J., Rasheed, A., Yang, G. J., Reynolds, M., Xia, X. C., et al. (2019). A rapid monitoring of NDVI across the wheat growth cycle for grain yield prediction using a multi-spectral UAV platform. *Plant Sci.* 282, 95–103. doi: 10.1016/j.plantsci.2018.10.022

Huang, B., Zhao, B., and Song, Y. M. (2018). Urban land-use mapping using a deep convolutional neural network with high spatial resolution multispectral remote sensing imagery. *Remote Sens. Environ.* 214, 73–86. doi: 10.1016/j.rse.2018.04.050

Huang, J. X., Tian, L. Y., Liang, S. L., Ma, H. Y., Becker-Reshef, I., Huang, Y. B., et al. (2015). Improving winter wheat yield estimation by assimilation of the leaf area index from Landsat TM and MODIS data into the WOFOST model. *Agric. For. Meteorol.* 204, 106–121. doi: 10.1016/j.agrformet.2015.02.001

Inoue, Y., Guerif, M., Baret, F., Skidmore, A., Gitelson, A., Schlerf, M., et al. (2016). Simple and robust methods for remote sensing of canopy chlorophyll content: A comparative analysis of hyperspectral data for different types of vegetation. *Plant Cell Environ.* 39, 2609–2623. doi: 10.1111/pce.12815

Jiang, Q., Fang, S. H., Peng, Y., Gong, Y., Zhu, R. S., Wu, X. T., et al. (2019). UAV-Based Biomass Estimation for Rice-Combining Spectral, TIN-Based Structural and Meteorological Features. *Remote Sens.* 11:890. doi: 10.3390/rs11070890

Jiang, Z. Y., Huete, A. R., Didan, K., and Miura, T. (2008). Development of a two-band enhanced vegetation index without a blue band. *Remote Sens. Environ.* 112, 3833–3845. doi: 10.1016/j.rse.2008.06.006

Jordan, C. F. (1969). Derivation of leaf area index from light quality of the forest floor. *Ecology* 50, 663–666. doi: 10.2307/1936256

Kimes, D. S., Markham, B. L., Tucker, C. J., and McMurtrey, J. E. (1981). Temporal relationships between spectral response and agronomic variables of a corn canopy. *Remote Sens. Environ.* 11, 401–411. doi: 10.1016/0034-4257(81)90037-7

Laliberte, A. S., Goforth, M. A., Steele, C. M., and Rango, A. (2011). Multispectral remote sensing from unmanned aircraft: Image processing workflows and applications for rangeland environments. *Remote Sens.* 3, 2529–2551. doi: 10.3390/rs3112529

Li, B., Xu, X. M., Zhang, L., Han, J. W., Bian, C. S., Li, G. C., et al. (2020). Above-ground biomass estimation and yield prediction in potato by using UAV-based RGB and hyperspectral imaging. *ISPRS J. Photogramm. Remote Sens.* 162, 161–172. doi: 10.1016/j.isprsjprs.2020.02.013

Li, Y., Zhou, Q. G., Zhou, J., Zhang, G. F., Chen, C., and Wang, J. (2014). Assimilating remote sensing information into a coupled hydrology-crop growth model to estimate regional maize yield in arid regions. *Ecol. Model.* 291, 15–27. doi: 10.1016/j.ecolmodel.2014.07.013

Liu, X. J., Zhang, K., Zhang, Z. Y., Cao, Q., Lv, Z. F., Yuan, Z. F., et al. (2017). Canopy chlorophyll density based index for estimating nitrogen status and predicting grain yield in rice. *Front. Plant Sci.* 8:1829. doi: 10.3389/fpls.2017.01829

Luo, S., He, Y. B., Li, Q., Jiao, W. H., Zhu, Y. Q., and Zhao, X. H. (2020). Nondestructive estimation of potato yield using relative variables derived from multi-period LAI and hyperspectral data based on weighted growth stage. *Plant Methods* 16:150. doi: 10.1186/s13007-020-00693-3

Maes, W. H., and Steppe, K. (2019). Perspectives for remote sensing with unmanned aerial vehicles in precision agriculture. *Trends Plant Sci.* 24, 152–164. doi: 10.1016/j.tplants.2018.11.007

Maimaitijiang, M., Sagan, V., Sidike, P., Hartling, S., Esposito, F., and Fritschi, F. B. (2020). Soybean yield prediction from UAV using multimodal data fusion and deep learning. *Remote Sens. Environ.* 237:111599. doi: 10.1016/j.rse.2019.111599

Noguera, M., Millan, B., Perez-Paredes, J. J., Ponce, J. M., Aquino, A., and Andujar, J. M. (2020). A new low-cost device based on thermal infrared sensors for olive tree canopy temperature measurement and water status monitoring. *Remote Sens.* 12: 723. doi: 10.3390/rs12040723

Peng, S. B., Garcia, F. V., Laza, R. C., and Cassman, K. G. (1993). Adjustment for specific leaf weight improves chlorophyll meter's estimate of rice leaf nitrogen concentration. *Agron. J.* 85, 987–990. doi: 10.2134/agronj1993.00021962008500050005x

Peng, Y., Zhu, T. E., Li, Y. C., Dai, C., Fang, S. H., Gong, Y., et al. (2019). Remote prediction of yield based on LAI estimation in oilseed rape under different planting methods and nitrogen fertilizer applications. *Agric. For.Meteorol.* 271, 116–125. doi: 10.1016/j.agrformet.2019.02.032

Qiu, F., Huo, J., Zhang, Q., Chen, X., and Zhang, Y. (2021). Observation and analysis of bidirectional and hotspot reflectance of conifer forest canopies with a multiangle hyperspectral UAV imaging platform. *J. Remote Sens.* 25, 1013–1024. doi: 10.11834/jrs.20219435

Raj, R., Walker, J. P., Pingale, R., Banoth, B. N., and Jagarlapudi, A. (2021). Leaf nitrogen content estimation using top-of-canopy airborne hyperspectral data. *Int. J. Appl. Earth Obs. Geoinform.* 104:102584. doi: 10.1016/j.jag.2021.102584

Rosas, J. T. F., Pinto, F. D. D., de Queiroz, D. M., Villar, F. M. D., Martins, R. N., and Silva, S. D. (2020). Low-cost system for radiometric calibration of UAV-based multispectral imagery. *J. Spat. Sci.* 15, doi: 10.1080/14498596.2020.1860146

Roy, D. P., Zhang, H. K., Ju, J., Gomez-Dans, J. L., Lewis, P. E., Schaaf, C. B., et al. (2016). A general method to normalize Landsat reflectance data to nadir BRDF adjusted reflectance. *Remote Sens. Environ.* 176, 255–271. doi: 10.1016/j.rse.2016.01.023

Sandmeier, S., Muller, C., Hosgood, B., and Andreoli, G. (1998). Physical mechanisms in hyperspectral BRDF data of grass and watercress. *Remote Sens.f Environ.*66, 222–233. doi: 10.1016/s0034-4257(98)00060-1

Smith, G. M., and Milton, E. J. (1999). The use of the empirical line method to calibrate remotely sensed data to reflectance. *Int. J. Remote Sens.* 20, 2653–2662. doi: 10.1080/014311699211994

Stow, D., Hope, A., Nguyen, A. T., Phinn, S., and Benkelman, C. A. (1996). Monitoring detailed land surface changes using an airborne multispectral digital camera system. *IEEE Transac. Geosci. Remote Sens.* 34, 1191–1203. doi: 10.1109/36.536536

Tucker, C. J. (1979). Red and photographic infrared linear combinations for monitoring vegetation. *Remote Sens. Environ.* 8, 127–150. doi: 10.1016/0034-4257(79)90013-0

Uddling, J., Gelang-Alfredsson, J., Piikki, K., and Pleijel, H. (2007). Evaluating the relationship between leaf chlorophyll concentration and SPAD-502 chlorophyll meter readings. *Photosynth. Res.* 91, 37–46. doi: 10.1007/s11120-006-9077-5

Wan, L., Cen, H. Y., Zhu, J. P., Zhang, J. F., Zhu, Y. M., Sun, D. W., et al. (2020). Grain yield prediction of rice using multi-temporal UAV-based RGB and multispectral images and model transfer - a case study of small farmlands in the South of China. *Agric. For. Meteorol.* 291:108096. doi: 10.1016/j.agrformet.2020.108096

Wang, C. Y., and Myint, S. W. (2015). A simplified empirical line method of radiometric calibration for small unmanned aircraft systems-based remote sensing. *IEEE J. Sel. Top Appl. Earth Obs. Remote Sens.* 8, 1876–1885. doi: 10.1109/jstars.2015.2422716

Wang, F. L., Wang, F. M., Zhang, Y., Hu, J. H., Huang, J. F., and Xie, J. K. (2019). Rice yield estimation using parcel-level relative spectra variables from UAV-based hyperspectral imagery. *Front. Plant Sci.* 10:12. doi: 10.3389/fpls.2019.00453

Wang, Y. P., Chang, Y. C., and Shen, Y. (2021). Estimation of nitrogen status of paddy rice at vegetative phase using unmanned aerial vehicle based multispectral imagery. *Precis. Agric.* 23, 1–17. doi: 10.1007/s11119-021-09823-w

Xie, Q. Y., Huang, W. J., Liang, D., Chen, P. F., Wu, C. Y., Yang, G. J., et al. (2014). Leaf area index estimation using vegetation indices derived from airborne hyperspectral images in winter wheat. *IEEE J. Sel. Top. Appl. Earth Obs. Remote Sens.* 7, 3586–3594. doi: 10.1109/jstars.2014.2342291

Xu, J. F., and Huang, J. F. (2008). Empirical line method using spectrally stable targets to calibrate IKONOS imagery. *Pedosphere* 18, 124–130. doi: 10.1016/s1002-0160(07)60110-6

Xu, X. Q., Lu, J. S., Zhang, N., Yang, T. C., He, J. Y., Yao, X., et al. (2019). Inversion of rice canopy chlorophyll content and leaf area index based on coupling of radiative transfer and Bayesian network models. *ISPRS J. Photogramm. Remote Sens.* 150, 185–196. doi: 10.1016/j.isprsjprs.2019.02.013

Yang, G. J., Liu, J. G., Zhao, C. J., Li, Z. H., Huang, Y. B., Yu, H. Y., et al. (2017). Unmanned aerial vehicle remote sensing for field-based crop phenotyping: Current status and perspectives. *Front. Plant Sci.* 8:26. doi: 10.3389/fpls.2017.01111

Yue, J. B., Yang, G. J., Tian, Q. J., Feng, H. K., Xu, K. J., and Zhou, C. Q. (2019). Estimate of winter-wheat above-ground biomass based on UAV ultrahigh-ground-resolution image textures and vegetation indices. *ISPRS J. . Photogramm. Remote Sens.* 150, 226–244. doi: 10.1016/j.isprsjprs.2019.02.022

Zhao, L., Zhou, W., Peng, Y. P., Hu, Y. M., Ma, T., Xie, Y. K., et al. (2021). A new AG-AGB estimation model based on MODIS and SRTM data in Qinghai Province. *Chin. Ecol. Indicators* 133:108378. doi: 10.1016/j.ecolind.2021.108378

Zheng, H. B., Cheng, T., Zhou, M., Li, D., Yao, X., Tian, Y. C., et al. (2019). Improved estimation of rice aboveground biomass combining textural and spectral analysis of UAV imagery. *Precis. Agric.* 20, 611–629. doi: 10.1007/s11119-018-9600-7

frontiers | Frontiers in Plant Science

TYPE Original Research
PUBLISHED 11 August 2022
DOI 10.3389/fpls.2022.955340

Check for updates

OPEN ACCESS

EDITED BY
Xiuliang Jin,
Institute of Crop Sciences (CAAS), China

REVIEWED BY
Qingfeng Song,
Center for Excellence in Molecular Plant Sciences (CAS), China
Norhashila Hashim,
Putra Malaysia University,
Malaysia

*CORRESPONDENCE
Yubin Lan
ylan@scau.edu.cn

†These authors have contributed equally to this work and share first authorship

SPECIALTY SECTION
This article was submitted to Sustainable and Intelligent Phytoprotection, a section of the journal Frontiers in Plant Science

RECEIVED 28 May 2022
ACCEPTED 08 July 2022
PUBLISHED 11 August 2022

CITATION
Zhang Y, Zhao D, Liu H, Huang X, Deng J, Jia R, He X, Tahir MN and Lan Y (2022) Research hotspots and frontiers in agricultural multispectral technology: Bibliometrics and scientometrics analysis of the Web of Science.
Front. Plant Sci. 13:955340.
doi: 10.3389/fpls.2022.955340

COPYRIGHT
© 2022 Zhang, Zhao, Liu, Huang, Deng, Jia, He, Tahir and Lan. This is an open-access article distributed under the terms of the Creative Commons Attribution License (CC BY). The use, distribution or reproduction in other forums is permitted, provided the original author(s) and the copyright owner(s) are credited and that the original publication in this journal is cited, in accordance with accepted academic practice. No use, distribution or reproduction is permitted which does not comply with these terms.

Research hotspots and frontiers in agricultural multispectral technology: Bibliometrics and scientometrics analysis of the Web of Science

Yali Zhang[1,2†], Dehua Zhao[1,2†], Hanchao Liu[1,2], Xinrong Huang[1,2], Jizhong Deng[1,2], Ruichang Jia[1,2], Xiaoping He[3], Muhammad Naveed Tahir[4] and Yubin Lan[2,5*]

[1]College of Engineering, South China Agricultural University, Guangzhou, China, [2]National Center for International Collaboration Research on Precision Agricultural Aviation Pesticide Spraying Technology, Guangzhou, China, [3]Department of Information Consulting, Library, South China Agricultural University, Guangzhou, China, [4]Department of Agronomy, Pir Mehr Ali Shah-Arid Agriculture University, Rawalpindi, Pakistan, [5]College of Electronic Engineering and College of Artificial Intelligence, South China Agricultural University, Guangzhou, China

Multispectral technology has a wide range of applications in agriculture. By obtaining spectral information during crop production, key information such as growth, pests and diseases, fertilizer and pesticide application can be determined quickly, accurately and efficiently. The scientific analysis based on Web of Science aims to understand the research hotspots and areas of interest in the field of agricultural multispectral technology. The publications related to agricultural multispectral research in agriculture between 2002 and 2021 were selected as the research objects. The softwares of CiteSpace, VOSviewer, and Microsoft Excel were used to provide a comprehensive review of agricultural multispectral research in terms of research areas, institutions, influential journals, and core authors. Results of the analysis show that the number of publications increased each year, with the largest increase in 2019. Remote sensing, imaging technology, environmental science, and ecology are the most popular research directions. The journal *Remote Sensing* is one of the most popular publishers, showing a high publishing potential in multispectral research in agriculture. The institution with the most research literature and citations is the USDA. In terms of the number of papers, Mtanga is the author with the most published articles in recent years. Through keyword co-citation analysis, it is determined that the main research areas of this topic focus on remote sensing, crop classification, plant phenotypes and other research areas. The literature co-citation analysis indicates that the main research directions concentrate in vegetation index, satellite remote sensing applications and machine learning modeling. There is still a lot of room for development of multi-spectrum technology. Further development can be carried out in the areas of multi-device synergy, spectral fusion, airborne equipment improvement, and real-time image processing technology, which will cooperate with each other

to further play the role of multi-spectrum in agriculture and promote the development of agriculture.

KEYWORDS

multispectral, agriculture, CiteSpace, remote sensing, Web of Science, NDVI

Introduction

Precision agriculture is currently in a phase of rapid development, which integrates technologies such as remote sensing, big data, and decision analysis, and aims to achieve efficient use of resources, rational inputs, and co-benefits in environmental and economic terms through variable and controllable scale farm management (Mazzia et al., 2020). Whereas information acquisition is the basis of precision agriculture, farming information is precisely the dynamic tracking of the agricultural environment and the state of plants at various growth periods (Huang et al., 2016), and plant phenotypes are important expressions of information on morphological characteristics that can be observed from plants (Huang et al., 2020). Both are important expressions of information in precision agriculture. Therefore, farming information and plant phenotypes reflect the information status of plants and provide reliable information for decision makers. In this case, how to obtain the required information becomes critical.

The advent of multispectral technology provides an effective and fast way to obtain agricultural information or plant phenotype information. Spectral imaging technology (Garini et al., 2006) emerged in the 1960s and was early applied in remote sensing, military and other fields. With the emergence of semiconductor photodetectors, spectral technology developed rapidly and its applications were extended to agriculture, environmental science, food engineering and other fields. Multispectral imaging technology is a kind of fusion technology of image and spectrum, which can acquire both spatial and spectral information of the object. In recent years, with the development of multispectral technology, its application in the field of agriculture has become more and more extensive. In the field of agriculture multispectral has been deeply applied in several aspects such as grain yield prediction (Zhou et al., 2017), pest and disease detection (Sankaran et al., 2010), nondestructiveness detection (Yu et al., 2018), remote sensing of agricultural drones Berni et al. (2009), weed identification (Pena et al., 2013; Sa et al., 2018), water content detection (Baluja et al., 2012), biomass (Kross et al., 2015), vegetation detection (Candiago et al., 2015), and inorganic matter detection (He et al., 2016). Agricultural multispectral technology is based on multidisciplinary fusion research, which makes use of data fusion techniques with multiple platforms, sensors, and remote sensing to provide data for research in the field of agriculture.

Bibliometrics and scientometrics are quantitative tools commonly used in scientific research. They are applied to analyze the frontiers of a topic or research field from macro- to micro-perspectives, which includes elements such as countries, institutions, authors, keywords, and journals (Raparelli and Bajocco, 2019; Zhang et al., 2019). These tools integrate computer engineering, big data applications, and statistics, and are widely applied in many fields (Chen, 2017) to provide rich assessments and analyses in different areas. The advantages of bibliometrics are reflected in stronger analytical efficiency for keyword analysis, research hotspot frontiers, and reference co-occurrence analysis. Scientometrics is an effective method for discovering research hotspots, and a powerful helper for researchers to understand the evolutionary path of research as well (Xie et al., 2020). It provides a systematic and comprehensive judgment.

The development and application of multispectral technology in agriculture promotes the development of precision agriculture and helps solve problems encountered in today's agricultural development. The bibliometrics and scientometrics analysis was conducted in this paper by reviewing publications related to agricultural multispectral research in agriculture between 2002 and 2021 from the Web of Science (WOS). Multiple softwares, CiteSpace, VOSviewer, and Microsoft Excel were adopted for analyzing and mapping of scientific knowledge to characterize the research hotspots and frontiers of agricultural multispectral technology. Comprehensive analysis was discussed in terms of research areas, institutions, influential journals, core authors, and keywords. Multiple research areas on agricultural multispectral research were identified through keyword co-citation analysis. The main research directions were proposed through literature co-citation analysis as well.

Materials and methods

Literature search strategy

The WOS database was taken as the data source with multispectral as the theme. Agriculture multispectral research mostly focus on crops, soil, moisture, biomass, etc. Therefore, the search formula was determined as: TS = (multispectral)AND TS = (Agricultural UAV or agriculture or crop or tomato or corn or wheat or rice or citrus or cotton or soybean or moisture or soil

or pest or weed or yield or potato or precision agriculture or Sugar cane or Nitrogen or tea or biomass or water fractions or Vegetables or Agricultural Remote Sensing or Chlorophyll or Pesticides). The literature data were searched for the time period from January 2002 to December 2021. Finally, 3,830 publication records were exported with each record containing author, title, source document, abstract, and cited references.

Methodology

Data mining, analysis and visualization were conducted for 3,830 literature related to agricultural multispectral research through CiteSpace 5.8.3, VOSviewer, and Microsoft Excel.

CiteSpace software[1] was developed by Prof. Chaomei Chen, Professor (tenure-track faculty) at School of Information Science and Technology, Drexel University, United States. The software is citation visualization and analysis software gradually developed in the context of scientometrics and data visualization (Chen, 2006; Chen et al., 2010). Thomas' and Kuhn's structure of scientific revolution provides the philosophical basis for CiteSpace. Another design inspiration for this software is a theory called structural holes, which was proposed by Burt at the University of Chicago in his study of social networks and social values (Chen, 2013). The software features dynamic complex network analysis and data visualization, and the visualization of CiteSpace can be divided into two main modes: cluster view and temporal view. The most prominent feature in CiteSpace is the co-citation analysis of the literature as a way to explore the knowledge structure of research. CiteSpace helps summarize clusters research frontiers and reveal the valuable knowledge points in the frontiers of agricultural multispectral research.

VOSviewer,[2] afree JAVA-based software developed by VanEck and Waltman at the Centre for Science and Technology Studies (CWTS), Leiden University, the Netherlands, in 2009 (van Eck and Waltman, 2010), is mainly oriented toward documentary data, relational knowledge units of documents construction. It is adapted to the analysis of one-mode undirected networks and focus on the visualization of scientific knowledge. VOSviewer draws scientific knowledge maps to show the inter-relationships between literatures in agricultural multispectral research. The most valuable advantage of VOSviewer over other bibliometric software is its graphical presentation capabilities, its suitability for large-scale data, and the versatility in adapting to source data in various formats from various databases. VOSviewer also provides text mining capabilities for constructing and visualizing co-occurrence of important terms extracted from scientific literatures about agricultural multispectral research. VOSviewer also provides text mining capabilities for building and visualizing co-occurrence networks of important terms extracted from these literatures.

Keywords are the core summary of a scientific paper. Analysis of the keywords gives a glimpse of the topic of the paper as that keywords given in a paper must have some kind of association. This association can be expressed by the frequency of co-occurrence. It is generally believed that the more frequent a word pair appears in the same literature, the closer the relationship between the two themes. Co-occurrence analysis investigates the common occurrence of lexical pairs of nouns or phrases in a literature set to determine the relationship between themes in the disciplines represented by that literature set. By counting the frequency of occurrences of two theme terms in the same document, a co-word network of these word-pair associations can be formed. The analysis of keywords can explore the research themes and hotspots of the literatures. The statistics of the frequency of keywords can analyze the hotspots of the research field. Two or more papers are cited by one or more papers at the same time, then these papers will constitute a co-citation relationship, and the co-citation relationship of the literature will change with time. A research hotspot is the focus and concentration of a technical field over a period of time, which is manifested by the emergence of a large number of papers and patents on a technical issue. The concept of research hotspot was first introduced by Plath in 1965, and has been developed and extended over the past 60 years to multiple levels. Analyses of research hotspots help clarify the development history, correctly understand the research lineage, and provide reference for future directions of agricultural multispectral technology.

Results

Basic data information

The searched literatures were first processed and removed irrelevant ones, and a total of 3,830 publications and 53,390 references were obtained. The average of 191.5 publications per year from 2002 to 2021 was available in the field of agricultural multispectral research. From the analysis results it is clear that multispectral study is flourishing in agriculture. These literatures involved 12,913 authors and generated a total of 12,899 keywords.

Evolution of publications

The trend of year-on-year growth can be seen in Figure 1, from 54 articles in 2002 to 608 articles in 2021, with an average annual growth rate of 13.5%. The number of publications exceeded 100 for the first time in 2008 and reached 104, then dropped below 100 in the next 2 years. From 2011 the number of publications exceeded 100 again and showed a stable growth trend. From 2002 to 2021, the number of publications increased by 10.25 times. The increasing number of publications year by year indicates that the application of multispectral technology in agriculture is attracting more and more attention.

1 https://sourceforge.net/projects/citespace/
2 https://www.vosviewer.com/

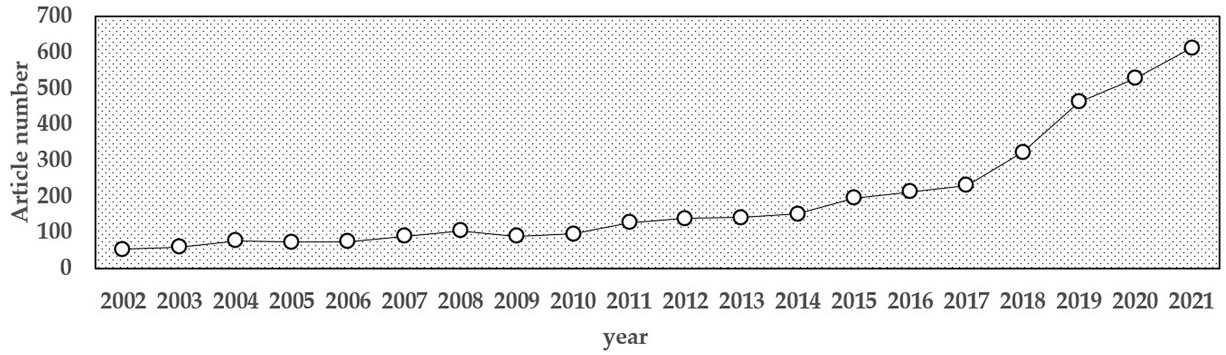

FIGURE 1
Annual distribution of the number of research publications on agricultural multispectral research in 2002–2021.

WOS Research Area

Table 1 lists the main agricultural fields of multispectral study from 2002 to 2021, which are remote sensing, imaging science, environmental science, geology, multi-discipline research, agriculture, electronic engineering, etc. Among them, remote sensing is the field with the largest proportion, followed by a variety of subjects, indicating that multispectral research is concerned by multiple fields and disciplines. From the current perspective, the research of multi-discipline integration will become a hot trend in the future about agricultural multispectral research.

TABLE 1 Main categories of multispectral research literature in agriculture from 2002 to 2021.

Subject categories	Number	Ration%
Remote Sensing	1,691	44.11
Imaging Science Photographic Technology	1,430	37.30
Environmental Sciences	1,124	29.32
Geosciences Multidisciplinary	868	22.64
Engineering Electrical Electronic	372	9.70
Geography Physical	295	7.69
Agriculture Multidisciplinary	265	6.91
Agronomy	239	6.23
Plant Sciences	194	5.06

Analysis of research countries and institutions

Analyzing research institutions help understand the publication and collaboration of major institutions. In total, 3,358 institutions are involved in agricultural multispectral research. Results show that the top five institutions with the highest number of publications are: USDA, Chinese Academy of Sciences, NASA, UNIVERSITY OF CALIFORNIA SYSTEM, and CNRS.A total of 746 articles were published by the above five institutions. The top two institutions have significantly more publications than the others, indicating an imbalance between the research publications of influential institutions. From 2002 to 2021, the USDA is the institution with the highest number of publications, with a total of 247 publications, taking the first place. The institutional co-occurrence mapping in Figure 2 was generated based on the analysis.

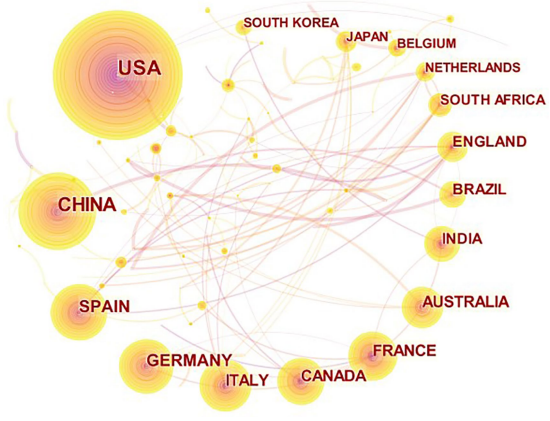

FIGURE 2
Co-current mapping of research institution collaboration on agricultural multispectral research in 2002–2021. The points to circles represent the individual countries, the size of the graph indicates how much literature comes from each country and how influential it is, and the lines represent how close each country is to other countries.

A total of 118 countries are involved in agricultural multispectral research. The density of cooperation among countries is visualized in Figure 3. The research countries analysis shows that the five countries with the highest number of publications are the United States (1,177), China (737), Spain (285), Germany (277), and Italy (231). In addition to the number of publications, centrality is one of the criteria to measure the strength of a country's research in this field. From the data obtained, the top five countries in terms of centrality are: United States, Germany, Italy, Australia, and England. China and Spain, despite being in the top five in terms of number of publications, are not in the top five in terms of centrality ranking.

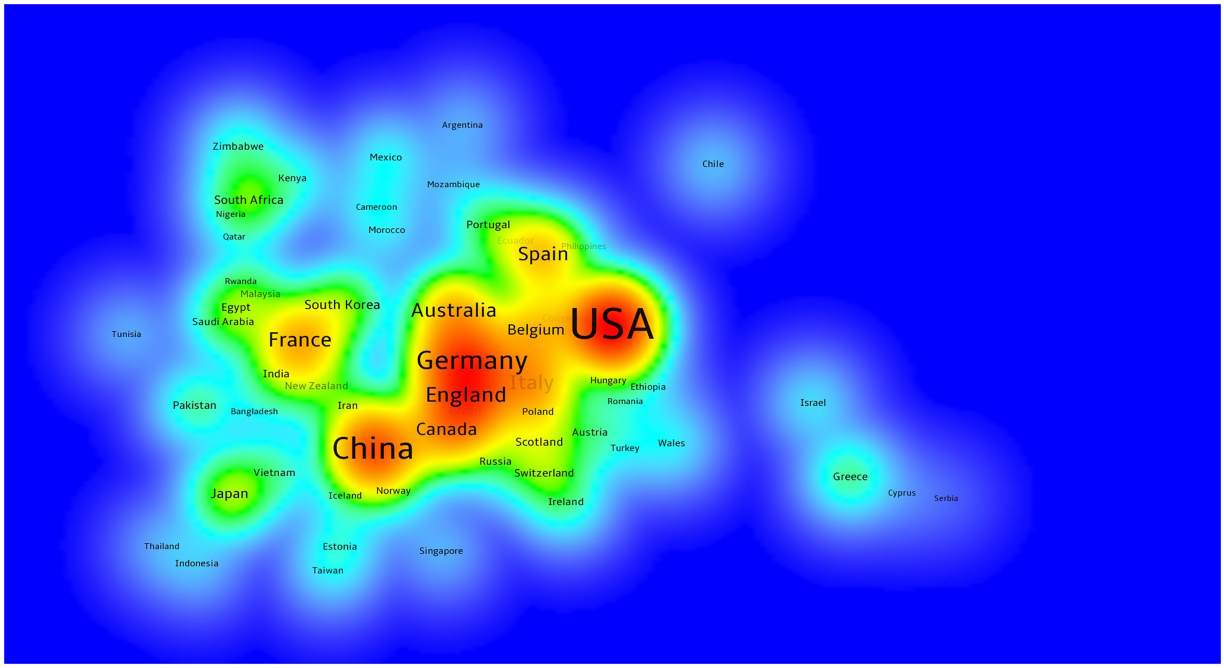

FIGURE 3
Visualization of agricultural multispectral research in terms of the density of cooperation between countries.

Influential journals

Multispectral research in agriculture was published in 702 journals, and the co-occurrence map of journals is shown in Figure 4. The top 20 (2.85%) journals published 2,021 papers, accounting for 52.8% of the total literature. There were 405 journals that published only one paper in agricultural multispectral research, accounting for 57.7% of the total number of journals. There were 200 journals that published 2–5 papers, accounting for 28.5% of the total number of journals. Less than 10 papers were published in 645 journals, representing 91.8% of the total number of journals. The top 3 publishers were Remote sensing (529), International journal of remote sensing (216), and Remote sensing of environment (207). According to this analysis, the agricultural multispectral publications become scattered. Most of the research achievement was published in 12 journals as shown in Table 2. These 12 journals can be considered as the core sources of multispectral research in agriculture, and these journals play an important role as well. Among them, Remote sensing is the most popular journal in the field of agricultural multispectral research with the largest proportion and the fastest growth rate, showing that it has played an important role in promoting multispectral research in agriculture.

Analysis of author groups

The collaborative network of authors enables the analysis of the core authors and collaborations within the field of agricultural multispectral study. The analysis of core authors and their collaborative relationships was performed by VOSviewer to generate a co-occurrence map of authors, as shown in Figure 5. Results show that the top 5 authors with the highest number of published papers are Onisimo Mutanga (52), Timothy Dube (25), Yu Zhang (24), James F. Bell (22), and Jeffrey R. Johnson (22). Zarco-Tejada, P. J. has the most cited papers with an average of 81.9 citations per paper. Authors with more than four publications in the field of study were considered core authors according to its definition, of which there are 675 core authors. The top 10 core authors are shown in Table 3. There are 3,830 papers that involve 12,913 authors, with an average of 0.29 papers per author and 3.37 authors per paper. This also indicates that multispectral research in agriculture is a multi-author collaborative field.

Keyword analysis

A total of 12,899 keywords were detected in 3,830 publications from 2002 to 2021 through software analysis. A total of nine clusters were generated by co-occurrence analysis. The clusters, based on the relationship between the weight of link attributes under different keywords and the strength of total links, are shown in Figure 6. The top 20 keywords in 3,212 publications were ranked by frequency, as shown in Table 4.

Figure 6 shows the keyword network presented by the co-occurrence method on agricultural multispectral research in 2002–2021. The keywords are divided into nine clusters and each cluster is identified by a different color. The thickness and number

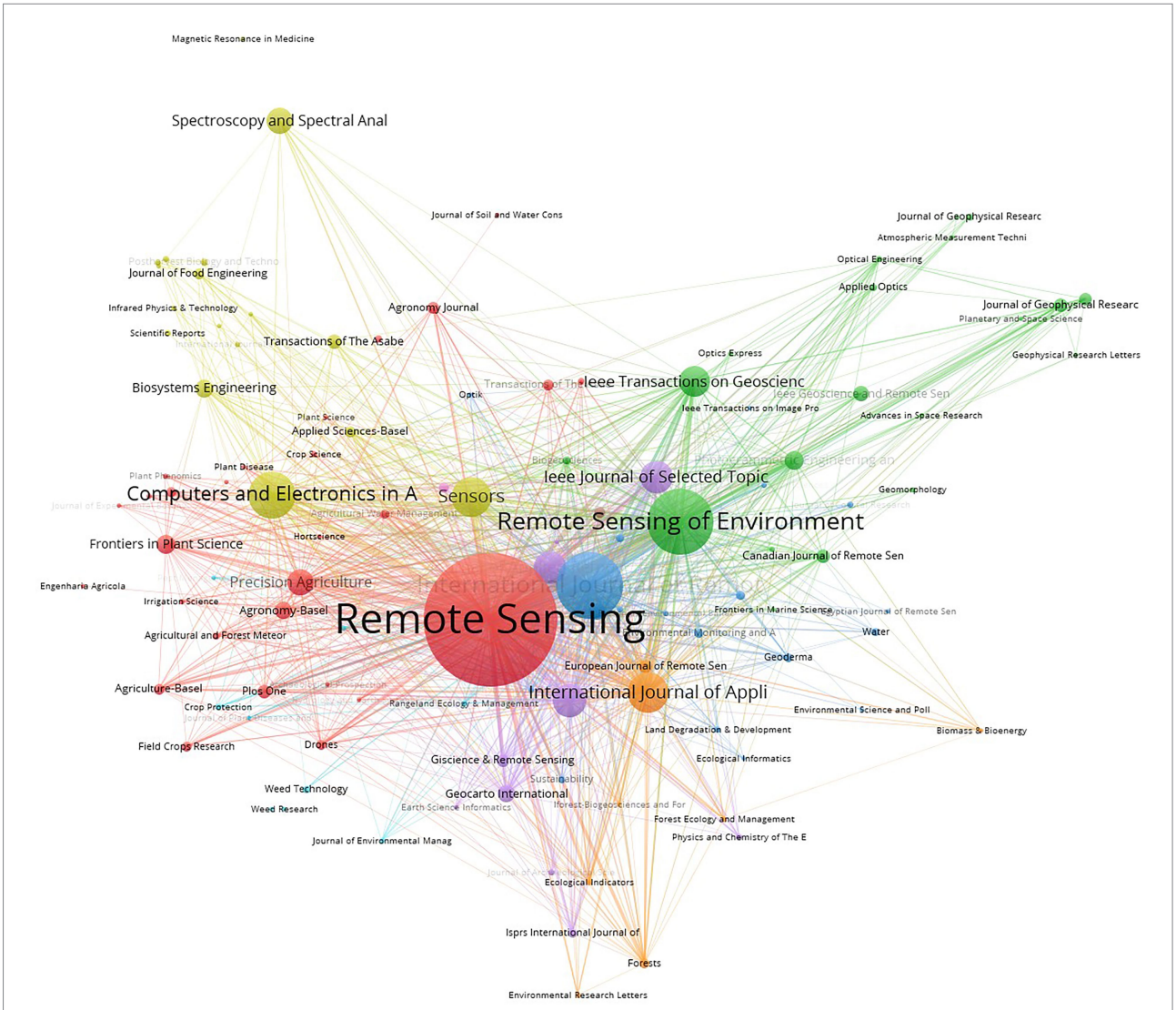

FIGURE 4
Co-occurrence map of influential journals on agricultural multispectral research in 2002–2021.

TABLE 2 Top 12 journals for local citation ranking of agricultural multispectral studies in 2002–2021.

Source	D	Citations	TS	WL
Remote Sensing	532	7,930	1,831	198
International Journal of Remote Sensing	216	4,934	560	123
Remote Sensing of Environment	207	17,268	1,216	172
Computers and Electronics in Agriculture	134	3,982	495	111
International Journal of Applied earth Observation and Geoinformation Sensors	107	2,766	501	106
Sensors	105	1782	400	92
Isprs Journal of Photogrammetry and Remote Sensing	85	3,293	525	89
Ieee Journal of Elected Topics in Applied Earth Observations and Remote Sensing	84	1743	259	54
Journal of Applied Remote Sensing	80	935	213	63
Ieee Transactions on Image Processing	79	4,137	309	75
Precision Agriculture	62	1952	275	29
Spectroscopy and Spectral Analysis	60	174	34	18

D, documents; TS, Total link strength; WL, weight links.

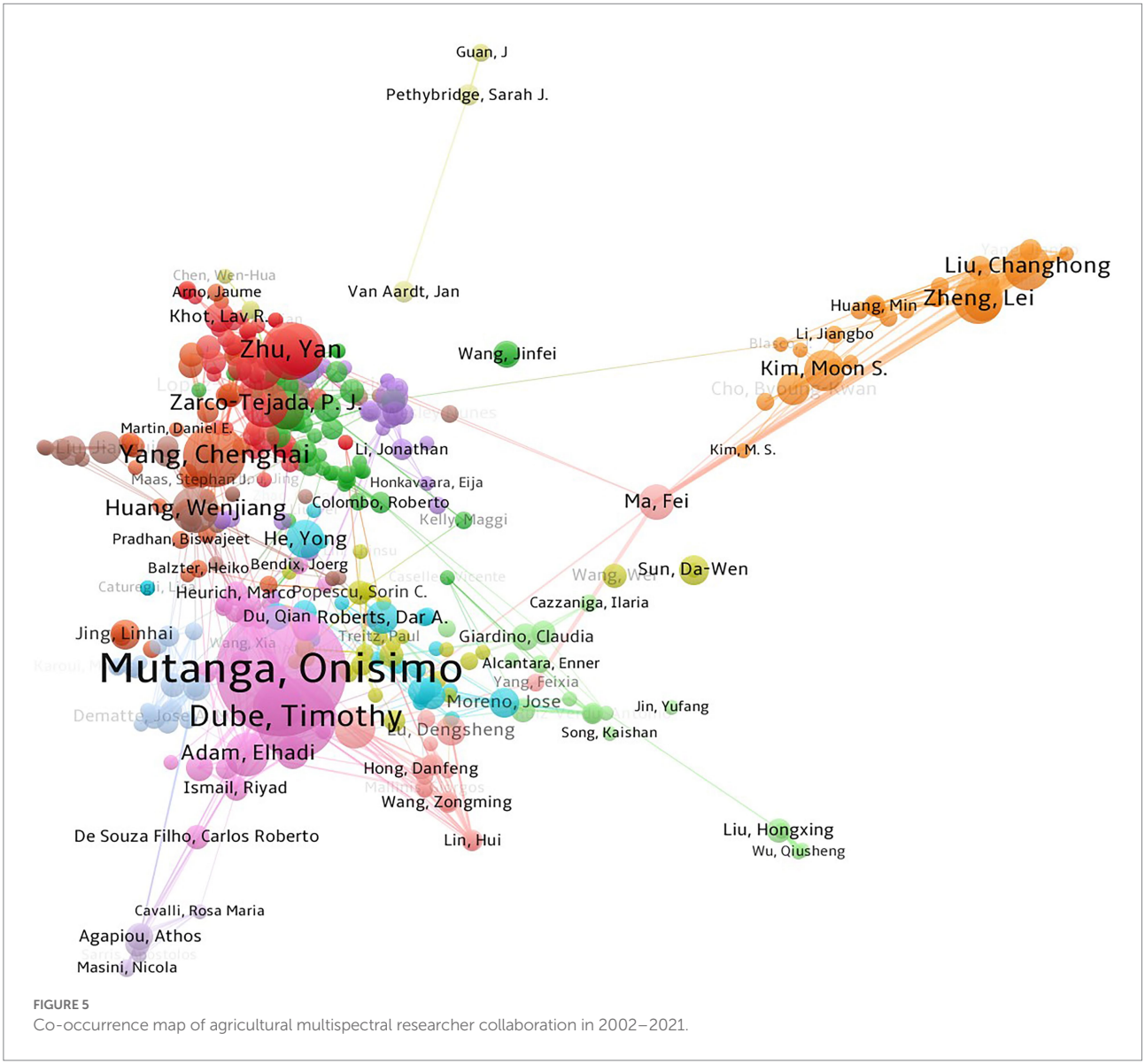

FIGURE 5
Co-occurrence map of agricultural multispectral researcher collaboration in 2002–2021.

TABLE 3 Top 10 authors ranked by total literature on agricultural multispectral research in 2002–2021.

Authors	Dc	Ct	TLS	Institutions	Countries
Onisimo Mutanga	52	1,672	813	University of KwaZulu-Natal	South Africa
Timothy Dube	30	591	427	University of Western Cape	South Africa
Yu Zhang	23	563	320	Chinese Academy of Sciences	China
James F. Bell	22	396	199	Arizona State University	United States
Jeffrey R. Johnson	22	1,228	260	U.S. Geological Survey	United States
Chenghai Yang	22	563	209	USDA-Agricultural Research Service	United States
Moon S. Kim	21	272	68	USDA-Agricultural Research Service	United States
Lopez-granados F	21	891	163	Spanish National Research Council	Spain
Lei Zheng	21	291	568	Hefei University of Technology	United States
Yan Zhu	21	396	199	Nanjing Agricultural University	China

Dc, Documents; Ct, Citations; TLS, Total link strength; JCICTA, Jiangsu Collaborative Innovation Center for the Technology and Application of Internet of Things; UKSARC, USDA-ARS Kika de la Garza Subtropical Agricultural Research Center.

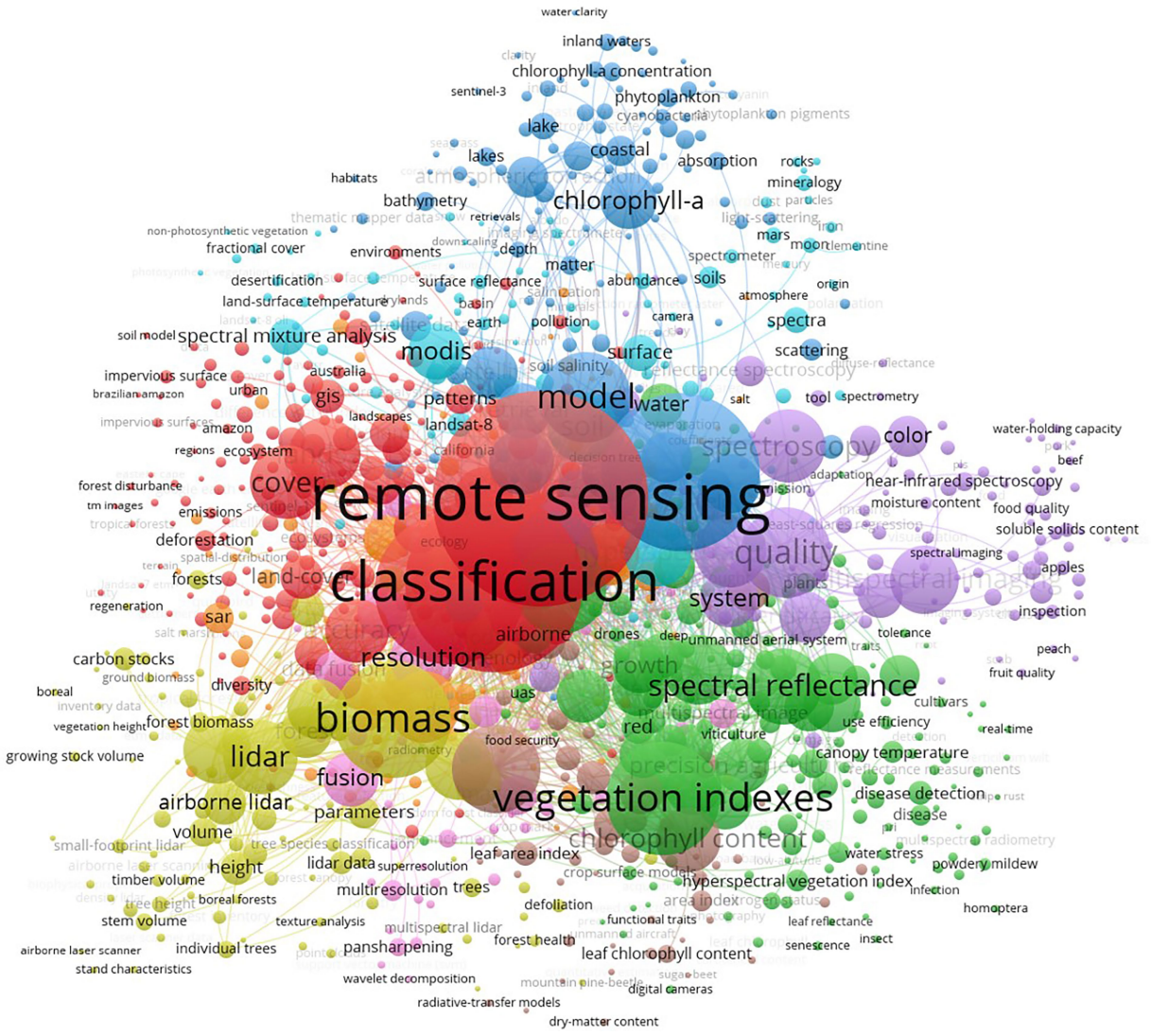

FIGURE 6
Network of keywords based on the co-occurrence method on agricultural multispectral research in 2002–2021.

of connecting lines between different clusters indicate the closeness of the connection between clusters. These nine clusters are cluster 1, red: remote sensing; cluster 2, green: vegetation indexes; cluster 3, cyan: reflectance; cluster 4, yellow: biomass; cluster 5, purple: quality; cluster 6, blue: soil; cluster 7, orange: random forest; cluster 8, brown: leaf-area index; cluster 9, pink: resolution. From the top 20 keywords given on Table 4, cluster 1 remote sensing, cluster 2 vegetation indexes, cluster 3 reflectance, cluster 4 biomass, cluster 5 quality account for the most weight, by clustering with the four keywords that account for the most, we can know the current research hotspots.

By keyword clustering found clustering 1 remote sensing in the field of agricultural multispectral is the most dominant research area, remote sensing technology is generally considered as one of the most important technologies for precision agriculture, and the development of technologies such as imaging of spectral information and multi-directional optical detection has improved the timeliness and operability of remote sensing technology (Tsouros et al., 2019). At present, remote sensing in the field of agriculture mainly focuses on: crop classification, crop coverage, and precise identification. Classification of weeds and crops in the field and accurate management of weeds, crop cover and vegetation coverage in agricultural fields, accurate identification of biomass and trace element content are the current research priorities in remote sensing (Huang et al., 2018; Näsi et al., 2018; Memon et al., 2019; Wijesingha et al., 2021). Remote sensing has made a great contribution to the development of precision agriculture.

Keyword clustering 2 led by vegetation indexes is likewise a current research hotspot in multispectral in agriculture, vegetation indexes have been widely used to qualitatively and quantitatively evaluate the information produced by vegetation,

TABLE 4 Top 20 keywords ranked by frequency on agricultural multispectral research in 2002–2021.

P	Keyword	N	C	L	TS	P	Keyword	N	C	L	TS
1	Remote sensing	532	1	1,267	4,212	11	NDVI	163	2	681	1,493
2	Classification	416	1	1,075	3,475	12	Lidar	160	4	570	1,339
3	Reflectance	374	3	1,062	3,188	13	Spectral reflectance	150	2	621	1,501
4	Vegetation	334	2	991	2,965	14	Uav	149	2	541	1,239
5	Biomass	302	4	791	2,288	15	Soil	145	6	544	1,324
6	Vegetation indexes	251	2	741	2,230	16	Yield	141	2	515	974
7	Leaf-area index	191	8	662	1,511	17	Cover	139	1	542	1,143
8	Imagery	174	5	654	1,446	18	Spectroscopy	137	5	564	1,140
9	Multispectral	171	4	584	1,325	19	Prediction	135	5	538	1,276
10	Model	165	3	605	1,615	20	Precision agriculture	132	5	518	1,137

P, position; N, number of articles; C, Cluster; L, Weight Links; TS, Total link strength.

and vegetation indexes have been applied in a particularly wide range of applications, in which yield prediction, spectral reflection studies, vegetation growth, and vegetation canopy information extraction are hot research directions (Zhou et al., 2017; Marston et al., 2020; Peng et al., 2021; Zhu et al., 2021). Among these research directions, accurate yield prediction of food crops, application research of specific wavelength bands, soil drought and salinity, foliar index, and crop pest monitoring are the focus of research (Farrell et al., 2018; Mazzia et al., 2020; Zhu et al., 2021), and a significant part of these studies use uavs as the main application platform, and the combination of UAVs and multispectral further promotes the development of vegetation indices in agriculture.

keyword clustering 3 reflectance is based on spectral reflectance information to carry out various studies in which the most important thing is to use reflectance information to construct models through which specific problems can be solved. For example, the simple algorithm yield model was used to estimate the foliar index by combining the light energy efficiency and leaf function of the crop (Peng et al., 2021) the SWAP-WOFOST model was used to predict the growth of sugarcane (Hu et al., 2019) and the improved casa model was used to map the crop biomass (Fang et al., 2021). The application of various models helped us to provide a great role in rapid crop monitoring as well as crop yield assessment.

Keywords clustering 4 biomass: Biomass is a common crop parameter based on remote sensing and with the rapid development of remote sensing technology biomass detection techniques have advanced tremendously with the rapid development of precision agriculture from 1980 to 2021. The rapid development of UAV technology, lightweight multispectral, and hyperspectral equipment has provided new tools for biomass detection and during these decades most of the studies on crop parameters were conducted based on spectral information and with the addition of 3D information technology the interplay of the two is a new progress in the detection of crop parameters (Candiago et al., 2015; Näsi et al., 2018; Zhu et al., 2019a; Fei et al., 2021; Jayakumari et al., 2021; Li et al., 2021; Yu et al., 2021).

Keywords clustering 5 quality: Improving the quality of production is one of the goals of agriculture and the development of multispectral technologies in improving the quality of production provides scientific tools to achieve the goal of high-quality agricultural development and the rapid development of UAVs with light and portable sensors capable of capturing multiple spectral images and new image processing methods have promoted high quality agricultural production (Messina et al., 2021). For example, six-band multispectral sensors and accurate orthorectified impact processing methods can improve spatial accuracy and can provide guidance for subsequent research (Mesas-Carrascosa et al., 2017); the use of deep learning methods to segment UAV images a new image alignment method that enables the fusion of information from two different sensors and improves detection accuracy (Kerkech et al., 2020).

Theme term analysis

Co-occurrence analysis of theme term

The theme term was analyzed by CiteSpace. Noun terms were extracted from the titles, author keywords, and system supplementary keywords of the dataset, and the top appearing terms were selected to generate a network time zone map (Figure 7). The time zone map collects the first occurrence of theme terms in the same year and the same time zone, which shows the evolution of the knowledge domain in the time dimension more clearly. Multispectral image, vegetation indices, normalized difference vegetation index (NDVI), the multispectral data, Unmanned aerial vehicle, overall accuracy, square error, spectral bands, random forest, high spatial resolution, hyperspectral data, remote sensing data, spatial distribution, growing season, etc., should be considered as the hot content of multispectral research in the field of agriculture in these years.

Burst Analysis of Theme Term

The theme terms with relatively high salience were analyzed by CiteSpace's burst detection algorithm in order to reflect the research trend and dig out the research hotspots, which are characterized by high frequency of changes within a certain phase in the software. The nodes that show up in red in Figure 7 indicate burst. Since there are relatively more red nodes with prominence from 2002 to 2021, the red nodes with prominence in the 6 years from 2015 to 2021 were selected as shown in Table 5. Satellite data, climate change, forest inventory, standard deviation, growing satellite data, climate change, forest inventory, standard deviation, growing seasons, plant height, sentinel-2 data, unmanned aerial, environmental condition, crop water stress index, point clouds, crop yield, etc., indicate that the recent years of multispectral research in agriculture are based on the above series of themes. The above-mentioned thematic terms have been used as a research method in the field of agriculture. From 2002 to 2010, burst themes included canopy reflectance, spectral mixture analysis, reflectance data, airborne multispectral imagery, aerial photography, and multispectral analysis. Burst themes in 2011–2021 associated with multispectral satellite imagery, remote sensing technique, high resolution, water quality parameter, partial least squares, crop water stress index, and biomass estimation, which indicate that the research and application of vegetation indices and algorithms were the main focus at this phase. Among them, vegetation index is the most researched part of multispectral in the field of agriculture.

Research frontiers

Agricultural multispectral research analysis selects the reference node and generates the cited literature analysis graph by

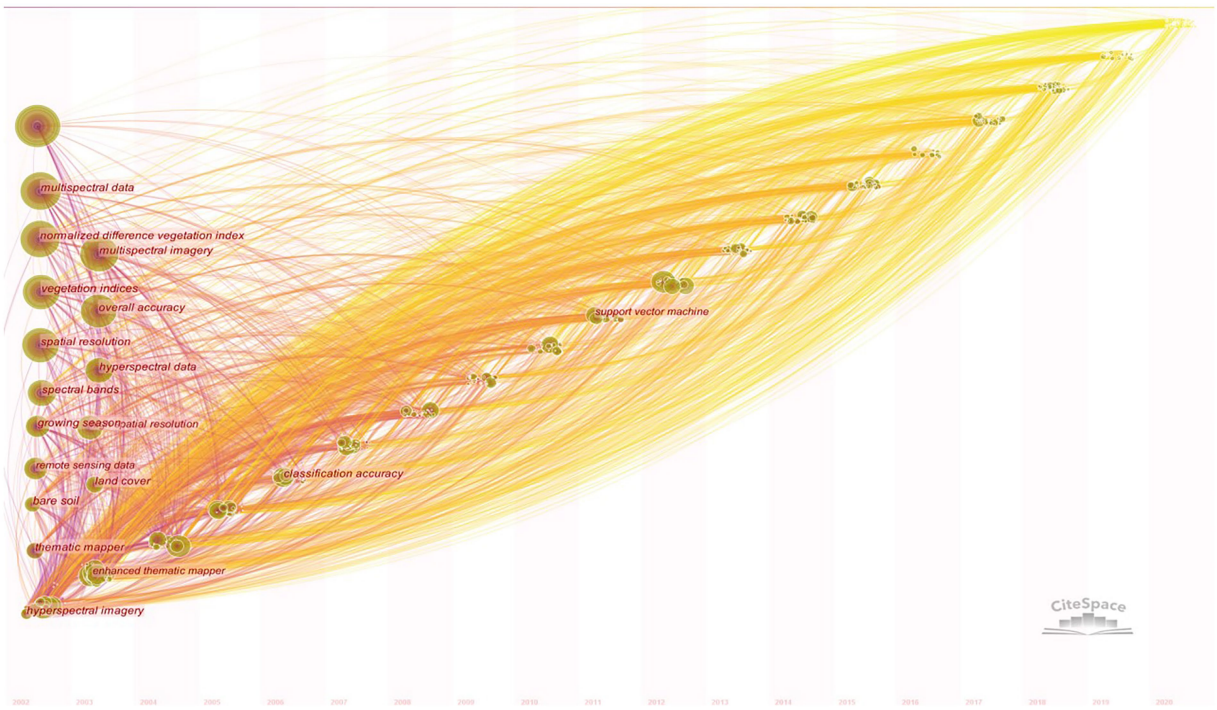

FIGURE 7
Co-occurrence time zone map of theme terms on agricultural multispectral research in 2002–2021. The horizontal axis represents the year, each node represents a topic, and the size of each node represents frequency of occurrence. The lines between each node represent connections to other topics. The circles in the vertical axis represent topics in the multispectral area of agriculture. The size of the circles represents the magnitude of the heat. The years with more topics were arranged in order from the largest to the smallest on the vertical axis.

CiteSpace. Clusters were formed by selecting keywords, and then a total of 17 clusters were generated by LLR algorithm. Each of these clusters represents the activity of its future direction, as shown in Figure 8. The denser and more active the clusters in the graph, the more they represent the current research frontier. The module values of the 17 clusters in Figure 8 are $Q = 0.8208$ and $S = 0.917$. The module values and the average profile values are indicators provided by CiteSpace based on the network structure and the clarity of the clusters, which are used to measure the clustering effect of the map. $Q > 0.3$ indicates that the clustering is significant, and $S > 0.7$ indicates that the clustering is highly convincing. Generally, the clustering above 0.5 can be considered reasonable. Therefore, the present clustering is reasonable and the structure is significant.

The color curves in the figure indicate co-citation links. More connected lines between clusters indicate a strong correlation between clusters. Large nodes indicate that they are worth exploring because they contain important cases that are overcited or mentioned. Nodes that are still active represent cutting-edge directions, scientific themes and novel trends in agricultural multispectral research field. According to the Figure 8, the largest cluster is #0 (vegetation index), located at the top of the image. The duration varies between clusters, with some lasting more than a decade and others having a shorter life span. The four clusters with higher activity and frequency were selected for further analysis.

The largest cluster #0 (UAV) contains 175 reference points between 2012 and 2021. The average reference year is 2016 and the average profile value $S = 0.855$, which was well visualized. This cluster is a corresponding study for vegetation indices in land cover, vegetation classification, crop yield estimation, drought monitoring, and environmental change using UAV remote sensing as the main application platform. UAV is an important vehicle for acquiring a variety of remote sensing data accurately, flexibly and efficiently in the low-altitude field, and UAV remote sensing is now very commonly used in precision agriculture, while UAV-based IoT technology is considered as the future of remote sensing in precision agriculture. Vegetation indices are formed by combining different bands of the spectrum according to the spectral characteristics of vegetation. More than 40 kinds of vegetation indices are available and widely used in the field of agricultural production. The most cited one in this cluster is Bendig et al. (2015), who used vegetation indices and plant height information to estimate summer barley biomass and verified the potential of visible bands to predict biomass. Candiago et al. (2015) demonstrated the great potential of UAVs in the multispectral field by monitoring vegetation indices with UAVs carrying imaging equipment. Zhou et al. (2017) verified that red-edge and infrared bands were more effective in predicting rice yield and foliar index based on a UAV-mounted multispectral photography platform, demonstrating the reliability of the platform for rice yield and growth estimation and identifying the most contraindicated virtual instrument for rice yield. Zaman-Allah et al. (2015) used a multispectral imaging sensor-mounted UAV platform to measure the N content in soil and derive crop performance indices for low N stress in maize fields, showing that the platform is effective in assessing field variability and crop performance. Duan et al. (2017) applied UAV based multispectral camera to detect NDVI indices in wheat field during the growing season through a high-throughput phenotyping platform, showing that NDVI before and after flowering had a strong

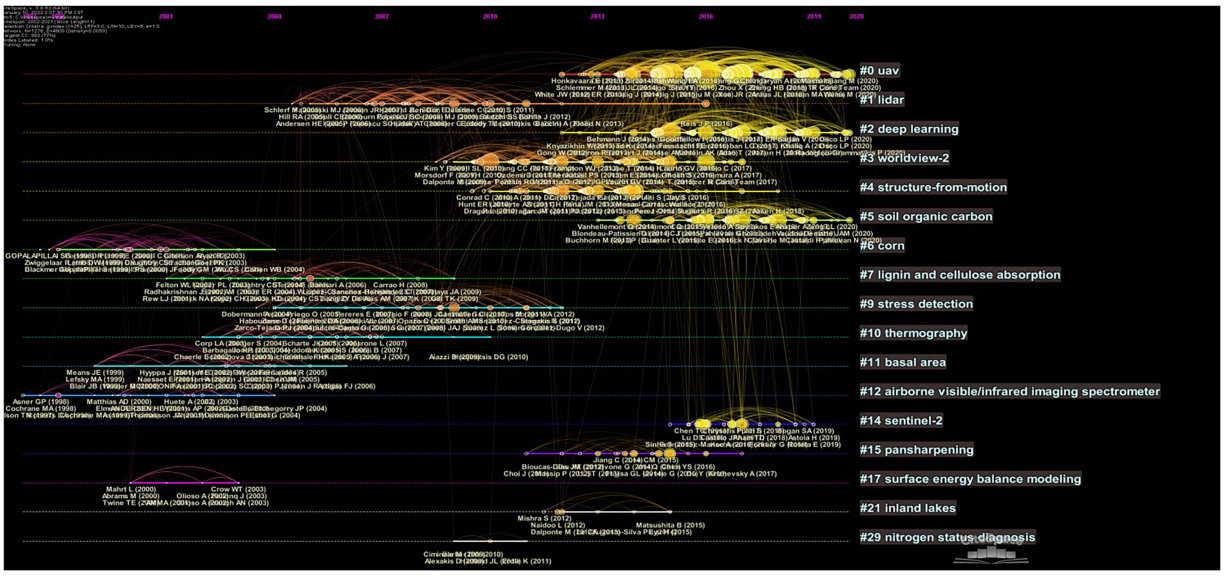

FIGURE 8
Co-citation timeline mapping of publications on agricultural multispectral research in 2002–2021. The horizontal axis represents the year, each node represents a popular cited reference, and the size of each node is proportional to its citation frequency. The line between each node represents the time evolution of the cited literature, and the thickness of the line represents the co-citation intensity.

TABLE 5 Burst theme terms on agricultural multispectral study in 2015–2021.

Term	Strength	Begin	End	2015–2021
Satellite data	3.81	2015	2017	
Climate change	3.44	2015	2017	
Forest inventory	3.15	2015	2018	
Spectral feature	5.07	2016	2018	
Hyperspectral image	4.73	2016	2017	
Standard deviation	3.77	2016	2021	
Growing seasons	3.69	2016	2021	
Soil property	5.91	2017	2018	
Optimal wavelengths	4.6	2017	2021	
Plant height	3.1	2017	2021	
Sentinel-2 data	8.1	2018	2021	
Unmanned aerial system	6.02	2018	2021	
RGB image	5.71	2018	2021	
Field scale	4.82	2018	2021	
Environmental condition	4.02	2018	2021	
Crop water stress index	4.02	2018	2021	
Point clouds	3.62	2018	2021	
Digital surface model	3.19	2018	2021	
Crop yield	3.19	2018	2021	

correlation with yield. From the clustering timeline, the cluster is still highly dynamic until 2021, and UAV remote sensing is still a hot spot for current research.

The average citation time for cluster #2 is 2016. This cluster focuses on the clustering of remote sensing-based algorithms, which summarizes a review of multispectral remote sensing and case studies of algorithm applications. Currently algorithms for remotely sensed vegetation indices is effective and convenient, which have been applied for vegetation cover and growth dynamics research with wide application of UAVs (Xue and Su, 2017). Torres-Sánchez et al. (2015a) newly developed a threshold segmentation OBIA algorithm by UAV images on the Otsu-based method. This algorithm was applied to the Excess Green Index (ExG) and Normalized Vegetation Index (NDVI). Torres-Sánchez et al. (2015b) proposed a method to calculate the 3D geometric features of individual trees and rows with an accuracy of 97% for area quantification with UAVs. Mathews and Jensen (2013) acquired UAV images to collect Leaf Area Index (LAI) of visualized and quantified vineyard canopy through a motion point cloud computer technique. Albetis et al. (2017) proposed a UAV-based images and operational flavescence dorée mapping technique for grape diseases detection. The duration of this clustering is 2012–2021 and, as with the vegetation index, machine learning is also a current hotspot. Machine learning has becomes a hot spot thanks to the development of artificial intelligence, which improves efficiency by combining various algorithms. Integration of machine learning and vegetation indices plays an important role in the field of agricultural multispectral research.

Cluster #3 is well visualized with a mean citation time of 2012 and a mean profile of $S = 0.897$. The clustering is mainly the analysis of ground information using high-altitude images from satellite multispectral remote sensing. Nowadays, more and more UAVs are joining the application of remote sensing mapping, but satellite remote sensing is still the most used method in high-altitude remote sensing. Satellite remote sensing has the characteristics of high point of view, wide field of view, and continuous and fast data collection. It has a broad application prospect in land resources, water resources survey, farming estimation, etc. Dube and Mutanga (2015) applied the medium-resolution multi-spectral Landsat 8 to analyze above-ground biomass in forest plantations. His study concluded that the data provided by satellite could be a more effective data source for analyzing above-ground biomass and spectral vegetation indices, demonstrating the potential and advantages of this Landsat dataset. Immitzer et al. (2016) adopted S2 satellites to map summer and winter crops and different deciduous and tree species to confirm the capability of S2 data for land cover mapping and the high value of red-edge and short-wave infrared bands for vegetation mapping. Clevers and Gitelson (2013) estimated chlorophyll and nitrogen content of crops and grass based on red-edge band remote sensing on Sentinel-2 and-3 satellites, confirming the importance of the red-edge band on satellites for agricultural applications. Ramoelo et al. (2015) used Worldview-2 satellite to monitor leaf nitrogen content and above-ground biomass, demonstrating the importance of high-altitude resolution and the red-edge band in rangeland assessment and detection. Mutanga et al. (2012) obtained red-edge-band images from Worldview-2 satellite and applied random forest regression algorithm to predict biomass in wetland areas. The duration of this clustering was 2009–2017, which indicates that multispectral research in terms of satellites

is no longer a hotspot for research at present. The current direction of research has moved toward multispectral remote sensing research represented by UAVs.

The average citation time for cluster #4 is 2012. The main research in this cluster is summarized for aerial detection. In addition, this cluster is a multispectral research mainly by UAVs. The main research in this cluster is remote sensing mapping of field vegetation by multispectral information, and building higher accuracy classification models, including research on weed identification and yield estimation in crop fields. Yu et al. (2016) adopted UAV platform to obtain multispectral data for soybean breeding, which led to significant improvement in yield estimation models through machine learning. Maimaitijiang et al. (2017) applied UAV multisensor data fusion to extract soybean plant phenotypes and developed a model for extracting plant phenotypes, demonstrating that low-cost multisensors can provide accurate data. Veeranampalayam Sivakumar et al. (2020) conducted experiments on weed identification with low altitude UAV image of soybean field, verifying the accuracy of the Faster RCNN model and fully affirming the importance of the model. Marston et al. (2020) conducted soybean aphid experiments with UAVs and found that NIR reflections are sensitive for aphids detection. The duration of clustering #4 was from 2010 to 2018, and the research on re-clustering provided a basis and reference for the subsequent development of multispectral technology in agriculture in terms of precision management of farmland, as well as crop identification. Along with the rise of vegetation indices as well as machine science, remote sensing mapping classification is gradually approaching this aspect.

In addition, based on the ranking of the burst literature according to the intensity, the top 15 articles were selected from total 162 strongly burst literatures, as shown in Table 6. From the content presented in these 15 literatures, the results are roughly the same as those of the above cluster analysis, with the research frontier trends focusing on the application and expansion of the UAV platform in various aspects, as well as various studies for vegetation indices. Data acquisition mostly relies on multispectral sensors carried by UAVs (Zhang and Kovacs, 2012) and to a lesser extent on satellites (Clevers and Gitelson, 2013), with UAVs gradually occupying the mainstream with their low-cost and flexibility advantages. Moreover, most of the studies are on crop parameters such as biomass (Bendig et al., 2015), species classification (Ke et al., 2010), plant phenotypes (Araus and Cairns, 2014), etc. Machine learning (Mountrakis et al., 2011) also plays a big role in this. The development of new and emerging technologies has played a great role in the development of agriculture.

Discussion

Based on the analysis of the publications searched, it is known that the current research on multispectral in agriculture is mainly focused on vegetation index (Chang et al., 2020; Kim et al., 2020; Mazzia et al., 2020), land cover (Laamrani et al., 2020), vegetation classification (Gibson et al., 2004), crop estimation (Zhou et al., 2017), drought monitoring (Periasamy and Shanmugam, 2016), and environmental change (Brook et al., 2020). Among them, the studies related to vegetation indices involves the most papers. Most of the current monitoring of crops uses remote sensing technology and ground data in conjunction with each other to invert the biological indicators of crops, such as normalized vegetation index and biomass (Li et al., 2020a). Vegetation indices are the key to qualitative and quantitative assessment of vegetation, and vegetation indices have been widely applied for crop monitoring. Research related to vegetation indices is also a hot area of research at present and also a hot area of research in the

TABLE 6 Top 15 highest prominence of cited references.

Begin	End	Strength	Year	References	2002–2021
2011	2015	15.5696	2010	Blaschke, 2010, ISPRS J Photogramm, V65, P2	
2013	2017	13.1026	2012	Zarco-Tejada PJ, 2012, Remote Sens Environ, V117, P322	
2017	2018	12.5081	2013	Clevers JGPW, 2013, Int J Appl Earth Obs, V23, P344	
2015	2018	12.1329	2013	Mulla DJ, 2013, Biosyst Eng, V114, P358	
2014	2017	11.6238	2012	Mutanga O, 2012, Int J Appl Earth Obs, V18, P399	
2012	2014	11.4153	2009	Berni JAJ, 2009, IEEE T Geosci Remote, V47, P722	
2017	2021	10.5978	2014	Bendig J, 2014, Remote Sens, V6, P10395	
2015	2017	9.5025	2012	Zhang CH, 2012, Precis Agric, V13, P693	
2006	2017	9.3241	2012	Berner L T, 2012, Biogeosciences, V9, P3943	
2011	2014	9.2223	2009	Chander G, 2009, Remote Sens Environ, V113, P893	
2018	2021	8.3433	2015	Bendig J, 2015, Int J Appl Earth Obs, V39, P79	
2012	2015	8.1168	2010	KeYH, 2010, Remote Sens Environ, V114, P1141	
2017	2021	7.7503	2014	Torres-Sanchez J, 2014, Comput Electron Agr, V103, P104	
2016	2021	7.1715	2014	Araus JL, 2014, Trends Plant Sci, V19, P52	
2012	2016	7.1502	2011	Mountrakis G, 2011, ISPRS J Photogramm, V66, P247	

future. Vegetation indices can be divided into linear combinations of bands or original band ratio design (RVI; Lee et al., 2020), improvement of original indices by physical and mathematical methods (with universal applicability; Zhu et al., 2019b), and indices born on the basis of remote sensing technology for hyperspectral and thermal infrared remote sensing (with difficulty in data acquisition and difficult to be promoted and developed; Berni et al., 2009). The early studies of vegetation indices were on chlorophyll and nitrogen measurements, and plant data were obtained by tgi indices in conjunction with related factors (Hunt et al., 2013). Many current studies address NDVI indices and are interwoven with various indices such as NDRE and NGRDI (Hassan et al., 2019). The best proof of the application of remote sensing in agricultural monitoring was demonstrated in crop yield estimation (Maimaitijiang et al., 2020). Combined with the 2021 research literature, there is now a shift from large scale and large area detection of satellite data to specific range detection with further improvement in accuracy and precision.

Before the rise of UAVs, land satellites were primary means of acquiring multispectral data. Satellites equipped with multispectral instruments have the capability to detect the full spectral band from visible to thermal infrared. Such satellites are used in land resources (Zanardo et al., 2016), environmental monitoring (Brook et al., 2020), etc. by higher applications. And in recent years the emergence of unmanned aircraft remote sensing detection gradually occupy the mainstream, but from 2002 to the present satellites still mainly undertake the task of data acquisition. The US landlast and sentinel series satellites are typical representatives of multispectral research. Early studies based on satellite data modeled drought environments (Theseira et al., 2002) and constructed drought early warning systems, that is, drought has been the focus of research. There have also been studies on crop leaf area monitoring (Chrysafis et al., 2020) and image classification and identification (Venkatesh and Kumar Raja, 2003; Gibson et al., 2004; Li et al., 2020b) through satellite data. Nowadays, the main research of satellites is for surface biomass (Khan et al., 2020) and monitoring of soil elements over a large area (Sullivan et al., 2004; Periasamy and Shanmugam, 2016; Ramos et al., 2020; Luo et al., 2021). In the future, as satellite technology continues to develop, the application of multispectral aspects will gradually advance, and the ability to monitor large areas as well as the types of objects to be monitored will be greatly improved.

Deep learning and machine algorithms are also extensively covered in the literature of search. The current strong emergence of UAV imaging systems has developed as a means of application in agriculture that can yield benefits. The application of machine learning algorithms (Eskandari et al., 2020; Maimaitijiang et al., 2020; Mazzia et al., 2020; Osco et al., 2020a) has improved the ability of UAV applications and likewise the ability of satellite data for agricultural applications (Datta et al., 2021). Through the study it was shown that 62% studies used regression models and 38% used classification models. With the technology development, machine learning has also gradually derived multiple medium algorithms, including artificial convolutional neural networks (Osco et al., 2020b), support vector machines (Fortin et al., 2014), etc. The early algorithms were simple development of machine vision such as detection of two-dimensional planes (Aleixos et al., 2002), for example, fruit integrity detection (Ariana et al., 2006). The integration of algorithms and equipment has achieved three-dimensional breakthroughs, for example, extraction of tree canopy volume (Li et al., 2020a; Minařík et al., 2020), etc. Currently in the field of remote sensing support vector machines and integrated classifiers are the focus of current development, while deep learning in the field of agricultural multispectral research mainly analyzes images, including image fusion, segmentation, recognition, target detection, obia, supervised training, etc. With the progress of hardware technology, the consequent acquisition of numerous data will also be beneficial to the development of machine learning, and currently big data cloud computing and machine learning are combined together to work on the development of agriculture. Deep learning is being applied to various fields of remote sensing.

In terms of multispectral detection equipment, it lacks of cooperation of ground and UAV and other aerial equipment. In some special terrain areas, the UAVs cannot shoot clearly. In this case, ground equipment will be able to make up for this shortcoming. The cooperation of multiple machinery and equipment in the future may be the focus of development research. Especially in crop modeling, UAVs and scanning instruments can cooperate with each other to combine mathematical models, build internal and external relationships, and generate complete plant images.

At present, it is difficult to achieve the simultaneous existence of multispectral and hyperspectral data on the same machine. The use of multispectral data to simulate hyperspectral data to obtain different data types by image fusion technology will be a valuable research direction in the future. Image fusion techniques can fuse different data types, not only multispectral data. The multispectral data can be extracted from the hyperspectral data or inverse performance data by specific methods such as mathematical equations, but this method is still incomplete and the current research is still focused on traditional linear algorithms. Future research should focus on studying new models or improving the accuracy by further improving machine algorithms.

UAVs play a great role with their unique advantages as the current main application platform of multispectral in agriculture. The most prominent problem with UAVs at present is the endurance problem. In the future, high endurance UAVs should be launched, while stability performance, detection accuracy, and load capacity are also necessary performance enhancements. In addition, economic and efficient multispectral equipment is needed as well. The simplicity of operation can reduce the user's learning costs. At the same time, sensor fusion technology can also improve its application level, eliminate the possible contradictory data between sensors, reduce uncertainty, and improve the speed and correctness of the system.

Real-time image processing technology can eliminate the time gap between data collection and data analysis, and provide the

basis for real-time control of operating equipment. Along with the rapid development of deep learning technology, the research on agricultural information analysis based on artificial intelligence has opened the era of intelligent research on unmanned farms. However, in the actual application operation, the uneven network coverage in the field limits the real-time transmission of images in the cloud, and the current computing performance of embedded chips also limits the real-time processing of images at the edge. Therefore, this technology is still in the early stage of research. In the future, with the popularization of 5G signal, the improvement of embedded chip computing power and the breakthrough of lightweight network model, the feasibility of real-time image processing will be gradually improved, and the foundation for the realization of unmanned and intelligent farms will be laid.

Conclusion

The bibliometrics and scientometric approach were applied to analyze the publications on multispectral research in agriculture from 2002 to 2021. It can be seen that the number of publications in agricultural multispectral research has a rapid growth trend. The growth rate is obviously significant in recent years, maintaining a high growth rate of the literature, which is closely related to the development of precision agriculture. The study shows that the United States, China, and Spain are the countries with the largest research share, with the Chinese Academy of Sciences from China being the institution with the most publications. The most influential journal is Remote Sensing with Mutanga, Dube.timothy, and Chenghai Yang as core authors.

Multispectral technology has undergone nearly 50 years of development from the launch of ground-accessible land satellites in the United States in the 1970s to the present. It is gradually developing from the initial exploration stage to the present mature model with commercialized equipment and system software, and spreading to multiple industries. Based on the analysis, the development of agricultural multispectral technology from 2002 to 2021 is accompanied by advanced sensors and sophisticated algorithms and numerical models in agriculture. Especially along with the development of UAV technology, the application of multispectral technology in agriculture has become more and more extensive, from organic matter monitoring such as crops, to inorganic matter monitoring such as soil, moisture, nitrogen elements. The future development prospect is also more extensive. The advancement of technology has jointly promoted the application of multi-spectrum in agriculture, and also promoted the development of precision agriculture.

Data availability statement

The raw data supporting the conclusions of this article will be made available by the authors, without undue reservation.

Author contributions

YZ and YL: conceptualization, project administration, and funding acquisition. DZ, XHu, and YZ: methodology. DZ: software, data curation, and visualization. DZ and YZ: validation and investigation. DZ and HL: formal analysis. YZ: resources. DZ, HL, and YZ: writing—original draft preparation. JD, RJ, XHe, and MT: writing—review and editing. YL: supervision. All authors contributed to the article and approved the submitted version.

Funding

This research was funded by Key Field Research and Development Plan of Guangdong Province, China, grant number 2019B020221001, Science and Technology Plan Project of Guangdong Province, China, grant number 2018A050506073, Guangdong Modern Agricultural Industry Generic Key Technology Research and Development Innovation Team Project, grant number 2021KJ133, and the 111Project, grant number D18019.

Acknowledgments

The authors would like to thank Chaomei Chen for the computational support of CiteSpace software.

Conflict of interest

The authors declare that the research was conducted in the absence of any commercial or financial relationships that could be construed as a potential conflict of interest.

Publisher's note

All claims expressed in this article are solely those of the authors and do not necessarily represent those of their affiliated organizations, or those of the publisher, the editors and the reviewers. Any product that may be evaluated in this article, or claim that may be made by its manufacturer, is not guaranteed or endorsed by the publisher.

References

Albetis, J., Duthoit, S., Guttler, F., Jacquin, A., Goulard, M., Poilvé, H., et al. (2017). Detection of flavescence dorée grapevine disease using unmanned aerial vehicle (uav) multispectral imagery. *Remote Sens. (Basel)* 9:308. doi: 10.3390/rs9040308

Aleixos, N., Blasco, J., Navarrón, F., and Moltó, E. (2002). Multispectral inspection of citrus in real-time using machine vision and digital signal processors. *Comput. Electron. Agric.* 33, 121–137. doi: 10.1016/S0168-1699(02)00002-9

Araus, J. L., and Cairns, J. E. (2014). Field high-throughput phenotyping: the new crop breeding frontier. *Trends Plant Sci.* 19, 52–61. doi: 10.1016/j.tplants.2013.09.008

Ariana, D., Guyer, D. E., and Shrestha, B. (2006). Integrating multispectral reflectance and fluorescence imaging for defect detection on apples. *Comput. Electron. Agric.* 50, 148–161. doi: 10.1016/j.compag.2005.10.002

Baluja, J., Diago, M. P., Balda, P., Zorer, R., Meggio, F., Morales, F., et al. (2012). Assessment of vineyard water status variability by thermal and multispectral imagery using an unmanned aerial vehicle (uav). *Irrig. Sci.* 30, 511–522. doi: 10.1007/s00271-012-0382-9

Bendig, J., Yu, K., Aasen, H., Bolten, A., Bennertz, S., Broscheit, J., et al. (2015). Combining uav-based plant height from crop surface models, visible, and near infrared vegetation indices for biomass monitoring in barley. *Int. J. Appl. Earth Obs. Geoinf.* 39, 79–87. doi: 10.1016/j.jag.2015.02.012

Berni, J., Zarco-Tejada, P. J., Suarez, L., and Fereres, E. (2009). Thermal and narrowband multispectral remote sensing for vegetation monitoring from an unmanned aerial vehicle. *IEEE Trans. Geosci. Remote Sens.* 47, 722–738. doi: 10.1109/TGRS.2008.2010457

Brook, A., De Micco, V., Battipaglia, G., Erbaggio, A., Ludeno, G., Catapano, I., et al. (2020). A smart multiple spatial and temporal resolution system to support precision agriculture from satellite images: proof of concept on aglianico vineyard. *Remote Sens. Environ.* 240:111679. doi: 10.1016/j.rse.2020.111679

Candiago, S., Remondino, F., De Giglio, M., Dubbini, M., and Gattelli, M. (2015). Evaluating multispectral images and vegetation indices for precision farming applications from uav images. *Remote Sens.* 7, 4026–4047. doi: 10.3390/rs70404026

Chang, A., Yeom, J., Jung, J., and Landivar, J. (2020). Comparison of canopy shape and vegetation indices of citrus trees derived from uav multispectral images for characterization of citrus greening disease. *Remote Sens.* 12:4122. doi: 10.3390/rs12244122

Chen, C. (2006). Citespace ii: detecting and visualizing emerging trends and transient patterns in scientific literature. *J. Am. Soc. Inf. Sci. Technol.* 57, 359–377. doi: 10.1002/asi.20317

Chen, C. (2013). Hindsight, insight, and foresight: a multi-level structural variation approach to the study of a scientific field. *Tech. Anal. Strat. Manag.* 25, 619–640. doi: 10.1080/09537325.2013.801949

Chen, C. (2017). Science mapping: a systematic review of the literature. *J. Data Inform. Sci.* 2, 1–40. doi: 10.1515/jdis-2017-0006

Chen, C., Ibekwe-SanJuan, F., and Hou, J. (2010). The structure and dynamics of co-citation clusters: a multiple-perspective co-citation analysis. *J. Am. Soc. Inf. Sci. Technol.* 61, 1386–1409. doi: 10.1002/asi.21309

Chrysafis, I., Korakis, G., Kyriazopoulos, A. P., and Mallinis, G. (2020). Retrieval of leaf area index using sentinel-2 imagery in a mixed mediterranean forest area. *ISPRS Int. J. Geo Inf.* 9:622. doi: 10.3390/ijgi9110622

Clevers, J. G. P. W., and Gitelson, A. A. (2013). Remote estimation of crop and grass chlorophyll and nitrogen content using red-edge bands on sentinel-2 and-3. *Int. J. Appl. Earth Obs. Geoinf.* 23, 344–351. doi: 10.1016/j.jag.2012.10.008

Datta, S., Das, P., Dutta, D., and Giri, R. K. (2021). Estimation of surface moisture content using sentinel-1 c-band Sar data through machine learning models. *J. Indian Soc. Remote Sens.* 49, 887–896. doi: 10.1007/s12524-020-01261-x

Duan, T., Chapman, S. C., Guo, Y., and Zheng, B. (2017). Dynamic monitoring of ndvi in wheat agronomy and breeding trials using an unmanned aerial vehicle. *Field Crop Res* 210, 71–80. doi: 10.1016/j.fcr.2017.05.025

Dube, T., and Mutanga, O. (2015). Evaluating the utility of the medium-spatial resolution landsat 8 multispectral sensor in quantifying aboveground biomass in umgeni catchment, South Africa. *ISPRS J. Photogramm. Remote Sens.* 101, 36–46. doi: 10.1016/j.isprsjprs.2014.11.001

Eskandari, R., Mahdianpari, M., Mohammadimanesh, F., Salehi, B., Brisco, B., and Homayouni, S. (2020). Meta-analysis of unmanned aerial vehicle (uav) imagery for agro-environmental monitoring using machine learning and statistical models. *Remote Sens.* 12:3511. doi: 10.3390/rs12213511

Fang, P., Yan, N., Wei, P., Zhao, Y., and Zhang, X. (2021). Aboveground biomass mapping of crops supported by improved casa model and sentinel-2 multispectral imagery. *Remote Sens.* 13:2755. doi: 10.3390/rs13142755

Farrell, M., Gili, A., and Noellemeyer, E. (2018). Spectral indices from aerial images and their relationship with properties of a corn crop. *Precis. Agric.* 19, 1127–1137. doi: 10.1007/s11119-018-9570-9

Fei, S., Hassan, M. A., Ma, Y., Shu, M., Cheng, Q., Li, Z., et al. (2021). Entropy weight ensemble framework for yield prediction of winter wheat under different water stress treatments using unmanned aerial vehicle-based multispectral and thermal data. *Front. Plant Sci.* 12:730181. doi: 10.3389/fpls.2021.730181

Fortin, J. G., Anctil, F., and Parent, L. E. (2014). Comparison of multiple-layer perceptrons and least squares support vector machines for remote-sensed characterization of in-field lai patterns - a case study with potato. *Can. J. Remote. Sens.* 40, 75–84. doi: 10.1080/07038992.2014.928182

Garini, Y., Young, I. T., and McNamara, G. (2006). Spectral imaging: principles and applications. *Cytometry A* 69A, 735–747. doi: 10.1002/cyto.a.20311

Gibson, K. D., Dirks, R., Medlin, C. R., and Johnston, L. (2004). Detection of weed species in soybean using multispectral digital images. *Weed Technol.* 18, 742–749. doi: 10.1614/WT-03-170R1

Hassan, M. A., Yang, M., Rasheed, A., Yang, G., Reynolds, M., Xia, X., et al. (2019). A rapid monitoring of ndvi across the wheat growth cycle for grain yield prediction using a multi-spectral uav platform. *Plant Sci.* 282, 95–103. doi: 10.1016/j.plantsci.2018.10.022

He, L., Song, X., Feng, W., Guo, B., Zhang, Y., Wang, Y., et al. (2016). Improved remote sensing of leaf nitrogen concentration in winter wheat using multi-angular hyperspectral data. *Remote Sens. Environ.* 174, 122–133. doi: 10.1016/j.rse.2015.12.007

Hu, S., Shi, L., Huang, K., Zha, Y., Hu, X., Ye, H., et al. (2019). Improvement of sugarcane crop simulation by swap-wofost model via data assimilation. *Field Crop Res* 232, 49–61. doi: 10.1016/j.fcr.2018.12.009

Huang, Y., Reddy, K. N., Fletcher, R. S., and Pennington, D. (2018). Uav low-altitude remote sensing for precision weed management. *Weed Technol.* 32, 2–6. doi: 10.1017/wet.2017.89

Huang, Y., Ren, Z., Li, D., and Liu, X. (2020). Phenotypic techniques and applications in fruit trees: a review. *Plant Methods* 16:107. doi: 10.1186/s13007-020-00649-7

Huang, Y., Thomson, S. J., Brand, H. J., and Reddy, K. N. (2016). Development and evaluation of low-altitude remote sensing systems for crop production management. *Int. J. Agric. Biol. Engineer.* 9:1. doi: 10.3965/j.ijabe.20160904.2010

Hunt, E. R., Doraiswamy, P. C., McMurtrey, J. E., Daughtry, C. S. T., Perry, E. M., and Akhmedov, B. (2013). A visible band index for remote sensing leaf chlorophyll content at the canopy scale. *Int. J. Appl. Earth Obs. Geoinf.* 21, 103–112. doi: 10.1016/j.jag.2012.07.020

Immitzer, M., Vuolo, F., and Atzberger, C. (2016). First experience with sentinel-2 data for crop and tree species classifications in central europe. *Remote Sens.* 8:166. doi: 10.3390/rs8030166

Jayakumari, R., Nidamanuri, R. R., and Ramiya, A. M. (2021). Object-level classification of vegetable crops in 3d lidar point cloud using deep learning convolutional neural networks. *Precis. Agric.* 22, 1617–1633. doi: 10.1007/s11119-021-09803-0

Ke, Y., Quackenbush, L. J., and Im, J. (2010). Synergistic use of quickbird multispectral imagery and lidar data for object-based forest species classification. *Remote Sens. Environ.* 114, 1141–1154. doi: 10.1016/j.rse.2010.01.002

Kerkech, M., Hafiane, A., and Canals, R. (2020). Vine disease detection in uav multispectral images using optimized image registration and deep learning segmentation approach. *Comput. Electron. Agric.* 174:105446. doi: 10.1016/j.compag.2020.105446

Khan, M. R., Khan, I. A., Baig, M. H. A., Liu, Z., and Ashraf, M. I. (2020). Exploring the potential of sentinel-2a satellite data for aboveground biomass estimation in fragmented himalayan subtropical pine forest. *J. Mt. Sci.* 17, 2880–2896. doi: 10.1007/s11629-019-5968-8

Kim, J., Popescu, S. C., Lopez, R. R., Wu, X. B., and Silvy, N. J. (2020). Vegetation mapping of no name key, florida using lidar and multispectral remote sensing. *Int. J. Remote Sens.* 41, 9469–9506. doi: 10.1080/01431161.2020.1800125

Kross, A., McNairn, H., Lapen, D., Sunohara, M., and Champagne, C. (2015). Assessment of rapideye vegetation indices for estimation of leaf area index and biomass in corn and soybean crops. *Int. J. Appl. Earth Obs. Geoinf.* 34, 235–248. doi: 10.1016/j.jag.2014.08.002

Laamrani, A., Joosse, P., McNairn, H., Berg, A., Hagerman, J., Powell, K., et al. (2020). Assessing soil cover levels during the non-growing season using multitemporal satellite imagery and spectral unmixing techniques. *Remote Sens.* 12:1397. doi: 10.3390/rs12091397

Lee, H., Wang, J., and Leblon, B. (2020). Intra-field canopy nitrogen retrieval from unmanned aerial vehicle imagery for wheat and corn fields. *Can. J. Remote. Sens.* 46, 454–472. doi: 10.1080/07038992.2020.1788384

Li, T., Cui, L., Xu, Z., Hu, R., Joshi, P. K., Song, X., et al. (2021). Quantitative analysis of the research trends and areas in grassland remote sensing: a scientometrics analysis of web of science from 1980 to 2020. *Remote Sens.* 13:1279. doi: 10.3390/rs13071279

Li, F., Piasecki, C., Millwood, R. J., Wolfe, B., Mazarei, M., and Stewart, C. N. Jr. (2020a). High-throughput switchgrass phenotyping and biomass modeling by uav. *Front. Plant Sci.* 11:574073. doi: 10.3389/fpls.2020.574073

Li, X., Yang, C., Huang, W., Tang, J., Tian, Y., and Zhang, Q. (2020b). Identification of cotton root rot by multifeature selection from sentinel-2 images using random forest. *Remote Sens. (Basel)* 12:3504. doi: 10.3390/rs12213504

Luo, X. R., Li, S. D., Liu, L., Yang, W. N., Zhang, Y. H., Chen, G., et al. (2021). Quantifying aboveground vegetation water storage combining landsat 8 oli and sentinel-1 imageries. *Geocarto Int.* 37, 2717–2734. doi: 10.1080/10106049.2020.1861662

Maimaitijiang, M., Ghulam, A., Sidike, P., Hartling, S., Maimaitiyiming, M., Peterson, K., et al. (2017). Unmanned aerial system (uas)-based phenotyping of

soybean using multi-sensor data fusion and extreme learning machine. *ISPRS J. Photogramm. Remote Sens.* 134, 43–58. doi: 10.1016/j.isprsjprs.2017.10.011

Maimaitijiang, M., Sagan, V., Sidike, P., Hartling, S., Esposito, F., and Fritschi, F. B. (2020). Soybean yield prediction from uav using multimodal data fusion and deep learning. *Remote Sens. Environ.* 237:111599. doi: 10.1016/j.rse.2019.111599

Marston, Z. P. D., Cira, T. M., Hodgson, E. W., Knight, J. F., Macrae, I. V., and Koch, R. L. (2020). Detection of stress induced by soybean aphid (hemiptera: aphididae) using multispectral imagery from unmanned aerial vehicles. *J. Econ. Entomol.* 113, 779–786. doi: 10.1093/jee/toz306

Mathews, A., and Jensen, J. (2013). Visualizing and quantifying vineyard canopy lai using an unmanned aerial vehicle (uav) collected high density structure from motion point cloud. *Remote Sens.* 5, 2164–2183. doi: 10.3390/rs5052164

Mazzia, V., Comba, L., Khaliq, A., Chiaberge, M., and Gay, P. (2020). Uav and machine learning based refinement of a satellite-driven vegetation index for precision agriculture. *Sensors.* 20:2530. doi: 10.3390/s20092530

Memon, M. S., Jun, Z., Sun, C., Jiang, C., Xu, W., Hu, Q., et al. (2019). Assessment of wheat straw cover and yield performance in a rice-wheat cropping system by using landsat satellite data. *Sustainability* 11:5369. doi: 10.3390/su11195369

Mesas-Carrascosa, F. J., Clavero Rumbao, I., Torres-Sánchez, J., García-Ferrer, A., Peña, J. M., and López Granados, F. (2017). Accurate ortho-mosaicked six-band multispectral uav images as affected by mission planning for precision agriculture proposes. *Int. J. Remote Sens.* 38, 2161–2176. doi: 10.1080/01431161.2016.1249311

Messina, G., Praticò, S., Badagliacca, G., Di Fazio, S., Monti, M., and Modica, G. (2021). Monitoring onion crop "cipolla rossa di tropea Calabria igp" growth and yield response to varying nitrogen fertilizer application rates using uav imagery. *Drones* 5:61. doi: 10.3390/drones5030061

Minařík, R., Langhammer, J., and Lendzioch, T. (2020). Automatic tree crown extraction from uas multispectral imagery for the detection of bark beetle disturbance in mixed forests. *Remote Sens.* 12:4081. doi: 10.3390/rs12244081

Mountrakis, G., Im, J., and Ogole, C. (2011). Support vector machines in remote sensing: a review. *ISPRS J. Photogramm. Remote Sens.* 66, 247–259. doi: 10.1016/j.isprsjprs.2010.11.001

Mutanga, O., Adam, E., and Cho, M. A. (2012). High density biomass estimation for wetland vegetation using worldview-2 imagery and random forest regression algorithm. *Int. J. Appl. Earth Obs. Geoinf.* 18, 399–406. doi: 10.1016/j.jag.2012.03.012

Näsi, R., Viljanen, N., Kaivosoja, J., Alhonoja, K., Hakala, T., Markelin, L., et al. (2018). Estimating biomass and nitrogen amount of barley and grass using uav and aircraft based spectral and photogrammetric 3d features. *Remote Sens.* 10:1082. doi: 10.3390/rs10071082

Osco, L. P., Arruda, M. D. S. D., Marcato Junior, J., Da Silva, N. B., Ramos, A. P. M., Moryia, E. A. S., et al. (2020a). A convolutional neural network approach for counting and geolocating citrus-trees in uav multispectral imagery. *ISPRS J. Photogramm. Remote Sens.* 160, 97–106. doi: 10.1016/j.isprsjprs.2019.12.010

Osco, L. P., Junior, J. M., Ramos, A. P. M., Furuya, D. E. G., Santana, D. C., Teodoro, L. P. R., et al. (2020b). Leaf nitrogen concentration and plant height prediction for maize using uav-based multispectral imagery and machine learning techniques. *Remote Sens.* 12:3237. doi: 10.3390/rs12193237

Pena, J. M., Torres-Sanchez, J., de Castro, A. I., Kelly, M., and Lopez-Granados, F. (2013). Weed mapping in early-season maize fields using object-based analysis of unmanned aerial vehicle (uav) images. *PLoS One* 8:e77151. doi: 10.1371/journal.pone.0077151

Peng, X., Han, W., Ao, J., and Wang, Y. (2021). Assimilation of lai derived from uav multispectral data into the safy model to estimate maize yield. *Remote Sens.* 13:1094. doi: 10.3390/rs13061094

Periasamy, S., and Shanmugam, R. S. (2016). Multispectral and microwave remote sensing models to survey soil moisture and salinity. *Land Degrad. Dev.* 28, 1412–1425. doi: 10.1002/ldr.2661

Ramoelo, A., Cho, M. A., Mathieu, R., Madonsela, S., van de Kerchove, R., Kaszta, Z., et al. (2015). Monitoring grass nutrients and biomass as indicators of rangeland quality and quantity using random forest modelling and worldview-2 data. *Int. J. Appl. Earth Obs. Geoinf.* 43, 43–54. doi: 10.1016/j.jag.2014.12.010

Ramos, T. B., Castanheira, N., Oliveira, A. R., Paz, A. M., Darouich, H., Simionesei, L., et al. (2020). Soil salinity assessment using vegetation indices derived from sentinel-2 multispectral data. Application to lezíria grande, Portugal. *Agric Water Manag* 241:106387. doi: 10.1016/j.agwat.2020.106387

Raparelli, E., and Bajocco, S. (2019). A bibliometric analysis on the use of unmanned aerial vehicles in agricultural and forestry studies. *Int. J. Remote Sens.* 40, 9070–9083. doi: 10.1080/01431161.2019.1569793

Sa, I., Chen, Z., Popovic, M., Khanna, R., Liebisch, F., Nieto, J., et al. (2018). Weednet: dense semantic weed classification using multispectral images and mav for smart farming. *IEEE Robot. Automat. Lett.* 3, 588–595. doi: 10.1109/LRA.2017.2774979

Sankaran, S., Mishra, A., Ehsani, R., and Davis, C. (2010). A review of advanced techniques for detecting plant diseases. *Comput. Electron. Agric.* 72, 1–13. doi: 10.1016/j.compag.2010.02.007

Sullivan, D. G., Shaw, J. N., Mask, P. L., Rickman, D., Luvall, J., and Wersinger, J. M. (2004). Evaluating corn nitrogen variability via remote-sensed data. *Commun. Soil Sci. Plant Anal.* 35, 2465–2483. doi: 10.1081/LCSS-200030339

Theseira, M. A., Thomas, G., and Sannier, C. A. D. (2002). An evaluation of spectral mixture modelling applied to a semi-arid environment. *Int. J. Remote Sens.* 23, 687–700. doi: 10.1080/01431160010019652

Torres-Sánchez, J., López-Granados, F., and Peña, J. M. (2015a). An automatic object-based method for optimal thresholding in uav images: application for vegetation detection in herbaceous crops. *Comput. Electron. Agric.* 114, 43–52. doi: 10.1016/j.compag.2015.03.019

Torres-Sánchez, J., López-Granados, F., Serrano, N., Arquero, O., and Peña, J. M. (2015b). High-throughput 3-d monitoring of agricultural-tree plantations with unmanned aerial vehicle (uav) technology. *PLoS One* 10:e130479. doi: 10.1371/journal.pone.0130479

Tsouros, D. C., Bibi, S., and Sarigiannidis, P. G. (2019). A review on uav-based applications for precision agriculture. *Information* 10:349. doi: 10.3390/info10110349

van Eck, N. J., and Waltman, L. (2010). Software survey: vosviewer, a computer program for bibliometric mapping. *Scientometrics* 84, 523–538. doi: 10.1007/s11192-009-0146-3

Veeranampalayam Sivakumar, A. N., Li, J., Scott, S., Psota, E., Jhala, A. J., Luck, J. D., et al. (2020). Comparison of object detection and patch-based classification deep learning models on mid-to late-season weed detection in uav imagery. *Remote Sens. (Basel)* 12:2136. doi: 10.3390/rs12132136

Venkatesh, Y. V., and Kumar Raja, S. (2003). On the classification of multispectral satellite images using the multilayer perceptron. *Pattern Recogn.* 36, 2161–2175. doi: 10.1016/S0031-3203(03)00013-X

Wijesingha, J., Dayananda, S., Wachendorf, M., and Astor, T. (2021). Comparison of spaceborne and uav-borne remote sensing spectral data for estimating monsoon crop vegetation parameters. *Sensors* 21:2886. doi: 10.3390/s21082886

Xie, H., Zhang, Y., Wu, Z., and Lv, T. (2020). A bibliometric analysis on land degradation: current status, development, and future directions. *Land* 9:28. doi: 10.3390/land9010028

Xue, J., and Su, B. (2017). Significant remote sensing vegetation indices: a review of developments and applications. *J. Sensors* 2017, 1–17. doi: 10.1155/2017/1353691

Yu, N., Li, L., Schmitz, N., Tiaz, L. F., Greenberg, J. A., and Diers, B. W. (2016). Development of methods to improve soybean yield estimation and predict plant maturity with an unmanned aerial vehicle based platform. *Remote Sens. Environ.* 187, 91–101. doi: 10.1016/j.rse.2016.10.005

Yu, J., Wang, J., and Leblon, B. (2021). Evaluation of soil properties, topographic metrics, plant height, and unmanned aerial vehicle multispectral imagery using machine learning methods to estimate canopy nitrogen weight in corn. *Remote Sens.* 13:3105. doi: 10.3390/rs13163105

Yu, D., Xu, T., and Song, K. (2018). Nondestructive testing of external defects on nanguo pear. *Spectrosc. Lett.* 51, 191–197. doi: 10.1080/00387010.2018.1447968

Zaman-Allah, M., Vergara, O., Araus, J. L., Tarekegne, A., Magorokosho, C., Zarco-Tejada, P. J., et al. (2015). Unmanned aerial platform-based multi-spectral imaging for field phenotyping of maize. *Plant Methods* 11:35. doi: 10.1186/s13007-015-0078-2

Zanardo, F. H., Rodrigues, R. A. F., Silva, H. R., Marques, A. P., and Faria, G. A. (2016). Geotechnology application for data acquisition for agricultural and environmental management of the municipality of vitória Brazil-sp. *Engenharia Agrícola* 36, 684–695. doi: 10.1590/1809-4430-Eng.Agric.v36n4p684-695/2016

Zhang, C., and Kovacs, J. M. (2012). The application of small unmanned aerial systems for precision agriculture: a review. *Precis. Agric.* 13, 693–712. doi: 10.1007/s11119-012-9274-5

Zhang, Y., Thenkabail, P. S., and Wang, P. (2019). A bibliometric profile of the remote sensing open access journal published by mdpi between 2009 and 2018. *Remote Sens.* 11:91. doi: 10.3390/rs11010091

Zhou, X., Zheng, H. B., Xu, X. Q., He, J. Y., Ge, X. K., Yao, X., et al. (2017). Predicting grain yield in rice using multi-temporal vegetation indices from uav-based multispectral and digital imagery. *ISPRS J. Photogramm. Remote Sens.* 130, 246–255. doi: 10.1016/j.isprsjprs.2017.05.003

Zhu, W., Rezaei, E. E., Nouri, H., Yang, T., Li, B., Gong, H., et al. (2021). Quick detection of field-scale soil comprehensive attributes via the integration of uav and sentinel-2b remote sensing data. *Remote Sens.* 13:4716. doi: 10.3390/rs13224716

Zhu, W., Sun, Z., Peng, J., Huang, Y., Li, J., Zhang, J., et al. (2019a). Estimating maize above-ground biomass using 3d point clouds of multi-source unmanned aerial vehicle data at multi-spatial scales. *Remote Sens.* 11:2678. doi: 10.3390/rs11222678

Zhu, W., Sun, Z., Huang, Y., Lai, J., Li, J., Zhang, J., et al. (2019b). Improving field-scale wheat lai retrieval based on uav remote-sensing observations and optimized vi-luts. *Remote Sens.* 11:2456. doi: 10.3390/rs11202456

frontiers | Frontiers in Plant Science

TYPE Original Research
PUBLISHED 12 August 2022
DOI 10.3389/fpls.2022.962391

Check for updates

OPEN ACCESS

EDITED BY
Xiuliang Jin,
Institute of Crop Sciences (CAAS), China

REVIEWED BY
Nirmal Mazumder,
Manipal Academy of Higher Education, India
Jiwan Han,
Shanxi Agricultural University, China

*CORRESPONDENCE
Dongmei Chen
chendongmei@hdu.edu.cn

SPECIALTY SECTION
This article was submitted to Sustainable and Intelligent Phytoprotection, a section of the journal Frontiers in Plant Science

RECEIVED 06 June 2022
ACCEPTED 18 July 2022
PUBLISHED 12 August 2022

CITATION
Yan L, Wu K, Lin J, Xu X, Zhang J, Zhao X, Tayor J and Chen D (2022) Identification and picking point positioning of tender tea shoots based on MR3P-TS model. *Front. Plant Sci.* 13:962391. doi: 10.3389/fpls.2022.962391

COPYRIGHT
© 2022 Yan, Wu, Lin, Xu, Zhang, Zhao, Tayor and Chen. This is an open-access article distributed under the terms of the Creative Commons Attribution License (CC BY). The use, distribution or reproduction in other forums is permitted, provided the original author(s) and the copyright owner(s) are credited and that the original publication in this journal is cited, in accordance with accepted academic practice. No use, distribution or reproduction is permitted which does not comply with these terms.

Identification and picking point positioning of tender tea shoots based on MR3P-TS model

Lijie Yan[1], Kaihua Wu[1], Jia Lin[1], Xingang Xu[2], Jingcheng Zhang[1], Xiaohu Zhao[1], James Tayor[3] and Dongmei Chen[1]*

[1]School of Automation, Hangzhou Dianzi University, Hangzhou, China, [2]Beijing Research Center for Information Technology in Agriculture, Beijing Academy of Agriculture and Forestry Sciences, Beijing, China, [3]School of Natural and Environmental Sciences, Newcastle University, Newcastle Upon Tyne, United Kingdom

Tea is one of the most common beverages in the world. In order to reduce the cost of artificial tea picking and improve the competitiveness of tea production, this paper proposes a new model, termed the Mask R-CNN Positioning of Picking Point for Tea Shoots (MR3P-TS) model, for the identification of the contour of each tea shoot and the location of picking points. In this study, a dataset of tender tea shoot images taken in a real, complex scene was constructed. Subsequently, an improved Mask R-CNN model (the MR3P-TS model) was built that extended the mask branch in the network design. By calculating the area of multiple connected domains of the mask, the main part of the shoot was identified. Then, the minimum circumscribed rectangle of the main part is calculated to determine the tea shoot axis, and to finally obtain the position coordinates of the picking point. The MR3P-TS model proposed in this paper achieved an mAP of 0.449 and an *F*2 value of 0.313 in shoot identification, and achieved a precision of 0.949 and a recall of 0.910 in the localization of the picking points. Compared with the mainstream object detection algorithms YOLOv3 and Faster R-CNN, the MR3P-TS algorithm had a good recognition effect on the overlapping shoots in an unstructured environment, which was stronger in both versatility and robustness. The proposed method can accurately detect and segment tea bud regions in real complex scenes at the pixel level, and provide precise location coordinates of suggested picking points, which should support the further development of automated tea picking machines.

KEYWORDS

image analysis, deep learning, *Camellia sinensis*, faster region-based convolutional neural network, fine tea picking

Introduction

The tea plant (*Camellia sinensis*) is grown to produce tea, a popular beverage, worldwide. There are many processing steps in tea production, which vary with the different types of tea produced, but tea harvesting is an essential prerequisite for all types of production (Tian et al., 2021). Traditionally, tea harvesting has been performed by hand. However, with the increasing labor cost, lack of specialists, and higher quality requirements from tea producers, mechanized tea picking is becoming an inevitable trend for the sustainable development of the tea industry (Zhu et al., 2021).

Mechanized tea harvesters have been researched and developed in many countries to conform to local production conditions, but harvesters can be mainly classified into a reciprocating cutting type, spiral hob type, horizontal-circle blade type, or spiral roll folding type (Han et al., 2014, 2019). Harvesters can reduce the cost and improve the efficiency of the tea harvest; however, they usually cut the top leaves without distinguishing between the desirable young shoots and older leaves. This leads to the harvested crop containing old and broken leaves and a lower quality of product (Madamombe et al., 2015). At the same time, mechanical harvesters may also damage the stems of trees and affect the germination of new shoots, and potential yield, for the next harvest (Abesinghe et al., 2020).

To improve crop quality from mechanized picking, the first and essential task is to be able to recognize the tender tea shoots and accurately localize the picking points in a complex vegetative system (Li et al., 2021). The more tender the leaves are, the higher the quality and the price achieved. The optimal picking situation is considered to be a single tip with two leaves (Madamombe et al., 2015; Yang et al., 2021). Some traditional image processing-based methods have been proposed to identify these two-leaf tips to achieve such a task (Chen et al., 2015; Ke and Lv, 2016). Wu et al. (2015) detected new tea bud leaves (tips) from among older leaves using color transformation, Otsu's thresholding, and *k*-means clustering. Thangavel and Murthi (2017) counted the number of tea shoots using key frame extraction, rice counting, optical flow, and the Prewitt operator. Karunasena and Priyankara (2020) applied a machine learning object detection technique to identify tea bud leaves and achieved 55% of overall accuracy, while Shao et al. (2018) segmented young leaves in tea images with the HSI color model and the improved *k*-means algorithm. However, the above research actions were performed under controlled conditions and poorly replicated the real conditions within tea fields with complex environments, including uncontrolled illumination and a high level of similarity between the foreground and background (Chen and Chen, 2020).

In comparison to the methods above, convolutional neural networks (CNN) constitute a deeper neural network that provides a hierarchical representation of the data with various convolutions (Lecun and Bengio, 1995; Schmidhuber, 2015). CNN models have shown remarkable performance in various imagery-related problems in agriculture with complex background, including target recognition and detection in unstructured environments (Kamilaris and Prenafeta-Boldú, 2018; Yu et al., 2019). Yang et al. (2019) trained a tea shoot detection model with the improved "you only look once" (YOLO) network and achieved a high accuracy for the validation data set. Chen et al. (2018) achieved tea shoot detection using a faster region-based convolutional neural network (Faster R-CNN), which Chen and Chen (2020) coupled with a fully convolutional network (FCN) to identify the picking point on the tea shoot region. However, the tea shoot picking point detection model of Chen and Chen (2020) is a two-stage model with complicated detection and segmentation steps. Another tea shoot segmentation model, based on the improved deep convolutional encoder-decoder Network (TS-SegNet) with a contrastive-center loss function and skip connections, has also been proposed (Qian et al., 2020), but this model can only realize the semantic segmentation of the tea without distinguishing different tea shoots.

Therefore, there is still an absence of a model that can directly detect the contour of each tea shoot in the image and produce the accurate location of the tea shoots' picking points. In this paper, a Mask R-CNN Positioning of Picking Point for Tea Shoots (MR3P-TS) model is proposed for the identification and picking point positioning of tender tea shoot. The main contributions are as follows: (1) separation of different tea shoots under the complex field background; (2) accurate extraction and counting of the edge information of tea shoots; and (3) end-to-end output of the picking point position coordinates and suggested knife angle.

Materials and methods

Image acquisition

The experimental images were collected in several tea gardens in the West Lake scenic area, Hangzhou, Zhejiang province, China. The target variety was "Longjing 43," which was bred by the tea research institute of the China agricultural science park. In the study, we took RGB images of tea buds with the iPhone rear camera at a distance of 60–80 cm from the tea tree with multiple angles in March 2021. The dual rear cameras we used are divided into wide-angle and ultra-wide-angle lenses. The wide-angle is a 1,200 W pixel camera with F1.6 + 7P lens OIS + dual-core focus, while the ultra wide-angle is a 1,200 W pixel lens with an equivalent focal length of 13 mm + 120° + F2.4. In order to ensure that the model had a good generalization ability and robustness, the image acquisition process included two different light scenarios: under sunny and cloudy conditions. The storage format was JPG. The original images were cropped in a 2*4 ratio to limit the number of shoots per image. After cropping, the pixel resolution of the tea shoot image used in this paper was 1512*1008. The images were visually assessed, and those with a clear shoot outline and a visible picking point were retained, resulting in a final dataset of 464 images. Examples of the acquired images are shown in Figure 1.

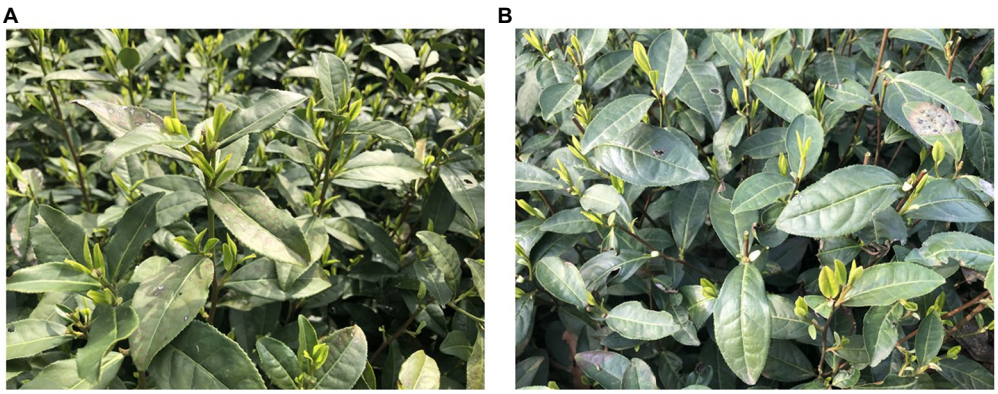

FIGURE 1
Examples of the 1,058 images collected in the study in a natural environment under **(A)** sun-lit conditions and **(B)** cloud-covered conditions.

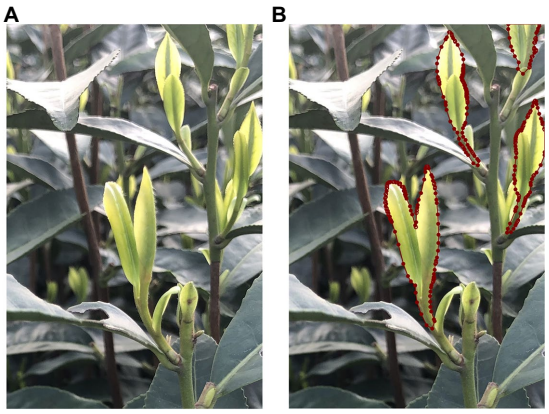

FIGURE 2
Instance segmentation example of tea shoots dataset **(A)** original image, **(B)** the visualization of the boundary points for the mask.

Data set construction and annotation

In order to prevent the model from overfitting during the training process, image augmentation was used to expand the dataset. The image-augmented data reduced the unbalanced distribution of samples and improved the generalization ability of the model. The methods of image augmentation used in the study mainly included scale transformation, flip transformation, and pixel value normalization.

After data augmentation processing, the imagery dataset was randomly divided into three groups, with the ratio of 70, 20, and 10%, to form the model training, model validation, and testing datasets, respectively. The training set was used to learn the weight parameters in the model training process, the validation set was used to optimize the network model structure, and the testing set was used to verify the accuracy of the proposed method. The image data of tea shoots were annotated by LabelMe (Russell, 2008), an open-source annotation tool from the Massachusetts Institute of Technology (MIT), to generate masks of the tea shoots. These masks were used for model training and parameter optimization, and the inverse loss was calculated and compared with the predicted results to evaluate the instance segmentation performance of the model. The tea shoot area in the image was labeled, and the rest of the image was denoted as the background by default. An example of a raw and annotated tea shoot image is shown in Figure 2.

MR3P-TS model

An overview of the proposed method, the MR3P-TS model for tea shoot identification and picking point positioning, is shown in Figure 3. The MR3P-TS model was extended from the Mask R-CNN framework (He et al., 2017) and can be divided into three stages. In the first stage, the backbone network is used to extract feature maps from the input image, and then, the feature maps are sent to the region proposal network (RPN) to generate regions of interest (RoIs). In the second stage, RoIs are mapped to the feature map to extract the corresponding target features, which are sent to the head network to predict the target box and mask. The head network includes a fully connected layer (FC layer) and a fully convolutional network (FCN). The third stage is the positioning method of the picking point. The mask obtained in the second stage is subjected to maximum connected domain processing to obtain the main part of the shoot. Then, the minimum circumscribed rectangle of the main body is calculated to determine the axis of the shoots from which the position coordinates of the picking point can be determined.

Feature extraction and generation of regions of interest

The backbone network is usually a neural network with a certain depth to extract feature maps from the input image. When the number of network layers is deepened, the model's expressive ability does not always theoretically strengthen, and the model will degenerate, that is, the network will converge slowly and the

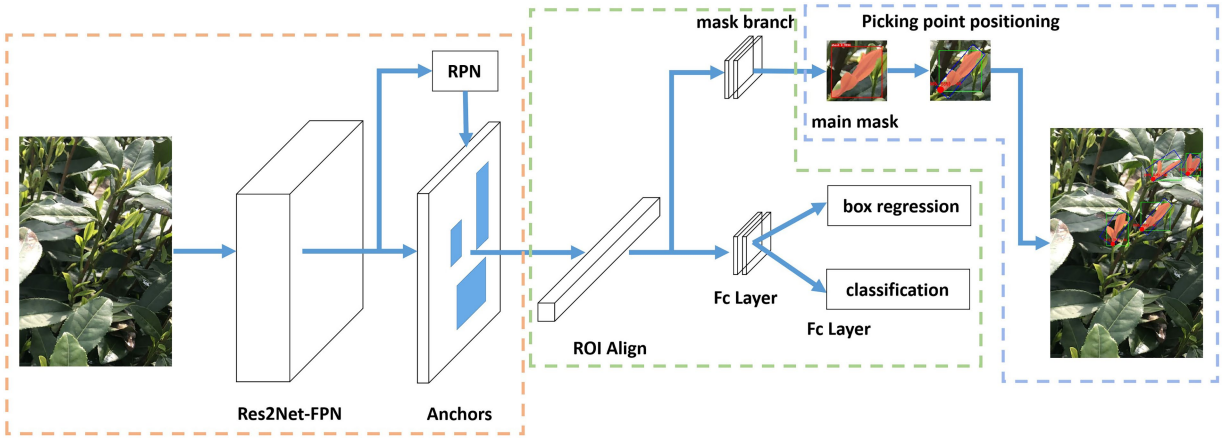

FIGURE 3
Schematic overview of the complete Mask R-CNN Positioning of Picking Point for TeaShoots (MR3P-TS) model structure.

training accuracy will decrease (He and Jian, 2015; Srivastava et al., 2015). The emergence of the residual network model (ResNet; He et al., 2016) has solved this problem. As a network structure with cross-layer connection, ResNet builds a residual structure on the basis of the VGG model, and connects the shallow network and the deep network across layers to enable deep training. Errors can be back-propagated to shallow layers, effectively alleviating the issue of training degradation. As an improvement of ResNet, Res2Net (Gao et al., 2019) adds a small residual block to the original residual unit structure, which enables the network to represent multi-scale features at a finer granularity and increases the receptive field of each layer of the network.

Feature pyramid network (FPN), as a feature extraction network, can be used to assist ResNet in feature extraction. Using a top-down architecture with horizontal connections, FPN can fuse feature maps with strong low-resolution semantic information and feature maps with weak high-resolution semantic information by providing rich spatial information with less computation. This makes feature maps of different sizes in each layer of the FPN network that have strong semantic information, and allows the prediction of the feature maps of each layer separately.

The feature map output by the backbone network is used as the input of the Region Proposal Network (RPN) to extract candidate boxes, and then, the boxes generate Regions of Interest (RoIs). The RPN network is a module specially used to extract candidate boxes. It slides over the feature map through nine anchor boxes of different scales and proportions and further filters the anchor boxes according to the foreground score before using the bounding box regression parameters to correct the anchor boxes. Anchor boxes that cross the image boundary after correction are discarded. During the training process, each image generated too many RoIs. In the study, RoIs with an Intersection over Union (IoU) greater than 0.7 by non-maximum suppression were removed. The threshold of 0.7 was chosen based on expert experience with these images.

Target detection and instance segmentation

In order to map the RoIs to the feature map to extract the corresponding target features, a region of interest alignment (RoI Align) method was used to replace the region of interest pooling (RoI Pooling) in the Faster R-CNN network. Pixel-level segmentation was achieved by using a mask branch, on the premise that the precise position of the input feature can be obtained. RoI Align eliminates the quantization operation and does not quantify the RoI boundary and unit. It preserves the decimal point and then uses bilinear interpolation to calculate the exact location of the sampling point in each unit, and uses max pooling or average pooling to output the final fixed-size RoI. Finally, it uses the head network to make predictions, including an FC layer for classification prediction, a regression layer for bounding box coordinate correction, and an FCN for instance segmentation to generate object masks.

Position of the tea shoots picking point

While maintaining the classification and bounding box regression, a parallel branch is added in the model structure (Figure 3) to output a binary mask that reflects the position and shape of the target object in the RoIs. Tea shoots generally grow vertically, and the picking points are generally distributed below the intersection of the shoot axis and the leaf. Therefore, the basis for positioning the tea picking point is to determine the direction of the shoot axis. Through empirical observation, it was found that the picking points are often located at a point of approximately 2% of the total shoot length starting from the bottom of the masked area. The final output also includes a suggested knife angle, i.e., the inclination angle of the shoot axis to the knife, which can meet the requirements of a simple shoot picking robot. The whole process of selecting the picking point is shown in Figure 4. Firstly, by looking for the maximum connected domain in the shoot identification result (Figure 4A), the picking point prediction regions are located, which are called as the main mask (Figure 4B), because picking points are often more likely to be found in connected domains with

larger areas. The minimum bounding rectangle of the main mask is calculated to obtain the shoot axis and the suggested knife angle (Figure 4C). The shoot axis is taken from the rotation angle of the minimum bounding rectangle, and the angle θ between the bottom edge of the rectangular box and the shoot axis is the suggested knife angle. Finally, the position of the picking point, at 2% of the total mask length starting from the bottom, is identified (Figure 4D).

Loss function

The loss function of the model consists of two parts, namely the RPN network loss and the head network loss. The loss function is defined as follows:

$$L = L_{RPN} + L_{head}.$$

Among them, L_{RPN} contains classification loss and bounding box regression loss, which is:

$$L_{RPN} = L_{cls} + L_{reg} = \frac{1}{N_{cls1}}\sum_i L_{cls}\left(p_i, p_i^*\right) + \lambda_1 \frac{1}{N_{reg1}}\sum_i p_i^* L_{reg}\left(t_i, t_i^*\right).$$

In the formula, i represents the anchor index, p_i represents the positive softmax probability, p_i^* represents the corresponding GT predict probability. When IoU > 0.7 between the ith anchor and GT, the anchor is supposed to be positive, $p_i^* = 1$. When IoU < 0.3, the anchor is supposed to be negative, $p_i^* = 0$. As for those anchors with 0.3 < IoU < 0.7, they do not participate in training. t represents the predict bounding box, t^* represents the GT box corresponding to the positive anchor, and $\lambda_1$is an adjustable parameter used to balance the number of anchors $N_{cls1}$and the number of bounding boxes N_{reg1}. L_{cls} uses the binary cross-entropy loss, and L_{reg} uses the smooth_{L1} loss.

L_{head} contains classification, bounding box regression and mask loss, which is:

$$L_{\text{head}} = \frac{1}{N_{\text{cls}2}}\sum_i L_{\text{cls}}\left(p_i, p_i^*\right) + \lambda_2 \frac{1}{N_{\text{reg}2}}\sum_i p_i^* L_{\text{reg}}\left(t_i, t_i^*\right) + \gamma \frac{1}{N_{\text{mask}}}\sum_i L_{\text{mask}}\left(s_i, s_i^*\right).$$

In the formula, s represents the binary predict mask, s^* represents the GT mask of the corresponding category. L_{mask} is the binary cross-entropy loss of a single category, and only calculates the loss of the corresponding category for each pixel, avoiding competition between classes. The calculation formulas of classification loss L_{cls} bounding box regression loss L_{reg} and mask loss L_{mask} are as follows:

$$L_{\text{cls}}\left(p_i^*, p_i\right) = -p^* \log p$$

$$L_{\text{reg}}\left(t_i^*, t_i\right) = \text{smooth}_{L1}\left(t^* - t\right),$$

$$\text{smooth}_{L1}(x) = \begin{cases} 0.5x^2 \text{ if } |x| < 1 \\ |x| - 0.5 \text{ otherwise} \end{cases}.$$

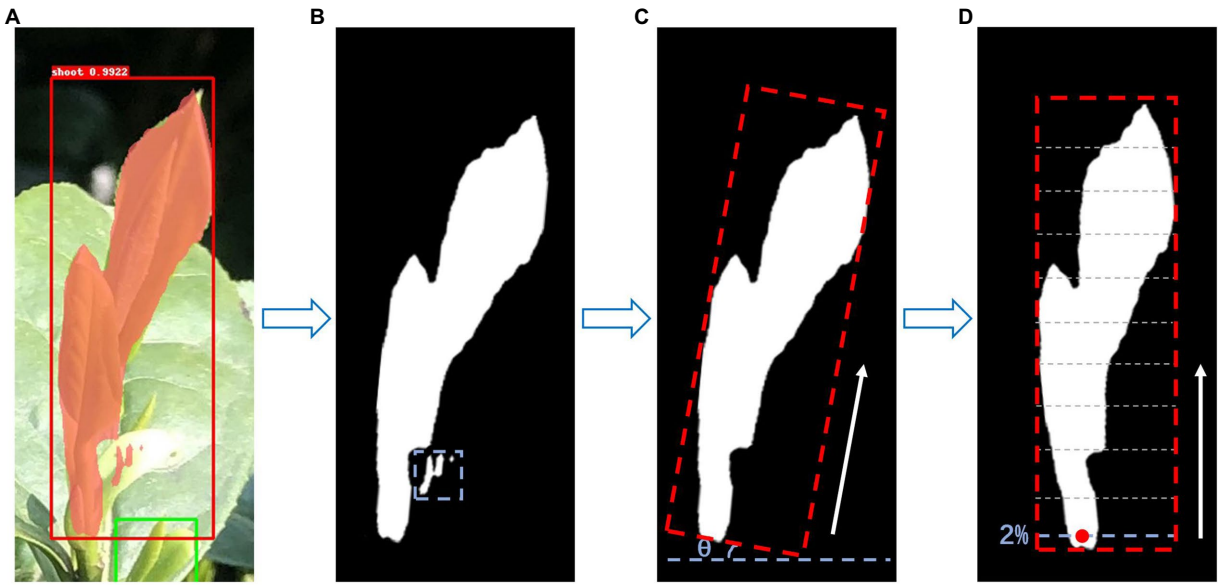

FIGURE 4
Implementation of picking point determination **(A)** the result of the contour of shoot identification, **(B)** the determination of the shoot main mask, **(C)** calculation of the minimum circumscribed rectangle, and **(D)** calculation of the 2D coordinate information of the picking point.

$$L_{\text{mask}}\left(s_i^*, s_i\right) = -\left(S^* \text{logs} + \left(1 - s^*\right)\log\left(1 - s\right)\right).$$

Evaluation

Evaluation of tea shoots identification

For the bounding box regression and mask output by the model, F_β was chosen as the performance metric to evaluate the shoot identification problem. F_β can express the different preferences of the task for precision mAP and recall mAR and is defined as:

$$F_\beta = \frac{\left(1+\beta\right)\times mAP \times mAR}{\left(\beta^2 \times mAP\right) + mAR}.$$

In the task of machine picking, the picking machine needs to capture images from multiple angles of the same cluster of tea trees, in order to alleviate the classic problem that the shoots are occluded and cannot be correctly identified due to the dense growth of tea leaves. The increase of the acquisition angle makes it more important to pay attention to whether the shoots can be correctly identified when evaluating the model, rather than missing the shoots as little as possible. So, the contribution of the precision rate to the performance measurement should be greater. Based on experience and the actual meaning of each parameter, we finally decided to set β to 2.

The IoU evaluates the overlap between the generated candidate box (Candidate bound, C) and the ground truth bound (ground truth bound, G), which is defined as follows:

$$\text{IoU} = \frac{area\left(c\right) \cap area\left(G\right)}{area\left(c\right) \cup area\left(G\right)}.$$

mAP and mAR are an average concept, which is the average of each precision rate and recall rate when IoU takes [0.45:0.05:0.95], which is defined as follows:

$$\text{mAP} = \frac{1}{11}\sum_{\text{IoU}=0.5}^{0.95} \frac{\text{TP@IoU}}{\text{TP@IoU} + \text{FP@IoU}}.$$

$$\text{mAR} = \frac{1}{11}\sum_{\text{IoU}=0.5}^{0.95} \frac{\text{TP@IoU}}{\text{TP@IoU} + \text{FN@IoU}}.$$

For tea picking machines, in addition to the localization performance of the model, the performance of real-time detection is also very important. A fast processing and decision speed is needed to improve picking efficiency. A common metric for evaluating speed is Frame Per Second (FPS). The higher the FPS, the more pictures can be processed per second, the faster the speed, and the more effective the model will be in operational situations.

The F_β and FPS were chosen as the performance metrics for the shoot identification task. The relationship between the two and the model evaluation is that the larger the value, the better the model.

Evaluation of the position for tea shoots picking points

Precision and recall were used as performance metrics for the picking point location:

$$\text{precision} = \frac{\text{ED}}{\text{ED} + \text{ND}},$$

$$\text{recall} = \frac{\text{ED}}{\text{ED} + \text{EN}},$$

where ED, EN, and ND are calculated from the confusion matrix, the row sum of the confusion matrix represents the number of true markers of the picking point, and the column sum represents the number of predicted markers of the picking point. In this paper, P represents the positive examples, and N represents the negative examples. The specific representation is shown in Table 1.

Results and discussion

The experimental computing platform is a Tesla V100 graphics processing unit (GPU) with 16 GB of video memory (NVIDIA, Santa Clara, CA, United States). The experimental training tasks are pre-trained based on the COCO dataset, which is a large-scale dataset used for various tasks, such as image classification, object detection, and image segmentation (Lin et al., 2014). By adjusting the parameters, the optimal model was

TABLE 1 Definition of confusion matrix.

Confusion matrix		Prediction category (Picking point detected)	
		P	N
Actual category (Picking point exists)	P	ED (Picking point exists and detected)	EN (Picking point exists but not detected)
	N	ND (Pick point does not exist but is detected)	/

obtained with the best learning rate, batch size, and backbone. Meanwhile, the MR3P-TS model was compared with several mainstream target detection model including YOLOv3 (Redmon and Farhadi, 2018) and FasterRCNN (Ren et al., 2017), and showed the practical performance on the testing dataset.

Parameter adjustment experiment

In order for the model to achieve the best results, it was necessary to design an experiment to tune the hyperparameters, such as the epoch number, the grid structure, and some function choices in the network. The sources of adjustment parameters can be divided into data processing, training, and network parameters. In this experiment, a set of parameters with the best performance was determined by testing different learning rates and batch sizes for the MR3P-TS model.

The decrease of the loss curve of the models with different learning rates during the training process is shown in Figure 5. A smaller learning rate, although it is possible for the loss value to drop even lower, converges significantly slower than other models with larger learning rates, and is more likely to fall into the local minima. So, the learning rate in this group of test values was set to 0.01.

TABLE 2 Evaluation results of different batch size.

Batch size	mAP	mAR	Training time
1	0.511	0.558	1 h 4 m (60 epoch)
2	0.389	0.441	1 h 35 m (100 epoch)
4	0.280	0.372	1 h 17 m (100 epoch)
8	0.274	0.374	1 h 21 m (100 epoch)
16	0.286	0.360	1 h 25 m (100 epoch)

The evaluation results of different batch sizes in the dataset are shown in Table 2. The training time remained at the same level due to the parallel computing power of the GPU. As the batch size increased, the evaluation data of the model in the training set and the test set declined. This is because a large batch size needed more training data to update the gradient, which means that the larger updated step size was easier to converge to the sharp minima (Keskar et al., 2016). In the model training, the optimal batch size was 1 in this study.

The evaluation results on the different backbone datasets are shown in Figure 6. The detection speed of the Res2Net network was slower than that of the ResNet101 network with similar F2 values, and the detection speed of HRNet was the slowest. From the detection results of the model, the HRNet was the best, but it cannot meet the requirements for real-time detection. Although the effect of Res2Net was slightly worse than HRNet, it was much higher than other networks. Therefore, combining the above two indicators, the optimal backbone in the experiment was Res2Net.

Figure 6B shows the actual detection results of different backbones for several example images. As shown in Figures 6B,C, there were holes (non-masked areas) within the identification results of the shoot mask when using ResNext101, which resulted in incomplete identification of the shoots. In the recognition results shown in Figure 6B, ResNet101 and HRNet had many missed detections. The results of ResNet50 were similar to Res2Net, but Res2Net's FPS and F2 indicators were better than ResNet50. As a

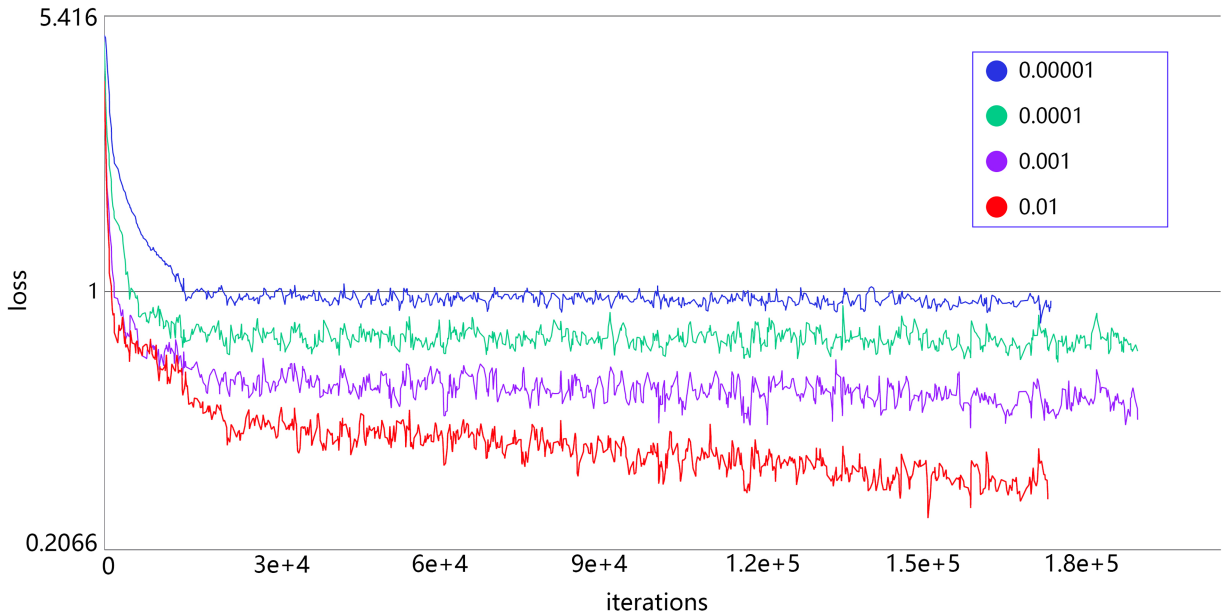

FIGURE 5
The decline of the loss curve of different learning rates during the training process.

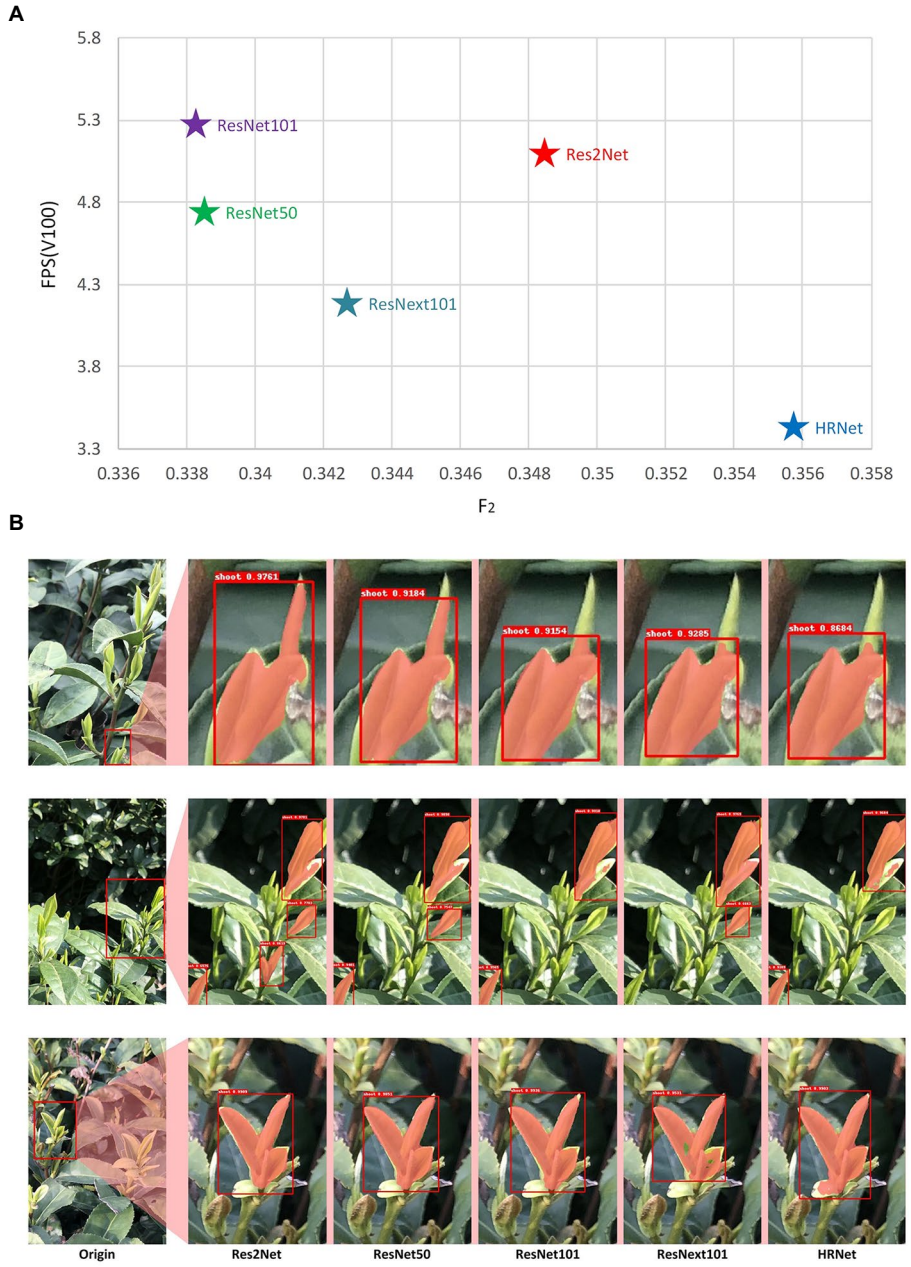

FIGURE 6
Evaluation results of different backbone **(A)** the relationship between F_2 and FPS of model with different backbones, **(B)** the practical performance of models with different backbones on selected areas of a larger scene.

result of these tests, the learning rate was set to 0.01, batch size to 1, and Res2Net was selected as the backbone network for all subsequent image analyses with the MR3P-TS method.

Comparison results of segmentation methods for tea shoots detection

The MR3P-TS model was compared with the YOLOv3 and Faster R-CNN algorithms for tea shoot location and segmentation to verify that the MR3P-TS model had better performance on the missed detection and overlapping problems.

In the actual picking operation, the method of detecting the same area from multiple angles can be adopted to solve the problem of tea shoot obscuration, so the focus here was on how well the segmentation approach detected shoots, rather than the reduction of missed shoots. Therefore, the F2 statistic was used as the primary performance measure as the accuracy was considered more important than the recall rate.

TABLE 3 Recognition results of several models.

Model	Evaluation indicators		
	mAP	mAR	F_2
MR3P-TS	0.449	0.544	0.313
YOLOv3	0.484	0.615	0.350
Faster R-CNN	0.446	0.555	0.317



FIGURE 7
Example illustrating local details of the instance segmentation results of the MR3P-TS, YOLO_V3, and Faster R-CNN models.

From the data of the study results (Table 3), the MR3P-TS model proposed in this paper obtained an mAP of 0.449 and an F2 value of 0.313 in the test set. The F2 values of YOLOv3 and Faster R-CNN algorithms were 0.350 and 0.317, respectively.

The prediction results of the various models obtained from the testing set were visualized and examples are shown in Figure 7. The Faster R-CNN model had obvious target overlap, and the YOLOv3 model had two obvious missed detection phenomena. In contrast, the proposed MR3P-TS model actually performed better in the detection task of overlapping objects and edge objects. To sum up, although the MR3P-TS model still needs to be optimized in terms of data indicators, its performance was excellent in the actual tests. Therefore, it can be considered that the proposed MR3P-TS model was more suitable for solving the problem of tea shoot identification and picking point location compared to the well-known YOLOv3 and Faster R-CNN methods.

Picking point position result

An example of the final result of the model evaluation with shoot identification and picking point positioning identified from the independent testing set is shown in Figure 8 (more detection results listed in the supplemental material). With the exception of some unfocused areas in the images, the model produced accurate representations of the shoot segmentation in complex scenes, and generated the coordinates of the two-dimensional picking point and the suggested knife angle. In total, the proposed MR3P-TS model identified 128 picking points in 42 images within the testing set, of which 111 were correctly identified, and the precision of the picking point positioning was 0.949, and the recall was 0.910.

As shown in Figure 8A, the set in parentheses represented the position coordinates of the picking point relative to the upper left corner of the image, and the following values are the angle information, which was the angle between the bottom edge of the rectangular box and the shoot axis.

General discussion

Compared with the indoor measurement images under ideal and stable lighting conditions, the shoot images acquired in the tea garden environment with complex background were affected by light and wind, which affects the accuracy of tea shoots detection. To further improve the accuracy of shoot recognition, it is intended to add an attention module to the model in future research. The attention mechanism has been shown to improve the accuracy of the model (Nie et al., 2020; Wang et al., 2022). At the same time, in order to apply the model to the actual mechanized tea picking task, the corresponding mechanical structure and a complete visual recognition system can be designed for the tea picking machine in the future, and the model can be deployed to the development board to achieve fine tea picking.

In order to apply the model to the actual mechanized tea picking task, the model can be deployed to the development board, and the corresponding mechanical structure and complete visual recognition system can be designed for the tea picking machine to realize the fine picking of tender shoots. At present, some literature has been reported to use binocular depth cameras to collect field fruit images, and design a fruit spatial positioning system (Zhang et al., 2021). Some other researchers have proposed methods of connecting the manipulator with the tea picking machine, which provides theoretical support for this line of

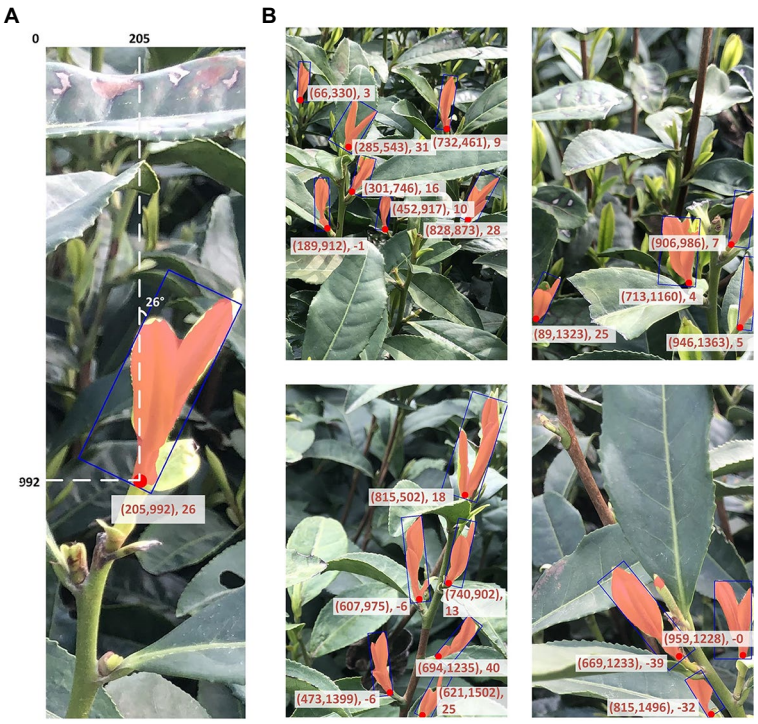

FIGURE 8
Examples of the resulting outcome of the MR3P-TS model **(A)** a single sample example of the shoot output, and **(B)** four images showing multiple tea shoots and picking point identification from the MR3P-TS model.

thinking (Yang et al., 2021). However, to realize a fully automated harvesting system there are still many aspects to work on, such as how to integrate the deployed model with the depth information provided by the binocular camera and how to debug the manipulator and other structures.

Conclusion

In this study, a novel approach was proposed to identify the contour and counting of tender tea shoots and locate the picking points under field conditions. It is a three-step model using Res2Net as the backbone network to generate candidate regions, extract features, discriminate feature categories, and correct the position of candidate boxes, and finally extract masks for localization of picking points. By using an image dataset containing different lighting information for the model learning, the MR3P-TS model can directly use the two-dimensional mask obtained from the parallel prediction mask branch for the localization of the picking points. In the test set, the proposed MR3P-TS model achieved an mAP of 0.449 and an F2 value of 0.313 in shoot identification, and achieved a precision of 0.949 and a recall of 0.910 in localization of picking points. The samples of the multi-target overlap in the target detection were obviously less than other target detection algorithms with better numerical values and better actual engineering effect. The MR3P-TS algorithm has provided the necessary basic information for the realization of an automated tea picking machine. In future research, the intent is to design a reasonable tea picking scheme to better identify the shoots and locate the picking point and to encapsulate the process within a web interface and within an embedded imaging system. This will undoubtedly improve the automation level of tea production and contribute to the cause of agricultural science and technology.

Data availability statement

The raw data supporting the conclusions of this article will be made available by the authors, without undue reservation.

Author contributions

DC, LY, and JL conceptualized the topic of the article and designed this study. LY and JL collected the tea sprout data and marked the data. JL and XZ performed method validation and results collation. LY, JL, and DC did the original draft preparation. DC, JT, XX, JZ, and KW commented and edited the draft. All authors contributed to the article and approved the submitted version.

Funding

This research was supported by the Zhejiang Provincial Natural Science Foundation of China under grant no. LGN19F030001, National Key R&D Program of China (2019YFE0125300); and Zhejiang Agricultural Cooperative and Extensive Project of Key Technology (2020XTTGCY04-02 and 2020XTTGCY01-05).

Conflict of interest

The authors declare that the research was conducted in the absence of any commercial or financial relationships that could be construed as a potential conflict of interest.

Publisher's note

All claims expressed in this article are solely those of the authors and do not necessarily represent those of their affiliated organizations, or those of the publisher, the editors and the reviewers. Any product that may be evaluated in this article, or claim that may be made by its manufacturer, is not guaranteed or endorsed by the publisher.

Supplementary material

The supplementary material for this article can be found online at: https://www.frontiersin.org/articles/10.3389/fpls.2022.962391/full#supplementary-material

References

Abesinghe, A., Ksp, A., Ekanayake, E., Kavindi, M., and Mohotti, A. (2020). Developing A selective tea plucking mechanism using image processing For A drone-based tea harvesting machine. *GSJ*. 8, 526–533.

Chen, Y., and Chen, S. (2020). Localizing plucking points Of tea leaves using deep convolutional neural networks. *Comput. Electron. Agric.* 171:105298. doi: 10.1016/J.Compag.2020.105298

Chen, J., Chen, Y., Jin, X., Che, J., Gao, F., and Li, N. (2015). "Research on a parallel robot for green tea flushes plucking." in *Proceedings of The 5th International Conference On Education, Management, Information and Medicine*; April 24-26, 2015; 22–26.

Chen, Y., Wu, C., and Chen, S. (2018). Application of deep learning algorithm on tea shoot identification and localization. ASABE annual international meeting, 2018. *Am. Soc. Agric. Biol. Eng.*, 1. doi: 10.13031/Aim.201801253

Gao, S., Cheng, M. M., Zhao, K., Zhang, X. Y., and Torr, P. (2019). Res2net: a new multi-scale backbone architecture. *IEEE Trans. Pattern Anal. Mach. Intell.* 43, 652–662. doi: 10.1109/Tpami.2019.2938758

Han, Y., Xiao, H., Qin, G., Song, Z., Ding, W., and Mei, S. (2014). Developing situations of tea plucking machine. *Engineering* 06, 268–273. doi: 10.4236/Eng.2014.66031

Han, Y., Xiao, R. H., Song, Y. Z., and Ding, Q. W. (2019). Design and evaluation of tea-plucking machine for improving quality of tea. *Appl. Eng. Agric.* 35, 979–986. doi: 10.13031/Aea.13116

He, K., Gkioxari, G., Dollár, P., and Girshick, R. (2017). Mask R-Cnn. *IEEE Trans. Pattern Anal. Mach. Intell.* 2961–2969. doi: 10.1109/Iccv.2017.322

He, K., and Jian, S. (2015). "Convolutional neural networks At constrained time cost." in *2015 IEEE Conference On Computer Vision and Pattern Recognition (Cvpr)*; June 1, 2015.

He, K., Zhang, X., Ren, S., and Sun, J. (2016). Deep residual learning for image recognition. *IEEE*. 770–778. doi: 10.1109/Cvpr.2016.90

Kamilaris, A., and Prenafeta-Boldú, F. X. (2018). Deep learning in agriculture: a survey. *Comput. Electron. Agric.* 147, 70–90. doi: 10.1016/J.Compag.2018.02.016

Karunasena, G., and Priyankara, H. (2020). Tea bud leaf identification by using machine learning and image processing techniques. *Int. J. Sci. Eng. Res.* 11, 624–628. doi: 10.14299/Ijser.2020.08.02

Ke, Z., and Lv, J. (2016). Study on automatic segmentation of tea sprouts under natural conditions. *J. Heilongjiang Bayi Agric. Univ.* 28, 100–104. doi: 10.3969/j.issn.1002-2090.2016.02.021

Keskar, N. S., Mudigere, D., Nocedal, J., Smelyanskiy, M., and Tang, P. T. P. (2016). On large-batch training for deep learning: generalization gap and sharp minima. Arxiv [Epub ahead of Preprint], doi:10.48550/Arxiv.1609.04836

Lecun, Y., and Bengio, Y. (1995). "Convolutional networks for images, speech, and time series," in *The Handbook Of Brain Theory And Neural Networks*. ed. M. A. Arbib (Cambridge, MA: MIT Press).

Li, Y., He, L., Jia, J., Lv, J., Chen, J., Qiao, X., et al. (2021). In-field tea shoot detection and 3d localization using an Rgb-D camera. *Comput. Electron. Agric.* 185:106149. doi: 10.1016/J.Compag.2021.106149

Lin, T. Y., Maire, M., Belongie, S., Hays, J., and Zitnick, C. L. (2014). *Microsoft Coco: Common Objects In Context*. Cham: Springer International Publishing.

Madamombe, G., Tesfamariam, E., and Taylor, N. (2015). Yield decline In mechanically harvested clonal tea (camellia Sinensis (L) O. Kuntze) As influenced by changes In source/sink and radiation interception dynamics in the canopy. *Sci. Hortic.* 194, 286–294. doi: 10.1016/J.Scienta.2015.08.009

Nie, X., Duan, M., Ding, H., Hu, B., and Wong, E. K. (2020). Attention mask R-Cnn for ship detection and segmentation From remote sensing images. *IEEE Access* 8, 9325–9334. doi: 10.1109/Access.2020.2964540

Qian, C., Li, M., and Ren, Y. (2020). Tea sprouts segmentation via improved deep convolutional encoder-decoder network. *IEICE Trans. Inf. Syst.* E103.D, 476–479. doi: 10.1587/Transinf.2019edl8147

Redmon, J., and Farhadi, A. (2018). Yolov3: an incremental improvement. *Arxiv* [Epub ahead of preprint]. doi:10.48550/Arxiv.1804.02767

Ren, S., He, K., Girshick, R., and Sun, J. (2017). Faster R-Cnn: towards real-time object detection with region proposal networks. *IEEE Trans. Pattern Anal. Mach. Intell.* 39, 1137–1149. doi: 10.1109/Tpami.2016.2577031

Russell, B. (2008). Labeme: a database and web-based tool for image annotation. *Int. J. Comput. Vis.* 77, 157–173. doi: 10.1007/S11263-007-0090-8

Schmidhuber, J. (2015). Deep learning In neural networks: An overview. *Neural Netw.* 61, 85–117. doi: 10.1016/J.Neunet.2014.09.003

Shao, P., Wu, M., Wang, X., Zhou, J., and Liu, S. (2018). "Research on the tea bud recognition based on improved k-means algorithm," *MATEC Web of Conferences.* 232:03050.

Srivastava, R. K., Greff, K., and Schmidhuber, J. (2015). Highway networks. *Comput. Sci.* doi: 10.48550/Arxiv.1505.00387

Thangavel, S. K., and Murthi, M. A. (2017). Semi automated system for smart harvesting of tea leaves. 2017 4th international conference on advanced computing and communication systems (ICACCS). *IEEE*, 1–10. doi: 10.1109/Icaccs.2017.8014724

Tian, J., Zhu, H., Liang, W., Chen, J., Wen, F., and Long, Z. (2021). Research on the application of machine vision in tea autonomous picking. *J. Phys. Conf. Ser.* 1952:022063. doi: 10.1088/1742-6596/1952/2/022063

Wang, G., Lin, J., Cheng, L., Dai, Y., and Zhang, T. (2022). Instance segmentation convolutional neural network based On multi-scale attention mechanism. *PLoS One* 17:E0263134. doi: 10.1371/Journal.Pone.0263134

Wu, X., Tang, X., Zhang, F., and Gu, J. (2015). Tea buds image identification based on lab color model and K-means clustering. *J. Chin. Agric. Mechanization.* 36, 161–164. doi: 10.13733/j.jcam.issn.2095-5553.2015.05.040

Yang, H., Chen, L., Chen, M., Ma, Z., Deng, F., Li, M., et al. (2019). Tender tea shoots recognition and positioning for picking robot using improved Yolo-V3 model. *IEEE Access* 7, 180998–181011. doi: 10.1109/Access.2019.2958614

Yang, H., Chen, L., Ma, Z., Chen, M., Zhong, Y., Deng, F., et al. (2021). Computer vision-based high-quality tea automatic plucking robot using Delta parallel manipulator. *Comput. Electron. Agric.* 181:105946. doi: 10.1016/J.Compag.2020.105946

Yu, Y., Zhang, K., Yang, L., and Zhang, D. (2019). Fruit detection For strawberry harvesting robot In non-structural environment based On mask-Rcnn. *Comput. Electron. Agric.* 163:104846. doi: 10.1016/J.Compag.2019.06.001

Zhang, X., Gao, Q., Pan, D., Cao, P. C., and Huang, D. H. (2021). Research on spatial positioning system of fruits to be picked in field based on binocular vision And Ssd model. *J. Phys. Conf. Ser.* 1748:042011. doi: 10.1088/1742-6596/1748/4/042011

Zhu, Y., Wu, C., Tong, J., Chen, J., He, L., Wang, R., et al. (2021). Deviation tolerance performance evaluation and experiment of picking end effector for famous tea. *Agriculture* 11:128. doi: 10.3390/Agriculture11020128

frontiers | Frontiers in Plant Science

TYPE Methods
PUBLISHED 25 August 2022
DOI 10.3389/fpls.2022.938216

Check for updates

OPEN ACCESS

EDITED BY
Surya Kant,
La Trobe University,
Australia

REVIEWED BY
Chengquan Zhou,
Zhejiang Academy of Agricultural Sciences,
China
Elvis Felipe Elli,
Iowa State University,
United States

*CORRESPONDENCE
Haikuan Feng
fenghk@nercita.org.cn

†These authors have contributed equally to this work

SPECIALTY SECTION
This article was submitted to Sustainable and Intelligent Phytoprotection, a section of the journal Frontiers in Plant Science

RECEIVED 28 June 2022
ACCEPTED 13 July 2022
PUBLISHED 25 August 2022

CITATION
Liu Y, Feng H, Yue J, Jin X, Li Z and Yang G (2022) Estimation of potato above-ground biomass based on unmanned aerial vehicle red-green-blue images with different texture features and crop height. *Front. Plant Sci.* 13:938216. doi: 10.3389/fpls.2022.938216

COPYRIGHT
© 2022 Liu, Feng, Yue, Jin, Li and Yang. This is an open-access article distributed under the terms of the Creative Commons Attribution License (CC BY). The use, distribution or reproduction in other forums is permitted, provided the original author(s) and the copyright owner(s) are credited and that the original publication in this journal is cited, in accordance with accepted academic practice. No use, distribution or reproduction is permitted which does not comply with these terms.

Estimation of potato above-ground biomass based on unmanned aerial vehicle red-green-blue images with different texture features and crop height

Yang Liu[1,2,3†], Haikuan Feng[1,4*†], Jibo Yue[5], Xiuliang Jin[6], Zhenhai Li[1] and Guijun Yang[1]

[1]Key Laboratory of Quantitative Remote Sensing in Agriculture of Ministry of Agriculture and Rural Affairs, Information Technology Research Center, Beijing Academy of Agriculture and Forestry Sciences, Beijing, China, [2]Key Laboratory of Smart Agriculture System, Ministry of Education, China Agricultural University, Beijing, China, [3]Key Laboratory of Agricultural Information Acquisition Technology, Ministry of Agriculture and Rural Affairs, China Agricultural University, Beijing, China, [4]College of Agriculture, Nanjing Agricultural University, Nanjing, China, [5]College of Information and Management Science, Henan Agricultural University, Zhengzhou, China, [6]Institute of Crop Sciences, Chinese Academy of Agricultural Sciences/Key Laboratory of Crop Physiology and Ecology, Ministry of Agriculture, Beijing, China

Obtaining crop above-ground biomass (AGB) information quickly and accurately is beneficial to farmland production management and the optimization of planting patterns. Many studies have confirmed that, due to canopy spectral saturation, AGB is underestimated in the multi-growth period of crops when using only optical vegetation indices. To solve this problem, this study obtains textures and crop height directly from ultrahigh-ground-resolution (GDS) red-green-blue (RGB) images to estimate the potato AGB in three key growth periods. Textures include a grayscale co-occurrence matrix texture (GLCM) and a Gabor wavelet texture. GLCM-based textures were extracted from seven-GDS (1, 5, 10, 30, 40, 50, and 60cm) RGB images. Gabor-based textures were obtained from magnitude images on five scales (scales 1–5, labeled S1–S5, respectively). Potato crop height was extracted based on the generated crop height model. Finally, to estimate potato AGB, we used (i) GLCM-based textures from different GDS and their combinations, (ii) Gabor-based textures from different scales and their combinations, (iii) all GLCM-based textures combined with crop height, (iv) all Gabor-based textures combined with crop height, and (v) two types of textures combined with crop height by least-squares support vector machine (LSSVM), extreme learning machine, and partial least squares regression techniques. The results show that (i) potato crop height and AGB first increase and then decrease over the growth period; (ii) GDS and scales mainly affect the correlation between GLCM- and Gabor-based textures and AGB; (iii) to estimate AGB, GLCM-based textures of GDS1 and GDS30 work best when the GDS is between 1 and 5cm and 10 and 60cm, respectively (however, estimating potato AGB based on Gabor-based textures gradually deteriorates as the Gabor convolution kernel scale increases); (iv) the AGB estimation based on a single-type texture is not as good as estimates based on multi-resolution GLCM-based and multiscale Gabor-based textures (with the latter being the best); (v) different forms of textures combined with crop height using the LSSVM technique improved by 22.97, 14.63, 9.74, and

8.18% (normalized root mean square error) compared with using only all GLCM-based textures, all Gabor-based textures, the former combined with crop height, and the latter combined with crop height, respectively. Therefore, different forms of texture features obtained from RGB images acquired from unmanned aerial vehicles and combined with crop height improve the accuracy of potato AGB estimates under high coverage.

KEYWORDS

UAV, RGB images, GLCM-/Gabor-based textures, crop height, above-ground biomass

Introduction

The above-ground biomass (AGB) of crops is the total dry organic mass of the above-ground vegetative organs per unit area at a particular time (Zhou et al., 2018). AGB is an essential phenotypic parameter for evaluating crop growth and predicting yield (Zhou et al., 2019). In addition, crop AGB information is a vital decision-making indicator for simulating nitrogen concentration dilution curves, which play an essential role in determining the nitrogen nutrition status and guiding fertilization management (Huang et al., 2015). Traditionally, manual measurement of AGB requires destructive sampling and weighing, which is a highly subjective, time-consuming, and labor-intensive manner to estimate from point to area (Liu et al., 2021a). At the same time, the constraints of sampling points and the variability of the field environment make this inefficient method to acquire AGB unsuited for large-scale real-time monitoring of crop growth (Castaldi et al., 2015). Therefore, new technologies are needed to quickly and accurately estimate the AGB of large-scale crops to provide scientific guidance for improving field management and increasing yield.

Remote-sensing technology is currently the most effective non-contact method for estimating crop AGB over large scales (David et al., 2020). To estimate the AGB of large-scale crops, satellite remote-sensing data (e.g., Sentinel-2, Landsat 8-OLI, and Worldview-2) is the best choice because of its advantages of wide coverage and free access by users (Dong et al., 2020; He et al., 2021). However, the satellite remote-sensing technology is difficult to fully exploit because of various factors such as satellite revisit cycle, atmospheric conditions, and spatial resolution, limiting the rapid development of precision agriculture (Li et al., 2020a). Although few restrictions encumber ground remote sensing based on backpacks or vehicle-mounted equipment, such an approach is unsuited for large-scale AGB monitoring because of the limitations of remote-sensing platforms (Ryu et al., 2020). Fortunately, remote sensing from unmanned aerial vehicles (UAVs) now fills the technology gap formed by and inadequacies of satellite and ground remote sensing. Given its simple operation, convenience, flexibility, efficient data acquisition, and high temporal and spatial resolution of the images obtained by UAV remote sensing, this approach has created a new paradigm for the quantitative estimation of crop AGB (Duan et al., 2021).

Vegetation indices (VIs) such as the normalized difference vegetation index, the renormalized difference vegetation index, and the ratio vegetation index obtained from broadband multispectral data from the visible to the near-infrared have been used with significant success to estimate crops AGB (Chen et al., 2009; Meng et al., 2013). At present, research into estimating AGB is mainly divided into two categories: (i) research based on physical models and (ii) research based on empirical regression models (Yang et al., 2019). Physical models (e.g., the PROSPECT and PROSAIL models) have robust mechanisms and applicability, but many parameters required by these models are difficult to obtain, which limits their use for estimating crop AGB (Wan et al., 2021; Yang et al., 2021a). In empirical models, different regression techniques are used to relate feature parameters to AGB (Meng et al., 2017; Xu et al., 2018). These regression techniques fall into two categories (Yue et al., 2018a): traditional regression techniques [e.g., multiple stepwise regression, partial least squares regression (PLSR), and principal component analysis] and machine-learning techniques [e.g., random forest, artificial neural networks, and extreme learning machine (ELM)]. Spectral VIs combined with various regression techniques to estimate crop AGB offer the advantages that (i) VIs and AGB are strongly correlated over the reproductive growth period of crops, and (ii) the model structure is simple, which facilitates applications in AGB estimation (Bao et al., 2020; Kumar et al., 2021).

However, numerous studies have challenged the wisdom of using VIs to estimate the crop AGB in the multi-growth periods. The main arguments brought to bear are that (i) VIs saturate easily under high crop coverage, and (ii) VIs lose their sensitivity to AGB in the multi-growth period, making it challenging to use VIs to estimate crop AGB in the multi-growth period (Ma et al., 2019; Zhang et al., 2020). At present, the four primary techniques used to enhance the accuracy of AGB estimates are (i) the synthetic aperture radar technique (Montesano et al., 2013, 2014), (ii) the laser intensity direction and ranging (LiDAR) technique (Cao et al., 2018; Hu et al., 2020), (iii) the narrowband hyperspectral technique (Filippi et al., 2014; Tao et al., 2020), and (iv) the crop-height model (CHM; Roth and Streit, 2018; Zhu et al., 2019a; Issa et al., 2020).

Given the use of long-wavelength electromagnetic radiation, synthetic aperture radar remote-sensing techniques can penetrate the crop canopy and are not affected by weather conditions, which means that they overcome the problem of premature saturation of AGB estimates by optical remote-sensing VIs and are thus highly suitable for long-term monitoring of AGB for areas with high crop coverage (Banda and Tebaldini, 2020). Previous studies have confirmed that using the backscattering coefficient of synthetic aperture radar remote sensing produces highly accurate estimates of crop AGB for wheat (Han et al., 2019), maize (Hosseini et al., 2019), and rice (Yang et al., 2016).

LiDAR remote-sensing techniques actively transmit electromagnetic wave pulses with a specific penetration ability to interact with ground objects. By statistically calculating the height or quantity of LiDAR echoes, different variables characterizing crop canopy structure (such as volume and coverage) can be obtained, which is very useful for estimating crop AGB (Malambo et al., 2018). For example, Walter et al. (2019) demonstrated that volume and height data acquired by LiDAR correlate strongly with wheat AGB. Wang et al. (2017) showed that VIs combined with metrics obtained through LiDAR improve estimates of maize AGB. Furthermore, because crop height is a good metric of crop growth, the canopy height determined by LiDAR to estimate crop AGB is a very promising method to resolve spectral saturation (Salum et al., 2020). At present, UAV-LiDAR is widely used, mainly because it is convenient, data collection is fast, it provides a digital elevation model and digital surface model of the field, and it promotes the production of a CHM, which provides a new avenue for estimating crop AGB (Zhu et al., 2019b).

Narrowband hyperspectral techniques have the capacity to continuously acquire crop canopy spectral reflectance data with high spectral resolution, which means that mining the hidden information in the spectrum is helpful for AGB estimation. Therefore, crop AGB estimation can be enhanced by using spectral differential analysis (Gnyp et al., 2014), band-depth analysis (Fu et al., 2014), continuous wavelet analysis (Yao et al., 2018), and red-edge-region analysis (Marshall and Thenkabail, 2015). For example, Yue et al. (2021) showed that the accuracy of estimates of winter wheat AGB during the multi-growth period could be improved by using wavelet coefficients and multiple stepwise regression methods. Yang et al. (2021b) proposed that, during the multi-growth period of crops, the red-edge region leads to more accurate AGB estimates than the use of traditional VIs.

Although the above-mentioned remote-sensing techniques accurately estimate AGB and allow for real-time monitoring of crop growth, obtaining the data incurs high cost, and data processing is complex, which prevents this approach from gaining wide acceptance in the private sector (Poley and McDermid, 2020). In contrast, UAV digital remote-sensing systems are more acceptable because of their low price, simple data structure, and convenient data processing (Guo et al., 2021; Wang et al., 2021). More importantly, UAV-based RGB images may be spliced together to obtain digital surface models (from which a CHM can be developed) and ultrahigh-ground-resolution (GDS) digital orthophoto images (from which crop canopy spectra can be extracted), which provides more avenues to accurately estimate crop parameters.

Previous reports have confirmed that the CHM generated from UAV-based RGB images can be used for AGB estimation (Yue et al., 2018b; Lu et al., 2019). However, estimating AGB in multiple growth periods based only on crop height is not reliable because the change in crop height (such as wheat, maize, and rice) is not apparent in the late growth period, whereas AGB continues to increase, making it unfeasible to estimate AGB in the whole growth period based only on crop height (Fu et al., 2021). Niu et al. (2019) reported that combining crop canopy height and VIs is more accurate for estimating maize AGB than the use of either crop height or VIs alone. Similarly, VIs calculated from RGB-based images also suffer from spectral saturation under high crop coverage, resulting in inaccurate AGB estimates (Christelle and Emmanuel, 2020). Thus, considering the limitations of VIs and crop height to estimate AGB, researchers have begun to mine image features from ultrahigh-GDS RGB images to enhance the accuracy of AGB estimation models.

UAV-based ultrahigh-GDS RGB images are helpful not only for estimating AGB (Batistoti et al., 2019) but also for estimating chlorophyll (Liu et al., 2021b), nitrogen content (Li et al., 2015), leaf area index (Yue et al., 2018a), and crop yield (Zeng et al., 2021). These studies show that ultrahigh-GDS RGB images are rich in crop canopy surface information for monitoring growth. Therefore, canopy texture features can be extracted from ultrahigh-GDS UAV-based RGB images for estimating AGB (Mao et al., 2021). For example, Yue et al. (2019) confirmed that textures based on the gray level co-occurrence matrix (GLCM) and extracted from UAV-based RGB images with various GDS produce more accurate winter wheat AGB estimates than the traditional narrow and wideband VIs. Zhu et al. (2021) also reported that GLCM-based textures from UAV-based RGB images can be used to estimate maize AGB.

A literature review shows that most studies only extract single-scale GLCM-based texture features from specific GDS images to estimate crop AGB. However, the Gabor-based transformation features provide information that can be used to describe image textures and have been fully applied in the field of image processing, despite receiving little attention in crop phenotyping research (Shen and Bai, 2006; Fu et al., 2021). The crop canopy structure and size are known to vary with the growth period, which makes it difficult to use single-scale texture features to reflect differences in canopy structure. If the multiscale texture features can be extracted, the morphology of the crop canopy structure could be described to maximum extent, allowing more accurate estimates of crop AGB over multiple growth periods.

Furthermore, the texture features extracted from ultrahigh-GDS UAV-based RGB images can represent the high-frequency information of crop canopy photos, which provides new information (e.g., lush vegetation) about the crop canopy. If

this information can be combined with the vertical height of the crop canopy, it could be used to accurately estimate AGB. On the one hand, different texture techniques offer different potentials for extracting high-frequency information. On the other hand, the high-frequency information contained in images of different GDS will vary. After a careful literature review, no study has been found that proposes using different multiscale texture techniques to extract high-frequency information for estimating potato AGB.

Therefore, the present study investigates the performance of GLCM- and Gabor-based textures and various textures combined with crop canopy height to estimate potato AGB. GLCM-based textures were extracted from seven-GDS (1, 5, 10, 30, 40, 50, and 60 cm) RGB images. Gabor-based textures were obtained from magnitude images on five scales (scales 1–5, denoted S1–S5, respectively). We estimate the potato AGB by applying a least-squares support vector machine (LSSVM), an ELM, and PLSR using, respectively, (i) GLCM-based textures from different GDS RGB images and their combinations, (ii) Gabor-based textures from different scales and their combinations, and (iii) GLCM-based textures, Gabor-based textures, and their combinations integrated with crop height.

Experiment and methods

Experiments

The experiment was conducted at the National Precision Agriculture Research Demonstration Base (40°10′N, 116°26′E), Changping District, Beijing, China. Changping District has a typical warm temperate semi-humid continental monsoon climate, where the main crops are summer maize and winter wheat.

To increase the spatial growth difference of potato crops in the field, we use Zhongshu 5 (Z5) and Zhongshu 3 (Z3) early maturing potato varieties planted with different planting densities, nitrogen, and potassium fertilizers treatments. Forty-eight plots were planted, with each plot covering 32.5 m^2 and with a row spacing of 0.6 m. Eighteen plots filled the density test area with three gradients [60,000 plants/hm^2 (T1), 72,000 plants/hm^2 (T2), and 84,000 plants/hm^2 (T3)] and six repetitions. Twenty-four plots occupied the nitrogen test area with four gradients [0 kg/hm^2 urea (N0), 244.65 kg/hm^2 urea (N1), 489.15 kg/hm^2 urea (N2, normal treatment, 15 kg pure N), and 733.50 kg/hm^2 urea (N3)] and six repetitions. Six plots occupied the potassium fertilizer test area with two gradients [0 kg/hm^2 potassium fertilizer (K0), 1941 kg/hm^2 potassium fertilizer (K2)] and three repetitions. The specific test plan is shown in Figure 1. The planting method is mulching, and the field management includes weeding, soil cultivation, and watering. To accurately correct the terrain for subsequent RGB images, eleven ground control points (G1–G11) were uniformly deployed around the test plot and accurately positioned by using differential global positioning with millimeter accuracy.

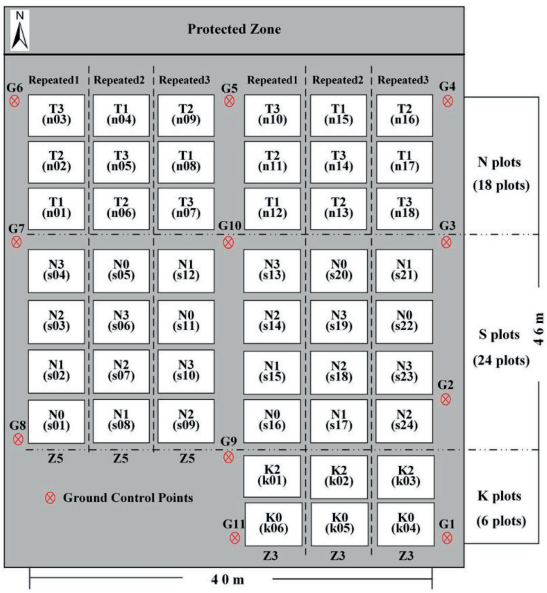

FIGURE 1
Potato planting plan at Changping District, 2019.

Collection and processing of crop height and AGB data

Ground crop height and AGB data were collected on 28 May 2019, 10 June 2019, and 20 June 2019, which corresponded to periods of potato tuber formation (P1), tuber growth (P2), and starch storage (P3), respectively. During each growth period, four plants representative of the overall growth level were selected from each plot. The vertical height of each plant was measured with a ruler, and the average value was taken as the measured crop height (in centimeters) for each plot.

To obtain the AGB data, three plants representative of the overall growth level were artificially selected from each plot. After artificial field sampling, put it into a white sealed bag and quickly took it back to the laboratory. The samples were washed with running water indoors. After the sample was naturally dried, the stems and leaves were cut into small pieces by using scissors. The separated samples were killed at 105°C, and dried at 80°C in a large bake oven until reaching constant mass. For each growth period, the plant density and dry mass of the stems and leaves of each plant sample as measured by a high-precision balance were used to calculate the potato AGB of each plot (in kg/hm^2).

Unmanned aerial vehicle RGB image acquisition and processing

After the ground collection work was completed, the DJI 4A series product produced by DJI Group, Ltd. was used to carry out UAV remote-sensing operations in the bare soil period (April 20, 2019) and the three critical growth periods of potatoes. The UAV

system was equipped with a three-channel CMOS sensor, with 20 million effective pixels and a maximum pixel value of 4,000 × 3,000. To ensure the generation of RGB images with high GDS, the UAV's flying height was manually set to 20 m, and the heading and side overlap were both 80%. By using its position and orientation system during flight, the UAV recorded the three-dimensional position of the sensor in real-time. The flights were conducted in clear, calm weather to reduce the variation of crop canopy reflection intensity caused by uneven illumination. The take-off position and flight path were essentially the same for each flight to accurately match the digital surface model (DSM) obtained in different growth periods.

Before extracting crop height and multiscale texture features from UAV RGB images, we used Agisoft PhotoScan Professional software to splice together digital images from the various periods. Next, the RGB images were topographically corrected based on the measured three-dimensional coordinates of G1–G11, and the correction error for each period was less than 2 cm. Finally, the DSM and digital orthophoto map of the test location were derived for each period. The specific image-processing flow followed that of Fu et al. (2021). A total of 48 regions of interest (ROIs) were delineated according to the boundary of each sample plot.

Generation of crop height model

Crop height represents the growth of groups and symbolizes the vertical structure of the crop canopy, which is closely related to AGB. Therefore, the accurate acquisition of crop-height information is important for monitoring crop growth and managing farmland production (Niu et al., 2019). First, in this study, the DSM of the three critical growth periods (P1–P3) and the bare soil period of potatoes were topographically corrected and established through high-density point clouds. The raster statistics tool of ArcGIS 10.2 software was then used to calculate the difference in DSM between potato critical growth periods and the bare soil period and obtain the crop height model of the corresponding growth period (Figures 2D–F). Finally, the average potato crop height of each plot was automatically extracted by using the ROI tool.

Extraction of GLCM- and Gabor-based texture features

The GLCM is a matrix function involving pixel distance and angle. It reflects spatial variations in the gray distribution of the image by calculating the correlation between the gray levels of two points separated by a certain distance and in a specific direction in the image (Fu et al., 2021). The flying height of the UAV in this study was 20 m, and the GDS of the obtained images was about 0.85 cm. The original image was sampled to 1 cm by resampling. GDS5, GDS10, GDS20, GDS30, GDS40, GDS50, and GDS60 cm images were acquired based on the GDS1-cm image using the nearest-neighbor pixel method. In this study, GLCM-based texture features in four directions (0°, 45°, 90°, 135°) were extracted from each channel of UAV RGB images. Four moving windows (3 × 3, 5 × 5, 7 × 7, 9 × 9) were set in each direction for extracting diverse textures. We selected eight standard GLCM-based texture features, including the mean (Mea), variance (Var), homogeneity (Hom), contrast (Con), dissimilarity (Dis), entropy (Ent), second moment (Sec), and correlation (Cor) for analyzing the performance of estimating AGB. To simplify the description, the texture features were prefixed with R-, G-, or B- to denote the GLCM-based extracted textures for the three channels (e.g., R-Con denotes the contrast of the R band).

The Gabor transform, also known as the windowed Fourier transform (Gaussian function as a window function), is a transformation from the time to the frequency domain and offers good characteristics for extracting local space and frequency domain information from the target (Shen and Bai, 2006). The Gabor filter is like the visual stimulus–response of simple cells in the human visual system. It is sensitive to the edge of the image, which can provide good direction-scale selection characteristics, and is insensitive to illumination changes, confronting changes in illumination with appropriate adaptation (Jones and Palmer, 1987; Fu et al., 2020). Therefore, the Gabor transform is often used to extract and analyze image texture features. In this study, four directions (0°, 45°, 90°, 135°) and five scales (S1–S5) were selected to generate a total of twenty filter banks. The other parameters were set to the same values as in Fu et al. (2021). For each ROI in the growth period of each potato, the RGB images were convolved with the Gabor filter banks to generate a total of sixty types of amplitude images. Based on these magnitude images, we obtained the same textures as GLCM-based textures. Therefore, 480 texture features were extracted from each plot. To simplify the description later, R-, G-, B- followed by the scale factors served to characterize the texture features of different bands and scales (e.g., R-S2-Ent denotes the entropy of scale 2 of the R-band). Figure 3 shows the specific process of extracting diverse GLCM- and Gabor-based textures.

Technical route and regression analysis

To verify the hypothesis proposed herein, repeats 2 and 3 data (32 groups) collected in each potato growth period in 2019 served as the calibration set to estimate AGB, and repeat 1 data (16 groups) served as the validation set to verify the reliability and stability of the model. Figure 4 shows the technical scheme of this study. The coefficient of determination R (Zhou et al., 2019), root mean square error (RMSE), mean absolute error (MAE), and normalized root mean square error (NRMSE) were used to evaluate the estimation accuracy of different models.

Results and analysis

Crop-height response to potato AGB

Figures 5A–C show the relative residuals of the extracted crop height based on UAV RGB images during the P1–P3 growth

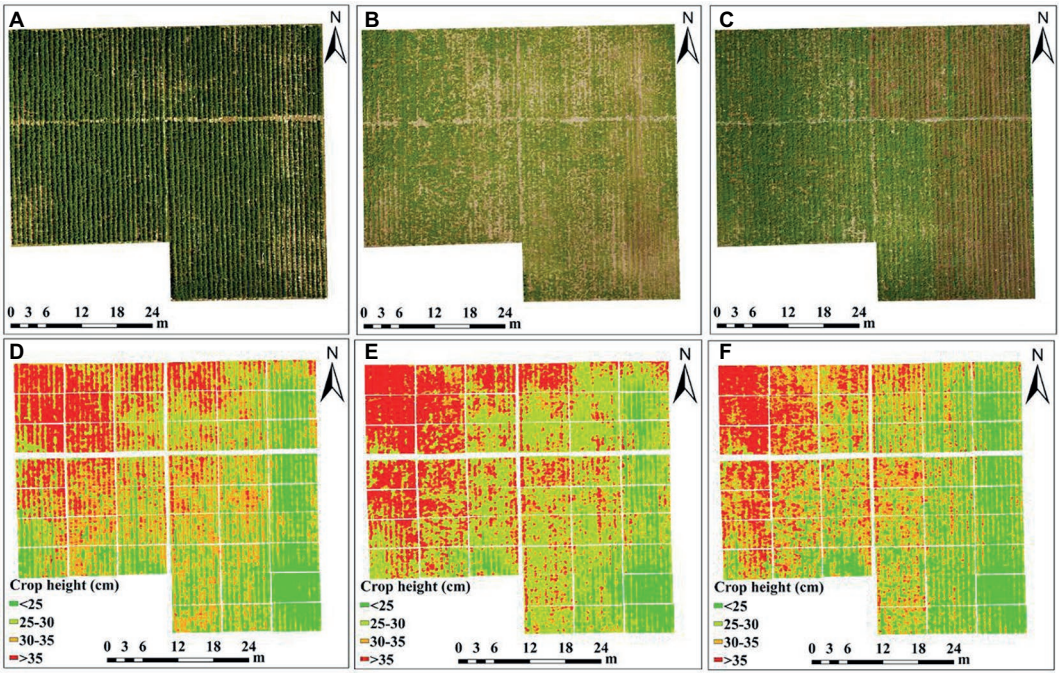

FIGURE 2
UAV RGB images and potato crop height of each plot. **(A,D)** P1, **(B,E)** P2, and **(C,F)** P3 periods.

period of potatoes. The results show that the extracted crop height in each growth period is generally low, and that most of the relative residuals are less than 20% (RMSE <3 cm), which indicates that the crop height extracted through the crop height model (Figure 2) is reliable. The result in Figure 5D shows that crop height and AGB correlate positively in all key potato growth periods ($p > 0.01$), which means that crop height may contribute to the potato AGB estimates over multi-growth periods.

Response of GLCM-based texture features to potato AGB

Response of GLCM-based textures from different windows and directions to potato AGB

Taking the RGB images of GDS1 as an example, Figures 6A–D examine the Pearson correlation coefficients between GLCM-based textures and potato AGB in different windows and directions. The results show that the correlation of GLCM-based textures with potato AGB is basically independent of direction and window size. To reduce the dimensionality of the data, we use GLCM-based textures with 45° orientation and a 5 × 5 window for potato AGB estimation. The results shown in Figures 6E,F indicate that GLCM-based texture correlates weakly with potato AGB in three single growth periods ($p < 0.05$), and that, when considering the multiple growth periods of crops, GLCM-based textures correlate positively (e.g., G-dis) or negatively (e.g., B-cor) with potato AGB ($p < 0.01$), which indicates that the use of GLCM-based textures may also improve the accuracy of AGB estimates of potatoes in multiple growth periods.

Response of GLCM-based textures of different ground resolution to potato AGB

The results shown in Figure 7 indicate that the Pearson correlation coefficients of GLCM-based textures with different GDS and potato AGB differ significantly. GLCM-based textures of GDS1 correlate strongly with AGB ($p < 0.01$). The GLCM-based textures of GDS5 and GDS10 correlate more weakly with AGB and the correlation coefficient has the opposite sign. The GLCM-based textures of GDS20 and GDS30; GDS40, GDS50, and GDS60 approximately correlate with AGB. These results show that the image GDS affects the relationship between GLCM-based textures and AGB. Therefore, we must evaluate the accuracy of GLCM-based textures at different resolutions to estimate potato AGB.

Response of Gabor-based texture features from different directions and scales to potato AGB

Figures 8A–D show the Pearson correlation coefficients of Gabor-based textures (GDS1) and potato AGB at different orientations and different scales. The size and sign of the correlation coefficient show that the correlation between Gabor-based textures and potato AGB is significantly more affected by scale than by direction, which differs completely from the result for GLCM-based textures. Therefore, we use Gabor-based textures

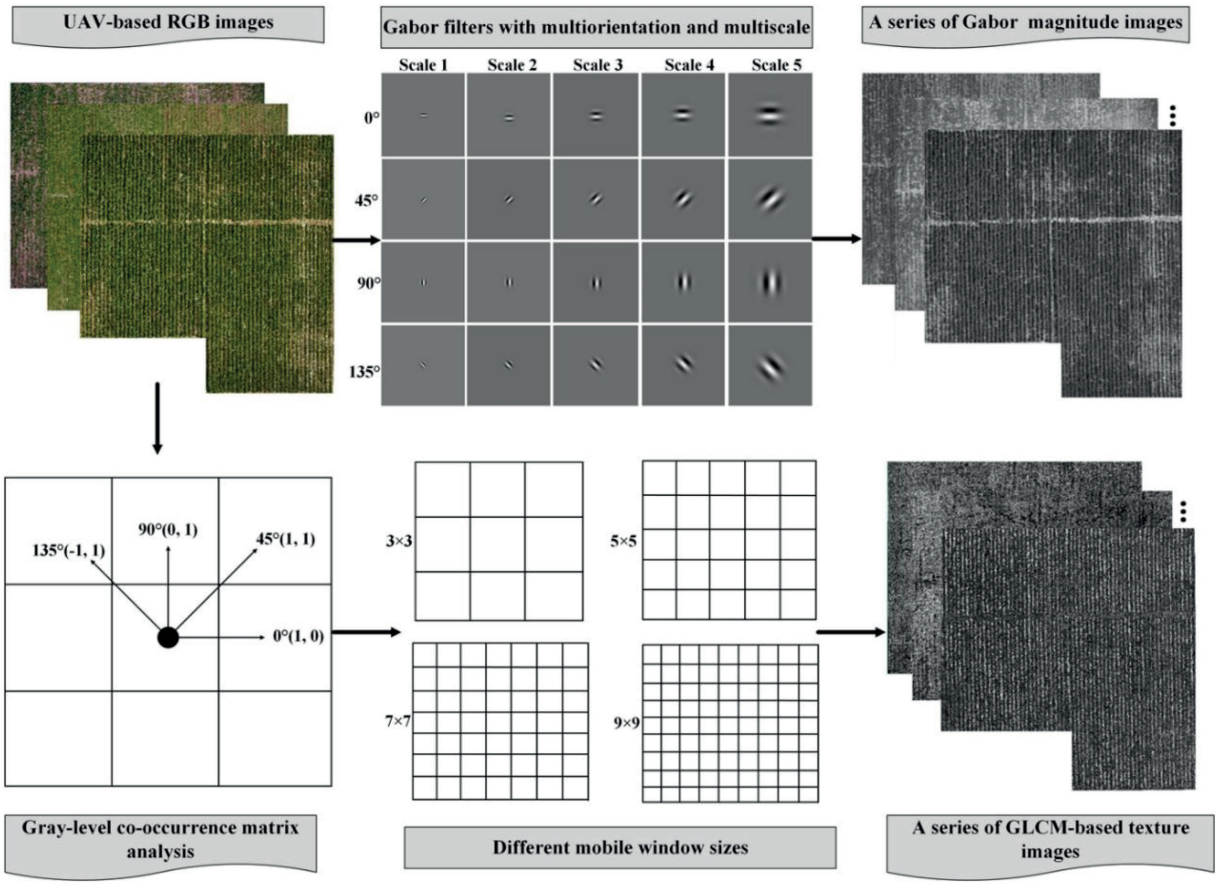

FIGURE 3
Multiform texture features extraction process from GLCM- and Gabor-based analysis.

with different scales in 45° orientation to estimate potato AGB. The results shown in Figures 8E,F indicate an excellent linear relationship between Gabor-based textures and potato AGB in single- or multi-growth periods under multiple scales ($p < 0.01$). Compared with the results in Figures 7E,F, when the AGB exceeds 1,000 kg/hm^2, the Gabor-based textures remain sensitive to AGB ($p < 0.01$), which indicates that the multiscale Gabor-based textures are more promising for AGB estimation than multi-resolution GLCM-based textures.

Using GLCM-based texture features to estimate potato AGB

As shown in Figure 7, five representative ground resolution images were selected to extract GLCM-based textures to estimate potato AGB. The selected ground resolution and GLCM-based textures (using the "findCorrelation" function in the Caret package of the R language, with a cutoff of 0.99) appear in Table 1.

Figure 9 shows potato AGB estimates using the LSSVM, ELM, and PLSR techniques based on image textures of GDS1, GDS5, GDS10, GDS30, GDS60, and their combinations. These results show that multi-resolution GLCM-based textures provide better estimates ($R^2 = 0.68–0.71$, RMSE = 261–269 kg/hm^2, MAE = 214–218 kg/hm^2, NRMSE = 21.94–22.65%) than others with single ground resolution textures. In addition, for GDS1 to GDS5, the GLCM-based textures of GDS1 provide the best AGB estimates ($R^2 = 0.63–0.67$, RMSE = 273–290 kg/hm^2, MAE = 216–236 kg/hm^2, NRMSE = 22.96–24.43%). Between GDS10 and GDS60, the GLCM-based textures of GDS30 provide the best AGB estimates ($R^2 = 0.59–0.64$, RMSE = 288–305 kg/hm^2, MAE = 246–256 kg/hm^2, NRMSE = 24.28–25.64%).

Using Gabor-based texture features to estimate potato AGB

The multiscale Gabor-based textures used in this study to estimate potato AGB are listed in Table 2 (the selection rules are given in Table 1). To compare the effect of single and multiscale Gabor-based textures for potato AGB estimation, we also use the LSSVM, ELM, and PLSR techniques to build AGB estimation models.

The results in Figure 10 show that (i) the use of multiscale Gabor-based textures produces more accurate AGB estimates than the use of GLCM-based textures with different GDS ($R^2 = 0.70–$

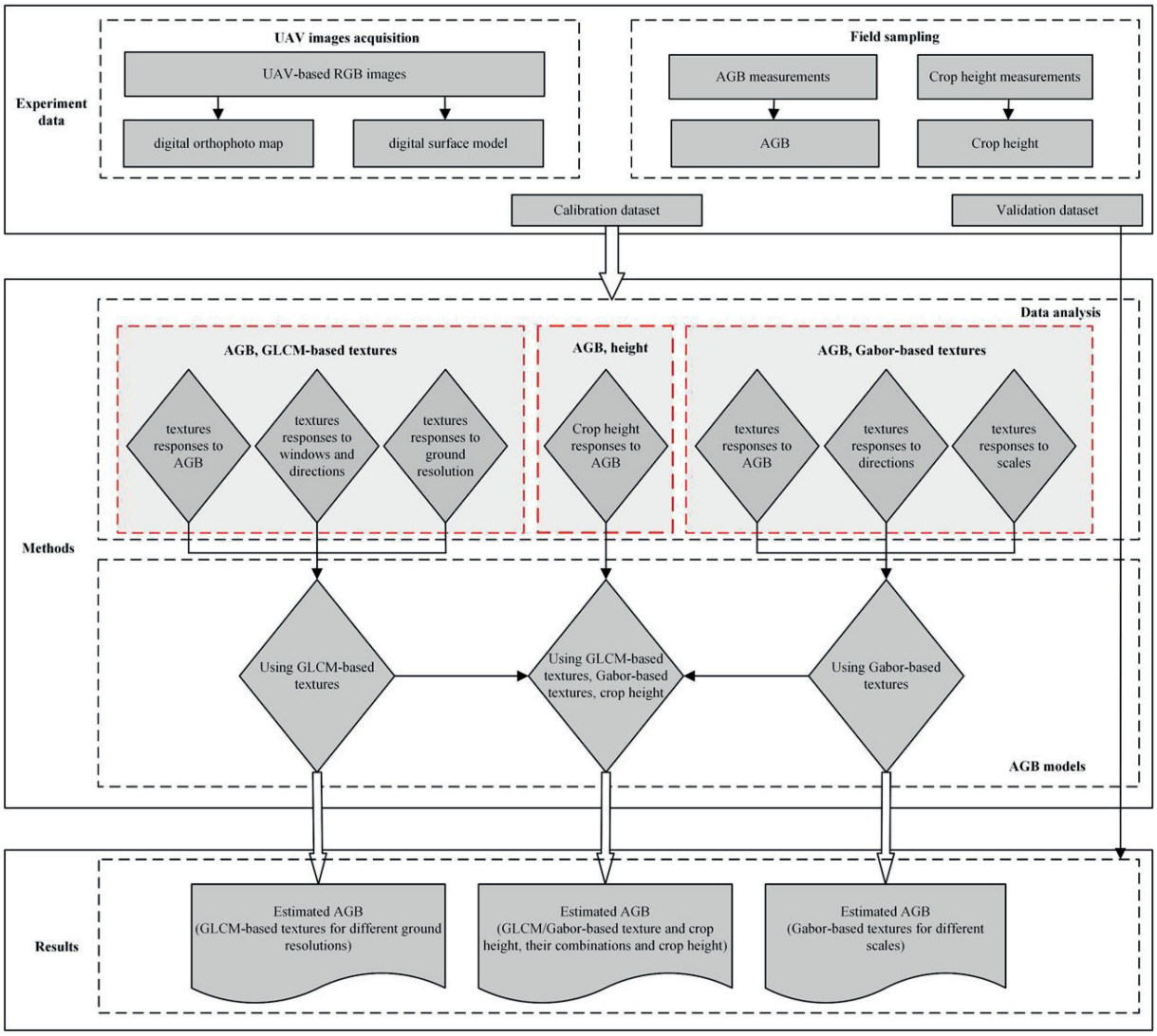

FIGURE 4
Technical route of the study.

0.74,RMSE = 244–271 kg/hm^2,MAE = 207–232 kg/hm^2,NRMSE = 20.55–22.80%). (ii) For different scales, the AGB estimation results gradually became less accurate with increasing scale. (iii) Finally, when the AGB exceeds 1,000 kg/hm^2, the multiscale Gabor-based textures (Figures 10F,L,R) overestimates the AGB more than does the GLCM-based textures of different GDS. These results confirm that the multiscale Gabor-based textures produce more accurate estimates of potato AGB than do multi-resolution GLCM-based textures.

Using texture features and crop height to estimate potato AGB

To determine whether the fusion of high-frequency information and vertical crop canopy structure information is helpful for AGB estimation, we estimate potato AGB by using (i) GLCM-based textures of different resolutions and crop height; (ii) Gabor-based textures of different scales and crop height; and (iii) GLCM- and Gabor-based textures of all forms and crop height. The results in Figure 11 show that (i) the LSSVM technique produces more accurate estimates of potato AGB (R^2 = 0.73–0.78, RMSE = 236–255 kg/hm^2,MAE = 187–199 kg/hm^2,NRMSE = 19.90–20.90%); (ii) combining textures of different resolutions and scales separately with the crop height enhances the accuracy of AGB estimates (and more so for the latter); (iii) different textures combined with crop height produce the most accurate estimates of potato AGB for the same regression technique (R^2 = 0.75–0.78, RMSE = 236–243 kg/hm^2,MAE = 187–209 kg/hm^2,NRMSE = 19.86–20.48%). More importantly, different textures combined with crop height are not underestimated when AGB exceeds 1,000 kg/hm^2. The results in Figures 11B,E,H than those in Figures 11A,D,G,

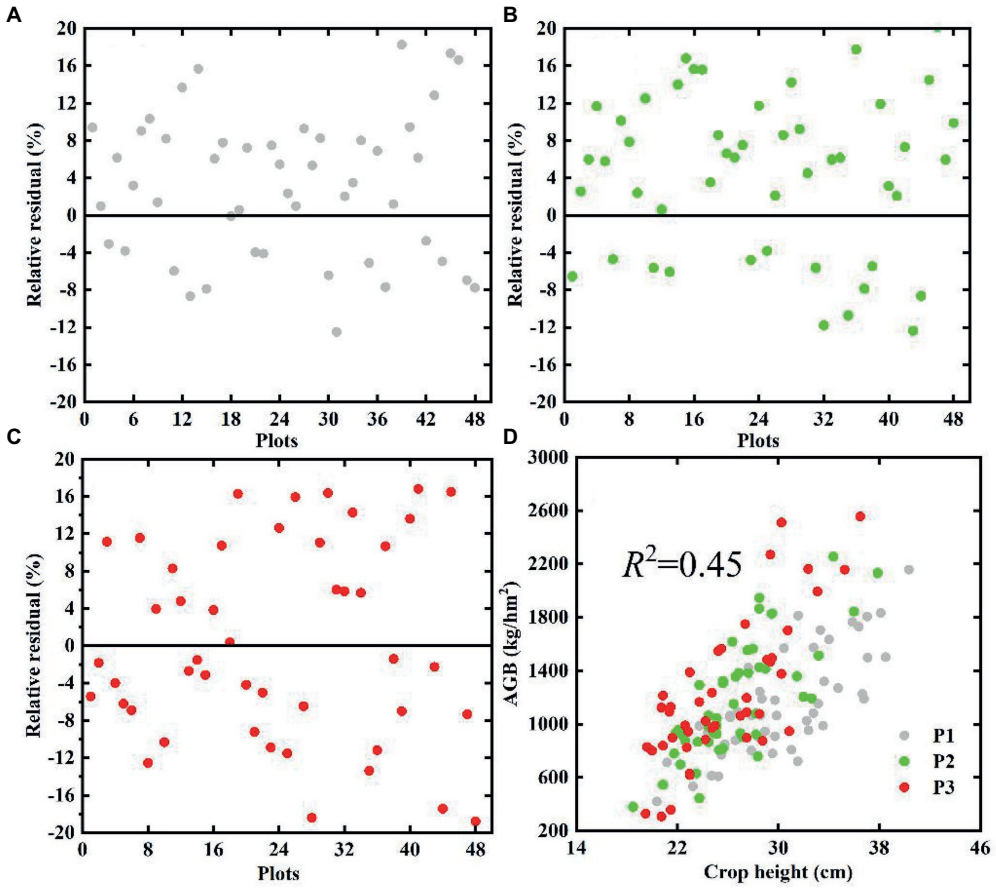

FIGURE 5
Comparison of the relative residuals (%) of the extracted crop height during the growth period of potato **(A)** P1, **(B)** P2, **(C)** P3, and **(D)** the relationship between AGB and estimated crop height based on UAV.

which validates the argument that multiscale Gabor-based textures are more promising than multi-resolution GLCM-based textures for estimating potato AGB.

Discussion

The use of different varieties, planting density, nitrogen fertilizer, and potassium fertilizer leads to significant differences in the growth of potato crops. At present, to obtain AGB information, crop-growth monitoring is done mainly by optical remote sensing. However, this approach has limitations (Zhang et al., 2020) because optical VIs lose their sensitivity to AGB for high crop coverage, resulting in the underestimation of potato AGB in reproductive growth periods. To improve the AGB estimation of potato crops in multiple growth periods and investigate the feasibility of using digital cameras for AGB estimation, this study obtained RGB images of potato canopies from an economic UAV remote-sensing platform and directly extracted different texture features and crop height to estimate potato AGB.

Response of crop height to AGB

Fluctuations in crop height can reflect crop health and nutritional status. At the same time, reasonable plant height is also the basis for stable and high-yield crops. Therefore, accurate acquisition of plant height information is vital for crop-growth monitoring and farmland production management (Lu et al., 2019). For example, Niu et al. (2019) and Yue et al. (2018a) used crop height to estimate maize and winter wheat AGB. Unfortunately, using crop height alone to estimate AGB during the whole growth period of maize and wheat may be of limited use because variations in height are not apparent in the later growth stage of maize and wheat, whereas AGB increases significantly (corn grain and ear formation). On the contrary, potato growth differs significantly from that of maize and wheat. In the early reproductive growth period, potato stem nodes elongate and leaves expand, increasing both AGB and crop height. However, in the later stage of reproductive growth, the underground tubers expand continuously so that the nutrients accumulated on the ground must be transferred underground, resulting in wilting and yellowing of the stems and leaves of

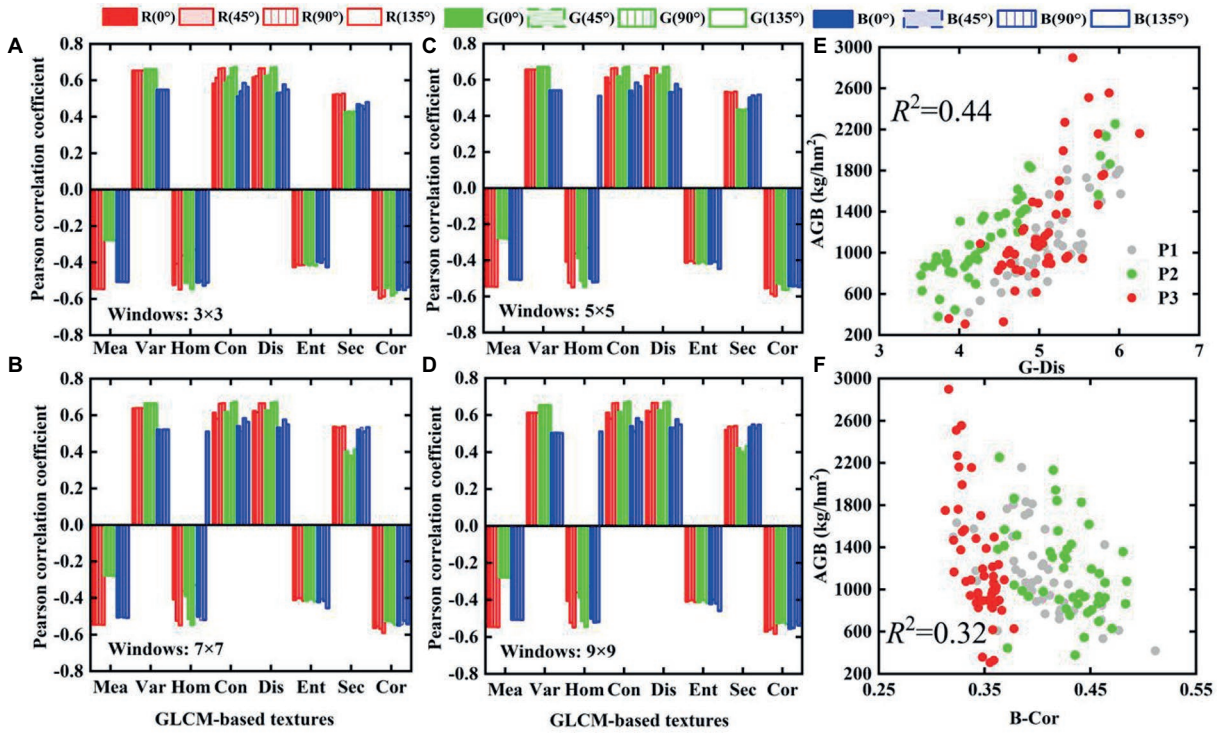

FIGURE 6
The relationship between GLCM-based textures and AGB in different directions and different windows: **(A)** 3×3, **(B)** 5×5, **(C)** 7×7, **(D)** 9×9, **(E,F)** scatter plots of G-Dis and B-Cor with AGB under 45° and 5×5 windows, respectively.

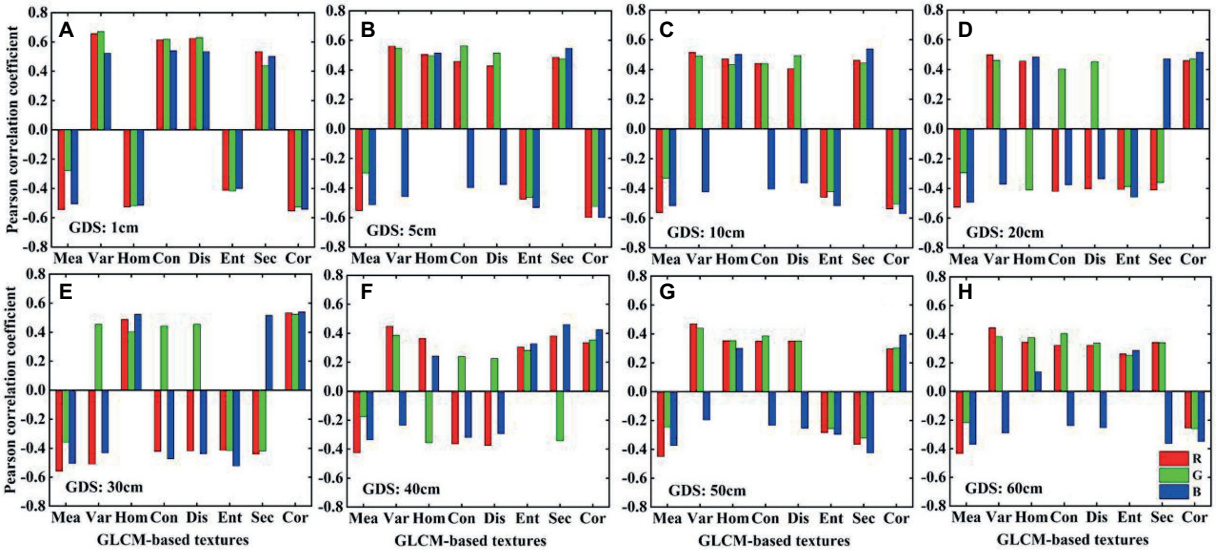

FIGURE 7
The relationship between different ground resolution (GDS) GLCM-based textures and AGB. **(A)** 1, **(B)** 5, **(C)** 10, **(D)** 20, **(E)** 30, **(F)** 40, **(G)** 50, **(H)** 60 cm image textures.

above-ground potato plants. A small number of leaves even fall off, which reduces the crop height and AGB simultaneously, as shown in plot s03 of Supplementary Figure 1.

The visualization in Figure 5D shows that both crop height and AGB maintains a positive linear correlation ($p < 0.01$) in single or multiple growth periods, which is consistent with potato crop

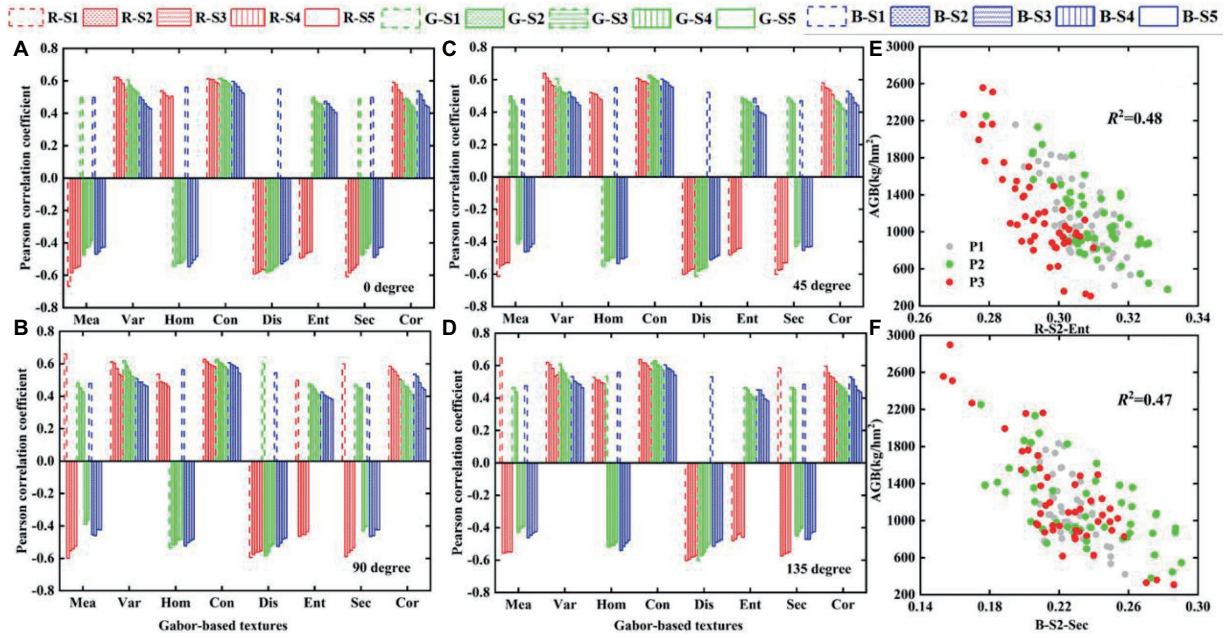

FIGURE 8
The relationship between Gabor-based textures and AGB in different directions and different scales: **(A)** 0-degree, **(B)** 45-degree, **(C)** 90-degree, **(D)** 135-degree, **(E,F)** scatter plots of R-S2-Ent and B-S2-Sec with AGB, respectively.

TABLE 1 Selected GLCM-based textures to estimate potato AGB.

Textures	Ground resolution (cm)	Parameters
GLCM-based textures	GDS1	R-Mea, R-Var, R-Con, R-Dis, R-Cor, G-Var, G-Con, G-Dis, B-Con, B-Cor
	GDS5	R-Mea, R-Cor, G-Con, G-Dis, G-Cor, B-Mea, B-Hom, B-Ent, B-Sec, B-Cor
	GDS10	R-Mea, R-Hom, G-Var, B-Mea, B-Var, B-Hom, B-Con, B-Ent, B-Sec
	GDS30	R-Mea, B-Mea, B-Var, B-Hom, B-Con, B-Dis,
	GDS60	R-Mea, G-Var, G-Con, G-Dis, B-Mea, B-Var, B-Dis

growth and indicates that potato crop height could be used for AGB estimation. The quantitative analysis results in Figure 11 show that the addition of crop height (R^2 increases, RMSE and MAE decrease) in different models improves the accuracy of AGB estimation and reduces the underestimation of AGB, which also confirms the hypothesis that crop height may support AGB estimation in multiple growth periods of potatoes. Li et al. (2020b) reported that the potato crop height correlates significantly with the AGB of early maturing potato varieties (the potato plant and canopy branches grow synchronously), whereas the correlation with the AGB of late-maturing varieties decreases (when the potato plant grows to a certain height, the canopy is not well developed). However, the potato varieties Zhongshu 5 and Zhongshu 3 planted in this study are both early maturing varieties, and the conclusions obtained based on these varieties are consistent, namely, that a significant linear relationship exists between crop height and AGB (see Figure 5D). This shows that the difference in varieties is the key factor restricting the use of crop height to estimate AGB. Therefore, relying only on crop height to estimate the AGB of different varieties of the same crop seems ill-advised.

Response of GLCM-based textures to AGB

The results show that the correlation between GLCM-based textures and AGB remains basically unaffected by the direction and window (Figure 6), which may be related to the principle of GLCM generation. It represents the occurrence frequency of a pixel pair. Little difference exists in the number of statistics in different directions and windows. Fu et al. (2021) and Yue et al. (2019) also reported that the correlation between GLCM-based textures and winter wheat AGB is largely unaffected by directions and windows. In contrast, the correlations between GLCM-based textures and AGB at different ground resolutions differ significantly (Figure 7), mainly because the amount of information contained in the potato canopy structure differs. Taking the G-band as an example, Table 3 shows the data range and variance statistics for each growth period. Although the range of G-band data obtained through the nearest pixel resampling method in each growth period remains basically unchanged, the variance decreases gradually with decreasing resolution, which is indicative

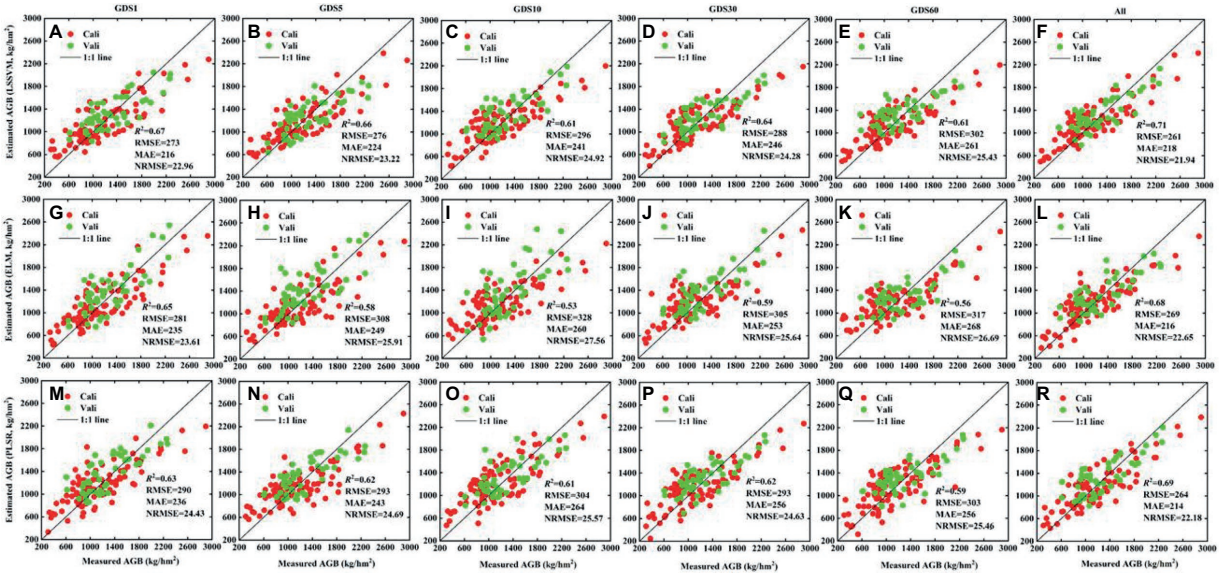

FIGURE 9
The fitted scatter plot of measuring and estimating potato AGB (kg/hm^2) using GLCM-based textures from GDS1, GDS5, GDS10, GDS30, GDS60 and all, respectively. **(A–F)** LSSVM; **(G–L)** ELM; **(M–R)** PLSR. "All" represent texture combinations of different ground resolutions. Cali and Vali represent calibration (repeat 2 and 3) and validation data sets (repeat 1), respectively. The estimation results of Cali and Vali are shown in Supplementary Table A1.

TABLE 2 Selected Gabor-based textures to estimate potato AGB.

Textures	Scales	Parameters
Gabor-based textures	S1	R-S1-Var, R-S1-Ent, R-S1-Cor, G-S1-Var, B-S1-Var, B-S1-Cor
	S2	R-S2-Hom, R-S2-Con, R-S2-Dis, R-S2-Ent, R-S2-Sec, R-S2-Cor, G-S2-Var, B-S2-Cor
	S3	R-S3-Mea, R-S3-Hom, R-S3-Con, R-S3-Dis, R-S3-Sec, B-S3-Var, B-S3-Cor
	S4	R-S4-Hom, R-S4-Con, R-S4-Dis, B-S4-Hom, B-S4-Var
	S5	R-S5-Mea, R-S5-Hom, R-S5-Con, R-S5-Dis, R-S5-Sec, B-S5-Var

of a decrease in the amount of information contained in the canopy image, modifying the correlations between GLCM-based textures and AGB at different resolutions.

We classified GLCM-based textures obtained with different ground resolutions into five categories: (i) GDS1, (ii) GDS5, (iii) GDS10, (iv) GDS20, GDS30, and (v) GDS40, GDS50, GDS60. As shown in Figure 7A, the GLCM-based textures of GDS1 remain strongly correlated with potato AGB because most pixels correspond to pure potato leaves or soil. However, the correlation between the GLCM-based textures of GDS5 and GDS10 and potato AGB begins to weaken and the sign of the correlation coefficient changes (Figures 7B,C) because a small number of pixels express potato canopy information in the original image. However, when using the nearest-neighbor resampling method, these pixels express soil information, so the mixed spectrum was extracted based on ROIs. Given that the potato row spacing was 60 cm, when the GDS changes from 20 to 30 cm, the fraction of soil pixels increases in the ROI (e.g., in the GDS30 cm image, the ROI may contain half vegetation and half soil, and the final extracted canopy spectra are similarly smoothed), which makes the correlation between GLCM-based textures of GDS30-cm and AGB greater than that between GDS20-cm and AGB (Figures 7D,E). However, when the ground resolution exceeds half the line spacing, a lower image resolution makes the fraction of soil in the pixels in the ROI more significant than vegetation, reducing the correlation between GLCM-based textures and AGB.

Consider the Dis of the B-band of plot s04 as an example. Under the same growth period, the Dis-texture gradually increases and then decreases from GDS1- to GDS30-cm. This shows that, when the GDS exceeds half the line spacing, the information contained in the ROI changes from high frequency (e.g., potato leaves) to low frequency (e.g., soil, shadow); that is, the texture changes from nonuniform (Supplementary Figure 2; GDS2-, GDS5-, GDS10-, GDS20-cm) to uniform (Supplementary Figure 2; GDS40-, GDS50-, GDS60-cm), which explains why the image resolution affects the correlation between GLCM-based texture and potato AGB. Potato AGB first increases and then decreases from the P1- to the P3-growth period, whereas the Dis-texture value of GDS1 (pure pixel; Supplementary Figure 2) maintains a significant positive correlation with AGB as the growth period changes (Figure 7A; Supplementary Figure 2; GDS1-cm). However, other ground resolution Dis-textures correlate negatively with AGB because most pixels in the ROI contain soil. Therefore, selecting an appropriate GDS is helpful for monitoring crop growth.

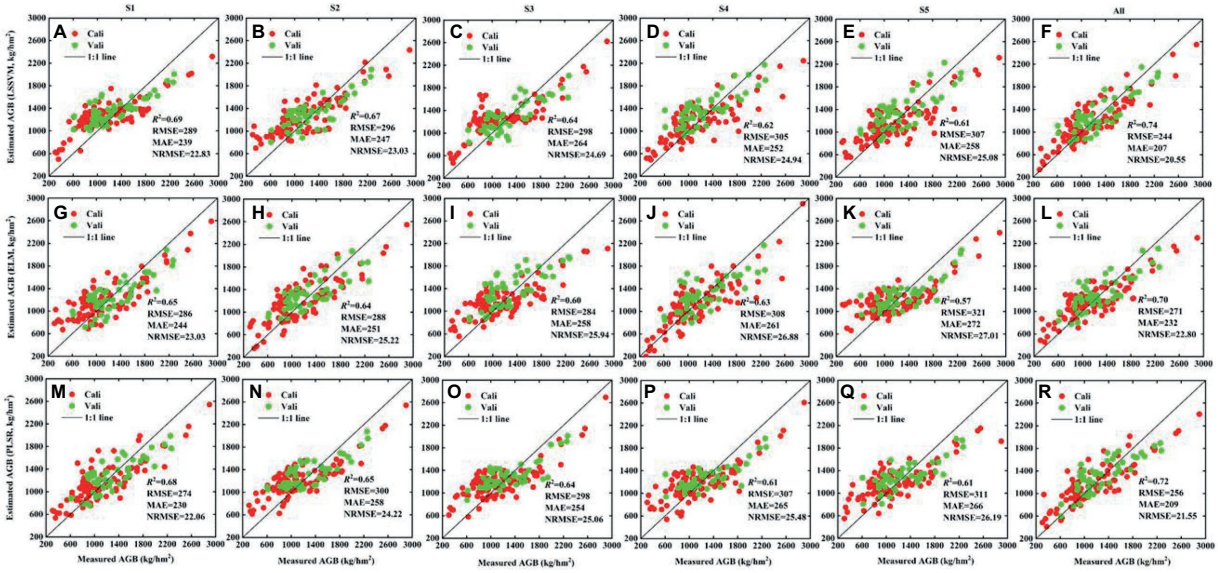

FIGURE 10
The fitted scatter plot of measuring and estimating potato AGB (kg/hm^2) using Gabor-based textures from S1, S5, S3, S4, S5 and all, respectively. **(A–F)** LSSVM; **(G–L)** ELM; **(M–R)** PLSR. "All" represent texture combinations of different scales. The estimation results of Cali and Vali are shown in Supplementary Table A2.

Response of Gabor-based textures to AGB

The Gabor filter produces an effect very similar to the human visual response and is not sensitive to local illumination, making it highly suitable for extracting fine texture features. Following the work of others (Fu et al., 2020), we set four orientations and five scales to form a total of 20 filters (Figure 3). Based on these filters, we extract multiscale Gabor-based textures. The results show that the correlation between Gabor-based textures and potato AGB are significantly more affected by scale than by direction, which differs significantly from the results obtained from GLCM-based texture (Figures 8A–D). This was also confirmed by Fu et al. (2021).

Consider as an example the B-band of the n01 plot for the P1-P3 growth period. The results show that the amplitude images generated by the convolution of Gabor wavelet kernels of different scales with the RGB images have different spatial characteristics (Supplementary Figure 3). As mentioned earlier, potato AGB first increases and then decreases as the growth period advances, whereas B-S1-Con, B-S2-Ent, B-S4-Cor change with changing AGB, which means that the three correlate positively with AGB (Figures 8C; Supplementary Figure 2). Conversely, B-S3-Hom and B-S5-Sec maintain a negative correlation with AGB (Figures 8C; Supplementary Figure 2).

The above results show that extracting multiscale Gabor-based textures more finely describes variations in potato canopy structure. The results show that the sign of the correlation coefficients of the Ent-, Cor-, Sec-texture (GLCM-based) and AGB change (analogous to Gabor-based textures), which indicates that estimates of potato AGB made by using Gabor-based textures may differ from estimates of potato AGB made by using CLCM-based textures. Furthermore, the results shown in Figures 7E,F show that the multiscale Gabor-based texture is linear in both the potato single- and multi-growth period AGB. Unlike the results in Figures 6E,F, when the AGB exceeds 1,000 kg/hm^2, the Gabor-based textures remain sensitive to AGB, which means that using multiscale Gabor-based textures to estimate AGB over multiple potato growth periods may produce more accurate result than GLCM-based textures, which is similar to the above hypothesis. The results in Supplementary Figure 3 show that the Gabor-based textures at different scales reflect the details of the potato canopy, which reminds us that the accuracy of Gabor-based textures must be evaluated at different scales to estimate potato AGB.

Evaluation of accuracy of AGB estimation model

RGB images of the potato canopy typically consist of soil, stems, leaves, weeds, and shade (Supplementary Figure 1), and the fraction of each component changes with the advancement of the potato growth period. During the tuber formation period (P1), potatoes gradually close the ridge, and the shadow between the ridges appears clearly on RGB images. During the tuber growth period (P2), the branching of the potato canopy becomes maximal, as is the vegetation coverage, so the potato canopy almost covers the background soil. During the starch-storage period (P3), the distribution and transfer of assimilates on the ground causes the leaves to yellow and fall off, and the soil and weeds become apparent. These changes in the potato canopy can

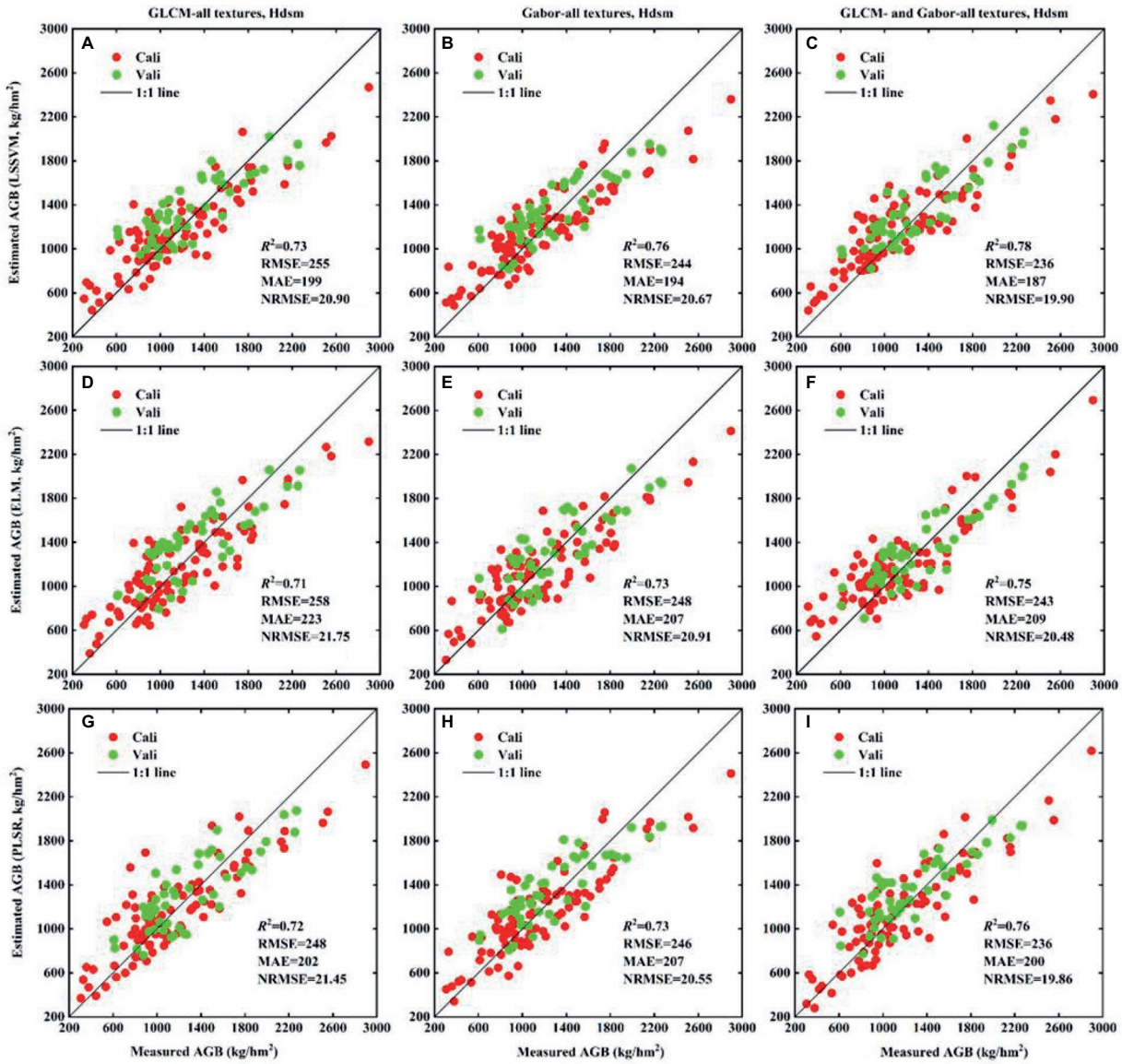

FIGURE 11
The fitted scatter plot of measuring and estimating potato AGB (kg/hm^2) using different ground resolution GLCM-based textures, different scales Gabor-based textures and crop height. **(A–C)** LSSVM; **(D–F)** ELM; **(G–I)** PLSR. GLCM-all textures, Hdsm represent combination of different ground resolution GLCM-based textures and crop height. The estimation results of Cali and Vali are shown in Supplementary Table A3.

be captured by image texture features. In addition, given different varieties, planting densities, and fertilization treatments, significant differences appear in the potato canopy, even in the same growth period. Therefore, describing this change based solely on single-scale textures would be difficult. Figures 9, 10 show that using only a single type of texture to estimate AGB with different regression techniques is less effective than using multi-type textures (multi-resolution GLCM-based and multiscale Gabor-based textures).

The use of GLCM-based textures of GDS1 produces the most accurate AGB estimates when the ground resolution ranges from 1 to 5 cm. While the ground resolution ranges from 10 to 60 cm, the use of GLCM-based textures of GDS30 produces the most accurate AGB estimate (Figure 9; Supplementary A1). This differs somewhat from the results of Yue et al. (2019), who report that the textures GDS1 and GDS30 produce the most accurate AGB estimates of winter wheat. This discrepancy may be related to the difference in crop canopy structure and image down-sampling. The width of potato leaves (greater than or equal to about 5 cm for vigorous growth) far exceeds that of winter wheat leaves, which allows fine GLCM-based textures to be extracted from GDS5-cm images. In the present study, the information on the potato canopy structure obtained by the nearest pixel resampling method (the ROI spectrum is smoothed only at low resolution, such as less than 30 cm) differs significantly from the information on the winter wheat canopy structure obtained by Yue et al. (2019)

TABLE 3 Statistical analysis of G band DN values at each growth period.

Images	P1		P2		P3	
	Data range	Variance	Data range	Variance	Data range	Variance
GDS1	255	66.92	255	60.72	255	53.74
GDS5	254	50.52	255	57.39	255	53.71
GDS10	254	50.61	243	57.34	250	43.32
GDS30	254	49.10	254	39.67	253	33.68
GDS60	252	48.54	241	37.64	252	32.75

through the average method (the degree of smoothness differs at different resolutions, and the smoothness increases as the image resolution decreases). Therefore, the estimation of potato AGB based on GDS30 cm images is inferior to that based on GDS5 cm images. Combining different ground resolution textures to estimate AGB is more accurate, so we conclude that textures with different GDS could provide complementary information from different perspectives to estimate AGB.

Similarly, we estimate potato AGB using single-scale Gabor-based textures (Figure 10; Supplementary A2). The results show that the estimation accuracy deteriorates with increasing scale (Figure 10; Supplementary A2), but samples with AGB exceeding 1,000 kg/hm^2 are less underestimated, which is consistent with the results of Fu et al. (2021). As shown in Figure 3, an increased scale would make the Gabor convolution kernel larger, and the final Gabor-based textures are like the textures after down-sampling. As shown earlier, GLCM-based textures down-sampled from GDS1 to GDS5 and used to estimate AGB produce less accurate results. Fortunately, combining Gabor-based textures with different scales leads to more accurate AGB estimates than combining GLCM-based textures with different ground resolutions, which confirms the assumption of Section 3.3. The Gabor filter can be seen as a microscope sensitive to orientation and scale (it has good spatial resolution and direction selectivity); it can capture local structural information corresponding to spatial frequency and is robust against illumination and pose. These advantages show that Gabor filtering is a powerful tool to describe the local gray distribution of the image (i.e., variations in texture). Therefore, Gabor filtering at different scales could be used to extract finer textures from images.

We estimated AGB using the LSSVM, ELM, and PLSR techniques by combining all GLCM-based textures, all Gabor-based textures, and the combined textures with crop height (Figure 11; Supplementary A3). The results show that all models combined with crop height significantly improve the estimation accuracy, which confirms the importance of crop height for estimating potato AGB and confirmed the speculation in the introduction (Figure 5) that high-frequency information combined with vertical structure information may improve AGB estimates. Note that different textures combined with crop height produce the most accurate AGB estimates, and the samples are closer to a 1:1 line (Figure 11). Taking the 1,000 kg/hm^2 AGB sample as the splitting point, we counted the NRMSE of the different models (Supplementary Figure 4). Using high AGB (1000–3,000 kg/hm^2) samples as benchmarks, the accuracy of the AGB estimation model improves (i) by 22.97% (NRMSE) when using different types of textures combined with crop height (GLCM-all and Gabor-all, Hdsm) with the LSSVM technique as opposed to using only GLCM-all textures, (ii) by 14.63% compared with using only Gabor-all textures, (iii) by 9.74% compared with GLCM-all textures combined with crop height (GLCM-all, Hdsm), and (iv) by 8.18% compared with Gabor-all textures combined with crop height (Gabor-all, Hdsm). This study used one-year data to estimate potato AGB based on crop morphological characteristics accurately, but it lacked validation analysis of multi-year experiments. In future research, we will collect potato data from different places and years to evaluate the model's performance, enhancing the reliability of the research results.

Conclusion

This work evaluates the performance of GLCM-based textures of differing resolutions and Gabor-based textures of differing scales and their combination with crop height for estimating potato AGB. The results lead to the following conclusions:

1. The correlation between GLCM-based textures and AGB is unaffected by the direction and window, but it is more affected by the ground resolution. The correlation between Gabor-based textures and potato AGB is significantly more affected by scale than by direction.
2. The GLCM-based textures of GDS1and GDS30 produce the most accurate AGB estimates when the ground resolution ranges from 1 to 5 cm and 10 to 60 cm, respectively. However, the accuracy of potato AGB estimates based on Gabor-based textures gradually deteriorates upon increasing the convolution kernel scale.
3. Both multi-resolution GLCM-based textures and multiscale Gabor-based textures are better than single-type textures for estimating AGB, and multiscale Gabor-based textures are the best for estimating AGB.
4. Gabor-based textures combined with crop height produce more accurate AGB estimates than GLCM-based textures. Optimistically, combining two different types of textures with crop height solves the problem

whereby potato samples with high AGB are underestimated, which is especially important for monitoring crop growth and advancing the development of precision agriculture.

Data availability statement

The original contributions presented in the study are included in the article/Supplementary material, further inquiries can be directed to the corresponding author.

Author contributions

HF, ZL, and GY designed the experiments. YL and HF collected the AGB, plant height and UAV digital images, analyzed the data, and wrote the manuscript. JY, XJ, and ZL provided comments and suggestions for the manuscript and checked the writing. All authors contributed to the article and approved the submitted version.

Funding

This study was supported by the Key scientific and technological projects of Heilongjiang province (2021ZXJ05A05), the Key Field Research and Development Program of Guangdong Province (2019B020216001) and the National Natural Science Foundation of China (41601346).

Conflict of interest

The authors declare that the research was conducted in the absence of any commercial or financial relationships that could be construed as a potential conflict of interest.

Publisher's note

All claims expressed in this article are solely those of the authors and do not necessarily represent those of their affiliated organizations, or those of the publisher, the editors and the reviewers. Any product that may be evaluated in this article, or claim that may be made by its manufacturer, is not guaranteed or endorsed by the publisher.

Supplementary material

The Supplementary material for this article can be found online at: https://www.frontiersin.org/articles/10.3389/fpls.2022.938216/full#supplementary-material

References

Banda, F., and Tebaldini, S. (2020). Ground and volume decomposition as a proxy for AGB from P-band SAR data. *Remote Sens.* 12, 240–253. doi: 10.3390/rs12020240

Bao, N. S., Li, W., Gu, X. W., and Liu, Y. H. (2020). Biomass estimation for semiarid vegetation and mine rehabilitation using worldview-3 and sentinel-1 SAR imagery. *Remote Sens.* 11, 2855–2879. doi: 10.3390/rs11232855

Batistoti, J., Marcato, J., Itavo, L., Matsubara, E., Gomes, E., Oliveira, B., et al. (2019). Estimating pasture biomass and canopy height in Brazilian savanna using UAV photogrammetry. *Remote Sens.* 11, 2447–2470. doi: 10.3390/rs11202447

Cao, L. D., Pan, J., Li, R. J., Li, J. L., and Li, Z. F. (2018). Integrating airborne LiDAR and optical data to estimate forest aboveground biomass in arid and semi-arid regions of China. *Remote Sens.* 10, 532–553. doi: 10.3390/rs10040532

Castaldi, F., Casa, R., Pelosi, F., and Yang, H. (2015). Influence of acquisition time and resolution on wheat yield estimation at the field scale from canopy biophysical variables retrieved from SPOT satellite data. *Int. J. Remote Sens.* 36, 2438–2459. doi: 10.1080/01431161.2015.1041174

Chen, J., Gu, S., Shen, M. G., Tang, Y. H., and Matsushita, B. (2009). Estimating aboveground biomass of grassland having a high canopy cover: an exploratory analysis of hyperspectral data. *Int. J. Remote Sens.* 30, 6497–6517. doi: 10.1080/01431160902882496

Christelle, G., and Emmanuel, D. (2020). RGB image-derived indicators for spatial assessment of the impact of broadleaf weeds on wheat biomass. *Remote Sens.* 12, 2982–3001. doi: 10.3390/RS12182982

David, A. J., Hernan, D. B., and Jocelyn, C. (2020). Graph-based data fusion applied to: change detection and biomass estimation in rice crops. *Remote Sens.* 12, 2683–2705. doi: 10.3390/RS12172683

Dong, L. F., Du, H. Q., Han, N., Li, X. J., Zhu, D., Mao, F. J., et al. (2020). Application of convolutional neural network on Lei Bamboo above-ground-biomass (AGB) estimation using Worldview-2. *Remote Sens.* 12, 958–982. doi: 10.3390/rs12060958

Duan, B., Fang, S., Gong, Y., Wu, X., and Zhu, R. (2021). Remote estimation of grain yield based on UAV data in different rice cultivars under contrasting climatic zone. *Field Crops Res.* 267, 108148–108166. doi: 10.1016/j.fcr.2021.108148

Filippi, A. M., Guneralp, I., and Randall, J. (2014). Hyperspectral remote sensing of aboveground biomass on a river meander bend using multivariate adaptive regression splines and stochastic gradient boosting. *Remote Sens. Lett.* 5, 432–441. doi: 10.1080/2150704X.2014.915070

Fu, Y., Yang, G. J., Li, Z. H., Song, X. Y., Li, Z. H., Xu, X. G., et al. (2020). Winter wheat nitrogen status estimation using UAV-based RGB imagery and Gaussian processes regression. *Remote Sens.* 12, 3778–3805. doi: 10.3390/rs12223778

Fu, Y., Yang, G., Song, X., Li, Z., Xu, X., Feng, H., et al. (2021). Improved estimation of winter wheat aboveground biomass using multiscale textures extracted from UAV-based digital images and hyperspectral feature analysis. *Remote Sens.* 13, 581–603. doi: 10.3390/rs13040581

Fu, Y., Yang, G., Wang, J., Song, X., and Feng, H. (2014). Winter wheat biomass estimation based on spectral indices, band depth analysis and partial least squares regression using hyperspectral measurements. *Comput. Electron. Agric.* 100, 51–59. doi: 10.1016/j.compag.2013.10.010

Gnyp, M. L., Miao, Y., Yuan, F., Ustin, S. L., Yu, K., Yao, Y., et al. (2014). Hyperspectral canopy sensing of paddy rice aboveground biomass at different growth stages. *Field Crops. Res.* 155, 42–55. doi: 10.1016/j.fcr.2013.09.023

Guo, Y., Fu, Y., Chen, S., Li, X., Sun, H., Wang, S., et al. (2021). Integrating spectral and textural information for identifying the tasseling date of summer maize using UAV based RGB images. *Int. J. Appl. Earth Obs. Geoinf.* 102, 102435–102452. doi: 10.1016/j.jag.2021.102435

Han, D., Yang, H., Qiu, C. X., Yang, G. J., Chen, E. X., Dong, Y., et al. (2019). Estimating wheat biomass from GF-3 data and a polarized water cloud model. *Remote Sens. Lett.* 10, 234–243. doi: 10.1080/2150704X.2018.1542184

He, L. M., Wang, R., Mostovoy, G., Liu, J. E., Chen, J. M., Shang, J. L., et al. (2021). Crop biomass mapping based on ecosystem modeling at regional scale using high resolution Sentinel-2 data. *Remote Sens.* 13, 806–829. doi: 10.3390/rs13040806

Hosseini, M., McNairn, H., Mitchell, S., Robertson, L. D., Davidson, A., and Homayouni, S. (2019). Synthetic aperture radar and optical satellite data for estimating the biomass of corn. *Int. J. Appl. Earth Obs. Geoinf.* 83, 101933. doi: 10.1016/j.jag.2019.101933

Hu, T. Y., Zhang, Y., Su, Y. J., Zheng, Y., Lin, G. H., and Guo, Q. H. (2020). Mapping the global mangrove forest aboveground biomass using multisource remote sensing data. *Remote Sens.* 12, 1690–1771. doi: 10.3390/rs12101690

Huang, S. Y., Miao, Y. X., Wang, T. T., Li, Y., Zhang, J., Sun, W. C., et al. (2015). Satellite remote sensing-based in-season diagnosis of rice nitrogen status in Northeast China. *Remote Sens.* 7, 10646–10667. doi: 10.3390/rs70810646

Issa, S., Dahy, B., Ksiksi, T., and Saleous, N. (2020). Allometric equations coupled with remotely sensed variables to estimate carbon stocks in date palms. *J. Arid Environ.* 182, 104264–104276. doi: 10.1016/j.jaridenv.2020.104264

Jones, J. P., and Palmer, L. A. (1987). An evaluation of the two-dimensional Gabor filter model of simple receptive fields in cat striate cortex. *J. Neurobiol.* 58, 1233–1258. doi: 10.1152/jn.1987.58.6.1233

Kumar, P., Krishna, A. P., Rasmussen, T. M., and Pal, M. K. (2021). Rapid evaluation and validation method of above ground forest biomass estimation using optical remote sensing in tundi reserved forest area. *India. Isprs. Int. J. Geo-Inf.* 10, 29–41. doi: 10.3390/ijgi10010029

Li, F., Cristiano, R. M., Benjamin, W., and Mitra, M. (2020a). High-throughput switchgrass phenotyping and biomass modeling by UAV. *Front. Plant Sci.* 11:574073. doi: 10.3389/fpls.2020.574073

Li, B., Xu, X., Zhang, L., Han, J., Bian, C., Li, G., et al. (2020b). Above-ground biomass estimation and yield prediction in potato by using UAV-based RGB and hyperspectral imaging. *ISPRS J. Photogramm. Remote Sens.* 162, 161–172. doi: 10.1016/j.isprsjprs.2020.02.013

Li, J. W., Zhang, F., Qian, X. Y., Zhu, Y. H., and Shen, G. X. (2015). Quantification of rice canopy nitrogen balance index with digital imagery from unmanned aerial vehicle. *Remote Sens. Lett.* 6, 183–189. doi: 10.1080/2150704X.2015.1021934

Liu, Y., Feng, H. K., Huang, J., Yang, F. Q., Wu, Z. C., and Sun, Q. (2021a). Estimation of potato above ground biomass based on hyperspectral characteristic parameters of UAV and plant height. *Spectrosc. Spect. Anal.* 41, 903–911. doi: 10.3964/j.issn.1000-0593(2021)03-0903-09

Liu, Y., Hatou, K., Aihara, T., Kurose, S., Akiyama, T., Kohno, Y., et al. (2021b). A robust vegetation index based on different UAV RGB images to estimate SPAD values of naked barley leaves. *Remote Sens.* 13, 686–708. doi: 10.3390/rs13040686

Lu, N., Zhou, J., Han, Z., Li, D., Cao, Q., Yao, X., et al. (2019). Improved estimation of aboveground biomass in wheat from RGB imagery and point cloud data acquired with a low-cost unmanned aerial vehicle system. *Plant Methods* 15, 17–39. doi: 10.1186/s13007-019-0402-3

Ma, J. C., Li, Y. X., Chen, Y. Q., Du, K. M., Zheng, F. X., Zhang, L. X., et al. (2019). Estimating above ground biomass of winter wheat at early growth stages using digital images and deep convolutional neural network. *Eur. J. Agron.* 103, 117–129. doi: 10.1016/j.eja.2018.12.004

Malambo, L., Popescu, S. C., Vidrine, M., McCutchen, B., Baltensperger, D., Bishop, M. (2018). Multitemporal field-based plant height estimation using 3D point clouds generated from small unmanned aerial systems high-resolution imagery. *Int. J. Appl. Earth Obs. Geoinf.* 64, 31–42. doi: 10.1016/j.jag.2017.08.014

Mao, P., Qin, L., Hao, M., Zhao, W., Luo, J., Qiu, X., et al. (2021). An improved approach to estimate above-ground volume and biomass of desert shrub communities based on UAV RGB images. *Ecol. Indic.* 125, 107494–107511. doi: 10.1016/j.ecolind.2021.107494

Marshall, M., and Thenkabail, P. (2015). Advantage of hyperspectral EO-1 Hyperion over multispectral IKONOS, GeoEye-1, WorldView-2, Landsat ETM+, and MODIS vegetation indices in crop biomass estimation. *ISPRS J. Photogramm. Remote Sens.* 108, 205–218. doi: 10.1016/j.isprsjprs.2015.08.001

Meng, J., Du, X., and Wu, B. (2013). Generation of high spatial and temporal resolution NDVI and its application in crop biomass estimation. *Int. J. Digit. Earth.* 6, 203–218. doi: 10.1080/17538947.2011.623189

Meng, B. P., Ge, J., Liang, T. G., Yang, S. X., Gao, J. L., Feng, Q. S., et al. (2017). Evaluation of remote sensing inversion error for the above-ground biomass of alpine meadow grassland based on multi-source satellite data. *Remote Sens.* 9, 372–394. doi: 10.3390/rs9040372

Montesano, P. M., Cook, B. D., Sun, G., Simard, M., Nelson, R. F., Ranson, K. J., et al. (2013). Achieving accuracy requirements for forest biomass mapping: A spaceborne data fusion method for estimating forest biomass and LiDAR sampling error. *Remote Sens. Environ.* 130, 153–170. doi: 10.1016/j.rse.2012.11.016

Montesano, P. M., Nelson, R. F., Dubayah, R. O., Sun, G., Cook, B. D., Ranson, K. R., et al. (2014). The uncertainty of biomass estimates from LiDAR and SAR across a boreal forest structure gradient. *Remote Sens. Environ.* 154, 398–407. doi: 10.1016/j.rse.2014.01.027

Niu, Y., Zhang, L., Zhang, H., Han, W., and Peng, X. (2019). Estimating above-ground biomass of maize using features derived from UAV-based RGB imagery. *Remote Sens.* 11, 1261–1284. doi: 10.3390/rs11111261

Poley, L. G., and McDermid, G. J. (2020). A systematic review of the factors influencing the estimation of vegetation aboveground biomass using unmanned aerial systems. *Remote Sens.* 12, 1052–1075. doi: 10.3390/rs12071052

Roth, L., and Streit, B. (2018). Predicting cover crop biomass by lightweight UAS-based RGB and NIR photography: an applied photogrammetric approach. *Precis. Agric.* 19, 93–114. doi: 10.1007/s11119-017-9501-1

Ryu, J. H., Jeong, H., and Cho, J. (2020). Performances of vegetation indices on paddy rice at elevated air temperature, heat stress, and herbicide damage. *Remote Sens.* 12, 2654–2671. doi: 10.3390/RS12162654

Salum, R. B., Souza, P. M., Simard, M., Silva, C. A., Fernandes, M. B., Cougo, M. F., et al. (2020). Improving mangrove above-ground biomass estimates using LiDAR. *Estuar. coast. Shelf S.* 236, 106585–106596. doi: 10.1016/j.ecss.2020.106585

Shen, L., and Bai, L. (2006). A review on Gabor wavelets for face recognition. *Pattern Anal. Appl.* 9, 273–292. doi: 10.1007/s10044-006-0033-y

Tao, H. L., Feng, H. K., Xu, L. J., Miao, M. K., Long, H. L., Yue, J. B., et al. (2020). Estimation of crop growth parameters using UAV-based hyperspectral remote sensing data. *Sensors* 20, 1296–1317. doi: 10.3390/s20051296

Walter, J. C., Edwards, J., McDonald, G., and Kuchel, H. (2019). Estimating biomass and canopy height with LiDAR for field crop breeding. *Front. Plant Sci.* 10:1145. doi: 10.3389/fpls.2019.01145

Wan, L., Zhang, J. F., Dong, X. Y., Du, X. Y., Zhu, J. P., Sun, D. W., et al. (2021). Unmanned aerial vehicle-based field phenotyping of crop biomass using growth traits retrieved from PROSAIL model. *Comput. Electron. Agr.* 187, 106304–106316. doi: 10.1016/j.compag.2021.106304

Wang, C., Nie, S., Xi, X. H., Luo, S. Z., and Sun, X. F. (2017). Estimating the biomass of maize with hyperspectral and LiDAR data. *Remote Sens.* 9, 11–24. doi: 10.3390/rs9010011

Wang, F., Yi, Q., Hu, J., Xie, L., Yao, X., Xu, T., et al. (2021). Combining spectral and textural information in UAV hyperspectral images to estimate rice grain yield. *Int. J. Appl. Earth Obs. Geoinf.* 102, 102397–102414. doi: 10.1016/j.jag.2021.102397

Xu, Q., Man, A., Fredrickson, M., Hou, Z. Y., Pitkanen, J., Wing, B., et al. (2018). Quantification of uncertainty in aboveground biomass estimates derived from small-footprint airborne LiDAR. *Remote Sens. Environ.* 216, 514–528. doi: 10.1016/j.rse.2018.07.022

Yang, Z., Li, K., Shao, Y., Brisco, B., and Liu, L. (2016). Estimation of paddy rice variables with a modified water cloud model and improved polarimetric decomposition using multi-temporal RADARSAT-2 images. *Remote Sens.* 8, 878–898. doi: 10.3390/rs8100878

Yang, H. B., Li, F., Wang, W., and Yi, K. (2021a). Estimating above-ground biomass of potato using random forest and optimized hyperspectral indices. *Remote Sens.* 13, 2339–2358. doi: 10.3390/rs13122339

Yang, Y. L., Wang, J. L., Chen, Y., Cheng, F., Liu, G. J., and He, Z. H. (2019). Remote-sensing monitoring of grassland degradation based on the GDI in Shangri-La. *China. Remote Sens.* 11, 3030–3054. doi: 10.3390/rs11243030

Yang, J., Zhang, Y., Du, L., Liu, X. G., Shi, S., and Chen, B. W. (2021b). Improving the selection of vegetation index characteristic wavelengths by using the PROSPECT model for leaf water content estimation. *Remote Sens.* 13, 821–841. doi: 10.3390/rs13040821

Yao, X., Si, H., Cheng, T., Jia, M., Chen, Q., Tian, Y., et al. (2018). Hyperspectral estimation of canopy leaf biomass phenotype per ground area using a continuous wavelet analysis in wheat. *Front. Plant Sci.* 9:1360. doi: 10.3389/fpls.2018.01360

Yue, J., Feng, H., Jin, X., Yuan, H., Li, Z., Zhou, C., et al. (2018a). A comparison of crop parameters estimation using images from UAV-mounted snapshot hyperspectral sensor and high-definition digital camera. *Remote Sens.* 10, 1138–1162. doi: 10.3390/rs10071138

Yue, J. B., Feng, H. K., Yang, G. J., and Li, Z. H. (2018b). A comparison of regression techniques for estimation of above-ground winter wheat biomass using near-surface spectroscopy. *Remote Sens.* 10, 66–89. doi: 10.3390/rs10010066

Yue, J., Yang, G., Tian, Q., Feng, H., Xu, K., and Zhou, C. (2019). Estimate of winter-wheat above-ground biomass based on UAV ultrahigh-ground-resolution image textures and vegetation indices. *ISPRS J. Photogramm. Remote Sens.* 150, 226–244. doi: 10.1016/j.isprsjprs.2019.02.022

Yue, J., Zhou, C., Guo, W., Feng, H., and Xu, K. (2021). Estimation of winter-wheat above-ground biomass using the wavelet analysis of unmanned aerial vehicle-based digital images and hyperspectral crop canopy images. *Int. J. Remote Sens.* 42, 1602–1622. doi: 10.1080/01431161.2020.1826057

Zeng, L., Peng, G. Z., Meng, R., Man, J. G., Li, W. B., Xu, B. Y., et al. (2021). Wheat yield prediction based on unmanned aerial vehicles-collected red-green-blue imagery. *Remote Sens.* 13, 2937–2959. doi: 10.3390/rs13152937

Zhang, M., Zhou, J., Sudduth, K., and Kitchen, N. (2020). Estimation of maize yield and effects of variable-rate nitrogen application using UAV-based RGB imagery. *Biosyst. Eng.* 189, 24–35. doi: 10.1016/j.biosystemseng.2019.11.001

Zhou, M., Huang, J. X., Li, L., Zhang, X. D., Ma, H. Y., Cao, X. R., et al. (2019). Assimilating soil moisture retrieved from sentinel-1 and sentinel-2 data into WOFOST model to improve winter wheat yield estimation. *Remote Sens.* 11, 1618–1635. doi: 10.3390/rs11131618

Zhou, C. Q., Liang, D., Yang, X. D., Xu, B., and Yang, G. J. (2018). Recognition of wheat spike from field-based phenotype platform using Mul-tisensor fusion and improved maximum entropy segmentation algorithms. *Remote Sens.* 10, 246–270. doi: 10.3390/rs10020246

Zhu, W., Sun, Z., Huang, Y., Yang, T., Li, J., Zhu, K., et al. (2021). Optimization of multi-source UAV RS agro-monitoring schemes designed for field-scale crop phenotyping. *Precis. Agric.* 22, 1768–1802. doi: 10.1007/s11119-021-09811-0

Zhu, W. X., Sun, Z. G., Peng, J. B., Huang, Y. H., Li, J., Zhang, J. Q., et al. (2019a). Estimating maize above-ground biomass using 3D point clouds of multi-source unmanned aerial vehicle data at multi-spatial scales. *Remote Sens.* 11, 2678. doi: 10.3390/rs11222678

Zhu, Y., Zhao, C., Yang, H., Yang, G., Han, L., Li, Z. H., et al. (2019b). Estimation of maize above-ground biomass based on stem-leaf separation strategy integrated with LiDAR and optical remote sensing data. *Peer J.* 7, e7593. doi: 10.7717/peerj.7593

frontiers | Frontiers in Plant Science

TYPE Original Research
PUBLISHED 06 October 2022
DOI 10.3389/fpls.2022.1001779

Check for updates

OPEN ACCESS

EDITED BY
Xiuliang Jin,
Institute of Crop Sciences (CAAS), China

REVIEWED BY
Dipankar Mandal,
Kansas State University, United States
Zheng Zhao,
Chinese Academy of Surveying and Mapping, China

*CORRESPONDENCE
Shuli Wang
shuli.wang1@hotmail.com
Long Liu
liulong@radi.ac.cn

†These authors have contributed equally to this work and share first authorship

SPECIALTY SECTION
This article was submitted to Sustainable and Intelligent Phytoprotection, a section of the journal Frontiers in Plant Science

RECEIVED 24 July 2022
ACCEPTED 20 September 2022
PUBLISHED 06 October 2022

CITATION
Wang Z, Wang S, Wang H, Liu L, Li Z, Zhu Y and Wang K (2022) Field-scale rice yield estimation based on UAV-based MiniSAR data with Ku band and modified water-cloud model of panicle layer at panicle stage. *Front. Plant Sci.* 13:1001779. doi: 10.3389/fpls.2022.1001779

COPYRIGHT
© 2022 Wang, Wang, Wang, Liu, Li, Zhu and Wang. This is an open-access article distributed under the terms of the Creative Commons Attribution License (CC BY). The use, distribution or reproduction in other forums is permitted, provided the original author(s) and the copyright owner(s) are credited and that the original publication in this journal is cited, in accordance with accepted academic practice. No use, distribution or reproduction is permitted which does not comply with these terms.

Field-scale rice yield estimation based on UAV-based MiniSAR data with Ku band and modified water-cloud model of panicle layer at panicle stage

Zhiyong Wang[1†], Shuli Wang[2*†], Hongxiang Wang[3], Long Liu[4*], Zhenjin Li[1], Yuandong Zhu[1] and Kai Wang[1]

[1]College of Geodesy and Geomatics, Shandong University of Science and Technology, Qingdao, China, [2]Institute of Intelligent Science and Technology, Shandong Cultural Industry Vocational College, Qingdao, China, [3]College of Information Science and Engineering, Shandong Agricultural University, Tai'an, China, [4]Laboratory of Target Microwave Properties (LAMP), Zhongke Deqing Academy of Satellite Application (DASA), Huzhou, China

Scientific and accurate estimation of rice yield is of great significance to food security protection and agricultural economic development. Due to the weak penetration of high frequency microwave band, most of the backscattering comes from the rice canopy, and the backscattering coefficient is highly correlated with panicle weight, which provides a basis for inversion of wet biomass of rice ear. To solve the problem of rice yield estimation at the field scale, based on the traditional water cloud model, a modified water-cloud model based on panicle layer and the radar data with Ku band was constructed to estimate rice yield at panicle stage. The wet weight of rice ear scattering model and grain number per rice ear scattering model were constructed at field scale for rice yield estimation. In this paper, the functional area of grain production in Xiashe Village, Xin'an Town, Deqing County, Zhejiang Province, China was taken as the study area. For the first time, the MiniSAR radar system carried by DJI M600 UAV was used in September 2019 to obtain the SAR data with Ku band under polarization HH of the study area as the data source. Then the rice yield was estimated by using the newly constructed modified water-cloud model based on panicle layer. The field investigation was carried out simultaneously for verification. The study results show: the accuracies of the inversion results of wet weight of rice ear scattering model and grain number per rice ear scattering model in parcel B were 95.03% and 94.15%; and the accuracies of wet weight of rice ear scattering model and grain number per rice ear scattering model in parcel C+D+E were over 91.8%. In addition, different growth stages had effects on yield estimation accuracy. For rice at fully mature, the yield estimation accuracies of wet weight of ear and grain number per ear were basically similar, both exceeding 94%. For rice at grouting stage, the yield estimation accuracy of wet weight of ear was 92.7%, better than that of grain number per ear. It was proved that it can effectively estimate rice yield using the modified

water-cloud model based on panicle layer constructed in this paper at panicle stage at field scale.

KEYWORDS

Rice yield estimation, Modified water-cloud model of panicle layer, Field scale, MiniSAR, Ku band

1 Introduction

As one of the three major food corps in the world, rice is an important survival necessity for human beings (Huang et al., 2020). China, as a major rice producer and exporter, ranks first in the world in annual rice output. Scientific and accurate estimation of rice yield is of great significance to national food security and agricultural economic development (Shen et al., 2009; Guo et al., 2020; Huang et al., 2020).

In the face of several unfavorable conditions, such as abnormal global climate change, frequent occurence of natural disaster and continuous population growth, it is an urgent problem to obtain timely and accurate information on rice growth and yield in China.

In the background of continuous development of science and technology, intelligent methods for monitoring rice gradually appear (Gu et al., 2022; Huang et al., 2022). With the development of satellite remote sensing technology and the improvement of agricultural remote sensing level, it has become a scientific and technological method of modern agriculture to monitor rice growth and estimate rice yield using remote sensing technology. At present, optical remote sensing, hyperspectral remote sensing, microwave remote sensing (including microwave scatterometer, synthetic aperture radar) and other remote sensing techniques have been successfully applied to monitor the rice growth and yield estimation (Jia et al., 2014; Guan. K et al., 2018; Setiyono et al., 2018; Wu et al., 2020; Alebele et al., 2021; Jing et al., 2022).

Different types of sensors also have their own advantages and disadvantages in rice yield estimation. Because rice is mainly grown in the cloudy and rainy tropical and subtropical regions, it is often covered by cloud and rain for a long time during its growth cycle. Such as Zhejiang province, Hunan province, Hubei province, Guangdong province and other provinces in South China, during the growth cycle of early rice, the probability of obtaining an optical remote sensing image with cloud amount less than 10% is only 7%. As a result, it is often influenced by weather when monitoring the rice by optical satellite remote sensing (Shen et al., 2009; Jia et al., 2014; Huang et al., 2020). This has limited the large-scale application and promotion of related yield estimation methods. Synthetic Aperture Radar (SAR) is not influenced by cloud, fog, rain, snow and other weather, and it can obtain image data with the advantages of day/night data acquisition, all-weather imaging capability, and strong penetrability (Li et al., 2022; Wang et al., 2022; Yu et al., 2022). Satellite remote sensing can observe the earth from space over a large area. At present, radar remote sensing has become one of the best observation techniques for monitoring the rice and yield estimation (Shen et al., 2009; Jia et al., 2014; Huang et al., 2020; Wu et al., 2020). At the same time, radar remote sensing technology can obtain the radar response characteristics of rice canopy under different polarization, including scattering intensity information and phase information, which can better reflect the rice canopy water content, plant structure and growth situation (Guan. K et al., 2018; Setiyono et al., 2018; Guo et al., 2020). Radar remote sensing is complementary to optical remote sensing. So it can provide abundant data support for establishing reliable and stable rice monitoring system based on radar remote sensing.

The methods and applications for monitoring rice and yield estimation based on radar remote sensing technology have been studied by many researchers. At present, radar remote sensing technology has been successfully applied in monitoring the rice planting area and mapping the rice classification (Yang et al., 2017; Yuzugullu et al., 2017; Guan. K et al., 2018; Guo et al., 2018; Mandal et al., 2018; Alebele et al., 2020; Dipankar et al., 2020; Yang et al., 2021). On this basis, many researchers began to focus on rice plant height inversion (Lee et al., 2018; Ndikumana et al., 2018; Guo et al., 2020) and rice yield estimation (Shen et al., 2009; Zhang et al., 2017; Kersten et al., 2018; Asilo et al., 2019; Huang et al., 2020), and achieved a series of achievements. Traditional SAR rice monitoring and yield estimation are often based on the SAR data with low frequency, such as X, C band and L band. Compared with the SAR data with high frequency, it has certain difficulties when usig SAR data with low frequency to estimate the rice yield: microwave with low frequency band could penetrate rice panicle layer, which makes the radar echo containing much information about stem and leaf layer and even the underlying surface. This increases the difficulty of the modeling, and reduces the yield estimation accuracy. To solve this problem, Jia et al. (2014) firstly established a forward microwave scattering model of rice, which contained a large number of parameter information on stem and leaf layer and the

underlying surface, and then constructed inversion model based on neural network to establish rice yield model. However, if more radar echoes of rice canopy are derived from rice panicle layer, the number of input parameters in forwarding modeling can be greatly reduced.

To overcome the disadvantages of radar data with low frequency when estimating the rice yield, the SAR data with high frequency can be used for rice yield estimation. At present, researches on monitoring the rice by SAR data with high frequency have been carried out internationally. As early as 1989, Toan et al. (1989) used airborne SAR in France to obtain dual-polarization and multi-temporal radar images of rice in X band during the growing stage and extracted radar backscattering characteristics. The study found that before rice was at tillering stage, the backscattering coefficient increased with the growth of rice, showing a strong correlation with the biomass of rice. This is the first application of SAR data with high frequency in monitoring rice. In 2000, Kim et al. (2000) used X band scatterometer to study the change of backscattering coefficient over time in rice fields, and obtained the continuous response value of incident angle (0-70°) for the first time. The study showed that the backscattering coefficient reached the maximum of about 43-60 days after rice transplanting. In 2002, Inoue et al. (2002) analyzed the relationship between backscattering coefficients of different frequencies and rice growth parameters by using multi frequency and full polarized scatterometer, and found that the backscattering coefficients of high frequency microwave (Ka, Ku, X band) were highly correlated with weight of ear. It provided a basis for ground measurement of rice panicle biomass inversion based on SAR data with high frequency. From 2013 to 2014, further experimental studies (Inoue and Sakaiya, 2013; Inoue et al., 2014) found that the backscattering coefficient under VV polarization decreased with the increase of panicle grain plumpness at the filling stage. The sensitivity of backscattering coefficient under VV polarization to the biomass of rice ear was explained experimentally, and the radar data with X band was significantly correlated with weight of ear at high incidence angle. In 2012, Nguyen et al. (2012) selected TerraSAR-X data of five time phases after rice sowing to perform linear regression fitting on rice field measurement data to estimate rice yield. Compared with official statistical data, the fitting accuracy of total output is up to 95%. The results showed that the high resolution X band SAR data is reliable in rice yield estimation. From 2015 to 2017, based on the high frequency dual polarization TanDEM-X data, Lopez-Sanchez, Erten, and Rossi et al. (Erten et al., 2015; Rossi and Erten, 2015; Erten et al., 2016; Lopez-Sanchez et al., 2017) monitored the changes of rice plant height during the growing stage, verified its potential in rice plant height inversion, and provided effective data support for rice yield estimation. Maki et al. (2017) used Cosmo-SkyMed data and rice leaf area index integrated crop model (SIMRIW-RS) to estimate regional rice yield in 2017. In conclusion, it is an effective data source to estimate rice yield using SAR data with high frequency. However, since the spaceborne SAR systems mostly work in X band or C band, it is still to be studied the feasibility and advantages of Ku band and other high frequency bands in rice yield estimation.

The water-cloud model is an effective model proposed by Attema and Ulaby in 1978 (Attema and Ulaby, 1978). On this basis, many modified water-cloud models have been proposed (Liu et al., 2012; Yang et al., 2016; Setiyono et al., 2019; Wu et al., 2020), such as the two layer water-cloud model. At present, rice yield estimation based on water-cloud model has achieved good results. Yang et al. (2016) estimated the change of wheat by using the modified water-cloud model (MWCM) and multi-temporal RADARSAT-2 images. The validation results showed that the MWCM could predict the temporal behaviors of the rice variables well during the growth cycle (R^2 >0.8). Setiyono et al. (2019) used SAR images and ORYZA crop growth model to realize the estimation of rice yield in a large area in South and Southeast Asian countries. Based on a single TerraSAR image, Wu et al. (2020) explored the effects of water-cloud model with different layers on rice yield estimation, indicating that single-layer water-cloud model is better than a double-layer water-cloud model in grain number estimation. In later developments, rice yield estimation based on remote sensing images also began to be combined to computer science, including physical scattering model, optimization algorithm, and gradient regression (Zhang et al., 2020; Arumugam et al., 2021). The results are better than those of the original models.

It can provide data support for fine agriculture research to realize the rice yield estimation at the field scale (Wang et al., 2019). At present, the Unmanned Aerial Vehicle (UAV) remote sensing has been widely used in rice yield estimation research work in field scale or small scale, but most of them are used the optical sensors or hyperspectral sensors (Zheng et al., 2018; Duan et al., 2019; Wang et al., 2019; Wang et al., 2022). Now, the research for rice yield estimation using UAV-based SAR data is very few, especially for the high frequency band, such as Ku band. When radar operates in Ku band, the backscattering is mainly from panicle layer. So the radar with Ku band is an effective sensor for rice yield estimation. It has advantages of convenience and maneuverability to estimate the rice yield using UAV-based MiniSAR. The research on rice yield estimation using UAV-based MiniSAR can enrich the technical approach to rice yield estimation at the field scale and it can provide a new means of rice yield estimation.

To verify the potential of radar data with Ku band in rice yield estimation and realize rice yield estimation at field scale, based on the radar data with Ku band acquired by the MiniSAR radar system mounted on the UAV platform, this paper constructed a rice yield estimation model suitable for the radar data with Ku band at panicle stage, and carried out rice yield estimation based on the backscattering coefficient of high-frequency SAR data and a modified water-cloud model.

The structure of this paper is arranged as follows: It introduces the study area and data in section 2. It mainly introduces the acquisition of UAV-based MiniSAR data, which can provide the radar data with Ku band. Section 3 is the method of this paper. In order to realize rice yield estimation at the field scale, a new modified water-cloud model based on panicle layer is constructed for rice yield estimation at panicle stage. It includes the wet weight of rice ear scattering model and grain number per rice ear scattering model. Section 4 is the experiment and results of this paper. The experiment is introduced in detail. Section 5 is the discussion and analysis part. Finally, some important conclusions of this study are given.

2 Study area and materials

2.1 Study area

The study area is located in the the functional area of grain production in Xiashe Village, Xin 'an Town, Deqing County, Zhejiang Province, China, which covers an area of 1 km^2. Its longitude ranges from 120°C10′40′′E to 120°C11′15′′E, and its latitude ranges from 30°C34′00′′N to 30°C34′25′′N, as shown in Figure 1. The study area is located in the HangJiaHu plain with the fertile land and belongs to grain mulberry area. It is also known as "land of fish and rice" and "home of silk". The study area has a subtropical humid monsoon climate, warm and humid, with distinct four seasons. The annual average temperature is 13-16°C, and the annual average precipitation is about 1379 mm, which are suitable for single-season rice growth. The functional area is dominated by rice and rape, with rice growing season from early June to the middle of November and rape growing season from November to the following May.

The main types of rice planted in the study area are Nanjing 46 and Nanjing 9108. Nanjing 46 is about 110 cm in plant height, compact plant type, medium with strong in tillering, large panicle type, upright panicle length of about 15cm, total grain number of 140-150 per panicle, setting percentage more than 90%, and 25-26 g per 1000 grains. Nanjing 9108 is about 96.4 cm in plant height, compact plant type and strong in tillering, total grain number of 125.5 per panicle, setting percentage about 94.2%, and 26.4 g per 1000 grains.

2.2 Data

2.2.1 MiniSAR data

MiniSAR is a radar system for UAVs independently developed by the Academy of Aerospace Information Innovation, Chinese Academy of Sciences (CAS). The radar system operates in the Ku band with the frequency of 14.6GHz and HH polarization. The undercenter look angle and incidence angle of the UAV-based MiniSAR image used in this study are both 50°. The MiniSAR radar system carried by the DJI M600 UAV platform was used to photograph the rice in the study area, obtain high resolution SAR images, and complete the acquisition of radar data of rice field. For the UAV-based MiniSAR data, we carried out speckle noise filtering, the radar backscatter information was presented in dB scale. The spatial resolution of the UAV-based MiniSAR image used in the experiment is 0.3m*0.3m. The area of the randomly selected sampling plot in the rice field survey sampling is 1.5m×1.5m, which theoretically includes 5*5 pixels in the SAR image. The backward

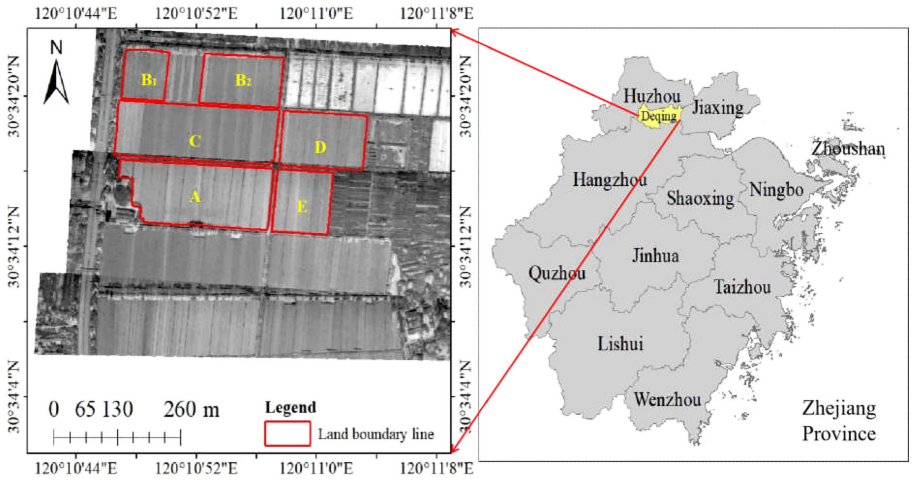

FIGURE 1
Geographical map of the study area. The left image shows the MiniSAR radar images and the locations of **(A–E)** parcels in the study area. The maps on the right show the geographical location of the study area.

scattering coefficients of 5*5 pixels are averaged to one when estimating the rice yield.

On the day of the experiment, the weather was clear with the north wind of level 1-2. The UAV was manually controlled to take off, and the flight altitude was 150 meters. The first flight was from 14:00 to 16:00 on September 24, 2019, and the second and third flights were from 9:00 to 11:00 on September 25, 2019, respectively. The acquisition of UAV-based MiniSAR data is about a week after the rainfall. Therefore, the research results of this paper are also basically not affected by seasonality. The flight range covered the whole rice study area. Table 1 shows the working parameters of the MiniSAR system. In the study area, five parcels (named parcel A, B, C, D and E) were selected for research and analysis.

2.2.2 Field investigation data

Field samples were collected from parcels B, C, D and E in the study area from September 23 to 25, 2019. Parcel B and parcel C are large, with an area of 22,759.4m^2(about 2.28 hectares) for parcel B and 24,579.35m^2(about 2.46 hectares) for parcel C. 40 sampling plots with an area of 1.5m×1.5m were randomly selected in parcel B and parcel C, and 40 rice pancel samples were collected, and numbered from 1 to 40. As a small area in the middle of parcel B is used for nitrogen fertilizer experiment, the amount of fertilizer application is different from other plots, and two varieties of Nanjing 46 and Nanjing 9108 are planted respectively, so this part of sampling is not carried out. Instead, rice fields outside this small area are selected, namely areas parcel B_1 and parcel B_2. All rice varieties in this area are Nanjing 9108 with uniform growth. Data collected in the two parcels were used for modeling and later validation. For parcel B, 40 original samples were collected, 28 samples were available after data cleaning, 18 were randomly selected for modeling, and the remaining 10 samples were used as validation data. For parcel C, 40 original samples were collected. The area of parcel D and parcel E is small, parcel D covers an area of about 12,763.98m^2(about 1.28 hectares), and parcel E covers an area of about 9,493.61m^2(about 0.95 hectares). 25 sampling plots with an area of 1.5m×1.5m were randomly selected in parcel D, 25 sampling plots with an area of 1.5m×1.5m were randomly selected in parcel E. 50 rice panicle samples were collected in parcel D and parcel E, and numbered from 1 to 50. Considering that the sowing and heading dates of rice in parcels C, D, and E were similar, the samples of the three parcels were combined to the parcel C+D+E to conduct yield estimation modeling and yield estimation. So for parcel C+D+E, a total of 90 original samples were collected. 10 samples were available for each parcel C, D and E after data cleaning, so a total of 30 samples for parcel C+D+E, and then 20 samples were randomly selected for modeling and the remaining 10 samples were used for validation. Figure 2 is some photos taken during the field investigation.

TABLE 1 The parameters of UAV-based MiniSAR data.

Item	Product Level
UAV platform	DJI M600
Sampling mode	Intermediate frequency sampling
Operating mode	Single channel
Radar band	Ku
Polarization	HH
Resolution (m)	0.3× 0.3
Center frequency (GHz)	14.6
Pulse bandwidth (MHz)	1200
Side direction	Right
Undercenter look angle (°)	50
Beam angle in range direction (°)	40
Beam angle in azimuth direction (°)	6

3 Method

To solve the problem of rice yield estimation at the field scale, we constructed a rice yield estimation method based on a new modified water-cloud model at panicle layer and the radar data with Ku band. Using the MiniSAR system mounted by DJI M600 UAV as the sensor, the synthetic aperture radar (SAR) data with Ku band during panicle stage in the study area were obtained, and the parameters of yield estimation model and rice yield in the study area were inverted. The overall technical flow chart of this paper is shown in Figure 3.

3.1 New modified water-cloud model based on panicle layer

The semi-empirical water-cloud model was firstly proposed by Attema and Ulaby et al. (Attema and Ulaby, 1978) in 1978. The water cloud model is suitable for rice biomass inversion because of its simple structure, fewer parameters and easy to get the reverse solution.

Yang et al. (2016) proposed the Modified Water-Cloud Model (MWCM), which considered phenology information and canopy level heterogeneity. Because the backscattering of high frequency band radar such as Ku band is mainly from the panicle layer of rice, n this paper, inspired by the MWCM model, the rice canopy is divided into two layers: panicle layer and stem and leaf layer, in order to obtain more accurate wet biomass of rice ear. Figure 4 is the simulation figure of the new water-cloud model based on panicle layer.

The expression of unit volume water content W (kg/m^3) of rice canopy can be expressed as follows:

$$W = W_1 + W_2 \quad (1)$$

$$W_1 = (m_{1w} - m_{1d}) \cdot n/h_1 \quad (2)$$



FIGURE 2
Photos taken during the field investigation in the study area.

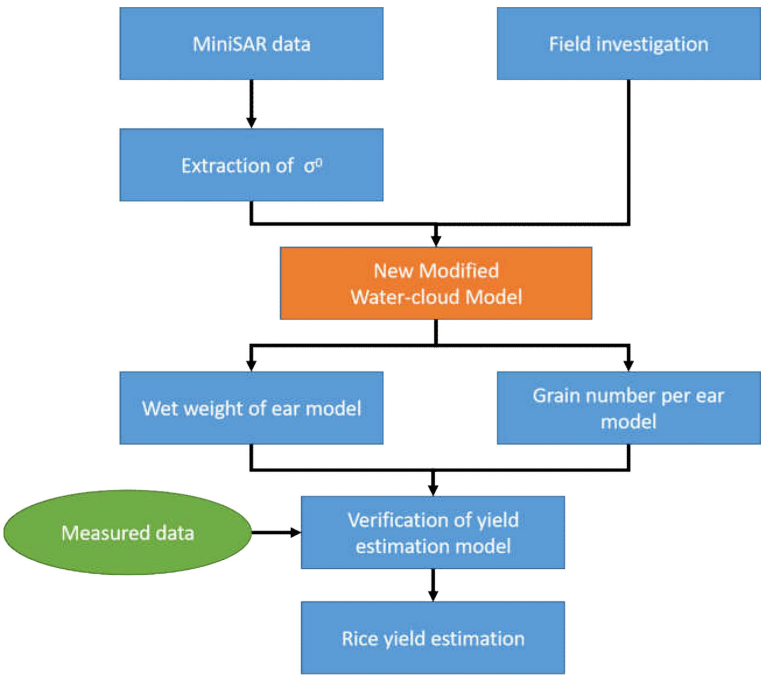

FIGURE 3
Overall technical flow chart.

$$W_2 = (m_{2w} - m_{2d}) \cdot n/h_2 \quad (3)$$

Where, W_1 and W_2 are water content per unit volume (kg/cm^3) of panicle layer and stem and leaf layer; h_1 and h_2 are height (m) of panicle layer and stem and leaf layer; m_{1w} and m_{2w} are wet weight (kg/plant) of panicle layer and stem and leaf layer for single plant respectively; m_{1d} and m_{2d} are dry weight (kg/plant) of panicle layer and stem and leaf layer for single plant respectively. Parmater n is the number of plants per unit area (plants/m^2).

The penetration of microwave with high frequency is poor. It is difficult to reach the ground through the stem and leaf layer. In general, for the total backscattering from the whole vegetation canopy, the proportion of multiple scattering from soil and vegetation canopy is very small. So we do not consider this kind of scattering when constructing new modified water-cloud model. Therefore, the following formula can be used to describe the total backscattering from rice canopy:

$$\sigma^0 = \sigma^0_{ear} + \tau^2_{ear} \cdot \sigma^0_{sl} + \tau^2_{ear} \cdot \tau^2_{sl} \cdot \sigma^0_{soil} \quad (4)$$

Where, σ^0 is the total backscattering from rice canopy; $\sigma^0 ear$ is the volume scattering from rice panicle layer; $\sigma^0 s\&l$ is the volume scattering from rice stem and leaf layer; $\sigma^0 soil$ is the radar scattering reflected by soil after the attenuation of canopy; $\tau^2 ear$ and $\tau^2 s\&l$ are the bidirectional attenuation coefficients of panicle layer and stem and leaf layer, and the canopy and soil layer respectively. The calculation formula of $\tau^2 ear$ and $\tau^2 s\&l$ are respectively expressed as:

$$\tau^2_{ear} = \exp(-2N_1 \cdot Q \cdot h_1/\cos\theta) \quad (5)$$

$$\tau^2_{sl} = \exp(-2N_2 \cdot Q \cdot h_2/\cos\theta) \quad (6)$$

Where, θ is the incidence angle of radar beam; N_i(i = 1 or 2) represents the number of water droplets in panicle layer, stem and leaf layer per unit volume respectively; and Q represents the attenuation cross section of a single water droplet.

Assuming that α denotes the attenuation coefficient of radar waves within the canopy and η denotes the radar cross section per unit volume in the vegetation canopy, which are defined as:

$$\eta = N_i \cdot \lambda \quad (7)$$

$$\alpha = N_i \cdot Q \quad (8)$$

Where λ is the scattering cross section of a single water droplet particle.

The volume scatterings from panicle layer and stem and leaf layer of rice are respectively expressed as:

$$\sigma^0_{ear} = (\lambda/2Q)[1 - \exp(-2N_1 \cdot Q \cdot h_1/\cos\theta)] \quad (9)$$

$$\sigma^0_{sl} = (\lambda/2Q)[1 - \exp(-2N_2 \cdot Q \cdot h_2/\cos\theta)] \quad (10)$$

The backscattering coefficient from soil is expressed as:

$$\sigma^0_{soil} = A\exp(B \cdot m_s) \quad (11)$$

Where, parameter A and B represent two parameters related to radar band, incidence angle, polarization mode and ground roughness; parameter λ represents the scattering cross section of a single water droplet; parameter m_s represents the water content per unit volume of soil.

Finally, considering the attenuation effect of rice canopy on radar wave, the new modified water-cloud model based on rice panicle layer is constructed in this paper as follows:

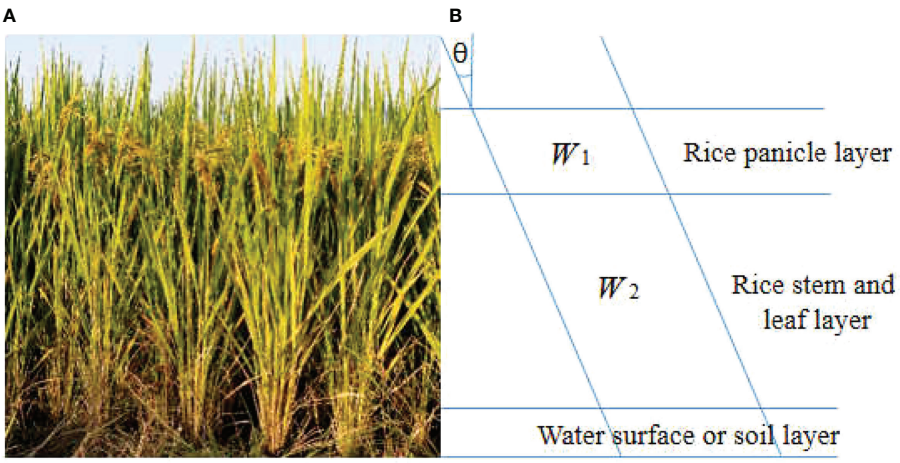

FIGURE 4
The simulation figure of the newly constructed water-cloud model based on panicle layer. **(A)** is the actual scene of the rice plant. **(B)** is the schematic diagram of new model. The canopy of rice is mainly divided into two parts: the pancicle layer, stem and leaf layer.

$$\sigma^0 = (\lambda/2Q)[1 - \exp(-2N_1 \cdot Q \cdot h_1/\cos\theta)] + (\lambda/2Q)[1 - \exp(-2N_2 \cdot Q \cdot h_2/\cos\theta)]\exp(-2N_1 \cdot Q \cdot h_1/\cos\theta) + A\exp(B \cdot m_s)\exp(-2N_1 \cdot Q \cdot h_1/\cos\theta)\exp(-2N_2 \cdot Q \cdot h_2/\cos\theta) \quad (12)$$

For ease of expression, we replace (7) with the parameter C. Since N is proportional to W, we replace NQ with DW, and the expression becomes:

$$\sigma^0 = C[1 - \exp(-2DW_1 \cdot h_1/\cos\theta)] + C[1 - \exp(-2DW_2 \cdot h_2/\cos\theta)]\exp(-2DW_1 \cdot h_1/\cos\theta) + A\exp(B \cdot m_s - 2DW_1 \cdot h_1/\cos\theta - 2DW_2 \cdot h_2/\cos\theta) \quad (13)$$

The above equation is simplified as:

$$\sigma^0 = C[1 - \exp(-2DW_1 \cdot h_1/\cos\theta - 2DW_2 \cdot h_2/\cos\theta)] + A\exp(B \cdot m_s - 2DW_1 \cdot h_1/\cos\theta - 2DW_2 \cdot h_2/\cos\theta) \quad (14)$$

σ^0 can also be expressed in decibels (dB) as:

$$\sigma^0 = 10 \cdot \log_{10}\{C[1 - \exp(-2DW_1 \cdot h_1/\cos\theta - 2DW_2 \cdot h_2/\cos\theta)] + A\exp(B \cdot m_s - 2DW_1 \cdot h_1/\cos\theta - 2DW_2 \cdot h_2/\cos\theta)\} \quad (15)$$

In the formula, the model parameters are denoted by A, B, C and D, which are obtained by regression analysis and fitting of the model to the measured rice backscatter coefficients. In some studies, the model coefficients A, B and D also are obtained by simulation with the soil backscatter model.

The study by Yang et al. (Shenbin, 2008) pointed out that there are two forms of rice water cloud models: (1) the rice water cloud model with the water layer as a special soil treatment; (2) the rice water cloud model based on the scattering mechanism. In this paper, we choose the model that is easier to derive its inverse function, the "rice water cloud model with the water layer as a special soil treatment" to carry out the inversion of rice biological parameters and complete rice yield estimation at the panicle stage.

During the maturity of rice, the depth of the water layer in the paddy field is usually 2 cm-5 cm, and some parcels are not covered by the water layer, and the soil of the paddy field is wet. Moreover, the penetration of high-frequency SAR microwaves is small and it is difficult to penetrate the stem and leaf layer to reach the ground, so the improved water cloud model for the rice panicle layer in the paper is the Equation (10).

$$\sigma^0 = C(1 - \exp(-2DW_1 \cdot h1/\cos\theta - 2DW_2 \cdot h_2/\cos\theta)) + \sigma^0_{BG}\exp(-2DW_1 \cdot h_1/\cos\theta - 2DW_2 \cdot h_2/\cos\theta) \quad (16)$$

Formula (16) can be simplified as follows:

$$\sigma^0 = C + (\sigma^0_{BG} - C)(\exp(-2DW_1 \cdot h_1/\cos\theta - 2DW_2 \cdot h_2/\cos\theta)) \quad (17)$$

Where, $\sigma^0{}_{BG}$ is a constant term, representing the backscattering coefficient of the water layer covering rice field. For the new modified water-cloud model, h_1 and h_2 represent the heights of rice panicle layer and stem and leaf layer; W_1 and W_2 represent the water content per unit volume of rice panicle layer and stem and leaf layer. Therefore, $W_1 \cdot h_1$ and $W_2 \cdot h_2$ represent the water content per unit area of rice panicle layer and stem and leaf layer respectively.

Formula (17) is the new modified water-cloud model based on panicle layer constructed in this paper for rice yield estimation at panicle stage, which is mainly suitable for the radar data with high frequency, such as Ku band. Considering that the Ku band is less penetrating, it will be more sensitive to the rice panicle layer. It is less sensitive to the stem and leaf layer, which affect the sensitivity of parameters such as leaf area index (LAI) and plant height. Therefore, the improved water cloud model in this paper was simplified by not considering information on other parameters affecting the model, the sensitivity analysis was not performed for the relevant parameters, and only considering the rice panicle layer.

3.2 Estimation of the model parameters

There are only three unknown parameters in the formula (17): C, D and $\sigma^0{}_{BG}$. The above parameters are usually obtained by fitting method after field measurement of backscattering coefficient and water content of rice.

By combining the similar terms of formula (17), we can obtain the formula (18) as follows:

$$(W_1 \cdot h_1 + W_2 \cdot h_2) = \frac{\cos\theta}{-2D}\ln\left(\frac{\sigma^0 - C}{\sigma^0_{BG} - C}\right) \quad (18)$$

Suppose that the parameter C satisfies $C>\sigma^0$, then $C > \sigma^0_{BG}$. We can get:

$$a = \frac{\cos\theta}{2D}\ln(C - \sigma^0_{BG}) \quad (19)$$

$$b = \frac{\cos\theta}{2D} \quad (20)$$

Then the final inversion formula is:

$$(W_1 \cdot h_1 + W_2 \cdot h_2) = a - b\ln(C - \sigma^0) \quad (21)$$

Its inverse function is:

$$\sigma^0 = C - \exp(-((W_1 \cdot h_1 + W_2 \cdot h_2) - a)/b) \quad (22)$$

Where, the parameter a and b represent the coefficients of the inversion formula; the parameter C represents the volume scattering coefficients when rice sealing line; the parameter W_1, W_2, h_1 and h_2 are obtained through field measurement experiments.

4 Results

4.1 Experimental results

Generally, in the relatively mature stage of rice, except for the dominant leaves, the scattering intensity of rice canopy is largely derived from the scattering of rice panicle. For rice field, the more ears of rice, the more grain number per ear. Panicle density (the number of ears of rice per square meter) and panicle length are also directly related to grain yield (Lee et al., 2018).

For parcel B, 18 samples from field investigation were randomly selected for modeling. For parcel C+D+E, 20 samples from field investigation were randomly selected for modeling.

Based on the inversion formula of $W_1 \cdot h_1$, wet weight of ear and grain number per ear of rice can be inverted. Statistical analysis of relevant experimental data obtained in this paper showed that $W_1 \cdot h_1$ had a linear relationship with wet weight of ear and grain number per ear of rice. Figure 5 is the inversion model of wet weight of ear and grain number per ear of rice, and formula (23)~(26) are the inversion model formulas.

The model of wet weight of ear of rice in parcel B and parcel C+D+E are as follows:

$$M_{wetB} = 2.5404 \times (W_1 \cdot h_1)_B + 0.2943 \; R_B^2 = 0.8401 \quad (23)$$

$$M_{wetCDE} = 2.8169 \times (W_1 \cdot h_1)_{CDE} + 0.1464 \; R_{CDE}^2 = 0.9061 \quad (24)$$

The model of grain number per ear of rice in parcel B and parcel C+D+E are as follows:

$$N_B = 78315 \times (W_1 \cdot h_1)_B + 5015.5 \; R_B^2 = 0.9433 \quad (25)$$

$$N_{CDE} = 94399 \times (W_1 \cdot h_1)_{CDE} - 6380.9 \; R_{CDE}^2 = 0.7912 \quad (26)$$

Where, M_{wetB} and M_{wetCDE} are respectively the wet weight of ear per square meter (kg/m^2) of rice in parcel B and parcel C+D+E; N_B and N_{CDE} are respectively the grain number per ear per square meter (thousand grains/m^2) of rice in parcel B and parcel C+D+E; R^2_B and R^2_{CDE} are the model correlation coefficients respectively.

The results of Figure 5 showed that there were two high linear correlations of rice between wet weight of ear and water content per unit area ($W_1 \cdot h_1$), and between grain number per ear and water content per unit area ($W_1 \cdot h_1$). By observing Figures 5A, B, it can be found that under HH polarization, the correlation between $W_1 \cdot h_1$ and wet weight of ear of rice in parcel B (Figure 5A) was much smaller than that in parcel C+D+E (Figure 5B). The reason for the difference in correlation was that the rice in parcel B was fully mature and about to be harvested, with less water content in panicle. The rice in parcel C+D+E was in the grouting stage with more water content. Similarly, under HH polarization, the correlation between $W_1 \cdot h_1$ and grain number per ear was more than 0.94 in parcel B (Figure 5C), but the result of parcel C+D+E (Figure 5D) was far worse than that of parcel B (Figure 5C). According to the analysis, the difference of rice varieties planted in parcel C+D+E leads to the difference in the grain number per ear, resulting in uneven distribution of panicle grains per unit area. However, the rice varieties in parcel B are all Nanjing 9108, with uniform growth. The above analysis shows that it is feasible and effective to estimate the rice yield using the new modified water-cloud model based on panicle layer constructed in this paper.

Figure 6 is the rice yield estimation map using the new modified water-cloud model based on panicle layer constructed in this paper. M_{wetB} and N_B, which have the smallest error with the field investigation, are selected to draw the rice yield estimation map. According to Figure 6, the estimated rice value at the field scale can be obtained.

4.2 Experimental verification

4.2.1 Verification of yield estimation model

In order to verify the accuracy of the rice yield estimation model constructed in this paper, some other samples were selected for verification. For parcel B, the other 10 samples from field investigation were selected; for parcel C+D+E, the other 10 samples from field investigation were selected. Figure 7 shows the validation of the inversion models of wet weight of ear and grain number per ear. Correlation (R^2) and Root Mean Square Error (RMSE) were used to evaluate the accuracy of the yield estimation model.

According to Figures 7A, B, the inversion results of wet weight of ear were close to the measured results, and the R^2 was 0.9477 in parcel B, with the lowest RMSE of 0.12. The R^2 and RMSE were 0.9182 and 0.39 respectively in parcel C+D+E. This indicats that the yield estimation model constructed in this paper can accurately estimate wet weight of ear of rice. As can be seen from Figures 7C, D, for the inversion results of grain number per ear, the inversion results in parcel B (Figure 7C) were closest to the measured results, with R^2 of 0.9414 and RMSE of 0.27. The inversion accuracy of parcel C+D+E (Figure 7D) was much lower than that of Figure 7C, with R^2 of 0.702 and RMSE of 2.14. This error may be caused by the difference of rice varieties planted in C+D+E parcel, which resulted in different grain number per ear. And the distribution of grain number per ear per unit area is not uniform.

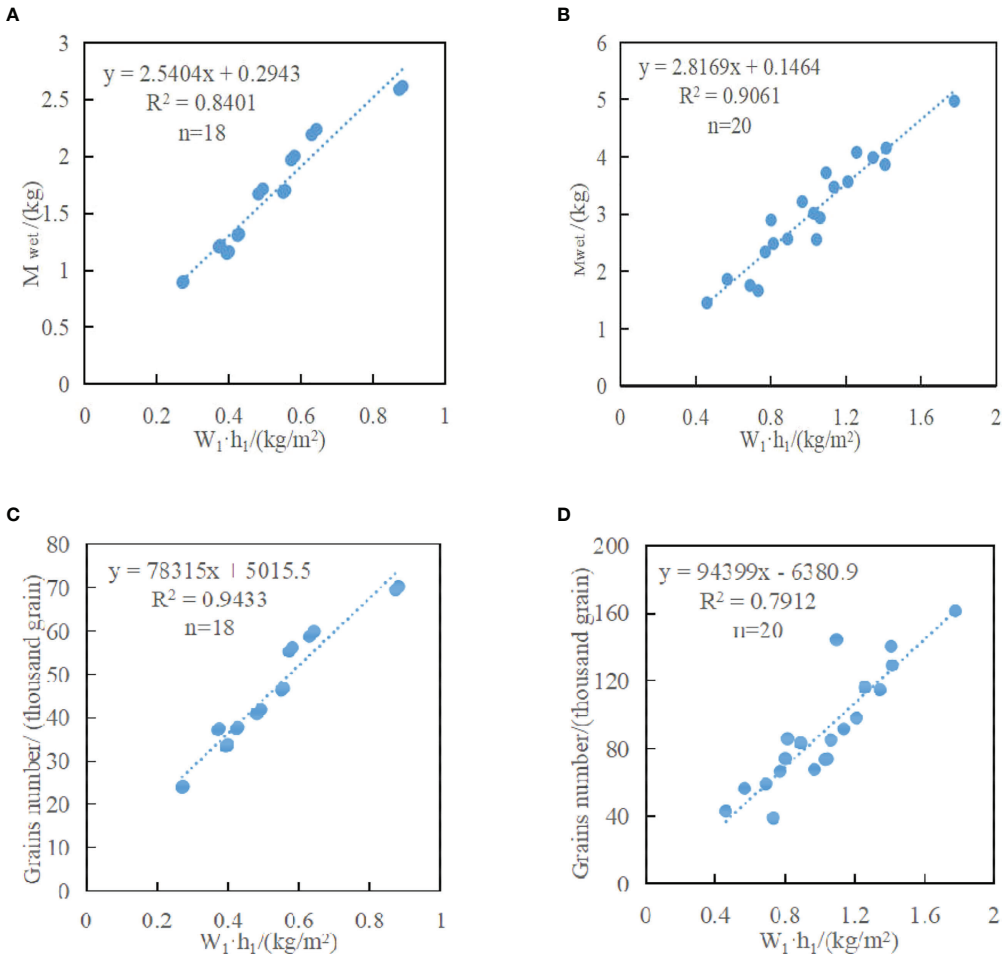

FIGURE 5
Inversion model of wet weight of ear and grain number per ear. **(A)** is the scatter diagram between $(W_1 \cdot h_1)_B$ and wet weight of rice ear scattering model M_{wetB}. **(B)** is the scatter diagram between $(W_1 \cdot h_1)_{CDE}$ and wet weight of rice ear scattering model M_{wetCDE}. **(C)** is the scatter diagram between $(W_1 \cdot h_1)_B$ and grain number per rice ear scattering model N_B. **(D)** is the scatter diagram between $(W_1 \cdot h_1)_{CDE}$ and grain number per rice ear scattering model N_{CDE}.

4.2.2 Verification between estimated yield and measured yield

The rice yield estimation model constructed in this paper was used to estimate the rice yield of parcel B and parcel C+D+E, and was compared with the rice yield data of field investigation to verify the accuracy obtained in this paper. The measured data of rice yield are shown in Table 2. Comparison of model yield estimates with measured data is shown in Table 3.

As can be seen from Table 3, for rice in parcel B, the estimated values based on wet weight of rice ear scattering model (M_{wetB}) and grain number per rice ear scattering model (N_B) were higher than the measured data. The absolute error (AE) of N_B was 27.68 kg/mu, the relative error (RE) was 4.97%, and the precision (P) was the highest, reaching 95.03%. The difference between model inversion yield and measured data was small. The AE, RE and P of M_{wetB} were 32.61 kg/mu, 5.85% and 94.15% respectively. For rice in parcel C+D+E, the estimated values of rice based on wet weight of rice ear scattering model (M_{wetCDE}) and grain number per rice ear scattering model (N_{CDE}) were still higher than the measured data, and the estimated yield of M_{wetCDE} was better than that of N_{CDE}. The AE, RE and P of M_{wetCDE} were 49.44 kg/mu, 7.28% and 92.72% respectively. The AE, RE and P of N_{CDE} were 55.22 kg/mu, 8.14% and 91.86% respectively.

The reasons for the higher estimated rice yield in parcel B by the model constructed in this paper are as follows: In the functional area of grain production, only rice in parcel B was sown earlier, had good growth conditions and was fully mature. However, many grains were eaten by birds, leading to a decrease in the measured yield. Based on the analysis of the parcel

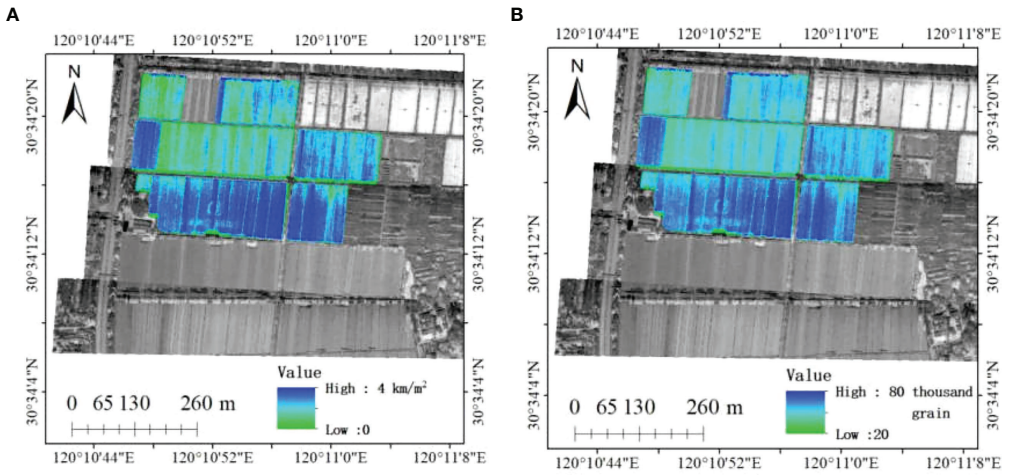

FIGURE 6
The estimation yield map based on the new modified water-cloud model of panicle layer. **(A)** is the estimation values based on M_{wetB} model of wet weight of rice ear; **(B)** is the estimation values based on N_B model of grain number per rice ear.

C+D+E, the estimated values of the model in this paper is still higher than the measured data, because rice is in the grouting stage, which is not fully mature, and has more water content. In the process of model construction, the panicle weight was calculated according to the state of full maturity of the samples collected, while the measured yield contained some depressed grains with insufficient grout. Therefore, some reduction in production is normal.

5 Discussion and analysis

5.1 Analysis of relationship between $W_1 \cdot h_1$ and $W_2 \cdot h_2$

To discuss the feasibility of using the radar data with high frequency Ku band for rice yield estimation, it is necessary to explore the penetration of the radar data with Ku band in rice plants, and to further explore the relationship between the water content per unit area of panicle layer ($W_1 \cdot h_1$) and the water content per unit area of stem and leaf layer ($W_2 \cdot h_2$). According to the measured data, the fitting relationship between water content per unit area of panicle layer ($W_1 \cdot h_1$) and water content per unit area of stem and leaf layer ($W_2 \cdot h_2$) was established. The fitting relationships of parcel B and parcel C+D+E were formula (27) and formula (28), respectively. Figure 8 shows the scatter diagram of water content per unit area of panicle layer and stem and leaf layer in different fields.

The fitting relationship of field B is:

$$(W_2 \cdot h_2)_B = 4.4297(W_1 \cdot h_1)_B + 0.1408\, R_{B^2} = 0.6825 \quad (27)$$

The fitting relationship of field C+D+E is:

$$(W_2 \cdot h_2)_{CDE} = 3.2385(W_1 \cdot h_1)_{CDE} + 1.255\, R_{CDE^2} = 0.8451 \quad (28)$$

Where, $(W_1 \cdot h_1)_B$ and $(W_1 \cdot h_1)_{CDE}$ are the water content per unit area of panicle layer (kg/m^2) of parcel B and parcel C+D+E; $(W_2 \cdot h_2)_B$ and $(W_2 \cdot h_2)_{CDE}$ are the water content per unit area (kg/m^2) of stem and leaf layer of parcel B and parcel C+D+E; R^2_B and R^2_{CDE} are fitting coefficients of regression formula.

According to Figure 8, the water content per unit area of panicle layer and stem and leaf layer of rice showed a certain linear correlation. Figures 8A, B both had the same trend. $W_1 \cdot h_1$ increased with the increase of $W_2 \cdot h_2$, that is, the water content of panicle layer increased with the increase of stem and leaf layer. The change of water content per unit area of parcel C+D+E (Figure 8B) was more obvious than that of parcel B (Figure 8A). Because rice in parcel B was in the fully mature stage and was about to be harvested, many leaves and stems withered, and the water content per unit area decreased significantly, which weakened the correlation between panicle layer and stem and leaf layer. The water content per unit area of panicle layer ranged from 0.3 to 0.8 (kg/m^2), the water content per unit area of stem and leaf layer ranged from 1.5 to 4.0 (kg/m^2), and the correlation coefficient R_B^2 was about 0.68. The correlation between $W_1 \cdot h_1$ and $W_2 \cdot h_2$ was good. The water content per unit area of panicle layer ranged from 0.5 to 1.7 (kg/m^2), and the water content per unit area of stem and leaf layer ranged from 3.5 to 7.0 (kg/m^2), with a correlation coefficient of 0.84. Therefore, it is difficult to penetrate stem and leaf layer and the pad surface layer for the SAR data with high frequency, such as Ku band. The radar echo

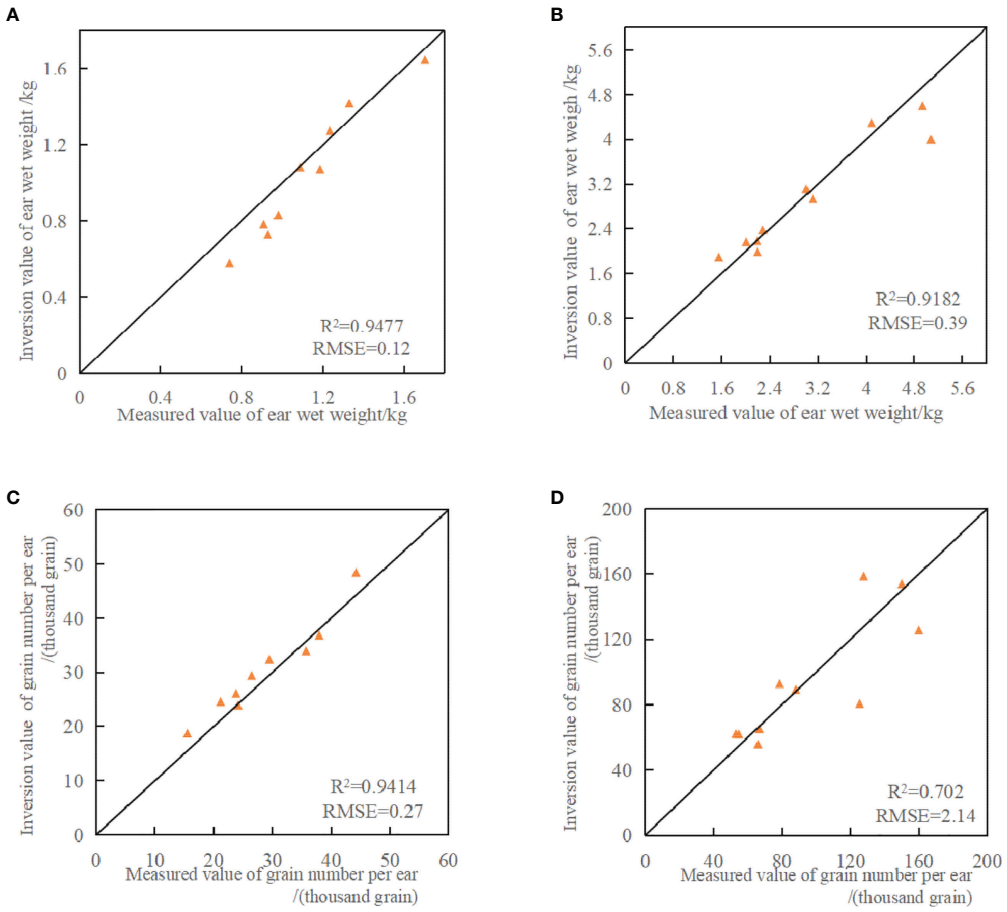

FIGURE 7
Verification diagram of inversion model of wet weight of ear and grain number per ear. **(A)** Model verification of measured values and inversion values of wet weight of rice ear M_{wetB}; **(B)** Model verification of measured values and inversion values of wet weight of rice ear M_{wetCDE}; **(C)** Model verification of measured values and inversion values of grain number per ear N_B; **(D)** Model verification of measured values and inversion values of grain number per rice ear N_{CDE}.

of rice canopy is more from rice panicle layer, which effectively overcomes the shortcoming of a large amount of information of stem and leaf layer and the pad surface layer contained in low frequency data source, and reduces the difficulty of yield estimation modeling.

5.2 Analysis of the relationship between σ^0 and $W_1 \cdot h_1$

According to formulas (21), (22), (27) and (28), the new modified water-cloud model at panicle layer was used to

TABLE 2 Field investigation data of rice yield in parcel B and C+D+E.

	Effective ear (ten thousand/hm^2)	Total number of particles (grain/ear)	Real income (grain/ear)	The weight of 1000 grains (g)	Total output (kg/hm^2)	yield per mu (kg/mu) (drying)
parcel B	406.5	158.9	141.2	23.6	8359.8	557.32
parcel C	363.8	451.1	279.9	25.4	10488	679.2
parcel D	357.8	439.1	349.8	26.4	11014.5	714.3
parcel E	327.7	446.6	292.3	25.3	9640.5	642.7
parcel C +D+E	349.76	445.6	307.33	25.7	10381	678.73*

*,the average yield of three fields.

TABLE 3 Verification of model yield estimate accuracy.

	Model	Estimated Ywet weight (kg/ mu) (wet)	Estimated production (kg/mu) (drying)	Real production (kg/mu)	Absolute error (kg/mu)	Relative error (%)	Precision (%)
parcel B	MwetB	854.97	589.93	557.32	32.61	5.85	94.15
	NB	——	585.0	557.32	27.68	4.97	95.03
parcel C +D+E	MwetCDE	1011.34	728.17	678.73	49.44	7.28	92.72
	NCDE	——	733.95	678.73	55.22	8.14	91.86

establish the relationship between SAR backscattering coefficient (σ^0) and the water content per unit area of panicle layer ($W_1 \cdot h_1$) for parcel B and parcel C+D+E. Figure 9 is the fitting result diagram of the model.

Figure 9 shows that there is a certain correlation between SAR backscattering coefficient (σ^0) and the water content per unit area of panicle layer ($W_1 \cdot h_1$), and the fitting formula is as follows:

For parcel B:

$$\sigma_B^0 = -10.57 - \exp\left(-\left((W_1 \cdot h_1)_B + 1.58\right)/0.6638\right) R_B^2 = 0.6166 \quad (29)$$

For parcel C+D+E:

$$\sigma_{CDE}^0 = -15.44 - \exp\left(-\left((W_1 \cdot h_1)_{CDE} + 1.203\right)/0.4669\right) R_{CDE}^2 = 0.4708 \quad (30)$$

As can be seen from Figure 9, the inversion results of the two models are similar, indicating that it has certain sensitivity to the change of water content in rice canopy for HH polarization mode. σ^0 increases with the increase of $W_1 \cdot h_1$ and gradually tends to saturation. Some sample points deviate far from the fitting curve, which is mainly because the backscattering coefficient of ground objects is a range rather than a fixed value. For rice, the backscattering coefficient in the fitting result is within the allowable range. Parameter C in formula (29) and formula (30) has a great difference. Considering that rice in parcel B is already in the mature stage, and the plant height and water content per unit area of stem and leaf layer are different, so the water content per unit area of panicle layer has a great difference. And this leads that the scattering of radar wave is also different. Compared with parcel B, parcel C+D+E has higher canopy density, large leaf area and large coverage. So the parcel C+D+E has a stronger degree of attenuation of radar wave, which makes that the scattering of radar signal shows a great difference. Therefore, the fitting accuracy is lower than that of parcel B.

6 Conclusions

Aiming at the problem of rice yield estimation at the field scale, this paper constructed a modified water-cloud model based on panicle layer and the radar data with Ku band to estimate the rice yield. Using the UAV-based MiniSAR radar data with Ku band and the new model, the relation model of rice

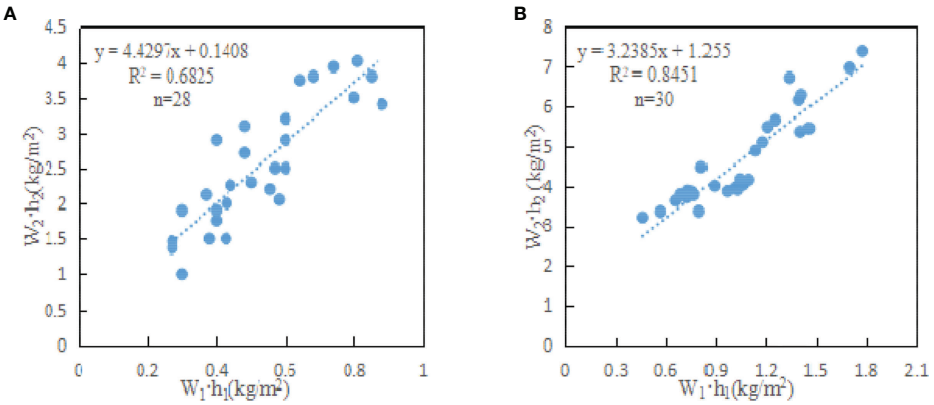

FIGURE 8
Fitting diagram of $W_1 \cdot h_1$ and $W_2 \cdot h_2$. **(A)** is the fitting diagram of $W_1 \cdot h_1$ and $W_2 \cdot h_2$ in parcel B; **(B)** is the fitting diagram of $W_1 \cdot h_1$ and $W_2 \cdot h_2$ in parcel C+D+E.

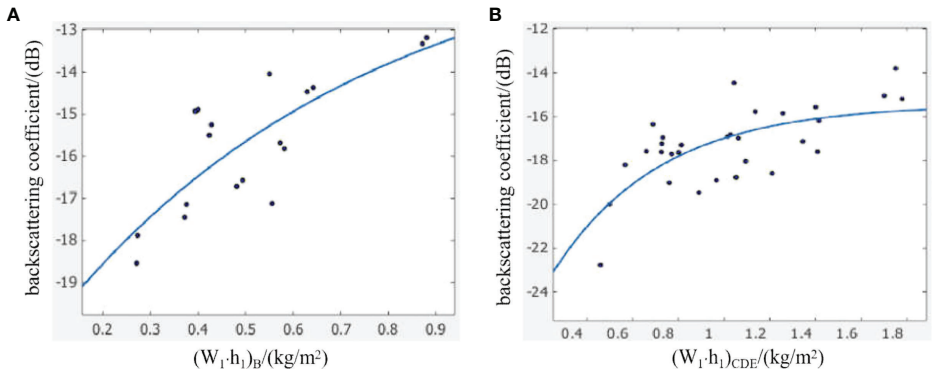

FIGURE 9
The relationship between the backscattering coefficients and $W_1 \cdot h_1$ under polarization HH. **(A)** is the relationship between the backscattering coefficients and $W_1 \cdot h_1$ under polarization HH in parcel B; **(B)** is the relationship between the backscattering coefficients and $W_1 \cdot h_1$ under polarization HH in parcel C+D+E.

panicle wet weight, grain number and water content per unit area ($W_1 \cdot h_1$) was established. The yield estimation of rice in panicle and mature stage at field scale can be realized.

Through the research, some valuable conclusions can be obtained as follows:

(1) For parcel B, compared with measured data, the estimation accuracies of M_{wetB} model and N_B model were 95.03% and 94.15%, respectively. For parcel C+D+E, the estimation accuracies of M_{wetCDE} and N_{CDE} were more than 91.8%. The variation trend of the estimated values were basically consistent with the measured values, which indicated that the model constructed in this paper could be applied to rice yield estimation well.

(2) The accuracy of rice yield estimation is influenced by the different growth stages of rice. The method in this paper is especially suitable for rice yield estimation at the mature stage. For rice at mature stage, the estimated yield accuracy of wet weight of rice ear scattering model was almost the same as that of grain number per rice ear scattering model, both of which were over 94%. For rice at grouting stage, the yield estimation accuracy of wet weight of rice ear scattering model was 92.7% better than that of grain number per rice ear scattering model.

(3) It is difficult to penetrate stem and leaf layer to reach the pad surface layer of rice for the SAR data with high frequency, such as Ku band, so the radar echoes of rice canopy are mostly from panicle layer, which effectively overcomes the shortcoming of the radar data with low frequency contains a large amount of information about stem and leaf layer and pad surface layer. It can reduce the difficulty of yield estimation modeling. Based on the modified water-cloud model of panicle layer constructed in this paper, under HH polarization in Ku band, the estimated yield of wet weight of rice ear scattering model and grain number per rice ear scattering model is similar to the measured results, with an estimated yield accuracy of more than 91%. This model can estimate rice yield effectively, and it provides a practical method for estimating rice yield in high frequency SAR data.

The method constructed in this paper can be applied to rice yield estimation at the field scale at the mature stage of rice, and is particularly suitable for SAR data with high frequency, such as Ku band. In the study of rice yield estimation, the proposed method achieved relatively high yield estimation accuracy. However, due to the simplified processing of the model, some structural parameters of rice (such as leaf density distribution in stem and leaf layer, blade incidence, panicle angle, etc.) were not sufficiently considered, which would influence the change of rice backscattering. In this yield estimation study, only the radar data with HH polarization and Ku band from UAV-based MiniSAR was used. In the next step, the radar data with different polarization and different frequencies will be combined to carry out more accurate rice yield estimation.

Data availability statement

The original contributions presented in the study are included in the article/supplementary material. Further inquiries can be directed to the corresponding authors.

Author contributions

ZW wrote the manuscript, designed its structure and revised the manuscript. SW wrote the manuscript, collected and analyzed the MiniSAR data and field investigation sampling data. ZW and SW contributed equally to this work. HW contributed to the data analysis, making charts and the paper modification. LL proposed and performed the experiments, completed the acquisition of MiniSAR radar data and

provided suggestions. ZL helped in collecting and analyzing the data. YZ and KW critically revised the manuscript. All authors contributed to the article and approved the submitted version.

Funding

This research is supported by funding from the National Natural Science Foundation of China (No. 41601375, 41876202) and Natural Science Foundation of Zhejiang Province (No. LGN20D010001).

Acknowledgments

Thanks to the Institute of Space and Space Information Innovation, Chinese Academy of Sciences for providing the MiniSAR system for this research.We want to thank the reviewers for their valuable suggestions and comments which improved the quality of the manuscript.

Conflict of interest

The authors declare that the research was conducted in the absence of any commercial or financial relationships that could be construed as a potential conflict of interest.

Publisher's note

All claims expressed in this article are solely those of the authors and do not necessarily represent those of their affiliated organizations, or those of the publisher, the editors and the reviewers. Any product that may be evaluated in this article, or claim that may be made by its manufacturer, is not guaranteed or endorsed by the publisher.

References

Alebele, Y., Wang, W. H., Yu, W. G., Zhang, X., Yao, X., Tian, Y. C., et al. (2021). Estimation of crop yield from combined optical and SAR imagery using Gaussian kernel regression. *IEEE J-Stars.* 14, 10520–10534. doi: 10.1109/JSTARS.2021.3118707

Alebele, Y., Zhang, X., Wang, W., Yang, G., Yao, X., Zheng, H., et al. (2020). Estimation of canopy biomass components in paddy rice from combined optical and SAR data using multi-target Gaussian regressor stacking. *Remote Sens.* 12 2564. doi: 10.3390/rs12162564

Arumugam, P., Chemura, A., Schauberger, B., and Gornott, C. (2021). Remote sensing based yield estimation of rice (Oryza sativa l.) using gradient boosted regression in India. *Remote Sens.* 13 2379. doi: 10.3390/rs13122379

Asilo, S., Nelson, A., De Bie, K., Skidmore, A., Laborte, A., Maunahan, A., et al. (2019). Relating X-band SAR backscattering to leaf area index of rice in different phenological phases. *Remote Sens.* 11 1462. doi: 10.3390/rs11121462

Attema, E. P. W., and Ulaby, F. T. (1978). Vegetation modeled as a water cloud. *Radio Sci.* 13, 357–364. doi: 10.1029/RS013i002p00357

Dipankar, M., Vineet, K., Debanshu, R., Lepoz-Sanchez, J. M., Avik, B., Heather, M., et al. (2020). Assessment of rice growth conditions in a semi-arid region of India using the generalized radar vegetation index derived from RADARSAT-2 polarimetric SAR data. *Remote Sens. Environ.* 237, 111561. doi: 10.1016/j.rse.2019.111561

Duan, B., Fang, S. H., Zhu, R. S., Wu, X. T., Wang, S. Q., Gong, Y., et al. (2019). Remote estimation of rice yield with unmanned aerial vehicle (UAV) data and spectral mixture analysis. *Front. Plant Sci.* 10. doi: 10.3389/fpls.2019.00204

Erten, E., Lopez-Sanchez, J. M., Yuzugullu, O., and Hajnsek, I. (2016). Retrieval of agricultural crop height from space: a comparison of SAR techniques. *Remote Sens. Environ.* 187, 130–144. doi: 10.1016/j.rse.2016.10.007

Erten, E., Rossi, C., and Yuzugullu, O. (2015). Polarization impact in TanDEM-X data over vertical oriented vegetation: the paddy-rice case study. *IEEE Geosci. Remote S.* 12, 1501–1505. doi: 10.1109/LGRS.2015.2410339

Guan. K, Y., Li, Z., Rao, L. N., Gao, F., Xie, D., Hien, N. T., et al. (2018). Mapping paddy rice area and yields over Thai binh province in Viet nam from MODIS, landsat, and ALOS-2/PALSAR-2. *IEEE J-Stars* 11, 2238–2252. doi: 10.1109/JSTARS.2018.2834383

Gu, C., Ji, S., Xi, X. B., Zhang, Z. H., Hong, Q. Q., Huo, Z. Y., et al. (2022). Rice yield estimation based on continuous wavelet transform with multiple growth periods. *Front. Plant Sci.* 13. doi: 10.3389/fpls.2022.931789

Guo, X. Y., Li, K., Shao, Y., LopezSanchez, J. M., and Wang, Z. Y. (2020). Inversion of rice height using multitemporal TanDEM-X polarimetric interferometry SAR data. *Spectrosc. Spect. Anal.* 40, 878–884. doi: 10.3964/j.issn.1000-0593(2020)03-0878-07

Guo, X. Y., Li, K., Shao, Y., Wang, Z. Y., Li, H. Y., Yang, Z., et al. (2018). Inversion of rice biophysical parameters using simulated compact polarimetric SAR c-band data. *Sensors* 18 2271. doi: 10.3390/s18072271

Huang, C. L., Li, W. K., Zhang, Z. F., Hua, X. D., Yang, J. Y., Liang, X. Y., et al. (2022). An intelligent rice yield trait extraction system based on threshed panicle compensation. *Front. Plant Sci.* 900408. doi: 10.3389/fpls.2022.900408

Huang, C., Xu, Z. X., Zhang, C., Li, H., Liu, Q. S., Yang, Z. K., et al. (2020). Extraction of rice planting structure in tropical region based on sentinel-1 temporal features integration. *Trans. Chin. Soc. Agric. Eng.* 36, 177–184. doi: 10.11975/j.issn.1002-6819.2020.0902

Inoue, Y., Kurosu, T., Maeno, H., Kozu, K., Zielinska, D., Qi, J., et al. (2002). Season-long daily measurements of multifrequency (Ka, Ku, X, C, and l) and full-polarization. backscatter signatures over paddy rice field and their relationship with biological variable. *Remote Sens. Environ.* 81, 194–204. doi: 10.1016/S0034-4257(01)00343-1

Inoue, Y., and Sakaiya, E. (2013). Relationship between X-band backscattering coefficients from high-resolution satellite SAR and biophysical variables in paddy rice. *Remote Sens. Lett.* 4, 288–295. doi: 10.1080/2150704X.2012.725482

Inoue, Y., Sakaiya, E., and Wang, C. Z. (2014). Potential of X-band images from high-resolution satellite SAR sensors to assess growth and yield in paddy rice. *Remote Sens.* 6, 5995–6019. doi: 10.3390/rs6075995

Jia, M. Q., Tong, L., Zhang, Y. Z., Chen, Y., and Chopra, R. (2014). Multi-temporal radar backscattering measurements and modelling of rice fields using a multi-frequency (L, s, c, and X) scatterometer. *Int. J. Remote Sens.* 35, 1253–1271. doi: 10.1080/01431161.2013.876117

Jing, X., Zhang, J., Wang, J. J., Ming, S. K., Fu., Y. Q., Feng, H. K., et al. (2022). Comparison of machine learning algorithmsfor remote sensing monitoringof rice yields. *Spectrosc. Spect. Anal.* 42, 1620–1627. doi: 10.3964/J.issn.1000-0593(2022)05-1620-08

Kersten, C., Marco, O., Patrick, L., and Claudia, K. (2018). Estimating rice production in the Mekong delta, Vietnam, utilizing time series of sentinel-1 SAR data. *Int. J. Appl. Earth Obs.* 73, 574–585. doi: 10.1016/j.jag.2018.07.022

Kim, S. B., Kim, B. K., Kong, T. K., and Kim, Y. S. (2000). Radar backscattering measurements of rice crop using X-band scatterometer. *IEEE T. Geosci. Remote* 38, 1467–1471. doi: 10.1109/36.843044

Lee, S.-K., Yoon, S. Y., and Won, J.-S. (2018). Vegetation height estimate in rice fields using single polarization TanDEM-X science phase data. *Remote Sens.* 10 1702. doi: 10.3390/rs10111702

Liu, L., Shao, Y., Li, K., and Gong, H. Z. (2012). "A two layer water cloud model," in *2012 IEEE international geoscience and remote sensing symposium*. (Munich, Germany), 5840–5843. doi: 10.1109/IGARSS.2012.6352281

Li, Z. J., Wang, Z. Y., Liu, X. T., Zhu, Y. D., Wang, K., and Zhang, T. G. (2022). Classification and evolutionary analysis of yellow river delta wetlands using decision tree based on time series SAR backscattering coefficient and coherence. *Front. Mar. Sci.* 9. doi: 10.3389/fmars.2022.940342

Lopez-Sanchez, J. M., Vicente-Guijalba, F., Erten, E., Campous-Taberner, M., and Garcia-Haro, F. J. (2017). Retrieval of vegetation height in rice fields using polarimetric SAR interferometry with TanDEM-X data. *Remote Sens. Environ.* 192, 30–44. doi: 10.1016/j.rse.2017.02.004

Maki, M., Sekiguchi, K., and Homma, K. (2017). Estimation of rice yield by SIMRIW-RS, a model that integrates remote sensing data into a crop growth model. *J. Agric. Meteorol.* 73, 2–8. doi: 10.2480/agrmet.D-14-00023

Mandal, D., Bhattacharya, A., and Rao, Y. S. (2021). *Radar remote sensing for crop biophysical parameter estimation* (Springer).

Mandal, D., Kumare, V., Bhattacharya, A., Rao, Y. S., Siqueira, P., and Bera, S. (2018). Sen4Rice: A processing chain for differentiating early and late transplanted rice using time-series sentinel-1 SAR data with Google earth engine. *IEEE Geosci. Remote S.* 15, 1947–1951. doi: 10.1109/LGRS.2018.2865816

Ndikumana, E., Ho Tong Minh, D., Dang Nguyen, H. T., Baghdadi, N., Courault, D., Hossard, L., et al. (2018). Estimation of rice height and biomass using multitemporal SAR sentinel-1 for camargue, southern France. *Remote Sens.* 10 1394. doi: 10.3390/rs10091394

Nguyen, L. D., Phung, H. P., Juliance, H., and Phung, C. V. (2012). Estimation of the rice yield in the Mekong Delta using dual polarisation TerraSAR-X data. VNU Journal of Science. *Earth Sciences 28* 28, 20–28.

Rossi, C., and Erten, E. (2015). Paddy-rice monitoring using TanDEM-X. *IEEE T. Geosci. Remote* 53, 900–910. doi: 10.1109/TGRS.2014.2330377

Setiyono, T. D., Quicho, E. D., Gatti, L., Campos-Taberner, M., Busetto, L., Collivignarelli, F., et al. (2018). Spatial rice yield estimation based on MODIS and sentinel-1 SAR data and ORYZA crop growth model. *Remote Sens.* 10, 293. doi: 10.3390/rs10020293

Setiyono, T. D., Quicho, E. D., Holecz, F. H., Khan, N. I., Romuga, G., Maunahan, A., et al. (2019). Rice yield estimation using synthetic aperture radar (SAR) and the ORYZA crop growth model: development and application of the system in south and south-east Asian countries. *Int. J. Remote Sens.* 40, 8093–8124. doi: 10.1080/01431161.2018.1547457

Shenbin, Y. (2008). *Study on rice mapping and rice yield estimation based on ASAR data* (Doctoral Dissertation in Nanjing University of Information Science and Technology).

Shen, S. H., Yang, S. B., Li, B. B., Tang, B., Li, Z. Y., and Le, T. S. (2009). A scheme for regional rice yield estimation using ENVISAT ASAR data. *Sci. China Ser. D.* 39, 763–773. doi: 10.1007/s11430-009-0094-z

Toan, T. L., Laur, H., and Mougin, E. (1989). Multitemporal and dual-polarization observations of agricultural vegetation covers by X-band SAR images. *IEEE T. Geosci. Remote* 27, 709–718. doi: 10.1109/TGRS.1989.1398243

Wang, J., Dai, Q., Shang, J., Jin, X., Sun, Q., Zhou, G., et al. (2019). Field-scale rice yield estimation using sentinel-1A synthetic aperture radar (SAR) data in coastal saline region of jiangsu province, China. *Remote Sens.* 11 2274. doi: 10.3390/rs11192274

Wang, Z. L., Ma, Y. M., Chen, P., Yang, Y. G., Fu, H., Yang, F., et al. (2022). Estimation of rice aboveground biomass by combining canopy spectral reflectance and UAV-based RGB imagery data. *Front. Plant Sci.* 13. doi: 10.3389/fpls.2022.903643

Wang, F. L., Wang, F. M., Zhang, Y., Hu, J. H., Huang, J. F., and Xie, J. K. (2019). Rice yield estimation using parcel-level relative spectral variables from UAV-based hyperspectral imagery. *Front. Plant Sci.* 10. doi: 10.3389/fpls.2019.00453

Wang, Z. Y., Ye, K. L., Zhang, M. Y., Li, Z. J., Zhu, Y. D., Li, H., et al. (2022). Monitoring the wetland of the yellow river delta by combining GF-3 polarimetric synthetic aperture radar and sentinel-2A multispectral data. *Front. Ecol. Evol.* 10. doi: 10.3389/fevo.2022.80697

Wu, X. X., Liu, L., Guo, X. Y., Liu, Z. Q., and Shao, Y. (2020). Comparison of water cloud models with different layers for rice yield estimation from a single TerraSAR image. *Remote Sens. Lett.* 11, 876–882. doi: 10.1080/2150704X.2020.1781284

Wu, X., Washaya, P., Liu, L., Li, K., Shao, Y., Meng, L. Y., et al. (2020). Rice yield estimation based on spaceborne SAR: A review from 1988 to 2018. *IEEE Access* 8, 157462–157469. doi: 10.1109/ACCESS.2020.3020182

Yang, Z., Li, K., Shao, Y., Brisco, B., and Liu, L. (2016). Estimation of paddy rice variables with a modified water cloud model and modified polarimetric decomposition using multi-temporal RADARSAT-2 images. *Remote Sens.* 8, 878. doi: 10.3390/rs8100878

Yang, H. J., Pan, B., Li, N., Wang, W., Zhang, J., and Zhang, X. L. (2021). A systematic method for spatio-temporal phenology estimation of paddy rice using time series sentinel-1 images. *Remote Sens. Environ.* 259, 112394. doi: 10.1016/j.rse.2021.112394

Yang, Z., Shao, Y., Li, K., Liu, Q. B., Liu, L., and Brisco, B. (2017). An modified scheme for rice phenology estimation based on time-series multispectral HJ-1A/B and polarimetric RADARSAT-2 data. *Remote Sens. Environ.* 97, 184–201. doi: 10.1016/j.rse.2017.04.016

Yu, Y. R., Wang, Z., Li, Z. J., Ye, K. L., Li, H., and Wang, Z. H. (2022). A lightweight anchor-free subsidence basin detection model with adaptive sample assignment in interferometric synthetic aperture radar interferogram. *Front. Ecol. Evol.* 10. doi: 10.3389/fevo.2022.840464

Yuzugullu, O., Erten, E., and Hajnsek, I. (2017). A multi-year study on rice morphological parameter estimation with X-band polsar data. *Appl. Sci.* 7, 602. doi: 10.3390/app7060602

Zhang, Y., Yang, B., Liu, X. H., and Wang, C. Z. (2017). Estimation of rice grain yield from dual-polarization radarsat-2 SAR data by integrating a rice canopy scattering model and a genetic algorithm. *Int. J. Appl. Earth Obs.* 5, 75–85. doi: 10.1016/j.jag.2016.12.014

Zhang, Y., Yan, W. J., Yang, B., Yang, T. P., and Liu, X. H. (2020). Estimation of rice yield from a c-band radar remote sensing image by integrating a physical scattering model and an optimization algorithm. *Precis. Agric.* 21, 245–263. doi: 10.1007/s11119-019-09664-8

Zheng, H. B., Cheng, T., Li, D., Yao, X., Tian, Y. C., Cao, W. X., et al. (2018). Combining unmanned aerial vehicle (UAV)-based multispectral imagery and ground-based hyperspectral data for plant nitrogen concentration estimation in rice. *Front. Plant Sci.* 9. doi: 10.3389/fpls.2018.00936

frontiers | Frontiers in Plant Science

TYPE Original Research
PUBLISHED 18 October 2022
DOI 10.3389/fpls.2022.1012070

Check for updates

OPEN ACCESS

EDITED BY
Carl J. Rosen,
University of Minnesota Twin Cities,
United States

REVIEWED BY
Yi Wang,
University of Wisconsin-Madison,
United States
Jan Clevers,
Wageningen University and Research,
Netherlands

*CORRESPONDENCE
Haikuan Feng
fenghk@nercita.org.cn

†These authors have contributed equally to this work

SPECIALTY SECTION
This article was submitted to Sustainable and Intelligent Phytoprotection, a section of the journal Frontiers in Plant Science

RECEIVED 05 August 2022
ACCEPTED 30 September 2022
PUBLISHED 18 October 2022

CITATION
Fan Y, Feng H, Jin X, Yue J, Liu Y, Li Z, Feng Z, Song X and Yang G (2022) Estimation of the nitrogen content of potato plants based on morphological parameters and visible light vegetation indices. *Front. Plant Sci.* 13:1012070. doi: 10.3389/fpls.2022.1012070

COPYRIGHT
© 2022 Fan, Feng, Jin, Yue, Liu, Li, Feng, Song and Yang. This is an open-access article distributed under the terms of the Creative Commons Attribution License (CC BY). The use, distribution or reproduction in other forums is permitted, provided the original author(s) and the copyright owner(s) are credited and that the original publication in this journal is cited, in accordance with accepted academic practice. No use, distribution or reproduction is permitted which does not comply with these terms.

Estimation of the nitrogen content of potato plants based on morphological parameters and visible light vegetation indices

Yiguang Fan[1,2†], Haikuan Feng[1,3*†], Xiuliang Jin[4], Jibo Yue[5], Yang Liu[1,6], Zhenhai Li[7], Zhihang Feng[8], Xiaoyu Song[1] and Guijun Yang[1]

[1]Key Laboratory of Quantitative Remote Sensing in Agriculture of Ministry of Agriculture and Rural Affairs, Information Technology Research Center, Beijing Academy of Agriculture and Forestry Sciences, Beijing, China, [2]School of Geographic, Liaoning Technical University, Fuxin, China, [3]College of Agriculture, Nanjing Agricultural University, Nanjing, China, [4]Key Laboratory of Crop Physiology and Ecology, Ministry of Agriculture, Institute of Crop Sciences, Chinese Academy of Agricultural Sciences, Beijing, China, [5]College of Information and Management Science, Henan Agricultural University, Zhengzhou, China, [6]Key Lab of Smart Agriculture System, Ministry of Education, China Agricultural University, Beijing, China, [7]College of Geomatics, Shandong University of Science and Technology, Qingdao, China, [8]School of Computer and Information Technology, Beijing Jiaotong University, Beijing, China

Plant nitrogen content (PNC) is an important indicator to characterize the nitrogen nutrition status of crops, and quickly and efficiently obtaining the PNC information aids in fertilization management and decision-making in modern precision agriculture. This study aimed to explore the potential to improve the accuracy of estimating PNC during critical growth periods of potato by combining the visible light vegetation indices (VIs) and morphological parameters (MPs) obtained from an inexpensive UAV digital camera. First, the visible light VIs and three types of MPs, including the plant height (*H*), canopy coverage (CC) and canopy volume (CV), were extracted from digital images of the potato tuber formation stage (S1), tuber growth stage (S2), and starch accumulation stage (S3). Then, the correlations of VIs and MPs with the PNC were analyzed for each growth stage, and the performance of VIs and MPs in estimating PNC was explored. Finally, three methods, multiple linear regression (MLR), k-nearest neighbors, and random forest, were used to explore the effect of MPs on the estimation of potato PNC using VIs. The results showed that (i) the values of potato *H* and CC extracted based on UAV digital images were accurate, and the accuracy of the pre-growth stages was higher than that of the late growth stage. (ii) The estimation of potato PNC by visible light VIs was feasible, but the accuracy required further improvement. (iii) As the growing season progressed, the correlation between MPs and PNC gradually decreased, and it became more difficult to estimate the PNC. (iv) Compared with individual MP, multi-MPs can more accurately reflect the morphological structure of the crop and can further improve the accuracy of estimating PNC. (v) Visible light VIs combined with MPs improved the accuracy of estimating PNC, with the

highest accuracy of the models constructed using the MLR method (S1: R^2 = 0.79, RMSE=0.27, NRMSE=8.19%; S2:R^2 = 0.80, RMSE=0.27, NRMSE=8.11%; S3: R^2 = 0.76, RMSE=0.26, NRMSE=8.63%). The results showed that the combination of visible light VIs and morphological information obtained by a UAV digital camera could provide a feasible method for monitoring crop growth and plant nitrogen status.

KEYWORDS

potato, plant nitrogen content, UAV, vegetation indices, morphological parameters

1 Introduction

Worldwide demand for food has increased dramatically owing to the constraints of arable land area and the increasing global population. Some studies suggest that the yield of agricultural systems must double by 2050 to meet the growing food demand of the worldwide population (White et al., 2012; Holman et al., 2016). Staple crops, such as rice (*Oryza sativa*), maize (*Zea mays*), and wheat (*Triticum aestivum*), have a limited scope for increasing yields and high requirements for irrigation systems, which results in high production costs and low potential. Alternatively, potato (*Solanum tuberosum*) is becoming increasingly important in ensuring global food security as the fourth largest food crop with a short growth cycle and the ability to adapt to the environment (Liu et al., 2022). In recent years, the excessive application of nitrogen (N) fertilizer to aggressively maximize potato yields in some regions has reduced the efficiency of N fertilizer use, resulting in increased production costs and wasted resources and triggering potential environmental risks (Nayak et al., 2015). Therefore, scientific N fertilizer management is a vital issue that needs to be addressed for the healthy and sustainable development of the potato industry.

Plant nitrogen content (PNC) is an important indicator that is used to characterize the nitrogen nutritional status of crops. Quickly and efficiently obtaining the PNC information of crops is highly significant for evaluating crop growth and scientifically applying N fertilizers (Fu et al., 2021a). Although traditional field surveys and destructive sampling methods can obtain more accurate PNC information, they are time-consuming and inefficient. Therefore, they cannot meet the current development needs of large-scale, rapid, and efficient monitoring of crop growth conditions in precision agriculture (Yue et al., 2019; Peter et al., 2021; Li et al., 2022). In recent years, the rapid development of remote sensing technology has provided a new option for the efficient, non-destructive, and real-time monitoring of the PNC status of crops.

Compared with ground and satellite remote sensing techniques, unmanned aerial vehicle (UAV) imaging technology can obtain higher temporal and spatial resolution and is more suitable for crop growth monitoring and estimating physicochemical parameters at the farm scale (Yue et al., 2021a). A substantial amount of research has been conducted on UAV imaging technology to monitor the N nutrition status of crops. For example, Feng et al. (Feng et al., 2016) combined the normalized difference red-edge index (NDRE) and floating-position water band index (FWBI) to construct a new vegetation index – the water-tolerant nitrogen index (WNI), which effectively improved the accuracy of estimating the N content in winter wheat leaves. Wang et al. (Wang et al., 2012) showed that the three-bands vegetation index with wavelengths of 423 mm, 703 mm, and 924 mm was significantly better than the two-bands vegetation index in monitoring the nutrient status of N in rice. Xu et al. (Xu et al., 2021) fused multi-source sensors information to construct coverage-adjusted spectral indices (CASIs) to estimate the content of leaf N of maize in three reproductive stages. The results showed that the CASIs outperformed conventional spectral indices. These studies showed that vegetation indices (VIs) can effectively characterize the N nutrient status of crops compared with the traditional methods, which will aid in the efficient management of nitrogen fertilization in the field. However, most of these indices contain wavelengths other than visible light, such as red-edge and near-infrared bands and require the integration of narrow-band reflectance (He et al., 2016; Lu et al., 2021). Simultaneously, the sensors used to acquire these bands, such as hyperspectral and multispectral, are expensive. They have complicated data processing processes that increase the cost of agricultural production and limit their large-scale application in agricultural remote sensing.

In contrast to sensors, such as hyperspectral and multispectral, high-definition digital cameras are inexpensive and have high spatial resolution, simple data processing, and stable performance (Li et al., 2020; Lu et al., 2021). The use of inexpensive digital cameras to monitor the N nutrition status of crops has gradually become favored by many researchers (Putra and Soni, 2018; Putra and Soni, 2020). However, owing to the

few wavelength channels of digital camera sensors, the red-edge and near-infrared bands closely related to the crop canopy structure cannot be obtained (Prey et al., 2018; Jin et al., 2021). Thus, there are certain limitations in monitoring crop N nutrition using VIs that have only been constructed with visible light (Wang et al., 2014).

Morphological parameters (MPs), such as plant height (*H*) and canopy cover (CC), are direct expressions of crop growth and nutritional status, as well as a comprehensive reflection of N metabolism in the crop (Yue et al., 2021b; Li et al., 2022). Similar to the red-edge and near-infrared bands, MPs can provide structural information closely related to crop growth. The combination of *H* and CC extracted from UAV digital images has been shown to significantly improve the accuracy of VIs in estimating crop growth parameters, such as yield, biomass, and the leaf area index (Lu et al., 2019; Wan et al., 2020; Qiao et al., 2022; Shu et al., 2022). Furthermore, most of the growth parameters described above are closely related to the N nutrient status of crops. Therefore, there should also be some connection between MPs and the N status of crops. However, whether the structural information provided by MPs can be used to monitor the nitrogen status of crops remains to be further investigated. The high spatial resolution of UAV digital cameras makes them unique at extracting crop MPs, which provides a new concept to effectively monitor the N nutrient status of crops using inexpensive digital cameras.

However, there are differences in the ability of different MPs to characterize the growth status of crops. For example, *H* and CC reflect the morphological information of crops in vertical and canopy structures, respectively (Bendig et al., 2015; Maimaitijiang et al., 2019). With the advance in growth period, the values of *H* and CC may tend to be stable and no longer change significantly (Tilly et al., 2015). The use of only a single MP may not be able to accurately reflect the dynamic changes of crop growth (Niu et al., 2019; Fu et al., 2021b). Thus, this study calculated the canopy volume (CV) of crops based on the product of *H* and CC, explored the relationship between multiple MPs (*H*, CC and CV) and the potato PNC, and used the three methods of multiple linear regression (MLR), k-nearest neighbors (KNN) and random forest (RF) to explore the performance of MPs and MPs combined with visible light VIs to estimate the potato PNC with the goal of providing a new method to effectively monitor the N status of crops with an inexpensive digital camera.

In summary, this study utilized potato as the research object and explored the potential of MPs extracted by inexpensive digital camera and those combined with visible light VIs to estimate the potato PNC to provide technical support for the scientific and precise management of potato N nutrition. The specific goals of this study were to: (1) evaluate the accuracy of extraction of potato MPs by a UAV digital camera; (2) compare the performance of different MPs and the combination of multi-MPs to estimate the potato PNC; and (3) investigate the effect of MPs on the estimation of potato PNC by visible light VIs and evaluate the potential of combining the two to improve the accuracy of estimating PNC.

2 Experiment and methods

2.1 Experimental design

The experiment was conducted from April to July 2019 at the National Precision Agriculture Experiment Station (40°10′N, 116°26′E), Changping District, Beijing, China. The average altitude is 36 m, and the climate type is a warm temperate semi-humid continental monsoon. Potato seed tubers were sown on 28 March 2019 and harvested on 9 July 2019. The experimental area was divided into the density experimental area (T plots), N experimental area (N plots) and potassium fertilizer experimental area (K plots) to increase the spatial difference of potato growth (Liu et al., 2022). Among them, three levels were established in the density test area, including 60,000 plants/hm^2 (T0), 72,000 plants/hm^2 (T1), and 84,000 plants/hm^2 (T2). Two early maturing potato varieties Zhongshu 5 (Z5) and Zhongshu 3 (Z3) were the two varieties under each density treatment and the experiments were conducted in triplicate with a total of 18 plots. Four levels of N were established in the N test area, including 0 kg/hm^2 urea (N0), 244.65 kg/hm^2 urea (N1), 489.15 kg/hm^2 urea (N2, normal treatment, 15 kg of pure N), and 733.50 kg/hm^2 urea (N3). The same two varieties (Z5 and Z3) were under each N treatment and three replicates for a total of 24 plots. Three levels were established in the potassium fertilizer test area, including 0 kg/hm^2 potassium fertilizer (K0), 970.50 kg/hm^2 potassium fertilizer (K1, the planting density and nitrogen test area received the K1 treatment), and 1,941 kg/hm^2 potassium fertilizer (K2)under one variety treatment (Z3), which was repeated three times for a total of six plots. Both N and K plots were treated under T1 density. There were 48 test plots in total, and the area of a single plot was 32.5 m^2. A total of 11 ground control points (k01~k11) were evenly buried around the test area to accurately obtain the spatial location of the test area and reduce the influence of the positional deviation of each growth period on the test results, and the three-dimensionality (3-D) of each ground control point (GCP) was measured by high-precision GPS. The location of the test field and the details of the test plan are shown in Figure 1.

2.2 UAV digital images acquisition and pre-processing

UAV flight operations were conducted on April 20, May 28, June 10, and June 20, 2019, to obtain digital images of the potato bare soil stage, tuber formation stage (S1), tuber growth stage (S2), and starch accumulation stage (S3). A DJI Genie 4Pro UAV (DJI Group, Ltd. Shenzhen, China) was used as the

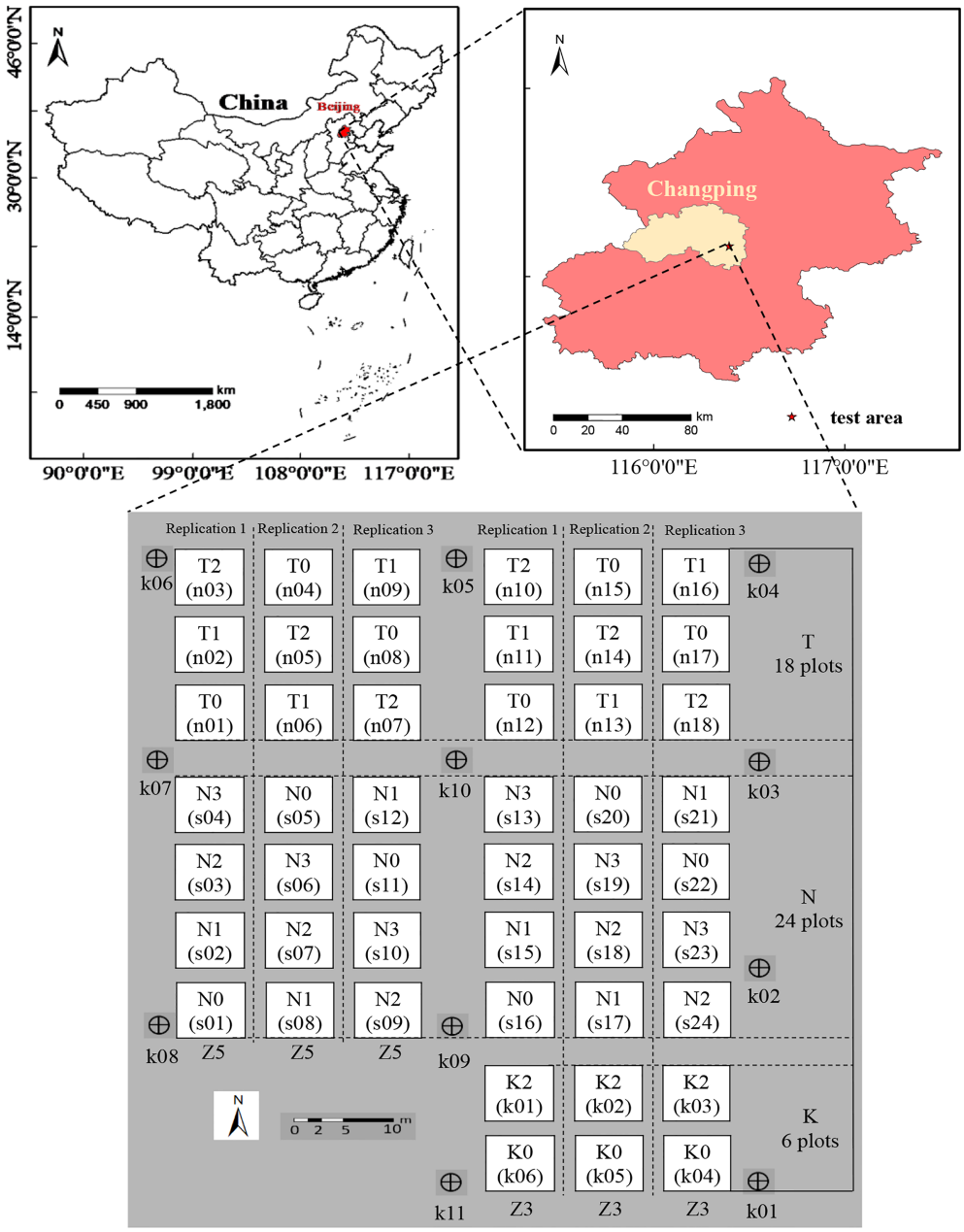

FIGURE 1
Potato field location and experimental design.

remote sensing system platform, and it carried a COMS sensor with 20 million effective pixels and three wavelength channels, including Red (R), Green (G), and Blue (B). In addition, the system was equipped with a position and orientation system (POS) to record the position and spatial altitude of the camera center during data acquisition. The UAV flights were operated in clear, cloudless, and calm weather conditions between 11 a.m. and 1 p.m. local time. The flight altitude was established to 20 m; the overlap rate of heading and collateral direction was 85%, and the spatial resolution of the images obtained was approximately 0.86 cm.

The digital images were pre-processed using Agisoft PhotoScan Professional software (Agisoft, LLC, St. Petersburg, Russia). The specific processing flow started with the digital images with POS data, and the 3-D coordinates of GCPs in the potato bare soil period and each growth period were imported into the software. Images with abnormal attitude angles were removed, and the images were initially aligned. The spatial position and attitude of the

photography center at the moment of image acquisition was restored. Secondly, the images were topographically corrected based on the 3-D coordinates of the GCPs to further optimize the spatial attitude and position of the images and generate a sparse point cloud with precise spatial information attributes in the flight area. Next, the dense point cloud of the flight area was constructed to generate a spatial grid and texture information. Finally, the digital orthophoto map (DOM) and digital surface model (DSM) of the test area were generated.

2.3 Ground data acquisition

The ground data collection was simultaneously conducted with the UAV flight operation and primarily included digital ground photos and measurements of the plant height and PNC at each growth stage. The digital ground photos were obtained by first placing a 1.3 m × 1.3 m white box (perpendicular and parallel to the test crop rows) randomly in each test plot and then using a Canon G16 digital camera to horizontally photograph at 2 m directly above the white box to obtain ground digital photo of each test plot to extract the ground coverage. The plant height was measured by selecting four representative plants in each plot and measuring the distance from the base of the stem to the tip of the leaf and recording it. Finally, the average height of the four plants was considered to be the measured plant height of the plot. The potato PNC was measured by selecting three representative plants in each plot, separating the stems and leaves, and then killing them at 105°C for 0.5 h. The plants were then dried at 80°C to a constant mass and weighed. The N contents of the stem and leaf parts were measured separately using a Kjeldahl nitrogen analyzer. Finally, the PNC was calculated based on the dry mass and nitrogen content of the samples (Fu et al., 2020). The statistical analysis of the measured plant height and PNC at each growth stage is shown in Table 1.

2.4 Vegetation index selection

Based on the existing research results in which visible light VIs were used to monitor crop N status, 10 VIs with potential performance for estimating the potato PNC were selected for follow-up studies as shown in Table 2. Among them, R, G, and B represent the digital number (DN) values of the red, green, and blue channels, respectively, and r, g, and b were calculated from equations(1)–(3), which represent the digital numbers of the normalized R, G, and B, respectively.

$$r = \frac{R}{R+G+B} \tag{1}$$

$$g = \frac{G}{R+G+B} \tag{2}$$

$$b = \frac{B}{R+G+B} \tag{3}$$

2.5 Extraction of morphological parameters

The acquisition of *H* in the different growth stages of potato was primarily determined by the difference between the DSM in each growth stage and that in the bare soil stage. The specific methods first included obtaining the high-definition digital images of the experimental field in the bare soil period and combining them with the 3-D coordinates of GCPs. The DSM of this period, namely DSM_0, was generated, which was used as the reference plane for the subsequent *H* extraction. Secondly, based on the digital images of different growth stages of potato, combined with GCPs, the DSM of the corresponding growth stage, namely DSM_i (i=1, 2, 3, denoted S1, S2, and S3, respectively) was generated. DSM_i was then differentiated from DSM_0 (Equation 4) to obtain the crop height models for the corresponding growth periods. Finally, the average plant height of each plot was extracted using ENVI 5.3 software (L3Harris Geospatial, Boulder, CO, USA) and the vector data of each experimental plot was used to obtain the *H* of each plot.

$$H_i = DSM_i - DSM_0 \ (i = 1, 2.3) \tag{4}$$

This study extracted the CC of potato in each growth period based on the ground digital photos and UAV digital images,

TABLE 1 Statistical analysis of plant height and nitrogen content of potato in different growth stages.

Growth stages	Crop parameters	Max	Min	Mean	Standard deviation	Coefficient of variation (%)
S1	*H*	40.50	20.38	30.29	4.76	15.71
	PNC	4.50	2.09	3.21	0.61	19.03
S2	*H*	40.88	20.42	27.72	5.20	18.75
	PNC	4.00	1.61	2.69	0.58	21.41
S3	*H*	40.35	15.12	25.78	5.15	19.97
	PNC/%	3.74	1.86	2.94	0.46	15.86

S1, tuber formation stage; S2, tuber growth stage; S3, starch accumulation stage.

TABLE 2 Visible light vegetation indices related to nitrogen.

Visible light vegetation indices	Definition	Reference
R	R	/
G	G	/
B	B	/
GRRI	r/g	(Lu et al., 2021b)
GLA	(2*g-r+b)/(2*g+r+b)	(Yue et al., 2021b)
GLI	(2*g-r-b)/(2*g+r+b)	(Yue et al., 2018; Zhou et al., 2018)
GRVI	(g-r)/(g+r)	(Bendig et al., 2015)
VARI	(g-r)/(g+r-b)	(Maimaitijiang et al., 2019)
EXG	2*g-b-r	(Fu et al., 2021a)
NDI	(r-g)/(r+g+0.01)	(Meyer and Neto, 2008)

respectively, and used the results extracted from the ground digital photos as the CC measured values to verify the results extracted by the UAV (Li et al., 2005; Meyer and Neto, 2008). Among them, the vegetation coverage extraction algorithm (VCEA) based on ground digital photos derived the concepts of CC extraction from several studies (Gitelson et al., 2003; Meyer and Neto, 2008) and optimized some of them. The basic process first involved transforming the test area based on the Hue-Saturation-Intensity (HSI) color space, and secondly, using the Excess Green Vegetation Index (EXG) to conduct green vegetation processing on the results of HSI processing. The soil background and weed noise were removed using the maximum interclass variance threshold and morphological threshold. Finally, the ratio of the number of pixels of vegetation in each plot to the total number of pixels in the plot was calculated, which is the measured CC value of the plot. The basic process of CC extraction based on UAV digital images included first processing the DOM of each growth period using the EXG index. The threshold value of vegetation and soil was then obtained using the bimodal method, and the number of pixels of vegetation and soil in each plot was obtained using the banding operation. Finally, the ratio of number of pixels of vegetation to the total number of pixels in each plot was calculated, which was the CC value of that plot based on UAV extraction.

In this study, the product of extracted H and CC was defined as the canopy volume (Qiao et al., 2022) to explore the association of multiple MPs with the potato PNC, and the CV was calculated as shown in Equation 5.

$$CV = CC{\star}H \tag{5}$$

2.6 Model building and evaluation

A total of 48 sets of data were obtained in each growth period of potato. To enhance the reliability of the experimental conclusions, the models were constructed with repetitions 1 and 3 (32) as the training set, and the data of repetition 2 (16) was used to validate the models. The methods used to build the potato PNC estimation models included MLR, KNN, and RF. Among them, MLR is an effective linear regression method, which is often used to describe the linear relationship between multiple independent variables and dependent variables. KNN is a mature machine learning algorithm that can determine the regression values of the samples to be tested based on the features of the k most similar samples in the feature space. RF is a supervised ensemble learning algorithm. It trains input samples to generate a decision tree training set based on bootstrap resampling technology, and then integrates the results of each decision tree to output the predicted target value. In this study, the coefficient of determination (R^2), root mean square error (RMSE), and normalized root mean square error (NRMSE) were used to evaluate the accuracy and stability of the models.

3 Results and analysis

3.1 Potato plant height extraction

The crop height models based on UAV digital images can visually represent the spatial distribution of potato plant height at different growth stages, which helps to monitor the growth of potato plants, and explore the effects of varying treatment factors on the height of potato plants. In this study, the DSM of different growth stages of potato and that of the bare soil stage were calculated to obtain the crop height models of corresponding growth stages, and the results are shown in Figure 2. It is apparent that the height of potato plant in each growth period was generally high in the west and low in the east. Among them, there were differences in the plant height between different varieties, nutrient and density treatments, and the difference in plant height of the different varieties of potato was the most obvious.

To verify the accuracy of H extraction based on the DSM, the measured plant height and extracted plant height were

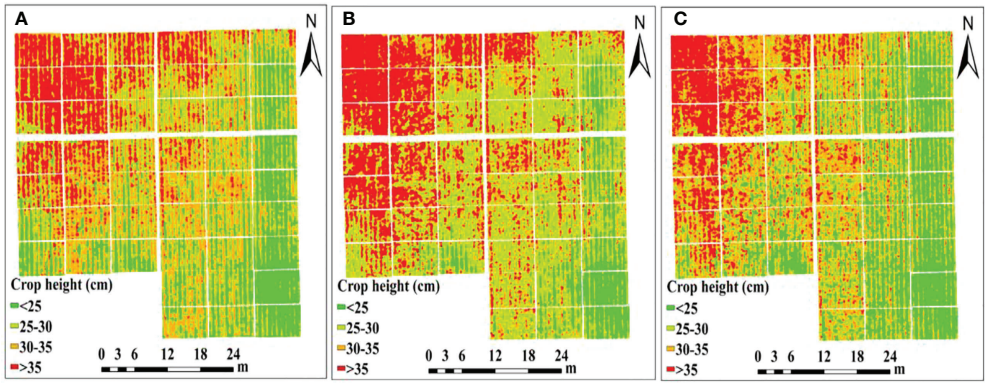

FIGURE 2
Crop height models of potato at **(A)** S1, **(B)** S2, **(C)** S3.

compared and analyzed for the three reproductive stages, and the results are shown in Figure 3. The coefficients of determination of the extracted plant height and the measured plant height in the three growth stages were 0.86, 0.87 and 0.76, respectively, and the RMSE were 2.29 cm, 2.47 cm, and 2.79 cm, respectively. These values indicated that the plant height extraction based on DSM had higher precision, and the extraction precision of potato in the early stages of growth was higher than that in the later stage of growth.

3.2 Potato coverage extraction

The ground digital photos and UAV digital images of three growth stages of the potato plants were processed by VCEA and EXG index bimodal threshold methods, respectively, and the CC values of each growth stage that were measured and extracted were obtained. The use of plot s20 as an example in Figure 4 compares the results of CC extraction by the two methods. The digital ground photos and the UAV digital images showed slight differences in potato canopy morphology. Among them, the digital ground photos more clearly reflected the interplant interlacing state of potato, which was more conducive to the extraction of potato canopy cover. UAV digital images can also better distinguish potato plants from soil background, and the CC values extracted based on the two methods can effectively reflect the potato canopy cover in general.

The CC that was extracted using the two methods for the three growth stages was compared and analyzed to quantitatively evaluate the accuracy of CC extraction based on the UAV digital images. The results are shown in Figure 5. The CC values of the S1 were primarily concentrated between 0.6 and 0.8, while the CC values of the S2 and S3 were primarily concentrated between 0.4 and 0.8. The coefficients of determination of the fit between the extracted CC and the measured CC in the S1, S2, and S3 were 0.83, 0.81, and 0.78, respectively. The RMSE were 0.02, 0.05, and 0.08, respectively, indicating that the accuracy of potato canopy cover extracted based on digital images is reliable and can be used to estimate crop physical and chemical parameters.

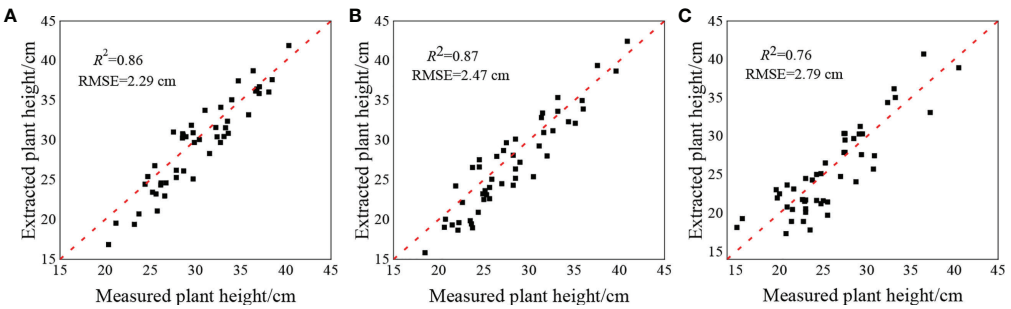

FIGURE 3
Contrastive analysis of plant height extracted from potato and measured plant height at **(A)** S1, **(B)** S2, **(C)** S3.

10.3389/fpls.2022.1012070

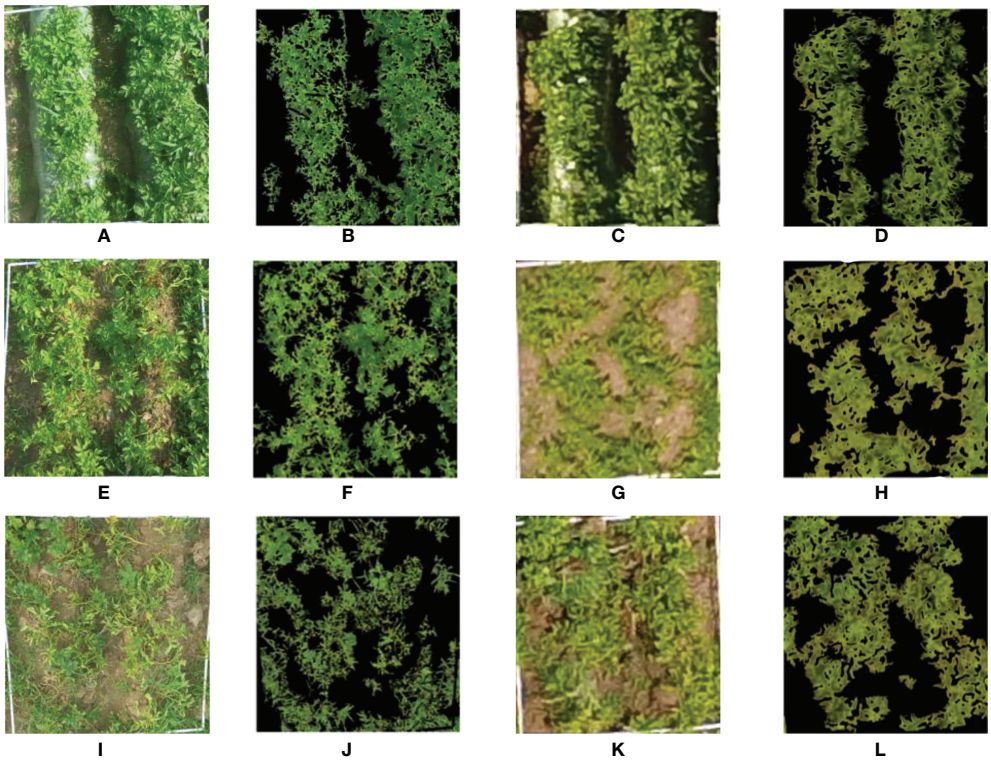

FIGURE 4
Comparison of two methods for extracting potato coverage.**(A, E, I)** Ground digital photos of the potato plants at S1-S3; **(B, F, J)** The effect of potato CC extraction using ground digital photo at S1-S3; **(C, G, K)** UAV digital images of potato plants at S1-S3; **(D, H, L)** The effect of potato CC extraction using UAV digital image at S1-S3.

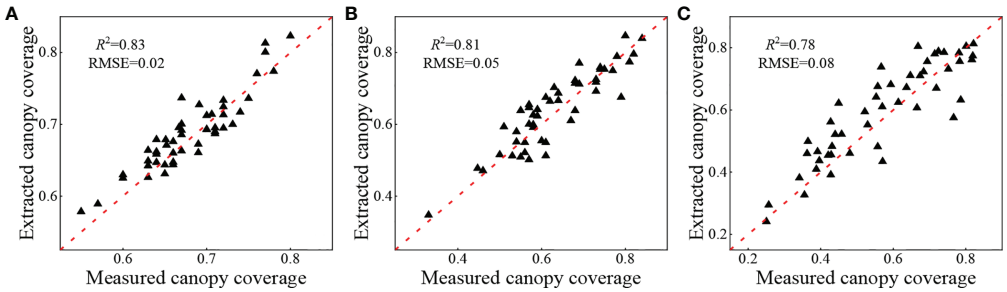

FIGURE 5
Comparative analysis of potato extraction coverage and measured coverage at **(A)** S1, **(B)** S2, **(C)** S3.

3.3 Correlation analysis between the parameters and PNC

Correlation analysis was performed between the visible light VIs and MPs obtained in each growth period of potato and PNC, and the results are shown in Figure 6. The correlation between most of the VIs and PNC tended to increase and then decrease from the S1 to S3. Among them, all the VIs except G reached a significance level of 0.01 for the correlation with the PNC during the S1 and S2, and the absolute values of correlation coefficients ranged from 0.40 to 0.74 and 0.54 to 0.83, respectively. All the VIs reached a significance level of 0.01 for the correlation with the PNC during the S3, and the absolute values of correlation coefficients ranged from 0.40 to 0.69. Unlike visible light VIs,

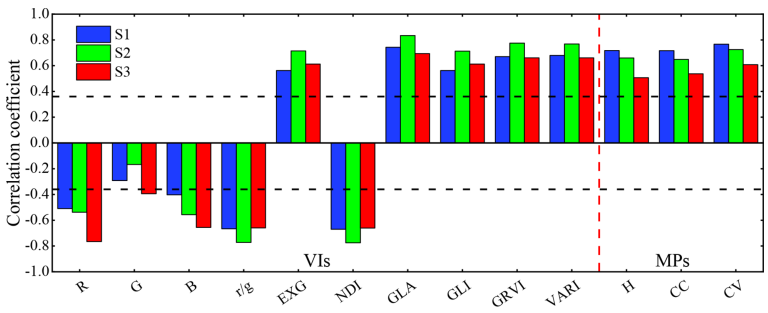

FIGURE 6
Correlation analysis results of each parameter and potato PNC. Note: the horizontal dashed line indicates a significance level of 0.01.

the correlation between MPs and PNC gradually decreased as the growing season progressed. Nevertheless, the correlation between all the MPs and PNC a significance level of 0.01 in all three growth stages. Furthermore, the correlations of CV were higher than those of *H* and CC, and the absolute values of the correlation coefficients were 0.77, 0.63, and 0.65 for the three growth stages S1, S2, and S3, respectively. Compared with the visible light VIs, the correlations between MPs and PNC in the three growth stages of potato were comparable to those of most of the visible light VIs, indicating that the association between MPs and PNC is stronger and that it is practical to monitor the potato PNC based on the MPs extracted from inexpensive digital cameras.

3.4 Estimation of the Potato PNC

3.4.1 Estimation of the potato PNC by visible light VIs

In this study, the top five VIs with higher correlations in each growth period were selected, and the three methods MLR, KNN and RF were used to construct estimation models for the potato PNC. The results are shown in Table 3. The R^2 of potato PNC estimation models constructed using the three methods > 0.5 for all three growth periods, indicating that the selected VIs could reflect the potato PNC status some extent. Thus, it was feasible to monitor the potato PNC status based on visible light VIs during the critical growth periods. A comparison of the results of the three reproductive stages indicated that the estimations of the S1 and S2 were clearly better than that of the S3. From the modeling and validation results, it can be seen that the potato PNC estimation models constructed by the three methods show similar R^2, RMSE, and NRMSE.

3.4.2 MPs to estimate the potato PNC

To investigate the association between MPs and the PNC, this study constructed estimation models of the potato PNC based on extracted *H*, CC, and constructed CV. The three were combined to investigate the effect of multiple MPs in estimating the potato PNC. The results are shown in Figure 7. The estimation of PNC by single or multiple MPs was better in the S1 and worse in the S3, whereas *H* and CC were the worst in the S3 (R^2< 0.4). The models constructed by CV had a higher R^2, lower RMSE, and NRMSE and better estimation of PNC than those of *H* and CC. The combination of multiple MPs effectively improved the accuracy of PNC estimation at all the growth stages of potato compared with the models constructed with single MPs. However, compared with visible light VIs (Table 3), the estimation effect of MPs requires further improvement.

TABLE 3 Visible light vegetation indices estimation of potato PNC.

Growth stages	Dataset	MLR			KNN			RF		
		R^2	RMSE/%	NRMSE/%	R^2	RMSE/%	NRMSE/%	R^2	RMSE/%	NRMSE/%
S1	Cali	0.75	0.31	9.76	0.72	0.33	10.45	0.75	0.31	9.95
	Vali	0.75	0.30	8.99	0.72	0.34	10.32	0.73	0.36	10.67
S2	Cali	0.74	0.27	10.43	0.69	0.31	11.44	0.73	0.28	10.70
	Vali	0.78	0.32	11.23	0.62	0.42	14.77	0.73	0.38	13.52
S3	Cali	0.69	0.24	8.42	0.62	0.27	9.37	0.68	0.26	8.83
	Vali	0.72	0.29	10.12	0.64	0.32	8.90	0.64	0.31	10.55

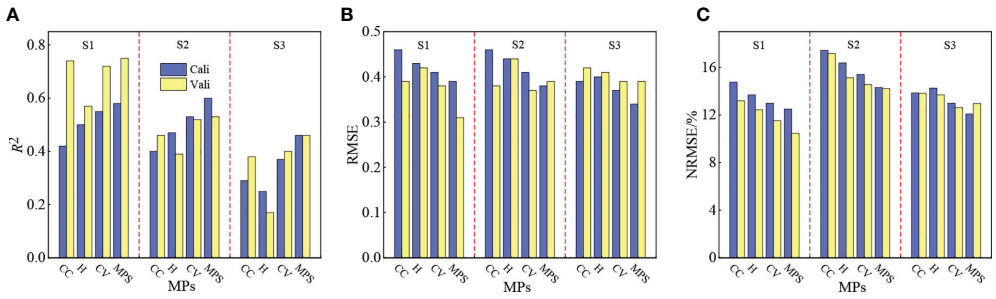

FIGURE 7
Estimation of the potato PNC effect by morphological parameters at **(A)** R^2, **(B)** RMSE, **(C)** NRMSE.

3.4.3 Estimation of the potato PNC by combining visible light VIs and MPs

To investigate the effect of inexpensive digital camera extraction of MPs on the visible light VIs to estimate the potato PNC, this study constructed the PNC estimation models for the three potato growth stages using three methods MLR, KNN, and RF based on the selected VIs and extracted MPs in Section 2.5. The results are shown in Table 4. The models used to estimate the PNC were constructed using three methods with visible light VIs combined with MPs. They were also more effective at estimating the S1 and S2 than the S3 for potato at all stages of growth. Combined with Tables 3, 4, it is apparent that during the same growth period, the R^2 of the models constructed by VIs combined with MPs increased compared with a single model variable. In addition, the RMSE and NRMSE decreased substantially, indicating that the addition of MPs improved the accuracy of visible light VIs in estimating the PNC. Comparing the estimation results of different methods in each growth stage, it can be seen that the three methods have achieved promising results. The scatter plot of the predicted and measured PNC values for each growth period are shown in Figure 8. The predicted and measured PNC values obtained by the three methods were mostly uniformly distributed around the 1:1 line for each potato growth period, indicating that the overall effect of estimating the PNC based on visible light VIs and MPs is suitable.

4 Discussion

4.1 Extraction of the morphological parameters

The highly accurate extraction of the potato *H* and CC at all growth stages is essential to explore the potential of MPs in combination with the visible light VIs to estimate the potato PNC. UAV remote sensing platforms are advantageous because of their operational flexibility and high spatial and temporal resolution; thus, they have more significant advantages in extracting crop MPs (Holman et al., 2016; Li et al., 2016; Niu et al., 2019; Johnson et al., 2020). In this study, based on the crop height models of potato, the plant height was extracted in three growth stages, and it is apparent in Figure 3 that the extraction of the plant height in all three growth stages of potato was highly accurate, and the accuracy of the S1 and S2 was better than that of the S3. The reason is that during the first two growth periods, the potato plants primarily grew vegetatively and reproduced, producing vigorous plants with a large area of leaf expansion. At

TABLE 4 Estimation of the potato PNC by visible light vegetation indices combined with morphological parameters.

Growth stages	Data set	MLR			KNN			RF		
		R^2	RMSE/%	NRMSE/%	R^2	RMSE/%	NRMSE/%	R^2	RMSE/%	NRMSE/%
S1	Cali	0.78	0.29	9.07	0.75	0.31	9.78	0.78	0.29	9.20
	Vali	0.79	0.27	8.19	0.76	0.29	8.84	0.81	0.35	10.58
S2	Cali	0.76	0.27	10.36	0.71	0.29	10.99	0.73	0.29	10.95
	Vali	0.80	0.27	8.11	0.70	0.36	12.73	0.75	0.34	11.90
S3	Cali	0.71	0.24	8.13	0.70	0.25	8.39	0.72	0.26	9.21
	Vali	0.76	0.26	8.63	0.70	0.29	9.65	0.73	0.28	9.53

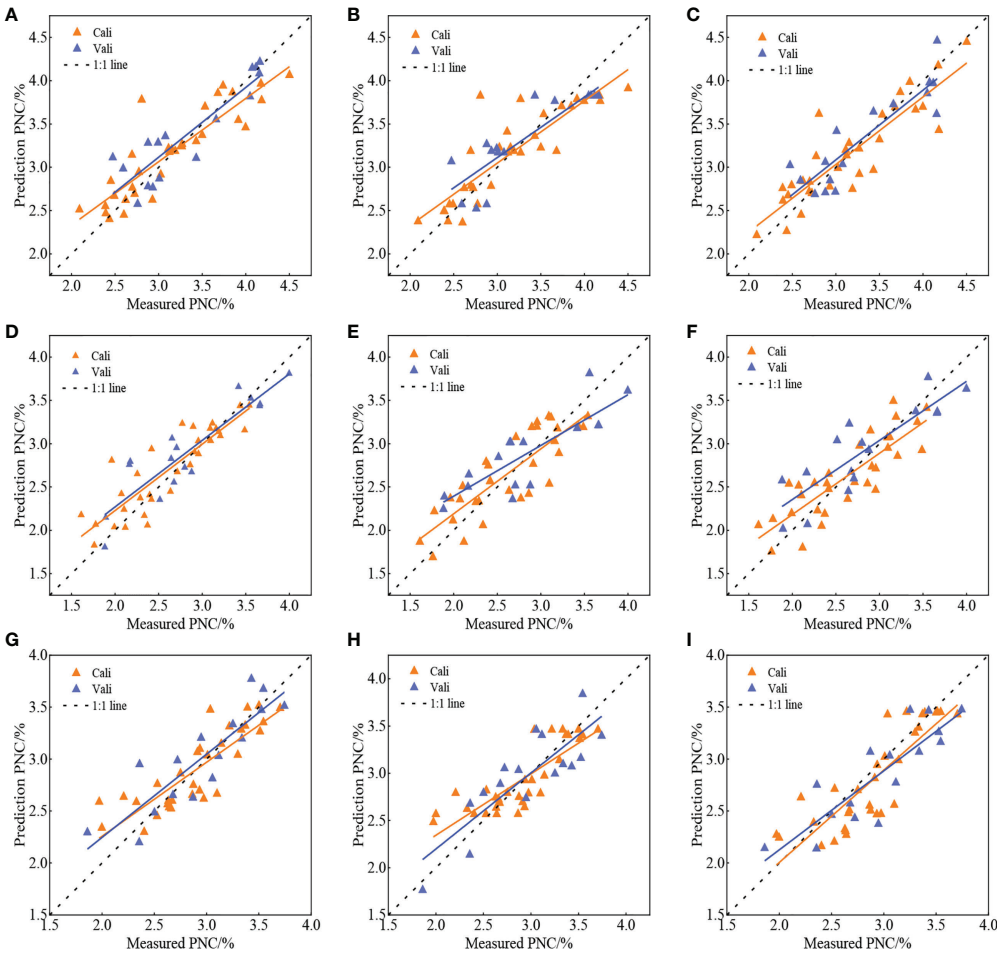

FIGURE 8
Validation effect of estimation of potato PNC based on fusion characteristics at each growth stage.**(A, D, G)** MLR, S1-S3; **(B, E, H)** RF, S1-S3; **(C, F, I)** KNN, S1-S3.

this time, the plant height extracted was less affected by mixed pixels and was highly precise. The potato tubers were bulking and maturing during the S3, and some potato leaves began to turn yellow and shrink, and the canopy coverage was reduced. At this time, the extracted plant height was substantially affected by the soil background, which reduced the accuracy. Similar to the plant height, the accuracy of extraction of the CC also showed that the S1 and S2 could be more effectively extracted than plants in the S3. The reason for this is that the extraction of CC was less influenced by soil and weeds and more accurate during the early growth periods of potato. In contrast, there was a larger difference between the CC values extracted based on digital ground photos and those based on UAV digital images during the S3. The accuracy of extraction of CC decreased owing to the influence of a small number of field weeds and soil background. As shown in Figures 3, 5, the extraction of the potato canopy MPs based on the UAV digital camera was highly accurate and more effectively reflected the growth conditions of potato, which enables their use to estimate physical and chemical parameters. In addition, measures, such as mulching and weeding, can be implemented in the field to reduce the interference of soil background and weeds and further improve the accuracy of extracting crop MPs.

4.2 Response of visible light VIs to the PNC

Based on the existing research results, this study selected 10 VIs that were closely linked to crop N and analyzed their correlation with the PNC in three key growth stages of potato. As shown in Figure 6, most of the VIs and PNC reached a significance level of 0.01 for the correlation, indicating that it is feasible to use visible light VIs to estimate the PNC. The

correlation between most VIs and PNC first increased and then decreased from the S1 to S3. The effect of estimating the PNC based on visible light VIs (Table 3) also showed that the estimation of the early growth stages of potato were better than those at the later stage.

The reason is that the vegetative and reproductive growth were the primary factors during the early stages of potato growth. The plants grew vigorously, and the extracted VIs were less affected by mixed pixels, such as soil, so they more effectively reflected the change in PNC. In contrast, the effect of spectral saturation rendered most of the VIs less sensitive to the evolution of PNC during the late stage of potato growth, and some potato plants began to senesce and turn yellow during this period. The spectral information extracted at this time was also substantially affected by the soil background. Therefore, the accuracy of estimation of PNC by visible light VIs was lower during the S3 than during the first two reproductive stages. In addition, compared with Nigon's result (Nigon et al., 2015) of estimating the content of N in potato leaves (R^2 = 0.79), the accuracy of this study was lower. There are several primary reasons for this. On the one hand, Nigon used the red edge information obtained by a hyperspectral camera to obtain more spectral information related to nitrogen (Raper and Varco, 2015). Alternatively, compared with the N content of plants, changes in the canopy spectrum were more closely related to the content of crop leaf N than that of the plant, and the spectral information is more suitable for estimating the leaf N content (Zhou et al., 2018).

4.3 Response of morphological parameters to the PNC

The MPs of crops have been widely used to monitor crop growth parameters (Bendig et al., 2015; Stevens et al., 2020). However, the status of response of PNC to different MPs at the various crop growth stages is unclear. As shown in Figures 6 and 7, the correlation between all three MPs and the PNC gradually decreased as the growth period advanced, and the constructed models gradually became less accurate. The reason for this is that the potato growth was most closely related to the nutritional status during the S1, and the accuracy of extraction of each MP was higher, which more effectively reflected the changing status of PNC. During the S2, *H* and CC tended to saturate, and no longer changed significantly (Wan et al., 2020; Qiao et al., 2022), and the link between MPs and PNC weakened. The growth of potato was primarily reproductive during the S3, and the N in plant continued to transfer to the tuber. While the changes of *H* and CC were not obvious, the accuracy of extraction also became worse. The connection between MPs and PNC was weakest at this stage, and the models constructed were the least effective at estimating the PNC.

Considering that a single MP cannot finely reflect the crop growth condition, this study constructed the CV based on the extracted *H* and CC. In addition, we explored the effect of multiple MPs in estimating the potato PNC by combining *H*, CC, and CV. Figures 6, 7 show that the correlation between CV and PNC was higher than that of *H* and CC for all three reproductive stages of potato, and the effect of estimating PNC based on the CV was better than that based on the *H* and CC. The reason is that the PNC was composed of two parts, which included the contents of leaf N and stem N, and the CV simultaneously reflected the growth status of potato in the canopy and vertical scales, which weakened the saturation phenomenon of PNC estimated by *H* or CC. The combination of *H*, CC and CV was much more accurate at estimating the PNC than a single MP because multiple MPs can characterize the morphological changes of potato from multiple dimensions and improve the sensitivity of MPs to PNC in each period (Lu et al., 2021).

4.4 Effect of the MPs on the estimation of PNC from visible light VIs

Existing studies have shown that both VIs and MPs can reflect the growth and nutritional status of crops. The visible light VIs and MPs obtained by UAV digital camera enabled this study to use the three methods of MLR, KNN, and RF to explore the effect of combining the VIs and MPs to estimate the potato PNC. As shown in Table 4, the combination of VIs with MPs improved the accuracy of estimating PNC compared with using the VIs alone, and the accuracy of the models constructed in the three growth stages was closer to the result of Nigon. The reason is that, on the one hand, the VIs and MPs combined the nutritional information and morphological information of crops, which can better characterize the law of crop growth and enhance the connection with PNC. Alternatively, the red-edge or near-infrared band was sensitive to crop canopy structure, while *H* and CC were the primary factors that affect the crop canopy structure; the combination of multiple MPs provides similar information to the red-edge and near-infrared bands (Wang et al., 2012; Wan et al., 2020), which enhanced the link between optical VIs and PNC. Thus, the combination of visible light VIs and MPs can improve the accuracy of estimating the PNC.

4.5 Implications for future study

In this study, digital images of the key growth periods of the potato were obtained using a UAV digital camera, and the visible light VIs and MPs, such as *H*, CC, and CV, were

extracted from them. Combined with different regression methods, the effect of different MPs and MPs combined with VIs in estimating the potato PNC were explored. The results showed that the morphological information of potato plant was closely related to the N nutrition status, and the combination of VIs and MPs could improve the accuracy of estimating the PNC, which was consistent with the existing research conclusions (Maimaitijiang et al., 2019; Shu et al., 2022). In addition, Figures 3 and 5 showed that the *H* and CC of potato plant extracted based on the UAV digital camera were highly accurate, which could provide a favorable reference for monitoring the growth of potato. The use of MPs extracted by an inexpensive UAV digital camera combined with the visible light VIs to estimate the potato PNC not only fully utilizes the advantages of high spatial resolution of the digital camera but also avoids the possible matching error between multi-source sensors, which can provide an effective manner to estimate the physical and chemical parameters with high precision.

This study only discussed the effect of using the MPs extracted from the UAV digital images to estimate the PNC in the critical growth periods of potato at a fixed flying height. However, the accuracy of extraction of the MPs is closely related to the spatial resolution of the digital images and the flying height of the UAV. These factors should also be considered in subsequent studies. In addition, future studies should also consider using potato data from different locations and years to verify the conclusions.

5 Conclusions

This study developed a method to effectively estimate the growth parameters and PNC status of potato at critical growth stages based on an inexpensive UAV digital camera. First, the UAV digital camera was used to extract visible light VIs and morphological information about the potato canopy. Next, the effect of MPs and VIs combined with MPs in estimating PNC was investigated by combining various methods. Several conclusions can be drawn from these results. (1) UAV digital images can obtain potato *H* and CC information with high accuracy, which can provide a reference to assess the growth of potato plants. (2) Both visible light VIs and MPs reflect the status of potato PNC, and VIs are more closely associated with the PNC. (3) Different MPs have different effects on estimating PNC, and multiple MPs can more effectively reflect the morphological structure of crops, which can further improve the accuracy of estimating PNC. (4) Visible light VIs combined with MPs can improve the accuracy of estimating the PNC. Based on these findings, the method can provide a reference to monitor crop growth and N nutrient status using a UAV digital camera to reduce agricultural production costs and improve precision agricultural management.

Data availability statement

The original contributions presented in the study are included in the article/supplementary material. Further inquiries can be directed to the corresponding author.

Author contributions

HF, YF, GY, ZL, and JY designed the experiments. HF, ZF, ZL, and YL collected the PNC and UAV digital images. YF and HF analyzed the data and wrote the manuscript. XJ and HF made comments and revised the manuscript. All authors contributed to the article and approved the submitted version.

Funding

This study was supported by the Key scientific and technological projects of Heilongjiang province (2021ZXJ05A05), the National Natural Science Foundation of China (41601346), the Platform Construction Funded Program of Beijing Academy of Agriculture and Forestry Sciences (No.PT2022-24), and the Key Field Research and Development Program of Guangdong Province (2019B020216001).

Acknowledgments

We thanks to the National Precision Agriculture Experiment Station for providing the test site and employees. We are also grateful to Hong Chang, Huiling Long, Yang Meng and Yu Zhao who worked hard in the field and lab to provide us with valuable data.

Conflict of interest

The authors declare that the research was conducted in the absence of any commercial or financial relationships that could be construed as a potential conflict of interest.

Publisher's note

All claims expressed in this article are solely those of the authors and do not necessarily represent those of their affiliated organizations, or those of the publisher, the editors and the reviewers. Any product that may be evaluated in this article, or claim that may be made by its manufacturer, is not guaranteed or endorsed by the publisher.

References

Bendig, J., Yu, K., Aasen, H., Bolten, A., Bennertz, S., Broscheit, J, et al. (2015). Combining UAV-based plant height from crop surface models, visible, and near infrared vegetation indices for biomass monitoring in barley. *Int. J. Appl. Earth Observation Geoinformation* 39, 79–87. doi: 10.1016/j.jag.2015.02.012

Feng, W., Zhang, H.-Y., Zhang, Y.-S., Qi, S.-L., Heng, Y.-R., Guo, B.-B., et al. (2016). Remote detection of canopy leaf nitrogen concentration in winter wheat by using water resistance vegetation indices from *in-situ* hyperspectral data. *Field Crops Research* 198, 238–246. doi: 10.1016/j.fcr.2016.08.023

Fu, Y., Yang, G., Li, Z., Song, X., Li, Z., Xu, X., et al. (2020). Winter wheat nitrogen status estimation using UAV-based RGB imagery and Gaussian processes regression. *Remote Sens.* 12, 3778–805. doi: 10.3390/rs12223778

Fu, Y., Yang, G., Pu, R., Li, Z., Li, H., Xu, X., et al. (2021a). An overview of crop nitrogen status assessment using hyperspectral remote sensing: Current status and perspectives. *Eur. J. Agron.* 124, 126241–57. doi: 10.1016/j.eja.2021.126241

Fu, Y., Yang, G., Song, X., Li, Z., Xu, X., Feng, H., et al. (2021b). Improved estimation of winter wheat aboveground biomass using multiscale textures extracted from UAV-based digital images and hyperspectral feature analysis. *Remote Sens.* 13, 581–603. doi: 10.3390/rs13040581

Gitelson, A. A., Vina, A., Arkebauer, T. J., Rundquist, D. C., Keydan, G., and Leavitt, B.. (2003). Remote estimation of leaf area index and green leaf biomass in maize canopies. *Geophysical Res. Lett.* 30, 1248–52. doi: 10.1029/2002gl016450

He, L., Zhang, H.-Y., Zhang, Y.-S., Song, X., Feng, W., Leavitt, B., et al. (2016). Estimating canopy leaf nitrogen concentration in winter wheat based on multi-angular hyperspectral remote sensing. *Eur. J. Agron.* 73, 170–185. doi: 10.1016/j.eja.2015.11.017

Holman, F. H., Riche, A. B., Michalski, A., Castle, M., Wooster, M. J., and Hawkesford, M. J.. (2016). High throughput field phenotyping of wheat plant height and growth rate in field plot trials using UAV based remote sensing. *Remote Sens.* 8, 1031–55. doi: 10.3390/rs8121031

Jin, X., Zarco-Tejada, P. J., Schmidhalter, U., Reynolds, M. P., Hawkesford, M. J., Varshney, R. K., et al. (2021). High-throughput estimation of crop traits: A review of ground and aerial phenotyping platforms. *IEEE Geosci. Remote Sens. Magazine* 9, 200–231. doi: 10.1109/mgrs.2020.2998816

Johnson, B. J., Manby, R., and Devine, G. J. (2020). Performance of an aerially applied liquidBacillus thuringiensisvar.israelensisformulation (strainAM65-52) against mosquitoes in mixed saltmarsh-mangrove systems and fine-scale mapping of mangrove canopy cover using affordable drone-based imagery. *Pest Manage. Sci.* 76, 3822–3831. doi: 10.1002/ps.5933

Li, X. B., Chen, Y. H., Yang, H., and Zhang, Y. X. (2005). Improvement, comparison, and application of field measurement methods for grassland vegetation fractional coverage. *J. Integr. Plant Biol.* 47, 1074–1083. doi: 10.1111/j.1744-7909.2005.00134.x

Li, H., Li, D., Xu, K., Cao, W., Jiang, X., Ni, J., et al. (2022). Monitoring of nitrogen indices in wheat leaves based on the integration of spectral and canopy structure information. *Agronomy-Basel* 12, 833–53. doi: 10.3390/agronomy12040833

Li, W., Niu, Z., Chen, H. Y., Li, D., Wu, M. Q., and Zhao, W.. (2016). Remote estimation of canopy height and aboveground biomass of maize using high-resolution stereo images from a low-cost unmanned aerial vehicle system. *Ecol. Indic.* 67, 637–648. doi: 10.1016/j.ecolind.2016.03.036

Liu, Y., Feng, H. K., Yue, J. B., Li, Z. H., Yang, G. J., Song, X. Y., et al. (2022). Remote-sensing estimation of potato above-ground biomass based on spectral and spatial features extracted from high-definition digital camera images. *Comput. Electron. Agric.* 198, 107089–102. doi: 10.1016/j.compag.2022.107089

Li, B., Xu, X., Zhang, L., Han, J., Bian, C., et al. (2020). Above-ground biomass estimation and yield prediction in potato by using UAV-based RGB and hyperspectral imaging. *Isprs J. Photogrammetry Remote Sens.* 162, 161–172. doi: 10.1016/j.isprsjprs.2020.02.013

Lu, J., Cheng, D., Geng, C., Zhang, Z., Xiang, Y., and Hu, T.. (2021a). Combining plant height, canopy coverage and vegetation index from UAV-based RGB images to estimate leaf nitrogen concentration of summer maize. *Biosyst. Eng.* 202, 42–54. doi: 10.1016/j.biosystemseng.2020.11.010

Lu, N., Zhou, J., Han, Z., Li, D., Cao, Q., Yao, X., et al. (2019). Improved estimation of aboveground biomass in wheat from RGB imagery and point cloud data acquired with a low-cost unmanned aerial vehicle system. *Plant Methods* 15, 17–33. doi: 10.1186/s13007-019-0402-3

Maimaitijiang, M., Sagan, V., Sidike, P., Maimaitiyiming, M., Hartling, S., Peterson, K. T., et al. (2019). Vegetation index weighted canopy volume model (CVMVI) for soybean biomass estimation from unmanned aerial system-based RGB imagery. *Isprs J. Photogrammetry Remote Sens.* 151, 27–41. doi: 10.1016/j.isprsjprs.2019.03.003

Meyer, G. E., and Neto, J. C. (2008). Verification of color vegetation indices for automated crop imaging applications. *Comput. Electron. Agric.* 63, 282–293. doi: 10.1016/j.compag.2008.03.009

Nayak, D., Saetnan, E., Cheng, K., Wang, W., Koslowski, F., Cheng, Y.-F., et al. (2015). Management opportunities to mitigate greenhouse gas emissions from Chinese agriculture. *Agric. Ecosyst. Environ.* 209, 108–124. doi: 10.1016/j.agee.2015.04.035

Nigon, T. J., Mulla, D. J., Rosen, C. J., Cohen, Y., Alchanatis, V., Knight, J., et al. (2015). Hyperspectral aerial imagery for detecting nitrogen stress in two potato cultivars. *Comput. Electron. Agric.* 112, 36–46. doi: 10.1016/j.compag.2014.12.018

Niu, Y., Zhang, L., Zhang, H., Han, W., and Peng, X. (2019). Estimating above-ground biomass of maize using features derived from UAV-based RGB imagery. *Remote Sens.* 11, 1261–82. doi: 10.3390/rs11111261

Peter, B. G., Messina, J. P., Carroll, J. W., and Chikowo, R. (2021). A case for green-based vegetation indices: Plot-scale sUAS imagery related to crop chlorophyll content on smallholder maize farms in Malawi. *Remote Sens. Lett.* 12, 778–787. doi: 10.1080/2150704x.2021.1938733

Prey, L., von Bloh, M., and Schmidhalter, U. (2018). Evaluating RGB imaging and multispectral active and hyperspectral passive sensing for assessing early plant vigor in winter wheat. *Sensors* 18, 2931–49. doi: 10.3390/s18092931

Putra, B. T. W., and Soni, P. (2018). Enhanced broadband greenness in assessing chlorophyll a and b, carotenoid, and nitrogen in robusta coffee plantations using a digital camera. *Precis. Agric.* 19, 238–256. doi: 10.1007/s11119-017-9513-x

Putra, B. T. W., and Soni, P. (2020). Improving nitrogen assessment with an RGB camera across uncertain natural light from above-canopy measurements. *Precis. Agric.* 21, 147–159. doi: 10.1007/s11119-019-09656-8

Qiao, L., Gao, D., Zhao, R., Tang, W., An, L., Li, M., et al. (2022). Improving estimation of LAI dynamic by fusion of morphological and vegetation indices based on UAV imagery. *Comput. Electron. Agric.* 192, 106603–15. doi: 10.1016/j.compag.2021.106603

Raper, T. B., and Varco, J. J. (2015). Canopy-scale wavelength and vegetative index sensitivities to cotton growth parameters and nitrogen status. *Precis. Agric.* 16, 62–76. doi: 10.1007/s11119-014-9383-4

Shu, M., Shen, M., Dong, Q., Yang, X., Li, B., and Ma, Y.. (2022). Estimating the maize above-ground biomass by constructing the tridimensional concept model based on UAV-based digital and multi-spectral images. *Field Crops Res.* 282, 108491–503. doi: 10.1016/j.fcr.2022.108491

Stevens, B., Diels, J., Vanuytrecht, E., Brown, A., Bayo, S., Rujweka, A., et al. (2020). Canopy cover evolution, diurnal patterns and leaf area index relationships in a mchare and Cavendish banana cultivar under different soil moisture regimes. *Scientia Hortic.* 272, 109328–338. doi: 10.1016/j.scienta.2020.109328

Tilly, N., Aasen, H., and Bareth, G. (2015). Fusion of plant height and vegetation indices for the estimation of barley biomass. *Remote Sens.* 7, 11449–11480. doi: 10.3390/rs70911449

Wan, L., Cen, H., Zhu, J., Zhang, J., Zhu, Y., Sun, D., et al. (2020). Grain yield prediction of rice using multi-temporal UAV-based RGB and multispectral images and model transfer - a case study of small farmlands in the south of China. *Agric. For. Meteorology* 291, 108096–111. doi: 10.1016/j.agrformet.2020.108096

Wang, Y., Wang, D., Shi, P., and Omasa, K. (2014). Estimating rice chlorophyll content and leaf nitrogen concentration with a digital still color camera under natural light. *Plant Methods* 10, 36–47. doi: 10.1186/1746-4811-10-36

Wang, W., Yao, X., Yao, X. F., Tian, Y. C., Liu, X. J., Ni, J., et al. (2012). Estimating leaf nitrogen concentration with three-band vegetation indices in rice and wheat. *Field Crops Res.* 129, 90–98. doi: 10.1016/j.fcr.2012.01.014

White, J. W., Andrade-Sanchez, P., Gore, M. A., Bronson, K. F., Coffelt, T. A., Conley, M. M., et al. (2012). Field-based phenomics for plant genetics research. *Field Crops Res.* 133, 101–112. doi: 10.1016/j.fcr.2012.04.003

Xu, X., Fan, L., Li, Z., Meng, Y., Feng, H., Yang, H., et al. (2021). Estimating leaf nitrogen content in corn based on information fusion of multiple-sensor imagery from UAV. *Remote Sens.* 13, 340–357. doi: 10.3390/rs13030340

Yue, J., Feng, H., Li, Z., Zhou, C., and Xu, K. (2021a). Mapping winter-wheat biomass and grain yield based on a crop model and UAV remote sensing. *Int. J. Remote Sens.* 42, 1577–1601. doi: 10.1080/01431161.2020.1823033

Yue, J. B., Feng, H. K., Yang, G. J., and Li, Z. H. (2018). A comparison of regression techniques for estimation of above-ground winter wheat biomass using near-surface spectroscopy. *Remote Sens.* 10, 66–89. doi: 10.3390/rs10010066

Yue, J., Guo, W., Yang, G., Zhou, C., Feng, H., and Qiao, H.. (2021b). Method for accurate multi-growth-stage estimation of fractional vegetation cover using unmanned aerial vehicle remote sensing. *Plant Methods* 17, 51–67. doi: 10.1186/s13007-021-00752-3

Yue, J., Yang, G., Tian, Q., Feng, H., Xu, K., and Zhou, C.. (2019). Estimate of winter-wheat above-ground biomass based on UAV ultrahigh-ground-resolution image textures and vegetation indices. *Isprs J. Photogrammetry Remote Sens.* 150, 226–244. doi: 10.1016/j.isprsjprs.2019.02.022

Zhou, Z. J., Jabloun, M., Plauborg, F., and Andersen, M. N. (2018). Using ground-based spectral reflectance sensors and photography to estimate shoot n concentration and dry matter of potato. *Comput. Electron. Agric.* 144, 154–163. doi: 10.1016/j.compag.2017.12.005

frontiers | Frontiers in Plant Science

TYPE Original Research
PUBLISHED 24 October 2022
DOI 10.3389/fpls.2022.1032170

Check for updates

OPEN ACCESS

EDITED BY
Zhenhai Li,
Shandong University of Science and Technology, China

REVIEWED BY
Haikuan Feng,
Beijing Research Center for Information Technology in Agriculture, China
Cheryl Dalid,
University of Florida, United States

*CORRESPONDENCE
Xinwei Li
lixw@ahstu.edu.cn

†These authors have contributed equally to this work

SPECIALTY SECTION
This article was submitted to Sustainable and Intelligent Phytoprotection, a section of the journal Frontiers in Plant Science

RECEIVED 30 August 2022
ACCEPTED 07 October 2022
PUBLISHED 24 October 2022

CITATION
Liu J, Zhu Y, Tao X, Chen X and Li X (2022) Rapid prediction of winter wheat yield and nitrogen use efficiency using consumer-grade unmanned aerial vehicles multispectral imagery. *Front. Plant Sci.* 13:1032170. doi: 10.3389/fpls.2022.1032170

COPYRIGHT
© 2022 Liu, Zhu, Tao, Chen and Li. This is an open-access article distributed under the terms of the Creative Commons Attribution License (CC BY). The use, distribution or reproduction in other forums is permitted, provided the original author(s) and the copyright owner(s) are credited and that the original publication in this journal is cited, in accordance with accepted academic practice. No use, distribution or reproduction is permitted which does not comply with these terms.

Rapid prediction of winter wheat yield and nitrogen use efficiency using consumer-grade unmanned aerial vehicles multispectral imagery

Jikai Liu[1,2†], Yongji Zhu[1,2†], Xinyu Tao[1,2], Xiaofang Chen[1,2] and Xinwei Li[1,2*]

[1]College of Resource and Environment, Anhui Science and Technology University, Fengyang, China, [2]Anhui Province Agricultural Waste Fertilizer Utilization and Cultivated Land Quality Improvement Engineering Research Center, Anhui Science and Technology University, Fengyang, China

Rapid and accurate assessment of yield and nitrogen use efficiency (NUE) is essential for growth monitoring, efficient utilization of fertilizer and precision management. This study explored the potential of a consumer-grade DJI Phantom 4 Multispectral (P4M) camera for yield or NUE assessment in winter wheat by using the universal vegetation indices independent of growth period. Three vegetation indices having a strong correlation with yield or NUE during the entire growth season were determined through Pearson's correlational analysis, while multiple linear regression (MLR), stepwise MLR (SMLR), and partial least-squares regression (PLSR) methods based on the aforementioned vegetation indices were adopted during different growth periods. The cumulative results showed that the reciprocal ratio vegetation index (repRVI) had a high potential for yield assessment throughout the growing season, and the late grain-filling stage was deemed as the optimal single stage with R^2, root mean square error (RMSE), and mean absolute error (MAE) of 0.85, 793.96 kg/ha, and 656.31 kg/ha, respectively. MERIS terrestrial chlorophyll index (MTCI) performed better in the vegetative period and provided the best prediction results for the N partial factor productivity (NPFP) at the jointing stage, with R^2, RMSE, and MAE of 0.65, 10.53 kg yield/kg N, and 8.90 kg yield/kg N, respectively. At the same time, the modified normalized difference blue index (mNDblue) was more accurate during the reproductive period, providing the best accuracy for agronomical NUE (aNUE) assessment at the late grain-filling stage, with R^2, RMSE, and MAE of 0.61, 7.48 kg yield/kg N, and 6.05 kg yield/kg N, respectively. Furthermore, the findings indicated that model accuracy cannot be improved by increasing the number

of input features. Overall, these results indicate that the consumer-grade P4M camera is suitable for early and efficient monitoring of important crop traits, providing a cost-effective choice for the development of the precision agricultural system.

KEYWORDS

DJI Phantom 4 Multispectral (P4M) camera, grain yield, vegetation indices (VIs), winter wheat, nitrogen use efficiency (NUE)

Introduction

Wheat (*Triticum aestivum L.*) is the most crucial global staple food that constitutes 20% of the required calories and proteins for humans (Curtis and Halford, 2014). Since the "Green Revolution" of the 1950s, wheat yield has increased significantly with the application of nitrogen fertilizer (Nguyen et al., 2019). To increase wheat yield sustainably, agricultural systems worldwide have been extensively applying nitrogen fertilizers (Han et al., 2015; Ali et al., 2018). However, accumulating evidence suggests that the goal of increasing wheat yield through nitrogen application rate has reached a bottleneck (Fischer et al., 2009; Curtis and Halford, 2014). Meantime, the continuous excessive application of nitrogen fertilizer leads to an increase of agricultural production cost and irreversible environmental pollution (Sharma and Bali, 2018). Hence, current research is focused on how to maximize nitrogen use efficiency (NUE) while maintaining a reasonable N fertilizer application rate, so as to achieve the ultimate goal of increasing wheat yields (Good et al., 2004; Han et al., 2015; Ali et al., 2018; Nguyen and Surya, 2018).

Obvious genotypic differences exist in the yield and NUE, and complex polygenic traits are influenced by the genotype, management practice, and environment (Curtis and Halford, 2014; Han et al., 2015; Sharma and Bali, 2018). Researchers need to systematically examine the level of variation in different varieties with different N gradients and environments (Monostori et al., 2017). The assessment of yield and NUE traits of different varieties under natural conditions in the field is typically performed at the time of crop maturity by manually operating simple machines and through complex chemical analyses performed in laboratories. These processes are laborious, inefficient, and destructive. Moreover, the inefficiency of phenotype data acquisition capacity restricts the high-throughput development of crop genetic improvement (Prey et al., 2020; Jin et al., 2021). Thus, low-cost, robust, high-throughput phenotype acquisition platforms and technologies are highly warranted.

Compared with satellites and ground-based proximal sensors, a high-throughput phenotyping platform with unmanned aerial vehicles (UAVs) is an economical, practical, efficient, and non-destructive solution to conveniently capture spatial resolution images on centimeter- or millimeter-scale without the constraints of weather conditions (Lin, 2015; Yang et al., 2017; Hassler and Baysal-Gurel, 2019). This approach ensures data collection at critical crop growth stages, facilitating the efficient management or monitoring of crops.

Spectral information from UAVs is mainly used in the form of vegetation indices (VIs) (Araus and Cairns, 2014; Svensgaard et al., 2019; Guo et al., 2021). VIs represent mathematical transformation of reflectance of two or more bands to characterize the canopy spectral characteristics of crops (Yang and Guo, 2008; Qiu et al., 2018), and it is the simplest, most effective, and most widely studied method for the estimation of crop parameters (Feng et al., 2021). To obtain the ideal crop yield prediction accuracy, researchers have used the UAVs to explore the combination of VIs and stages that suits their respective research needs. For instance, Zhou et al. (2017) predicted rice yield by using UAVs-based RGB and multispectral imagery and demonstrated that airborne RGB and multispectral VIs could be used as reliable platforms for crop growth and yield estimation. Zhu et al. (2018) also used the UAVs equipped with a multispectral camera to acquire images of wheat at different growth stages and assessed the yield by using nine VIs. The analysis results showed that the most effective estimation model was presented from the heading to the filling stage, and the optimal vegetation index was an enhanced vegetation index without a blue band (EVI2). Fu et al. (2020) used a multispectral camera to obtain canopy images of wheat at the critical growth stages and predicted wheat yield by machine learning methods. The results revealed that the vegetation indices at the jointing, flowering, and filling stages showed reasonable fit efforts with the yield. Normalized difference vegetation index (NDVI) at the jointing stage, normalized difference red-edge index (NDRE) at the flowering stage, and canopy chlorophyll content index (CCCI) at the filling stage showed the best yield estimation. The study by Shafiee et al. (2021), on the other hand, concluded that NDVI for wheat yield was the strongest predictor, while the addition of MERIS terrestrial chlorophyll index (MTCI) in the pre-filling period

could improve the predictive power of yield models. Wan et al. (2020) developed the best rice yield prediction model based on NDVI, normalized difference yellowness index (NDYI), canopy height, and canopy cover by using a UAVs high-throughput platform equipped with RGB and multispectral cameras. Moreover, the initial heading stage was considered the best stage for yield prediction. Results of previous studies suggest that the best predictive VIs and stage for yield modeling generally differ across the growth season. In other words, such yield estimation models can be applied at specific time points, and they show limited extrapolation capability under any other growth stage during the growing season. This point undoubtedly raises the threshold for spectral vegetation indices in applied production. Practitioners without specialized remote sensing knowledge prefer using a single vegetation index during multiple stages of the growing season.

Unlike yield prediction, the NUE traits have been less frequently evaluated by UAVs. Yang et al. (2020) evaluated the NUE of wheat varieties by using a UAV_mounted multispectral camera. The results revealed that the NDRE had a high consistency and accuracy for NUE, particularly in the mid to late-grain filling stage. In addition, the nitrogen dynamics time-series curves of the two rice populations were captured by UAVs' multispectral imagery, which were used to identify an available spectral index (NDRE) and a high NUE variety (Liang et al., 2021). Therefore, more studies are needed to explore the potential of UAVs imagery in NUE prediction.

With the proliferation of the UAVs and sensor markets, increasing numbers of consumer-grade UAVs are being used for agricultural remote sensing research, and their use is being promoted by actual agricultural managers (Gallardo-Salazar and Pompa-García, 2020; Lu et al., 2020; Di Gennaro et al., 2022). The advent of the DJI Phantom 4 Multispectral (P4M) camera (SZ DJI Technology Co., Shenzhen, China) brings multispectral sensors into the consumer-grade category. However, there are few studies have evaluated cereal yield and NUE by using P4M multispectral imagery.

In this study, we used a P4M camera to develop rapid prediction models of yield and NUE traits that can be applied to different growth stages. In summary, we aimed to (1) determin the optimal VIs that can be applied to multiple periods within a growing season for yield and NUE traits assessment; (2) compare the performance of several linear regression (LR) models based on optimal VIs at different growth periods, and (3) validate the potential of the P4M camera for wheat grain yield or NUE prediction of precision agricultural systems. Based on a literature review and discussion of the current methodology, we present our research findings and discuss the optimal screening VIs and estimation models suitable for wheat trait monitoring during multiple growth periods. Our study can provide an efficient, convenient, and reliable high-throughput phenotype selection method to construct intelligent agricultural systems.

Materials and methods

Design of field experiment

The experimental area was set up in Xiaogang Village, Anhui Province, China, located on the bank of Huai River. Typical warm temperate semi-humid continental monsoon climate of Xiaogang Village is 15.4°C annual average temperature with mean annual precipitation of 1236.2 mm, and summer maize and winter wheat are the major crops grown in this region. The experiment was conducted during the 2020–2021 wheat season, and was laid out using a split-plot design with three replicates, with nitrogen fertilizer levels assigned to the primary plots, whereas the winter wheat varieties were set up in subplots. There were four nitrogen fertilizer levels (N0 = 0, N1 = 100, N2 = 200, and N3 = 300 kg/ha) and three wheat varieties (V1: Huaimai 44, V2: Yannong 999, and V3: Ningmai 13). The three winter wheat varieties are newly released in Huang-Huai-Hai areas of China, and have the potential of high yield and stability. Black plastic films with 4 mm thickness were deposited between primary plots with different nitrogen fertilizer gradients to prevent water and fertilizer diffusion. Nine subplots of the primary plots were designed with 50-cm spacing. The whole study area comprised 36 wheat plots, with an area of 16 m^2 (2 m×8 m) for each plot (Figure 1). Winter wheat seeds were sown on November 7, 2020, following rice harvest, and the rice stubble was treated in time, with a row spacing of 30 cm and artificial drilling. Irrigation was then performed to maintain the soil moisture content. In late February 2021, winter wheat enters the turning green and rising period. Then, in late April, it enters the flowering stage. In May, the winter wheat enters the grain-filling stage, and hence, the harvest was performed on June 3, 2021. Nitrogen fertilizers were applied at 60% and 40% during the sowing and jointing stages, respectively. Phosphate (P = 90 kg/ha) and potassium (K = 135 kg/ha) fertilizers were applied as basal fertilizers prior to sowing. For field management, local high-yield cultivation methods and pest and disease control strategies were adopted. Fortunately, the weather conditions were ideal throughout the winter wheat growing season, and no meteorological disasters such as drought or waterlogging occurred during this period.

UAVs multispectral image acquisition

The DJI P4M camera was used for multispectral imagery acquisition; it is the latest consumer-grade quad-rotor

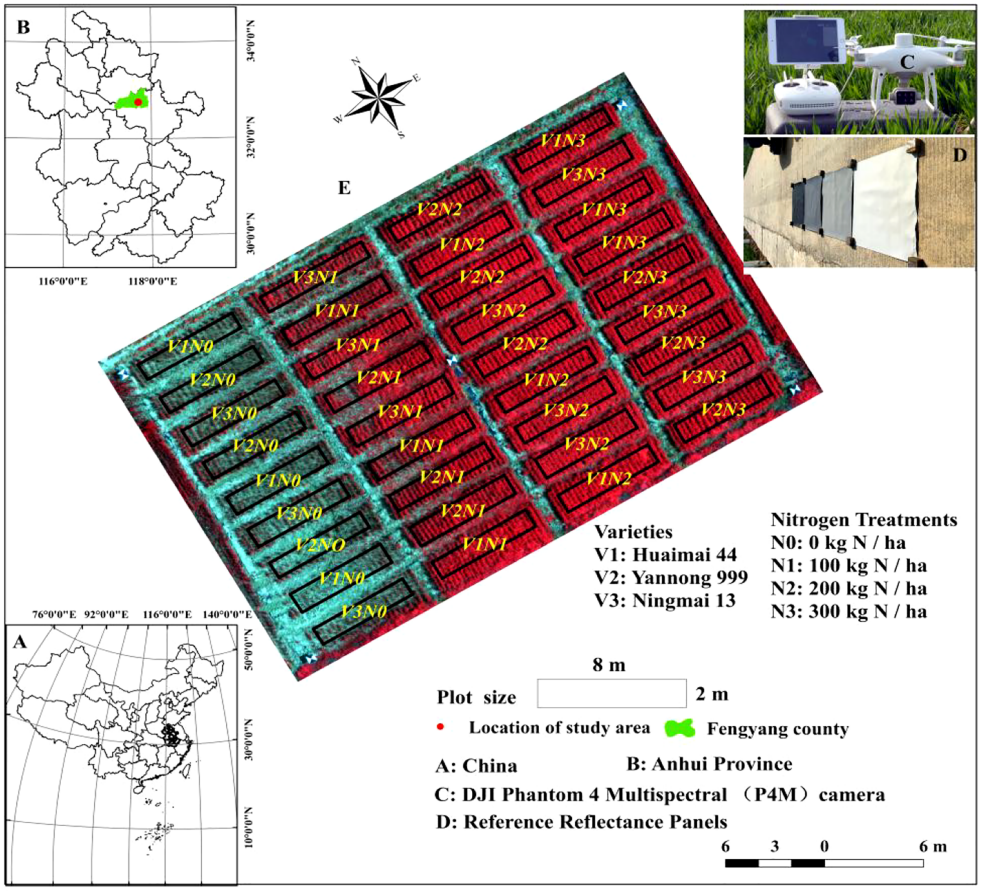

FIGURE 1
Experimental location **(A, B)**, plot design **(E)**, P4M platform **(C)**, and calibration panels **(D)** in the present study.

multispectral imaging system that can be used for agricultural applications launched by DJI. It consists of 5 monochrome sensors of 12.08 megapixels and is configured on a 3-axis gimbal to obtain clear and stable images. In addition, the camera is equipped with a real-time kinematic (RTK) system to obtain images with centimeter-level positioning accuracy. Table 1 describes the technical specifications of the camera.

The UAVs campaigns were conducted in clear, cloudless, and calm weather conditions between 11:00 and 13:00 local time. We employed the software DJI GS PRO software (https://www.dji.com/cn/ground-station-pro/) to pre-plan the routes and examine the aerial photography performance in real-time during the flight. Multispectral images were acquired from 30 m above the ground level, with a flight speed of 2.0 m/s, under automatic exposure mode, and 90% and 85% of overlap in the flight and side directions, respectively. A series of 6 campaigns with identical flight plans were developed using the P4M camera (Table 2). The photos were saved in the.tiff format, and 785 images were captured per flight.

Ground hyperspectral data acquisition

Spectral measurements of the winter wheat canopy were conducted using the ASD FieldSpec HandHeld2 (ASD HH2) portable spectrometer (Analytical Spectral Devices, Boulder, Colorado, USA). The spectroradiometer can take continuous spectrum measurements in the 325–1075 nm wavelength range, with a spectral resolution of <3.0 nm at 700 nm, wavelength accuracy of 1 nm, and a view angle of 25°C. The measurements were performed under stable sunlight conditions before or after the drone flight, and radiation correction was performed with a standard whiteboard before measurements. Three representative uniform areas were selected for the measurement of each plot. The detector was downward, while the vertical distance was approximately 50 cm above the canopy. All spectra collected from the same plot were averaged to represent the mean reflectance of this plot. Considering the lack of spectral response functions of the P4M camera, we compared and analyzed the differences between the reflectance of the P4M bands and the

TABLE 1 DJI P4M camera technical specifications.

Parameters	Values
Sensor	1/2.9 inch CMOS(5)
Pixel resolution(px*px)	1600*1300
Acquisition mode	snapshot
Optics	f/2.20
Focal length(mm)	5.74
FOV(°)	62.7
Battery life(minutes)	27
RTK accuracy(m)	vertical: ± 0.1; horizontal: ± 0.1
Photo format	.tiff
Bands set	Blue:450 nm ± 16 nm
	Green:560 nm ± 16 nm
	Red:650 nm ± 16 nm
	Red Edge:730 nm ± 16 nm
	NIR:840 nm ± 26 nm

field-measured mean spectral measurement at the plot scale to illustrate the reliability of the P4M multispectral camera.

UAVs multispectral image preprocessing

Preprocessing is fundamental for ensuring better image quality and consistency in subsequent analyses, and it mainly includes orthophoto image generation, radiometric calibration, and geometric correction. The original multispectral photos (.tiff format) were evaluated to exclude images with any noticeable distortion. To generate orthophoto images, we used DJI Terra software (https://www.dji.com/cn/downloads/softwares/dji-terra), which ensures the extraction of accurate quantitative information by performing positional error registration and radiation distortion correction from exposure, vignetting, file format, and spectral sensitivity. Then, the 5 single-band orthophoto images were merged into a multispectral file (.tiff) by using ENVI software (Exelis Visual Information Solutions, Boulder, Colorado, USA). The unified coordinate system used was WGS_84 UTM 50N. Following preprocessing, multispectral images of the experimental field were obtained, and the spatial resolution was resampled to 1.5 cm.

TABLE 2 Flight details for the entire growth season.

Date	Growth stages	Heights (m)	Spatial resolution (cm*cm)
03/14/21	Jointing(J)	30	1.64*1.44
04/08/21	Booting(B)		1.85*1.54
04/18/21	Heading(H)		1.74*1.44
04/29/21	Late flowering(LF)		1.74*1.45
05/09/21	Initial grain-filling (IGF)		1.74*1.46
05/24/21	Late grain-filling(LGF)		1.74*1.47

We applied the empirical line method (ELM) to each band based on four reference panels with known reflectance values. Di Gennaro et al. (2022) demonstrated the effectiveness of the ELM model for radiometric correction of the P4M camera. To eliminate the boundary effect, an area of approximately 0.2 m × 0.2 m was selected in the central part of the reference panels, and the average value was extracted and used as the DN value of the reference panels. The DN values were further transformed into reflectance values by using the following equation:

$$R_{(i,j)} = DN_{(i,j)} * a_i \ , \ \ i \in [1,5], \ j \in [1,4] \tag{1}$$

where $R_{(i,j)}$ and $DN_{(i,j)}$ are the reflectance and DN values of the reference panel j in band i, respectively, and a_i is the slope coefficient of ELM.

Removal of the soil background

During the early growth period of winter wheat (i.e., at the tillering and jointing stages), the plants were short, and the soil background occupied a major proportion in the field of view, which led to an underestimation of the VI value. Zhu reported that the impact of soil background on early winter wheat yield estimation was remarkable (Zhu et al., 2018). In addition, plants in the non-fertilized (N0) area had less tillering and weak growth, and the vegetation coverage was low throughout the growing season. Referring to a previous study (Jay et al., 2019), we selected the visible atmospherically resistant index (VARI) and adopted the threshold method to remove the soil background. The winter wheat accuracy evaluation results after background removal based on the VARI threshold were presented in Supplementary Table S1.

Calculation of vegetation indices

The reflectance of the 5 bands was extracted from the background-removed multispectral images, and nine vegetation indices, which have been widely used to assess crop yield and biochemical parameters, were calculated. Among these indices, MTCI used the red-edge band, which effectively weakened the reflectance changes caused by leaf orientation and specular reflection and had a positive effect on accuracy of the crop physiological parameter prediction (Dash and Curran, 2004). Modified normalized difference blue index (mNDblue)

could effectively reduce the radiation error caused by the soil background and illumination changes, and it was insensitive to the canopy structure (Jay et al., 2017). Normalized green, red difference index (NGBDI) is calculated by bands in the visible light range, which is sensitive to the reproductive growth of crops, and it showed better for rice grain yield prediction than VARI (Wan et al., 2020). In another study, this index has been referred to as NDYI (John and Dan, 2016). Based on the ratio vegetation index (RVI), the present study proposes the reciprocal ratio vegetation index (repRVI), which was calculated by dividing the NIR band by the red band. The vegetation indices are detailed in Table 3.

Agronomic data acquisition and preprocessing

At the physiological maturity stage of winter wheat, three representative and uniform 0.5-m double-row areas in each plot were selected for sampling. The harvested ears were transferred to the laboratory and sun-dried until the weight remained unchanged. The average yield of the 3 sampling sub-plots served as the final yield of the plot, and this yield was uniformly converted to kg/ha.

Several definitions have been developed for NUE, and most of these definitions are based on grain yield, meaning the input-output ratio of nitrogen fertilizers (Moll et al., 1982; Good et al., 2004; Hawkesford, 2017). Agronomical NUE (aNUE) is calculated based on the grain yield under N application when compared with that under the 0 level, and it was used to assess the utilization efficiency of the fertilizer applied on top of the residual N in the soil, In addition, the N partial factor productivity (NPFP) is adjusted for the grain yield with the direct application of the N supply under each treatment (Wan et al., 2020). Both indicators emphasized the nitrogen fertilizer input-output ratio, which indicated the ability of the crop to efficiently use the applied nitrogen fertilizer to increase grain yield. aNUE and NPFP were calculated according to the formulas (2) and (3), respectively, which are as follows (Kefauver et al., 2017; Wan et al., 2020)

$$aNUE = \frac{GY_{Ni} - GY_{N0}}{Ni} \quad i \in [1,3] \tag{2}$$

$$NPFP = \frac{GY_{Ni}}{Ni} \quad i \in [1,3] \tag{3}$$

where GY_{Ni} and GY_{N0} represent the grain yield of the plot at the i ($i \neq 0$) level and 0 levels, respectively; and Ni represents the N supply at the i ($i \neq 0$) level.

Variance analysis was implemented to describe the differences among the different N levels and varieties in terms of grain yield and NUE by using Wilcoxon rank sum and signed rank tests in RStudio (version 1.4.1106) (https://www.rstudio.com/) with R version 4.04 (https://www.r-project.org/).

Model development and performance assessment

Linear regression (LR) is a simple model that incorporates the concept of naive machine learning modeling and serves as the basis for highly complicated linear models. The least-square method based on the minimization of mean square error is the basic method employed for solving the LR model. Multiple LR (MLR) model involves two or more independent variables and considers the comprehensive effect of multiple independent variables on the dependent variable. In the MLR model, multiple correlations among variables affect the estimation of parameters, thereby decreasing the estimation accuracy. Therefore, other methods are preferred to eliminate multicollinearity (Fu et al., 2020). Stepwise MLR (SMLR) is a modeling method that eliminates covariance by removing unnecessary independent variables through AIC value

TABLE 3 Multispectral vegetation indices used in this study.

VIs name	Algorithm formula	Reference
Visible atmospherically resistant index (VARI)	$(R_{green}-R_{red})/(R_{green}+R_{red}-R_{blue})$	Gitelson et al., 2003a
Normalized green, red difference index (NGBDI)	$(R_{green}-R_{blue})/(_{green}+R_{blue})$	Hunt et al., 2005
Normalized difference vegetation index (NDVI)	$(R_{NIR}-R_{red})/(_{NIR}+R_{red})$	Rouse et al., 1974
Normalized difference red edge index (NDRE)	$(R_{NIR}-R_{rededge})/(_{NIR}+R_{rededge})$	Barnes et al., 2000
Green normalized difference vegetation index (GNDVI)	$(R_{NIR}-R_{green})/(_{NIR}+R_{green})$	Gitelson et al., 1996
Red edge chlorophyll index (CIrededge)	$R_{NIR}/R_{rededge}-1$	Gitelson et al., 2003b
MERIS terrestrial chlorophyll index (MTCI)	$(R_{NIR}-R_{rededge})/(R_{rededge}-R_{red})$	Dash and Curran, 2004
Modified normalized difference blue index (mNDblue)	$(R_{blue}-R_{rededge})/(R_{NIR}+R_{blue})$	Jay et al., 2017
Reciprocal ratio vegetation index (repRVI)	R_{red}/R_{NIR}	Jordan, 1969

repRVI is in a reciprocal relationship to RVI (Jordan, 1969).

minimization iterations and selecting significant independent variables to obtain the optimal regression model. The SMLR model has simple logic and clear physical meaning of the independent variables, indicating that it is an interpretable machine learning model (Yu et al., 2016; Han et al., 2019; Zhang et al., 2022). Partial least-squares regression (PLSR) is one of the widely used machine learning methods that combines the basic functions of MLR, canonical correlation analysis, and principal component analysis. This method can avoid the non-normal distribution of data, eliminate the multi-linear relationship between independent variables, and maintain the relationship between independent variables and factors. PLSR has demonstrated satisfactory performance in agricultural remote sensing research (Fu et al., 2014; Kasim et al., 2017; Shu et al., 2021). Considering the limited number of samples in the current study, complex machine learning algorithms such as random forest (RF), support vector machine (SVM), and neural network (NN), which are recommended for processing high-dimensional features, were not applied in this study.

The winter wheat grain yield and NUE estimation models were established by using the aforementioned four models based on the vegetation indices. Considering the significant differences in the agronomic traits under different nitrogen levels (Figure 2), stratified sampling was performed according to the nitrogen levels; two-thirds of the samples were randomly selected as the training set to develop the model, and the remaining one-third of the samples were used as the test dataset for model performance evaluation. The coefficient of determination (R^2), root mean square error (RMSE), and mean absolute error (MAE) were applied to evaluate the model's performance. Considering the randomness of sample selection, each model was repeated 20 times to enhance the robustness of the analysis, each time with a different random sampling seed number. The average value of 20 times was considered to evaluate the performance and stability of the model. Specifically, R^2, RMSE, and MAE were calculated as follows:

$$R^2 = \frac{\sum_{i=1}^{N}\left(Y_{iact} - \overline{Y_{act}}\right)\left(Y_{ipre} - \overline{Y_{pre}}\right)}{\sqrt{\sum_{i=1}^{N}\left(Y_{iact} - \overline{Y_{act}}\right)^2\left(Y_{ipre} - \overline{Y_{pre}}\right)^2}} \quad (4)$$

$$RMSE = \sqrt{\frac{\sum_{i=1}^{N}\left(Y_{iact} - Y_{ipre}\right)^2}{N}} \quad (5)$$

$$MAE = \frac{1}{N}\sum_{i=1}^{N}\left|\left(Y_{iact} - Y_{ipre}\right)\right| \quad (6)$$

where Y_{iact} and Y_{ipre} represent the actual measured values and the predicted values of i sample, respectively; $\overline{Y_{act}}$ and $\overline{Y_{pre}}$ represent the average actual measured values and the average predicted values of all samples, respectively; and N is the number of samples.

The establishment and evaluation of the above-mentioned estimation models were performed using the RStudio (version 1.4.1106) (https://www.rstudio.com/) with R version 4.04 (https://www.r-project.org/). The four estimation models were implemented using the lm (LR and MLR), lmStepAIC (SMLR), and pls (PLSR) methods in the machine learning package *caret*, respectively. Stratified sampling employed the strata function from the *sampling*

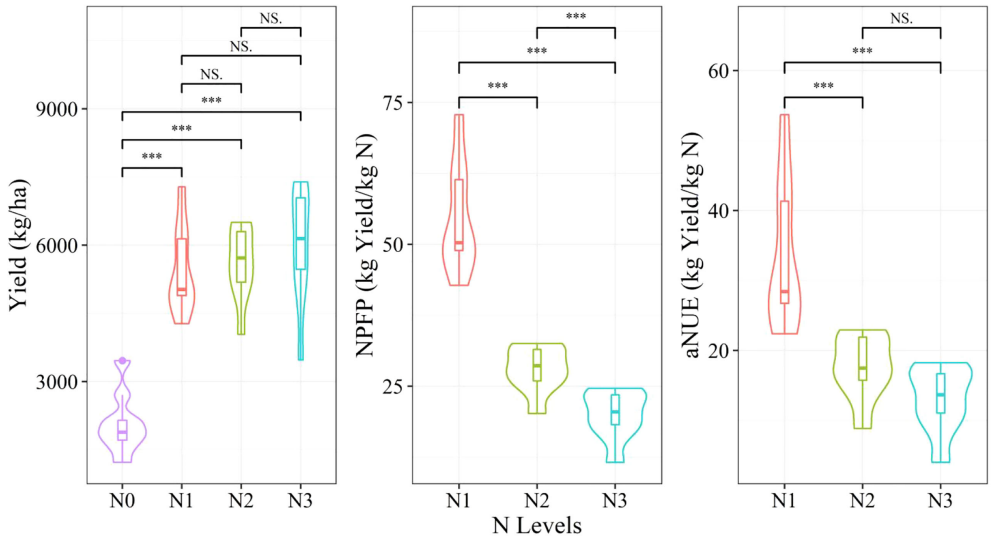

FIGURE 2
Yield, nitrogen partial factor productivity (NPFP), and agronomical nitrogen use efficiency (aNUE) under different nitrogen levels are shown with the mean and standard deviation. NS, not significant; ***p < 0 by Wilcox's test.

package. The PLSR model showed a hyperparameter "ncomp", which uses a 5-fold cross-validation for determination. To ensure the comparability of the models, the same random number seed was set for each model in each cycle, and the features were standardized.

Results

Effect of nitrogen levels on the yield and NUE

Figure 2 depicts the effects of different N levels on the yield and NPFP, as well as aNUE. The yield parameter showed an increasing trend with the increase in N levels and varied significantly under N0 and other N treatments. By contrast, both NPFP and aNUE showed a decreasing trend with an increase in N levels, with the former showing a steeper decline. Significant differences were observed in NPFP between different N treatments. For aNUE, significant differences were observed among different N treatments, except for N2 and N3. Figure 3 depicts the differences in the aforementioned 3 agronomic traits across different varieties. No significant differences were recorded in these parameters among the varieties, except for the yields of varieties V1 and V2, which showed a significant difference. The variety V1 clearly showed the highest yield and NUE, whereas V3 showed the lowest values. In summary, only the nitrogen level was found to significantly affect the yield, NPFP, and aNUE. Therefore, building a predictive model using a stratified sampling strategy is crucial for monitoring wheat yield and NUE under different N treatments.

Correlations of vegetation indices with yield and NUE

Correlation analysis results for the relationship between agronomic traits and multispectral vegetation indices are shown in Figure 4. Multispectral vegetation indices significantly are correlated with the yield (r = −0.92 to 0.92) under all N treatments, and the correlation in the middle growth period (from booting to the initial grain-filling stage) was higher than that in the early and late growth periods. repRVI demonstrated strong significant negative correlations in the growing season, with high correlation coefficients ranging from −0.77 to −0.92. It showed the best correlation compared with other indices, particularly in the jointing and late grain-filling stages. NDVI and green normalized difference vegetation index (GNDVI) did not differ from repRVI and were slightly lower than the latter throughout the growing season. NGBDI showed a weak correlation with the yield.

Vegetation indices strongly correlated with NUE at the jointing stage, with NGBDI and GNDVI showing the highest correlation coefficient, followed by repRVI. The correlations of most vegetation indices at the jointing stage were higher than those observed at other stages. However, such a close relationship cannot be synchronized with the growth and development of winter wheat, limiting the indices' further application in the middle and late growth periods. Throughout the growing season, MTCI and mNDblue showed stable and strong correlations with NPFP (r = −0.65 to −0.78 and r = −0.60 to −0.74, respectively). Notably, the correlation coefficients of these two vegetation indices were much higher than those of the

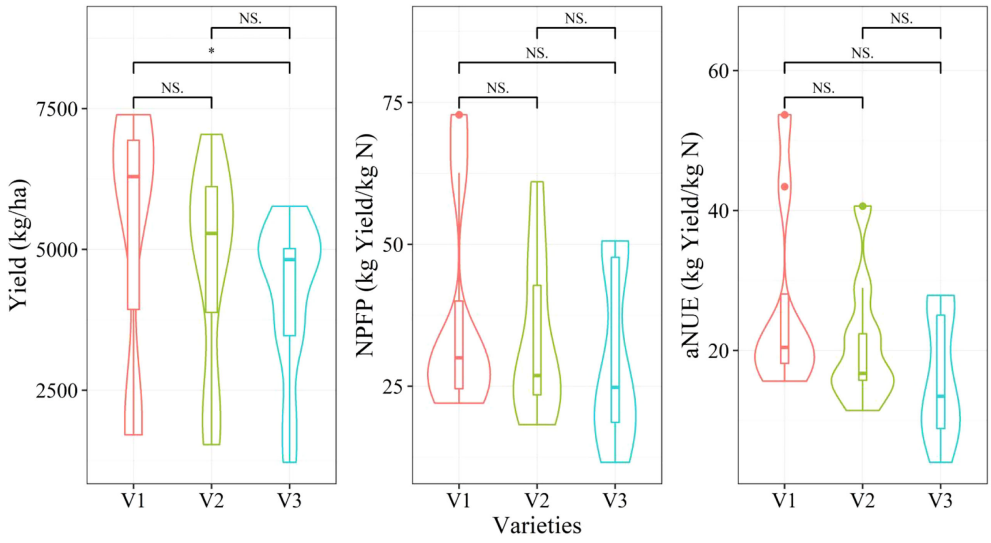

FIGURE 3
Yield, NPFP, and aNUE under different varieties are shown with the mean and standard deviation. NS, not significant; *p < 0.05 by using Wilcox's test.

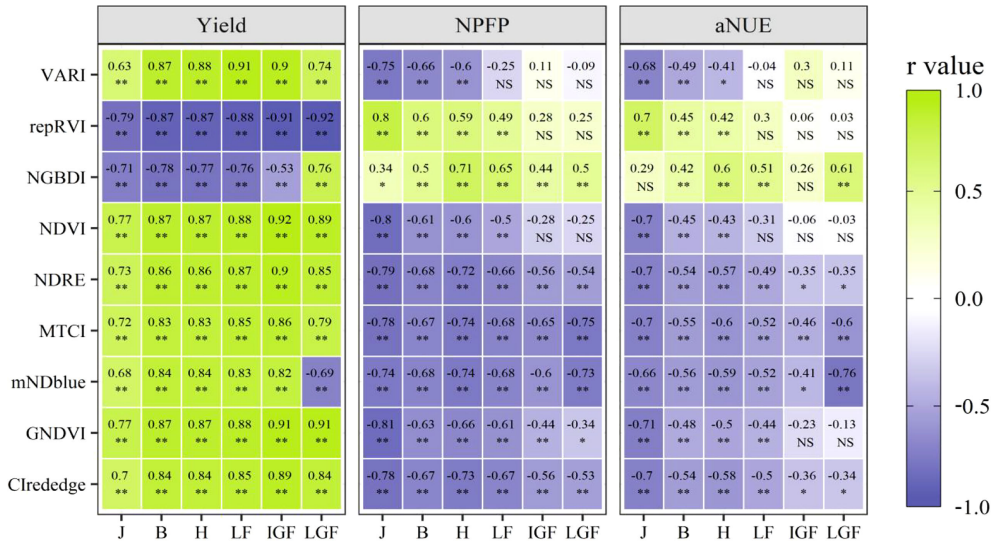

FIGURE 4
Heatmap for the correlation between vegetation indices and agronomic traits under different growth stages. J, Jointing stage; B, Booting stage; H, Heading stage; LF, Late flowering stage; IGF, Initial grain-filling stage; LGF, Late grain-filling stage; NS, not significant; *: $p < 0.05$; **: $p < 0.01$.

other vegetation indices in the reproductive growth period, and they reached the highest at the maturity stage (r = −0.75 and −0.73, respectively). Middle to strong correlations were also detected between NPFP and other multispectral indices such as NDRE (r = −0.54 to −0.79) and CIrededge (r = −0.53 to −0.78). A similar trend was observed in the correlations between UAVs-based multispectral indices and aNUE. Throughout the growth period, MTCI and mNDblue performed relatively well. Specifically, mNDblue exhibited the highest correlation coefficient (r = −0.76) at the maturity stage. NDRE and CIrededge also achieved middle to strong correlations over the entire season.

Estimation of yield and NUE for a single critical growth stage

The repRVI presented a high potential for yield assessment throughout the growing season, except for the jointing stage (Figures 5A–C). This finding is important for researchers to make better yield prediction before flowering. The best accuracy was achieved at the late grain-filling stage, with R^2 = 0.85, RMSE = 793.96 kg/ha, and MAE = 654.56 kg/ha.

No significant difference was noted in the predictive performance of MTCI and mNDblue during the entire growth period (Figures 5D–F). Considering the stability of the model, the jointing stage was proven to be the optimal stage to conduct NPFP prediction, with R^2, RMSE, and MAE of 0.65, 10.53 kg yield/kg N, and 8.90 kg yield/kg N, respectively, and followed by the late grain-filling with mNDblue. The initial grain-filling stage showed the worst prediction.

As a similar prediction performance to NPFP, mNDblue provided the best assessment of aNUE (R^2 = 0.61, RMSE = 7.48 kg yield/kg N, and MAE = 6.05 kg yield/kg N) at the late grain-filling stage (Figures 5G–I). MTCI in the jointing stage provided a better prediction, and the worst prediction was obtained in the initial grain-filling stage.

Estimation of yield and NUE for the vegetative and reproductive growth periods

Spectral information showed apparent differences in vegetative growth and reproductive growth, which are contributed by the difference in the crop structure of the observation field of view. We then analyzed the performance of vegetation indices on yield and NUE prediction in the two periods. No differences were noted in the prediction performance among the three linear models. Table 4 shows the results of repRVI for winter wheat yield prediction. In the reproductive period, higher performance was achieved, with the average R^2, RMSE, and MAE of 0.85, 801.05 kg/ha, and 668.53

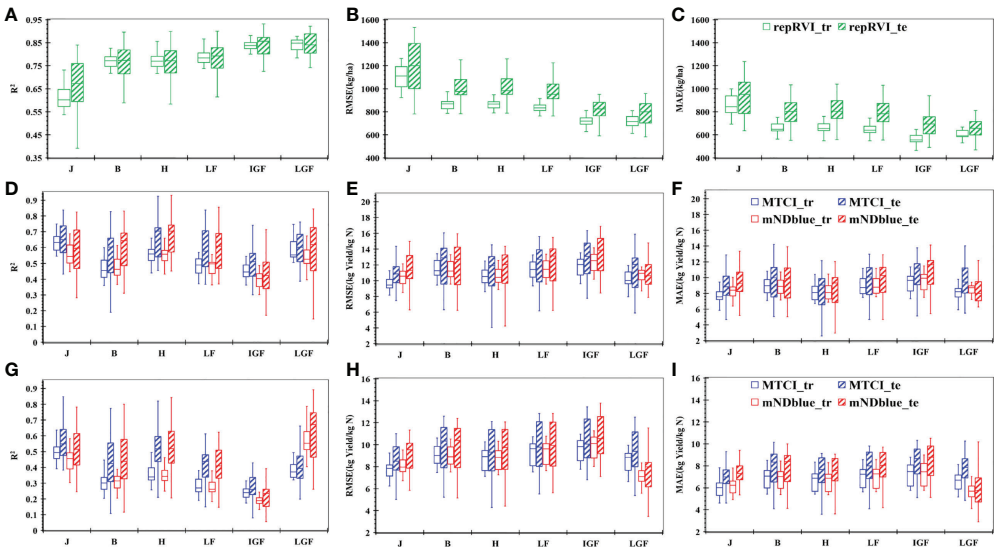

FIGURE 5
Results of yield **(A-C)** and NUE **(D-I)** prediction for a single critical growth stage using the LR model based on the selected VIs. **(A)** the value of determination coefficient (R^2) for yield prediction; **(B)** the value of root-mean-squared error (RMSE) for yield prediction; **(C)** the value of mean absolute error(MAE) for yield prediction; **(D)** the value of R^2 for NPFP prediction; **(E)** the value of RMSE for NPFP prediction; **(F)** the value of MAE for NPFP prediction; **(G)** the value of R^2 for aNUE prediction; **(H)** the value of RMSE for aNUE prediction, and **(I)** the value of MAE for aNUE prediction. MTCI indicates the MERIS terrestrial chlorophyll index; mNDblue indicates the modified normalized difference blue index; repRVI indicates the reciprocal ratio vegetation index; XXX_tr indicates the result based on the training dataset and XXX vegetation index (RepRVI or MTCI or mNDblue); XXX_te indicates the result based on the test dataset and XXX vegetation index (RepRVI or MTCI or mNDblue). J, Jointing stage; B, Booting stage; H, Heading stage; LF, Late flowering stage; IGF, Initial grain-filling stage; LGF, Late grain-filling stage.

kg/ha, respectively. Compared with that under the single critical growth stage, the prediction accuracy of yield improved.

For NUE prediction, MTCI was a better variable in the vegetative period, while mNDblue was anther better variable in the reproductive period (Tables 5, 6). The NUE predicted better on the MTCI and MLR in the vegetative growth period; in the reproductive growth period, the mNDblue and SMLR provided better results for NUE prediction. Similarly, the predictive performance of NUE did not exhibit a significant improvement when compared with that at the single critical growth stage.

Estimation of yield and NUE for the entire growth season

According to the aforementioned results, repRVI, MTCI, and mNDblue showed a good assessment performance for yield and NUE during multiple growth stages, however, the effects of the three linear models in the entire growth season remain unclear.

Among the three linear models, the PLSR model achieved the best yield prediction performance (Figures 6A–C). The R^2 of

TABLE 4 Yield estimation results with multiple linear regression (MLR), stepwise multiple linear regression (SMLR), and partial least-squares regression (PLSR) models for the vegetative and reproductive growth periods based on the repRVI index.

Yield			Vegetative growth period						Reproductive growth period					
			Training dataset			Test dataset			Training dataset			Test dataset		
			R^2	RMSE	MAE	R^2	RMSE	MAE	R^2	RMSE	MAE	R^2	RMSE	MAE
repRVI	PLSR	mean	0.78	837.84	658.11	0.74	1057.35	859.94	0.87	640.81	512.54	0.85	812.47	676.90
		std	0.04	62.18	51.96	0.09	137.52	134.76	0.03	59.21	44.20	0.06	141.50	128.76
	SMLR	mean	0.78	838.08	657.28	0.74	1045.04	841.67	0.88	622.31	503.42	0.85	803.66	669.09
		std	0.03	60.81	50.95	0.08	125.13	135.77	0.02	52.32	45.07	0.05	151.44	140.85
	MLR	mean	0.79	829.13	655.80	0.74	1060.53	867.07	0.88	618.27	504.36	0.86	787.01	659.61
		std	0.03	59.28	52.05	0.09	130.69	135.65	0.02	51.76	46.03	0.05	146.01	133.61

the unit of RMSE and MAE is kg/ha.

TABLE 5 NPFP estimation results with MLR, SMLR, and PLSR models for the vegetative and reproductive growth periods based on the MTCI and mNDblue indices.

NPFP			Vegetative growth period						Reproductive growth period					
			Training dataset			Test dataset			Training dataset			Test dataset		
			R^2	RMSE	MAE	R^2	RMSE	MAE	R^2	RMSE	MAE	R^2	RMSE	MAE
MTCI	PLSR	mean	0.66	9.11	7.19	0.61	11.34	9.08	0.59	10.10	8.08	0.55	12.05	10.25
		std	0.07	1.15	0.94	0.15	2.26	2.00	0.08	1.39	1.10	0.11	2.99	2.45
	SMLR	mean	0.68	8.94	7.18	0.61	11.25	9.23	0.59	10.03	7.99	0.58	11.46	9.76
		std	0.06	1.12	0.99	0.15	2.59	2.18	0.08	1.33	1.04	0.12	3.14	2.61
	MLR	mean	0.70	8.69	6.97	0.65	10.63	8.65	0.61	9.86	7.79	0.54	11.98	10.05
		std	0.05	0.97	0.85	0.15	2.34	2.08	0.08	1.35	1.00	0.13	3.03	2.48
mNDblue	PLSR	mean	0.64	9.45	7.41	0.59	11.83	9.58	0.69	8.73	6.84	0.61	10.63	8.95
		std	0.08	1.05	0.94	0.15	1.93	1.71	0.07	1.01	0.92	0.18	2.55	2.32
	SMLR	mean	0.68	8.86	7.14	0.62	11.25	9.04	0.69	8.65	6.70	0.64	10.21	8.59
		std	0.04	0.85	0.92	0.16	2.10	1.81	0.07	1.02	0.88	0.19	2.66	2.53
	MLR	mean	0.69	8.81	7.05	0.64	10.97	8.90	0.70	8.56	6.80	0.63	10.38	8.93
		std	0.04	0.83	0.85	0.14	1.95	1.75	0.07	1.03	0.94	0.18	2.59	2.35

the unit of RMSE and MAE is kg yield/kg N.

the test dataset was 0.85, the RMSE was 814.61 kg/ha, and the MAE was 642.69 kg/ha, which were comparable to the accuracy of the yield estimation model in the late grain-filling stage.

A similar approach was applied to estimate NUE by using MTCI and mNDblue indices. mNDblue performed significantly better than MTCI (Figures 6D–I). Although the three linear models did not show differences, better results for NPFP assessment were achieved based on the mNDblue and MLR, with R^2, RMSE, and MAE of 0.70, 9.59 kg yield/kg N, and 7.70 kg yield/kg N, respectively (Figures 6D–F). This result outperformed the prediction results obtained using only the critical growth stage, as shown in Figure 5.

Similar to the results of NPFP, no noticeable difference was noted among the three linear models, and the best results were also obtained based on the mNDblue and MLR (R^2 = 0.60, RMSE = 8.11 kg yield/kg N, and MAE = 6.58 kg yield/kg N) for

TABLE 6 aNUE estimation results with MLR, SMLR, and PLSR models for the vegetative and reproductive growth periods based on the MTCI and mNDblue indices.

aNUE			Vegetative growth period,						Reproductive growth period					
			Training dataset			Test dataset			Training dataset			Test dataset		
			R^2	RMSE	MAE	R^2	RMSE	MAE	R^2	RMSE	MAE	R^2	RMSE	MAE
MTCI	PLSR	mean	0.53	7.39	5.66	0.55	8.84	7.11	0.39	8.50	6.58	0.37	9.97	8.32
		std	0.10	0.94	0.84	0.15	1.94	1.71	0.11	1.25	1.04	0.10	2.29	1.95
	SMLR	mean	0.56	7.22	5.59	0.52	8.84	7.07	0.41	8.35	6.41	0.39	9.87	8.28
		std	0.06	0.89	0.92	0.13	1.76	1.52	0.08	1.09	0.92	0.14	2.38	1.98
	MLR	mean	0.57	7.11	5.48	0.55	8.63	6.81	0.44	8.12	6.15	0.41	9.49	7.67
		std	0.05	0.82	0.86	0.15	1.98	1.78	0.09	1.12	0.91	0.14	2.49	2.09
mNDblue	PLSR	mean	0.49	7.68	5.91	0.50	9.62	7.67	0.59	6.85	5.39	0.52	8.38	7.03
		std	0.11	0.91	0.88	0.18	1.50	1.24	0.09	0.77	0.82	0.22	2.28	2.20
	SMLR	mean	0.56	7.21	5.60	0.49	9.39	7.48	0.59	6.91	5.51	0.55	8.11	6.82
		std	0.06	0.81	0.86	0.17	1.36	1.20	0.10	0.81	0.78	0.24	2.12	2.06
	MLR	mean	0.57	7.12	5.56	0.53	9.04	7.19	0.61	6.69	5.39	0.53	8.30	7.07
		std	0.05	0.73	0.83	0.17	1.54	1.21	0.09	0.79	0.86	0.23	2.31	2.22

the unit of RMSE and MAE is kg yield/kg N.

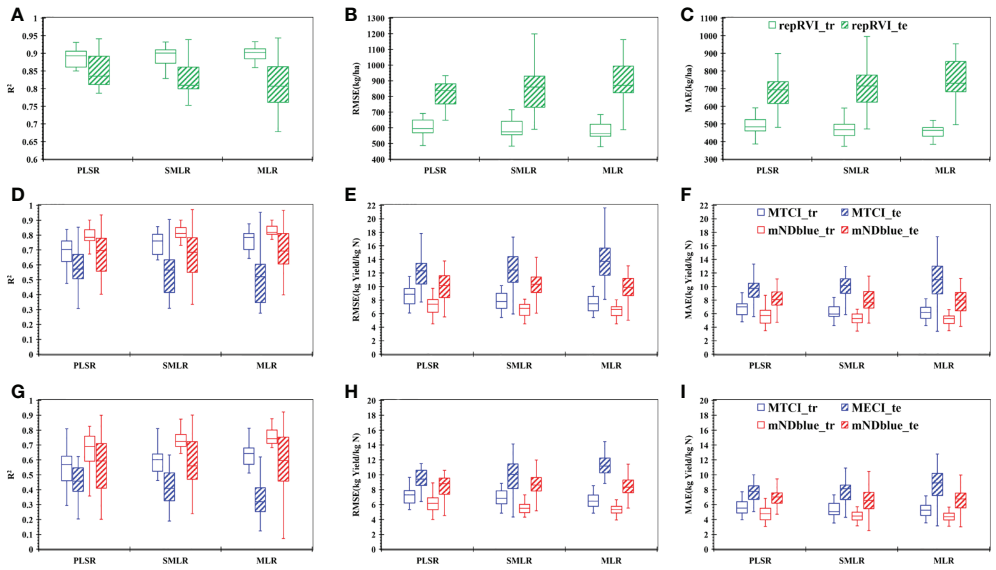

FIGURE 6
Results of yield **(A-C)** and NUE **(D-I)** prediction with MLR, SMLR, and PLSR models for the entire growing season based on the selected VIs. **(A)** the value of determination coefficient (R^2) for yield prediction; **(B)** the value of root-mean-squared error (RMSE) for yield prediction; **(C)** the value of mean absolute error(MAE) for yield prediction; **(D)** the value of R^2 for NPFP prediction; **(E)** the value of RMSE for NPFP prediction; **(F)** the value of MAE for NPFP prediction; **(G)** the value of R^2 for aNUE prediction; **(H)** the value of RMSE for aNUE prediction, and **(I)** the value of MAE for aNUE prediction. MTCI indicates the MERIS terrestrial chlorophyll index; mNDblue indicates the modified normalized difference blue index; repRVI indicates the reciprocal ratio vegetation index; XXX_tr indicates the result based on the training dataset and XXX vegetation index (RepRVI or MTCI or mNDblue); XXX_te indicates the result based on the test dataset and XXX vegetation index (RepRVI or MTCI or mNDblue). J, Jointing stage; B, Booting stage; H, Heading stage; LF, Late flowering stage; IGF, Initial grain-filling stage; LGF, Late grain-filling stage.

aNUE (Figures 6G–I), which were comparable to the results at the late grain-filling stage.

Estimation of yield and NUE using all vegetation indices

Further analysis was performed to determine whether redundant independent variables affect the prediction results. Figures 7A–C describes the effect of all VIs on the yield, indicating that the yield assessment performance of SMLR and MLR increased from the jointing stage to the initial grain-filling stage and then decreased at the late grain-filling stage. Taking MLR as an example, the R^2 (RMSE and MAE) values changed from 0.62 (1322.23 kg/ha and 1055.07 kg/ha) to 0.82 (900.71 kg/ha and 725.50 kg/ha), which then fluctuated to 0.78 (989.24 kg/ha and 811.37 kg/ha). Conversely, the prediction result of PLSR was satisfactory with R^2, RMSE, and MAE of 0.70, 1120.59 kg/ha, and 908.77 kg/ha, respectively, at the jointing stage, which then gradually increased to 0.86, 776.83 kg/ha, and 642.69 kg/ha, respectively. The performance was slightly improved when compared to a linear model based on a single critical stage by using repRVI.

Figures 7D–I depicts the prediction performance for NUE of all vegetation indices at different stages in terms of R^2. Although the PLSR model showed a lower accuracy than SMLR and MLR models on the training dataset than SMLR and MLR, the accuracy on the test dataset was better than with the other two models, and the R^2 distribution was concentrated. In short, the PLSR model was more effective in overcoming the problem of unbalanced prediction accuracy on the test dataset and the training datasets caused by overfitting and performed better on the test dataset. Compared with the single-stage estimation model, the prediction performance based on all VIs did not improve. These results suggested that improving the prediction performance by increasing the number of input features is not necessarily a good choice.

Discussions

Reliability of the P4M camera

UAVs are increasingly being used for crop growth monitoring and field phenotyping. In the recent decade, UAVs have entered the consumer goods market in parallel with the continuous development of low-cost sensing technology. The appearance of DJI P4M has made the multispectral remote-sensing system available in the market. Although there are cheap CIR cameras that can capture NIR images by modifying the

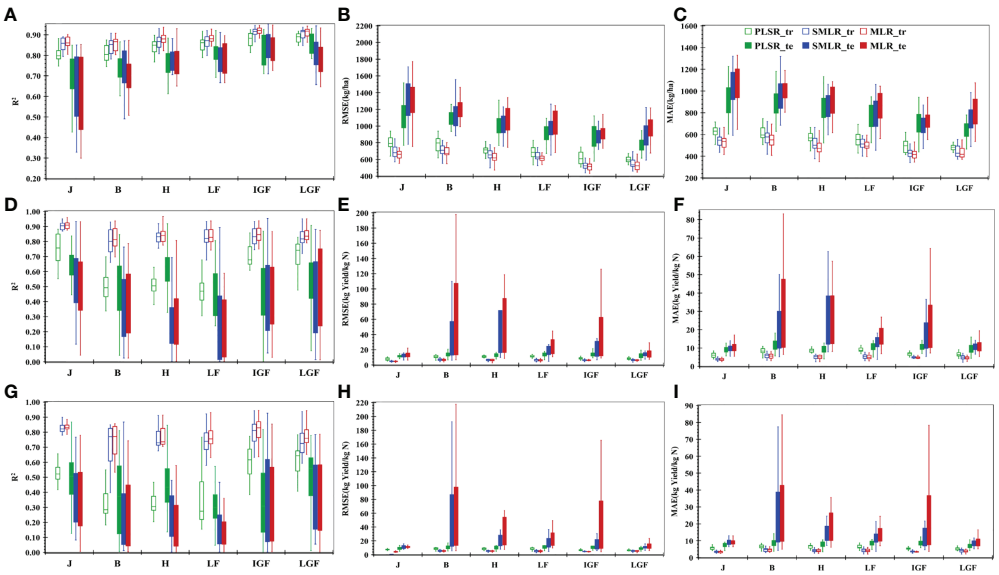

FIGURE 7
Results of yield **(A-C)** and NUE **(D-I)** prediction with MLR, SMLR, and PLSR models at different stages based on all vegetation indices. **(A)** the value of determination coefficient (R^2) for yield prediction; **(B)** the value of root-mean-squared error (RMSE) for yield prediction; **(C)** the value of mean absolute error(MAE) for yield prediction; **(D)** the value of R^2 for NPFP prediction; **(E)** the value of RMSE for NPFP prediction; **(F)** the value of MAE for NPFP prediction; **(G)** the value of R^2 for aNUE prediction; **(H)** the value of RMSE for aNUE prediction, and **(I)** the value of MAE for aNUE prediction. MTCI indicates the MERIS terrestrial chlorophyll index; mNDblue indicates the modified normalized difference blue index; repRVI indicates the reciprocal ratio vegetation index; XXX_tr indicates the result based on the training dataset and XXX vegetation index (RepRVI or MTCI or mNDblue); XXX_te indicates the result based on the test dataset and XXX vegetation index (RepRVI or MTCI or mNDblue). J, Jointing stage; B, Booting stage; H, Heading stage; LF, Late flowering stage; IGF, Initial grain-filling stage; LGF, Late grain-filling stage.

images obtained through ordinary RGB cameras, the red-edge band, which is of great significance to crop monitoring, remains a luxury. Nevertheless, P4M integrates this band to the consumer level, which positively promotes the significance of the popularization of agricultural remote sensing. It is especially well-received by users with limited funds. Lu et al. (2020) compared the consistency of the spectral features of Parrot Sequoia and P4M and noted a high correlation among the green, red, red-edge, and near-infrared bands. In their study, the consistency between P4M-NDVI and the ground measured ASD_NDVI was compared to reveal a correlation coefficient of >0.85. However, it remains questionable that the processing of P4M reflectance in the study was replaced by dividing 10^5 based on the original DN value, which lacked radiometric calibration in remote sensing. It is well-known that NDVI is calculated based on reflectance rather than DN value. Although satisfactory results were obtained in the study Lu et al. (2020), the methods used for data processing remain questionable. A recent study (Di Gennaro et al., 2022) discussed the exposure mode and radiometric calibration of P4M in detail and exhibited that irrespective of whether the exposure mode was set manually or automatically, there was no difference in data obtained and users can obtain professional-quality data without any background in optics. On the other hand, they compared the influence of 4 radiometric calibration methods (M1-M4 for short; M1 and M2 performed no radiometric calibration, while M3 and M4 performed radiometric calibration with ELM) on the accuracy of vegetation indices. Their results showed that M3 (empirical linear correction performed on the orthophoto images by the DJI Terra software with multiple reference reflectance panels of known reflectance) had high accuracy. The authors also reported that the accuracy in the crop canopy of the VIs calculated after the correction by this method was equivalent to that of the improved Micasense RedEdge camera (Lu et al., 2020). These results mainly suggest the spectral reliability of the P4M camera and its effectiveness in vegetation monitoring. However, another ambiguity is raised as a result of the use of VIs instead of band reflectance values by the authors during the authenticity test of the spectral performance of P4M. It is well-known that band reflectance is the basis for calculating spectral VIs. If the authenticity of band reflectance can be verified, numerous VIs can be calculated or created according to the corresponding formula to meet the diversified agricultural application scenarios. Another consideration was that although three VIs were used in this study, more than 50 VIs calculated based on reflectance were initially referenced (data not shown). The comparison of the spectral consistency among a few VIs in past studies could not cover this huge index group. Therefore, the reflectance of the P4M bands was compared with the measured reflectance of the ground ASD HH2 spectrometer to

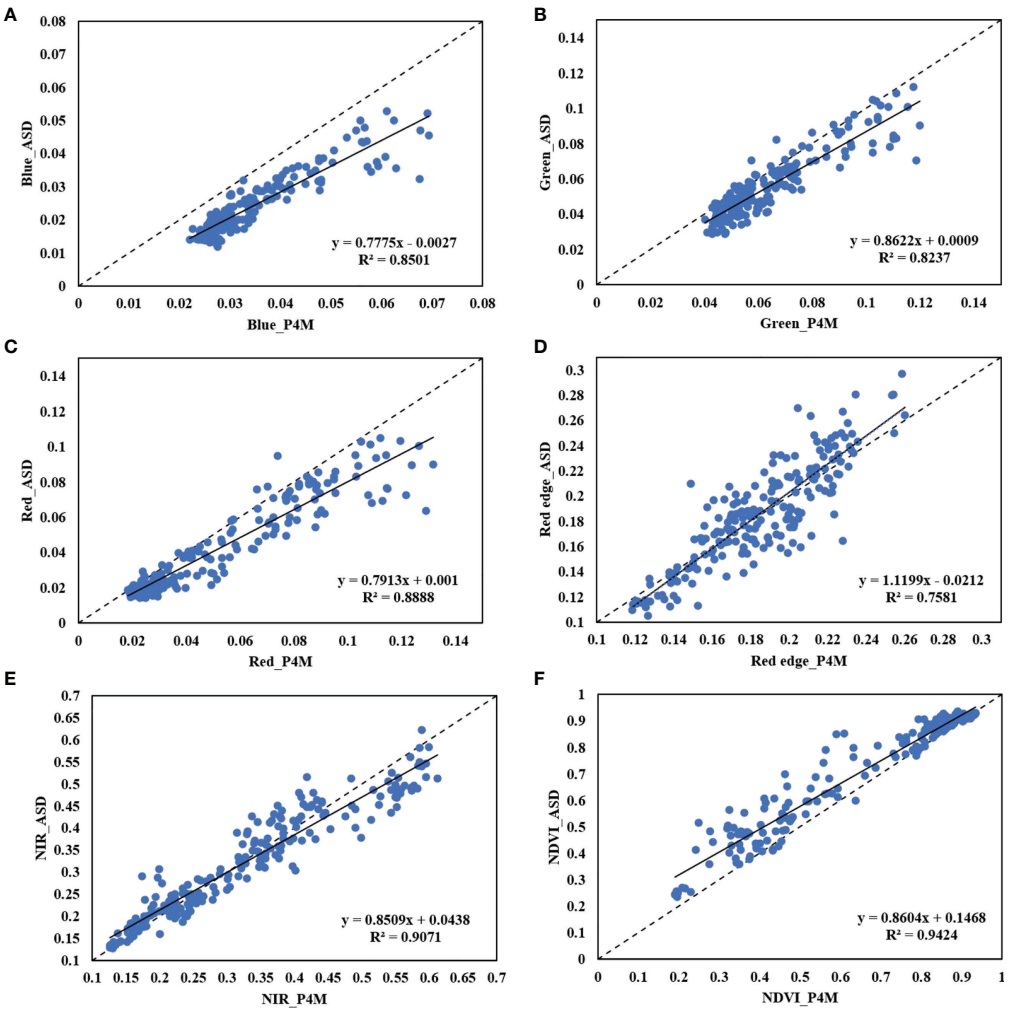

FIGURE 8
Analysis of the correlation between the reflectance of P4M bands and ground measured reflectance of the ASD HH2 spectrometer **(A–E)** and corresponding NDVI **(F)**. The dotted line indicates a 1:1 line.

establish a solid theoretical basis for further research, as well as for its wider and deeper application in the future.

Figures 8A–E shows the scatter distribution of the reflectance of P4M bands after radiometric calibration and the mean reflectance measured by the ground ASD HH2 spectrometer, respectively. The correlation between the reflectance of the remaining four P4M bands, except for the red-edge band, and the measured reflectance exceeded $R^2 = 0.82$. The correlation between the red and near-infrared bands was higher, and the scatter distribution was closer to the 1:1 line. The comparison of NDVI also suggested a significant correlation with $R^2 = 0.94$ (Figure 8F), which is higher than that reported by Lu et al. (2020) ($R^2 = 0.88$). This may benefit from the efficient radiometric calibration method adopted in this study. Compared with the results of Di Gennaro et al. (2022), the NDVI in this study also obtained a good percentage error (PE) in the wheat canopy (this study: PE = 9.5%, the study of Di et al.: PE = 9.9%). The correlation between the reflectance of the red-edge band and the ground measured reflectance was the lowest. The NDRE calculated by the calibrated red-edge reflectance and near-infrared reflectance elsewhere (Di Gennaro et al., 2022) showed poor PE accuracy (PE = 19.4%), however, the authors did not analyse this result further. We believe that this can be deemed to be associated with the setting of the red-edge band with a bandwidth of 32 nm, which is greater than the setting of similar multispectral cameras (Supplementary Table S2). A large bandwidth setting contributes to imprecise determination of the position of the red edge. The red edge may get missed at the steepest slope of the sharp rise region of the typical green vegetation reflectance spectrum from the red light to near-infrared light. Furthermore, Holman et al. (2019) demonstrated that the spectral reflectance of 30 wheat varieties

obtained by the Parrot Sequoia camera under 4 nitrogen treatments was compared to that measured by the Tec5 HandySpec Field Spectrometer. Holman et al. (2019) reported that the correlation of the NIR band with R^2 = 0.74, which is consistent with that of the red-edge band with R^2 = 0.76 in this study. In comparison with the wide application of the Parrot Sequoia camera in agricultural research, the correlation of the red-edge band of P4M was within the acceptable range. Moreover, P4M has been used in several studies with ambiguous calibration methods to obtain data, which further proves the effectiveness of this camera (Gallardo-Salazar and Pompa-García, 2020). Considering that this study is the first to verify the accuracy of the reflectance of the P4M bands from the perspective of reflectance, whether the weak correlation of the red-edge band is an exception remains unestablished. Further work is needed in this direction to validate the current findings.

Physiological interpretation of UAVs-based VIs

VIs shows good potential in crop growth monitoring by UAVs (Yang and Guo, 2008; Qiu et al., 2018). Using suitable VIs, instead of the complex methods based on VIs, is the key for agronomic trait estimation. This study developed generic evaluation models for early yield and NUE monitoring based on three promising VIs that can be applied to multiple growth stages during the growing season of wheat. One of these VIs — repRVI, was an index of yield; the other two indices, MTCI, and mNDblue, showed relatively consistent performance in the estimation of two NUE traits.

The results revealed that repRVI performed best in grain yield assessment at the LGF stage, which is consistent with previous studies (Hassan et al., 2019; Fei et al., 2021a; Fei et al., 2021b; Ganeva et al., 2022), because the LGF stage is close to maturity and the information in the UAVs field of view is mainly provided by the mature spikes. The signal is minimally affected by moisture and other green parts of the rice plant.

Furthermore, repRVI performed best at the LGF stage, which may be related to the construction of this index. The green signal is relatively less prominent and the reflectance of the red band is relatively higher in LGF stage. The high value of Red band makes the NIR/Red value lower overall when Red band is used as the denominator, but the fact that the magnitude of NIR band is more than 10 times higher than that of the Red band cannot be ignored, thus, the NIR/Red is more dependent on the numerator NIR, which makes it difficult to effectively capture the weak changes brought about by the elevation of Red band. However, the repRVI uses Red band as a molecule and NIR band as a denominator, which can better capture rising trends of Red band and is sensitive to weak information. Thus, the repRVI index is more conducive to monitoring vegetation information in the grain-filling stage.

The MTCI and mNDblue performed stably and demonstrated significant correlations with NUE throughout the growing season. Another interesting finding is that MTCI was more suitable for NUE prediction in the vegetative growth period, while mNDblue was more suitable for evaluation in the reproductive growth period. Chlorophyll is closely related to nitrogen, and high chlorophyll and N contents in the plant are obvious signs of effective nitrogen fertilization supply (Tian et al., 2011). Due to the red edge band, MTCI is sensitive to the chlorophyll content and should not be saturated at a high chlorophyll concentration (Dash and Curran, 2004). At a high chlorophyll concentration in the vegetative growth stage, other vegetative indices may be saturated to varying degrees, whereas MTCI can help avoid this problem and thus better reflect the photosynthetic capacity of rice, which is conducive to adequate nitrogen uptake and increased yield (Tian et al., 2011). mNDblue was improved by Jay et al. (2017), who found that mNDblue was sensitive to canopy chlorophyll content when the effect of soil background is weak. During the reproductive growth period of winter wheat, the effect of soil background was minimized, thus maximizing the performance of the mNDblue. We also found correlation coefficient of more than 0.97 between the two indices, which may explain the similarity and difference in NUE prediction by these two indices.

Furthermore, we also calculated the weighted mean/maximum-rank sums (WMMRS) score, which evaluates the optimum vegetation index that is robust towards date-specific effects through linear relationship (Prey et al., 2020) for 9 vegetation indices. These three indices obtained the highest scores among all indices in terms of generalized performance throughout the whole growing season (Supplementary Table S3 and Appendix document A), which is a major motivation for our selection.

Accuracy and stability of yield and NUE prediction models

In recent years, several studies on the yield and/or NUE of different genotypes of crops based on remote sensing have proved the applicability of UAVs in the field. The technical system for yield prediction is mature and advanced, however, the current studies on NUE have been limited in quantity or quality. Only one study used the UAVs to evaluate the NUE of winter wheat (Yang et al. 2020). Notably, NUE was distinguished from the nitrogen content. Although the nitrogen content in plant reflects the ability of a crop to absorb nitrogen, NUE emphasizes the extent to which crops can utilize external nitrogen applications.

Our study showed that the model has high accuracy for yield prediction and moderate accuracy for NUE prediction. Despite a gap between NUE prediction accuracy and yield prediction accuracy, the models have equivalent or higher accuracy compared with those reported in similar studies (Table 7).

TABLE 7 Previous research results similar to those of the present study.

Platforms	Traits	Sensors	Crops	Stage	Best results	Reference
Ground	Yield \NutEff_grain	PhenoTrac 4 multi-sensor	wheat	initial grain-filling	LR: Yield:R^2 = 0.52; NutEff_grain: R^2 = 0.21 PLSR: Yield:R^2 = 0.33 RMSE = 1891kg/ha	Prey et al., 2019
	Yield\NUtE	Ocean Optics USB2000 spectrometers	wheat	heading to initial grain-filling	LR: Yield: R^2 = 0.47; NUtE: R^2 = 0.44 PLSR: Yield: R^2 = 0.42,RMSE = 792kg/ha; NUtE: R^2 = 0.41,RMSE = 2.2	Pavuluri et al., 2015
	Yield\NPFP	JAZ portable field spectrometer	wheat	heading	MLR: Yield: R^2 = 0.83,RMSE = 565.29kg/ha MLR: NPFP: R^2 = 0.85 under low N conditions MLR: NPFP: R^2 = 0.77 under normal N conditions	Frels et al., 2018
UAVs	Yield \aNUE \NPFP	Tetracam mini MCA	barley	grain-filling	MLR: Yield: R^2 = 0.827	Kefauver et al., 2017
	aNUE	Parrot sequoia	wheat	mid to late grain-filling	LR: R^2 = 0.78, RMSE = 0.004	Yang et al. 2020
	Yield	Micasens- RedEdge-M	wheat	initial grain-filling	SVR: R^2 = 0.91, MSE = 0.14	Shafiee et al., 2021
	Yield	Airphen	wheat	whole	RF: R^2 = 0.78, RMSE =103 kg/ha	Fu et al., 2020
	Yield	Parrot Sequoia	wheat	tillering and grain-filling	LR: R^2 = 0.62, RMSE = 972 kg/ha	Zhou et al., 2021
	Yield	Parrot Sequoia	wheat	late grain-filling	SLR: R^2 = 0.89	Hassan et al., 2019
	Yield	MultiSPEC 4C	wheat	heading to grain-filling	MLR: R^2 = 0.70, RMSE = 618.30 kg/ha	Zhu et al., 2018
	Yield	multispectral camera MQ022MG-CM	rice	whole	RF: R^2 = 0.78, RMSEP = 370 kg/ha, rRMSE = 3.20%	Wan et al., 2020
	Yield	Tetracam mini MCA	rice	booting and heading	MLR: R^2 = 0.75, RMSE = 926.46 kg/ha	Zhou et al., 2017
	Yield	Parrot Sequoia	maize	anthesis	ANN: R^2 = 0.97, RMSE = 425kg/ha, MAE = 249kg/ha	García-Martínez et al., 2020

NutEff_grain indicates the grain N utilization efficiency; NutE indicates N utilization efficiency; LR indicates linear regression; MLR indicates multiple linear regression; SMLR indicates stepwise multiple linear regression; PLSR indicates partial least-squares regression; RF indicates the random forest; SVR indicates support vector machine regression, and ANN indicates artificial neural network regression.

The results of yield prediction were compared with those of past studies, and the present study results are equivalent to or better than the prediction results of wheat yield reported in previous studies (Table 7). We believe that the main difference between these studies with higher accuracy was that the input features not limited to VIs, plant height, canopy coverage, or density were included and the machine learning method was applied in these studies (Fu et al., 2020; García-Martínez et al., 2020; Klompenburg et al., 2020; Wan et al., 2020; Shafiee et al., 2021). For instance, previous studies have used the RF model (Fu et al., 2020; Wan et al., 2020), the neural network model (García-Martínez et al., 2020), and SVR regression models (Shafiee et al., 2021).

Regarding the prediction of NUE, the values reported in this study are lower than those reported by Yang et al. (2020) and Pavuluri et al. (2015) (Table 7). Unlike the approach adopted in these studies, different N treatments were simultaneously considered in our study to establish models. Another explanation for this was the significant difference in the wheat genotype used in these studies. However, there was no difference in the NUE parameters of the three varieties in the present study. The NDRE at the middle and late grain-filling stages in a past study (Yang et al., 2020) showed the best mean R^2 and RMSE. NDRE was also applied in this study, which showed a moderate correlation with NUE. The MTCI was also considered in the studies by Prey et al. (2020) and Frels et al. (2018); however, it showed the worst performance on the test dataset. This result can be explained by three possible reasons: (1) the dependent variable in the study Fresl et al. (2018) was NutE (NutEff_grain). Although it also emphasized NUE, the calculation method was different (yield/nitrogen uptake), with the denominator being the plant nitrogen content, rather than the amount of fertilizer applied; (2) the MTCI was first developed based on broadband and was calculated by the reflectance in the narrow hyperspectral bands in these studies (Frels et al., 2018; Prey et al., 2020); (3) several wheat genotypes (22–75 genotypes) have been used in past studies (Pavuluri et al., 2015; Prey et al., 2020), which could have resulted in low R^2.

Machine learning is being increasingly applied in the estimation of crop parameters (Jin et al., 2021). It complements big data and high-performance computing. We used only 3 varieties and 4 nitrogen levels in this study, totaling 36 samples with only 9 features involved, which did not show the characteristics of high-dimensional data. Hence, significant improvements may not be necessarily obtained by machine learning, as also verified by Zhou et al. (2021). Another key consideration is that machine learning is in a black box. Consequently, there are certain obstacles for personnel without a background in data analysis science, which limits its further

popularization. If the applied research remains limited to the laboratory level, its value will be greatly reduced (Klompenburg et al., 2020). Considering the aim of this study was to further verify the reliability of P4M camera for yield and NUE rapidly evaluation and to provide a cost-effective and practical approach for agricultural practitioners lacking remote sensing experience, several understandable and operatable linear models were used in this study. The results support our choices.

According to the results depicted in Figures 2, 3, the three agronomic parameters were sensitive to the nitrogen level but not to the variety. Therefore, when establishing regression models, varieties were not differentiated. Stratified sampling was adopted when dividing the training and test datasets according to the nitrogen level. It allowed the division of an equal proportion of samples for each nitrogen level to participate in modeling. Regression models were established according to the nitrogen level as in a past study to obtain more accurate models. However, the sample size was smaller (N = 9). The models at the middle and late grain-filling stages adopted elsewhere (Yang et al. 2020) used 9 samples (3 samples/year), and the training dataset was not distinguished from the test dataset. The stability and applicability of such models are uncertain. To establish a more robust model, we adopted 20 cycles in this study to calculate the average value of the model evaluation indices to display the stability of the model. The modeling results showed that the training dataset was much more stable than the test dataset. When more independent variables were input, the PLSR model was more stable and had fewer outliers because the PLSR model could better deal with the collinearity of multidimensional variables. Generally, the stability of the prediction model for yield was higher than that for NUE. The robustness of the prediction model trained by multiple cycles has rarely been examined in past studies. Our study demonstrated that the error of model performance caused by the difference in random sampling was also worth considering. Random sampling is approximately unbiased only when the population is sufficiently large. For a small sample size, it cannot be ensured whether the samples collected each time are unbiased or depict an approximately unbiased estimate of the population. Therefore, confirming the stability of the model by increase the number of sampling cycles for a small sample size is highly recommended.

Implications for future work

Compared with ground assessment, the non-destructive UAVs remote-sensing evaluation is repeatable and flexible and provides real-time data. The popularity of the consumer drone market has further promoted the in-depth application of UAVs remote-sensing technology in the field of agricultural research, however, only a few studies have used P4M cameras to predict wheat yield and nitrogen use efficiency. Our research aims to explore and establish a general strategy for better prediction of yield and NUE across multiple growth periods, thereby providing a low-cost data analysis strategy for potential non-expert users of consumer-grade multispectral UAVs. In this study, three P4M-based vegetation indices with good performance were proposed. The combination of these vegetation indices and linear models can provide a rapid and cost-effective method to assess yield and NUE, demonstrating the great potential of P4M camera for quantifying important crop traits.

Although our model based on three genotypes adequately accounted for the differences in varieties and nitrogen levels, the performance of the model must be tested on multiple wheat varieties where the differences between varieties were more significant. The model can be applied in practice and accepted by researchers and applicators only by developing it as a general prediction model for yield and NUE assessments by considering different N gradients and varieties. In addition, continued multi-year trials are warranted, and future attention should be paid to seasonal differences in the proposed general strategy to compensate for the lack of inter-year variation characteristics in the current study. Considering the increasing application of UAVs remote sensing in agriculture, developing a comprehensive and shared database to support mutual verification of the same research purposes and future in-depth exploration of precision agriculture is essential.

Conclusions

In this study, we explored the potential of a consumer-grade multispectral P4M camera for monitoring the winter wheat grain yield and NUE traits. For this purpose, three universal vegetation indices showing high correlations with the target-dependent variables were determined. The results revealed that the repRVI presented a high potential for grain yield assessment during the entire growing season, except at the jointing stage. The late grain-filling stage was identified as the optimal single stage to predict the grain yield and achieve the prediction results, with R^2 = 0.85, RMSE = 793.96 kg/ha, and MAE = 656.31 kg/ha. The performance of the yield estimation combining multiple stages improved slightly but not significantly. Both MTCI and mNDblue exhibited a significant correlation with NUE. The simple LR model based on the MTCI index at the jointing stage showed a good performance in NPFP assessment, with R^2 = 0.65, RMSE = 10.53 kg yield/kg N, and MAE = 8.90 kg yield/kg N, followed by the mNDblue at the late grain-filling stage. Good performance with the mNDblue index for aNUE was observed at the late

grain-filling stage, with R^2 = 0.61, RMSE = 7.48 kg yield/kg N, and MAE = 6.05 kg yield/kg N, followed by MTCI at the jointing stage. Combining multiple stages did not improve NUE traits assessment accuracy. Moreover, MTCI and mNDblue were suitable for NUE prediction in the vegetative growth period and reproductive growth period, respectively.

The differences among the three linear models became evident with an increase in the number of input independent variables. The PLSR model with all VIs as input features showed better robustness than the other regression models, albeit the accuracy did not improve noticeably.

Importantly, our study demonstrated the effectiveness of the DJI P4M camera as a high-throughput phenotyping platform for small-scale crop monitoring tasks, and the selected indices can serve as effective indicators for timely and accurate prediction of yield and NUE prior to harvest. In the future research, the potential of P4M camera in different climates, seasons, and varieties should be studied and the capabilities of UAV remote sensing for diversified agricultural applications should be thoroughly explored.

Data availability statement

The original contributions presented in the study are included in the article/Supplementary Materials. Further inquiries can be directed to the corresponding author. The Supplementary material and Appendix document for this article can be found online at: https://figshare.com/s/fa258c55dd6bd9fc69b9 named as Supplementary Material.zip.

Author contributions

XL, JL, and YZ designed and developed the research idea. YZ, XC, and XT conducted the field data collection. JL and YZ performed the data analysis. JL wrote the manuscript. JL, YZ, XT, XC, and XL contributed to the results and data interpretation, discussion, and revision of the manuscript. All the authors revised and approved the manuscript. All authors have read and agreed to the published version of the manuscript.

Funding

This research were funded by the Xinjiang Construction Corps Oasis Ecology Key Laboratory Open Project Development Fund Project (201903), a university-level scientific research project of Anhui Science and Technology University (2021gnny02). Major science and technology projects of Anhui Province of China (201903a06020001) and Sub-project under National Science and Technology Support Program of China (2018YFD0300901-2).

Acknowledgments

We are very grateful to Jun Li, Xueqing Zhu, and Qingyang Liu for their assistance in data collection and we would also like to thank Jie Liu and Fang Gao for their valuable suggestions on the paper.

Conflict of interest

The authors declare that the research was conducted in the absence of any commercial or financial relationships that could be construed as a potential conflict of interest.

Publisher's note

All claims expressed in this article are solely those of the authors and do not necessarily represent those of their affiliated organizations, or those of the publisher, the editors and the reviewers. Any product that may be evaluated in this article, or claim that may be made by its manufacturer, is not guaranteed or endorsed by the publisher.

Supplementary material

The Supplementary Material for this article can be found online at: https://www.frontiersin.org/articles/10.3389/fpls.2022.1032170/full#supplementary-material

References

Ali, J., Jewel, Z. A., Mahender, A., Anandan, A., Hernandez, J., and Li, Z. (2018). Molecular genetics and breeding for nutrient use efficiency in rice. *Int. J. Mol. Sci.* 19 (6), 1762. doi: 10.3390/ijms19061762

Araus, J. L., and Cairns, J. E. (2014). Field high-throughput phenotyping: the new crop breeding frontier. *Trends Plant Science.* 19, 52–61. doi: 10.1016/j.tplants.2013.09.008

Barnes, E. M., Clarke, T. R., Richards, S. E., Colaizzi, P., Haberland, J., Kostrzewski, M., et al. (2000). "Coincident detection of crop water stress, nitrogen status and canopy density using ground-based multispectral data"," in *Proceedings of the international conference on precision agriculture and other resource management* (Bloomington, MN, USA).

Curtis, T., and Halford, N. G. (2014). Food security: the challenge of increasing wheat yield and the importance of not compromising food safety. *Ann. Appl. Biol.* 64, 354–372. doi: 10.1111/aab.12108

Dash, J., and Curran, P. J. (2004). The MERIS terrestrial chlorophyll index. *Int. J. Remote Sens.* 25, 5403–5413. doi: 10.1080/0143116042000274015

Di Gennaro, S. F., Toscano, P., Gatti, M., Poni, S., Berton, A., and Matese, A. (2022). Spectral comparison of UAV-based hyper and multispectral cameras for precision viticulture. *Remote Sens.* 14, 449. doi: 10.3390/rs14030449

Fei, S., Hassan, M. A., He, Z., Chen, Z., Shu, M., Wang, J., et al. (2021a). Assessment of ensemble learning to predict wheat grain yield based on UAV-multispectral reflectance. *Remote Sens.* 13 (12), 2338. doi: 10.3390/rs13122338

Fei, S., Hassan, M. A., Ma, Y., Shu, M., Chen, Q., Li, Z., et al. (2021b). Entropy weight ensemble framework for yield prediction of winter wheat under different water stress treatments using unmanned aerial vehicle-based multispectral and thermal data. *Front. Plant Sci.* 12. doi: 10.3389/fpls.2021.730181

Feng, L., Chen, S., Zhang, C., Zhang, Y., and He, Y. (2021). A comprehensive review on recent applications of unmanned aerial vehicle remote sensing with various sensors for high-throughput plant phenotyping. *Comput. Electron. Agric.* 182, 106033. doi: 10.1016/j.compag.2021.106033

Fischer, R. A., Byerlee, D., and Edmeades, G. O. (2009). "Can technology deliver on the yield challenge to2052, 050?," in *How feed World2052, 050* (Rome: FAO Expert Meet).

Frels, K., Baenziger, P. S., Guttieri, M., Joyce, B., and Leavitt, B. (2018). Evaluating canopy spectral reflectance vegetation indices to estimate nitrogen use traits in hard winter wheat. *Field Crops Res.* 217, 82–92. doi: 10.1016/j.fcr.2017.12.004

Fu, Z., Jiang, J., Gao, Y., Krienke, B., Wang, M., Zhong, K., et al. (2020). Wheat growth monitoring and yield estimation based on multi-rotor unmanned aerial vehicle. *Remote Sens.* 12, 508. doi: 10.3390/rs12030508

Fu, Y., Yang, G., Wang, J., Song, X., and Feng, H. (2014). Winter wheat biomass estimation based on spectral indices, band depth analysis and partial least squares regression using hyperspectral measurements. *Comput. Electron. Agric.* 100, 51–59. doi: 10.1016/j.compag.2013.10.010

Gallardo-Salazar, J. L., and Pompa-García, M. (2020). Detecting individual tree attributes and multispectral indices using unmanned aerial vehicles: applications in a pine clonal orchard. *Remote Sens.* 12, 4144. doi: 10.3390/rs12244144

Ganeva, D., Roumenina, E., Dimitrov, P., Gikov, A., Jelev, G., Dragov, R., et al. (2022). Phenotypic traits estimation and preliminary yield assessment in different phenophases of wheat breeding experiment based on UAV multispectral images. *Remote Sens.* 14 (4), 1019. doi: 10.3390/rs14041019

García-Martínez, H., Flores-Magdaleno, H., Ascencio-Hernández, R., Khalil-Gardezi, A., Tijerina-Chávez, L., Mancilla-Villa, O. R., et al. (2020). Corn grain yield estimation from vegetation indices, canopy cover, plant density, and a neural network using multispectral and RGB images acquired with unmanned aerial vehicles. *Agriculture* 10, 277. doi: 10.3390/agriculture10070277

Gitelson, A. A., Gritz, Y., and Merzlyak, M. N. (2003b). Relationships between leaf chlorophyll content and spectral reflectance and algorithms for non-destructive chlorophyll assessment in higher plant leaves. *J. Plant Physiol.* 160, 271–282. doi: 10.1078/0176-1617-00887

Gitelson, A. A., Kaufman, Y. J., and Merzlyak, M. N. (1996). Use of a green channel in remote sensing of global vegetation from EOS-MODIS. *Remote Sens. Environ.* 58, 289–298. doi: 10.1016/S0034-4257(96)00072-7

Gitelson, A. A., Vina, A., Arkebauer, T. J., Rundquist, D. C., Keydan, G., and Leavitt, B. (2003a). Remote estimation of leaf area index and green leaf biomass in maize canopies. *Geophysical Res. Letters* 30, 335–343. doi: 10.1029/2002GL016450

Good, A. G., Shrawat, A. K., and Muench, D. G. (2004). Can less yield more? is reducing nutrient input into the environment compatible with maintaining crop production? *Trends Plant Sci.* 9, 597–605. doi: 10.1016/j.tplants.2004.10.008

Guo, W., Carroll, M. E., Singh, A., Swetnam, T. L., Merchant, N., Sarkar, S., et al. (2021). UAS-based plant phenotyping for research and breeding applications. *Plant Phenomics.* 2022 (021), 9840192. doi: 10.34133/2021/9840192

Han, M., Okamoto, M., Beatty, P. H., Rothstein, S. J., and Good, A. G. (2015). The genetics of nitrogen use efficiency in crop plants. *Annu. Rev. Genet.* 49 (1), 269–289. doi: 10.1146/annurev-genet-112414-055037

Han, L., Yang, G., Dai, H., Xu, B., Yang, H., Feng, H., et al. (2019). Modeling maize above-ground biomass based on machine learning approaches using UAV remote-sensing data. *Plant Methods* 15, 10. doi: 10.1186/s13007-019-0394-z

Hassan, M. A., Yang, M., Rasheed, A., Yang, G., Reynolds, M., Xia, X., et al. (2019). A rapid monitoring of NDVI across the wheat growth cycle for grain yield prediction using a multi-spectral UAV platform. *Plant Sci.* 282, 95–103. doi: 10.1016/j.plantsci.2018.10.022

Hassler, S. C., and Baysal-Gurel, F. (2019). Unmanned aircraft system (UAS) technology and applications in agriculture. *Agronomy* 9, 618. doi: 10.3390/agronomy9100618

Hawkesford, J. M. (2017). Genetic variation in traits for nitrogen use efficiency in wheat. *J. Exp. Botany.* 10, 2627–2632. doi: 10.1093/jxb/erx079

Holman, F. H., Riche, A. B., Castle, M., Wooster, M. J., and Hawkesford, M. J. (2019). Radiometric calibration of 'Commercial off the shelf' cameras for UAV-based high-resolution temporal crop phenotyping of reflectance and NDVI. *Remote Sensing* 11, 1657. doi: 10.3390/rs11141657

Hunt, E. R., Cavigelli, M., Daughtry, C. S. T., Mcmurtrey, J. E., and Walthall, C. L. (2005). Evaluation of digital photography from model aircraft for remote sensing of crop biomass and nitrogen status. *Precis. Agricul.* 6, 359–378. doi: 10.1007/s11119-005-2324-5

Jay, S., Baret, F., Dutartre, D., Malatesta, G., Heno, S., Comar, A., et al. (2019). Exploiting the centimeter resolution of UAV multispectral imagery to improve remote-sensing estimates of canopy structure and biochemistry in sugar beet crops. *Remote Sens. Environ.* 231, 110898. doi: 10.1016/j.rse.2018.09.011

Jay, S., Gorretta, N., Morel, J., Maupas, F., Bendoula, R., Rabatel, G., et al. (2017). Estimating leaf chlorophyll content in sugar beet canopies using millimeter- to centimeter-scale reflectance imagery. *Remote Sens. Environ.* 198, 173–186. doi: 10.1016/j.rse.2017.06.008

Jin, X., Zarco-Tejada, P., Schmidhalter, U., Reynolds, M., Hawkesford, M., Varshney, R. K., et al. (2021). High-throughput estimation of crop traits: A review of ground and aerial phenotyping platforms. *IEEE Geosci. Remote Sens. Magazine* 9, 200–231. doi: 10.1109/MGRS.2020.2998816

John, J. S., and Dan, S. L. (2016). Spectral considerations for modeling yield of canola. *Remote Sens. Environ.* 184, 161–174. doi: 10.1016/j.rse.2016.06.016

Jordan, C. F. (1969). Derivation of leaf-area index from quality of light on the forest floor. *Ecology* 50, 663–666. doi: 10.2307/1936256

Kasim, N., Shi, Q., Wang, J., Sawut, R., Nurmemet, I., and Isak, G. (2017). Estimation of spring wheat chlorophyll content based on hyperspectral features and PLSR model. *Trans. Chin. Soc. Agric. Engineer.* 33, 208–216. doi: 10.11975/j.issn.1002-6819.2017.22.027

Kefauver, S. C., Vicente, R., Vergara-Díaz, O., Fernandez-Gallego, J. A., Kerfal, S., Lopez, A., et al. (2017). Comparative UAV and field phenotyping to assess yield and nitrogen use efficiency in hybrid and conventional barley. *Front. Plant Sci.* 8. doi: 10.3389/fpls.2017.01733

Klompenburg, T. V., Kassahun, A., and Catal, C. (2020). Crop yield prediction using machine learning: A systematic literature review. *Comput. Electron. Agricult.* 177, 105709. doi: 10.1016/j.compag.2020.105709

Liang, T., Duan, B., Luo, X., Ma, Y., Yuan, Z., Zhu, R., et al. (2021). Identification of high nitrogen use efficiency phenotype in rice (Oryza sativa l.) through entire growth duration by unmanned aerial vehicle multispectral imagery. *Front. Plant Sci.* 12. doi: 10.3389/fpls.2021.740414

Lin, Y. (2015). Lidar: An important tool for next-generation phenotyping technology of high potential for plant phenomics? *Comput. Electron. Agricult.* 9, 61–73. doi: 10.1016/j.compag.2015.10.011

Lu, H., Fan, T., Ghimire, P., and Deng, L. (2020). Experimental evaluation and consistency comparison of UAV multispectral mini-sensors. *Remote Sensing* 12, 2542. doi: 10.3390/rs12162542

Moll, R. H., Kamprath, E. J., and Jackson, W. A. (1982). Analysis and interpretation of factors which contribute to efficiency of nitrogen utilization. *Agron. J.* 74 (3), 562–564. doi: 10.2134/agronj1982.00021962007400030037x

Monostori, I., Szira, F., Tondelli, A., Árendás, T., Gierczik, K., Cattivelli, L., et al. (2017). Genome-wide association study and genetic diversity analysis on nitrogen use efficiency in a central European winter wheat (Triticum aestivum l.) collection. *PLoS One* 12 (12), e0189265. doi: 10.1371/journal.pone.0189265

Nguyen, G. N., Maharjan, P., Maphosa, L., Vakani, J., Thoday-Kennedy, E., and Kant, S. (2019). Robust automated image-based phenotyping method for rapid vegetative screening of wheat germplasm for nitrogen use efficiency. *Front. Plant Sci.* 10. doi: 10.3389/fpls.2019.01372

Nguyen, G. N., and Surya, K. (2018). Improving nitrogen use efficiency in plants: effective phenotyping in conjunction with agronomic and genetic approaches. *Funct. Plant Biol.* 45, 606–619. doi: 10.1071/FP17266

Pavuluri, K., Chim, B. K., Griffey, C. A., Reiter, M. S., Balota, M., and Thomason, W. E. (2015). Canopy spectral reflectance can predict grain nitrogen use efficiency in soft red winter wheat. *Precis. Agricult.* 16, 405–424. doi: 10.1007/s11119-014-9385-2

Prey, L., Hu, Y., and Schmidhalter, U. (2020). High-throughput field phenotyping traits of grain yield formation and nitrogen use efficiency: Optimizing the selection of vegetation indices and growth stages. *Front. Plant Sci.* 10. doi: 10.3389/fpls.2019.01672

Qiu, R., Wei, S., Zhang, M., Zhang, M., Li, H., Sun, H., et al. (2018). Sensors for measuring plant phenotyping: A review. *Int. J. Agric. Biol. Engineering.* 11, 1–17. doi: 10.25165/j.ijabe.20181102.2696

Rouse, J. W., Haas, R. H., Schell, J. A., and Deering, D. W. (1974). "Monitoring vegetation systems in the great plains with ERTS," in *Third earth resources technology satellite-1 symposium*, vol. 1 . Eds. S. C. Freden, E. P. Mercanti and M. Becker (Washington, DC: Technical Presentations, NASA SP-351. National Aeronautics and Space Administration), 309–317.

Shafiee, S., Lied, M. L., Burud, I., Dieseth, J. A., Alsheikh, M., and Lillemo, M. (2021). Sequential forward selection and support vector regression in comparison

to LASSO regression for spring wheat yield prediction based on UAV imagery. *Comput. Electron. Agricult.* 183, 106036. doi: 10.1016/j.compag.2021.106036

Sharma, L. K., and Bali, S. K. (2018). A review of methods to improve nitrogen use efficiency in agriculture. *Sustainability* 10, 51. doi: 10.3390/su10010051

Shu, M., Shen, M., Zuo, J., Yin, P., Wang, M., Xie, Z., et al. (2021). The application of UAV-based hyperspectral imaging to estimate crop traits in maize inbred lines. *Plant Phenomics.* 2022 (021), 9890745. doi: 10.34133/2021/9890745

Svensgaard, J., Jensen, S. M., Westergaard, J. C., Nielsen, J., Christensen, S., and Rasmussen, J. (2019). Can reproducible comparisons of cereal genotypes be generated in field experiments based on UAV imagery using RGB cameras? *Eur. J. Agronomy* 106, 49–57. doi: 10.1016/j.eja.2019.03.006

Tian, Y. C., Yao, X., Yang, J., Cao, W. X., Hannaway, D., and Zhu, Y. (2011). Assessing newly developed and published vegetation indices for estimating rice leaf nitrogen concentration with ground- and space-based hyperspectral reflectance. *Field Crops Res.* 120 (2), 299–310. doi: 10.1016/j.fcr.2010.11.002

Wan, L., Cen, H., Zhu, J., Zhang, J., Zhu, Y., Sun, D., et al. (2020). Grain yield prediction of rice using multi-temporal UAV-based RGB and multispectral images and model transfer – a case study of small farmlands in the south of China. *Agric. For. Meteorol* 10, 8096. doi: 10.1016/j.agrformet.2020.108096

Yang, Z., and Guo, B. (2008). "Image mosaic based on SIFT," in *Proceedings of the2002, 008 international conference on intelligent information hiding and multimedia signal processing (IIH-MSP2002, 008)* (USA: IEEE Computer Society), 1422–1425. doi: 10.1109/IIH-MSP.2008.335

Yang, M., Hassan, M. A., Xu, K., Zheng, C., Rasheed, A., Jin, X., et al. (2020). Assessment of water and nitrogen use efficiencies through UAV-based multispectral phenotyping in winter wheat. *Front. Plant Science.* 11. doi: 10.3389/fpls.2020.00927

Yang, G., Liu, J., Zhao, C., Li, Z., Huang, Y., Yu, H., et al. (2017). Unmanned aerial vehicle remote sensing for field-based crop phenotyping: Current status and perspectives. *Front. Plant Sci.* 8. doi: 10.3389/fpls.2017.01111

Yu, X., Liu, Q., Wang, Y., Liu, X., and Liu, X. (2016). Evaluation of MLSR and PLSR for estimating soil element contents using visible/near-infrared spectroscopy in apple orchards on the jiaodong peninsula. *Catena*, 137, 340–349. doi: 10.1016/j.catena.2015.09.024

Zhang, X., Zhang, K., Sun, Y., Zhao, Y., Zhuang, H., Ban, W., et al. (2022). Combining spectral and texture features of UAS-based multispectral images for maize leaf area index estimation. *Remote Sens.* 14, 331. doi: 10.3390/rs14020331

Zhou, X., Kono, Y., Win, A., Matsui, T., and Tanaka, T. S. T. (2021). Predicting within-field variability in grain yield and protein content of winter wheat using UAV-based multispectral imagery and machine learning approaches. *Plant Production Science* 24, 137–15154. doi: 10.1080/1343943X.2020.1819165

Zhou, X., Zheng, H. B., Xu, X. Q., He, J. Y., Ge, X. K., Yao, X., et al. (2017). Predicting grain yield in rice using multi-temporal vegetation indices from UAV-based multispectral and digital imagery. *ISPRS J. Photogrammetry Remote Sensing* 130, 246–255. doi: 10.1016/j.isprsjprs.2017.05.003

Zhu, W., Li, S., Zhang, X., Li, Y., and Sun, Z. (2018). Estimation of winter wheat yield using optimal vegetation indices from unmanned aerial vehicle remote sensing. *Trans. Chin. Soc. Agric. Engineering* 34, 78–86. doi: 10.11975/j.issn.1002-6819.2018.11.010

frontiers | Frontiers in Plant Science

TYPE Original Research
PUBLISHED 07 November 2022
DOI 10.3389/fpls.2022.1021398

Check for updates

OPEN ACCESS

EDITED BY
Joe Mari Maja,
Clemson University, United States

REVIEWED BY
Ying Zhang,
Beijing Research Center for Information Technology in Agriculture, China
Tugrul Oktay,
Erciyes University, Turkey

*CORRESPONDENCE
Wanjun Ren
rwjun@126.com
Xiuliang Jin
jinxiuliang@caas.cn

†These authors have contributed equally to this work

SPECIALTY SECTION
This article was submitted to Sustainable and Intelligent Phytoprotection, a section of the journal Frontiers in Plant Science

RECEIVED 17 August 2022
ACCEPTED 07 October 2022
PUBLISHED 07 November 2022

CITATION
Sun B, Zhou W, Zhu S, Huang S, Yu X, Wu Z, Lei X, Yin D, Xia H, Chen Y, Deng F, Tao Y, Cheng H, Jin X and Ren W (2022) Universal detection of curved rice panicles in complex environments using aerial images and improved YOLOv4 model. *Front. Plant Sci.* 13:1021398. doi: 10.3389/fpls.2022.1021398

COPYRIGHT
© 2022 Sun, Zhou, Zhu, Huang, Yu, Wu, Lei, Yin, Xia, Chen, Deng, Tao, Cheng, Jin and Ren. This is an open-access article distributed under the terms of the Creative Commons Attribution License (CC BY). The use, distribution or reproduction in other forums is permitted, provided the original author(s) and the copyright owner(s) are credited and that the original publication in this journal is cited, in accordance with accepted academic practice. No use, distribution or reproduction is permitted which does not comply with these terms.

Universal detection of curved rice panicles in complex environments using aerial images and improved YOLOv4 model

Boteng Sun[1†], Wei Zhou[1†], Shilin Zhu[1], Song Huang[1], Xun Yu[2], Zhenyuan Wu[1], Xiaolong Lei[1], Dameng Yin[2], Haixiao Xia[1], Yong Chen[1], Fei Deng[1], Youfeng Tao[1], Hong Cheng[1], Xiuliang Jin[2*] and Wanjun Ren[1*]

[1]State Key Laboratory of Crop Gene Exploration and Utilization in Southwest China, Key Laboratory of Crop Ecophysiology and Farming System in Southwest China, Ministry of Agriculture, Sichuan Agricultural University, Chengdu, Sichuan, China, [2]Key Laboratory of Crop Physiology and Ecology, Ministry of Agriculture, Institute of Crop Sciences, Chinese Academy of Agricultural Sciences, Beijing, China

Accurate and rapid identification of the effective number of panicles per unit area is crucial for the assessment of rice yield. As part of agricultural development, manual observation of effective panicles in the paddy field is being replaced by unmanned aerial vehicle (UAV) imaging combined with target detection modeling. However, UAV images of panicles of curved hybrid Indica rice in complex field environments are characterized by overlapping, blocking, and dense distribution, imposing challenges on rice panicle detection models. This paper proposes a universal curved panicle detection method by combining UAV images of different types of hybrid Indica rice panicles (leaf-above-spike, spike-above-leaf, and middle type) from four ecological sites using an improved You Only Look Once version 4 (YOLOv4) model. MobileNetv2 is used as the backbone feature extraction network based on a lightweight model in addition to a focal loss and convolutional block attention module for improved detection of curved rice panicles of different varieties. Moreover, soft non-maximum suppression is used to address rice panicle occlusion in the dataset. This model yields a single image detection rate of 44.46 FPS, and mean average precision, recall, and F1 values of 90.32%, 82.36%, and 0.89%, respectively. This represents an increase of 6.2%, 0.12%, and 16.24% from those of the original YOLOv4 model, respectively. The model exhibits superior performance in identifying different strain types in mixed and independent datasets, indicating its feasibility as a

general model for detection of different types of rice panicles in the heading stage.

KEYWORDS

curved rice panicle, panicle recognition model, YOLOv4, MobileNetv2, UAV, convolutional block attention module

1 Introduction

There is a great need to improve rice yield as rice (indica hybrid rice (*Oryza Satiua* L.)) is the staple food of 60% of China's population (Zhou et al., 2016). Effective panicles per unit area is a key determinant of rice yield and its accurate detection can guide the development of cultivation techniques for high-yield and high quality rice (Slafer et al., 2014). Currently, manual selection statistics are used to predict effective rice panicles per unit, which is labor-intensive, inefficient, and error-prone (Madec et al., 2019; Zhao et al., 2019). Therefore, an efficient and accurate method for automatic detection and counting of rice panicles is necessary.

The application of rice panicle recognition technology in agricultural production under field conditions is limited by the accuracy of rice panicle recognition in complex environments and the detection speed of the model. Deep learning and image processing technology, which can quickly identify the number of rice panicles per unit area, have been widely used in agriculture in recent years (Fu et al., 2020). Rice panicle recognition is primarily divided into image segmentation and target detection. Xiong et al. (2017) proposed a rice panicle segmentation algorithm (panicle-SEG) that can accurately segment rice panicles in different varieties and complex environments. An unsupervised Bayesian approach was used to segment the unmanned aerial vehicle (UAV) rice panicle images of different varieties and panicle types during the tasseling period with a mean F1 score of 82.10%. However, this method was only applied to upright panicles (Hayat et al., 2020). Zhou et al. (2019) proposed an improved region-based fully convolutional network (R-FCN) algorithm for UAV rice panicle image recognition with an F-measure of 87.4%. However, this method had limitations in training time and image background. Additionally, only one type of rice panicle was used for testing, which limited its application. Yang et al. (2020) used the FPN-Mask (feature pyramid network mask) method to segment rice panicles with an accuracy of 0.99; however, the effect of rice panicle type on segmentation accuracy was not considered. Shao et al. (2021) proposed a localization-based FCN combined with a watershed algorithm for dense rice panicle recognition and counting, with an accuracy of 89.88%. The aforementioned study that uses image segmentation for the actual panicle detection counts, as well as for investigating the effect of spike type on panicle detection, has limitations.

Compared with the traditional image segmentation techniques, the deeper features of rice panicles in the complex field environment can be extracted by using deep learning target detection. You only look once version 4 (YOLOv4) is a representative deep learning model with high speed and accuracy, which is widely used in agriculture, including crop and fruit detection (Yang et al., 2021; Sozzi et al., 2022; Wang et al., 2022a), disease identification (Roy et al., 2022), and lightweight model deployment (Li et al., 2022). However, it is rarely applied to panicle recognition. Compared with two-stage models, such as faster regions with convolutional neural network (Faster-RCNN), the YOLOv4 target detection model offers enhanced detection accuracy while reducing model size, which makes it suitable for future mobile deployment. A feature pyramid-based rice panicle detection method was proposed based on the images Nanjing 46 rice varieties in small-scale complex field environments. This method achieved a recall rate and accuracy rate of 90.82% and a accuracy rate of 99.05%, respectively (Jiang et al., 2020). This indicates the algorithm's ability to recognize small-sized rice panicles for local occlusion. However, the algorithm was not developed considering UAV and is limited for large-scale applications. The improved Faster-RCNN algorithm was proposed and used to identify rice panicles in potted conditions, and the mAP of this algorithm achieved 80.3% (Zhang et al., 2021). However, this method is designed to detect rice panicles under pot conditions and cannot be directly applied to complex field environments. A multi-scale hybrid window rice panicle detection method was proposed to detect panicles of Nanjing 46 rice varieties at the maturity stage and afforded better robustness for high-density rice panicle counting (Xu et al., 2020). However, when the number of rice panicles in the images increased to 71–80, the recognition accuracy decreased to 86.9%. Zhang et al. (2022a) improved Faster-RCNN to identify multi-growth period rice panicles and the mAP reached 92.47%. However, there were difficulties in actual field testing for mobile applications. Wang et al. (2022b) proposed a new method to remove repeated detections and achieved an accuracy of 92.77%. The methods, however, need to be optimized for UAV images and different density identification.

Although UAV photography considerably improves the efficiency of image acquisition (Oktay et al., 2018; Zhang et al., 2022b), the shape of panicles, occlusion, overlap, background changes, and reduced image quality due to the high density of rice panicles, light intensity, as well as differences in varieties can pose additional difficulties for the model in recognizing rice panicles (Zhao et al., 2021). In particular, the presence of sword leaf shading and scattered rice panicle overlap reduces accuracy of rice panicle detection. Therefore, improving the recognition of different spike types using a model in complex environments remains a challenge. Most of the current research focuses on the improvement of algorithm accuracy and the upright spike type of Japonica rice (Jiang et al., 2020; Xu et al., 2020). Few studies (Zhang et al., 2021) have focused on identifying different varieties and curved panicle types of hybrid Indica rice using UAV images in large-scale complex environments.

To address these challenges, this study establishes a universal model for curved rice panicle identification considering different Indica hybrid rice varieties from multiple regions in the Sichuan province. Images of multiple varieties of rice panicles were acquired using UAV from different ecological points. The model was trained to detect rice panicles based on the improved YOLOv4 model. MobileNetv2 was introduced to replace CSPDarkNet53 as the backbone YOLOv4 feature extraction module to make the model lightweight. Moreover, the convolutional block attention module (CBAM) attention mechanism and focal loss function were introduced for accurate recognition of rice panicle images in a mixed dataset. Finally, soft non-maximum suppression (soft-NMS) was utilized to address the dense shading of similar samples. The enhanced detection performance of this model enables its use as a general detection counting model for different varieties, ecological regions, and types of curved rice panicles in complex environments, making it a useful tool for rice yield prediction and identification of rice panicles.

2 Materials and methods

2.1 Experimental materials

The images of rice panicles were collected in the demonstration areas of high-yield rice production at four different ecological sites in the Sichuan province: Dayi County, Shehong City, Nanbu County, and Chongzhou City (Figure 1A). Sichuan is located in a subtropical monsoon climate zone. The location and pattern of the image collection are shown in Figure 1A. Different types of rice panicles—spike-above leaf, leaf-above spike, and middle types—were used as testing materials. The rice varieties and classification of types for each testing location are listed in Table 1. The UAV images of the three types of materials are shown in Figures 1B-D, respectively. Cultivation management measures of different rice varieties in different ecological sites are shown in Table S1.

2.2 UAV image acquisition

A UAV (DJI PHANTOM 4 RTK) was used to collect large-scale images of rice panicles under complex field environments. Under actual field production conditions, rice panicles are easily blocked by leaves. Therefore, to reduce the detection error of rice panicles, images were acquired seven days after the full heading stage in early August 2021. Another set of images were collected at maturity stage in mid-September to ascertain the suitable period for the detection of different types of rice panicles. Clear

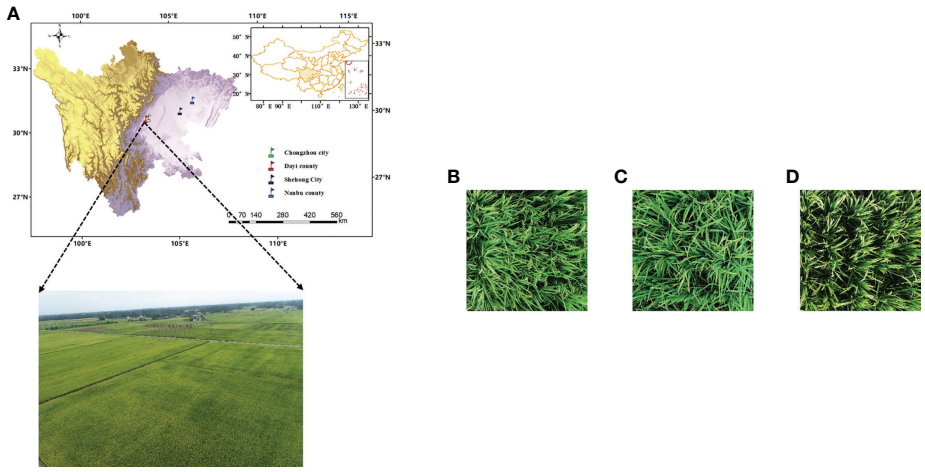

FIGURE 1
Experimental site and photos of different types of rice panicles. Experimental site of Dayi County **(A-D)** represent spike above leaf, leaf above spikes, and middle type, respectively.

TABLE 1 Experimental rice varieties and their classifications.

Study area	Leaf above spike	Spike above leaf	Middle type
Dayi County	Shen9you28 Chuankangyousimiao Chuanyou6709 Quanyou822	Jingliangyou534	Chuankangyou2115 Yixiangyou2115
Nanbu County		Tianyouhuazhan JingliangYou534	
Chongzhou City			Yixiangyou2115
Shehong City	Chuanzhongyou3877	Jingliangyou534	Chuankangyou2115

and cloudless weather conditions were selected for image collection (9:00–11:00 am, 3:00–5:00 pm). The manual flight mode was used with a flight level of 3 m and gimbal tilt angle of 90°. The collected rice panicle images were uniformly 5742 × 3648 pixels in size. In addition, we set up an independent dataset (Jingyou781) in the experiment to verify the model. The independent validation set Jingyou 781 was collected from the experimental field with different panicle fertilizers (Table S2) in Dayi County. The collection time and other factors were kept consistent for all images. The remaining camera settings were: ISO-Automatic, Aperture- f/2.2, Focal length-5.74mm.

2.3 Data annotation

The field environment had a significant influence on the detection of the panicles. Data associated with multiple varieties of genotypes and ecological points were included in the panicle image dataset. The accurate identification of rice panicles was hindered by the inconsistent and scattered positioning of the panicles. The leaf-above type panicles were particularly difficult to identify as the panicles are naturally hidden beneath the leaves. The image and processing flow chart are shown in Figure 2A. To reduce the cost of data processing annotation and model training time, the original rice panicle images were cropped randomly to 10 images of 608 × 608 pixels using MATLAB (2018b, The MathWorks, USA). Then, for the pre-processed images, the open-source software LabelImg was used for rice panicle labeling (GitHub - tzutalin/labelImg, 2022). For overlapping rice panicles, only the exposed parts were marked. The annotation category label is rice panicle (Figure 2B), and the annotation information was saved in the form of a Pascal VOC dataset. Finally, the dataset was amplified by up-and-down, adding noise, emboss filter and sharpening, as shown in Figure 2C. There were 10,285 images after image enhancement, including 8,330 images in the training set, 926 images in the validation set, and 1,029 images in the test set.

2.4 Rapid detection method for curved rice panicles

2.4.1 YOLOv4 model

Based on the initial YOLO family of networks, YOLOV4 was optimized to varying degrees in terms of model training,

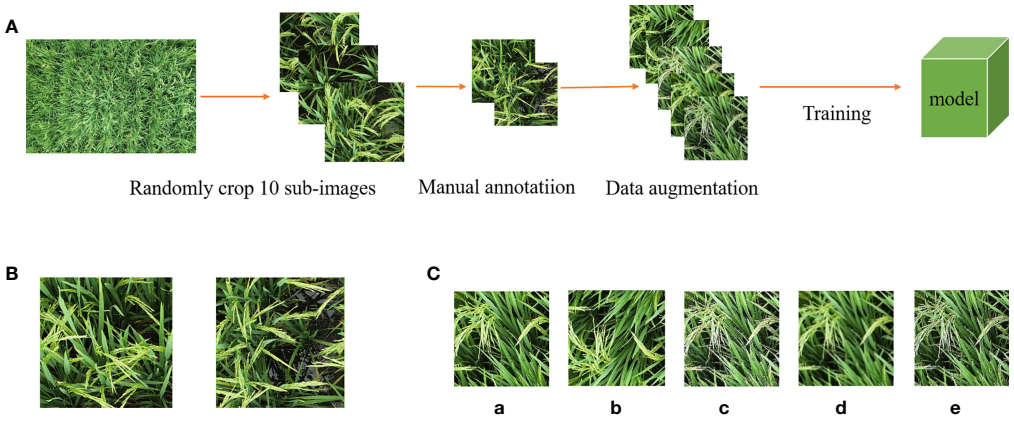

FIGURE 2
Data pre-processing process. **(A)** Image pre-processing process. **(B)** Example of data labeling. **(C)** Panicle image enhancement (a-e) Original image; flip up and down; image sharpening; Gaussian noise; e: Emboss filter.

activation functions, loss functions and backbone networks. As a two-stage representative network, Faster-RCNN is characterized by low recognition error rate and high accuracy (Ren et al., 2016). Compared to the Faster-RCNN two-stage algorithm, YOLOv4 has a better balance of speed and accuracy, a significant improvement in detection speed, and is widely used in agriculture (Bochkovskiy et al., 2020). The YOLOv4 model primarily consists of the CSPDarknet53 backbone feature extraction network, spatial pyramid pooling (SPPNET), path aggregation network (PANET), and YOLO-Head modules, which generate the coordinates, width, and height, of the candidate frames and final rice panicle prediction frame. CSPDarknet53 comprises several residual modules, which are composed of CSP-X and CBM modules stacked on top of each other. Furthermore, SPPNET can significantly improve the size of the receptive field and extract the most salient contextual features (He et al., 2015). In addition, PANet improves the bottom-up strategy to construct feature pyramids, which can achieve improved feature extraction for targets of different scales and sizes.

2.4.2 Improvement of the YOLOv4 model

YOLOv4 stacks multiple residual modules in the backbone extraction network CSP-Darknet53, resulting in numerous model parameters. This limits the further application of the rice panicle recognition model in agriculture. We aimed to further improve the detection accuracy and speed of this research method for curved rice panicles, with the complexity of the mixed datasets of UAV images of different ecological zones, varieties, and rice panicle types in the complex field environment. To this end, we propose the lightweight MobileNetV2 as the backbone feature extraction network. The CBAM is added to the image feature fusion stage, and soft-NMS is used to handle dataset occlusion as some of the curved panicles overlap and block each other approximately 7 days after the full heading stage. Further, focal loss was used to optimize the category loss function of the original YOLOv4 model. The model architecture of the improved rice panicle detection network is depicted in Figure 3.

2.4.3 Improvement of the YOLOv4 backbone

The YOLOv4 network has better detection accuracy and detection speed (Li et al., 2021). Although the YOLOv4 backbone network CSPDarknet53 can effectively extract depth feature information, the limitation of the number of parameters and computational resources leads to difficulties in applying it in practical agricultural production. Therefore, we improved the original YOLOv4 model to make it more embeddable into mobile devices in the future.

In this study, MobileNetv2 was used to replace CSPDarkNet53, which is the backbone feature extraction network of the YOLOv4 model. MobileNetv2, a lightweight feature extraction network, is an improved version of MobileNet, which uses the depthwise convolution module of MobileNetv1 and prevents the destruction of the RELU6 function when applied to the features of a low-dimensional

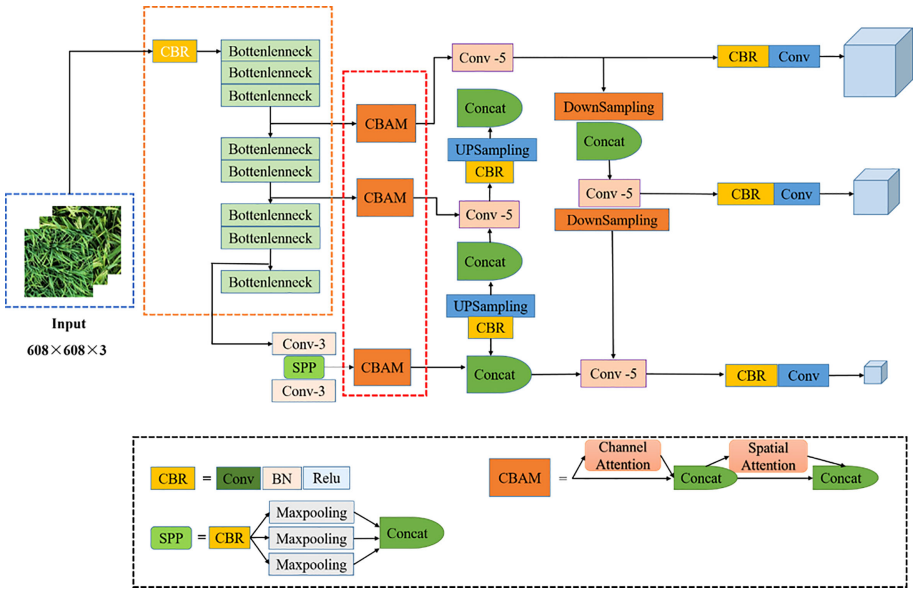

FIGURE 3
Improved YOLOv4 model structure. The dashed boxes represent improvements to the module. SPP and CBAM represent the SPPNET and attention mechanism modules respectively, Conv represents the convolution operation.

rice panicle. The linear bottleneck structure is introduced instead of RELU6 and then combined with the inverse residual module to form the MobileNetv2 network. The inverse residual structure is proposed by combining the depth-separable convolution, linear bottleneck structure, and residual network to enhance the accuracy of the algorithm. The inverse residual and overall structures of MobileNetv2 are shown in Figures 4A, B, respectively. The left part of Figure 4A represents the backbone, and the right green part represents the residual structure, which connects the input to the output directly. The inverse residual structure lifts the low dimension of the input by a 1×1 convolution, and a depthwise convolution is used to extract the features. Finally, a 1×1 convolution is used for dimensionality reduction. Figure 4B shows the overall MobileNetV2 network structure; Conv2D represents the convolution operation, bottleneck represents the inverse residual module, and Avgpool is the global pooling operation.

2.4.4 Attention module

The attention mechanism is divided into spatial, channel, and mixed spatial and channel attention mechanisms. In this study, CBAM (Woo et al., 2018) is the combined channel and spatial attention mechanism, which was inserted into the feature-enhanced network module in the YOLOv4 model. CBAM is an efficient module with negligible computational overhead and is given an intermediate feature mapping layer as input. The CBAM attention mechanism was used to assign more weight to the rice panicle's feature region in the image through the spatial and channel learning of rice panicle features and focuses on the extraction of important features of rice panicles during training. It also suppressed distracting factors such as rice leaves and water reflection in the field to improve the accuracy of the model. The channel and spatial attention mechanism expressions of CBAM are given in the following equations:

$$Mc(F) = \sigma(\mathrm{MLP}(\mathrm{AvgPool}(F)) + \mathrm{MLP}(\mathrm{MaxPool}(F))) = \sigma\left(W_1\left(W_0\left(F^c_{\mathrm{avg}}\right)\right) + W_1\left(W_0\left(F^c_{\mathrm{max}}\right)\right)\right); \quad (1)$$

$$Ms(F) = \sigma\left(f^{7\times7}\left(\left[F^s_{\mathrm{avg}}; F^s_{max}\right]\right)\right); \quad (2)$$

where MLP is a multilayer perceptron with a hidden layer, σ is the sigmoid operation and the convolution kernel size is 7×7. F^c_{avg} and F^c_{max} represent average-pooled features and max-pooled features. $W_0 \in \mathbb{R}^{C/r\times C}$, $W_1 \in \mathbb{R}^{C/r\times C/r}$ indicates the weight of MLP.

2.4.5 Soft-NMS

This study focused on different types of bent rice panicles, which exhibit different degrees of shading. Owing to the density of the rice plants in the images, the overlapping of leaves or panicles causes an obstruction which reduces the detection accuracy of the model. NMS typically misses certain rice panicles because of overlapping and is not suitable for rice panicle detection using UAV images. By contrast, Soft-NMS can significantly improve the recognition rate of the model in the presence of occlusion (Bodla et al., 2017). Therefore, Soft-NMS was introduced in the YOLOv4 model instead of NMS. Soft-NMS accounts for both the score and degree of overlap as follows:

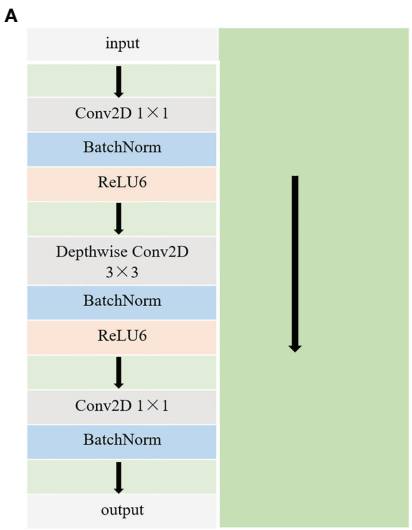

B

input	Operators	output channels	Stride
$416^2 \times 3$	Conv2d	32	2
$208^2 \times 32$	1×Bottleneck	16	1
$208^2 \times 16$	6×Bottleneck	24	2
$104^2 \times 24$	6×Bottleneck	32	2
$52^2 \times 32$	6×Bottleneck	64	2
$26^2 \times 64$	6×Bottleneck	96	1
$26^2 \times 96$	6×Bottleneck	160	2
$13^2 \times 160$	6×Bottleneck	320	1
$13^2 \times 320$	Conv2d 1×1	1280	1
$13^2 \times 1280$	Avgpool 7×7	-	-
1×1×1280	Conv2d 1×1	Class	-

FIGURE 4
Inverse residual structure **(A)** and structure of MobileNetv2 **(B)**.

$$s_i = \begin{cases} s_i, & Iou(M, b_i) < N_t \\ s_i(1 - \mathrm{Iou}(M, b_i)), & Iou(M, b_i) \geq N_t \end{cases} \quad (3)$$

where s_i is the final score, i is the subscript, M is the box with the highest score in the prediction box set, b_i is the box in the prediction box set B, and N_t is the intersection-over-union (IoU) threshold of M and b_i.

2.4.6 Improvement of the loss function

The loss functions, including the complete intersection over union (CIOU), classification, and confidence losses, were used in the YOLOv4 model. CIOU loss also considers the overlap area, centroid distance, and aspect ratio of the bounding box regression. The original loss function was the crossover loss function, which was calculated as follows:

$$\mathcal{L}_{CIoU} = 1 - IoU + \frac{\rho^2(\mathbf{b}, \mathbf{b}^{gt})}{c^2} + \alpha \mathrm{v}; \quad (4)$$

$$R_{\mathrm{CIoU}} = \frac{\rho^2(\mathbf{b}, \mathbf{b}^{\mathbf{gt}})}{\mathrm{c}^2} + \alpha \mathrm{v}; \quad (5)$$

$$\mathrm{v} = \frac{4}{\pi^2}\left(\arctan\frac{\mathrm{w}^{\mathrm{gt}}}{\mathrm{h}^{\mathrm{gt}}} - \arctan\frac{\mathrm{w}}{\mathrm{h}}\right)^2; \quad (6)$$

$$\alpha = \frac{\mathrm{v}}{(1 - \mathrm{IoU}) + \mathrm{v}}; \quad (7)$$

where $\rho^2(b,b^{gt})$ represents the Euclidean distance between the center points of the predicted and real boxes, respectively; c represents the diagonal distance that can contain both the prediction box and true box minimum closure region; v represents the aspect ratio parameters; and α represents the positive trade off parameters. Further, w and h denote the width and height of the prediction box, respectively, and w^{gt} and h^{gt} denote the width and height of the real box, respectively.

In the curved rice panicle data set, the model ignored samples that are difficult to classify when there are overlaps and rice panicle occlusions in the image. Hence, the appropriate loss function must be selected to balance the contribution of positive and negative samples to the total loss. Therefore, by improving the loss function, the model network can focus more on the samples that are difficult to classify. The focal loss equation is expressed as follows:

$$\mathrm{L_{fl}} = \begin{cases} -(1 - \hat{\mathrm{p}})^{\gamma} log(\hat{\mathrm{p}}) & \text{if } y = 1 \\ -\hat{\mathrm{p}}^{\gamma} log(1 - \hat{\mathrm{p}}) & \text{otherwise} \end{cases} \quad (8)$$

Here, $\hat{p}$ represents the probability of correctly classifying a rice panicle. The classification loss function of the original YOLOv4 model is optimized using the focal loss without increasing the computational overhead of the model. Note that $1 - \hat{p}$ approaches 1 as $\hat{p}$ decreases, indicating that the overall loss has a negligible effect on accuracy. Thus, replacing the category loss function with the focal loss function enables the model to focus on rice panicles with overlapping occlusion in the image.

2.4.7 Model training

Processing was performed using an AMD 5900X CPU, 32GB memory, Windows 10, RTX3060 GPU, 12G video memory, the operating environment was PyTorch 1.7.1, Python 3.7, CUDA 11.0. The model training is based on the transfer learning technique to speed up the model convergence. The k-means clustering algorithm was used to generate the anchor coordinates of (25, 21), (32, 43), (54, 28), (63, 49), (42, 73), (101, 51), (70, 97), (135, 81), and (111, 136). Mosaic data augmentation, label smoothing, cosine smoothing, cosine annealing decay, and other training techniques were used in the training process to improve model accuracy. The other training parameters are shown in Table 2. The training loss of the improved model is shown in Figure 5A. The model training loss decreases and converges as the number of iterations increases. The model converges by the 300th epoch, and the model loss value is 0.124. The influence of label smoothing training techniques on model loss is compared in Figure 5A. Using label smoothing techniques improves the generalization ability of the model. Figure 5B shows the P-R plots of the improved model; the area enclosed under the curve represents the AP value of the model.

2.4.8 Evaluation metrics

In this study, precision (P), recall (R), mean average precision (mAP), F1-score, detection speed, and detection time of the model were calculated to objectively evaluate the detection effect of this model for curved rice panicles in a complex field environment. In the experiment, IOU greater than 0.5 was defined as a positive sample. By definition, P, R, mAP, and the F1-score can be expressed as

$$P(\%) = \frac{T_P}{T_P + F_P} \times 100; \quad (9)$$

$$R(\%) = \frac{T_P}{T_P + F_N} \times 100; \quad (10)$$

TABLE 2 Network training hyperparameters.

Parameters	Set value
Optimizer	SGD
Momentum	0.9
Initial learning rate	1×10^{-2}
Label smoothing	0.01
Epoch	300
Decay weights	5×10^{-4}

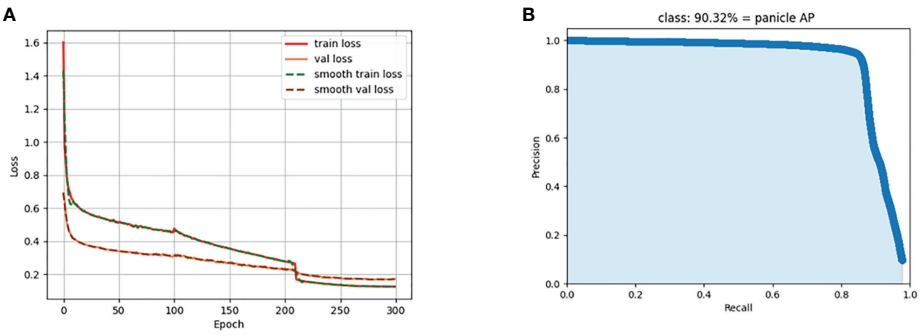

FIGURE 5
(A) Training loss curve and **(B)** P-R curve of panicle detection for the proposed method.

$$F1 = 2 \times \frac{PR}{P+R}; \tag{11}$$

$$mAP = \int_0^1 P(R)dR; \tag{12}$$

where TP, FP, TN, and FN represent true positive, false positive, true negative, and false negative, respectively, based on the true and predicted classes of the target object. mAP is the average of AP across the total number of classes, which indicates the detection performance of the model for rice panicles; higher mAP values represent better models. The model detection speed is evaluated by frames per second (FPS) transmission, and the larger the attained FPS, the better the model fluency and the faster the detection speed.

In addition, quantitative model count accuracy metrics including root-mean-square error (RMSE) and R^2 were used. The lower the RMSE, and the larger the R^2 value, the better is the model performance. They are expressed as follows:

$$R^2 = 1 - \frac{\sum_{i=1}^{n}(t_i - c_i)^2}{\sum_{i=1}^{n}(t_i - \bar{t}_i)^2} \tag{13}$$

$$\mathrm{RMSE} = \sqrt{\frac{1}{n}\sum_{i=1}^{n}(t_i - c_i)^2} \tag{14}$$

$$\text{Statistical accuracy} = 1 - \left|\frac{Predict - True}{True} \times 100\,\%\right|. \tag{15}$$

3 Results

3.1 Ablation study

The results of the ablation experiments showed the effectiveness of the improved model, as shown in Table 3. The model achieved a mAP of 82.92%, only by replacing the MobileNetv2 backbone feature extraction network. Using the CBAM attention mechanism module to join in the feature fusion stage, the model mAP reached 83.10%. Then, using Soft-NMS to replace NMS resulted in a mAP of 87.02%. Finally, focal loss is used to replace the category loss function in the YOLOv4 loss function to improve the detection effect of the model for identifying samples with overlapping rice panicles, increasing the mAP to 90.32%.

3.2 Detection effect of improved models

Compared to the MobileNetv2-YOLOv4 model, the mAP of MobileNetv2-YOLOv4-DepthwiseConv decreased by 4.79% when the model training parameters were kept consistent, as can be observed in Table 4. Compared with Our method and the YOLOv4 model, the mAP of Our-method-Depthwise-Conv, a feature enhancement module using depthwise convolution, decreased by 9.56% and 3.36%, respectively. Furthermore, the

TABLE 3 Ablation study.

MobileNetv2	CBAM	Soft-NMS	Focal loss	mAP (%)
✓				82.92
✓	✓			83.10
✓	✓	✓		87.02
✓	✓	✓	✓	**90.32**

The symbol "✓" means adding an improvement strategy.

detection time of Our-method-Depthwise-Conv only increased by 0.016s compared to Our Method. These results showed that although the detection speed of Our Method was slightly reduced, the detection accuracy was significantly improved.

The rice panicle dataset is a hybrid dataset of UAV images, composed of different varieties, panicle types, and ecological points in a complex environment in a large field. The rice panicle detection model mAP in this study reached 90.32% of our method compared with the YOLOv4 model and Faster-RCNN (Table 5). Our improved model in this paper has the highest mAP, F1, and recall, which increased by 6.2%, 0.12, 16.24% respectively, as compared to the original YOLOv4 model. With respect to the Faster-RCNN model, our improved model increased the same values by 45.68%, 0.50, 29.24%, respectively. The test time of our model was the lowest, which decreased by 0.0036–0.0655 s, compared with the other models. The above results indicate that our improved model performs better than previous models in terms of detection accuracy with slightly decreased but comparable speed for the identification of curved rice panicles in a complex field environment.

3.3 Recognition effect of different types of rice panicles

As shown in Figure 6, the independent dataset of Jingyou781 varieties was used for model validation (Figure 6A). The YOLOv4 model showed misrecognition in the presence of occlusion, and our method performs better in the independent dataset. The leaf-above spike type, scattered spike type, and small target panicles were all missed in the original YOLOv4 algorithm, while our method did not misidentify the small scattered panicle type in the image (Figure 6B). The spike-above leaf type showed more scattered panicle types, leading to false recognition in both the YOLOv4 model and our method (Figure 6C). For the middle type rice panicle (Figure 6D), YOLOv4 misrecognized the small target panicle owing to the different extraction time in the actual field environment; however, the recognition of our improved algorithm showed excellent performance.

3.4 Accuracy validation of model counting

The improved model yielded better detection performance for the three types of curved rice panicles (Table 6). One hundred images of each type from the training set were randomly selected, and the model was used to identify and compare the images with that of the actual labeled frames. Results showed that for the middle, spike-above leaf, and leaf-above spike types of panicles, the R^2 value was 0.84, 0.89, and 0.92 respectively, and the RMSE was 2.56, 1.95, and 4.39, respectively. The larger RMSE of the leaf-above spike type is because of the presence of more panicles obscured by leaves in the image, resulting in more rice panicles being missed. The manual labeling of the three types of rice panicles in the 100 images found 1589, 1961, and 3510 panicles, respectively. Comparatively, our improved model recognized 1699, 1965, and 3754 panicles, respectively. The original YOLOv4 model recognized 1325, 1518, and 2505. Thus, the accuracy of our method was 93.08%, 99.80%, and 93.05% for the three types of rice spike counts, respectively. The accuracy of YOLOv4 for the three types of rice spikes was 83.39%, 74.41%, and 71.37%, respectively. The original YOLOv4 model performed the worst in the leaf-above spike type count.

3.5 Model accuracy in different periods

The maturity stage of the rice crop when the images were taken also had a significant impact on the accuracy of the

TABLE 4 Experimental results of rice panicle recognition with different target detection models.

Model	mAP (%)	Test time (s)	FPS
MobileNetv2-YOLO	82.92	0.161	62.13
MobileNetv2-YOLO4-Depthwise Conv	78.73	0.0152	65.95
Our-method-Depthwise Conv	80.76	0.0209	47.92
Our method	90.32	0.0225	44.46

TABLE 5 Recognition effects of different advanced target detection models.

Model	mAP (%)	F1	Recall (%)	Test time (s)	FPS
YOLOv4	84.12	0.77	66.12	0.0261	38.32
Faster-RCNN	44.64	0.49	53.12	0.0880	11.31
Our method	90.32	0.89	82.36	0.0225	44.46

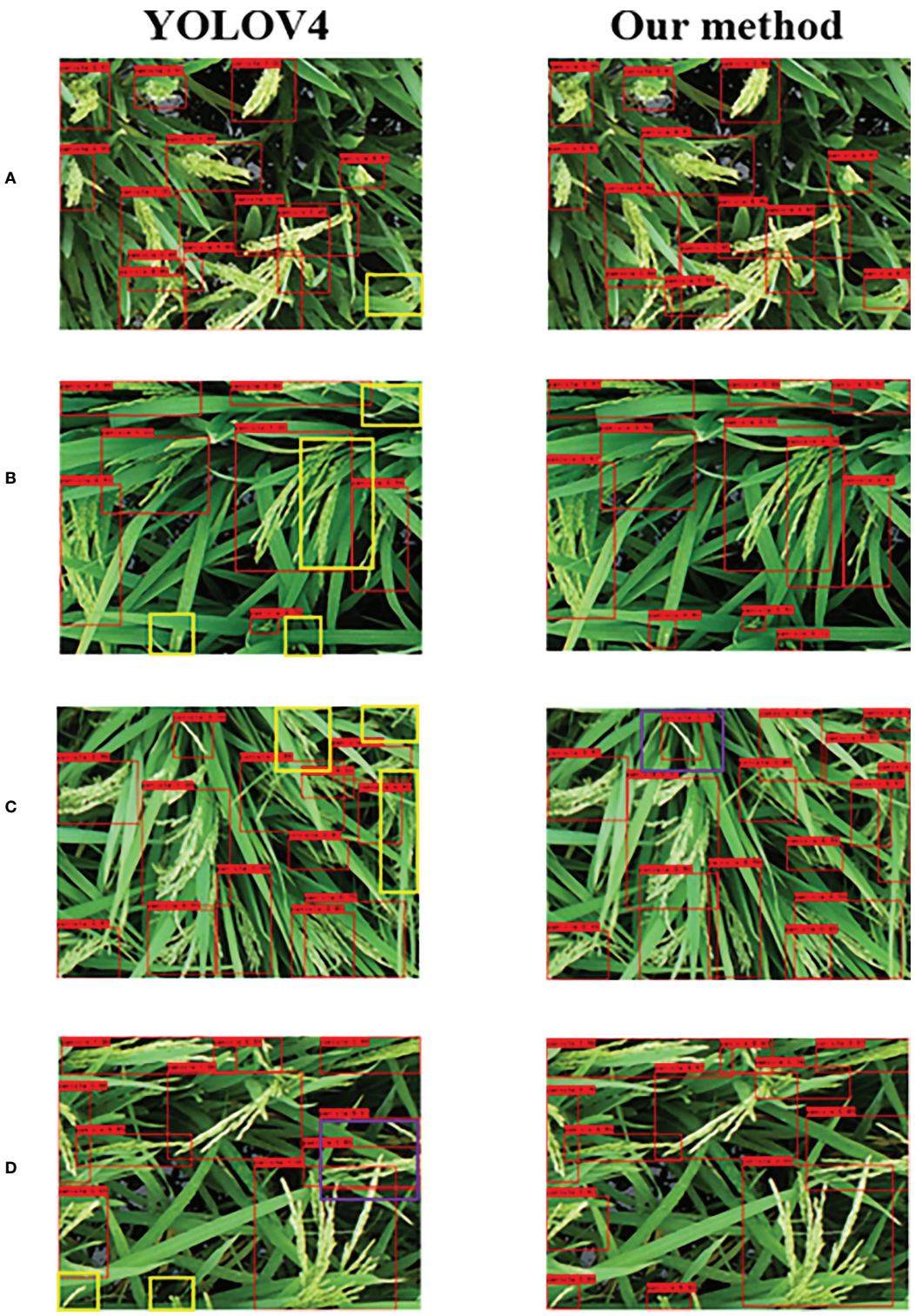

FIGURE 6
Recognition effects of YOLOv4 model (left) and the improved algorithm in this study (right). **(A)** Independent dataset recognition; **(B)** leaf-above spike type; **(C)** spike-above leaf type; **(D)** middle type. The yellow and purple boxes represent missed and false detection, respectively.

TABLE 6 The accuracy of our method for identifying different types of panicles.

Type	Seven days after the full heading stage			Mature stage		
	R^2	RMSE	rRMSE	R^2	RMSE	rRMSE
Middle type	0.84	2.56	0.1741	0.46	2.77	0.4567
Spike above leaf	0.89	1.95	0.0986	0.38	2.86	0.4321
Leaf above spike	0.92	4.39	0.1520	0.31	3.28	0.4097

models. This is due to the presence of more bent and dispersed rice panicles, and the fact that both leaves and panicles turn yellow at maturity. This also had an impact on manual labeling. In this study, 514 images of different varieties of rice at different ecological points were labeled at maturity. After data enhancement for model training, the mAP of the model had only 79.66% at maturity stage (Table 7). This result indicated that data collection is more appropriate at 7 days after the full heading stage for the identification and counting of rice panicles. A comparison of 100 randomly selected marker images of the three rice panicle types with the number predicted by the model is shown in Figure 7. The model performed poorly in identifying the three types at maturity, with R^2 values of only 0.46, 0.38, and 0.31, for the middle, spike-above leaf, and leaf-above spike types of panicles, respectively.

4 Discussion

Most rice panicle identification studies focus on upright spikes and potted plants. Our study targeted the curved spike type of Indica rice in the actual field production environment, which significantly increased the difficulty of recognition. Compared to the method of Zhang et al. (2021), our method's mAP was 10.02% greater, and the detection speed improved by 146.6 ms (Table S4). In a previous study, the addition of the CBAM attention mechanism for YOLOv4 improved wheat detection accuracy in the presence of occlusion (Yang et al., 2021). Compared with the recognition of rice panicles using UAV images based on improved R-FCN (Zhou et al., 2019), our method improves the recognition accuracy of different varieties by 3.52%. The mAP of our method improves by 45.68% and 6.2% compared to the Faster-RCNN and YOLOv4 models, respectively (Ren et al. 2017). The above results indicate the better performance of our improved model in the mixed dataset. The weight ratio of fertilizer formulations are shown in Table S2. In addition, the results of the panicle count for different fertilization treatments for the independent dataset demonstrates the feasibility of our method to build a universal model for the mixed dataset (Table S3). The mAP of the proposed method achieves 90.32% while accounting for the speed of detection (Table 4). This experiment shows that the proposed method effectively addresses challenges associated with different varieties, panicle types, and ecological regions to achieve accurate rice panicle identification and counting.

The type of the rice panicle and the variety of the rice crop influenced the accuracy of model detection (Xu et al., 2020). We established a general method by collecting different varieties at the same period, and the mAP value of the model was 90.32% (Table 4). The results from the independent dataset counts in Table S3 showed that it is feasible to develop a generic rice panicle detection model for different varieties in the same period. However, in the G-BLACK processing, because the heads of the panicles are scattered, there were many repeated detections.

The photo environment also affects the image quality, and thus affects the recognition accuracy of the rice panicles. Figure 8 shows the effect of this study's improved algorithm on rice panicle recognition under different complex environmental disturbances. For example, there are inconsistent light conditions when using a UAV for rice panicle image acquisition. When the improved algorithm was used for the recognition of rice panicles under strong light conditions, there were no misrecognitions (Figure 8A). Due to the canopy disturbance caused by the UAV rotor, the image is blurred and model detection is affected, leading to the lack of recognition of spikelets under the leaf shade in the proposed method (Figure 8B). The proposed method is based on the existence of dispersed rice panicle types in the image, which can easily cause multiple recognition for dispersed spike types (Figure 8C). Building a universal detection model for dispersed-type rice panicles in a complex field environment is complex, as the scattered state of the rice panicles at 7 days after full heading

TABLE 7 Influence of sampling period on model accuracy.

Stage	mAP (%)	F1	Recall (%)	Number of training images	Number of images after data enhancement
Seven days after the full heading stage	90.32	0.89	82.36	2056	10280
Mature stage	79.66	0.75	62.05	514	2570

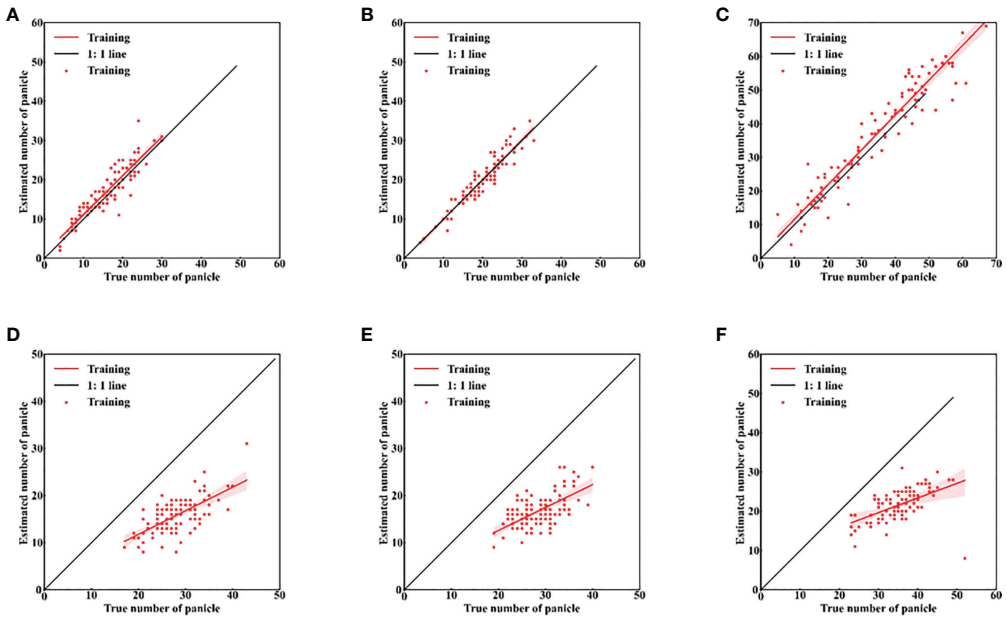

FIGURE 7
Accuracy of rice panicles identification in different data sets. **(A–C)** seven days after the full heading stage; **(D–F)** mature stage; **(A, D)** middle type; **(B, E)** spikes above leaves type; **(C, F)** leaves above spikes type.

has an impact on the integrity of the other rice panicles, resulting in misidentification and misrecognition.

To further explore the possibility of generalizing the improved model for image detection in a wide field of UAV view (Figure 9), this study discussed the rice panicle images from a UAV at a distance 3 m from the rice canopy. The UAV view improvement algorithm did not achieve better results at maturity because of the increase in dispersed spike types at this stage (Figure 9C). The presence of scattered rice panicles in the image leads to multiple model recognitions, which makes it difficult to maintain the integrity of the rice panicles (Figure 9D). Then, the improved model was employed to detect and evaluate the collected image. The poor recognition of dispersed rice panicles photographed by a UAV is mainly caused by the following reasons: the obscuration of sword leaves (Figure 9D), small rice panicles in the UAV image (Figure 9E), and multiple dispersed rice panicles interacting with each other (Figure 9F). For scattered rice panicles, the more accurate and easier identification period should be selected by counting the dynamic changes of rice panicles. Future research will focus on establishing a specific recognition model that can be combined with the collection of images during a specific period of time in order to establish accurate detection of rice panicles. To achieve large-scale application, lightweight and universal models must be developed. In addition, we must establish a single model to detect the dispersed panicle type in the curved panicle type to reduce misidentification by the model.

5 Conclusion

In this study, a universal rice panicle detection model was developed using a mixed dataset to identify panicle images of different Indica hybrid rice varieties grown in different ecological regions in large-scale complex field environments. The improved method outperformed the original YOLOv4 and Faster-RCNN models in terms of detection performance and accuracy for the leaf-above-spike type, spike-above-leaf type, and middle type. The F1 scores improved by 0.12 and 0.40 from those of the two original models, respectively. The detection accuracy of different models at 7 days after full heading stage was significantly higher than that at maturity stage, and the RMSE of the spike-above-leaf type at 7 days after full heading stage was also improved. Different rice varieties were divided into different types for detection and analysis, and all three types obtained improved identification results with our model. The current study illustrates the feasibility of establishing a general rice panicle identification model for a certain period with a mixed dataset of Indica hybrid rice. However, when there are more dispersed panicles in the hybrid Indica rice, a separate rice panicle detection model is needed to improve detection accuracy. In future, we will focus on the detection of scattered spike count and

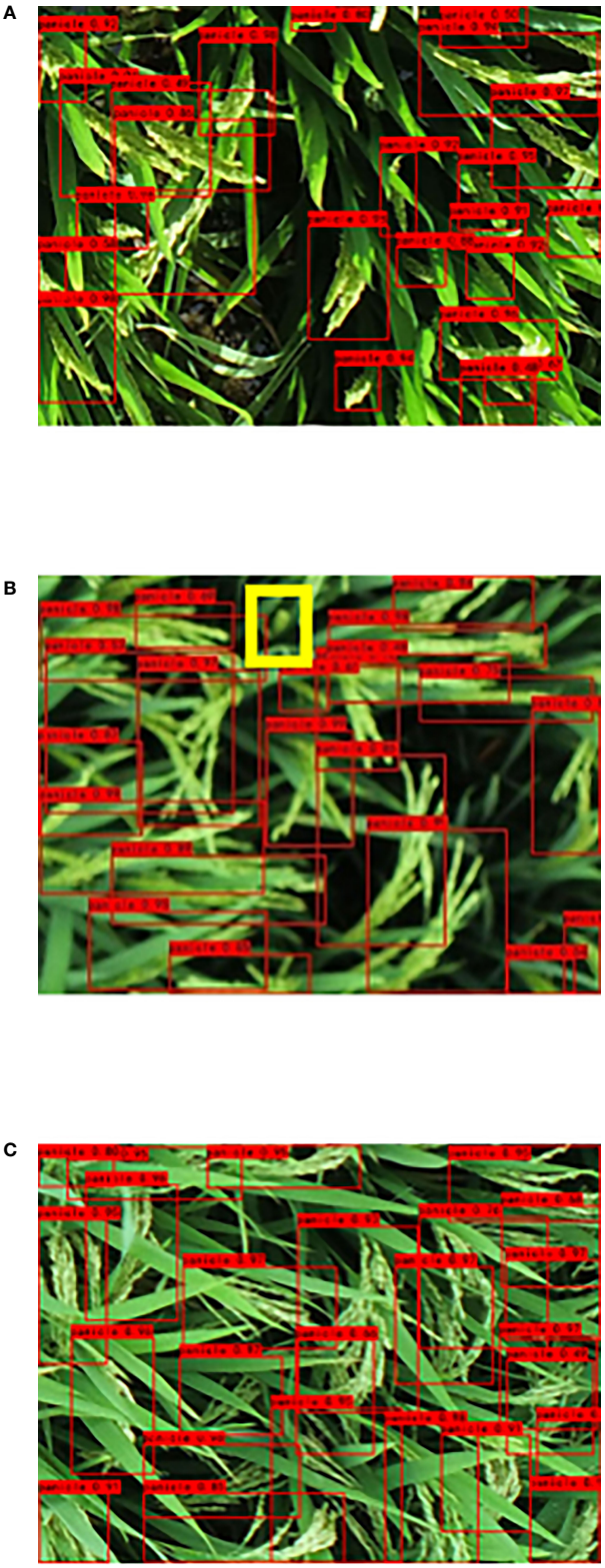

FIGURE 8
Effect of different complex environments on the recognition of scattered panicle in a large field. **(A)** Image taken using strong exposure; **(B)** UAV image of canopy disturbance; **(C)** Scattered panicle in complex environment.

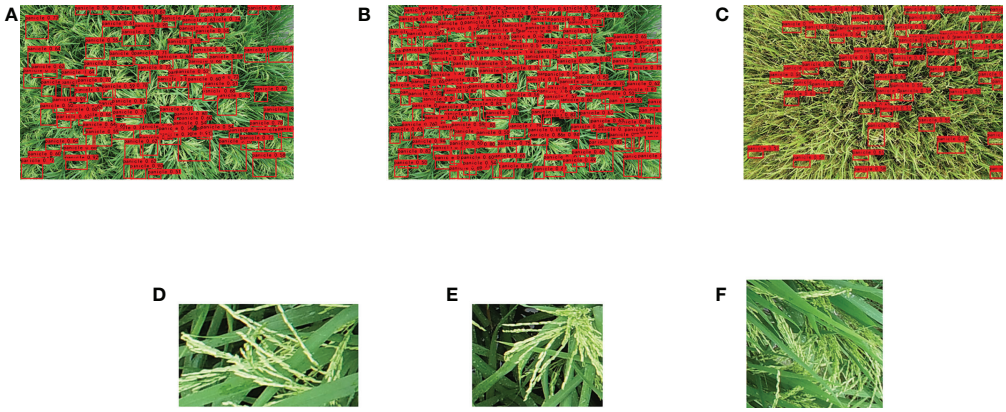

FIGURE 9
Recognition results of UAV images using the large-scale dispersion spike model. **(A)** Recognition results of the original YOLOv4 model, and **(B)** Recognition results of the improved algorithm **(C)** Improved algorithm recognition during maturity. **(D–F)** Large-scale UAV view prediction frame analysis.

model deployment on mobile devices. The best prediction identification date should be chosen based on dynamic analysis of the three types to build identification models for the characteristics of Indica hybrid rice with more scattered spike types in the future.

Data availability statement

The original contributions presented in the study are included in the article/Supplementary Material. Further inquiries can be directed to the corresponding authors.

Author contributions

BS: Conceptualization, Writing- Original draft preparation, Data curation, Formal analysis. WZ: Conceptualization, Supervision, Writing- Original draft preparation, Visualization, Software, Writing-Reviewing and Editing. SZ, SH, XY, and ZW: Methodology, Investigation. XL, DY, HX, YC, YT, FD, and HC: Writing- Reviewing and Editing, Resources. WR and XJ: Conceptualization, Supervision, writing-Reviewing and Editing. All authors contributed to the article and approve the submitted version.

Funding

This work was supported by the Natural Science Foundation of China (grant numbers U20A2022), the Sichuan Science and Technology Program (grant number 2021YJ0492), the Agricultural Science and Technology Innovation Program of the Chinese Academy of Agricultural Sciences, Hainan Yazhou Bay Seed Lab (B21HJ0221), Nanfan special project, CAAS (YJTCY01, YBXM01), and Research and application of key technologies of smart brain for farm decision-making platform (2021ZXJ05A03).

Acknowledgments

The authors would like to gratefully thank all the members of the Paddy Laboratory of Sichuan Agriculture University of China for their suggestions and help. We would like to thank Editage [www.editage.cn] for English language editing.

Conflict of interest

The authors declare that the research was conducted in the absence of any commercial or financial relationships that could be construed as a potential conflict of interest.

Publisher's note

All claims expressed in this article are solely those of the authors and do not necessarily represent those of their affiliated organizations, or those of the publisher, the editors and the reviewers. Any product that may be evaluated in this article, or claim that may be made by its manufacturer, is not guaranteed or endorsed by the publisher.

Supplementary material

The Supplementary Material for this article can be found online at: https://www.frontiersin.org/articles/10.3389/fpls.2022.1021398/full#supplementary-material

References

Bochkovskiy, A., Wang, C. Y., and Liao, H. (2020). YOLOv4: Optimal speed and accuracy of object detection. *arXiv* 2004, 10934.

Bodla, N., Singh, B., Chellappa, R., and Davis, L. S. (2017). Soft-NMS – improving object detection with one line of code. *arXiv* 1704, 04503. doi: 10.1109/ICCV.2017.593

Fu, L., Song, Z., Zhang, X., Li, R., Wand, D., Cui, Y., et al. (2020). Applications and research progress of deep learning in agriculture. *J. China Agric. Univ.* 25, 105–120. doi: 10.11841/j.issn.1007-4333.2020.02.12

GitHub - tzutalin/labelImg. (2022). In: *LabelImg is a graphical image annotation tool and label object bounding boxes in images*. Available at: https://github.com/tzutalin/labelImg (Accessed 2022/4/29).

Hayat, M. A., Wu, J., and Cao, Y. (2020). Unsupervised Bayesian learning for rice panicle segmentation with UAV images. *Plant Methods* 16, 18. doi: 10.1186/s13007-020-00567-8

He, K., Zhang, X., Ren, S., and Sun, J. (2015). Spatial pyramid pooling in deep convolutional networks for visual recognition. *IEEE Trans. Pattern Anal. Mach. Intell.* 37, 1904–1916. doi: 10.1109/TPAMI.2015.2389824

Jiang, HY., Xu, C., Yao, C., and Yongkang, C. (2020). Detecting and counting method for small-sized and occluded rice panicles based on in-field images. *Transactions of the Chinese Society for Agricultural Machinery* 51, 152–162.

Li, G., Suo, R., Zhao, G., Gao, C., Fu, L., Shi, F., et al. (2022). Real-time detection of kiwifruit flower and bud simultaneously in orchard using YOLOv4 for robotic pollination - ScienceDirect. *Comput. Electron. Agric.* 193, 106641. doi: 10.1016/j.compag.2021.106641

Li, W., Feng, X., Zha, K., Li, S., and Zhu, H. (2021). Summary of Target Detection Algorithms. *Journal of Physics: Conference Series*. 1757, 012003. doi: 10.1088/1742-6596/1757/1/012003.

Madec, S., Jin, X., Lu, H., De Solan, B., Liu, S., Duyme, F., et al. (2019). Ear density estimation from high resolution RGB imagery using deep learning technique. *Agric. For. Meteorol.* 264, 225–234. doi: 10.1016/j.agrformet.2018.10.013

Oktay, T, Celik, H, and Turkmen, I. (2018). Maximizing autonomous performance of fixed-wing unmanned aerial vehicle to reduce motion blur in taken images. *Proceedings of the Institution of Mechanical Engineers, Part I: Journal of Systems and Control Engineering*. 232 (7), 857–868. doi: 10.1177/0959651818765027

Ren, S., He, K., Girshick, R., and Sun, J. (2016). Towards real-time object detection with region proposal networks. *IEEE* 6 (2017), 1137–1149.

Ren, S., He, K., Girshick, R., and Sun, J. (2017). Faster r-CNN: Towards real-time object detection with region proposal networks. *IEEE Trans. On Pattern Anal. Mach. Intell.* 39, 1137–1149. doi: 10.1109/TPAMI.2016.2577031

Roy, A. M., Bose, R., and Bhaduri, J. (2022). A fast accurate fine-grain object detection model based on YOLOv4 deep neural network. *Neural Computing Appl.* 34, 3895–3921. doi: 10.1007/s00521-021-06651-x

Shao, H., Tang, R., Lei, Y., Mu, J., Guan, Y., and Xiang, Y. (2021). Rice ear counting based on image segmentation and establishment of a dataset. *Plants (Basel)* 10, 1625. doi: 10.3390/plants10081625

Slafer, G. A., Savin, S., and Vo., C. (2014). Coarse and fine regulation of wheat yield components in response to genotype and environment. *Field Crops Res.* 157, 71–83. doi: 10.1016/j.fcr.2013.12.004

Sozzi, M., Cantalamessa, S., Cogato, A., Kayad, A., and Marinello, F. (2022). Automatic bunch detection in white grape varieties using YOLOv3, YOLOv4, and YOLOv5 deep learning algorithms. *Agronomy* 12, 319. doi: 10.3390/agronomy12020319

Wang, L., Zhao, Y., Liu, S., Li, Y., Chen, S., Lan, Y., et al. (2022a). Precision detection of dense plums in orchards using the improved YOLOv4 model. *Front. Plant Sci.* 13. doi: 10.3389/fpls.2022.839269

Wang, X., Yang, W., Lv, Q., Huang, C., Liang, X., Chen, G., et al. (2022b). Field rice panicle detection and counting based on deep learning. *Front. Plant Sci.* 13. doi: 10.3389/fpls.2022.966495

Woo, S., Park, J., Lee, J. Y., and Kweon, I. S. (2018) CBAM: Convolutional block attention module. *Springer Cham*. doi: 10.1007/978-3-030-01234-2_1

Xiong, X., Duan, L., Liu, L., Tu, H., Yang, P., Wu, D., et al. (2017). Panicle-SEG: A robust image segmentation method for rice panicles in the field based on deep learning and superpixel optimization. *Plant Methods* 13, 104. doi: 10.1186/s13007-017-0254-7

Xu, C., Jiang, H., Yuen, P., Zaki Ahmad, K., and Chen, Y. (2020). MHW-PD: A robust rice panicles counting algorithm based on deep learning and multi-scale hybrid window. *Comput. Electron. Agric.* 173, 105375. doi: 10.1016/j.compag.2020.105375

Yang, B., Gao, Z., Gao, Y., and Zhu, Y. (2021). Rapid detection and counting of wheat ears in the field using YOLOv4 with attention module. *Agron. (Basel)* 11, 1202. doi: 10.3390/agronomy11061202

Yang, Z., Gao, S., Xiao, F., Li, G., Ding, Y., Guo, Q., et al. (2020). Leaf to panicle ratio (LPR): A new physiological trait indicative of source and sink relation in japonica rice based on deep learning. *Plant Methods* 16, 117. doi: 10.1186/s13007-020-00660-y

Zhang, Y., Xiao, D., Chen, H., and Liu, Y. (2021). Rice panicle detection method based on improved faster r-CNN. *Trans. Chin. Soc. Agric. Machinery* 52, 231–240. doi: 10.6041/j.issn.1000-1298.2021.08.023

Zhang, Y., Xiao, D., Liu, Y., and Wu, H. (2022a). An algorithm for automatic identification of multiple developmental stages of rice spikes based on improved faster r-CNN. *Crop J.* 10 (5), 1323–1333doi: 10.1016/j.cj.2022.06.004

Zhang, J., Min, A., Steffenson, B. J., Su, W., Hirsch, C. D., Anderson, J., et al. (2022b). Wheat-net: An automatic dense wheat spike segmentation method based on an optimized hybrid task cascade model. *Front. Plant Sci.* 13. doi: 10.3389/fpls.2022.834938

Zhao, J. Q., Zhang, X. H., Yan, J. W., Qiu, X. L., Yao, X., Tian, Y. C., et al. (2021). A wheat spike detection method in UAV images based on improved YOLOv5. *Remote Sens.* 13, 3095. doi: 10.3390/rs13163095

Zhao, S., Zheng, H., Chi, M., Chai, X., and Liu, Y. (2019). Rapid yield prediction in paddy fields based on 2D image modelling of rice panicles. *Comput. Electron. Agric.* 162, 759–766. doi: 10.1016/j.compag.2019.05.020

Zhou, W., Lv, T., Zhang, P. P., Huang, Y., and Ren, W. (2016). Regular nitrogen application increases nitrogen utilization efficiency and grain yield in indica hybrid rice. *Agron. J.* 108, 1951–1961. doi: 10.2134/agronj2016.03.0137

Zhou, C., Ye, H., Hu, J., Shi, X., Hua, S., Liu, Y., et al. (2019). Automated counting of rice panicle by applying deep learning model to images from unmanned aerial vehicle platform. *Sensors* 19, 3106. doi: 10.3390/s19143106

frontiers | Frontiers in Plant Science

TYPE Original Research
PUBLISHED 13 December 2022
DOI 10.3389/fpls.2022.1012293

Check for updates

OPEN ACCESS

EDITED BY
Daobilige Su,
China Agricultural University, China

REVIEWED BY
Chunlei Xia,
CAS, China
Bin Liu,
Northwest A&F University, China
Salah Elsayed Mohamed Elsayed,
University of Sadat City, Egypt
Tugrul Oktay,
Erciyes University, Turkey

*CORRESPONDENCE
Ying-hui Li
liyinghui@caas.cn
Li-juan Qiu
qiulijuan@caas.cn
Xiuliang Jin
jinxiuliang@caas.cn

†These authors have contributed equally to this work

SPECIALTY SECTION
This article was submitted to Sustainable and Intelligent Phytoprotection, a section of the journal Frontiers in Plant Science

RECEIVED 05 August 2022
ACCEPTED 28 November 2022
PUBLISHED 13 December 2022

CITATION
Bai D, Li D, Zhao C, Wang Z, Shao M, Guo B, Liu Y, Wang Q, Li J, Guo S, Wang R, Li Y-h, Qiu L-j and Jin X (2022) Estimation of soybean yield parameters under lodging conditions using RGB information from unmanned aerial vehicles. *Front. Plant Sci.* 13:1012293. doi: 10.3389/fpls.2022.1012293

COPYRIGHT
© 2022 Bai, Li, Zhao, Wang, Shao, Guo, Liu, Wang, Li, Guo, Wang, Li, Qiu and Jin. This is an open-access article distributed under the terms of the Creative Commons Attribution License (CC BY). The use, distribution or reproduction in other forums is permitted, provided the original author(s) and the copyright owner(s) are credited and that the original publication in this journal is cited, in accordance with accepted academic practice. No use, distribution or reproduction is permitted which does not comply with these terms.

Estimation of soybean yield parameters under lodging conditions using RGB information from unmanned aerial vehicles

Dong Bai[1†], Delin Li[1†], Chaosen Zhao[2†], Zixu Wang[1], Mingchao Shao[1], Bingfu Guo[2], Yadong Liu[1], Qi Wang[1,3], Jindong Li[1,4], Shiyu Guo[1,3], Ruizhen Wang[2], Ying-hui Li[1*], Li-juan Qiu[1*] and Xiuliang Jin[1,4*]

[1]The National Key Facility for Crop Gene Resources and Genetic Improvement (NFCRI)/Key Laboratory of Crop Gene Resource and Germplasm Enhancement (MOA)/Key Laboratory of Soybean Biology (Beijing) (MOA), Institute of Crop Science, Chinese Academy of Agricultural Sciences, Beijing, China, [2]Nanchang Branch of National Center of Oil Crops Improvement, Jiangxi Province Key Laboratory of Oil Crops Biology, Crops Research Institute of Jiangxi Academy of Agricultural Sciences, Nanchang, China, [3]College of Agriculture, Northeast Agricultural University, Harbin, China, [4]National Nanfan Research Institute (Sanya), Chinese Academy of Agricultural Sciences, Sanya, China

The estimation of yield parameters based on early data is helpful for agricultural policymakers and food security. Developments in unmanned aerial vehicle (UAV) platforms and sensor technology help to estimate yields efficiency. Previous studies have been based on less cultivars (<10) and ideal experimental environments, it is not available in practical production. Therefore, the objective of this study was to estimate the yield parameters of soybean (Glycine max (L.) Merr.) under lodging conditions using RGB information. In this study, 17 time point data throughout the soybean growing season in Nanchang, Jiangxi Province, China, were collected, and the vegetation index, texture information, canopy cover, and crop height were obtained by UAV-image processing. After that, partial least squares regression (PLSR), logistic regression (Logistic), random forest regression (RFR), support vector machine regression (SVM), and deep learning neural network (DNN) were used to estimate the yield parameters. The results can be summarized as follows: (1) The most suitable time point to estimate the yield was flowering stage (48 days), which was when most of the soybean cultivars flowered. (2) The multiple data fusion improved the accuracy of estimating the yield parameters, and the texture information has a high potential to contribute to the estimation of yields, and (3) The DNN model showed the best accuracy of

training (R^2=0.66 rRMSE=32.62%) and validation (R^2=0.50, rRMSE=43.71%) datasets. In conclusion, these results provide insights into both best estimate period selection and early yield estimation under lodging condition when using remote sensing.

KEYWORDS

UAV, yield, soybean, lodging, machine learning

1 Introduction

Global soybean (*Glycine max* (L.) Merr.) production steadily increased during the last two decades, primarily in the United States, Brazil, Argentina, China, Paraguay, and India, which accounted for 94.3% of the global soybean production in 2021 (Agriculture, 2021). Accurately estimating the yields at the early crop growth stage is important for the government to deploy the appropriate share of imports.

Traditional ways of estimating soybean yield rely on destructive sampling and manual experience (Jin et al., 2021), they are time-consuming. Traditional methods of estimating yields utilize plot yield as a qualitative indices (Geipel et al., 2014), it is strongly influenced by the environment and a variety of biotic factors (Hamblin et al., 1978) if there are a lot of cultivars and a small plot area. So more stable yield parameters (grain number of seeds per plant and grain weight per plant) were used as field yield study data (Hamblin et al., 1978). Most types of yield estimation neglect the effects of micro-environmental factors owing to the large plot areas and a limited number of cultivars (Ji et al., 2022), so they were highly accurate in approximating the mean value of the yield of cultivars but not were not effective at truly identifying germplasm resources.

In recent years, high-throughput phenotyping has garnered increasing attention, particularly the use of unmanned aerial vehicles (UAVs) as a phenotyping platform combined with high-quality image sensors (Guo et al., 2021). High-throughput UAV phenotyping can not only reduce the threshold of traditional phenotyping but can also efficiently locate genes (Sukumaran et al., 2018) and provide basic data support for molecular biology and the genetic breeding of crops (Venkatalaxmi et al., 2004). With the developments of multi-spectral sensors (Maimaitijiang et al., 2017), hyperspectral sensors (Yue et al., 2018) and lidar (Jin et al., 2015), it can provide tens of millions of MB data support for the identification of diverse phenotypes and genotypes and molecular breeding (Potgieter et al., 2017). But previous yield estimates have utilized relatively inaccessible multispectral, hyperspectral (Paulus and Mahlein, 2020), and even radar data, which are highly accurate but unsuitable in real field plots.

In previous studies the UAV-derived datasets were used to estimate multiple vegetation traits (Maimaitijiang et al., 2017) and yield. The primary methods of estimating yields include physical models and machine learning models. Crop growth models have been proposed to estimate crop yields under different scenarios, including climate, genotype, soil properties, and management factors (Araus et al., 2021). For example, Ma et al. (2022) used the single algorithm for yield (SAFY) crop growth model to estimate the yields of wheat (*Triticum aestivum* L.). The results obtained an R^2 of 0.73, 0.83, and 0.49 for the leaf area index (LAI), biomass, and yield with root mean square error (RMSE) values of 0.72, 1.13 t/ha and 1.14 t/ha (Ma et al., 2022). Jin et al. (2022) conducted research on the ChinaAgrosys crop model on wheat. The R^2 of estimated maturity, LAI, and yield were higher than 0.73, 0.44, and 0.60 (Jin et al., 2022). These models can provide reasonable explanations for a variety of biochemical mechanisms and responses, but there are deficiencies in the input parameters to estimate the yield under complex and unpredictable scenarios (Zhao et al., 2013). In addition, previous studies estimated yields using multispectral images for machine learning or deep learning. Khaki and Wang (2019) applied deep neural networks to estimate the yield of maize (*Zea mays* L.) hybrids using environmental data. The use of weather data reduced the RMSE to 11% of the average yield and 46% of the standard deviation (SD) (Khaki and Wang, 2019). Feng et al. (2021) proposed a geographically and temporally weighted neural network (GTWNN) model for 12 years of data from 2008 to 2019, and the GTWNN outperformed other models (Feng et al., 2021). Maimaitijiang et al. (2020) used five machine learning algorithms to estimate the yield of soybeans, and DNN-F2 was the most accurate with an R^2 of 0.72 and a relative root mean square error (RMSE%) of 15.90% (Maimaitijiang et al., 2020). PLSR and RFR were used for quantifying soil salinity (Wang et al., 2018). The validation accuracy showed that the RFR model performed better than the model of PLSR. The most effective model was built based on the 1.5th order derivative of RF with respect to absorbance with

the best values of R^2 (0.93), RMSE (4.57 dS m(-1)). SVM is mostly used for disease classification and monitoring, and known studies include A. O. Conrad et al. (2020) used SVM to build and evaluate the accuracy of disease prediction models based on supervised classification. Sparse partial least squares discriminant analysis was used to confirm the results. The most accurate model comparing mock-inoculated and inoculated plants was SVM-based with an overall test accuracy of 86.1% (N = 72), while the most accurate SVM model had an overall test accuracy of 73.3% (N = 105) (Conrad et al., 2020).

In summary, although studies on estimating yield have been conducted quite frequently, these data are basically from a limited number of cultivars (<10), and thus, are not widely applicable and can only be considered to be an exploration of the technique. In addition, they rarely consider the yield status under specific environmental conditions, while the constant environmental variability in the field has crucial effects on yield.

Therefore, in this study, the performance of five algorithms to estimate yield parameters under lodging conditions was estimated, and the optimal time point to estimate yield during the early dates was studied based on more than 1,500 soybean germplasm cultivars. The aims of this study were to 1) Find the most suitable time point to estimate the yield parameters of soybean. 2) Test the multi-data fusion of vegetation indices, canopy cover, and crop height based on a Digital Elevation Model (DEM), lodging, and texture indices to estimate yield using different machine learning algorithms, and 3) To assess the effect of lodging on the grain number of seeds per plant and grain weight per plant.

2 Materials and methods

2.1 Materials

2.1.1 Study area

The experiment was conducted from July to November 2020 in Nanchang, Jiangxi Province, China (115°27' ~116°35' E, 28° 10' ~29° 11' N), which has a humid subtropical monsoon climate, abundant precipitation of 2,167.9 mm in 2020 (Nanchang weather station NO.58606), average annual sunshine of 1,772~1,845 hours, long summer and winter and short spring and autumn throughout the year, and an average annual temperature of 17.0°C-17.7°C. The experimental terrain is a plain, with an average elevation of 22 m. The experimental area of 0.92 acres was located in the southwestern suburbs of Nanchang City (Figure 1).

A total of 1,615 cultivars and 190 plots of controls (30 cultivars) were sown on July 15, 2020, and the UAV photos were collected at 17 time points (Li et al., 2022), which represented different growing stages. Some of those cultivars that had either a low germination or were under abiotic/biotic stresses were also studied to maintain high diversity, instead of dropping in the previous study (Li et al., 2022). The soybean cultivars came from worldwide and the largest number of cultivars were from China (70%), followed by the USA and Europe, and covered a wide range of ecotypes. The growth states of the different cultivars differed significantly. The plots were 1.8 m × 0.8 m with two rows and 10 cm plant spacing, so there were 1,805 plots in total. They were separated by furrows. Conventional N P K compound fertilizer of potassium sulfate 15:15:15 was applied once (K_2O_4S, 50%, 112.5kg/ha).

2.1.2 Image collection parameters

A DJI Phantom 4 (DJI Technology Co., Shenzhen, China) was used to collect the image data. As detailed in Table 1, the image was outputted in the tiff format. The UAV (unmanned aerial vehicle) platform was implemented with an autopilot system (Şahin et al., 2022) to execute a predefined flight from 10:00 to 14:00 every 3 days for 20 minutes. To avoid the partial loss of image texture feature information owing to cloud cover, weather with stable solar radiation intensity and a clear and cloudless sky was selected to acquire the images. The images had a resolution of 1,600*1,300 pixels, and all the flight missions were planned at the flight altitude and speed of 12 m and 1.2 m/s with the lateral and forward overlaps (Kose and Oktay, 2020) of 75% and 60% (before 13 September)/75% (after 13 September), respectively. Real-time kinematic (RTK) was used for positioning. The RTK accuracy that was enabled was ± 0.1 m vertically and horizontally (Oktay and Coban, 2017). The quality of images was checked after the flight.

The experimental field design required that the soybean planting site be treated with weed control in advance. Therefore, the effect of weeds on each indices of the image was not considered in this study. The 0.5 m × 0.5 m image ground control points (GCPs) set between the different routes were kept constant throughout the soybean growing stages. Agisoft PhotoScan software (Agisoft LLC, St. Petersburg, Russia) was used to stitch the UAV digital images. The software can perform image geometry correction and eliminate the effects of UAV attitude changes based on GCPs.

2.2 Methods

2.2.1 Overview for data process

This work used the UAV data and manually collected data. The UAV data consisted of RGB (red, green, blue) and DEM (digital elevation model) data. The degree of lodging and yield parameters (grain number of seeds per plant and grain weight per plant) were collected manually. The RGB data were calculated for vegetation indices, including texture information and canopy cover. The normalized results of crop height were calculated using DEM. After the Indices and data had been screened, the datasets were divided into a training dataset (70%) and a testing dataset (30%), followed by modeling using five

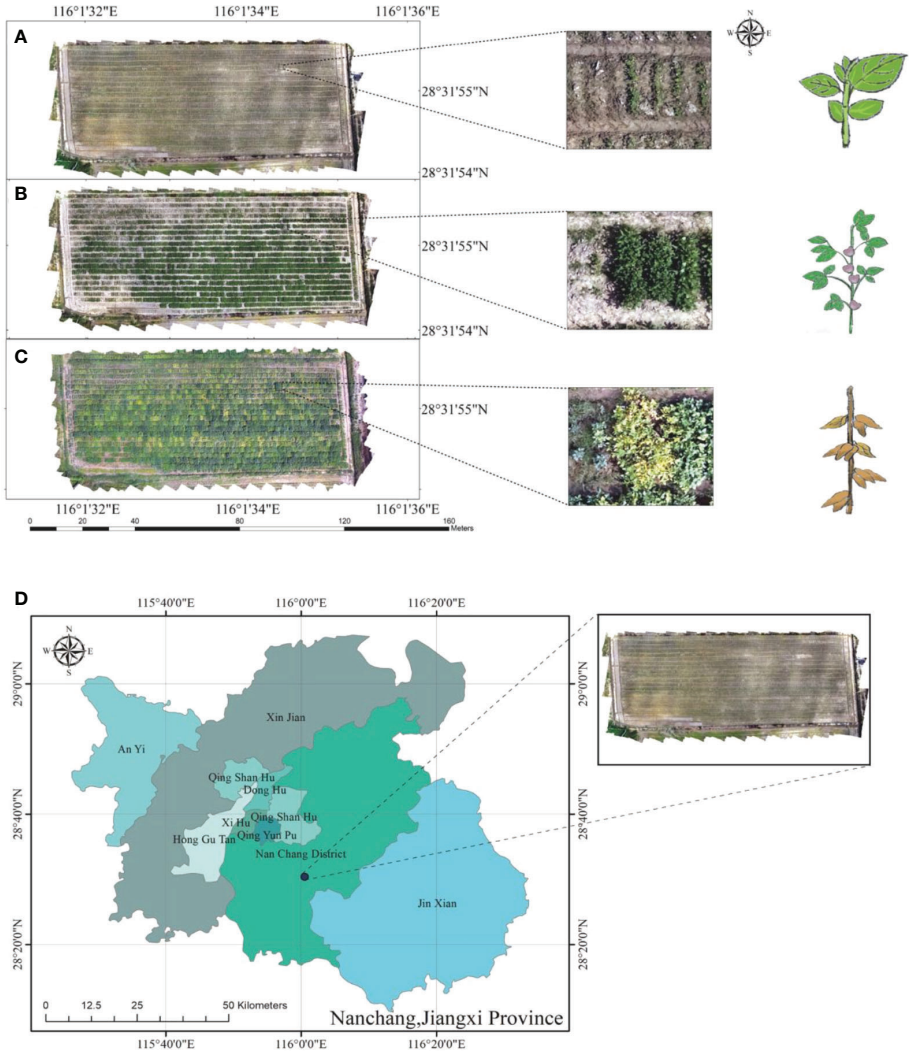

FIGURE 1
Study area. **(A)** RGB orthomosaic map on August 1, 2020. **(B)** RGB orthomosaic map on August 20, 2020. **(C)** RGB orthomosaic map on September 24, 2020. **(D)** The test field was in Nanchang, Jiangxi Province, China.

machine learning algorithms, and the performance of the models was finally evaluated to estimate the yield parameters. The flowchart is shown in Figure 2, and the details are discussed below.

2.2.2 Measurements of yield parameters

The yield parameters used in this work were the grain number of seeds per plant and the grain weight per plant Figure 3A. The mean value was calculated after 10~15 plants were randomly selected in each plot after harvest. The lodgings were monitored by experts from the Jiangxi Academy of Agricultural Sciences (Nanchang, China) to ensure reliable data during the whole growth stage. The levels of lodging severity were divided into five classifications (1-5) (Kato et al., 2021). The degree of tilting stalks at maturity was used to divide the plots with level 1 indicating that all the plants in plot were upright, and level 5 indicating that all the plants in plot had lodged Figures 3B, C. Stalk strength, root traits, and biological yield, which are closely related to lodging, were not considered mechanistically. Thus, a comprehensive index approach was not utilized to evaluate lodging resistance.

2.2.3 Image pre-processing

(i) Stitching images. Agisoft Photo-Scan Professional Version 1.2.2 (Agisoft LLC) was used to stitch images, it can process photos based on multi-view 3D reconstruction technology. (ii) Georeferencing used map coordinates to locate the image. By georeferencing raster data, multi-period raster

TABLE 1 Drone technical details.

Project	Technical details
Time per flight	Approximately 20 minutes
Hover accuracy	When RTK is enabled and RTK is working properly: Vertical: ± 0.1 m; Horizontal: ± 0.1 m
Controlled rotation range	Pitch: -90 degrees to +30 degrees
Image sensor	6 1/2.9-inch CMOS; Single sensor: 2.08 million effective pixels (2.12 million total pixels)
Lens	FOV: 62.7 degrees; Focal length: 5.74 mm (35 mm format equivalent: 40 mm); Infinity fixed focal length; Aperture : f/2.2
The resolution of the image	1600×1300(4:3.25)

CMOS, complementary metal oxide semiconductor (an image sensor); RTK, real-time kinematic.

data can be viewed, queried, and analyzed together. Typically, raster data is georeferenced using existing spatial data in the desired map coordinate system. Images from August 1, 2020 were used in this study. This process involved identifying a series of GCPs (with known x, y coordinates) to link the location of the raster dataset with the location of the spatial reference data (target data). The control points were precisely identifiable locations in the raster dataset and actual coordinates. More than 10 coordinate points for each plot were selected for georeferencing in this study. (iii) The images were cropped after georeferencing using ESRI ArcGIS 10.7 (Redlands, CA, USA) to outline the mask data, the software can be used to create maps, perform spatial analysis, and manage data. Since each plot was not strictly the same size during pre-planting, the specific criteria for outlining plots were to remove roads and furrows. Interactive data language (IDL) was then used to crop the images. The IDL code was written by ENVI 5.3 (Exelis Visual Information Solutions, L3Harris Geospatial, Boulder, CO, USA) (Figure 4). ENVI provides professional spectrum analysis tools, extended functions can also be written using IDL.

2.2.4 Vegetation indices Extraction

The vegetation indices were extracted using RGB images and MATLAB R2021a (MathWorks, Portola Valley, CA USA). Vegetation Indices can be constructed to enhance the interpretation of remote sensing images through the linear or nonlinear combination of two or more characteristic bands and play an important role in crop growth monitoring. ExG and ExGR are two common visible bands used as vegetation indices. They provide a near binary intensity image that outlines the vegetation area of interest, and then the vegetation information can be extracted through threshold segmentation. The color index of vegetation extraction (CIVE) integrates the red, green, and blue bands to enhance the vegetation information. In addition, the Green-Red Ratio Index (GRI), Green-Red Vegetation Index (GRVI), Modified Green-Red Ratio Vegetation Index (MGRVI), Visible Atmospheric Resistance Index (VARI), and Warbeck Index (WI) change the linear exponential to form a ratio to enhance the differences among different cultivars. The Soil Adjusted Vegetation Index (SAVI) reduces the sensitivity of soil to traditional vegetation indices and thus, reduces their impact. The red green blue VI (RGBVI) is defined as the normalized difference of the squared green reflectance and the product of blue × red reflectance. The

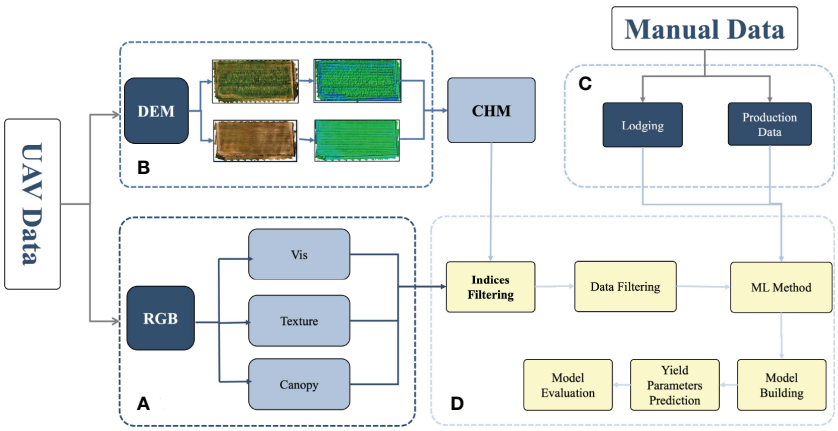

FIGURE 2
Flowchart for estimating the yield parameters. **(A)** RGB indices extraction process. **(B)** Calculation of the plant height using DEM. **(C)** Manual data, including lodging and yield parameters, such as the grain number of seeds per plant and grain weight per plant. **(D)** Data cleaning and model building. DEM, digital elevation model; RGB, red green blue.

10.3389/fpls.2022.1012293

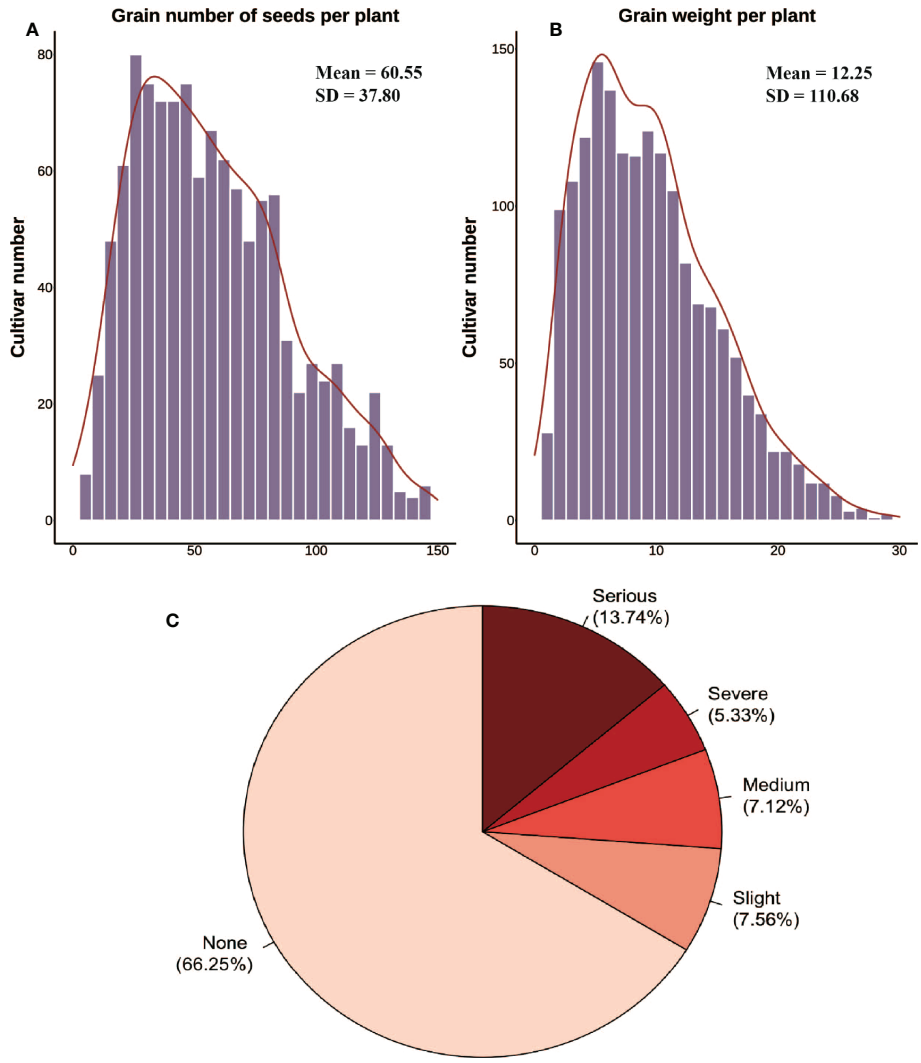

FIGURE 3
Yield parameters and inversions collected manually. **(A, B)** Histogram distribution of the grain number of seeds per plant and the grain weight per plant from manual surveys. **(C)** Lodging classification and percentage.

vegetative index (VEG) was designed to manage the variability of natural daylight illumination. The VDVI (visible-band difference vegetation index) was constructed based on the normalized diffuse vegetation index (NDVI) but only used the visible band, which can render the vegetation and non-vegetation index values more compact. comb1 and comb2 are indices that are specifically used to determine greenness. They are linear combinations of ExG, ExGR, CIVE, and VEG. The plant pigment ratio (PPR) is an index that produces an output image in which strongly pigmented foliage presents a high PPR, while weakly pigmented foliage has a low PPR. In summary, these 15 visible bands vegetation indices were used in this study as shown in Table 2.

2.2.5 Canopy coverage extraction

Threshold segmentation is a simple method to extract interesting regions from grayscale images. In this experiment, the binary images were generated using the excess green index (EGI, (2G-R-B)/G). The threshold value ($Green_{threshold}$) was established as 0.05 for canopy cover and background segmentation. First, the EGI was calculated using the three channels (R, G, B) of the image, and the EGI values > the green threshold corresponded to the canopy (binary value = 1). The values < $Green_{threshold}$ corresponded to the soil (binary value = 0). The percentage of canopy (binary value = 1) pixels in an image was calculated as the canopy coverage. Finally, the canopy coverage of all the plots was calculated in turn.

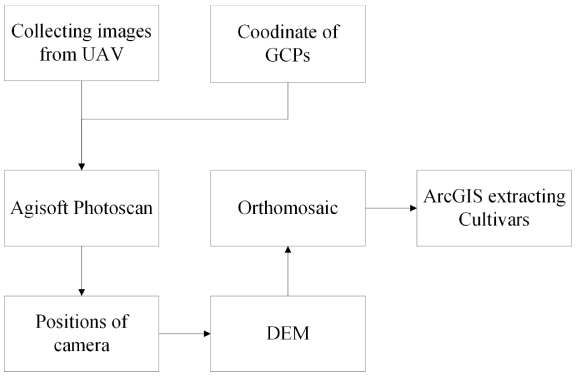

FIGURE 4
Flowchart of the UAV RGB image mosaic processing.

2.2.6 Crop height extraction

In this study, crop height (CH) was extracted from the RGB image point clouds and used as a canopy structure indicesto estimate the yield parameters. UAV-based RGB images were collected at an earlier stage of plant emergence on August 1, 2020, to create a bare ground DEM using a photogrammetric three-dimensional (3-D) point cloud. Height peaks within the plot were segmented using the Otsu algorithm (Qiao and Sun, 2014), and the lower peaks were used as the bare ground height. Digital surface models (DSM) were created from UAV-based RGB images collected after August 1, 2020. After that, a crop height model (CHM) was obtained from pixel-level subtraction of the DSM and DEM with subsequent normalization. A total of 190 manually collected ground CH measurements were used to assess the accuracy of the CHM (Figure 5). OBM is manually collected crop height. The distribution of CH reflects the different genotypes and the heterogeneity of soybean fields.

2.2.7 Texture information extraction

The texture information was extracted using Python version 3.8 (Python Software Foundation, Wilmington, DE, USA) and PyCharm version 2021.3.3 (JetBrains, Prague, Czechia). The texture is a common method used to extract image information in digital image processing. Although there is no formal definition of texture, this descriptor intuitively measures its properties. Calculating the texture consists of two methods: statistical and spectral methods, with statistical methods producing texture information, such as smoothness, roughness, and graininess. Spectral methods are based on the nature of Fourier spectrum and focus on detecting global periodicity in an image by identifying high-energy narrow peaks in the spectrum (Bharati et al., 2004). The spectral texture information of the canopy was calculated using RGB

TABLE 2 Summary of the RGB-based vegetation index.

VI	Abbreviation	Equation	Reference
R_n	R_n	=R/R(max)	Arroyo, Guijarro, & Pajares et al. (2016) (Arroyo et al., 2016)
G_n	G_n	=G/G(max)	
B_n	B_n	=B/B(max)	
r	r	$=R_n/(R_n+G_n+B_n)$	Guijarro et al. (2011) (Guijarro et al., 2011)
g	g	$=G_n/(R_n+G_n+B_n)$	
b	b	$=B_n/(R_n+G_n+B_n)$	
Color Index of Vegetation Extraction	CIVE	=18.78745+(0.44r)-(0.88g)+(0.385b)	Kataoka et al. (2003) (Kataoka et al., 2003)
Combined 1	COMB1	=(0.25ExG)+(0.3EXGR)+(0.33CIVE)+(0.12VEG)	Guijarro et al. (2011)
Combined 2	COMB2	=(0.36ExG)+(0.47CIVE)+(0.17VEG)	Guijarro et al. (2011)
Excess Green	ExG	=(2g)-r-b	Woebbecke et al. (1995) (Woebbecke et al., 1995)
Excess Green Minus Excess Red	EXGR	=ExG-(1.4r)-g	Guijarro, & Pajares (2011) (Guijarro et al., 2011)
Ratio Green Red Index	GRI	=G/R	Li et al. (2010) (Li et al., 2010)
Green Red Vegetation Index	GRVI	=(G-R)/G+R	Gitelson et al. (2002) (Gitelson et al., 2002)
Modified Green Red Vegetation Index	MGRVI	$=(G^2-R^2)/(G^2+R^2)$	Bendig et al. (2015) (Bendig et al., 2015)
Plant Pigment Tatio	PPRb	=(G-B)/(G+B)	Metternicht et al. (2010) (Metternicht, 2010)
RGB Vegetation Index	RGBVI	$=((G^2-(R*B))/((G^2+(R*B))$	Bendig et al. (2015)
Soil Adjusted Vegetation Index	SAVI	=1.5(G-R)/(G+R+0.5)	Li et al. (2010)
Visible Atmospherically Resistant Index	VARI	=(G-R)/(G+R-B)	Gitelson et al. (2002)
Visible Difference Vegetation Index	VDVI	=(2G-R-B)/(2G+R+B)	Wang et al. (2015) (Wang et al., 2015)
Vegetation Index	VEG	$=g/r^a b^{(1-a)}$.∴a=0.667	Hague, Tillett, & Wheeler (2006) (Hague et al., 2006)
Woebbecke Index	WI	=(g-b)/|r-g|	Woebbecke et al. (1995)

R, G, and B represent the DN variables from digital image red, green, and blue bands, respectively.

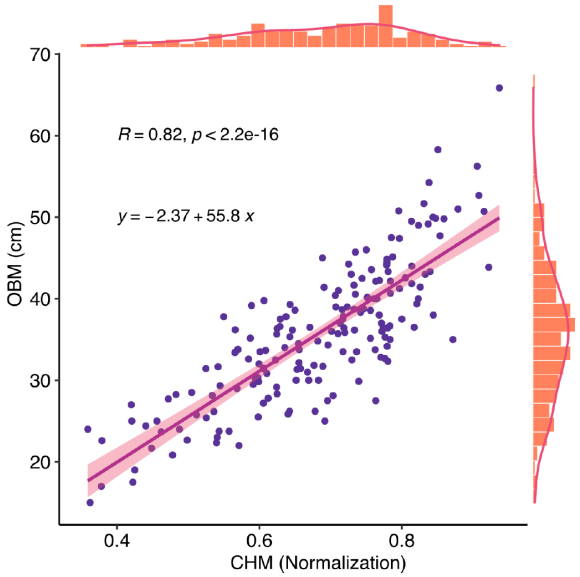

FIGURE 5
Correlation between CHM and Observation. CHM is crop height model, it is the plant height estimated data.

data. This texture information was extracted from the RGB-based grayscale co-occurrence matrix (GLCM) of the red, green, and blue bands. The GLCM texture consists of nine indices, including the mean, variance, homogeneity, contrast, dissimilarity, entropy, energy, correlation, and autocorrelation. The processing window is 3 rows x 3 columns. To obtain more texture information, the mean, minimum, maximum, SD, and coefficient of variation (CV) values of the GLCM metrics within each plot were calculated. Thus, nine (GLCM indices) × three (bands) × five (statistical metrics) = 135 RGB texture variables that were generated.

2.2.8 Indices selection

Indices selection is an important step in machine learning. The indices determine the upper bound of the model if the algorithm determines the lower bound of it. In addition, it is important to note that the model with as many indices as possible will not always perform better. Sometimes several indices will provide the desired result, and the high correlation indices cannot always be deleted directly to obtain a better performing model. This study tried many methods to filter the indices. Boruta (Kursa and Rudnicki, 2010) used a random forest approach based on the Boruta algorithm to screen the initial 72 Indices, the complete list of indices is given in the supplementary table (Table S1). It disrupts the order of indices and calculates the importance of indices. In this study, the lodging and canopy cover were not participants in the screening process. The indices matrix was then shuffled, and the shadow indices were combined with the real indices to form a new Indices matrix. The indices were selected or removed in order of importance.

The steps for running the Boruta algorithm are as follows:

1. First, it adds randomness to a given dataset by creating mixed copies of all the indices (shuffled features).
2. It then trains an extended dataset for random forest classification and uses an indices importance measure (set by default to an average reduction in precision) to evaluate the importance of each indicator, with a higher meaning indicating greater importance.
3. In each iteration, it checks whether a true indices has higher importance than the best-shaded indices (whether the indices scores higher than the largest shuffled indices) and keeps removing indices that it considers to be very unimportant.
4. Finally, the algorithm stops when all the indices have been confirmed or rejected, or when the algorithm reaches a prescribed limit for the operation of the random forest.

Boruta follows all the relevant indices selection methods, which capture all the indices related to the outcome variable. In contrast, most traditional indices selection algorithms follow a minimal optimization approach, which relies on a small subset of indices and produces a minimal error in selecting the classification. Compared to traditional indices selection algorithms (recursive feature elimination algorithms [RFE] (Liu and Wang, 2021)). Boruta can generate better results on the importance of the indices and is also easy to interpret.

2.2.9 Data filtering

Outliers from the remaining indices were removed using the One-Class-SVM outlier detection algorithm, which uses the appropriate Python version 3.8 (Python Software Foundation, Wilmington, DE, USA) packages and environment. One-class-SVM uses a spherical rather than a planar approach and the algorithm obtains a spherical boundary around the data in the feature space, a hypersphere whose volume is minimized, thus minimizing the effect of outliers.

One-Class-SVM (Tax and Duin, 1999) can be a good outlier detection method when the data dimensionality is very high, or there are no assumptions about the distribution of the data. It finds the hyperplane for the partition and the support vector machines using the support vector domain description (SVDD) idea. All the samples that are not anomalies are expected to be positive classes for SVDD, and it uses a hypersphere instead of a hyperplane to divide. The algorithm obtains a spherical boundary around the data in the feature space and expects to minimize the volume of this hypersphere, thus, minimizing the effect of outlier data. It is possible to determine whether the data is within or not after the LaGrange dual solution was used. If the

distance ≤ to the radius, it is not an anomaly, and if it is outside the hypersphere, it is an anomaly.

In this study, a radial basis function kernel is used with a gamma value of 0.001, a lower bound on the support vector fraction of 0.03, a residual convergence condition of $1e^{-3}$, and the remaining parameters as default. The values are based on experience or multiple attempts to select the most suitable parameter value. To satisfy this condition means wrapping all the suitable data points in the sphere to achieve unsupervised outlier detection.

In scikit-learn version 0.23.2 (Pedregosa et al., 2012), One-Class-SVM (Pedregosa et al., 2012) was used to detect outliers using the SVM package.

2.2.10 Machine learning

Five machine learning algorithms were used to estimate yields in this study, including support vector machine regression (SVM), logistic regression (Logistic), random forest regression (RFR), partial least squares regression (PLSR), and DNN networks. All the model methods are based on the R language version 4.1.1 (R Foundation, Vienna, Austria) with the computation of DNN network using the h2o package version 3.34.0.3 (H2O.ai, Mountain View, CA, USA) package, which is based on Java but provides a computational interface between the R and Python. A total of 1,615 cultivars were divided into two parts, 0.7 and 0.3, as the training set and the validation datasets.

In this study, there were five principal components before calculations to elucidate the mean center of all the data in PLSR. During the process of data processing, leave-one-out cross-validation was performed serially; the cross-validation was optimized for speed, and some generality was sacrificed. In particular, the model matrix was calculated only once for the complete cross-validation. The jackknife method was also used to correct for bias (Seasholtz and Kowalski, 1992).

The Logistic were 10 folds. The first was to obtain the lambda sequence and calculate the result of the fit omitting each fold. The errors accumulated, and the mean error and SD of the folds were calculated. The alignment is "lambda", and the lambda values from the autonomous fit (all data) were used to rank the predicted values from each fold (Simon et al., 2011). The other parameters were set to default.

The random forest is the randomization of column variables and row observations of a dataset to generate multiple classifiers, and finally, the classification tree results are aggregated. Two important parameters are the number of variables preselected by tree nodes and the number of trees in the random forest. In this study, the number of variables preselected by the tree nodes was one-third of the dataset, and there were 500 trees in the forest (Edwards et al., 2018).

SVM can be formalized as a problem of solving convex quadratic programming and is also equivalent to the problem of minimizing the loss function of a regularized hinge. The learning algorithm of SVM is the optimization algorithm for solving convex quadratic programming. Radial was used as the kernel function here; gamma is 1/(data dimension); the termination criterion was 0.001, and epsilon in the insensitive-loss function was 0.01 (Fan et al., 2005).

DNN is a feedforward multilayer artificial neural network. In this study, the hidden layer has two hidden layers, each with 200 neurons, and 10 iterations are needed to make the network converge; the target ratio of communication overhead to computation was 0.05, and the learning rate was 0.005. These parameter settings are based on empirical or model-recommended optimal parameters (Xu et al., 2016).

2.2.11 Statistical indices

The coefficient of determination (R^2), root mean square error (RMSE) and relative root mean square error (rRMSE) were selected to test the training and validation models (Liu et al., 2021).

3 Results

3.1 Selection of the best estimation dates

All the indices (162 for every date) were used to identify the most suitable time point to estimate the yield parameters. Data were collected on 17 dates. Each of the data points for 17 days was used to provide a result to estimate the yield parameters. In general, the estimations for grain number per plant were poor before emergence to second trifoliolate stage (21 days after sowing), with a gradual increase at the third trifoliolate to the sixth trifoliolate stage (24~44 days after sowing) until the peak at flowering stage (48 days), and then a slow decline. The trend of the grain weight per plant was the same before flowering stage (44 days after sowing). The changes after seeds to maturity stage (48 days after sowing) were not obvious, and there were many abrupt changes. This was probably owing to the changes in the pixel colors that were impacted by weather. In addition, they can be affected by maturity (Figure 6). In this study, we wanted to obtain the earliest time point as the result, so on balance we chose the time point with the highest accuracy for early estimation and the critical fertility period of common interest in soybean production as the most appropriate time point for estimating yield parameters.

3.2 Selection of indices

The 48-day red band texture information and RGB vegetation indices were selected. These 72 indices (Table S1)

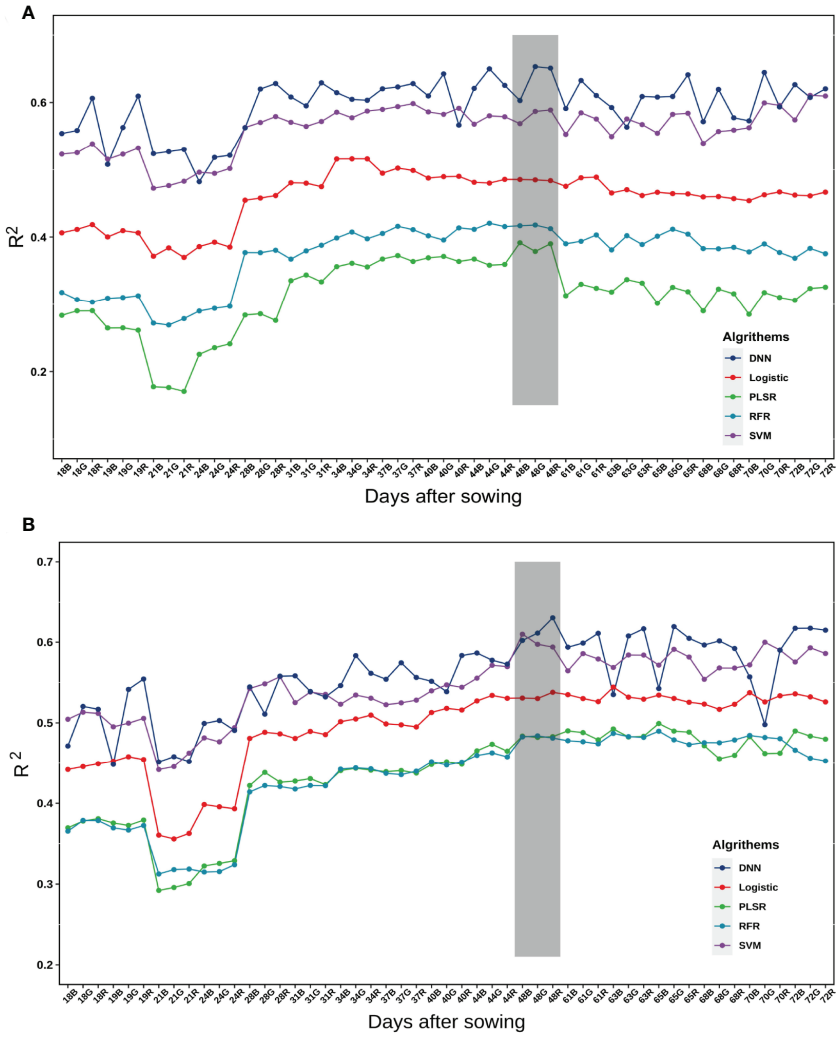

FIGURE 6
Accuracy of the estimation of different models on yield parameters at different dates. **(A)** Grain number of seeds per plant. **(B)** Grain weight per plant. The digital numbers represent the days after sowing, and R, G, and B represent the spectral bands. The grey background represents the selected optimal estimation model from day 48.

included 45 texture indices, 24 RGB vegetation indices, canopy cover, crop height, and lodging.

The indices of grain number of seeds per plant and the grain weight per plant were screened separately using the Boruta algorithm, which gave an average ranking of importance and a recommendation to eliminate data points (red) or retain them (blue) based on the results of 100 times ranking. The top indices for the grain weight per plant were the texture indices, while the vegetation indices were in the middle. Out of the 100 times importance rankings provided by the Boruta algorithm, indices with 80 times importance rankings below the shadow indices were marked red and removed. Thus, the nine indices associated with the maximum and minimum values in the red box plot in Figure 7B were deleted. The top importance for the grain number of seeds per plant was vegetation indices. The top one was lodging, and crop height was also advanced, but all the texture indices were ranked at the bottom (outside the top 10). The analysis of the grain weight per plant was the same as the grain number of seeds per plant. The nine indices that were deleted were the texture indices related to the maximum and minimum values with the red box plot in Figure 7A.

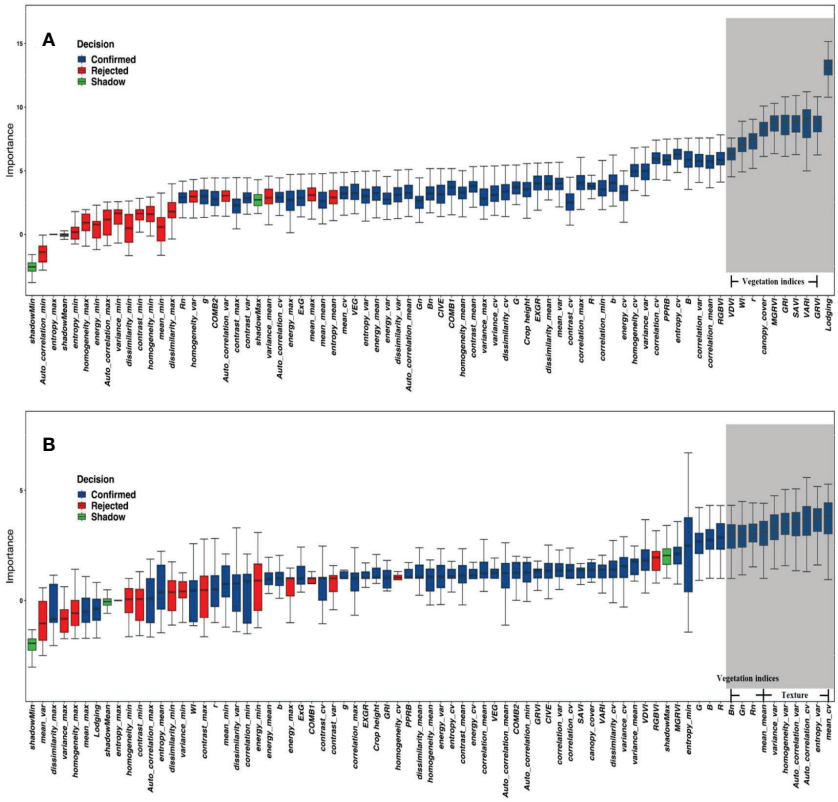

FIGURE 7
The importance of indices for yield parameters. **(A)** Grain weight per plant. **(B)** Grain number of seeds per plant. The red box plot was the indices recommended for removal; the blue box plot was the Indices recommended to be retained. The grey background represents the top 10 indices.

3.3 Study on the estimation of yield parameters by different indices and machine learning algorithms

3.3.1 Grain number of seeds per plant

The spectral information extracted from the RGB images was used to obtain texture information, canopy structure information, and crop height. Machine learning algorithms (support vector machines, random forests, partial least squares, logistic regression, and DNN neural networks) were used to estimate the grain number of seeds per plant in soybean.

As shown in Table 3, the combination of spectral and canopy structure information improved the accuracy of estimation of yield parameters. As the number of indices increased, the R^2 increased, resulting in a decrease in both the RMSE and rRMSE. The accuracy of estimation improved with the addition of texture indices for support vector machines and the DNN, while the others had limited changes. All the models had roughly the same optimization with the addition of crop height, and a significant change with the addition of lodging.

All the model methods performed similarly for single categories of indices. The SVM method performed slightly better, but the DNN network quickly outperformed the SVM when the indices were increased. They were clearly split into three levels. The RFR and PLSR methods were relatively poor, and the logistic method was in the middle, while the SVM and DNN methods performed better. The best yield estimates were $r^2 = 0.66$ and rRMSE=32.62% when the DNN method was used with 63 Indices (Figure 11).

The r^2 gradually increased as the number of input indices increased, and the rRMSE gradually decreased for all the regression methods, indicating that all the methods can handle the fusion of multimodal data to some extent. The DNN outperformed other methods because of the large amount of data in this study, but it has been demonstrated (Bonazza et al., 2019) that traditional machine learning algorithms may work better when there is less data. The DNN tends to perform better when analyzing larger sample sizes and more complex non-linear datasets.

Although the DNN neural network also performed well at estimating the grain number of seeds per plant, there was a

TABLE 3 The accuracy of estimation of different models for the grain number of seeds per plant.

Type	No. of indices	Metrics	PLSR	RFR	Logistic	SVM	DNN
VIs	25	R^2	0.40	0.37	0.41	0.44	0.43
		RMSE	26.69	27.46	26.41	25.98	26.30
		rRMSE	45.00%	46.30%	44.60%	43.92%	43.84%
VIs+TI	60	R^2	0.41	0.37	0.45	0.55	0.58
		RMSE	26.38	27.31	25.55	23.41	24.27
		rRMSE	44.52%	46.13%	43.15%	39.56%	42.34%
VIs+TI+CC	61	R^2	0.42	0.37	0.45	0.55	0.58
		RMSE	26.36	27.37	25.52	23.41	22.51
		rRMSE	44.56%	46.25%	43.17%	39.58%	38.76%
VIs+TI+CC+CHM	62	R^2	0.43	0.39	0.46	0.56	0.61
		RMSE	25.97	26.98	25.16	23.11	21.50
		rRMSE	43.80%	45.50%	42.50%	39.00%	38.00%
VIs+TP+CC+CHM+Lodging	63	R^2	**0.45**	**0.41**	**0.48**	**0.58**	**0.66**
		RMSE	**25.39**	**26.39**	**24.76**	**22.5**	**21.00**
		rRMSE	**42.97%**	**44.65%**	**41.86%**	**41.80%**	**41.70%**

VIs, vegetation index; TI, texture information; CC, canopy cover; CHM, crop height; DNN, deep learning network; Logistic, logistic regression; PLSR, partial least square regression; RFR, random forest regression; SVM, support vector machine regression. The best results in terms of R^2, RMSE, and rRMSE values through different indices with various modeling methods are shown in bold.

decrease in the validation dataset, which could be owing to errors in the manual measurement of data (Figure 8).

A comparison of the estimated dataset from each regression method with the observed dataset indicated that each method had a similar distribution of estimated yield parameters. In common with the performance of the existing studies (Maimaitijiang et al., 2017), all the regression methods underestimated the higher yield parameters of cultivars. Theoretically, this should not be an issue because we used flowering data in which the nutritional growth had ceased. In theory, there was no longer a significant increase in pod number. However, 48 days may not be the flowering period for all the cultivars, and some flowered late. This resulted in the lack of determination of the grain number of seeds per plant during this period (Figure 8).

3.3.2 Grain weight per plant

As shown in Table 4, the combination of all the information (r^2 = 0.64 in the training dataset and r^2 = 0.49 in the validation dataset) resulted in the most accurate estimation, and the accuracy of the model increased with each additional category of indices. Moreover, unlike the grain number of seeds per plant, the 48-day vigorous growth state (specifically the photosynthetic state) determined the final amount of biomass that accumulated in the final plant to some extent, i.e., the result of the grain weight per plant.

The combination of all the information was more accurate than single category data for estimating the yield regardless of the method used. The r^2 ranged from 0.47 to 0.63 where the grain weight per plant was more accurate than the grain number of seeds per plant, possibly because the plant nutrition influenced by canopy information was more likely to change the grain weight than the grain number of seeds. However, the texture information had a more pronounced effect on the grain weight than the grain number of seeds, possibly because the texture is related to photosynthesis (Heckmann et al., 2017). It should be noted that the improvement in the estimation of yield parameters with texture information compared with the vegetation indices was not only substantial but suggested that, although some methods have been used to remove redundant data, it still contains a large proportion of redundant information (Figure 9).

When all the data were combined to estimate yield, the DNN neural network performed better for both the grain number of seeds per plant and the grain weight per plant. DNN outperformed the other machine learning algorithms for both training datasets and validation datasets by a large margin. SVM also performed well on the training dataset, but it performed the validation dataset less accurately (Figure 10).

Unlike the grain number of seeds per plant, the estimation for grain weight was not underestimated at higher values. There are two likely reasons for this. (1) They were easier to measure and gave more accurate results without too many outliers. (2) The state of canopy was a greater determinant for the formation of grain weight. There could be a deeper reason for this different performance in estimating the grain number of seeds per plant and grain weight per plant, and more experiments can be designed to determine the answer.

10.3389/fpls.2022.1012293

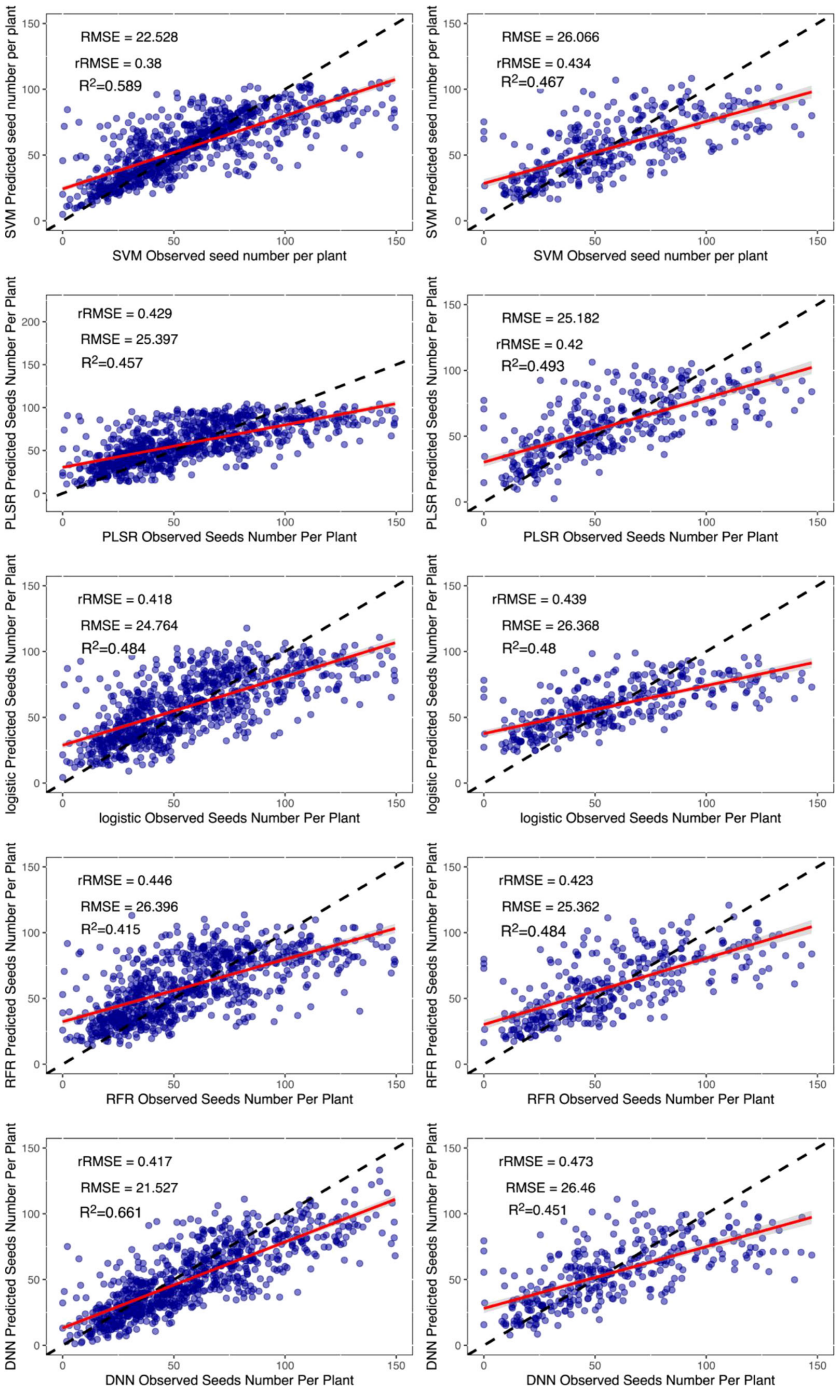

FIGURE 8
Results of machine learning algorithms to estimate the grain number of seeds per plant. The left column is the training dataset, and the right column is the validation dataset. The black dashed line is the 1:1 line, and the red solid line is the data fitted line. SVM, support vector machines regression; RFR, random forests regression; PLSR, partial least squares regression; Logistic, logistic regression; DNN, deep neural network.

TABLE 4 The accuracy of estimation of different models for grain weight per plant.

Type	No. of indices	Metrics	PLSR	RFR	Logistic	SVM	DNN
VIs	25	R^2	0.43	0.42	0.45	0.48	0.48
		RMSE	3.98	3.97	3.98	3.83	3.88
		rRMSE	42.96%	42.53%	41.42%	41.26%	43.52%
VIs+TI	60	R^2	0.45	0.45	0.51	0.58	0.58
		RMSE	3.89	3.86	3.67	3.4	3.541
		rRMSE	41.72%	41.31%	39.33%	36.34%	39.45%
VIs+TI+CC	61	R^2	0.45	0.46	0.51	0.59	0.61
		RMSE	3.9	3.85	3.67	3.40	3.28
		rRMSE	41.75%	41.26%	39.32%	36.47%	35.29%
VIs+TI+CC+CHM	62	R^2	0.48	0.49	0.52	0.61	0.62
		RMSE	3.78	3.74	3.60	3.31	3.25
		rRMSE	40.4%	40.00%	38.52%	35.40%	35.32%
VIs+TI+CC+CHM+Lodging	63	**R^2**	**0.48**	**0.49**	**0.53**	**0.62**	**0.64**
		RMSE	**3.78**	**3.76**	**3.6**	**3.287**	**3.16**
		rRMSE	**40.43%**	**40.22%**	**38.54%**	**35.18%**	**33.80%**

VIs, vegetation index; TI, texture information; CC, canopy cover; CHM, crop height; DNN, deep neural network; Logistic, logistic regression; PLSR, partial least squares regression; RFR, random forest regression; SVM, support vector machine regression. The best results in terms of R^2, RMSE, and rRMSE values through different sensors with various modeling methods are shown in bold.

4 Discussion

The optimal time point to estimate the yield parameters in this paper was 48 days (flowering). In maize and rice studies, Li et al. (2021) showed that crop yields can be satisfactorily forecasted one to three months before harvest (Li et al., 2021). Zhou et al. (2017) used three soybean cultivars to produce results that indicated that the best estimation period is the gestation period (Zhou et al., 2017). Previous research has provided results comparable to those of this study. However, there are some differences between them that could be attributed to two reasons. (1) The soybeans are dried by hand after harvest, which usually takes place when the plants are still green. Therefore, it is difficult to obtain data for soybeans during this stage. (2) In earlier studies, the limitation of the number of cultivars (usually < 5) resulted in the spectral information of the flowering period not being very distinguishable, while the later stage effects on yield were more obvious owing to the cumulative effects. That suggests that the results of these studies could be limited. In contrast, this study found that the flowering period was the best period to distinguish the cultivars, and the spectral information was more easily distinguished in this stage. Physiologically, this result is also supported by the fact that the flowering stage is a peak period for soybean growth and development. Although 48 days after sowing was used as the base data in this paper, in the future, a combination of Indices with a high correlation of yield (possibly from different times) could improve the accuracy of estimation. However, this would increase the difficulty of interpreting the established models to estimate yield. Another option could be to use a more reasonable time series-based model approach.

Previous studies used correlation (Hall, 1999) or recursive feature elimination (RFE) (Granitto et al., 2006) algorithms to remove indices. In comparison, the Boruta algorithm removed Indices that were maximum or minimum values for texture information. These values are usually unchanged or changed only slightly. They provide almost no information and create considerable interference information in the estimation results, thus, affecting the accuracy of estimating the experimental results. Overall, seven of the top 10 indices of the importance for grain weight per plant were texture indices, suggesting that the canopy structure is more influential for grain weight per plant than the vegetation indices. The mean of texture (top one) information reflects the degree of the neatness of growth, and a neater state of growth is likely to result in a higher grain weight per plant. The top 10 importance indices for the grain number of seeds per plant were vegetation indices that reflected the physiological status, while all the texture indices ranked lower, with lodging ranked first, followed closely by GRVI and VARI, which are all closely related to the biomass or NDVI. Zhou et al. (2017) also found that NDVI-related indices had a higher effect on yield (Zhou et al., 2017), and this study found that this effect could be attributed more to the grain number of seeds per plant than the grain weight per plant. Canopy cover reflects the ability of the vegetation to receive energy, suggesting that the state of the soybean itself may have a more pronounced effect on the grain number of seeds per plant. The effect of lodging on the grain number of seeds per plant was much greater than that for grain weight per plant, indicating its importance. The effect of lodging on yield has been evaluated very ambiguously in traditional agronomic research. Cooper (1971) studied the effect of early lodging on yield outcomes and identified a 21%

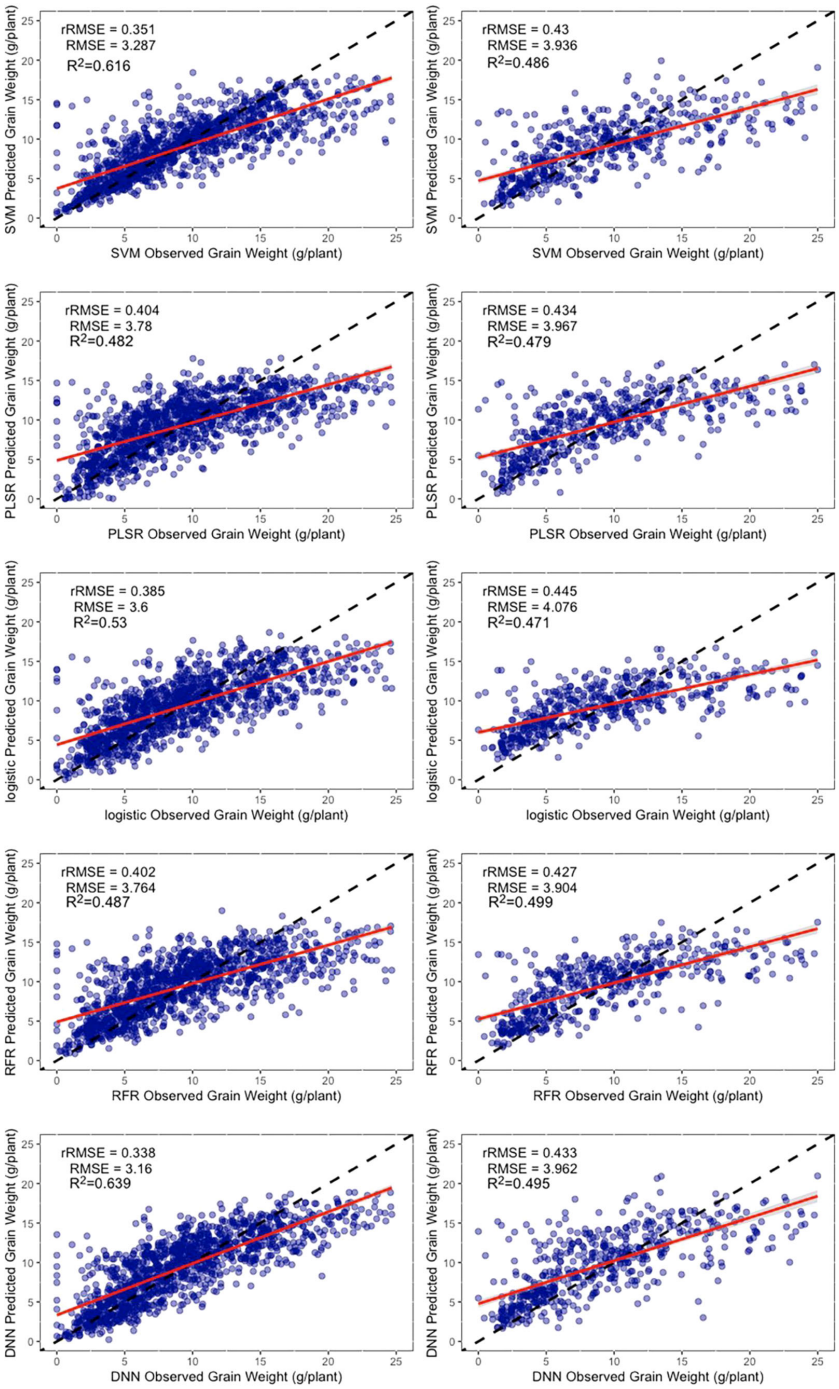

FIGURE 9
Results of the machine learning algorithms to estimate the grain weight per plant. The left column is the training dataset, and the right column is the validation dataset. The black dashed line is the 1:1 line, and the solid red line is the data fitted line. SVM, support vector machines regression; RFR, random forest regression; PLSR, partial least squares regression; Logistic, logistic regression; DNN, deep neural network.

decrease in yield (Cooper, 1971). However, they did not address the effect of lodging in more detail. This is primarily because lodging is a combination of several complex traits. A separate discussion of the different parameters of yield data could be a valid approach, and existing evaluation indices should be updated or reconstructed.

In contrast to the previous study, Maimaitijiang et al. (2020) also used some algorithms. They found less of a difference

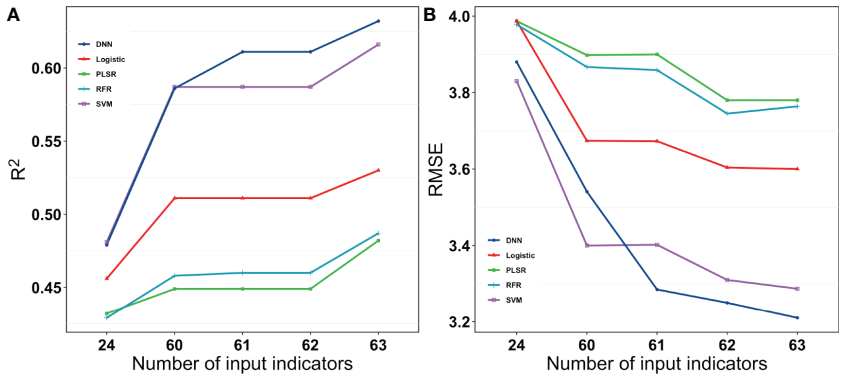

FIGURE 10
R^2 and RMSE for the different models with different input indices for grain weight per plant. 24 were vegetation indices. 60 were vegetation indices and texture indices. 61 were vegetation indices, texture indices, and canopy cover. 62 were vegetation indices, texture indices, canopy cover, and crop height. 63 were vegetation indices, texture indices, canopy cove, crop height, and lodging.

between the different algorithms, with an R^2 that ranged from 0.65 to 0.72 (Maimaitijiang et al., 2020). This could be because their results were based on only three cultivars. However, this study was based on a large number of cultivars to better distinguish the performance of the different algorithmic models. As for Figures 10 and 11, the five machine learning algorithms were clearly divided into three parts, which exhibit very different results. In addition, machine learning methods performed similarly to DNN-based regression when fewer indices were inputted, while the DNN outperformed other methods when more indices were utilized. An increase in the number of indices resulted in an increase in R^2 and a decrease in RMSE for all the regression methods. However, the magnitude of increase or decrease varied. The DNNs performed better than the other regression algorithms owing to the large amount of data in this study, but they do not have a very clear advantage when the dataset is smaller. This could be owing to the ability of deep learning to often outperform machine learning methods when processing larger sample sizes and complex non-linear datasets.

This work has some practical implications, firstly it given more accurate conclusions of existing modeling methods based on >1,500 cultivars, and we found a pronounced stratification of the model, which will have a positive impact between the technology and practical production. Secondly, instead of estimating traditional yields, we estimated two yield parameters and found that the effect of lodging was different, it provided with ideas for doing some other complex traits later.

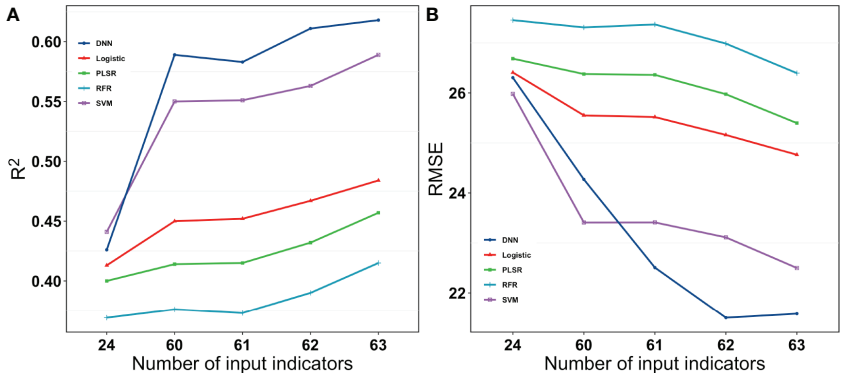

FIGURE 11
R^2 and RMSE for different models with different numbers of input Indices for the grain number of seeds per plant. 24 were vegetation indices. 60 were vegetation indices and texture indices. 61 were vegetation indices, texture indices, and canopy cover. 62 were vegetation indices, texture indices, canopy cover, and crop height. 63 were vegetation indices, texture indices, canopy cove, crop height, and lodging.

Finally, we evaluated the accuracy of the estimated yield parameters with early stage, these allowing breeders to evaluate the performance of specific cultivars at an earlier stage.

Although this study has extracted as many indices as possible to estimate the final yield parameters, the RGB itself contains limited information, which resulted in the poor accuracy of estimation. In addition, the diversity of cultivars that numbered >1,500 exacerbated this result. But RGB is more economical and practical than multiple spectral sensors, and it is impractical to use hyperspectral in large test field currently. Although existed hyperspectral methods will get better results, they are often obtained by only 5-10 cultivars and have not been validated over a large number of cultivars. Although only RGB data were used in this study, our conclusions will be more realistic and credible based on data from more than 1500 cultivars, apart from this, the process of moving from method to field may require more experiments, such as multi-year and multi-point experiments. In this study, the grain number of seeds per plant and the grain weight per plant were used as yield parameters instead of the traditional plot yield. There were several reasons for this. First, analyzing such a large number of cultivars, including the control cultivars, that totaled 1,805 plots, with the land arrangement and post-survey was an enormous task. The plot size could only be reduced to one plot with two rows. Secondly, the plot yield can be too severely affected by chance factors, including occasional biotic and abiotic effects, such as seedling deficiency and diseases. These factors could have too much influence on the final plot yield, which interfered with the representation of the real yield data. The mean value of the plots was also calculated for different vegetation indices and textures, so that more reasonable yield parameters were used as the final indicator. The grain number of seeds per plant and grain weight per plant would also be easier to interpret. Use of the Boruta algorithm to eliminate indices is not the best way to do this, but it will provide suggestions for indices in the middle of the range of importance, and the final selection can be artificially conducted. Although the DNN had the best training and accuracy of estimation, the recent rapid development of deep learning algorithms will increase the likelihood of improvements in modeling algorithms. Promising algorithms include the use of long and short-term memory learning (LTSM) or an improved RNN algorithm in combination with time-series data.

5 Conclusions

This study explored the potential of RGB data to estimate yield parameters. UAVs provide canopy spectra, structure, and texture information, and five machine learning methods were used to estimate the yield parameters under lodging conditions. The main conclusions are as follows:

1. The most accurate time point for yield parameters estimation is 48 days after sowing when most cultivars are flowering. However, not all the indices correlate best with yield parameters at the flowering stage.
2. A combination of all the screened indices most effectively estimated the yield parameters. Spectral information offers a substantial potential for estimating the yield parameters, and the accuracy of estimating higher yield parameters is the highest when all the information indices are used.
3. The DNN-based model outperforms the PLSR, RFR, logistic, and SVM when the input indices are increased.
4. The effect of lodging levels on yield parameters are significant, and they affect both the grain number of seeds per plant and the grain weight per plant. However, the grain number of seeds per plant is more effective at generating accurate results.

The results suggest that there is substantial potential to estimate the yield parameters using multiple types of data fusion combined with deep neural networks. However, there are some limitations. First, as for breeders and cultivators, multi-year multi-area performance is an important indices of model stability, and it is difficult to judge the effectiveness of the model when we have only one year data. Secondly, our model only considered data from one time-point but considering multiple periods data may increase the estimation accuracy of yield parameters. Finally, we were numerically unable to the effect of lodging on yield parameters, so it was impossible to estimate the impact of lodging. To further improve the accuracy of estimating yield parameters, a larger amount of data is needed to support the estimation of yield parameters for so many genotypes. A future goal is to try to use more efficient methods to improve the stability of the estimated yield model.

Data availability statement

The raw data supporting the conclusions of this article will be made available by the authors, without undue reservation.

Author contributions

XJ, LQ, YL, DB, and DL conceived the research. DB completed the first manuscript version, XJ, YL, and DL contributed most of the key changes to the manuscript text. DB, DL, ZW, MS, BG, YL, QW, SG, and JL made significant contributions to the UAV data collection, data processing, and interpretation of the experimental data. DB, BG and DL led the trial design, management of experimental cultivation and collection of agronomic data at harvest. All authors contributed to the article and approved the submitted version.

Funding

This research was supported by the National Key Research and Development Program of China (2021YFD1201601 and 2021YFD1201602), the Agricultural Science and Technology Innovation Program of the Chinese Academy of Agricultural Sciences, Hainan Yazhou Bay Seed Lab (B21HJ0221), the earmarked fund for CARS (CARS-04-PS01) and Nanfan Special Project, CAAS (YJTCY01 and YBXM01).

Conflict of interest

The authors declare that the research was conducted in the absence of any commercial or financial relationships that could be construed as a potential conflict of interest.

Publisher's note

All claims expressed in this article are solely those of the authors and do not necessarily represent those of their affiliated organizations, or those of the publisher, the editors and the reviewers. Any product that may be evaluated in this article, or claim that may be made by its manufacturer, is not guaranteed or endorsed by the publisher.

Supplementary material

The Supplementary Material for this article can be found online at: https://www.frontiersin.org/articles/10.3389/fpls.2022.1012293/full#supplementary-material

References

Agriculture, U. S. D. O (2021). *2021 U.S. soybean outlook remains strong after record first quarter export volume* (International Agricultural Trade Report). Available at: https://www.fas.usda.gov/data/2021-us-soybean-outlook-remains-strong-after-record-first-quarter-export-volume.

Araus, J. L., Kefauver, S. C., Diaz, O. V., Gracia-Romero, A., Rezzouk, F. Z., Segarra, J., et al. (2021). Crop phenotyping in a context of global change: what to measure and how to do it. *J. Integr. Plant Biol.* 64, 27–88. doi: 10.1111/jipb.13191

Arroyo, J., Guijarro, M., and Pajares, G. (2016). An instance-based learning approach for thresholding in crop images under different outdoor conditions. *Comput. Electron. Agric.* 127, 669–679. doi: 10.1016/j.compag.2016.07.018

Bendig, J., YU, K., Aasen, H., Bolten, A., Bennertz, S., Broscheit, J., et al. (2015). Combining UAV-based plant height from crop surface models, visible, and near infrared vegetation indices for biomass monitoring in barley. *Int. J. Appl. Earth Observation Geoinformation* 39, 79–87. doi: 10.1016/j.jag.2015.02.012

Bharati, M. H., Liu, J. J., and Macgregor, J. F. (2004). Image texture analysis: methods and comparisons. *Chemometrics Intelligent Lab. Syst.* 72, 57–71. doi: 10.1016/j.chemolab.2004.02.005

Bonazza, P., Miteran, J., Ginhac, D., and Dubois, J. (2019). Traditional machine learning or deep learning methods for embedded computer vision study on biometric application. *Biostatistics Biometrics Open Access J.* 9, 1234–1235. doi: 10.19080/BBOAJ.2019.09.555755

Conrad, A. O., Li, W., Lee, D. Y., Wang, G. L., Rodriguez-Saona, L., and Bonello, P. (2020). Machine learning-based presymptomatic detection of rice sheath blight using spectral profiles. *Plant Phenomics* 2020, 8954085. doi: 10.34133/2020/8954085

Cooper, R. L. (1971). Influence of early lodging on yield of soybean [Glycine max (L.) merr.]. *Agron. J.* 63, 449–450. doi: 10.2134/agronj1971.00021962006300030030x

Edwards, J., Santos-Medellín, C., Liechty, Z. S., Nguyen, B., Lurie, E., Eason, S., et al. (2018). Compositional shifts in root-associated bacterial and archaeal microbiota track the plant life cycle in field-grown rice. *PloS Biol.* 16, e2003862. doi: 10.1371/journal.pbio.2003862

Fan, R.-E., Chen, P.-H., and Lin, C.-J. (2005). Working set selection using second order information for training support vector machines. *J. Mach. Learn. Res.* 6, 1889–1918. doi: 10.5555/1046920.1194907

Feng, L., Wang, Y., Zhang, Z., and Du, Q. (2021). Geographically and temporally weighted neural network for winter wheat yield prediction. *Remote Sens. Environ.* 262, 112514–112529. doi: 10.1016/j.rse.2021.112514

Geipel, J., Link, J., and Claupein, W. (2014). Combined spectral and spatial modeling of corn yield based on aerial images and crop surface models acquired with an unmanned aircraft system. *Remote Sens.* 6, 10335–10355. doi: 10.3390/rs61110335

Gitelson, A. A., Kaufman, Y. J., Stark, R., and Rundquist, D. (2002). Novel algorithms for remote estimation of vegetation fraction. *Remote Sens. Environ.* 80, 76–87. doi: 10.1016/S0034-4257(01)00289-9

Granitto, P. M., Furlanello, C., Biasioli, F., and Gasperi, F. (2006). Recursive feature elimination with random forest for PTR-MS analysis of agroindustrial products. *Chemometrics intelligent Lab. Syst.* 83, 83–90. doi: 10.1016/j.chemolab.2006.01.007

Guijarro, M., Pajares, G., Riomoros, I., Herrera, P. J., Burgos-Artizzu, X. P., and Ribeiro, A. (2011). Automatic segmentation of relevant textures in agricultural images. *Comput. Electron. Agric.* 75, 75–83. doi: 10.1016/j.compag.2010.09.013

Guo, W., Carroll, M. E., Singh, A., Swetnam, T. L., Merchant, N., Sarkar, S., et al. (2021). UAS-based plant phenotyping for research and breeding applications. *Plant Phenomics* 2021, 9840192–9840204. doi: 10.34133/2021/9840192

Hague, T., Tillett, N. D., and Wheeler, H. (2006). Automated crop and weed monitoring in widely spaced cereals. *Precis. Agric.* 7, 21–32. doi: 10.1007/s11119-005-6787-1

Hall, M. A. (1999). Correlation-based feature selection for machine learning. *Phd Thesis Waikato Univer Sity*, 1–38.

Hamblin, J., Knight, R., and Atkinson, M. J. (1978). The influence of systematic micro-environmental variation on individual plant yield within selection plots. *Euphytica* 27, 497–503. doi: 10.1007/BF00043175

Heckmann, D., Schluter, U., and Weber, A. P. M. (2017). Machine learning techniques for predicting crop photosynthetic capacity from leaf reflectance spectra. *Mol. Plant* 10, 878–890. doi: 10.1016/j.molp.2017.04.009

Ji, Y., Chen, Z., Cheng, Q., Liu, R., Li, M., Yan, X., et al. (2022). Estimation of plant height and yield based on UAV imagery in faba bean (Vicia faba l.). *Plant Methods* 18, 26–38. doi: 10.1186/s13007-022-00861-7

Jin, N., Tao, B., Ren, W., He, L., Zhang, D., Wang, D., et al. (2022). Assimilating remote sensing data into a crop model improves winter wheat yield estimation based on regional irrigation data. *Agric. Water Manage.* 266, 107583–107595. doi: 10.1016/j.agwat.2022.107583

Jin, X., Yang, G., Xu, X., Yang, H., Feng, H., Li, Z., et al. (2015). Combined multi-temporal optical and radar parameters for estimating LAI and biomass in winter wheat using HJ and RADARSAR-2 data. *Remote Sens.* 7, 13251–13272. doi: 10.3390/rs71013251

Jin, X., Zarco-Tejada, P. J., Schmidhalter, U., Reynolds, M. P., Hawkesford, M. J., Varshney, R. K., et al. (2021). High-throughput estimation of crop traits: a review of ground and aerial phenotyping platforms. *IEEE Geosci. Remote Sens. Magazine* 9, 200–231. doi: 10.1109/MGRS.2020.2998816

Kataoka, T., Kaneko, T., Okamoto, H., and Hata, S. (2003). *Crop growth estimation system using machine vision* (Proceedings 2003 IEEE/ASME International Conference on Advanced Intelligent Mechatronics), 2, 1079–1083. doi: 10.1109/AIM.2003.1225492

Kato, S., Samanfar, B., Morrison, M. J., Bekele, W. A., Torkamaneh, D., Rajcan, I., et al. (2021). Genome-wide association study to identify soybean stem pushing resistance and lodging resistance loci. *Can. J. Plant Sci.* 101, 663–670. doi: 10.1139/cjps-2020-0187

Khaki, S., and Wang, L. (2019). Crop yield prediction using deep neural networks. *Front. Plant Sci.* 10, 621–631. doi: 10.3389/fpls.2019.00621

Kose, O., and Oktay, T. (2020). Simultaneous quadrotor autopilot system and collective morphing system design. *Aircraft Eng. Aerospace Technol.* 92, 1093–1100. doi: 10.1108/AEAT-01-2020-0026

Kursa, M. B., and Rudnicki, W. R. (2010). Feature selection with the boruta package. *J. Stat. Software* 361 -, 13. doi: 10.18637/jss.v036.i11

Li, D., Bai, D., Tian, Y., Li, Y. H., Zhao, C., Wang, Q., et al. (2022). Time series canopy phenotyping enables the identification of genetic variants controlling dynamic phenotypes in soybean. *J. Integr. Plant Biol.* doi: 10.1111/jipb.13380

Li, Y., Chen, D., Walker, C. N., and Angus, J. F. (2010). Estimating the nitrogen status of crops using a digital camera. *Field Crops Res.* 118, 221–227. doi: 10.1016/j.fcr.2010.05.011

Liu, S., Jin, X., Nie, C., Wang, S., Yu, X., Cheng, M., et al. (2021). Estimating leaf area index using unmanned aerial vehicle data: shallow vs. deep machine learning algorithms. *Plant Physiol.* 187, 1551–1576. doi: 10.1093/plphys/kiab322

Liu, W., and Wang, J. (2021). Recursive elimination–election algorithms for wrapper feature selection. *Appl. Soft Computing* 113, 107956. doi: 10.1016/j.asoc.2021.107956

Li, L., Wang, B., Feng, P., Wang, H., He, Q., Wang, Y., et al. (2021). Crop yield forecasting and associated optimum lead time analysis based on multi-source environmental data across China. *Agric. For. Meteorology* 308–309:108558. doi: 10.1016/j.agrformet.2021.108558

Maimaitijiang, M., Ghulam, A., Sidike, P., Hartling, S., Maimaitiyiming, M., Peterson, K., et al. (2017). Unmanned aerial system (UAS)-based phenotyping of soybean using multi-sensor data fusion and extreme learning machine. *ISPRS J. Photogrammetry Remote Sens.* 134, 43–58. doi: 10.1016/j.isprsjprs.2017.10.011

Maimaitijiang, M., Sagan, V., Sidike, P., Hartling, S., Esposito, F., and Fritschi, F. B. (2020). Soybean yield prediction from UAV using multimodal data fusion and deep learning. *Remote Sens. Environ.* 237, 111599–111619. doi: 10.1016/j.rse.2019.111599

Ma, C., Liu, M., Ding, F., Li, C., Cui, Y., Chen, W., et al. (2022). Wheat growth monitoring and yield estimation based on remote sensing data assimilation into the SAFY crop growth model. *Sci. Rep.* 12, 5473–5489. doi: 10.1038/s41598-022-09535-9

Metternicht, G. (2010). Vegetation indices derived from high-resolution airborne videography for precision crop management. *Int. J. Remote Sens.* 24, 2855–2877. doi: 10.1080/01431160210163074

Oktay, T., and Coban, S. (2017). Simultaneous longitudinal and lateral flight control systems design for both passive and active morphing TUAVs. *Elektronika ir elektrotechnika* 23, 15–20. doi: 10.5755/j01.eie.23.5.19238

Paulus, S., and Mahlein, A. K. (2020). Technical workflows for hyperspectral plant image assessment and processing on the greenhouse and laboratory scale. *Gigascience* 9, 1–10. doi: 10.1093/gigascience/giaa090

Pedregosa, F., Varoquaux, G., Gramfort, A., Michel, V., Thirion, B., Grisel, O., et al. (2012). Scikit-learn: machine learning in python. *Jornal Mach. Learn. Res.* 12, 2825–2830. doi: 10.5555/1953048.2078195

Potgieter, A. B., George-Jaeggli, B., Chapman, S. C., Laws, K., Suarez Cadavid, L. A., Wixted, J., et al. (2017). Multi-spectral imaging from an unmanned aerial vehicle enables the assessment of seasonal leaf area dynamics of sorghum breeding lines. *Front. Plant Sci.* 8, 1532–1543. doi: 10.3389/fpls.2017.01532

Qiao, N., and Sun, P. (2014). Study of improved otsu algorithm and its ration evaluation analysis for PCB photoelectric image segmentation. *Optik* 125, 4784–4787. doi: 10.1016/j.ijleo.2014.04.060

Şahin, H., Kose, O., and Oktay, T. (2022). Simultaneous autonomous system and powerplant design for morphing quadrotors. *Aircraft Eng. Aerospace Technology*. 94 (8), 1228–1241. doi: 10.1108/AEAT-06-2021-0180

Seasholtz, M. B., and Kowalski, B. R. (1992). The effect of mean centering on prediction in multivariate calibration. *J. Chemometrics* 6, 103–111. doi: 10.1002/cem.1180060208

Simon, N., Friedman, J. H., Hastie, T., and Tibshirani, R. (2011). Regularization paths for cox's proportional hazards model *via* coordinate descent. *J. Stat. Software* 391 -, 13. doi: 10.18637/jss.v039.i05

Sukumaran, S., Reynolds, M. P., and Sansaloni, C. (2018). Genome-wide association analyses identify QTL hotspots for yield and component traits in durum wheat grown under yield potential, drought, and heat stress environments. *Front. Plant Sci.* 9, 81–97. doi: 10.3389/fpls.2018.00081

Tax, D. M. J., and Duin, R. P. W. (1999). Support vector domain description. *Pattern Recognition Lett.* 20, 1191–1199. doi: 10.1016/S0167-8655(99)00087-2

Venkatalaxmi, A., Padmavathi, B. S., and Amaranath, T. (2004). A general solution of unsteady stokes equations. *Fluid Dynamics Res.* 35, 229–236. doi: 10.1016/j.fluiddyn.2004.06.001

Wang, J., Ding, J., Abulimiti, A., and Cai, L. (2018). Quantitative estimation of soil salinity by means of different modeling methods and visible-near infrared (VIS-NIR) spectroscopy, ebinur lake wetland, Northwest China. *PeerJ* 6, e4703. doi: 10.7717/peerj.4703

Wang, X., Wang, M., Wang, S., and Wu, Y. (2015). Extraction of vegetation information from visible unmanned aerial vehicle images. *Nongye Gongcheng Xuebao/Transactions Chin. Soc. Agric. Eng.* 31, 152–159. doi: 10.3969/j.issn.1002-6819.2015.05.022

Woebbecke, D., Meyer, G., Bargen, K., and Mortensen, D. (1995). Color indices for weed identification under various soil, residue, and lighting conditions. *Trans.* 38 (1), 259–269. doi: 10.13031/2013.27838

Xu, C., Lu, C., Liang, X., Gao, J., Zheng, W., Wang, T., et al. (2016). Multi-loss regularized deep neural network. *IEEE Trans. Circuits Syst. Video Technol.* 26, 2273–2283. doi: 10.1109/TCSVT.2015.2477937

Yue, J., Feng, H., Jin, X., Yuan, H., Li, Z., Zhou, C., et al. (2018). A comparison of crop parameters estimation using images from UAV-mounted snapshot hyperspectral sensor and high-definition digital camera. *Remote Sens.* 10, 1138–1154. doi: 10.3390/rs10071138

Zhao, Y., Chen, S., and Shen, S. (2013). Assimilating remote sensing information with crop model using ensemble kalman filter for improving LAI monitoring and yield estimation. *Ecol. Model.* 270, 30–42. doi: 10.1016/j.ecolmodel.2013.08.016

Zhou, X., Zheng, H. B., Xu, X. Q., He, J. Y., Ge, X. K., Yao, X., et al. (2017). Predicting grain yield in rice using multi-temporal vegetation indices from UAV-based multispectral and digital imagery. *ISPRS J. Photogrammetry Remote Sens.* 130, 246–255. doi: 10.1016/j.isprsjprs.2017.05.003

frontiers | Frontiers in Plant Science

TYPE Original Research
PUBLISHED 17 January 2023
DOI 10.3389/fpls.2022.979103

Check for updates

OPEN ACCESS

EDITED BY
Yuzhen Lu,
Mississippi State University, United States

REVIEWED BY
Muhammad Ali Raza,
Islamia University of Bahawalpur, Pakistan
Haikuan Feng,
Beijing Research Center for Information Technology in Agriculture, China
Yanbo Huang,
United States Department of Agriculture (USDA), United States
Joby Czarnecki,
Mississippi State University, United States

*CORRESPONDENCE
Wenbin Wu
wuwenbin@caas.cn
Xiuliang Jin
jinxiuliang@caas.cn

†These authors share first authorship

SPECIALTY SECTION
This article was submitted to Sustainable and Intelligent Phytoprotection, a section of the journal Frontiers in Plant Science

RECEIVED 27 June 2022
ACCEPTED 28 December 2022
PUBLISHED 17 January 2023

CITATION
Liu Y, Nie C, Zhang Z, Wang Z, Ming B, Xue J, Yang H, Xu H, Meng L, Cui N, Wu W and Jin X (2023) Evaluating how lodging affects maize yield estimation based on UAV observations.
Front. Plant Sci. 13:979103.
doi: 10.3389/fpls.2022.979103

COPYRIGHT
© 2023 Liu, Nie, Zhang, Wang, Ming, Xue, Yang, Xu, Meng, Cui, Wu and Jin. This is an open-access article distributed under the terms of the Creative Commons Attribution License (CC BY). The use, distribution or reproduction in other forums is permitted, provided the original author(s) and the copyright owner(s) are credited and that the original publication in this journal is cited, in accordance with accepted academic practice. No use, distribution or reproduction is permitted which does not comply with these terms.

Evaluating how lodging affects maize yield estimation based on UAV observations

Yuan Liu[1,2,3†], Chenwei Nie[2,3†], Zhen Zhang[1], ZiXu Wang[2,4], Bo Ming[2], Jun Xue[2], Hongye Yang[2], Honggen Xu[2], Lin Meng[2,3], Ningbo Cui[5], Wenbin Wu[6*] and Xiuliang Jin[1,2,3*]

[1]School of Geomatics, Anhui University of Science and Technology, Huainan, China, [2]Institute of Crop Sciences, Chinese Academy of Agricultural Sciences/Key Laboratory of Crop Physiology and Ecology, Ministry of Agriculture, Beijing, China, [3]National Nanfan Research Institute (Sanya), Chinese Academy of Agricultural Sciences, Sanya, China, [4]Engineering Mapping and Geographical Information Division, Henan Provincial Communications Planning & Design Institute Co., LTD, Zhengzhou, China, [5]State Key Laboratory of Hydraulics and Mountain River Engineering & College of Water Resource and Hydropower, Sichuan University, Chengdu, China, [6]Institute of Agricultural Resources and Regional Planning, Chinese Academy of Agricultural Sciences, Beijing, China

Timely and accurate pre-harvest estimates of maize yield are vital for agricultural management. Although many remote sensing approaches have been developed to estimate maize yields, few have been tested under lodging conditions. Thus, the feasibility of existing approaches under lodging conditions and the influence of lodging on maize yield estimates both remain unclear. To address this situation, this study develops a lodging index to quantify the degree of lodging. The index is based on RGB and multispectral images obtained from a low-altitude unmanned aerial vehicle and proves to be an important predictor variable in a random forest regression (RFR) model for accurately estimating maize yield after lodging. The results show that (1) the lodging index accurately describes the degree of lodging of each maize plot, (2) the yield-estimation model that incorporates the lodging index provides slightly more accurate yield estimates than without the lodging index at three important growth stages of maize (tasseling, milking, denting), and (3) the RFR model with lodging index applied at the denting (R5) stage yields the best performance of the three growth stages, with R^2 = 0.859, a root mean square error (RMSE) of 1086.412 kg/ha, and a relative RMSE of 13.1%. This study thus provides valuable insight into the precise estimation of crop yield and demonstra\tes that incorporating a lodging stress-related variable into the model leads to accurate and robust estimates of crop grain yield.

KEYWORDS

remote sensing, maize yield, lodging levels, random forest regression, UAV images

1 Introduction

Given the population growth, the demand for food supplies is increasing all over the world (Mishra et al., 2021). Furthermore, limited arable land and frequent extreme weather events have resulted in significant stress on food security. Maize, one of the most important grain crops in the world, is a staple grain crop in China (Jin et al., 2020), where 273 million

tons were harvested in 2021, accounting for 40% of global grain production. Timely, accurate, and nondestructive pre-harvest estimation of maize yield is vital for the authorities to formulate corresponding regulation policies and ensure the stability of grain prices and food security (Yu et al., 2020; Feng et al., 2021; Wu et al., 2021). Such estimates also facilitate the development of precision agriculture.

Remote sensing technology can quickly and accurately obtain wall-to-wall information on the land surface and has been widely used to estimate the yield of various food crops (Ju et al., 2021; Maimaitijiang et al., 2021; Nagy et al., 2021). However, satellite remote sensing is often limited by low spatial resolution, long revisit period, and cloudy weather, which prevents image acquisition at certain time points (Xu et al., 2021a). The development of unmanned aerial vehicles (UAVs) provides a way to solve these problems (Peng et al., 2021). As a new tool of information acquisition, UAV remote sensing has irreplaceable advantages in agricultural production (Duan et al., 2021), achieving accurate results with low cost, convenient operation, high spatial-temporal resolution and more (Tao et al., 2020; Wang et al., 2021).

Two main methods exist for crop yield estimation based on UAV remote sensing: data-assimilation methods and statistical models. Data assimilation methods involve crop growth models, which simulate crop growth, development, and yield by combining crop and environment parameters, such as crop species, soil-plant dynamics, water status, and meteorological data (Palosuo et al., 2011; Wu et al., 2021). Assimilating remote sensing data with crop growth models, including WOFOST (van Diepen et al., 1989), AquaCrop (Steduto et al., 2009), DSSAT (Jones et al., 2003), and SWAP (Van Dam et al., 1997), have achieved good results in crop yield estimation. However, these models require a set of biotic and abiotic parameters for model calibration (Kang and Özdoğan, 2019), which undoubtedly increases the complexity of the model because some of the parameters are difficult to obtain. In addition, a certain amount of error exists in most of the environment data acquired from remote sensing data. Consequently, the applicability of the data-assimilation methods is limited in large-scale-yield modeling (Zhang et al., 2019). Statistical models are the earliest and simplest methods to estimate crop yield and are favored by numerous researchers. The basis of statistical models is to establish a linear or nonlinear regression between remote sensing data and measured crop yield (Duan et al., 2017; Zhou et al., 2017). Crop yield estimated by this approach does not address the physiological mechanisms that determine plant growth (Crane-Droesch, 2018), so fewer auxiliary measurements are required. Statistical models to estimate crop yield can be further divided into two categories: linear and nonlinear models. The linear models directly construct the relationship between vegetation indices and crop yield based on linear regressions. However, empirical relationships between crop yield and estimators (e.g., vegetation indices, canopy height, and canopy coverage) usually present nonlinearities (Johnson et al., 2016). Given the generally high degree of autocorrelation of these estimators, yield-estimation models using these variables over time are prone to overfitting. In view of these limitations, machine-learning algorithms were developed to better deal with nonlinearities and reduce overfitting, which is the second type of statistical model. The most successful machine-learning methods for yield estimation include random forest regression (RFR) (Wan et al., 2020; Li et al., 2021), support vector regression (Shafiee et al., 2021), and partial least squares regression (Rischbeck et al., 2016).

Estimating crop yield based on statistical models usually uses spectral, structural, and textural information. Spectral vegetation indices derived from multispectral or hyperspectral data are closely related to some vegetation parameters, such as leaf area index (Tan et al., 2020), green biomass (Li et al., 2020), and crop yield (Panek and Gozdowski, 2021). They describe the average tonal variations in various bands. Structural information such as canopy height and canopy coverage have been used to depict the physiological and geometric characteristics of vegetation and are good indicators of plant growth and crop yield (Malambo et al., 2018). Texture information, characterized by the spatial distribution of tonal variations within a band (Haralick et al., 1973), highlights the structural and geometric features of the plant canopy. Numerous previous studies have estimated crop biomass and yield based on texture (Zheng et al., 2018; Yue et al., 2019; Maimaitijiang et al., 2020). Most studies have focused on using these three common predictors for maize-yield estimates (Rischbeck et al., 2016; Wan et al., 2020). However, few studies have considered how lodging affects crop yield estimation, despite lodging being a common occurrence during the growing season. When lodging occurs, the photosynthetic capacity and dry matter production capacity decrease (Luo et al., 2022), and the transport of water, nutrients, and carbohydrates through the xylem and phloem is cut off (Kashiwagi et al., 2015). During the 12-leaf stage, stalk and root lodging can reduce maize yield by 14% and 28%, respectively (Xue et al., 2017). Every 1% increase in lodging reduces maize yield by an average of 108 kg/ha (Liu et al., 2021). As a result, lodging leads to the loss of crop yield and the reduction of grain quality (Tan et al., 2021). Therefore, lodging may affect yield estimates. To improve crop yield, studies on maize lodging have investigated the factors that cause or affect lodging and have screened lodging-resistant varieties (Chen et al., 2021; Li et al., 2022). In studies of crop yield estimation using agricultural remote sensing, the crop-yield response to lodging has been widely discussed (Acreche and Slafer, 2011; Mi et al., 2011). However, few investigations have focused on how lodging affects model performance and robustness (Chauhan et al., 2019).

To accurately estimate maize yield after lodging, we develop herein a lodging index to represent the degree of lodging of each plot. In addition, we propose a method to estimate maize yield based on spectral features, structural features, texture features, and the lodging index extracted from UAV-based RGB and multispectral images. The analyses were conducted at three different maize growth stages (tasseling stage, milking stage, and denting stage). The specific objectives of this study are (1) to develop an index that represents the degree of maize lodging, (2) to explore how the lodging index correlates with the current model used to estimate maize yield, and (3) to develop a method to accurately estimate maize yield under lodging conditions.

2 Materials and methods

2.1 Study area and experimental setup

The study area was located at the Xinxiang Experimental Station of the Chinese Academy of Agricultural Sciences (35°7′51.6″N, 113° 45′58″E; elevation 75 m), Henan Province in China (Figure 1). Xinxiang County is in the North China Plain and has a warm continental monsoon climate characterized by four distinct seasons. The main crop grown in the summer is maize. The average annual precipitation and temperature are 560.6 mm and 14.3 °C, respectively. The average annual precipitation is unevenly distributed, being mostly concentrated between June and September, when about 75% of the annual rainfall occurs.

Maize was planted in 132 plots with different varieties and fertilizer treatments (Figure 1) to ensure the generalizability of the proposed method and avoid overfitting. In the variety experiment, 98 maize varieties with different genotypes and lodging resistance were planted, each in a 3 m × 10 m plot. The same fertilizer treatment was applied in each plot. In the nitrogen-treatment experiment, two maize varieties widely planted in north China (JNK728 and ZD958) were planted in 34 plots, with varied fertilizer treatment (0–400 kg/ha) and application time (from before sowing to the silking stage). In all the plots, urea (CH_4N_2O) was used as nitrogen source. The planting density was 75 000 plants/ha, with a row spacing of 60 cm, and a plant spacing of 23 cm.

2.2 Data acquisition

2.2.1 UAV images acquisition

This study used a DJI M600 pro UAV (Figure 2A, DJI Innovation Co., Ltd., Shenzhen, China) equipped with a Sony α7RII and a RedEdge-MX camera to collect RGB images and multispectral images, respectively (Figure 2B). The Sony α7RII digital camera uses a complementary 35.9 × 24.0 mm^2 metal-oxide semiconductor sensor with a resolution of 42.4 million pixels. The RedEdge-MX multispectral camera includes five bands (blue or B, green or G, red or R, red edge or RE, and near-infrared or NIR) within the spectral region of 400–1000 nm. The details of each sensor are given in Table 1.

UAV images of summer maize were collected in 2020 at the stages of tasseling (VT), milking (R3), and denting (R5). Three flight missions were undertaken at 30 m height and a speed of 2.1 m/s. Each flight mission took about 30 minutes. The lateral and forward overlaps were 80% and 90%, respectively. Each flight campaign was conducted during clear and sunny weather between 12 p.m. and 2 p.m. to reduce the impact on image quality of cloud cover and changes in solar zenith angle. To calibrate the multispectral camera, the FieldSpec 4s spectroradiometer (Analytical Spectral Devices, Boulder, Colorado, USA) was used to measure the reflectivity of tarpaulins with six different colors (gray, red, white, green, blue, and black) at various wavelengths in the study area (Figure 2C). The spectral range of the spectrometer was from 350 to 2500 nm, each color tarp was measured ten times during the UAV flight and the average was taken as the reflectance result of the corresponding calibration tarp. The six color tarpaulins were placed in the field perpendicular to the flight path, allowing their reflectance data to be acquired during the UAV flight. Meanwhile, to facilitate the georegistration of images, 12 ground control points (GCPs) were evenly marked around the plots (Figure 1).

2.2.2 Collection of yield data

The yield of the 132 plots was measured by using the following procedure: For each plot, all maize plants in six 5-m-long rows were harvested. Ten maize ears of representative size and weight were

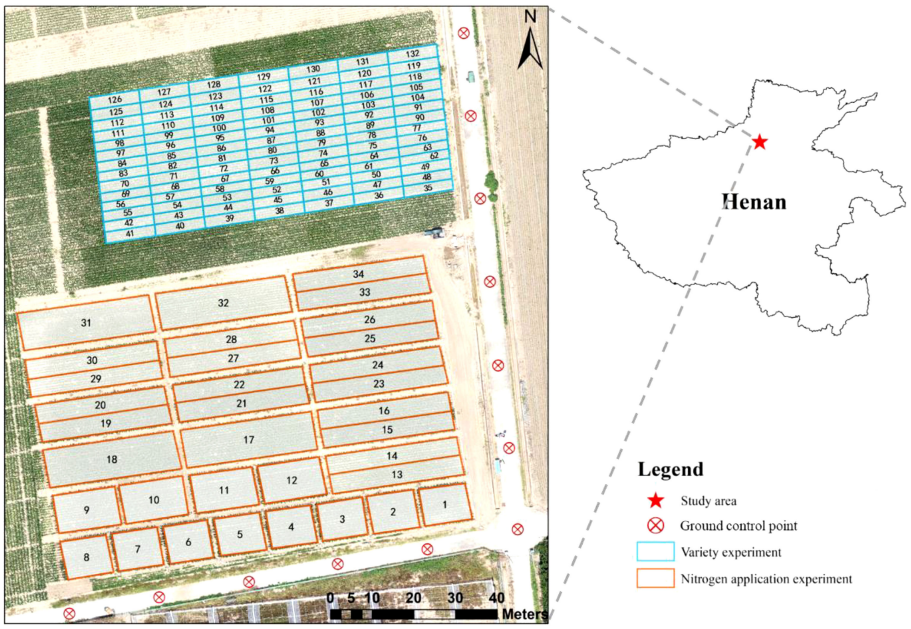

FIGURE 1
Study area location and layout of the experimental site.

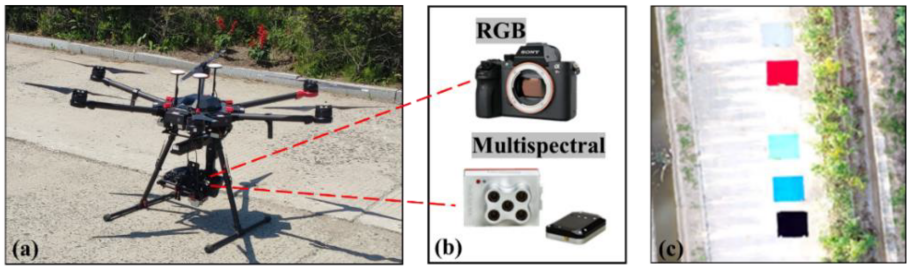

FIGURE 2
The UAV platform and sensors: **(A)** DJI M600 pro, **(B)** Sony α7RII and MicaSense RedEdge-MX, and **(C)** six tarpaulins of different colors.

selected for indoor measurement of water content and grain weight. The relative water content of the grain was measured with a PM-8188-A Grain Moisture Meter (Kett Electric Laboratory Co., Ltd., Tokyo, Japan). Finally, the grain yield at 14% water content of each plot was calculated and is shown in Figure 3. The lowest yield (1291.08 kg/ha) was from plot 69. The highest yield (13781.02 kg/ha) was from plot 117.

2.3 Image preprocessing

The orthoimages of RGB and multispectral data were generated using the Agisoft PhotoScan software (version 1.4.5, Agisoft LLC, St. Petersburg, Russia), facilitated by the GPS and IMU (Inertial Measurement Unit) data recorded by the UAV flight control system. Georegistration of the orthoimages obtained at different times was conducted so that the positional displacements were removed, and the images were geographically well aligned. This step was done by the ArcGIS software (version 10.4, Environmental Systems Research Institute, Inc., Redlands, CA, USA) according to the 12 GCPs (Figure 1).

For the multispectral images, radiometric correction was conducted to convert image digital number (DN) values into reflectance to extract spectral information. Linear, quadratic, exponential, logarithmic, and power functions were used to fit the relationship between the DN values of six color tarpaulins (Figure 2C) extracted from the images and their reflectance based on the FieldSpec 4s spectroradiometer measurements. The optimal functions were used to separately calibrate each band in each growth stage (Figure 4). The exponential function was selected for the blue band in the VT and R5 stages, and for the green band in the R5 stage, with R^2 reaching 0.93, 0.95, and 0.98, respectively. The quadratic function, with R^2 varying from 0.93 to 0.99. The overall workflow of this study is shown in Figure 5, including the acquisition of indicators, the establishment of models, and the research objectives.

2.4 Features extraction from multimodal images

Integrating multimodal features for crop yield estimation has been validated in previous studies (Rischbeck et al., 2016; Feng et al., 2020; Ramadanningrum et al., 2020). Estimating maize yields by integrating spectral, structural, and textural information can provide more information related to yield and overcome the inherent asymptotic saturation of single canopy features (Maimaitijiang et al., 2017). In this study, the lodging information was also considered.

2.4.1 Canopy spectral information

The spectral characteristics of crops are affected mainly by the absorption, reflection, and transmission of electromagnetic radiation caused by the physiological structure of plants, which makes spectral indices good predictors of crop yield (Berger et al., 2020; Yang et al., 2021). In this study, radiometrically calibrated multispectral images were used to extract the canopy spectral features. Fourteen spectral indices that have been widely used in yield estimation were selected (Sui et al., 2018; Maimaitijiang et al., 2020), as shown in Table 2. The extraction was implemented in the ArcGIS software.

TABLE 1 Basic parameters of the sensors mounted on the UAV.

Sensor name	Sony α7RII	RedEdge-MX
Sensor type	RGB (Red-Green-Blue)	Multispectral
Dimension (mm)	126.9×95.7×60.3	87×59×45.4
Spectral region (μm)	N/A	Blue:0.475, Green:0.560, Red:0.668, Red-edge:0.717, Near-infrared:0.842
Resolution (pixels)	7952×5304	1280×960
Focal length (mm)	70	5.4
Mass (g)	625	231.9

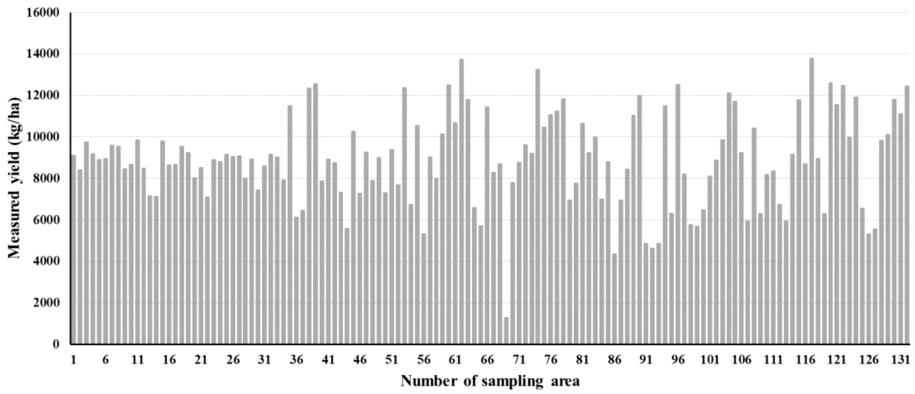

FIGURE 3
Bar plot showing the measured maize yield in the sampling plots.

2.4.2 Canopy structure information

The canopy-structure information is directly related to light use efficiency (Xu et al., 2021b), which contains independent information from spectral and texture feature (Stanton et al., 2017). Two indicators, canopy coverage (CC) and canopy height (CH), were extracted to characterize the structure of the maize. Both were extracted from the UAV-RGB images.

Canopy height was extracted by generating a crop height model (CHM) from UAV high-resolution RGB images. At each of the three growth stages, the structure-from-motion (SfM) algorithm was implemented in Agisoft PhotoScan software to create a three-dimensional (3D) points cloud and a digital surface model (DSM) (Xie and Yang, 2020). In addition, a bare-earth digital elevation model (DEM) was created based on photogrammetric 3D point clouds generated before maize emergence (Maimaitijiang et al., 2019). Subsequently, the CHM was calculated by subtracting DEM from DSM using the raster calculator tool in the ArcGIS software.

The calculation of CC depends on the correct recognition of crop pixels from among the background (soil and weeds). Previous studies have shown that vegetation and soil can be separated based on indices calculated from RGB images, such as the color index of vegetation extraction (CIVE), excess green index (ExG), and excess green minus excess red (ExG – ExR) (Hamuda et al., 2016; Castillo-Martínez et al., 2020). In this study, the CIVE [Eq. (1)] is used with a threshold interval set at [−28, 5]. The CC is thus expressed as the fraction of maize canopy pixels to all pixels in the sampled plot [Eq. (2)]:

$$CIVE = 0.441R - 0.811G + 0.385B + 18.787 \quad (1)$$

$$CC = \frac{P_{maize}}{P_{total}} \times 100\,\% \quad (2)$$

where P_{maize} is the number of maize canopy pixels the plot, and P_{total} is the total number of pixels in the plot.

2.4.3 Canopy texture information

Canopy texture can provide additional information related to spatial canopy architecture and spectral characteristics (Xu et al., 2022). The inclusion of texture features can reduce the bias of yield estimates beyond what is possible using spectral indices alone; this is helpful for early monitoring of grain yield (Wang et al., 2021). In this study, texture features were extracted from UAV-RGB images based on the gray-level co-occurrence matrix (GLCM), which is a popular method to extract texture features (Mohanaiah et al., 2013). This step was implemented in the ENVI software (version 5.3; Esri Inc.) with a window size of 7 × 7. The meanings and formulas (Haralick et al., 1973) of the texture indices are presented in Table 3.

2.4.4 Lodging stress information

Around August 3, 2020 (tasseling stage), a sudden rainstorm accompanied by strong winds (wind force level 5 to 6) hit the experiment site, resulting in varying degrees of lodging in the maize plots. The distribution and degree of lodging were investigated in the field the day after. Different degrees of lodging occurred in the same plot at the pixel level. In this study, the lodging degree at the pixel level was extracted as per Wang (2021) and then divided into three categories: no lodging (NL), light lodging (LL), and severe lodging (SL). NL means that the maize remained upright, and the angle between the plant and the ground was between 0° and 30°. LL means that the angle between the maize plant and the ground was 30° to 60°. SL means that the maize plant was close to or completely on the ground. An index representing the degree of lodging of each plot was developed based on the pixel-level degree of lodging and the lodging area in each plot. The calculation was implemented in the ArcGIS software. The formula for calculating the lodging index is

$$LI = \sum_{i=1}^{3} LD_i \times S_i \quad (3)$$

where LI is the lodging index of a plot, LD_i is the pixel-level lodging degree, and S_i is the area fraction of lodging degree i in the plot.

2.5 Random forest regression algorithm

We selected the RFR machine-learning algorithm because it has already produced accurate and robust estimates of crop yield (Aghighi et al., 2018; Cai et al., 2019). The RFR algorithm is an ensemble method that uses bootstrap sampling. Multiple samples are extracted from the original sample with replacement, each bootstrap sample is modeled by a decision tree, and then multiple decision trees are combined by voting to determine the final estimation (Breiman,

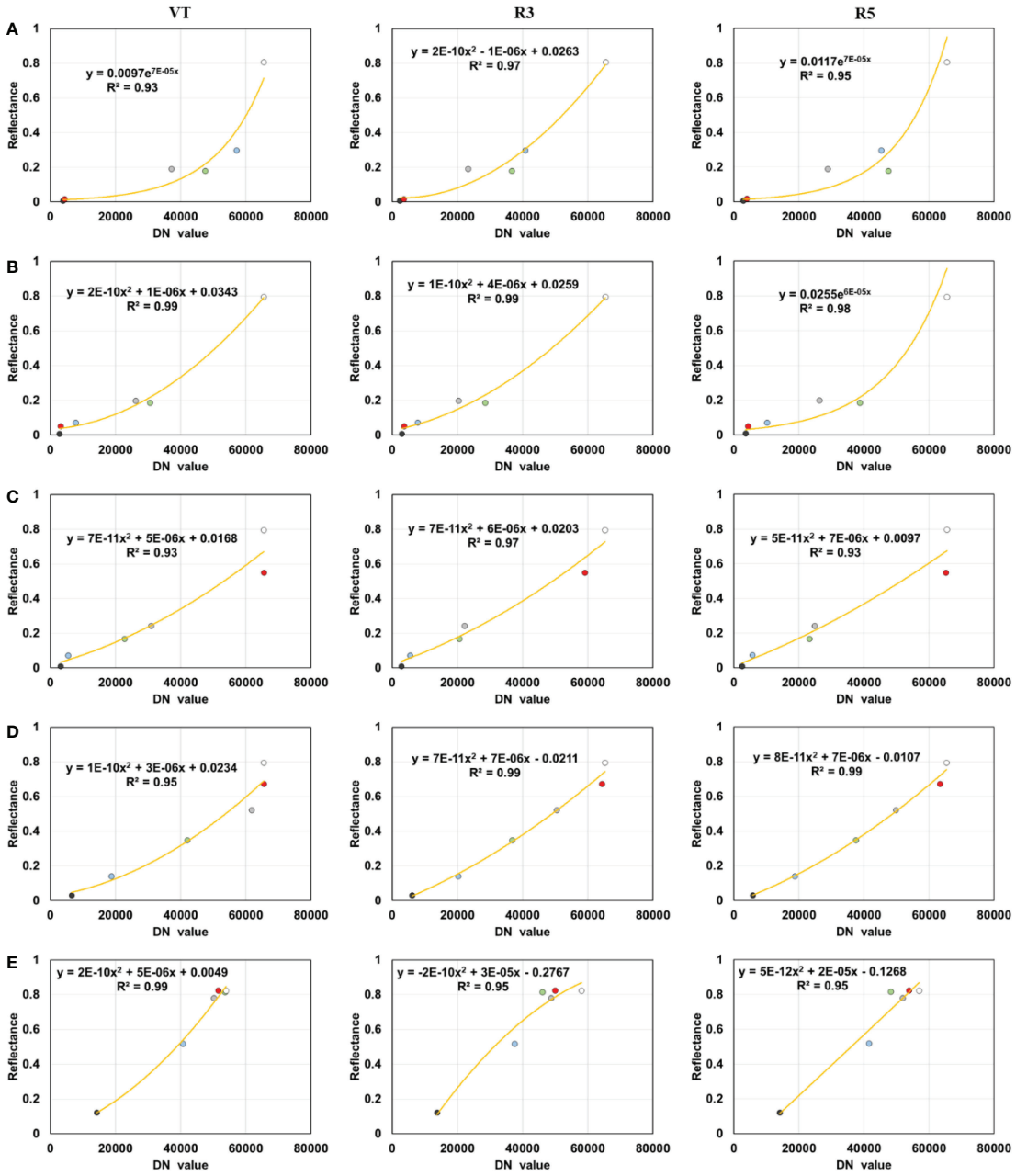

FIGURE 4
Multispectral radiometric calibration fitting models. **(A)** blue band, **(B)** green band, **(C)** red band, **(D)** red-edge band, and **(E)** near-infrared band.

2001). Because multiple different decision trees are integrated, RFR is robust against overfitting (Yu et al., 2016).

The RFR models were implemented using Python version 3.7 (Google Inc., Mountain View, California, USA). The number of RFR decision trees was set to 100, the number of seeds used by the random number generator was set to 15, and the maximum depth of the decision tree was determined so that each leaf is "pure" or until all leaves contain less than the minimum number of samples needed to split the internal nodes. The other parameters used the default settings of the Python sklearn package.

To ensure a fair and comprehensive evaluation of the constructed model, we randomly selected 80% of the samples of the measured maize yields to train the model and used the remaining 20% to determine the accuracy of the yield estimates produced by this method.

2.6 Assessment of model accuracy

Three evaluation indicators were used to test the model accuracy: the coefficient of determination R^2, the root mean square error (RMSE), and relative RMSE (rRMSE). These evaluation metrics are calculated as follows:

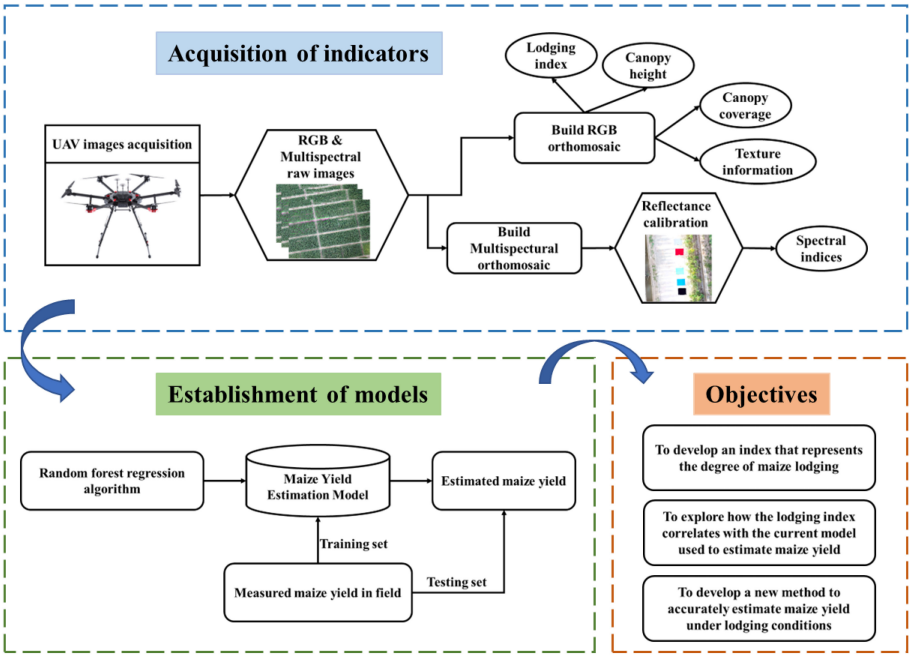

FIGURE 5
Workflow for preprocessing, feature extraction, model building, and target research using multimodal data.

$$R^2 = 1 - \frac{\sum_{i=1}^{n}\left(X_{model,i} - \overline{X_{obs}}\right)^2}{\sum_{i=1}^{n}\left(X_{obs,i} - \overline{X_{obs}}\right)^2} \quad (4)$$

$$RMSE = \sqrt{\frac{\sum_{i=1}^{n}\left(X_{model,i} - X_{obs,i}\right)^2}{n}} \quad (5)$$

$$rRMSE = \frac{RMSE}{\overline{X_{obs}}} \times 100\,\% \quad (6)$$

where $X_{model,i}$ and $X_{obs,\ i}$ are the estimated yield and observed yield for plot i, respectively, $\overline{X_{obs}}$ is the average of the observed yields, and n is the number of samples.

TABLE 2 Definitions of the features extracted from multispectral imagery.

Spectral index	Formula	References
Normalized difference vegetation index	$NDVI=(NIR-R)/(NIR+R)$	(Rouse et al., 1974)
Ratio vegetation index	$RVI=NIR/R$	(Tucker, 1979)
Green-red vegetation index	$GRVI=(G-R)/(G+R)$	(Tucker, 1979)
Optimized soil adjusted vegetation index	$OSAVI=(NIR-R)/(NIR-R+L)(L=0.16)$	(Rondeaux et al., 1996)
Normalized difference red-edge	$NDRE=(NIR-RE)/(NIR+RE)$	(Gitelson and Merzlyak, 1997)
Modified chlorophyll absorption in reflectance index	$MCARI=[(RE-R)-0.2*(RE-G)]*(RE/R)$	(Daughtry et al., 2000)
Transformed chlorophyll absorption in reflectance index	$TCARI=3*[(RE-R)-0.2*(RE-G)*(RE/R)]$	(Haboudane et al., 2002)
Green normalized difference vegetation index	$GNDVI=(NIR-G)/(NIR+G)$	(Gitelson et al., 2003)
Wide dynamic range vegetation index	$WDRVI=(a*NIR-R)/(a*NIR+R)(a=0.12)$	(Gitelson, 2004)
Green chlorophyll index	$GCI=(NIR/G)-1$	(Gitelson et al., 2005)
Red-edge chlorophyll index	$RECI=(NIR/RE)-1$	(Gitelson et al., 2005)
Two-band enhanced vegetation index	$EVI2=2.5*(NIR-R)/(NIR+2.4*R+1)$	(Jiang et al., 2008)
Normalized difference red-edge index	$NDREI=(RE-G)/(RE+G)$	(Hassan et al., 2018)

TABLE 3 Meanings and formulas of the selected texture indices based on GLCM.

Texture index	Formula	Meaning
Mean	$\mu_i = \sum_{i,j=0}^{N-1} i(P_{i,j})$ $\mu_j = \sum_{i,j=0}^{N-1} j(P_{i,j})$	Average gray level in the window.
Variance	$\sigma_i = \sum_{i,j=0}^{N-1} P_{i,j}(i-\mu_i)^2$ $\sigma_j = \sum_{i,j=0}^{N-1} P_{i,j}(j-\mu_j)^2$	Variance of gray level in the window.
Homogeneity	$HOM = \sum_{i,j=0}^{N-1} P_{i,j}/[1+(i-j)^2]$	Measure of the homogeneity across the window.
Contrast	$CON = \sum_{i,j=0}^{N-1} P_{i,j}(i-j)^2$	Metric of the local change in pixel value between adjacent pixels.
Dissimilarity	$DIS = \sum_{i,j=0}^{N-1} P_{i,j}\lvert i-j\rvert$	Metric that reflects the difference in grayscale.
Entropy	$ENT = \sum_{i,j=0}^{N-1} P_{i,j}(-\ln P_{i,j})$	Measure of the disorder across an image.
Angular Second Moment	$ASM = \sum_{i,j=0}^{N-1} P_{i,j}^2$	Metric of the uniformity of the image gray level distribution.
Correlation	$COR = \sum_{i,j=0}^{N-1} P_{i,j}[(i-\mu_i)(j-\mu_j)/\sqrt{(\sigma_i^2)(\sigma_j^2)}]$	Metric of linearity between adjacent pixels.

From Hall-Beyer (2017); Park and Guldmann (2020), and Haralick et al. (1973).
N is the number of gray levels. i and j are the column and row labels of the GLCM, respectively. $P_{i,j}$ is the probability that values i and j appear in the adjacent pixels of the original image within the window that defines the neighborhood. μ is the mean and σ is the standard deviation, defined by the GLCM mean and the GLCM variance equation in the table.

3 Results

3.1 Construction of lodging index

The pixel-level map of lodging degree (Figure 6) for each test plot is derived from the pixel-size degree of lodging extracted by Wang (2021). The classification accuracy of using the random forest classifier for lodging degree at pixel size is 86.96%; for more details, see Wang (2021). The result shows that the degree of lodging differs at different positions within the same plot. Therefore, it is hard to describe the degree of lodging of the plot only by lodging area or the lodging degree at pixel size. The lodging index of each plot is shown in Figure 7, where a larger lodging index indicates a greater degree of lodging in the plot, and a lower degree of lodging means that the lodging degree of the plot is lighter. The lodging degree of each plot represented by the lodging index (Figure 7) is consistent with the spatial distribution of the pixel-level lodging degree (Figure 6). Thus, the lodging index is used to analyze how lodging affects yield estimates.

To further describe the relationship between the lodging index and yield, we plot the measured yield versus the lodging index in Figure 8. There was no obvious increasing or decreasing trend in the measured maize yield with increasing lodging index.

3.2 Estimation of maize yield without lodging index

Differences appear in the estimated maize yield in different growth stages, and the yield-estimation model identifies the optimal harvest time. The results show that the models developed based on UAV images obtained at different growth stages perform at various levels (Figure 9). The model developed at the R5 stage performs best, with R^2 = 0.806, RMSE = 1106.67 kg/ha, and rRMSE = 13.4%. The model developed at the VT stage performs the worst, with R^2 = 0.170, RMSE = 1799.01 kg/ha, and rRMSE = 21.7%. The results indicate that models developed at later growth stages perform better than models developed at early growth stages, which is consistent with previous results (Johansen et al., 2020; Li et al., 2021).

To further explore whether lodging affects yield estimation, the deviation between the estimated and measured yields is plotted as a function of lodging index. As shown in Figure 10, no clear relationship appears between the estimation error and the lodging index. Large estimation errors appear mainly in plots with small lodging index or larger lodging index. In addition, at all three growth stages of maize, the yield of plots with a small degree of lodging tends to be underestimated with respect to the actual yield, whereas the yield of the plots with severe lodging degree is clearly overestimated.

10.3389/fpls.2022.979103

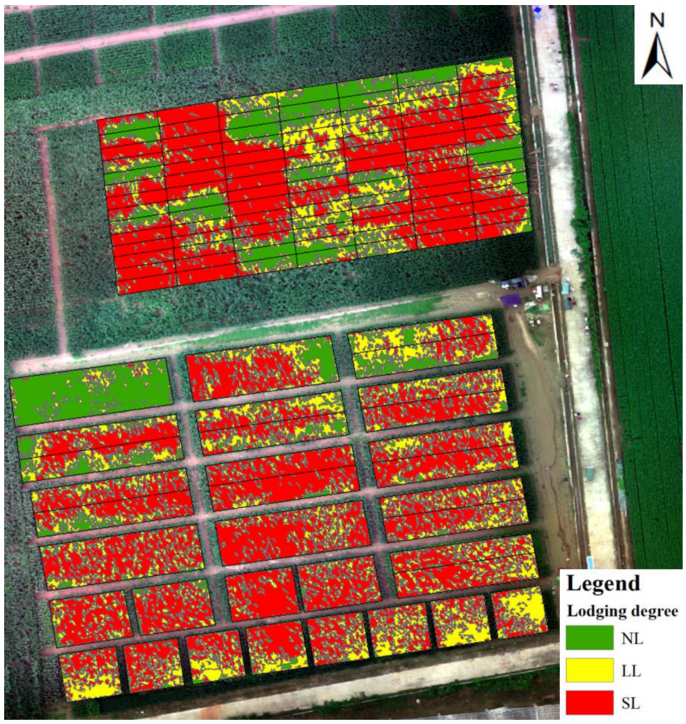

FIGURE 6
Distribution of pixel-level degree of maize lodging.

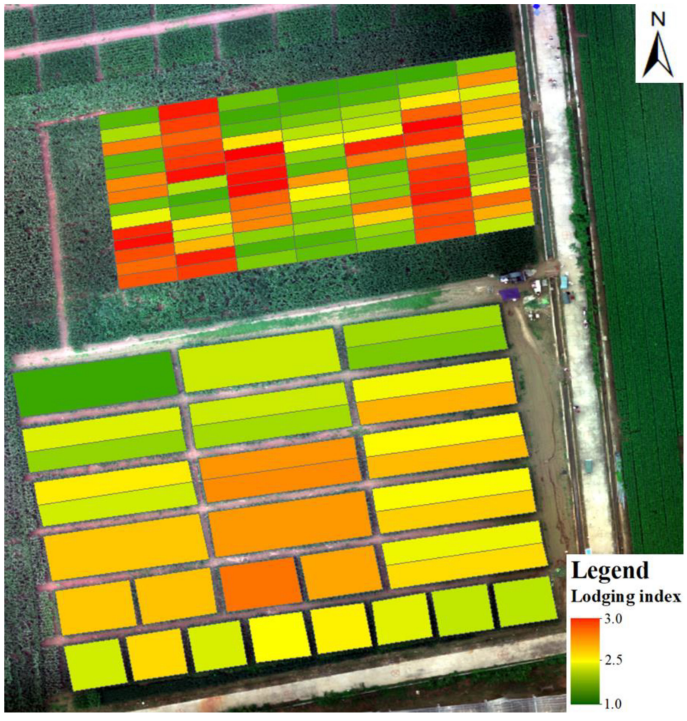

FIGURE 7
Distribution of lodging index for each plot.

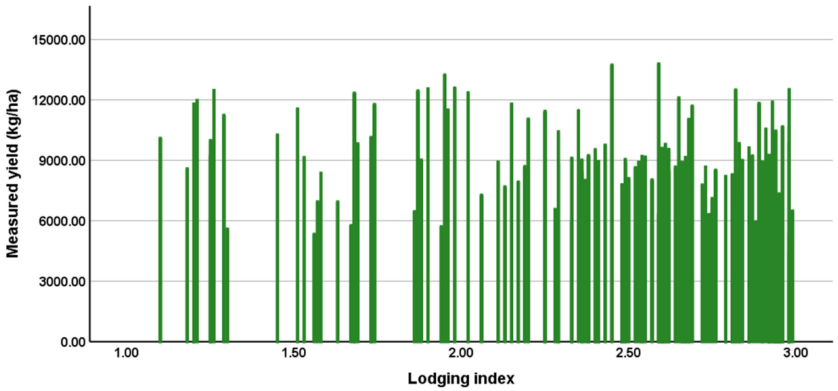

FIGURE 8
One-to-one correspondence between the lodging index and the measured yield of each plot.

The results indicate that the yield estimates are influenced by lodging. Thus, lodging must be considered to accurately estimate yields under lodging conditions.

3.3 Accurate estimation of maize yield with lodging index

Figure 11 shows the yield estimated by integrating into the model the canopy spectral, structural, and textural information and the lodging index. For the model developed at the same growth stage, the model including the lodging index performs better than without the lodging index. For models including the lodging index, a model developed at the later growth stages performs better than a model developed at early growth stages, which performs similarly to a model without the lodging index. For a model developed at the VT stage, R^2 increases from 0.170 to 0.242 and the RMSE decreases from 1799.01 to 1700.60 kg/ha. For a model developed at the R3 stage, R^2 increases from 0.434 to 0.533 and the RMSE decreases from 1466.87 to 1401.75 kg/ha. For a model developed at the VT stage, R^2 increases from 0.806 to 0.859 and the RMSE decreases from 1106.67 to 1086.41 kg/ha. These results indicate that the lodging index is a useful variable for accurately estimating maize yield when lodging occurs.

To test the importance of the lodging index in yield estimation, Figure 12 shows the relationship between the residual of the estimation model (i.e., the estimated yield minus the measured yield) and the lodging index. Upon integrating the lodging index into the maize yield estimation model for all three maize growth stages, plots with a low (high) lodging index experience more (less) overestimation but less (more) underestimation. In addition, the estimation residuals are smaller at the R5 stage than at the VT and R3 stages, although adding the lodging index. In general, adding lodging information to the model reduces the underestimation of yield in areas of slight lodging and reduces overestimation in areas of severe lodging, so the model performs better in the early stage after lodging than in the later stage.

4 Discussion

The construction of the lodging index should consider not only the degree of lodging but also the lodging area (Kendall et al., 2017). The lodging index proposed herein integrates the pixel-level degree of lodging and the fraction of the lodging area in the plot. The calculated lodging index well characterizes the degree of lodging of each plot (cf. Figures 6, 7), but subtle differences still exist where the lodging degree is underestimated. In addition, the lodging index represents the entire plot, but omits details within plots. Future work should construct a lodging index that represents more comprehensively the lodging situation of each community.

This study uses the spectral, structural, and textural information of the maize canopy to estimate maize yields. The model developed at the R5 stage has R^2 = 0.806, RMSE = 1106.67 kg/ha, and rRMSE = 13.4%, which is consistent with previous studies (Rischbeck et al.,

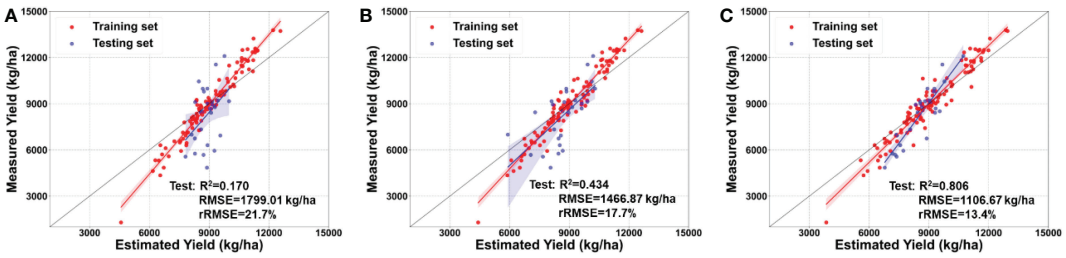

FIGURE 9
Estimation of maize yield by integrating multimodal data, but without considering the lodging index, at the **(A)** tasseling stage (VT), **(B)** milking stage (R3), and **(C)** denting stage (R5).

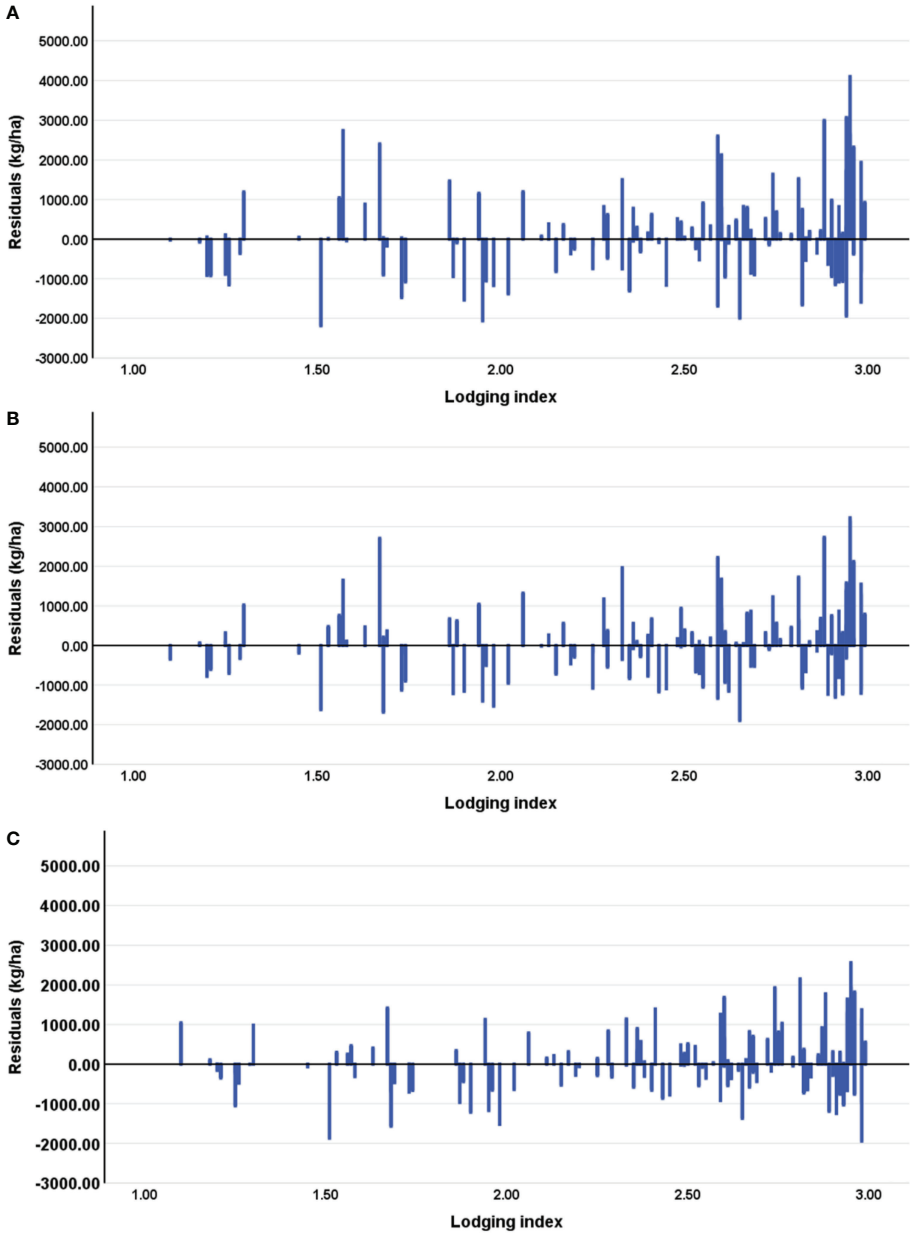

FIGURE 10
Residuals of yields estimated without considering the lodging index at the **(A)** tasseling stage (VT), **(B)** milking stage (R3), and **(C)** denting stage (R5).

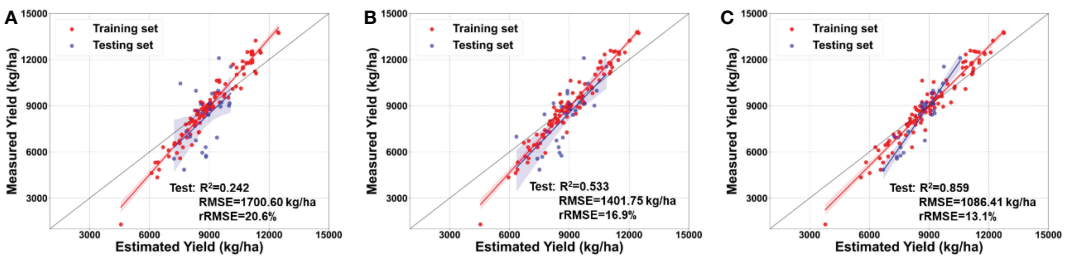

FIGURE 11
Maize yield estimated by integrating multimodal data with lodging index at the **(A)** tasseling stage (VT), **(B)** milking stage (R3), and **(C)** denting stage (R5).

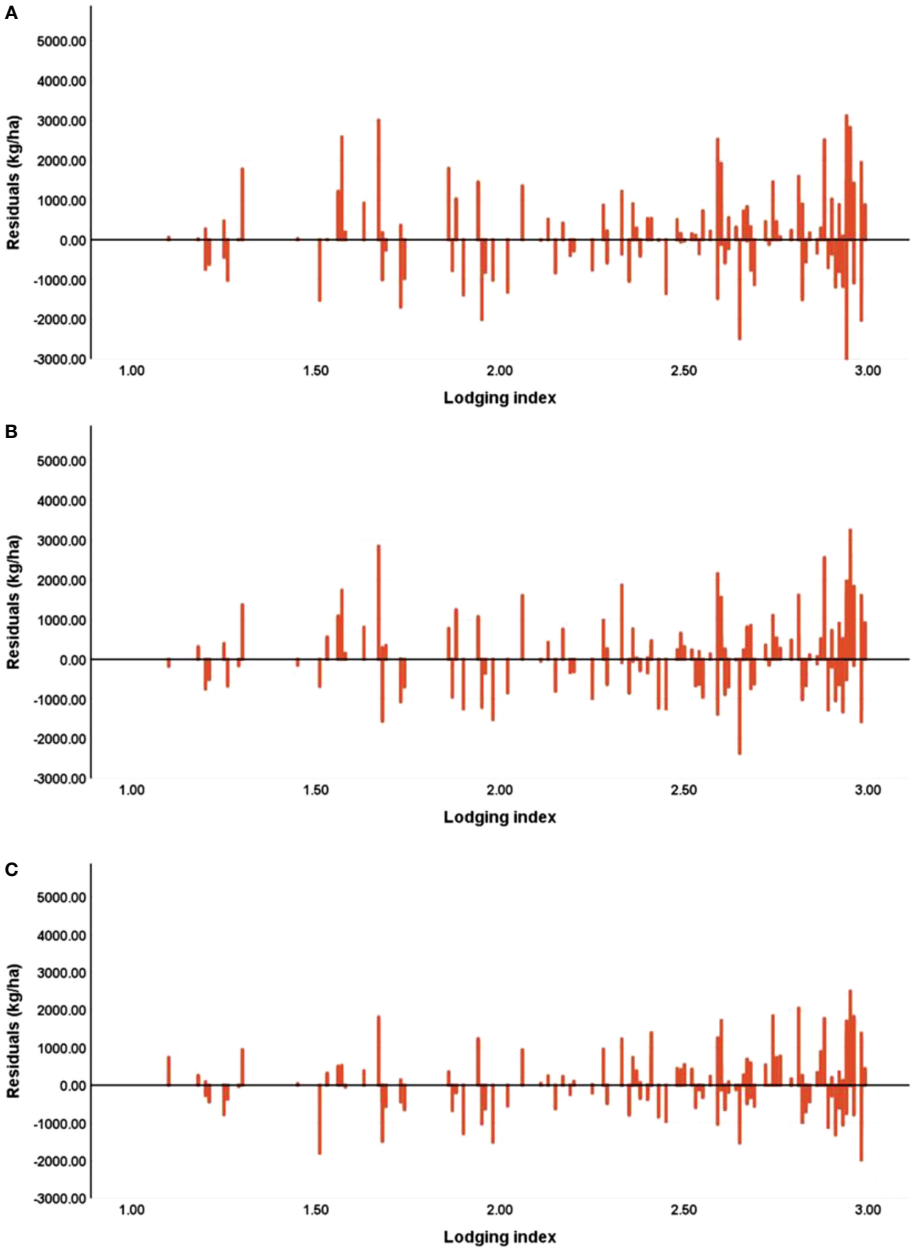

FIGURE 12
Estimation bias between measured yield and estimated yield, at the **(A)** tasseling stage (VT), **(B)** milking stage (R3), and **(C)** denting stage (R5).

2016; Feng et al., 2020; Ramadanningrum et al., 2020). Integrating the lodging index with canopy spectral, structural, and textural information improves maize-yield estimates (Figures 8, 10) because lodging occurred in the field. The main reason for these results may be that the lodging index constructed herein provides useful information about the degree of lodging of each plot under natural conditions.

The variable importance at different growth stages presented in Figure 13 also shows that the CC and lodging index are important for estimating maize yields at all three growth stages. This shows that the lodging index may offer additional information associated with the growth status of maize. In addition, different variables are not screened to improve the performance of the model. Previous studies have shown that a strong linear correlation exists between vegetation indices, whereas each variable produces different effects on retrieving vegetation parameters (Zeng et al., 2022). Therefore, multiple variables must be integrated to estimate yield with better accuracy.

The improved accuracy of yield estimation in the VT and R3 stages is slightly greater than that in the R5 stage, indicating a decreased response of maize plants to lodging as they grow. This is consistent with the varying importance at different growth stages presented in Figure 13. The importance of the lodging index in RFR modeling decreases as the growth stage approaches maturity. Such decreases may be attributed to the natural self-recovery of maize plants and the manual measures taken. The self-recovery of maize plants could change the canopy characteristics (Hu et al., 2021), which leads to less difference between lodged and non-lodged plants. Moreover, manual measures were applied within 3 days after lodging

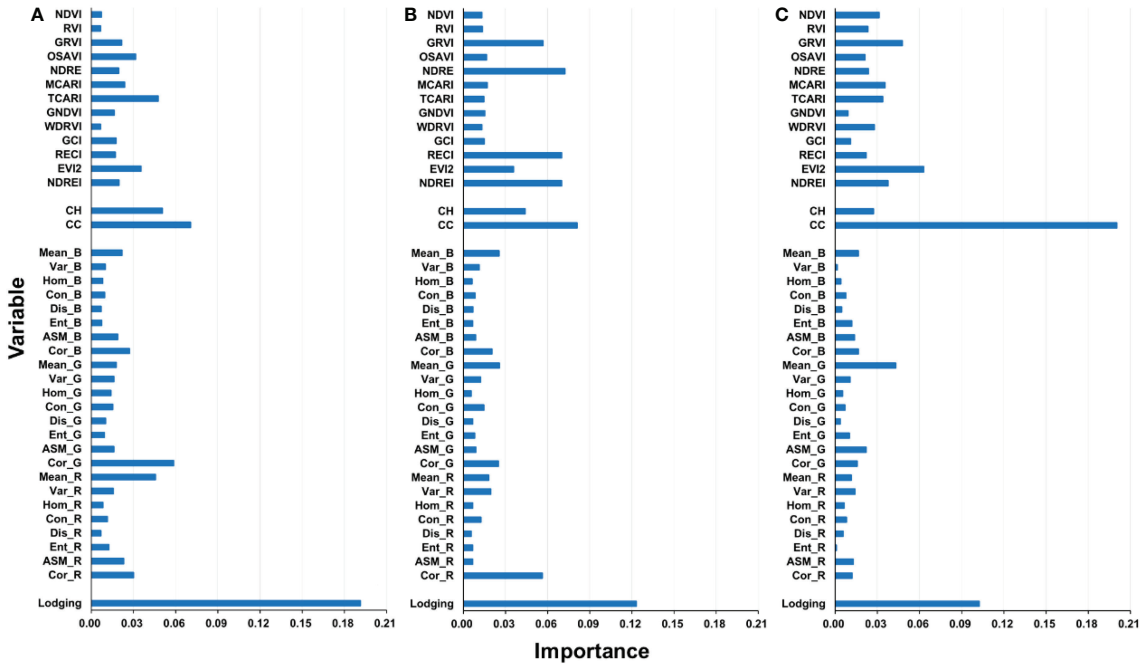

FIGURE 13
Variable importance of yield estimating model in different growth stages: **(A)** VT stage, **(B)** R3 stage, and **(C)** R5 stage.

occurred to help the maize plants return to the upright state. These measures may also reduce the influence of lodging on yields and thereby weaken the effect of the lodging index on yield estimation. In addition, the response of maize plants to lodging decreases with the growth of maize plants. In this study, all experimental plots were analyzed together to verify the stability of the model, and the role of lodging in yield estimation in a variety of experiments and nitrogen treatments was not considered. Thus, future studies should take this into consideration.

Regardless of whether the lodging index is included in the yield estimation model, the model developed in the R5 stage is the most accurate of the three growth stages, and the model developed in VT stage is the least accurate. The main reason for this result may be that pollination does not start at the VT stage, and many factors can later affect the development of seeds. For example, the canopy characteristics might change with the rapid growth of the crop after lodging occurs due to the self-recovery of maize (Han et al., 2018). As the maize plants grow closer to harvesting, the development of seeds the canopy characteristics tend to stabilize (Song et al., 2016), which would improve the correlation between the final grain yields and the canopy characteristics. Therefore, estimating crop yield at the early growth stage produces greater error than estimating crop yield at later growth stages.

5 Conclusion

In this study, the RGB and multispectral images obtained from a low-altitude UAV are used to estimate the grain yield of various varieties of maize with different nitrogen fertilization treatments. The canopy spectral, structural, and textural information were integrated into the RFR algorithm for estimating maize yield. In addition, to study how lodging affects yield estimation, a lodging index was developed to quantify the degree of lodging of each plot. The results lead to the following main conclusions: (1) The lodging index developed herein accurately quantifies the degree of lodging of each plot. (2) Including the lodging index into the yield-estimation model leads to more accurate crop yield estimates, and the model performs better in the early stage of maize growth than that in the later stage of maize growth. (3) The maize yield can be accurately estimated by integrating spectral, structural, textural, and structure information of the maize canopy with the lodging index, especially in the R5 stage, which gives R^2 = 0.859, RMSE = 1086.41 kg/ha, and rRMSE = 13.1%, followed by the R3 stage, with the VT stage producing the least accurate yield estimates.

Future efforts to improve UAV-based maize-yield estimation under various lodging conditions should focus on developing a more comprehensive lodging index, exploring how lodging affects yield estimation, and seeking new ways to integrate lodging information into yield estimation.

Data availability statement

The raw data supporting the conclusions of this article will be made available by the authors, without undue reservation.

Author contributions

BM, JX, HY, NC, WW and HX contributed to conception and design of the study. YL and LM organized the database. YL and ZW performed the statistical analysis. YL and CN wrote the first draft of the

manuscript. YL, XJ and CN wrote sections of the manuscript. All authors contributed to the article and approved the submitted version.

Funding

This research was supported by Central Public-interest Scientific Institution Basal Research Fund for Chinese Academy of Agricultural Sciences (Y2020YJ07, Y2022XK22), National Natural Science Foundation of China (42071426, 51922072, 51779161, 51009101), the National Key Research and Development Program of China (2021YFD1201602), the Agricultural Science and Technology Innovation Program of the Chinese Academy of Agricultural Sciences, Hainan Yazhou Bay Seed Lab (JBGS+B21HJ0221), Nanfan Special Project, CAAS (YJTC01, YBXM01), and the Special Fund for Independent Innovation of Agricultural Science and Technology in Jiangsu, China (CX(21)3065).

Conflict of interest

Author ZW is employed byHenan Provincial Communications Planning & Design Institute Co., LTD.

The remaining authors declare that the research was conducted in the absence of any commercial or financial relationships that could be construed as a potential conflict of interest.

Publisher's note

All claims expressed in this article are solely those of the authors and do not necessarily represent those of their affiliated organizations, or those of the publisher, the editors and the reviewers. Any product that may be evaluated in this article, or claim that may be made by its manufacturer, is not guaranteed or endorsed by the publisher.

References

Acreche, M. M., and Slafer, G. A. (2011). Lodging yield penalties as affected by breeding in Mediterranean wheats. *Field Crops Res.* 122 (1), 40–48. doi: 10.1016/j.fcr.2011.02.004

Aghighi, H., Azadbakht, M., Ashourloo, D., Shahrabi, H. S., and Radiom, S. (2018). Machine learning regression techniques for the silage maize yield prediction using time-series images of landsat 8 OLI. *IEEE J. Selected Topics Appl. Earth Observations Remote Sens.* 11 (12), 4563–4577. doi: 10.1109/JSTARS.2018.2823361

Berger, K., Verrelst, J., Féret, J-B., Wang, Z., Wocher, M., Strathmann, M., et al. (2020). Crop nitrogen monitoring: Recent progress and principal developments in the context of imaging spectroscopy missions. *Remote Sens. Environ.* 242, 111758. doi: 10.1016/j.rse.2020.111758

Breiman, L. (2001). Random forests. *Mach. Learn.* 45 (1), 5–32. doi: 10.1023/A:1010933404324

Cai, Y., Guan, K., Lobell, D., Potgieter, A. B., Wang, S., Peng, J., et al. (2019). Integrating satellite and climate data to predict wheat yield in Australia using machine learning approaches. *Agric. For. Meteorol.* 274, 144–159. doi: 10.1016/j.agrformet.2019.03.010

Castillo-Martínez, M.Á., Gallegos-Funes, F. J., Carvajal-Gámez, B. E., Urriolagoitia-Sosa, G., and Rosales-Silva, A. J. (2020). Color index based thresholding method for background and foreground segmentation of plant images. *Comput. Electron. Agric.* 178 (2020), 105783. doi: 10.1016/j.compag.2020.105783

Chauhan, S., Darvishzadeh, R., Boschetti, M., Pepe, M., and Nelson, A. (2019). Remote sensing-based crop lodging assessment: Current status and perspectives. *ISPRS J. Photogrammetry Remote Sens.* 151, 124–140. doi: 10.1016/j.isprsjprs.2019.03.005

Chen, L., Yi, Y., Wang, W., Zeng, Y., Tan, X., Wu, Z., et al. (2021). Innovative furrow ridging fertilization under a mechanical direct seeding system improves the grain yield and lodging resistance of early indica rice in south China. *Field Crops Res.* 270, 108184. doi: 10.1016/j.fcr.2021.108184

Crane-Droesch, A. (2018). Machine learning methods for crop yield prediction and climate change impact assessment in agriculture. *Environ. Res. Lett.* 13 (11), 114003. doi: 10.1088/1748-9326/aae159

Daughtry, C. S. T., Walthall, C. L., Kim, M. S., de Colstoun, E. B., and McMurtrey, J. E. (2000). Estimating corn leaf chlorophyll concentration from leaf and canopy reflectance. *Remote Sens. Environ.* 74 (2), 229–239. doi: 10.1016/S0034-4257(00)00113-9

Duan, T., Chapman, S. C., Guo, Y., and Zheng, B. (2017). Dynamic monitoring of NDVI in wheat agronomy and breeding trials using an unmanned aerial vehicle. *Field Crops Res.* 210, 71–80. doi: 10.1016/j.fcr.2017.05.025

Duan, B., Fang, S., Gong, Y., Peng, Y., Wu, X., Zhu, R., et al. (2021). Remote estimation of grain yield based on UAV data in different rice cultivars under contrasting climatic zone. *Field Crops Res.* 267, 108148, 71–80. doi: 10.1016/j.fcr.2021.108148

Feng, L., Wang, Y., Zhang, Z., and Du, Q. (2021). Geographically and temporally weighted neural network for winter wheat yield prediction. *Remote Sens. Environ.* 262, 112514. doi: 10.1016/j.rse.2021.112514

Feng, A., Zhou, J., Vories, E. D., Sudduth, K. A., and Zhang, M. (2020). Yield estimation in cotton using UAV-based multi-sensor imagery. *Biosyst. Eng.* 193, 101–114. doi: 10.1016/j.biosystemseng.2020.02.014

Gitelson, A. A. (2004). Wide dynamic range vegetation index for remote quantification of biophysical characteristics of vegetation. *J. Plant Physiol.* 161 (2), 165–173. doi: 10.1078/0176-1617-01176

Gitelson, A. A., Gritz, Y., and Merzlyak, M. N. (2003). Relationships between leaf chlorophyll content and spectral reflectance and algorithms for non-destructive chlorophyll assessment in higher plant leaves. *J. Plant Physiol.* 160 (3), 271–282. doi: 10.1078/0176-1617-00887

Gitelson, A. A., and Merzlyak, M. N. (1997). Remote estimation of chlorophyll content in higher plant leaves. *Int. J. Remote Sens.* 18 (12), 2691–2697. doi: 10.1080/014311697217558

Gitelson, A. A., Vina, A., Ciganda, V., Rundquist, D. C., and Arkebauer, T. J. (2005). Remote estimation of canopy chlorophyll content in crops. *Geophysical Res. Lett.* 32 (8), L08403. doi: 10.1029/2005GL022688

Haboudane, D., Miller, J. R., Tremblay, N., Zarco-Tejada, P. J., and Dextraze, L. (2002). Integrated narrow-band vegetation indices for prediction of crop chlorophyll content for application to precision agriculture. *Remote Sens. Environ.* 81 (2), 416–426. doi: 10.1016/S0034-4257(02)00018-4

Hall-Beyer, M. (2017). Practical guidelines for choosing GLCM textures to use in landscape classification tasks over a range of moderate spatial scales. *Int. J. Remote Sens.* 38 (5), 1312–1338. doi: 10.1080/01431161.2016.1278314

Hamuda, E., Glavin, M., and Jones, E. (2016). A survey of image processing techniques for plant extraction and segmentation in the field. *Comput. Electron. Agric.* 125, 184–199. doi: 10.1016/j.compag.2016.04.024

Han, L., Yang, G., Feng, H., Zhou, C., Yang, H., Xu, B., et al. (2018). Quantitative identification of maize lodging-causing feature factors using unmanned aerial vehicle images and a nomogram computation. *Remote Sens.* 10 (10), 1528. doi: 10.3390/rs10101528

Haralick, R. M., Shanmugam, K., and Dinstein, I. (1973). Textural features for image classification. *IEEE Trans. Syst. Man Cybernetics* SMC-3 (6), 610–621. doi: 10.1109/TSMC.1973.4309314

Hassan, M. A., Yang, M., Rasheed, A., Jin, X., Xia, X., Xiao, Y., et al. (2018). Time-series multispectral indices from unmanned aerial vehicle imagery reveal senescence rate in bread wheat. *Remote Sens.* 10 (6), 809. doi: 10.3390/rs10060809

Hu, X., Sun, L., Gu, X., Sun, Q., Wei, Z., Pan, Y., et al. (2021). Assessing the self-recovery ability of maize after lodging using UAV-LiDAR data. *Remote Sens.* 13 (12), 2270. doi: 10.3390/rs13122270

Jiang, Z., Huete, A. R., Didan, K., and Miura, T. (2008). Development of a two-band enhanced vegetation index without a blue band. *Remote Sens. Environ.* 112 (10), 3833–3845. doi: 10.1016/j.rse.2008.06.006

Jin, X., Li, Z., Feng, H., Ren, Z., and Li, S. (2020). Estimation of maize yield by assimilating biomass and canopy cover derived from hyperspectral data into the AquaCrop model. *Agric. Water Manage.* 227, 105846. doi: 10.1016/j.agwat.2019.105846

Johansen, K., Morton, M. J.L., Malbeteau, Y., Aragon, B., Al-Mashharawi, S., Ziliani, M. G., et al. (2020). Predicting biomass and yield in a tomato phenotyping experiment using UAV imagery and random forest. *Front. Artif. Intell.* 3, 28. doi: 10.3389/frai.2020.00028

Johnson, M. D., Hsieh, W. W., Cannon, A. J., Davidson, A., and Bédard, F. (2016). Crop yield forecasting on the Canadian prairies by remotely sensed vegetation indices and machine learning methods. *Agric. For. Meteorol.* 218-219, 74–84. doi: 10.1016/j.agrformet.2015.11.003

Jones, J. W., Hoogenboom, G., Porter, C. H., Boote, K. J., Batchelor, W. D., Hunt, L. A., et al. (2003). The DSSAT cropping system model. *Eur. J. Agron.* 18 (3), 235–265. doi: 10.1016/S1161-0301(02)00107-7

Ju, S., Lim, H., Ma, J. W., Kim, S., Lee, K., Zhao, S., et al. (2021). Optimal county-level crop yield prediction using MODIS-based variables and weather data: A comparative

study on machine learning models. *Agric. For. Meteorol.* 307, 108530. doi: 10.1016/j.agrformet.2021.108530

Kang, Y., and Özdoğan, M. (2019). Field-level crop yield mapping with landsat using a hierarchical data assimilation approach. *Remote Sens. Environ.* 228, 144–163. doi: 10.1016/j.rse.2019.04.005

Kashiwagi, T., Sasaki, H., and Ishimaru, K. (2015). Factors responsible for decreasing sturdiness of the lower part in lodging of rice (Oryza sativaL.). *Plant Production Sci.* 8 (2), 166–172. doi: 10.1626/pps.8.166

Kendall, S. L., Holmes, H., White, C. A., Clarke, S. M., and Berry, P. M. (2017). Quantifying lodging-induced yield losses in oilseed rape. *Field Crops Res.* 211, 106–113. doi: 10.1016/j.fcr.2017.06.013

Li, B., Xu, X., Zhang, L., Han, J., Bian, C., Li, G., et al. (2020). Above-ground biomass estimation and yield prediction in potato by using UAV-based RGB and hyperspectral imaging. *ISPRS J. Photogrammetry Remote Sens.* 162, 161–172. doi: 10.1016/j.isprsjprs.2020.02.013

Li, L., Wang, B., Feng, P., Wang, H., He, Q., Wang, Y., et al. (2021). Crop yield forecasting and associated optimum lead time analysis based on multi-source environmental data across China. *Agric. For. Meteorol.* 308–309, 108558. doi: 10.1016/j.agrformet.2021.108558

Li, W.-q., Han, M.-M., Pang, D.-W., Chen, J., Wang, Y.-Y., Dong, H.-H., et al. (2022). Characteristics of lodging resistance of high-yield winter wheat as affected by nitrogen rate and irrigation managements. *J. Integr. Agric.* 21 (5), 1290–1309. doi: 10.1016/S2095-3119(20)63566-3

Liu, X.-m., Gu, W.-r., Li, C.-f., Li, J., and Wei, S. (2021). Effects of nitrogen fertilizer and chemical regulation on spring maize lodging characteristics, grain filling and yield formation under high planting density in heilongjiang province, China. *J. Integr. Agric.* 20 (2), 511–526. doi: 10.1016/S2095-3119(20)63403-7

Luo, X., Wu, Z., Fu, L., Dan, Z., Yuan, Z., Liang, T., et al. (2022). Evaluation of lodging resistance in rice based on an optimized parameter from lodging index. *Crop Sci.* 62 (3), 1318–1332. doi: 10.1002/csc2.20712

Maimaitijiang, M., Ghulam, A., Sidike, P., Hartling, S., Maimaitiyiming, M., Peterson, K., et al. (2017). Unmanned aerial system (UAS)-based phenotyping of soybean using multi-sensor data fusion and extreme learning machine. *ISPRS J. Photogrammetry Remote Sens.* 134, 43–58. doi: 10.1016/j.isprsjprs.2017.10.011

Maimaitijiang, M., Sagan, V., Sidike, P., Maimaitiyiming, M., Hartling, S., Peterson, K. T., et al. (2019). Vegetation index weighted canopy volume model (CVMVI) for soybean biomass estimation from unmanned aerial system-based RGB imagery. *ISPRS J. Photogrammetry Remote Sens.* 151, 27–41. doi: 10.1016/j.isprsjprs.2019.03.003

Maimaitijiang, M., Sagan, V., Sidike, P., Hartling, S., Esposito, F., and Fritschi, F. B. (2020). Soybean yield prediction from UAV using multimodal data fusion and deep learning. *Remote Sens. Environ.* 237, 111599. doi: 10.1016/j.rse.2019.111599

Maimaitijiang, M., Sagan, V., and Fritschi, F. B. (2021). "Crop Yield Prediction using Satellite/Uav Synergy and Machine Learning," 2021 IEEE International Geoscience and Remote Sensing Symposium IGARSS, pp. 6276–6279, doi: 10.1109/IGARSS47720.2021.9554735.

Malambo, L., Popescu, S. C., Murray, S. C., Putman, E., Pugh, N. A., and Horne, D. W.. (2018). Multitemporal field-based plant height estimation using 3D point clouds generated from small unmanned aerial systems high-resolution imagery. *Int. J. Appl. Earth Observation Geoinformation* 64, 31–42. doi: 10.1016/j.jag.2017.08.014

Mi, C., Zhang, X., Li, S., Yang, J., Zhu, D., and Yang, Y. (2011). Assessment of environment lodging stress for maize using fuzzy synthetic evaluation. *Math. Comput. Model.* 54 (3), 1053–1060. doi: 10.1016/j.mcm.2010.11.035

Mishra, V., Cruise, J. F., and Mecikalski, J. R. (2021). Assimilation of coupled microwave/thermal infrared soil moisture profiles into a crop model for robust maize yield estimates over southeast united states. *Eur. J. Agron.* 123, 126208. doi: 10.1016/j.eja.2020.126208

Mohanaiah, P., Sathyanarayana, P., and Gurukumar, L. (2013). Image texture feature extraction using GLCM approach. *Int. J. Sci. Res. Publications* 3 (5), 1–5.

Nagy, A., Szabó, A., Adeniyi, O. D., and Tamás, J. (2021). Wheat yield forecasting for the tisza river catchment using landsat 8 NDVI and SAVI time series and reported crop statistics. *Agronomy* 11 (4), 652. doi: 10.3390/agronomy11040652

Palosuo, T., Kersebaum, K. C., Angulo, C., Hlavinka, P., Moriondo, M., Olesen, J. E., et al. (2011). Simulation of winter wheat yield and its variability in different climates of Europe: A comparison of eight crop growth models. *Eur. J. Agron.* 35 (3), 103–114. doi: 10.1016/j.eja.2011.05.001

Panek, E., and Gozdowski, D. (2021). Relationship between MODIS derived NDVI and yield of cereals for selected European countries. *Agronomy* 11 (2), 340. doi: 10.3390/agronomy11020340

Park, Y., and Guldmann, J.-M. (2020). Measuring continuous landscape patterns with Gray-level Co-occurrence matrix (GLCM) indices: An alternative to patch metrics? *Ecol. Indic.* 109, 105802. doi: 10.1016/j.ecolind.2019.105802

Peng, X., Han, W., Ao, J., and Wang, Y. (2021). Assimilation of LAI derived from UAV multispectral data into the SAFY model to estimate maize yield. *Remote Sens.* 13 (6), 1094. doi: 10.3390/rs13061094

Ramadanningrum, D. P., Kamal, M., and Murti, S. H. (2020). Image-based tea yield estimation using landsat-8 OLI and sentinel-2B images. *Remote Sens. Applications: Soc. Environ.* 20, 100424. doi: 10.1016/j.rsase.2020.100424

Rischbeck, P., Elsayed, S., Mistele, B., Barmeier, G., Heil, K., and Schmidhalter, U. (2016). Data fusion of spectral, thermal and canopy height parameters for improved yield prediction of drought stressed spring barley. *Eur. J. Agron.* 78, 44–59. doi: 10.1016/j.eja.2016.04.013

Rondeaux, G., Steven, M., and Baret, F. (1996). Optimization of soil-adjusted vegetation indices. *Remote Sens. Environ.* 55 (2), 95–107. doi: 10.1016/0034-4257(95)00186-7

Rouse, J., Haas, R. H., Schell, J. A., and Deering, D. W. (1974). Monitoring vegetation systems in the great plains with ERTS. In: *NASA SP-351, Third ERTS-1 Symposium* NASA, Washington DC. 1, pp. 309–317.

Shafiee, S., Lied, L. M., Burud, I., Dieseth, J. A., Alsheikh, M., and Lillemo, M. (2021). Sequential forward selection and support vector regression in comparison to LASSO regression for spring wheat yield prediction based on UAV imagery. *Comput. Electron. Agric.* 183, 106036. doi: 10.1016/j.compag.2021.106036

Song, R., Cheng, T., Yao, X., Tian, Y., Zhu, Y., and Cao, W.. (2016). "Evaluation of landsat 8 time series image stacks for predicitng yield and yield components of winter wheat," in *2016 IEEE International Geoscience and Remote Sensing Symposium (IGARSS)*. 2016, 6300–6303. doi: 10.1109/IGARSS.2016.7730647

Stanton, C., Starek, M. J., Elliott, N., Brewer, M., Maeda, M. M., Chu, T., et al. (2017). Unmanned aircraft system-derived crop height and normalized difference vegetation index metrics for sorghum yield and aphid stress assessment. *J. Appl. Remote Sens.* 11 (2), 026035. doi: 10.1117/1.JRS.11.026035

Steduto, P., Hsiao, T. C., Raes, D., and Fereres, E. (2009). AquaCrop–the FAO crop model to simulate yield response to water: I. concepts and underlying principles. *Agron. J.* 101 (3), 426–437. doi: 10.2134/agronj2008.0139s

Sui, J., Qin, Q., Ren, H., Sun, Y., Zhang, T., Wang, J., et al. (2018). Winter wheat production estimation based on environmental stress factors from satellite observations. *Remote Sens.* 10 (6), 962. doi: 10.3390/rs10060962

Tan, C. W., Zhang, P. P., Zhou, X. X., Wang, Z. X., Xu, Z. Q., Mao, W., et al. (2020). Quantitative monitoring of leaf area index in wheat of different plant types by integrating NDVI and beer-Lambert law. *Sci. Rep.* 10 (1), 929. doi: 10.1038/s41598-020-57750-z

Tan, S., Mortensen, A. K., Ma, X., Boelt, B., and Gislum, R. (2021). Assessment of grass lodging using texture and canopy height distribution features derived from UAV visual-band images. *Agric. For. Meteorol.* 308–309, 108541. doi: 10.1016/j.agrformet.2021.108541

Tao, H., Feng, H., Xu, L., Miao, M., Yang, G., Yang, X., et al. (2020). Estimation of the yield and plant height of winter wheat using UAV-based hyperspectral images. *Sensors (Basel)* 20 (4), 1231. doi: 10.3390/s20041231

Tucker, C. J. (1979). Red and photographic infrared linear combinations for monitoring vegetation. *Remote Sens. Environ.* 8 (2), 127–150. doi: 10.1016/0034-4257(79)90013-0

Van Dam, J. C., Huygen, J., Wesseling, J., Feddes, R., Kabat, P., Van Walsum, P., et al. (1997). Theory of SWAP version 2.0. *Tech. Document* 45, 167.

van Diepen, C. A., Wolf, J., van Keulen, H., and Rappoldt, C. (1989). WOFOST: a simulation model of crop production. *Soil Use Manage.* 5 (1), 16–24. doi: 10.1111/j.1475-2743.1989.tb00755.x

Wan, L., Cen, H., Zhu, J., Zhang, J., Zhu, Y., Sun, D., et al. (2020). Grain yield prediction of rice using multi-temporal UAV-based RGB and multispectral images and model transfer – a case study of small farmlands in the south of China. *Agric. For. Meteorol.* 291, 108096. doi: 10.1016/j.agrformet.2020.108096

Wang, Z. (2021). Detection and analysis of degree of maize lodging using UAV-RGB image multi-feature factors and V arious classification methods. *ISPRS Int. J. Geo-Information.* 10, 309. doi: 10.3390/ijgi 10050309

Wang, F., Yi, Q., Hu, J., Xie, L., Yao, X., Xu, T., et al. (2021). Combining spectral and textural information in UAV hyperspectral images to estimate rice grain yield. *Int. J. Appl. Earth Observation Geoinformation* 102, 102397. doi: 10.1016/j.jag.2021.102397

Wu, S., Yang, P., Ren, J., Chen, Z., and Li, H. (2021). Regional winter wheat yield estimation based on the WOFOST model and a novel VW-4DEnSRF assimilation algorithm. *Remote Sens. Environ.* 255, 112276. doi: 10.1016/j.rse.2020.112276

Xie, C., and Yang, C. (2020). A review on plant high-throughput phenotyping traits using UAV-based sensors. *Comput. Electron. Agric.* 178, 105731. doi: 10.1016/j.compag.2020.105731

Xue, J., Xie, R.-Z., Zhang, W.-F., Wang, K.-R., Hou, P., Ming, B., et al. (2017). Research progress on reduced lodging of high-yield and -density maize. *J. Integr. Agric.* 16 (12), 2717–2725. doi: 10.1016/S2095-3119(17)61785-4

Xu, W., Chen, P., Zhan, Y., Chen, S., Zhang, L., Lan, Y., et al. (2021a). Cotton yield estimation model based on machine learning using time series UAV remote sensing data. *Int. J. Appl. Earth Observation Geoinformation* 104, 102511. doi: 10.1016/j.jag.2021.102511

Xu, X., Nie, C., Jin, X., Li, Z., Zhu, H., Xu, H., et al. (2021b). A comprehensive yield evaluation indicator based on an improved fuzzy comprehensive evaluation method and hyperspectral data. *Field Crops Res.* 270, 108204. doi: 10.1016/j.fcr.2021.108204

Xu, L., Zhou, L., Meng, R., Zhao, F., Lv, Z., Xu, B., et al. (2022). An improved approach to estimate ratoon rice aboveground biomass by integrating UAV-based spectral, textural and structural features. *Precis. Agric.* 23, 1276–1301. doi: 10.1007/s11119-022-09884-5

Yang, W., Nigon, T., Hao, Z., Dias Paiao, G., Fernández, F. G., Mulla, D., et al. (2021). Estimation of corn yield based on hyperspectral imagery and convolutional neural network. *Comput. Electron. Agric.* 184, 106092. doi: 10.1016/j.compag.2021.106092

Yue, J., Yang, G., Tian, Q., Feng, H., Xu, K., and Zhou, C. (2019). Estimate of winter-wheat above-ground biomass based on UAV ultrahigh-ground-resolution image textures and vegetation indices. *ISPRS J. Photogrammetry Remote Sens.* 150, 226–244. doi: 10.1016/j.isprsjprs.2019.02.022

Yu, N., Li, L., Schmitz, N., Tian, L. F., Greenberg, J. A., Diers, B. W., et al. (2016). Development of methods to improve soybean yield estimation and predict plant maturity with an unmanned aerial vehicle based platform. *Remote Sens. Environ.* 187, 91–101. doi: 10.1016/j.rse.2016.10.005

Yu, D., Zha, Y., Shi, L., Jin, X., Hu, S., Yang, Q., et al. (2020). Improvement of sugarcane yield estimation by assimilating UAV-derived plant height observations. *Eur. J. Agron.* 121, 126159. doi: 10.1016/j.eja.2020.126159

Zeng, Y., Hao, D., Huete, A., Dechant, B., Berry, J., Chen, J. M., et al. (2022). Optical vegetation indices for monitoring terrestrial ecosystems globally. *Nat. Rev. Earth Environ.* 3 (7), 477–493. doi: 10.1038/s43017-022-00298-5

Zhang, Z., Jin, Y., Chen, B., and Brown, P. (2019). California Almond yield prediction at the orchard level with a machine learning approach. *Front. Plant Sci.* 10, 809. doi: 10.3389/fpls.2019.00809

Zheng, H., Cheng, T., Zhou, M., Li, D., Yao, X., Tian, Y., et al. (2018). Improved estimation of rice aboveground biomass combining textural and spectral analysis of UAV imagery. *Precis. Agric.* 20 (3), 611–629. doi: 10.1007/s11119-018-9600-7

Zhou, X., Zheng, H. B., Xu, X. Q., He, J. Y., Ge, X. K., Yao, X., et al. (2017). Predicting grain yield in rice using multi-temporal vegetation indices from UAV-based multispectral and digital imagery. *ISPRS J. Photogrammetry Remote Sens.* 130, 246–255. doi: 10.1016/j.isprsjprs.2017.05.003

frontiers | Frontiers in Plant Science

TYPE Original Research
PUBLISHED 18 January 2023
DOI 10.3389/fpls.2022.1048479

Check for updates

OPEN ACCESS

EDITED BY
Xiuliang Jin,
Key Laboratory of Crop Physiology and Ecology (CAAS), China

REVIEWED BY
Haikuan Feng,
Beijing Research Center for Information Technology in Agriculture, China
Yansheng Li,
Wuhan University, China

*CORRESPONDENCE
Changping Huang
huangcp@aircas.ac.cn

SPECIALTY SECTION
This article was submitted to Sustainable and Intelligent Phytoprotection, a section of the journal Frontiers in Plant Science

RECEIVED 19 September 2022
ACCEPTED 28 December 2022
PUBLISHED 18 January 2023

CITATION
Lang P, Zhang L, Huang C, Chen J, Kang X, Zhang Z and Tong Q (2023) Integrating environmental and satellite data to estimate county-level cotton yield in Xinjiang Province.
Front. Plant Sci. 13:1048479.
doi: 10.3389/fpls.2022.1048479

COPYRIGHT
© 2023 Lang, Zhang, Huang, Chen, Kang, Zhang and Tong. This is an open-access article distributed under the terms of the Creative Commons Attribution License (CC BY). The use, distribution or reproduction in other forums is permitted, provided the original author(s) and the copyright owner(s) are credited and that the original publication in this journal is cited, in accordance with accepted academic practice. No use, distribution or reproduction is permitted which does not comply with these terms.

Integrating environmental and satellite data to estimate county-level cotton yield in Xinjiang Province

Ping Lang[1,2], Lifu Zhang[1,2], Changping Huang[1,2]*, Jiahua Chen[1,2], Xiaoyan Kang[1], Ze Zhang[3] and Qingxi Tong[1]

[1]State Key Laboratory of Remote Sensing Science, Aerospace Information Research Institute, Chinese Academy of Sciences, Beijing, China, [2]University of Chinese Academy of Sciences, Beijing, China, [3]Xinjiang Production and Construction Crops Oasis Eco-Agriculture Key Laboratory, College of Agriculture, Shihezi University, Shihezi, China

Accurate and timely estimation of cotton yield over large areas is essential for precision agriculture, facilitating the operation of commodity markets and guiding agronomic management practices. Remote sensing (RS) and crop models are effective means to predict cotton yield in the field. The satellite vegetation indices (VIs) can describe crop yield variations over large areas but can't take the exact environmental impact into consideration. Climate variables (CVs), the result of the influence of spatial heterogeneity in large regions, can provide environmental information for better estimation of cotton yield. In this study, the most important VIs and CVs for estimating county-level cotton yield across Xinjiang Province were screened out. We found that the VIs of canopy structure and chlorophyll contents, and the CVs of moisture, were the most significant factors for cotton growth. For yield estimation, we utilized four approaches: least absolute shrinkage and selection operator regression (LASSO), support vector regression (SVR), random forest regression (RFR) and long short-term memory (LSTM). Due to its ability to capture temporal features over the long term, LSTM performed best, with an R^2 of 0.76, root mean square error (RMSE) of 150 kg/ha and relative RMSE (rRMSE) of 8.67%; moreover, an additional 10% of the variance could be explained by adding CVs to the VIs. For the within-season yield estimation using LSTM, predictions made 2 months before harvest were the most accurate (R^2 = 0.65, RMSE = 220 kg/ha, rRMSE = 15.97%). Our study demonstrated the feasibility of yield estimation and early prediction at the county level over large cotton cultivation areas by integrating satellite and environmental data.

KEYWORDS

remote sensing, climate variables, GEE, deep learning, yield estimation, cotton

Introduction

Cotton is an important cash crop used in fabrics, cloth, and oil. According to the International Cotton Advisory Committee (ICAC), China is the largest cotton consumer and second largest cotton producer in the world, and Xinjiang Province accounts for > 80% of the total cotton production of China. Precise estimation of the cotton yield of Xinjiang Province could inform Chinese and international policy decisions, and promote stable operation of agricultural commodity markets. Besides different genotype and management practices, extreme weather (e.g. droughts, floods, and high temperatures) also makes crop yield vary from year to year (Bauer et al., 2015). To prevent losses, it is necessary to measure the cotton yield in an accurate and timely manner for effective agronomic management practices (Xu et al., 2021a; Li et al., 2022b).

Satellite remote sensing (RS) is widely applied in agricultural research. Vegetation indices (VIs) calculated from satellite data are the most common means of predicting crop yield (Bian et al., 2022). VIs can describe such biotic features as the canopy structure, chlorophyll, and nitrogen content of crops and different indices indicate different features. The Normalized Difference Vegetation Index (NDVI), Enhanced Vegetation Index (EVI) and Near-Infrared Reflectance of Vegetation (NIRv) have been used to explain variation in wheat, corn, rice and soybean yields (Johnson, 2014; Meng et al., 2017; Fan et al., 2021). However, it is still not clear which RS VIs are optimal for predicting cotton yield and which biotic features are most relevant to the yield. Additionally, genotype (G), environment (E) and management (M), namely biotic and abiotic conditions have the greatest influence on crop growth and production (Jones et al., 2003; Tao et al., 2009). VIs alone have limited ability to estimate yield. Therefore, Climate variables (CVs) have also been applied by taking abiotic features into consideration at the same time. Temperature and precipitation are the most influential abiotic factors in crop breeding (Mathieu and Aires, 2018; Kang et al., 2020). However, their predictive power varies among regions. Precipitation does not precisely reflect the moisture available for plants between the sowing and mellowing stages. Since except for inevitable algorithm error in estimating precipitation value, the processes of crop growth are complicated. Water evaporation of leaves, and irrigation and drainage management practices, also affect moisture (Folberth et al., 2016; Chen et al., 2018). Vapor pressure (vap), vapor pressure deficit (vpd), reference evapotranspiration (pet), land surface temperature (LST), and the soil moisture resulting from the interaction of liquid and solar radiation in soil and vegetation have been used in analyses of the effects of climate changes on crop production (Rigden et al., 2020). Recent researches have shown that each satellite and climate index has advantages and disadvantages for predicting yield that depend on the diversity of the terrain and topography, spatial distribution of crops, and phenology (Tao et al., 2009; Kern et al., 2018). Therefore, it is necessary to investigate the relationships between VIs and environmental stress in the context of cotton crops over a large area.

The main approaches to crop yield estimation are crop models and regression methods. Biophysical models provide mathematical descriptions of crop growth and development in terms of radiation, photosynthetic production, respiration, transpiration, dry matter generation, and distribution (Sinclair and Seligman, 1996; Dorigo et al., 2007; Kheir et al., 2022). Process-based crop models consider all the G×E×M factors and their interactions. These models use daily crop type, soil, meteorology and field management data as input (Sinclair and Seligman, 1996; Keating et al., 2003; de Wit et al., 2019). However, the use of these high-quality inputs throughout the breeding and reproductive period is computationally intense (Tao et al., 2018). Although crop models for monitoring and predicting yield at a single location, or at the field scale, have made great progress, application to the regional scale is difficult due to the intricate data collection and huge calculation costs (Curnel et al., 2011; Wu et al., 2021). Statistical regression models are powerful tools applicable to large scales. They use fewer parameters and simpler inputs than the crop models, and are less computationally intense. Regression methods for yield prediction typically use optical satellite data instead of daily inputs over the entire growth stage. Moreover, they perform better than process-based crop models when there is a sufficient amount of training data (Liu et al., 2012). However, conventional linear regression methods have difficulty capturing the sophisticated relationships between various features, and may oversimplify the nonlinear relationships. Machine learning (ML) and deep learning (DL) algorithms can overcome the drawbacks of traditional statistical-based models. They disentangle the complicated relationships among input and target variables by fully training the model before practical application (LeCun et al., 2015; Ashapure et al., 2020). As well as having lower computational costs than biophysical models, DL and ML models can also assess the yield of numerous crops with greater accuracy and less error than linear regression approaches. DL methods have made particularly significant progress. They routinely involve hidden layers that abstract non-linear features to another dimensional space for linear partition as a black-box, thus simplifying the relationships among various inputs and outputs (LeCun et al., 2015; Chu and Yu, 2020). At the same time, these non-linear models are usually complex and difficult to interpret, highly dependent on data volume and need test sets to avoid overfitting. Nevertheless, ML and DL methods show excellent performance in terms of capturing the spatiotemporal variation of input data (van Klompenburg et al., 2020; Xu et al., 2021b). Recent studies have demonstrated the superiority of ML and DL methods for crop yield prediction. Support vector regression (SVR), random forest regression (RFR), convolution neural networks (CNNs), and long short-term memory networks (LSTM) have successfully estimated the yield of various crop types, considering the effects of climate change at the pixel or county scale (Gopal and Bhargavi, 2019; Sun et al., 2019; Khaki et al., 2020). To enhance ML and DL methods, the ensemble Bayesian model averaging (EBMA) and You Look Only Once version 5 (YOLOv5) which are improved models also applied (Wang et al., 2022; Fei et al., 2023). Furthermore, deep learning adaptive crop model (DACM) is proposed considering the spatial heterogeneity of large areas for yield estimation (Zhu et al., 2022). However, the basic ML and DL methods for cotton yield estimation are not sufficiently advanced for direct application to production and practice, especially in Xinjiang Province, China.

Regression models, including those based on ML and DL, require various parameters that are closely related to crop growth to narrow the gap between actual and potential (i.e. predicted) yield. The

application of comprehensive RS and environmental data has improved crop yield predictions because different datasets contain diverse information on crop growth and development (Kamir et al., 2020; Zhang et al., 2020). For example, the green chlorophyll vegetation index (GCVI) combined with LST and other climatic indices explained about 70% of the variance in maize yield across China, with the LSTM showing the best performance (Zhang et al., 2021). Various environmental data for single and double rice systems have been integrated with the NDVI and EVI to predict rice yield in China (Cao et al., 2021). NDVI, Maximum temperatures and accumulated rainfall data were used to monitor Australian wheat yield (Kamir et al., 2020). Considering climate or weather conditions of crops within season, prediction of corn and wheat have been reached (Johnson, 2014; Jin et al., 2022). While for cotton yield estimation, most of the studies are limited to the field scale by means of remote sensing (Ashapure et al., 2020; Meng et al., 2021; Wang et al., 2021). These study areas are often dedicated to cotton fields in small areas. When we expand the study regions, spatial heterogeneity must be considered. Therefore, it is difficult to apply the methods and processes of the field scale over a large area. However, the optimum VIs and CVs for cotton yield estimation remain unclear, and the ability of ML and DL methods to predict early cotton yield also needs to be further explored.

Here, we used satellite data and environmental parameters to build regression models for accurate prediction of cotton yield from 2012 to 2019 at the county level in Xinjiang Province. Based on the extracted cotton field, we calculated VIs and CVs to screen out the best ones for model establishment. We used one linear (least absolute shrinkage and selection operator, LASSO), two ML (SVR and RFR), and one DL (LSTM) model. Our overall workflow is shown in Figure 1. We sought answers to three questions: (1) which VIs and CVs can most precisely describe the county-level cotton yield in Xinjiang Province? (2) which regression model best simulates cotton yield over a large area? (3) how long before harvest could the yield be predicted?

Materials and methods

Study region and cotton yield

This study attempted to estimate cotton yields in Xinjiang Province (Figure 2), which produces more than 85% of the cotton grown in China. The study area, between 34°22′N-49°10′N and 73°40′E-96°23′E, covers approximately 166 million hectares. Xinjiang is among the districts in China most susceptible to climate change, as it spans the mid-temperate, south-temperate, and plateau climatic zones from north to south, with average daily air temperatures ranging from −28°C to 41°C and annual precipitation of about 150 mm. In Xinjiang, cotton is commonly planted in spring (April) and harvested in autumn (September–October; mostly in September). Therefore, we define the cotton growing season as the period from April to September.

County cotton yields (in kg/ha) from 2012 to 2019 were obtained from the agricultural statistical yearbook (https://www.yearbookchina.com). To reduce uncertainty, a preliminary quality check was used to identify and filter outliers, i.e. data points that were more than two standard deviations above or below the mean. Because of the special administrative structure of Xinjiang, the yield data did not cover the entire province. We selected counties with available cotton yield as yield records. In total, 355 yield records were used to define the study area (Figure 2).

Satellite remote sensing and environmental data

Surface reflectance (SR) images of the cotton cultivation areas for 2012–2019 were acquired from MODIS (MOD09A1) and Sentinel-2 (L2A), and radiometrically calibrated and atmospherically corrected within the Google Earth Engine (GEE). After removing images with > 10% clouds, we masked the clouds in the remaining valid images using cloud-free bands. Based on these pre-processed images, 14 satellite VIs,

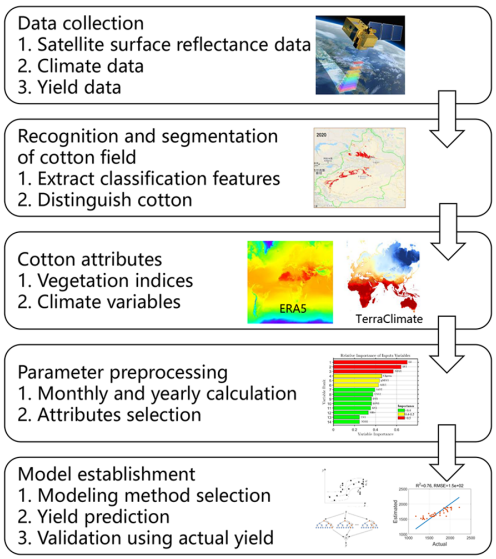

FIGURE 1
Workflow of county-level cotton yield prediction in this study.

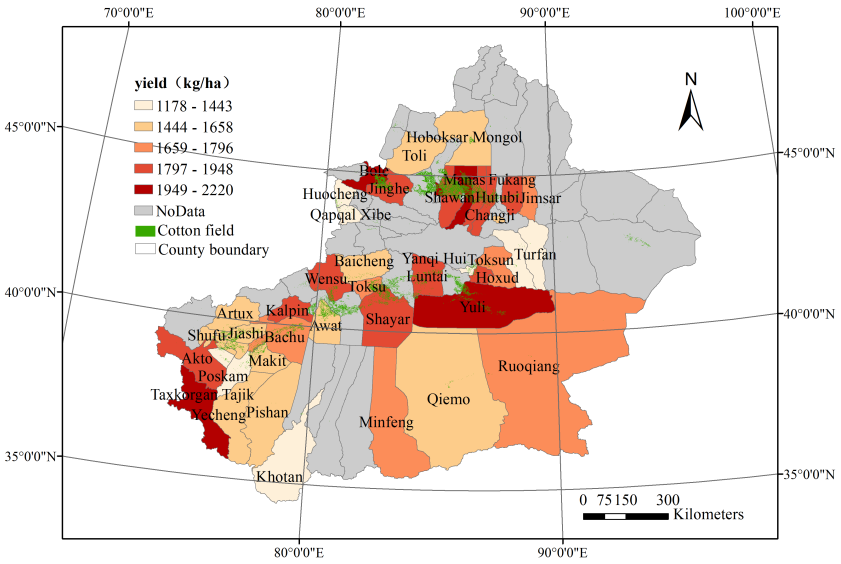

FIGURE 2
The study areas, cotton cultivation area and counties with recorded yield in Xinjiang Province in 2019. yields are from the Statistical Yearbook.

including the NDVI, EVI, and Universal Normalized Vegetation Index (UNVI), were computed for yield prediction (Table 1). Annual and monthly averages of the MOD09A1 VIs were produced for 2012–2019, while only monthly averages for 2019 were produced for the Sentinel-2 L2A VIs. The annual values obtained by averaging the monthly means from April to September were used to predict cotton yield in 2012-2019. The monthly values were used to predict the yield before the cotton harvest and to explore the temporal pattern of cotton growth. To validate the feasibility of the MODIS dataset for estimating, the Sentinel-2 data of 2019 were used.

Since precipitation, temperature, and soil all play important roles in plant growth, they are widely used for estimating crop yield (Kamir et al., 2020; Schwalbert et al., 2020; Gomez et al., 2021). We collected historical Climate Hazards Group Infrared Precipitation with Station data (CHIRPS) for daily precipitation (pre), ERA5 monthly temperature data [including maximum (Tmax), minimum (Tmin), and mean (Tmean) values], and TerraClimate data for monthly actual evapotranspiration (aet), climate water deficit (def), the palmer drought severity index (pdsi), precipitation accumulation (pr), soil moisture (soil), vapor pressure (vap), vapor pressure deficit (vpd) and reference evapotranspiration (pet) as climate parameters for the yield prediction models (Table 2). Yearly and monthly average values of the CVs were produced for 2012–2019. The same with VIs, the yearly and monthly values were for cotton yield estimation and prediction, respectively.

Cotton cultivation area

The cotton maps used to mask satellite and climate parameters during 2012–2019 were from our previous work. Based on high-spatial-resolution time series images that integrated Sentinel-2 and Landsat 8 satellite data, we explored the effects of image synthesis, the spectral index, and spatial texture on cotton identification accuracy, while also considering agricultural zoning. We applied the LSWI to a 10-day composite period analysis according to the farming division in Xinjiang, with texture features added at days 100, 200, and 260 to distinguish cotton from maize, wheat, and other main crops, and finally drew a spatial distribution map of cotton in Xinjiang in 2020. The map was verified with 5061 field samples obtained from ground surveys, with 3082, 466, 154, 341, and 1018 samples for cotton, maize, wheat, other crops, and non-farm land, respectively. The overall accuracy (OA) of cotton identification reached 0.8851, with a kappa coefficient of 0.8294, user precision of 0.9246, and producer precision of 0.9677. The specific spatial distribution of cotton cultivation areas shows in Figure 2

Assessment of variable importance

To identify the most important yield predictors and discard unimportant variables, the relative importance of each input variable was calculated using the Boruta algorithm. It is essentially the same as the Random Forest Importance. They both were originated from the Random Forest but expressed in slightly different forms. The Boruta algorithm is a wrapper built around the random forest classification algorithm implemented in the R package randomForest in 2010 (Liaw and Wiener, 2002; Kursa and Rudnicki, 2010). It has also been introduced into Python, and the current Boruta version of Python is BorutaPy (https://github.com/scikit-learn-contrib/boruta_py). Boruta can iteratively remove less important features while running RFR. Based on the original feature, a shadow feature is derived *via* a shuffling process that extends the feature matrix. Then, the *z*-score is computed and the maximum value is used as the threshold. During each random forest run, original features with importance values exceeding the threshold are marked as important, while those with importance values below the threshold are marked as unimportant. In subsequent runs, the important features are included and unimportant ones are removed. When every original feature is marked as important or

TABLE 1 Vegetation indices (VI) and their calculations.

Vegetation Index	Formulation	Reference
Normalized Difference Vegetation Index (NDVI)	$NDVI = \frac{Nir - Red}{Nir + Red}$	(Rouse, 1974)
Enhanced Vegetation Index (EVI)	$EVI = \frac{2.5 \times (Nir - Red)}{Nir + 6 \times Red - 7.5 \times Blue + 1}$	(Huete et al., 2002)
Green NDVI (gNDVI)	$gNDVI = \frac{Nir - Green}{Nir + Green}$	(Kaufman and Merzlyak, 1996)
Triangular Chlorophyll Absorption Ratio Index (TVI)	$TVI = 60 \times Nir - Green - 100 \times (Red - Green)$	(Broge and Leblanc, 2001)
Land Surface Water Index (LSWI)	$LSWI = \frac{Nir - Swir1}{Nir + Swir1}$	(Tucker, 1979)
Green Index (GI)	$GI = \frac{Green}{Red}$	(Gitelson et al., 2003a)
Near-Infrared Reflectance of Vegetation (NIRv)	$NIR_V = Nir \times \frac{Nir - Red}{Nir + Red}$	(Badgley et al., 2017)
Ratio Vegetation Index (RVI)	$RVI = \frac{Nir}{Red}$	(Jordan., 1969)
Difference Vegetation Index (DVI)	$DVI = Nir - Red$	(Tucker, 1979)
Normalized Difference Built-up Index (NDBI)	$NDBI = \frac{Swir1 - Nir}{Swir1 + Nir}$	(Zha et al., 2003)
Soil-Adjusted Vegetation Index (SAVI)	$SAVI = \frac{1.5 \times (Nir - Red)}{Nir + 0.5 + Red}$	(Huete, 1988)
Atmospherically Resistant Vegetation Index (ARVI)	$ARVI = \frac{Nir - (2 \times Red - Blue)}{Nir + (2 \times Red - Blue)}$	(Kaufman and Tanre, 1992)
Green Chlorophyll Index (CIgreen)	$CI_{green} = \frac{Nir}{Green} - 1$	(Gitelson et al., 2003b)
Universal Normalized Vegetation Index (UNVI)	$UNVI = \frac{C_v - 0.1 \times C_s - C_4}{C_v + C_v + C_s}$	(Zhang et al., 2019)

unimportant, or the random forest runs reach a previously defined limit, the algorithm ends.

Prediction models

We first normalized the input variables using the *z*-score method, and then built regression models to determine their impact on yield. Four regression models were used to estimate cotton yield at the county level, i.e. a LASSO linear regression model, two ML models (SVR and RFR), and a DL model (LSTM), and their performances were compared. Due to insufficient valid data in the yearbook, 10-fold cross-validation, which can make full use of limited data, was applied. In the 10-fold cross-validation process, the dataset is evenly divided into 10 copies and each sample is labelled from 1-10. The cross-validation was repeated 10 times, once for each label as a test. During each run, the data with the same label are deemed as testing sets while the others are for training. For each prediction model, the averaged R^2, root mean square error (RMSE) and relative RMSE (rRMSE) of 10 runs were used in the training and testing datasets for evaluating the performance. For within-season prediction result, the averaged R^2, RMSE, rRMSE of 10 testing datasets were used.

TABLE 2 Summary of the dataset used in this study.

Category	Variables	Spatial Resolution	Temporal Resolution	Time Coverage	Source
Crop yield	Cotton yield	Statistical division	Yearly	2012-2019	https://www.yearbookchina.com
Satellite data	MODIS VIs	500 m	8-day	2012-2019	https://lpdaac.usgs.gov https://doi.org/10.5067/MODIS/MOD09A1.006
	Sentinel-2 VIs	20 m	5-day	2019	https://sentinel.esa.int
Climate data	Pre	0.05°	Daily	2012-2019	CHIRPS (Funk et al., 2015)
	Tmax, Tmin, Tmean	10 km	Monthly	2012-2019	ERA5 (Horanyi, 2017; Hersbach et al., 2020)
	aet, def, pdsi, pet, pr, soil, vap, vpd	4 km	Monthly	2012-2019	TerraClimate (Abatzoglou et al., 2018)

$$R^2 = 1 - \frac{\sum_{i=1}^{n}\left(y_{act,i} - y_{pre,i}\right)^2}{\sum_{i=1}^{n}\left(y_{act,i} - y_{ave}\right)^2} \quad (1)$$

$$RMSE = \sqrt{\frac{1}{n}\sum_{i=1}^{n}\left(y_{act,i} - y_{pre,i}\right)^2} \quad (2)$$

$$rRMSE = \frac{RMSE}{y_{ave}} \quad (3)$$

where y_{act} is the actual true yield,y_{pre} is the model predictive yield, y_{ave} is the averagey_{act} value, and$n$ is the sample size. Details of the four models follow: LASSO regression is a shrinkage method characterized by variable selection and regularization that fits a generalized linear model (Tibshirani, 2011). The loss function can reduce the weight of input features to zero, which helps avoid overfitting. The LASSO uses the L1-regularization method to minimize the weight coefficient ω in the cost function [equation (4)]. The L1-penalty is the absolute value, which can't get derivation directly. Therefore, the gradient descent method is used to approach the optimal solution gradually by iteratively updating the values of the weight coefficients along one of the coordinate axes. We ran the LASSO model from the *linear_model* package and let the parameter *alpha* to be optimized through the *GridSearchCV* function from the *sklearn* package in Python 3.8.

$$Cost(\omega) = \sum_{i=1}^{N}\left(y_i - \omega^T x_i\right)^2 + \lambda\omega \quad (4)$$

where y_i is the response value, x_i is the standardized predictors,λ is the penalty coefficient,ω is the vector of weight coefficient, and$N$ is the sample size.

SVR is a variant of a support vector machine that uses kernels to map input data in higher dimensional feature space, such that we can identify relationships between input and output variables (Drucker et al., 1996; Hsu and Lin, 2002). SVR uses hyperplanes that can minimize the error arising from training samples and make all data have the shortest distance from the plane [equation (5)]. This is a convex quadratic programming problem that can be solved by the Lagrange method. Of the various kernel functions, we used the radial basis function (RBF) instead of linear, sigmoid, or polynomial kernels due to its greater accuracy in terms of localized and finite responses. We ran the SVR from the *svm* package and tuned the parameter *C*, *epsilon*, and *gamma* through the *GridSearchCV* function from the *sklearn* package in Python 3.8.

$$\min \frac{1}{2}\omega^2 \quad s.t. \quad y_i - \left(\omega^T x_i + b\right) \le \epsilon, \quad i = 1, 2, \ldots, l \quad (5)$$

where (ω, b) is the hyperplane, (x_i, y_i) is the sample point, ϵ is the tolerance deviation, and$l$ is the sample size.

RFR is a bagging ensemble learning method for model training and prediction that integrates numerous decision trees lying on a collection of random variables sampled independently; the trees are then aggregated to produce a forest. Each decision tree yields a prediction from the samples and features drawn, and by combining the results of all the trees and taking the average, the regression prediction for the whole forest is obtained. By calculating the arithmetic mean, RFR can produce accurate predictions without a high computational burden (Breiman, 2001). The RFR ran in the *ensemble* package and the parameters *n_estimators*, *max_depth*, and *max_features* were tuned through the *RandomizedSearchCV* function from the *sklearn.ensemble* package in Python 3.8.

LSTM is a special type of recurrent neural network (RNN) that can solve the problems of gradient disappearance and explosion and learn time-dependent information to understand crop growth processes (Hochreiter and Schmidhuber, 1997). These models include an input layer, one or more LSTM layers (consisting of LSTM cells), and an output layer. Figure 3 shows the architecture of the LSTM model. Each LSTM cell contains forget, input, and output gates to determine which information to forget, retain, and output in the LSTM layers. Through the activation (σ) and tanh functions, the hidden neurons (h_t) and internal memory cells (C_t) renewed continuously, contributing to the memory ability of the network. We ran the LSTM model in MATLAB 2020, which contains the *lstmLayer* structure. The hyper-parameters were optimised by an *optimiseParameters* function that is created by ourselves to compare the accuracy of different parameter combinations and select the highest precision one. In this study, the networks were run for 60 epochs; the batch size was 10 in the learn rate drop period and the factors were 100 and 0.02. Table 3 shows the specific parameters of the four models.

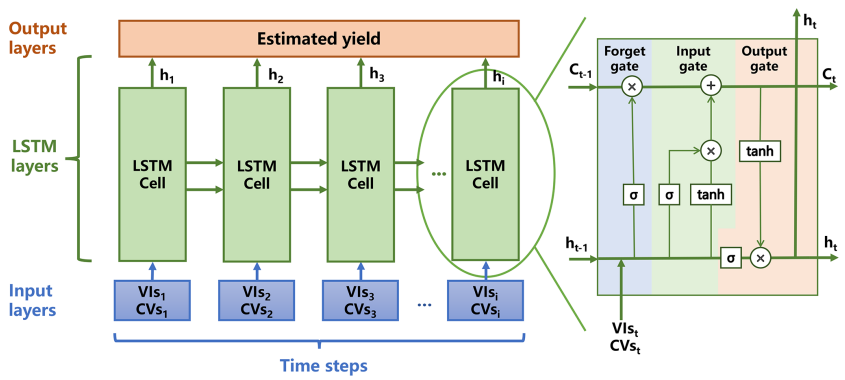

FIGURE 3
The architecture of long short-term memory (LSTM) model. The VIs variables refer to GI, RVI, NDVI. The CVs variables are soil, pet and vap.

TABLE 3 The detail list of parameters used for the regression models.

Model	Parameters
LASSO	alpha = 0.1
SVR	C = 5000, gamma = 10, epsilon = 0.01
RFR	n_estimators = 120, max_depth = 12, max_features = 4
LSTM	miniBatchSize = 10, MaxEpochs = 60, LearnRateDropPreriod = 100, LearnRateDropFactor = 0.02

Results

Most important variables for estimating cotton yield

The ability of the 14 typical VIs listed in Table 1 to predict cotton yield was evaluated using LASSO, SVR, RFR, and LSTM approaches. According to the relative importance of the variables, as illustrated in Figure 4, the green index (GI), ratio vegetation index (RVI), and NDVI contributed most to predictions of cotton yield in the study area, with importance values > 0.5; these were followed by CIgreen, gNDVI, and ARVI, with importance values of 0.4–0.5. The importance of the remaining variables did not exceed 0.4, indicating that cotton yield was little affected by them.

The three most important climate features for predicting yield were soil moisture, pet, and vap, with relative importance values of 0.47, 0.44, and 0.43, respectively. The other variables had importance values< 0.4. The least significant climate feature was pdsi, with an importance value< 0.1.

Performance of satellite and climate data for cotton yield estimation

Table 4 summarizes the yield estimation performance (mean values of 10-fold for training and testing results) achieved by applying the four regression algorithms using various parameters from 2012 to 2019. The important parameters were divided into VIs groups and VIs plus CVs groups. In experiments using both groups, the LSTM model outperformed the other models, followed by the two ML models (RFR and SVR). The linear regression model based on LASSO performed the worst, with non-linear relationships seen among the different predictors and cotton yield. Only the LSTM method had an R^2 > 0.6, RMSE< 200 kg/ha and rRMSE< 11%. The two ML methods explained only 30-50% of the variance in cotton yield, with SVR performing slightly worse than RFR. We found that, with combined use of satellite and climate data as input variables, greater accuracy was achieved compared with the individual satellite data; R^2 increased by 10%, and RMSE decreased by > 10 kg/ha, indicating that climate data provide complementary information that merits consideration. Our results suggest that the two datasets explain 66% and 76% of the cotton yield variability when using LSTM, respectively.

Within-season predicting performance

Using the most suitable variables and algorithms for predicting yearly yield, the seasonal cycles were examined (Figure 5). Generally, the values of all VIs (both MODIS and Sentinel-2 derived) increased gradually from April to July and the mid-summer peak during the cotton-blooming season (July–August), but peaked at different times between the two satellite systems. The three VIs peaked in July in the MODIS system, while in the Sentinel-2 system, only GI peaked in July and the seasonal cycles of RVI and NDVI lagged by 1 month. However, the difference between peak timings was very small. The satellite-derived VIs for July were very close to those for August. The GI and RVI derived from MODIS were clearly distinct from July to August, and dropped from 1 to 0.9. The NDVI derived from MODIS, and all three VIs derived from Sentinel-2, remained high, as in July. From August to September, the GI and NDVI declined the most and least rapidly, respectively. Since GI is the most important VIs, we explored the spatiotemporal pattern for Manas County (a large cotton

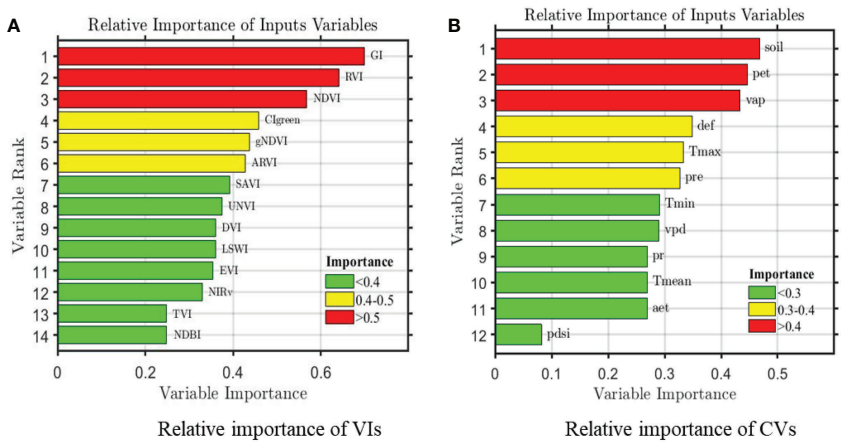

FIGURE 4
Relative importance of county-level remote sensing **(A)** and climate **(B)** variables on cotton yields during 2012-2019. Note: the aet, def, pdsi, pr, vap, vpd, pet, pre, soil, Tmax, Tmin, and Tmean represent actual evapotranspiration (mm), climate water deficit (mm), the palmer drought severity index, precipitation accumulation (mm), vapor pressure (kPa), vapor pressure deficit (kPa), reference evapotranspiration (mm), daily precipitation (mm), soil moisture (mm), monthly maximum, minimum and mean temperature (°C), respectively.

TABLE 4 The training and testing model performances (R^2, RMSE and rRMSE in the average of 10-fold cross-validation) at county-level from 2012 to 2019 .

Model	Variables	Training R^2	Training RMSE (kg/ha)	Training rRMSE	Testing R^2	Testing RMSE (kg/ha)	Testing rRMSE
LASSO	VIs	0.25	223	13.94%	0.23	229	15.42%
	VIs+CVs	0.31	216	13.31%	0.27	207	13.74%
SVR	VIs	0.85	95	5.51%	0.35	224	12.93%
	VIs+CVs	0.95	85	4.94%	0.38	218	12.60%
RFR	VIs	0.85	83	5.03%	0.37	215	12.86%
	VIs+CVs	0.96	78	4.74%	0.47	208	12.50%
LSTM	VIs	0.98	65	3.60%	0.66	182	10.53%
	VIs+CVs	0.99	23	1.34%	0.76	150	8.67%

growing area commonly used for research) in 2019 (Figure 6), verifying the reality of the whole county.

Of the CVs, pet and vap increased from April to July, peaking in July and August, respectively. The VIs had similar seasonal cycles, although pet decreased dramatically from the peak and reached its lowest value in September. The monthly variation in soil moisture had a different pattern from all other parameters examined. From the beginning of April to the end of September, it declined gradually from 1 to 0. There were no obvious differences among the green-up stage, blooming period, and cotton boll opening stage.

Table 4 indicates that the LSTM model best predicted the yearly cotton yield at the county level. Hence, we used LSTM for the final regression model to analyze the within-season predicting performance for cotton in different months. To validate the MODIS satellite data, which has a spatial resolution of 500 m and may exceed the cotton field scale, we used Sentinel-2 data with a spatial resolution of 20 m to predict the yield in 2019, after training the model using data for 2012–2018. Figure 7 shows the time series of the 10-fold averaged R^2, RMSE and rRMSE, achieved with the LSTM method from April to September. The model showed poor performance during the early seedling and germination stages. As the cotton grew and developed, the information derived from the satellite data became more important. The estimation accuracy also increased gradually, peaking in July before starting to drop slightly in August. In September, when the cotton bolls began to open, the prediction accuracy decreased to a level close to that in June. The addition of CVs improved the ability of VIs to predict within-season production. From July to September R^2 increased by 10%, RMSE and rRMSE decreased by 40 kg/ha and 3.25%, respectively; these values were much better compared with those for the green-up stage. Compared with the MODIS data, the Sentinel-2 data better predicted the cotton yield every month. After adding CVs to VIs as inputs, MODIS had essentially the same accuracy as Sentinel-2, revealing the feasibility of using MODIS data for county-level cotton yield prediction. Moreover, the 2019 validation experiment showed that MODIS can satisfactorily predict the cotton yield about 2 months before harvest (R^2 = 0.65, RMSE = 220 kg/ha, rRMSE = 15.97% in July; R^2 = 0.62, RMSE = 244 kg/ha, rRMSE = 17.39% in August). The Sentinel-2 data had slightly greater accuracy.

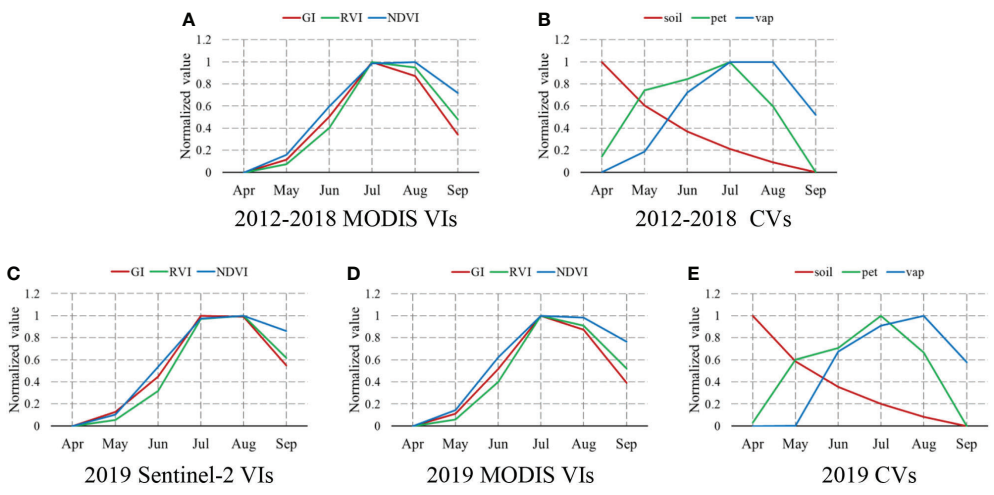

FIGURE 5
Normalized monthly means of the satellite (**A**, **C**, **D**) and climate (**B**, **E**) variables for the cotton study area for 2012-2018 (top row) and 2019 (bottom row), with raw values normalized to 0-1 to match their minimum and maximum values.

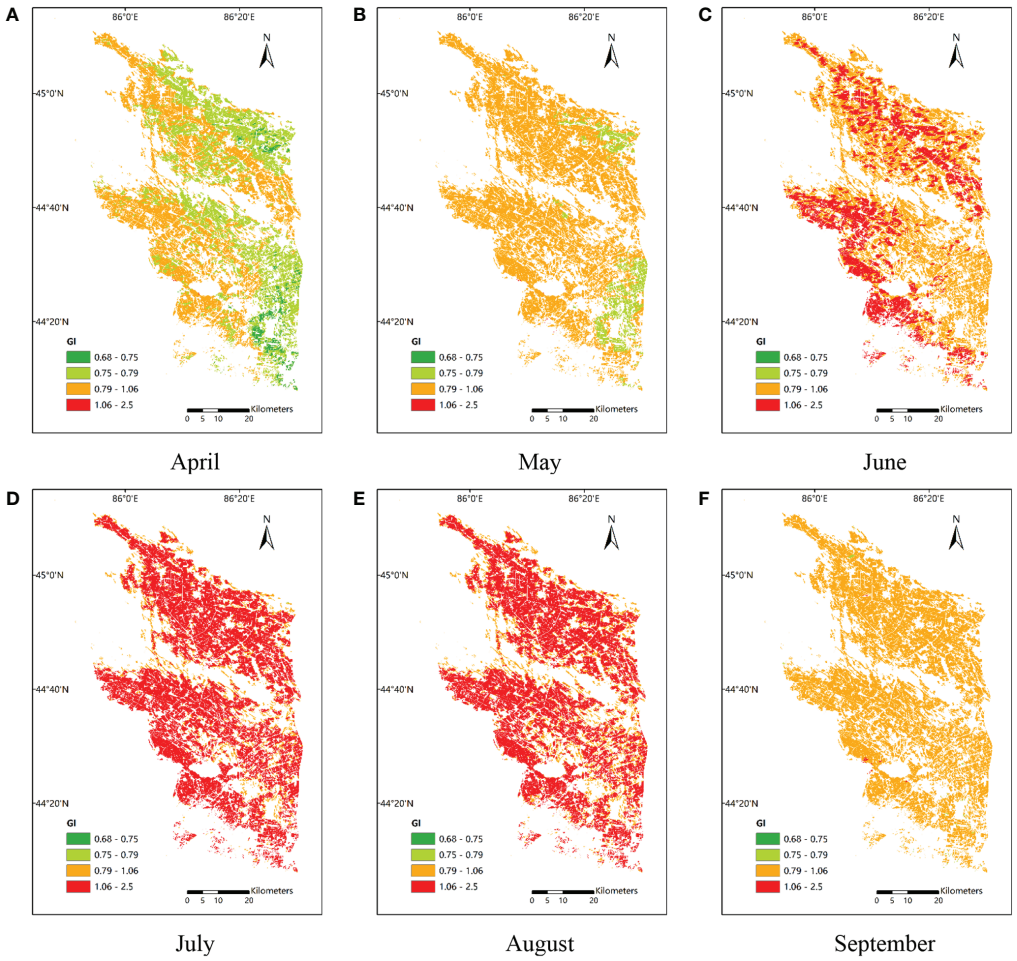

FIGURE 6
The spatiotemporal distributions of GI in Manas County in 2019, **(A–F)** refer to the different growth periods of cotton.

Discussion

The most suitable parameters for estimating Xinjiang cotton yield

Our first experiment examined which satellite data and CVs are most important for cotton yield estimation. After screening 14 VIs and 12 CVs, 3 of each showed clear superiority over the other parameters. The VIs GI, RVI and NDVI that with importance values > 0.5, and the CVs soil moisture, pet, and vap that with importance values > 0.4, performed best. They are significantly more important than the later ones. Like most plants, the reflectance for cotton is highest in the near-infrared band, with relatively less reflectance seen in the green band and an absorption valley occurring in the red band. VIs are an efficient way to measure crop growth and, ultimately, production (Meng et al., 2017; Ren et al., 2018). GI is defined as the ratio of the green and red bands. It is mainly influenced by the canopy chlorophyll concentration, and best explained the variability in cotton yield in this study. RVI is the ratio of the near-infrared and red bands. It is affected by vegetation structure and canopy nitrogen content, and is sensitive to atmospheric correction of the red band. Previous studies showed that NDVI is effective for estimating maize, rice, and soybean yield (Lambert et al., 2018; Cao et al., 2021). However, it often reaches a saturation point and is sensitive to the soil background, which may explain why it did not outperform GI and RVI in this study. Among the VIs with importance values exceeding 0.5, the red band was the most important. The first five VIs utilized only the information in the green, red, and near-infrared bands, illustrating their utility for estimating cotton yield. It's due to the presence of chlorophyll, green plants strongly absorb radiation energy in the red band (> 90%) and form a green reflective peak in the green band (10% - 20%). Therefore, we think the importance of chlorophyll in cotton growth can't be ignored. On adding the blue and short-wave infrared bands, the effects of the other VIs decreased gradually. DVI and TVI were unable to eliminate sensor and atmospheric effects. NIRv is multiplied by the near-infrared band and NDVI, and has been successfully applied for crop monitoring; however, it may eliminate certain types of canopy structure information (Zeng et al. 2022). NIRv did not estimate cotton yield well, suggesting that structure information cannot be ignored when making yield predictions. Overall, the VIs chosen herein to predict the Xinjiang cotton yield were characterized by high correlations with crop growth conditions in the canopy structure and the chlorophyll contents.

Among the CVs, soil moisture, pet, and vap best reflected the yield variation according to environmental factors. All three of these

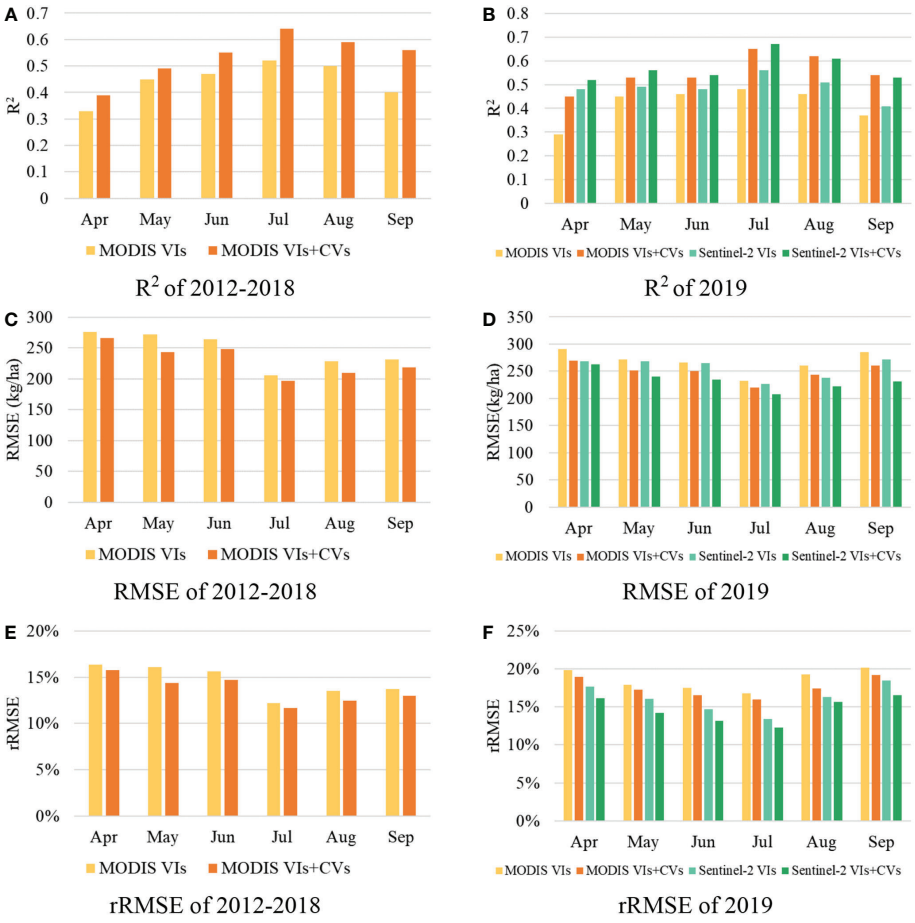

FIGURE 7
Testing performance [R2 **(A, B)**, RMSE **(C, D)** and rRMSE **(E, F)**] of cotton yield prediction only with remote sensing variables and combined with climate variables using the LSTM model for the whole growing season during 2012-2018 and 2019, respectively.

CVs are related to water, demonstrating that moisture greatly affects cotton yield. This is in line with the growth characteristics of cotton. In a field survey, we observed that cotton farmers used drip irrigation to overcome water shortages caused by insufficient rainfall. For most crops, precipitation and temperature are vital for yield prediction. However, the three CVs that we selected showed that precipitation was slightly more important than temperature. Based on a literature review, this discrepancy has two antecedents. First, the geographical vastness of our study area and great differences in altitude and terrain complexity lead to uneven rainfall and large differences in temperature, pressure, and soil type. Second, unlike precipitation and temperature, which are single indicators, soil moisture, pet, and vap are composite variables calculated from the former two variables. For growth, cotton must absorb water from soil and breathe *via* leaf evapotranspiration. Therefore, combining CVs with conventional satellite RS data can provide complementary information, thereby improving the accuracy of cotton yield estimation.

Potential of the LSTM network for yield prediction

The results showed that the four statistical approaches performed differently. The two ML methods (SVR and RFR) and DL method (LSTM) performed better than the linear regression model (LASSO), consistent with previous studies (Gopal and Bhargavi, 2019; Zhang et al., 2021; Jeong et al., 2022). The reason for this may be that the LASSO algorithm lacks the ability to identify potential nonlinear and complicated relationships among input variables, which is the main strength of the other three models. The two ML methods exhibited average performance; SVR could not capture the relationship between yield and the other variables as well as RFR. We attributed this to an algorithm difference; RFR has excellent robust generalization ability, while SVR is limited by the quadratic programming problem. The limited sample size could be another reason why the ML models did not perform as well as expected, although we used 10-fold cross validation. LSTM can efficiently and effectively extract key temporal features hidden within input variables without the need for thousands of samples. Due to its RNN structure, LSTM is a useful DL approach for predicting crop yield. Furthermore, other studies have shown that RS data and climate features can reveal the complex reasons for yield variation (Cai et al., 2019; Kim et al., 2019; Cao et al., 2021). Therefore, we integrated satellite RS data and CVs to predict cotton yield at the county level. Compared with satellite VIs alone, all models performed better after the addition of CVs. This suggests that environmental data supplies additional information that RS data are unable to provide, and verified the effectiveness of combining the two types of data for cotton yield estimation. On the other hand, it seems that our results have worse

performances than other studies (Ashapure et al., 2020; Jeong et al., 2022). Meanwhile, some yield prediction performances are even worse than ours (Zhang et al., 2021; Li et al., 2022b). Through comprehensive analysis, we attribute the reasons for poor results to the following two parts. The first one is the study scale. Compared with the county level, the pixel or field scale that can capture more details without the influence of complex background is much more elaborate. The second is the kinds of data sources. Rather than MODIS satellite data only, the climate data, soil property, geography, and topography can provide extra information. The more types of data sources, the higher the accuracy of yield estimation (Zhang et al., 2020; Cheng et al., 2022; Li et al., 2022b). However, apart from satellite and climate data, we have no access to other data for our study region, resulting in relatively poor results. All in all, our results demonstrate the advantage of integrating satellite and climate data for the prediction of cotton yield.

Finally, since LSTM outperformed all of the other algorithms, we explored how early it can predict the cotton yield and validated this using Sentinel-2 satellite data for 2019. Exploring the within-season performance of the selected variables, we also found phenological changes in Xinjiang cotton. After planting cotton seeds in April, we could predict cotton yield increasingly accurately until July, with the accuracy then decreasing in August and September. In rice and wheat crops, prediction accuracy is stable from July to harvest. Why does this discrepancy arise? Regarding the monthly changes of the selected VIs shown in Figure 5, we found the same trend as for the cotton estimation accuracy, which is in accordance with the process of cotton growth, but not that of rice and wheat. As cotton grows, the leaves become thicker and less soil is exposed from April to July. The bolls begin to open in August, which affects the satellite VIs directly; these start to decrease in August, thereby reducing the connection between the green VIs and yield. Furthermore, given the possibility of errors accumulating due to the low spatial resolution of the MODIS sensors, we also used Sentinel-2 data to estimate the cotton yield. The patterns were similar in both cases, demonstrating that MODIS satellite data can predict county-level yield accurately. The three CVs also varied with cotton growth, with pet and vap changing like the VIs, while soil moisture progressively decreased. Overall, the cotton yield estimate was most accurate 2 months before harvest. The accuracy of county-level cotton yield estimates did not increase with time after planting, although many factors influence the development and production of cotton in the full growth stage. Early yield estimation plays an important role in precision agriculture. It can assist farmers with field management before harvest, thus helping them to avoid further losses, and also helps the Department of Agriculture make marketing decisions pertaining to foods to maintain economic balance.

Uncertainties and prospects

This study found that a combination of satellite and climate data can estimate cotton yield at the county level more accurately through the application of different approaches using the GEE and python platforms. LSTM showed the best performance. We successfully predicted the cotton yield 2 months before harvest using the LSTM model. However, like many other studies, ours had a few uncertainties and limitations. First, our yield estimation did not include all counties in Xinjiang Province. Xinjiang consists not only of counties, but also of "construction crops". Moreover, these regions sometimes intersect, which makes it difficult for the national statistical office to collect yield data by county. Hence, after removing invalid data, production data were available only for part of Xinjiang. Second, our cotton distribution areas remained static in the period 2012–2019, but in actuality they differed over time. The cotton crop map for 2020 was used for the entire study period, which probably led to errors when generating VIs and CVs (as the land use varied from year to year between cotton and other fields). Future studies should consider updating the cotton maps annually to reduce errors in cotton yield estimation. In addition, more data types should be considered to predict cotton yield, by making full use of complementary information (Clevers and vanLeeuwen, 1996; Guan et al., 2017; Franz et al., 2020; Zhang et al., 2020). We used common VIs and CVs, and did not consider other data types. Solar-induced chlorophyll fluorescence (SIF) and synthetic aperture radar (SAR) data can also contribute to yield estimation. SIF is good at capturing the photosynthetic activity of plants (Duveiller and Cescatti, 2016; Kang et al., 2022), while SAR microwave data can assess plant structure due to its multi-polarization, multi-perspective scattering characteristics (Setiyono et al., 2019; Wu et al., 2020). Furthermore, the specific attributes of bolls compared with other crops and the spatial distribution characteristics of small and scattered cotton fields in Xinjiang should be considered. The domain knowledge-aware deep networks that take into account the enormous importance of small categories may offer a new way to conquer this problem (Li et al., 2022a). Finally, the spatial resolution of our major datasets was insufficient to reduce most of the errors affecting county-level predictions of cotton yield at the local scale; the satellite SR data and CVs used are only available at low spatial resolution, and the mixed pixels cannot distinguish cotton from other features, which reduces the accuracy of cotton yield prediction (Hunt et al., 2019; Meng et al., 2019). In the future, we may combine satellite data from different sensors with a higher temporal and spatial resolution to better extract the unique traits of cotton and improve cotton yield estimation accuracy.

Conclusions

In this study, we pre-processed satellite data and CVs on the GEE platform and then identified the most important variables for cotton yield prediction at the county level in Xinjiang, using one linear regression (LASSO) and two ML (SVR and RFR) models, and one DL model (LSTM), with different combinations of input variables. The results showed that LSTM performed best, with an R^2 of 0.76, RMSE of 150 kg/ha and rRMSE of 8.67% after an average of 10 runs. The performance was better after integrating RS and climate features. We used the LSTM algorithm, with VIs and CVs incorporated, to monitor cotton cropland during its growth and development. Finally, the within-season yield prediction suggested that cotton yield could be predicted reasonably accurately in July, 2 months before harvest, with an R^2 of 0.65, RMSE of 220 kg/ha and rRMSE of 15.97%. The model using high-spatial-resolution Sentinel-2 data performed slightly better than the coarse MODIS data for yield predictions for 2019. The MODIS and Sentinel-2 data had the same monthly prediction accuracy, indicating that MODIS satellite data can satisfactorily estimate cotton yield in advance, thus facilitating cotton

management decisions. To remove redundant features, the Boruta algorithm was used to determine which VIs and CVs were most sensitive to the county-level cotton yield in Xinjiang; this identified three VIs and three CVs. The VIs GI, RVI, and NDVI contain green, red and near-infrared bands, indicating that information on cotton canopy structure and chlorophyll contents can be useful for yield estimation. Because cotton fields are scattered throughout Xinjiang, only parts of each county are used to grow cotton, so the problem of mixed pixels must be considered. The most important CVs in this study were soil moisture, pet, and vap, which reflect moisture. Overall, MODIS satellite data integrated with CVs based on the LSTM model were superior for county-level cotton yield prediction in Xinjiang. In the future, the VIs characterizing canopy structure and chlorophyll and CVs related to moisture can be further investigated for cotton growth, and the LSTM method can be widely applied in crop yield prediction over large areas.

Data availability statement

The original contributions presented in the study are included in the article/supplementary material. Further inquiries can be directed to the corresponding author.

Author contributions

PL, LZ, and CH designed the research and wrote the original draft. PL and JC contributed to data processing and analysis. CH, XK, ZZ, and QT revised the manuscript. All authors reviewed and contributed to the organization of the manuscript.

Funding

This research was funded by the National Natural Science Foundation of China (grant numbers 41971321 and 41830108), Key Research Program of Frontier Sciences, CAS (grant number ZDBS-LY-DQC012), and Open Fund of Key Laboratory of Oasis Eco-agriculture, XPCC (grant numbers 201801 and 202003). CH was supported by Youth Innovation Promotion Association, CAS (grant number Y2021047).

Conflict of interest

The authors declare that the research was conducted in the absence of any commercial or financial relationships that could be construed as a potential conflict of interest.

Publisher's note

All claims expressed in this article are solely those of the authors and do not necessarily represent those of their affiliated organizations, or those of the publisher, the editors and the reviewers. Any product that may be evaluated in this article, or claim that may be made by its manufacturer, is not guaranteed or endorsed by the publisher.

References

Abatzoglou, J. T., Dobrowski, S. Z., Parks, S. A., and Hegewisch, K. C. (2018). Data descriptor: TerraClimate, a high-resolution global dataset of monthly climate and climatic water balance from 1958-2015. *Sci. Data* 5. doi: 10.1038/sdata.2017.191

Ashapure, A., Jung, J., Chang, A., Oh, S., Yeom, J., Maeda, M., et al. (2020). Developing a machine learning based cotton yield estimation framework using multi-temporal UAS data. *ISPRS J. Photogrammetry Remote Sens.* 169, 180–194. doi: 10.1016/j.isprsjprs.2020.09.015

Badgley, G., Field, C. B., and Berry, J. A. (2017). Canopy near-infrared reflectance and terrestrial photosynthesis. *Sci. Adv.* 3 (3). doi: 10.1126/sciadv.1602244

Bauer, P., Thorpe, A., and Brunet, G. (2015). The quiet revolution of numerical weather prediction. *Nature* 525 (7567), 47–55. doi: 10.1038/nature14956

Bian, C. F., Shi, H. T., Wu, S. Q., Zhang, K. F., Wei, M., Zhao, Y. D., et al. (2022). Prediction of field-scale wheat yield using machine learning method and multi-spectral UAV data. *Remote Sens.* 14 (6). doi: 10.3390/rs14061474

Breiman, L. (2001). Random forests. *Mach. Learn.* 45 (1), 5–32. doi: 10.1023/a:1010933404324

Broge, N. H., and Leblanc, E. (2001). Comparing prediction power and stability of broadband and hyperspectral vegetation indices for estimation of green leaf area index and canopy chlorophyll density. *Remote Sens. Environ.* 76 (2), 156–172. doi: 10.1016/s0034-4257(00)00197-8

Cai, Y. P., Guan, K. Y., Lobell, D., Potgieter, A. B., Wang, S. W., Peng, J., et al. (2019). Integrating satellite and climate data to predict wheat yield in Australia using machine learning approaches. *Agric. For. Meteorology* 274, 144–159. doi: 10.1016/j.agrformet.2019.03.010

Cao, J., Zhang, Z., Tao, F., Zhang, L., Luo, Y., Zhang, J., et al. (2021). Integrating multi-source data for rice yield prediction across China using machine learning and deep learning approaches. *Agric. For. Meteorology* 297, 108275. doi: 10.1016/j.agrformet.2020.108275

Cheng, M. H., Penuelas, J., McCabe, M. F., Atzberger, C., Jiao, X. Y., Wu, W. B., et al. (2022). Combining multi-indicators with machine-learning algorithms for maize at the-level in China. *Agric. For. Meteorology* 323. doi: 10.1016/j.agrformet.2022.109057

Chen, Y. L., Lu, D. S., Luo, L. F., Pokhrel, Y., Deb, K., Huang, J. F., et al. (2018). Detecting irrigation extent, frequency, and timing in a heterogeneous arid agricultural region using MODIS time series, landsat imagery, and ancillary data. *Remote Sens. Environ.* 204, 197–211. doi: 10.1016/j.rse.2017.10.030

Chu, Z., and Yu, J. (2020). An end-to-end model for rice yield prediction using deep learning fusion. *Comput. Electron. Agric.* 174. doi: 10.1016/j.compag.2020.105471

Clevers, J., and vanLeeuwen, H. J. C. (1996). Combined use of optical and microwave remote sensing data for crop growth monitoring. *Remote Sens. Environ.* 56 (1), 42–51. doi: 10.1016/0034-4257(95)00227-8

Curnel, Y., de Wit, A. J. W., Duveiller, G., and Defourny, P. (2011). Potential performances of remotely sensed LAI assimilation in WOFOST model based on an OSS experiment. *Agric. For. Meteorology* 151 (12), 1843–1855. doi: 10.1016/j.agrformet.2011.08.002

de Wit, A., Boogaard, H., Fumagalli, D., Janssen, S., Knapen, R., van Kraalingen, D., et al. (2019). 25 years of the WOFOST cropping systems model. *Agric. Syst.* 168, 154–167. doi: 10.1016/j.agsy.2018.06.018

Dorigo, W. A., Zurita-Milla, R., de Wit, A. J. W., Brazile, J., Singh, R., and Schaepman, M. E. (2007). A review on reflective remote sensing and data assimilation techniques for enhanced agroecosystem modeling. *Int. J. Appl. Earth Observation Geoinformation* 9 (2), 165–193. doi: 10.1016/j.jag.2006.05.003

Drucker, H., Burges, C. J. C., Kaufman, L., Smola, A., and Vapnik, V. (1996). "Support vector regression machines"," in *10th Annual Conference on Neural Information Processing Systems (NIPS)), MIT Press*, Denver, Co. 155–161.

Duveiller, G., and Cescatti, A. (2016). Spatially downscaling sun-induced chlorophyll fluorescence leads to an improved temporal correlation with gross primary productivity. *Remote Sens. Environ.* 182, 72–89. doi: 10.1016/j.rse.2016.04.027

Fan, H. Y., Liu, S. S., Li, J., Li, L. T., Dang, L. N., Ren, T., et al. (2021). Early prediction of the seed yield in winter oilseed rape based on the near-infrared reflectance of vegetation (NIRv). *Comput. Electron. Agric.* 186. doi: 10.1016/j.compag.2021.106166

Fei, S. P., Chen, Z., Li, L., Ma, Y. T., and Xiao, Y. G. (2023). Bayesian Model averaging to improve the yield prediction in wheat breeding trials. *Agric. For. Meteorology* 328. doi: 10.1016/j.agrformet.2022.109237

Folberth, C., Skalsky, R., Moltchanova, E., Balkovic, J., Azevedo, L. B., Obersteiner, M., et al. (2016). Uncertainty in soil data can outweigh climate impact signals in global crop yield simulations. *Nat. Commun.* 7. doi: 10.1038/ncomms11872

Franz, T. E., Pokal, S., Gibson, J. P., Zhou, Y. Z., Gholizadeh, H., Tenorio, F. A., et al. (2020). The role of topography, soil, and remotely sensed vegetation condition towards predicting crop yield. *Field Crops Res.* 252. doi: 10.1016/j.fcr.2020.107788

Funk, C., Peterson, P., Landsfeld, M., Pedreros, D., Verdin, J., Shukla, S., et al. (2015). The climate hazards infrared precipitation with stations-a new environmental record for monitoring extremes. *Sci. Data* 2. doi: 10.1038/sdata.2015.66

Gitelson, A. A., Gritz, Y., and Merzlyak, M. N. (2003a). Relationships between leaf chlorophyll content and spectral reflectance and algorithms for non-destructive chlorophyll assessment in higher plant leaves. *J. Plant Physiol.* 160 (3), 271–282. doi: 10.1078/0176-1617-00887

Gitelson, A. A., Vina, A., Arkebauer, T. J., Rundquist, D. C., Keydan, G., and Leavitt, B. (2003b). Remote estimation of leaf area index and green leaf biomass in maize canopies. *Geophysical Res. Lett.* 30 (5). doi: 10.1029/2002gl016450

Gomez, D., Salvador, P., Sanz, J., and Casanova, J. L. (2021). Regional estimation of garlic yield using crop, satellite and climate data in Mexico. *Comput. Electron. Agric.* 181. doi: 10.1016/j.compag.2020.105943

Gopal, P. S. M., and Bhargavi, R. (2019). A novel approach for efficient crop yield prediction. *Comput. Electron. Agric.* 165. doi: 10.1016/j.compag.2019.104968

Guan, K. Y., Wu, J., Kimball, J. S., Anderson, M. C., Frolking, S., Li, B., et al. (2017). The shared and unique values of optical, fluorescence, thermal and microwave satellite data for estimating large-scale crop yields. *Remote Sens. Environ.* 199, 333–349. doi: 10.1016/j.rse.2017.06.043

Hersbach, H., Bell, B., Berrisford, P., Hirahara, S., Horanyi, A., Munoz-Sabater, J., et al. (2020). The ERA5 global reanalysis. *Q. J. R. Meteorological Soc.* 146 (730), 1999–2049. doi: 10.1002/qj.3803

Hochreiter, S., and Schmidhuber, J. (1997). Long short-term memory. *Neural Comput.* 9 (8), 1735–1780. doi: 10.1162/neco.1997.9.8.1735

Horanyi, A. (2017). Some aspects on the use and impact of observations in the ERA5 Copernicus climate change service reanalysis. *Idojaras* 121 (4), 329–344.

Hsu, C. W., and Lin, C. J. (2002). A comparison of methods for multiclass support vector machines. *IEEE Trans. Neural Networks* 13 (2), 415–425. doi: 10.1109/72.991427

Huete, A. R. (1988). A SOIL-ADJUSTED VEGETATION INDEX (SAVI). *Remote Sens. Environ.* 25 (3), 295–309. doi: 10.1016/0034-4257(88)90106-x

Huete, A., Didan, K., Miura, T., Rodriguez, E. P., Gao, X., and Ferreira, L. G. (2002). Overview of the radiometric and biophysical performance of the MODIS vegetation indices. *Remote Sens. Environ.* 83 (1-2), 195–213. doi: 10.1016/s0034-4257(02)00096-2

Hunt, M. L., Blackburn, G. A., Carrasco, L., Redhead, J. W., and Rowland, C. S. (2019). High resolution wheat yield mapping using sentinel-2. *Remote Sens. Environ.* 233. doi: 10.1016/j.rse.2019.111410

Jeong, S., Ko, J., and Yeom, J. M. (2022). Predicting rice yield at pixel scale through synthetic use of crop and deep learning models with satellite data in south and north Korea. *Sci. Total Environ.* 802, 149726. doi: 10.1016/j.scitotenv.2021.149726

Jin, H. D., Li, M., Hopwood, G., Hochman, Z., and Bakar, K. S. (2022). Improving early-season wheat yield forecasts driven by probabilistic seasonal climate forecasts. *Agric. For. Meteorology* 315. doi: 10.1016/j.agrformet.2022.108832

Johnson, D. M. (2014). An assessment of pre- and within-season remotely sensed variables for forecasting corn and soybean yields in the united states. *Remote Sens. Environ.* 141, 116–128. doi: 10.1016/j.rse.2013.10.027

Jones, J. W., Hoogenboom, G., Porter, C. H., Boote, K. J., Batchelor, W. D., Hunt, L. A., et al. (2003). The DSSAT cropping system model. *Eur. J. Agron.* 18 (3-4), 235–265. doi: 10.1016/s1161-0301(02)00107-7

Jordan, C. F. (1969). Derivation of leaf-area index from quality of light on the forest floor. *Ecology* 50, 663–666. doi: 10.2307/1936256

Kamir, E., Waldner, F., and Hochman, Z. (2020). Estimating wheat yields in Australia using climate records, satellite image time series and machine learning methods. *Isprs J. Photogrammetry Remote Sens.* 160, 124–135. doi: 10.1016/j.isprsjprs.2019.11.008

Kang, X., Huang, C., Zhang, L., Zhang, Z., and Lv, X. (2022). Downscaling solar-induced chlorophyll fluorescence for field-scale cotton yield estimation by a two-step convolutional neural network. *Comput. Electron. Agric.* 201, 107260. doi: 10.1016/j.compag.2022.107260

Kang, Y. H., Ozdogan, M., Zhu, X. J., Ye, Z. W., Hain, C., and Anderson, M. (2020). Comparative assessment of environmental variables and machine learning algorithms for maize yield prediction in the US Midwest. *Environ. Res. Lett.* 15 (6). doi: 10.1088/1748-9326/ab7df9

Kaufman, Y. J., and Merzlyak, M. N. (1996). Use of a green channel in remote sensing of global vegetation from eos-modis. *Remote Sens. Environ.* 58 (3), 289–298. doi: 10.1016/s0034-4257(96)00072-7

Kaufman, Y. J., and Tanre, D. (1992). ATMOSPHERICALLY RESISTANT VEGETATION INDEX (ARVI) FOR EOS-MODIS. *IEEE Trans. Geosci. Remote Sens.* 30 (2), 261–270. doi: 10.1109/36.134076

Keating, B. A., Carberry, P. S., Hammer, G. L., Probert, M. E., Robertson, M. J., Holzworth, D., et al. (2003). An overview of APSIM, a model designed for farming systems simulation. *Eur. J. Agron.* 18 (3-4), 267–288. doi: 10.1016/s1161-0301(02)00108-9

Kern, A., Barcza, Z., Marjanovic, H., Arendas, T., Fodor, N., Bonis, P., et al. (2018). Statistical modelling of crop yield in central Europe using climate data and remote sensing vegetation indices. *Agric. For. Meteorology* 260, 300–320. doi: 10.1016/j.agrformet.2018.06.009

Khaki, S., Wang, L. Z., and Archontoulis, S. V. (2020). A CNN-RNN framework for crop yield prediction. *Front. Plant Sci.* 10. doi: 10.3389/fpls.2019.01750

Kheir, A. M. S., Hoogenboom, G., Ammar, K. A., Ahmed, M., Feike, T., Elnashar, A., et al. (2022). Minimizing trade-offs between wheat yield and resource-use efficiency in the Nile delta – a multi-model analysis. *Field Crops Res.* 287, 108638. doi: 10.1016/j.fcr.2022.108638

Kim, N., Ha, K. J., Park, N. W., Cho, J., Hong, S., and Lee, Y. W. (2019). A comparison between major artificial intelligence models for crop yield prediction: Case study of the Midwestern united state 2006-2015. *Isprs Int. J. Geo-Information* 8 (5). doi: 10.3390/ijgi8050240

Kursa, M. B., and Rudnicki, W. R. (2010). Feature selection with the boruta package. *J. Stat. Software* 36 (11), 1–13. doi: 10.18637/jss.v036.i11

Lambert, M. J., Traore, P. C. S., Blaes, X., Baret, P., and Defourny, P. (2018). Estimating smallholder crops production at village level from sentinel-2 time series in mali's cotton belt. *Remote Sens. Environ.* 216, 647–657. doi: 10.1016/j.rse.2018.06.036

LeCun, Y., Bengio, Y., and Hinton, G. (2015). Deep learning. *Nature* 521 (7553), 436–444. doi: 10.1038/nature14539

Liaw, A., and Wiener, M. (2002). Classification and regression by random forest. *R News* 2 (3), 18–22.

Li, Z., Ding, L., and Xu, D. (2022b). Exploring the potential role of environmental and multi-source satellite data in crop yield prediction across northeast China. *Sci. Total Environ.* 815, 152880. doi: 10.1016/j.scitotenv.2021.152880

Liu, J. G., Pattey, E., and Jego, G. (2012). Assessment of vegetation indices for regional crop green LAI estimation from landsat images over multiple growing seasons. *Remote Sens. Environ.* 123, 347–358. doi: 10.1016/j.rse.2012.04.002

Li, Y. S., Zhou, Y. H., Zhang, Y. J., Zhong, L. H., Wang, J., and Chen, J. D. (2022a). DKDFN: Domain knowledge-guided deep collaborative fusion network for multimodal unitemporal remote sensing land cover classification. *Isprs J. Photogrammetry Remote Sens.* 186, 170–189. doi: 10.1016/j.isprsjprs.2022.02.013

Mathieu, J. A., and Aires, F. (2018). Assessment of the agro-climatic indices to improve crop yield forecasting. *Agric. For. Meteorology* 253, 15–30. doi: 10.1016/j.agrformet.2018.01.031

Meng, L., Liu, H., Ustin, S. L., and Zhang, X. (2021). Assessment of FSDAF accuracy on cotton yield estimation using different MODIS products and landsat based on the mixed degree index with different surroundings. *Sensors (Basel)* 21 (15). doi: 10.3390/s21155184

Meng, L. H., Liu, H. J., Zhang, X. L., Ren, C. Y., Ustin, S., Qiu, Z. C., et al. (2019). Assessment of the effectiveness of spatiotemporal fusion of multi-source satellite images for cotton yield estimation. *Comput. Electron. Agric.* 162, 44–52. doi: 10.1016/j.compag.2019.04.001

Meng, L. H., Zhang, X. L., Liu, H. J., Guo, D., Yan, Y., Qin, L. L., et al. (2017). Estimation of cotton yield using the reconstructed time-series vegetation index of landsat data. *Can. J. Remote Sens.* 43 (3), 244–255. doi: 10.1080/07038992.2017.1317206

Ren, H. R., Zhou, G. S., and Zhang, F. (2018). Using negative soil adjustment factor in soil-adjusted vegetation index (SAVI) for aboveground living biomass estimation in arid grasslands. *Remote Sens. Environ.* 209, 439–445. doi: 10.1016/j.rse.2018.02.068

Rigden, A. J., Mueller, N. D., Holbrook, N. M., Pillai, N., and Huybers, P. (2020). Combined influence of soil moisture and atmospheric evaporative demand is important for accurately predicting US maize yields. *Nat. Food* 1 (2). doi: 10.1038/s43016-020-0028-7

Rouse, J. W. (1974). Monitoring vegetation systems in the great plains with ERTS: Proceedings of the third earth resources technology satellite-1 symposium. *NASA* SP 35, 301–317.

Schwalbert, R. A., Amado, T., Corassa, G., Pott, L. P., Prasad, P. V. V., and Ciampitti, I. A. (2020). Satellite-based soybean yield forecast: Integrating machine learning and weather data for improving crop yield prediction in southern Brazil. *Agric. For. Meteorology* 284. doi: 10.1016/j.agrformet.2019.107886

Setiyono, T. D., Quicho, E. D., Holecz, F. H., Khan, N. I., Romuga, G., Maunahan, A., et al. (2019). Rice yield estimation using synthetic aperture radar (SAR) and the ORYZA crop growth model: Development and application of the system in south and south-east Asian countries. *Int. J. Remote Sens.* 40 (21), 8093–8124. doi: 10.1080/01431161.2018.1547457

Sinclair, T. R., and Seligman, N. G. (1996). Crop modeling: From infancy to maturity. *Agron. J.* 88 (5), 698–704. doi: 10.2134/agronj1996.00021962008800050004x

Sun, J., Di, L. P., Sun, Z. H., Shen, Y. L., and Lai, Z. L. (2019). County-level soybean yield prediction using deep CNN-LSTM model. *Sensors* 19 (20). doi: 10.3390/s19204363

Tao, F. L., Rotter, R. P., Palosuo, T., Diaz-Ambrona, C. G. H., Minguez, M. I., Semenov, M. A., et al. (2018). Contribution of crop model structure, parameters and climate projections to uncertainty in climate change impact assessments. *Global Change Biol.* 24 (3), 1291–1307. doi: 10.1111/gcb.14019

Tao, F., Yokozawa, M., and Zhang, Z. (2009). Modelling the impacts of weather and climate variability on crop productivity over a large area: A new process-based model development, optimization, and uncertainties analysis. *Agric. For. Meteorology* 149 (5), 831–850. doi: 10.1016/j.agrformet.2008.11.004

Tibshirani, R. (2011). Regression shrinkage and selection *via* the lasso: A retrospective. *J. R. Stat. Soc. Ser. B-Statistical Method.* 73, 273–282. doi: 10.1111/j.1467-9868.2011.00771.x

Tucker, C. J. (1979). Red and photographic infrared linear combinations for monitoring vvgetation. *Remote Sens. Environ.* 8 (2), 127–150. doi: 10.1016/0034-4257(79)90013-0

van Klompenburg, T., Kassahun, A., and Catal, C. (2020). Crop yield prediction using machine learning: A systematic literature review. *Comput. Electron. Agric.* 177. doi: 10.1016/j.compag.2020.105709

Wang, L., Liu, Y., Wen, M., Li, M., Dong, Z., He, Z., et al. (2021). Using field hyperspectral data to predict cotton yield reduction after hail damage. *Comput. Electron. Agric.* 190, 106400. doi: 10.1016/j.compag.2021.106400

Wang, L. L., Zhao, Y. J., Xiong, Z. J., Wang, S. Z., Li, Y. H., and Lan, Y. B. (2022). Fast and precise detection of litchi fruits for yield estimation based on the improved YOLOv5 model. *Front. Plant Sci.* 13. doi: 10.3389/fpls.2022.965425

Wu, X. X., Washaya, P., Liu, L., Li, K., Shao, Y., Meng, L. Y., et al. (2020). Rice yield estimation based on spaceborne SAR: A review from 1988 to 2018. *IEEE Access* 8, 157462–157469. doi: 10.1109/access.2020.3020182

Wu, S. R., Yang, P., Ren, J. Q., Chen, Z. X., and Li, H. (2021). Regional winter wheat yield estimation based on the WOFOST model and a novel VW-4DEnSRF assimilation algorithm. *Remote Sens. Environ.* 255. doi: 10.1016/j.rse.2020.112276

Xu, W., Chen, P., Zhan, Y., Chen, S., Zhang, L., and Lan, Y. (2021a). Cotton yield estimation model based on machine learning using time series UAV remote sensing data. *Int. J. Appl. Earth Observation Geoinformation* 104, 102511. doi: 10.1016/j.jag.2021.102511

Xu, Y. J., Liu, X., Cao, X., Huang, C. P., Liu, E. K., Qian, S., et al. (2021b). Artificial intelligence: A powerful paradigm for scientific research. *Innovation* 2 (4). doi: 10.1016/j.xinn.2021.100179

Zeng, Y. L., Hao, D. L., Huete, A., Dechant, B., Berry, J., Chen, J. M., et al. (2022). Optical vegetation indices for monitoring terrestrial ecosystems globally. *Nat. Rev. Earth Environ.* 3 (7), 477–493. doi: 10.1038/s43017-022-00298-5

Zha, Y., Gao, J., and Ni, S. (2003). Use of normalized difference built-up index in automatically mapping urban areas from TM imagery. *Int. J. Remote Sens.* 24 (3), 583–594. doi: 10.1080/01431160304987

Zhang, L. F., Qiao, N., Baig, M. H. A., Huang, C. P., Lv, X., Sun, X. J., et al. (2019). Monitoring vegetation dynamics using the universal normalized vegetation index (UNVI): An optimized vegetation index-VIUPD. *Remote Sens. Lett.* 10 (7), 629–638. doi: 10.1080/2150704x.2019.1597298

Zhang, L. L., Zhang, Z., Luo, Y. C., Cao, J., and Tao, F. L. (2020). Combining optical, fluorescence, thermal satellite, and environmental data to predict county-level maize yield in China using machine learning approaches. *Remote Sens.* 12 (1). doi: 10.3390/rs12010021

Zhang, L., Zhang, Z., Luo, Y., Cao, J., Xie, R., and Li, S. (2021). Integrating satellite-derived climatic and vegetation indices to predict smallholder maize yield using deep learning. *Agric. For. Meteorology* 311, 108666. doi: 10.1016/j.agrformet.2021.108666

Zhu, Y. L., Wu, S. S., Qin, M. J., Fu, Z. Y., Gao, Y., Wang, Y. Y., et al. (2022). A deep learning crop model for adaptive yield estimation in large areas. *Int. J. Appl. Earth Observation Geoinformation* 110. doi: 10.1016/j.jag.2022.102828

frontiers | Frontiers in Plant Science

TYPE Original Research
PUBLISHED 24 July 2023
DOI 10.3389/fpls.2023.1016890

Check for updates

OPEN ACCESS

EDITED BY
Ming-Guo Ma,
Beijing Forestry University, China

REVIEWED BY
Gang He,
Northwest A&F University, China
Tong Qiu,
The Pennsylvania State University (PSU), United States

*CORRESPONDENCE
Zhenhai Li
lizh323@126.com

RECEIVED 11 August 2022
ACCEPTED 28 June 2023
PUBLISHED 24 July 2023

CITATION
Liu X, Li X, Gao L, Zhang J, Qin D, Wang K and Li Z (2023) Early-season and refined mapping of winter wheat based on phenology algorithms - a case of Shandong, China.
Front. Plant Sci. 14:1016890.
doi: 10.3389/fpls.2023.1016890

COPYRIGHT
© 2023 Liu, Li, Gao, Zhang, Qin, Wang and Li. This is an open-access article distributed under the terms of the Creative Commons Attribution License (CC BY). The use, distribution or reproduction in other forums is permitted, provided the original author(s) and the copyright owner(s) are credited and that the original publication in this journal is cited, in accordance with accepted academic practice. No use, distribution or reproduction is permitted which does not comply with these terms.

Early-season and refined mapping of winter wheat based on phenology algorithms - a case of Shandong, China

Xiuyu Liu[1,2,3], Xuehua Li[1], Lixin Gao[3], Jinshui Zhang[1,2], Dapeng Qin[4], Kun Wang[5] and Zhenhai Li[3]*

[1]State Key Laboratory of Remote Sensing Science, Beijing Normal University, Beijing, China, [2]Institute of Remote Sensing Science and Engineering, Faculty of Geographical Science, Beijing Normal University, Beijing, China, [3]College of Geodesy and Geomatics, Shandong University of Science and Technology, Qingdao, China, [4]Roquette Management (Shanghai) Com. Ltd, Shanghai, China, [5]Key Laboratory of Digital Earth Science, Aerospace Information Research Institute, Chinese Academy of Sciences, Beijing, China

Winter wheat is one of the major food crops in China, and timely and effective early-season identification of winter wheat is crucial for crop yield estimation and food security. However, traditional winter wheat mapping is based on post-season identification, which has a lag and relies heavily on sample data. Early-season identification of winter wheat faces the main difficulties of weak remote sensing response of the vegetation signal at the early growth stage, difficulty of acquiring sample data on winter wheat in the current season in real time, interference of crops in the same period, and limited image resolution. In this study, an early-season refined mapping method with winter wheat phenology information as priori knowledge is developed based on the Google Earth Engine cloud platform by using Sentinel-2 time series data as the main data source; these data are automated and highly interpretable. The normalized differential phenology index (NDPI) is adopted to enhance the weak vegetation signal at the early growth stage of winter wheat, and two winter wheat phenology feature enhancement indices based on NDPI, namely, wheat phenology differential index (WPDI) and normalized differential wheat phenology index (NDWPI) are developed. To address the issue of " different objects with the same spectra characteristics" between winter wheat and garlic, a plastic mulched index (PMI) is established through quantitative spectral analysis based on the differences in early planting patterns between winter wheat and garlic. The identification accuracy of the method is 82.64% and 88.76% in the early overwintering and regreening periods, respectively, These results were consistent with official statistics (R2 = 0.96 and 0.98, respectively). Generalization analysis demonstrated the spatiotemporal transferability of the method across different years and regions. In conclusion, the proposed methodology can obtain highly precise spatial distribution and planting area information of winter wheat 4_6 months before harvest. It provides theoretical and methodological guidance for early crop identification and has good scientific research and application value.

KEYWORDS

winter wheat, early mapping, phenological information, contemporaneous crops, Sentinel-2

1 Introduction

Food security is critical for the worldwide community, national economic development, social harmony, and people's daily lives. Food security is eliciting increasing attention as a result of urbanization, global climate change, and the loss of farmland due to deterioration (Liu et al., 2014; Song et al., 2018). With the rapid growth of Earth observation data in the past decades, remote sensing has been widely recognized in informative agricultural applications because of its advantages of broad spatial coverage, high revisit frequency, low cost and simple accessibility (Griffiths et al., 2019; Jin et al., 2019). Remote sensing technology can perform timely and accurate mapping of crop types with high accuracy, and it has been proven to be one of the most effective ways to determine the spatial distribution of crop cultivation (Pan et al., 2012; Griffiths et al., 2019). Crop identification and crop acreage estimation in early or in-season can help in crop cultivation management, food security scenario analysis and related policy formulation and also have important applications in crop yield forecasting, agricultural insurance, agricultural subsidies and agricultural restructuring.

Currently, the identification of crop types usually requires the use of image data on their entire growth period, so the results of crop distribution maps are often obtained after the season or in the following year, with a certain delay. For example, the United States Department of Agriculture Cropland Data Layer (CDL) Dataset is published about five months after the end of the crop harvest, and the Agriculture and Agri-Food Canada Annual Crop Inventory (ACI) is usually published about eight months after harvest (Fisette et al., 2014; Kussul et al., 2018). Although CDL and ACI datasets have high accuracy, they both have time delay. Therefore, the importance of in-season or early-season crop type mapping based on remote sensing has become a valuable research topic.

The amount of information available for early crop remote sensing identification is smaller than that for post-season identification. The first manifestation is the reduction in remote sensing data, which are limited to the early crop growth time period. At the early stage of crop growth, the characteristic response on the remote sensing image of crop growth is not significant due to the effect of mixed image units caused by vegetation and soil; therefore, fully exploiting the phenological and spectral information in the early stage of crop growth can contribute to highly accurate early crop mapping. Dong et al. (2016) developed a pixel-level rice mapping method based on the Google Earth Engine (GEE) platform by using the water signal characteristics at the rice transplanting stage, and accomplished rice mapping in Northeast China by using the enhanced vegetation index (EVI) and the land surface water index (LSWI). Basing on the fact that corn is seeded earlier than soybean in the United States, Sakamoto et al. (2014) accomplished mapping and yield calculation for both crops. The second manifestation is that early identification studies have little opportunity to obtain sample dates in the current year (Johnson and Mueller, 2021). A common strategy is to use a migration learning approach that utilizes sample data from previous years to train the model and apply it to the current year. Cai et al. (2018) completed early-season mapping of maize and soybean by using a transfer learning algorithm based on Landsat time series data. Zhang et al. (2019) adopted artificial neural networks to predict the spatial distribution of future crop plantings before the start of the growing season on the basis of historical information and effectively completed pre-season crop mapping and crop yields estimation for a normal year.

In addition to the reduction in available remote sensing information, the spatial resolution of remote sensing images is another factor that affects identification accuracy. In previous studies, MODIS data were the main data source for crop mapping in large regions. Hao et al. (2015) employed MODIS time series data to investigate the effect of time length on crop mapping by using Kansas, USA, as the study area and achieved high crop identification accuracy after five months of the sowing period. However, most of China's cultivated land is fragmented, and villages, towns, and wheat are interspersed. The average planting area per household is only 1.37 hectares, which account for 5% of the MODIS image size, and the planting structure is complex. Moreover, the mixed image phenomenon at the boundary of the land is serious, so accurately identifying the winter wheat planting area is difficult (Zhang, 2008; Qiu et al., 2017). Tian et al. used multi-source remote sensing data based on a phenological algorithm to map the crop distribution and subsequently compared and analyzed the difference in the accuracy of identifying winter wheat by using Landsat-7, Landsat-8, and Sentinel-2 remote sensing data and MODIS data (including 250 and 500 m) under the same method. The results showed that image spatial resolution has a considerable influence on the remote sensing recognition results, and the mapping accuracy increases with the increase in spatial resolution. Moreover, MODIS data cannot accurately identify village boundaries, rural roads, and other features, and the overall accuracy of identification using high-resolution remote sensing data is improved by 14.1% compared with the overall accuracy of identification using MODIS data (Tian, 2019; Tian et al., 2019). Song et al. studied Landsat, Sentinel-2, Sentinel-1 and MODIS remote sensing data at different spatial resolutions for crop type mapping of soybean and corn in the Continental United States (Song et al., 2021). Another study evaluated the application efficiency and effectivity of rice mapping based on the GEE cloud platform in Southern Punjab, Pakistan, from coarse to fine resolution multispectral satellites (Sentinel-2 [10 m], Landsat-8 [30 m] and MODIS [250 m]) (Waleed et al., 2022). These studies proved that the higher the spatial resolution of optical remote sensing data is, the better the mapping accuracy of crop types is; moreover, Sentinel-2 data can effectively enable field-scale crop mapping, and the identification accuracy is affected by parcel size, planting density, and crop diversity. However, Landsat and Sentinel-2 data are usually studied in a small area due to their massive data volume (Belgiu and Csillik, 2018). After GEE was made available to the public in 2012, its powerful cloud computing capabilities have facilitated extensive, high spatial-resolution crop mapping based on Landsat and Sentinel series satellites. Gumma developed a spatial distribution map of agricultural land in South Asia on the basis of a machine learning algorithm by using Landsat time series data on GEE (Gumma et al., 2020). Nasrallah extracted the 10 m resolution winter wheat distribution in the Bekaa Valley of Lebanon by using Sentinel-2 time series data (Nasrallah et al., 2018).

The use of remote sensing data with high spatial resolution helps alleviate the low identification accuracy caused by parcel fragmentation. In addition, high-spatial-resolution remote sensing images help describe farmland cropping patterns at the landscape level and achieve highly effective extraction of crop phenology information at the parcel scale (Pan et al., 2015; Qiu et al., 2020).

In North China, In North China, winter crops are usually sown from September to October, with seedlings emerging before the over-wintering period and harvested around June. Winter wheat, garlic, and rapeseed are the principal winter crops of the North China Plain, with winter wheat accounting for the majority of production (Dong et al., 2020). Winter wheat and garlic are the two primary crops grown throughout the winter in the Shandong region. However, existing studies have focused on winter wheat, and little importance has been given to remote sensing mapping and area estimation of garlic (Chai et al., 2019). Garlic's economic value has increased recently, resulting in an increase in planting areas. Given that winter wheat and garlic have almost the same phenological period and vegetation characteristics, the phenomenon of " different objects with the same spectra characteristics " arises, and garlic is easily as winter wheat, which makes the identification of winter wheat erroneous.

In summary, to address the problems of early-season identification of winter wheat, such as weak vegetation signal, limited spatial resolution of remote sensing data, heavy reliance on training samples, and the " different objects with the same spectra characteristics " of winter wheat and garlic, this study has completed a refined early-season mapping of winter wheat in Shandong Province with 10-m resolution on the basis of the GEE cloud platform, by using Sentinel-2 time series data supplemented by Landsat-8 data. In the study, a phenology feature index was developed for weak vegetation signal enhancement of winter wheat, and early-season identification discriminative rules were designed in combination with other information for different periods of winter wheat. In addition, a unique spectral feature was developed based on the growth differences between winter wheat and garlic. The proposed method does not require training samples and can achieve refined early-season identification of winter wheat with automated premise. The winter wheat identification results can be advanced to 4-6 months before the harvesting period, with high identification accuracy.

2 Materials

2.1 Study area

Shandong Province is located on the eastern coast of China, and it is between 34°22′N-38°24′N and 114°47′E-122°42.3′E. It is situated in the lower reaches of the Yellow River and has a land area of about 155,800 km^2, as shown in Figure 1. The climate of Shandong Province is warm-temperate monsoon, characterized by concentrated precipitation in summer, rain and heat in the same season, and coldness and dryness in winter. The average annual temperature is between 11°C and 14°C, and the temperature difference between the east and west is greater than that between the north and south. The annual precipitation is between 550 and 950 mm and decreases from southeast to northwest (Chen et al., 2012). The average annual amount of light is between 2,290 and 2,890 hours, and the sufficient heat conditions meet the needs of crops to mature twice a year (Xu et al., 2019). The central part of Shandong Province is mountainous, the southwest and northwest parts are low-lying and flat, and the eastern part is gently undulating. Plains account for 65.6% of the province's area and are mainly located in the northwest and southwest of Shandong.

The soil type in Shandong Province is mainly brown loam and brown soil. The fertile soil and good climatic conditions make Shandong Province the second major production center of winter

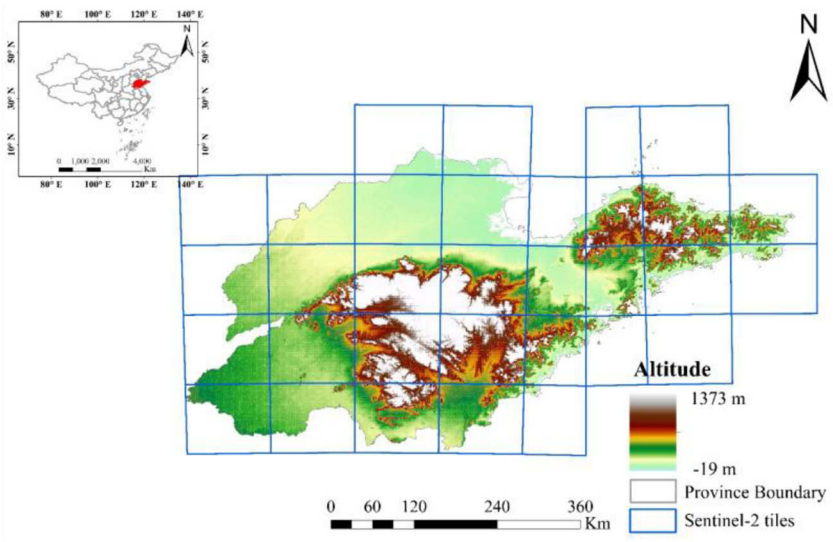

FIGURE 1
Location of the study area (It includes the location of Shandong Province in China, the coverage of Sentinel-2 relative orbits and the elevation data of Shandong Province).

wheat aside from Henan Province (Li et al., 2021). In 2021, 39,493,530,800 ha of winter wheat, which is the largest winter crop in Shandong Province, was planted in the said province Garlic, oilseed rape, vegetables, and greenhouse crops are also grown in the region, with garlic being the most widely planted. The phenological periods of winter wheat and garlic are basically the same; the sowing period is from September to October, and the harvesting period is in June. The specific phenological periods are shown in Figure 2.

2.2 Data and preprocessing

In this study, the processing and analysis of remote sensing images were carried out on the GEE, and the remote sensing data mainly included Sentinel-2A/B MSI data and Landsat-8 OLI data. This study also used SRTM elevation data, field sample data, and winter wheat planting area statistics The elevation data were directly derived from GEE (https://developers.google.com/earth-engine/datasets/catalog/USGS_SRTMGL1_003), and the statistical data were obtained from Shandong Provincial Bureau of Statistics (http://tjj.shandong.gov.cn/tjnj/nj2021/indexch.htm).

2.2.1 Remote sensing image data

This study used two types of Sentinel-2 optical images are used in the study, which are surface reflectance data and top-of-atmosphere reflectance data. The surface reflectance data were employed to construct a time-series winter wheat phenology curve, and the top-of-atmosphere reflectance data were adopted to extract winter wheat phenology characteristics. Both types of data were pre-processed via radiometric calibration, geometric correction, and topographic correction, and the temporal resolution of the data was five days. Landsat-8 surface reflectance data were invoked on the GEE cloud platform and had already been pre-processed via radiometric calibration and geometric correction. The main purpose of these data was to compensate for the lack of effective observations of Sentinel-2 optical images due to poor weather, with a revisit period of 16 days. The spectral parameters of Landsat-8 and Sentinel-2 are shown in Table 1.

2.2.2 Field sampling data source

The data on winter wheat sample points were obtained from the field survey of the national agricultural department, and the sampling period was between November and December 2021, with a total of 3,885 winter wheat sample points in Shandong Province. Samples of other surface types were automatically generated in GEE by using a sampling method. The detailed operation is to used ESA-2020 and AGLC-2015 as the base data, and calculate the concatenation of cropland types in the two datasets was calculated to define them as cropland areas. Then random points were generated in the non-cultivated area, and the land type and coordinate information of the random points were

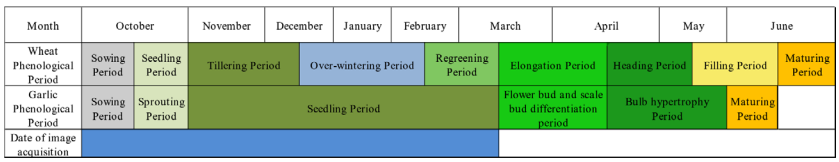

FIGURE 2
Winter wheat and garlic phenological calendar in Shandong Province.

TABLE 1 Remote sensing image waveband parameters.

Bands Name	Landsat-8 wavelength range (μm)	Sentinel-2 band center wavelength (S2A/S2B)
Aerosols	B1(0.43~0.45)	B1(443.9nm/442.3nm)
Blue	B2(0.45~0.51)	B2(496.6nm/492.1nm)
Green	B3(0.53~0.59)	B3(560nm/559nm)
Red	B4(0.64~0.67)	B4(664.5nm/665nm)
NIR	B5(0.85~0.88)	B8(835.1nm/833nm)
SWIR 1	B6(1.57~1.65)	B11(1613.7nm/1610.4nm)
SWIR 2	B7(2.11~2.29)	B12(2202.4nm/2185.7nm)
Red Edge 2		B5(703.9nm/703.8nm)
Red Edge 2		B6(740.2nm/739.1nm)
Red Edge 3		B7(782.5nm/779.7nm)
Red Edge 4		B8A(864.8nm/864nm)

extracted In the end, a total of 2,500 random non-wheat sample points were generated. A total of about 6,385 sample points were obtained for the accuracy verification of the identification results.

2.2.3 Detection of clouds and cloud shadows

In this study, cloud and cloud shadow removal was performed in accordance with the clouds presenting different features from other ground features in an image (Lewis and Brown, 2001). The details of the process are as follows: Clouds are bright and moist in the cirrus band, blue band, and all visible bands, so the cloud score of the image is calculated and the cloud probability is detected using data from four bands (aerosol, blue, green and red bands) together with two spectral indices (normalized difference humidity index and normalized difference snow index). Cloud shadows are then judged based on the solar geometry features and the position clouds, so clouds and cloud shadows can be detected and removed accurately at the same time. This method is more effective than the QA60 band for cloud and shadow removal (You and Dong, 2020).

3 Methods

3.1 Weak signal enhancement in early winter wheat

At the early stage of winter wheat growth, the winter wheat leaves are small and cannot cover the ground completely. The winter wheat vegetation signal is also mixed with background information, such as soil and snowmelt. The vegetation signal features on remote sensing images are not noticeable due to the background information, and the vegetation changes shown on time-series images are less sensitive because of the slow growth of winter wheat at the early growth stage. A new vegetation index called normalized differential phenology index (NDPI) was selected in this research to enhance the weak vegetation signal characteristics at the start of winter wheat growth (Wang et al., 2017). NDPI can suppress soil and snow cover compared with the traditional vegetation index and can reduce the influence of weak vegetation response at the early stage of winter wheat growth and winter snow. NDPI is calculated as shown in Equation 1:

$$NDPI = \frac{\delta_{NIR} - (\alpha \times \delta_{RED} + (1-\alpha) \times \delta_{SWIR})}{\delta_{NIR} + (\alpha \times \delta_{RED} + (1-\alpha) \times \delta_{SWIR})}, \quad (1)$$

where δ_{NIR} is the NIR band reflectance, δ_{RED} is the red band reflectance, δ_{SWIR} is the shortwave infrared reflectance, and α is set at 0.74 since it is the most potent value for reducing changes in the soil and snow backdrop (Wang et al., 2017).

Extraction of time series variation characteristics based on NDPI was performed using Sentinel-2 data. First, cloud and cloud shadow removal and five-day-interval time-series NDPI index median composition were conducted. Second, NDPI index reconstruction was performed using the Savitzky-Golay filtering algorithm. Lastly, NDPI feature images with a five-day interval at 10 m spatial resolution were acquired (Savitzky and Golay, 1964). In the study area for winter wheat and other major surface types (including woodlands, grasslands, water bodies, and impervious surfaces), 100 sample points were evenly selected for each surface type. Their mean values were calculated to generate the phenological curves and conduct a comparative analysis, as shown in Figure 3.

The analysis of Figure 3 shows that, the first window period was in the winter wheat sowing period (light yellow background), where the NDPI value of winter wheat was the smallest, that is, about 0.1. The NDPI values of forest and grassland (i.e., about 0.3) were higher than that of winter wheat. The NDPI values of impervious surfaces was low, generally less than 0.1, and the NDPI value of water bodies was less than 0. The second window period ① (blue background, black solid line area)was the early over-wintering period and over-wintering period of winter wheat, in which the chlorophyll content of winter wheat increased, so and the NDPI value also increased. The NDPI of winter wheat was greater than 0.35. The NDPI values of water bodies and impermeable surfaces were mostly unchanged, whereas those of forest, grassland, and other withering vegetation typically decreased to below 0.2. The second window period ② (the region with a green background and a blue dotted box) had a start time that was similar to that of the second window period ① and an end time that was the regreening period of forest and grassland (before March 15). At this time, winter wheat had entered the regreening period for 2_3 weeks. At the end of the second window period ②, the NDPI value of winter wheat increased from a low value during the over-wintering period to be at par with the maximum value of NDPI during the early over-wintering period, with an NDPI value greater than 0.45. During the second window period ②, forest and grassland had just entered the regreening period; their NDPI values increased slightly, but most of the forest and grassland NDPI values were still in the low-value period. The NDPI value of impervious surfaces slightly increased because the vegetation in the residential land returned to green and formed a mixed image with the buildings. The NDPI value of water bodies slightly increased but was lower than 0.1, which could be well distinguished.

To further enhance the weak vegetation signal characteristics of winter wheat and highlight the time-series vegetation variation of winter wheat, this study proposed two phenological indices for early-season identification of winter wheat based on the phenological characteristics of early winter wheat growth; the two indices are winter wheat phenology differential Index (WPDI) and the normalized differential wheat phenology index (NDWPI). The formulas are as follows:

$$WPDI = Max\{NDPI_{Pho_2}\} - Min\{NDPI_{Pho_1}\}, \quad (2)$$

$$NDWPI = \frac{Max\{NDPI_{Pho_2}\} - Min\{NDPI_{Pho_1}\}}{Max\{NDPI_{Pho_2}\} + Min\{NDPI_{Pho_1}\}}, \quad (3)$$

where $NDPI_{pho_1}$ denotes the time series data of NDPI in the first time window of winter wheat, $NDPI_{pho_2}$ denotes the time series data of NDPI in the second time window of winter wheat.

$Min\{NDPI_{pho_1}\}$ denotes the minimum value of the NDPI calculated in the first time window, and $Max\{NDPI_{pho_2}\}$ denotes

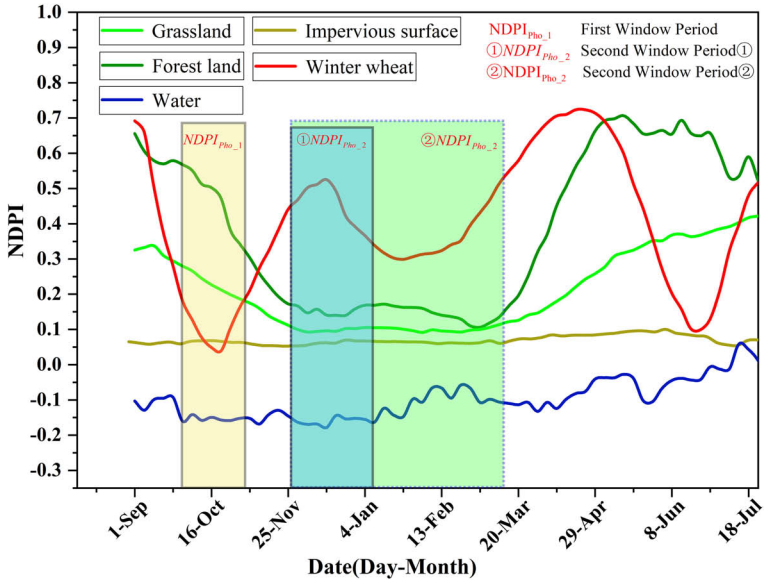

FIGURE 3
Time-series NDPI curves for winter wheat and other landforms.

the maximum value of the NDPI calculated in the second time window. The settings of the time windows are shown in Figure 3.

In addition, the day of year (DOY) corresponding to the maximum value of NDPI in the early over-wintering period is set as an important feature for judging winter wheat.

$$DOY_{\max} = \arg\max\left\{NDVI_{pho} | pho_1 \le pho \le pho_2\right\}, \quad (4)$$

where $DOY_{\max}$ is the DOY corresponding to the maximum value of NDPI, pho_1 corresponds to the winter wheat sowing period, pho_2 corresponds to the winter wheat early over-wintering period, and argmax $\{f(x)\}$ indicates the x corresponding to the maximum of $f(x)$, that is, DOY.

The DOY corresponding to the maximum value of NDPI represents the date of the most vigorous growth of winter wheat. According to the winter wheat growth phenology calendar and the analysis of Figure 3, the peak growth date of winter wheat is generally after mid-November, and the peak growth period of woodland and grassland is before winter wheat sowing. Therefore, DOY can be used to help distinguish winter wheat from woodland and grassland.

In this study, NDPI was used to mitigate the mixed pixel effect and enhance the weak vegetation signal in the early growth period of winter wheat. Two feature indices, WPDI and NDPI, were also developed based on the phenological characteristics to increase the distinguishability of winter wheat from other ground features in the time dimension. However, because garlic and winter wheat have similar phenological characteristics, they cannot be effectively distinguished from each other by using the abovementioned method.

3.2 Spectral characterization of winter wheat and garlic

Winter wheat and garlic have similar phenological characteristics, and both belong to green vegetation, as shown in Figure 4A. The two time-series NDPI curves in this study were similar, although garlic had slightly lower NDPI values than winter wheat throughout the growth stage. However, some variations in NDPI values without obvious boundaries were observed. Additionally, the harvest period for garlic was a little bit earlier than the harvest period for winter wheat, but considering the length of the harvest period and the interval satellite observations, precisely differentiating between the two based on vegetation or phenological characteristics was challenging. Nevertheless, garlic and winter wheat have a few different planting practices, though. Winter wheat is more resistant to cold than garlic is, so when garlic is seeded, the mulch is often covered to prevent frost damage during the overwintering season, as shown in Figure 4B.

In this study, a mulch characteristic index was created to differentiate garlic from winter wheat by using the specific qualities of plastic mulch utilized during the early stages of garlic growth. In this study, 100 sample points from the winter wheat-and garlic-growing regions were collected for spectrum analysis through a field survey and visual interpretation of high-resolution Google pictures. The data are displayed in Figure 5A. The plastic mulch used at the earliest stage of the garlic planting process is often colorless and transparent, and the ground surface it covers has higher brightness characteristics than bare soil. The primary chemical component of the plastic mulch is polyvinyl chloride, which has a higher transmittance in the 1500–2500 μm range than the visible near infrared band in terms of spectral characteristics. Figure 5A shows that although the reflectance values of plastic mulch decreased in the short-wave infrared band range, they increased in the visible to near-infrared band range in the garlic-growing region compared with the winter wheat-growing area. In the study, a plastic mulched index (PMI) was developed based on the special spectral characteristics of plastic mulch. PMI is expressed as

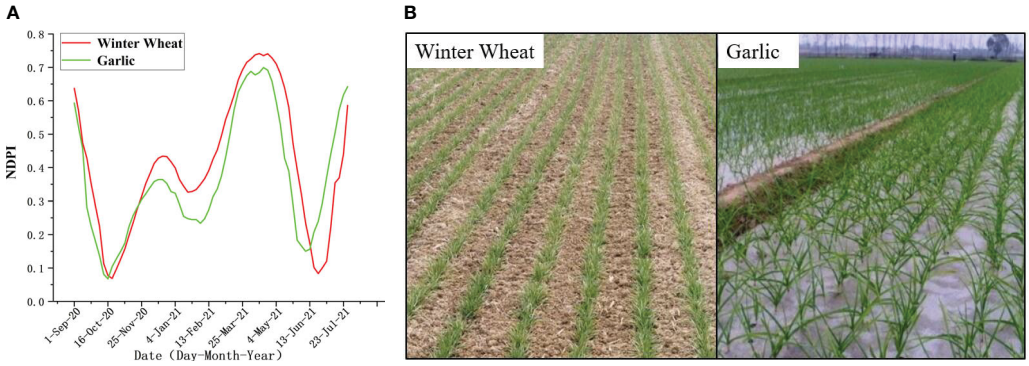

FIGURE 4
Differences between winter wheat and garlic [**(A)** displays the phenology curves for winter wheat and garlic, and **(B)** displays fieldwork photos of winter wheat and garlic at the early growth stage].

$$PMI = \frac{\delta_{NIR} - \delta_{SWIR1}}{\delta_{NIR} + \delta_{SWIR1}}, \quad (5)$$

where δ_{NIR} is the reflectance of the NIR band and δ_{SWIR1} is the reflectance of the shortwave infrared1 band. The reflectance of the NIR and shortwave infrared1 bands was chosen in this study because the PMI results are highly stable with a small range of data fluctuations while maintaining a large difference.

As illustrated in Figure 5A, discerning between winter wheat and garlic by using NDPI and NDVI vegetation indices is difficult. Given that PMI data fluctuate less and the feature is stable, using the PMI feature index suggested in the study allows for easy distinction between winter wheat and garlic as a contemporaneous crop. The PMI feature index is negative in areas where winter wheat is grown and positive in areas where garlic is grown.

3.3 Decision tree algorithm classification

The decision tree technique is a popular classifier for classifying remote sensing images. The fundamental idea behind this algorithm is to create a set of rules using expert knowledge, divide them into levels in accordance with the tree structure, and make logical decisions at each level in accordance with the rules until the classification is complete at the final leaf node. The decision tree method has a clear structure, good interpretability, and quick and easy operation (Friedl and Brodley, 1997).

On the basis of the findings presented in Sections 4.1 and 4.2, a tree was constructed for refined early-season mapping of winter wheat in this study, and the classification rules of the decision tree are illustrated in Figure 6.

First, removal of clouds and cloud shadows was performed on the GEE platform for Sentinel-2 and Landsat-8 data. Second, a time-series vegetation index dataset was constructed. Owing to the influence of cloud removal, remote sensing images in some areas or times have no-data values. In this study, the median composition algorithm was used to generate spatio-temporal continuous data at five-day intervals. The three phenological periods' time windows were selected based on the results of the analysis in Section 4.1 and Figure 3, and the defining images of each period were filtered in accordance with the time windows.

Image composition based on the time window of the winter wheat phenological period can enhance the image features of early

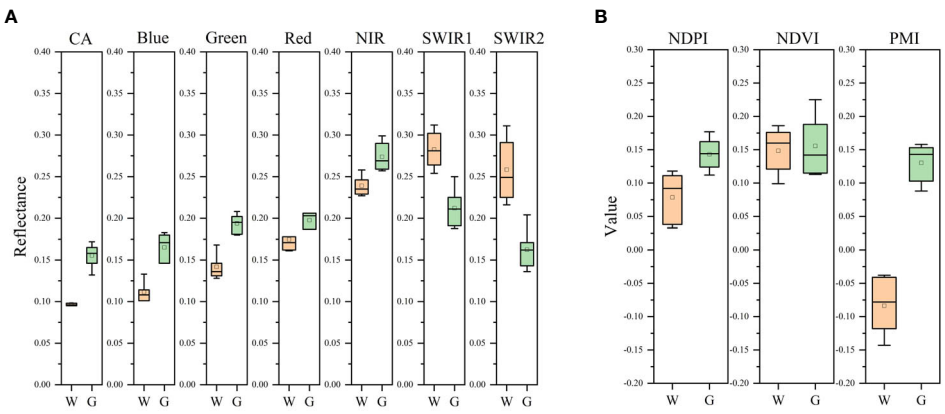

FIGURE 5
Spectral analysis of winter wheat and garlic W represents winter wheat, G represents garlic, **(A)** shows the spectral band information, and **(B)** shows the spectral index information].

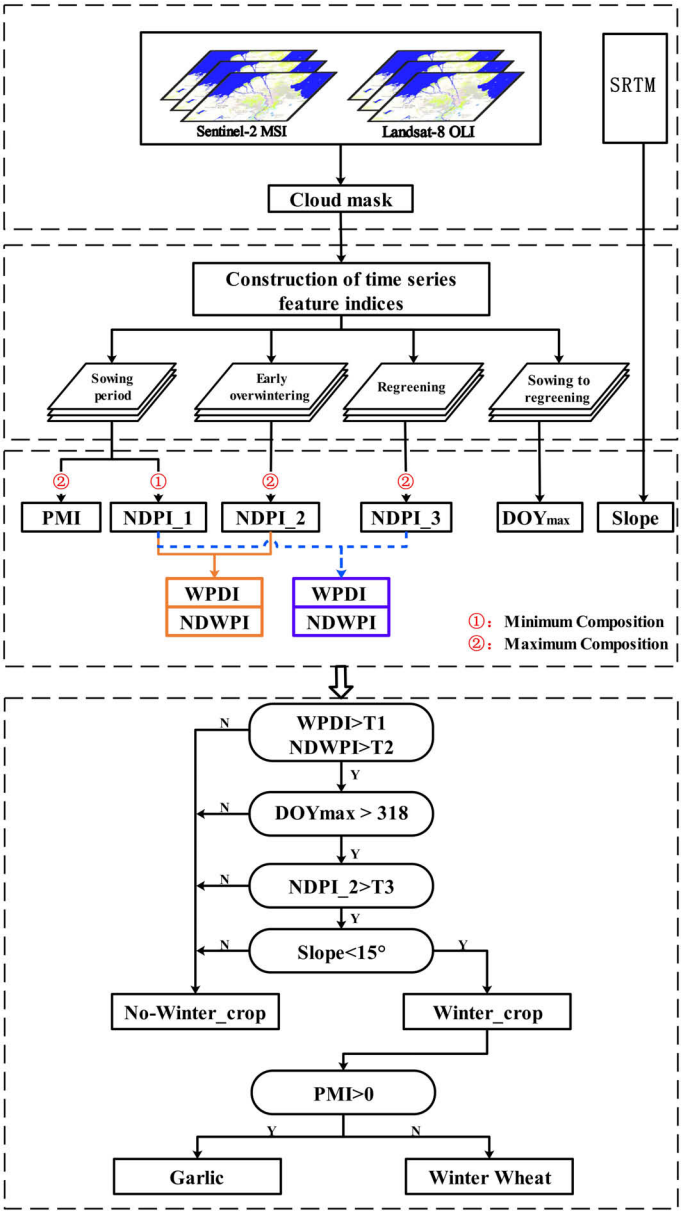

FIGURE 6
Flow chart of early refinement mapping of winter wheat with the decision tree algorithm.

winter wheat growth and reduce data redundancy. We completed the minimum composite of time-series NDPI in the sowing period, the maximum composite of time-series NDPI in the early overwintering period, and the maximum composite of time-series NDPI in regreening period. From to the winter wheat phenology calendar and phenology curve in Shandong Province, we found that NDPI reached the maximum value in the tillering period, and we set the threshold value of DOY corresponding to NDPI to 318. DOY greater than the threshold value of 318 refers to a winter crop. Winter wheat is often planted in plain areas with mild slopes, and less land is cultivated in central and eastern mountainous areas (Valero et al., 2021). In addition, 15° is used as the slope threshold, and winter wheat is grown in areas where the slope is less than 15°. Other characteristics including water bodies, forests, grasslands, and impervious surfaces may be distinguished based on the five abovementioned rules to extract the spatial distribution of winter crops, but garlic, a contemporaneous crop of winter wheat, cannot be extracted.

On the basis of the spatial distribution map of winter crops, garlic was distinguished from winter wheat by using the PMI index developed in this study. With the analysis conclusion in Section 3.2, the PMI maximum composite of the sowing period was calculated, and the area with PMI greater than 0 was established as the garlic planting area with mulching. The other areas were winter wheat planting areas.

Automated early-season refined mapping of winter wheat was achieved in all regions of Shandong Province without a large number of training samples and by using only *a priori* knowledge of winter wheat phenology.

3.4 Accuracy assessment

Accuracy verification is necessary to evaluate the recognition performance and is mainly divided into type accuracy and quantitative accuracy. Type accuracy is usually assessed using the confusion matrix. Quantitative accuracy describes how closely a particular type area matches the actual area. In this study, the overall area accuracy was used to evaluate the quantitative accuracy of recognition, and the area consistency index was adopted to evaluate the consistency between the extracted area and the actual area; the higher the area consistency was, the higher the extraction accuracy was.

The confusion matrix is generally calculated based on the acquired samples and classification results, and the specific evaluation metrics include overall accuracy (OA), user accuracy (UA), production accuracy (PA), kappa coefficient, and the derived F1 score (Lewis and Brown, 2001). OA and kappa are used to evaluate the overall classification results, and the F1 score is a combined metric consisting of PA and UA; it provides a comprehensive evaluation of each type of classification accuracy.

$$OA = \frac{\sum_{i=1}^{n} A_{ii}}{N} \times 100\,\%, \tag{6}$$

$$Kappa = \frac{N\sum_{i=1}^{n} A_{ii} - \sum_{i=1}^{n}(A_{i+} \times A_{+i})}{N^2 - \sum_{i=1}^{n}(A_{i+} \times A_{+i})}, \tag{7}$$

$$PA = \frac{A_{ii}}{A_{+i}} \times 100\,\%, \tag{8}$$

$$UA = \frac{A_{ii}}{A_{i+}} \times 100\,\%, \tag{9}$$

$$\mathrm{F1_}Score = 2 \times \frac{\mathrm{PA} * \mathrm{UA}}{\mathrm{PA} + \mathrm{UA}}, \tag{10}$$

where n represents the number of classes, and it is also the total number of rows or columns of the matrix; A_{ii} represents the number of image elements on the first row and column; and N represents the total number of real samples. A_{i+} represents the sum of the pixels on row i, and A_{i+} represents the sum of the pixels on column i.

Total area accuracy (TA) refers to the closeness of the extracted area to the true area. The true area uses the yearbook results published by local and municipal statistical offices, as follows:

$$TA = 1 - \frac{|X - Y|}{X} \times 100\,\%, \tag{11}$$

where X is the statistical area in the yearbook and Y is the area of the extraction results.

Area consistency accuracy is achieved through a regression analysis of the crop area published in the yearbook of the municipal statistical office with the results of identification, and calculation of the coefficient of determination (R^2) (Phalke et al., 2020). Large values indicate a high correlation of the dependent variable, which also indicates good area consistency between the extracted area and the statistical data. A comparison is then made between the linear fit line and the 1:1 line, which is used to reflect the direction of deviation. R^2 is shown as

$$R^2 = 1 - \frac{\Sigma(y_i - \widehat{y_i})^2}{\Sigma(y_i - \overline{y_i})^2}, \tag{12}$$

where y_i is the identification area of the i municipal unit, $\hat{y}$ is the statistical area, and $\bar{y}$ is the average of the area.

4 Results

4.1 Winter wheat and garlic early-season mapping

The judgment indices for constructing the decision tree are shown in Figure 7. For the two characteristic indices, WPDI and NDPI, the results obtained from the sowing and early over-wintering periods were selected as examples. Their large values indicated that the vegetation change was great and that the increasing trend of NDPI was obvious. Although the NDPI of winter wheat increased a little relative to that of garlic, the distinction between the two was not obvious because both winter wheat and garlic were green in the early over-wintering period. The comparison showed that the trend of DOY max had a strong correlation with the trend of WPDI and NDPI, and the macroscopic change trend was consistent.

On the basis of the decision tree algorithm, Figure 8A shows the identification results of the early over-wintering period with the date of January 15, and Figure 8B shows the identification results of the regreening period with the date of March 15. The identified winter wheat area in the regreening period was slightly larger than the identified area in the early over-wintering period, and the increased area was mainly in the eastern part of Shandong Province. A comprehensive analysis revealed that the winter wheat planting areas in Shandong Province were mainly distributed in the western, northern, and southern regions, in which four cities, namely, Heze, Dezhou, Liaocheng, and Jining, had large and concentrated planting areas. This distribution was mainly due to the wide distribution of mountains and hills in the central and northeastern regions of Shandong, which are unsuitable for the cultivation of winter wheat. Moreover, the soil texture in the eastern coastal region was relatively poor, and the planting suitability of winter wheat i was low; hence, the planting area of winter wheat was small and scattered.

This study completed the early spatial distribution of winter wheat in Shandong Province, and also acquired the spatial distribution map of early mapping of garlic. Garlic cultivation in Shandong Province was mainly distributed in Jinxiang County of Jining City and its surrounding areas, among which Jinxiang had the widest garlic cultivation area and the most concentrated distribution. Meanwhile, garlic cultivation in the rest of the areas was relatively fragmented. In this study, we adopted Jinxiang County of Jining as an example to show the identification results

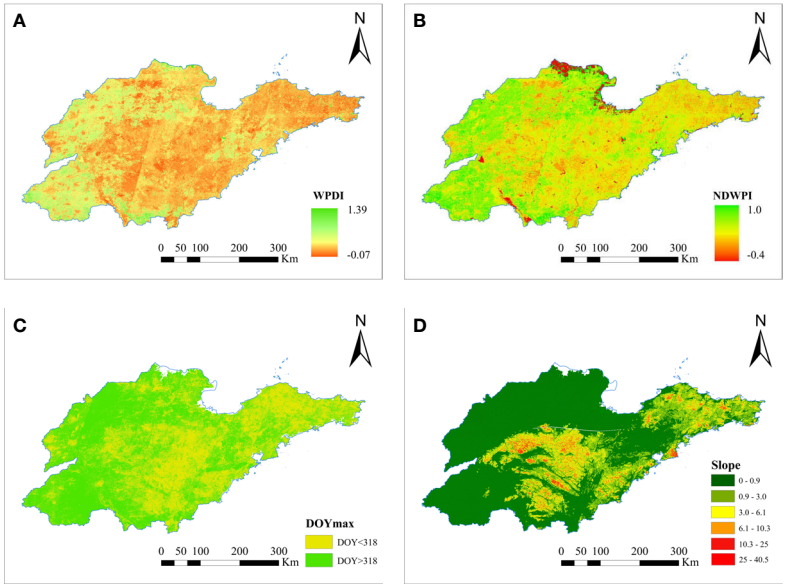

FIGURE 7
Example of decision rule feature image. [**(A–D)** respectively show the images of four feature indices: WPDI, NDWPI, DOY max, and slope].

of garlic, as indicated in Figure 9. Garlic is the main plantation in Jinxiang County, and the distribution of garlic is relatively concentrated. The main plantation zones are the central, eastern, and western parts. The distribution of winter wheat is fragmented, and the planting area is mostly in long and narrow patches. The distribution of winter wheat in the north and south of Jinxiang County is relatively concentrated, which is basically consistent with the background survey of crop cultivation.

4.2 Accuracy verification

Early-season identification mapping of winter wheat was conducted in two phenological periods, namely, early over-wintering and regreening. We used three methods for accuracy evaluation: calculation of the confusion matrix, statistical area validation of municipal administrative units, and zoomed maps of local areas.

4.2.1 Validation on sample points

On the basis of the data of 3,885 winter wheat sample points and 2,500 non-winter wheat sample points, the accuracy of the early-season identification results of winter wheat was evaluated by calculating the confusion matrix for the early over-wintering and regreening period. The results are shown in Figure 10. The analysis revealed that the accuracy of the early-season identification results of winter wheat in the regreening period was higher than that in the early over-wintering period, with an overall accuracy of 82.64%, F1 score of 0.84, and kappa coefficient of 0.78. The accuracy of the identification results in the regreening period was improved to some extent, with an overall accuracy of 88.76%, F1 score of 0.89, and kappa coefficient of 0.84. The reason for the higher accuracy of the

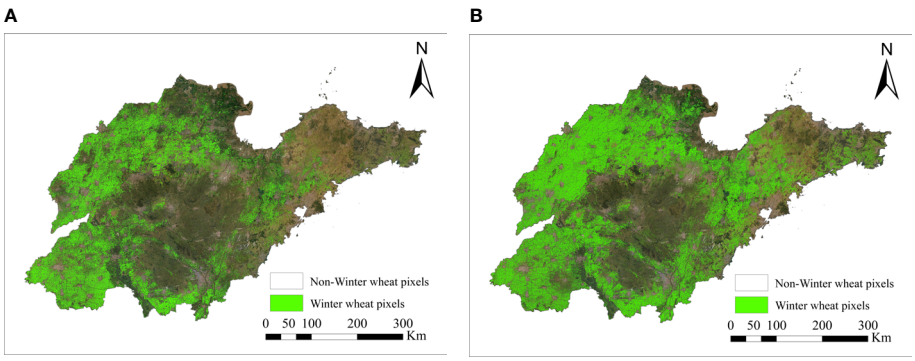

FIGURE 8
Spatial distribution of winter wheat in Shandong Province.

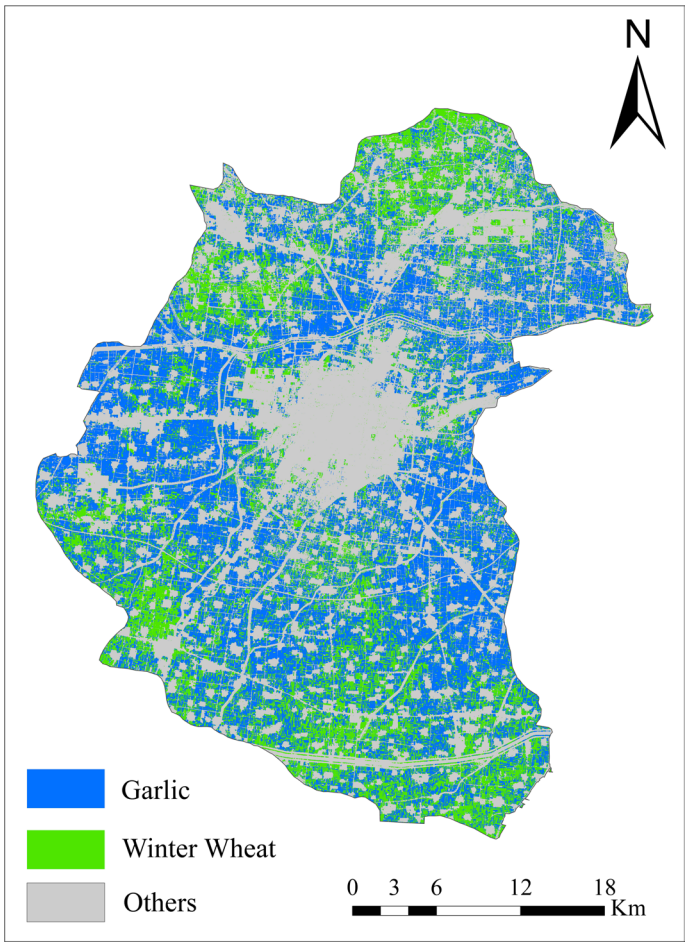

FIGURE 9
Early-season identification results of winter wheat and garlic in Jinxiang County.

identification results in the regreening period is that the growth of winter wheat in the regreening period is better and more uniform than that in the early over-wintering period, and the vegetation signal of wheat is more prominent. In conclusion, the early-season identification results of winter wheat in the study have high accuracy.

4.2.2 Verification of official statistics

To further verify the identification accuracy, this study calculated the planted area in accordance with the early-season identification results of winter wheat. The official statistics of winter wheat planted area in Shandong Province in 2021 was 3,949,353 ha. Meanwhile, the identified area in the early over-wintering period was 3,206,666.8 ha and the identified area in the regreening period was 3,990,686.7 ha; the overall area accuracy of the two periods was 81.2% and 98.9%, respectively. The identification results in the early over-wintering period were underestimated, and the identification results in the regreening period were overestimated. The reasons for the underestimated results in the early over-wintering period include the inconsistent growth of winter wheat in this period and the late sowing and un-sowing, which lead to missed identifications. The overestimated results in the regreening period may be due to the situation of winter wheat being harvested for green storage before the harvest stage, in addition to misclassification. Another main reason is that the area of winter wheat has been reduced by natural meteorological disasters or pests' diseases. Furthermore, to validate the consistency of the identification results, this study verified the area of winter wheat identified in this work based on official statistics in 16 municipalities in Shandong Province. The results are shown in Figure 11. The analysis revealed that the early-season identification results of winter wheat in both periods had good consistency, and the R^2 values were both above 0.95. The identified area in the over-wintering period was slightly lower than the statistical area.

In this study, we could not obtain garlic field sample points, so the confusion matrix was not calculated for accuracy evaluation. This study adopted Jinxiang County, a large garlic planting county, as an example to verify the statistical area. A total of 35,933.5 ha of garlic was planted in Jinxiang County in 2021, and the early-season identification area of garlic in the study was 31,666.8 ha, with an overall area accuracy of 88.13%. After excluding the garlic planting area, the overall accuracy of the winter wheat area identification was improved from 65.2% to 96.8%, which increased the identification accuracy.

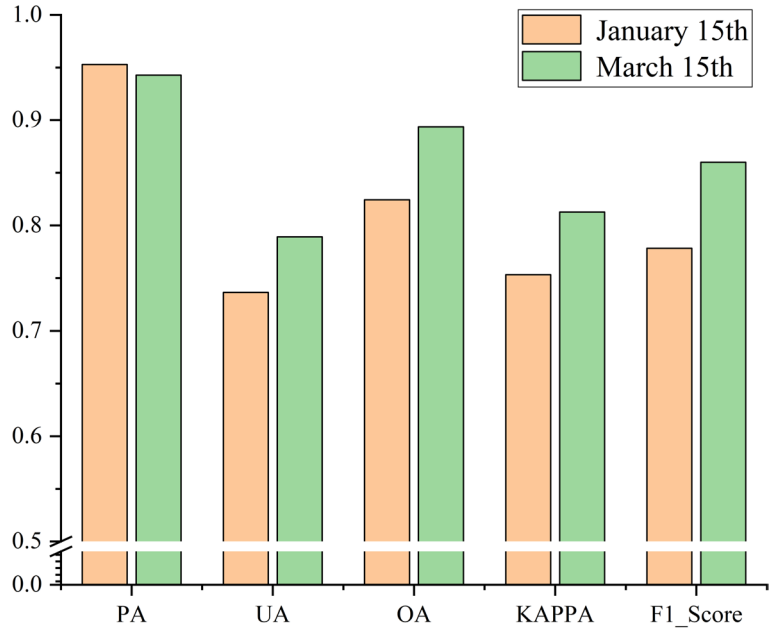

FIGURE 10
(A, B) Evaluation results of the confusion matrix for early-season identification of winter wheat.

4.2.3 Classification result subset analysis

As shown in Figure 12, the early-season identification results of winter wheat in the northern, eastern, southern and central-eastern parts of Shandong Province were randomly selected with one sample each, and the Google image was obtained from Google Earth with a resolution of 1 m. The NDPI image was the result obtained from using the Sentinel-2 image in the April elongation period with a resolution of 10 m. The remote sensing features of winter wheat in this period were relatively obvious. The third column shows the early-season identification results. The results indicate that the recognition of winter wheat distribution based on the Sentinel-2 image with 10 m resolution was good, and roads, settlements, bare land, water bodies, and wide farmland boundaries could be distinguished. The identified farmland details were relatively rich, which cannot be achieved by lower-resolution remote sensing data.

To further evaluate the effectiveness of this study on differentiating winter wheat and garlic, four validation samples were selected in Jinxiang County for an accuracy assessment, as shown in Figure 13. The first column is the Google image, the second column is the calculated PMI index, and the third column is the identification result.

The results of the four validation regions showed that the method in the study could identify garlic and winter wheat well. Region 1 had an interspersed distribution of garlic and winter wheat, and the PMI index could be used to distinguish them well.

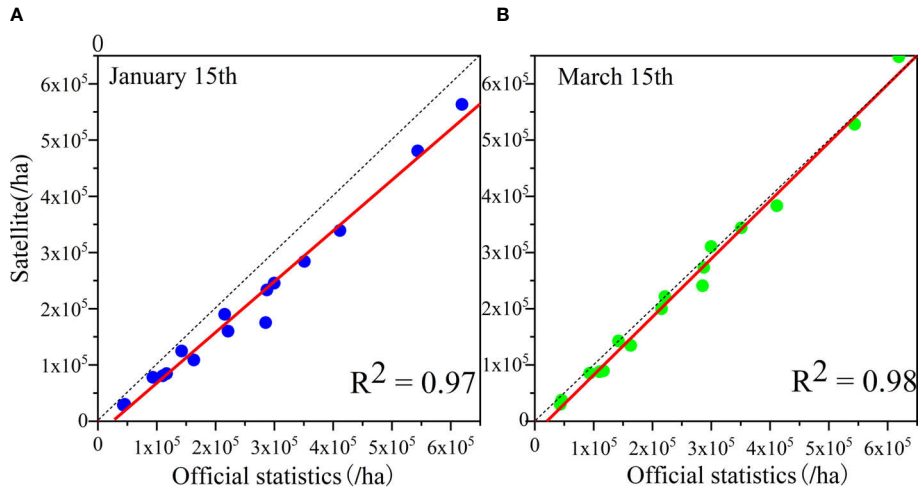

FIGURE 11
(A, B) Verification of consistency between the identification results and official statistics.

10.3389/fpls.2023.1016890

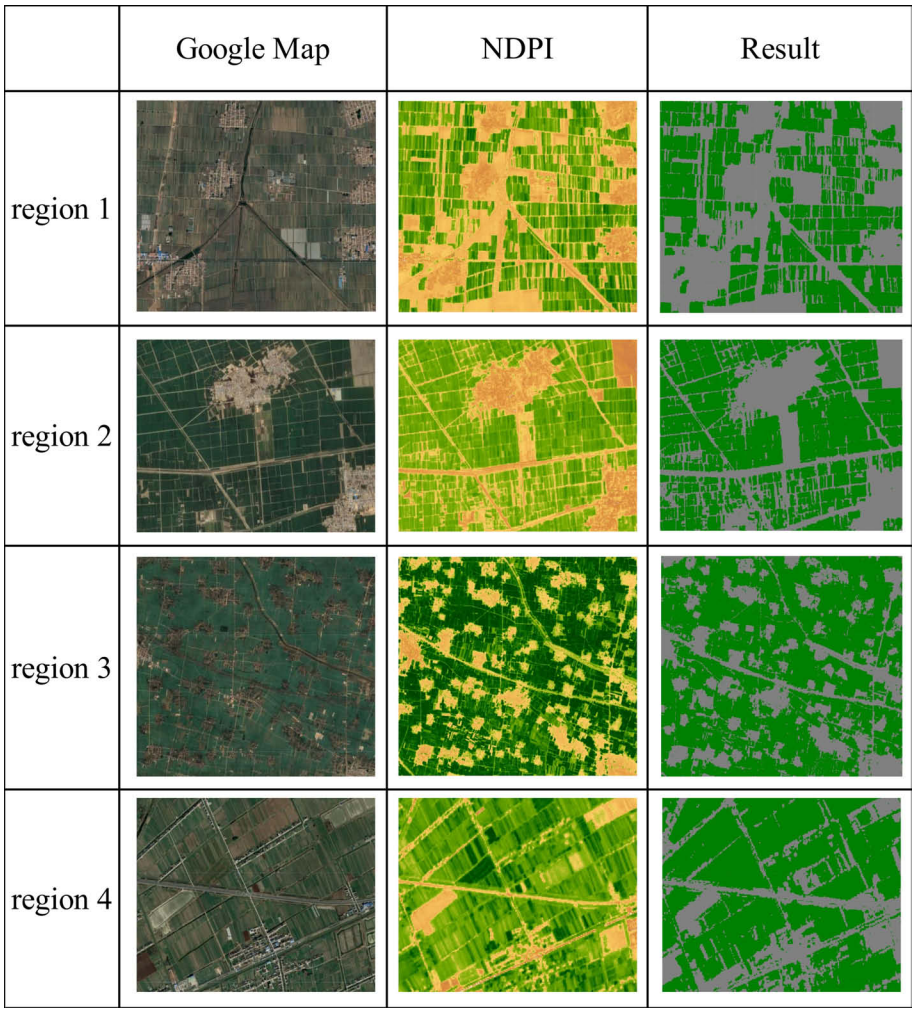

FIGURE 12
Validation of winter wheat identification results.

Region 2 contained many other objects, such as buildings, water bodies, bare land and woodland. The developed method could also accurately identify garlic and wheat without interference from the other objects. Region 3 was mainly a large garlic planting area, and the spatial continuity of the recognition results was good, almost without the interference of noise points, and some main roads between fields could be recognized. Region 4 mainly had an interlaced distribution of winter wheat and garlic, and many narrow parcels had high fragmentation. From the analysis, we found that the recognition effect for narrow fields was not ideal, but the overall recognition accuracy basically met the requirements.

5 Discussion

5.1 Comparison and analysis of vegetation indices

At present, the main approach to extract phenological information based on remote sensing technology is to construct time-series curves from vegetation indices, and vegetation indices are often used as the main discriminative feature for crop identification. Common vegetation indices include RVI, NDVI, and EVI (Huete et al., 2002; Ji and Peters, 2003). The main goal of was to achieve an early-season identification of winter wheat. Winter wheat grows slowly at the early stage of growth, and the leaf area is small and cannot cover the ground completely, resulting in a weak vegetation signal; meanwhile, the traditional vegetation index is affected by soil and snow cover (Dong et al., 2020). To verify the advantage of NDPI over other vegetation indices in enhancing the weak signal characteristics of vegetation in winter wheat at the early growth stage, this study used NDVI and EVI for a comparative analysis. NDVI and EVI are calculated as follows:

$$NDVI = \frac{\delta_{NIR} - \delta_{RED}}{\delta_{NIR} + \delta_{RED}}, \tag{13}$$

$$EVI = 2.5 \times \frac{\delta_{NIR} - \delta_{RED}}{\delta_{NIR} + 6 \times \delta_{RED} - 7.5 \times \delta_{BLUE} + 1}, \tag{14}$$

where δ_{NIR} is the NIR band reflectance, δ_{RED} is the red band reflectance, and $\delta_{BLUE}$is the blue band reflectance.

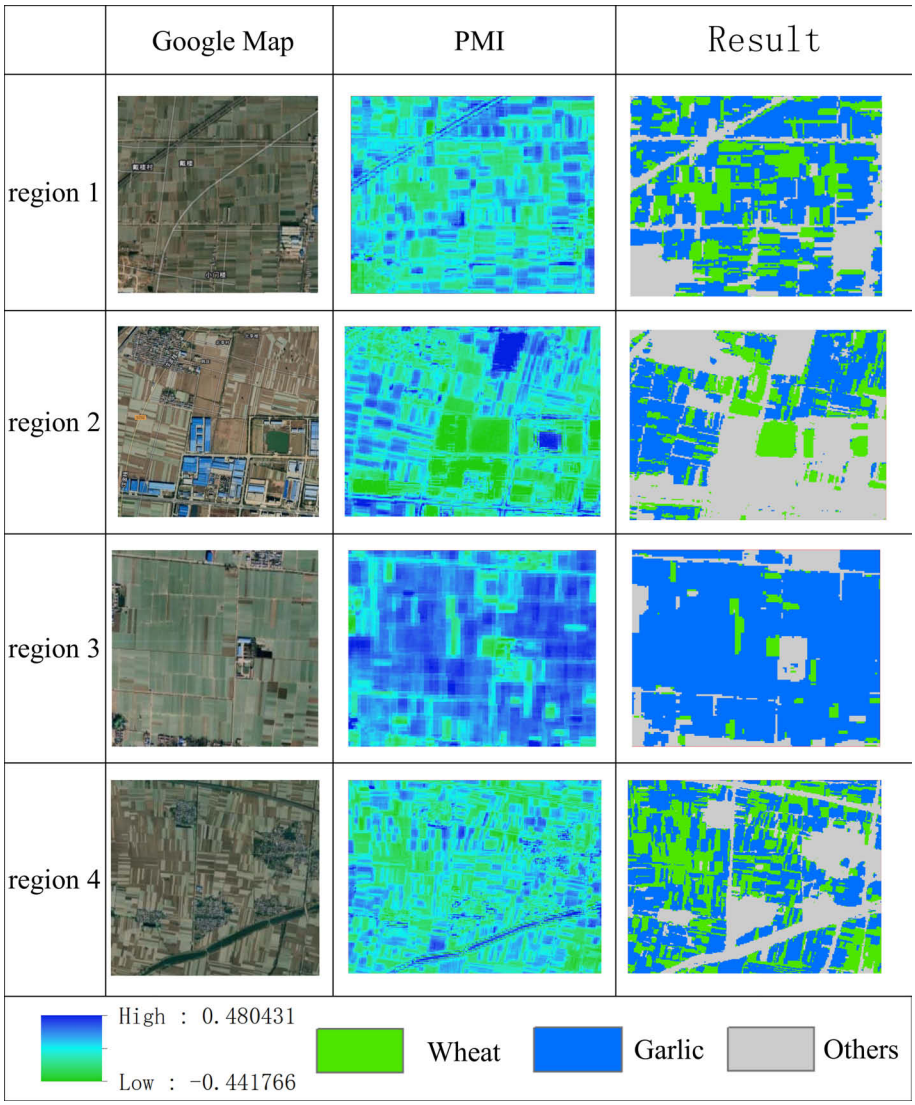

FIGURE 13
Validation of winter wheat and garlic identification results.

In the study area, 200 winter wheat sample points were selected. We constructed the phenological curves of NDPI, NDVI and EVI. The results are shown in Figure 14A that NDPI had a more sensitive response to vegetation changes in early winter wheat compared with the other vegetation indices. To quantitatively evaluate the change in the three vegetation indices, the quantitative evaluation index of Greenness Change Before Winter (GCBW) was defined in this study with the following equation 15.The results are shown in Figure 14B. The analysis showed that NDPI had the largest amount of variation, with a mean value of about 0.25. NDVI and EVI had a mean value of about 0.15, and the mean value of NDVI was slightly higher than that of EVI. The results of the quantitative analysis showed that NDPI index could more effectively reflect the changes in vegetation at the early stage of wheat growth compared with the other indices. This finding fully supports the selection of NDPI in this study. NDPI can effectively enhance the weak signal characteristics of winter wheat vegetation at the early stage of growth, and it has greater advantages in early mapping of winter wheat compared with NDVI and EVI.

$$GCBW = VI_{\max} - VI_{\min}, \tag{15}$$

where VI_{max} is the maximum value of the vegetation indices before the over-wintering period, and VI_{min} is the minimum value of the vegetation indices before the over-wintering period.

5.2 Transferability analysis

To more comprehensively evaluate the migration ability of the model in the study, we generalized the model in temporal and spatial dimensions to verify its effectiveness in early-season winter wheat refinement identification in other years and other regions. We extended the model to the early-season refinement identification of winter wheat in Shandong Province in 2020, and because the crop types in Shandong Province hardly change from year to year, we used the winter wheat samples in 2021 to verify the

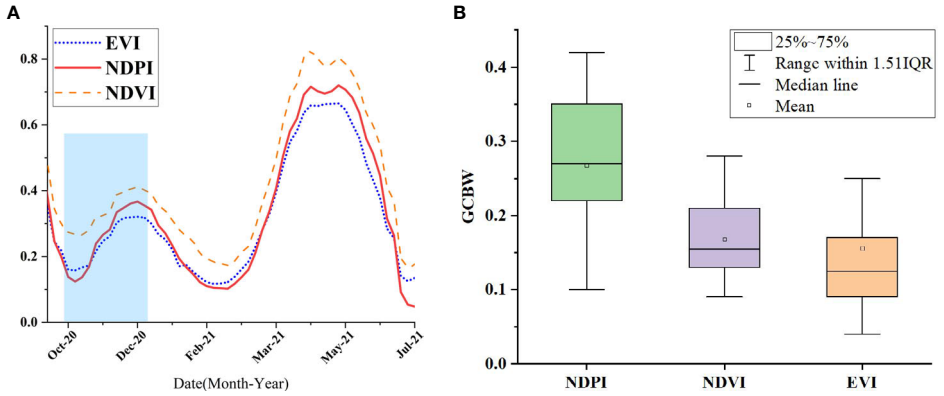

FIGURE 14
Comparison of vegetation indices for winter wheat. [**(A)** displays the Winter wheat phenology curve, **(B)** displays the Vegetation index GCBW statistical results].

accuracy. The results are shown in Figure 15. The results of the confusion matrix calculation were as follows. In the early over-wintering period the overall accuracy was 79.43%, the F1 score was 0.82, and the kappa coefficient was 0.76. The accuracy of identification in the regreening period was improved compared with that in the early over-wintering period. The overall accuracy was 87.31%, F1 score is 0.85, and Kappa coefficient is 0.80. The accuracy of early-season winter wheat identification in 2020 was slightly reduced compared with that in 2021. Specifically, the overall accuracy was reduced by about 2% on the average, the F1 score and kappa coefficient were reduced by 0.03 on the average, and the identification effect was basically unchanged. The slight decrease in accuracy may be due to the differences in winter wheat sowing dates between years and differences in winter wheat growth due to different temperatures and precipitation. Nevertheless, the model still exhibited a strong transfer ability between years.

To verify the ability to transfer geospatially, the model was applied to Henan Province, the largest winter wheat growing area in China, for the early-season refinement identification of winter wheat. Henan Province, located in the west of Shandong Province, has the largest winter wheat cultivation area and production in China. The climate is basically similar to that of Shandong Province, which has a warm temperate monsoon climate, and the province is mostly a plain area, which is highly favorable for the cultivation of winter wheat in large areas. And there are nearly have 800,004,000 ha of garlic planting area in Qixian and Zhongmou counties in Henan province. The planting structure of winter crops in Henan Province is basically the same as that of

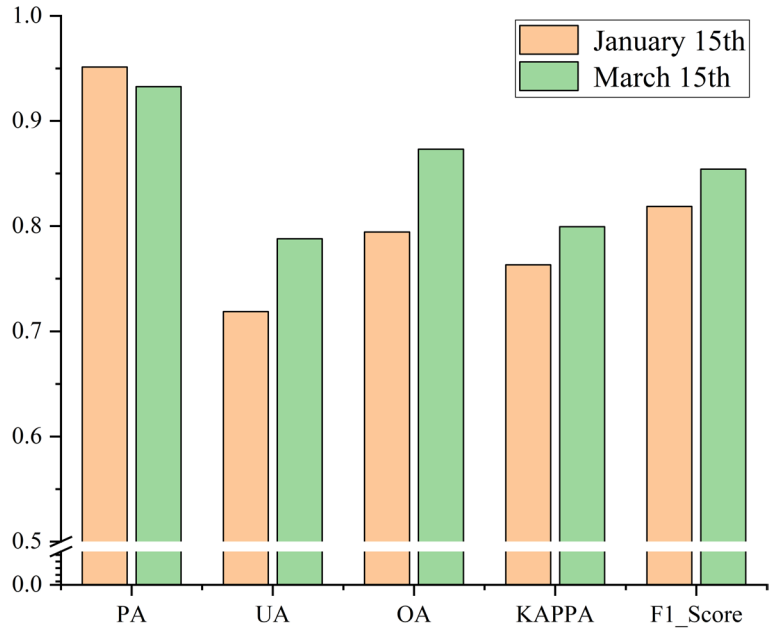

FIGURE 15
Evaluation results of the confusion matrix for early-season identification of winter wheat in 2020.

Shandong Province. The early-season mapping of winter wheat in the early over-wintering (January 15) and regreening (March 15) periods was completed using the developed method, and the identification results are shown in Figure 16. The analysis showed that the identification results of the two periods were basically the same, but the identification area of the regreening period was slightly higher than that of the early over-wintering period. Notably, winter wheat in Henan Province is mainly planted on the eastern plains, and the area planted in western hilly areas is relatively small.

Given that a sufficient amount of field sample point data in Henan Province could not be obtained, this study used only the official statistics released by Henan Province for accuracy verification. A consistency test between the early-season identification results of winter wheat and statistical data was conducted for 17 prefectural cities in Henan Province, and the results are shown in Figure 17. The early-season identification results of winter wheat in Henan Province in both periods showed high identification accuracy and were in good agreement with the official statistics; the R^2 of both reached 0.98. According to the official statistics, 6,102,030 ha were planted with winter wheat in Henan Province in 2021, and the identified winter wheat area in the study was 5,465,360 ha in the early over-wintering period and 5,901,362.8 ha in the regreening period, with an overall area accuracy of 89.6% and 96.3%, respectively. The recognition accuracy in the early over-wintering period in Henan Province was even better than that of Shandong Province possibly due to the wider plain area in Henan Province, better natural conditions for winter wheat cultivation, and higher degree of mechanized cultivation compared with Shandong Province. Thus, the developed method of this study has strong spatial generalization ability and can be applied to other regions for high-precision early-season winter wheat refinement recognition under automated methods.

5.3 Impact factors of classification results

The decision tree model constructed in the study based on *a priori* knowledge such as winter wheat phenology information, as a fully automated classification method, has a great advantage in early-season refinement recognition of winter wheat. It can complete the mapping of winter wheat spatial distribution 4-6 months before the winter wheat harvest period, and the method has a strong generalization ability. In this study, we showed through an experimental analysis that the present method can be extended to temporal and spatial dimensions, and can complete the refined mapping of winter wheat in historical years and other regions with high recognition accuracy. Compared with supervised classification methods (e.g., random forest and support vector machine), the developed method does not require the manual labeling of a large number of training samples (Dong et al., 2020; Zhang et al., 2021). Although the developed method is not limited by samples, the classification results are affected by the number of effective observations of images, spatial inconsistency of winter wheat phenology and other factors (Sun et al., 2012). Valid observation data on complete and intensive time series could not be obtained due to the influence of the revisit cycle and cloudy and rainy weather, so this study could not complete winter wheat mapping in the whole area of Shandong Province by using Sentinel-2 data. We plotted the number of effective observations in Shandong Province based on the time window of the phenological period for early-season mapping of winter wheat, as shown in Figure 18. The larger the number of effective observations, the more abundant the vegetation information on the early growth of winter wheat is and the better the mapping results are. However, as shown in Figure 18, the number of effective observations in some areas was fewer than three, reflecting little information on winter wheat, and this situation is not conducive to the identification of winter wheat. Therefore, supplementation with Landsat-8 data is necessary to increase the number of effective observations, that is, to increase the number of acquired cloud-free images.

In this study, the rules for building the decision tree were mainly based on phenological information at the early stage of winter wheat growth, and the precision of the phenological information determined the accuracy of the mapping. In Shandong Province, the eastern part is adjacent to the sea, the western part is a plain, and the central part is hilly and mountainous; thus, the phenological information is relatively complex. To verify the differences in winter wheat phenology at early growth stages, this study

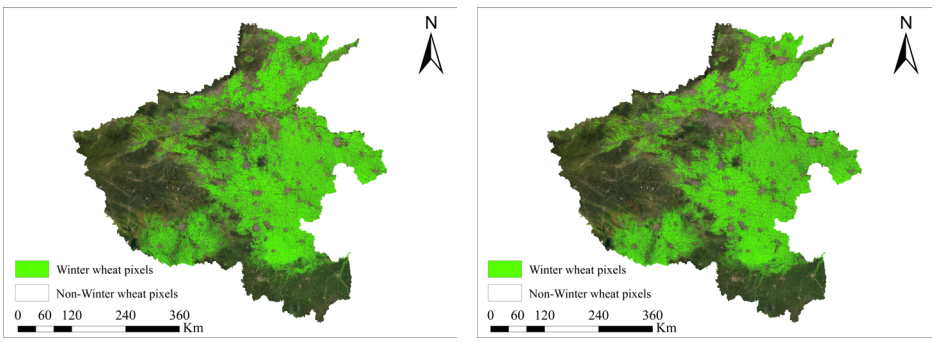

FIGURE 16
Spatial distribution of winter wheat in Henan Province.

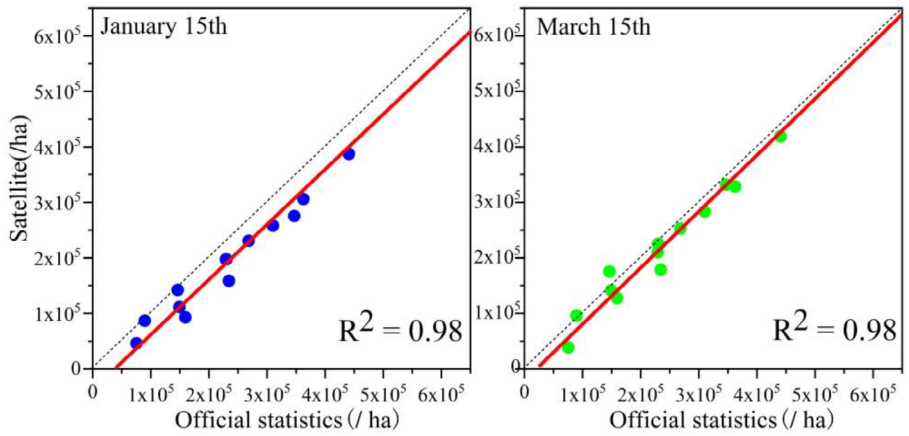

FIGURE 17
Verification of the consistency between winter wheat identification results and official statistics in Henan Province.

extensively collected winter wheat phenology information from all counties in the province. The results showed that the DOYmax corresponding to the maxima NDPI of winter wheat in the early over-wintering period ranged from 335 to 352, and the spatial distribution exhibited the patterns of being later in southern Shandong than in northern Shandong and being later in the inland than in the coast. The DOYmax corresponding to the regreening periods was between 45 and 65, and the spatial distribution of NDPI in the greening period was earlier in southern Shandong than in northern Shandong and earlier in the inland than in the coastal areas. The maximum difference in the phenology period in the different regions was about 20 days, and obvious spatial differences were observed, which made the effective extraction of winter wheat features difficult. To reduce the errors caused by inconsistent phenology, this study adopted the method of time window synthesis to extract the most obvious phenological features for enhancing the vegetation characteristics of the early growth stage of winter wheat. The decision tree algorithm built based on multiple rules in this study is affected by other factors, such as crop conditions, sowing dates, and natural conditions, but it has a good generalization ability. Delayed sowing and poor weather conditions, such as temperature and precipitation, can lead to poor crop growth when the NDPI increase in winter wheat is reduced. In addition, when cultivated land has poor soil fertility or insufficient sunlight, the growth of winter wheat can be reduced. In particular, winter wheat is grown at low latitudes under satisfactory natural conditions such as sufficient light, temperature, and precipitation, and winter wheat phenology may skip the over-wintering period and grow non-stop, during which the threshold needs to be adjusted.

5.4 Outlook

The proposed method has some advancements and advantages in early-season identification of winter wheat, but it also has some limitations that can be further improved in future research. First, only NDPI and its derived phenological feature indices were used in the study. This limitation can be further investigated in the future via multi-feature fusion or by developing other effective weak vegetation signal feature enhancement indices. Second, the decision tree algorithm used in the study requires manual setting of thresholds, which are based on the results of the phenology analysis and may change under varying external conditions (e.g., temperature, precipitation and anthropogenic factors). Hence, a dynamic adaptive threshold method could be developed to further

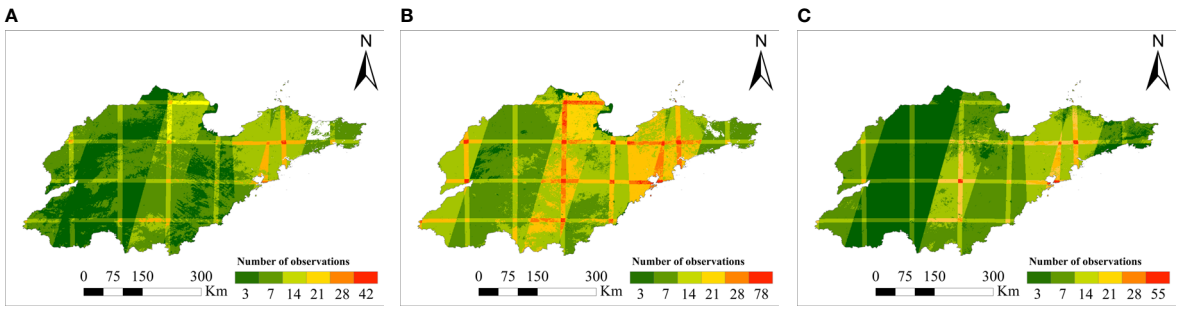

FIGURE 18
Availability of Sentinel-2 images. [**(A)** corresponds to the temporal window of the sowing period, **(B)** corresponds to the temporal window of the early over-wintering period, and **(C)** corresponds to the temporal window of the regreening period].

improve the automation and applicability of the model. Third the phenology of the study area presents some inconsistencies. When early-season identification of winter wheat in a large area is carried out, partitioning based on the phenological differences should be considered to ensure the consistency in all zones, which is conducive to achieving high-precision, automated, early-season identification in large areas. Fourth, with the in-depth application of deep learning technology in remote sensing, deep learning methods can now automatically extract the features of images and distinguish the importance of features autonomously. Therefore, we can conduct the early-season identification of winter wheat by using deep learning methods (Xu et al., 2021). At the same time, we can perform research on the early-season identification algorithm of winter wheat on a large scale by using domestic satellite images.

6 Conclusions

Using the GEE cloud platform and the Sentinel-2 and Landsat-8 remote sensing data provided by it, this paper investigates the theory and algorithm of early-season refinement mapping of winter wheat by analyzing the characteristics and phenological features of winter wheat of early growth stage. As an example, early-season refinement mapping of winter wheat with 10m resolution was completed in Shandong Province, and the earliest identification time was 4_6 months before the harvesting period. The main conclusions are as follows:

(1) In response to the weak remote sensing response of the vegetation signal in the early period of winter wheat growth, an enhanced index of the weak vegetation signal characteristics of winter wheat was developed. Two winter wheat phenological feature indices, namely, WPDI and NDPI, were developed to enhance winter wheat information, and applied to the early-season identification of winter wheat. The indices achieved good identification effects.

(2)The problem that winter wheat and garlic are difficult to be distinguished from each other due to the "different objects with the same spectra characteristics" phenomenon was solved. By analyzing the planting habits and quantitative spectral differences between winter wheat and garlic, this study developed a PMI index that can effectively achieve early-season identification of winter wheat and garlic. Ideal early mapping results on garlic were obtained for Shandong Province (especially in Jinxiang County).

(3). An automated algorithm for early refinement of winter wheat mapping was constructed based on winter wheat phenological information. The overall accuracy of the model was 82.64% and 88.76% in the early over-wintering and regreening periods, respectively. The identification results showed good agreement with the official municipal statistics, with the R^2 of the two being 0.96 and 0.98, respectively. We also performed temporal and geospatial transfer learning by using our algorithm and proved its effectiveness and strong generalization capability for large-scale early-season mapping of winter wheat.

Data availability statement

The original contributions presented in the study are included in the article/Supplementary Material. Further inquiries can be directed to the corresponding author.

Author contributions

XYL: conceptualization, investigation, methodology, writing - original draft, writing - review & editing. XHL, LG and JZ: resources, supervision, writing - review & editing. DQ and KW: resources, data curation. ZL: resources, formal analysis, writing - review & editing, supervision. All authors contributed to the article and approved the submitted version.

Funding

This study was supported by the National Key Technologies of Research and Development Program (No. 2021YFB3901303), the Key R&D plan of Shandong Province (Grant No. 2021LZGC026), and the National Natural Science Foundation of China Major Program (42192580, 42192584).

Acknowledgments

We would like to thank all the scientists and students who participated in the field observation and provided relevant information. We also want to thank the editors and reviewers for their valuable opinions on the paper.

Conflict of interest

Author DQ was employed by the company Roquette Management Shanghai Com. Ltd, Shanghai, China.

The remaining authors declare that the research was conducted in the absence of any commercial or financial relationships that could be construed as a potential conflict of interest.

Publisher's note

All claims expressed in this article are solely those of the authors and do not necessarily represent those of their affiliated organizations, or those of the publisher, the editors and the reviewers. Any product that may be evaluated in this article, or claim that may be made by its manufacturer, is not guaranteed or endorsed by the publisher.

Supplementary material

The Supplementary Material for this article can be found online at: https://www.frontiersin.org/articles/10.3389/fpls.2023.1016890/full#supplementary-material

References

Belgiu, M., and Csillik, O. (2018). Sentinel-2 cropland mapping using pixel-based and object-based time-weighted dynamic time warping analysis. *Remote Sens. Environ.* 204, 509–523. doi: 10.1016/j.rse.2017.10.005

Cai, Y., Guan, K., Peng, J., Wang, S., Seifert, C., Wardlow, B., et al. (2018). A high-performance and in-season classification system of field-level crop types using time-series landsat data and a machine learning approach. *Remote Sens. Environ.* 210, 35–47. doi: 10.1016/j.rse.2018.02.045

Chai, Z., Zhang, H., Xu, X., and Zhang, L. (2019). "Garlic mapping for sentinel-2 time-series data using a random forest classifier," in *IGARSS 2019-2019 IEEE International Geoscience and Remote Sensing Symposium*, Yokohama, Japan. 7224–7227. doi: 10.1109/IGARSS.2019.8900617

Chen, G., Liu, H., Zhang, J., Liu, P., and Dong, S. (2012). Factors affecting summer maize yield under climate change in Shandong province in the huanghuaihai region of China. *Int. J. Biometeorol.* 56 (4), 621–629. doi: 10.1007/s00484-011-0460-3

Dong, Q., Chen, X., Chen, J., Zhang, C., Liu, L., Cao, X., et al. (2020). Mapping winter wheat in north China using sentinel 2A/B data: a method based on phenology-time weighted dynamic time warping. *Remote Sens.* 12 (8), 1274. doi: 10.3390/rs12081274

Dong, J., Fu, Y., Wang, J., Tian, H., Fu, S., Niu, Z., et al. (2020). Early-season mapping of winter wheat in China based on landsat and sentinel images. *Earth Syst. Sci. Data* 12 (4), 3081–3095. doi: 10.5194/essd-12-3081-2020

Dong, J., Xiao, X., Menarguez, M. A., Zhang, G., Qin, Y., Thau, D., et al. (2016). Mapping paddy rice planting area in northeastern Asia with landsat 8 images, phenology-based algorithm and Google earth engine. *Remote Sens. Environ.* 185, 142–154. doi: 10.1016/j.rse.2016.02.016

Fisette, T., Davidson, A., Daneshfar, B., Rollin, P., Aly, Z., and Campbell, L. (2014). "Annual space-based crop inventory for Canada: 2009–2014," in *2014 IEEE Geoscience and Remote Sensing Symposium*, Quebec City, QC, Canada. 5095–5098. doi: 10.1109/IGARSS.2014.6947643

Friedl, M. A., and Brodley, C. E. (1997). Decision tree classification of land cover from remotely sensed data. *Remote Sens. Environ.* 61 (3), 399–409. doi: 10.1016/S0034-4257(97)00049-7

Griffiths, P., Nendel, C., and Hostert, P. (2019). Intra-annual reflectance composites from sentinel-2 and landsat for national-scale crop and land cover mapping. *Remote Sens. Environ.* 220, 135–151. doi: 10.1016/j.rse.2018.10.031

Gumma, M. K., Thenkabail, P. S., Teluguntla, P. G., Oliphant, A., Xiong, J., Giri, C., et al. (2020). Agricultural cropland extent and areas of south Asia derived using landsat satellite 30-m time-series big-data using random forest machine learning algorithms on the Google earth engine cloud. *GIScience Remote Sens.* 57 (3), 302–322. doi: 10.1080/15481603.2019.1690780

Hao, P., Zhan, Y., Wang, L., Niu, Z., and Shakir, M. (2015). Feature selection of time series MODIS data for early crop classification using random forest: a case study in Kansas, USA. *Remote Sens.* 7 (5), 5347–5369. doi: 10.3390/rs70505347

Huete, A., Didan, K., Miura, T., Rodriguez, E. P., Gao, X., and Ferreira, L. G. (2002). Overview of the radiometric and biophysical performance of the MODIS vegetation indices. *Remote Sens. Environ.* 83 (1-2), 195–213. doi: 10.1016/S0034-4257(02)00096-2

Ji, L., and Peters, A. J. (2003). Assessing vegetation response to drought in the northern great plains using vegetation and drought indices. *Remote Sens. Environ.* 87 (1), 85–98. doi: 10.1016/S0034-4257(03)00174-3

Jin, Z., Azzari, G., You, C., Di Tommaso, S., Aston, S., Burke, M., et al. (2019). Smallholder maize area and yield mapping at national scales with Google earth engine. *Remote Sens. Environ.* 228, 115–128. doi: 10.1016/j.rse.2019.04.016

Johnson, D. M., and Mueller, R. (2021). Pre-and within-season crop type classification trained with archival land cover information. *Remote Sens. Environ.* 264, 112576. doi: 10.1016/j.rse.2021.112576

Kussul, N., Mykola, L., Shelestov, A., and Skakun, S. (2018). Crop inventory at regional scale in Ukraine: developing in season and end of season crop maps with multi-temporal optical and SAR satellite imagery. *Eur. J. Remote Sens.* 51 (1), 627–636. doi: 10.1080/22797254.2018.1454265

Lewis, H. G., and Brown, M. (2001). A generalized confusion matrix for assessing area estimates from remotely sensed data. *Int. J. Remote Sens.* 22 (16), 3223–3235. doi: 10.1080/01431160152558332

Li, Y., Sun, Z., Accatino, F., Hang, S., Lv, Y., and Ouyang, Z. (2021). Comparing specialised crop and integrated crop-livestock systems in China with a multi-criteria approach using the emergy method. *J. Clean. Prod.* 314, 127974. doi: 10.1016/j.jclepro.2021.127974

Liu, J., Kuang, W., Zhang, Z., Xu, X., Qin, Y., Ning, J., et al. (2014). Spatiotemporal characteristics, patterns, and causes of land-use changes in China since the late 1980s. *J. Geogr. Sci.* 24 (2), 195–210. doi: 10.1007/s11442-014-1082-6

Nasrallah, A., Baghdadi, N., Mhawej, M., Faour, G., Darwish, T., Belhouchette, H., et al. (2018). A novel approach for mapping wheat areas using high resolution sentinel-2 images. *Sensors* 18 (7), 2089. doi: 10.3390/s18072089

Pan, Z., Huang, J., Zhou, Q., Wang, L., Cheng, Y., Zhang, H., et al. (2015). Mapping crop phenology using NDVI time-series derived from HJ-1 A/B data. *Int. J. Appl. Earth Obs. Geoinf.* 34, 188–197. doi: 10.1016/j.jag.2014.08.011

Pan, Y., Li, L., Zhang, J., Liang, S., Zhu, X., and Sulla-Menashe, D. (2012). Winter wheat area estimation from MODIS-EVI time series data using the crop proportion phenology index. *Remote Sens. Environ.* 119, 232–242. doi: 10.1016/j.rse.2011.10.011

Phalke, A. R., Özdoğan, M., Thenkabail, P. S., Erickson, T., Gorelick, N., Yadav, K., et al. (2020). Mapping croplands of Europe, middle east, russia, and central asia using landsat, random forest, and google earth engine. *ISPRS J. Photogramm. Remote Sens.* 167, 104–122. doi: 10.1016/j.isprsjprs.2020.06.022

Qiu, B., Luo, Y., Tang, Z., Chen, C., Lu, D., Huang, H., et al. (2017). Winter wheat mapping combining variations before and after estimated heading dates. *ISPRS J. Photogramm. Remote Sens.* 123, 35–46. doi: 10.1016/j.isprsjprs.2016.09.016

Qiu, T., Song, C., and Li, J. (2020). Deriving annual double-season cropland phenology using landsat imagery. *Remote Sens.* 12 (20), 3275. doi: 10.3390/rs12203275

Sakamoto, T., Gitelson, A. A., and Arkebauer, T. J. (2014). Near real-time prediction of US corn yields based on time-series MODIS data. *Remote Sens. Environ.* 147, 219–231. doi: 10.1016/j.rse.2014.03.008

Savitzky, A., and Golay, M. J. (1964). Smoothing and differentiation of data by simplified least squares procedures. *Anal. Chem.* 36 (8), 1627–1639. doi: 10.1021/ac60214a047

Song, X. P., Hansen, M. C., Stehman, S. V., Potapov, P. V., Tyukavina, A., Vermote, E. F., et al. (2018). Global land change from 1982 to 2016. *Nature* 560 (7720), 639–643. doi: 10.1038/s41586-018-0411-9

Song, X. P., Huang, W., Hansen, M. C., and Potapov, P. (2021). An evaluation of landsat, sentinel-2, sentinel-1 and MODIS data for crop type mapping. *Sci. Remote Sens.* 3, 100018. doi: 10.1016/j.srs.2021.100018

Sun, H., Xu, A., Lin, H., Zhang, L., and Mei, Y. (2012). Winter wheat mapping using temporal signatures of MODIS vegetation index data. *Int. J. Remote Sens.* 33 (16), 5026–5042. doi: 10.1080/01431161.2012.657366

Tian, H. (2019). *Study on mapping for winter wheat distribution in China based on sentinel-1&2 images* (Beijing, China: Institute of Remote Sensing and Digital Earth, Chinese Academy of Sciences).

Tian, H., Huang, N., Niu, Z., Qin, Y., Pei, J., and Wang, J. (2019). Mapping winter crops in China with multi-source satellite imagery and phenology-based algorithm. *Remote Sens.* 11 (7), 820. doi: 10.3390/rs11070820

Valero, S., Arnaud, L., Planells, M., and Ceschia, E. (2021). Synergy of sentinel-1 and sentinel-2 imagery for early seasonal agricultural crop mapping. *Remote Sens.* 13 (23), 4891. doi: 10.3390/rs13234891

Waleed, M., Mubeen, M., Ahmad, A., Habib-ur-Rahman, M., Amin, A., Farid, H. U., et al. (2022). Evaluating the efficiency of coarser to finer resolution multispectral satellites in mapping paddy rice fields using GEE implementation. *Sci. Rep.* 12 (1), 1–5. doi: 10.1038/s41598-022-17454-y

Wang, C., Chen, J., Wu, J., Tang, Y., Shi, P., Black, T. A., et al. (2017). A snow-free vegetation index for improved monitoring of vegetation spring green-up date in deciduous ecosystems. *Remote Sens. Environ.* 196, 1–2. doi: 10.1016/j.rse.2017.04.031

Xu, F., Guo, B., Ye, B., Ye, Q., Chen, H., Ju, X., et al. (2019). Systematical evaluation of GPM IMERG and TRMM 3B42V7 precipitation products in the Huang-Huai-Hai plain, China. *Remote Sens.* 11 (6), 697. doi: 10.3390/rs11060697

Xu, J., Yang, J., Xiong, X., Li, H., Huang, J., Ting, K. C., et al. (2021). Towards interpreting multi-temporal deep learning models in crop mapping. *Remote Sens. Environ.* 264, 112599. doi: 10.1016/j.rse.2021.112599

You, N., and Dong, J. (2020). Examining earliest identifiable timing of crops using all available sentinel 1/2 imagery and Google earth engine. *ISPRS J. Photogramm. Remote Sens.* 161, 109–123. doi: 10.1016/j.isprsjprs.2020.01.001

Zhang, P. (2008). Revitalizing old industrial base of northeast China: process, policy and challenge. *Chin. Geogr. Sci.* 18 (2), 109–118. doi: 10.1007/s11769-008-0109-2

Zhang, C., Di, L., Lin, L., and Guo, L. (2019). Machine-learned prediction of annual crop planting in the US corn belt based on historical crop planting maps. *Comput. Electron. Agric.* 166, 104989. doi: 10.1016/j.compag.2019.104989

Zhang, H., Du, H., Zhang, C., and Zhang, L. (2021). An automated early-season method to map winter wheat using time-series sentinel-2 data: a case study of Shandong, China. *Comput. Electron. Agric.* 182, 105962. doi: 10.1016/j.compag.2020.105962

Frontiers in Plant Science

Cultivates the science of plant biology and its applications

The most cited plant science journal, which advances our understanding of plant biology for sustainable food security, functional ecosystems and human health.

Discover the latest Research Topics

See more →

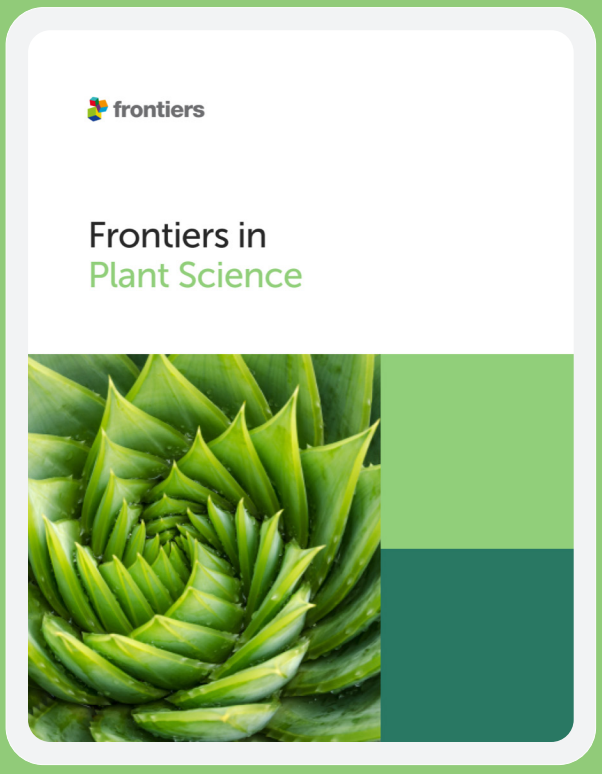

Frontiers

Avenue du Tribunal-Fédéral 34
1005 Lausanne, Switzerland
frontiersin.org

Contact us

+41 (0)21 510 17 00
frontiersin.org/about/contact